



# FLOMEKO2019

18<sup>th</sup> International Flow Measurement Conference

Portugal | Lisbon | LNEC | 26-28 june 2019

PROCEEDINGS



Instituto Português da  Qualidade



LABORATÓRIO NACIONAL  
DE ENGENHARIA CIVIL





inotech Meter Calibration Systems GmbH



**UBERTONE**

**REN** 



 **JANZ**



## TABLE OF CONTENTS

Michael Reader-Harris – IMEKO TC9 .....	1
Álvaro Ribeiro – FLOMEKO2019 .....	2
KEYNOTE SPEAKERS	
Erik Smits .....	3
José Pedro Salema .....	4
Vania Silverio .....	5
Technical Exhibition plan .....	6
SPONSORS .....	7
Overall schedule .....	13
Congress Center plan .....	14
CONFERENCE PROGRAMME .....	15
Themes .....	18
PROCEEDINGS .....	19





## Michael Reader-Harris – IMEKO TC9



Dear all,

Welcome to FLOMEKO. The first IMEKO Conference on Flow Measurement - FLOMEKO - took place in 1978 in the Netherlands. The 11th, from 12 to 14 May 2003 returned to the same place, Groningen, 25 years later. But FLOMEKO is very international, conferences have also taken place in Africa (South Africa), America (Brazil), Asia (China, Japan, Korea, Taiwan), Australia, and Europe (France, Germany, Hungary, Sweden, UK). This is the 18th FLOMEKO.

FLOMEKO covers not only the measurement of the quantity of flowing fluids, but also calibrations and calibration facilities, traceability and quality control, uncertainty, instrumentation, numerical simulation, flow visualisation, flow conditioning, practical experience with existing measuring methods, specific metering principles, wet-gas and multiphase flow measurement and other topics.

FLOMEKO provides a wonderful opportunity to meet fellow flow metrologists.

It is particularly delightful to come to Portugal, to enjoy its history, warmth and welcome. I hope that many of you will take the opportunity to explore Lisbon, to go a little further afield, to Sintra, for example, and maybe to travel to the Algarve or to the Douro Valley.

Best wishes,

Michael

Dr Michael Reader-Harris,

Chairman IMEKO TC9



## Álvaro Ribeiro – FLOMEKO2019



Dear Colleagues,

FLOMEKO is an event of IMEKO TC9 very special for many people around the world who, since 1978, have found in this community a space for sharing, dialogue and development of applied knowledge in industry, research, teaching and resource management.

For the entities that organize this event for the first time in Portugal, it is an honor but also a challenge, to try to establish bridges between stakeholders, to involve different areas of interest, to join partners and to promote synergies for the future. A grateful message should be addressed to the sponsors and entities that have supported this initiative, to the committees, speakers and participants who make it a success and the team that make it happen.

We hope that, as in previous events, FLOMEKO 2019 will be a major contribution to the innovation and creativity that promote scientific and technological development in this context of flow, helping to consolidate key foundations for the organizations and companies that apply this knowledge in the day-to-day activities impacting on technological, political, social, economic and environmental domains.

In the social context Lisbon is a welcoming city, with immense light, friendliness and diversified cultural and social opportunities, so we hope that you can enjoy what Portugal has to offer you and that you have lasting memories and a desire to return.

Welcome to the FLOMEKO2019 experience and Welcome to Lisboa!

Álvaro Ribeiro

Chairperson of FLOMEKO2019

## Erik Smits



For over 26 years Erik Smits has travelled around the world to work on metering systems and flow meter calibration facilities of customers of VSL. Erik started his career at NMI-VSL in the hydrocarbon and water flow meter calibration facilities next to the liquid volume laboratory as a calibration and verification engineer. Many of the flow meters he calibrated needed a second stage verification in their metering system on location of operation. Through the years Erik developed his skills as a metrologist being responsible for the Dutch National Reference Standards for liquid flow and volume.

Erik was the project manager for modernizing the hydrocarbon facilities and the construction of the water flow calibration facility of VSL. VSL's water flow calibration facility has one of the lowest measurement uncertainties in the world. His experience in this type of work gives him the basis to take up new challenges around the world and to advise operators and manufacturers of flow meters and calibration facilities. Traceability to the SI through VSL has been provided around the world for all kinds of instruments including pipe provers. Erik started the program "VSL CMC Certified" to review calibration facilities for measurement uncertainties.

After 24 years Erik was asked to step up and be one of the managers for the Calibration and Reference Materials department at VSL. From June 1st, 2019 he has been the Manager of Flow Metrology leading a team of about 15 flow scientists and metrologists. Erik is a member of Euramet TC-Flow, Working Group for Fluid Flow of BIPM, EuReGa and Convenor for ISO/TC 28/WG 20 working on a standard for LNG flow measurement. Erik also provides technical expertise to several accrediting bodies during audits of companies that are accredited, or are seeking accreditation, according to ISO/IEC17025.

Keynote:

How do we provide and maintain flow measurement traceability for the fluids of the future?



## José Pedro Salema



José Pedro Salema is the Chief Executive Officer of EDIA – the public company that manages the Alqueva project – since 2013. Before this he was the co-founder and managing partner of AGROGESTÃO - a consultancy firm focused on farm management software tools and training services.

He is a certified trainer with extensive experience in lecturing at college level. He has an Agronomic Engineering degree from Lisbon's University, a Master's degree in Management and a MBA in E-Business from the Portuguese Catholic University.

Keynote:

Water flow measurement in the Alqueva multipurpose project

## Vania Silverio



Vania Silverio is currently involved in scientifically innovative and challenging R&D projects combining nanotechnology with simulation tools for the design, fabrication, integration and test of microfluidic devices and sensors (INESC-MN, [www.inesc-mn.pt](http://www.inesc-mn.pt)). Additionally, she is engaged on the definition of ISO Standards and Processes for Microfluidics [CEN/TC-332/WG7; ISO/TC48/WG3].

She is author of more than 35 research publications in the areas of fluid dynamics at the microscale and microfluidics device fabrication. She combines her research with advanced training, teaching and theses supervision at the Master and PhD level at Instituto Superior Técnico, ULisboa (<http://tecnico.ulisboa.pt>), where she is an Invited Assistant Professor (Microfluidics course; Micro and Nanofabrication Techniques course).

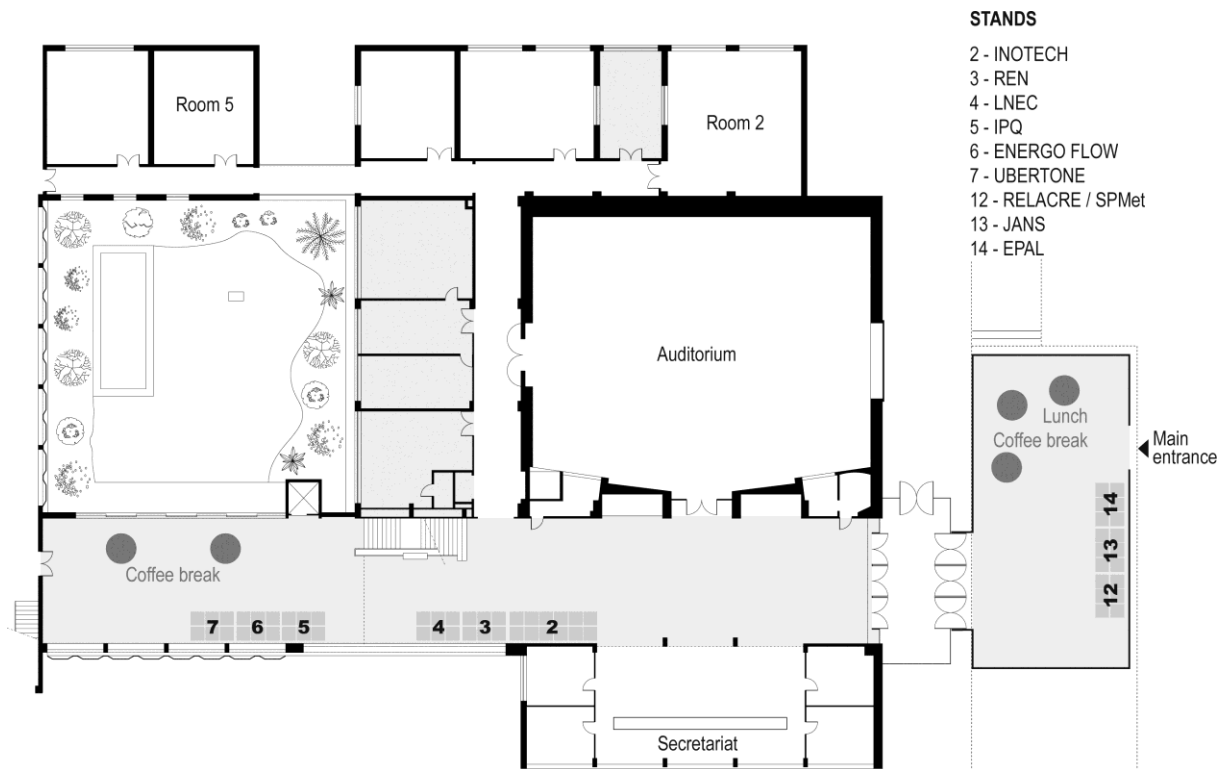
Silverio is regular Peer Reviewer of several Scientific Journals and is currently involved in the organization of 3 International Meetings on Micro and Nanotechnology. She is member of the International Microfluidics Association, of the IEEE Society USA, of the Portuguese Physical Society and of the European Physical Society. She holds a PhD degree in Mechanical Engineering (Tecnico, ULisboa) and a Licenciatura degree in Technological Chemistry (5 years, FCUL, ULisboa).

Keynote:

Microfluidics: the science and technology for miniaturized laboratories on-chip



## TECHNICAL EXHIBITION PLAN





## SPONSORS



Welcome at inotech – Perfection in precision ...

26 years of inotech – 26 years of continuous development in innovative energy supply products

In the last, now almost 27 years the inotech Meter Calibration Systems GmbH has evolved into a leading manufacturer of test equipment for gas meters, testing facilities and calibration facilities and has a reputation as an expert and reliable partner for meter manufacturers and independent test centers throughout the entire world. In the last few years we have also established ourselves in the field of water meter and heat meter test equipment and this has also effectively extended our product portfolio. Millions of different types of meters are calibrated with our test equipment every year.

Test equipment is our core business. Every day we combine our know-how with our customers demands to improve our products constantly. Our customer requirements in the focus of all our product developments and production and are always state of the art development.

The current inotech developments are focused on the new PS 8 software generation that transfers the test equipment of single systems into a network of testing systems. Consequently, the PS 8 version is particularly interesting for all test centers with multiple testing units. Of course, considerable attention is paid to the world of smart meters and the testability of these new meters is given priority.

Come and talk to us and we will be happy to introduce you to the new generation of developments.

As our company is owner-led, we have flat hierarchies and rapid decision-making processes and we can respond flexibly to the demands of the market. This flexibility is our strength and makes us a reliable partner for our customers. Due to the changing meter market towards the Smart Meter, the continuous further development and adaptation in close coordination with our customers is a basic precondition for successful products. These are the challenges we set ourselves and we constantly work towards being even better.



Energoflow AG operates to meet the requirements of a constantly evolving industry and always seeks the best ways to incorporate its state-of-the-art, competitive products and services on-line as well as implements advanced innovative solutions to accomplish the goals and provide excellent performance on a global basis.

We strive to provide state-of-the-art, cost effective turnkey technical solutions to our valued clients throughout the globe for gas and liquid measurement and monitoring and in related fields across a wide range of industries and applications. Our gas meters and flow meters are reliable, accurate and capable of functioning as satisfactorily in the harshest process and ambient conditions.

And we use the principle of the 3 E's for achieving this: Experience, Expertise & Efficiency !



# UBERTONE

UBERTONE is specialized in the design and manufacturing of high resolution velocity and acoustic turbidity profilers for scientific applications and OEM acoustic based instruments for industries. Ubertone's devices allow to measure instantaneous velocity profiles, as well as echo amplitude and acoustic turbidity profiles. The company provides two families of products: one component velocity profilers (known as UVP) and two components velocity profilers (known as ADVP). Ubertone offers solutions for various applications such as detailed flow visualization, turbulence and sediment transport studies, opaque liquids characterization, with instruments that can be used in open channel flows (sewage networks, wastewater treatment plants, physical models, small rivers...) as well as in closed-conduit flows (pipes, experimental setups...).

Read more: <http://ubertone.com/>

Come visit our stand!



The Laboratory of Metrology of REN Gasodutos, is composed of a Fixed Laboratory (located in Pombal) and a Mobile Unit. Since 2015, its activity has been accredited in accordance with NP EN ISO / IEC 17025, and is mainly focused on the calibration of the gas metering and instrumentation systems that make up the National Natural Gas System (SNGN)

The services provided by the Metrology Laboratory and its capabilities are:

- Calibration of Gas Volumetric Counters (Turbines, Rotary Pistons) with air at atmospheric pressure, for flows between 10 - 2500 m<sup>3</sup>/h;
- Calibration of Gas Volume Conversion Electronic Devices;
- Calibration of pressure measuring elements for pressures between 0 and 200 bar;
- Calibration of temperature measuring elements between -20 °C and 100 °C;

The Metrology Laboratory of REN Gasodutos has the most advanced technical means and a highly specialized and experienced team, thus enabling us to present ourselves as a national reference in the natural gas sector.



EPAL is a reference company in the water sector, nationally and internationally, that for more than 150 years produces, transports and distributes water for consumption.

The supply system of EPAL serves more than 2.9 million inhabitants, is developed between the bay of Castelo do Bode and the city of Lisbon, along more than 2000 km. It replenishes a set of management entities on the north bank of the river Tagus and in Lisbon is responsible for the home supply to more than 350 thousand direct customers.

To guarantee the production and distribution of water with quality and in quantity, it has Water Treatment Stations and accredited Laboratories equipped with the highest technology.

Because innovation is a company's goal, over time there are several services and products related to the water cycle and the efficiency of the systems that the company has been developing and marketing.

Since 2015, within the scope of the restructuring of the water sector, EPAL has been delegated management of the multi-municipal system Águas do Vale do Tejo, whose activity includes water supply and wastewater sanitation services to the municipalities of Beiras and Alentejo.

EPAL and Águas do Vale do Tejo cover 33% of the national territory, serve 87 municipalities and 3.5 million inhabitants.



In business for more than 100 years, our company is recognized by a profound knowledge in mechanical water meters production.

Janz has a leading role in the water measurement sector worldwide being state-of-the-art in industry developments and meeting demanding production standard.

We offer all the necessary certifications that enable us to offer a wide range of solutions and, above all, to satisfy and exceed our customers expectations.

For more information, please visit our website: [www.janz.pt](http://www.janz.pt)

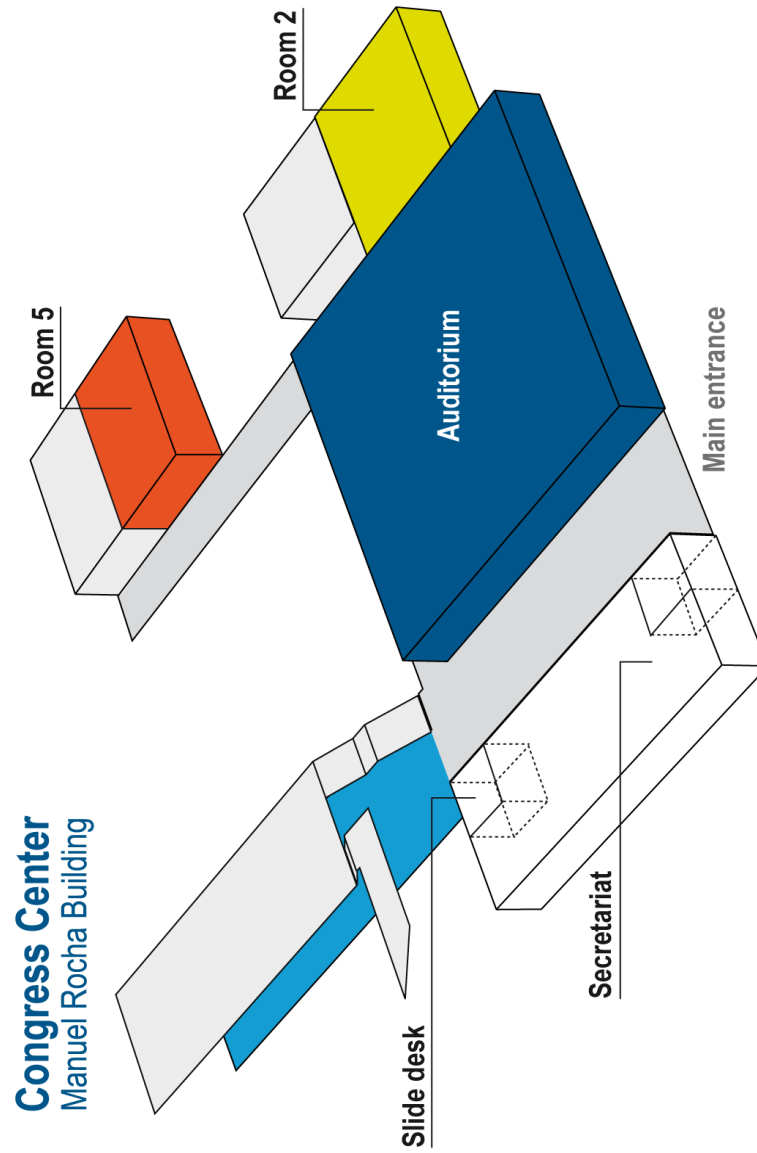


## OVERALL SCHEDULE

Date & Time/Planned Activity	Location
<b>Monday – 24 June 2019</b>	
9:00 – 16:00	WGFF meeting
17:00 – 18:00	Welcome Reception at the City Hall
<b>Tuesday – 25 June 2019</b>	
9:00 – 16:00	WGFF meeting
18:00 – 19:00	Get Together
19:00 – 20:00	Registration
<b>Wednesday – 26 June 2019</b>	
8:00 – 9:00	Registration
9:00 – 11:00	Opening Ceremony+Keynote speaker – Erik Smits
11:00 – 11:30	networking@coffee
11:30 – 13:00	Conference Sessions & Presentations
13:00 – 14:00	networking@lunch
14:00 – 15:30	Conference Sessions & Presentations
15:30 – 16:00	networking@coffee
16:00 – 17:30	Conference Sessions & Presentations
<b>Thursday – 27 June 2019</b>	
9:00 – 10:00	Keynote speaker – José Pedro Salema
	Group photo (Main Entrance)
10:00 – 11:00	Poster Session
11:00 – 11:30	networking@coffee
11:30 – 13:00	Conference Sessions & Presentations
13:15 – 13:45	IMEKO TC9 members meeting
13:00 – 14:00	networking@lunch
14:00 – 15:30	Conference Sessions & Presentations
16:00 – 19:00	<i>"Discover Lisboa with us"</i>
19:30 – 23:00	Conference Gala Dinner
<b>Friday – 28 June 2019</b>	
9:00 – 10:00	Keynote speaker – Vania Silverio
10:00 – 11:00	Conference Sessions & Presentations
11:00 – 11:30	networking@coffee
11:30 – 13:00	Conference Sessions & Presentations
13:00 – 14:00	networking@lunch
14:00 – 15:00	Poster Session
15:00 – 15:30	networking@coffee
15:30 – 17:00	Conference Sessions & Presentations
17:00 – 17:30	Closing ceremony



## CONGRESS CENTER PLAN





## CONFERENCE PROGRAMME

Time	Tuesday 25 June		
18:00 – 20:00	Get-Together Party		
19:00 – 20:00	<b>REGISTRATION</b>		
Time	Wednesday 26 June		
08:00 – 09:30	<b>REGISTRATION</b>		
09:30 – 10:00	<b>OPENING CEREMONY</b>		
10:00 – 11:00	<b>PLENARY SESSION</b> KEYNOTE SPEAKER – ERIK SMITS		
11:00 – 11:30	networking@coffee		
11:30 – 13:00	<b>AUDITORIUM</b> S1.1 Liquid Flow Standards	<b>ROOM 5</b> S2.9 Coriolis Meter Technology	<b>ROOM 2</b> S3.12 CFD and Simulation
13:00 – 14:00	networking@lunch		
14:00 – 15:30	<b>AUDITORIUM</b> S4.1 Gas Flow	<b>ROOM 5</b> S5.5 Flow Standards	<b>ROOM 2</b> S6.8 Uncertainty Determination
15:30 – 16:00	networking@coffee		
16:00 – 17:30	<b>AUDITORIUM</b> S7.10 Microflow	<b>ROOM 5</b> S8.9 Flow Metering Technology	<b>ROOM 2</b> S9.6 Critical Flow Venturi Nozzels



Time	Thursday 27 June		
9:00 – 10:00	PLENARY SESSION KEYNOTE SPEAKER – JOSÉ PEDRO SALEMA		
10:00 – 11:00	POSTER SESSION 1		
11:00 – 11:30	networking@coffee		
11:30 – 13:00	AUDITORIUM S10.5 Flow Standards	ROOM 5 S11.1 Wet Gas	ROOM 2 S12.2 Air Speed
13:00 – 14:00	networking@lunch		
14:00 - 15:30	AUDITORIUM S13.5 Flow Standards	ROOM 5 S14.1 Multiphase Flow	ROOM 2 S15.9 Flow Metering Technology
16:00 – 19:00	"DISCOVER LISBOA WITH US"		
19:30 – 23:00	CONFERENCE GALA DINNER		



Time	Friday 28 June		
9:00 – 10:00	<b>PLENARY SESSION</b> KEYNOTE SPEAKER – VANIA SILVERIO		
10:00 – 11:00	<b>AUDITORIUM</b> S16.1 Uncertainty and Traceability	<b>ROOM 5</b> S17.5 Flow Performance Studies	<b>ROOM 2</b> S18.7/8 Legal Metrology
11:00 – 11:30	networking@coffee		
11:30 – 13:10	<b>AUDITORIUM</b> S19.9 Flow Metering Technology	<b>ROOM 5</b> S20.8 Intercomparisons	<b>ROOM 2</b> S21.10/11 Microflow
13:10 – 14:00	networking@lunch		
14:00 – 15:00	POSTER SESSION 2		
15:00 – 15:30	networking@coffee		
15:30 – 17:10	<b>AUDITORIUM</b> S22.1/12 Liquid Flow	<b>ROOM 5</b> S23.5 Gas Standards	<b>ROOM 2</b> S24.2 Natural Gas
17:10 – 17:30	<b>CLOSING CEREMONY</b>		



## THEMES

- 1 - Liquid, gas & multi-phase flows
- 2 - Air speed, volume
- 3 - Fluid properties
- 4 - Hydrocarbon flows, e.g.: LNG, CNG and so forth
- 5 - Primary standards, new calibration and inter-comparison facilities
- 6 - Critical Flow Venturi Nozzles
- 7 - Legal Metrology in Flow Measurement
- 8 - Analysis and assessment of uncertainties
- 9 - Development and performance of flow metering technology
- 10 - Micro-flow technology
- 11 - New applications in healthcare, saving energy and protecting the environment
- 12 - Computer-modelling applications



# FLOMEKO2019

PROCEEDINGS



# Design of a Calibration System for Miniature Carbon Dioxide Sensors

Mengna Li<sup>1</sup>, Heming Hu<sup>1</sup>, Jing Zhang<sup>1</sup>

*1Division of Thermophysics and Process Measurements, National Institute of Metrology, No. 18 Bei San Huan Dong Lu, Chaoyang District, Beijing 100013, China  
E-mail (corresponding author): limn@nim.ac.cn*

---

## Abstract

Anthropogenic activities such as combustion of fossil fuel and changes in land use release carbon dioxide (CO<sub>2</sub>) into the atmosphere which impacts climate. Cities, with high energy consumption, are main emitters of CO<sub>2</sub>. Therefore, acquiring the concentration and movement of CO<sub>2</sub> in cities is the key to the mitigation of CO<sub>2</sub> emission and the implementation of policies designed for climate change adaption. To quantify the CO<sub>2</sub> emission from cities and investigate its contribution to the regional carbon budget, it is necessary to employ a multi-point observation method. The miniature non-dispersive infrared (NDIR) sensor, which is inexpensive, stable and can provide with high spatial and temporal resolution data, is preferable. However, the emission status of CO<sub>2</sub> can not be well researched without high-quality observed data. It is important to correct the sensors' outputs to enhance the accuracy. Focusing on this, we develop a calibration system of the NDIR CO<sub>2</sub> sensors (Senseair K30). A theoretical transmission model is established based on the Beer-Lambert law. Observed signals of K30 sensor and high-precision Picarro CO<sub>2</sub> analyzer are recorded, along with temperature and pressure obtained by BME sensor, and then theoretical transmission using the experimentally observed variations is calculated. Finally, the theoretical transmission is fitted to the experimental data using a polynomial function, and a reasonable correction formula is established. In this study, we explore the measurement principle of NDIR sensors and develop a feasible methodology for the calibration of miniature CO<sub>2</sub> sensors. This paper provides a reference for improving the accuracy of miniature CO<sub>2</sub> sensors, which is essential for a comprehensive understanding of the CO<sub>2</sub> emission status.

---

## 1. Introduction

Anthropogenic activities such as combustion of fossil fuel and changes in land use release carbon dioxide (CO<sub>2</sub>) into the atmosphere which impacts climate [1, 2]. Cities, with high energy consumption, are main emitters of CO<sub>2</sub>. Therefore, acquiring the concentration and movement of CO<sub>2</sub> in cities is the key to the mitigation of CO<sub>2</sub> emission and implementation of policies designed for climate change adaption.

Quantifying the CO<sub>2</sub> emission from cities and investigating its contribution to the regional carbon budget, it is necessary to employ a multi-point observation method using as many fixed stations or observation vehicles as possible [3]. For multi-point observation, low-cost but accurate sensors are preferable. The miniature non-dispersive infrared (NDIR) sensors, which are inexpensive, stable and can provide with high spatial and temporal resolution data, are widely in high-density CO<sub>2</sub> observation network.

Performance of miniature NDIR sensors can significantly impact the accuracy of the CO<sub>2</sub> emission measurement. The output of sensors is affected by many factors such as temperature, atmospheric pressure, and length of use [4-6]. Without high-quality data, the emission status of CO<sub>2</sub> can not be well researched. To enhance the accuracy of miniature NDIR sensors, it is important to correct the sensors' outputs. Therefore, a calibration method to improve the precision and accuracy of recently developed miniature CO<sub>2</sub> sensors is required. However, few studies focused on the performance and calibration methods of small commercial CO<sub>2</sub> sensors [7, 8].

The objectives of this study are to explore the principle of NDIR sensor and develop a feasible methodology for the calibration of miniature CO<sub>2</sub> sensors. Focusing on this, we develop a calibration system of the NDIR CO<sub>2</sub> sensors (Senseair K30) to improve the accuracy of the measurement. In this study, theoretical data based on the experimental variables is calculated. The observed data

is recorded and compared with the data measured by a highly accurate CO<sub>2</sub> analyzer (Picarro-G2401). Using analytical methodology, the theoretical data is fitted to the observed data, and a reasonable correction formula is established. This paper provides a reference for the calibration system of improving the accuracy of miniature CO<sub>2</sub> sensors, which is essential for a comprehensive understanding of the CO<sub>2</sub> emission status.

## 2. The miniature CO<sub>2</sub> sensor

### 2.1 Senseair K30 overview

The Senseair K30 non-dispersive infrared (NDIR) CO<sub>2</sub> sensor, which is shown in Figure 1, is used commercially for monitoring CO<sub>2</sub> concentration. The measurement range is 0 to 5000 ppm, with an accuracy of ± 3%. The rate of measurement is 0.5Hz. It is small, lightweight and the dimensions are 51 x 57 x 14 mm (Length x Width x approximate Height).



Figure 1: A Senseair K30 NDIR CO<sub>2</sub> sensor

### 2.2 Measurement principle

The Beer-Lambert law relates the intensity  $I$  of radiation, after passage through a length  $L$  of a species with concentration  $c$  and absorption cross-section  $\sigma$ , to its initial intensity  $I_0$ :

$$I = I_0 e^{-c\sigma L} \quad (1)$$

The NDIR sensor measures the intensity signal  $I$  of infrared signal after passing through the sample gas. The average transmittance  $\tau$  is calculated, and the relationship between transmittance and the ratio of sample gas to be measured is established.

The equation can also be expressed as transmission  $\tau = I / I_0$ ;  $\tau$  is the fraction of incoming radiation that passes through the sample.

$$\tau = \exp(-\sigma(T, P, \nu)cL) \quad (2)$$

The equation can be converted to the relationship with mixing ratio, temperature and pressure.

$$\tau = \exp\left(-\sigma(T, P, \nu) \frac{PXN_A}{RT} L\right) \quad (3)$$

where  $X$  is the mixing ratio of the gas to be measured,  $T$  the temperature of the air chamber and  $P$  is the pressure.  $N_A$  is Avogadro constant, and  $R$  is the ideal gas constant.

The absorption cross-section  $\sigma(T, P, \nu)$ , which is the function of temperature and pressure, can be further expressed as the convolution form of the spectral line strength  $S_i$  and linear function  $\phi_i$  of each spectral line in the wavelength range, and the integral is within the wavelength range of the sensor spectral band filter. The equation can be expressed as follows,

$$\tau = \frac{1}{\Delta\nu} \exp\left(-\sum_i S_i(T) \phi_i(T, P, \nu) \frac{PXN_A}{RT} L\right) d\nu \quad (4)$$

CO<sub>2</sub> absorbs strongly in the thermal infrared (IR) centred around 2348 cm<sup>-1</sup>, or 4.26 μm. The relatively high intensity of the peaks in this band makes this wavelength range the most appropriate for a CO<sub>2</sub> sensor [9]. Hence, the spectral band pass filter included in the sensors allows transmission between 2280 and 2400 cm<sup>-1</sup>. The pass band coincides with a frequency range over which CO<sub>2</sub> absorbs strongly, but H<sub>2</sub>O absorbs weak.

## 3. Methods

### 3.1 Apparatus

Apparatuses include BME 680 sensors, Picarro-G2401 CO<sub>2</sub> concentration analyzer, pump, thermostat, external vents and drying chamber. Connections between different apparatus are shown in Figure 2.

BME680 sensor was used to measure the pressure and temperature in the thermostat during the experiment. The BME680 is a digital 4-in-1 sensor with gas, humidity, pressure and temperature measurement based on proven sensing principles. In addition, highly accurate Picarro-G2401 CO<sub>2</sub> concentration analyzer was used for comparison. The analyzer provides simultaneous and continuous measurement of gas. It has a high precision and accuracy, with a parts-per-billion sensitivity. The experimental apparatus is shown in Figure 3.

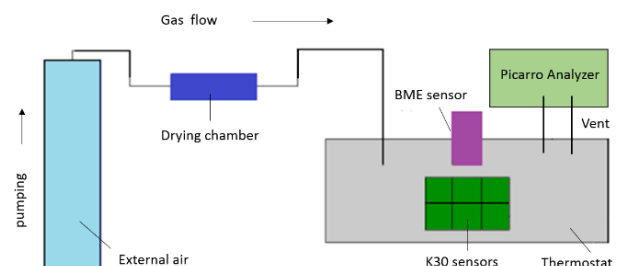


Figure 2: Connections between the apparatus



**Figure 3:** The experimental apparatus

### 3.2 Analytical methodology overview

Analytical methodology is used to explore the relationship between the observed data and theoretical data. The process of experiment and data analysis is as follows; Section 3.4 to Section 3.6 provide more detailed information on these steps.

Firstly, a theoretical transmission model as a function of temperature, pressure and CO<sub>2</sub> concentration is established based on the Beer-Lambert law. Secondly, the observed signal obtained by K30 and Picarro is recorded, along with temperature and pressure by BME sensor. Thirdly, theoretical transmission based on the experimentally observed variations is calculated using the transmission model. In addition, to compare the experimentally measured data and theoretical data, the theoretical transmission is fitted to the experimental data using a polynomial function. Finally, a reasonable correction formula is established for the calibration of miniature CO<sub>2</sub> sensors.

### 3.3 Transmission calculation model

#### 3.3.1 The spectral line strength

The spectral line strength  $S$  of CO<sub>2</sub> can be calculated using the following equation:

$$S = S(T_s) \frac{Q_V(T_s)Q_r(T_s)}{Q_V(T)Q_r(T)} \exp\left[\frac{1.439E''(T-T_s)}{TT_s}\right] \quad (5)$$

where  $S(T_s)$  is the the spectral line strength under standard temperature,  $E''$  is the low-state energy of the transition.  $Q_V$  is vibration distribution function, and  $Q_r$  is rotation distribution function. Both of them are the function of temperature. Within the temperature range of the 175 ~ 325K,  $Q_V$  of CO<sub>2</sub> can be expressed in the following formula [10]:

$$Q_V(T) = 1.05385 - 8.11142 \times 10^{-4}T + 3.18772 \times 10^{-6}T^2 \quad (6)$$

And  $Q_r$  can be expressed as:

$$Q_r(T) = Q_r(T_s) \left(\frac{T}{T_s}\right) \quad (7)$$

The CO<sub>2</sub> spectral data used in the calculation is taken from the HITRAN 2016 spectroscopic database [11].

#### 3.3.2 The linear function

The linear function reflects the variation of absorption cross-section with frequency, that is, the line broadening. A transition between two given quantum mechanical energy levels of a molecule occurs at a single, well-defined frequency. Theoretically, a spectroscopic line at this exact frequency should be observed. However, experimentally observed lines have a finite width. This is due to line broadening effects, which cause small differences in transition frequency from the quantum mechanical result. This gives rise to probability distributions around the central line frequency, and a non-zero line width [12].

For gas, the main type of the line broadening are the Doppler non-uniform broadening (Gauss line shape) caused by molecular thermal motion, and uniform broadening (Lorentz line shape) caused by the collision. Pressure broadening is due to collisions between molecules, which lead to some variation in the energies of the rotational and vibrational states of the absorbing species [13]. The line shape in this study is dictated by pressure broadening. Pressure broadening depends not only on pressure, but also the collision between the molecules. There are contributions from the absorbing species and other species in the gas mixture, and the combined effects can be approximated by a Lorentz probability distribution. The Lorentz line shapes:

$$\varphi(T, P, \nu) = \frac{\alpha_L}{\pi[(\nu-\nu_0)^2 + \alpha_L^2]} \quad (8)$$

where  $\alpha_L$  is the half-width of Lorentz broadening, and can be calculated using

$$\alpha_L(P, T) = \gamma \left(\frac{P}{P_s}\right) \left(\frac{T}{T_s}\right)^{-n} \quad (9)$$

where  $\nu_0$  is the centre frequency,  $\gamma$  is the spectral line half-width at standard pressure  $P_s$  (1 atmospheric pressure) and standard temperature  $T_s$  (296K),  $n$  is the temperature coefficient. The value of  $\gamma$  and  $n$  are taken from the HITRAN 2016 spectroscopic database.

#### 3.3.3 Integration of the IR absorption spectrum

The calculation of absorption cross-section is based on integration of the IR absorption spectrum. For actual atmospheric molecular spectra, a spectral interval often contains a number of spectral lines. Hence the contributions of all spectral lines should be taken into account when calculating the absorption coefficient at a specific sampling point. Line-by-line integration was adopted in the study.

For all spectral lines, weighted average half-width is used instead.

$$\bar{\alpha}_L = \left( \frac{\sum_{i=1}^n \sqrt{S_i} \alpha_{Li}}{\sum_{i=1}^n \sqrt{S_i}} \right)^2 \quad (10)$$

In addition, spectral line center which is not exactly at the integral sampling point was moved to the sampling point. The strength of all spectral lines at the same integral point is summed up and then treated as a single line [14, 15]. In order to compensate the error caused by truncation, the line strength can be modified as follows,

$$S' = S / \left( 1 - \frac{2}{\beta\pi} \right) \quad (11)$$

According to the measurement principle of NDIR sensors, the transmission  $\tau$  of a fixed mixing ratio of CO<sub>2</sub>, can be calculated using the Beer-Lambert law. The calculation model is established and then tested using variables ( $P$  and  $T$ ) that were similar to those in the experiment environment. The value of temperature  $T$  was set between 273 K and 323 K, and pressure  $P$  between 0.96 atm and 1.08 atm. The transmission surface is shown in Figure 4.

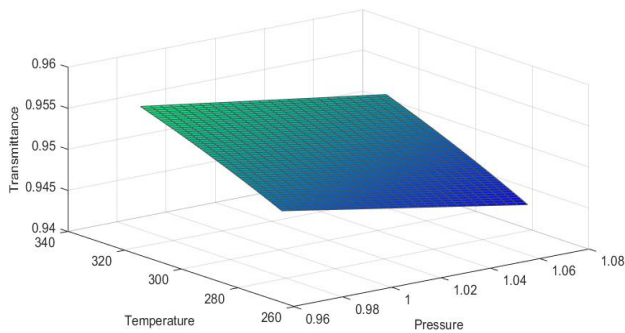


**Figure 4:** Transmission surfaces

### 3.4 Experimentally observed data

Experiments were successfully performed over timescale from 16:30 (25 September 2018) to 15:00 (26 September 2018). During the experiment, K30 sensor and BME sensor were placed in the thermostatic box. In series of experiments, external air was pumped through the drying chamber from the atmosphere, and then into the

thermostat. In the process of measurement, the inlet of the external air was closed. Picarro analyzer, which has been calibrated using standard gas, was connected to the thermostat through the inlet and outlet vents to provide measurement of the CO<sub>2</sub> concentration.

Continuous observed time-series data during the experiment was recorded. The variation of pressure and temperature were recorded by BME sensor. The CO<sub>2</sub> concentration was measured by K30 sensor and a high-precision Picarro CO<sub>2</sub> analyzer throughout the experiment. Raw signal of K30 sensor is also obtained, which is used to investigate and analyze the correction method of the sensor. The recorded temperature and pressure of BME sensor, and the observed signal of K30 sensor and Picarro analyzer are shown in Figure 5.

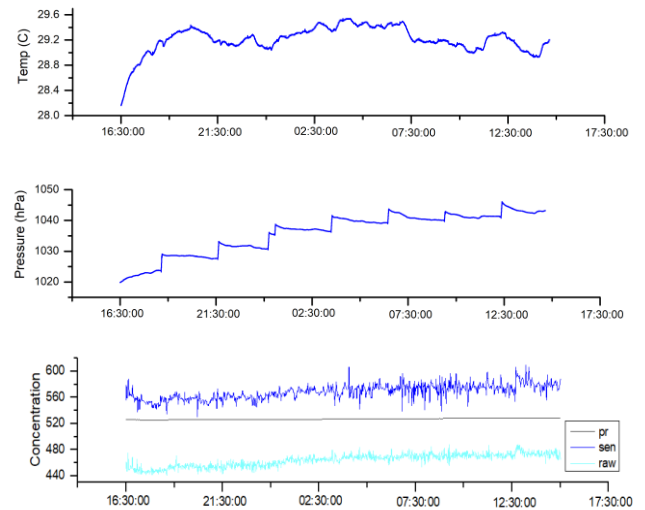


**Figure 5:** Temperature, pressure recorded by BME sensor; the observed signal by K30 sensors and Picarro analyzer. Line pr represents the data observed by Picarro. Line sen and raw is the observed signal and raw signal of K30, respectively.

### 3.5 Transmission calculation

Theoretically transmission, based on the variations obtained in the experiment, described in Section 3.4, can therefore be calculated.

The experimental pressure  $P$  and temperature  $T$  are recorded by BME sensor, and  $C$  is acquired during the experiment using the Picarro analyzer. Initially, using the observed pressure and temperature for the experiment, theoretical transmission is calculated at the CO<sub>2</sub> mixing ratio measured in the experiment. Then the curves of transmission, as a function of pressure and temperature are plotted in Figure 6. This provides a measure of theoretical transmission to distinguish small changes at different pressures and temperature.

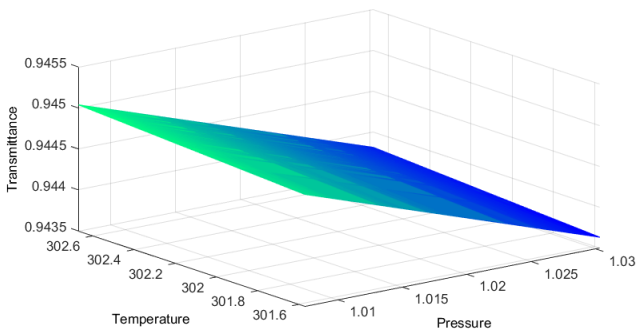


**Figure 6:** Theoretical transmission surfaces

### 3.6 Fitting transmission to observed signal

Theoretical transmission can be calculated for a given temperature, pressure and concentration. Correlation analysis is carried out to explore and analyze the relationship between theoretical transmission and the raw signal of K30.

In addition, experimentally observed signal of K30, based on the analytical methodology, is fitted with exponential function to the theoretically derived transmission. The fitting function is of the cubic form  $ax^3 + bx^2 + cx + d$  for an observed signal, where a, b, c and d are constants. Adding a further term has very little effect on the fit.

Regression analysis was used to clarify the relationship between the raw signal of K30 sensor and the output of Picarro analyzer. Accordingly, the correction formula is obtained.

## 4. Result and Discussion

### 4.1 Variables dependence

Temperature shows small and rapid changes coincide with the changes during the experiment. Experiments were performed over a timescale of several hours with a sealed apparatus, changes of temperature are due to the change external environment. Pressure profile of the experiment has a typical stepwise variation during the experimental procedure. Pressure increases due to the increase of water vapor in the thermostat. The effect of water vapour on the observed signal suggests that absorption is significant at high water vapour mixing ratios over the spectral range of the sensors.

The curves of transmission as a function of temperature and pressure are not linear because the concentration is sufficient to make the CO<sub>2</sub> effectively opaque in this spectral region at higher pressures. For large values of C, the Beer-Lambert exponent becomes very large and negative.

### 4.2 Statistical analysis

Using Correlation analysis, the goodness-of-fit between theoretical transmission and raw signal is analyzed. The coefficient of determination ( $R^2$ ) is 0.9812, indicating a high correlation between theoretical transmission and raw signal. The result is shown in Figure 7, where trans is the theoretical transmission, and raw is the value of raw signal.

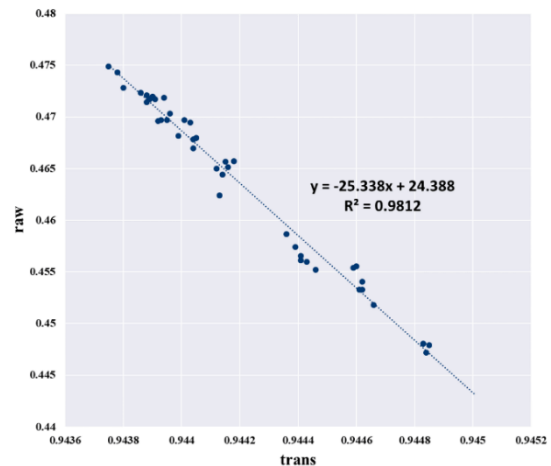


**Figure 7:** Relationship between theoretical data and the raw signal

The relationship of the sensor output and theoretical calculated transmission is analyzed. The result is shown in Figure 8, which indicates that there is a conversion from the transmission to concentration, and the original signal is corrected using a non-linear function in K30 sensor.

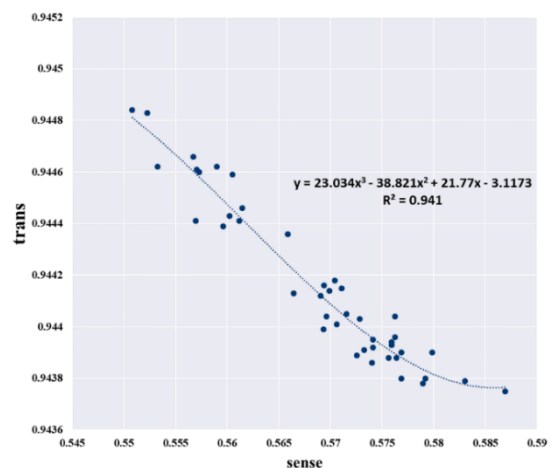


**Figure 8:** Theoretical data with observed signal of K30

Using Regression analysis, the raw signal of K30 sensors can be fitted to the concentration measured by Picarro analyzer, the result is shown in Figure 9.

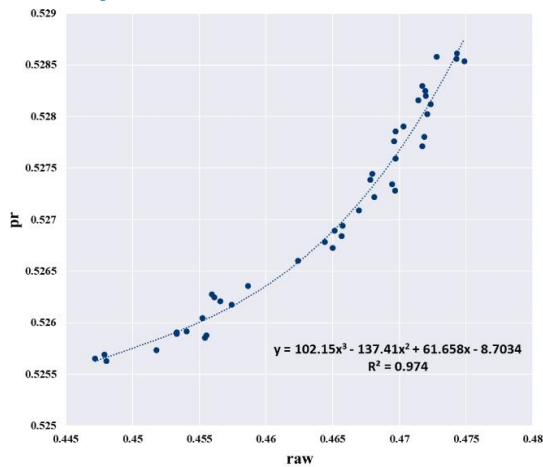


**Figure 9:** Measurement of Picarro with raw signal of K30

#### 4.3 Validation test

The CO<sub>2</sub> concentration was measured by a high-precision Picarro CO<sub>2</sub> analyzer and K30 sensor using the apparatus described in Section 3.1. The raw signal of the K30 sensor was corrected based on the regression function, and then compared to the measured CO<sub>2</sub> concentration data obtained by the Picarro analyzer. The result is shown in Figure 10.

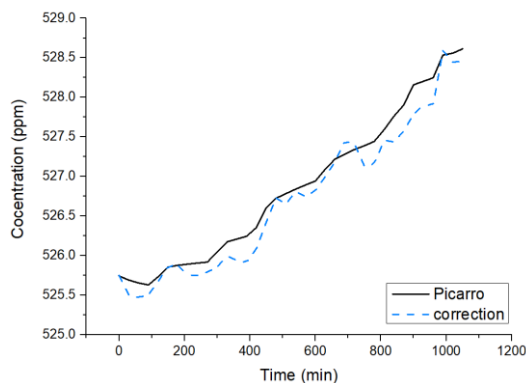


**Figure 10:** Comparison of CO<sub>2</sub> concentration measured by Picarro and corrected result of K30

Subsequently, the relative root mean squared error (RRMS) difference of the corrected value against the measurement of Picarro analyzer was calculated. The RRMS difference is 0.46%, indicating a good agreement between the corrected value of K30 sensor and the measurement of high-precision Picarro CO<sub>2</sub> analyzer.

## 5. Conclusion

The principle of miniature NDIR sensors is explored and a theoretical transmission model as a function of temperature, pressure and CO<sub>2</sub> concentration is established based on the Beer-Lambert law.

In addition, the experimentally observed signal of sensors, along with temperature and pressure are obtained. Using analytical methodology, the theoretical data is calculated and fitted with the observed data. Accordingly, a calibration method of miniature NDIR CO<sub>2</sub> sensors (Senseair K30) to improve the accuracy of the measurement is developed. This study provides a reference for improving the accuracy of miniature CO<sub>2</sub> sensors, which is essential for quantifying and understanding the CO<sub>2</sub> emission status.

There was insufficient time to calculate a theoretical data affected by H<sub>2</sub>O absorption, mainly due to a lack of data of fixed H<sub>2</sub>O. To quantify the interferent effect of H<sub>2</sub>O, further experiment can be conducted to perform the calculation, and fit the signal to sets of data at a series of fixed H<sub>2</sub>O values.

## Acknowledgments

This paper is currently supported by The National Key R&D Program of China (project/subject SN. 2017YFB0504003)

## References

- [1] IPCC, Contribution of Working Group I to the Fourth Assessment Report of the Intergovernmental Panel on Climate Change, *The Physical Science Basis*, p. 996, 2007.
- [2] Hofmann, D.J., et al., The role of carbon dioxide in climate forcing from 1979 to 2004: introduction of the Annual Greenhouse Gas Index, *Tellus B: Chemical and Physical Meteorology*, **58(5)**, p. 614-619, 2006.
- [3] Idso, C.D., S.B. Idso, and R.C. Balling Jr, The urban CO<sub>2</sub> dome of Phoenix, Arizona. *Physical Geograph*, **19(2)**, p.95-108,1998.
- [4] Hodgkinson, J., et al., Non-dispersive infra-red (NDIR) measurement of carbon dioxide at 4.2 μm in a compact and optically efficient sensor, *Sensors and Actuators B: Chemical*, **186**, p. 580-588, 2013.
- [5] Wong, J.Y., Self-calibration of an NDIR gas sensor, *Google Patents*, 1994.
- [6] Mizoguchi, Y. and Y. Ohtani, Comparison of response characteristics of small CO<sub>2</sub> sensors and an improved method based on the sensor response, *Journal of Agricultural Meteorology (Japan)*, 2005.
- [7] Grimmond, C., et al., Local-scale fluxes of carbon dioxide in urban environments: methodological challenges and results from Chicago, *Environmental Pollution*, **116**,p. S243-S254, 2002.
- [8] Pandey, S. and K.-H.Kim, The relative performance of NDIR-based sensors in the near

- real-time analysis of CO<sub>2</sub> in air, *Sensors*, **7(9)**, p. 1683-1696, 2007.
- [9] Johns, J., Absolute intensity and pressure broadening measurements of CO<sub>2</sub> in the 4.3- $\mu$ m region, *Journal of Molecular Spectroscopy*, **125(2)**, p. 442-464, 1987.
- [10] McClatchey, R.A., et al., AFCRL atmospheric absorption line parameters compilation, *Air Force Cambridge Research Labs HANSCOM AFB MA*, 1973,
- [11] Gordon, I.E., et al., The HITRAN 2016 molecular spectroscopic database, *Journal of Quantitative Spectroscopy and Radiative Transfer*, **203**, p. 3-69, 2017.
- [12] Ward, J., J. Cooper, and E.W. Smith, Correlation effects in the theory of combined Doppler and pressure broadening—I. Classical theory, *Journal of Quantitative Spectroscopy and Radiative Transfer*, **14(7)**, p. 555-590, 1974.
- [13] Hollas, J.M., *Modern spectroscopy* (John Wiley & Sons), 2004
- [14] Aoki, T., An accurate representation of the transmission functions of the H<sub>2</sub>O and CO<sub>2</sub> infrared bands, *Journal of Quantitative Spectroscopy and Radiative Transfer*, **24(3)**, p. 191-202, 1980.
- [15] Hurst, S., A. Durant, and R. Jones, A low cost, disposable instrument for vertical profile measurements of atmospheric CO<sub>2</sub>, *Chemistry Research Project Report*, 2011.

# Traceability of pulsed flow rates consisting of constant delivered volumes at given time interval

H. Bissig, M. Tschannen, M de Huu

Federal Institute of Metrology, Lindenweg 50, 3003 Bern-Wabern, Switzerland  
E-mail (corresponding author): [hugo.bissig@metas.ch](mailto:hugo.bissig@metas.ch)

## Abstract

Very low flow calibrations are important in several areas of pharmaceutical, microfluidic and health care applications where volumetric dosage or delivery at given flow rates are crucial for the process. Not only continuous flow rates are commonly used in the health sector, but also pulsed flow rates consisting of constant delivered volumes at given time intervals. One known application is the delivery of Insulin with tethered or patch pumps. These constant volumes can be of the order of several tens or hundreds of nanoliters. As the delivery times can vary up to several minutes, it is not appropriate to determine an average flow rate of the delivered volume. It is more advisable to determine the average volume and the average time interval of delivery.

The METAS Microflow facility has been upgraded to perform measurements with insulin pumps delivering a volume of 500 nl at a given time interval of several minutes. The updated design and new aspects of the discontinuous volume collection from the tethered or patch pumps are discussed in this paper. First calibration results of insulin pumps are also presented.

## 1. Introduction

Dosing small amounts of liquids at a well-defined interval in time are implemented in several areas of pharmaceutical, microfluidic and health care applications. Examples for this application are the tethered pump and patch pump for the delivery of insulin. The characterization of one of each pump for flow rates from 70 nL/min to 500 nL/min is presented in this paper. Very low flow rates are often determined by collecting the water continuously in a beaker placed on a balance for the gravimetric method. However, in this case the flow is not generated by a continuous method, but by the stepwise delivery of a constant volume per unit time.

## 2. Microflow facility

### 2.1 Gravimetric method

METAS has developed the Microflow facility for flow rates applied in microfluidics covering flow rates from 50 nl/min up to 1 ml/min [1]. Only the main component being the beaker for continuous water collection is emphasized in this paper. The beaker is placed in the weighing environment shown in Figure 1. To control the evaporation rate, the conventional method of adding water in an evaporation trap in the weighing zone is applied to saturate the air with humidity.

The weighing data are continuously collected by a Real Time system (RT), which communicates with the balance at 20 Hz and pairs the weight value directly with the time stamp of the RT.

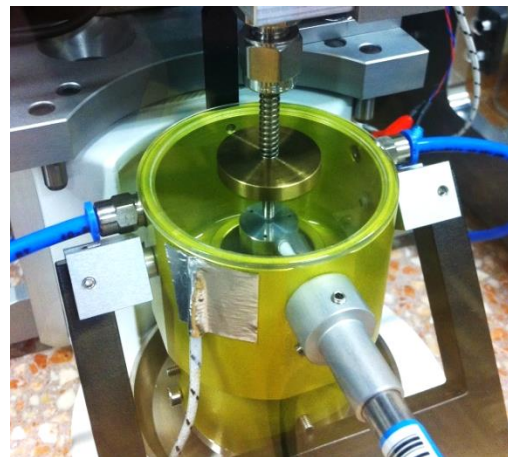


**Figure 1:** Insight in the weighing zone with its evaporation trap filled with water and the holes at the top of the weighing zone housing acting as humidity exchanger. Details can be found in [1].

### 2.2 Standard flow rate determination

The collected weighing data are then fitted by means of a least square linear fit to obtain the mass flow rate. A fixed time window of the order of 3600 s or larger is

chosen for the data presented in this paper. By increasing the starting time of this fixed time window by time steps of the corresponding data the moving average of the flow rate in time can be followed. More details of this procedure are beyond the scope of this paper and can be found in the references [1] and [2].

### 2.3 Volume increment per unit time

As the investigated insulin pumps deliver a certain amount of liquid per unit time, it is more appropriate to determine the increment of volume per unit time. The increment of volume per unit time can also be expressed as a flow rate if desired.

## 3. Setup for the insulin pumps

### 3.1 Setup for the tethered pump

The tethered pump is like a small syringe pump with a fixed tubing at the outlet of the small syringe. This tubing is connected to the gravimetric method of the Microflow facility. The setup is shown in Figure 2, where also a thermal mass flow meter is connected in between to follow the flow rate variation with a second technique.



**Figure 2:** Setup of the tethered pump connected to the METAS Microflow facility.

### 3.2 Setup for the patch pump

The patch pump has a fixed tubing of a length of 12 mm, where the fluid is extruded. Therefore, a special holder for the patch pump was constructed to position the tubing in the beaker on the glass filter. Details of the water collecting beaker can be found in the reference [1]. A picture of the setup is shown in Figure 3.

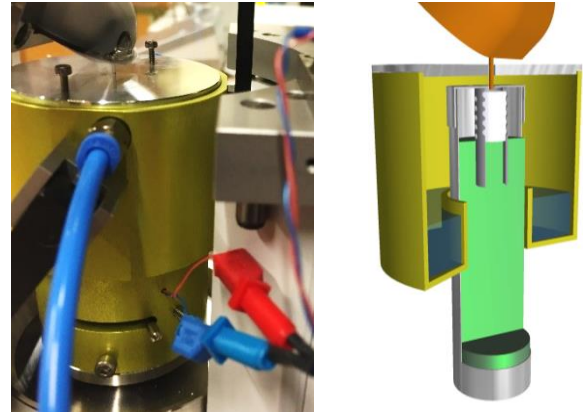


**Figure 3:** The patch pump is fixed above the weighing zone in order that the tubing is placed on the glass filter in the beaker, which is under the cover.

Another setup was also constructed for the patch pump where the tubing is immersed into water with an oil layer on top to prevent evaporation (Figure 4). This technique is also widely used to collect the water on the balance [3].

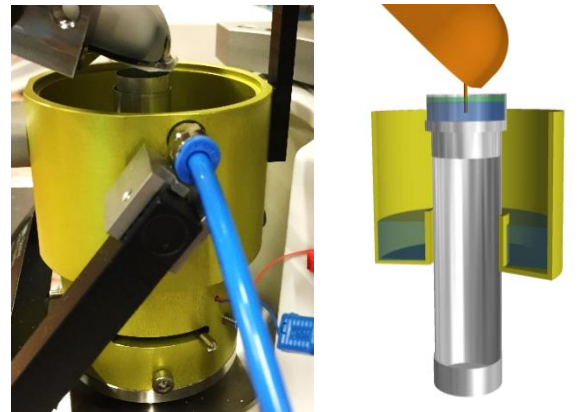


**Figure 4:** The patch pump is fixed above the weighing zone in order that the tubing is immersed into water in the open beaker. To prevent evaporation an oil layer is added on top of the water.

## 4. Results for the tethered pump

The flow rates are first determined by the standard flow rate determination method and the deviations are calculated according to the preset flow rate at the tethered pump. The deviations are shown in Figure 5 (black circles) and Table 1. The deviations are between 0 % and 1.3 %, which are within the specified accuracy of  $\pm 5$  %.

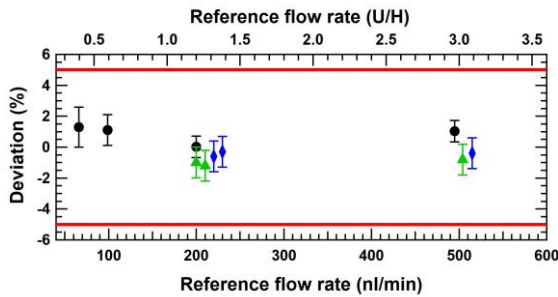


**Figure 5:** Deviations of tethered pump with respect to the standard flow rate determination method (black circles) and the delivered volume per unit time by using the peak of the histogram (green triangles) or the maximum of the Gaussian fit (blue diamonds). Calibration results are well within the specifications of the manufacturer for the accuracy of 5% (red solid line). The data at 200 nL/min and 500 nL/min are slightly shifted in flow rate for better illustration.

**Table 1:** Tethered pump standard method

Water T (°C)	Q <sub>REF</sub> (nL/min)	Selected flow rate (U100)		Dev (%)	U (%)
		(nL/min)	(U/H)		
22.2	494.9	500.0	3.0	+1.0	0.7
22.2	200.0	200.0	1.2	+0.0	0.7
22.2	98.9	100.0	0.6	+1.1	1.0
22.2	65.8	66.7	0.4	+1.3	1.5

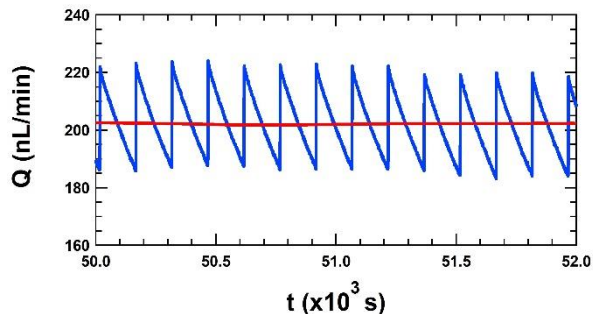


**Figure 6:** Instantaneous flow rate measured by a thermal mass flow meter (blue line). The average taken over 3600 s is close to 200 nL/min (red line).

To illustrate the delivery of 500 nL per unit time, we show in Figure 6 the flow rate at 200 nL/min measured by a thermal mass flow meter. The instantaneous delivered volume increases the pressure at the outlet of the tethered pump, but the pressure is decreasing along the tubing due to the impedance of the tubing. This is smoothening the flow rate and a stepwise increment of the flow rate at the delivery of the volume followed by a slowly decrease of the flow rate is observed. The same feature is observed at a flow rate of 200 nL/min in the data of the balance shown Figure 7. As the volume is delivered the increment in weight is clearly visible, which is flattening out before the next delivery. The instantaneous flow rate determined by the gravimetric method at 200 nL/min shown in Figure 8 reflects this

behaviour as the strong increase of the flow rate is always followed by a decrease.

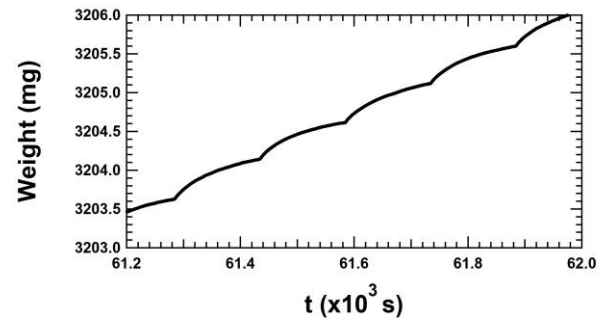


**Figure 7:** Zoom in of the increase of weighing data. It is a smooth increase of weight in steps and not a sharp step function.

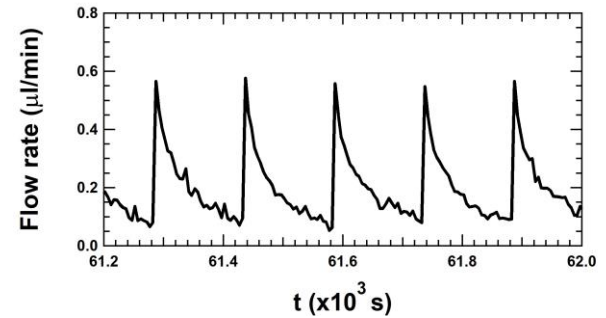


**Figure 8:** Instantaneous flow rate at 200 nL/min obtained by the weight increase shown in Figure 7. The fit window is 5 s for the determination of the flow rate by means of the linear least square fit.

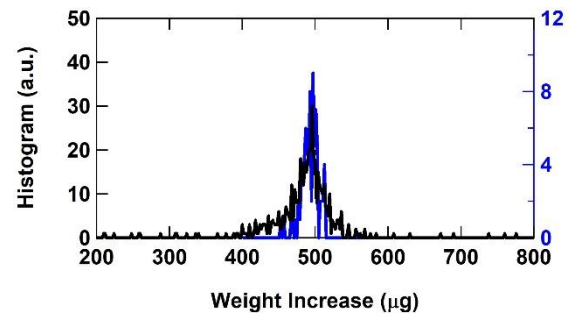


**Figure 9:** Histogram of the weight increments of all the data of the measurement (black line) and of a selected period being 75 ks – 85 ks (blue line) at 200 nL/min. The second distribution is slightly narrower than the first one. The data of the histogram are raw data without corrections.

Therefore, it is more appropriate to determine the increment of volume per unit time. The histogram of the weight increments per unit time of all data and a selected period is shown in Figure 9. The peak of the histogram for all data resp. a selected period is at 496 µg resp. 497 µg. Performing a Gaussian fit on the histograms leads to a maximum at 492.6 µg resp. 494.1 µg for all data resp. a selected period. Converting

the mass into volume by applying the water density of  $997.7 \text{ kg/m}^3$  and adding the evaporated amount of water being  $7.75 \text{ nL}$  in  $2.5 \text{ min}$  we obtain  $504.9 \text{ nL}$  resp.  $505.9 \text{ nL}$  in  $2.5 \text{ min}$  starting from the peak values and  $501.5 \text{ nL}$  resp.  $503.0 \text{ nL}$  starting from the maximum value of the Gaussian fit. These different values differ only by  $0.9 \%$ . Expressing this in flow rates we have obtained the flow rates and deviations represented in Table 2, Table 3 and Figure 5 (green triangles and blue diamonds). The deviations obtained are between  $-0.3 \%$  and  $-1.2 \%$  for both flow rates. The same delivered volume is expected for all the flow rates as only the time interval is changing. Also, the capillary force is not constant any more at the outlet needle with the strong variations in flow rate, but it can be assumed that for each cycle of the delivery of volume the changes in the capillary forces are similar. This contribution to the uncertainty has not yet been investigated und several contributions due to the flow rate determination have to be re-evaluated. A rather empiric estimation of the total uncertainty is  $1.0 \%$ .

**Table 2:** Tethered pump with the method of the volume delivered per unit time. Taking the peak of the histogram.

Data	$Q_{REF}$	Selected flow rate (U100)		Dev (%)	U (%)
	(nL/min)	(nL/min)	(U/H)		
all	504.3	500.0	3.0	-0.8	1.0
all	202.0	200.0	1.2	-1.0	1.0
75-85 ks	202.4	200.0	1.2	-1.2	1.0

**Table 3:** Tethered pump with the method of the volume delivered per unit time. Taking the maximum of the Gaussian fit of the histogram.

Data	$Q_{REF}$	Selected flow rate (U100)		Dev (%)	U (%)
	(nL/min)	(nL/min)	(U/H)		
all	502.2	500.0	3.0	-0.4	1.0
all	200.6	200.0	1.2	-0.3	1.0
75-85 ks	201.2	200.0	1.2	-0.6	1.0

The largest differences between the two flow rate determination techniques are  $1.2 \%$  resp  $1.8 \%$  for the flow rate of  $200 \text{ nL/min}$  resp.  $500 \text{ nL/min}$ . The results obtained with the standard flow rate determination and the delivered volume per unit time are with the assumption of the uncertainty for the volume delivered per unit time for the first case consistent. This example highlights also that for this type of delivered volume per unit time the analysis method has to be adapted. The standard flow rate determination might not be the best method for this case. A possibility to investigate additional contributions to the uncertainty of this technique can be investigated with the METAS piston provers [2]. A stepwise delivery of a small volume by the METAS piston provers at a given time interval can simulate the stepwise extraction of volumes by insulin pumps. Then, all the effects can be studied, as the generated constant volume per unit time is traceable. FLOMEKO 2019, Lisbon, Portugal

With such investigations a more realistic uncertainty could be obtained.

## 5. Results for the patch pump

For the patch pump, we had the possibility to apply two different water collection techniques. The first one is the standard method, where the water is flowing through a glass filter and collected in the beaker [1] (see Figure 3). The second one is the collection of the water with the immersed needle in water with a layer of oil on top of it [3] (see Figure 4).

The flow rates are first determined by the standard flow rate determination method and the deviations are calculated according to the preset flow rate at the patch pump. The deviations for both water collection techniques are shown in Figure 10 and Table 4 and Table 5.

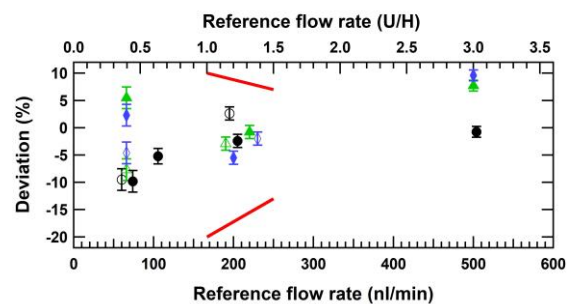


**Figure 10:** Deviations of the patch pump with respect to the standard flow rate determination method. Two water collection techniques are compared: the standard water collection technique (full black circles) and the water collection technique with the immersed needle in water covered by an oil layer (open black circles). The red lines are the accuracies reported in the reference [4]. Volume increment per unit time for the standard collection technique (Peak - full green triangles; Gaussian - full blue diamonds) and the collection technique with immersed needle (Peak - open green triangles; Gaussian - open blue diamonds). See text for more details.

**Table 4:** Results of the patch pump with the standard flow rate determination method and the standard water collection technique

Water T (°C)	$Q_{REF}$	Selected flow rate (U100)		Dev (%)	U (%)
	(nL/min)	(nL/min)	(U/H)		
22.2	503.8	500.0	3.0	-0.8	1.0
22.2	204.9	200.0	1.2	-2.4	1.2
22.2	105.5	100.0	0.6	-5.2	1.4
22.2	74.0	66.7	0.4	-9.8	2.0

**Table 5:** Results of the patch pump with the standard flow rate determination method and the water collection technique with immersed tubing in water with oil cover.

Water T (°C)	$Q_{REF}$	Selected flow rate (U100)		Dev (%)	U (%)
	(nL/min)	(nL/min)	(U/H)		
22.2	194.9	200.0	1.2	+2.6	1.2
22.2	73.7	66.7	0.4	-9.5	2.0

The results at 66.7 nL/min are consistent with both techniques. However, the deviations at 200 nL/min are not consistent with a difference of 5 %. The reasons for this discrepancy are not yet known.

For the standard water collection technique, the tubing of the patch pump is not as stiff as the standard outlet needle used and therefore the capillary force between the tubing and the glass filter might not be as stable as expected. As the tubing is only 12 mm long, the delivered volume creates a strong step increase on the balance, as shown in Figure 11 (black curve) at flow rate 66.7 nL/min with a volume of 500 nL every 7.5 min. The strong peaks at each step reflect the strong variations of the capillary force.

For the water collection technique with the immersed needle, the buoyancy correction force due to the immersed needle has not been determined for this method. It is not clear if a stick-slip effect influences the weighing values at each delivery of the volume. The typical increments of weight are shown in Figure 11 (blue curve). It is surprising to see that after each delivered volume the weight is still slightly increasing during the time before the next delivery of volume. We would expect that the strong increase in weight at the delivery of the volume flatten out over this period or would slightly decrease due to a small evaporation contribution. However, the increase in weight is not expected and further investigations are needed.

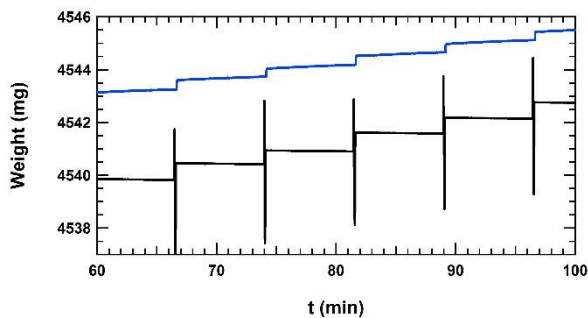


**Figure 11:** The increase of weight of the two water collection techniques at 66.7 nL/min (500 nL every 7.5 min) are presented: the standard water collection technique (black line) and the water collection technique with the immersed needle in water covered by an oil layer (blue line).

For both water collection technique the increment of volume per unit time is investigated at 200 nL/min. Figure 12 resp. Figure 13 shows the weighing data and the step increments of weight for the standard water collection technique resp. the water collection technique with the immersed needle in water covered by an oil layer. We clearly see in Figure 12 the changes in the capillary force (peaks downwards) when the volume is delivered and water flows on the glass filter. The histograms of the weight increment per unit time of both techniques are shown in Figure 14. The distributions are very broad, but we observe 3 distinct peaks for both FLOMEKO 2019, Lisbon, Portugal

water collection techniques. This leads to the assumption that the delivered volume is not always constant and possibly some stick-slip effects inside the pumps lead to delivered volumes of the order of 400 nL, 500 nL and 600 nL. We identify the main peak and the maximum of the Gaussian fit to estimate the delivered volume per unit time, reported in Table 6 and Table 7. When the distribution is very broad and shows 3 distinct peaks, the Gaussian fit is not very representative. Nevertheless, it is a first attempt for the analysis. The slight differences of the histograms indicate also that the water collection technique and the data analysis for these patch pumps have to be improved and further investigations are needed.

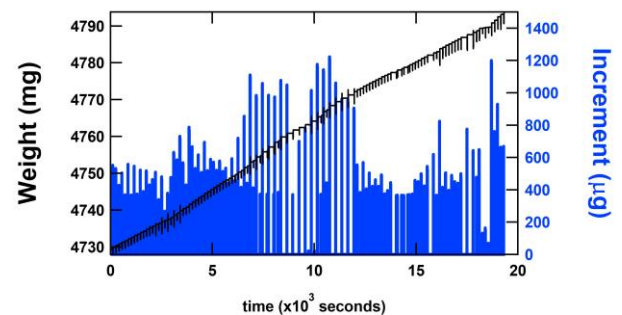


**Figure 12:** Weighing data (black line) and the step increment of weight for the standard water collection technique (blue line) at 200 nL/min.

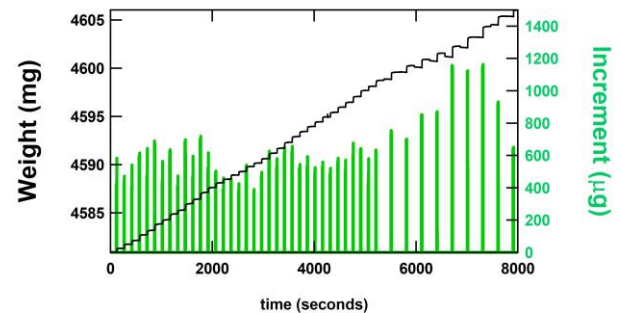


**Figure 13:** Weighing data (black line) and the step increment of weight for the water collection technique with the immersed needle in water covered by an oil layer (green line) at 200 nL/min.

The same techniques were applied for the analysis of the data at 500 nL/min and 66 nL/min. All the results are presented in Figure 10, Table 6 for the "peak technique" (green triangles) and Table 7 for the "Gaussian fit technique" (blue diamonds) with the full symbols for the standard water collection technique and the open symbols for the water collection technique with the immersed needle. All the differences in the results indicate that the water collection technique and the data analysis for these patch pumps have to be improved and further investigations are needed to avoid systematic

measurement errors and determine a realistic measurement uncertainty.

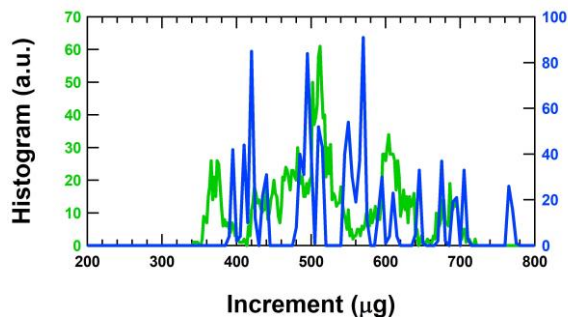


**Figure 14:** Histograms of the step increments of weight for the standard water collection technique (blue line) and for the water collection technique with the immersed needle in water covered by an oil layer (green line) at 200 nL/min.

**Table 6:** Patch pump with the method of the volume delivered per unit time. Taking the peak of the histogram.

Method & Data	Q <sub>REF</sub>	Selected flow rate (U100)		Dev	U
	(nL/min)	(nL/min)	(U/H)	(%)	(%)
Standard 1-12 ks	464.2	500.0	3.0	+7.7	1.0
Immersed needle 1-5 ks	206.0	200.0	1.2	-2.9	1.2
Standard 3-7 ks	201.6	200.0	1.2	-0.8	1.2
Immersed needle 47-54 ks	72.2	66.7	0.4	-7.7	2.0
Standard 1-70 ks	63.2	66.7	0.4	+5.5	2.0

**Table 7:** Patch pump with the method of the volume delivered per unit time. Taking the maximum of the Gaussian fit of the histogram.

Data	Q <sub>REF</sub>	Selected flow rate (U100)		Dev	U
	(nL/min)	(nL/min)	(U/H)	(%)	(%)
Standard 1-12 ks	456.1	500.0	3.0	+9.6	1.0
Immersed needle 1-5 ks	204.0	200.0	1.2	-2.0	1.2
Standard 3-7 ks	211.6	200.0	1.2	-5.5	1.2
Immersed needle 47-54 ks	69.9	66.7	0.4	-4.6	2.0
Standard 1-70 ks	65.2	66.7	0.4	+2.3	2.0

## 6. Conclusion

The METAS Microflow facility has been upgraded to perform measurements with insulin pumps delivering a volume of 500 nl at a given time interval of several minutes. A tethered pump and a patch pump have been

characterized for flow rates from 70 nL/min to 500 nL/min. The standard flow rate determination due to the continuous collection of water on the balance and the determination of the delivered volume per unit time were applied to the weighing data.

For the tethered pump, the results were consistent or close to consistency with a difference of 1.8 % with measurement uncertainties of 1 %. For all the flow rates, the deviations were between -1.2 % and +1.3 %. This is expected as on average the same amount of volume is delivered, but only the time interval between two deliveries is changing.

For the patch pump, the setup was slightly more complicated to realise. Using the standard flow rate determination, we obtained similar results for the two water collection techniques. The results at 66.7 nL/min were consistent, while at 200 nL/min the difference is 5 %. The reason for this is yet unknown and further investigations are needed. The second technique determining the delivered volume per unit time shows a large discrepancy for the patch pump. Furthermore, it is not clear, why the standard flow rate determination shows larger negative deviations for lower flow rates. It seems that the stepwise weight increment and other effects occurring due to this non-continuous increase influence the reference flow rate determined with the standard flow rate determination. Further investigations are needed to clarify this issue.

Overall, the upgrade of the METAS Microflow facility enables the determination of constant volume increments at different time intervals. Several issues have to be investigated and the analysis of the weighing data has to be improved.

## References

- [1] H. Bissig, M. Tschannen and M. de Huu, "Micro-flow facility for traceability in steady and pulsating flow", *Flow Meas. and Instrum.*, Vol. 44, 34-42, 2015.
- [2] H. Bissig, M. Tschannen and M. de Huu, "Recent Innovations in the field of traceable calibration of liquid milli-flow rates with liquids other than water", in *Flomeko Proc.*, 2016.
- [3] H. Bissig, H.T. Petter, P. Lucas et al., "Primary standards for measuring flow rates from 100 nl/min to 1 ml/min – gravimetric principle", *Biomed Eng – Biomed Tech*, Vol. 60(4), 301-316, 2015.
- [4] Zisser H. "Siphon Effects on Continuous Subcutaneous Insulin Infusion Pump Delivery Performance", *J Diabetes Sci Technol*, Vol 4(1):98-103, 2010.

# Liquid properties effects on Coriolis and thermal mass flow meters at very low flow rates

H. Bissig, M. Tschannen, M de Huu

Federal Institute of Metrology, Lindenweg 50, 3003 Bern-Wabern, Switzerland  
E-mail (corresponding author): [hugo.bissig@metas.ch](mailto:hugo.bissig@metas.ch)

---

## Abstract

Calibration of flow devices are important in several areas of pharmaceutical, flow chemistry and health care applications where volumetric dosage or delivery at given flow rates are crucial for the process. Although most of the flow devices are measuring flow rates of process-oriented liquids their calibrations are often performed with water as calibration liquid. It is recommended to perform the calibrations of the flow devices with process-oriented liquids as the liquid itself might influence the performance of the flow devices. Therefore, METAS has developed facilities with METAS flow generators to address the issue of measuring with process-oriented liquids for flow rates from 400 ml/min down to 50 nl/min with uncertainties from 0.07 % to 0.9 %.

The effects of liquids with different viscosities and thermal properties on the measurement accuracy of Coriolis and thermal mass flow meters have been investigated at these very low flow rates. Calibrations with water and several reference oils with traceable viscosity were performed to study the viscosity effect on the flow meter performance and the dependency on the thermal properties for the thermal mass flow meter. The results will be discussed in this paper.

---

## 1. Introduction

Calibration of flow devices are important in several areas of pharmaceutical, flow chemistry and health care applications where volumetric dosage or delivery at given flow rates are crucial for the process. Although most of the flow devices are measuring flow rates of process-oriented liquids, their calibrations are often performed with water as calibration liquid. It is recommended to perform the calibrations of the flow devices with process-oriented liquids as the liquid itself might influence the performance of the flow devices. In this paper, we present calibrations results of two Coriolis flow meter with reference oils of different viscosities ranging from 1.0 mPa·s to 7.5 mPa·s. The Coriolis flow meters are known to have a very small dependency of viscosities. On the other hand, calibration results of a thermal mass flow meter with the same liquids are presented in this paper. However, the scaling behaviour is much more difficult as the heat capacity and the heat conductivity play an important role and the scaling behaviour is not linear with respect to the properties of water. In most cases, the manufacturer of liquid thermal mass flow meters propose calibrations with water and IPA (Isopropanol alcohol) with corresponding calibration parameters stored in the flow sensors. For liquids consisting of hydrocarbon chains the behaviour of the thermal mass

flow sensor is linearly scalable with the calibration parameters obtained with IPA as it is a good thermal representative for most hydrocarbons [1, 2].

After developing a facility for the micro-flow range [3, 4], METAS has developed facilities with METAS piston provers to address the issue of measuring with process-oriented liquids. The METAS piston provers are homemade and allow measurements with liquids other than water in the range from 400 ml/min down to 50 nl/min [5, 6]. Traceability is guaranteed through the calibration of the generated flow rates of the METAS piston provers by means of the dynamic gravimetric method where a liquid of well-known density and a well-controlled evaporation rate is used. In a later stage, it will be directly traceable to length and time as it is usually done for piston provers. As the METAS piston prover is a volumetric flow generator, it can be operated with any liquid acting as a transfer standard to perform calibrations of flow devices. The advantage of traceable calibrations of a flow device with the process-oriented liquid is to enhance the quality of the measurements results of the flow device during the production process. Different types of flow devices are stated from the manufacturer with accuracies between 0.5 % and 10 % depending of the flow rate range and the working principle of the flow devices. Obviously, a traceable calibration with uncertainties ranging from 0.07 % to 0.9 % for steady flow rates ranging from 400 ml/min to

50 nl/min will enhance the accuracy of the measurements as the stated deviations of the flow devices are corrected in the application and the measurement uncertainties are known and much smaller than the accuracies stated by the manufacturer.

## 2. The METAS piston provers

The METAS piston provers consist of a high precision linear stage with a fixed linear measuring system, mounting parts to fix commercially available syringes or homemade prover cylinders in front of the table and mounting parts to fix and move the piston in the prover cylinder in order to generate the flow rate (see Figure 1 and Figure 2), [5]. The position of the linear stage is determined by counting the pulses sent by the linear measuring system by means of an FPGA, which is a Field Programmable Gate Array with hard coded program code running on a defined constant cycle time of the order of 25 ns (40 MHz). For each additional pulse in any direction, a time stamp of the FPGA is recorded and a pair with the position and the timestamp is formed. This pair of values is then read from the main software and the real time position can be recorded. The real time speed is then determined by a linear fit of several pairs of position data with the corresponding time stamps as the slope corresponds to the speed. Multiplying the speed with the cross section of the syringe gives the volume flow rate. The speed range for the METAS piston prover of the Microflow facility resp. of the Milliflow facility is from 0.1 mm/s to 0.1  $\mu\text{m/s}$  resp. from 4.0 mm/s to 4.0  $\mu\text{m/s}$ .

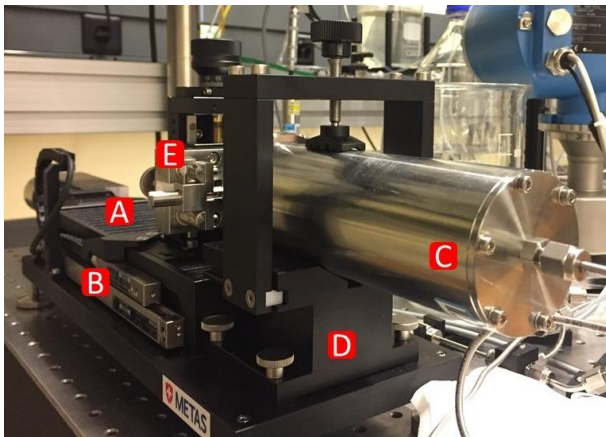


**Figure 1:** METAS piston prover of the Milliflow facility, (A) high precision linear stage, (B) linear measuring system, (C) piston cylinder, (D) mounting piston cylinder, (E) mounting and positioning for the piston.

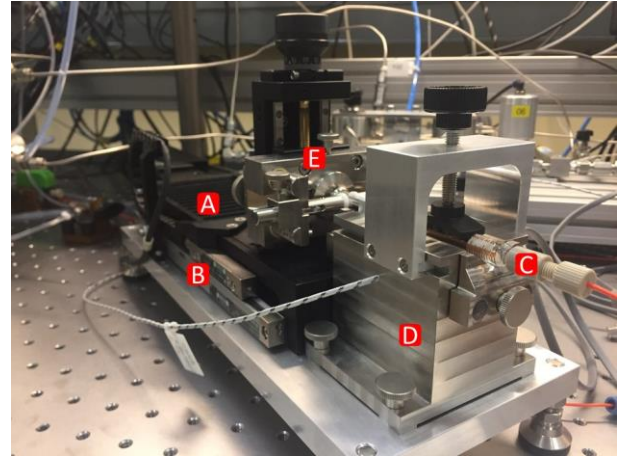


**Figure 2:** METAS piston prover of the Microflow facility, (A) high precision linear stage, (B) linear measuring system, (C) syringe, (D) mounting syringe body, (E) mounting and positioning for syringe plunger.

## 3. Liquid properties

The relevant properties of the reference oils that are used for the measurements with the Coriolis mass flow meters and a thermal mass flow meter are listed in Table 1.

**Table 1:** Properties of the reference oils and water at approx. 21.4 °C.

Property	Water	Reference oil 2BW <sup>1</sup>	Reference oil 5BW <sup>1</sup>	Reference oil 10AW <sup>1</sup>
Dyn Viscosity $\eta$ ( $\text{kg}\cdot\text{m}^{-1}\cdot\text{s}^{-1}$ )	0.9624 $\cdot 10^{-3}$	2.361 $10^{-3}$	5.903 $10^{-3}$	8.419 $10^{-3}$
Spec. Heat capacity $c_p$ ( $\text{J}\cdot\text{kg}^{-1}\cdot\text{K}^{-1}$ )	4184	2130	2067	2046
Th. conductivity $\lambda$ ( $\text{W}\cdot\text{m}^{-1}\cdot\text{K}^{-1}$ )	0.600	0.143	0.151	0.147
Density $\rho$ ( $\text{kg}\cdot\text{m}^{-3}$ )	997.9	767.5	796.4	805.9

<sup>1</sup> the reference oils are commercially available at <https://zmk-wolfen.de/>, ZMK & ANALYTIK GmbH in Germany.

## 4. Coriolis and thermal mass flow meters

The Coriolis and thermal mass flow meters are calibrated with the liquids water and the reference oils 2BW, 5BW and 10AW, where the properties are listed in Table 1. The METAS piston provers are used as traceable volumetric flow generators and are filled with each of these liquids. As the Coriolis mass flow meters measure mass flow rates, the volumetric flow rate of the piston prover is converted into mass flow rate by multiplying with the density of the liquid. The thermal mass flow meter indicates the volumetric flow rate.

### 4.1 Coriolis mass flow meters

The following Coriolis mass flow meters were calibrated with these liquids: Cubemass DCI DN01

from Endress+Hauser AG and miniCori M12 from Bronkhorst High-Tech B.V. For both Coriolis flow meters the zeroing procedure was applied prior to the measurement with water. Afterwards, for the measurements with the other liquids, no zeroing procedure was performed, but the zero flow was measured in all cases.

#### 4.2 Cubemass DCI DN01 from Endress+Hauser AG

The calibration results of the Cubemass DCI DN01 from Endress+Hauser AG are shown in Figure 3, Figure 4 and Figure 5, where the deviation is shown as a function of the reference mass flow rate, the Reynolds number and for the last figure with the zero flow correction applied after the measurements. It is common to use the Reynolds number instead of the mass flow rate as it takes into account the mass flow rate and the dynamic viscosity of the liquid.

In Figure 3, the results show a constant deviation for mass flow rates larger than 30 g/min for all liquids. For the mass flow rates around 10 g/min, the deviations seem to be widely spread for the different liquids. However, if we plot the deviations as a function of the Reynolds number as shown in Figure 4, we can observe a trend in the data, which is highlighted by black dashed trend-line drawn by hand.

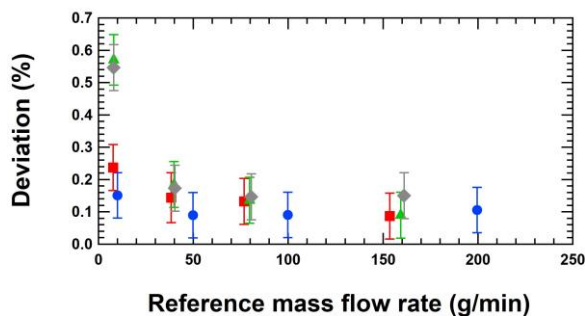


**Figure 3:** Cubemass DCI DN01. Deviations as a function of reference mass flow rate for the different liquids: water (blue circles), liquid 2BW (red squares), liquid 5BW (green triangles), liquid 10AW (gray diamonds).

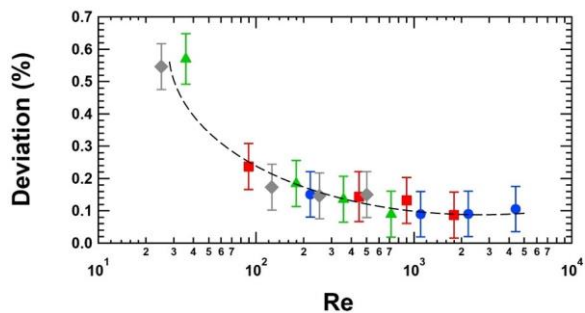


**Figure 4:** Cubemass DCI DN01. Deviations as a function of Reynolds number for the different liquids: water (blue circles), liquid 2BW (red squares), liquid 5BW (green triangles), liquid 10AW (gray diamonds). The black dashed line is only a trend-line.

Applying the zero flow correction by subtracting the measured zero flow (Table 2) from the measured flow rate, we obtain the deviations presented in Figure 5, which are close to a constant deviation for all liquids (except for the liquid 2BW at  $Re \sim 100$ ). No obvious dependency of the various liquids with different viscosities could thus be observed in this case.

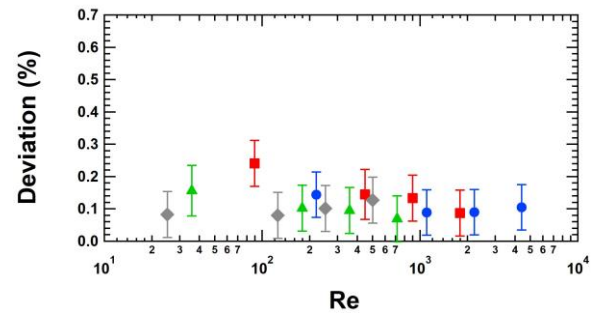


**Figure 5:** Cubemass DCI DN01. Deviations of the zero-flow corrected flow rates of the Coriolis mass flow meter as a function of Reynolds number for the different liquids: water (blue circles), liquid 2BW (red squares), liquid 5BW (green triangles), liquid 10AW (gray diamonds).

**Table 2:** Measured Zero flows of the Coriolis mass flow meters with the reference oils and water.

Coriolis flow meter	Water	Reference oil 2BW	Reference oil 5BW	Reference oil 10AW
Cubemass DCI DN01 (mg/min)	+0.65	-0.30	+33.0	+37.3
miniCori M12 (mg/min)	+0.2	+0.0	+0.0	+0.0002

#### 4.3 miniCori M12 from Bronkhorst High-Tech B.V.

The calibration results of the miniCori M12 from Bronkhorst High-Tech B.V. are shown in Figure 6, Figure 7 and Figure 8, where the deviation is shown as a function of the reference mass flow rate, the Reynolds number and for the last figure with the zero flow correction applied after the measurements.

Also for these measurements, the results look more consistent when the deviations are plotted against the Reynolds number as shown in Figure 7. However, applying the zero flow correction by subtracting the measured zero flow (Table 2) from the measured flow rate does not change the results as the measured zero flow rates are already negligible (see Figure 8). We observe rather constant deviations for Reynolds numbers larger than 20 and a wider spread of the deviations for smaller Reynolds numbers. No systematic dependency on the various liquids with different viscosities could be observed for this Coriolis flow meter. The spread of the data for Reynolds numbers smaller than 10 are due to the larger inaccuracy of the

Coriolis measurement principle at lower flow rate rather than due to the any viscosity effect.

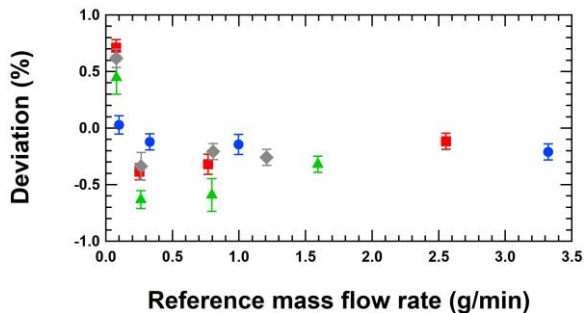


**Figure 6:** miniCori M12. Deviations as a function of reference mass flow rate for the different liquids: water (blue circles), liquid 2BW (red squares), liquid 5BW (green triangles), liquid 10AW (gray diamonds).

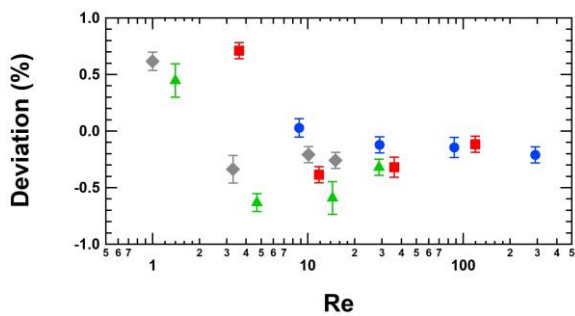


**Figure 7:** miniCori M12. Deviations as a function of Reynolds number for the different liquids: water (blue circles), liquid 2BW (red squares), liquid 5BW (green triangles), liquid 10AW (gray diamonds).

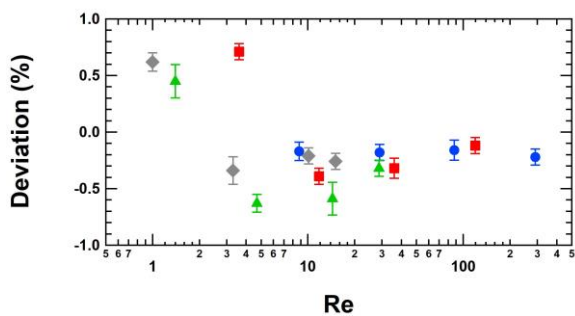


**Figure 8:** miniCori M12. Deviations of the zero-flow corrected flow rates of the Coriolis mass flow meter as a function of Reynolds number for the different liquids: water (blue circles), liquid 2BW (red squares), liquid 5BW (green triangles), liquid 10AW (gray diamonds).

#### 4.4 Thermal mass flow meter SLI-0430 from Sensirion

The thermal mass flow meter SLI-0430 from Sensirion AG was calibrated with the liquids water and the reference oils 2BW, 5BW and 10AW (properties listed in Table 1).

As mentioned above, the manufacturer of liquid thermal mass flow meters propose calibrations with water and IPA with corresponding calibration parameters stored in

the flow sensors. The calibration parameters of water were set in the flow sensor for the measurements showed in this paragraph. The results are presented in Figure 9 and Table 3. The indicated flow rates of the SLI-0430 are much smaller than the reference flow rate for the reference oils 2BW, 5BW and 10AW. The ratios between the indicated flow rates of water and any of the reference oils is dependent on the flow rate. Therefore, it is very difficult to find a scaling behaviour depending only on thermal properties of the liquids. The fact that the Zero flow of the SLI-0430 with the different reference oils indicates already non-negligible contributions (see Table 4) emphasizes these scaling difficulties.

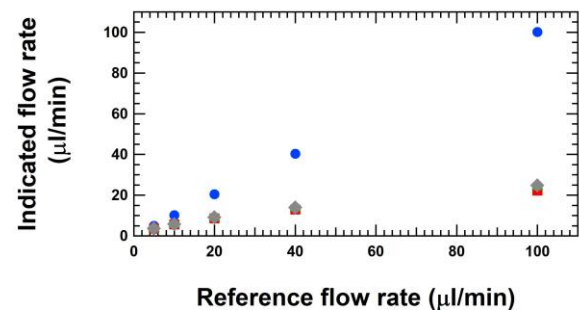


**Figure 9:** SLI-0430. Indicated flow rate as a function of the reference flow rate for the different liquids: water (blue circles), liquid 2BW (red squares), liquid 5BW (green triangles), liquid 10AW (gray diamonds). Uncertainties are smaller than the data symbols.

**Table 3:** Measured flow rates for the SLI-0430 with the different liquids and the corresponding uncertainties.

Ref. flow rate (µl/min)	Indicated flow rate of the SLI-0430 (µl/min)				Uncert. (k=2) (µl/min)
	Water	Ref. oil 2BW	Ref. oil 5BW	Ref. oil 10AW	
99.96	100.07	22.277	24.287	24.844	0.17
39.984	40.266	12.937	13.808	14.012	0.089
19.990	20.425	8.666	9.061	9.162	0.066
9.995	10.175	5.598	5.738	5.785	0.028
4.998	4.963	3.542	3.602	3.619	0.021

**Table 4:** Measured Zero flows of the Thermal mass flow meter with the reference oils and water.

Thermal mass flow meter	Water	Reference oil 2BW	Reference oil 5BW	Reference oil 10AW
SLI-0430 (µl/min)	+0.030	+0.859	+0.868	+0.870

Therefore, it would have been advisable to load the calibration parameters of the IPA calibration in the SLI-0430. Thus, measurements with IPA and the reference oils would probably have led to a scaling behaviour between these liquids. However, this points out the difficulty to perform measurements with different liquids of very different thermal properties and thermal

behaviour. This also underlines the fact that the flow devices measuring flow rates of process-oriented liquids should be calibrated with the process-oriented liquids. This would limit the influence of the theoretical scaling behaviour on the measurement uncertainty and increase the accuracy of the measurements.

#### 4.5 Thermal mass flow meter SLI-1000 from Sensirion

To illustrate a possible scaling behaviour the thermal mass flow meter SLI-1000 from Sensirion AG has been calibrated with water and liquids that are aqueous solutions: 0.0111 g Ethanol per 1 g water (solution 1) and 0.0222 g Ethanol per 1 g water (solution 2). The thermal properties have been taken from the literature at a temperature of 20 °C and are summarized in Table 5. The specific heat capacity and the thermal conductivity have been calculated according to the mass weighted mean of the individual components of the solutions according to Equation (1) and (2). These values are approximate, but they are useful to explain the calibration data obtained with different liquids for the SLI-1000.

$$c_{p,sol} = \frac{m_{H_2O} \cdot c_{p,H_2O} + m_{Ethanol} \cdot c_{p,Ethanol}}{m_{H_2O} + m_{Ethanol}} \quad (1)$$

$$\lambda_{sol} = \frac{m_{H_2O} \cdot \lambda_{H_2O} + m_{Ethanol} \cdot \lambda_{Ethanol}}{m_{H_2O} + m_{Ethanol}} \quad (2)$$

**Table 5:** Properties of water and the aqueous solutions at 20.0 °C.

Property	Water	Ethanol	Solution 1 (1.1 %wt)	Solution 2 (2.2 %wt)
Dyn Viscosity $\eta$ [7] ( $\text{kg} \cdot \text{m}^{-1} \cdot \text{s}^{-1}$ )	1.002 · 10 <sup>-3</sup>	1.189 · 10 <sup>-3</sup>	1.040 · 10 <sup>-3</sup>	1.078 · 10 <sup>-3</sup>
Spec. Heat capacity $c_p$ ( $\text{J} \cdot \text{kg}^{-1} \cdot \text{K}^{-1}$ )	4184	2430	4164.7	4145.9
Th. conductivity $\lambda$ ( $\text{W} \cdot \text{m}^{-1} \cdot \text{K}^{-1}$ )	0.600	0.200	0.596	0.591
Density $\rho$ ( $\text{kg} \cdot \text{m}^{-3}$ )	998.21	789.34	996.18	994.17

For the anemometric regime with flow rates larger than 2 g/h (33  $\mu\text{l}/\text{min}$ ), the relation between the mass flow rate  $q_m$  and the heater power  $P_{\text{heater}}$  is  $P_{\text{heater}} \sim q_m^{0.33}$  [8]. Assuming that the heater power is linearly dependent on the heat capacity of the liquid, the conversion factor should be as described in Equation (3):

$$q_{m,sol} \cong q_{m,H_2O} \cdot (c_{p,H_2O}/c_{p,sol})^3 \quad (3)$$

And for volume flow rate ( $q_V$ ) we get Equation (4):

$$q_{V,sol} \cong q_{V,H_2O} \cdot (\rho_{H_2O}/\rho_{sol}) \cdot (c_{p,H_2O}/c_{p,sol})^3 \quad (4)$$

Applying Equation (4) to the measured data, we obtain the theoretical flow rates for the solution 1 and solution 2, reported in Table 6 and the deviations as a function of the Reynolds number shown in Figure 10.

**Table 6:** Theoretical flow rates for the solution 1 and solution 2.

Reference flow rate ( $\mu\text{l}/\text{min}$ )	SLI-1000 ( $\mu\text{l}/\text{min}$ )				
	Water	Sol. 1	Sol. 1 scaled	Sol. 2	Sol. 2 scaled
559.9	542.0	551.2	550.7	557.2	559.3
509.9	493.6	501.9	501.5	507.4	509.4
459.9	445.3	452.8	452.4	457.5	459.6
359.9	351.5	356.8	357.1	360.6	362.7
260.0	256.4	260.3	260.5	263.1	264.6

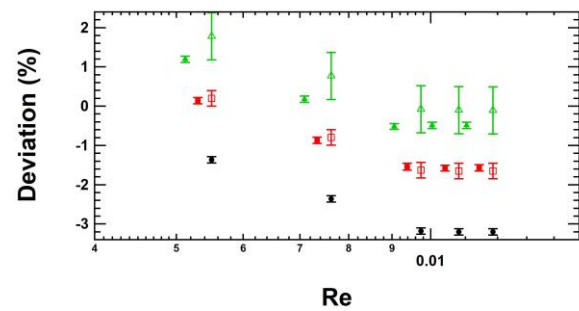


**Figure 10:** SLI-1000. Deviations as a function of Reynolds number for the different liquids: water (black circles), solution 1 (red squares), solution 2 (green triangles). Full symbols are measured data and open symbols are theoretical values.

The deviations of the measured flow rates and the theoretical expected flow rates for the SLI-1000 and the corresponding uncertainties are reported in Table 7 resp. Table 8.

Table 8.

**Table 7:** Deviations of the measured flow rates and the theoretical expected flow rates for the SLI-1000 in Table 6.

Deviation of the SLI-1000 (%)				
Water	Sol. 1	Sol. 1 scaled	Sol. 2	Sol. 2 scaled
-3.20	-1.57	-1.65	-0.49	-0.11
-3.20	-1.58	-1.65	-0.49	-0.10
-3.18	-1.54	-1.63	-0.52	-0.08
-2.36	-0.87	-0.80	0.18	0.76
-1.37	0.14	0.20	1.19	1.78

**Table 8:** Uncertainties of the measured deviations and the scaled deviations for the SLI-1000 in Table 7.

Uncertainties (k=2) (%)				
Water	Sol. 1	Sol. 1 scaled	Sol. 2	Sol. 2 scaled
0.08	0.08	0.20	0.08	0.60
0.08	0.07	0.20	0.08	0.60
0.08	0.09	0.20	0.07	0.60
0.08	0.08	0.20	0.08	0.60

0.08	0.08	0.20	0.08	0.60
------	------	------	------	------

The uncertainties for the theoretical expected flow rates (scaled) were chosen in a way that the measured and the theoretical data are consistent within the uncertainties. This means that by applying a scaling factor to data measured with one liquid and to estimate the flow rate for another liquid it has to be taken into account that the theoretical value is more uncertain than the measured value. This example also shows the importance to calibrate the flow sensor with the process-oriented liquid that will be used for the measurements. This will increase the quality of the measurements results and considerably decrease the uncertainty, if needed.

## 5. Conclusion

Calibration results of Coriolis and thermal mass flow meters performed with the METAS piston provers with the liquids water and the reference oils 2BW, 5BW and 10AW were discussed in this paper.

No obvious dependency of the various liquids with different viscosities could be observed for the Coriolis mass flow meters.

The thermal mass flow meters showed obviously strong dependencies on the thermal properties of the liquids. Estimating a scaling behavior for the reference oils with the sensor parameters set to the water calibration turned out to be a very difficult task and is beyond of the scope of this paper. The calibrations of a thermal mass flow meter with water and aqueous solutions offered a scaling behaviour and an estimation of the uncertainty of these theoretical predictable flow rates. As these scaling effects are already important, no effect of the viscosity on the flow meter performance could be investigated.

These measurements show the importance of calibrating the flow sensor with the process-oriented liquid that will be used for the measurements. This will increase the quality of the measurements results and considerably decrease the uncertainty, if needed.

## References

- [1] [www.sensirion.com](http://www.sensirion.com), datasheet SLI Liquid Flow Meter Series.
- [2] [www.bronkhorst.com](http://www.bronkhorst.com), datasheet e.g.  $\mu$ Flow series L01.
- [3] H. Bissig, M. Tschannen and M. de Huu, "Micro-flow facility for traceability in steady and pulsating flow", *Flow Meas. and Instrum.*, Vol. 44, 34-42, 2015.
- [4] H. Bissig, H.T. Petter, P. Lucas et al., "Primary standards for measuring flow rates from 100 nl/min to 1 ml/min – gravimetric principle", *Biomed Eng – Biomed Tech*, Vol. 60(4), 301-316, 2015.
- [5] H. Bissig, M. Tschannen and M. de Huu, "Recent Innovations in the field of traceable calibration of liquid milli-flow rates with liquids other than water", in *Flomeko Proc.*, 2016.
- [6] H. Bissig, M. Tschannen and M. de Huu, "Improving process quality by means of accurate and traceable calibration of flow devices with process oriented liquids", *CHIMIA*, Vol. 72, 124-129, 2018.
- [7] I.S. Khattab et al., "Density, viscosity, and surface tension of water+ethanol mixtures from 293 to 323 K", *Korean J. Chem. Eng.*, Vol. 29(6), 812-817, 2012.
- [8] F.P. Incropera, D.P. DeWitt, *Fundamentals of Heat and Mass Transfer*, John Wiley & Sons, 1996

# From Disturbance to Measurement: Application of Coriolis Meter for Pattern Identification of Gas Bubbles

Hao Zhu<sup>1</sup>, Alfred Rieder<sup>1</sup>, Wolfgang Drahm<sup>1</sup>, Yaoying Lin<sup>1</sup>, Andreas Guettler<sup>1</sup>, Michael Wiesmann<sup>1</sup>, Josef Hubensteiner<sup>1</sup>

<sup>1</sup>Endress+Hauser Flowtec AG, Am Lohmuehlbach 12, 85356 Freising, Germany  
E-mail (corresponding author): hao.zhu@endress.com

## Abstract

Entrained gas has been regarded as disturbance to measurements based on Coriolis meters, since measurement accuracy can be degraded because of this disturbance. Recent research from Endress+Hauser has discovered that different types of gas bubbles, namely free bubbles and suspended bubbles, have various impact on the meter measurement performance. It is crucial to identify the bubble pattern in the measuring tube of a Coriolis meter to make a diagnosis and reduce the negative influence of the disturbance accordingly. For free bubbles that typically cause inhomogeneity of a medium, the fluctuation of the resonance frequency of the measuring tube in a Coriolis meter is directly correlated to the existence of this type of bubbles, since this medium under a flowing condition causes density fluctuation to the meter as gas density is typically much lower than that of a liquid. For homogenous suspended bubbles that lead to a significantly increased compressibility of a medium, the innovative Multi-Frequency Technology in Promass Q sensor offers the means to qualitatively detect the existence of this type of bubbles and quantitatively calculate the volume fraction of the gas phase, based on its ability to derive the speed of sound in a medium containing such bubbles. Identification of the type of bubbles helps not only for crediting the measurement reliability, but also for obtaining more detailed medium properties, and in turn a better process insight, with which a process optimization can be enabled to improve the quality of production.

## 1. Introduction

In recent decades, Coriolis Mass Flowmeters (CMFs) have been widely used in industry for mass flow and density measurements. The measuring technique has reached a high degree of acceptance and new fields of applications emerge every year. Together with this high acceptance, Coriolis meters are utilized as a multivariable sensor with not only mass flow and density, but also temperature and viscosity measurements [1]. There is a trend to use those additional measured parameters, for example density and viscosity, for monitoring product quality.

Figure 1 shows a typical Coriolis meter, which consists of two parallel measuring tubes, a housing that protects the inner part as well as other components adhering to the measuring tube such as a driver for exciting the tube and sensors for sensing the tube motion. The measuring tube, which in commercial designs can be of various shapes, is the core element of a Coriolis meter. In order to be energy efficient, the tube is continuously

excited at its natural frequency. This measured natural frequency is a function of the medium density in the tube, therefore, forms the basis of the density measurement. The induced tube vibration generates an angular velocity. Together with the mass flow of a medium inside the tube, Coriolis forces are generated, which causes an anti-symmetrically distortion of the tube. The magnitude of this distortion sensed by the sensors is directly proportional to the mass flow rate and forms the basis of the mass flow measurement.

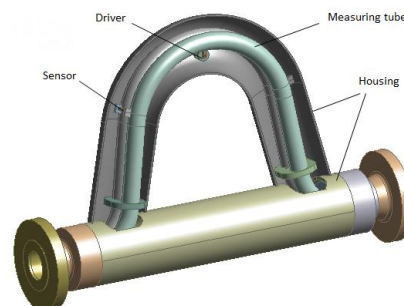


Figure 1: Typical structure of a Coriolis mass flow meter.

Similar to many other measuring principles, it is known that accuracy of a Coriolis meter can be affected by the existence of entrained gas in a liquid flow. A number of research activities have been carried out in the past to understand the error mechanisms of Coriolis metering under two-phase conditions, which is summarized in [2]. According to the effects on Coriolis metering, gas bubbles in liquid flows are classified as “free bubble” and “suspended bubble” that lead to “bubble effect” and “resonator effect”, respectively [3]. Therefore, it is important to detect the existence of entrained gas and identify the type of entrained bubbles that has relevance to the measurement reliability. Furthermore, very often entrained gas bubbles affect product quality in an adverse way, for example in chemical industry when a glue is produced. However, sometimes homogeneous suspended micro-bubbles are wanted as a product feature, for example in food industry when cream cheese is produced. But exactly for this product, big free bubbles are unwanted and regarded as being disadvantageous for product quality. In the meanwhile, the existence of big “free bubbles” also indicates a less optimal manufacturing process, in which the injected gas is not well mixed into the cream cheese for generating homogeneous micro-bubbles. Therefore, the detection of gas bubbles and the identification of the bubble types are crucial for product quality control and optimization of production process.

## 2. Identification of gas bubbles

### 2.1 Free bubble

The definition of free bubble is based on the “bubble effect” theory developed by Hemp et al [4]. According to the theory, a free bubble in the measuring tube of a Coriolis mass flowmeter does not strictly follow the oscillation of the surrounding liquid with the same amplitude because the liquid cannot “hold” the bubble well. The amplitude of the bubble is greater than that of the tube vibration. Based on the bubble effect theory, a holding coefficient is defined in Equation (1) to describe the degree of a bubble being “free” in a liquid subject to an oscillation [3].

$$\delta = \sqrt{\frac{\mu}{d^2 f \rho_l}}, \quad (1)$$

where  $\mu$ ,  $d$ ,  $f$  and  $\rho_l$  are the viscosity of the liquid, the bubble diameter, the tube vibration frequency and the liquid density, respectively. Following this FLOMEKO 2019, Lisbon, Portugal

definition, the vibration amplitude ratio  $J$  between the gas bubble and the measuring tube can be calculated and only the result is given in Figure 2 below.

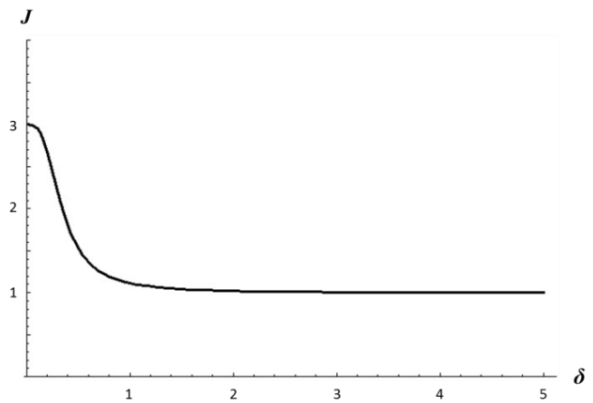


Figure 2: Amplitude ratio as a function of  $\delta$ .

If the amplitude ratio is 3, the bubble is defined as “free bubble”, as it reaches its maximum vibration amplitude that is different to that of the measuring tube. Deviations for density and mass flow measurements occur due to this difference in vibration amplitude, which is named as “bubble effect”.

If the amplitude ratio is 1, the bubble is defined as “suspended bubble”, as it exactly follows the tube oscillation with the same amplitude and is therefore “held” by the surrounding liquid. Under such circumstance, there is no measurement deviations caused by the bubble effect. However, “resonator effect” that also leads to measurement deviations can become significant for homogeneously distributed suspended bubbles. This effect is discussed in the next subsection.

If the amplitude ratio is between 1 and 3, it is defined as the transition region that is typically of less importance for most practical applications.

It can be seen in Equation (1) that the bubble diameter is the most important parameter that almost dominates the holding coefficient, considering that the other parameters such as density and viscosity can only vary in a limited range for a certain application. Therefore, a free bubble is typically featured with a big diameter as a “big” bubble; while a suspended bubble usually has a small diameter and is known as “small” or “micro” bubble. It should be borne in mind that “big” and “small” here are relative. The precise definition of free or suspended bubble should follow the previously defined holding coefficient.

When practical application is concerned and the source of the generation of different bubble types is also considered, free bubbles are typically discrete and big in size, causing inhomogeneity to the process medium for density, as gas density is usually much smaller than that of a liquid even under a relatively high process pressure. A non-optimal process is very often the source of free bubbles, e.g. batching from empty, or insufficient liquid level such that the downstream pump sucks in air. To detect a medium containing free bubbles, the inhomogeneity of this medium can be used by a Coriolis meter that measures density. A simple density model for a Coriolis meter to measure fluid density is given by

$$\rho = c_0 + c_1 \frac{1}{f^2}, \quad (2)$$

where  $c_0$  and  $c_1$  are density coefficients that are determined by a density calibration and stored in the Coriolis device. The inhomogeneity of the flowing medium causes fluctuation of the density measurement of the meter over time. A derivative with respect to time can be built directly to the above equation, which in turn gives

$$\frac{\partial \rho}{\partial t} = c_1 \frac{-2 \partial f}{f^3 \partial t}. \quad (3)$$

Therefore, a derived parameter  $I_{FB}$ , as given in Equation (4), can be defined to indicate the existence of free bubbles.

$$I_{FB} = c_1 \frac{-2 \partial f}{\rho f^3 \partial t}. \quad (4)$$

As  $f$  is the resonance frequency of the measuring tube,  $\partial f / \partial t$  can be obtained by building the standard deviation of the raw signal  $f$  over a certain period, for example, over a second, and  $\rho$  can take the average value over the same period.

For practical use, the parameter  $I_{FB}$  is actually not only related to gas bubbles, but also to the existence of a second phase that has a different density to the first carrier phase and leads to an inhomogeneous mixture status. A bigger this parameter is, a greater inhomogeneity the two-phase mixture has.

## 2.2 Suspended bubble

Homogeneous suspended small or micro bubbles are often seen in Food industry, for example in ice cream where gas is injected and well mixed in a form of micro bubble to increase the softness for a better taste of the product; or in Oil&Gas industry,

for example in a heavy oil where the viscosity is high and a lot of small or micro bubbles can be held. Because this type of bubbles is generated often as a product feature or due to the characteristics of the base liquid, the resulted two-phase mixture is usually homogeneous and does not really cause a significant density fluctuation to a Coriolis meter when it is flowing. Figure 3 shows two pictures of typical free bubbles and suspended bubbles.

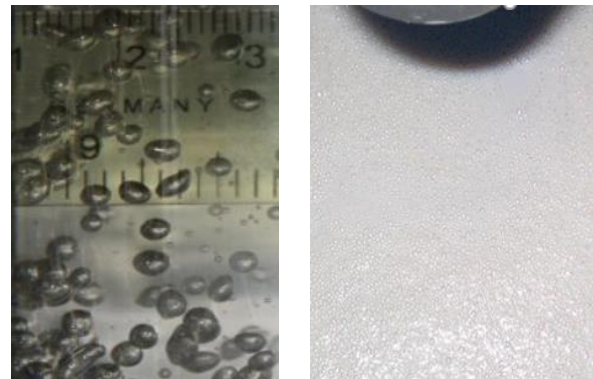


**Figure 3:** Typical inhomogeneous free bubbles (left) and homogeneous suspended bubbles (right)

Since a medium containing suspended small or micro bubbles is typically homogenous, the method provided in Section 2 is not able to detect such type of bubbles. However, the recently developed Multi-Frequency Technology (MFT) [3] in the Coriolis sensor, Promass Q, enables the possibility. This technology is invented to cope with the resonator effect that is related to the compressibility of a medium for a Coriolis meter. The detailed explanation of the resonator effect is given in [2]. For convenience, its basic theory is briefly presented again in this paper.

It has been known that speed of sound in a gas-liquid two-phase mixture is calculated by the following equation:

$$c = \left( \frac{\alpha}{c_g^2} + \frac{(1-\alpha)^2}{c_l^2} + \frac{\alpha(1-\alpha)\rho_l}{\gamma P} \right)^{-\frac{1}{2}}, \quad (5)$$

where  $c$ ,  $\alpha$ ,  $\rho$ ,  $P$  and  $\gamma$  are speed of sound, Gas Void Fraction (GVF), density, pressure and the adiabatic constant. The indices  $g$  and  $l$  represent gas phase and liquid phase, respectively. Equation (5) is plotted in the figure below. It can be seen that speed of sound decreases significantly even a small GVF is present. The lowest acoustic resonance frequency of a fluid in a tube  $f_0$  is determined by

$$f_0 = c \frac{\lambda_1}{2\pi R_0}, \quad (6)$$

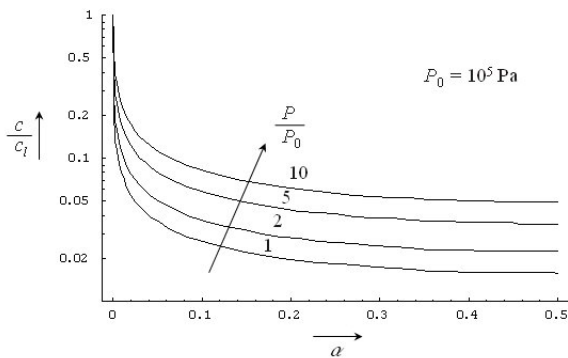


**Figure 4:** speed of sound as a function of GVF and pressure

where  $\lambda_1$  is the lowest eigenvalue, and  $R_0$  is the radius of the tube. Therefore,  $f_0$  reduces with a reduced speed of sound when gas is present in a liquid. Typically, the speed of sound in a single-phase fluid is relatively high, such that the corresponding  $f_0$  is also high, for example of the order of  $10^4$  Hz. Its distance to the tube resonance frequency  $f$  is too big to cause any noticeable deviation for Coriolis density measurement. However, it is not the case when GVF starts to increase from zero. The measurement deviation can be calculated by

$$\rho_a = \rho \left( r_0 + r_1 \frac{1}{1 - \frac{f^2}{f_0^2}} \right), \quad (7)$$

where  $\rho_a$  is the apparent density reading from the Coriolis meter,  $r_0$  and  $r_1$  are constants.

With MFT, the two measuring tubes in the meter are excited for the basic tube mode and a higher tube mode simultaneously, as depicted in Figures 5 and 6. It should be noted that the two modes have two different resonance frequencies. For each mode, an independent density measurement can be performed for the same medium inside the meter. Therefore, Equation (7) can be established twice, as given by

$$\rho_{ai} = \rho \left( r_0 + r_1 \frac{1}{1 - \frac{f_i^2}{f_0^2}} \right), \quad (8)$$

where  $i = 1$  and  $2$ , corresponding to the basic mode and the higher mode, respectively. Combining the two equations of the modes leads to a solution of  $f_0$ , and the true density of the two-phase mixture  $\rho$ . The latter is used as the output of the density FLOMEKO 2019, Lisbon, Portugal

measurement of Promass Q with MFT, instead of an apparent density reading without the correction for the resonator effect. It should be noted that mass flow measurement is also affected by suspended bubbles in a similar way. As a matter of fact, this influence on mass flow measurement is eliminated with the help of MFT in Promass Q, similar to that for density measurement.

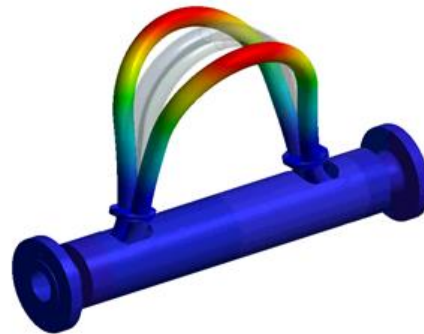


**Figure 5:** Modal shape of the basic tube mode in numerical simulation (shown in heightened form)

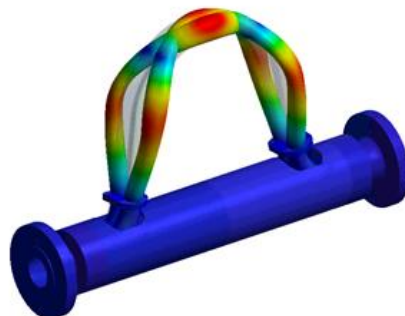


**Figure 6:** Modal shape of the higher tube mode in numerical simulation (shown in heightened form)

It is interesting to see that the measured apparent density can be different for the two modes, because of the different driving frequencies. Table 1 gives a calculation example of a DN50 meter for the measured apparent densities under the two tube modes of MFT. The tube radius is assumed to be 0.014 meter, and the medium density is  $1000 \text{ kg/m}^3$ . The tube mode frequencies are fixed for the calculation for simplicity, although they can slightly vary for the two conditions, i.e. speed of sound  $1400 \text{ m/s}$  and  $100 \text{ m/s}$  respectively, in this example.

**Table 1:** Example of measured densities for the two modes of a DN50 meter

Medium density	f1	f2	c	f0	f1 mode apparent density	f2 mode apparent density
[kg/ m <sup>3</sup> ]	[Hz]	[Hz]	[m/s]	[Hz]	[kg/ m <sup>3</sup> ]	[kg/ m <sup>3</sup> ]
1000	200	1200	1400	29316	1000.04	1001.40
			100	2094	1007.71	1409.27

The calculated results show that for case 1, where speed of sound is 1400 m/s like in water, the Coriolis meter measures the density effect of the medium with only a deviation of 0.04 kg/m<sup>3</sup> with the basic mode, which is the basic working mode of a Coriolis meter. It should be noted that this small density deviation is not shown in the final Coriolis density measurement because a factory calibration with a correction reference density already includes this effect and thus eliminates this influence. With the higher mode, the apparent density has a deviation of 1.40 kg/m<sup>3</sup>, which is still considerably small for such a single-phase medium. However, when entrained gas is present, the speed of sound can significantly drop, for example to 100 m/s as previously introduced, the Coriolis density measurement will show a deviation of 7.71 kg/m<sup>3</sup> with the basic mode, and a deviation of 409.27 kg/m<sup>3</sup> with the higher mode. The effect can be so strong for suspended bubbles that an indicator for the detection of such bubbles can be built based the measured density difference, as shown by

$$d\rho = \rho_{a2} - \rho_{a1}. \quad (9)$$

It has been proven by experimental data that  $d\rho$  is a very sensitive indicator for homogeneous suspended bubbles. However, using  $d\rho$  for the detection does not directly show how much gas content there is, and also normal users have no direct physical feeling with this parameter. Therefore, an intuitive indicator is of more practical use and has been developed.

It is shown by Equation (6) that the speed of sound  $c$  can be obtained with the help of the knowledge of  $f_0$ , which is the outcome of Equation (8) with MFT. The GVF of the homogeneously distributed suspended bubbles can then be derived by using Equation (5). Certain simplification can be made to this equation to facilitate the GVF calculation. As explained, MFT directly outputs the true mixture density for a medium with suspended bubbles. It is known that a two-phase mixture density is calculated by

$$\begin{aligned} \rho &= \rho_l(1 - \alpha) + \rho_g\alpha \\ &\approx \rho_l(1 - \alpha). \end{aligned} \quad (10)$$

Therefore, Equation (5) can be rewritten as

$$c = \left[ \frac{\alpha}{c_g^2} + \frac{(1 - \alpha)^2}{c_l^2} + \frac{\alpha\rho}{\gamma P} \right]^{-\frac{1}{2}}. \quad (11)$$

Equation (11) enables a solution of  $\alpha$ , the gas content of suspended bubbles, based on the knowledge of the fluid properties of the gas and the liquid phases, together with the pressure in the measuring tube of the meter.

For the purpose of detection, the corresponding indicator can thus be defined as

$$I_{SB} = \alpha. \quad (12)$$

### 3. Application of the two indicators

To validate the two derived indicators, a field test was performed in one application in Chemical industry, where a chemical material in a big tank is processed and then pumped into smaller containers in small batches, as depicted in Figure 7. This product captures large amount of suspended micro bubbles during the manufacturing process because of its high viscosity. In the meanwhile, free bubbles can exist when the liquid level in the big tank is so low that the pump starts to suck in air. For the sake of product quality, entrained gas, no matter suspended bubbles or free bubbles, should be removed to a minimum level. Therefore, it is crucial to identify the bubble type, because the identification provides the process insight, enabling the possibility for process optimization based on this information. If certain amount of homogeneous suspended micro bubbles is detected, which is above the allowed threshold, a corresponding measure, for example more vacuum time in the tank to extract bubbles out of the liquid, should be applied to improve the product quality. On the other hand, the detection of free bubbles indicates an insufficient liquid level in the big tank and requires corresponding operations to handle this problem, for example, raising the liquid level in the tank.

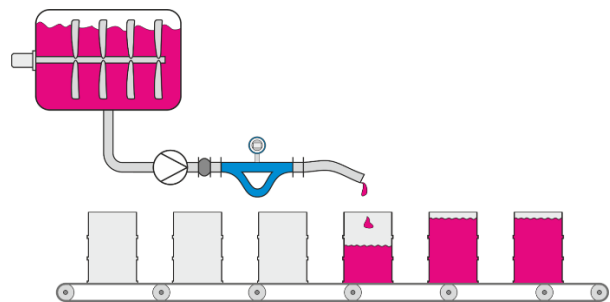


Figure 7: Production process

To generate unwanted process conditions that lead to bad product quality, two scenarios were created for the validation test: 1) low liquid level in the tank for some batches to generate free bubbles; 2) less vacuum time than the normal one applied in the tank

for some batches to generate suspended bubbles. The test results shown in Figures 8 and 9 clearly validated the ability of the two indicators for the detection of corresponding bubble pattern: the red markers represent the upset conditions, and the indicators accordingly gave high values than the others under normal conditions.

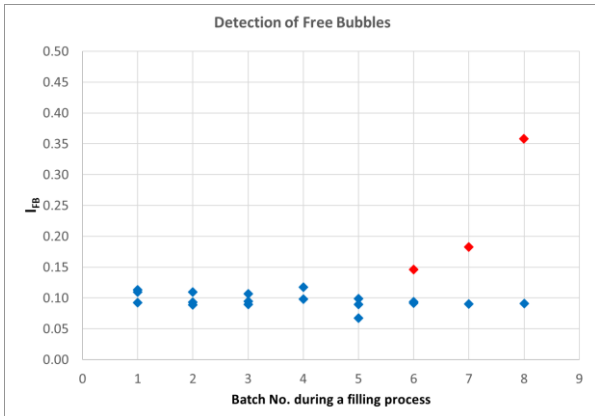


Figure 8: Detection of free bubbles (red: low liquid level)

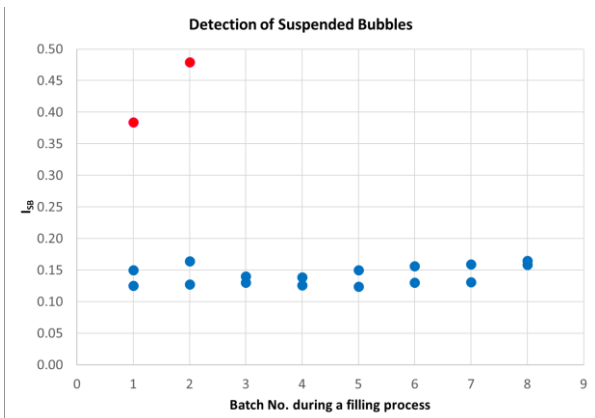


Figure 9: Detection of suspended bubbles (red: less vacuum time)

#### 4. Conclusion

Free bubbles and suspended bubbles have different influence on Coriolis metering, and also cause the corresponding changes of different measurement signals. Free bubbles typically lead to an inhomogeneous density reading of a Coriolis meter when the medium is flowing, which can directly be used for the detection. A unique feature of MFT in Promass Q enables the quantitative calculation of the amount of suspended bubbles, although they are usually homogeneously distributed and show a constant medium density to the meter. Identification of the type of bubbles helps not only for crediting the measurement reliability, but also for obtaining more

detailed medium properties, and in turn a better process insight, with which a process optimization can be enabled to improve the quality of production.

#### References

- [1] M. Fuchs, W. Drahm, C. Matt and A. Wenger, "Coriolis mass flow meter with direct viscosity measurement", *Flomeko 2003*, 2003
- [2] H. Zhu, *Application of Coriolis Mass Flowmeters in Bubbly and Particulate Two-Phase Flows*, Shaker, 2009
- [3] H. Zhu, A. Rieder and Y. Lin, "an innovative technology for Coriolis metering under entrained gas condition", *Flomeko 2016*, 2016
- [4] J. Hemp and G. Sultan, "on the theory and performance of Coriolis mass flow meter", in *Proceedings of the International Conference on Mass Flow Measurement*, 1989

# Molten salt flow calibration facility by dynamic weighing method base on argon pressure balance principle

Chao Chen<sup>1</sup>, Jin Song<sup>2</sup>, Yiping Liu<sup>3</sup>, Jinchuan Wu<sup>4</sup>

<sup>1</sup>Shanghai Institute of Measurement and Testing Technology, No1500 Zhangheng Rd., Shanghai, China

<sup>2</sup>Shanghai Institute of Measurement and Testing Technology, Shanghai, China

<sup>3</sup>Shanghai Institute of Measurement and Testing Technology, Shanghai, China

<sup>4</sup>Shanghai Institute of Measurement and Testing Technology, Shanghai, China

E-mail: chenc@simt.com.cn

## Abstract

Thorium-based molten salt has the characteristics of high temperature, low pressure, high chemical stability and high heat capacity, which can be used as coolant for the molten salt reactor. The high-temperature molten salt flow meters need to measure, display and record the flow parameters in the reactor of molten salt circuit, and monitor the operating conditions of the molten salt reactor equipment, ensuring the safe and reliable operation of the reactor. However, there is no good calibration method for the high-temperature molten salt flow meter in China.

We have established high-temperature molten salt flow calibration facility by dynamic weighing method base on argon pressure balance principle. The flow range is (1~30) m<sup>3</sup>/h, and the operating temperature range is from 600°C to 650 °C. The expanded uncertainty is  $U_{rel}=1.3\%$  ( $k=2$ ). The calibration facility has the characteristics of using less amount of molten salt, fast response and stable temperature. The configuration of the facility, working principle, main technical specification, data processing methods and uncertainty evaluation are described in this paper. High-temperature molten salt flowmeter of DN25-DN50 can be calibrated in the facility, the traceability problem of the high-temperature molten salt flowmeters can be solved.

## 1. Introduction

Molten Salt Reactor (MSR) is one of the six candidate nuclear energy systems selected by the Fourth Generation Nuclear Energy International Forum (GIF). MSR has many advantages in radioactive waste treatment, inherent safety and nuclear proliferation prevention. It is the development trend of nuclear energy in various countries. Through the comprehensive utilization of nuclear energy, it can alleviate the problems of carbon emissions and environmental pollution.

In order to ensure safe and reliable operation of the reactor, the high-temperature molten salt flowmeters are used in the molten salt reactor. Therefore, it is necessary to calibrate the high-temperature molten salt flowmeters. The liquid flow standard facility can be divided into three types, volumetric method, gravimetric method and master meter method. At present, the majority of liquid flow standard facility's working medium is oil or water,

and the operating temperature of the facility is usually normal temperature. If the high-temperature molten salt flowmeters with medium temperature higher than 600 °C is calibrated with normal liquid flow standard facility, it will cause the problem that the calibration condition is inconsistent with the actual working conditions, so the flowmeters cannot be calibrated accurately.



Figure 1: The photograph of molten salt flow calibration facility

Moreover, most of high-temperature molten salt flowmeters are ultrasonic flowmeters, the velocity of ultrasonic in the high-temperature molten salt is different from the velocity of ultrasonic in water or oil, which will also cause greater impact for the high-temperature molten salt flowmeters.

In order to solve the calibration problem of high-temperature molten salt flowmeters, molten salt flow calibration facility is established in China, calibration facility is shown in Figure 1, which is based on argon pressure balance principle. The calibration facility has the characteristics of using less amount of molten salt, fast response and stable temperature.

## 2. Composition and working principle

### 2.1 Composition of standard facility

Calibration facility is made of electric balances, molten tanks, measuring pipeline, argon pressure control system, heating and insulation system, level meters, pressure transmitter, temperature transmitter, data acquisition system and control system. Because of strong corrosion and toxicity of the high temperature molten salt, the standard facility adopts a closed loop structure to ensure the safe operation. The schematic diagram of standard facility is shown in Figure 2. Two measuring pipelines are connected to the bottom of the molten salt tanks respectively, argon pressure control pipeline are connected to the upper part of the molten salt tank, and the level meters are installed the top of molten salt tank to monitor the molten salt level. The pressure transmitter and temperature transmitter are installed on two molten salt tanks to measure the temperature and pressure in the molten salt tank. The high temperature molten salt flow meter under test is installed on the horizontal measuring pipeline.

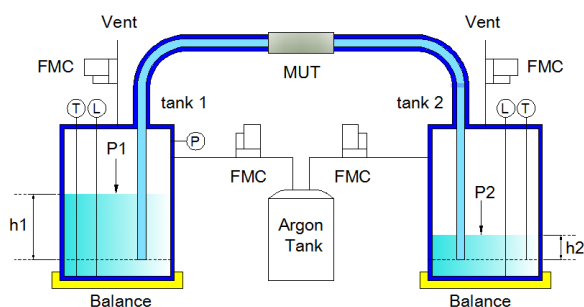


**Figure 2:** The schematic diagram of standard facility

In order to minimize to use the amount of molten salt and ensure the temperature stability of the medium, the standard facility uses argon pressure as the water head for the medium in the molten salt tank rather than using the conventional pump. The differential pressure in the two molten salt tanks will realize the flow of the high-temperature molten salt by controlling the pressure of the two molten salt tanks. The siphon phenomenon is

generated in the measuring pipeline, so the measuring pipe is in fully charged in the molten salt. The different calibration flow can be controlled by adjusting the differential pressure between the molten salt tanks.

### 2.2 Working principle

Before operating, the high temperature molten salt is heated to the required working temperature, adjusting the pressure in the tank 2 is a little bit higher than the pressure of the tank1, so that the molten salt is completely back to the tank 1.

At the beginning of the calibration, the pressure control system fills the tank 1 with argon quickly, and simultaneously opens the tank 2 exhaust valve to release the argon pressure of the tank 2. At this time, a differential pressure is generated between the two tanks. Then the molten salt in the tank 1 flows through the meter under test, and flows into the tank 2. The pressure control system adjusts the differential pressure continuously between the two tanks to make the flowrate stable, and the data acquisition system records the initial mass  $M_0$  of the molten salt in the tank 1, meanwhile system recording the output signal of the meter under test. During the measurement, the parameter of mass, temperature, pressure and liquid level in the two molten salt tanks are monitored. The pressure of the argon in the two molten salt tanks is controlled by the mass flow controller to maintain molten salt flow stability. When the measurement time is up, the finishing mass  $M_1$  of the molten salt in the tank 1 is recorded, meanwhile stoping recording the output signal of the meter under test, and the first time of calibration is completed.

Closing the intake valve of the tank 1, and opening the exhaust valve to release the pressure in the tank 1 to reduce the pressure of the tank 1, then opening the intake valve of tank 2 to refill the argon, increasing the pressure in the tank 2 to make the all molten salt back to tank 1, and waiting for the next measurement.

## 3. Mathematical model of flow controlling

Since the molten salt is an incompressible fluid, it conforms to the Bernoulli equation:

$$\frac{P_1}{\rho g} + \frac{v^2}{2g} + h_1 = \frac{P_2}{\rho g} + \frac{v^2}{2g} + h_2 + \sum \lambda \frac{Lv^2}{2dg} + \sum \xi \frac{v^2}{2g} \quad (1)$$

Where  $P_1$  is the pressure of tank 1,  $P_2$  is the pressure of tank 2,  $\rho$  is the density of molten salt,  $g$  is the gravity acceleration,  $v$  is the velocity of measuring pipe,  $h_1$  is the molten salt level of the tank 1,  $h_2$  is the molten salt level of the tank 2,  $\lambda$  is coefficient of friction losses,  $L$  is the length of pipe,  $d$  is diameter of pipe, and  $\xi$  is coefficient of local losses.

After deforming the formula (1):

$$(P_1 - P_2) + \rho g(h_1 - h_2) = \left( \sum \lambda \rho \frac{L}{d} + \sum \xi \rho \right) \frac{v^2}{2}$$

Assuming:

$$\Delta P = (P_1 - P_2) + \rho g(h_1 - h_2)$$

$\Delta P$  includes two items, the first item ( $P_1 - P_2$ ) is the pressure difference between the two tanks; the second item is the pressure difference caused by the difference in the level of the molten salt in the two tanks. Under the action of argon pressure, the molten salt flows from the tank 1 to the tank 2 continuously,  $h_1$  will continue to decrease the molten salt level in tank 1, while  $h_2$  increase continuously. To maintain  $\Delta P$  stability, the pressure  $P_1$  in tank 1 needs continue to increase, and the pressure  $P_2$  in tank 2 needs to decrease constantly, and the pressure difference ( $P_1 - P_2$ ) between the two tanks varies with the liquid level of the molten salt.

Assuming:

$$K = \left( \sum \lambda \rho \frac{L}{d} + \sum \xi \rho \right)$$

Then the velocity of the pipe can be expressed as:

$$v = \sqrt{\frac{2\Delta P}{\rho K}} \quad (2)$$

The flow rate in the pipe can be expressed as:

$$q_v = \frac{\pi d^2}{4} v = \frac{\pi d^2}{4} \sqrt{\frac{2\Delta P}{\rho K}} \quad (3)$$

During the measurement, the molten salt properties and the pipe characteristics will not change, it can be considered that  $\rho$ 、 $K$  and  $d$  are constant, so the flowrate will stabilize as long as  $\Delta P$  is stable.

#### 4. The method of data processing

The standard facility is based on the principle of dynamic gravimetric method, and there is no diverter to start and stop the chronometer. Therefore, there is a certain difference between the actual measuring time and the measuring time of the flowmeter. It is necessary to correct the actual measuring time of the standard facility to the time of meter under test, and then the indication error of the flowmeter can be calculated accurately.

The measured mass of the standard facility at the measurement time is:

$$M_s = M_1 - M_0 \quad (4)$$

The actual molten salt volume of the standard facility is:

$$V_a = C_f \frac{M_s}{\rho} \quad (5)$$

Since the measurement time of the actual volume  $V_a$  and the indicated volume  $V_i$  of the flowmeter are inconsistent, it is necessary to correct the actual volume  $V_a$  to the volume of meter under test in  $t_i$ . The corrected indication error of the flowmeter is:

$$E_m = \frac{V_i - \frac{t_i}{t_a} V_a}{\frac{t_i}{t_a} V_a} \times 100\% = \left( \frac{V_i \bullet t_a}{V_a \bullet t_i} - 1 \right) \times 100\%$$

$$= \left( \frac{V_i \bullet \rho \bullet t_a}{\Delta M \bullet C_f \bullet t_i} - 1 \right) \times 100\% \quad (6)$$

Where  $t_i$  is the measurement time of meter under test and  $t_a$  is the actual measurement time of the standard facility.

#### 5. Experiments

Flowrate stability is a very important performance of the liquid flow standard facility. It is an important parameter for evaluating the measurement performance of the liquid flow standard facility. The method for evaluating the flowrate stability of the liquid flow standard facility has two methods, flowrate stability within the integration interval, the former mainly considers the long-term stability of the standard facility and it is well known. The high-temperature molten salt flow standard facility is based on argon pressure balance, so using the method of flowrate stability within the integration interval to evaluate flowrate stability is more scientific.

##### 5.1 the method of flowrate stability

The output signal of the flowrate  $q_{1i}$  is recorded continuously ( $i = 1, 2, 3, \dots, n \geq 60$ ).

The average flowrate is:

$$q_1 = \frac{\sum_{i=1}^n q_{1i}}{n} \quad (7)$$

The relative error is:

$$E_i = \frac{q_{1i} - q_1}{q_1} \times 100\% \quad (8)$$

The autocorrelation function  $R_j$  is calculated.

The autocorrelation function:

$$R_j = \frac{\sum_{i=1}^{n-j} E_i \cdot E_{i+j}}{n-j} \quad (9)$$

Where  $j=0,1,2,\dots,n-1$  is the succession step,  $i$  is the running succession number.

The normalized autocorrelation function, the combination of the coefficients of correlation is determined from :

$$r_j = \frac{R_j}{R_0} \quad (10)$$

The flowrate within the integration interval is :

$$E_{q1} = k \left[ \frac{2}{n} \sum_{j=1}^{j_{\min}} |R_j| \right]^{1/2} \times 100\% \quad (11)$$

Where  $j=0,1,\dots, j_{\min}$  ( $j_{\min}$  is the smallest rank from which  $r_j$  is less than or equal to 0.1).

### 5.2 Measurement datas

According to the method of flowrate stability within the integration interval, the flowrate stability is carried out at maximum flowrate and at minimum flowrate respectively. The flowrate stability test results are shown in Table 1 and Table 2.

**Table 1:** The test results at minimum flowrate  $\text{m}^3/\text{h}$

No. 1-10	No. 11-20	No. 21-30	No. 31-40	No. 41-50	No. 51-60
0.9876	0.9893	0.9788	0.9551	0.9615	0.9886
0.9814	1.0137	0.9494	0.9691	0.9768	0.9798
0.9899	1.0016	0.9836	0.9748	0.9987	0.9781
0.9981	0.9936	0.9550	1.0066	1.0074	0.9489
0.9855	0.9617	0.9929	1.0017	0.9915	0.9719
1.0073	0.9561	0.9519	0.9817	0.9657	0.9649
0.9964	0.9583	0.9924	0.9865	0.9894	0.9656
0.9964	0.9625	0.9924	0.9827	0.9838	0.9727
0.9613	0.9849	0.9898	0.9812	0.9822	0.9638
0.9937	0.9871	0.9900	0.9652	0.9613	0.9644

**Table 2:** The test results at maximum flowrate  $\text{m}^3/\text{h}$

No. 1-10	No. 11-20	No. 21-30	No. 31-40	No. 41-50	No. 51-60
18.871	18.851	18.829	18.941	19.000	18.874
18.646	18.909	19.023	19.057	18.969	18.683
18.670	19.080	18.960	18.963	18.907	18.668
18.817	19.096	19.022	18.880	18.830	18.720
18.978	19.080	18.749	18.777	18.912	18.708
19.116	18.978	18.872	18.814	18.742	18.721
18.922	18.853	18.839	18.909	18.896	18.754
18.879	18.790	18.957	18.964	18.936	18.739
18.867	18.750	18.753	18.935	19.078	18.862
18.891	18.785	18.787	19.035	18.917	18.821

### 5.3 The results of flowrate stability

The flowrate is relatively stable at minimum flowrate, However, the flowrate has a little bit decrease within the measuring time. Because the flowrate is small, the flowrate stability duration time can last up to 400s. The minimum flowrate stability of the standard facility is

0.32% can be achieved. Then the control flowrate stable is very difficult at maximum flowrate, the flowrate fluctuation is more obvious than the minimum flowrate, and the duration of the flow stability is relatively short. The maximum flowrate stability of the standard facility is 0.87% can be calculated. The flowrate stability test results at different flowrates are shown in Figure 3 and Figure 4.

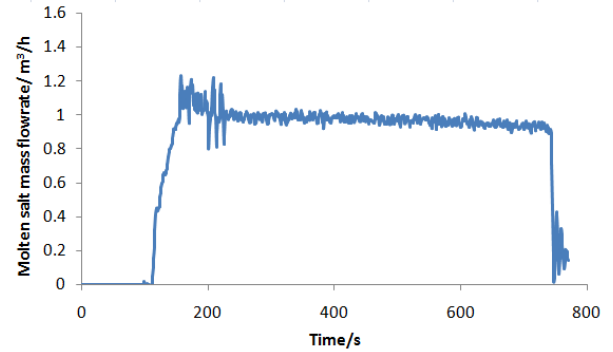


**Figure 3** Flowrate stability results of minimum flowrate

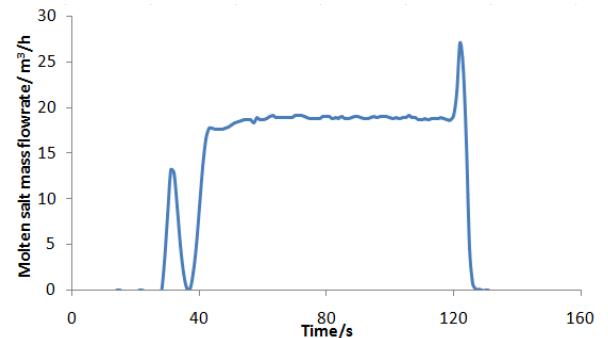


**Figure 4** Flowrate stability results of maximum flowrate

## 6. Uncertainty evaluation

When the high-temperature molten salt flow meters calibrated with molten salt flow calibration facility, it needs to convert display mass of electronic balance to actual volume based on density of molten salt, During the actual working condition, the reference volume is also related to the temperature change of the molten salt and the bubbles in the molten salt. The reference volume of the standard facility at the high temperature molten salt flowmeter is:

$$V_{ref} = \frac{M_s}{\rho} C_f + \Delta V_P + \Delta V_B \quad (12)$$

Where  $V_{ref}$  is the reference volume of the standard pressure at meter under test,  $M_s$  is the actual mass of the electrical balance,  $\rho$  is the density of molten salt,  $C_f$  is the coefficient of buoyancy,  $\Delta V_P$  is the

changeable volume of the measuring pipe,  $\Delta V_B$  is the volume of the bubble in molten salt.

### 6.1 Standard uncertainty of electrical balance $u_{M_s}$

#### 6.1.1 Uncertainty of calibrating electrical balance $u_{M_{s1}}$

The full scale of the electrical balance is 1500 kg being used in the molten salt flow calibration facility, the electrical balance is used at 3 fixed points, which is 800kg at the maximum flowrate, 400kg at the medium flowrate and 200kg at minimum flowrate respectively. According to the calibration certification of the electrical balance, the expanded uncertainty is 0.5kg ( $k=2$ ) at 800kg.

The standard uncertainty caused by the calibration of the electrical balance at maximum flowrate is:

$$u_{M_{s1}} = \frac{0.5}{2} = 0.25 \text{ kg}$$

#### 6.1.2 Standard uncertainty of deviation of electrical balance $u_{M_{s2}}$

According to the calibration certification of the electrical balance, the deviation of electrical balance is 1.0kg, ( $k=2$ ) at 800kg.

The standard uncertainty caused by the deviation of the electrical balance at maximum flowrate is:

$$u_{M_{s2}} = \frac{1.0}{\sqrt{3}} = 0.58 \text{ kg}$$

#### 6.1.3 Standard uncertainty caused by resolution of the electrical balance $u_{M_{s3}}$

According to the display of the electrical balance, the resolution of electrical balance is 0.5kg.

The standard uncertainty caused by resolution of the electrical balance is:

$$u_{M_{s3}} = \frac{0.5}{\sqrt{3}} = 0.29 \text{ kg}$$

#### 6.1.4 Standard uncertainty caused by connecting pipe stress $u_{M_{s4}}$

Because the high-temperature molten salt flow calibration facility is a sealing system, the connecting pipe will stress the electronic balance when the molten salt flows. The maximum uncertainty caused by connecting pipe stress is 1.2kg. The standard uncertainty caused by the connecting pipe stress at maximum flowrate is:

$$u_{M_{s4}} = \frac{1.2}{\sqrt{3}} = 0.69 \text{ kg}$$

#### 6.1.5 The calculation of standard uncertainty of input quantity $M_s$

The standard uncertainty of  $M_s$  is :

$$u_{M_s} = \sqrt{u_{M_{s1}}^2 + u_{M_{s2}}^2 + u_{M_{s3}}^2 + u_{M_{s4}}^2}$$

$$= \sqrt{0.25^2 + 0.58^2 + 0.29^2 + 0.69^2} = 1.0 \text{ kg}$$

Sensitivity coefficient is:

$$c(M_s) = \frac{\partial V_{ref}}{\partial M_s} = \frac{C_f}{\rho} = 0.0005 (\text{m}^3/\text{kg})$$

### 6.2 Standard uncertainty of molten salt density $u_\rho$

#### 6.2.1 Standard density uncertainty caused by temperature transmitter $u_{\rho 1}$

The range of the temperature transmitter is (0 ~ 1000) °C, the maximum permissible error of the temperature transmitter is  $\pm 5$  °C. The maximum deviation of density caused by the temperature is 3.2kg/m<sup>3</sup>. The standard density uncertainty caused by temperature transmitter is:

$$u_{\rho 1} = \frac{3.2}{\sqrt{3}} = 1.9 \text{ kg/m}^3$$

#### 6.2.2 Standard uncertainty caused by the deviation between the molten salt density function and the actual value of the molten salt $u_{\rho 2}$

Since the molten salt density is calculated by the temperature, and then calculating the density of the molten salt, there is a certain deviation between the calculated density and the actual density. According to the relevant reference information, it is known that the maximum deviation of the molten salt density is 16 kg/m<sup>3</sup>. The standard density uncertainty caused by the deviation between the molten salt density function and the actual value of the molten salt is :

$$u_{\rho 2} = \frac{16}{\sqrt{3}} = 9.2 \text{ kg/m}^3$$

#### 6.2.3 Standard uncertainty caused by measurement position of the temperature $u_{\rho 3}$

Because the temperature sensor cannot measure the temperature of the medium at the right position of high-temperature molten salt flowmeter, which will cause some difference of the temperature. The maximum temperature deviation that measured in different positions is 3 °C, The maximum density deviation 1.9 kg/m<sup>3</sup>. The standard density uncertainty caused by the measurement location of the temperature is:

$$u_{\rho 1} = \frac{1.9}{\sqrt{3}} = 1.1 \text{ kg/m}^3$$

#### 6.2.4 The calculation of standard uncertainty of input quantity $\rho$

The standard uncertainty of  $\rho$  is :

$$u_\rho = \sqrt{u_{\rho 1}^2 + u_{\rho 2}^2 + u_{\rho 3}^2}$$

$$= \sqrt{1.9^2 + 9.2^2 + 1.1^2} = 9.5 \text{ kg/m}^3$$

Sensitivity coefficient at maximum flowrate is:

$$c(\rho) = \frac{\partial V_{ref}}{\partial \rho} = -\frac{M_s C_f}{\rho^2} = -0.0002 \text{ (m}^3\text{)}^2/\text{kg}$$

### 6.3 Standard uncertainty of air buoyancy coefficient

$u_{C_f}$

Standard uncertainty of air buoyancy coefficient mainly depends on the density of the molten salt and the density of the air in the laboratory environment, the maximum changeable of the buoyancy correction factor is 0.0001. The standard uncertainty caused by air buoyancy coefficient is:

$$u_{C_f} = \frac{0.0001}{\sqrt{3}} = 0.000058$$

Sensitivity coefficient at maximum flowrate is:

$$c(C_f) = \frac{\partial V_{ref}}{\partial C_f} = \frac{M_s}{\rho} = 0.40 \text{ m}^3$$

### 6.4 Standard uncertainty caused by changeable volume of the measuring pipe $u_p$

The temperature of molten salt will not change more than 5 °C during one measurement, the volume from the molten salt inlet line to the high temperature molten salt flowmeter is 0.1 m<sup>3</sup>. The volume expansion coefficient of molten salt is  $2.6 \times 10^{-4}/^\circ\text{C}$ , The changeable volume is:

$$\Delta V_p = V_p \times \beta_w \times \Delta t$$

$$= 0.1 \times 0.00026 \times 5 = 0.00013 \text{ m}^3$$

The standard density uncertainty caused by the changeable volume of the measuring pipe is:

$$u_p = \frac{0.00013}{\sqrt{3}} = 0.00008 \text{ m}^3$$

Sensitivity coefficient is:

$$c(V_p) = \frac{\partial V_{ref}}{\partial V_p} = 1$$

### 6.5 Standard uncertainty caused by the bubble in molten salt $u_B$

Small bubbles may be exist in the molten salt medium during the test, the working pressure of the standard facility is 0.2MPa, The volume of bubbles in the molten salt is 0.06L. The standard uncertainty caused by the bubble in molten salt is:

$$u_B = \frac{0.06 \times 0.4}{\sqrt{3}} = 0.014 \text{ L}$$

Sensitivity coefficient is:

$$c(V_E) = \frac{\partial V_{ref}}{\partial V_E} = 1$$

### 6.6 Calculation of expanded uncertainty

Based on the calculated standard uncertainty of each input quantity, the expanded uncertainty of the uncertainty can be calculated at maximum flowrate, The uncertainty summary is shown in Table 3.

**Table 1:** The uncertainty summary at minimum flowrate

No	Uncertainty	Source	$u(x_i)$	$C_i$	$ c_i u(x_i)$
1	$u_{M_s}$	Mass	1.0kg	0.0001 m <sup>3</sup> /kg	0.0005m <sup>3</sup>
2	$u_\rho$	density	9.5m <sup>3</sup> /kg	-0.0002 (m <sup>3</sup> ) <sup>2</sup> /kg	0.0019m <sup>3</sup>
3	$u_{C_f}$	Buoyancy	0.000058	0.4 m <sup>3</sup>	0.00002m <sup>3</sup>
5	$u_P$	Pipe volume	0.00008 m <sup>3</sup>	1	0.00008m <sup>3</sup>
6	$u_B$	Bubble	0.000014 L	1	0.000014m <sup>3</sup>

Combined standard uncertainty:  $u_c = 0.0020 \text{ m}^3$

Relative uncertainty at maximum flowrate:

$$u_{rc} = \frac{0.0020 \times 2022}{800} \times 100\% = 0.50\%$$

Expanded uncertainty at maximum flowrate:

$$U_{rel} = k u_{rc} = 2 \times 0.50\% = 1.0\%$$

Using the same method, the expanded uncertainty at minimum flowrate also can be calculated  $U_{rel} = 1.3\%$  ( $k=2$ ).

## 7. Conclusion

High-temperature molten salt flow calibration facility by dynamic weighing method base on argon pressure balance principle is established in China. The unique flowrate driving method is used in the standard facility, The calibration facility has the characteristics of using less amount of molten salt, fast response and stable temperature. Test results show that the flowrate stability is better than 0.9%, which can be meet the requirement of calibrating high-temperature molten salt flowmeters.

## References

- [1] JIN Yuan, CHENG Jinhui, WANG Kun, *Thermal study several typical molten salt coolant*. Nuclear Technology, 2016, 39(5).
- [2] Yanxun Su, Guowei Liang, Jian Sheng, *Flow Metrology and Measurement (second edition)*
- [3] Chi Wang, *Analysis on uncertainty of flow measurement*, Beijing: China Metrology Publishing House, 2002.
- [4] Gill D D, Kolb W J, Briggs R J, *An evaluation of pressure and flow measurement in the molten salt test loop system*. SAND2013-5366, US: Sandia National Laboratories, 2013.

# Flow Measurement Turn Down Analysis for DP Flow Meter using Multiple Multivariable Transmitters

Akio Ito<sup>1</sup>, Hiromasa Takiguchi<sup>1</sup>, Aya Morokata<sup>1</sup>, Vince Cisar<sup>2</sup>

<sup>1</sup>Yokogawa Electric Corporation, Musashino-shi, Tokyo, Japan

<sup>2</sup>VERIS Flow Measurement Group, Armstrong International, Frederick, CO, USA

E-mail (corresponding author): Akio.Itou@jp.yokogawa.com

## Abstract

We conducted differential pressure (DP) flow meter calibration at CEESI and observed that the combined linearity of VERIS Accelabar® flow primary element and Yokogawa EJX910 multivariable transmitter DP measurement indicated excellent performance. The observation result was that linearity with reference flow rate was 0.5% with 15:1 turndown for the EJX910 H range with the 4" VERIS Accelabar® during the 800 psia air test. EJX910 has also L range and we show that adding L range, flow measurement turndown will be increased beyond 15:1 until 20:1. Firstly we show flow rate equation and uncertainty of the combined flow meter. We assume that VERIS Accelabar® flow uncertainty contribution is 0.5% with 20:1 turndown derived by previous experiments. Also, we assume the density contribution as 0.1%. Then, EJX910 L range DP uncertainty at 20:1 turndown point is analysed. With assumption of using L range data tested at the factory, DP measurement uncertainty including reference accuracy and static pressure (SP) span effects is assumed as 0.24%. Flow uncertainty is calculated as 0.52%, which is almost 0.5%. EJX910 is designed with multi-sensing capabilities using built-in silicon resonant sensor technology. EJX910 dynamically & continuously minimizes the effect of SP fluctuation with two resonators incorporated into one sensor tip and provides precise DP measurement. This shows that EJX910 has an advantage of low DP measurement under high SP condition. This indicates the latest progress of DP flow meter technology and the DP flow meter has still big potential for use in industry widely.

## 1. Introduction

We conducted differential pressure (DP) flow meter calibration at CEESI located at Nunn, Colorado, USA in 2015 and observed that the combined linearity of VERIS Accelabar® flow primary element and Yokogawa EJX910 multivariable transmitter DP measurement indicated excellent performance [1] (See Figure 1 to 3). The VERIS Accelabar® is a flow primary element which combines a unique toroidal nozzle design with the VERIS Verabar® averaging pitot tube [2]. The Yokogawa EJX910 is a multivariable transmitter based on pressure transmitter, which is designed with multi-sensing capabilities using built-in silicon resonant sensor technology [3].

The observation result was that linearity with reference flow rate was 0.5% with 15:1 turndown for the EJX910 H range (DP: 2000inH<sub>2</sub>O) with the 4" VERIS Accelabar® during the SP: 800 psia air test. CEESI flow facility reference flow uncertainty was 0.3%-0.46% during the flow range.

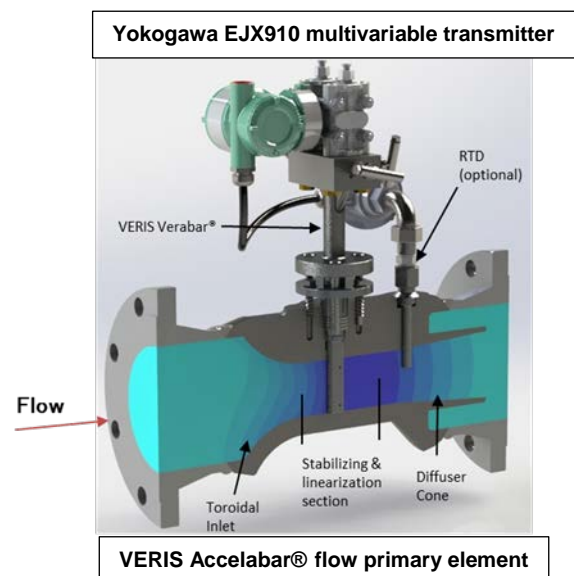
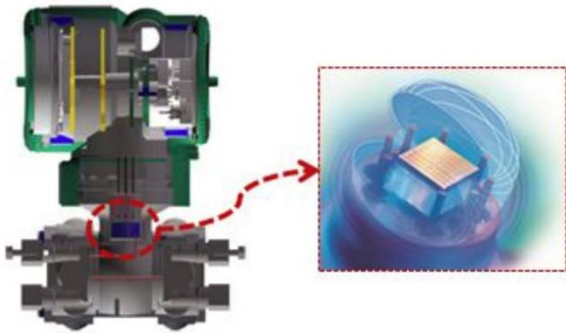
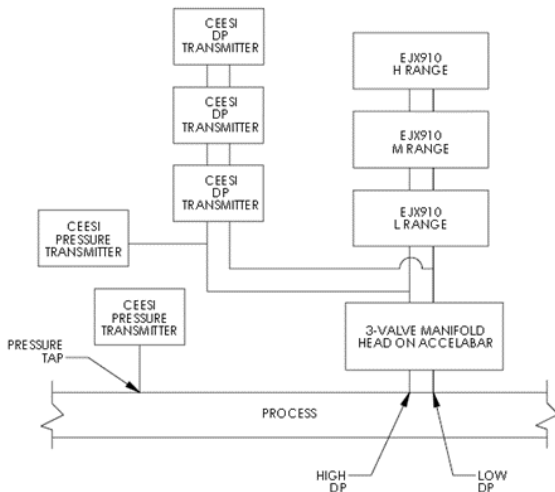


Figure 1: Combined DP flow meter VERIS Accelabar® and Yokogawa EJX910



**Figure 2: EJX910 multivariable transmitter with silicon resonant sensor**



**Figure 3: Instrument connections at CEESI calibration**

EJX910 has also L range (DP: 40inH2O) transmitter and capability of using for low flow rate measurement. In this paper, we show that adding L range transmitter with H range transmitter, flow measurement turndown will be increased beyond 15:1 until 20:1. Also we show that EJX910 has an advantage of low DP measurement under high static pressure (SP) condition.

## 2. Flow calibration result at CEESI

### 2.1 Result using single multivariable transmitter

The combined linearity of VERIS Accelablar® flow primary element and Yokogawa EJX910 DP measurement was 0.5% with 15:1 turndown. The result was obtained using single EJX910 H range (2000inH2O). The result is shown in Figure 4 [1].

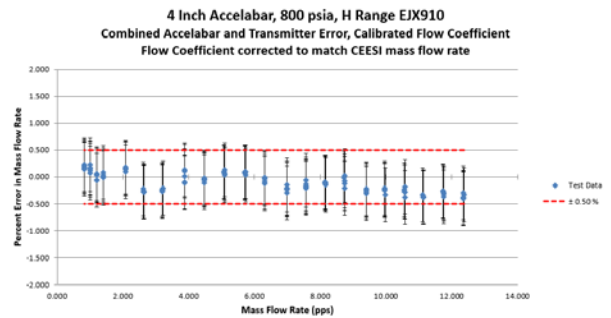


**Figure 4: Flow measurement result using single multivariable transmitter (0.50% Accuracy, 15:1 Turndown).**

### 2.2 Flow rate equation at the CEESI test

We show flow rate equation of the combined flow meter EJX910 and VERIS Accelablar® [4].

$$q_m = \frac{\pi}{4} K \epsilon D^2 \sqrt{2 \Delta P \rho_f} \quad (1)$$

Where

- K stands for flow coefficient
- $\epsilon$  stands for expansibility
- D stands for diameter of the conduit
- $\Delta P$  stands for DP
- $\rho_f$  stands for density

The maximum flow rate at the test is around 12.4 lb/sec where DP is around 890inH2O. Minimum flow rate is around 0.62 lb/sec where DP is around 3.9inH2O. The flow turndown is calculated as below.

$$\text{Flow turn down} = \frac{12.4 \text{ lb/sec}}{0.62 \text{ lb/sec}} = 15.1 \quad (2)$$

The flow turndown 20:1 flow rate from the maximum flow point 12.4 lb/sec is as below.

$$20:1 \text{ flow point} = \frac{12.4 \text{ lb/sec}}{20} = 0.62 \text{ lb/sec} \quad (3)$$

Corresponding DP  $\Delta P_{20:1}$  is as below, assuming K and  $\epsilon$  difference is small around 15:1 flow rate  $q_{m(15:1)}$  and 20:1 flow rate  $q_{m(20:1)}$ .

$$q_{m(15:1)} = \frac{\pi}{4} K \epsilon D^2 \sqrt{2 \Delta P_{15:1} \rho_f} \quad (4)$$

$$q_{m(20:1)} = \frac{\pi}{4} K \epsilon D^2 \sqrt{2 \Delta P_{20:1} \rho_f} \quad (5)$$

$$\Delta P_{20:1} = \frac{q_{m(20:1)}^2}{q_{m(15:1)}^2} \times \Delta P_{15:1} = \frac{0.62^2}{0.82^2} \times 3.9 = 2.2 \text{ inH2O} \quad (6)$$

We will analyse 20:1 flow point uncertainty and confirm if flow measurement turndown will be increased beyond 0.5% 15:1 until 20:1 in case of adding L range transmitter.

### 3. Combined flow uncertainty

We show general equation of combined flow uncertainty of the flow meter [4].

$$\frac{\delta q_m}{q_m} = \sqrt{\left(\frac{\partial K}{K}\right)^2 + \left(\frac{\partial \varepsilon}{\varepsilon}\right)^2 + \left(\frac{2\partial D}{D}\right)^2 + \left(\frac{\partial \Delta P}{2\Delta P}\right)^2 + \left(\frac{\partial \rho}{2\rho}\right)^2} \quad (7)$$

The uncertainty contribution of VERIS Accelabar®  $Uncert_{pe}$  is as below.

$$Uncert_{pe} = \left(\frac{\partial K}{K}\right)^2 + \left(\frac{\partial \varepsilon}{\varepsilon}\right)^2 + \left(\frac{2\partial D}{D}\right)^2 \quad (8)$$

In this paper, we assume that VERIS Accelabar® flow uncertainty contribution is 0.5% with 20:1 turndown derived by previous experiments [5].

$$\sqrt{\left(\frac{\partial K}{K}\right)^2 + \left(\frac{\partial \varepsilon}{\varepsilon}\right)^2 + \left(\frac{2\partial D}{D}\right)^2} = 0.5\% \quad (9)$$

Using the assumption, below is calculated.

$$Uncert_{pe\_as} = \left(\frac{\partial K}{K}\right)^2 + \left(\frac{\partial \varepsilon}{\varepsilon}\right)^2 + \left(\frac{2\partial D}{D}\right)^2 = (0.5\%)^2 \quad (10)$$

The uncertainty contribution of the density  $Uncert_{\rho}$  is as below.

$$Uncert_{\rho} = \left(\frac{\partial \rho}{2\rho}\right)^2 \quad (11)$$

We assume below equation by current EJX910 specification [6].

$$\left(\frac{\partial \rho}{\rho}\right) = 0.1\% \quad (12)$$

Using the assumption, below is calculated.

$$Uncert_{\rho\_as} = \left(\frac{\partial \rho}{2\rho}\right)^2 = (0.05\%)^2 \quad (13)$$

After next section, we will show 0.5% turn down 20:1 is achieved by analysing EJX910 DP uncertainty under above assumption.

### 4. DP measurement uncertainty

The uncertainty contribution of the EJX910  $Uncert_{dp}$  is as below.

$$Uncert_{dp} = \left(\frac{\partial \Delta P}{2\Delta P}\right)^2 \quad (14)$$

EJX910 flow uncertainty contribution are DP uncertainty which consists of reference accuracy, ambient temperature effects, and SP effects. EJX910 L range uncertainty is described as below [6].

- Reference accuracy is defined as  $\pm 0.04\%$  of span. In this case, we assume span is configured as 40inH<sub>2</sub>O same as maximum range value.
- Ambient temperature effect per 28°C (50°F) change is defined as  $\pm (0.055\% \text{ Span} + 0.09\% \text{ URL})$ . In this test, the temperature is kept in room temperature and this effect can be ignored.
- SP effects consist of span effects and effects on zero. SP span effects per 6.9 MPa (1000 psi) change is defined as  $\pm 0.075\%$  of span. SP effect on zero per 6.9 MPa (1000 psi) change is defined as  $\pm 0.05\% \text{ URL}$ . In this test, DP zero adjustment is conducted at 800 psia condition. So, zero effect can be ignored.

### 5. L range DP comparison with CEESI master meter

We also used EJX910 L range transmitter when we conducted DP flow meter calibration at CEESI (See Figure 3). In the ISFFM paper, we only showed DP comparison between EJX910 H range and CEESI master meter [1]. Here we show L range and H range combined data in Figure 5 below 200inH<sub>2</sub>O. L range data is available below 40inH<sub>2</sub>O.

The minimum data point is around 3.9 inH<sub>2</sub>O where flow turndown is 15:1. The EJX910 L range data difference between the EJX910 H range and CEESI master meter at the point is around 2%. The EJX910 uncertainty calculated by general specification is around 1%. The CEESI master meter uncertainty is 0.8%. The uncertainty of EJX910 and the reference CEESI master meter at the point is relatively bigger than the difference. It is not possible to obtain DP uncertainty value below 3.9 inH<sub>2</sub>O point from Figure 5. In the next section, we will calculate DP uncertainty at 2.2 inH<sub>2</sub>O point corresponding to 20:1 flow point.

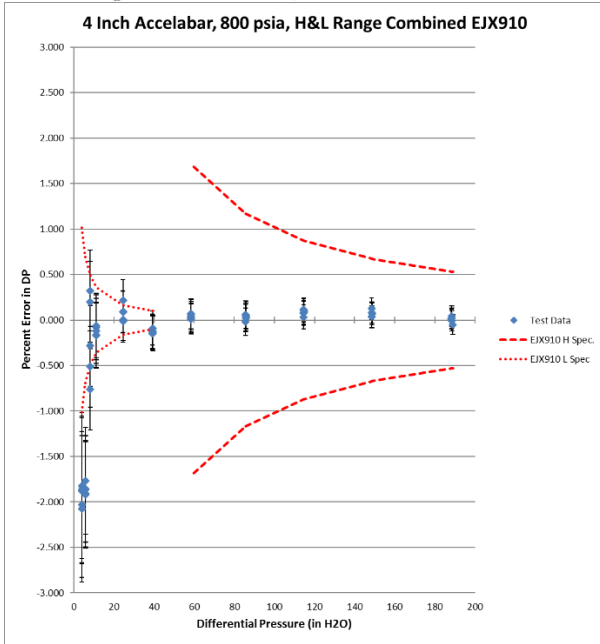


**Figure 5:** DP difference between EJX910 and CEESI master meter.

## 6. L range DP uncertainty analysis under CEESI calibration condition

EJX910 L range DP uncertainty assumption at 2.2 inH2O point under CEESI calibration condition is shown.

### 6.1 Reference accuracy

Reference accuracy is defined as  $\pm 0.04\%$  of span. From this defined accuracy, uncertainty at 2.2 inH2O point  $\left(\frac{\partial \Delta P}{\Delta P}\right)_{ref}$  is as below.

$$\left(\frac{\partial \Delta P}{\Delta P}\right)_{ref} = 0.04\% \times \frac{40 \text{ inH2O}}{2.2 \text{ inH2O}} = 0.7\% \quad (15)$$

On the contrary, L range EJX910 used at the CEESI test is tested at the factory. The result at 10 inH2O point is 0.005% of span. Also, the result at 0 inH2O point is 0.003% of span. If we assume the actual reference accuracy at 2.2 inH2O is 0.005% of span. Then, assumed uncertainty at 2.2 inH2O point  $\left(\frac{\partial \Delta P}{\Delta P}\right)_{ref\_as}$  is as below.

$$\left(\frac{\partial \Delta P}{\Delta P}\right)_{ref\_as} = 0.005\% \times \frac{40 \text{ inH2O}}{2.2 \text{ inH2O}} = 0.09\% \quad (16)$$

### 6.2 SP span effects

SP span effects per 6.9 MPa (1000 psi) change is defined as  $\pm 0.075\%$  of span. From this defined accuracy, uncertainty at 2.2 inH2O point  $\left(\frac{\partial \Delta P}{\Delta P}\right)_{span}$  is as below.

$$\left(\frac{\partial \Delta P}{\Delta P}\right)_{span} = 0.075\% \times \frac{800 \text{ psia}}{1000 \text{ psia}} \times \frac{40 \text{ inH2O}}{2.2 \text{ inH2O}} = 1.1\% \quad (17)$$

If we assume the actual span effects at 2.2 inH2O is 0.01% of span from the data tested at the factory, then, assumed uncertainty at 2.2 inH2O point  $\left(\frac{\partial \Delta P}{\Delta P}\right)_{span\_as}$  is as below.

$$\left(\frac{\partial \Delta P}{\Delta P}\right)_{span\_as} = 0.01\% \times \frac{800 \text{ psia}}{1000 \text{ psia}} \times \frac{40 \text{ inH2O}}{2.2 \text{ inH2O}} = 0.15\% \quad (18)$$

### 6.3 DP measurement uncertainty

From Equation (16) and (18), assumed uncertainty at 2.2 inH2O point  $\left(\frac{\partial \Delta P}{\Delta P}\right)_{as}$  is as below.

$$\left(\frac{\partial \Delta P}{\Delta P}\right)_{as} = \left(\frac{\partial \Delta P}{\Delta P}\right)_{ref\_as} + \left(\frac{\partial \Delta P}{\Delta P}\right)_{span\_as} = 0.09\% + 0.15\% = 0.24\% \quad (19)$$

Then, from Equation (14) and (19),

$$Uncert_{dp\_as} = \left\{ \left( \frac{\partial \Delta P}{2 \Delta P} \right)_{as}^2 \right\} = \left( \frac{1}{2} \times \left( \frac{\partial \Delta P}{\Delta P} \right)_{as} \right)^2 = \left( \frac{1}{2} \times 0.24\% \right)^2 = (0.12\%)^2 \quad (20)$$

## 7. Extending flow turn down to 20:1

From Equation (7), (8), (10), (11), (13), (14), and (20).

$$\begin{aligned} \left(\frac{\delta q_m}{q_m}\right)_{as} &= \sqrt{(Uncert_{pe\_as} + Uncert_{\rho\_as} + Uncert_{dp\_as})} = \\ &= \sqrt{((0.5\%)^2 + (0.05\%)^2 + (0.12\%)^2)} = \\ &= \sqrt{(0.25\% + 0.0025\% + 0.0144\%)} = \sqrt{0.2669} = 0.52\% \quad (21) \end{aligned}$$

If we assume condition (9), (12), and (19), L range uncertainty 2.2 inH2O point which corresponds to 20:1 flow turn down point is 0.52%, which is almost 0.5%. Then flow turn down 20:1 will be achieved using L range transmitter in addition to H range under CEESI test condition.

## 8. DP measurement contribution for flow measurement

EJX910 is designed with multi-sensing capabilities using built-in silicon resonant sensor technology [7] (See Figure 3). The pressure sensor based on advanced silicon resonant sensor structure contributes to the flow measurement performance which realizes uncertainty 0.5% turn down 20:1 by multiple multivariable transmitters.

### 8.1 Pressure sensor structure

Left drawing in Figure 6 shows two resonators which are incorporated into one sensor tip inside EJX910 using MEMS technology at the location of the silicon diaphragms. Two resonators are located where tensile strain and compressive strain occur. One of the specific characteristics of EJX910 sensor structure is that the SP is simultaneously measured along with the DP by this one sensor tip.

For typical flow application, SP is measured on high-side and DP is measured between high- and low- side. The pressure applied to the high-side diaphragm is conveyed to the front side of the sensor tip and the pressure applied to the low-side diaphragm is conveyed to another side of the sensor tip.

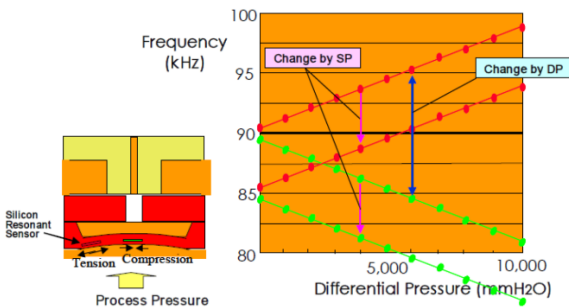


Figure 6: EJX910 pressure sensor structure and signal

### 8.2 Pressure sensor signal

The DP and SP signals can be calculated by making differential computations and summation computations of the two resonators respectively. Changes ( $\Delta f^2$ ) in resonance frequencies  $f_1$  and  $f_2$  of the two resonators due to pressure are simply given as below [7].

$$\Delta f_1^2 = \Delta f_{01}^2 \cdot G_{f1} (+\varepsilon_{dp1} + \varepsilon_{sp1}) \quad (22)$$

$$\Delta f_2^2 = \Delta f_{02}^2 \cdot G_{f2} (-\varepsilon_{dp2} + \varepsilon_{sp2}) \quad (23)$$

where

$f_0$  stands for the resonance frequency when the tensile force is zero

$G_f$  stands for the squared sensitivity of the resonator ( $=0.2366 \cdot (1/h)^2$ )

$h$  stands for thickness of the resonator

$\varepsilon_{dp}$  stands for change in the tensile force due to DP

$\varepsilon_{sp}$  stands for change in the tensile force due to SP

DP and SP change is calculated as below.

$$\Delta DP = \Delta f_1^2 - a \cdot \Delta f_2^2 \quad (24)$$

$$\Delta SP = \Delta f_1^2 + b \cdot \Delta f_2^2 \quad (25)$$

where

$\Delta DP$  stands for DP change

$\Delta SP$  stands for SP change

Equation (24) eliminates the term  $\varepsilon_{sp1}$  in (22) and  $\varepsilon_{sp2}$  in (23) related to SP and provides a DP signal. Equation (25) eliminates the term  $\varepsilon_{dp1}$  in (22) and  $\varepsilon_{dp2}$  in (23) related to DP and provides a SP signal. By previously determining each coefficient from actual measured appropriate data, DP and SP signals can be calculated. This indicates that DP and SP signals are both generated using two resonator's frequency signals inside one sensor tip.

EJX910 dynamically & continuously minimize the effect of SP fluctuation inside the transmitter based on above feature. It provides precise DP measurement under real conditions which is explained in Equation (15) to (18).

### 8.3 Pressure sensor characteristics

EJX910 pressure sensor has advanced characteristics indicated as below.

- EJX910 silicon resonant sensor is made of single crystal which is tetrahedral structure with strong bonding. It reacts ideal elastic deformation from outside force.
- EJX910 pressure whole range measurement is conducted under elastic deformation state. The deformation is proportional and uniform and the hysteresis is small. The two resonators deformation precisely match the theoretical Equation (22) and (23).
- Two resonators are incorporated into one sensor tip and the compensations (24) and (25) are achieved precisely.
- The silicon resonant sensor is inside the vacuum cavity and the resonance is robust from outside disturbance.

**8.4 Low DP measurement under high SP condition**  
Right drawing in Figure 6 indicates the two resonators signals influenced by the DP and the SP. The resonators frequency shifts according to the DP and the SP changes keeping two resonators frequency relation.

The changes are proportional and uniform and the hysteresis is small. SP compensations of DP signal for whole ranges are achieved precisely. This indicates that the uncertainty of the DP is small even at the condition of low DP under high SP. This shows that EJX910 has an advantage of low DP measurement under high SP condition.

## 9. Conclusion

In this paper, combined DP flow meter VERIS Accelabar® flow primary element and Yokogawa EJX910 multivariable transmitter is analysed. It indicates that adding EJX910 L range transmitter with H range transmitter, combined flow measurement turndown will be increased beyond 15:1 until 20:1 under 0.5% linearity with reference flow rate.

EJX910 is designed with multi-sensing capabilities using built-in silicon resonant sensor technology. EJX910 dynamically & continuously minimizes the effect of SP fluctuation with two resonators incorporated into one sensor tip and provides precise DP measurement under real conditions.

EJX910 has an advantage of low DP measurement under high SP condition with built-in silicon resonant sensor technology. This indicates the latest progress of DP flow meter technology and the DP flow meter has still big potential for use in industry widely.

## References

- [1] Ito, A., Cisar, V., "DP Flowmeter Calibration Performance and Flow Coefficient/Density Effects Study", *10<sup>th</sup> ISFFM, 2018*
- [2] Hodges, C., "New differential producing meters-ideas, implementations, and issues", *15th Flow Measurement Conference (FLOMEKO), 2010*
- [3] Ito, A., Mimura, S., Koyama, E., Odohira, T., Nikkuni, M., and Miyauchi, T., "EJX910 Multivariable Transmitter", *Yokogawa Technical Report*, No42, 2006, pp.13-16
- [4] ASME MFC 12M, Measurement of Fluid Flow in Closed Conduits Using Multiport Averaging Pitot Primary Elements, 2006

[5] Product Literature Accelabar, [https://www.armstronginternational.com/sites/default/files/resources/files/479-EN\\_0.pdf](https://www.armstronginternational.com/sites/default/files/resources/files/479-EN_0.pdf)

[6] General Specifications EJX910A Multivariable Transmitter, GS 01C25R01-01EN, [https://web-material3.yokogawa.com/GS01C25R01-01EN.pdf?\\_ga=2.166938622.1561879310.1555225837-133218096.1479342716](https://web-material3.yokogawa.com/GS01C25R01-01EN.pdf?_ga=2.166938622.1561879310.1555225837-133218096.1479342716)

[7] Ishikawa T., Odohira, T., Nikkuni, S., Koyama, E., Tsumagari, T., Asada, R., "New DPharp EJX Series of Pressure and Differential Pressure Transmitters", *Yokogawa Technical Report*, No.37,2004, pp9-14

Accelabar® and Verabar® are registered trademarks of VERIS, Inc. All company name, product name and logo etc. mentioned in this material are registered trademarks or trademarks of Yokogawa Electric Corporation and their respective companies.

# LNG Mid-Scale Loop flow metering – Preliminary Test Results

M.D. Schakel<sup>1</sup>, O. Kerkhof<sup>2</sup>, M.P. van der Beek<sup>3</sup>, P. van den Herik<sup>2</sup>, R. van Hof<sup>2</sup>, P. Lucas<sup>4</sup>, S. Wulffers<sup>2</sup>

<sup>1</sup>VSL, *mschakel@vsl.nl, Delft, The Netherlands*

<sup>2</sup>VSL, *Delft, The Netherlands*

<sup>3</sup>Euroloop, *Rotterdam, The Netherlands*

<sup>4</sup>TNO, *Delft, The Netherlands*

*E-mail (corresponding author): mschakel@vsl.nl*

---

## Abstract

The LNG Mid-Scale Loop (MSL) has been taken into use in 2019. Instead of making use of surrogate fluids, the facility will be able to perform calibrations with cryogenic liquid directly, and under actual operating conditions. Consequently, insight on surrogate-fluid calibration transferability will be obtained. The Cryogenic Research and Calibration facility allows for metrologically traceable cryogenic flow meter calibrations. At the time of writing, calibrations with liquid nitrogen (LiN) can be performed. By performing traceable calibrations with cryogenic liquids directly, market confidence in LNG custody transfer will be established which in turn allows the uptake of LNG on a larger scale. Notably, in addition to economic benefits of using LNG, the use of LNG as a transport fuel for trucks and ships has considerable environmental benefits. The Cryogenic Research and Calibration facility is based on a closed-loop system where cryogenic liquid is circulated. The cryogenic primary mass flow standard (PSL) is fully integrated into the facility. The target maximum flow rate of the facility is 200 m<sup>3</sup>/h. A metrologically traceable LNG composition primary standard allows to calibrate alternative composition measurement systems. Thus, the facility provides the means to traceably calibrate flow meter and composition measurement systems with cryogenic liquid directly, which in turn allows the calibration of systems for measuring the quantity of LNG-energy transferred. This article will describe the facility, its operating principles, preliminary test-results, and future plans. The facility allows for systematic research into flow meter performance in varied circumstances, such as the effects of flow-meter insulation, (upstream) flow disturbances, and multi-phase flow. Prototypes and models of cryogenic flow meters can be tested and calibrated in a metrologically traceable manner.

---

## 1. Introduction

Liquefied Natural Gas (LNG) is traded between the exporter and the importer during custody transfer. Typical applications of LNG are (at the large scale) to regassify it and inject it into the gas grid, and (at the small to midscale) as a transport fuel. LNG is an alternative to pipeline gas, with strategic and, for long distances, economic benefits [1]. Further LNG has considerable environmental benefits. Engines running on LNG will meet the (new) limits set on NO<sub>x</sub> and CO<sub>2</sub> emissions and produce less noise than diesel operated engines. LNG fuelled trucks are an alternative to diesel fuelled trucks for long-distance road freight transport. LNG shipments may overtake inter-regional pipeline shipments in the 2020s [2]. Clearly, the global trade in LNG is growing and there is a need for metrological infrastructure to facilitate

it. The quantity of LNG traded is based on the amount of energy transferred [3]. To determine this amount, current practice is to measure the volume of LNG which, in combination with the mass density and the measurement of LNG composition, allows to compute the amount of energy transferred (see for example [3]).

One method to measure the volume is based on level gauges and calibration tables in the LNG carrier. Another method is to measure the flow when custody transfer takes place, such as when fuelling an LNG truck or in LNG ship bunkering. Typical instruments used in the second method are ultrasonic flow meters (USM) and Coriolis Mass Flow (CMF) meters. Currently, CMF meters are calibrated with water and interpolation methods are applied to compensate for temperature effects at

cryogenic conditions when measuring LNG flow (see for example [4,5]). Clearly traceable calibrations with LNG will help to establish confidence in LNG flow metering and therefore in LNG custody transfer.

Within the European Metrology Research Programme (EMRP), the European Metrology Programme for Innovation and Research (EMPIR), and the “Regeling Nationale EZ subsidies” (Dutch Ministry of Economic Affairs and Climate Policy) research and innovation projects were undertaken to establish metrological infrastructure for LNG applications. In 2019 VSL completed the construction of the Cryogenic Research and Calibration facility to enable traceable cryogenic flow meter calibrations with a target maximum flow rate of 200 m<sup>3</sup>/h and a target measurement uncertainty of 0.15% in mass flow rate (which equates to about 0.20% in volume flow rate). The facility will serve the needs of small-scale to mid-scale LNG flow meter calibrations. The LNG composition primary standard allows to calibrate alternative composition measurement systems as well. Thus, the facility provides the means to traceably calibrate flow meter and composition measurement systems, which in turn allows the calibration of the quantity of LNG-energy transferred in LNG trade.

An LNG roadmap is displayed in Figure 1. A primary standard was built in 2013 and documented [6]. It is now integrated into the Cryogenic Research and Calibration Facility, which was completed in 2019 and where this paper is about. The facility can, in principle, be expanded to larger flow rates (range 400 – 1000 m<sup>3</sup>/h). The ultimate aim is to allow for traceable LNG flow meter calibrations at the large scale (10,000 m<sup>3</sup>/h).

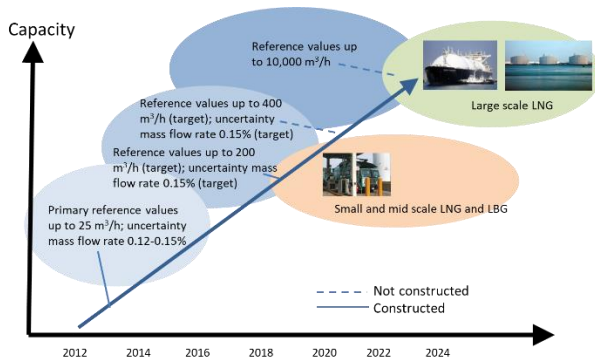


**Figure 1:** Roadmap for traceable LNG flow meter calibrations. LBG denotes liquified biogas.

Figure 2 shows the metrological traceability scheme for LNG composition, density, and flow, which are the inputs to compute the amount of LNG energy transferred on which LNG trade is based [3]. The composition analysers are made traceable by reference gases derived from primary standard mixtures. The reference gases are liquified by a liquefier. These liquids are used to calibrate the composition analyzers at the Cryogenic Research and Calibration facility. Pressure and temperature sensors embedded in the facility are made metrologically traceable by direct calibration with primary standards. Combining pressure, temperature, composition with an equation of state enables the LNG density to be computed. Mass and time are made metrologically traceable by the gravimetric mass flow primary standard which contains a weighing scale on which a cryostat-vessel rests. By combining the density with the mass flow the volume flow rate is computed.

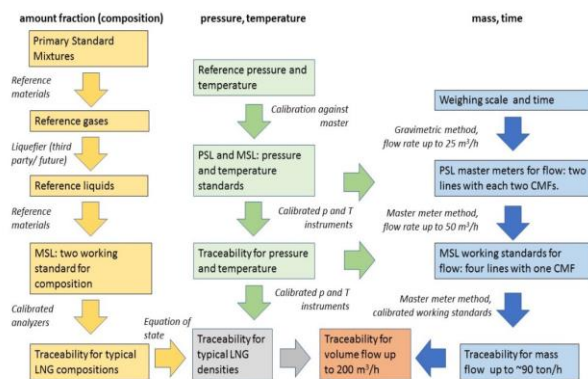


**Figure 2:** Metrological traceability scheme.

This paper will describe the main components of the Cryogenic Research and Calibration facility, the operating principles of the facility, preliminary test-results, and future plans. The facility allows for systematic research into flow meter performance in varied circumstances, such as the effects of flow-meter insulation, (upstream) flow disturbances, multi-phase flow, and variable subcooled conditions. Prototypes and models of cryogenic flow meters and cryogenic liquid composition analysers can be tested and calibrated in a metrologically traceable manner.

## 2. Cryogenic Research and Calibration facility components

Figure 3 shows an overview of the main components of the Cryogenic Research and Calibration facility.

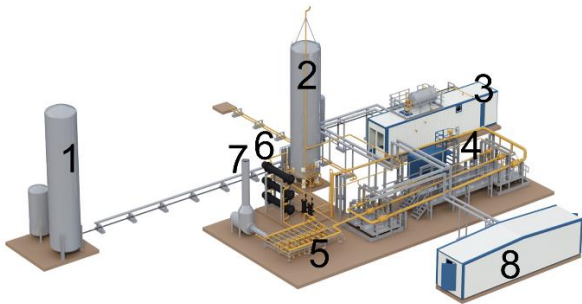


Figure 3: The Cryogenic Research and Calibration facility: 1) Liquid Nitrogen (LiN) storage tank, 2) cryogenic liquid storage tank, 3) primary Standard (PSL) for mass flow utilizing the gravimetric method to calibrate the Coriolis mass flow meters in the PSL, 4) Meter under Test (MuT) section, 5) working standards, a set of Coriolis mass flow meters, 6) heat exchangers and pumps, 7) Nitrogen (N<sub>2</sub>)-warmer and 8) control room.

1) The LiN storage tank is used as supply of LiN. LiN is used for varied purposes such as liquid coolant, source for instrumentation nitrogen, source of purging gas, etc.

2) The cryogenic liquid storage tank is used to store the cryogenic liquid (for example LiN or LNG). Since the tank is a cryostat, the cryogenic liquid can be kept into the storage tank without it being converted to gas.

3) The Primary Standard Loop (PSL) is a gravimetric primary standard for mass flow which is used to provide metrological traceability for mass flow to the working standards of the MSL.

4) In the Meter-under-Test (MuT) section cryogenic flow meters can be calibrated.

5) MSL flow working standards. Figure 4 shows a picture of the four Coriolis mass flow meter working standards. The working standards are refrigerated with cold N<sub>2</sub>-gas boiled off from the heat exchangers.



Figure 4: working standards, a set of Coriolis mass flow meters.

6) Pumps generate flow in the MSL by pumping the liquid from the cryogenic liquid storage tank through the MSL in which it is circulated in a loop. The heat exchangers refrigerate the cryogenic liquid below its boiling point to create a sub-cooled state of the cryogenic liquid. Figure 5 shows the pumps and Figure 6 shows the heat exchangers.



Figure 5: cryogenic pumps.



Figure 6: heat exchangers. LiN is guided past the cryogenic liquid to cool it down towards a sub-cooled state.

7) The N<sub>2</sub>-warmer heats the relatively cold waste nitrogen released from the heat exchanger (boiled of nitrogen from the sub-cooling process) and guides the heated gas towards a safe point into the atmosphere.

8) The facility is operated from the control room.

### 3. Operating principles

The Cryogenic Research and Calibration facility is based on a closed-loop system where cryogenic liquid is pumped (Figure 3, item 6) from the cryogenic vessel (Figure 3, item 2) to the working standard Coriolis mass flow meters (Figure 3, item 5), then towards the Meter(s)-under-Test (Figure 3, item 4), and then recirculated by the pumps towards the working standards (Figure 3, item 5). LiN (Figure 3, item 1) is used to subcool the cryogenic liquid, which occurs in the heat exchanger (Figure 3, item 6). Subcooling avoids boiling and concomitant two-phase flow of the circulated cryogenic liquid. Heating of cryogenic liquid occurs due to the heat transfer from the air at ambient temperatures towards the cryogenic liquid at cryogenic temperatures. A composition measurement primary standard (not shown) is located downstream of the Meter(s)-under-Test. This is a logical place as it will be assured that their connections to the loop will not affect the flow profile in the flow metering loop.

The PSL (Figure 3, item 3) is fully integrated into the facility. It was modified with respect to an earlier version with the aims to reduce the measurement uncertainty, to integrate it into the MSL of the Cryogenic Research and Calibration Facility, and to improve the metrological robustness of the primary standard Coriolis mass flow meters. Metrologically traceable calibrations of Coriolis mass flow meters in the primary standard can be performed and used to transfer traceability towards the working

standards of the MSL through a bootstrapping procedure. This procedure must be performed periodically (for example each year) and the flow loop will then be diverted from the MSL towards the PSL. After having (re)established the metrological traceability, the flow will be diverted back towards the MSL to perform traceable calibrations of Meter(s)-under-Test in a loop from the MSL working standards towards the Meter(s)-under-Test and then back to the working standards.

### 4. Preliminary test results

Stable flow rates with LiN have been achieved within the loop. This applies to flow from the pumps to the PSL and then towards the MSL as well as for the flow within the MSL. This is considerable better performance than initially expected, as the LiN is not actively cooled by another liquid coolant. This shows the high potential of the facility.

### 5. Future plans – A Cryogenic Field Laboratory

The facility was taken into use for metrologically traceable calibrations for LNG flow meter and LNG composition analysers. Naturally future plans are to flow LNG through the loop instead of LiN. This flow can be expanded to higher flow rates (range 400 – 1000 m<sup>3</sup>/h) completely serving the full range of the small- to mid-scale LNG market for refuelling and bunkering applications.

The commissioning of the facility with LiN has provided further insights. The facility opens up possibilities for cryogenic research not limited to:

- Systematic research into flow meter performance in varied circumstances, such as the effects of flow-meter insulation, (upstream) flow disturbances, multi-phase flow, and variable subcooled conditions
- Research into improved accuracy and robustness of cryogenic temperature measurements
- Metrologically traceable calibrations of prototype cryogenic measuring devices for mass and volume flow, density, speed-of-sound, etc.
- Metrologically traceable calibrations of prototype cryogenic liquid composition measuring devices
- Cryogenic training for operators and metering experts
- Research on new cryogenic measurement methods
- Cryogenic equipment field testing

## 6. Conclusion

The LNG research and calibration facility was commissioned with LiN. Even with LiN stable flow rates can be achieved both in the PSL as in the MSL. As the LiN is not actively cooled by a liquid coolant, this implies that it will be easier to create stable flow with any cryogenic liquid with a boiling point higher than LiN (such as LNG). Thus, the facility provides the means to traceably calibrate flow meter and composition measurement systems with cryogenic liquid directly, which in turn allows the calibration of systems for measuring the quantity of LNG-energy transferred.

The LiN commissioning results indicate the high potential of the facility as a Cryogenic Field Laboratory for cryogenic research into fields not limited to flow, composition, temperature, pressure, alternative and surrogate cryogenic liquids.

## 7. Acknowledgements

The research leading to the results discussed in this report has received funding from the European Metrology Programme for Innovation and Research (EMPIR) (Project Numbers: ENG60 and 16ENG09) and “Topsector Energiesubsidie” from the Dutch Ministry of Economic Affairs and Climate Policy (Project Numbers: TELN115006 and TELN116063). The EMPIR programme is jointly funded by the EMPIR participating countries within Euramet and the European Union.

## References

- [1] Nieuwenkamp, G., Pelevic, N., Li, Jianrong, Bükler, O., Arrhenius, K., Stolt, K., Rasmussen, K., Kondrup, J., Maury, R., Richter, M., Lner, R., Alberto Albo, P., Lago, S., Brown, A., Murugan, A., Gieseking, B., Tompkins, J., Eilts, P., Klare L., Moshammer K., Lucassen, A., Hadidi, K., “Metrology for LNG custody transfer and transport fuel applications”, in *18<sup>th</sup> International Congress of Metrology*. (EDP Sciences), 08001, 2017.
- [2] BP, BP Energy outlook 2018, <https://www.bp.com/content/dam/bp/en/corporate/pdf/energy-economics/energy-outlook/bp-energy-outlook-2018.pdf>
- [3] GIIGNL, *LNG custody transfer handbook*, 5th edition (Paris, GIIGNL), 2017.
- [4] Marfenko, I., Endress + Hauser Flowtec AG, Long Term Stability of Coriolis Flowmeters in Cryogenic Fluids, North Sea Flow Measurement Workshop 2018 / Metrology for LNG, [https://Ingmetrology.info/wp-content/uploads/2018/11/Long-Term-Stability-](https://Ingmetrology.info/wp-content/uploads/2018/11/Long-Term-Stability-of-Coriolis-Flowmeters-in-Cryogenic-Fluids.pdf)

[of-Coriolis-Flowmeters-in-Cryogenic-Fluids.pdf](https://Ingmetrology.info/wp-content/uploads/2018/11/CORIOLIS-APPLICATION-AT-LNG-CONDITIONS.pdf)

- [5] Pitti, S., Emerson, Transparency is a must for meter performance evaluation at LNG applications; an example with a Coriolis meter, North Sea Flow Measurement Workshop 2018 / Metrology for LNG <https://Ingmetrology.info/wp-content/uploads/2018/11/CORIOLIS-APPLICATION-AT-LNG-CONDITIONS.pdf>
- [6] van der Beek, M., Lucas, P., Kerkhof, O., Mirzaei, M., Blom, G., “*Results of the evaluation and preliminary validation of a primary LNG mass flow standard*”, *Metrologia*, 51(5), 539, 2014.

# Improvements to the Primary LNG Mass Flow Standard

**M.D. Schakel<sup>1</sup>, M.P. van der Beek<sup>2</sup>, Ilko Rahneberg<sup>3</sup>, Jan Schleichert<sup>4</sup>, Tobias Einkenkel<sup>4</sup>, Norbert Rogge<sup>4</sup>, Thomas Fröhlich<sup>4</sup>**

<sup>1</sup>VSL, *mschakel@vsl.nl, Delft, The Netherlands*

<sup>2</sup>VSL, *Delft, The Netherlands*

<sup>3</sup>SIOS Messtechnik GmbH, *Ilmenau, Germany*

<sup>4</sup>*Institute of Process Measurement and Sensor Technology, Ilmenau University of Technology, Ilmenau, Germany*

*E-mail (corresponding author): mschakel@vsl.nl*

---

## Abstract

In 2013 LNG mass flow meters were traceably calibrated by the gravimetric primary LNG mass flow standard with an estimated Calibration and Measurement Capability (CMC) of 0.12% to 0.15%. Dominant uncertainty sources included the uncertainty associated with the correction for so-called parasitic forces. Modifications to the primary standard were made with the objective to reduce the measurement uncertainty associated with the parasitic forces. A Level Compensation System (LCS) was installed to control the level of the weighing vessel during the weighing process. Several experiments were performed, and the results analysed. It was demonstrated that the LCS has the potential to reduce the measurement uncertainty associated with the parasitic forces. An alternative method to reduce parasitic forces was made possible by the installation of a dry-break coupling. Future activities will aim to provide a proof of principle of the improvements due to the LCS and the dry-break coupling when using liquid medium (e.g., LNG) in the weighing process.

---

## 1. Introduction

Liquefied Natural Gas (LNG) is traded between the exporter and the importer during custody transfer. Typical applications of LNG are (at the large scale) to regassify it and inject it into the gas grid, and (at the small to midscale) as a transport fuel. LNG is an alternative to pipeline gas, with strategic and, for long distances, economic benefits [1]. Further LNG has considerable environmental benefits. Engines running on LNG will meet the (new) limits set on NO<sub>x</sub> and CO<sub>2</sub> emissions and produce less noise than diesel operated engines. LNG fuelled trucks are an alternative to diesel fuelled trucks for long-distance road freight transport. LNG shipments may overtake inter-regional pipeline shipments in the 2020s [2]. Clearly, the global trade in LNG is growing and there is a need for metrological support to facilitate it. The quantity of LNG traded is based on the amount of energy transferred [3]. To determine this amount, current practice is to measure the volume of LNG which, in combination with the mass density and the measurement of LNG composition, allows to compute the amount of energy transferred (see for example [3]).

One method to measure the volume is based on level gauges and calibration tables in the LNG

carrier. Another method is to measure the flow when custody transfer takes place, such as when fuelling an LNG truck or in LNG ship bunkering. Typical instruments used in the second method are ultrasonic flow meters (USM) and Coriolis Mass Flow (CMF) meters. Currently, CMF meters are calibrated with water and interpolation methods are applied to compensate for temperature effects at cryogenic conditions when measuring LNG flow (see for example [4,5]). Clearly traceable calibrations with LNG will help to establish confidence in LNG flow metering and therefore in LNG custody transfer.

Within the European Metrology Research Programme (EMRP), the European Metrology Programme for Innovation and Research (EMPIR), and the “Regeling Nationale EZ subsidies” (Dutch Ministry of Economic Affairs and Climate Policy) research and innovation projects were undertaken to establish metrological support for LNG applications. Originating from these projects is the roadmap for the development of SI-traceable LNG flow meter calibrations shown in Figure 1. A gravimetric primary LNG mass flow standard was realised with an estimated Calibration and Measurement Capability (CMC) of 0.12% to 0.15% [6]. Subsequently a facility was built in the port of

Rotterdam, The Netherlands, to enable cryogenic liquid SI-traceable calibrations with a targeted maximum flow rate of about 200 m<sup>3</sup>/h and associated targeted uncertainty of 0.15% in mass flow rate. In the future, larger flow rates can be targeted that serve the small scale LNG market for transportation ( $\leq 1000$  m<sup>3</sup>/h) and the large scale custody transfer market (up to 10,000 m<sup>3</sup>/h).

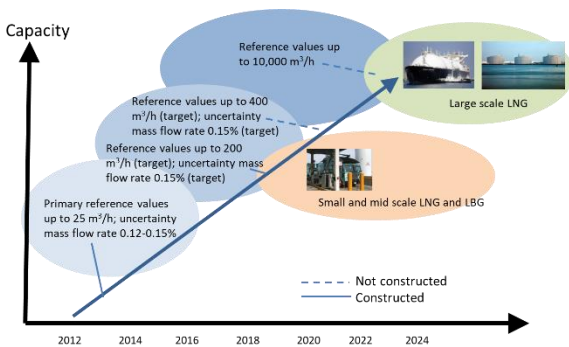


**Figure 1:** Roadmap for traceable LNG flow meter calibrations. LBG denotes liquified biogas.

In 2013 LNG mass flow meters were calibrated by the gravimetric primary LNG mass flow standard. Typical deviations of the flow meters with respect to the primary standard are within 0.5% in terms of mass flow rate [7]. The primary standard CMC of 0.12-0.15% in mass flow rate, equates to about 0.2% in volume flow rate. The primary standard flow rate is limited implying that the CMC of larger flow rate facilities will increase (i.e., will have a larger measurement uncertainty) when relying on the primary standard for their traceability. Conventional fuels have a typical flow rate measurement uncertainty of about 0.5%. To enable the usage of LNG as a transport fuel, a similar measurement uncertainty is required for the so-called small-scale to mid-scale applications which coincide with LNG truck fuelling and ship bunkering and flow rates  $<1000$  m<sup>3</sup>/h [8].

Dominant uncertainty sources of the primary mass flow standard are associated with the correction for so-called parasitic forces, calibration time uncertainty and temperature uncertainty. The parasitic forces arise as the appendages attached to the weighing vessel on the balance exhibit minor displacements during the weighing process. This paper describes modifications to the primary standard which were made with the objective to reduce the measurement uncertainty associated with the parasitic forces. A Level Compensation System (LCS) was installed to maintain the level of the weighing vessel close to its reference (starting) state during the weighing process. An alternative

method to reduce parasitic forces was made possible by the installation of a dry-break coupling.

## 2. Level Compensation System

### 2.1 Description of the LCS

The LCS was installed in the primary LNG mass flow standard in 2017. Figure 2 illustrates how an upward (parasitic) force is created when filling the tank of the gravimetric standard. The filling pipe is lowered relative to its initial state as the load cells below the balance top plate on which the tank rests are loaded. Due to the stiffness of the filling pipe (and other appendages), a resulting force is exerted on the tank which acts in opposite direction as the weight. Therefore, a smaller mass reading than the actual mass is expected.

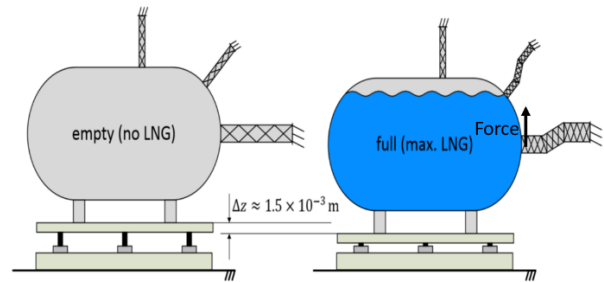


**Figure 2:** When the tank is loaded during the filling process of the weighing tank, a resulting force is created due to the lowering of the tank and the stiffness of the filling pipe (and other appendages).

Figure 3 shows the components of the LCS system. The balance (1) and weighing vessel (2) are supported by a floor board (3) which reduces the fluctuations during the weighing process. Actuators (4) attached to the frame (5) on which the weighing vessel rests compensate the displacement during filling/loading of the tank. Typical vertical displacement is in the order of several hundreds of  $\mu\text{m}$ 's. The control system (6) translates measured displacement of the system to vertical compensation enforced by three actuators along the tank frame in a closed loop servo control scheme. Calibration weights (7) are used to calibrate the balance and to provide traceability to the mass measurement.

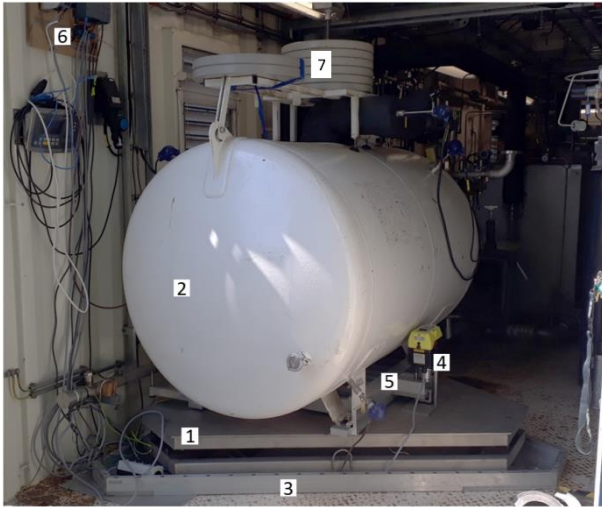


**Figure 3:** The LCS, balance, and weighing vessel of the primary LNG mass flow standard. Components are: balance (1), weighing vessel (2), floor board (3), actuators (4), tank frame (5) LCS control system (6), and calibration weights (7).

An elaborate description of the LCS functional requirements, assembly, and construction is described in a MSc thesis [9].

### 2.2 LCS preliminary experiments and results

In a first experiment calibration mass pieces were sequentially placed on the weighing vessel in 100 kg steps to simulate the filling of the vessel during the weighing process. Figure 4 shows the results with the LCS on (solid) and with the LCS off (blue) as a function of time.

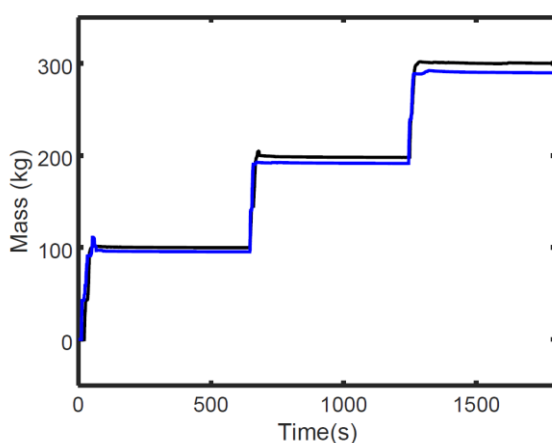


**Figure 4:** Mass readings as a function of time with LCS on (black) and LCS off (blue).

The mass readings with LCS on are higher than with the LCS off. The mass readings with the LCS on turn out to be closer to the corresponding calibration masses. This is expected as the LCS is compensating the vertical displacement and the

tilting of the tank relative to the pipes and is thus compensating the parasitic forces. Independent measurements with level gauges showed that the LCS kept the vessel in place during the weighing process with some retardation (less than 30 s) while the balance plate was lowered due to the calibration weights. A drift on the order of g/s occurs after loading with the calibration weights. During the experiments a rigid (filling) pipe of 2-3 m length was attached to the weighing vessel. It is speculated that this resulted in large relaxation effects. The experiment indicates that the LCS is reducing the parasitic forces. Thus, it is also expected that the corresponding uncertainty due to correcting for the parasitic forces will have a smaller contribution to the measurement uncertainty of the primary LNG mass flow standard.

In a second experiment, using the LCS on open loop mode to intentionally lift the tank up and down, the stiffness corresponding to the parasitic forces was determined by enforcing negative and positive displacements and measuring the corresponding apparent mass deviation. Figure 5 (top) shows the discrete displacements set by the LCS and Figure 5 (bottom) shows the corresponding mass deviations. The stiffness  $k$  is estimated from  $F = k\Delta z$  or  $\Delta mg = k\Delta z$ , where  $\Delta m$  is the apparent mass deviation corresponding to displacement  $\Delta z$ , and  $g = 9.81 \text{ m/s}^2$ . From the regression in Figure 4 (bottom) a stiffness of  $3 \times 10^3 \text{ N/m} \pm 3 \times 10^3 \text{ N/m}$  ( $k = 2$ ) is obtained. An independent measurement on the (detached) filling pipe directly yielded a value of  $7.84 \times 10^3 \text{ N/m} \pm 2.14 \times 10^3 \text{ N/m}$  ( $k = 2$ ). While these values are somewhat in correspondence it could also be expected that the estimated stiffness value from the experiment with the tank and filling pipe would be larger than the independent value measured directly on the (detached) filling pipe since the filling tank has more pipes/appendages attached to it than the filling pipe alone. Further experimentation is needed to explain the difference.

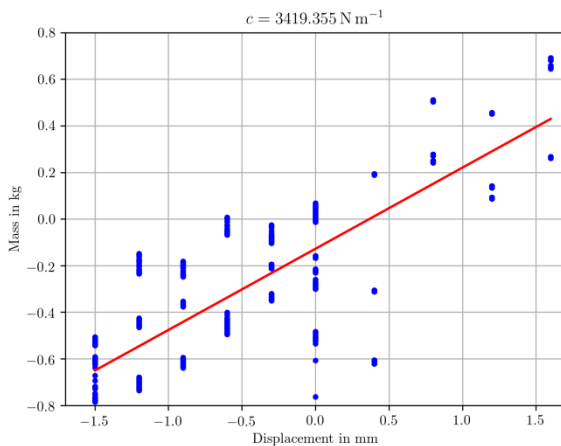
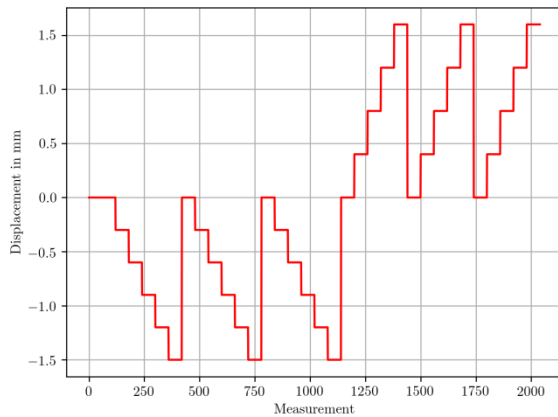


**Figure 5:** Actual displacements enforced by the LCS (top; negative is lowering) and corresponding measured mass deviations (bottom). From the linear regression a stiffness value of the filling pipe and other tank appendages is estimated.

### 3. Dry-break coupling

The filling pipe attached to the weighing vessel is a significant contributor to the parasitic forces and thereby a significant uncertainty source. For this reason, a dry-break coupling was installed into the primary standard. Figure 6 shows the filling pipe (1), the dry-break coupling (2), and the swivel pipe (3). The dry-break coupling allows to detach the filling pipe appendage prior to and after the weighing process. The swivel pipe is flexible in the vertical and flow direction, which is expected to further reduce parasitic forces. The swivel pipe and dry-break coupling are supported by flexible supports (chains).

The dry-break coupling has the expected potential to reduce the uncertainty contribution of the parasitic forces by detaching the weighing tank prior and after the calibration, to achieve an approximate equivalent geometry of the tank, filling pipe and other appendages when determining the increase in mass during the calibration.



**Figure 6:** Dry-break coupling in the primary LNG mass flow standard. Components indicated are: filling pipe (1), dry-break coupling (2), and the swivel pipe (3).

### 4. Discussion

Two approaches were chosen with the aim to reduce the contribution of parasitic forces to the measurement uncertainty of the primary LNG mass flow standard.

The LCS system shows higher readings closer to the corresponding calibration masses, and independent measurements showed that the LCS kept the vessel in place during the weighing process. This provides a strong indication that the LCS is compensating the parasitic forces due to the filling pipe and appendages attached to the weighing tank during the weighing process. Thus, it is also expected that the corresponding uncertainty due to correcting for the parasitic forces will have a smaller contribution to the measurement uncertainty of the primary LNG mass flow standard. Further investigation is needed to fully characterize the reduction of parasitic forces in an actual calibration process. The difference in the inferred and measured stiffness values indicates that the parasitic forces are not caused by the stiffness of the filling pipe alone.

The dry-break coupling is the second approach with the expected potential to reduce the uncertainty contribution due to parasitic forces.

Future activities will aim to provide a proof of principle of the improvements due to the LCS and the dry-break coupling when using cryogenic liquid in the weighing process.

### 5. Conclusion

Two systems were installed in the existing LNG primary mass flow standard that have the potential to reduce the uncertainty caused by parasitic forces.

These forces are a dominant uncertainty source of the primary standard Calibration and Measurement Capability (CMC). For the LCS initial results indicate that the parasitic forces are reduced indeed, and therefore the corresponding uncertainty contribution of the correction for the parasitic forces to the CMC is expected to be reduced as well. The dry-break coupling has not yet been tested for its potential to reduce the uncertainty contribution of the parasitic forces. Future activities will aim to provide a proof of principle of the improvements due to the LCS and the dry-break coupling when using cryogenic liquid in the weighing process

## 6. Acknowledgements

The research leading to the results discussed in this paper has received funding from the European Metrology Programme for Innovation and Research (EMPIR) (Project Numbers: ENG60 and 16ENG09) and "Topsector Energiesubsidie" from the Dutch Ministry of Economic Affairs and Climate Policy (Project Numbers: TELN115006 and TELN116063). The EMPIR programme is jointly funded by the EMPIR participating countries within Euramet and the European Union.

## References

- [1] Nieuwenkamp, G., Pelevic, N., Li, Jianrong, Bükler, O., Arrhenius, K., Stolt, K., Rasmussen, K., Kondrup, J., Mauray, R., Richter, M., Lner, R., Alberto Albo, P., Lago, S., Brown, A., Murugan, A., Gieseking, B., Tompkins, J., Eilts, P., Klare L., Moshammer K., Lucassen, A., Hadidi, K., "Metrology for LNG custody transfer and transport fuel applications", in *18<sup>th</sup> International Congress of Metrology*. (EDP Sciences), 08001, 2017.
- [2] BP, BP Energy outlook 2018, <https://www.bp.com/content/dam/bp/en/corporate/pdf/energy-economics/energy-outlook/bp-energy-outlook-2018.pdf>
- [3] GIIGNL, *LNG custody transfer handbook*, 5th edition (Paris, GIIGNL), 2017.
- [4] Marfenko, I., Endress + Hauser Flowtec AG, Long Term Stability of Coriolis Flowmeters in Cryogenic Fluids, North Sea Flow Measurement Workshop 2018 / Metrology for LNG, <https://lngmetrology.info/wp-content/uploads/2018/11/Long-Term-Stability-of-Coriolis-Flowmeters-in-Cryogenic-Fluids.pdf>
- [5] Pitti, S., Emerson, Transparency is a must for meter performance evaluation at LNG applications; an example with a Coriolis meter, North Sea Flow Measurement Workshop 2018 / Metrology for LNG <https://lngmetrology.info/wp-content/uploads/2018/11/CORIOLIS-APPLICATION-AT-LNG-CONDITIONS.pdf>
- [6] van der Beek, M., Lucas, P., Kerkhof, O., Mirzaei, M., Blom, G., "Results of the evaluation and preliminary validation of a primary LNG mass flow standard", *Metrologia*, 51(5), 539, 2014.
- [7] Schakel, M., VSL, LNGIII metrology training, North Sea Flow Measurement Workshop 2018 / Metrology for LNG
- [8] Euramet, Publishable Summary for 16ENG09 LNGIII Metrological support for LNG and LBG as transport fuel, [https://www.euramet.org/research-innovation/search-research-projects/details/?eurametCtcp\\_project\\_show%5Bproject%5D=1468&eurametCtcp\\_project%5Bback%5D=40&cHash=f1905637ac6d4d7c8cf2410b1e411cef](https://www.euramet.org/research-innovation/search-research-projects/details/?eurametCtcp_project_show%5Bproject%5D=1468&eurametCtcp_project%5Bback%5D=40&cHash=f1905637ac6d4d7c8cf2410b1e411cef)
- [9] Eienkel, T., *Gravimetric compensation system for LNG calibration*, MSc thesis, Ilmenau University of Technology, 2017.
- [10] S. Vasilyan, et. al., *Towards metering tap water by Lorentz Force Velocimetry*, Measurement, Science and Technology, vol. 26, no. 115302 2015. DOI: doi:10.1088/0957-0233/26/11/115302.
- [11] S. Vasilyan and T. Fröhlich, *Direct lorentz force compensation flowmeter for electrolytes*, Applied Physics Letters, vol. 105, no. 22, 2014. DOI: 10.1063/1.4903235.
- [12] C. Diethold, M. Kühnel, F. Hilbrunner, T. Fröhlich, E. Manske, *Determination of force to displacement curves using a nanopositioning system based on electromagnetic force compensated balances*, Measurement, 2014, <https://doi.org/10.1016/j.measurement.2014.02.034>.

# Gas Flow Meters with Thermal Time-of-Flight Technology

L.J. Huang

*Siargo Ltd., 3100 De La Cruz Boulevard, Suite 210, Santa Clara, CA 95054, USA  
E-mail: Liji@Siargo.com*

---

## Abstract

The thermal mass flow meters based on the calorimetry for utility gas metering have been recently deployed in a few countries and in a fast growth, but several technical issues including the compliance with the existing tariff standards have also been under scrutiny which prevents the desired massive installation. In this paper, we present a new utility gas meter with the thermal time-of-flight sensing technology that can simultaneously measure the mass flow rate, flow velocity, gas pressure, temperature and gas composition variations with the state-of-the-art electronics. These values can be further relayed to the thermal values of the measured gases providing the possibility for the future metrology and tariffs as well as the energy management of the distribution of the city gas. The multi-parameter data acquired from the integrated sensing elements on the other hand challenge the conventional verification process specially when the cost-effectiveness is also critical for the applications. The current meter design with integrated data output, which employs the multi-parameter acquisition and signal modulation, is substantially different from the traditional flow meter for which the metrology standard is normally having a single parameter standard being referenced. The meter also has an integrated harvester that can convert the flow energy induced temperature gradient into electrical energy that can be used for powering the flow measurement.

---

## 1. Introduction

Demands for better gas distribution management have continuously driven the development of the smart utility gas meters. On the other hand, the utility industry is however very conservative and traditional in accepting new technologies as the sensitivity in tariffs. As of today, the key technology advancement is largely limited in data transmission and management. Even this development was mostly due to a wave of governmental funding for economy stimulus in a decade ago. In a report by the market research firm IHS earlier in 2019 [1], the current annual worldwide utility gas meter shipment is about 50 million units, of which however only 20% have data communication capability and the original metrology technologies invented over two centuries ago are nearly intact. This is vastly in contrast to the pace of the contemporary electronic technologies.

The phenomenon could also reflect the complexity of a flow meter for utility applications where accuracy, long-term reliability, cost as well as regulatory requirements including the difficulties in change of the tariff system have less tolerance for the technology imperfection, which in turn prevents

the investment for the innovation in a wide scale and for a long run [2]. The utility gas meters based on ultrasonic technology have been a success for distribution tariff as the precision can be guaranteed with multiple channel detection and precise compensation of the environmental variants but the deployment to the residential gas metering has been limited by the cost and some technical difficulties for long-term performance. Further, the velocity only gas meters with ultrasonic technology are losing their attractiveness to the gas distributors, and even with a European standard in place in 2007, the shipment and installation of ultrasonic meters have not been substantiated for the deployment [3]. The concept of a calorimetric utility gas meter proposed by a few companies in earlier this century using micromachined calorimetric mass flow sensors that have a low power consumption as well as a better metrology performance has also a brilliant point of the mass metering metrology which could provide the much fairer tariffs and the better gas distribution management. It is also an all-electronic meter that enjoys a seamlessly data transmission without any mechanical or optical to electronic data conversion. The deployment of this new utility gas meter has been started in China

since 2007 for commercial users and in Italy since 2012 for both commercial and residential users. Italy has published its standard for the utility gas meters based on the calorimetric sensing technology [4], and an estimation of more than 2 million units have been installed as of today with a failure rate of about 0.26% in the field [5]. Europe community is now in discussion to convert the Italian standard into a European one.

There are several technical issues being intensively discussed for the calorimetric sensing technology for its wider acceptance by the utility gas industry, as the traditional thermal mass flow sensing is not applicable for tariff due to its measurement uncertainties often are much larger than those required by the tariff meters. The micromachining technology together with the advanced electronics has shown its significantly improvement in metrology performance as well as the measurement dynamic range. Another key issue is the gas compatibility or the additional metrology errors due to the variation of the natural gas compositions as it is well known that the gas composition may vary even in the same distribution line due to the supply sources. The calorimetric sensing is dependent on the thermal properties of the gases, the uncertainties based on the traditional thermal mass flow concept are then unpredictable. Although it has been shown that using additional thermal property sensor such as a thermal conductivity sensor can help to compensate the deviation of the metrology due to gas composition variations but some uncertainties need to be acknowledged. Moreover, the calorimetric sensing flow measurement is utilizing thermistors which are also dependent on the temperature of the medium that they measure. Hence compensation of the thermistor properties due to the variation of the medium temperature must also be done properly. In the Italian national standard, the above two factors both yield metrology uncertainties. As the micromachined sensing element has a small dimension, contamination shall be always a concern as the long-term reliability requirement for the tariff meters. Finally, compared to the mechanical metrology technology, the electronic meters shall add labour cost for after sales even though the remote data may catch up such abnormal precisely.

In this paper, we report a new thermal time-of-flight sensing technology that is designed and made to address the above concerns in the current calorimetric utility gas meters, while to provide additional data sensing capability that shall ultimately beneficial for the industry.

## 2. Design of the thermal time-of-flight gas flow meter

### 2.1 Thermal time-of-flight sensing principle

Thermal time-of-flight sensing has been proposed for over 70 years but no major branded products have been made available with this technology. For an ideal thermal time-of-flight sensing with one-dimensional proximity, the change of the temperature  $T$  with time  $t$  in the flow direction  $x$  can be expressed as below,

$$\frac{\partial T}{\partial t} = D \left( \frac{\partial^2 T}{\partial x^2} \right) - V_x \left( \frac{\partial T}{\partial x} \right) \quad (1)$$

where  $D$  represents the fluid properties and  $V_x$  is the fluid velocity. Therefore, in order to obtain a fluid property independent measurement, at least two sensing elements (receivers) with different distances to the thermal transmitter (microheater) shall be required:

$$V_x = \sqrt{(d_1^2/t_1 - d_2^2/t_2)/(t_1 - t_2)} \quad (2)$$

where  $d_i$  is the distance between the thermal transmitter and the receiver, the two distances must not be the same in order to obtain the above proximity. In addition, the thermal transmitter and receiver shall be thermally isolated, and the distances between the transmitter and receiver shall be reasonable such that other thermal effects can be minimized. In an earlier report [6], a hot-wire thermal time-of-flight technology was used to build a prototype for the natural gas metering which was shown to be gas composition independent and the pure volumetric flow rate could be established. However, the hot wire construction was very fragile in a real gas flow medium. The prototype could only be a laboratory demonstration of the concept for the technology and the conversion into a product was not feasible.

The main purpose for a fluid property independent velocity or volumetric measurement is to establish the compliance with the existing metrology and tariff standard that is based on the mechanical measurement technologies, as the differences in the measurement principles would lead to a significant debating on the tariff standard and the consumer sensitivity. However, the desired tariff system shall have the temperature and pressure compensation for the pure velocity measurements, which then requires additional metrological budget for the incorporated temperature and pressure sensors, which on the other hand inevitably shall cost tariffs. Therefore, it is not the desired one to develop a meter only being capable of pure volumetric data acquisition. This could also be one

of the reasons that a pure thermal time-of-flight flow meter would not justify the efforts of development.

### 2.2 Micromachined thermal time-of-flight sensor

Compared to the traditional hot wire approach, the micromachined sensors have much more spaces as more sensors can be integrated onto the same sensing chip that shall be able to acquire the desired data. The design of a micromachined thermal time-of-flight sensor can be therefore not only to have the capability of measuring volume and mass flow rate that is fluid property independent in order to be in compliance with the existing metrology standards, but it is to further explore the addition capabilities that can address the other technical issues with the current calorimetric meters.

The basic structure of a micromachined thermal time-of-flight sensor can be found in the earlier disclosure [7] that also detailed the basic process for making of the actual sensor. Such a structure nevertheless did not address the current technical issues associated with the calorimetric meters. In the present work, we added an additional sensor to ensure the data acquisition is gas property independent. The thermal isolation shall be kept via the openings around the thermistors (sensors). The major changes in the current sensor design from the disclosed ones are the addition of a pair of the thermal energy harvesters located at the edge of the membrane on the same sensor chip.

### 2.3 Gas flow meter design

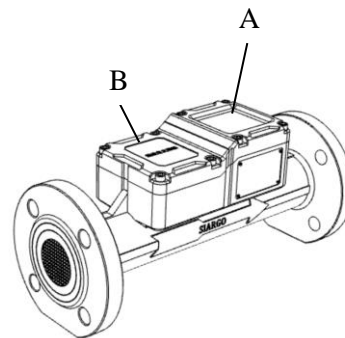
Even with the current advanced electronics, it is still desired to have the electronics for the smart gas meters being split into two major functional modules: one of the modules will be only designated to the metrology and another one for data communication. Such a design is based on the consideration that the communication module shall be the one that consumes most of the power while the metrology module shall be the one for tariffs. The communication protocol may change or vary depending on the local customers' requirements, but the metrology shall be universal once installed. In the practical case, the end users can be granted the access to the communication module such as to change the battery, but the metrology module shall be kept from access by untrained personnel.

For the metrology module, the electronics shall drive the microheater with a pulsar, and modulate the pulsar such that frequency can be tuned accordingly. The signals received by the two sensors at the downstream shall be processed to extract the time lag as well as the amplitude changes. The time lags shall be used for the

volumetric flow while the amplitude changes shall be a direct register of the mass flow as it is measured with the same principle as that for the calorimetric sensing. With the on-chip temperature sensor, the pressure could also be calculated by

$$V_{mass} = C \times V_{volume} \times (P/T) \quad (3)$$

where  $C$  is the constant related to the pressure and temperature at the reference conditions.



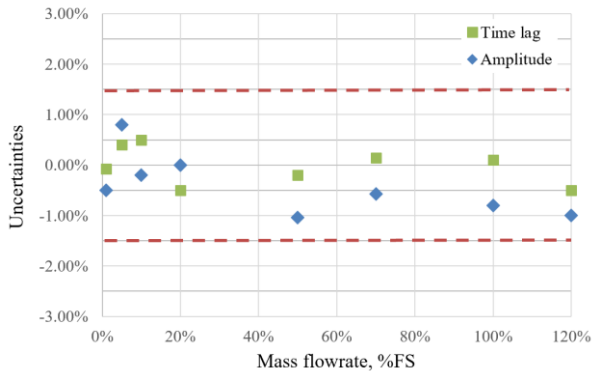
**Figure 1:** Design of a utility gas flow meter with micromachined time-of-flight sensing element. A – the metrology module; and B – the battery power chamber with data transmission module options.

Figure 1 shows the design of the utility meters for the commercial applications. Flow conditioner is installed at the inlet where flange connection is opted. The meter head has two chambers where chamber A is the metrology chamber that shall be sealed after calibration and/or verification. Chamber B contains the power pack with lithium ion batteries and the interface/module for data transmission. The modules are readily available and can be customized with communication protocols such as NB-IoT, LPWA or GPRS. In this paper, we shall not discuss the detailed design and options of the data transmission protocols.

## 3. Meter performance

### 3.1 Metrology performance in air

The meter was first calibrated with air at a sonic nozzle test bench that is described in a previous work [8]. Both the time lag and the amplitude data are registered during calibration. At the reference conditions (20°C, 101.325kPa), either the time lag or the amplitude data could be calibrated to the 150:1 dynamic range with the  $\pm 1.5\%$  uncertainties based on the design target. In general, the meter had a better accuracy in the dynamic range using the time lag data, while the amplitude (calorimetric) data were required to be applied with the offset stability algorithm.



**Figure 2:** The uncertainties measured from time lag and amplitude data at the reference conditions.

The meter was then subject to the verification of the metrology performance at conditions deviated from the reference to confirm the design goals of both volumetric and mass flow rate measurement. In the experiment, air was applied as the flow medium, and the reference meter is a laminar block mass flow meter with the volumetric value available simultaneously from Alicat Scientific with an uncertainty of  $\pm 0.4\%$ . The time lag data were compared for the reference condition (101.325kPa) and a positive pressurized flow at 170.182kPa while the mass flow rates were kept the same for both measurements. The temperature during the measurements were kept at the same ambient, which was 19.5°C in an air-conditioned environment. The amplitude (calorimetry) data verification for mass flow rate was also performed but it shall not be shown here since the calorimetric measurement principle was well known.

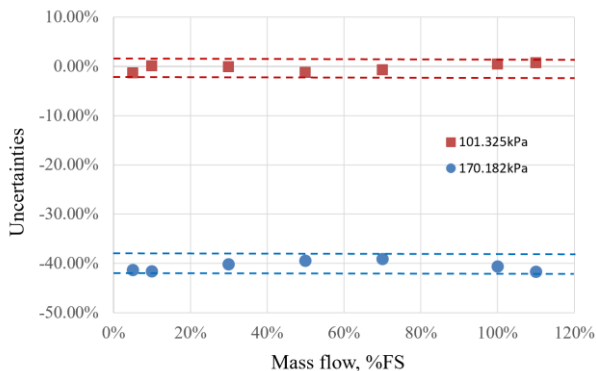


**Figure 3:** Time lag data verification against different pressure at the reference temperature.

The data shown in Figure 3 verified the volumetric flow measurement character as the pressure increases, the gas volume is compressed at the same mass flow rate. The volumetric flow will yield a smaller value vs mass flow rate with the increase of the line pressure if the temperature of the medium

is kept the same. In the above measurement shown in Figure 3, as the temperature was the same for both measurements, the relationship between the mass flow the volumetric flow then shall be determined by the pressure only,

$$(V_1 - V_0)/V_0 = (P_0/P_1) - 1 = 101.325/170.182 - 1 = -0.404$$

which matches well to the measured data. The data also indicated that if a temperature sensor is installed, for a specific gas with calibration, the pressure could be calculated via the simultaneously acquired time lag and amplitude data. In the micromachined sensing chip, since all sensors are made of thermistors, the temperature information is readily available. This would however be more complicated if the measured flow medium does not have a constant gas composition. The measured deviations between the amplitude and time lag data would not be registered correctly during the calibration. In such a case, direct calculate the pressure value would be difficult, it will then require an additional pressure sensor for the data.

### 3.2 Metrology performance in the natural gases of different gas compositions

For the current calorimetric metering technology with the micromachined sensing elements, to compensate the metrology uncertainties due to the gas composition change in flow medium, a thermistor that is not in the flow stream or perpendicular to the flow stream was used as a thermal conductivity sensor to metering the composition changes and calculate back for the corrected "volume". This is simply to have the measurement in compliance with the current tariff scheme which is based on the volume measurement. However, because of the thermistor is also temperature sensitive, there could be dependence on the flow rate as well, and the complete volumetric conversion scheme by the thermal conductivity values in a real product would be very challenging, making the conversion a proximity in most of the cases. This would be part of the reasons that the published Italian national standard allows additional metrology errors due to the gas composition variations [4].

Since the present thermal time-of-flight sensing could eliminate the gas property effects and lands on a volumetric measurement without additional compensation, the gas composition effects were tested for its metrology performance. The meter calibrated in air was then connected to a gas line that can supply pre-mixed gases. The reference meter was the same laminar block flow meter by Alicat Scientific. Two pre-mixed CH<sub>4</sub> based gases

with different gas compositions were selected to verify the metrology data of the air calibrated meter. The composition of these two gases are shown in Table 1. Both of the measurements with the time-of-flight time lag data (-TL) and the amplitude data (-A) were acquired for comparison.

**Table 1:** Compositions of the natural gases tested.

Gas \ Con.	CH4	C2H6	C3H8	Others
CH4	100%	0	0	0
CxHy	86.9%	8.5%	2.3%	2.3%

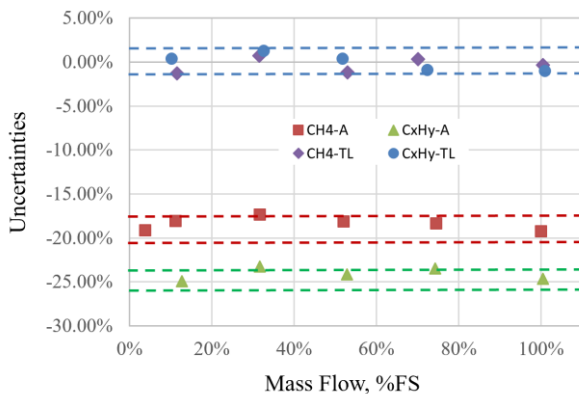


**Figure 4:** Verification measurements for gases with different compositions.

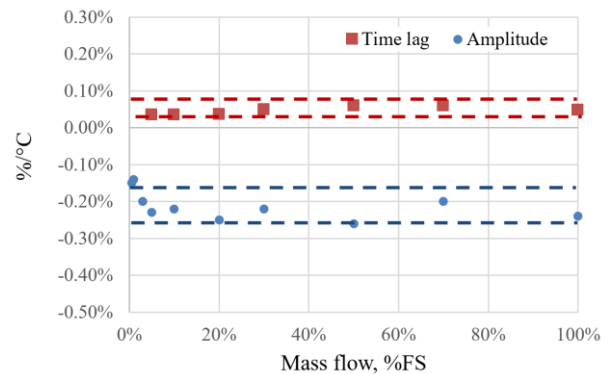
Figure 4 shows both of the acquired time lag data and amplitude data from two CH<sub>4</sub> based pre-mixed gases with the meter calibrated in air. The data indicated that the time lag data are not sensitive to the gas composition which is in consistence with the previous conclusions of the volumetric sensing character. Whereas the amplitude data are gas composition dependent, which was also in consistent with the calorimetric sensing characteristics. It is also showing that the time lag measurement would be more accurate if the volumetric tariff must be observed, although the conversion of the amplitude data to the volumetric data was feasible since the deviations were in parallel and the correction would then be readily achievable by applying a constant correction factor. However, it would be a directly observation that the conversion for an unknown gas composition could not be done without additional measurement, or additional sensing elements would be required to determine the gas properties which in turn would introduce additional uncertainties that were also registered in the Italian national standard [4].

### 3.2 Metrology performance due to temperature variations

Thermal mass (calorimetric) flow sensing was often mistaken by a claim that the measurement is intrinsically compensated with both temperature and pressure per the *mass flow* concept. However,

as the measurement actually utilizes the thermistors as the sensing elements, and the thermistors have a temperature dependence. Therefore, it is necessary to eliminate or compensate the thermistor temperature effects in order to have an accurate measurement which is a must for tariff. This compensation then inevitably shall introduce additional measurement uncertainties, which is also acknowledged in the Italian national standards. For thermal time-of-flight sensing, the time lag measurement shall have less effects by nature as the time domain data acquisition shall be dependent only on the delay of the thermal energy transferred with the flow medium. However, in the practical case, the thermal response and diffusivity might still play a role, and then the compensation would be required for the high precision data acquisition.

To test the temperature effects, the meter was connected to a copper pipeline with a temperature sensor inserted and the complete unit was placed into an environmental chamber that can have temperature varied. The same reference meter used in the experiment discussed in the previous sections was placed outside the environmental chamber at ambient. The data acquisition was started at a serial of set flow and temperature combinations after the temperature reading from the sensor was stabilized (<1% changes in 5 minutes).



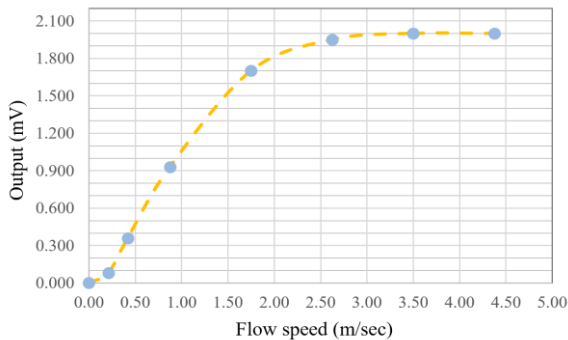
**Figure 5:** Verification measurements for gases with different compositions.

Figure 5 shows the averaged deviations of the measurement uncertainties per degree Celsius. The time lag sensing data were acquired from a circuitry without a feedback loop based on the environment temperature whereas the amplitude sensing data did operate at the constant temperature mode. The temperature effects were clearly much smaller for the time lag measurement and the temperature effects were opposite to the calorimetry revealing the characteristics of the mass flow and volumetric flow, respectively. A slightly flow rate dependence for both sets of data could be

observed. Therefore, to achieve a high precision measurement, temperature compensation would be required for the thermal time-of-flight measurement scheme as well, which could be due to the complete elimination of the thermal response and other related effects would not be feasible even with calibrations.

#### 4. Integration of an energy harvester

Another concern for the all-electronic utility meters is the power failure, as no battery manufacturer is willing to guarantee a zero-failure rate and the discharge pattern for each battery would not be 100% the same. Failure of the power shall directly lead to the cease of tariff records.



**Figure 6:** Direct output from a thermal (temperature) energy harvester.

Therefore, it has been a challenge whether the flow energy can be utilized to generate the power for metrology such that the tariff would not be lost due to power failure. For the utility gases, there would be three possibilities for energy harvesting: 1) the gas energy; 2) the flow (wind) energy; and 3) the thermal (temperature) energy. Among these three, the first two shall require some complicated physical process, and the reliability and safety would be also a challenge with the current status quo. The thermal energy would then be a possible and viable option. Figure 6 showed the direct output of voltage from such a device on the same sensor chip. The output started from a flow speed at about 0.05 m/sec and to about 2.5m/sec the output became unchanged. The large voltage output enables the circuitry to be waken up from a sleep mode which is another approach for power conservation. For a typical utility meter for residential applications, this would also make it possible for metering the flow from about 0.1 to 3 m<sup>3</sup>/hr without the microheater that is the main power consumption source. Hence, another than multiple onboard memories for data safety, the harvester could assist the basic functions of the meter even at the situation that the battery fails to power.

#### 5. Other considerations

The dual data acquisition scheme with the thermal time-of-flight sensing makes it possible to have the meter alarms for any possible presence of contaminants, as for the same reason that the time lag signal shall be less sensitive to the surface conditions of the sensing elements whereas the amplitude data have a close correlation.

#### 6. Concluding remarks

The current work presents a new flow measurement approach with the micromachined thermal time-of-flight sensing elements to obtain not only the volumetric but also the mass flow rate at the same time. This approach addresses the current concerns in existing tariff compliance for utility gases, and provide the mass flow capability for value added tariff. With further studies, the additional thermal values of thermal capacitance and thermal conductivity could also be measured from the modulated signals leading to the possibility of the ultimately desired thermal value metrology for the fairness of utility gas distributions.

The energy harvester shall be a direction for future work to a perfection of an electronic meter that shall be operated without a large battery source, or even without any external sources.

#### References

- [1] Deshpande, L T, "Gas meter growth movers from EMEA to APAC in long term", technology.ihs.com, 2019
- [2] Huang L J, "City natural gas metering", Chapter 9, *Natural Gas* (Rijeka, INTECH), 2012.
- [3] EN 14236: Ultrasonic Domestic Gas Meters, 2007.
- [4] UNI 11625: Gas Meters – Gas Meters with Mass Measurement Element – Thermal Capillary, 2016.
- [5] MeteRSit S.R.L, Facts and Figures, <http://www.metersit.com>.
- [6] Kang S S, and Nutt W E, "Development of a compact flow meter for residential natural gas metering, (New Hampshire, Creare Corporation), 1992.
- [7] Huang L J, Wu X, Yao Y and Chen C, "MEMS time-of flight thermal mass flow meter", US Patent 8,794,082, 2014.
- [8] Deng W et al., "Calibration and verification of MEMS mass flow meters for custody transfer", Proc. of the 15<sup>th</sup> Flow Measurement Conference, Taipei, 2010.

# Gas Cylinder Meter with Cloud Data Management

M. Dai, C. Zou, R. Liu, Y. Feng, W. Deng, L.J. Huang

*Siargo Ltd., 3100 De La Cruz Boulevard, Suite 210, Santa Clara, California 95054 USA  
E-mail: Liji@Siargo.com*

---

## Abstract

A thermal mass flow meter with micromachined sensing elements is designed and manufactured to address the accurate gas consumption, remote data and connectivity of gas cylinders in particular for medical, food and fuel supply industries. The designed flow meter has a rugged and compact enclosure whereas the flow dynamic range is over 100:1 with the mass flow totalizer capability. Verification of the metrology properties of this design was performed with a precise scale which weighted the gas consumption directly from the weight loss of the cylinder during usage, and compared to the totalized mass flow measured by the meter. The data transmission is realized via a Bluetooth and a smart device APP, or with a 3G/4G network or a NB-IoT or similar wireless network. For the grouped gas cylinders, the meter could also register each cylinder before usage or via a programmed consecutive register alert that can be timely sent to the end user. The data relayed to the cloud via the smart device/APP or a concentrator enable the gas cylinder user and suppliers to instantly access the cylinder status. The system enables the effective management of the gas cylinder manufacture, inventory and delivery. It also provides added value services to the end user who shall be timely notified for any programmed gas consumption.

---

## 1. Introduction

Gas cylinders have a variety of applications from medical operation to daily clean cooking. Gas cylinders are regulated via a mechanical valve with low accuracy pressure gauges and management of such is largely based on estimation only. Australian gas company El Gas is teaching its domestic customers to use a cup of hot water to alter the surface temperature of a cylinder resulting in a metering of the gas volume remained in a home fuel gas cylinder [1]. Some recommendations in the web-based knowledge even suggest a shaking of the cylinder would give the user a hint for the amount of the gas left inside the cylinder. These approaches are by far the accurate ones but also all have potential safety issues.

The domestic usage of the fuel cylinders would be mostly a matter of convenience, but in other applications instant knowledge of the gas status in a cylinder could be critical and helpful for not only gas consumers but gas cylinder suppliers. For example, medical oxygen cylinders have a large user base in a metropolis where the home care patient who needs oxygen therapy is still relying on the telecommunication with the suppliers. In this application, the suppliers could not manage the delivery of the needed cylinders in advance without

the knowledge of the instant status of the cylinders. In a large city, even the unexpected traffic conditions may prevent a promised delivery leading to customer complains. In addition, the suppliers must also constantly keep excessive inventory at various locations to meet the unexpected demands. In some cases, the failure of the timely supply would have even cost the loss of human life. Therefore, it is desired to develop not only a smart meter but a system that shall facilitate the usage of the cylinders. In a most recent disclosure [2,3], a special device is proposed to monitor the remaining gas volume of a gas container. Inside the special device a flow meter is used to measure a plurality of flowrates that vary when the gas is being consumed. However, the disclosed device for the gas consumption is based on a rolling mean or average of a plurality of non-continuous measured flow rate that may be quite deviated from the actual mass as it also requires the knowledge of the gas density, pressure and temperature. The disclosed device has a capability to be remotely connected to a system for the remote gas data management. This device requires external power sources and additional valves since it is an add-on unit, if direct attached to the high pressurized gas cylinder, it may have some safety risks, and particularly not all locations where a gas cylinder is placed would have an accessible power source, which then eliminates

the claimed application potentials. In another efforts, Linde Gas has developed an EVOS gas valve with electronic data transmission capability [4]. This valve utilizes the pressure sensor to estimate the consumption of gas volume and relay the data to the control centre for cylinder management. Nevertheless, both of the above systems are extremely costly compared to that for the current mechanical regulator and would not be practical for domestic applications.

In this paper, a battery powered device using mass flow sensing technology with micromachined thermal calorimetric sensors and cloud data enabled functions for the gas cylinder management is reported, and the corresponding applications are discussed.

## 2. Design of the device

### 2.1 Mass flow meter design

For a typical gas cylinder, a pressure regulator with mechanical pressure gauges is a standard accessory since the pressure inside the cylinder shall be too high to be directly connected to the devices for the end user. The traditional regulator for the cylinder is normally having two mechanical pressure gauges, one gauge is to measure the pressure inside the cylinder and another one to gauge the pressure in the pipeline to the end user. As the meter is designed to precisely measure the gas consumption via the pipeline to the end user, the mechanical pressure gauge at the outlet of the regulator is then not necessary and can be completely replaced by the meter. In order to have an easy adaption, the design of the flow meter is desired to be compact and easy to be connected to the outlet of the traditional pressure cylinder regulators.

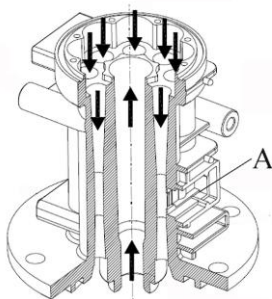


**Figure 1:** The flow metrology module mechanical design for the smart cylinder mass flow meter. A - is the location where the flow sensing elements are placed.

For the most of the industrial and medical gas cylinder applications, the end user pipeline pressure is within 10 bar and the mass flow rate is within 50

SLPM. In order to have the flow meter's mechanical dimension compatible to the most of the pressure regulator while the performance of the meter should meet these requirements, the conventional straight or bypass flow channel design would then not be feasible, and alternative design approach was considered. Figure 1 shows the designed flow metrology module with split flow channels, where the flow inlet is at the bottom central position and then the flow path splits into eight channels after it entered into a small buffer chamber at the top of the flow metrology mechanical module and the gas is further released from the bottom of the module. The channels are identical in its mechanical dimensions and distributed symmetrically with respect to the central flow inlet channel. The micromachined flow sensing element chip (indicated by letter A in Figure 1) is placed at the wall of one of these eight channels which have the configuration of the Venturi structure. The sensing elements are at the throat of the Venturi flow channel which helps for maintaining a better measurement stability.

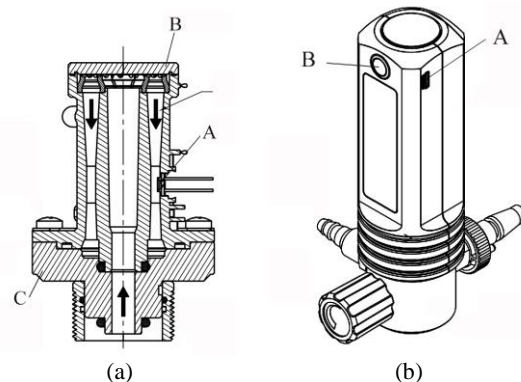


**Figure 2:** (a) the cross-section of the complete flow metrology module assembly where B is the top buffer chamber cap and A is where the flow sensing elements are located; and (b) the fully assembled smart flow meter for gas cylinders. The wired data port and external power socket is indicated by A, while B is the reset and functional selection button.

Figure 2 shows the assembly of the meter design. Figure 2(a) is the cross-section of the metrology module assembly. The flow metrology module shown in Figure 1 is made of polycarbonate inject mould and is installed onto a metal base C where the flow inlet and outlet are respectively at the central and outer circular path such that the base can also accommodate a manual control valve (Figure 2(b)) providing the capability of precisely adjusting and control of the gas supply, which is particularly important for medical applications. The capability of addition or removal of the mechanical connection ports from the meter base also provides the full spectrum of compatibility for different gas cylinder applications. For industrial applications, the manual valve would not be required, while for

medical applications such as oxygen delivery the adjust valve will be mandatory and this configuration also made the connection to a humidifier water cup much easier. The flow conditioners can be added to the buffer chamber B at the flow module to ensure the flow measurement stability. The reset and menu button B shown in Figure 2(b) provides the easy access to the meter for setting the password, switching the display from totalized readings to instant flow readings and resetting the totalizer. The completed assembled meter as shown in Figure 2(b) also has the battery chamber that accommodates two AA-size batteries or the same sized rechargeable batteries. For continuous measurement, the battery could work up to 90 days. A new sensor chip is being designed with a target for 180-day continuous measurement. The meter is incorporated with a wireless module that can be interchangeable depending on the application requirements. The available modules include a low energy Bluetooth (BLE), a 2G/3G/4G, a LoRa or a NB-IoT module. The APP is downloadable directly from Apple Store or Google Play Store under the name of *SmartCylinder* by Siargo. For gas cylinders delivered in a rack, the meter could also register each cylinder before usage or via a programmed consecutive register alert that can be timely sent to the end user as well as to the cloud server. The data relayed to the cloud via the smart device/APP enable the gas cylinder supplier as well as end user to instantly access the gas consumption information at each gas cylinder installed with the smart meter. A wired data port A shown in Figure 2(b) is also made available for wired data transmission or download the stored data in the meter in case the data transmission failure or power failure. The meter together with the cloud platform forms a system that allows the effective management of the gas cylinders for gas cylinder supplier for its management system for manufacture, inventory and delivery. It also provides added value services to the end user who could gain the accurate gas consumption and be alerted for the usage instantly.

The complete connected smart mass flow meter design utilizes an integrated control electronics with the micromachined sensing element targeting at a cost comparable to the quality mechanical pressure regulator for the gas cylinders, and can be massive manufactured and deployed.

## 2.2 Cloud data and system

Figure 3 shows the sketch of the smart gas cylinder system. The smart gas cylinder mass flow meter shall replace the outlet mechanical pressure gauge of the gas regulator. Depending on the specific applications, the mass flow meter shall opt one of

the wireless or even wired communication protocols to transmit the data to the cloud server. For example, if both local wireless and remote data are required, and a local smart device is readily available, then the mass flow meter with a BLE module shall be preferred, and the data can be relayed to the local smart device such as a smart phone with the designated APP. The local user with the smart phone will have direct access to the connected cylinder status while the data shall be simultaneously logged and transmitted to the cloud server via the data connected smart phone. In this example, the smart phone could also interact with the mass flow meter to reset the initial gas volume, timer, and perform other user defined functions, such as set the alarm level of the gas volume in the cylinder. Additionally, any relevant and authorized party can access the data anywhere via the cloud server to interact with the meter via the smart phone. This will be particularly helpful in case of a safety alarm or tariff related issue for the remote service providers. In case that a local smart device is unavailable or local data is not desired or required, the mass flow meter with a 2G/3G/4G wireless module can be selected. The data acquired from the mass flow meter can then directly be relayed to the cloud server for the authorized party to process. Per the common data safety practice, the acquired gas cylinder data by the mass flow meter shall also be stored into the plural number of memories in the control electronics inside the mass flow meter. These data can be readily downloaded to the authorized devices via the USB data port on the mass flow meter.

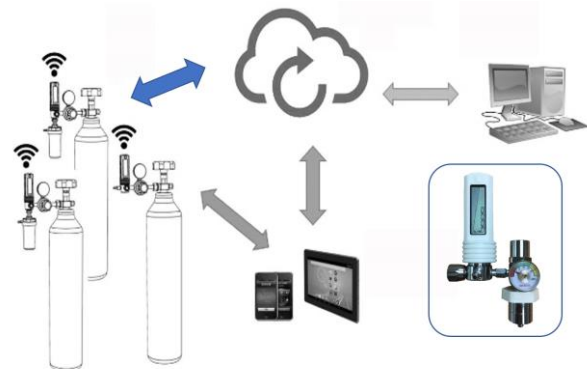


**Figure 3:** Schematic presentation of the smart gas cylinder management system where the smart gas cylinder meter is installed at each of the cylinder in the loop and the data are relayed to the cloud server directly or indirectly. Authorized users can interact with the gas cylinder via the cloud server. The insert shows an actual meter with a pressure regulator for medical gas cylinder

The complete meter-cloud server system discussed above can be fully customizable and the instant

data will make the close loop beneficial for both end users as well as the gas cylinder suppliers when the manufacture and inventory as well as delivery could be fully controlled.

### 3. Flow meter metrology verifications

Verification of the metrology properties of the designed mass flow meter was performed with a precise scale with an accuracy of  $\pm 1\%$  which weighted the cylinder before and after gas consumption and compared to the mass flow totalization measured by the meter installed on the same gas cylinder. For the cases of interests, a 12 kg capacity LPG gas cylinder connected to the LPG cooking appliance is used for this purpose. By adjusting the difference burning/cooking conditions, the different gas consumption can be obtained, then the data from each measurement were recorded and the comparison can be then corresponded. Another verification was done with an oxygen gas cylinder for home care, and similar procedure for comparison of the scale measured weight loss and flow meter obtained totalized mass flowrate were performed.

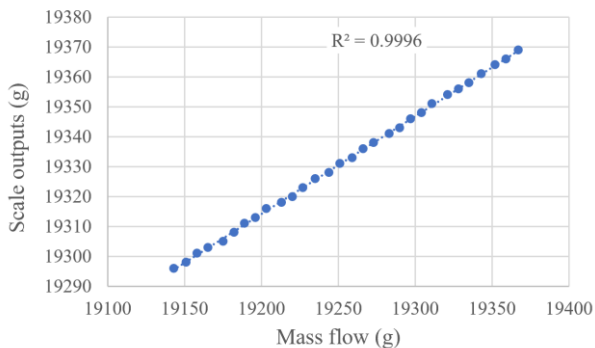


**Figure 4:** Mass flow meter readings against the scale outputs for a 12 kg LPG gas cylinder.

Figure 4 showed the measurement results from the comparison of the scale readings and the mass flow meter totalizer data from a 12 kg LPG gas cylinder connected to a cooking appliance. The mass flow meter was calibrated by air and converted to the LPG with a LPG gas conversion factor that was previously determined. The meter was reset to synchronize the readings by the scale before starting the verification measurement. The set of the measured data was acquired in a thirty-minute time period and each increment was one minute. It can be seen clearly a linearity of these two readings was well demonstrated which led to a narrow error band within about  $\pm 1\%$  that was beyond the accuracy attested.

Further verification measurements were performed with the same sized LPG cylinders having the scale as the reference as well but the data were collected at a random time period. Figure 5 shows the data collected from 10 such measurements. The verification measurement exhibited an  $\pm 2\%$  uncertainty, which is well within the design target.

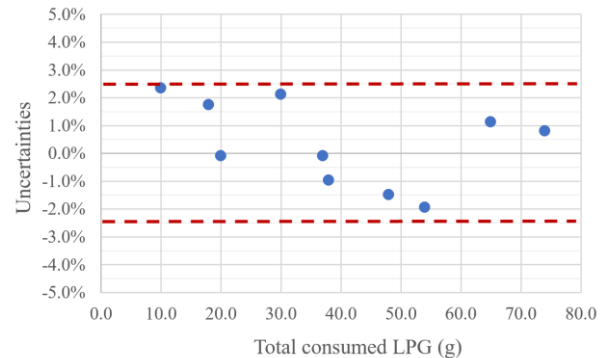


**Figure 5:** LPG gas consumption test data.

### 4. Application examples

There are vast numbers of gas cylinders on market. Some applications obviously may not require the connectivity and remote data, but the connectivity and cloud data can certainly provide critical benefits to a number of applications. These applications include:

- Medical gas cylinders, in particular for home care oxygen therapy supplied with cylinders. Currently the oxygen cylinder status is reported by the users and suppliers do not have any remote access to the status. There were reports of life lost due to the failure of timely delivery of the oxygen cylinders. On the other hands, the remote data access helps the manufacturer significantly in inventory and delivery management. Other than the home care oxygen cylinders, the connectivity can also effectively assist the management of the anesthesia gas cylinders used inside the ambulance or oxygen cylinders in hospitals.
- For clean energy gas home applications, LPG or LNG cylinders are main sources in many countries where energy gas pipeline sources are not available or too costly, for example, in many African countries, India, Australia etc. The connectivity and remote data shall help the energy saving, tariff management and a better lifestyle.
- For food industry, to preserve the freshness of the sea food, oxygen supply in vehicle via gas cylinders would be necessary during long

distance transportation. Management of these cylinders are very labor costly as each cylinder is required to be checked for its remaining volume before a new load of transportation. In some countries, food truck serving lunches or hot fast food often has its cooking energy supplied by the gas cylinders, status of those would certainly ease the efficiency of the performance.

- Other demanded applications include the industrial processing gases supplied by gas cylinders such as welding gases. Some special and expensive gas cylinders shall also appreciate the remote data for the management and cost saving.

## 5. Concluding remarks

The paper presents a design of a precise mass flow meter powered by batteries with wireless or wired connectivity for gas cylinders. The design is with a cost-effective approach targeted to replace one of the mechanical pressure gauge on the standard gas cylinder pressure regulator. The cost for the final product including the pressure regulator is comparable to that for current high-end mechanical pressure regulators. The connectivity and remote data from a cloud server significantly boost the gas cylinder management, cost saving, process control, user experience as well as safety. The connectivity may also reduce the loss of cylinder or facilitate to cylinder cycling. It benefits both the gas cylinder suppliers and end users.

## References

- [1] [www.elgas.com.au/blog/353](http://www.elgas.com.au/blog/353);  
[https://www.youtube.com/watch?time\\_continue=4&v=M85N6T0LI9w](https://www.youtube.com/watch?time_continue=4&v=M85N6T0LI9w)
- [2] Agnes H B, "New products for cylinders improve profitably", *Gas World US Edition*, **V56 (No.8)**, 32, 2018.
- [3] Wise E C, "Method and apparatus for monitoring, communicating and analyzing the amount of fluid in a tank", US Patent 9,435,675, September 6, 2016.
- [4] Bush S, "Smart IoT valve allows remote gas cylinder management" *Electronics Weekly*, online article, January 18, 2018.
- [5] Huang L. and Chen C., "Digital regulated gas dispensing apparatus with a MEMS flow meter", US Patent 10,240,723, March 26, 2019.

# Bilateral Comparison in the Calibration of Atmospheric Tank Provers by Volumetric and Gravimetric Methods

Kazuto Kawakita<sup>1</sup>, Valmir Ruiz<sup>1</sup>, Cezar Augusto Gonçalves<sup>2</sup>,  
Marcos Teruya<sup>2</sup>, William Escaletti dos Anjos<sup>2</sup>

<sup>1</sup>Institute for Technological Research of the State of Sao Paulo (IPT), São Paulo/SP, Brazil

<sup>2</sup>Weights and Measures Institute of the State of Sao Paulo (IPEM-SP), São Paulo/SP, Brazil  
kawakita@ipt.br, valmir@ipt.br, cagoncalves@ipem.sp.gov.br, mteruya@ipem.sp.gov.br,  
wanjos@ipem.sp.gov.br

---

## Abstract

Calibration of liquid quantity meters may be carried out volumetrically by collecting a known volume of liquid in a standard vessel. In this volumetric method, the standard vessel often known as atmospheric tank prover takes the form of a container with a calibrated volume. In its turn, calibration of the tank prover volume can be carried out by weighing the water contained in the vessel, or carried out using smaller volumetric measures which are themselves traceable to national standards by weighing methods. This paper presents a bilateral interlaboratory comparison in the calibration service of atmospheric tank provers carried out by Institute for Technological Research of the State of Sao Paulo (IPT) and Weights and Measures Institute of the State of São Paulo (IPEM-SP). The main objectives of the comparison were to validate the calibration results of two accredited laboratories and to comply with the requirements established by the accreditation standards regarding the participation of calibration laboratories in proficiency tests. Another important objective was to evaluate the comparability of the calibration methods used by the laboratories. IPT used the gravimetric weighting method and IPEM-SP used the volumetric method. The performances of the laboratories in the calibrations were quite satisfactory for both atmospheric tank provers used in the comparison. The normalized errors obtained were between 0.08 and 0.15 for the 20 L tank prover and 0.05 to 0.22 for the 1 000 L tank prover, indicating a very satisfactory comparability between the two calibration methods.

---

## 1. Introduction

Atmospheric tank provers are measurement standards often used in the calibration of liquid volume provers, which in turn are used in the calibration of oil flow meters installed in petroleum fiscal and production allocation measurement systems, in hydrocarbon custody transfer metering stations and also in the verification of volume totalizers of liquid fuels sold directly to consumers in gas stations. These devices are fundamental standards for establishing traceability in the measurement of these products and thus must have their volumes determined with accuracy and reliability. In Brazil, this equipment must be calibrated by accredited calibration laboratories at maximum intervals of three years.

In turn, the satisfactory participation of calibration laboratories in proficiency testing activities and in other types of interlaboratorial comparisons consists in a mechanism established by the ISO/IEC 17025 [1] standard

for the laboratories to ensure the validity of their measurement results. Among the many benefits of a laboratory participation in interlaboratory comparisons, it is worth mentioning the possibility of the laboratory comparing its metrological performance in measuring the value of a given quantity with another similar laboratory. Another benefit is the opportunity for the results obtained in the comparison to serve as a subsidy to improve the quality and reliability of the services provided by the laboratory.

## 2. Bilateral interlaboratory comparison

Based on the context presented previously and under a common interest and agreement, the Institute for Technological Research of the State of São Paulo (IPT) and the Weights and Measures Institute of the State of Sao Paulo (IPEM-SP) planned and carried out a bilateral interlaboratory comparison in the calibration service of atmospheric tank provers.

### 2.1 Objectives

The main objectives of the comparison were to validate the calibration results of both conformity assessment bodies and to comply with the requirements established by the accreditation standards regarding the regular participation of calibration laboratories in proficiency testing activities. Another important objective was to evaluate the comparability of the different calibration methods used by the laboratories.

Considering that it was a bilateral comparison between two public laboratories accredited by the Cgcre-General Coordination of Accreditation, the Brazilian ILAC member laboratory accreditation body, it was decided not to define a reference laboratory. Thus, the results obtained by one laboratory were directly compared with the results obtained by the other.

### 2.2 The tank provers used in the comparison

Two atmospheric tank provers with the characteristics presented in Table 1 were used for the comparison:

**Table 1:** Tank provers used in the comparison.

Tank prover	Characteristics
Tank prover of 20 L	Stainless steel atmospheric tank prover of 20 L, mark Impar, with carrying handle, identification number IE-02361, indication interval of $\pm 200$ cm <sup>3</sup> and resolution of the scale of 20 cm <sup>3</sup> .
Tank prover of 1000 L	Stainless steel atmospheric tank prover of 1000 L, unmarked, mounted on tripod, ball drain valve for discharge, identification number IE-09644, indication interval of $\pm 15$ L and resolution of the scale of 0.5 L.

Figures 1 and 2 show the two tank provers.



**Figure 1:** Tank prover of 20 L.      **Figure 2:** Tank prover of 1000 L.

According to the guidelines defined in the comparison protocol, the laboratories were not allowed to make any type of adjustment in the tank provers and, to provide

independence and impartiality, they should not know the results of the other laboratory until the calibrations were finished.

### 2.3 Calibrated scale points

Calibrations were performed in three points of the tank provers scales: the zero point corresponding to the nominal volume of the tank prover, an upper point and a lower point as shown in the Table 2.

**Table 2:** Chosen scale points for each calibrated tank prover.

Scale point	20 L tank prover		1 000 L tank prover	
	Scale mark	Nominal volume	Scale mark	Nominal volume
Lower	-200 mL	19.8 L	-10 L	990 L
Zero	0 mL	20.0 L	0 L	1 000 L
Upper	+200 mL	20.2 L	+10 L	1 010 L

After calibration, each participating laboratory prepared a calibration certificate for each tank prover, including the calibrated items data, calibration procedure used and the results obtained. After that, a technical meeting was held at IPEM-SP with representatives from both laboratories in order to disclose and compare the results.

The performance evaluation of the participants of the interlaboratory comparison was made using the criterion of normalized error calculated for the measurement bias quantity determined by the laboratories for each artifact.

## 3. Calibration methods

For the calibration of the tank provers each laboratory used its own method of calibration and calculation of results and uncertainties. IPEM-SP used the volumetric method and IPT used the gravimetric method of static weighing of the water contained in the tank prover.

### 3.1 Volumetric method

Calibration of an atmospheric tank prover by volumetric method consists on transfers of liquids (usually water) from standard volume measures from which the transferred volume and its measurement uncertainty required for calibration is known [2]. Since the volume of the transferred liquid is known, the scale of the atmospheric tank prover under calibration is compared with the meniscus of liquid formed during the calibration.

#### 3.1.1 Preparing the tank prover for calibration

Before carrying out the measurements, the atmospheric tank prover must be filled with clean water and after this water is poured (small prover) or drained through the drain discharge valve (large prover). After most of the water is released from the tank, a period of 30 seconds must be taken so that the discharge valve is opened and closed three times so as to deplete the residual water that has drained from the inner walls of the reservoir.

### 3.1.2 Measurements on the neck scale reading of zero of the tank provers

For the 1 000 L tank prover under calibration, a standard volume measure with nominal volume of 100 L was used ten times in order to transfer about 1 000 L of water into it. For the 20 L tank prover under calibration, a standard volume measure with nominal volume of 20 L was used once. Then the meniscus of water in both tank provers were adjusted to the respective zero point of the scale using standard glasswares.

The volumes of water transferred by the standard volume measures and by the standard glasswares give the reference volumes of the tank provers scales at zero point.

### 3.1.3 Measurements on the upper point

Since the zero point was measured, standard glasswares were used to provide more water into each tank prover until the meniscus of water reaches the chosen upper point of the scale. So its volume is calculated from the reference volume determined at zero point plus the volumes transferred by the standard glasswares.

### 3.1.4 Measurements on the lower point

Once the volume of upper point is calculated, standard glasswares were used to remove water from each tank prover until the meniscus of water reaches the chosen lower point. Thus the volume of lower point is calculated by the volume determined on the upper point minus the volume of water removed by the standard glasswares.

For each point measured, the temperature of water is determined using a digital thermometer. Once the measurements of the three points are finished, the steps described from 3.1.1 to 3.1.4 are repeated twice in order to determine the average volumes and their uncertainties.

### 3.1.5 Environmental parameters

The environmental parameters prevailing during the execution of both calibrations are shown in Table 3.

**Table 3:** Environmental parameters during calibrations.

Tank prover	Water temperature (°C)	Air temperature (°C)	Relative humidity (%)
1 000 L	19,1 ± 0,6	19,8 ± 0,4	63,7 ± 2,9
20 L	20,0 ± 0,2	19,7 ± 0,2	61,6 ± 1,4

### 3.1.6 Corrections on the volume determinations

Environmental parameters, especially temperature, are able to modify the volume of liquids and containers. The volume of a tank prover is usually referred as it is used at 20 °C, so the reference volume results should correspond to the volumes of the tank provers at 20 °C. Since the calibrations are generally performed at temperatures other than 20 °C, the measured volumes must be corrected to 20 °C as follows:

$$V_{Pt1} = V_{P20} \cdot [1 + \gamma_P \cdot (t_1 - 20)] \quad (1)$$

$$V_{ob20} = V_{Pt1} \cdot [1 - \gamma_{ob} \cdot (t_2 - 20)] \quad (2)$$

where:

- $V_{Pt1}$  : liquid volume in the standard at temperature  $t_1$ ;
- $V_{P20}$  : liquid volume in the standard at 20 °C;
- $V_{ob20}$  : corrected liquid volume on the object at 20 °C;
- $t_1$  : water temperature on the standard;
- $t_2$  : water temperature on the tank prover;
- $\gamma_P$  : thermal expansion coefficient of the standard;
- $\gamma_{ob}$  : thermal expansion coefficient of the tank prover.

Equation (1) corrects the volume of water delivered by the standard measures when its temperature is different from 20 °C. Then Equation (2) corrects the volume of the tank prover under calibration as it should be at 20 °C [3].

### 3.1.7 Sources of measurement uncertainties

Basically, the measurement uncertainties of each calibration results consider the standard deviation of the three volume measurements and the uncertainties from the standard volume measures, standard glasswares and temperature measurements. The uncertainties are calculated as described in reference [4].

### 3.2 Gravimetric method

The gravimetric method of calibration of atmospheric tank provers used by IPT is based on the static weighing of the mass of water contained in the tank prover using an electronic scale. The reference volume is determined from the value of the measured mass of water and its density at measuring conditions [6].

At IPT, calibration of tank provers with volumetric capacity up to 500 L is carried out in a single weighing. For vessels of capacities above 500 L, calibration is performed by means of multiple weighing and where the sum of the collected weighing matches the total volume of the tank prover. In this case, it is recommended to use the lowest number of weighing to minimize the final uncertainty associated to the measured volume.

#### 3.2.1 Calibration assembly

Assemblies presented in Figures 3 and 4 were used for the calibration of the 20 L and the 1 000 L tank provers according to the gravimetric method.

#### 3.2.2 Preparation for calibration

Tank provers are used to measure volumes of various types of liquid products that can contaminate the clean water used in the calibration. In order to avoid this type of problem, tank provers were checked for cleanliness before being calibrated. After that, tank provers were filled with clean water and inspected to check for leaks.

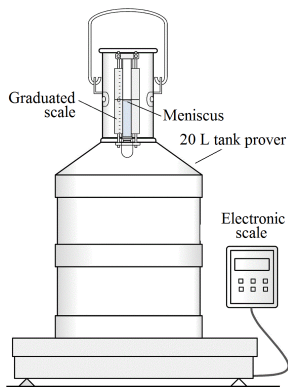


Figure 3: Schematic for calibration of the 20 L tank prover.

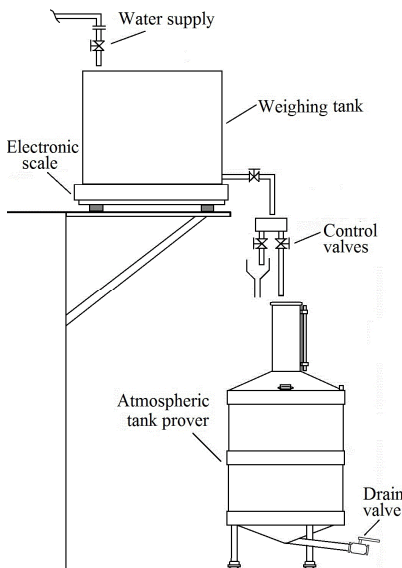


Figure 4: Schematic for calibration of the 1000 L tank prover.

The stability of the water temperature is a key factor for the success of the calibration. So, the water temperature during calibration should remain as stable as possible. The ideal calibration condition occurs with a maximum difference between the ambient air temperature and the water temperature of  $\pm 1$  °C.

### 3.2.3 Calibration of the tank prover nominal volume

Calibration of the 20 L tank prover was performed by directly comparing the volume of water collected in the prover and the mass of water measured using an electronic scale. For that, the dry tank prover was carefully filled with water to the point of the scale to be calibrated. The water density at the calibration temperature was used for determination of the tank prover volume.

Calibration of the 1000 L tank prover was carried out according to the following steps:

- The scale was reset after verifying its normal operation.
- Carefully, place the weighing tank on the scale.
- Level the tank prover.
- Fill the tank prover with clean water up to the neck.
- Drain the tank prover by observing the flow of the water in the drain valve; when the drain is no longer a continuous water fillet, that is when the water begins to drip at the outlet of the drain valve, start timing with a stopwatch, and after 30 seconds close the drain.
- Take note of the initial mass value indicated in the scale (Important: the scale should not be zeroed).
- Fill the tank prover with water to the point of the scale to be calibrated; use a pipette when the water level is close to the mark to minimize the effect of the meniscus that is normally formed during the filling process.
- Wait for a period of stabilization of the temperatures of the water and the tank prover wall; start reading the parameters by entering the following values:
  - volume indicated in the tank prover,
  - initial mass value indicated in the scale with tank prover empty,
  - final mass value indicated in the scale with tank prover filled with water,
  - tank prover wall temperature,
  - water temperature inside the tank prover,
  - atmospheric pressure and
  - ambient air temperature and relative humidity.
- Empty the tank prover and repeat the procedure twice.
- Enter the data obtained in the three measurements in the calculation software and analyse the results.

### 3.2.4 Calculation Methodology

The volume of water contained in the tank prover by the gravimetric method is determined by equation (3):

$$V_{\text{water}} = \frac{m_{\text{water}}}{\rho_{\text{water}}} \quad (3)$$

where:

- $V_{\text{water}}$  : volume of water contained in the tank prover [m<sup>3</sup>];
- $m_{\text{water}}$  : mass of water measured by the scale [kg];
- $\rho_{\text{water}}$  : density of the water in the tank prover temperature when filled with water [kg/m<sup>3</sup>].

- *Correction of the apparent initial mass indicated on the scale according to its calibration certificate*

$$m_{\text{init\_ind\_corr}} = m_{\text{init\_ind}} + k_1 \quad (4)$$

where:

- $m_{\text{init\_ind\_corr}}$  : initial mass indicated on the scale and corrected by its calibration certificate [kg];
- $m_{\text{init\_ind}}$  : initial mass indicated on the scale [kg];
- $k_1$  : initial mass correction value, obtained from the scale calibration certificate [kg].

The method of calculating the apparent final mass indicated on the scale follows the same procedure.

• *Determination of the initial reference mass*

Correction of apparent initial mass of water for air buoyancy effect:

$$m_{\text{init\_refer}} = (m_{\text{init\_ind\_corr}}) \cdot \frac{\rho_{\text{water\_scale}} \cdot (\rho_{\text{std\_mass}} - \rho_{\text{air\_scale\_cal}})}{\rho_{\text{std\_mass}} \cdot (\rho_{\text{water\_scale}} - \rho_{\text{air\_tank\_cal}})} \quad (5)$$

where:

- $m_{\text{init\_refer}}$  : initial reference mass [kg];
- $\rho_{\text{water\_scale}}$  : density of the water at the temperature inside the weighing tank [kg/m<sup>3</sup>];
- $\rho_{\text{std\_mass}}$  : density of the standard mass used in the calibration of the scale [8000 kg/m<sup>3</sup>];
- $\rho_{\text{air\_scale\_cal}}$  : density of the ambient air during calibration of the scale [1.2 kg/m<sup>3</sup>];
- $\rho_{\text{air\_tank\_cal}}$  : density of the ambient air during tank prover calibration [kg/m<sup>3</sup>].

The method of calculating the final reference mass follows the same procedure.

• *Determination of the net reference mass of water*

$$m_{\text{ref}} = m_{\text{final\_refer}} - m_{\text{init\_refer}} \quad (6)$$

where:

- $m_{\text{ref}}$  : reference mass [kg];
- $m_{\text{final\_refer}}$  : final reference mass [kg];
- $m_{\text{init\_refer}}$  : initial reference mass [kg].

• *Density of water used in tank prover calibration*

Calibration of the 20 L tank prover was performed using distilled water. Density of the distilled water used to convert the mass of water to an equivalent volume of the liquid is given by the following state equation [5]:

$$\rho_{\text{dist\_water}} = 999,8395639 + 0,06798299989 \cdot T_{\text{tank}} - 0,009106025564 \cdot T_{\text{tank}}^2 + 0,0001005272999 \cdot T_{\text{tank}}^3 - 0,000001126713526 \cdot T_{\text{tank}}^4 + 0,000000006591795606 \cdot T_{\text{tank}}^5 \quad (7)$$

where:

- $T_{\text{tank}}$  : water temperature at the tank prover temperature [°C];
- $\rho_{\text{dist\_water}}$  : density of water at the tank prover temperature [kg/m<sup>3</sup>].

Calibration of the 1 000 L tank prover was carried out using clean water and the water density was determined using a calibrated density meter.

• *Determination of the tank prover reference volume at the calibration temperature*

Reference volume of the tank prover at the calibration temperature is calculated using the following equation:

$$V_{\text{refer}} = \frac{m_{\text{refer}}}{\rho_{\text{water\_tank}}} \quad (8)$$

where:

- $V_{\text{refer}}$  : reference volume at tank prover temperature [m<sup>3</sup>];
- $\rho_{\text{water\_tank}}$  : water density at the tank prover temperature [kg/m<sup>3</sup>].

• *Calculation of the volume of the tank prover referred to the temperature of 20 °C*

$$V_{20\text{ °C}} = \frac{V_{\text{refer}}}{CTS} \quad (9)$$

where:

- $V_{20\text{ °C}}$  : volume of the tank prover at the reference temperature of 20 °C [L];
- $V_{\text{refer}}$  : volume of the tank prover at the tank prover temperature [m<sup>3</sup>];
- $CTS$  : correction factor by thermal expansion of the tank prover material.

• *Correction factor by thermal expansion of the tank prover material (CTS)*

$$CTS = 1 + G_c \cdot (T_{\text{tank}} - 20) \quad (10)$$

where:

- $CTS$  : thermal expansion correction factor of the tank prover material;
- $G_c$  : volumetric thermal expansion coefficient of the tank prover material [1/°C];
- $T_{\text{tank}}$  : tank prover temperature [°C];
- 20 : reference temperature of 20 °C.

• *Measurement bias calculation*

$$E = 100 \cdot \left( \frac{V_{\text{nom\_vol}} - V_{\text{refer}}(20\text{ °C})}{V_{\text{refer}}(20\text{ °C})} \right) \quad (11)$$

where:

- $E$  : measurement bias of volume indication of the tank prover [L];
- $V_{\text{refer}}(20\text{ °C})$  : reference volume of tank prover corrected for the reference condition of 20 °C [L];
- $V_{\text{nom\_vol}}$  : volume indicated on the mark scale [L].

3.2.5 Sources of measurement uncertainties

In the gravimetric method, the measurement uncertainties of each calibration results consider the standard deviation of the three volume measurements and the uncertainties associated to the reference mass measurements, water density, air density, tank material expansion factor and temperature measurements. The uncertainties are calculated according to the guidelines of reference [4].

#### 4. Calibration results

Tables 4 to 7 present the results obtained by IPEM-SP and IPT in the calibration of the two tank provers.

**Table 4:** Results of IPEM-SP for calibration of 20 L tank prover.

(Mark scale) Nominal volume (L)	Reference volume (L)	Measurement bias (L)	Expanded uncertainty (L)	Coverage factor <i>k</i>
(-02) 19,8	19,805	-0,005	0,005	2,0
(0) 20,0	20,003	-0,003	0,005	2,0
(+0,2) 20,2	20,202	-0,002	0,005	2,0

**Table 5:** Results of IPT for calibration of 20 L tank prover.

(Mark scale) Nominal volume (L)	Reference volume (L)	Measurement bias (L)	Expanded uncertainty (L)	Coverage factor <i>k</i>
(-02) 19,8	19,804	-0,004	0,012	2,02
(0) 20,0	20,004	-0,004	0,012	2,02
(+0,2) 20,2	20,204	-0,004	0,012	2,02

**Table 6:** Results of IPEM-SP for calibration of 1 000 L tank prover.

(Mark scale) Nominal volume (L)	Reference volume (L)	Measurement bias (L)	Expanded uncertainty (L)	Coverage factor <i>k</i>
(-10) 990	989,79	0,21	0,12	2,0
(0) 1000	1000,04	-0,04	0,12	2,0
(+10) 1010	1010,48	-0,48	0,12	2,0

**Table 7:** Results of IPT for calibration of 1 000 L tank prover.

(Mark scale) Nominal volume (L)	Reference volume (L)	Measurement bias (L)	Expanded uncertainty (L)	Coverage factor <i>k</i>
(-10) 990	989,7	0,3	0,4	2,03
(0) 1000	1000,1	-0,1	0,4	2,03
(+10) 1010	1010,5	-0,5	0,4	2,03

#### 5. Evaluation of the results

The evaluation of the performance of the participants in the interlaboratory comparison was performed using the normalized error (*NE*) criterion calculated for the measurement bias parameter, according to the expression:

$$NE = \left| \frac{E_{IPEM} - E_{IPT}}{\sqrt{U_{IPEM}^2 + U_{IPT}^2}} \right| \quad (12)$$

where:

$E_{IPEM}$  : result obtained by IPEM-SP laboratory;

$E_{IPT}$  : result obtained by IPT laboratory;

$U_{IPEM}$  : expanded uncertainty associated to the results of IPEM-SP laboratory;

$U_{IPT}$  : expanded uncertainty associated to the results of IPT laboratory.

Tables 8 and 9 show the results of the evaluation of normalized error obtained in the comparison of the results of the calibrations carried out by IPEM-SP and IPT for the tank provers of 20 L and 1000 L.

**Table 8:** Normalized error for the results of 20 L tank prover.

(Mark scale) Nominal volume (L)	Difference between measurement bias Values (L)	Normalized error <i>NE</i>
(-02) 19,8	-0,001	0,08
(0) 20,0	0,001	0,08
(+0,2) 20,2	0,002	0,15

**Table 9:** Normalized error for the results of 1000 L tank prover.

(Mark scale) Nominal volume (L)	Difference between measurement bias Values (L)	Normalized error <i>NE</i>
(-10) 990	-0,094	0,22
(0) 1000	0,064	0,14
(+10) 1010	0,019	0,05

#### 6. Conclusion

In summary, results presented in Tables 4 to 9 show that the performance of the laboratories in the calibrations were quite satisfactory for both atmospheric tank provers used in the comparison, especially considering that different calibration methods were used for determination of the reference volumes. The normalized errors obtained were between 0.08 and 0.15 for the 20 L tank prover and 0.05 to 0.22 for the 1000 L tank prover, indicating a very satisfactory comparability between the two calibration methods.

#### References

- [1] ISO/IEC 17025 *General requirements for the competence of testing and calibration laboratories*, 2017, Geneva, Switzerland.
- [2] OIML R120: *Standard capacity measures for testing measuring systems for liquids other than water*, 2010.
- [3] ISO 4787: *Laboratory glassware - Volumetric instruments - Methods for testing of capacity and for use*, 2010.
- [4] ISO/IEC Guide 98-3: *Uncertainty of measurement - Part 3: Guide to the expression of uncertainty in measurement (GUM:1995)*, 2005.
- [5] PTB Handbook 1968 Mitt, Vol. 81, N° 6, pages 412, 414 and 197.
- [6] API - MPMS – Chapter 4.9.4 – *Proving Systems, Section 9 – Methods of Calibration for Displacement and Volumetric Tank Provers, Part 4 Determination of Volume of Displacement and Tank Provers by the Gravimetric Method of Calibration*.

# Design of gravimetric primary standards for field testing of hydrogen refuelling stations

M. de Huu, M. Tschannen, H. Bissig

Federal Institute of Metrology METAS, Lindenweg 50, 3003 Bern-Wabern, Switzerland  
E-mail (corresponding author): marc.dehuu@metas.ch

---

## Abstract

The Federal Institute of Metrology METAS developed a Hydrogen Field Test Standard (HFTS) that can be used for field verification and calibration of hydrogen refuelling stations. The testing method is based on the gravimetric principle. The experimental design of the HFTS as well as the description of the method are presented here. The HFTS has been tested at METAS with nitrogen gas at  $-40^{\circ}\text{C}$  to mimic a refuelling process in the field. Laboratory tests have shown that icing on the pipes of the HFTS have a non-negligible impact on the results. The major uncertainty components have been identified and assigned values. The required expanded uncertainty of 0.3% could be achieved. A detailed uncertainty budget has been presented and shows that the scale is the largest contributor; buoyancy corrections only play a minor role. For the lowest uncertainty measurements, appropriate waiting times or cleaning methods to get rid of icing are required.

---

## 1. Introduction

A large hydrogen infrastructure is currently in development across Europe. The industry faces the dilemma that they are required to meet certain measurement requirements set by legislation that currently cannot be followed due to the lack of available methods and standards. One important metrological challenge is the accurate measurement of the amount of delivered hydrogen during refuelling.

Hydrogen refuelling stations look and operate in a very similar way to petrol stations, the only difference being that the delivered amount is given in kg. The SAE J2601 [1] establishes the protocol and process limits for hydrogen fuelling of light duty vehicles so that the vehicle storage tanks don't overheat or overfill. Vehicles are typically refuelled with precooled hydrogen gas from dispensers within 3 min to 5 min from banks of pressurized cylinders. Fuel delivery temperature, the maximum fuel flow rate, the rate of pressure increase and the ending pressure are all parameters that are defined by process limits and are affected by ambient temperature, fuel delivery temperature and initial pressure in the vehicle's hydrogen tank. During a fill, temperature and pressure span wide ranges: pressure can go from 0.1 MPa up to a nominal working pressure of 70 MPa; to allow short filling times, hydrogen can be precooled down to  $-40^{\circ}\text{C}$ . Mass flow is determined

by a pressure-ramp rate (PRR) that depend on initial pressure, available volume and temperature. We are thus far from steady conditions and only limited studies of high pressure hydrogen flow meters and transients conditions have been performed [2, 3].

International requirements propose accuracies for meters used in hydrogen refuelling station [4] and only very limited studies have been performed on how to test, inspect and verify such systems under laboratory conditions and in the field.

In the EMPIR Metrology for Hydrogen Vehicles (MetroHyVe) project, this is addressed through the development of several mobile gravimetric standards for field verification as well as an investigation into the use of substitute fluids for laboratory testing or calibration of flow meters used in hydrogen refuelling stations (HRS). In the gravimetric method, the dispensed mass is determined by weighing the amount of delivered hydrogen collected in a pressure vessel on a scale. We chose the gravimetric method because it is a well-known method that should allow obtaining the needed expanded uncertainty of 0.3%, one fifth of the proposed requirement of 1.5% Maximum Permissible Error (MPE) for flow meters.

In the course of the MetroHyVe project, three field test standards are being developed by members of the consortium: Justervesenet, METAS and VSL while CESAME Exadebit is using a standard built by Air Liquide.

In this work, we constructed a Hydrogen Field Test Standard certified for measurements in an environment with explosive atmosphere and performed measurements in the laboratory using nitrogen gas cooled down to  $-40^{\circ}\text{C}$  to mimic real conditions as encountered in a HRS. The major uncertainty components have been identified and assigned values. The required expanded uncertainty of 0.3% could be achieved and a field test phase will follow this work.

## 2. Experimental design

### 2.1 Mechanical design

The Hydrogen Field Test Standard (HFTS) consists of two 36 L pressure tanks mounted into an aluminium frame. The tanks are type 4 cylinders (carbon fibre-reinforced epoxy with a plastic liner) with a service pressure of 70 MPa (at  $15^{\circ}\text{C}$ ), corresponding to a capacity of 1.44 kg  $\text{H}_2$  each. The nominal empty mass of each tank is 33 kg with dimensions of 320.8 mm x 910.3 mm. Figure 1 shows the HFTS in its frame resting on its aluminium base plate (1900 mm x 1000 mm). The total weight is around 400 kg. The HFTS alone weighs around 150 kg.

The HFTS is equipped with two 27 cm long Pt 100 probes inserted at one end of each tank and two digital pressure transducers with a 100 MPa range. Additional Pt 100 probes are mounted on the HFTS to monitor temperature in the tubing and around the scale. Passive pressure gauges are also mounted before the tanks. A Coriolis mass flow meter is also part of the HFTS and can be placed in series with the piping leading to the tanks for monitoring or eventual calibration purposes.

The frame is mounted on a 300 kg scale with 0.1 g resolution for gravimetric measurements. The weight of the frame can be lifted from the scale by a load removal system activated by a hand pump. The complete system (HFTS + scale) is placed on an aluminium base plate, which can be lifted with a forklift and placed into a van for transport.

Accompanying the HFTS are a secondary ESD plastic frame to protect the scale from the environment (shown in Figure 2), a mobile data acquisition system with laptop and a 4 m tall stainless steel vent stack with support for venting the hydrogen gas in the field after a fill. During transport, the HFTS's load is removed from the scale and held in place by locking nuts. A detailed description of the operating instructions is part of the internal documentation of the HFTS.



**Figure 1:** HFTS resting on its base plate.



**Figure 2:** HFTS with housing, here partially closed. The open space between base plate and housing is 25 cm. The housing is not leak tight.

### 2.2 Flow scheme

Figure 3 shows the Piping and Instrumentation Diagram (P&ID) of the HFTS. The system is composed of three lines: an inlet line connected to the hydrogen dispenser, a purge line to flush the system with  $\text{N}_2$  and an outlet line for blowing the tanks down. The components located in the blue box are part of the frame that is being weighed on the scale. The hydrogen from the dispenser enters the HFTS through a nozzle as mounted on a car and is guided into the tanks. The gas can pass through the Coriolis mass flow meter, depending on the position of the needle valves V-4, V-1 and V-5. After filling, the tanks are emptied through a vent stack after passing through a cascade of pressure reducing valves PR-1 and PR-2 located after the needle valve V-9.

The base plate accommodates the piping for the load removal system (in red in Figure 3) as well as the piping for flushing and purging the tanks of all hydrogen gas before transport. Several nozzles placed around the frame allow flooding the ESD

housing with an inert gas during the measurements to prevent eventual icing on the pipes. All the piping in contact with hydrogen is made of medium pressure ¼" tubing, NPT and FK series fittings and valves in 316-stainless steel.

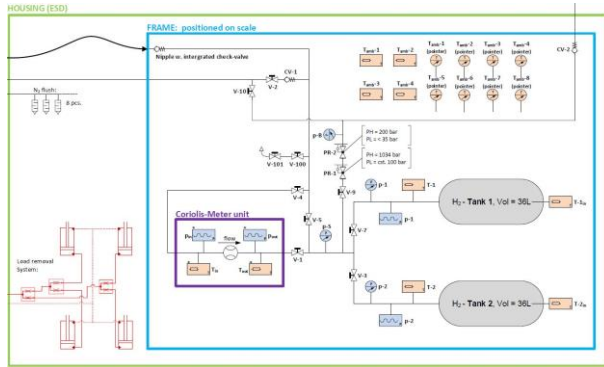


Figure 3: HFTS Piping and Instrumentation Diagram.

### 2.3 Electrical scheme and Data acquisition

The HFTS will store high-pressure hydrogen during field-testing and is therefore considered as equipment in an environment with explosive atmosphere (ATEX Zone 2). This puts some constraints on the design of the electrical scheme and data acquisition (DAQ) system as well as on the choice of sensors.

Figure 4 shows the electrical scheme of the HFTS. The components in the coloured part are located in the explosive atmosphere zone and are all certified. This includes the temperature probes, the pressure sensors, the scale and the Coriolis mass flow meter. These last two instruments are considered as non-arcing and are connected to the DAQ system through their own transmitters or readout modules. The remaining sensors are connected through terminal boxes to safety barriers located in the DAQ rack outside the ATEX Zone. An earth monitoring system (in yellow in Figure 4) guarantees that the HFTS and its DAQ system are continuously grounded with the hydrogen refuelling station to prevent electrostatic charges as ignition sources.

The DAQ system is shown in Figure 5 and acquires data from the scale and the temperature and pressure sensors. All cables can be plugged or unplugged from the HFTS to eliminate torqueing of the scale during weighing. The Coriolis mass flow meter is connected through a dedicated transmitter that is not part of the DAQ system.

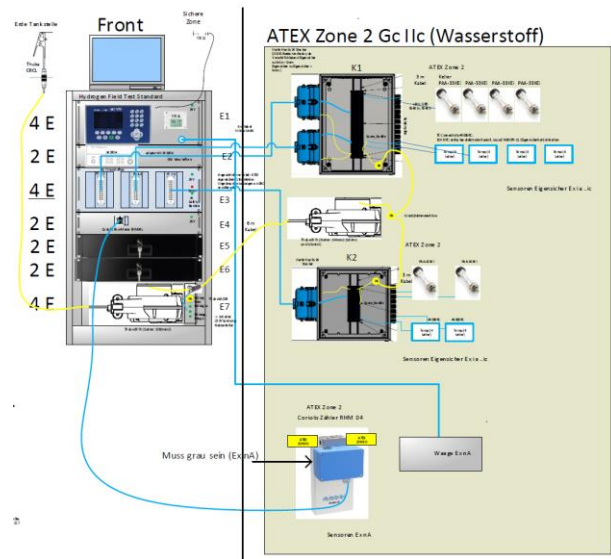


Figure 4: Electrical connections from the DAQ system to the ATEX Zone 2.



Figure 5: DAQ system with the various components (top to bottom): scale display, ambient conditions monitoring, multimeter and connection cables to the HFTS.

### 3. Description of the method

The HFTS is used to measure the mass of gas delivered into a vehicle. The method will be presented here.

The dispensed mass into the HFTS is calculated by:

$$m_{H_2} = m_2 - m_1 \quad (1)$$

Where  $m$  is the true mass and the subscripts denote the mass of the HFTS before and after the filling, respectively. The mass indicated by the

scale needs to be buoyancy corrected and for that we need the volume of the tank and of the frame. The HFTS tank volume is a function of pressure and temperature and is given by:

$$V_{tank} = V_0 \cdot (1 + 3 \cdot \alpha \cdot \Delta T) \cdot (1 + \lambda \cdot \Delta P) \quad (2)$$

where  $V_0 = 59.5$  L is the external tank volume at ambient conditions with no internal pressure,  $\alpha = 2.0 \cdot 10^{-6} \text{ } ^\circ\text{C}^{-1}$  the linear thermal expansion coefficient,  $\lambda = 2.2 \cdot 10^{-10} \text{ Pa}^{-1}$  the pressure expansion coefficient,  $\Delta T$  and  $\Delta P$  are the difference of the temperature and pressure from the reference values, respectively. If we take into account a maximum temperature difference of  $80 \text{ } ^\circ\text{C}$ , one obtains a volume correction factor of 1.00048. The pressure expansion coefficient has been determined experimentally during a refuelling up to 70 MPa and from manufacturer's data. The thermal and pressure expansion coefficients are very similar to values published elsewhere [3] and have been assigned an uncertainty of 10% ( $k=1$ ). Taking a maximum pressure difference of 87.5 MPa gives a correction factor of 1.01925. Thermal expansion will be completely neglected in the remaining description of the method as its correction factor is much smaller compared to the pressure correction. The external volume of the tank has been given an uncertainty of 5 L ( $k=1$ ). The volume of the frame has been determined using the CAD drawing of the HTFS (70 L) and has been assigned an uncertainty of 5 L ( $k=1$ ). From Equations (1) and (2), we can now calculate the dispensed mass into the HFTS corrected for buoyancy and apparent mass reading from the scale:

$$m_{H2} = (W_2 - W_1) \cdot \left(1 - \frac{\rho_0}{\rho_N}\right) \quad (3)$$

$$+ V_0 \cdot [\rho_{air2} \cdot (1 + \lambda \Delta P_2) - \rho_{air1} \cdot (1 + \lambda \Delta P_1)] + V_{frame} \cdot (\rho_{air2} - \rho_{air1}),$$

where  $W$  are the readings of the scale and the subscripts denote the reading before and after the filling, respectively. The factor  $\left(1 - \frac{\rho_0}{\rho_N}\right)$  turns apparent mass into true mass where  $\rho_0 = 1.2 \frac{\text{kg}}{\text{m}^3}$  and  $\rho_N = 8000 \frac{\text{kg}}{\text{m}^3}$  are the densities of air and stainless steel at reference conditions,  $\rho_{air}$  is the density of the air around the scale and the tanks before and after the fill and is calculated using the formula by Giacomo [5].

To obtain a feeling for orders of magnitude, a complete fill in the HFTS corresponds to 2.9 kg of hydrogen gas in the tanks at a pressure of 70 MPa. This yields a volume expansion of 0.92 L for

each tank. Under identical ambient conditions before and after the fill, we obtain a buoyancy correction of 2.12 g (0.08%) for both tanks. The term due to the volume of the frame only plays a role if ambient conditions change.

Laboratory tests were performed to reproduce field tests as closely as possible. The aim was to elaborate a testing procedure and practice using the HFTS before going into the field.

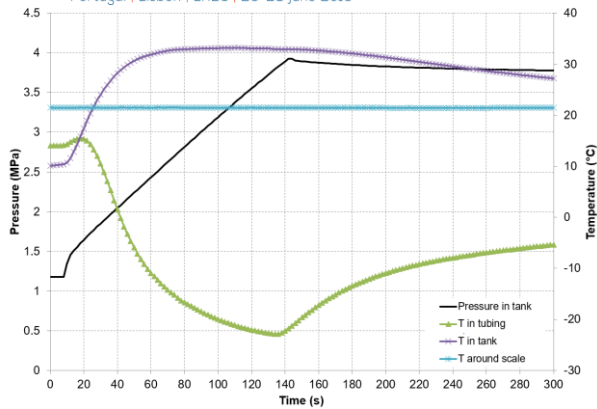
All laboratory measurements were performed with nitrogen gas from a bundle as a 5.5 MPa gas source to fill the HFTS. Before entering the HFTS, the gas was cooled down to  $-40 \text{ } ^\circ\text{C}$  by a heat exchanger to reproduce the temperature conditions of hydrogen as delivered by a HRS. Pressure and temperature in the tanks was monitored continuously during the fill. The frame was always enclosed or partially enclosed by the housing, the latter geometry leads to a better air circulation around the scale.

To perform the measurements, we followed several steps:

1. Disconnect all the cables and hoses from the frame, lower the HFTS onto the scale and weigh the empty HFTS, record the ambient conditions
2. Lift the HFTS from the scale, connect all sensors and measure tank pressure and temperature as well as temperature of the air in the frame
3. Connect the gas source to the HFTS inlet and fill the tanks. During the fill, all sensors are monitoring and recording data.
4. Disconnect all the cables and hoses from the frame and lower the HFTS onto the scale
5. Wait until scale reading stabilises and record value
6. Lift the HFTS from the scale and connect all sensors. Connect the vent stack and blow down the gas.

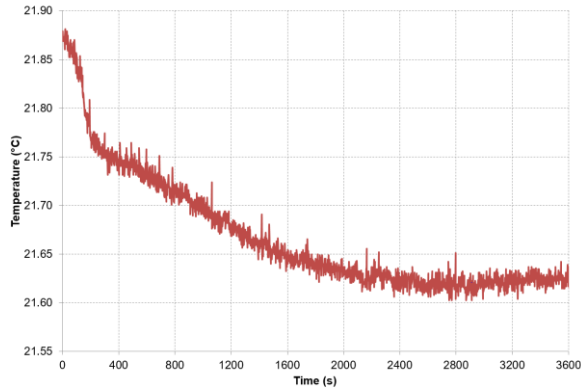
#### 4. Results

Typical results for the pressure rate and temperature profiles for a fill up to 4 MPa are shown in Figure 7. The pressure ramp rate (PRR) during the fill is around 1.14 MPa/min. During this period, temperature in the tanks increased due to compression heating while temperature of the tubing decreased below the freezing point of water due to the cold nitrogen gas flow. The air temperature around the scale remains more or less constant. After the fill, all temperatures converge more or less slowly toward the current ambient condition.



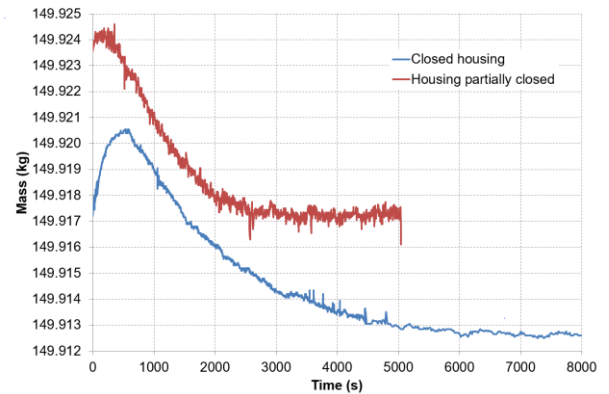
**Figure 6:** Pressure (in black) and temperature profiles from the HFTS during a fill, PRR = 1.14 MPa/min.

Figure 7 shows the temperature profile around the scale starting 60 s after the fill during 1 hour with the HFTS housing closed. Due to the temperature increase in the tanks, heat is transferred to the air around the scale, which then returns to ambient temperature after around 40 minutes. This can be considered as a worst case because of the poor air circulation around the HFTS and yields a maximum drift of 0.3 °C.



**Figure 7:** Temperature profile around the scale after a fill with closed housing.

The cold gas flowing through the HFTS causes part of the humidity present around the HFTS to condense and freeze on the pipes. This quantity of ice will be weighed but should not be part of the determination of the mass of dispensed gas. Figure 8 shows the scale reading profile shortly after the fill with a closed and a partially closed housing (opening of 25 cm). We notice an increase in mass due to condensation that reaches a maximum before a slow decrease because of melting and evaporation, eventually reaching a constant scale value. The maximum quantity of lost mass seems to be independent of the position of the housing and amounts to more or less 7 g in our case.



**Figure 8:** Scale reading profile as a function of time after the fill with a closed and partially closed housing. .

This is by far not negligible. On a brighter side, closing the housing partially accelerates the loss of mass and leads to a stable scale value with less than 1 g of spread after approximately 30 minutes. We also performed similar measurements with a closed housing flooded with nitrogen or argon gas. We chose argon because it is heavier than air and filled the housing up to the top and remained in the housing, contrary to nitrogen. With both gases, we still observed icing on the pipes but less than with air. Flooding with an inert gas brings more unknowns in the buoyancy correction because the flooding level is not well defined. In addition, the amount of gas needed is quite large.

It looks like the best solution is to measure with a partially closed housing, cleaning/drying the pipes after the fill and wait for the scale to show a stable value.

## 5. Uncertainty budget

The various contributions to the uncertainty budget are addressed in this section. The uncertainty of the gravimetric measurement can be calculated by

$$\left[ \frac{u(m_{H_2})}{m_{H_2}} \right]^2 = \sum_i S_{x_i}^2 \cdot \left( \frac{u(x_i)}{x_i} \right)^2 \quad (4)$$

where  $x_i$  are the measurands from Equation (3) and  $S_{x_i}$  are the normalised sensitivity coefficients for each variable and can be calculated by

$$S_{x_i} = \frac{\partial m_{H_2}}{\partial x_i} \cdot \frac{x_i}{m_{H_2}} \quad (5)$$

The scale has a resolution of 0.1 g and was calibrated against METAS standard masses with the frame on the scale. We observed a maximum deviation of 0.5 g. The calibration was checked over time and the scale showed a drift of 0.4 g over

90 minutes. The scale will always be calibrated on site in the field during measurements. As the effect of field use could not be determined yet, we consider a conservative uncertainty value of 0.7 g ( $k=1$ ) for the scale.

Air density depends mainly on the parameters pressure, temperature and humidity. These quantities are continuously logged with uncertainties of 50 Pa, 0.3 °C and 5%, respectively and allow the determination of air density with an uncertainty of 0.15% ( $k=1$ ) during measurements.

The digital pressure transducers have a resolution 2 kPa and a long-term stability of 100 kPa according to the specifications. The sensors have been calibrated and shown to lie within the specifications of 200 kPa.

Table 1 presents a summary of the uncertainty components and their magnitude for the gravimetric method for a test collection of 1 kg of gas. As expected, the scale is the largest contributor to the uncertainty, followed by the air density. The values presented here yield an expanded uncertainty of 0.22% or 2.2 g for 1 kg of gas collected.

**Table 1:** Summary of uncertainty components and their magnitude for the gravimetric method for 1 kg of gas collected.

Uncertainty component	Nominal value	$u(x_i)$ %	Contribution %
Initial mass	150.0000 kg	$4.7 \cdot 10^{-4}$	40.5
Final mass	151.0000 kg	$4.7 \cdot 10^{-4}$	40.5
Tank volume	0.120 m <sup>3</sup>	4.17	0.16
Frame volume	0.070 m <sup>3</sup>	7.14	< 0.1
Initial air density	1.1500 kg/m <sup>3</sup>	0.15	8.9
Final air density	1.1500 kg/m <sup>3</sup>	0.15	9.0
Initial tank pressure	0.10 MPa	20	< 0.1
Final tank pressure	35.00 MPa	0.057	< 0.1
Pressure coefficient	$2.2 \cdot 10^{-10}$ Pa <sup>-1</sup>	10	0.93

The uncertainty contribution due to condensation and icing of the pipes can be minimised if we wait at least 20 minutes or clean the pipes before reading the value of the scale. A 1 g spread as considered in section 4 under the assumption of a rectangular distribution yields an uncertainty contribution of 0.58 g ( $k=1$ ) and leads to an expanded uncertainty of 2.5 g (0.25%) for 1 kg of gas collected. The required expanded uncertainty of 0.3% or less is therefore achieved. Further measurements in the field under real conditions are planned to validate some of the assumptions taken in the present uncertainty budget.

## 7. Conclusion

The design of the HFTS and its associated gravimetric measuring method have been presented in this paper. Experimental results obtained with the HFTS under laboratory conditions with cold nitrogen gas at -40°C to mimic real fill conditions in a hydrogen refuelling station showed varying temperature and scale reading profiles. Condensation on the HFTS leads to a change in mass over time of up to 7 g, which is not negligible compared to the minimum quantity of 1 kg to be weighed during field-testing. A complete uncertainty budget has been presented and we obtained an expanded measuring uncertainty for the HFTS of 0.25%. The results presented in this paper can serve as a guide for future designs of similar field testing instruments based on the gravimetric principle.

## References

- [1] SAE J2601: Fueling protocols for light duty gaseous hydrogen surface vehicles, 2016.
- [2] J.G. Pope, J.D. Wright, "Performance of Coriolis meters in transient gas flows", *Flow Measurement and Instrumentation*, **37**, 42-53, 2014
- [3] J.G. Pope, J.D. Wright, "Hydrogen field test standard: Laboratory and field performance", *Flow Measurement and Instrumentation*, **46**, 112-124, 2015
- [4] OIML R139: *Compressed Gaseous Fuel Measuring Systems for Vehicles*, 2018.
- [5] P. Giacomo, "Equation for the Determination of the Density of Moist Air", *Metrologia*, **18**, 33-40, 1982

# Effect of Reynolds number and Boundary Layer Thickness on the Performance of V-cone Flowmeter using CFD

Sheikh Nasiruddin<sup>1</sup>, S N Singh<sup>1\*</sup>, S V Veeravalli<sup>1</sup> and S Hegde<sup>1</sup>

<sup>1</sup>Department of Applied Mechanics, IIT Delhi, Hauz Khas, New Delhi-110016

<sup>1\*</sup>E-mail (corresponding author): sidhnathsingh@hotmail.com

---

## Abstract

The effect of Reynolds number and boundary layer thickness on the performance of V-cone flowmeter has been evaluated using computational fluid dynamics (CFD). The shear stress transport  $k-\omega$  (SST  $k-\omega$ ) turbulence model has been adopted for closure. The performance of two V-cone flowmeters with different beta ratios ( $\beta$ ) viz., 0.6 and 0.7 for a fixed vertex angle ( $\phi$ ) of  $60^\circ$  has been analysed as a function of Reynolds number ( $Re$ ). The results show that the coefficient of discharge ( $C_d$ ) increases with Reynolds number in the laminar and transition flow regimes whereas it is nearly constant in turbulent flow regime. From the results, it can be concluded that  $C_d$  is independent of  $Re$  for values equal to 4000 and beyond. Further, it is also seen that the performance of the V-cone flowmeter is not affected by the upstream boundary layer thickness if the velocity profiles having different boundary layer thickness are extracted from an axial distance of  $10D$  and more are fed at  $5D$  upstream of the meter. However, the meter is sensitive to the extracted velocity profile from an axial distance of  $5D$  and uniform velocity profile being fed at  $5D$  upstream. The value of  $C_d$  may be sensitive as a result of the pressure variation due to the obstruction.

---

## 1. Introduction

Flow measurement plays an important role in our day to day life as well as in many industries. There are large numbers of flow measuring instruments commercially available for different applications. From an engineering application, flow measuring instruments are selected on the basis of space available for installation, fluid being handled and the level of accuracy required. For industries involved in commercial activity, accuracy is of prime importance as it is one of the determinants of profit or loss in flow handling business. In other industries, flow rate measuring instruments are used for accurate monitoring and flow control of a process or operation of a device or machine. Conventional obstruction flow metering devices such as orifice meter, venturi meter and nozzle meter are used extensively in various fields due to their simplicity in design and low maintenance. In industries, the use of these flowmeters is restricted due to the space constraints for installation and accuracy in measurement for wide ranges of flow conditions. The concept of V-cone flowmeter was introduced in late 1980s [1] to overcome these drawbacks of conventional obstruction flowmeters. Today it is extensively being used in place of conventional flowmeters where there are space constraints and the accuracy required for flow measurement is high. The performance of the V-cone flowmeter has been studied by many researchers ever since it was introduced commercially by McCrometer [2]. Ifft et al. [3] carried out experiments using equivalent diameter ratios ( $\beta$ ) of 0.5 and 0.75 and concluded that requirement of upstream and downstream lengths of the pipe for the V-cone flowmeter are 0 to  $3D$  and

3 to  $5D$  respectively whereas the conventional flowmeter requires any length above  $16D$  depending on the upstream flow conditions. They also reported that the presence of the cone directs the high velocity fluid from the core towards the pipe wall where low velocity exists forcing flow uniformity. This phenomenon causes flattened velocity profiles just upstream of the cone element. Prabhu et al. [4] conducted experiments on cone meter and orifice meter with  $\beta$ -value of 0.75 in the Reynolds number range of  $3 \times 10^4$  to  $5 \times 10^4$  using water as the working fluid. They measured the pressure distribution downstream of the orifice meter and cone flowmeter in order to estimate and compare the permanent pressure loss. They also investigated the effect of inlet swirl and observed that V-cone flowmeter is less sensitive to swirl flow and the overall pressure loss for cone flowmeter is 50% less than that of the orifice meter. Erdal and Anderson [5] using CFD evaluated the performance of V-cone flowmeter and showed that the predictions using standard  $k-\epsilon$  turbulence model have significant deviation from experimental results. Joshi [6] carried out extensive studies on V-cone flowmeter over a wide range of Reynolds number and concluded that performance of V-cone flowmeter is better under all conditions than any other obstruction type flow measuring device. Singh et al. [7] conducted an experimental study for  $\beta$ -values of 0.64 and 0.77 to establish the effect of Reynolds number and skewed velocity profile on the coefficient of discharge ( $C_d$ ). They established that  $C_d$  was independent of inlet Reynolds number and increases with increase in skewness of the inlet velocity at  $5D$  upstream of the cone. Weiguang Liu et al. [8] carried out a study on a dual support structure cone (DSSC) considering

the safety of the cone element. They concluded that V-cone flowmeter with DSSC possess better repeatability and safety. Within the range of  $\beta$ -value between 0.45 and 0.65, they optimized the location of the rear support as 0.8D downstream of the cone. They further observed that if the low-pressure tapping point is placed at 0.05D downstream of the cone, linearity of the  $C_d$  with respect to the Reynolds number increases. Singh et al. [9] also used CFD to establish the effect of swirl on the performance of V-cone flowmeter. Based on the validation studies they have shown that the RNG  $k$ - $\epsilon$  turbulence model provides a much better flow prediction and the deviation between experimental and predicted results was less than 4%.

Ying et al.[10] carried out numerical experiments for the performance evaluation of the V-cone flowmeter using turbulence model  $RNG$   $k$ - $\epsilon$  in the Reynolds number range of  $8 \times 10^4$  to  $1.2 \times 10^7$ . They have chosen three geometrical parameters for the study. These are i)  $\beta$ -values (0.50, 0.65 and 0.85), ii) fore-vertex angles ( $40^\circ$ ,  $45^\circ$  and  $50^\circ$ ) and iii) aft-vertex angles ( $120^\circ$ ,  $130^\circ$  and  $140^\circ$ ). They have reported that the variation of  $C_d$  is an inverse function of  $\beta$ -values. Further they have observed that for a fixed value of  $\beta$ , the aft-vertex angle has an impact on the linearity of the coefficient of discharge up to certain extent. They have also observed that the coefficient of discharge tends to become independent of Reynolds number with increase in fore-vertex angle.

Nasiruddin et al. [11] has carried out numerical experiments to establish the effect of vertex angle and vertex tip radius on the performance of the V-cone flowmeter. They have chosen a fixed beta value ( $\beta$ ) of 0.6 and studied different vertex angles ( $\phi$ ) for three modes of cone arrangement namely without support, front and rear support. The evaluation was done on the basis of coefficient of discharge ( $C_d$ ) and the extent of uncertainty ( $U_{Cd}$ ) present in predictions within the range of Reynolds number ( $1 \times 10^3 \leq Re \leq 1 \times 10^6$ ) studied. They have reported that the cone element with vertex angle of  $75^\circ$  gives nearly constant discharge coefficient for  $Re \geq 1000$  with minimum uncertainty and it is true for all the three modes of the cone arrangement. They further claimed that vertex tip radius has no effect on the performance of the V-cone flowmeter.

Nasiruddin et al.[12] have introduced a curved surface at the base of the cone to establish its effect. The study was conducted for a fixed  $\beta$ -value of 0.6 and three fore-vertex angles ( $\phi$ ) namely  $60^\circ$ ,  $75^\circ$  and  $90^\circ$  in the Reynolds number range of  $1 \times 10^3$  to  $1 \times 10^6$  using CFD. They replaced the aft-cone with curved surface for four non-dimensionalized radii of curvature ( $R/d$ ) namely 0.5 (hemispherical), 0.55, 0.625 and 0.6905. In addition, a semi-elliptical based cone with 20 mm semi-major axis and 10 mm semi-minor axis has also been studied. In all the cases, the chord length is kept constant and arc length is varied gradually. The radii of the curvature were chosen so as to locate the centre of the spheres and ellipse on the axis either in the frustum or cylindrical part of the cone. They have shown that the introduction of curved surface at the cone base improves the

performance of the V-cone flowmeter. Further, they have concluded that the V-cone flowmeter with curved base of  $R/d = 0.55$  has higher  $C_d$  value and smaller standard deviation compared to a device with an aft vertex cone. Their close scrutiny also reveals that for the hemispherical and semi-elliptical based V-cone flowmeter, the coefficient of discharge is dependent on Reynolds number.

The V-cone flowmeter is a novice device among the differential pressure flowmeters and very recently it has been included in ISO-5167-5:2016 [13]. The recommendations given in ISO-5167-5:2016 for the geometrical parameters fore, aft-vertex angles and range of  $\beta$ -values are  $52^\circ \pm 10^\circ$ ,  $135^\circ \pm 5^\circ$  and  $0.45 \leq \beta \leq 0.75$  respectively for the range of flow conditions of  $8 \times 10^4 \leq Re \leq 1.2 \times 10^7$ . However, ISO-5167-5:2016 suggests calibrating all the V-cone flowmeters for their accuracy.

The literature shows that there are many flow parameters whose effect on the performance of the flowmeter has not been investigated and one of the parameters is the inlet velocity profile with varying boundary layer thickness. Secondly, the effect of Reynolds number in the lower range is also not well documented. The present study is aimed to analyse the effect of Reynolds number in the lower range and the inlet boundary layer thickness on the performance of V-cone flowmeter using CFD after establishing the most appropriate turbulence model.

## 2. Working Principle

The working principle of V-Cone flowmeter is similar to other types of differential pressure flowmeters. The composite cone element is placed co-axially in the pipe as shown in the figure 1. The annulus space between the cone and the pipe restricts the fluid flow and the flow separates downstream of the cone. This causes a differential pressure between the pressure tap locations upstream and downstream of the cone.

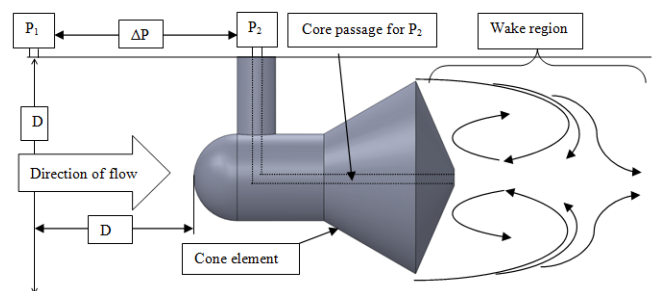


**Figure 1:** Schematic diagram of V-Cone flowmeter

The upstream pressure ( $P_1$ ) is measured from a pressure tap fixed at 1D upstream of the cone on the pipe wall and  $P_2$  is the pressure in the wake of the cone on the pipe axis. The calculated differential pressure ( $\Delta P$ ) is invoked in equation (1) to evaluate the theoretical flow rate and the actual flow rate fed at inlet allows evaluation of the value of  $C_d$ .



$$Q_{th} = \frac{1}{\sqrt{1-\beta^4}} \frac{\pi}{4} (D^2 - d^2) \sqrt{2\rho\Delta P} \text{ kg/s} \dots\dots\dots(1)$$

Where,  $\beta$  is the equivalent diameter ratio and is given by

$$\beta = \sqrt{1 - \frac{d^2}{D^2}}$$

### 3. Equations and mathematics

CFD has provided a platform by replacing the time consuming and cumbersome experiments for understanding any physical phenomena provided well documented data sets are available to establish the authenticity of CFD for that physical phenomena. This section describes the mathematical formulation in brief for the sake of completeness.

#### 3.1 Governing equations

The conservation forms of mass continuity and momentum equations for steady state incompressible flow are:

$$\frac{\partial}{\partial x_i} (\rho \bar{u}_i) = S_m \dots\dots\dots(2)$$

$$\frac{\partial}{\partial x_j} (\rho \bar{u}_i \bar{u}_j) = -\frac{\partial P_i}{\partial x_i} + \frac{\partial \tau_{ij}}{\partial x_j} + \rho g_i + F_i + \frac{\partial}{\partial x_j} (-\rho \overline{u'_i u'_j}) \dots\dots\dots(3)$$

Where  $S_m$  is the source term,  $P_i$  is the static pressure,  $\rho g_i$  is the body force per unit volume due to gravity and  $F_i$  is the external body force. The term  $\tau_{ij}$  represents the stress tensor.

The Reynolds stress terms  $(-\rho \overline{u'_i u'_j})$  need to be modelled to have closed form solution. Boussinesq hypothesis relates the Reynolds stresses to the mean velocity gradient using proportionality constant  $\frac{\mu_t}{\rho}$ .

$$-\overline{u'_i u'_j} = \mu_t \left( \frac{\partial \bar{u}_i}{\partial x_j} + \frac{\partial \bar{u}_j}{\partial x_i} \right) - \frac{2}{3} \delta_{ij} \left( \rho k + \mu_t \frac{\partial \bar{u}_i}{\partial x_i} \right) \dots\dots\dots(4)$$

In the equation (4),  $k$  is the turbulent kinetic energy and  $\mu_t$  is the turbulent viscosity. Various two equation turbulence models have been proposed by researchers to get the closure solution. None of the turbulence model is universally applicable to all type of flows. As the flow across the V-cone is highly turbulent and separated, different two equation turbulence models have been tried for closure solution and it was found that SST k- $\omega$  turbulence model predicts the performance reasonably well.

#### 3.2 Turbulence model

The two equation SST k- $\omega$  turbulence model has been adopted for the closure solution based on the recommendation of [11, 12]. Mentor [14] developed this model with effective and accurate blending of the k- $\omega$  model for near wall region and k- $\epsilon$  model in the free stream zone. Thus, the flow statistics at near wall as well as in the far field are captured effectively. The kinetic energy and specific dissipation equations of SST k- $\omega$  turbulence model are:

$$\frac{\partial}{\partial x_i} (\rho k \bar{u}_i) = \frac{\partial}{\partial x_j} \left( \Gamma_k \frac{\partial k}{\partial x_j} \right) + \tilde{G}_k - Y_k + S_k \dots\dots\dots(5)$$

$$\frac{\partial}{\partial x_j} (\rho \omega \bar{u}_j) = \frac{\partial}{\partial x_j} \left( \Gamma_\omega \frac{\partial \omega}{\partial x_j} \right) + G_\omega - Y_\omega + S_\omega + D_\omega \dots\dots\dots(6)$$

$\tilde{G}_k$  represents generation of turbulent kinetic energy ( $k$ ) due to mean velocity gradient,  $G_\omega$  represents the generation of vorticity/specific dissipation ( $\omega$ ).  $\Gamma_k$  and  $\Gamma_\omega$  represent effective diffusivity of  $k$  and  $\omega$  respectively.  $Y_k$ ,  $Y_\omega$  are the dissipation of  $k$  and  $\omega$  due to turbulence.  $S_k$ ,  $S_\omega$  are user defined source terms.  $D_\omega$  is cross-diffusion term. The details of these terms are given in Fluent Manual [15].

### 4. Validation

Numerically obtained results are acceptable if these have been validated against experimental results for similar geometries. Validation against experimental results also helps in evaluating the most appropriate turbulence model for closure solution as there is no universal turbulence model to predict all types of flow. The author has carried out the validation study [16] after reproducing the experimental set up and flow conditions of [7] considering all two equation turbulence models. He has found that the simulation results using SST k- $\omega$  turbulence model matched well with the experimental findings of Singh et al. [7] with a deviation in mean value of  $C_d$  being 3.1% only. However, the variation in mean value of coefficient of discharge obtained from RNG and Realizable k- $\epsilon$  turbulence model was lower than SST k- $\omega$  turbulence model for the range of flow conditions adopted in the experiments. To examine this further, the flow conditions were simulated extending it up to laminar and transition flow regime. The result revealed an interesting observation that the performance of both RNG and Realizable k- $\epsilon$  turbulence model was poor at lower Reynolds number ( $Re \leq 4000$ ) and the coefficient of discharge became dependent on Reynolds number. Whereas, SST k- $\omega$  turbulence model showed consistency in the result over the entire ranges of flow conditions (from laminar to turbulence). Thus, SST k- $\omega$  turbulence model was chosen as the appropriate turbulence model for simulating the present work.

### 5. Details of geometrical parameters studied

Flow predictions are carried out to study the effect of boundary layer thickness on the performance of V-cone flowmeter for two  $\beta$ -values namely 0.6 and 0.7 with fixed vertex angle of  $60^\circ$  in the Reynolds number range of 500 to 500000. The V-cone is mounted coaxially in a circular pipe of diameter 50 mm. The maximum cone diameters for the two values of  $\beta$  are 40 mm and 37.5 mm respectively. No supporting struts were simulated as the pressure tap holder is strong enough to hold the cone element [9]. The computational domain is chosen as 5D and 30D long in the upstream and downstream regions of the V-cone respectively. In order to nullify the constraining effects of

outlet boundary condition on cone element, the downstream length is kept reasonably long. The 3D cone element has been modelled using SolidWorks-2014 [17] software and imported in Ansys 15.0 DesignModeler [15] where the rest of the geometry was modelled. The cone element and related parameters are shown in figure 2. After the modelling, the mesh generation for the computational flow domain is carried out. Grid generation is the most important part of simulation work as it determines the level of accuracy in the results. Fine grids are required in the flow domain where high velocity gradients exist and reasonably coarse grids can be applied to the regions with smooth flow condition. On the pipe and cone wall boundaries inflation layers were generated in order to produce fine meshes for capturing the steep velocity gradient. Grid refinement leads to better accuracy but it also increases the cost of simulation in terms of CPU hours. However, a reasonable grid resolution is required for the flow simulation to achieve the acceptable accuracy level in results.

Grid independence checks were carried out in order to reach to a state after which the results do not change significantly

with further refinement of the grids. To study grid independence, nine different sizes of mesh elements were chosen. The value of  $C_d$  at Reynolds numbers of  $2.18 \times 10^5$  has been calculated for each mesh size. The optimum number of mesh elements for rough pipe was determined as  $13.31 \times 10^5$  because further refinement of the grid resulted in insignificant changes in  $C_d$  value. Grids consist of mixed tetrahedron and hexahedron elements which were converted into polyhedral cells in Fluent [15]. This conversion into polyhedral mesh reduces the cell counts to one-third and the solutions get converged within 5000 iterations. The same sizes grids are used for the present study. The boundary conditions are velocity-inlet, pressure outlet as zero-gauge pressure and pipe and cone surfaces as wall with roughness height of 0.5 mm and roughness constant of 0.5. Turbulent intensity and hydraulic diameter are calculated from the relations  $I=0.16 \times (\text{Re})^{-0.125}$  and  $H=4A/P$  where  $A$  is cross-sectional area of the pipe and  $P$  is wetted perimeter. A total of 160 converged runs are conducted.

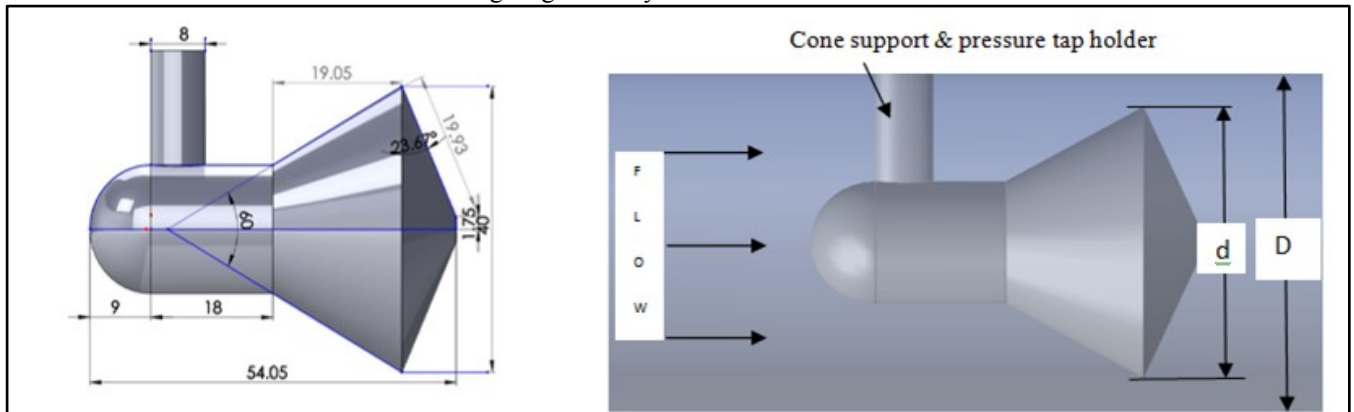


**Figure 2:** Geometrical details of one of the V-cone flowmeters with beta ratio 0.6 and vertex angle  $60^\circ$  used for present study (All dimensions are in 'mm').

## 6. Results and discussions

The present numerical study reports the effect of Reynolds number and boundary layer thickness on the performance of front supported V-cone flowmeter. Prior to carrying out simulations for the cone flowmeter with different velocity profiles being fed at 5D upstream of the cone, it was essential to generate the different velocity profiles.

### 6.1 Inlet velocity profiles

Two flow simulations were done in pipe separately, one in a straight pipe of length 60D and another in 83D long pipe with a V-cone coaxially placed at an axial distance of 60D from inlet. For both the cases, a uniform velocity profile of same magnitude was fed at the inlet to establish if there was any effect of obstruction on the velocity profiles in the pipe. Fig. 3 gives the comparison of velocity profiles at 50D axial distance from inlet for the two cases. From the figure it is

seen that the presence of V-cone has a tendency to flatten the velocity just before the cone. This implies that any

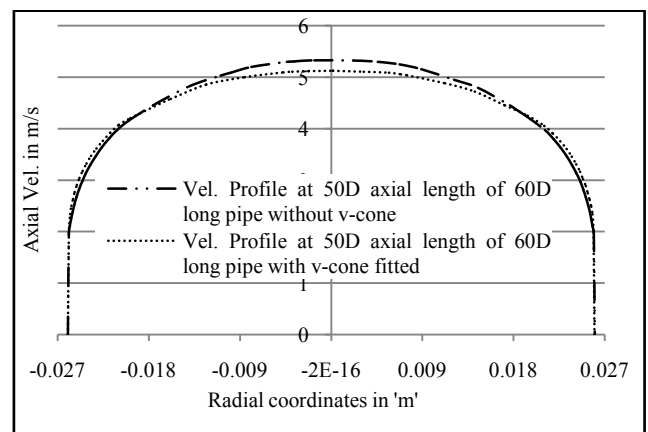


**Figure 3:** Comparison of velocity profiles for pipe flow simulation with and without V-cone fitted.

velocity profile fed at any distance from the cone will have a tendency to flatten the velocity profile before the cone. After establishing this effect, in the present study, two pipe simulations were carried out for the range of Reynolds number considered. One was straight pipe from where the velocity profiles at different axial distances namely 05D, 10D, 20D, 30D, 40D, 50D and 60D were extracted. The another pipe fitted with V-cone was simulated after feeding these extracted velocity profiles at the inlet (5D upstream of the cone). In addition, simulations are also done for uniform flow. Feeding different velocity profiles helps to establish the effect of the boundary layer thickness on the value of  $C_d$  without increasing the actual domain length.

### 6.2 Results with $\beta=0.6$

The effect of boundary layer thickness on the performance of the V-cone flowmeter has been investigated by feeding the extracted velocity profiles at 5D upstream of the cone. Fig.4a gives the variation of coefficient of discharge as a function of Reynolds number. The study reveals that the value of  $C_d$  is nearly constant if uniform velocity is fed at 5D upstream of the V-cone for Reynolds number greater than 1000 with deviation of  $\pm 0.32\%$  from the mean value ( $C_d=0.7839$ ). Fig 4a also gives the variation of  $C_d$  for different extracted velocity profiles. For 5D extracted velocity profile the  $C_d$  value increases linearly upto Reynolds number of 4000 and beyond 4000 the values of  $C_d$  are nearly constant and has an average value of 0.7161 with  $\pm 0.76\%$  deviation. For 10D extracted profile the variation of  $C_d$  is oscillatory upto Re value of 2500 and  $C_d$  becomes weak function of Re in the range of 2500 to 20,000 and then it is nearly constant. Treating the value of  $C_d$  as constant beyond  $Re=4000$ , the average value of  $C_d$  is 0.6912 with  $\pm 0.85\%$  deviation. The value of  $C_d$ 's for other extracted velocities being fed at 5D also follow the similar trend beyond  $Re=4000$ . The average values of  $C_d$ 's are given in Table 1 along with deviations. The mean values of  $C_d$  reduces continuously upto 20D extracted velocity beyond which it increases back and is nearly constant for extracted velocity of 30D and beyond. Further, if the Reynolds number is greater than 4000 we can conclude that  $C_d$  is independent of Re and is not affected by the boundary layer thickness upstream of the cone (for the velocity profile 10D and beyond). The value of  $C_d$  is

sensitive to the uniform velocity and 5D extracted velocity due to the pressure variation as a result of the obstruction.

### 6.3 Results with $\beta=0.7$

The effects of boundary layer thickness on discharge coefficient for V-cone configuration with beta value of 0.7 is shown in Fig. 5a. The variation in  $C_d$  is seen to be nearly same as  $\beta=0.6$ . The average value of  $C_d$  beyond 4000 for different extracted velocity profiles along with deviations are also given in Table 1. Feeding uniform velocity at 5D upstream of the V-cone results show linear variation in  $C_d$  with Reynolds number upto 4000 thereafter the value of  $C_d$  is nearly constant ( $C_d=0.7906$ ) with  $\pm 0.44\%$  deviation from mean value. For all extracted velocity profiles fed (at inlet i.e. 5D upstream of the cone), the value of  $C_d$  increases linearly upto Reynolds number 2500 and this linear increase shows a strong dependence on Reynolds number in the laminar range. The linear increase in  $C_d$  beyond Reynolds number 2500 and upto 20000 shows weak dependence on Reynolds number. Neglecting this weak dependency for 5D extracted profile fed at the inlet, one can treat the value of  $C_d$  is nearly constant for  $Re=4000$  and beyond with an average value of 0.725 and  $\pm 0.67\%$  deviation. For other extracted velocity profiles the trend looks to be similar to the cone configuration of  $\beta=0.6$ .

Close scrutiny of the results given in Table 1, show that for extracted velocity profiles from 10D onwards and fed at 5D upstream of the cone, the mean value of discharge coefficient is nearly same for all allextacted velocity profiles. Hence a mean value for extacted velocity profiles can be taken. This value for  $\beta=0.6$  is 0.6904 whereas it is 0.6959 for  $\beta=0.7$ . The respective adjusted standard deviations are  $\pm 0.0040$  and  $\pm 0.0039$ . The deviations of the mean  $C_d$  value for each extracted velocity profile from the mean  $C_d$  value taking all the extracted velocity profiles are plotted in figure 4b (for  $\beta=0.6$ ) and 5b (for  $\beta=0.7$ ) with 2% error bar. From the analysis it can be concluded that the effect of boundary layer thickness on discharge coefficient is negligible except for uniform velocity profile and extracted 5D velocity profile. Further, the  $C_d$  values for both the  $\beta$ -ratios of 0.6 (0.7839) and 0.7 (0.7906) for uniform velocity fed at 5D upstream of the cone lie within  $\pm 5\%$  of the  $C_d$  value (0.82) given in ISO-5167-5:2016.

**Table 1:** Values of Mean  $C_d$  for  $Re \geq 4000$  and its % deviation for  $\beta=0.6$  &  $0.7$

Velocity Profile Extracted from the pipe flow without V-cone fitted	Velocity Profile fed at 5D upstream of the V-cone	Mean $C_d$ and % deviation for $\beta=0.6$		Mean $C_d$ and % deviation for $\beta=0.7$	
		Mean $C_d$	% Deviation	Mean $C_d$	% Deviation
NIL	Uniform Velocity	0.7839	0.32	0.7906	0.44
05D	Extracted Velocity Profiles	0.7161	0.76	0.7217	0.67
10D		0.6912	0.85	0.6964	0.76
20D		0.6825	0.66	0.6882	0.55
30D		0.6907	0.98	0.6964	0.86
40D		0.6932	1.06	0.6986	0.94
50D		0.6925	1.07	0.6980	0.95
60D		0.6925	1.04	0.6977	0.92

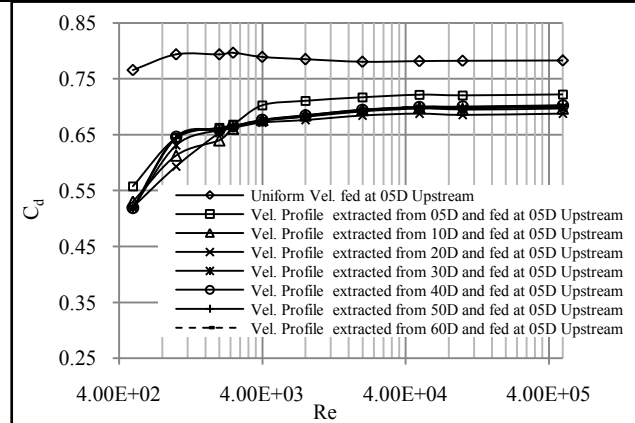


**Figure 4a:** Variation of  $C_d$  with  $Re$  for  $\beta=0.6$  &  $\varphi=60^\circ$

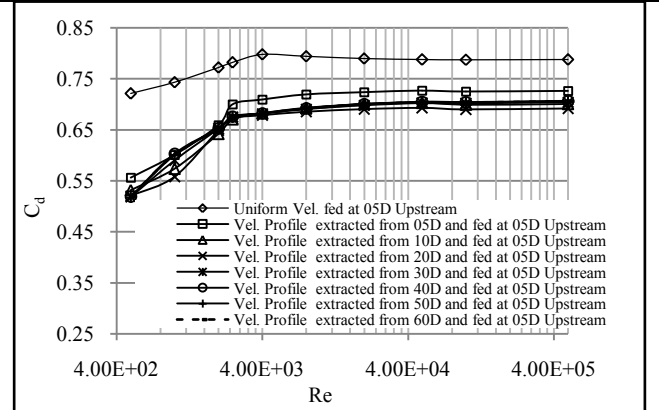


**Figure 5a:** Variation of  $C_d$  with  $Re$  for  $\beta=0.7$  &  $\varphi=60^\circ$

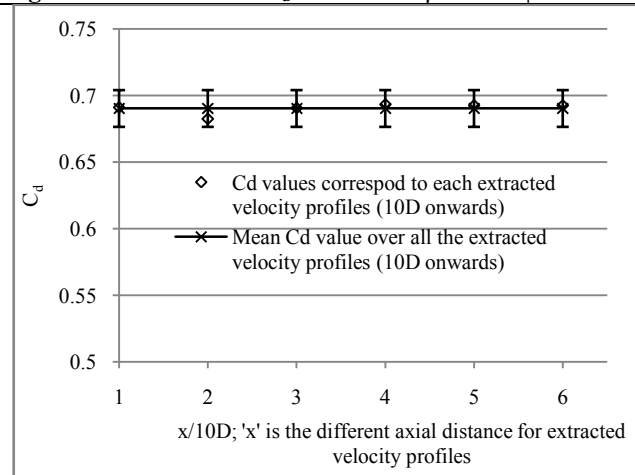


**Figure 4b:**  $C_d$  value for different extracted profiles with  $\pm 2\%$  error bar ( $\beta=0.6$  &  $\varphi=60^\circ$ ) for  $Re \geq 4000$

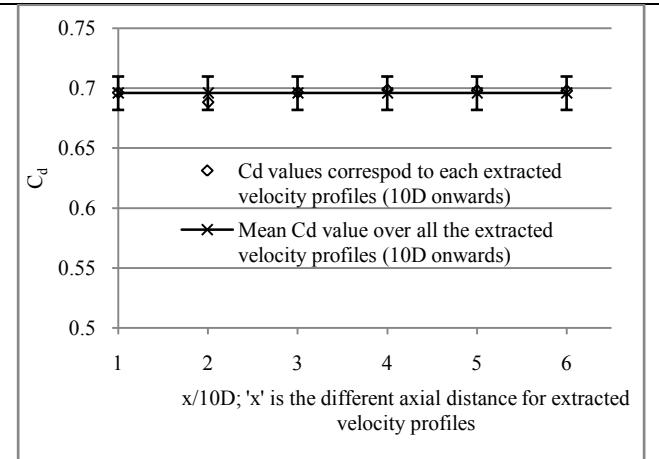


**Figure 5b:**  $C_d$  value for different extracted profiles with  $\pm 2\%$  error bar ( $\beta=0.7$  &  $\varphi=60^\circ$ ) for  $Re \geq 4000$

## 7. Conclusions

On the basis of the results obtained the following observations are enumerated.

1. For the chosen  $\beta$ -values of 0.6 and 0.7, the coefficient of discharge is linearly dependent on Reynolds number in the laminar and transition regimes. The  $C_d$  value is nearly constant for turbulent flow regime beyond Reynolds number of 4000.

2. The performance of the V-cone flowmeter is not affected by the boundary layer thickness except for the uniform flow and 5D extracted velocity profile (negligible boundary layer thickness) which were fed at 5D upstream of the meter. For the uniform flow fed, the deviation is around 14%. Whereas, feeding the boundary layer thickness formed due to 5D extracted profile, at the inlet the deviation is less than 4%. This is true for both the  $\beta$ -values.

## References

[1]. Miller RW, Flow measurement engineering handbook.

2nd ed. New York: McGraw Hill Publishing Company; 1989. p. 7.1–7.8.

[2]. www.mccrometer.com.

[3]. Ifft SA and Mikkelsen ED, Pipe elbow effects on the V-cone flow meter, in: Proceedings of the Fluids Engineering Conference, June 20–24, 1993, Publ. by ASME, Washington, DC, USA, 1993, pp. 37–41.

[4]. Prabhu SV, Mascomani R and Balakrishanan K, Effect of upstream pipe fittings on performance of orifice and conical flow meters. Flow Measurement Instrumentation 1996;7(1):49–54.

[5]. Erdal A and Andersson HI, Numerical aspects of flow computation through orifices, Flow Measurement and Instrumentation 1997;8(1):27–37.

[6]. Joshi SM, Eureka flow meter. In: International conference on hydrocarbon flow measurement. Palghat (India): FCRI; 2003. pp. 42–7.

[7]. Singh SN, Seshadri V, Singh R.K and Gawhade R, Effect of upstream flow disturbances on the performance characteristics of a V-cone flowmeter, Flow Measurement and Instrumentation (2006) 291–297, 1.



- [8]. Weiguang Liu, Ying Xu, Tao Zhang, Fengfeng Qi, Experimental optimization for dual support structures cone flowmeters based on cone wake flow field characteristics. *Sensors and Actuators A* 232 (2015) 115–131.
- [9]. Singh RK, Singh SN and Seshadri V, Study on the effect of vertex angle and upstream swirl on the performance characteristics of cone flow meter using CFD, *Flow Measurement and Instrumentation*20 (2009) 69–74.
- [10]. Ying Xu, Yang Hui-feng, Jing-wei Wu, Gang Li and Wang Hua-xiang; Numerical Simulation and Optimization Design for Cone Differential Pressure Flow sensor Micronanoelectronic Technology; July ~ August 2007; Issue 7/8 2007.
- [11]. Sheikh Nasiruddin, S.N. Singh, S.V. Veeravalli, S. Hegde, Effect of vertex angle and vertex tip radius on the performance of V-cone flow meter using CFD, *Measurement*, Volume 138,2019, pp. 536-544.
- [12]. Sheikh Nasiruddin, S.N. Singh, S.V. Veeravalli, S. Hegde, Shape optimization of the cone body for the improved performance of the V-cone flowmeter: A numerical study, *Flow Measurement and Instrumentation*, Volume 66 2019, pp.111-118.
- [13]. ISO-5167-5:2016(E), Measurement of Fluid Flow by means of Pressure Differential Devices inserted in Circular cross-section Conduits Running Full-Part-5; 01Mar 2016.
- [14]. Mentor FR, Two-Equation Eddy-Viscosity Turbulence Models for Engineering Applications, *AIAA Journal*. 32(8). 1598–1605. August 1994.
- [15]. Ansys 15.0 User guide, ANSYS Inc., Southpointe, 2600 Ansys Drive, Canonsburg, PA 15317, USA.
- [16]. Sheikh Nasiruddin (2018). Effects of some geometrical and dynamical parameters on the Flow characteristics of V-cone flowmeter (Doctoral Thesis). IIT Delhi, India.
- [17]. Solid Works-2014 User guide, Dassault Systems Solid Works Corporation, 175 Wyman Street, Waltham, MA 02451, USA.

# Diagnosis Method of Vortex Flowmeter Based on IoT

Yu Gu<sup>1</sup>, Chao Feng<sup>2</sup>, HanSheng Ye<sup>3</sup>, ZhongJun Han<sup>4</sup>

*<sup>1</sup>HeFei Comate Smart Sensor co.,LTD, Floor 2,building D2,Innovation industrial park,*

*No 800 Wangjiang west Road, HeFei,Anhui,China*

*<sup>2</sup>HeFei Comate Smart Sensor co.,LTD, HeFei, China*

*<sup>3</sup>HeFei Comate Smart Sensor co.,LTD, HeFei, China*

*<sup>4</sup>HeFei Comate Smart Sensor co.,LTD, HeFei, China*

*E-mail: yehsheng@comatemeter.com*

## Abstract

Vortex flowmeter is widely used in various applications because it can measure a wide range of media. When the flowmeter fails, the traditional on-site trouble shooting method has the disadvantages of time-consuming and difficult to ascertain the cause due to the complexity of the field conditions. This paper presents a convenient diagnostic method based on the Internet of Things transmission technology, which consists of the hardware, server and website. The hardware is a vortex flowmeter itself, which is to respond to server-side requests and data feedback, the server-side is used for the information interaction between device-side and web-side and data processing, and the web-side is used for the interaction between human-computer. The server can automatically complete the abnormal checking of the flowmeter's settings. More importantly, it can perform the FFT transformation and feature analysis on the original signal of the vortex sensor. After trouble-shooting, a firmware package containing the corresponding solution can be selected to upgrade the firmware of the flow meter on site remotely. Before the flowmeter is delivered from the factory, all parameters will be saved in the cloud as backup. During the process of diagnosis, the original setting parameters are firstly found according to the serial number of the flowmeter, and then the server will one-to-one match the currently settings and the back up data. After matching, the discrepant parameters will be marked and the parameter modification commands will be sent automatically. After the parameter modification, the server will read the parameters again to ensure the correctness of the amendment. The server will push the info of successful amendment and the detailed information of the amendment to the web after the amendment is completed, and the web will show the specific reasons for the failure. If there is no problem with the parameter setting, the original signal of the vortex sensor is to be obtained, and the server will perform FFT transformation on the acquired time domain signal to obtain the amplitude spectrum, and completes the statistical analysis of the frequency variance and the high frequency component. The server will cross check the abnormal data template with the signal characteristics and the corresponding firmware package is automatically upgraded according to the matching result. After the diagnosis is completed, the field data is saved to improve and enrich the template data. The method presented in this paper offers a simple and

FLOMEKO 2019, Lisbon, Portugal

intuitive human-computer interaction, and diagnose a vortex flow meter accurately and swiftly to reduce the maintenance cost of the flowmeter.

## 1. Introduction

When a non-linear bluff body planted vertically into a pipeline, as the fluid flows by the bluff body, the phenomenon of vortex separation occurs. There forms series of vortices on both left and right after the bluff body and they rotate reversely. Such vortices are known as Karman Vortex Street. Base on the theory above, vortex flow meter is invented ,which measure the flow rate according to the relationship between the frequency of the vortices leaves the bluff body and the flow rate.

When a vortex flowmeter fails, it is troublesome to find the cause of the problem due to its special structure, which means there is great disadvantage on the diagnosis of the vortex flowmeter. To solve the above problems, an IoT-based vortex flowmeter diagnosis method is proposed.

## 2. System Composition and Overview

The System consists of the hardware, server and website. The hardware is the vortex flowmeter itself, which is to respond to server-side requests and data feedback, the server-side is used for the information interaction between device-side and web-side and data processing, and the web-side is used for the interaction between human-computer.

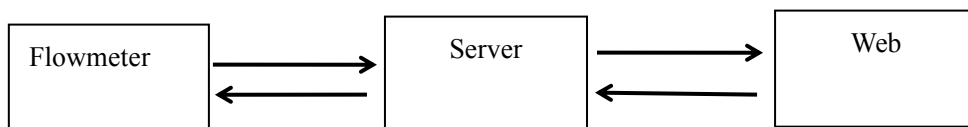


Figure 1: System Block

## 3. Diagnostic process

### 3.1 Parameter Settings Check

Website will firstly check if hardware is uploading any error code. If an error code is found, will cross check the parameters related to such error according to the error code. For instance, if find an error code of Err22, which means the max and min flow rate setting incorrect, the system will configure the hardware back to the setting which is preset in factory , according to the series number of the hardware and relevant data stored in database. If there find no error code, system will match and check all parameter and setting to find the abnormal one.

The detailed method for the match and check is as following: Say the acquired parameter is (attr, value), and the default setting of this parameter found in database is (attr', value'). When it is an int parameter, it will be judged as a match if value=value', otherwise a not match.

When it is an float parameter, it will be judged as a match if  $\left| \frac{value - value'}{value'} \right| < 1e-5$  ,

otherwise a not match. After match checking , the parameters judged as not matching will be marked and corrected automatically. The system will also match check the hardware again after the correction to ensure all amendments have been processed and are correct. All amendment of all parameters will be saved in database as analyzing report for checking in the future.

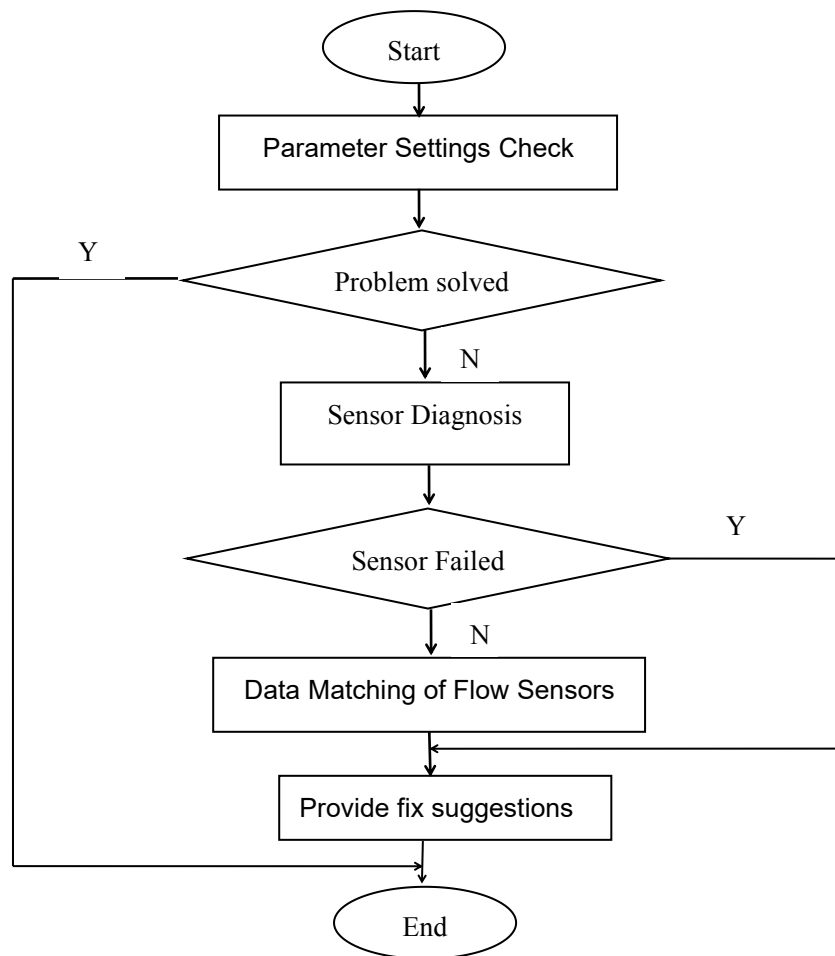


**Figure 2:** Diagnosis flow chart

### 3.2 Sensor Checking

The original data of flow sensor is acquired through Website, if the original data curve of flow sensor is straight when there is of flow in pipeline, the system will judge as flow sensor failure. In this case, the server will notify the maintenance engineer to replace the flow sensor on site or return the flow meter back to the factory for repairing.

### 3.3 Application condition checking

Perform similarity calculations between the origin sensor data with known standard data to decide the cause of abnormal measurement.

The detailed procedure of the similarity calculation are as following: Say Y0 is standard database of normal measurement, and Y1, Y2,~~~Y8 are database of abnormal caused by flow rate too small, flow rate too big, vibration too strong, improper installation, bluff body blocked, mixed-phase fluid, electromagnetic interference and leakage of pipeline. Figure 3 and figure 4 shows different signal curve sample of normal measurement and abnormal measurement caused by bluff body blockage.

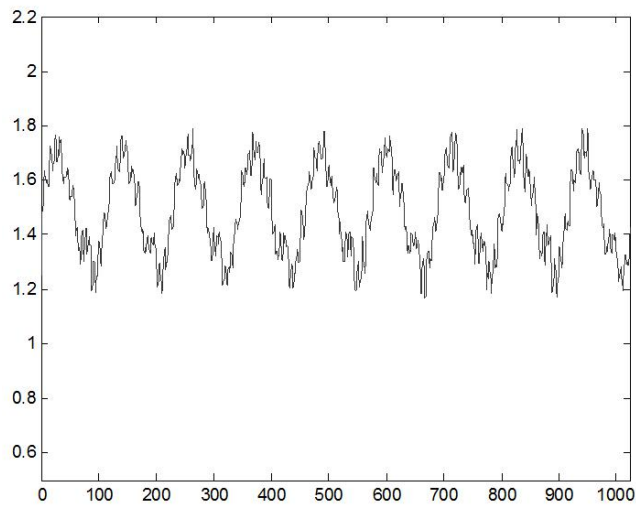


**Figure 3:** Normal measurement

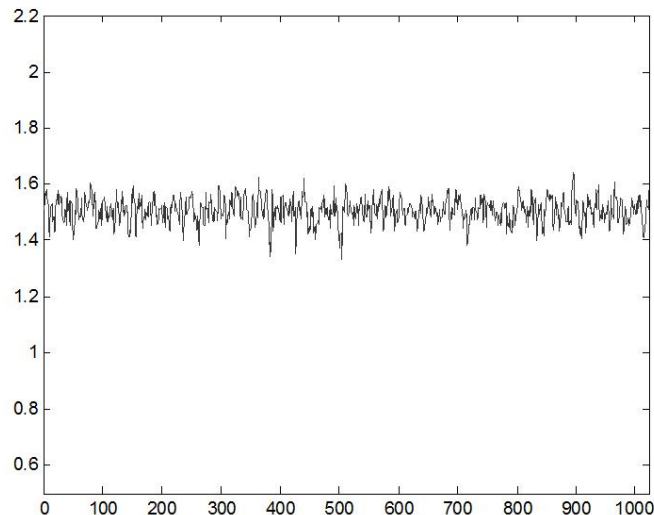


**Figure 4:** Abnormal measurement caused by bluff body blockage

Say X is origin data from field, C is the nominal size of the flow meter, M is the fluid, T is process temperature and P is process pressure.

Check the standard database and every database of abnormal measurement according to  $C$ 、 $M$ 、 $[T-T_0, T+T_0]$ 、 $[P-P_0, P+P_0]$  parameters.  $T_0$ 、 $P_0$  are preset values for

the temperature and pressure range to check. Acquire 20 sets of data samples which is more similar to application condition, say they are  $Y0'$ ,  $Y1'$ ,  $Y2'$ , ...  $Y8'$ .

Perform similarity calculation between X the origin data array X and  $Y0'$ , with the method of Algorithm of Pearson correlation coefficient (Equation 1)

$$\rho_{xy} = \frac{Cov(X,Y)}{\sqrt{D(X)}\sqrt{D(Y)}} = \frac{E\{[X - E(X)][Y - E(Y)]\}}{\sqrt{D(X)}\sqrt{D(Y)}} \quad (1)$$

In the equation above,  $X$  is the origin data from field,  $Y$  is data sample from database.  $\sqrt{D(X)}$ ,  $\sqrt{D(Y)}$  are the standard deviation of  $X$  and  $Y$ .  $E\{[X - E(X)][Y - E(Y)]\}$  is the covariance of  $X$  and  $Y$  as  $Cov(X,Y)$ . The quotient of the standard deviation and the covariance of  $X$  and  $Y$  are so called the correlation coefficient of  $X$  and  $Y$  ( $\rho_{xy}$ ).

Compare the average correlation of origin data and standard database against preset threshold. If average correlation is larger than threshold value, the origin data will be judged as normal. This judgement can be a proof of the correctness of the measurement in field and eliminate user's doubt on the measurement. If the average correlation is smaller than threshold, will proceed as following

Calculate the correlation of  $X$  and  $Y1'$ ,  $Y2'$ ... $Y8'$  one by one.

Get the the average correlation of each and every array,  $\bar{\rho} = \frac{\sum_{i=1}^n \rho_i}{n}$ .

Calculate the max value of the average correlation of each array.

Compare the correlation with preset threshold. If correlation is larger than threshold, we can judge that the relevant cause is the cause of the abnormal measurement. We can also recommend relevant signal processing method or advise on application condition improving. In case the signal processing method need to be improved, system will adopt the method provided by Chinese Invention Patent (Publication No. 106775588A) to update the program. If the correlations are smaller than thresholds, engineers shall pay a field visit for trouble shooting locally, system will store the abnormal data in the abnormal database after the judgement. So make the database more resourceful and improve the completeness of future diagnose and improve the efficiency of troubleshooting.

#### 4. Conclusion

To solve the disadvantage of inconvenient of traditional troubleshooting method of vortex flow meter, this paper proposes a new online diagnosis method based on the Internet of FLOMEKO 2019, Lisbon, Portugal

Things technology. The human-computer interaction is intuitive and simple. The method provide an accurately and quickly diagnose on vortex flowmeter and reduce the maintenance cost of flow meter efficiently.

### **References**

- [1] Masanori Hondoh, Masami Wada. A Vortex Flowmeter with Spectral Analsis Signal Processing. SIcon'01 Sensors for Industry Conference Rosement, Illinois, USA, 5-7, November 2001
- [2] F.A. Bower, D.J. Sorin, S. Ozev. A mechanism for online diagnosis of hard faults in microprocessors. 38th Annual IEEE/ACM International Symposium on Microarchitecture (MICRO'05). 12-16 Nov. 2005.
- [3] M.M Mukaka. A guide to appropriate use of Correlation coefficient in medical research. Malawi Medical Journal; 24(3): 69-71 September 2012

# A method of flow measurement based on the reaction force. Reaction flowmeters

H. M. Moțit

Control and Instrumentation Association of Romania

[hmotit@aair.org.ro](mailto:hmotit@aair.org.ro), Bucuresti, Romania

## Abstract

It is presented a worldwide new flow measurement method and the configurations of the first types of „reaction flowmeters” (both without and with moving parts) achieved thereof, both elaborated by the author. Also a global analysis of the functional equations and of the experimental and theoretical calibration of the reaction flowmeters without moving parts it is provided.

## 1. Preliminary considerations

Both this worldwide new flow measurement method and the different types of the configured flowmeters achieved thereof, are the subject matter of the patent application filed, with European Patent Office, EP 19020006.3.

The author named this method „Reaction force method of flow measurement” and the related flowmeters „Reaction flowmeters”.

These new types of flowmeters (both without and with moving parts) have been configured as a result of the first practical use of the „Unitary Synthesis and Design Method of Flowmeters”, recently elaborated by the author and of the developments from [1].

## 2. The principle of the method

The principle of this new method consists in the measurement of the fluid mass flow rate  $Q_m$  by putting in evidence the reaction force  $F_R = F_R(Q_m)$  of the measured fluid, which is proportional to  $Q_m$ , and the measurement of its different effects. The reaction force  $F_R$  is generated by a common basic specific configuration, developed for the fluid flow path through flowmeter. The force  $F_R$  is exerted by fluid on the wall of this specific configuration, and is measured, directly or indirectly, by the measurement of its derived effects (torque, differential pressure, force, frequency), proportional with  $F_R$ , according to the analytical dependence of  $F_R$  on  $Q_m$ .

## 3. Reaction flowmeters classification

Following the principle of „the reaction force method of flow measurement” the common basic configuration of the fluid flow path through reaction flowmeter (named „the reaction measurement system”) has been developed for all types of reaction flowmeters, and consists of a pair of two distinct functional parts: the inlet tube and the reaction element (reaction tube or reaction drum).

The „reaction measurement system” ensures the input of the measured fluid into the flowmeter through the inlet tube, which is an immobile and rigid tube to flowmeter housing, for all types of reaction flowmeters and then the fluid is transferred by a coupling to the reaction element.

The reaction element (reaction tube or reaction drum) performs by its specific configuration, two mandatory requirements, of the reaction flowmeters namely, on the one hand to get the maximum effect of the reaction force  $F_R(Q_m)$  exerted by the measured fluid on the reaction element and, on the other hand, to ensure the constructive facility that this effect of reaction force  $F_R$  be measured with precision.

Because the operating mode of the reaction flowmeters

is determined by the operation of their measuring system, it results the following classification of the reaction flowmeters:

- *Reaction flowmeters without moving parts.*

The reaction element is practically immobile, during the measurement, and it is usually achieved by a reaction tube.

- *Reaction flowmeters with moving parts.*

The reaction element is mobile during the measurement, and it is achieved by a reaction tube, or by a reaction drum in an evolved variant.

The reaction flowmeters in each above group have different coupling configuration, correlated with relative positions between inlet/outlet flowmeter connections (horizontal collinear axis, vertical collinear axis, perpendicular axis).

Further both groups of the reaction flowmeters are successively presented.

## 4. Reaction flowmeters without moving parts

### 4.1 Common reaction measurement system.

In Figure 1 is presented the basic configuration of “the reaction measurement system”, common for all reaction flowmeters without moving parts.

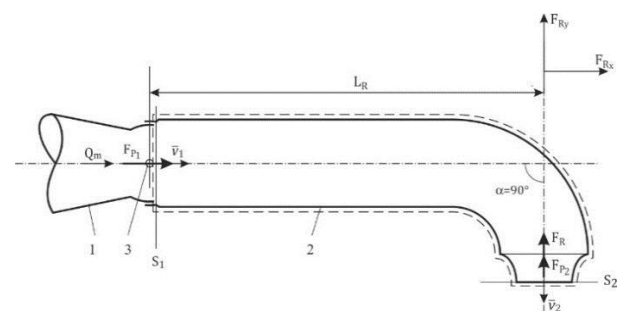


Figure 1: Configuration and the operating principle of the reaction measurement system

The reaction measurement system consists of the pair of immobile inlet tubes 1, configured as an extension of inlet connection of flowmeter, and the reaction tube 2.

Following the both mandatory requirements, mentioned in Section 3, the reaction tube 2 is specifically configured, on the one hand bent at  $90^\circ$  at its outlet end, the fluid discharge end, (to solve the first requirement), and on the other hand, is provided at its inlet with a shaft 3, perpendicular on it, which ensures a potential rotation mobility of the tube around the shaft (to solve the second requirement).

So configured, the reaction tube of the reaction flowmeters without moving parts ensures the possibility to detect and to measure the moment  $M_R$  of the reaction

force  $F_R$  to its rotation shaft, and by its processing to be calculated the mass flow rate  $Q_m$ .

#### 4.1.1 Functional equations

##### 4.1.1.1 Reaction force equation

The analysis is related to the reference control volume, marked with interrupted line in Figure 1, with faces at the inlet (section S1), which is the outlet from connection 1, with inner area  $A_1$ , and at the outlet (section S2) with inner area  $A_2$  of the reaction tube 2, encompassing the reaction tube walls.

According to the momentum theorem, the rate of change of momentum through the control volume, for a fluid which has a steady flow in a non-uniform flowing in a stream tube, is the total force exerted on the fluid and has the vector equation:

$$Q_m \times (\bar{v}_2 - \bar{v}_1) = \bar{F}_{RT} + \bar{F}_P + \bar{F}_G \quad (1)$$

where:

$Q_m$  - mass flow rate of fluid

$\bar{v}_1$  - inlet velocity of fluid into the control volume, (the outlet velocity from the connection 1)

$\bar{v}_2$  - outlet velocity of fluid from the reaction tube

$\bar{F}_{RT}$  - force exerted on the fluid by the reaction tube, touching the control volume

$\bar{F}_G$  - force exerted on the fluid body (e.g. fluid weight of control volume)

$\bar{F}_P$  - force exerted on the fluid by fluid pressure outside the control volume

$\bar{F}_P = \bar{F}_{P1} + \bar{F}_{P2}$

$\bar{F}_{P1}$  - force exerted on the fluid at the inlet of the control volume

$\bar{F}_{P2}$  - force exerted on the fluid at the outlet of the control volume

According to Newton's 3<sup>rd</sup> Law, regarding the "Principle of Action and Reaction", the force exerted by the fluid on the solid body (e.g. reaction tube), touching the control volume is opposite to  $\bar{F}_{RT}$  force, with the reaction force  $\bar{F}_R$ .

So the reaction force is given by expression:

$\bar{F}_R = -\bar{F}_{RT}$ , and has the vector equation:

$$F_R = Q_m \times (\bar{v}_1 - \bar{v}_2) + \bar{F}_{P1} + \bar{F}_{P2} + \bar{F}_G \quad (2)$$

Because the reaction tube shown in Figure 1 is placed in horizontal plane (a two dimensional  $x, y$  reference system), it is normally to use, instead of  $\bar{F}_R$  vector equation, its corresponding scalar equations, respectively its components  $\bar{F}_{Rx}$  (in  $x$  - direction) and  $\bar{F}_{Ry}$  (in  $y$  - direction).

It is convenient to choose the co-ordinate axis so that one is pointing in the direction of inlet velocity.

So in Figure 1 the  $x$  - axis points in the direction of the inlet velocity  $\bar{v}_1$ , and as a consequence the  $y$  - axis points in the direction of the outlet velocity  $\bar{v}_2$ .

On the one hand, the only fluid body force is that exerted by gravity, which acts into the paper plane, a direction that is not relevant in this analysis (for all types of reaction flowmeters that are horizontally placed).

On the other hand, it is known from continuity that  $Q_V = A_1 \times v_1 = A_2 \times v_2$ ,

Generally it is calculated the resultant reaction force  $F_{R_{resultant}}$  by combining its components,  $F_{Rx}$  and  $F_{Ry}$ .

Specifically for reaction tube from Figure 1 it is observed that the component  $F_{Rx}$ , of reaction force in the  $x$  - direction, does not contribute to the displacement of the reaction tube, because its effect is integrally take

over by the rotation shaft 3, which ensures the mobility of the tube for any its potential rotation.

Following these considerations, respectively by using the Bernoulli equation, and by replacing  $v_1$  and  $v_2$ , for the control volume which is open at both its ends, it results:

$$F_{R_v} = Q_m^2 \times k_1 \times \rho^{-1} \quad (3)$$

where:

$\rho$  - density of the measured fluid

$k_1 = 1/A_2 + 0,5 \times (A_2/A_1^2 - 1/A_2)$ - constructive constant

##### 4.1.1.2. Flow rate equations

*A. Flow rate equation of the reaction flowmeter with the measurement of reaction torque.*

This equation is deduced and with reference to the Figure 2, which presents the configuration of this basic type of the reaction flowmeters without moving parts.

The moment of the reaction force  $F_R$ , which tends to rotate the reaction tube 2 about its shaft 3, is named the reaction moment  $M_R$  and has the equation:

$$M_R = F_{R_y} \times L_R \quad (4)$$

where:  $L_R$  - moment arm

The reaction moment  $M_R$  is permanently balanced by the torque  $\tau$  of the torque sensor, according to equation:

$$M_R = \tau \quad (5)$$

Remark:

$\tau = \theta \times C$ , where  $C$  is the coefficient of torsional rigidity, and  $\theta$  is the torsion angle, with an insignificant maximum value of only  $0,2^0 \dots 0,8^0$ .

Consequently this type of reaction flowmeter is basically considered a flowmeter without moving parts.

By replacement of  $F_{R_y}$  in  $M_R$  expression, from previous equation (3), it results:

$$Q_m^2 \times \left[ \frac{1}{A_2} + \frac{1}{2} \times \left( \frac{A_2}{A_1^2} - \frac{1}{A_2} \right) \right] \times \rho^{-1} \times L_R = \tau \quad (6)$$

Respectively:

$$Q_m = (\rho \times \tau \times k_1^{-1} \times L_R^{-1})^{1/2} \quad (7)$$

*B. Flow rate equation of the reaction flowmeter with the differential measurement of pushing (reaction) pressure.*

This equation is deduced and with reference to the second configuration of reaction flowmeters, related to Figure 3, that ensures, proportionally to the component  $F_{R_y}$  of reaction force  $F_R$ , the force  $F_S$  which pushes, by a pin, on a face of a separation membrane, with pushing (reaction) pressure  $p_S$ . This pressure has the expression:

$$p_S = F_S/A_m = F_{R_y} \times L_R / (L_S \times A_m) \quad (8)$$

where:

$L_R$  - arm of moment  $M_R$

$L_S$  - arm of force  $F_S$  moment

$A_m$  - active area of separation membrane

According to flowmeter configuration, on the same face of the separation membrane acts simultaneously with  $F_S$ , the static pressure  $p_f$  of measured fluid with the equivalent force  $F_f = p_f \times A_m$

So the opposite face of the membrane (respectively the transmissions liquid) takes over the total pressure  $p_S + p_f = (F_S + F_f)/A_m$ , that is the result of the action of these two forces.

A differential pressure sensor measures the difference  $\Delta p = p_S$  between these pressures ( $p_S + p_f$ ) and  $p_f$

that acts on its (+) and (-) inlets.

By processing of the previous  $p_s$  expression, it results:

$$F_{Ry} = \Delta p \times L_S \times A_m / L_R \quad (9)$$

By replacing in equation (9) of  $F_{Ry}$  from equation (3) and by processing is obtained the measured mass flow rate equation:

$$Q_m = (\rho \times \Delta p \times k_2)^{1/2} \quad (10)$$

where:

$$k_2 = L_S \times A_m \times L_R^{-1} \times k_1^{-1} - \text{constructive constant}$$

#### 4.2 Basic configurations of reaction flowmeters

The connection of these flowmeters to the related pipe can be achieved in two ways (mostly with horizontal collinear inlet/outlet connections or in some cases with inlet/outlet connections with perpendicular axis).

With reference to their specific measurement systems, two configurations of reaction flowmeter are presented further.

A first embodiment is the reaction flowmeter with the direct measurement of the reaction torque, in the fluid (Figures 2a, b).

The measuring fluid enters the flowmeter through the inlet connection 1 and continues to flow through the reaction tube 2, by passing through the spherical coupling made of a nozzle (bumped head) 3 belonging to the inlet connection 1 and a nozzle (bumped head) 4 of the reaction tube.

The reaction tube is bent at the other end by 90°, and terminates with a convergent nozzle. The fluid exiting the reaction tube is taken up by a suitable convergent nozzle of the outlet connection 5 through which it is discharged from the flowmeter, and so is not disturbed the evacuation of the fluid from reaction tube.

Connections 1 and 5 are fixed rigidly and tightly to the housing 6 of the flowmeter, having their symmetry axes collinear, on the same horizontal line.

The radial equidistance between the nozzles (bumped heads) 3 and 4 is constructively achieved by two small bosses 7 of the bumped head 4 of the reaction tube, placed vertically, up and down around the vertical shaft 8, and so it is ensured an insignificant contact friction between the nozzles 3 and 4.

Their rigorously concentric positioning is accomplished by a metal shaft 8.

The rigorous positioning of the reaction tube with respect to the inlet connection is ensured by the rigorous concentric positioning of the bumped heads 3 and 4, achieved by rigorous positioning on the same vertical line of the upper bore of the bumped head 3 with the shaft 8. The spatial positioning ( $x, y, z$ ) between the two bumped heads 3 and 4 is thus rigorously assured, and by threading a nut 9 on the upper outer boss of the reaction tube, is ensured a permanent locking of the shaft 8 in this position.

By means of a wedge 10, the measuring shaft 11 of the torque sensor 12 being rigidly blocked relative to the reaction tube, respectively to its outer boss with which it is provided also at its lower side, fully takes over the torque of the reaction tube.

Correct measurement of the torque is ensured by blocking the rotation of a torque transducer by locking its support shaft 13 relative to the housing of the flowmeter, with a wedge 14 positioned between it and the support 15 which in its turn is rigidly fixed to the housing by screws 16.

The housing of the flowmeter is closed by a cover 17 which screws 19.

The reaction force  $F_R$  exerted by the mass flow  $Q_m$  at the outlet of the reaction tube, determines the torque

$$M_R = F_R \times L_R \text{ which is proportional to flow rate } Q_m.$$

This rotation torque is taken up by the measuring shaft 11 and implicitly by the torque sensor which output signal  $\tau$ , proportional to  $Q_m$ , is taken over by the electronic block 20.

Because the measuring shaft 11 requires a very low torsion angle of 0,2° ... 0,8° to measure its maximum torque, implicitly, the reaction tube, which is rigid with this shaft, will have the same insignificant rotation angle for the entire flow measurement range ( $Q_{m_{min}} \dots Q_{m_{max}}$ ).

So, the rotation angle of the reaction tube being practically insignificant, this type of reaction flowmeter is basically a flowmeter without moving parts.

In the electronic block, on the one hand, is stored, the calibration curve of flowmeter, for the specific nominal operating parameters of measured fluid, and on the other hand, it can provide the polynomial compensation of  $Q_m$  with temperature, and pressure, measured by sensors 21 and 22.

Thus, electronic block renders the compensated mass flow rate  $Q_m$  with  $P$  and  $T$ .

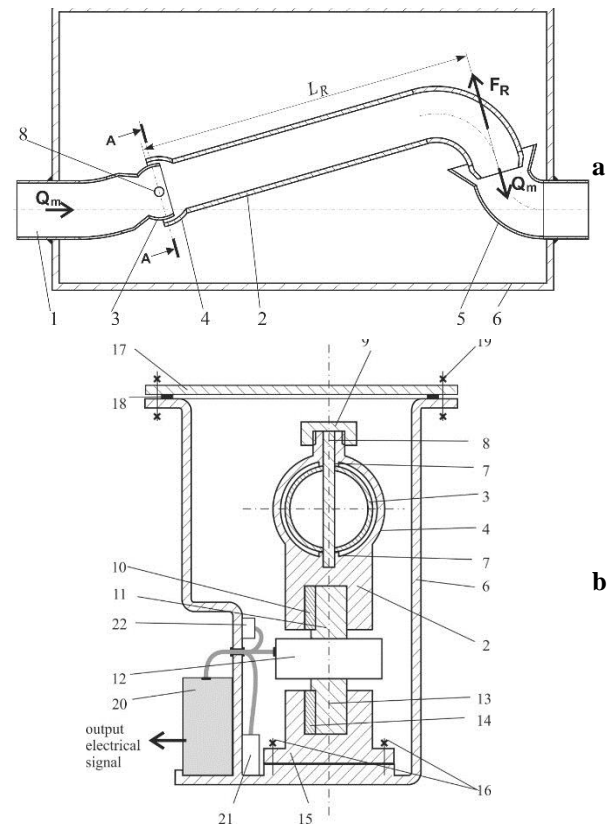


**Figure.2** Reaction flowmeter with torque measurement and horizontal collinear connections  
a- longitudinal section, b- cross section with a plane A-A

We mention that a similar configuration of reaction flowmeter with the measurement of reaction torque from outside the measured fluid, by magnetic coupling, was also elaborated.

Another type of reaction flowmeter, presented in Figure 3, ensures the measuring of reaction force by the differential measurement of the pushing (reaction) pressure produced by it.

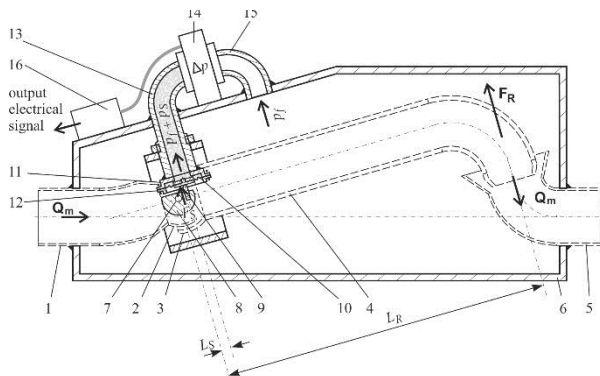


**Figure 3.** Reaction flowmeter with the measuring of the reaction force by the differential measurement of pushing (reaction) pressure.

The measuring fluid enters the flowmeter through inlet connexion 1 ending with in nozzle (bumped head) 2 which enters a nozzle (bumped head) 3 of the reaction tube 4.

The fluid flows through the reaction tube, which is bent at the other end at  $90^{\circ}$ , and ends with a convergent nozzle and then it is taken up by the outlet connection 5 through which it is discharged from the flowmeter, being provided at its inlet with a suitable converging nozzle in order to be not disturbed the fluid discharge from reaction tube.

Connections 1 and 5 are rigidly and sealed tighten to flowmeter housing 6, being horizontal collinear.

The radial equidistance between the nozzle (bumped head) 2 of the inlet connection and the nozzle (bumped head) 3 of the reaction tube 4 is made up constructively by two bosses, similarly to the solution presented in Figure 2b. The bosses are placed vertically, up and down, around the vertical shaft 7 and, being very small, provide a minimum contact friction between the bumped head 2, of inlet connection 1 and the bumped head 3 of the reaction tube.

The rigorous positioning of the reaction tube relative to the inlet connexion is ensured by the rigorous concentric positioning of the bumped heads 2 and 3, achieved by the vertical shaft.

The rigorous positioning of the shaft 7 in both the horizontal and vertical plane, is accomplished by its passing through two holes placed on the upper and lower walls of the reaction tube support. The centres of the two holes (bearings) being rigorously located on the same vertical axis, it is ensured the insignificant values both for horizontal play and friction of the shaft 7.

The reaction tube 4 is stiffened with the shaft 7 that rests on its support, that is stiffened related to housing 6. In the boss 8 at a distance  $L_S$  from the shaft centre, the pin 9 is rigidly embedded. It remains in permanent contact with the separation membrane 10 to which it permanently transmits the pushing force  $F_S$  of the reaction tube 4 as long as fluid flows through it and implicitly is generated by the reaction force  $F_R$ .

Since the  $L_R/L_S$  ratio is greater than 1, and  $F_S$  force is amplified relative to the  $F_R$  reaction force.

The pin 9 pushes the separation membrane through a workpiece which directly takes over the  $F_S$  force. The membrane takes over the  $F_S$  force, and is rigidly tighten and sealed externally between flanges 11 and 12 which are fastened by a screws/ nuts system.

Consequently, on the side towards the fluid, on the separation membrane operates both the static pressure  $p_f$  of the fluid and the pushing pressure  $p_s = F_S/A_m$  of the pin 9 ( $A_m$  being the active area of membrane) of  $F_S$  pushing force.

The connection 13, is welded to flange 11 and stiffened

against this by a nut, respectively being rigidly and tightly mounted to the housing 6 and connected to the high pressure inlet (+) of the differential pressure sensor 14. So, by connection 13 is transmitted to the sensor 14 the sum of the pressure  $p_s$  of pushing force  $F_S$  and the static pressure  $p_f$  of fluid, provided by the transmission liquid, with which is previously fully filled the volume between the separation membrane and the sensing element of the sensor 14.

At the low pressure inlet (-) of the sensor 14, is coupled the static pressure  $p_f$  of fluid, taken by the connection 15, which is rigidly and sealed mounted on the housing. Sensor 14 ensures a fully rigorous measurement of the differential pressure  $\Delta p = (p_f + p_s) - p_f = p_s$ , respectively the reaction pressure being structurally provided with the compensation function with the temperature and the pressure of the measuring fluid.

Thus the sensor 14 indirectly measures the pushing force  $F_S$ , implicitly the reaction force  $F_R$  and consequently measures the mass flow rate  $Q_m$ . The output signal of the sensor 14 is applied to the electronic block 16, where are stored both the calibration curve  $Q_m = Q_m(\Delta p)$  according to the normal operating parameters of the measured fluid and the facility to be ensured the flow rate compensation with pressure and temperature of fluid. Thus the electronic block 16 renders the compensated value of the measured mass flow  $Q_m$  with P and T.

Since the pressure transmitting liquid between the separation membrane 10 and the differential pressure sensor is practically incompressible, the displacement of this membrane, implicitly of the pin 9, is therefore very small, almost null, to measure the entire range  $Q_{mmin} \dots Q_{mmax}$ . Correspondingly, the reaction tube displacement is extremely small and consequently, this type of flowmeter is practically a flowmeter without moving

## 5. Reaction flowmeters with moving parts

These flowmeters are grouped, depending on the type of their reaction element, as follows:

- Reaction flowmeters with rotating reaction tube
- Reaction flowmeters with rotating reaction drum

Due to limited length of this paper, these flowmeters will be presented in another paper, and we now continue with the presentation of the experimental results regarding the reaction flowmeters without moving parts.

## 6. Experimental results and analysis

### 6.1 Reaction flowmeters with torque measurement

Further there are presented, the results of the experimental calibration successively achieved with water and air, for the reaction flowmeters with torque measurement.

Also the values of each experimental calibrations are presented in comparison with the values of the corresponding theoretical calibration.

#### 6.1.1 Calibration with water

A reaction flowmeter of DN25 having a torque sensor (with  $\tau_{max} = 0,5$  Nm and accuracy 0,1%FS) has been calibrated with water ( $t = 20 \pm 0,2^{\circ}\text{C}$ ) by the gravimetric method. Table 1 presents the values both of the measured and of the calculated mass flow rate  $Q_m$  corresponding to the measured torque  $\tau$  by the torque sensor of the calibrated flowmeter.

Corresponding to the measured torque range (0,0102.....0,5Nm) of its torque sensor, the potential measured flow rate range (310,152....2171,501 Kg/h) of

the calibrated reaction flowmeters was determined, experimentally and by theoretical calculation.

**Table 1:** Comparison between experimental and theoretical calibration with water

Torque	Pressure drop $\Delta p$	Average measured flow rate $Q_{m_{meas}}$	Theoretically calculated flow rate $Q_{m_{calc}}$	$\frac{Q_{m_{calc}} - Q_{m_{meas}}}{Q_{m_{meas}}} \times 100$
Nm	bar	kg/h	kg/h	%
0,01020	0,015	311,531	310,153	-0,44
0,02015	0,017	435,970	435,926	-0,01
0,02500	0,018	486,290	485,560	-0,15
0,03000	0,020	532,248	531,907	-0,07
0,04800	0,028	678,521	672,215	-0,93
0,07300	0,039	835,707	829,724	-0,71
0,10700	0,055	1014,740	1004,539	-0,98
0,15000	0,071	1199,002	1189,380	-0,80
0,20400	0,089	1400,101	1387,044	-0,93
0,25000	0,104	1549,122	1535,483	-0,88
0,32400	0,124	1761,315	1748,625	-0,72
0,35000	0,130	1830,906	1816,808	-0,77
0,40000	0,145	1957,716	1942,250	-0,79
0,45000	0,153	2076,891	2060,068	-0,81
0,50000	0,165	2189,455	2171,501	-0,82

The accuracy of the reaction flowmeter depends on the accuracy of the used torque sensor.

So, since the calibrated flowmeter used o torque sensor with  $\tau_{max} = 0,5Nm$  and accuracy of, 0,1% FS, it has an accuracy of  $-(0,1\% \text{ to } 2\% \text{ o.r.})$  corresponding to a theoretical turndown of 4,47, according to relationship  $Q_{m_{max}}/Q_{m_{min}} = (\tau_{max}/\tau_{min})^{1/2} (0,5Nm/0,025Nm)^{1/2}$

This value is confirmed and exceeded by the experimental turndown of 4,50, the ratio 2189,455Kg/h / 486,290Kg/h between the values of measured flow rate  $Q_m$  at torques 0,500Nm, respectively 0,025Nm.

The analysis of the Table 1 demonstrates a very good matching of the experimental and theoretical calibration, the percentage differences between the values of calculated and measured mass flow rate  $Q_m$ , being placed in a very narrow band of values of  $-(0,01 \dots 0,98)\%$ .

The theoretical calculation of  $Q_m$  has been achieved using the customized form of general functional equation (7), according to construction of the calibrated reaction flowmeter, respectively:

$$Q_m = 97,2 \times (\rho \times \tau)^{1/2} \quad (11)$$

where:

$Q_m$  - mass flow rate, in kg/h

$\rho = 998,2 \text{ kg/m}^3$  - density of water for  $t = 20^\circ C$

$\tau$  - measured torque, in Nm

97,2 - customized constructive constant, in  $m \times s$

Another positive conclusion it results from positioning of water velocities across the flowmeter with their maximum value ( $v_{max} = 1,22 \text{ m/s}$ ) in the center of the recommended economical velocity range.

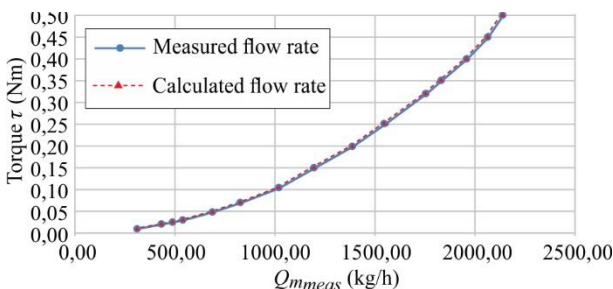


**Figure 4:** Mass flow rate of water depending on the measured torque

In Figure 4 there are plotted the dependence curves of  $Q_m$  by  $\tau$ , both for theoretically calculated  $Q_{m_{calc}}$  (red curve) and for measured  $Q_{m_{meas}}$  (blue curve) flow rates, the density of water being practically constant during the calibration, at  $20 \pm 0,20^\circ C$ . It result a very good matching between these two convergent approaches, that ensures a strong basis for a predictable and coherent synthesis and design of any new type of reaction flowmeter.

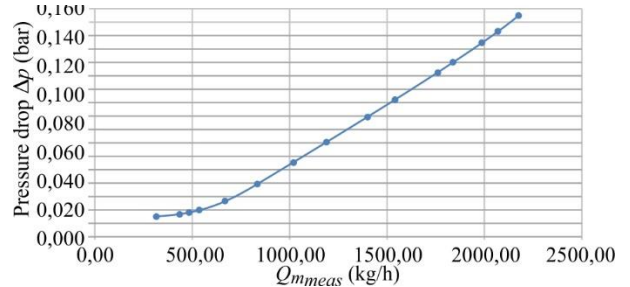


**Figure 5:** Pressure drop depending on measured flow rate of water

In Figure 5 is presented the curve of pressure drop  $\Delta p$  depending on flow rate  $Q_m$ .

It is observed that pressure drop  $\Delta p$  has a moderate value.

Regarding the installation these reaction flowmeters needs Inlet/Outlets of  $0 \times DN$ , being very economically.

### 6.1.2 Calibration with air

Another reaction flowmeter DN25 was calibrated with air. It has a dual-range torque sensor with measurement error 0,1% FS (that is custom-built to measure two ranges synchronously without chance-over) with the 1<sup>st</sup> range 0,5Nm and the 2<sup>nd</sup> range 1/10 of the 1<sup>st</sup> range, respectively 0 - 0,05Nm.

**Table 2:** Comparison between experimental and theoretical calibration with air

Torque	Inlet parameters of air				Pressure drop $\Delta p$	Average measured flow rate $Q_{m_{meas}}$	Calculated flow rate $Q_{m_{calc}}$	$\frac{Q_{m_{calc}} - Q_{m_{meas}}}{Q_{m_{meas}}} \times 100$
	Pressure $P_1$	Temperature $t_1$	Humidity	Density $\rho$				
O	bara	°C	%rH	kg/m3	bara	kg/h	kg/h	%
0,0025	0,9421	24,00	42,5	1,1030	0,0011	5,1120	5,1042	-0,15
0,0050	0,9432	23,67	42,7	1,1065	0,0020	7,2320	7,2298	-0,03
0,0100	0,9455	23,68	43,1	1,1110	0,0045	10,3740	10,2453	-1,24
0,0250	0,9520	24,12	42,6	1,1150	0,0110	16,5270	16,2284	-1,81
0,0500	0,9638	24,78	40,5	1,1270	0,0228	23,5340	23,0735	-1,96
0,1000	0,9855	26,51	35,5	1,1460	0,0445	33,5450	32,9048	-1,91
0,1500	1,0059	29,20	28,8	1,1580	0,0649	41,2950	40,5104	-1,90
0,2000	1,0286	32,81	24,4	1,1720	0,0876	47,9550	47,0593	-1,87
0,2500	1,0510	44,98	12,1	1,1500	0,1070	53,0620	52,1178	-1,78
0,3000	1,0690	44,99	12,2	1,1680	0,1280	58,4160	57,5372	-1,50
0,3500	1,0912	43,20	14,8	1,2010	0,1460	63,4000	63,0192	-0,60
0,3700	1,1008	34,10	20,7	1,2380	0,1575	66,0020	65,7852	-0,33
0,4200	1,1210	38,90	19,2	1,2500	0,1750	71,0020	70,4282	-0,81
0,4500	1,1277	40,02	18,5	1,3070	0,1910	74,7310	74,5437	-0,25
0,5000	1,1515	40,60	17,5	1,3320	0,2105	79,4190	79,3239	-0,12

The master slave method was used for the calibration. In Table 2 is presented the comparison between the average values of the measured mass flow rate (according to experimental calibration) and the theoretically calculated flow rate, according to equation (7), corresponding to each measured torque  $\tau$ , by the sensor of the calibrated flowmeter.

Also, in Table 2 for a complete analysis, the inlet parameters of air and the pressure drop are presented, for each value of the measured torque.

The torque sensor of the flowmeter being a dual - range sensor, when the torque value decreases along the 1<sup>st</sup> range, from 0,5Nm to 0,05Nm, the measurement error progressively increases from 0,1% o.r. to 1% o.r.

Then when the torque decreases, along the 2<sup>nd</sup> range, from 0,05Nm to 0,0025Nm, the measurement error progressively increases from 0.1% o.r. to 2% o.r.

It results that the whole used range of the torque sensor is characterized by the ratio

$$\tau_{max} / \tau_{min} = 0,5 \text{ Nm} / 0,0025 \text{ Nm} = 200.$$

Depending on the accuracy of the used torque sensor, results the accuracy of the reaction flowmeter.

In consequence, the measured errors of the reaction flowmeter repeats the variation of the dual - torque sensor, from 0,1% o.r. for  $Q_{m_{min}}$  to 2% for  $Q_{m_{max}}$ .

This variation of the measurement errors corresponds to a turndown of the reaction flowmeters of  $Q_{m_{min}}/Q_{m_{max}} = (\tau_{max} / \tau_{min})^{1/2} = (200)^{1/2} = 14,14$ , according to their functional equation (7).

The analysis of Table 2 demonstrates a very good matching of the flow rate values, experimental measured  $Q_{m_{meas}}$  and theoretically calculated  $Q_{m_{calc}}$ ; their percentage differences being placed in a narrow band of the values - (0,12... 1,96)%.

The theoretical calculation of  $Q_{m_{calc}}$  has been made with the equation (11), the customized form of the functional equation (7), that was established for using the torque sensor, according to constructive dimensions, and the values of the air density  $\rho$ .

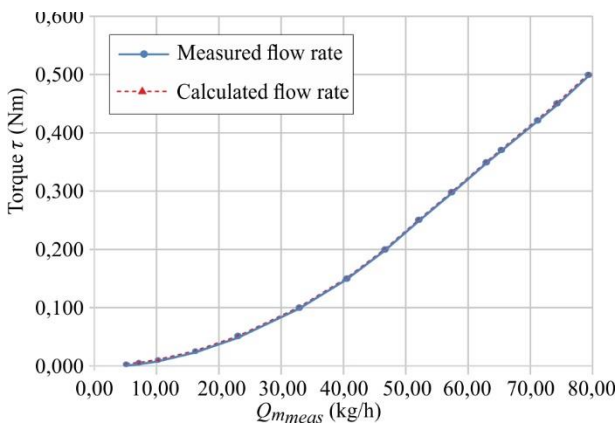


**Figure 6:** Mass flow rate of air depending on the measured torque

In Figure 6 is plotted the dependence curve  $Q_m$  by  $\tau$ , both for the theoretically calculated  $Q_{m_{calc}}$  (red curve), and for the measured  $Q_{m_{meas}}$  (blue curve).

In result a very good matching between these two convergent approaches, that ensures a strong basis for a predictable and coherent synthesis and design of any new type of reaction flowmeter.

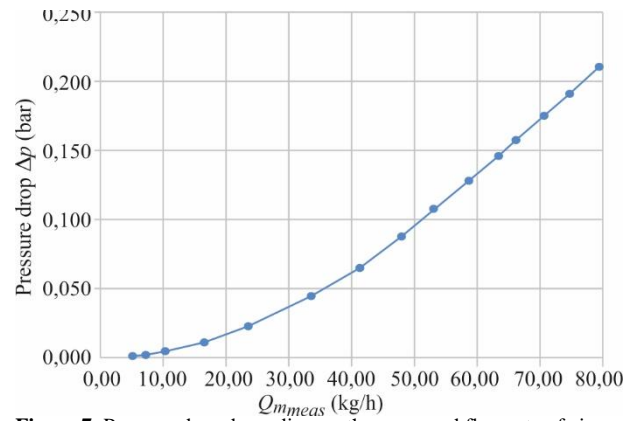


**Figure 7:** Pressure drop depending on the measured flow rate of air

In Figure 7 is presented the curve pressure drop  $\Delta p$  depending on the measured mass flow rate  $Q_{m_{meas}}$ . It is observed that  $\Delta p$  has a moderate value.

The comparison between the curves  $Q_m = Q_m(\tau)$  achieved with water and air, for these two flowmeters DN25, demonstrates on the one hand, the correctness of the general functional equation (7) of the reaction flowmeters.

On the other hand it results the practical usefulness of the equation to be ensured for the calculation, with a good precision, of the flow rate value converted from a measured fluid to other measured fluid.

### 6.2 Reaction flowmeters with differential measurement of reaction pressure

This type of reaction flowmeters, with configuration presented in Figure 3, using a differential pressure sensor with a high accuracy of 0,02% FS, can ensure the measuring of mass flow rate  $Q_m$  with the accuracy of (0,1...2)% o.r., for a turndown of  $(Q_{m_{max}}/Q_{m_{min}})^{1/2} = (\Delta p_{max}/\Delta p_{min})^{1/2} = 100^{1/2} = 10$ .

The own microprocessor of the difference pressure sensor and respectively the electronic block of the whole reaction flowmeter ensure the complete compensation of measured  $Q_m$  with temperature ( $T$ ) and pressure ( $P$ ) of measured fluid.

These reaction flowmeters have advantage that can be used for a wide range of fluids (liquids and gases), including aggressive fluids, due to the fact that the material in contact with media of the differential pressure sensor is stainless steel ANSI 316 or viton.

## 7. Conclusion

This new flow measurement method offers, the theoretical basis of the design of a wide diversity of new types of flowmeters, for a large area of applications.

For the reaction flowmeters without moving parts there are established: the functional equations, the good fit between experimental and theoretical calibration, the main technical features (accuracy, turndown, pressure drop) and the possibilities of their future progressive improvements.

## References

- [1] Horia Mihai Moșit, *Unitary Analysis, Syntesis, and Classification of Flow Meters* (Boca Raton, USA, CRC Press Taylor & Francis Group), 2018

# Exploration of Hydrogen Influence on Physical Properties of Natural Gas and Metrological Characteristics of Its Metering Systems

A. Stetsenko, V. Naumenko

A. Stetsenko, [andrii.energo@gmail.com](mailto:andrii.energo@gmail.com), Olten, Switzerland  
V. Naumenko, [naumenko@energo.kh.ua](mailto:naumenko@energo.kh.ua), Kharkiv, Ukraine

---

## Abstract

Due to the predicted exhaustion of oil and natural gas resources by the end of this century, all industrialized countries are taking steps to find alternatives for hydrocarbon fuels. Nuclear energy is expected to be the main source of electricity production by the end of the XXI century. Electricity, however, has some disadvantages related to storage and losses in case of long-distance transmission. Among other sources of energy, the use of which can be possible in the nearest future, hydrogen is the most promising one. The advantages of using hydrogen as a fuel can be summarized as follows: using hydrogen as fuel can be one of the comprehensive solutions to the problem of environmental protection; hydrogen is an excellent energy carrier; as of today, society is largely dependent on fossil energy, while the contribution of sustainable fuel to global energy demand is limited.

Taking into consideration the above, and the possibility of using a mixture of hydrogen and natural gas as a source of energy, the research has been aimed in the following directions:

- Influence of hydrogen impurities on the physical properties of natural gas;
- the effect of adding hydrogen into natural gas on the metrological characteristics of metering systems.

---

## 1. Statement of the problem

To determine the effect of hydrogen on the above list of factors, research is aimed at solving the following problems:

1. Conducting studies on the effect of hydrogen injection in natural gas on the physical properties of the mixture requires determining the dependence of the following gas parameters on the percentage of hydrogen in the natural gas: density, Reynolds number, dynamic viscosity, compressibility factor, high heat value, Wobbe number, sound speed, adiabatic exponent.

2. Determining the permissible fraction (permissible concentration) of hydrogen in natural gas in modern gas-transport and gas-consuming systems.

3. Examining the effect of hydrogen injection on metrological characteristics of measuring equipment and gas custody transfer metering systems in the following areas:

- research and assessment of the possibility of using contemporary gas meters to measure the

volumetric flow rate and volume of hydrogen and natural gas mixture;

- study of the effect of hydrogen injection on the results of measuring the volumetric flow rate and volume adjusted to basic conditions. Evaluation of the possibility of using existing flow computers and gas correctors to adjust the measured volumetric flow rates and mixture volumes to basic conditions;
- the influence of hydrogen injection on the calorific value of the mixture within the framework of the transition of gas metering systems of power plant units.

## 2. The main material

### 2.1 Conducting research on the effect of injecting hydrogen into natural gas on the physical properties of the mixture

Various samples of natural gas with different component mixtures were prepared to perform objective research and modeling.

Analysis of the following physical characteristics of these gas compositions and calculations of their physical criterion were carried out:

- adiabatic index and speed of sound;

- density;
- compressibility factor;
- higher heat of combustion;
- Wobbe index.

The calculation of the adiabatic index (the ratio of the relative change in pressure to the relative change in density without heat exchange with the environment) of gases was carried out according to the Kobza formula [1] for the component composition and density of each component at base conditions:

$$k = 1,556(1 + 0,074x_a) - 3,9 \cdot 10^{-4} T(1 - 0,68x_a) - 0,208\rho_b + (p/T)^{1,43} [384(1 - x_a)(p/T)^{0,8} + 26,4x_a] \quad (1)$$

where:  $x_a$  - nitrogen content in gas;

$p$  - pressure, MPa;

$T$  - absolute temperature, K;

$\rho_b$  - density of natural gas at base conditions, kg/m<sup>3</sup>.

The speed of sound in natural gas is determined by the formula AGA 10 [2]:

$$u = 18,591 \left( \frac{T \cdot Z \cdot K}{\rho_b} \right)^{0,5} \quad (2)$$

where:  $\rho_b$  - density of natural gas at base conditions, kg/m<sup>3</sup>;

$T$  - absolute temperature, K;

$k$  - adiabatic index;

$Z$  - compressibility factor.

The compressibility factor (the ratio of the actual volume of real gas at a certain pressure and temperature to the volume of an ideal gas under the same conditions) is calculated by the formula (3) ISO 6976:1995/Cor.2:1997, Cor.3:1999 [3]:

$$z_{mix}(t_2, p_2) = 1 - \left[ \sum_{j=1}^N x_j \cdot \sqrt{b_j} \right]^2 \quad (3)$$

where:  $x_j$  - the content of the j-th component in the gas;

$\sqrt{b_j}$  - summation of the coefficient for j-th component of natural gas.

The relative density (the ratio of the density of the gas to the density of dry air of standard composition at the same pressure and temperature) is calculated by the formula (14) ISO 6976:1995/Cor.2:1997, Cor.3:1999 [3]:

$$d(t, p) = \frac{d^\circ \cdot Z_{air}(t, p)}{Z_{mix}(t, p)} \quad (4)$$

where:  $d^\circ$  - the relative density of an ideal gas;

$Z_{air}(t, p)$  - compressibility factor of dry air of standard composition;

$Z_{mix}(t, p)$  - gas compressibility factor.

The relative density of an ideal gas is calculated by the formula (11) ISO 6976:1995/Cor.2:1997, Cor.3:1999 [3]:

$$d^\circ = \sum_{j=1}^N x_j \frac{M_j}{M_{air}} \quad (5)$$

where:  $x_j$  - the content of the j-th component in the gas;

$M_j$  - the molar mass of the j-th component;

$M_{air}$  - molar mass of dry air compressibility standard composition.

The density is calculated by the formula (15) ISO 6976:1995/Cor.2:1997, Cor.3:1999 [3]:

$$\rho(t, p) = \frac{\rho^\circ(t, p)}{Z_{mix}(t, p)} \quad (6)$$

where:  $\rho^\circ(t, p)$  - ideal gas density;

$Z_{mix}(t, p)$  - gas compressibility factor.

The ideal gas density is calculated by the formula (11) ISO 6976:1995/Cor.2:1997, Cor.3:1999:

$$\rho^\circ(t, p) = \left( \frac{p}{RT} \right) \sum_{j=1}^N x_j \cdot M_j \quad (7)$$

where:  $x_j$  - the content of the j-th component in the gas;

$M_j$  - the molar mass of the j-th component;

$p$  - pressure, MPa;

$T$  - absolute temperature, K;

$R$  - universal gas constant, equal to  $8,314510 \text{ J}\cdot\text{mol}^{-1}\cdot\text{K}^{-1}$ .

The determination of the values of the lowest and highest calorific values of gas is carried out in accordance with the formula (10) ISO 6976:1995/Cor.2:1997, Cor.3:1999:

$$\overline{H}[t_1, V(t_2, p_2)] = \frac{\overline{H}^\circ(t_1)}{Z_{mix}(t_2, p_2)} \quad (8)$$

where:  $\overline{H}^\circ(t_1)$  - the value of the ideal heat of combustion (higher or lower);  
 $Z_{mix}(t_2, p_2)$  - gas compressibility factor under base conditions.

The determination of the values of the lowest and highest ideal heat of combustion of a gas is made in accordance with the formula (4) ISO 6976:1995/Cor.2:1997, Cor.3:1999:

$$\overline{H}^\circ(t_1) = \sum_{j=1}^N x_j \cdot \overline{H}_j^\circ(t_1) \quad (9)$$

where:  $x_j$  - the content of the  $j$ -th component in the gas;  
 $\overline{H}_j^\circ(t_1)$  - the value of the ideal heat of combustion of the  $j$ -th component (higher or lower).

The calculation of the Wobbe number was performed according to the formula (16) ISO 6976:1995/Cor.2:1997, Cor.3:1999 [3]:

$$W[t_1, V(t_2, p_2)] = \frac{\overline{H}_s[t_1, V(t_2, p_2)]}{\sqrt{d(t_2, p_2)}} \quad (10)$$

where:  $\overline{H}_s[t_1, V(t_2, p_2)]$  - the value of the highest calorific value;  
 $d$  - relative density.

The results of the analysis of the physical parameters of the four natural gas samples are shown in Tables 1 - 4.

**Table 1**

Hydrogen	0	2	10	23
Methane	93.031	91.170	83.728	71.634
Ethane	3.541	3.470	3.187	2.727
Propane	0.835	0.818	0.752	0.643
i - Butane	0.105	0.103	0.095	0.081
n - Butane	0.136	0.133	0.122	0.105
neo - Pentane	0.013	0.013	0.012	0.010
i - Pentane	0.029	0.028	0.026	0.022
n - Pentane	0.023	0.023	0.021	0.018
Hexan	0.008	0.008	0.007	0.006
Nitrogen	1.125	1.103	1.013	0.866
Carbon Dioxide	1.149	1.126	1.034	0.885
Oxygen	0.008	0.008	0.007	0.006
Calorific value MJ/m3	38.650	38.116	35.980	32.516
Shift, %	-	-1.38	-6.91	-15.87
Wobbe index MJ/m3	49.8571	49.611	48.623	47.015
Shift, %	-	-0.49	-2.48	-5.70

**Table 2**

Hydrogen	0	2	10	23
Methane	90.779	88.963	81.701	69.900
Ethane	4.555	4.464	4.100	3.507
Propane	1.056	1.035	0.950	0.813
i - Butane	0.110	0.108	0.099	0.085
n - Butane	0.174	0.171	0.157	0.134
neo - Pentane	0.002	0.002	0.002	0.002
i - Pentane	0.045	0.044	0.041	0.035
n - Pentane	0.038	0.037	0.034	0.029
Hexan	0.034	0.033	0.031	0.026
Nitrogen	1.519	1.489	1.367	1.170
Carbon Dioxide	1.684	1.650	1.516	1.297
Oxygen	0.008	0.008	0.007	0.006
Calorific value MJ/m3	38.811	38.273	36.124	32.638
Shift, %	-	-1.39	-6.92	-15.90
Wobbe index MJ/m3	49.428	49.184	48.205	46.613
Shift, %	-	-0.49	-2.47	-5.70

**Table 3**

Hydrogen	0	2	10	23
Methane	89.425	87.637	80.483	68.857
Ethane	5.179	5.075	4.661	3.988
Propane	1.191	1.167	1.072	0.917
i - Butane	0.115	0.113	0.104	0.089
n - Butane	0.185	0.181	0.167	0.142
neo - Pentane	0.003	0.003	0.003	0.002
i - Pentane	0.047	0.046	0.042	0.036
n - Pentane	0.040	0.039	0.036	0.031
Hexan	0.054	0.053	0.049	0.042
Nitrogen	1.646	1.613	1.481	1.267
Carbon Dioxide	2.111	2.069	1.900	1.625
Oxygen	0.007	0.007	0.006	0.005
Calorific value MJ/m3	38.904	38.364	36.208	32.709
Shift, %	-	-1.39	-6.93	-15.92
Wobbe index MJ/m3	49.156	48.913	47.940	46.359
Shift, %	-	-0.49	-2.47	-5.69

**Table 4**

Hydrogen	0	2	10	23
Methane	89.213	87.428	80.291	68.694
Ethane	5.114	5.012	4.603	3.938
Propane	1.163	1.140	1.047	0.895
i - Butane	0.118	0.115	0.106	0.091
n - Butane	0.209	0.205	0.188	0.161
neo - Pentane	0.003	0.003	0.003	0.002
i - Pentane	0.059	0.058	0.053	0.046
n - Pentane	0.047	0.046	0.042	0.036
Hexan	0.05	0.049	0.045	0.039
Nitrogen	1.509	1.479	1.358	1.162
Carbon Dioxide	2.510	2.460	2.259	1.933
Oxygen	0.0055	0.005	0.005	0.004
Calorific value MJ/m <sup>3</sup>	38.809	38.271	36.122	32.636
Shift, %	-	-1.39	-6.92	-15.91
Wobbe index MJ/m <sup>3</sup>	48.905	48.665	47.701	46.135
Shift, %	-	-0.49	-2.46	-5.66

The results of calculations allow to draw conclusions that when adding hydrogen to the natural gas in an amount from 2 % to 23 % physical parameters of the obtained mixture vary accordingly in the following ranges:

- the speed of sound increases by (1 - 13.5) %;
- density (relative density) of the mixture is reduced by (1,7 - 20,5) %;
- compressibility factor at atmospheric pressure varies within the limits (0,01 - 0,1) % at atmospheric pressure;
- the high heat value decreases by approximately (1.4 - 16) %;
- the Wobbe index decreases in the range (0.49 - 5.7) %.

### 2.2 Finding out the permissible rate (concentration) of hydrogen in natural gas in existing gas transmission and gas consuming facilities.

Determination of the permissible fraction (permissible concentration) of hydrogen in natural gas was performed to satisfy the following requirements and limitations:

- the possibility of using the mixture in existing gas transmission and gas-consuming systems without additional reconstructions, modifications;
- requirements and limitations of regulatory and metrological documentation;
- safety and explosion protection requirements.

Analysis of regulatory documentation and modeling showed the following:

- According to the European standard EN 437 Tested gases - Test pressures - Appliance categories [4], natural gas is classified into "H" and "L" groups depending on the Wobbe index values. Simulations showed that with the addition of hydrogen in a volume of up to 23%, all four samples of natural gas remained in the "H" group;
- In accordance with the requirements of the international standard ISO 12213-3: 2006 [5],

FLOMEKO 2019, Lisbon, Portugal

restrictions are imposed on the use of natural gas for domestic purposes according to the following parameters:

- absolute pressure (from 0 to 12 MPa);
- the molar fraction of hydrogen (from 0 to 10%);
- relative density (from 0.55 to 0.8).

The simulation results carried out in the first section showed that, by the criterion of permissible values of the relative density, the fraction of hydrogen in natural gas should be in the range from 0 to 10%. Further increase in the proportion of hydrogen (up to 23%) depends on the quality (Wobbe number) of natural gas and requires the search and use of other algorithms for calculating the physical parameters of gas (described by other regulatory documents).

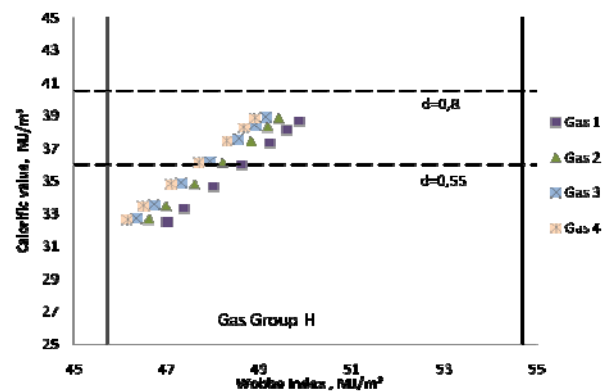


Figure 1

c) The algorithms for calculating the compressibility factor carried out according to GERG 88, also introduce a limit on the proportion of hydrogen in natural gas not more than 10%.

d) Analysis of the hydrogen explosion hazard showed that hydrogen ignites at a concentration of 4 to 74.5% (methane ignites at concentrations of 2.1 to 9.5%), although explosive concentrations for hydrogen are much higher than for natural gas (between 18.3 and 59% in concentration with air for hydrogen, compared with 6.3-14% for methane). This means that adding up to 59% of hydrogen to natural gas does not require changing the degree of explosion-proof, therefore, does not require additional modifications and certification of existing ex-proof equipment.

### 2.3 Analysis of the effect of hydrogen injection on the metrological characteristics of measuring instruments and gas metering systems

Currently, the most frequent systems (facilities, components) of fiscal metering of gas consumption include: a gas meter, a gas volume corrector (flow computer), pressure and temperature transducers, a measuring pipeline with straight pipe runs before and after the gas meter, communication lines between component parts of the system (complex, node) and auxiliary devices.

From the above list, only the gas meter and the volume corrector (calculator) are sensitive to hydrogen injections. Therefore, the study of the effect of the addition of hydrogen on the metrological characteristics of measuring instruments and systems for the fiscal accounting of natural gas was conducted in the following directions:

- research and evaluation of the possibility of using existing (ultrasonic) gas meters to account for the volumetric flow rate and the volume of the mixture of hydrogen and natural gas;
- learning the influence of hydrogen additives on the results of taking into consideration the volumetric flow rate and the volume reduced to base conditions. Evaluation of the possibility of using existing gas calculators and proofreaders to bring measured volumetric flow rates and mixture volumes to basic conditions;
- studying the influence of hydrogen additives on the heat of combustion of the mixture within the framework of the transition of gas metering systems to energy units.

Estimating the possibility of the use of existing gas meters was carried out only for measuring devices based on ultrasonic technology, whose functioning is based on measuring the propagation time of acoustic waves in the current medium. The main physical parameters of gas that affect the measurement results of meters are its density and acoustic velocity.

Analysis of the simulation results showed that when hydrogen is added to natural gas, the specified parameters change within the permissible limits, at which the metrological characteristics of the meter remain unchanged.

The calculation of the volume of gas in basic conditions on the values of volume in the measurement conditions is performed by the formula:

$$V_b = \frac{T_b \cdot P_m \cdot V_m \cdot Z_m}{T_m \cdot P_b \cdot Z_b} \quad (11)$$

where:  $V_m$  - volume in measurement conditions,  $m^3/h$ ;  
 $T_b$  - temperature at base conditions, K;  
 $T_m$  - temperature in measurement conditions, K;  
 $P_b$  - base pressure, MPa;  
 $P_m$  - measurement pressure, MPa;  
 $Z_b$  - compressibility factor under base conditions;  
 $Z_m$  - compressibility factor under measurement conditions.

The proper reduction of volume (volumetric flow rate) of a mixture of natural gas and hydrogen and the influence of the compressibility factor to the percentage of hydrogen is of great importance.

The simulation results showed a slight change (from 0.01% to 0.1%) of the compressibility factor when hydrogen is added to 23% at atmospheric pressure.

According to ISO 12213-3: 2006 [5], the expected uncertainty of the compressibility factor with hydrogen content up to 10% does not exceed 0.1% for pressures up to 10 MPa and 0.2% for pressures from 10 to 12 MPa.

The evaluation of the changeability of the calculation of compression index factors outside the limits of factors specified in ISO 12213-3: 2006 [5] requires additional calculations and research.

Taking into consideration current trends in the transition of gas metering systems in power plants, i.e., switching to natural gas metering based on its energy value (caloric content), the effect of hydrogen additives on the heat of combustion of the mixture was analyzed.

The results of the analysis of the calculations showed that with the addition of hydrogen up to 10%, the higher heat of combustion of the mixture decreases by about 7%, while the Wobbe index decreases by no more than 3%.

This allows us to conclude about the possibility of adding hydrogen to natural gas in the amount of up to 10% without any modifications of both gas transmission and gas-consuming systems and algorithms for calculating the physical parameters of gas.

### 3. Conclusion

Adding hydrogen to natural gas in a volume of up to 10% allows to operate existing gas-transport and gas-consumption systems without any reconstructions, modifications, changes in algorithms for calculating the physical parameters of the gas mixture and (volume) volumetric flow rate for custody transfer purposes.

Adding hydrogen in the volume of more than 10%, and also, the use of the mixture at high pressures requires additional study and the development of new algorithms.

### References

- [1] Kobza Z., Dobrovolska B., Gontarek J. (Polish Higher Engineering School). Analysis of the impact of the sources of adiabatic index determination on the error in calculating the flow rate.
- [2] AGA REPORT NO. 10, Speed of sound in natural gas and other related hydrocarbon gases
- [3] ISO 6976:1995/Cor. 2:1997, Cor. 3:1999 Natural gas - Calculation of calorific values, density, relative density and Wobbe index from composition
- [4] EN 437:2018 Test gases – Test pressures – Appliance categories
- [5] ISO 12213-3:2006 Natural gas – Calculation of compression factor – Part 3: Calculation using physical properties

# Orifice plate pressure loss ratio: theoretical work in compressible flow and experimental work in CO<sub>2</sub>

M J Reader-Harris<sup>1</sup>, J Barnett<sup>2</sup>, K Mistry<sup>2</sup>

<sup>1</sup> TUV SUD NEL, East Kilbride, Glasgow G75 0QF, UK

<sup>2</sup>National Grid, Solihull, UK

E-mail (corresponding author): [mreader@tuvnel.com](mailto:mreader@tuvnel.com)

## Abstract

An 8" (200 mm) nominal diameter orifice plate assembly with a nominal diameter ratio,  $\beta$ , of 0.4 was tested in gaseous phase carbon dioxide (CO<sub>2</sub>). The assembly had been calibrated in water using the TUV SUD NEL water flow test facilities at East Kilbride in Scotland. The orifice plate assembly incorporated flange tapings, with additional downstream tapings used for measurement of pressure loss ratio.

The test loop was filled with nitrogen, evacuated and then filled with CO<sub>2</sub> up to a pressure of 20 barg giving an estimated composition of 99.6% CO<sub>2</sub> by mol. Testing was carried out at 20 barg and 15 barg with additional test points at 12 barg.

Data on pressure loss ratio was collected from the orifice plate.

A correlation for pressure loss ratio in gas based on theory has been obtained, which deviates from the experimental data by only 0.0008, but further work with different orifice plate diameter ratios, pipe sizes and gases is required to prove the correlation.

## 1. Introduction

The tests were carried out in the TUV SUD NEL gas flow calibration loop. This calibration loop is normally configured for the calibration and testing of dry- and wet-gas flowmeters using nitrogen as the test gas and, for wet-gas testing, water and/or kerosene as the liquid. The loop is constructed to operate at pressures up to 60 barg. Test meters are normally tested using a reference ultrasonic meter which, like all the other instrumentation, is calibrated and traceable to national standards.

## 2. Meter, test installation and instrumentation

### 2.1 NEL Orifice plate meter

An 8" (200 mm) nominal diameter orifice plate meter was tested. The orifice plate had a nominal diameter ratio,  $\beta$ , of 0.4. The orifice diameter was measured, at 20 °C, as 81.011 mm and the pipe internal diameter as 202.56 mm.

The plate and installation were compliant with ISO 51672:2003. Flange tapings were utilised for the

measurements being reported. The test section had 6.5 m ( $> 30 D$ ) of straight unrestricted upstream pipework and 2.5 m ( $13 D$ ) of straight downstream pipework. An additional pressure tapping had been fitted  $6 D$  downstream of the plate to be used for the diagnostic testing.

The orifice and associated pipework had previously been calibrated in water to give a measured discharge coefficient. This measured discharge coefficient provided a correction to the theoretical discharge coefficient at the Reynolds numbers used in gaseous phase CO<sub>2</sub> testing conducted. The calibration data and fitted curve are given in Figure 1, where the Reader-Harris/Gallagher (1998) Equation is shown together with a parallel equation based on the water calibration extrapolated to the Reynolds numbers for this gas test programme:

$$C = 0.59921 + 0.00087 \left( \frac{10^6}{Re_D} \right)^{0.5} \quad (1)$$

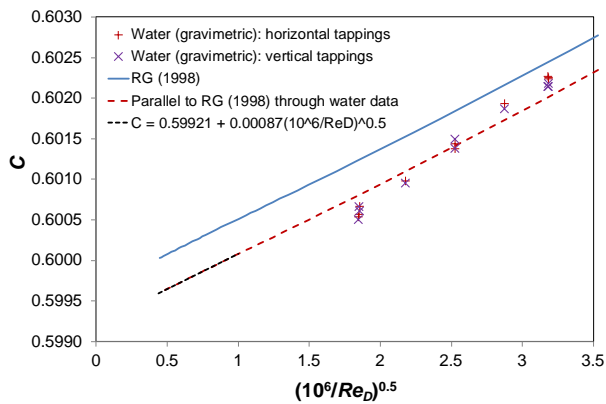


**Figure 1** Discharge coefficient of the  $\beta = 0.4$  orifice plate tested (RG (1998) is the Reader-Harris/Gallagher (1998) equation in 5.3.2.1 of ISO 5167-2:2003)

The flow calibration loop is shown in Figure 2.

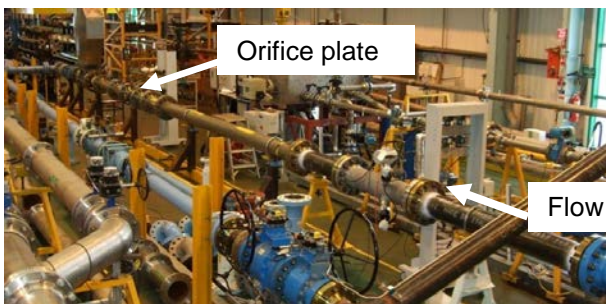


**Figure 2** Installation of the orifice plate meter

## 2.2 Calculations

The properties of  $\text{CO}_2$  were calculated from pressure, temperature and composition using the REFPROP [1] software package, which was verified by comparison with the TUV SUD NEL PPDS (Physical Properties Data Service) [2] properties package (see also Appendix A). For the purposes of the calculations, 100%  $\text{CO}_2$  has been assumed rather than 99.6% concentration: this has a negligible effect on the results presented here.

The primary calculated property is density, which was calculated from the measured pressure, temperature and composition. This allows the calculation of mass flow from the orifice plate readings.

Viscosity, isentropic exponent and Joule-Thomson coefficient were also calculated and used in the orifice plate calculation.

Two additional differential pressure measurements were taken from the orifice plate: pressure loss and pressure recovery.

The orifice meter temperature was measured  $8D$  downstream of the plate, and the Joule-Thomson correction was applied to provide the upstream temperature for the calculated density. The static pressure was measured at the upstream flange tapping.

## 2.3 Filling and operating the Loop

The loop was prepared for  $\text{CO}_2$  following a defined procedure.

Air was diluted and removed by pressurising the rig with nitrogen, circulating and venting to atmosphere. The rig was then evacuated with a nitrogen purge at 100 mbara to remove the last traces of air and water vapour. Finally, the rig was evacuated to a pressure of 60 mbara. The flow calibration loop was then filled with  $\text{CO}_2$  to the required pressure. Subsequently  $\text{CO}_2$  was added or vented to obtain the required pressure for testing.

It was calculated that, using this method, the  $\text{CO}_2$  should have a concentration of approximately 99.6% with nitrogen. This concentration was estimated from the absolute pressure in the flow loop when evacuated, the pressure when filled, the use of REFPROP's equations of state and assuming a constant rig volume and temperature. For flow testing it is not required to estimate the concentrations of other possible minor materials.

Tests were carried out at nominally 20 barg and 15 barg. In addition, an additional test over a limited number of flowrates was carried out at nominally 12 barg.

## 3. Orifice plate pressure loss ratio

### 3.1 Introduction

In any differential pressure flowmeter, the upstream pressure is reduced as the flow passes through the throat of the device, giving a differential pressure which is proportional to the square of the flowrate. The pressure then recovers a proportion of the differential pressure further downstream.

The pressure loss ratio is required for the design of orifice metering systems; the measured pressure loss ratio (see 3.3) is used in the orifice meter validation system developed by Steven of DP Diagnostics [3-7].

### 3.2 Theoretical work

The theory and practical testing in incompressible flow have been explored and reported in [8] and [9]. In compressible flow the pressure loss calculations are slightly different from those in [8] and are given

below. The calculation in incompressible flow was first undertaken by Urner [10].

The momentum theorem is obtained by integrating the equation of motion over a fixed volume so that:

$$\rho \frac{Du_i}{Dt} = \rho F_i + \frac{\partial \sigma_{ij}}{\partial x_j}, \quad (2)$$

where  $\rho$  is the density,  $u_i$  the velocity in the  $x_i$ -direction,  $F_i$  the body force,  $\sigma_{ij}$  the stress tensor and  $D/Dt$  the derivative following the motion of the fluid, becomes, on expanding the derivative following the motion of the fluid and using mass conservation and the divergence theorem,

$$\begin{aligned} \iiint_V \frac{\partial(u_i \rho)}{\partial t} dV &= - \iint_A \rho u_i u_j n_j dA \\ &+ \iiint_V F_i \rho dV + \iint_A \sigma_{ij} n_j dA \end{aligned} \quad (3)$$

where the fixed volume  $V$  is bounded by surface  $A$ .

The stress tensor consists of two terms: the pressure term is sufficient for the approximation here; so  $\sigma_{ij} = -p\delta_{ij}$ . The flow is steady and the body force (gravity) makes a contribution to the pressure that will make no contribution to the pressure loss.

Equation (3) is applied to the volume marked  $V$  on Figure 3.

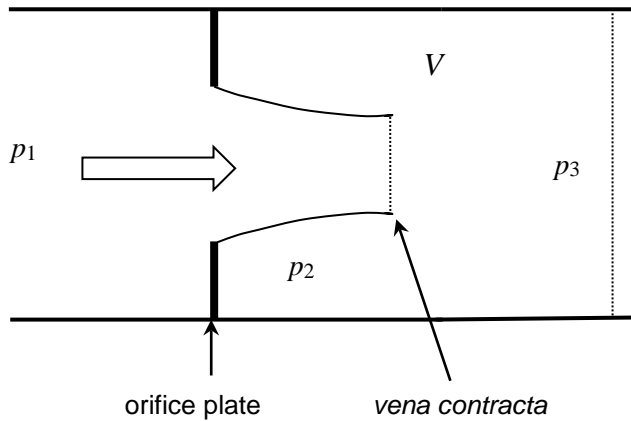


**Figure 3** Flow through an orifice plate

Then, assuming that the pressure has the same value on the back of the orifice plate, on the edge of the orifice jet as far as the *vena contracta* and at the *vena contracta*, and using the divergence theorem:

$$0 = \rho_2 A_c u_c^2 - \rho_3 A_p u_3^2 - p_3 A_p + p_2 A_p \quad (4)$$

where  $A_p$  and  $A_c$  are the area of the pipe and the *vena contracta* respectively,  $u_c$  is the mean velocity at the *vena contracta*,  $p_2$  and  $\rho_2$  are the pressure and density downstream of the orifice plate, and  $p_3$ ,  $\rho_3$  and  $u_3$  are the pressure, density and mean velocity respectively around  $6D$  downstream of the orifice plate.

In practice it would be desirable to include frictional pressure loss. Using the estimate in [9], which corresponds to a loss due to a pipe of length  $4.5\beta D$  of friction factor  $\lambda = 0.0125$ :

$$p_3 = \rho_2 u_c^2 \frac{A_c}{A_p} - \rho_3 u_3^2 + p_2 - 0.05625 \beta \frac{1}{2} \rho_3 u_3^2. \quad (5)$$

The flow is isentropic from a tapping point around  $1D$  upstream to the throat. So:

$$\rho_2 = \rho_1 \left( \frac{p_2}{p_1} \right)^{1/\kappa}, \quad (6)$$

where  $p_1$  and  $\rho_1$  are the pressure and density around  $1D$  upstream of the orifice plate.

Bernoulli's Theorem applies to the isentropic flow between the upstream  $1D$  location and the *vena contracta*. In this case (see, e.g., equation (1.2) of [11]):

$$\frac{\kappa}{\kappa-1} \frac{p_1}{\rho_1} + \frac{1}{2} u_1^2 = \frac{\kappa}{\kappa-1} \frac{p_2}{\rho_2} + \frac{1}{2} u_c^2, \quad (7)$$

where  $u_1$  is the mean velocity around  $1D$  upstream of the orifice plate, and  $\kappa$  is the isentropic exponent.

The orifice discharge-coefficient equation (equation (1) of ISO 5167-2:2003) can be used to determine  $u_1$ :

$$u_1 = \frac{\beta^2 C \varepsilon}{\sqrt{1-\beta^4}} \sqrt{\frac{2(p_1 - p_2)}{\rho_1}}, \quad (8)$$

where  $C$  is the discharge coefficient using tappings  $1D$  upstream and at the location downstream where  $p_2$  is measured, and  $\varepsilon$  is the expansibility factor.

Mass is conserved; so:

$$A_p \rho_1 u_1 = A_c \rho_2 u_c = A_p \rho_3 u_3. \quad (9)$$

Following [9] the downstream pressure location for determination of  $p_2$  (and hence  $C$ ) was taken as  $0.125D$  downstream of the plate (it has to be between the downstream corner and the *vena contracta*). It is now required to solve equations (5) to (9), but, whereas for incompressible flow a closed-form solution was found to the equivalent set of equations, here no closed-form solution was found. Although there is no closed-form solution to the equations, they can be solved by iteration.

In practice tapings are not at  $1D$  upstream and  $0.125D$  downstream of the orifice plate (most commonly flange tapings are used, as they were used for the data collected here); so it is necessary to calculate the difference between  $p_1$  and the pressure at the upstream tapping and between  $p_2$  and the pressure at the downstream tapping using the Reader-Harris/Gallagher (1998) Equation as in [8] and [9]. Then, using equations (5) to (9), the equations for the effect of different tapping locations and physical property data, the predicted values of the pressure loss ratio, using the orifice plate meter, were obtained and are shown in Figure 4. They are about 0.0008 (0.1%) below the measured values.

It is desirable to have an equation for the predicted pressure loss ratio for all gases, diameter ratios and tapping positions. So, although at present only one set of experimental compressible data in one fluid has been obtained, the pressure loss ratio was calculated for the following cases:

- $\beta = 0.2, 0.4, 0.6$  and  $0.75$
- $\Delta p = 50, 100, 200, 500, 1000$  mbar
- $p = 4, 13.3$  and  $22$  bar for  $\text{CO}_2$  and  $p = 4, 15$  and  $60$  bar for nitrogen
- $8''$  (200 mm) flange tapings

After considerable work it was found that these calculated values are fitted by the following equation with a standard deviation of 0.00021:

$$\frac{\Delta \bar{\omega}_{meas}}{\Delta p_{flange}} = \frac{\frac{P_{rise}}{\Delta p_{DandP}} + \frac{\sqrt{1-\beta^4(1-C_{DandP}^2)} - C_{DandP}\beta^2}{\sqrt{1-\beta^4(1-C_{DandP}^2)} + C_{DandP}\beta^2}}{1 + \frac{P_{rise}}{\Delta p_{DandP}} - \frac{\Delta p_{fdowntoP}}{\Delta p_{DandP}}} + \frac{0.05625\beta^5 C_{DandP}^2 \varepsilon^2}{1-\beta^4} + 0.52(1-\varepsilon)\kappa\beta^{2.2} \quad (10a)$$

$$\frac{P_{rise}}{\Delta p_{DandP}} = \frac{2}{C_{DandP}} \frac{14.78}{14.30} (0.123e^{-7L_1} - 0.080e^{-10L_1} - 0.00011) \frac{\beta^4}{1-\beta^4} \quad (10b)$$

$$\frac{\Delta p_{fdowntoP}}{\Delta p_{DandP}} = \frac{2}{C_{DandP}} 0.031 (M'_{2P} - 0.8M'_{2P}{}^{1.1} - (M'_2 - 0.8M'_2{}^{1.1})) \beta^{1.3} \quad (10c)$$

where  $C_{DandP}$  is determined from the Reader-Harris/Gallagher (1998) Equation with  $L_1 = 1$  and  $L_2' = 0.125$ . In equations (10b) and (10c),  $L_1$  and  $M_2'$  are based on the actual tapping positions and  $M_2'_{\text{P}}$  on  $L_2' = 0.125$ . Equation (10) is shown on Figure 4.

Equation (10) is equation (2) of [9] with the addition of the final term in (10a) and the change in the penultimate term in (10a) to account for compressibility. It may be noted that the Joule-Thomson coefficient does not appear in these equations.

Equation (10) was tested by using calculated values with an ideal gas (Joule-Thomson coefficient equal to 0):

- $\beta = 0.2, 0.4, 0.6$  and  $0.75$
- $\Delta p = 50, 100, 200, 500, 1000$  mbar
- $\kappa = 1.2, 1.4$  and  $1.67$
- $p = 4, 13.3, 22$  and  $60$  bar
- $100$  mm,  $200$  mm and  $400$  mm flange tapings

The standard deviation was 0.00024, very similar to the value with the two real gases.

### 3.3 Experimental work

For the testing of the orifice plate in  $\text{CO}_2$  gaseous phase flow, three differential pressures were recorded, and the results analysed. The following three differential pressures were measured:

1. the differential pressure: from the upstream flange tapping to the downstream flange tapping,  $\Delta P$ .
2. the measured pressure loss: from the upstream flange tapping to  $6D$  downstream

of the orifice plate, PL (note that the actual pressure loss may be different).

- the measured pressure recovery from the downstream flange tapping to  $6D$  downstream of the orifice plate, PR.

These three measured differential pressures are used in the orifice meter validation system developed by Steven of DP Diagnostics [3-7].

The measured (apparent) pressure loss ratio, PLR ( $=PL/\Delta P$ ) and the value of PLR deduced from the pressure recovery ( $=1-PR/\Delta P$ ) are shown in Figure 4. Data with PR < 15 mbar are omitted as it was found that the scatter increased for smaller values of PR. Measured values in water [9] are also shown. Equation (2) from [9], the correlation for incompressible flow, is also shown.

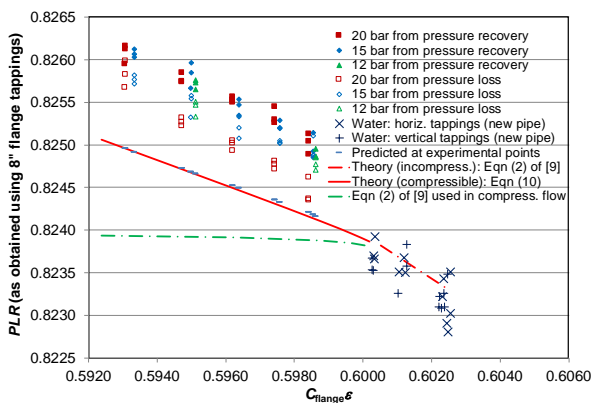


**Figure 4** The measured (apparent) pressure loss ratio for the data collected in CO<sub>2</sub>

Equation (10), the correlation for *PLR* in dry gas derived in Section 3.2, deviates from the set of data that has been obtained by only 0.0008, but further experimental work with different diameter ratios, different pipe diameters and different gases is required to prove the correlation.

#### 4. Conclusions

A correlation for pressure loss ratio in dry gas based on theory has been obtained; it deviates from the experimental data that have been obtained in CO<sub>2</sub> by only 0.0008, but further work with different diameter ratios, different pipe diameters and different gaseous phase compositions is required to prove the correlation.

No difficulties in measuring CO<sub>2</sub> with orifice plates were found.

#### Acknowledgments

This paper is published by permission of the Managing Director, TUV SUD NEL.

The authors are grateful for funding from the Innovation Funding Initiative (IFI) provided by National Grid.

#### References

- LEMMON, E. W., HUBER, M. L., McLINDEN, M. O. NIST Standard Reference Database 23: Reference Fluid Thermodynamic and Transport Properties-REFPROP, Version 9.0. National Institute of Standards and Technology, Standard Reference Data Program, Gaithersburg, 2010.
- PPDS for Windows: NEL, East Kilbride, UK; www.tuvnel.com.
- STEVEN, R. Diagnostic methodologies for generic differential pressure flow meters. *In Proc. 26<sup>th</sup> Int. North Sea Flow Meas. Workshop*, St Andrews. East Kilbride, Glasgow: TUV NEL, October 2008.
- STEVEN, R. Significantly improved capabilities of DP meter diagnostic methodologies. *In Proc. 27<sup>th</sup> Int. North Sea Flow Meas. Workshop*, Norway, October 2009.
- SKELTON, M., AYRE, J., BARRON, S., and STEVEN, R. Developments in the self-diagnostic capabilities of orifice plate meters. *In Proc. 28<sup>th</sup> Int. North Sea Flow Meas. Workshop*, St Andrews. East Kilbride, Glasgow: TUV NEL, October 2010.
- RABONE, J., BRYCE, A., MORRISON, M., VIJAY, D., GLOVER, B., and STEVEN, R. DP meter diagnostic systems – operator experience. *In Proc. 30<sup>th</sup> Int. North Sea Flow Meas. Workshop*, St Andrews. East Kilbride, Glasgow: TUV NEL, October 2012.
- RABONE, J., PEEBLES, R., KIDD, G., SAFONOV, A., and KINNEY, J. Advanced DP meter diagnostics – Developing dynamic pressure field monitoring (and other developments). *In Proc. 32<sup>nd</sup> Int. North Sea Flow Meas. Workshop*, St Andrews. East Kilbride, Glasgow: TUV NEL, October 2014.
- READER-HARRIS, M. J., LEE, W. K., BARNETT, J., and MISTRY, K. Diagnostics and orifice plates: theoretical

- and computational work. In Proc. FLOMEKO 17, Sydney, Australia, September 2016.
- [9] READER-HARRIS, M. J., ADDISON, D., BARNETT, J., and MISTRY, K. Diagnostics and orifice plates: experimental work. In Proc. 34<sup>th</sup> Int. North Sea Flow Meas. Workshop, St Andrews. East Kilbride, Glasgow: TUV NEL, October 2016.
- [10] URNER, G. Pressure loss of orifice plates according to ISO 5167-1. *Flow Measurement and Instrumentation*, **8(1)**: 39-41, 1997.
- [11] READER-HARRIS, M. J. *Orifice plates and Venturi tubes*. Springer, 2015.

## APPENDIX A

### NOTES ON PROPERTIES CALCULATIONS

#### A.1 REFPROP

REFPROP [1] is the properties of fluids software package available from the United States National Institute of Standards and Technology (NIST). For the calculation of properties of CO<sub>2</sub>, CO<sub>2</sub> mixtures and Hydrocarbon mixtures, REFPROP uses the Helmholtz-energy-based equations of state to calculate the properties of the fluids from an input of pressure, temperature and composition. The default for REFPROP is to use the NIST-defined equation coefficients; however, the GERG 2008 industry standard can be selected as an alternative. This uses slightly truncated coefficients. For CO<sub>2</sub> and CO<sub>2</sub> mixtures the differences are insignificant. As the selection of the GERG 2008 implementation is not easy to enable via the Excel interface, the default setting was used for this work.

#### A.2 Joule–Thomson coefficient

As gas passes through a restriction it drops in pressure and hence is subjected to Joule-Thomson cooling. As the density of the gas is required upstream of an orifice plate, and temperature is normally monitored downstream to avoid flow disturbance on the orifice plate, the temperature measured has to be corrected to the upstream condition. This correction is specified in ISO 5167; however it depends on the Joule-Thomson coefficient of the gas. For natural gas the coefficient is around 0.4 K/bar, for nitrogen it is around 0.2 K/bar, but for pure CO<sub>2</sub> it is around 1.2 K/bar, some 3 to 6 times greater.

This means that for CO<sub>2</sub> applications the temperature correction is significantly greater than in other common applications. Although this correction is specified as a standard procedure for natural gas fiscal and custody transfer applications, it is often considered unnecessary to apply the correction elsewhere. It is recommended that this correction is always applied to CO<sub>2</sub> metering applications.

#### A.3 Isentropic exponent

The expansibility factor (or expansion factor) is applied to the equation for flowrate measured through a differential-pressure meter. The equation to calculate expansibility factor is dependent on the isentropic exponent, which is normally designated as  $\kappa$ .

REFPROP provides isentropic exponent as an output. The NEL PPDS, in common with other calculation models, does not. PPDS provides the isentropic compressibility which, when multiplied by the pressure, is the inverse of the isentropic exponent.

Isentropic exponent is commonly believed to be the ratio of specific heats  $C_p/C_v$ , usually designated as  $\gamma$ . This definition can be found in some reference texts. Although this is true for an ideal gas it is not true for a real gas. For some gases at certain pressures the absolute difference between  $\kappa$  and  $\gamma$  may be insignificant. For CO<sub>2</sub> it can be significant, with a difference of 0.25.

Care should be taken in evaluating isentropic exponent correctly for CO<sub>2</sub> applications.

# Wet Gas Performance of Coriolis Meters: Laboratory and the Field Evaluation of a New Method

J. Hollingsworth<sup>1</sup>, D. Morett<sup>1</sup>

<sup>1</sup>Emerson Automation Solutions, 7070 Winchester Cir, Boulder, CO, USA  
E-mail: Justin.Hollingsworth@Emerson.com

## Abstract

The rapid growth in unconventional gas production has brought with it increased demand for a method of measuring flow rates of both gas and liquid at the wellhead that is more cost effective and reliable than traditional methods (i.e. separator or compensated differential pressure), while remaining reasonably accurate. This paper describes research efforts to determine to what degree a single Coriolis meter is capable of measuring gas and liquid flow rates in wet gas processes, without compositional fluid analysis or other inputs beyond readily available process measurements. This research builds on more than 10 years of development in Coriolis multiphase performance, although previous work has largely focused on small amounts of gas in a liquid process. Coriolis meters have the ability to measure multiple relevant variables: mass flow, density, temperature, tube damping (an indicator of phase fraction conditions), and time. By combining these variables with readily available process variables, such as density of liquid and gas, it is possible to make corrections to errors in Coriolis measurements due to multiphase process conditions and calculate the phase fraction, to apportion the overall mass flow to gas and liquid components.

## 1. Introduction

One of the greatest advantages of Coriolis flow meter technology is relative flexibility in specification and installation – generally no flow conditioning needed and high rangeability, and low sensitivity to secondary effects or fluid properties. Certainly, some designs offer a more robust flow measurement than others (a straight tube meter will be affected quite differently than a U-shaped meter to changes in temperature, pressure, viscosity, etc.) but all Coriolis meters, like all flow measurements, are affected by multi-phase conditions. For many years, this meant that Coriolis meters had been limited to strictly single-phase use, but research into the underlying physical behaviour that caused errors, such as decoupling [1] and compressibility of bubbles in a liquid [2], along with improved electronics have enabled new capabilities for Coriolis meters in liquid processes with some bubbles. This understanding of bubbly regimes and meter technology improvements have growth in the understanding and acceptance of Coriolis as a viable technology in limited, liquid-dominant multiphase conditions [3], but current literature tends to identify Coriolis technology as wholly unsuited for wet gas applications [4] [5]. More recent lab testing [6] and field experiences [7] have indicated that the technological improvements in Coriolis meters may provide better performance than indicated in existing industry guidelines and

literature, and a path towards viable wet gas measurement systems with Coriolis meters.

## 2. Coriolis Technology Improvements

With the improved understanding of bubbly two-phase behaviour (some gas in mostly liquid flow) gained from research in the early 2000's, improvements were made to sensor designs with two-phase performance in mind. Modal separation, balance between flow tubes, vibration isolation and minimizing the natural frequency were elements in sensor design improvements.

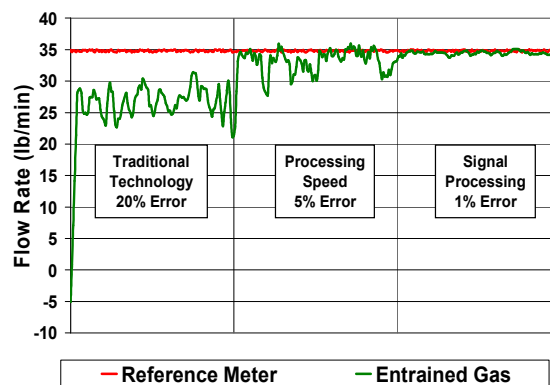


**Figure 1:** Improvements in bubbly two-phase due to electronics development

Faster processing speeds and improvements to signal processing (see Figure 1) and vibration control also made Coriolis technology better suited for service where liquid processes could have some gas phase contamination.

Many of the industry guidelines and best practices precede this development, or were written based on testing meters that had not been optimized for two-phase performance and therefore indicate “Coriolis meters can have an unpredictable behaviour in wet gas conditions but there is current research into their use in this area” [5], but have not yet been updated to reflect further research. The research into wet gas performance discussed in this paper shows that current Coriolis meter technology – the results of efforts in developing Coriolis meters for bubbly two-phase, have more stable and promising wet gas performance characteristics.

Diagnostics for identifying phase contamination were also further developed during this time, and although Coriolis manufacturers developed these primarily with bubbly two-phase conditions in mind, they can be quite sensitive to liquid phase contamination in gas processes [8].

### 3. Common Technology in the Field

#### 3.1 Periodic Separator Testing

The most common method by far of monitoring well performance is periodic testing using a 3-phase separator. The most common form of separator is a tank with one or more weirs that uses gravity and time to separate oil, water and gas. The level of each phase must be controlled to achieve perfect separation efficiency. Wells are diverted to the test separator, which may be mobile or permanently installed, for a period of time and results for that period are averaged to create a single flow rate data point for each phase. A typical testing period and interval would be one day-long test per month. A separator is a simple, easy to understand method of flow rate for each phase.

Separators are often quite large and expensive, especially for high flow rates or emulsions that require long residence times to separate. In order to reduce capital expenditure and footprint, separators are kept as small as possible, but under sizing can cause incomplete separation and measurement errors. The valve and level control systems also require maintenance to avoid cross contamination of phases. The end result is a large, expensive piece of equipment that can require frequent attention and still may not provide desired accuracy.

#### 3.2 Multiphase Flow Meters (MPFMs)

The term MPFM can encompass a wide array of technologies, combining flow meters, densitometers, fluid analysis inputs, and/or partial separation. The MPFM may be one self-contained device, or a small skid with various measurement devices, but the central theme is that they are meant to have much small footprint, less maintenance needs, and lower overall cost.

As attractive as a self-contained multiphase meter measurement can be, multiphase meters represent a significant investment for the average asset in both initial spending and in maintenance (particularly for nuclear based devices) and tend to have higher uncertainties than 3-phase separators. To date, the adoption rate of multiphase measurement has been significantly higher for subsea applications thanks to the greater initial investment and expected rate of return. While partial separation skids can offer reasonable accuracy, these meters often have a narrow operating range and represent a significant footprint and investment.

#### 3.3 Differential Pressure with Correction

Differential pressure is a ubiquitous and relatively straightforward technology for continuously monitoring gas wells. When the process is dry gas, differential pressure can provide an accurate gas flow rate, but when differential pressure is used in wet gas measurement, they have errors (referred to as ‘overread’). This overread is due to the flow measurement now including the liquid, as well as errors in the bulk (gas and liquid combined) flow rate.

The magnitude of these overread errors varies with the amount of liquid, pressure, flow rate, flow regime, etc [9]. There is a large body of empirical data regarding overread in differential pressure measurement of wet gas, which has been used to generate correction algorithms. Single differential pressure meters require an input of Lockhart-Martinelli Parameter for the correction algorithms, but with the addition of a third pressure measurement the meter effectively becomes 3 differential pressure measurements in one, allowing for additional diagnostics and empirical correction algorithms that do not require additional inputs from sampling.

Differential pressure meters are fundamentally simple and compact instruments but require straight runs upstream and downstream that can greatly increase the cost and footprint of installations and in wet gas conditions, they rely heavily on complex

empirical correction algorithms that have a narrow range of applicability that can result in higher than expected errors or even non-convergence (no output) when in operation in the field. With limited diagnostics available, it can be difficult to validate the accuracy of the meter in-situ.

### 3.4 Coriolis Meters

Coriolis meters offer multi-variable measurement, often at a lower installed cost than the technologies mentioned above, since they don't require straight runs or flow conditioning. Coriolis meters can independently measure mass flow rate and density, and some manufacturers have variables that indicate severity of multiphase conditions by monitoring tube damping. There are also diagnostics available that verify the sensor calibration in-situ. With all of this data available in a technology that has been widely accepted as robust and reliably accurate in single phase measurement, it seems there should be potential for viable 2-phase applications.

As it will be shown in this paper, Coriolis meters have the potential to produce accurate measurements on wet gas conditions without the need for laboratory or field calibration on specific wet gas applications or need for correction factors obtained from field test separators or additional equipment.

## 4. Applicable Flow Regimes

When addressing multiphase conditions in a Coriolis meter, it can be helpful to divide the problem into two parts: intermittent, irregular phase contaminations, including slugging flow regimes; and continuous, dispersed phase contamination. This approach is practical because in many applications, the distribution of phase contamination is known and knowing that reduces the complexity of the solution required. In the case of processes that are predominantly single phase (all liquid or all gas – for this paper, consider two-phase to be gas-liquid mix) with intermittent two-phase conditions, such as separators with dump valves or plunger lift wells, using an approach that categorizes data as single phase or two-phase in real time and treats that data as such is an effective way to greatly improve Coriolis volume and liquid measurement performance [10].

### 4.1 Intermittent Two-Phase Detection and Remediation

Performance of Coriolis meters in two-phase flow is not necessarily limited by the improvements discussed in section 2. Correction techniques can

be applied to improve their performance in limited two-phase applications. The first step in remediating gas measurement errors in two-phase conditions is identifying when single-phase and two-phase conditions occur within the sensor. With the sensitivity to detection of two-phase conditions, the correction algorithm can use real-time data validation to employ different methods for single-phase conditions, intermittent two-phase (slugging), and continuous two-phase. Additionally, diagnostic and trending information can be derived from the meter to help customers better understand their application.

### 4.2 Improving gas measurement

Similar techniques to those used to detect entrained gas in a liquid process can be used to detect liquid mist in a gas process, with certain Coriolis sensor designs. Testing at Southwest Research Institute [8] shows drive gain in Coriolis meters with a large "U" shaped geometry are very sensitive to even small amounts of liquid.

Figure 2 shows that with as little as 0.013% liquid by volume, drive gain is a clear and immediate indicator in one Coriolis meter but does not register with the other.

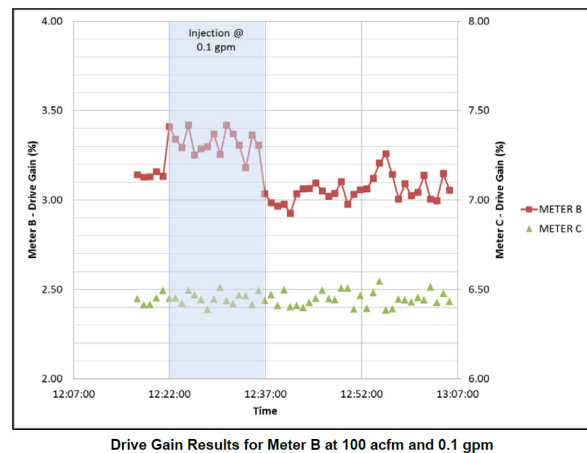


**Figure 2:** Drive gain response, 0.013% liquid

Once liquid is detected, the algorithm described below can be used to remediate gas flow rate measurement. Equation 1 showed that it is very easy for the mass flow rate of liquid to overshadow the mass flow rate of gas:

**Equation 1**

$$\dot{M}_{mixture} = \dot{M}_{liquid} + \dot{M}_{gas}$$

$$\dot{M}_{gas} \ll \dot{M}_{liquid}$$

$$\dot{M}_{mixture} \sim \dot{M}_{liquid}$$

In a gas process, this is detrimental to the measurement, since the desired output is often gas volume at standard pressure and temperature, which is simply:

**Equation 2**

$$\dot{V}_s = \dot{m} \cdot \rho_s$$

where  $\dot{V}_s$  is the volume rate flow at standard condition,  $\dot{m}$  is the mass flow rate at line conditions, and  $\rho_s$  is the density of the gas at standard conditions. The standard density of the gas is constant, provided the gas composition doesn't change, so mass flow rate is the critical measurement for gas processes.

To avoid the large errors in gas mass flow measurement that would be incurred by measuring liquid as well (often called "overread"), when two-phase conditions are detected by increases in drive gain, the mass flow rate from a few seconds before the two-phase conditions can be substituted for the bulk measurement, until the process returns to single phase gas. If the mass flow rate of the dry gas before and after the wet gas period is different, then a small adjustment can be made (see G in Figure 3) to the flow rate, so that the total will reflect a linear change in dry gas flow rate during the two-phase period, rather than a step change as the process transitions back to single-phase gas.

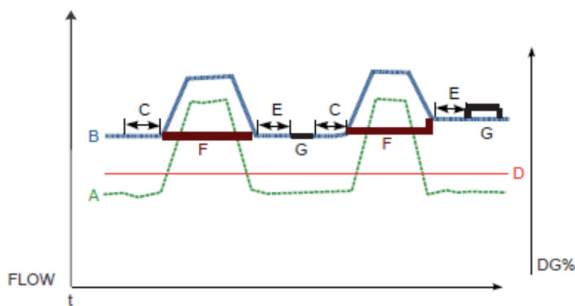


**Figure 3:** Gas remediation method for intermittent two-phase flow

In Figure 3, the letters represent the following:

- A – Drive Gain
- B – Bulk Mass Flow Rate
- C – Pre-Mist averaging of flow rate
- D – Drive Gain Threshold
- E – Post-Mist Delay
- F – Held Mass Flow Rate
- G – Post-Mist Adjustment

For the algorithm to work properly, the process should have a flow regime that has periods of single-phase gas and periods of two-phase or wet gas conditions. These conditions were created in the 4-inch wet gas test facility at Colorado Experiment Engineering Station, Inc (CEESI) [11] by installing a liquid injection point directly upstream of the meter, so that the flow regime could quickly transition from dry to wet and back to dry. Test points consisted of a dry period, a two-phase test point and followed by another dry period. Data points represent a 2-minute average of the two-phase test point. Gas flow rate error falls largely between 0% and -2%, regardless of pressure. This contrasts quite starkly with the gas 'overread' if the standard mass flow output is used. Since the algorithm detects and ignores liquid in the process, much of the 'overread' can be avoided.

**4.2 Continuous Two-Phase Detection and Remediation**

When the process condition consists of continuous wet gas conditions, a new challenge consists on the ability of the Coriolis meter to quantify the liquid to gas ratio first, and then to correct the overall mass flow error without periods of dry gas conditions to allow adjustments. The latest advances in Coriolis technology allows for more repeatable and reproducible behavior on wet gas conditions which in turn allows for the characterization of 'overreading' which can be corrected with empirical methods, with similar success as current dP meters, but with the benefit of having additional variables or sensor responses available from a Coriolis meter to correlate liquid loading.

Some Coriolis users are already successfully using this technique in the field. Figure 4 shows condensate/gas ratio (CGR) versus measured density from 5 meters with large "U" shape, in a field in Qatar [7]. The liquid/gas ratio can be calculated directly from the density measurement, using input densities of gas and liquid phases. Errors in density measurement from decoupling will cause a negative bias, but since it is expected for there to be well test data when a well is brought on line, the density

measurement from the Coriolis meter can be correlated to the liquid/gas ratio from well testing to give a repeatable and reasonably accurate indication of liquid flow rate and a way to correct the bulk rate to reflect the dry gas flow rate.

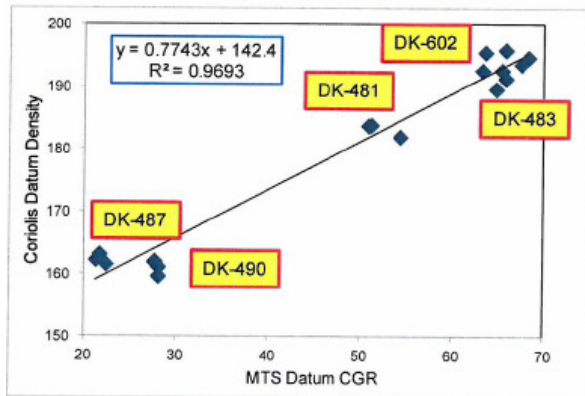


**Figure 4:** CGR vs Measured Density

With the understanding of liquid content gained by using the density measurement and input from a pressure measurement, there are two methods to obtain a separate liquid and gas output from a single Coriolis meter, which can operate simultaneously. Having an indication of the wetness of the process also provides a basis for flow measurement correction that responds to changing conditions in real time, without the need for additional sampling.

There is an ongoing research program by the authors to develop a more robust model based on the wet gas physics that would allow for digital processing of the sensor behavior in a similar fashion as previous work on decoupling for small amounts of gas in liquid phase [1].

Using this previous knowledge on entrained gas model it can be inferred that decoupling in wet gas conditions causes some of the liquid or gas mass in the tubes to move so that it is undetected by the flow meter. The further the particles decouple from the carrier fluid on each oscillation of the tubes (i.e. greater particle amplitude to fluid amplitude ratio), the larger the undetected mass of fluid will be and the larger the resulting flow error. The wet gas physical model will build from and complement the current entrained gas theory.

### 5. A New Method

Recent advances in wet gas metering using Coriolis meters have resulted in better prediction of liquid loading and flow measurement deviation from dry gas. A new method that relies on multivariable

analysis correlations can produce wet gas measurements in the order of +/- 5% flow overreading with respect to dry gas. This improved accuracy is significant considering the unremediated overreading can be as high as 400% with respect to dry gas.

The new method was tested using an Emerson Micro Motion CMF300 meter at CEESI [11] with natural gas at 25 and 50 bar (absolute pressure) and Exxol D80 at different oil loadings. The meter was initially tested on dry gas conditions producing the mass flow error curve shown in Figure 5.

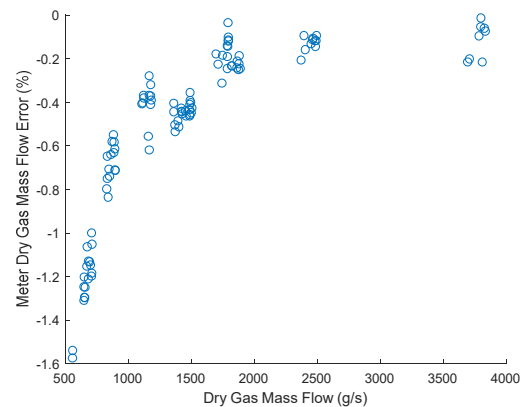


**Figure 5:** Dry gas performance of CMF300 at 25 and 50 bar

As shown in Figure 6, there is a linear correlation between dry gas overreading as a function of the Lockhart-Martinelli parameter. This dry gas overreading corresponds to the unremediated or total mass flow rate measured by a CMF300 on wet gas conditions at 25 and 50 bar. The new method can then correct the meter's mass flow and predict dry gas mass flow within 5% error.

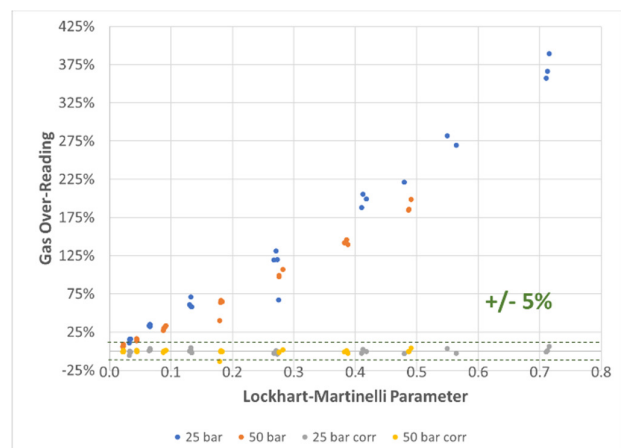


**Figure 6:** Unremediated and corrected dry gas overreading from CMF300 mass flow measurement on wet gas conditions

This is a significant achievement considering the dry gas performance of the meter itself is within 1.6% error and the corrected performance is linear on a wide range of wet gas conditions including multi-phase region where the Lockhart-Martinelli parameter is greater than 0.3.

The correction factors from this new method are obtained using direct measurements from the Coriolis meter and it doesn't rely on the Lockhart-Martinelli parameter. This allows for direct wet gas measurements using a single Coriolis meter without the need for periodic measurements of liquid loading as other instruments rely on for corrections. Additionally, the total mass flow rate output can be corrected for decoupling errors and separated into individual gas and liquid flow rate outputs.

Figure 7 and Figure 8 show additional wet gas data on a CMF100 from a new research pilot unit at one of Micro Motion's experimental facilities. The wet gas research program has provided valuable information on the physics behind the wet gas conditions and the behaviour of Coriolis meters with the ultimate goal of developing digital processing technique that enables higher accuracy on wet gas conditions based on physical models.

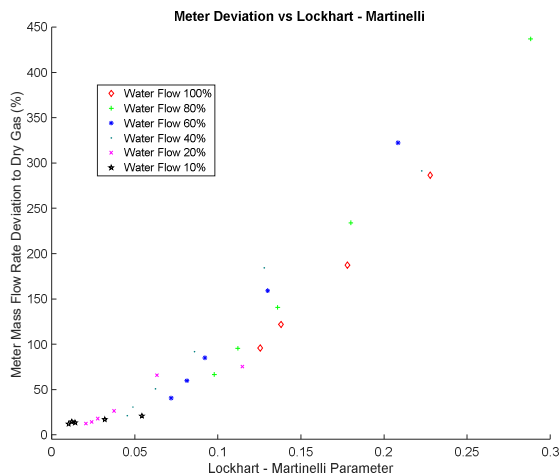


**Figure 7:** CMF100 overreading as a function of Lockhart-Martinelli parameter and water flow rate

Figure 7 shows the meter mass flow deviation (or overreading) at different Lockhart-Martinelli values within the wet gas region (lower than 0.3). As the percent of liquid flow varied there seems to be a linear response with Lockhart-Martinelli parameter. The water flow percent indicates the amount of liquid flowrate that was kept constant for various gas

flow rates, and the percentage indicates the different liquid flow points on the test matrix.

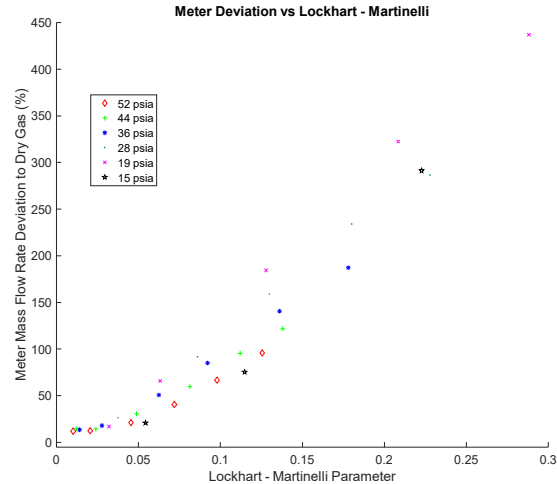


**Figure 8:** CMF100 overreading as a function of Lockhart-Martinelli parameter and pressure

Figure 8 shows the meter response at different line pressures, this data was obtained from the same test matrix as Figure 7 and it shows a dependency to pressure and Lockhart-Martinelli parameter.

Additional to the data presented, the wet gas research station at Micro Motion allows for inexpensive testing with the flexibility for testing different meter designs and it includes flow visualization ports that facilitates the physical model development.

## 6. Conclusions

The perception that all coriolis meters are unpredictable in wet gas conditions should be updated with further research, using meters that have been designed to handle multiphase conditions. There are several methods that could be used to drive further improvements in performance. Each approach has application spaces that they can work in. As the methods are developed, it is critical to understand the limitations and appropriate operating envelope.

## References

- [1] J. Weinstein, "The motion of bubbles and particles in oscillating liquids with applications to multiphase flow in Coriolis meters," 2008.
- [2] J. Hemp and J. Kutin, "Theory of errors in Coriolis flowmeter readings due to compressibility of the fluid being metered,"

*Flow Measurement and Instrumentation*, vol. 17, no. 6, pp. 359-369, 2006.

- [3] American Petroleum Institute, "Manual of Petroleum Measurement Standards Chapter 20.2: Production Allocation Measurement Using Single-phase Devices," API Publishing Services, Washington, DC, 2016.
- [4] "Wet Gas Flowmetering Guideline," New York, 2008.
- [5] D. G. Stewart, "The Evaluation of Dry Gas Meters in Wet Gas Conditions," TÜV NEL Ltd, East Kilbride, 2002.
- [6] R. Steven and J. Kinney, "Coriolis Meters & Wet Gas Service," in *South East Asia Flow Measurement Conference*, Kuala Lumpur, 2017.
- [7] O. Salama and M. C. Chandramohan, "Coriolis well head measurement - Alternative to traditional well testing," in *Emerson Global Users Exchange*, 2013.
- [8] A. G. Hawley and J. L. Thorson, "Turbine and Coriolis Meter Diagnostics with Entrained Liquids," Southwest Research Institute, San Antonio, Texas, USA, 2015.
- [9] TÜV SÜD NEL, "Good Practice Guide: An Introduction to Wet-Gas Flow Metering," The National Measurement System.
- [10] J. C. Hollingsworth, "A Method for Identifying and Reducing Errors in Wet Gas Measurement with Coriolis Meters," in *Canadian School of Hydrocarbon Measurement*, Calgary, 2017.
- [11] R. Steven, E. Harman and J. Kinney, "Wet Natural Gas Flow Test of Vertically Installed 3" Coriolis Meter," Colorado Engineering Experiment Station Inc. , Nunn, CO, 2018.
- [12] H. Zhu, A. Rieder and Y. Lin, "An Innovative Technology for Coriolis Metering under Entrained Gas Condition," in *Flomeko International Flow Measurement Conference*, Sydney, 2016.

# The bilateral comparison between NIM and PTB for small gas flow

Chunhui Li<sup>1</sup>, Bodo Mickan<sup>2</sup>, Shan Gao<sup>3</sup>

<sup>1</sup>NIM, No.18 Beisanhuan Donglu, Beijing, China

<sup>2</sup>PTB, Braunschweig, Germany

<sup>3</sup>Hebei University, Baoding, China

E-mail: lich@nim.ac.cn

---

## Abstract

With the development in the field of biomedicine, environmental monitoring, and so on, the requirement on the accuracy of small gas flow measurement is dramatically increased, which results in the increasing requirement on the accuracy of small gas flow facility. In NIM, the 100L pVTt facility was developed for small gas flow rate, which was built in 2010. But, the leakage and the big mass change in the inventory volume showed significant impact on the accuracy of the facility, especially for small gas flow rate, which was solved at the end of 2017. The uncertainty of the discharge coefficient for the sonic nozzle could be 0.15% ( $k=2$ ) when the flow rate is larger than 0.1 m<sup>3</sup>/h, while it could be 0.25% ( $k=2$ ) for smaller flow rate. The bilateral comparison between NIM and PTB for small gas flow rate was carried out with 4 sonic nozzles with flow rate 0.02 m<sup>3</sup>/h, 0.04 m<sup>3</sup>/h, 0.13 m<sup>3</sup>/h, 0.50 m<sup>3</sup>/h, and pressure range (85~1000) kPa. On the base of the good consistency of the comparison results, the uncertainty and the measurement capability of the 100 L pVTt facility were verified.

---

## 1. Introduction

With the development of biology medicine and environment monitoring, the accuracy requirement was significantly increased for small gas flow. For example, the uncertainty should be smaller than 0.65% ( $k=2$ ) for the gas sampler in the environment monitoring. In general, the small gas meter is traceable small gas flow facility. So, the accuracy of the small gas flow facility is the key parameter to guarantee the accuracy of the gas flow meter.

The piston prover [1~3] was widely used in many NIMs as the primary standard, especially for small rate. The double piston prover was used to achieve the smallest flowrate (0.005-5) L/h with the uncertainty of 0.05% ( $k=2$ ) in PTB [2], which can be used to calibrate sonic nozzle, laminar flowmeter, mass flowmeter and so on. The piston was driven by step motor for the double piston prover, which was typically called passive type piston prover. The piston prover was utilized in KRISS [3] for the smallest flowrate (0.002-20) L/min with the uncertainty of 0.11% ( $k=2$ ). The piston was driven by the working medium, which was typically called active type piston prover.

In 2005, Nakao et al [4] built the small pVTt facility in NMIJ. The minimum flowrate could be 0.01 mg/min with the uncertainty of 0.21% ( $k=2$ ). Berg et

al [5] presented the similar pVTt facility. The flow range could be (0.1 mL/min ~ 1 L/min) with uncertainty of 0.05% ( $k=2$ ).

Since 1986, the pVTt facility with collection tank of 2 m<sup>3</sup> and 20 m<sup>3</sup> in NIM had been as the national primary standard in China. The working medium is the humid air with the atmospheric pressure. At the end of 2014, the new pVTt facility with collection tank of 100 L and 2 m<sup>3</sup> was built in NIM. The working medium is the dry air with the pressure range of (0.1~2.5) MPa. The capability of the new pVTt facility with collection tank 2 m<sup>3</sup> was verified with the comparison among PTB, LNE, NIST and NIM [6].

The technical improvement for the new pVTt facility with the collection tank of 100 L was made, especially for the leakage control and evaluation, the mass cancellation in the inventory volume. From 2017 to 2018, the comparison between PTB and NIM was conducted to verify the capability of the facility.

## 2. The technical improvement for 100 L pVTt facility in NIM

### 2.1 The structure of pVTt facility

There are two compressors with dryer and filter to produce the high pressure dry air. The dry air from the compressors is saved in the buffer tank. There

are two stages of buffer tank. The first stage buffer tank is consisted with 2 tanks with the volume of 10 m<sup>3</sup> individually, and the second stage buffer tank is consisted with 2 tanks with the volume of 7.5 m<sup>3</sup>

individually. The maximum pressure in the first stage buffer tank is 10 MPa, while it is 5 MPa in the second stage.

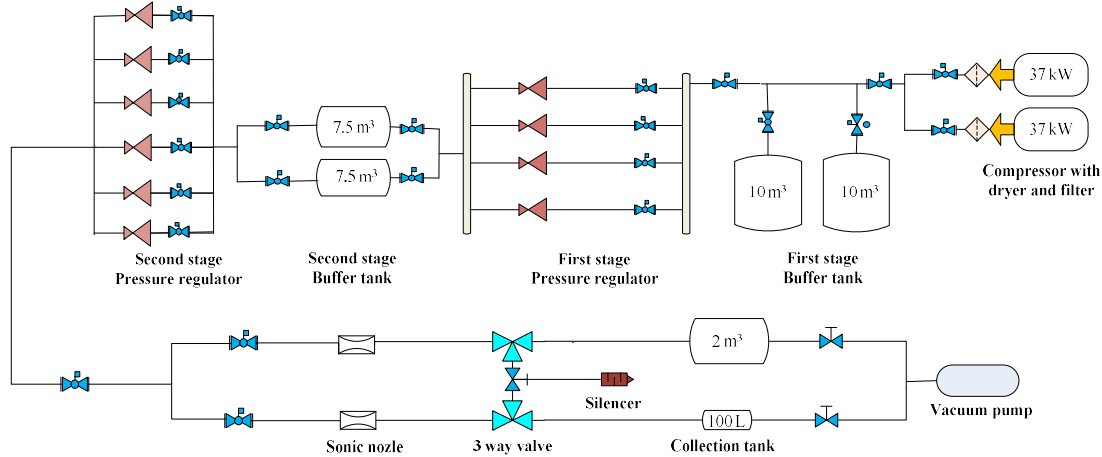


**Figure 1** the systematic diagram of pVTt facility

In general, the flowrate measured by the pVTt facility could be expressed [7],

$$q_m = \frac{\Delta m}{t} \quad (1)$$

where  $q_m$  is the flowrate measured by the pVTt facility;  $\Delta m$  is the mass change measured by the density change in the collection tank;  $t$  is the test time.

In reality, the leak and the mass change in the inventory volume directly influence the flowrate, furthermore, Equ.(1) could be expressed as,

$$q_m = \frac{\Delta m + m_{leak} + \Delta m_{inv}}{t} = \frac{\Delta m}{t} \left( 1 + \frac{m_{leak}}{\Delta m} + \frac{\Delta m_{inv}}{\Delta m} \right) \quad (2)$$

where  $\Delta m_{leak}$  is the total leak during the measurement process;  $\Delta m_{inv}$  is the mass change in the inventory volume during the measurement process.

So, the uncertainty of the pVTt facility can be expressed as

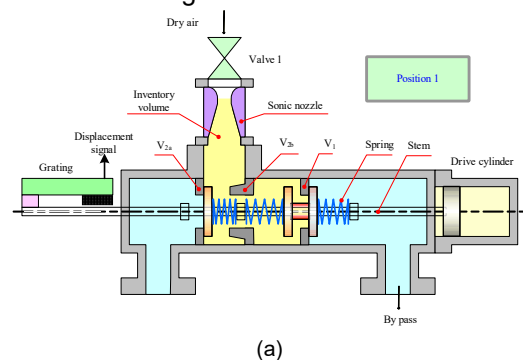
$$u_r(q_m) = \left\{ \begin{aligned} & \left[ \frac{1}{1 + \frac{m_{leak}}{\Delta m} + \frac{\Delta m_{inv}}{\Delta m}} u_r(\Delta m) \right]^2 \\ & + \left[ \frac{\frac{m_{leak}}{\Delta m}}{1 + \frac{m_{leak}}{\Delta m} + \frac{\Delta m_{inv}}{\Delta m}} u_r(m_{leak}) \right]^2 \\ & + \left[ \frac{\frac{\Delta m_{inv}}{\Delta m}}{1 + \frac{m_{leak}}{\Delta m} + \frac{\Delta m_{inv}}{\Delta m}} u_r(\Delta m_{inv}) \right]^2 + u_r(t)^2 \end{aligned} \right\}^{0.5} \quad (3)$$

To improve the uncertainty of the pVTt facility, it is required to minimize the effect of leak and mass change inventory volume.

### 2.2 The leakage control and evaluation

In the pVTt facility, the special designed 3 way valve was developed. The basic structure of the 3 way valve was show in Figure.1. There are three independent sealing positions.

- **Position 1:** the sealing is in the position  $V_{2a}$ , and the dry air flow through by pass. This position is the original condition for pVTt facility.
- **Position 2:** the sealing is in the position  $V_{2a}$  and the positon  $V_1$ , and the dry air flow in the inventory volume. This position is the condition, where the timer was switched on and off.
- **Position 3:** the sealing is in the position  $V_1$ , and the dry air flow through the collection tank. This position is the condition, where the collection tank was filling.



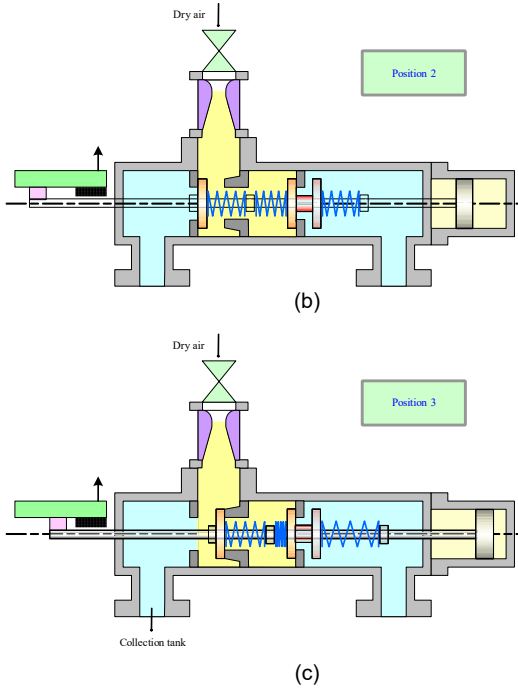


Figure 2 the systemic diagram of 3 way valve

During the test process, the leak could happen in Position 1 and Position 2, so, the total leak can be consisted of two parts

$$m_{leak} = m_{leak,1} + m_{leak,2} \quad (4)$$

Where,  $m_{leak,1}$  is the leak coming from the filling process;  $m_{leak,2}$  is the leak coming from the waiting process after filling process.

When the temperature is assumed stable, Equ. (4) can be simplified as,

$$m_{leak} = V(\Delta p_{leak,1} + \Delta p_{leak,2}) \frac{M}{R_u T Z} \quad (5)$$

Where,  $V$  is the volume of the collection tank;  $\Delta p_{leak,1}$  is the pressure change during the filling process due to leak;  $\Delta p_{leak,2}$  is the pressure change during the waiting process after the filling process due to leak;

Furthermore,  $\Delta p_{leak,1}$  could be expressed as,

$$\Delta p_{leak,1} = \frac{t_{filling}}{p_f - p_i} \int_{p_i}^{p_f} \Delta p_{leak}(p) dp \quad (6)$$

$\Delta p_{leak,2}$  could be expressed as,

$$\Delta p_{leak,2} = \Delta p_{leak,p_f} t_{wait} \quad (7)$$

The pressure change at different pressure in the collection tank was measured, on the base of which the curve fitting was made to compensate the leak effect for 100 L pVTt facility. The test result for the leak during the filling was shown in Figure 3.

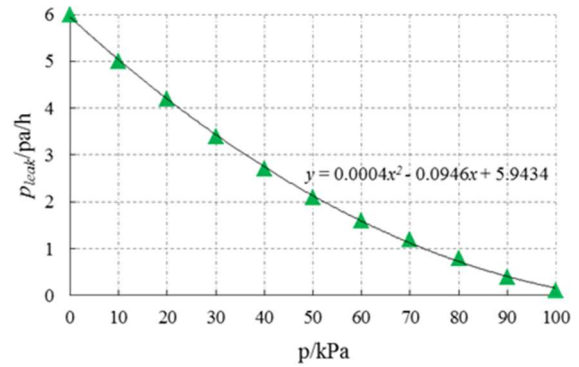


Figure 3 the leak measure during the filling

### 2.3 The mass cancellation in the inventory volume

During the opening and closing of the 3 way valve, the position of the stem was measured by the displacement signal from the grating with the resolution of 20  $\mu$ m. At the same time, the pressure with high speed in the inventory volume was measured and recorded with frequency above 5000 Hz.

For different flowrate, the typical pressure change in the inventory volume was shown in Figure 4.

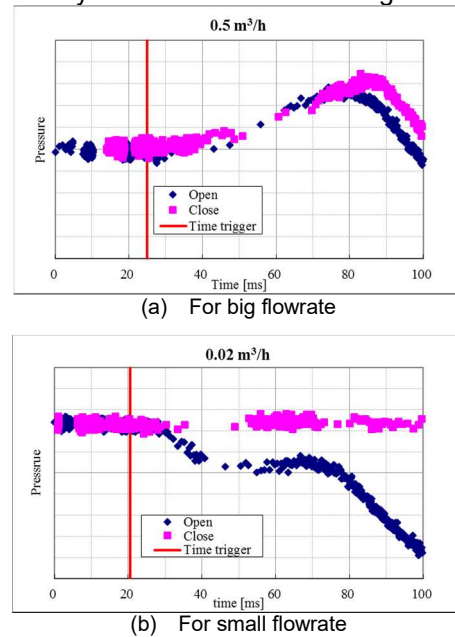


Figure 4 the pressure change in the inventory volume during filling process

It was clear that

- For large flowrate, the pressure overlap occurred, so the time correction almost could be neglected, and the mass cancellation could be achieved [8].
- For small flowrate, there was no obviously pressure overlap, the time correction was determined by the geometrical parameter of

the valve, which was consistent with the number of the signal.

### 3. Comparison results and analyses

With the technical improvement of the 100 L pVTt facility, the uncertainty of the discharge coefficient for the sonic nozzle was 0.15% ( $k=2$ ) when the flow rate was larger than 0.1 m<sup>3</sup>/h, while it was 0.25% ( $k=2$ ) for smaller flow rate.

To verify the capability of the 100 L pVTt facility, the bilateral comparison was conducted between NIM and PTB from 2017 to 2018.

According to the flowrate, the small sonic nozzle facility and two other gas facilities were used in PTB. The uncertainty of the discharge coefficient was 0.10% ( $k=2$ ) when the flowrate is bigger than 0.1 m<sup>3</sup>/h, which was 0.15% ( $k=2$ ) for smaller flowrate.

Due the high accuracy and long term stability, the critical flow Venturi nozzle (CFVN) was chosen as the transfer meter in this comparison [9]. The information on the CFVNs was shown in Table 1.

**Table 1** the information on the comparison

SN	Nominal flowrate [m <sup>3</sup> /h]	NIM [kPa]	PTB [kPa]
625	0.5	200~1000	85~230
623	0.13		
03574_320	0.04	85~230	
03575_250	0.02		

- The SN.625 and SN.623 were the transfer standards in NIM, which were calibrated in NIM in July, 2018. Then, they were calibrated in PTB in August, 2018.
- The SN.03574\_320 and SN.03575\_250 were the transfer meters in PTB, which were calibrated in PTB twice in March, 2017. Then, they were calibrated in NIM in November, 2018.

All the comparison data were shown in Figure 5.

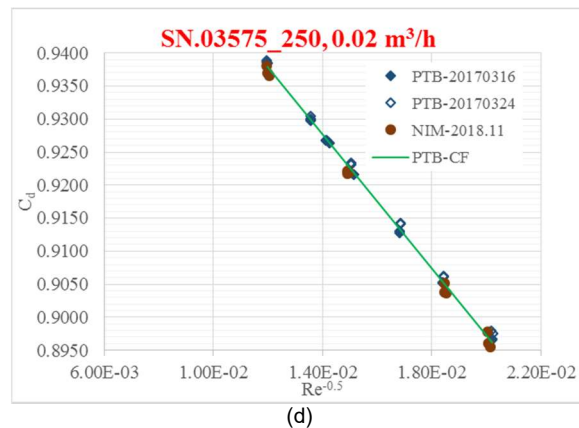
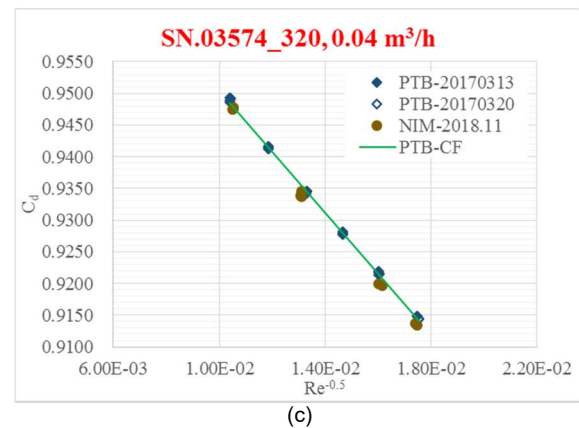
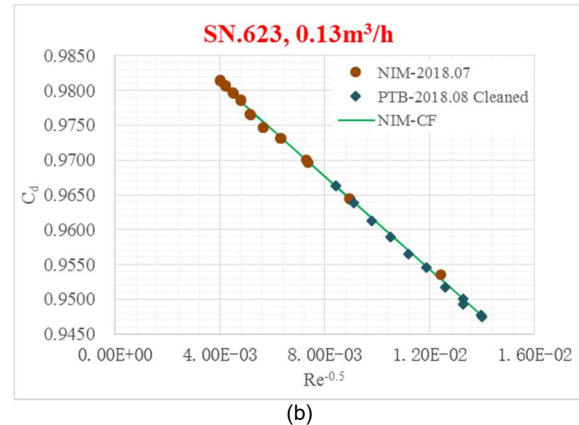
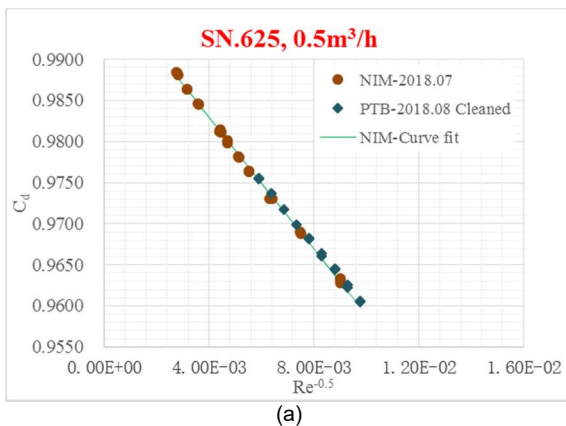


**Figure 5** the comparison results

The curve fitting was made to analyse the consistent of the result. For this comparison, the flow was within laminar region, the curve fitting was expressed as,

$$C_{d,CF} = a - \frac{b}{\sqrt{Re}} \quad (8)$$

- For the results of the SN.625 and SN.623, the curve fitting was based on the result of NIM.
- For the results of the SN.03574\_320 and SN.03575\_250, the curve fitting was based on the result of PTB.

The  $E_n$  value [10~11] was used to evaluate the result,

$$E_n = \frac{|C_{d,CF} - C_{d,NMI}|}{\sqrt{U_{NIM}^2 + U_{PTB}^2 + U_{CF}^2}} \quad (10)$$

where  $C_{d,CF}$  is the discharge coefficient was calculated according to the curve fitting, at the same Reynolds number,  $C_{d,NMI}$ . Due to the curve fitting, the additional curve fitting uncertainty,  $U_{CF}$ , which was evaluated by the residual between the test data and the curve fitting results.

$$U_{CF} = 2\sqrt{\frac{(C_{d,CF} - C_d)^2}{N - 2}} \quad (11)$$

The comparison results analyses were shown in Table 2.

**Table 2** the comparison results analyses

SN	$U_{NIM}$ , %	$U_{PTB}$ , %	$U_{CF}$ , %	$E_n$
625	0.15	0.10	0.06	0.07~0.47
623	0.15	0.10	0.09	0.02~0.34
03574_320	0.25	0.15	0.07	0.01~0.18
03575_250	0.25	0.15	0.13	0.02~0.38

The detailed value for each CFVN was shown in Figure 6.

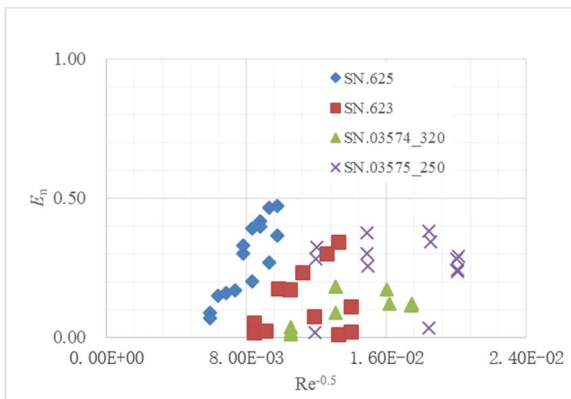


**Figure 6** the  $E_n$  value for this comparison

With the combination of Table 2 and Figure 5, all the  $E_n$  value was smaller than 1, which meant the uncertainty of the 100 L pVTt facility was verified.

#### 4. Conclusion and discussion

For the 100 L pVTt facility, the leak evaluation and mass evaluation in the inventory volume were analyzed and qualified in this paper. The uncertainty of the discharge coefficient for the sonic nozzle was 0.15% ( $k=2$ ) when the flow rate was larger than 0.1 m<sup>3</sup>/h, while it was 0.25% ( $k=2$ ) for smaller flow rate. With 4 CFVNs as the transfer meter, the bilateral comparison were conducted to verify the uncertainty of 100 L pVTt facility. On the base of the good consistency of the comparison results, the

uncertainty and the measurement capability of the 100 L pVTt facility were verified.

During this comparison, the maximum diameter was about 1 mm. The surface quality took significant effect on the test result.

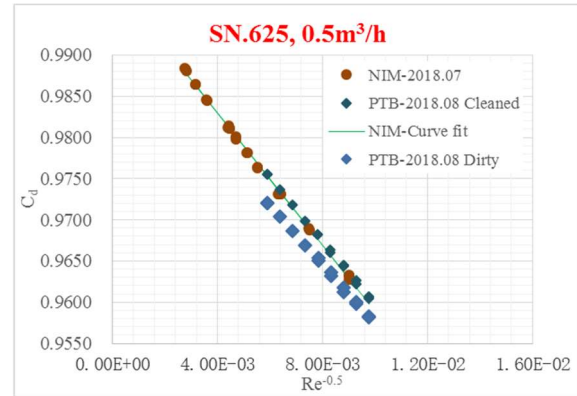


**Figure 7** the surface quality effect

As shown in Figure 7, the change of the discharge coefficient could be larger than 0.3% for the same sonic nozzle with different surface quality, which was larger than the uncertainty of the test results.

The surface quality could be qualified with microscope as shown in Figure 8.

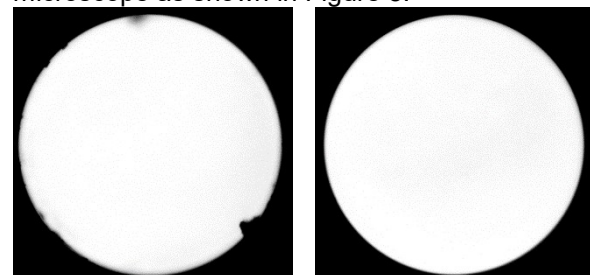


**Figure 8** the surface quality

It was clear that there was dust near to the throat, which affected the results very much. So, the clean of CFVN was necessary, especially for small size. In this comparison, the CFVNs were clean with ultrasonic bath before the test.

**Acknowledge:** this work is supported by The National Key Research and Development Program of China “Research and application of national quality infrastructure” (project/subject SN. 2017YFF0205305)

#### References

- [1] Ruis V, Hernandez, “Uncertainty Analysis in Piston Prover Calibration”, FLOMEKO, 2000.
- [2] Kramar R, Mickan B, Dopheide D, “Double piston prover usable as flowrate comparator for various gases”, Metrology for a Sustainable Development, 2006.

- [3] Choi H M, Park K A, Oh Y K, et al, "Improvement and uncertainty evaluation of mercury sealed piston prover using laser interferometer", *Flow Measurement and Instrumentation*, 20(4-5): 200-5, 2009.
- [4] Nakao S, "Development of the pVTt System for Very Low Gas Flow Rates", *Flow Measurement and Instrumentation*, 17(3): 193-200, 2006.
- [5] Berg R F, Tison S A. "Two Primary Standards for Low Flows of Gases", *Journal of Research of the National Institute of Standards and Technology*, 109 (4): 435-450, 2004.
- [6] Mickan B, Jean-Pierre Vallet, Li C H, J. Wright, "Extended data analysis of bilateral comparisons with air and natural gas up to 5 MPa", *Flomeko*, Sydney, 2016.
- [7] Wright J D, Johnson A N, "Design and Uncertainty Analysis for a PVTt Gas Flow Standard", *Journal of Research of the National Institute of Standards and Technology*, 108 (1):21-47, 2003.
- [8] Li C H, Cui L S, Wang C, "The uncertainty analysis and capability verification for the high pressure pVTt gas flow facility of NIM", *Flomeko*, Sydney, 2016.
- [9] Wright J D, "What is the "best" transfer standard for gas flow", *Flomeko*, 2003.
- [10] Cox M G, "Evaluation of key comparison data", *Metrologia*, 39: 589-595, 2002.
- [11] Cox M G, "The evaluation of key comparison data: determining the largest consistent subset", *Metrologia*, 44:187-200, 2007.

# The high pressure sonic nozzle gas flow standard facility in NIM

Chunhui Li<sup>1</sup>, Bodo Mickan<sup>2</sup>, Lishui Cui<sup>1</sup> and Chi Wang<sup>1</sup>

<sup>1</sup>NIM, No.18 Beisanhuan Donglu, Beijing, China

<sup>2</sup>PTB, Braunschweig, Germany

E-mail (corresponding author): lich@nim.ac.cn

---

## Abstract

The high pressure sonic nozzle gas flow facility in China was built in NIM at the end of 2014. There were 16 sonic nozzles used as the reference meters in the facility. The flow range is within (2~400) m<sup>3</sup>/h, while the pressure range is within the (190~2500) kPa. The sonic nozzles were traceable to the pVTt primary standard facility in NIM. To cover the pressure range, the curve fitting between discharge coefficient and Reynolds number was made for each sonic nozzle. To decrease pressure measurement uncertainty, there is an absolute pressure instrument in the manifold in the upstream of the MUT. The expanded uncertainty of meter factor for meter under test (MUT) is 0.15% ( $k=2$ ). To verify the uncertainty of the sonic nozzle facility, a comparison between NIM and PTB was made with three Dn 100 turbine meters as transfer meters. The three turbine meters were calibrated by PTB in 2013 with natural gas, which were calibrated in NIM in 2016 and recalibrated in 2017~2018 with dry air. On the base of the good consistency of the comparison results, the uncertainty and the measurement capability of the sonic nozzle facility were verified.

---

## 1. Introduction

The coal is the main primary energy source in China, which takes about 70% among all the primary energy consumption. Due to the heavy air pollution resulted from the combustion of coal, the natural gas was more and more widely utilized in China. The annual increase of natural gas consumption had been more than 10%, since 2000. The total consumption was 240.4 billion m<sup>3</sup> in 2017, which took about 6.6% among all the primary energy consumption [1].

With the fast development of natural gas, the requirement on the calibration for the high pressure gas flowmeter was increased for the fair of the trade, especially for the natural gas field. The first natural gas station was built in China at Chengdu in 1994. Now, there are 3 natural gas stations with whole transfer chain including primary standard, secondary standard and working standard, respectively located in Chengdu, Nanjing and Wuhan. In the available natural gas station in China, the natural gas supply is coming from the bypass of the main pipeline. Due to the pressure is different for each station, there was no formal domestic comparison for high pressure gas flow. So, the

value of quantity for the high pressure gas was not consistent until now.

As the national institute of metrology of China (NIM), there were only atmospheric pressure air facility before 2010. To meet the requirement of the high accurate calibration for the high pressure gas flowmeter and achieve the value of quantity consistent for the high pressure gas flow in China, the designing of high pressure gas system in NIM was started in 2010. With consideration of the traceability for the value of quantity the economics, the maximum pressure was fixed at 2.5 MPa, and the whole system was consisted with 3 sections.

### ➤ Primary standard

The pVTt facility with nominal volume of collection tank 100 L and 2 m<sup>3</sup> was treated as the primary standard. With the limit of the pressure resistance grade of the collection tank, the flowrate for the facility was within (0.019~1367) kg/h, with the best measurement capabilities 0.08% ( $k=2$ ), which was verified with the comparison among PTB, LNE, NIST and NIM [2].

### ➤ Secondary standard

There were 16 critical flow Venturi nozzles (CFVNs) used as the master in the secondary standard. The CFVNs could be traceable to the pVTt primary standard facility. The maximum flowrate was

expected to 400 m<sup>3</sup>/h with the uncertainty of 0.15% ( $k=2$ ).

➤ **Working standard**

To meet the requirement of the flow meter in application. The close loop facility was built as the working standard. The maximum flowrate could be 1300 m<sup>3</sup>/h at the pressure of 2.5 MPa with the expected uncertainty of 0.20% ( $k=2$ ).

In this paper, the detailed information the sonic nozzle facility will be presented, including the structure of the facility, the uncertainty analyses, and the verification on the uncertainty.

**2. The sonic nozzle facility**

**2.1 The structure of sonic nozzle facility**

There are two compressors with dryer and filter to produce the high pressure dry air. The dry air from the compressors is saved in the buffer tank. There are two stages of buffer tank. The first stage buffer tank is consisted with 2 tanks with the volume of 10 m<sup>3</sup> individually, and the second stage buffer tank is consisted with 2 tanks with the volume of 7.5 m<sup>3</sup> individually. The maximum pressure in the first stage buffer tank is 10 MPa, while it is 5 MPa in the second stage.

There are two stage of the pressure regulators. The pressure in the sonic nozzle facility was controlled by the second stage of the pressure regulator.

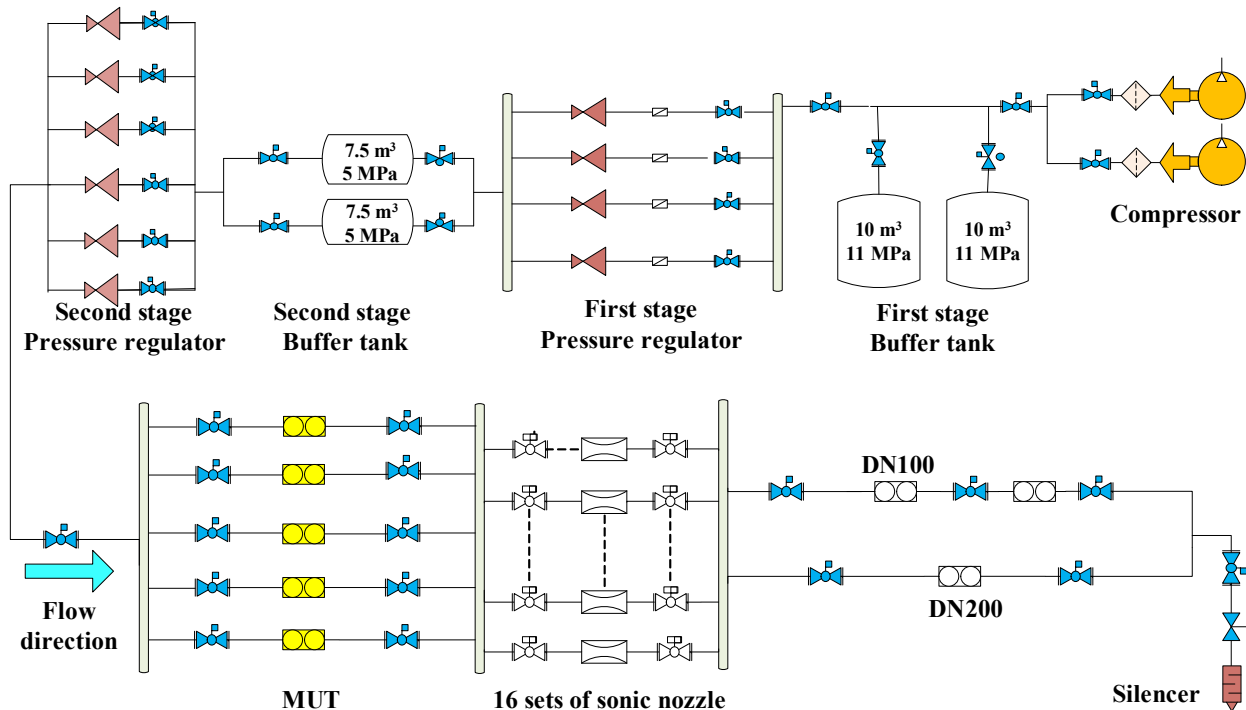


**Figure 1** the systematic diagram of the high pressure gas flow system



(a) The overview of the facility  
**Figure 2** the sonic nozzle facility

(b) the sonic nozzle

(c) the MUT

The meter under test (MUT) was located in the upstream of the facility, while the sonic nozzles were located in the downstream of the facility.

➤ The 16 sets of sonic nozzle were mounted in 4 rows, and there were 4 sets of sonic nozzle in each row.

- There were 5 pipelines for the MUT. There were 4 fixed pipelines for the reference meters in the close loop facility. One pipeline for the customer.

The real meter factor of the meter under test (MUT),  $K_{MUT,real}$ , could be calibrated with the sonic nozzle facility, which could be expressed as,

$$K_{MUT,real} = \frac{N_{MUT}}{t_{MUT} q_{MUT,real}} \quad (1)$$

Where,  $N_{MUT}$  is the pulse number;  $t_{MUT}$  is the test time;  $q_{MUT,real}$  is the real flowrate of the MUT.

According to the mass conservation,  $q_{MUT,real}$  could be expressed as,

$$q_{MUT,real} = \frac{q_{SN}}{\rho_{MUT}} = C_d A_* C_* \frac{p_{SN}}{\sqrt{\frac{R_u}{M} T_{SN}}} \left/ \frac{p_{MUT}}{\frac{R_u}{M} T_{MUT} z_{MUT}} \right. \quad (2)$$

$$= C_d A_* C_* \left/ \left( \frac{p_{MUT}}{p_{SN}} \cdot \frac{\sqrt{T_{SN}}}{T_{MUT}} \cdot \frac{1}{z_{MUT}} \cdot \sqrt{\frac{M}{R_u}} \right) \right.$$

So, Equ. (1) could be expressed as,

$$K_{MUT,real} = \frac{N_{MUT}}{t_{MUT}} \cdot \frac{1}{C_d} \cdot \frac{p_{SN}}{p_{MUT}} \cdot \frac{\sqrt{T_{SN}}}{T_{MUT}} \cdot \left( \frac{1}{A_* C_*} \cdot \frac{1}{z_{MUT}} \cdot \sqrt{\frac{M}{R_u}} \right) \quad (3)$$

Here,

- $A_*$  is the area of the throat of sonic nozzle, it was the same value when the sonic nozzle was calibrated by the pVTt facility and used as the reference meter in the sonic nozzle facility. So, the uncertainty was neglected.
- $R_u$  is the universal gas constant, which is fixed at 8314.4598 J/kmol/K. So, the uncertainty was neglected.
- $M$  is the molecular mass of dry air, which is fixed at 28.965294 kg/kmol. So, the uncertainty was neglected.
- $C_*$  is the critical flow function of the sonic nozzle,  $Z_{MUT}$  is the compressibility factor of MUT, which were calculated by the REFPROP 9.1. The uncertainty was neglected.

So, the uncertainty could be expressed as, [4]

$$u(K_{MUT,real}) = \sqrt{u(C_d)^2 + u(p_{SN})^2 + u(p_{MUT})^2 + 0.25u(T_{SN})^2 + u(T_{MUT})^2 + u(N_{MUT})^2 + u(t_{MUT})^2 + u_R(K_{MUT,real})^2} \quad (4)$$

## 2.2 The calibration for sonic nozzles

The sonic nozzles were traceable to the pVTt primary standard facility in NIM.

**Table 1** the parameters of the sonic nozzles

SN	Nominal throat [mm]	Nominal flowrate [m <sup>3</sup> /h]	Amount
01	1.92	2	1
02	2.71	4	1
03	3.78	8	1
04	5.36	16	1
05~16	7.35	32	12

The calibration procedure is following,

- Each sonic was calibrated at least 9 pressures, ie, 100 kPa, 150 kPa, 220 kPa, 330 kPa, 500 kPa, 750 kPa, 1150 kPa, 1670 kPa and 2500 kPa.
- For each pressure, the calibration was repeated 2~3 times.

To cover the pressure range, the curve fitting between discharge coefficient and Reynolds number was made for each nozzle.

- For SN.01, the curve fitting was shown in Equ. (5-a), due to the slight boundary transition .

$$C_{d,CF} = a + \frac{b}{\sqrt{Re}} + \frac{c}{Re} \quad (5-a)$$

The comparison between the test results and the curve fitting (CF) results based on Equ. (5-a) for SN.01 was shown in Figure 2.

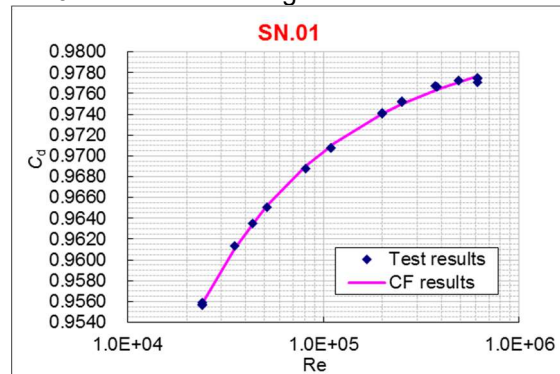


**Figure 2** the comparison between the test results and the CF results for SN.01

- For SN.02~16, the curve fitting was shown in Equ. (5-b) due to the obviously boundary layer transition, with the reference of Ishibashi's research [5].

$$C_{d,CF} = \left( a + \frac{b}{\sqrt{Re}} \right) + \frac{c + \frac{d}{\sqrt{Re}}}{1 + \exp\left(e - \frac{Re}{7000}\right)} \quad (5-b)$$

The comparison between the test results and the CF results based on Equ. (5-b) for SN.07 was shown in Figure 3.

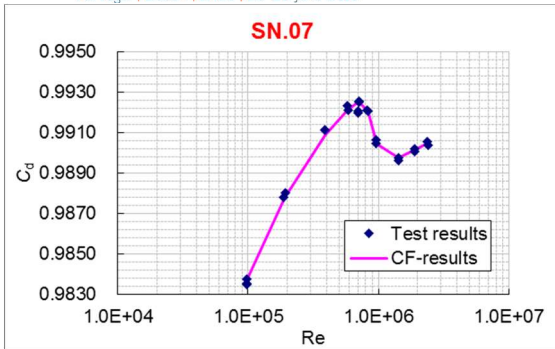


**Figure 3** the comparison between the test results and the CF results for SN.07

The additional residual from the curve fitting was considered in the uncertainty analyses, which was smaller than 0.035%.

$$u(C_{d,CF}) = \sqrt{\frac{(C_{d,CF} - C_d)^2}{N - m}} \quad (6)$$

Where,  $m=3$  for SN.01;  $m=5$  for SN.02~16.

When the sonic nozzle was calibrated at the atmospheric pressure, about 100 kPa with the pVT facility, the uncertainty of discharge coefficient was 0.10% ( $k=2$ ) [6]; when the sonic nozzle was calibrated at other higher pressures with the pVT facility, the uncertainty was 0.08% ( $k=2$ ) [2]. So, the maximum uncertainty of  $C_d$  could be expressed as,

$$u(C_d) = \sqrt{u(C_{d,pVT})^2 + u(C_{d,CF})^2} \quad (7)$$

$$= \sqrt{0.05^2 + 0.035^2} \% = 0.0602\%$$

### 2.3 The “absolute + differential” pressure measurement

To decrease the pressure measurement uncertainty, there is an absolute pressure instrument in the manifold in the upstream of the reference meters,  $p_{abs}$ , the differential pressure

transducers were used for the sonic nozzle and MUT,  $\Delta p_{SN}$ ,  $\Delta p_{MUT}$ . Due to  $\Delta p_{SN}, \Delta p_{MUT} \ll p_{abs}$  so, the pressure measurement in Equ. (1) could be expressed as

$$\frac{p_{MUT}}{p_{SN}} = \frac{p_{abs} + \Delta p_{MUT}}{p_{abs} + \Delta p_{SN}} = 1 + \frac{\Delta p_{MUT}}{p_{abs}} - \frac{\Delta p_{SN}}{p_{abs}} \quad (8)$$

So,

$$u(p_{SN}) = \frac{\Delta p_{SN}}{p_{abs}} \sqrt{u(\Delta p_{SN})^2 + u(p_{abs})^2} \quad (9-a)$$

$$u(p_{MUT}) = \frac{\Delta p_{MUT}}{p_{abs}} \sqrt{u(\Delta p_{MUT})^2 + u(p_{abs})^2} \quad (9-b)$$

In the sonic nozzle facility,

- $U(p_{abs}) = 0.01\%$ ,  $U(\Delta p_{SN}) = U(\Delta p_{MUT}) = 0.05\%$ , the distribution could be assumed as rectangle. At the maximum pressure, 2500 kPa, the maximum differential pressure for the reference meter and MUT was about 50 kPa. So, the sensitivity factor could be evaluated as  $\frac{\Delta p_{SN}}{p_{abs}} = \frac{\Delta p_{MUT}}{p_{abs}} = \frac{50}{2500} = 0.02$ .
- $U(T_{SN}) = U(T_{MUT}) = 0.1^\circ\text{C}$  ( $k=2$ ), the temperature could be assumed  $20^\circ\text{C}$ .
- With the application of the pulse interpolation technique,  $U(N) = 0.1$ , the distribution could be assumed as rectangle. The minimum pulses collection was 2000.
- The resolution of the timer is 0.1 ms, the distribution could be assumed as rectangle. The minimum time was 30 s.

With the combination of Equ. (4) and (9-a), (9-b), the detailed uncertainty component of sonic nozzle facility was shown in Table 1. The total uncertainty of  $K_{MUT,real}$  was 0.15% ( $k=2$ ).

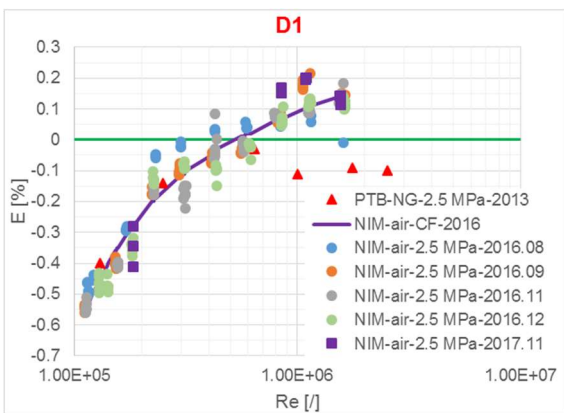
**Table 1** the uncertainty component of sonic nozzle facility

SN	Symbols	Meaning	$u$	$c$	$u \cdot c$
			[%]	[ ]	[%]
1	$u(C_d)$	The discharge coefficient	0.0602	1	0.0602
2	$u(p_{abs})$	The absolute pressure	0.0058	0.028	0.0002
3	$u(\Delta p_{SN})$	The differential pressure of sonic nozzle	0.0289	0.02	0.0006
4	$u(\Delta p_{MUT})$	The differential pressure of MUT	0.0289	0.02	0.0006
5	$u(T_{SN})$	The temperature of sonic nozzle	0.0085	0.5	0.0085
6	$u(T_{MUT})$	The temperature of MUT	0.0085	1	0.0085
7	$u(N_{MUT})$	The pulse number of MUT	0.0029	1	0.0029
8	$u(t_{MUT})$	The time of MUT	0.0002	1	0.0002
9	$u_R(K_{MUT,real})$	The repeatability	0.040	1	0.040
			$u(K_{MUT,real}) = 0.073\%$ , $U(K_{MUT,real}) = 0.15\%$ ( $k=2$ )		

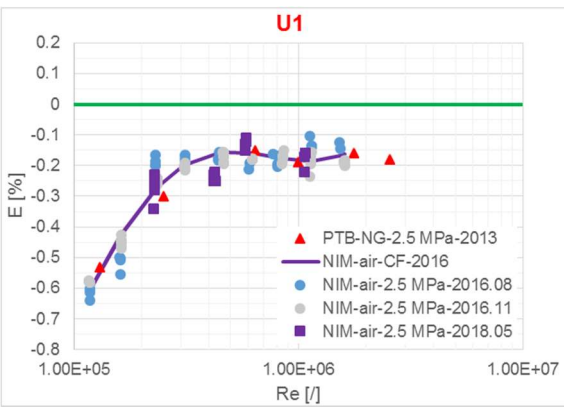
### 3. The verification on the measurement capabilities for the sonic nozzle facility

The expanded uncertainty of meter factor for meter under test (MUT) is 0.15% ( $k=2$ ).

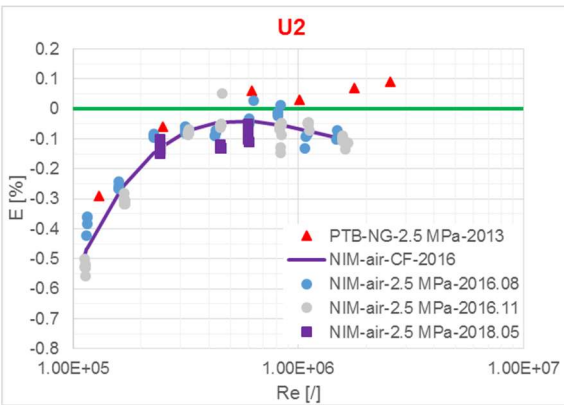
To verify the uncertainty of the sonic nozzle facility, a comparison between NIM and PTB with turbine meter facility was made with 3 Dn 100 turbine meters. The 3 turbine meters were calibrated in PTB in 2013 with natural gas, which were calibrated in NIM within 2016~2018 with air. The comparison results was shown in in Figure. 1. For turbine meter facility in PTB, the expanded uncertainty of meter factor for meter under test (MUT) is 0.13% ( $k=2$ ).



(a)



(b)



(c)

Figure 4 the comparison results

The consistence of the comparisons was evaluated with the value of  $E_n$ . Instead of meter factor, the error was used in the analyses, whose uncertainty was the same as the meter factor.

$$E_n = \frac{|E_{NIM,CF} - E_{PTB}|}{\sqrt{U_{NIM}^2 + U_{PTB}^2 + U_{NIM,CF}^2 + U^2}} \quad (10)$$

The turbine meter is a kind of velocity type meter, so, the error of the turbine meter is strongly related with the Reynolds number. In this comparison, the Reynolds number cannot be exactly matched, due to the different working fluid. Therefore, the curve fitting between the error and the Reynolds number as shown in Equ. (6), was made for each meter [7].

$$E_{NIM,CF} = a_0 + a_1 \ln(\text{Re}) + a_2 \ln(\text{Re})^2 + a_3 \ln(\text{Re})^{-1} + a_4 \ln(\text{Re})^{-2} \quad (11)$$

With the Equ. (6), the  $E_{NIM,CF}$  was calculated at the same Reynolds number as the PTB's result.

For the better freedom of the curve fitting, the individual test point was used. The residual of the curve fitting was evaluated with the following Equ. (7) with the consideration of the freedom.

$$U_{NIM,CF} = 2 \left[ \frac{\sum_{i=1}^N (E_{NIM,i} - E_{NIM,i,CF})^2}{N - 5} \right]^{\frac{1}{2}} \times 100\% \quad (12)$$

On the other hand, the additional uncertainty  $U$  was considered in Equ. (5), with the long term stability and the working fluid effect for the turbine meter.

The each uncertainty component for Equ. (5) for each turbine meter was shown in Table 2.

Table 2 The uncertainty component

SN	$U_{NIM}$ [%]	$U_{PTB}$ [%]	$U_{NIM,CF}$ [%]	$U$ [%]
D1	0.15	0.13	0.10	0.05
U1	0.15	0.13	0.08	0.05
U2	0.15	0.13	0.08	0.05

So, the value of  $E_n$  for each turbine meter is shown in Figure 5

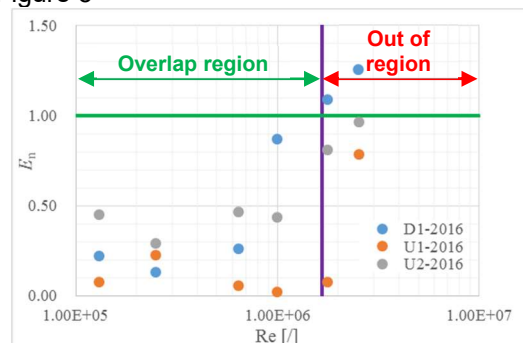


**Figure 5** the comparison results analyses

It was clear from Figure 5, all the  $E_n$  value was smaller than 1 within the overlap region of Reynolds number, which meant the uncertainty of the sonic nozzle facility was verified.

The recalibration of the 3 transfer meters was conducted from 2017 to 2018 as shown in Figure 4. Due to the pressure and temperature change, the test condition could not be matched very well. The reproducibility of the facility was evaluated with the following equation

$$\Delta E = E_{NIM,new} - E_{NIM,CF,2016} \quad (13)$$

Where  $E_{NIM,new}$  is the newest test result,  $E_{NIM,CF,2016}$  is the calculation result from the curve fitting based on the test result in 2016.

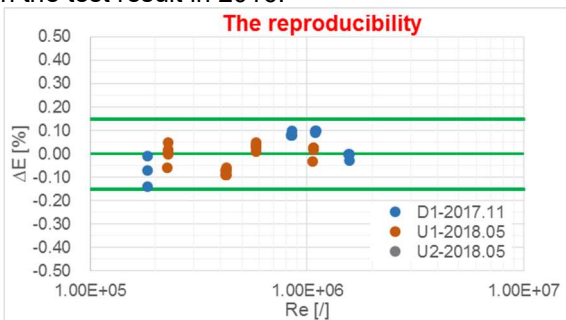


**Figure 6** the reproducibility of the sonic nozzle facility  
It was clear that the reproducibility was smaller than the uncertainty of the close loop facility.

#### 4. Conclusion

With 16 sonic nozzles used as the reference meters, the sonic nozzle facility was built in NIM. The flow range is within (2~400) m<sup>3</sup>/h, while the pressure range is within the (190~2500) kPa. The sonic nozzles were traceable to the pVTt primary standard facility in NIM. To cover the pressure range, the curve fitting between discharge coefficient and Reynolds number was made for each sonic nozzle. To decrease pressure measurement uncertainty, there is an absolute pressure instrument in the manifold in the upstream of the MUT. The expanded uncertainty of meter factor for meter under test (MUT) is 0.15% ( $k=2$ ). To verify the uncertainty of the sonic nozzle facility, a comparison between NIM and PTB was made with three Dn 100 turbine meters as transfer meters. The three turbine meters were calibrated by PTB in 2013 with natural gas, which were calibrated in NIM in 2016. On the base

of the good consistency of the comparison results, the uncertainty and the measurement capability of the sonic nozzle facility were verified.

Due to the limited of the volume of the storage tank as shown in Figure 1, the temperature stability for the maximum flowrate of 400 m<sup>3</sup>/h at 2.5 MPa was relative poor. So, the maximum  $E_n$  value occurred for D1 at the maximum flowrate 400 m<sup>3</sup>/h as shown in Figure 5. Therefore, the maximum flowrate for the sonic nozzle facility was generally claimed as 7200 Nm<sup>3</sup>/h, which was the normalized flowrate at pressure 100 kPa and 20°C, referring to the flowrate 288 m<sup>3</sup>/h at 2.5 MPa.

**Acknowledge:** this work is supported by The National Key Research and Development Program of China “Research and application of national quality infrastructure” (project/subject SN. 2017YFF0205305)

#### References

- [1] www.BP.com, BP statistical review of world energy, June, 2018.
- [2] Mickan B, Jean-Pierre Vallet, Li C H, J. Wright, “Extended data analysis of bilateral comparisons with air and natural gas up to 5 MPa”, Flomeko, Sydney, 2016.
- [3] ISO 9300, Measurement of Gas Flow by means of Critical Flow Venturi Nozzles, 2005
- [4] ISO/IEC Guide 98-3:2008 (Uncertainty of measurement – Part 3: Guide to the expression of uncertainty in measurement, GUM, 2008.
- [5] Ishibashi M, “Discharge coefficient equation for critical-flow toroidal-throat Venturi nozzle covering the boundary-layer transition regime”, Flomeko, 2013.
- [6] Li C H, Mickan B and Isaev I, “The comparison of low pressure gas flowrate among NIM, PTB and VNIIR”, Flomeko, Sydney, 2016.
- [7] Zhang H, Jia L, et al, “The error model of turbine flowmeter based on Reynolds number, Flomeko, Sydney, 2016.
- [8] Cox M G, “Evaluation of key comparison data”, Metrologia, 39: 589-595, 2002.
- [9] Cox M G, “The evaluation of key comparison data: determining the largest consistent subset”, Metrologia, 44:187-200, 2007.

# The high pressure close loop gas flow standard facility in NIM

Chi Wang<sup>1</sup>, Chunhui Li<sup>1</sup>, Ming Xu<sup>2</sup>, Wencan Yan<sup>2</sup>

<sup>1</sup>NIM, No.18 Beisanhuan Donglu, Beijing, China

<sup>2</sup>Sinopec, Gas Company, Wuhan, China

E-mail (corresponding author): lich@nim.ac.cn

---

## Abstract

The first high pressure close loop gas flow facility in China was built in NIM at the end of 2014. The 4 sets of Dn 100 turbine meters were used as the reference meters in the facility. The flow range is within (40~1300) m<sup>3</sup>/h, while the pressure range is within the (190~2500) kPa. The turbine meter is a kind of velocity type flow meter, which is easily affected by installation. To avoid the installation effect, the reference meters were designed to be calibrated in “original position” without dismounted. To decrease the pressure measurement uncertainty, there is an absolute pressure instrument in the manifold in the upstream of the reference meters, the differential pressure transducers were used for the reference meter and meter under test (MUT). The expanded uncertainty of meter factor for MUT is 0.20% ( $k=2$ ). The uncertainty of the close loop facility was verified with a comparison between the sonic nozzle facility and close loop facility, in which one Dn 100 turbine meter was chosen as the transfer meter. On the base of the good consistency of the comparison results, the uncertainty and the measurement capability of the close loop facility were verified.

---

## 1. Introduction

The coal is the main primary energy source in China, which takes about 70% among all the primary energy consumption. Due to the heavy air pollution resulted from the combustion of coal, the natural gas was more and more widely utilized in China. The annual increase of natural gas consumption had been more than 10%, since 2000. The total consumption was 240.4 billion m<sup>3</sup> in 2017, which took about 6.6% among all the primary energy consumption [1].

With the fast development of natural gas, the requirement on the calibration for the high pressure gas flowmeter was increased for the fair of the trade, especially for the natural gas field. The first natural gas station was built in China at Chengdu in 1994. Now, there are 3 natural gas stations with whole transfer chain including primary standard, secondary standard and working standard, respectively located in Chengdu, Nanjing and Wuhan. In the available natural gas station in China, the natural gas supply is coming from the bypass of the main pipeline. Due to the different pressure for each station, there was no formal domestic comparison for high pressure gas flow. So, the value of quantity for the high pressure gas was not consistent until now.

As the national institute of metrology of China (NIM), there were only atmospheric pressure air facility before 2010. To meet the requirement of the high accurate calibration for the high pressure gas flowmeter and achieve the value of quantity consistent for the high pressure gas flow in China, the designing of high pressure gas system in NIM was started in 2010. With consideration of the traceability for the value of quantity the economics, the maximum pressure was fixed at 2.5 MPa, and the whole system was consisted with 3 sections.

### ➤ Primary standard

The pVTt facility with nominal volume of collection tank 100 L and 2 m<sup>3</sup> was treated as the primary standard. With the limit of the pressure resistance grade of the collection tank, the flowrate for the facility was within (0.019~1367) kg/h, with the best measurement capabilities 0.08% ( $k=2$ ), which was verified with the comparison among PTB, LNE, NIST and NIM [2].

### ➤ Secondary standard

There were 16 critical flow Venturi nozzles (CFVNs) used as the master in the secondary standard. The CFVNs was traceable to the primary standard, pVTt facility. The maximum flowrate could be 400 m<sup>3</sup>/h with the best measurement capabilities 0.15% ( $k=2$ ), which was verified with comparison between PTB and NIM [3].

In reality, the maximum flowrate for the sonic nozzle facility was 7200 Nm<sup>3</sup>/h, which is the normalized flowrate at pressure 100 kPa and 20°C, due to the

limited of the volume of the storage tank as shown in Figure 1.

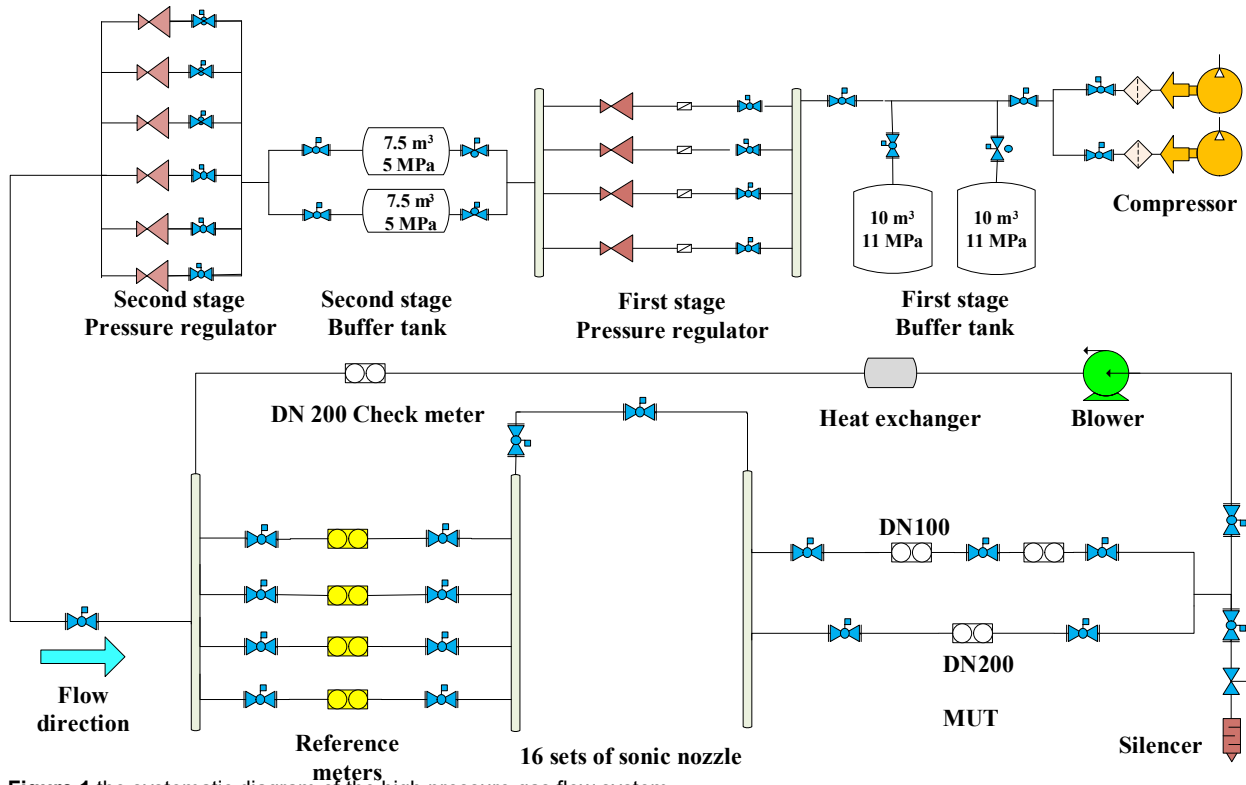


Figure 1 the systematic diagram of the high pressure gas flow system

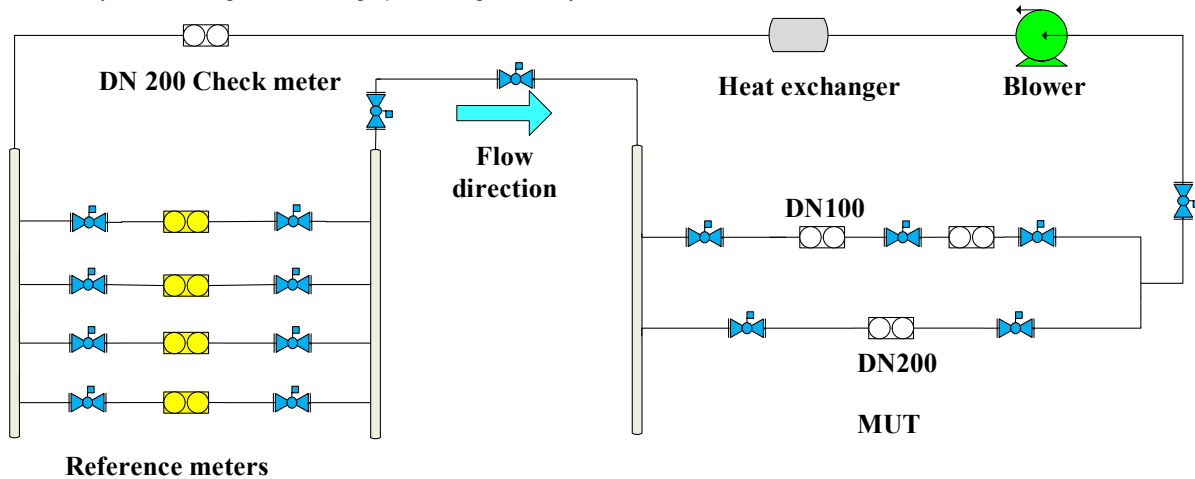


Figure 2 the detailed diagram of the close loop facility

### Working standard

The working standard are used for the daily calibration for the customer. The typical technologies in use are turbine meter or rotary meter [4 错误!未找到引用源。] because of their well-proven reproducibility and high flexibility regarding operating of different flow rates and reasonable pressure loss (energy efficiency of the test rigs).

To meet the requirement of the flow meter in application. The close loop facility was built. The

maximum flowrate could be 1300 m<sup>3</sup>/h at the pressure of 2.5 MPa, with the expected best measurement capabilities 0.20% ( $k=2$ ).

In this paper, the close loop facility will be introduced in detail, including the structure of the facility, the uncertainty analyses, and the comparison between the close loop facility and the sonic nozzle facility to verify the uncertainty.

## 2. The close loop facility

### 2.1 The structure of close loop facility

As shown in Figure 1, there are two compressors with dryer and filter to produce the high pressure dry air. The dry air from the compressors is saved in the buffer tank. There are two stages of buffer tank. The first stage buffer tank is consisted with 2 tanks with the volume of 10 m<sup>3</sup> individually, and the second stage buffer tank is consisted with 2 tanks with the volume of 7.5 m<sup>3</sup> individually. The maximum pressure in the first stage buffer tank is 10 MPa, while it is 5 MPa in the second stage.

As shown in Figure 2, the references meters were located in the upstream, while the MUT was located in the downstream. The blower was used to circulate the air in the loop. The heat exchanger was used to keep the temperature stable.

The real meter factor,  $K_{MUT,real}$ , could be calibrated with the close loop facility, which could be expressed as,

$$K_{MUT,real} = \frac{N_{MUT}}{t_{MUT} q_{MUT,real}} \quad (1)$$

Where,  $N_{MUT}$  is the pulse number of the meter under test (MUT);  $t_{MUT}$  is the test time of the MUT;  $q_{MUT,real}$  is the real volumetric flowrate of the MUT.

According to the mass conservation,  $q_{MUT,real}$  could be expressed as,

$$q_{MUT,real} = q_{ref} \cdot \frac{\rho_{ref}}{\rho_{MUT}} \quad (2)$$

$$= \frac{N_{ref}}{K_{ref} \cdot t_{ref}} \cdot \left( \frac{p_{ref}}{p_{MUT}} \cdot \frac{T_{MUT}}{T_{ref}} \cdot \frac{z_{MUT}}{z_{ref}} \right)$$

Where,  $q_{ref}$  is the real volumetric flowrate of the reference meter;  $K_{ref}$  is the real meter factor of the reference meter;  $p$  is the pressure;  $T$  is the temperature;  $z$  is the compressibility factor. The subscript of “*ref*” referring the reference meter, while “*MUT*” referring the meter under test.

So, Equ. (1) could be expressed as,

$$K_{MUT,real} = K_{ref} \cdot \frac{p_{MUT}}{p_{ref}} \cdot \frac{T_{ref}}{T_{MUT}} \cdot \frac{z_{ref}}{z_{MUT}} \cdot \frac{N_{MUT}}{N_{ref}} \cdot \frac{t_{ref}}{t_{MUT}} \quad (3)$$

The compressibility factor for MUT and master meter was calculated by the REFPROP 9.1, the uncertainty was neglected.

So, the uncertainty of the  $K_{MUT,real}$  can be expressed as [5],

$$u(K_{MUT,real}) = \sqrt{\begin{matrix} u(K_{ref})^2 + u(p_{ref})^2 + u(p_{MUT})^2 \\ + u(T_{ref})^2 + u(T_{MUT})^2 \\ + u(N_{ref})^2 + u(N_{MUT})^2 \\ + u(t_{ref})^2 + u(t_{MUT})^2 \\ + u_R(K_{MUT,real})^2 \end{matrix}} \quad (4)$$

## 2.2 The “original position” calibration for reference meters

The turbine meter is a kind of velocity type flow meter, which is easily affected by installation. To avoid the installation effect, the reference meters could be directly in “original position” traceable to the sonic nozzle facility in NIM without dismounted.

The calibration procedure is following,

- Each reference meter was calibrated at 5 pressures, ie, 190 kPa, 360 kPa, 690 kPa, 1300 kPa, and 2500 kPa.
- For each pressure, the meter was calibrated with 8 flow rate, ie, 40 m<sup>3</sup>/h, 54 m<sup>3</sup>/h, 76 m<sup>3</sup>/h, 106 m<sup>3</sup>/h, 147 m<sup>3</sup>/h, 206 m<sup>3</sup>/h, 288 m<sup>3</sup>/h and 400 m<sup>3</sup>/h.
- For each flow rate, the calibration was repeated at least 5 times.

**Note: due to the limited of the capability of the sonic nozzle facility, the maximum flowrate is about 288 m<sup>3</sup>/h at 2500 kPa, referring to the 7200 Nm<sup>3</sup>/h at pressure 100 kPa and 20°C.**

To cover the flow range, the curve fitting between error, instead of meter factor, and Reynolds number was made for each pressure.

The curve fitting was used to cover the flow range of the [6]

- For the pressure range within (190~400) kPa, the curve fitting was expressed as, Equ. (5-a),

$$E_{ref,CF} = a_0 + a_1 \ln(\text{Re}) + a_2 \ln(\text{Re})^2 + a_3 \ln(\text{Re})^3 \quad (5-a)$$

- For the pressure range within (400~2500) kPa, the curve fitting was expressed as, Equ. (5-b),

$$E_{ref,CF} = a_0 + a_1 \ln(\text{Re}) + a_2 \ln(\text{Re})^2 \quad (5-b)$$

The additional residual from the curve fitting was considered in the uncertainty analyses, which could be evaluated as,

$$u(E_{ref,CF}) = \sqrt{\frac{(E_{ref,CF} - E_{ref})^2}{N - m}} = u(K_{ref,CF}) \quad (6)$$

Where,  $m=4$  when the pressure is within (190~400) kPa;  $m=3$  when the pressure is within (400~2500) kPa. The maximum of  $u(E_{ref,CF})$  was smaller than 0.05%.

So, the maximum uncertainty of  $K_{ref}$  could be expressed as,

$$u(K_{ref}) = \sqrt{u(K_{ref,SN})^2 + u(K_{ref,CF})^2} \quad (7)$$

$$= \sqrt{0.075^2 + 0.05^2} \% = 0.0885\%$$

The test results for SN.U1 were shown in Figure 3.

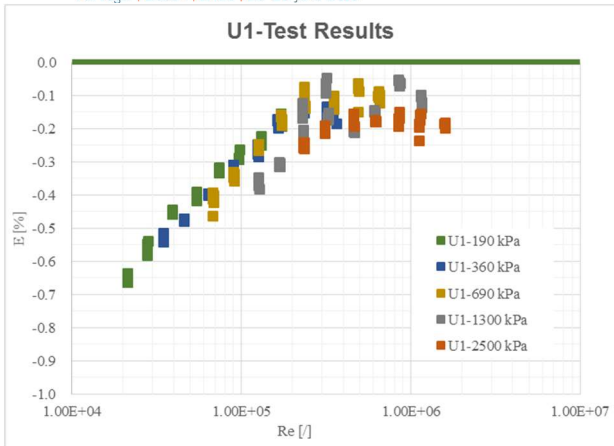


**Figure 3** the test results for U1 at different pressures

With the prediction from Equ. (5-a), the comparison between the test and curve fitting (CF) at pressure 360 kPa as shown in Figure 4.

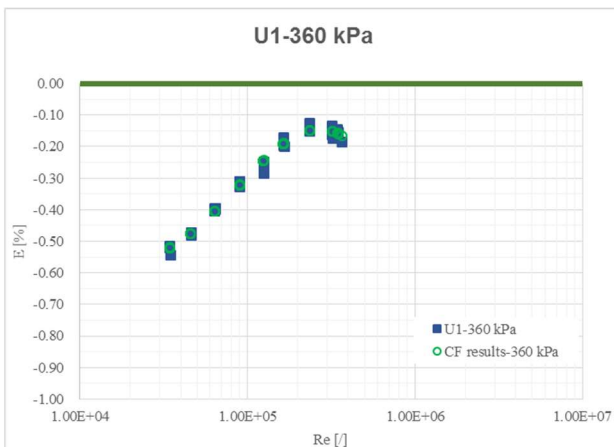


**Figure 4** the comparison between test and CF

With the prediction from Equ. (5-b), the comparison between the test and curve fitting (CF) at pressure 2500 kPa as shown in Figure 5.

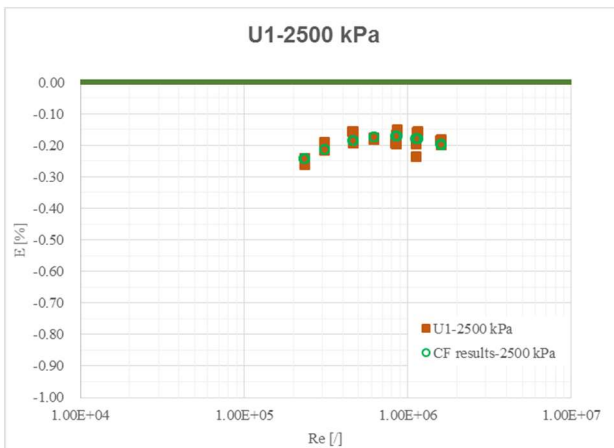


**Figure 5** the comparison between test and CF

### 2.3 The “absolute + differential” pressure measurement

To decrease the pressure measurement uncertainty, there is an absolute pressure instrument in the manifold in the upstream of the reference meters,  $p_{abs}$ , the differential pressure transducers were used for the reference meter and MUT,  $\Delta p_{ref}$ ,  $\Delta p_{MUT}$ . Due to  $\Delta p_{ref}, \Delta p_{MUT} \ll p_{abs}$  so, the pressure measurement in Equ. (1) could be expressed as

$$\frac{p_{MUT}}{p_{ref}} = \frac{p_{abs} + \Delta p_{MUT}}{p_{abs} + \Delta p_{ref}} = 1 + \frac{\Delta p_{MUT}}{p_{abs}} - \frac{\Delta p_{ref}}{p_{abs}} \quad (8)$$

So,

$$u(p_{ref}) = \frac{\Delta p_{ref}}{p_{abs}} \sqrt{u(\Delta p_{ref})^2 + u(p_{abs})^2} \quad (9-a)$$

$$u(p_{MUT}) = \frac{\Delta p_{MUT}}{p_{abs}} \sqrt{u(\Delta p_{MUT})^2 + u(p_{abs})^2} \quad (9-b)$$

In the close loop facility,

- $U(p_{abs}) = 0.01\%$ ,  $U(\Delta p_{ref}) = U(\Delta p_{MUT}) = 0.05\%$ , the distribution could be assumed as rectangle. At the maximum pressure, 2500 kPa, the maximum differential pressure for the reference meter and MUT was about 50 kPa. So, the sensitivity factor could be evaluated as  $\frac{\Delta p_{ref}}{p_{abs}} = \frac{\Delta p_{MUT}}{p_{abs}} = \frac{50}{2500} = 0.02$ .
- $U(T_{ref}) = U(T_{MUT}) = 0.1^\circ\text{C}$  ( $k=2$ ), the temperature could be assumed  $20^\circ\text{C}$ .
- With the application of the pulse interpolation technique,  $U(N) = 0.1$ , the distribution could be assumed as rectangle. The minimum pulses collection was 2000.
- The resolution of the timer is 0.1 ms, the distribution could be assumed as rectangle. The minimum time was 30 s.

With the combination of Equ. (4) and (9-a), (9-b), the detailed uncertainty component of close loop facility was shown in Table 1. The total uncertainty of  $K_{MUT,real}$  was 0.20% ( $k=2$ ).

### 3. The verification on the measurement capabilities for the close loop facility

To verify the capability of the close loop facility, one Dn 100 turbine meter was used as the transfer meter to make the comparison between the sonic nozzle facility and the close loop facility.

The comparison results were shown in Figure 6 with different pressures, 690 kPa, 1300 kPa and 2500 kPa. The curve fitting, the similar as Equ. (5-b) was made to analyse the consistent of the result.

$$E_{MUT,CF} = a_0 + a_1 \ln(\text{Re}) + a_2 \ln(\text{Re})^2 \quad (10)$$

Within the overlap region of Reynolds number, the  $E_n$  value [7~8] was used to evaluate the result,

**Table 1** the uncertainty component of close loop facility

SN	Symbols	Meaning	$u$	$c$	$u \cdot c$
			[%]	[/]	[%]
1	$u(K_{ref})$	The meter factor of reference meter	0.0899	1	0.0899
2	$u(p_{abs})$	The absolute pressure	0.0058	0.028	0.0002
3	$u(\Delta p_{ref})$	The differential pressure of reference meter	0.0289	0.02	0.0006
4	$u(\Delta p_{MUT})$	The differential pressure of MUT	0.0289	0.02	0.0006
5	$u(T_{ref})$	The temperature of reference meter	0.0085	1	0.0085
6	$u(T_{MUT})$	The temperature of MUT	0.0085	1	0.0085
7	$u(N_{ref})$	The pulse number of reference meter	0.0029	1	0.0029
8	$u(N_{MUT})$	The pulse number of MUT	0.0029	1	0.0029
9	$u(t_{ref})$	The time of the reference meter	0.0002	1	0.0002
10	$u(t_{MUT})$	The time of MUT	0.0002	1	0.0002
12	$u_R(K_{MUT,real})$	The repeatability	0.040	1	0.040

$u(K_{MUT,real})=0.098\%$ ,  $U(K_{MUT,real})=0.20\%$  ( $k=2$ )

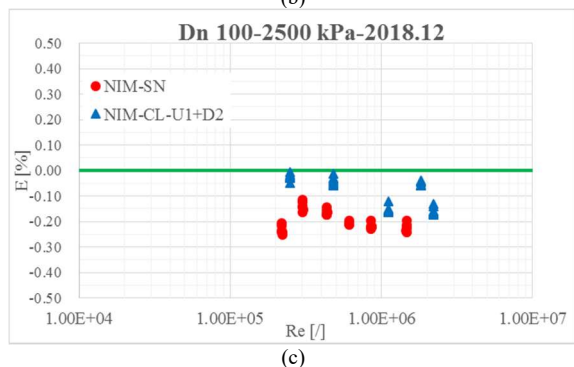
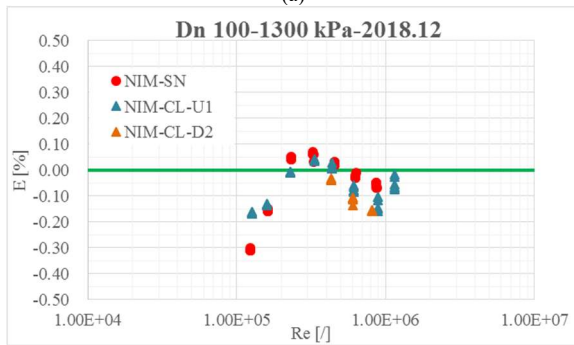
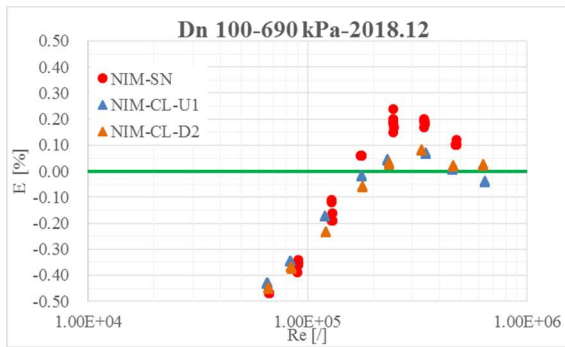


**Figure 6** the comparison results between sonic nozzle facility and close loop facility

$$E_n = \frac{|E_{MUT,CL,CF} - E_{MUT,SN}|}{\sqrt{U_{MUT,CL}^2 + U_{MUT,SN}^2 + U_{CF}^2}} \quad (11)$$

- For sonic nozzle facility, the expanded uncertainty of meter factor for meter under test (MUT) is 0.15% ( $k=2$ ).
- For close loop facility, the expanded uncertainty of meter factor for meter under test (MUT) is 0.20% ( $k=2$ ).

Due to the curve fitting, the additional curve fitting uncertainty, the same as Equ. (6),  $U_{CF}$ , which was evaluated by Equ. (12),

$$U_{CF} = 2 \sqrt{\frac{(E_{MUT,CF} - E_{MUT})^2}{N - 3}} \quad (12)$$

The comparison results were shown Figure 7 in detail, which were summarized in Table 2.

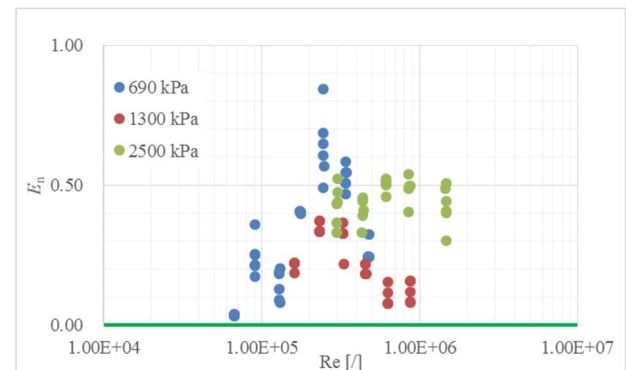


**Figure 7** the detailed comparison results

It was clear that all the value of  $E_n$  was smaller than 1, which meant that the 0.20% ( $k=2$ ) uncertainty of the close loop facility was verified.

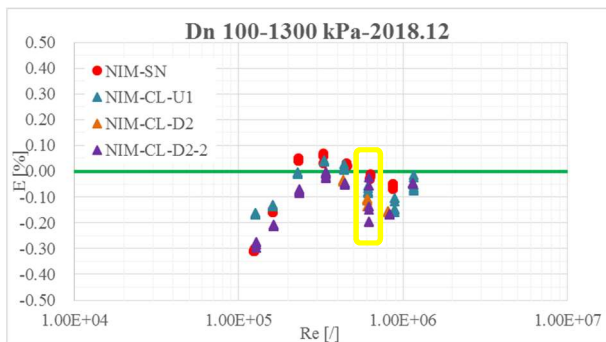
**Table 2** The comparison results

Pressure [kPa]	Re range for CF	$U_{cr}$ [%]	$E_n$
690	$6.5 \times 10^4 \sim 6.4 \times 10^5$	0.06	0.03~0.84
1300	$1.3 \times 10^5 \sim 1.2 \times 10^6$	0.11	0.08~0.37
2500	$2.5 \times 10^5 \sim 2.2 \times 10^6$	0.09	0.30~0.54

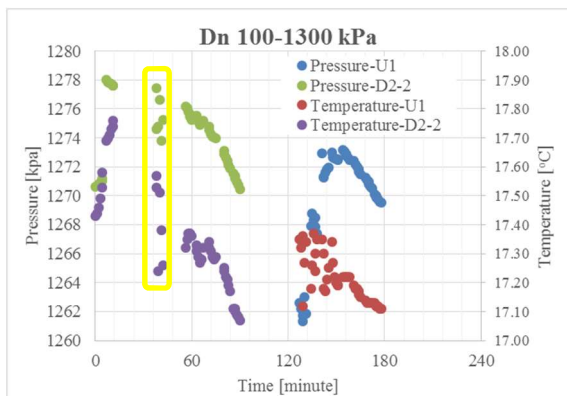
For the close loop facility, the pressure and temperature stability was the important parameter, which influence the repeatability very much. In general, the repeatability was smaller than 0.04%,  $u_R(K_{MUT,real})$  which was used in the uncertainty analyses in Table 1.

As shown in Figure 8 (a) with yellow square, the poor repeatability, 0.07%, occurred, when the flowrate was about 210 m<sup>3</sup>/h. The pressure and temperature change during the test was shown in Figure 8 (b).

From the Figure 8 (b), it was clear that the temperature changed about 0.3 °C within 4 minutes. Due to the slow response of the temperature sensor, the real temperature change might not be caught. So, the temperature change was kept within 0.3 °C in one hour for the close loop facility.



(a) The poor repeatability for error



(b) The pressure and temperature change

**Figure 8** the pressure and temperature effect

#### 4. Conclusion

The close loop facility with 4 sets of Dn 100 turbine meters as the reference meters was built in NIM. The flow range is within (40~1300) m<sup>3</sup>/h, while the pressure range is within the (190~2500) kPa. To avoid the installation effect, the reference meters were designed directly in “original position” traceable to the sonic nozzle facility (SN). To decrease the pressure measurement uncertainty, there is an absolute pressure instrument in the manifold in the upstream of the reference meters, the differential pressure transducers were used for the reference meter and MUT. So, the expanded uncertainty of meter factor for meter under test (MUT) was 0.20% ( $k=2$ ), which was verified with the comparison between sonic nozzle facility and close loop facility.

**Acknowledge:** this work is supported by The National Key Research and Development Program of China “Research and application of national quality infrastructure” (project/subject SN. 2017YFF0205305)

#### References

- [1] www.BP.com, BP statistical review of world energy, June, 2018.
- [2] Mickan B, Jean-Pierre Vallet, Li C H, J. Wright, “Extended data analysis of bilateral comparisons with air and natural gas up to 5 MPa”, Flomeko, Sydney, 2016.
- [3] Li C H, Mickan Bodo and Lishui Cui, et al., “The high pressure sonic nozzle gas flow standard facility in NIM”, Flomeko, Lisbon, 2019.
- [4] Bremser W, Hasselbarth W and Hirlehei U, et al., “Uncertainty analysis and long-term stability investigation of the German primary high-pressure natural gas test facility Pigsar, Flomeko, Groningen, 2003.
- [5] ISO/IEC Guide 98-3:2008 (Uncertainty of measurement – Part 3: Guide to the expression of uncertainty in measurement, GUM, 2008.
- [6] Su Y L, “The investigation on the characteristics of turbine flowmeter based on high pressure sonic nozzle gas flow standard facility”, Master thesis, in Chinese, 2017.
- [7] Cox M G, “Evaluation of key comparison data”, Metrologia, 39: 589-595, 2002.
- [8] Cox M G, “The evaluation of key comparison data: determining the largest consistent subset”, Metrologia, 44:187-200, 2007.

# EDF R&D new test bench for liquid industrial flow meters calibration

E. Thibert<sup>1</sup>, S. Blairon<sup>1</sup>, D. Boldo<sup>1</sup>, E. Nanteau<sup>1</sup>, J. Veau<sup>1</sup>

<sup>1</sup>EDF R&D, 6 quai Watier, BP49, 78401 Chatou Cedex, France  
E-mail (corresponding author): emmanuel.thibert@edf.fr

---

## Abstract

Since 1997, EDF Research and Development Division has been carrying out liquid flow metering studies on the EVEREST experimental loop at EDF Lab Chatou (France). In the last twenty years, industrial flow meters designs have been continuously improved by manufacturers. In the same time, the need for industrial flow measuring instruments with a high accuracy has tremendously increased due to the required economic cost-effectiveness in the energy sector. Flow meters metrological assessment tests consequently need to be upgraded in order to remain relevant. In 2016, EDF R&D has then initiated a complete revamping of the EVEREST test bench which was achieved at the beginning of 2019. This comprehensive retrofit leads to a significant calibration accuracy improvement. The EVEREST reference volume flow uncertainty is now better than 0.1% from 50 m<sup>3</sup>.h<sup>-1</sup> up to 1200 m<sup>3</sup>.h<sup>-1</sup>. Moreover, in order to characterize the velocity profile impact on industrial meter metrological performance, two laser velocimetry measurement systems have been purchased. This effort leads also to the design of a mini-loop, called MONT-BLANC, whose purpose is to mimic EVEREST calibration features under a smaller size and a lower flow rate rangeability (from 13 m<sup>3</sup>.h<sup>-1</sup> up to 150 m<sup>3</sup>.h<sup>-1</sup>). This test bench will allow not only to ease optical adjustments of laser-based velocity measurement techniques and their future implementations on EVEREST but also to provide an effective tool to investigate the influence of scale effect on flow meters and pipes flow physics.

---

## 1. Introduction

EDF (the French Electricity Generation company) operates 58 “Pressurized Water Reactor type” nuclear units in France (PWR). In these particular power plants, flow monitoring is essential not only for safety reasons but also for economical ones. For instance, accurate measurement of feedwater flow in PWR plants is necessary to quantify the turbine cycle heat rate of the plant, which is a major component of the overall plant efficiency.

Twenty years ago, EDF appointed its Research and Development Division (EDF Lab Chatou, France) to carry out experimental tests on usual or innovative flow meters for evaluating their metrological performance. These tests aimed at assessing flow meters metrological behaviour in a semi real industrial conditions prior to a potential PWR on-site installations. EDF R&D consequently designed a specific test bench for this mission. This loop was called EVEREST.

The basic design concept of EVEREST had two main objectives: one was to duplicate the behaviour of an industrial liquid pipe flow process as closely as

possible, and the second was to generate an accurate and steady reference flow rate.

In the last twenty years, industrial flow meters designs have been continuously improved by manufacturers. In the same time, the need of industrial flow measuring instruments with a high accuracy has tremendously increased due to the required economic cost-effectiveness in the energy sector. Flow meters metrological assessment tests consequently need to be upgraded in order to remain relevant.

In 2016, EDF R&D has then initiated a complete revamping of the EVEREST test bench [1] [2]. This task was challenging because it required not only to maintain the specificity of the old bench (generation of a steady liquid flow rate for test/calibration purposes in a semi-industrial scale) but also to add new features such as a better calibration accuracy and a liquid velocity profile characterization for real pipe flow configurations.

This objective was achieved at the beginning of 2019 and led to the design of two similar test benches but at different scales: an upgrade version of the old EVEREST loop and a mini EVEREST called MONT-

BLANC for smaller flow rates calibration and an easier modularity for laser-based velocity measurement techniques implementation.

## 2. EVEREST loop global design

The new EVEREST facility is a closed loop with a liquid flow rate regulation (figure 1). Fluid is clean tap water.

EVEREST consists in three parts: a flow metering reference section, an operation section and a modular flow metering test section (figure 2).



Figure 1: EVEREST test facility overview.

Table 1: Overview of the design specification of EVEREST.

Prime Features	Details
Calibration test type	Closed regulated loop
Flow meter reference	Master meters method
Test section pipe size	From DN100 up to DN350
Pipe compositions	Stainless steel
Fluid	Tap liquid water
Pressure range	From 1 up to 10 bar
Fluid temperature range	From 20°C up to 40°C
Environment Temperature	Minimum and maximum ambient temperature are (respectively) 10°C and 35°C
Flow rate range	From 50 m <sup>3</sup> .h <sup>-1</sup> up to 1200 m <sup>3</sup> .h <sup>-1</sup>
Flow metering uncertainty	0.1% (volume flow rate)

## 3. EVEREST operation section

Table 1 shows the new EVEREST design specifications. The test bench provides a steady water stream from  $5 \cdot 10^4$  up to  $2 \cdot 10^6$  Reynolds number. Flow circulation is provided with a variable centrifugal pump (315 kW). Depending on the test section geometrical configuration, flow range generally goes from 50 m<sup>3</sup>.h<sup>-1</sup> up to 1200 m<sup>3</sup>.h<sup>-1</sup>. Thanks to regulation systems, a steady flow rate is maintained in the reference and the test sections.

Pump energy is converted into heat which is absorbed by the pumped liquid. Due to EVEREST loop FLOMEKO 2019, Lisbon, Portugal

configuration, this phenomenon consequently increases fluid temperature in the test and reference sections. To compensate this phenomenon, water temperature is regulated thanks to a plate heat exchanger (215 kW). The cooling system is provided by a fan coils unit located at the outside of the experimental hall. Fluid temperature can thus be set at a specific value according to the desired test conditions, generally between 20°C and 40°C. Fluid pressure regulation is regulated from 1 bar up to 10 bar thanks to a pressuriser.

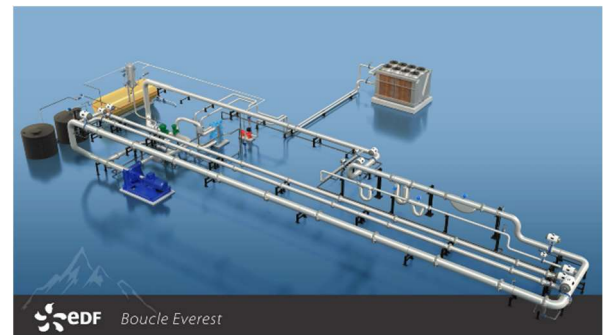


Figure 2: EVEREST test facility layout design.

EVEREST loop is designed to minimize its environmental impact by managing efficiently its water consumption. Two water storage tanks are used for filling and emptying the EVEREST hydraulic circuits between two test campaigns which required different pipe configurations. Moreover, a third tank has been implemented in order to store the entire test bench water volume. When needed, this “waste” water is analysed before a classic evacuation or, if necessary, a reprocessing in a water treatment plant.

## 4. EVEREST flow metering reference section

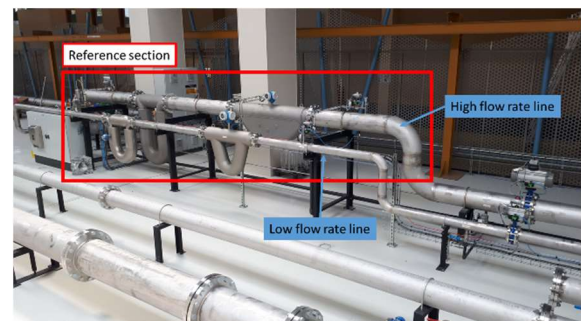


Figure 3: EVEREST flow metering reference section.

The major characteristic of EVEREST loop is the generation of a steady liquid flow rate for test/calibration purposes. This reference flow rate is calculated with the use of four different master meters based on Coriolis technology (Table 2). As shown in

Figure 3, two meters are used for low flow rate calibration tests, from  $50 \text{ m}^3 \cdot \text{h}^{-1}$  up to  $350 \text{ m}^3 \cdot \text{h}^{-1}$ . They are installed on DN100 stainless steel pipe. The other two devices operate under high flow rate calibration tests conditions, from  $150 \text{ m}^3 \cdot \text{h}^{-1}$  up to  $1200 \text{ m}^3 \cdot \text{h}^{-1}$ . They are installed on DN250 stainless steel pipe. This configuration aims at decreasing uncertainty all over the loop flow rate rangeability, for each meter is used in its nominal operative flow rate. The EVEREST reference flow rate is calculated as a volume flow rate. Reference volume flow uncertainty is better than 0.1% for the overall flow rate range [3] [4].

**Table 2:** EVEREST Coriolis reference meters specifications.

	Flowmeter	pipe diameter	Flow rate ( $\text{m}^3 \cdot \text{h}^{-1}$ )	
			Min.	Max.
High flow rate line	$Q_{1\text{ref}}$	DN250	150	1200
	$Q_{2\text{ref}}$			
Low flow rate line	$Q_{3\text{ref}}$	DN100	50	350
	$Q_{4\text{ref}}$			

Usual experimental tests are carried out on steady flow rate. At the beginning of a test, bench operator selects the flow rate on the monitoring screen and consequently the corresponding master meter line which has to be used.

For each reference line, one Coriolis meter is used as the reference flow rate and the other is used as a “drift detection” meter. This choice allows to monitor and to detect any reference sensor drift between two consecutive calibrations.

Furthermore, due to the Coriolis technology, there is no need for a high upstream straight lengths before the meters implementation zone. This feature leads to benefit from a bigger area available for the test section in the experimental hall (figure 4).

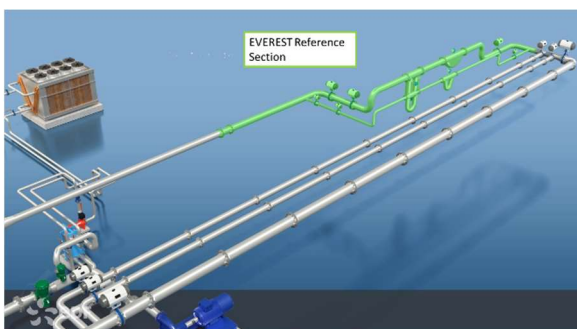


**Figure 4:** EVEREST flow metering reference section digital model.

## 5. EVEREST flow metering test section

The last but not least section of EVEREST is the flow metering test section. Tested devices are generally mounted on stainless steel pipes and can be invasive as well as non-invasive according to the sensor technology.

This inner room section constitutes an available space with a length of 25 m, a width of 5 m and with a high ceiling of 5 m. This test section is designed to perform calibration tests not only under ideal thermo-hydraulic conditions (fully developed and swirl-free velocity profile thanks to a high straight lengths at the upstream of the tested meter) but also calibrations tests under non-ideal thermo-hydraulic conditions due to the presence of various fittings located upstream or downstream the tested meter. Figure 4 shows a common test section modification, from a 100Dh (hydraulic diameter) straight lengths DN200 pipe up to a test area located between two double 90° elbow pipes.

The default test section configuration includes three piping lines with different sizes (DN350, DN200 and DN100). However, several pipe configurations can be arranged depending on the meter calibration purposes (figure 5).

This modularity was a key feature of the previous loop and greatly contributed to its recognition within EDF. This characteristic was obviously kept for the new one.

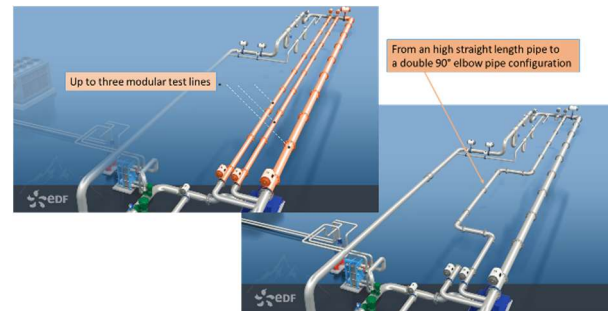


**Figure 5:** EVEREST modular flow metering test section example.

Thus, the new loop test section is still a multi-purpose test area which allows to re-create numerous process pipeworks or to install a reduced scale mock-up of typical industrial components for metrological purpose. This flexibility will allow EDF R&D to keep on investigating the real installation conditions impacts on flowmeters accuracy: orifice plate installation with no ISO 5167-2 [6] required upstream and/or downstream straight lengths of piping, electromagnetic or ultrasonic flow metering systems under severely perturbed flow conditions, ...

## 6. MONT-BLANC layout

Flow meters metrological assessment tests need to be upgraded in order to remain relevant. EDF R&D has come to the conclusion that, improving flow meters accuracy investigations requires a comprehensive velocity profile understanding. This feature was one of the main cornerstone for the revamping of EVEREST. Some velocity measurements have been performed in 2014 and 2015 with the previous loop [5]. These tests were performed in a semi-realistic scale pipe configuration which turned out to be quite a challenge for collecting accurate velocity data.

This test campaign led EDF R&D to the idea of designing a smaller version of EVEREST loop dedicated to prepare and adjust velocity measurement systems and configurations prior to any experimental campaigns on a semi-realistic test bench.

This bench, which was named MONT-BLANC, was built during the revamping of EVEREST. It nearly shares the main thermo-hydraulic features with EVEREST except for the size and the flow rate rangeability (figure 6). Table 3 shows the MONT-BLANC design specifications.

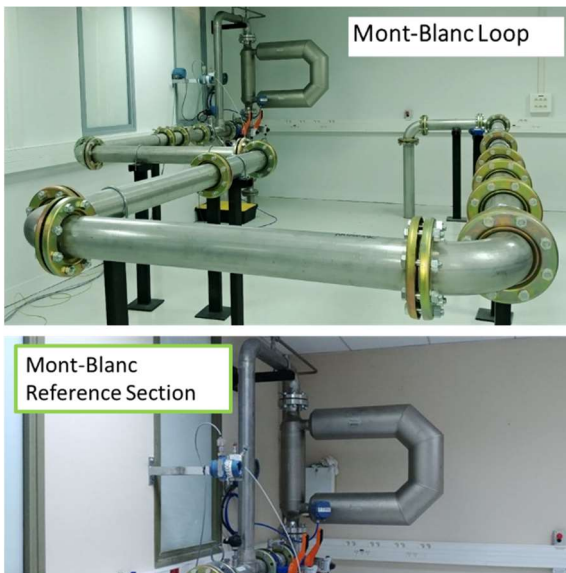


**Figure 6:** MONT-BLANC test facility overview (top) and details of the reference section (bottom).

In addition to ease velocity profile investigations MONT-BLANC allows also to perform calibration tests under low flow rate (from  $13 \text{ m}^3 \cdot \text{h}^{-1}$  up to  $150 \text{ m}^3 \cdot \text{h}^{-1}$ ). Maximum flow rate was set up to  $150 \text{ m}^3 \cdot \text{h}^{-1}$  which provides some possible inter-comparison calibration tests with EVEREST. Reference flow rate is elaborated thanks to a Coriolis meter. Reference volume flow

uncertainty is better than 0.1% for the overall flow rate range [3] [4].

Usual experimental tests are carried out on steady flow rate. Reference and test sections are set in the same floor while the operation section is set at the lower floor. It includes the circulation pump, the regulation valves, and the heat exchanger (cooling unit). A by-pass pipe is implemented in the reference section in order to inject, where appropriate, seeding particles for velocimetry measurements which use Laser-based technologies.

**Table 3:** Overview of the design specification of MONT-BLANC.

Prime Features	Details
Calibration test type	Closed regulated loop
Flow meter reference	Coriolis master meter
Test section pipe size	From DN40 up to DN150
Pipe compositions	Stainless steel
Fluid	Tap liquid water
Pressure range	From 1 up to 8 bar
Fluid temperature range	From 23.5°C up to 24.5°C
Environment Temperature	ambient temperature is regulated near 20°C
Flow rate range	From $13 \text{ m}^3 \cdot \text{h}^{-1}$ up to $150 \text{ m}^3 \cdot \text{h}^{-1}$
Flow metering uncertainty	0.1% (volume flow rate)

Since March 2019, some preliminary tests have been performed on MONT-BLANC with Particle Image Velocimetry (2D 3C PIV) system (figure 7). Later this year, some 3D3C PIV tests are scheduled before hopefully planning the implementation of this system on EVEREST loop next year.

With such a feature, MONT-BLANC constitutes also a tremendous experimental tool for assessing Computational Fluids Dynamics (CFD) software for liquid industrial pipe flow configurations.

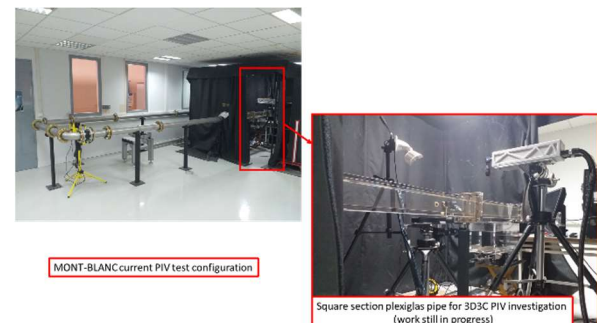


**Figure 7:** MONT-BLANC velocity profile investigation with 3D3C PIV system.

## 7. Conclusion

In 2016, EDF R&D has initiated a complete revamping of the EVEREST test bench which was achieved at the beginning of 2019. This comprehensive retrofit leads to a significant calibration accuracy improvement. The EVEREST reference volume flow uncertainty is now better than 0.1% from 50 m<sup>3</sup>.h<sup>-1</sup> up to 1200 m<sup>3</sup>.h<sup>-1</sup>. Moreover, in order to characterize the velocity profile impact on industrial meter metrological performance, two laser velocimetry measurement systems have been purchased. This effort leads also to the design of a mini-loop, called MONT-BLANC, whose purpose is to mimic EVEREST calibration features under a smaller size and a lower flow rate rangeability (from 13 m<sup>3</sup>.h<sup>-1</sup> up to 150 m<sup>3</sup>.h<sup>-1</sup>). This test bench will allow not only to ease Particle Image Velocimetry and Laser Doppler Velocimetry system preparations, adjustments and future implementations on EVEREST but also to provide an effective tool to investigate the influence of scale effect on flow meters and pipes flow physics.

## References

- [1] E. THIBERT, *Note d'opportunité du projet de rénovation et d'amélioration du banc d'essais EVEREST*, H-P1E-2015-05006-FR, EDF R&D, 2016.
- [2] S. BLAIRON, *CR - Comité d'engagement du projet de rénovation de la boucle Everest et compléments d'information*, 6125-3117-2016-14628-FR, EDF R&D, 2016.
- [3] D. BOLDO, *Référentiel qualité du laboratoire débitmétrie: incertitudes et contrôles intermédiaires*, 6125-3117-2019-00295-FR, EDF R&D, 2019.
- [4] NF ISO/CEI GUIDE 98-3, *Uncertainty of measurement — Part 3: Guide to the expression of uncertainty in measurement (GUM: 1995)*, ICS: 17.020, 2014.
- [5] N. LANCIAL, M. ARENAS, H. GAMEL, N. DESSACHY, E. THIBERT, J. VEAU, “*Pressure loss prediction by numerical simulations through a square-edged orifice in a round pipe*”, FLOMEKO (2016).
- [6] ISO 5167-2, *Measurement of fluid flow by means of pressure differential devices inserted in circular-cross section conduits running full - Part 2: Orifice plates*, Classification index: X 10-102-2, ICS: 17.120.10, June 2003.

# INVESTIGATION OF IN-LINE PRESSURE EFFECT ON PITOT TUBE MEASUREMENTS

I. CARE<sup>1</sup>, F. FOURNEAUX<sup>1</sup>

<sup>1</sup>CETIAT, Domaine scientifique de la Doua, 25 avenue des Arts, Villeurbanne, France  
E-mail (corresponding author): [isabelle.care@cetiat.fr](mailto:isabelle.care@cetiat.fr)

## Abstract

Pitot tubes are commonly used to measure gas flow in ducts. The integration of the velocity profile which allows the calculation of the gas flow is described in several international standards such as ISO 3966 or ISO 10780.

The common working principle of Pitot tubes is based on the measurement of the differential pressure between the two different pressure taps. The gas velocity is related to this differential pressure through a flow coefficient depending on the Pitot tube type.

In case of stable flow, in a pressurised duct, fluctuations of the in-line pressure, even low, can occur. If the response times of the two pressure lines (static and total) between the Pitot tube head and the differential pressure sensor are not equal, these fluctuations can be seen as fluctuations of the measured differential pressure and then of the calculated velocity.

This phenomenon is investigated for different design of Pitot tubes and the difference in behaviour of the two pressure lines is highlighted.

## 1. Introduction

In the middle of the past century, significant work was undertaken on Pitot tubes. This research led to recommendations for proper calibration and use to minimize the measurement uncertainty.

Some of these recommendations are summarized in ISO 3966 [1], for L-type Pitot tubes, in which different error sources are listed. When the conditions are fulfilled, an uncertainty of about 2% ( $k=2$ ) can be achieved on the flow rate when using L-type Pitot tubes.

However, if fluctuations, even small, of the static pressure occur inside the duct, an artificial differential pressure measured by the pressure sensor could be generated if the response time is not the same at the two pressure taps of the Pitot tube. As a consequence, unexpected fluctuations in the velocity (and flow) would be measured.

This has already been observed in industrial applications when measuring an air flow rate of a slightly pressurised flow with a L-type Pitot tube, as shown in Figure 1.

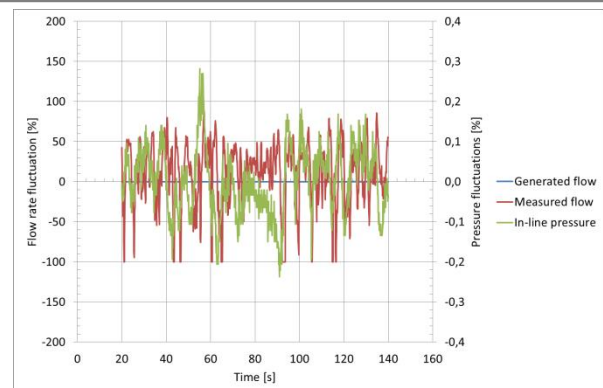


**Figure 1:** Results of unexpected fluctuating flow rate observed in a pressurized duct

In this application, a flow is generated at a rate of  $3.2 \text{ m}^3/\text{h}$  and an overpressure of 150 mbar in the pipe. This flow rate is measured with a mass flow meter. The observed fluctuations of flow (blue line, left axis) and pressure (green line, right axis) are both less than 0.2% of the flow rate.

When measuring the flow with a Pitot tube inserted in the pipe, the observed fluctuations (red line, left axis) are 60% of the rate.

In order to contribute to the understanding of this phenomenon, this paper presents some analysis for different types of Pitot tube.

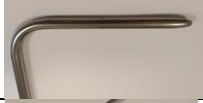
## 2. Preliminary results

### 2.1 Pitot tubes

In 2018, preliminary results were presented at ISFFM [2] for 8 Pitot tubes of different design. In this paper, 7 of these 8 ones are under investigation:

- 6 are L-type Pitot tubes designed according ISO 3966 [1] and are of different head diameter: 2 are of NPL type, 1 is of AMCA type and 3 are of CETIAT type. They differ by the shape of the nozzle
- 1 is a straight Pitot tube manufactured by TSI Inc.

**Table 1:** The tested Pitot tubes

Pitot tube type		Designation and head diameter (mm)
NPL		MAG1 (Ø8) MAG2 (Ø4)
AMCA		MAG4 (Ø5)
CETIAT		ANEMO2 (Ø4) MAG3 (Ø3) MAG5 (Ø8)
TSI		ANEMO3

When using a Pitot tube, the relation between the measured differential pressure,  $\Delta P$ , and the velocity,  $V_{Pitot}$ , is given by Equation (1):

$$V_{Pitot} = K \times \sqrt{\frac{2 \times \Delta P}{\rho}} \quad (1)$$

with:

- $\rho$ , the density of air
- K, the coefficient of the Pitot tube, closed to one for the Pitot tubes designed according ISO 3966 [1] or specified by the manufacturer for the others

### 2.2 Experiment facility and results

In 2018, preliminary results were presented at the ISFFM conference [2]. A fast decrease of pressure in a closed chamber was generated and the measured differential pressure by the Pitot tube recorded, as well as the pressure inside the volume.

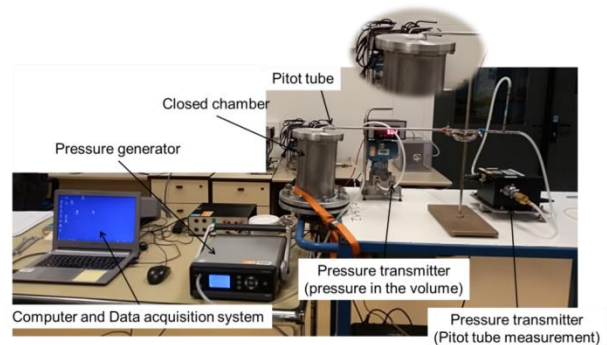


**Figure 2:** Experimental setup for characterization of Pitot tube

In the setup (Figure 2), the differential pressure is measured with a MKS 220D pressure transmitter (range  $\pm 2$  torr), the pressure in the chamber with a Rosemount 3051 pressure transmitter (range 0 – 400 Pa). The measurements are recorded with an Agilent 34972A data acquisition system. The closed chamber is a cylinder with a height of 27 cm and a diameter of 13.5 cm.

A pressure generator was used to set the pressure in the closed chamber at a given value over the atmospheric pressure. The tests were performed at a pressure of 50, 100 and 150 Pa.

The Pitot tube was put tightly in the closed chamber in such a way that the total pressure tap was not directly submitted to the flow generated by the pressure decrease.

The results of the tests were drawn as in Figure 3 for the Pitot tube named MAG4 and an initial pressure of 150 Pa in the closed volume.

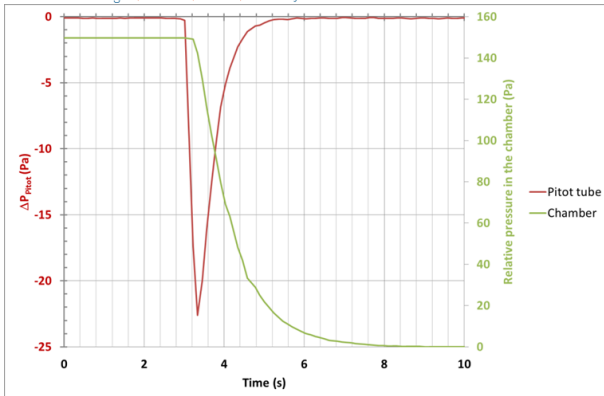


**Figure 3:** Differential pressure measured by the Pitot tube (MAG4) and pressure in the chamber over time

At the beginning and the end of the test, the measured differential pressure (red line, left axis) is zero as there is no flow in the volume. During the decrease of the static pressure (green line, right axis), a peak is observed in the differential pressure measurement.

In 2018, it has been shown that the value of this peak is depending on the Pitot tube type, its head diameter as shown in Figure 4.

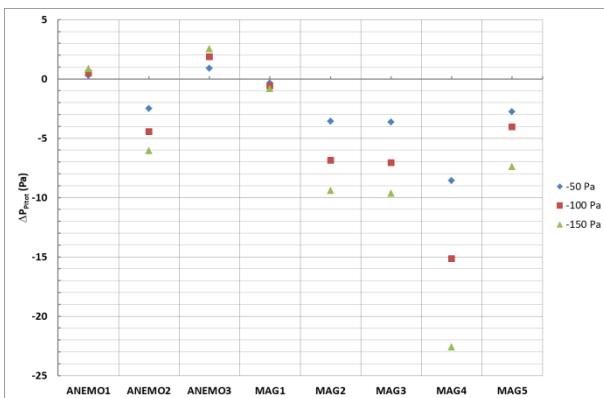


**Figure 4:** Maximum differential pressure measured by the Pitot tubes

It depends also on the length of the tubing between the "+" or the "-" ports of the pressure transmitter and the pressure taps at the Pitot tube.

### 3. Characterization of the pressure lines of the Pitot tubes

#### 3.1 Experimental setup

In 2018, it was then demonstrated that the observed fluctuations were due to a difference in the response time of the two pressure lines of a Pitot tube. The response time of the line is depending both on its resistance and on the encapsulated volume.

In 2019, a new experiment has been set up (Figure 5) to evaluate separately the resistance of the static pressure and total pressure lines of a Pitot tube.

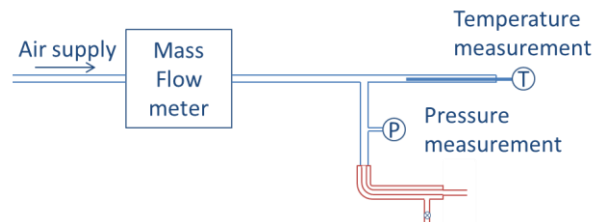


**Figure 5:** Scheme of the set up for the measurement of the resistance of a Pitot tube pressure line

In this experiment, the objective is to measure the flow rate at a pressure line (total or static) for a given upstream pressure while the second pressure line is kept at atmospheric pressure.

The upstream pressure is measured with a MKS 220D pressure transmitter (range  $\pm 2$  torr) and adjusted between 10 and 200 Pa.

At each upstream pressure, the mass flow rate is measured with a:

- Molbloc L meter above 75 cm<sup>3</sup>/min
- Brooks 5850E mass flow controller between 7 and 75 cm<sup>3</sup>/min
- Alicat MC-10SCCM mass flow controller below 7 cm<sup>3</sup>/min

Nota: The flow rate is expressed at normal conditions of temperature and pressure (0°C, 101325 Pa).

#### 3.2 Results and discussion

The measurements are performed for the seven Pitot tubes listed in Table 1 and the results are presented in Figure 6a and 6b as the upstream pressure against the measured mass flow.

For all the tests, the used tubing is the same and the observed difference in the resistance of the Pitot tubes is then the one due to the Pitot tube pressure line itself.

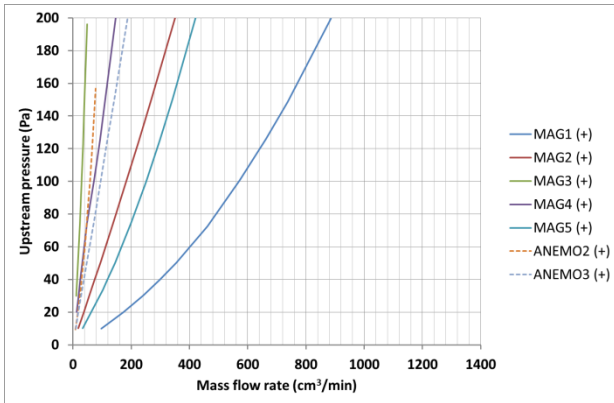


**Figure 6a:** Resistance of the total pressure line for the different Pitot tubes

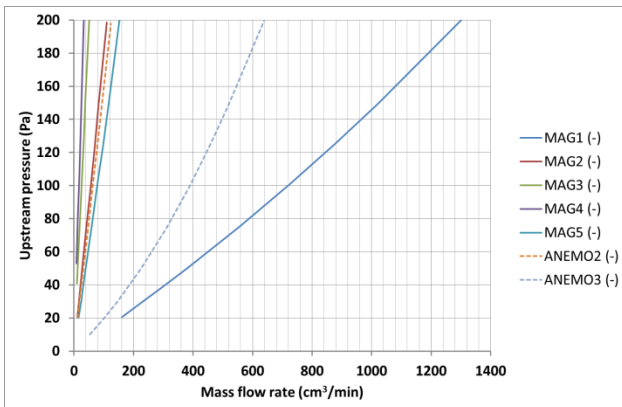


**Figure 6b:** Resistance of the static pressure line for the different Pitot tubes

Considering an upstream pressure, the higher the flow rate is, the faster the pressure balances in the encapsulated volume of a given Pitot tube line.

For the different Pitot tubes, the pressure is related to the mass flow rate as a linear function or a combination of a linear and a function of degree 2.

Several situations can be found. The pressure lines of the MAG4 Pitot tube are both related with a linear function to the mass flow rate as shown in Figure 7 below.

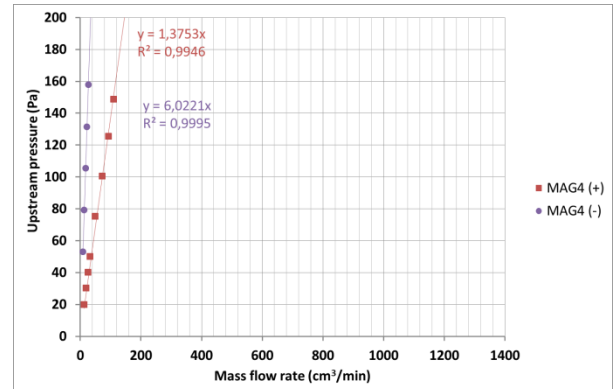


**Figure 7:** Resistance of the two pressure lines of the MAG4 Pitot tube

The pressure lines of the MAG1 Pitot tube are both related with a sum of a linear and a quadratic function to the mass flow rate as shown in Figure 8 below.

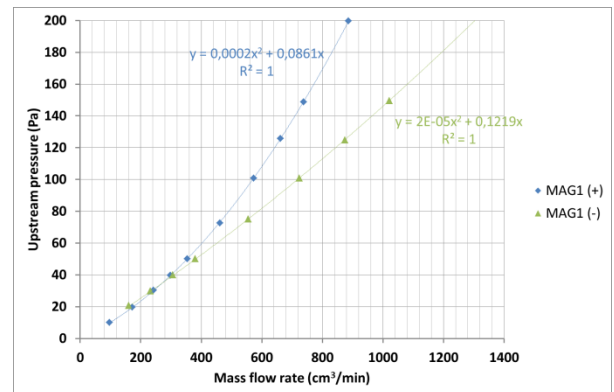


**Figure 8:** Resistance of the two pressure lines of the MAG1 Pitot tube

Moreover, some intermediate situation can be found, as for Pitot tube MAG5 with a static pressure line presenting a linear function when the total one is the sum of a linear function and a quadratic one.

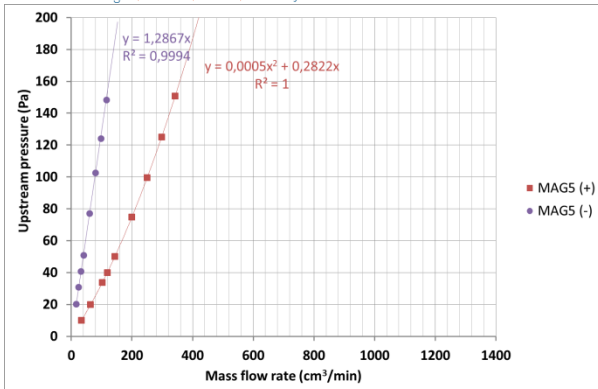


**Figure 9:** Resistance of the two pressure lines of the MAG5 Pitot tube

Furthermore, it can be noticed that for all Pitot tubes the resistance is almost equivalent for the two pressure lines except for the straight and non-normalized one, named ANEMO3 for which the total pressure line is much more resistant than the static one as shown in Figure 10.

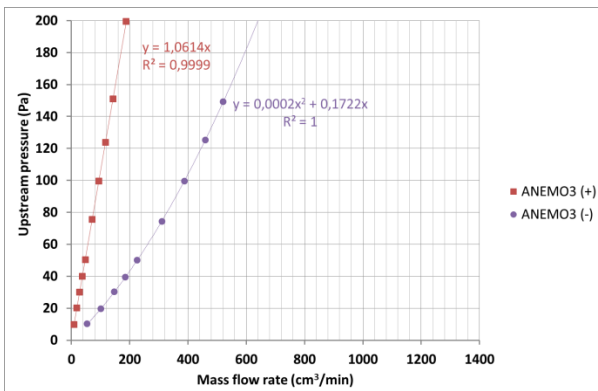


**Figure 10:** Resistance of the two pressure lines of the ANEMO3 Pitot tube

When the resistance is high, it is then driven by a linear relation to the mass flow rate whereas it is driven by the sum of a linear and a quadratic function when it is low. This behaviour is neither explicitly related to the type of the Pitot tube nor by its diameter.

When the resistance of the static pressure line is low (MAG1, see Figure 8 and ANEMO3, see Figure 10), the time to reach the equilibrium in the encapsulated volume is small. As a consequence, the error on the measurement of the fluctuations of the static pressure in a pipe is small. The differential pressure measured by the Pitot tube when submitting to a step change of pressure is

then close to zero for the MAG1 Pitot tube which presents also a low resistance on the total pressure line and slightly positive for the ANEMO3 Pitot tube with a higher resistance on the total pressure line.

#### 4. Conclusion

Unexpected of fluctuations in flow can be observed when using a Pitot tube in a pressurized pipe. In 2018, this phenomenon has been highlighted for different types of Pitot tubes.

The objective of the tests carried out this year was to highlight the characteristics of the static and total pressure lines separately.

It has been identified that the phenomenon is mainly driven by the resistance of the static pressure line.

Some further investigations should be performed to be able to give recommendations for the design a low resistance static pressure line of a Pitot tube, and to deduce a predictive model allowing the determination of the expected fluctuations for a given Pitot tube.

#### References

- [1] ISO 3966: *Measurement of fluid flow in closed conduits — Velocity area method using Pitot static tubes*, 2008.
- [2] Care I, Fourneaux F, "Investigation of in-line pressure effect on Pitot tube measurements" in *ISFFM Proc.*, 2018.

# Numerical Simulation and Experiment of Gas Mass in pVTt Standard Container under Isothermal Boundary Condition

Ruo-xuan LIU, Ming-zheng ZHU, Yu-ming SHEN

University of Shanghai for Science and Technology, 516 Jungong Road, Shanghai, China  
E-mail (corresponding author): ym-shen@usst.edu.cn

---

## Abstract

Focusing on a 36m<sup>3</sup> horizontal pVTt standard container, the intake process and homogeneous process of the gas in the container were numerically simulated in constant wall temperature and constant velocity as the inlet boundary condition. A new algorithm for calculating the average temperature in the standard pVTt container was proposed, whose name was mass temperature average. The simulation results showed that in the natural convection process after gas intake, the average mass temperature  $\bar{T}$  of the gas in the container slowly decreased with time in parabolic shape and tended to wall temperature, while the average pressure drops sharply and quickly reached uniformity. Through numerical simulation and experimental verification, it was found that the gas mass in the container was linear with  $\ln \bar{T}$ .

---

## 1. Introduction

The gas calibration facility to pVTt technique mostly uses a horizontal standard container. The container needs to be pumped and inflated when a sonic nozzle is calibrated on the facility. The temperature and pressure of the gas in the vessel are stable and uniform after the gas undergoes a long period of natural convection in the vessel.

Two methods are generally used to shorten the time when the temperature field in the standard container reaches a stable and uniform state: water bath or oil bath cooling<sup>[1-2]</sup>.

For example, NMIJ from Japan uses the interlayer water bath constant temperature cooling method in pVTt container, which eliminates the seasonal influence and time-varying characteristics of environmental temperature gradient. The stabilization time is about 30 minutes, and the uncertainty of the facility is better than 0.05% (k=2)<sup>[3]</sup>. This is also the method commonly used in China today.

The other one is to install a fan and air duct in the container<sup>[4]</sup> to force the gas in the container to convective movement. For example, a high-flow pVTt standard container in NIST is equipped with air ducts and agitator fans, while the gas reaches a stable state after being forced convection heat

transfer for 45 minutes, and the uncertainty of the facility is 0.13% (k=2)<sup>[5-6]</sup>. However, due to the heat of the fan itself and the influence of the ambient temperature, the gas stability effect in the actual measurement does not achieve the desired effect.

However, the methods above cannot completely avoid the influence of temperature inhomogeneity caused by intake and exhaust. So the scholars use numerical simulation technology to study the uncertainty characteristics of temperature field.

For example, Lihong Yang<sup>[7]</sup> of Shanghai Jiao Tong University used software FLUENT to numerically simulate the deflation process of empty containers and isothermal vessels, and obtained the velocity field distribution, temperature field distribution and their variation law during deflation. Ruiqin Bai et al<sup>[2]</sup> from Zhe Jiang institute of econometrics used software FLUENT to carry out unsteady simulation research on the temperature field characteristics of pVTt method facility under natural environment and constant temperature of water bath. They concluded that the stable time of constant temperature of water bath is shorter than that of natural environment, and they gave the idea of temperature measuring point layout. Xuening Zhao<sup>[8]</sup>, from Shanghai University of Science and Technology, has carried out numerical simulation on the process of inlet and exhaust of pVTt standard container under two boundary conditions

of adiabatic wall and constant temperature wall. The results show that under the condition of adiabatic wall, the stable time of gas temperature in the container is shorter.

Most of the literatures above only discussed the temperature field and pressure field in the pVTt container, but did not directly discuss the mass (or mass distribution) of the gas in the container.

In this paper, the numerical simulation model is optimized to explore the gas mass distribution law and internal relations in the container. Under the condition of constant wall temperature, the natural convection process of the air in a horizontal pVTt standard container with a volume of 36 m<sup>3</sup> was simulated, and the distribution cloud chart of the temperature and pressure of the air in the container was obtained. A new temperature averaging method, namely "mass average temperature  $\bar{T}$ ", is proposed, and the functions of  $\bar{T} \sim t$ ,  $p \sim t$  and  $p/\bar{T} \sim \ln \bar{T}$  are obtained. The numerical simulation shows that  $p/\bar{T}$  is inversely proportional to  $\ln \bar{T}$ . The 30 sets of experiments were carried out during the intake and natural convection processes of the facility. The experimental data were used to fit the trend curve, and the correctness of the inverse proportional linear relationship obtained via the numerical simulation was verified.

## 2. Working Principle

During the time interval  $\Delta t$ , the pVTt standard container of volume  $V$  is evacuated and inhaled, and when the process is completed and the temperature and pressure are both stable and uniform, the temperature  $T$  and the pressure  $p$  of the gas in the vessel are respectively measured. Regardless of the compression factor and the container temperature correction, the mass flow rate  $q_m$  of the gas flowing into the standard vessel can be calculated based on the ideal gas state equation.

$$q_m = \frac{\Delta m}{\Delta t} = \left( \frac{V}{R/M} \right) \left[ \left( \frac{p}{T} \right)_2 - \left( \frac{p}{T} \right)_1 \right] / \Delta t \quad (1)$$

Where  $R$  is the universal gas constant and  $M$  is the molecular weight of the gas, so  $\left( \frac{V}{R/M} \right)$  is a constant. So,  $(p/T)_2 - (p/T)_1$  can qualitatively represent the mass of the gas in the container.

## 3. Governing Equation

By establishing the governing equation and solving the change of the air temperature  $T$  and the pressure  $p$  in the container over time after air intake, the internal relation between the gas mass in the container and the average temperature in the changing container were found. In theory, the average temperature of the gas in the vessel gradually approaches the wall temperature due to the boundary conditions of constant wall temperature.

Assuming that the air is a viscous compressible ideal gas, the continuity equation, the momentum equation and the energy equation are satisfied in the process of natural convection.

*Continuity Equation*

$$\frac{\partial \rho}{\partial t} + \nabla \cdot (\rho \bar{u}) = 0 \quad (2)$$

Where,  $\rho$  is the density of air (kg/m),  $t$  is time (s),  $\bar{u}$  is the velocity of air (m/s).

*N-S Equation*

$$\rho \frac{D\bar{u}}{Dt} = \rho \bar{F} - \nabla p - \nabla \cdot \left( \frac{2}{3} \mu \nabla \cdot \bar{u} \right) + \mu \Delta \bar{u} \quad (3)$$

Where,  $\mu$  is the aerodynamic viscosity coefficient (Pa.s),  $p$  for pressure (Pa).

*Energy Equation*

$$\rho c_v \frac{DT}{Dt} = -\rho \nabla \cdot \bar{u} + \nabla \cdot (k \nabla T) + \rho q \quad (4)$$

Where,  $c_v$  is the specific heat at constant volume J/(kg.K),  $T$  is the thermodynamic temperature in units (K),  $k$  is the thermal conductivity W/(m.K),  $q$  is the heat given by the heat source to the fluid per unit mass in unit time,  $-\rho \nabla \cdot \bar{u}$  is the work done by the normal pressure  $p$  when the air volume is deformed relative to the line, and the item  $\nabla \cdot (k \nabla T) + \rho q$  is the heat intake for other reasons such as heat radiation and heat conduction.

In the equations (2)~(4) above, there are six physical quantities ( $\rho$ ,  $\bar{u}$ ,  $T$ ,  $p$ , etc.) unknown.. But there are only five equations. In order to make the system closed, we need to add an equation of state.

*Ideal gas equation of state*

$$pV = m \left( \frac{R}{M} \right) T \quad (5)$$

Where  $m$  is the air mass (kg),  $M$  is the average molar mass of air (kg/mol),  $R$  is the general ideal gas constant J/(mol.K) and  $V$  is the standard

volume (m<sup>3</sup>) of the vessel. At this point, all the equations are closed.

#### 4. Mass average temperature

At present, in the calibration practice,  $n$  temperature sensors are arranged in the standard container, and the  $n$  temperature sensors are processed by arithmetic mean, which is

$$T = \frac{1}{n} \sum_{i=1}^n T_i$$

The obtained  $T$  is substituted into the formula (1) to calculate the gas mass. When the temperature of the gas in the vessel is uniform, the gas mass can be calculated with the arithmetic mean temperature to obtain a sufficiently accurate gas quality.

We believe that it is meaningless to perform arithmetic averaging of  $n$  temperature sensors when the temperature in the vessel has not reached uniformity. However, each temperature sensor can be used to calculate the mass of the gas in the vicinity of the temperature sensor. Assuming that the sensors are evenly distributed in the container, the gas mass in the  $1/n$  region near each temperature sensor can be expressed as

$$m_i = \frac{\rho \left( \frac{V}{n} \right)}{\left( \frac{R}{M} \right) T_i} \quad (6)$$

Where  $p$  is the uniform and stable gas pressure. The total mass of the gas in the container is

$$m = \sum_{i=1}^n m_i = \frac{\rho V}{\left( \frac{R}{M} \right)} \left( \sum_{i=1}^n \frac{1}{T_i} \right) n^{-1} \quad (7)$$

Define

$$\tilde{T} = n \left( \sum_{i=1}^n \frac{1}{T_i} \right)^{-1} \quad (8)$$

The temperature expressed by the formula (8) is referred to as "mass average temperature".

According to the calculation, when the temperature unevenness deviation is 10K at 293K, the calculation of the gas mass in the container by the "mass average temperature" can improve the calculation accuracy by 0.03% compared to the arithmetic average temperature calculation method. The larger the deviation of temperature uniformity, the larger the deviation of gas mass calculated by arithmetic mean temperature. Unless otherwise stated herein, mean temperature means "mass average temperature".

## 5. Modeling and boundary conditions

### 5.1 Modeling and grid generation

The physical model is a horizontal pVTt standard container with a diameter of about 2.2m and a total volume of about 36m<sup>3</sup>. The inlet pipe has a diameter of 150mm and is located at the side of the horizontal tank, as shown in Figure 1.

Considering the advantages of fast generation of the structured mesh, the good mesh quality, and the easier convergence of calculations, structural meshing is used. Among them, the middle cylinder part is divided into hexahedral meshes, and the hemispheres on both sides are divided into tetrahedral meshes. In order to achieve better grid accuracy and a calculation speed, the left and right hemispheres, the air inlet, the inlet pipe and the cylinder connection part and the vicinity of the container are all encrypted.

The number of grids calculated by the container is about 3.5 million. The mesh quality parameter of more than 88% is greater than 0.85, the total mass parameter of the grid is greater than 0.6, the minimum angle is  $\geq 45^\circ$ , and the number of negative grids is 0. The container 3D model and its meshing are shown in Figure 1.

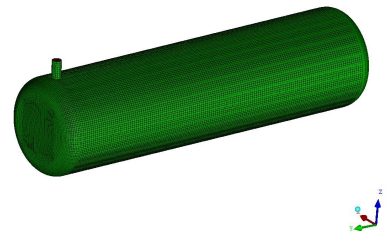


**Figure 1:** 36m<sup>3</sup> horizontal pVTt standard container model with grid division.

### 5.2 Control parameters and boundary conditions

In this paper, the pVTt standard container calibration process is simulated, that is, in the process of air inlet, after the calibration is completed and the valve is closed, in the process of natural convection of the gas in the container, the air temperature and the pressure in the container change over time, which belongs to unsteady, viscous compressible gas flow. The coupling, density-based and absolute velocity implicit transient solver is used in CFD calculation. The governing equations described in the third part of the paper are used, and the Realizable  $k$ - $\epsilon$  turbulence model is used. The medium is air and satisfies the ideal gas state equation. In addition,

considering the influence of the gas mass force, a negative gravitational acceleration is added to the z-axis.

The wall surface of the container satisfies the condition of no slip boundary; the temperature of the wall surface of the vessel and the initial temperature of the container are both set to 297.3 K, which is consistent with the measured temperature; the initial pressure is 0.1 kPa, that is, the gas state after the end of the pumping and stabilization.

The inlet process was set as the boundary condition of the inlet with a constant flow rate, and the air flow rate was 0.284m<sup>3</sup>/s, that is, the velocity of flow of the inlet air was 16.082m/s, which was also consistent with the actual flow rate of the sonic nozzle tested.

## 6. Numerical simulation and analysis

Due to space limitations, this article only describes the process of gas convection after the gas enters the container. Among them, the intake end time is taken as the initial state of the natural convection process.

From the ideal gas state equation, the gas temperature deviation is 0.5K at 20°C and the gas mass will produce a calculation error of 0.17%. When the pressure deviation is 10Pa, the gas mass will produce a calculation error of 0.02%. For the actual measurement practice, ignoring the sensor error, it is obvious that the temperature and pressure unevenness deviation should be as small as possible, for example, the temperature uniformity is controlled to be 0.1K and the pressure unevenness is controlled within 5 Pa.

In order to shorten the calculation time, when the average temperature difference in the container is less than 0.5k and the pressure difference is less than 10Pa, it is deemed that the average temperature and the pressure in the container have reached a uniform state, and the calculation is completed.

### 6.1 Intake Process

When the intake is about 1 minute, close the valve and the intake is over. When the valve closes, the temperature distribution cloud in the standard container is shown in Figure 2.

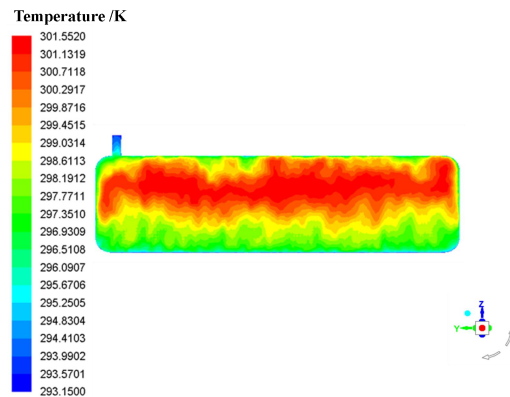


**Figure 2:** Cloud diagram of gas temperature distribution in the longitudinal section of the container at the end of inlet.

As can be seen from Figure 2, the temperature difference of the air in the container at the end of inlet is >8K. The temperature along the axial direction (x axis) of the container presents a zonal distribution, indicating that the temperature gradient in this direction is not obvious. And along the vertical direction of the container (that is, along the diameter of the container), there is a large temperature gradient. Because of the constant wall temperature, the gas temperature near the wall is low.

Due to the continuous filling of low-temperature air in the intake process, the inlet pipe temperature is relatively low. The gas temperature in the area where the inlet pipe is connected to the container is higher, which is due to the large flow rate of air filled and the violent movement of gas molecules. It can also be seen from Fig. 2 that the temperature in the hemisphere region at the left and right ends of the container is high due to insufficient heat exchange of the air; and because the density of the hot air is small, the temperature in the upper region of the container is also high.

### 6.2 Natural Convection Process

When the intake valve is closed, natural convection occurs in the air in the container. The numerical simulation shows that after about 10 minutes of convection heat transfer, the average temperature and the pressure of the air in the container are basically stable.

Figure 3 is the temperature distribution cloud diagram after the air in the container is basically uniform.

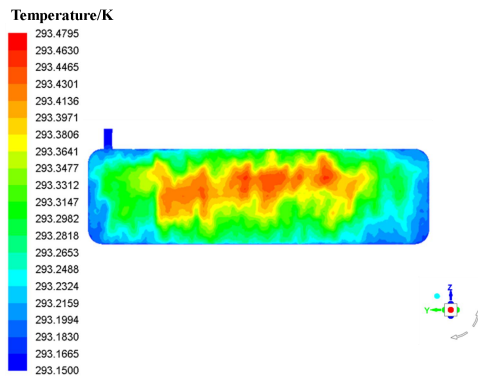


**Figure 3:** Temperature distribution cloud diagram after uniform air intake.

It can be seen that when the temperature field is in a stable state, it is symmetrically distributed along the axis of the container (x axis), and the maximum temperature difference in each region is  $< 0.3K$ . After the stability of convection heat transfer, the average temperature of the air in the container is close to the wall temperature. The isotherm is a circle along the axis of the container, and the temperature in the middle region is slightly higher than that in other regions.

Figure 4 is the pressure distribution cloud diagram after the air in the container is basically uniform.

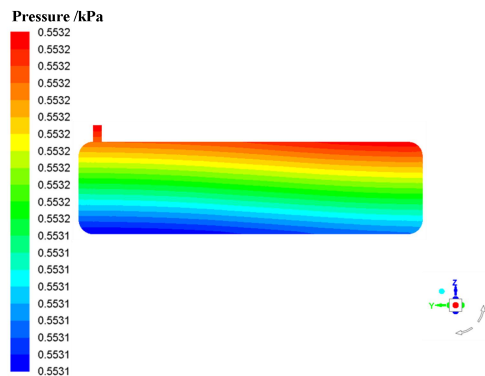


**Figure 4:** Cloud diagram of pressure distribution after uniform air intake.

It can be seen that when the pressure field is in a stable state, the pressure in the container presents a stratified and zonal uniform distribution.

## 7. Gas Mass Analysis and Experiment

The mass of gas in the vessel is calculated by determining the temperature and the pressure of the gas in the vessel. Figure 5 shows the comparison between the simulated and experimental results of the curve of the average temperature  $\bar{T}$  of air in the container with time  $t$  in the process of natural convection.

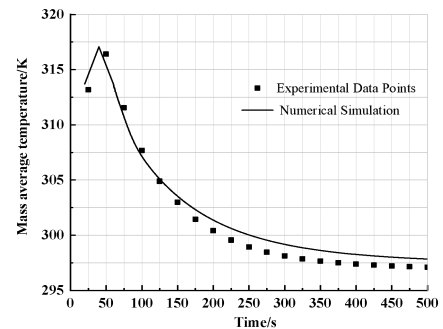


**Figure 5:** Curve of average temperature change of mass in homogeneous process.

According to the observation curve and the experimental results, the average temperature of the air in the container at the end of inlet is about 300.6K. At the beginning of natural convection, the mean temperature rises slightly and then decreases monotonously. At about 500s, the temperature field in the container is basically stable, and the average temperature tends to the wall temperature of 297.3K. This shows that the constant wall temperature condition can promote the natural convection of air in the container, effectively inhibit the fluctuation of the temperature field, and accelerate the temperature field to reach a uniform state.

Figure 6 is a graph showing the average pressure  $p$  of the air in the container during the natural convection process as a function of time  $t$ .

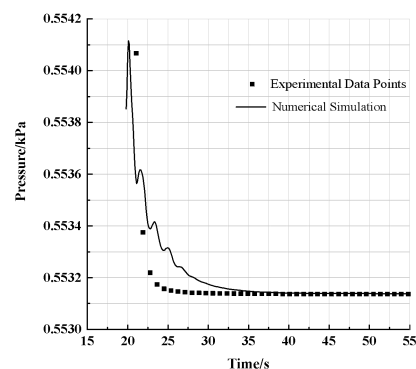


**Figure 6:** Curve of mean pressure change in uniform process.

It can be seen that in the early stage of natural convection, the average pressure fluctuation in the container fluctuates frequently and monotonously drops sharply, and then gets steadily and slowly.

The pressure field in the container is basically stable at about 35s and the average pressure at the time of stabilization tends to 0.5531 kPa.

The numerical simulation data in the uniform process is used to make a relationship between  $p/\bar{T}$  and  $\ln \bar{T}$ , as shown in Figure 7.

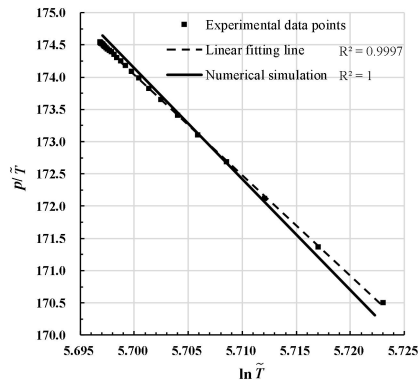


**Figure 7:** Numerical simulation results of the relationship between  $p/\bar{T}$  and  $\ln \bar{T}$  in a homogeneous process.

It can be seen that  $p/\bar{T}$  representing the mass of the gas is inversely proportional to  $\ln \bar{T}$ . The horizontal standard vessel was tested in a constant temperature environment. In the experiment, the temperature values of 40 temperature sensors and the average pressure at the recording time were recorded every 1 minute. Thirty experiments were carried out over a period of two months.

The relative error statistics of 30 groups of experimental data and simulated values are shown in Figure 8.

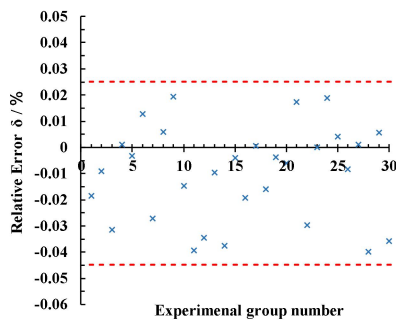


**Figure 8:** Relative error statistics of 30 groups of experiments.

By calculating the relative error between the theoretical linear equation and the experimental data, the absolute value of the average relative error is about  $|\bar{\delta}| \approx 0.0158\%$ , of which the experimental data of 15 groups is  $|\delta| < 0.0098\%$ .

It can be seen from the Figure 8 that the error of the experimental data of a small group is  $>0.04\%$ , which is due to the unstable water temperature of the container spacer during the experiment.  
FLOMEKO 2019, Lisbon, Portugal

## 8. Conclusion

Under the condition of constant wall temperature, numerical simulation and experiment were carried out on the process of natural convection and air inlet of the  $36\text{m}^3$  pVTt standard container, and the following conclusions were obtained:

(1) The algorithm of vessel mass average temperature is derived. The calculation precision of gas mass can be improved by using mass average algorithm compared with arithmetic average algorithm.

(2) In the process of natural convection, it is verified by numerical simulation and experimental data that  $p/\bar{T}$  and  $\ln \bar{T}$  satisfy the inverse proportional linear relationship, and the average relative error between the simulated theoretical value and the experimental results of the 30 groups is about 0.0158%.

## References

- [1] Johnson A N, Wright J D, Moldover M R, et al. Temperature characterization in the collection tank of the NIST 26 m<sup>3</sup> PVTt gas flow standard[J]. Metrologia, 2003, 40(5): 211.
- [2] Ruiqin Bai, Jia Cheng, Dongsheng Li, et al. Simulation study on temperature field of gas flow standard device using constant temperature pVTt method in water bath [J]. Sensor and microsystem, 2011, 30(12): 43-46.
- [3] Ishibashi M, Morioka T. The renewed airflow standard system in Japan for 5–1000 m<sup>3</sup>/h[J]. Flow measurement and instrumentation, 2006, 17(3): 153-161.
- [4] Wright J D, Johnson A N, Moldover M R. Design and uncertainty analysis for a PVTt gas flow standard[J]. Journal of research of the National Institute of Standards and Technology, 2003, 108(1): 21.
- [5] Johnson A N, Wright J D, Moldover M R, et al. Temperature characterization in the collection tank of the NIST 26 m<sup>3</sup> PVTt gas flow standard[J]. Metrologia, 2003, 40(5): 211.
- [6] Johnson A N, Wright J D. Gas Flowmeter Calibrations with the 26 m<sup>3</sup> PVTt Standard[J]. NIST Special Publication, 2005, 1046.
- [7] Lihong Yang. Numerical simulation and thermodynamic model study of vessel venting process [D]. Shanghai jiaotong university, 2007.
- [8] Xuening Zhao. PVTt standard container flow field simulation based on software FLUENT [J]. Software guide, 2008, 17(02): 154-157.

# Simulation and Research on Flow-field of Butterfly Valve in Standard Variable Head Flow Device

F. Lu<sup>1</sup>, J.M. Zhang<sup>2</sup>, Y.M. Shen<sup>3</sup>

<sup>1,3</sup> University of Shanghai for Science and Technology, 516 JunGong Road, Shanghai, China  
<sup>2</sup> Shanghai Institute of Metrology and testing Technology, 1500 ZhangHeng Road, Shanghai, China  
E-mail : ym-shen@usst.edu.cn

---

## Abstract

For the butterfly flow-regulating valve commonly used in the variable head flow standard device, the three-dimensional flow field in the valve body was simulated during the flow regulating process by CFD dynamic mesh technology. The flow field changes with cloud maps in the internal and downstream piping of the valve body under several operating conditions of 10°, 30°, 45°, 60° and 90° opening was proposed in the condition of constant water head. The simulation results also show that there are two opposite vortices in the flow field downstream of the valve body at 10° and 30° opening, and the valve opening has a nonlinear function relationship with the flow. Meanwhile, The flow control function of butterfly valve was presented to keep the flowrate constant under variable head conditions. Experiments were carried out on a variable head simulation device with an effective head of 3m and a pipe diameter of 150mm. Experiments show that the control function can be used to open-loop control the butterfly valve, and the control accuracy of flow fluctuation less than 1% can be obtained.

---

## 1. Introduction

The butterfly valve is a flow control device for start-stop control or flow regulation in the standard flow device of constant and variable head. In the variable head device, the flow rate in the calibration line is controlled to be close to a stable value by controlling the opening degree of the butterfly valve. In order to obtain the ideal flow characteristics, domestic and foreign scholars have conducted extensive research on butterfly valves. For example, Leutwyler and Shen Yang<sup>[3,4]</sup> et al. studied the fluid-pneumatic torque characteristics of the centerline butterfly valve under steady-state conditions, and obtained the relationship between the aerodynamic torque and the valve opening under different pressure differences; Using three-dimensional numerical simulation technology, the flow of incompressible fluid inside the butterfly valve under the fixed opening was analyzed by Huang and Kim<sup>[5]</sup>. The three-dimensional steady-state simulation calculation on the hydrodynamic characteristics of the butterfly valve were performed by Henderson and Yang Zhixian<sup>[6,7]</sup> respectively. The phenomenon of flow separation and vortex formation in the downstream pipeline of butterfly valve was analyzed, and the variation law of dynamic torque coefficient with valve opening degree was discussed. Most of these studies

discuss the torque characteristics of the flow field to the butterfly valve. In this paper, using dynamic grid and CFD technology, three-dimensional dynamic simulation of the internal and upper flow fields of the butterfly valve during the opening process is carried out under the condition of constant water head; the evolution process of the flow field vortex downstream of the butterfly valve is simulated; and for the specific variable head standard device, under the unsteady condition, the butterfly valve-based control function is used to obtain a constant flow with a fluctuation of less than 1% control precision.

## 2. Modeling and Gridding

Taking the DN150 butterfly valve as an example, take the butterfly valve and the upstream pipe  $L_1 = 2D$  ( $D$  is the inner diameter of the pipe) and the downstream pipe  $L_2 = 10D = 10D$  as the calculation domain. The valve is horizontally placed in the +X flow direction and ignoring the mass force.

The calculation domain is divided into grid using ANSYS ICEM. The calculation domain of the dynamic grid in the 0.5D length range of the upstream and downstream of the butterfly valve is divided into triangle unstructured grids and the grids is encrypted. The total number of grids is

about 450,000. The upstream and downstream pipelines of the butterfly valve are divided into tetrahedral grid and connected to the dynamic grid pipeline through the interface. The total number of grids is about 340,000. By programming the UDF code, UDF (User Defined Functions) method is adopted to realize the process of opening the butterfly valve at a uniform rotation speed of 0.05 rad/s. In the process of numerical simulation, the dynamic grids region of the butterfly valve motion is reconstructed by the Smoothing, Layering and Remeshing methods, and the iterative iteration is used to solve the dynamic grid problem of the unsteady flow field during the butterfly valve opening process.

The UDF program for the butterfly revolution:

```
#include "udf.h"
DEFINE_CG_MOTION(moving_body, dt, vel,
omega, time, dtime)
{
    omega[0] = 0.0;
    omega[1] = 0.0;
    omega[2] = 3.14/20;
}
```

The dynamic grid computing domain is shown in Figure 2.

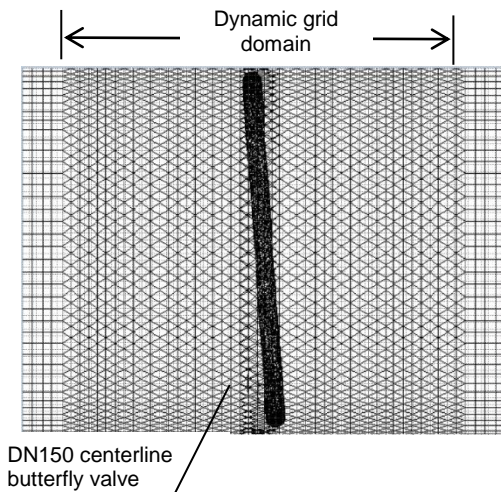


Figure 1: Butterfly valve gridding

### 3. Control equations and boundary conditions

Assuming that the inside of the butterfly valve is an unsteady, incompressible viscous liquid flow, the Reynolds equations (continuity equation and NS momentum equation) and the Realizable k-ε model with swirl correction are used to form a closed

equation group. Among them, the Reynolds average equation is:

$$\frac{\partial \rho}{\partial t} + \nabla \cdot (\rho \vec{U}) = 0 \quad (1)$$

$$\frac{\partial}{\partial t} (\rho \vec{U}) + \nabla \cdot (\rho \vec{U} \vec{U}) = -\nabla p + \mu \nabla^2 \vec{U} + \vec{S}_M \quad (2)$$

Where:  $\vec{U}$  is the velocity vector of the liquid;  $p$  is the liquid pressure;  $\rho$  and  $\mu$  is the density and dynamic viscosity of the liquid respectively.

The transport equations for the turbulent flow energy and dissipation of the Realizable k-ε model are:

$$\frac{\partial}{\partial t} (\rho k) + \frac{\partial}{\partial x_i} (\rho k u_i) = \frac{\partial}{\partial x_i} \left[ \left( u + \frac{u_t}{\sigma_k} \right) \frac{\partial k}{\partial x_j} \right] + G_k + G_b - \rho \varepsilon \quad (3)$$

$$\frac{\partial}{\partial t} (\rho \varepsilon) + \frac{\partial}{\partial x_j} (\rho \varepsilon u_j) = \frac{\partial}{\partial x_j} \left[ \left( u + \frac{u_t}{\sigma_\varepsilon} \right) \frac{\partial \varepsilon}{\partial x_j} \right] + \rho C_{1\varepsilon} S_\varepsilon + C_{1\varepsilon} \frac{\varepsilon}{k} C_{3\varepsilon} G_b - \rho C_{2\varepsilon} \frac{\varepsilon^2}{k + \sqrt{u \varepsilon}} \quad (4)$$

Where,  $C_1 = \max \left[ 0.43 \frac{\delta}{\delta + 5} \right]$ ,  $\delta = S \frac{k}{\varepsilon}$ ,  $k$  is the turbulent flow energy,  $\varepsilon$  is the turbulent flow dissipation,  $C_{1\varepsilon}$ ,  $C_2$ ,  $C_{3\varepsilon}$  are constants,  $G_k$ ,  $G_b$  is the turbulent energy generated by the velocity

gradient and buoyancy.  $\sigma_k$ ,  $\sigma_\varepsilon$  is the turbulent Prandtl number, the turbulent viscosity

$u_t = \rho \frac{1}{A_0 + A_s} \frac{k^2}{\varepsilon} \frac{kU}{\varepsilon}$ ,  $U$  is a function of laminar flow strain and rotation.  $S_\varepsilon$  is the user-defined turbulent dissipative source.

Numerical simulations were carried out at two water heads of 3.5m and 2.5m respectively. The boundary conditions are shown in Table 1. The medium is water and is assumed to be an incompressible fluid. Among them, at the water head of 3.5m, the flow rate at the valve opening degree of 20° is simulated; and under the condition that the valve is fully open, the curve of the flow variation from the head of 3.5m head until zero is simulated. At the same time, the opening of the valve from 0° to 90° is simulated separately to observe the flow field change and flow characteristics of water under different opening degrees of the butterfly valve.

Table 1: Boundary conditions

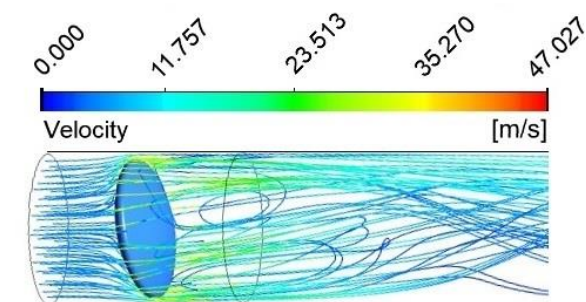
Name	Boundary Type	Value
Inlet	Pressure-inlet	30000 pa

Inlet	Pressure-inlet	25000 pa
Outlet	Pressure-outlet	0 pa
Pipe wall, valve plate	Wall	No slip

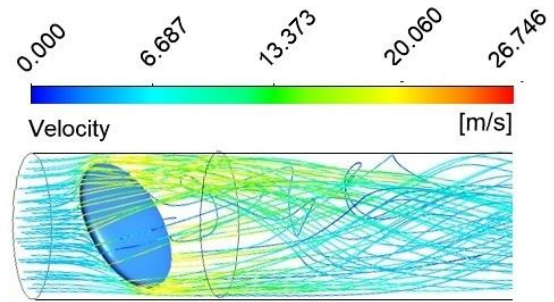
#### 4. Simulation Results and Analysis

##### 4.1 Flow field evolution behind valve

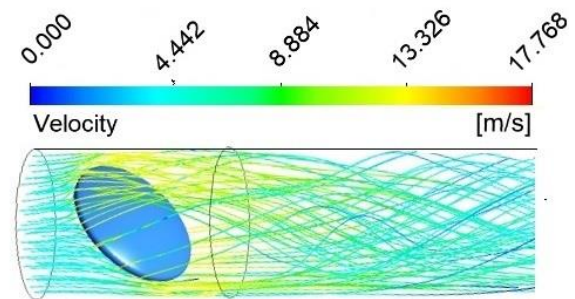
It is assumed that the butterfly valve has the same physical characteristics during the opening and closing process. In this paper, only the opening of the butterfly valve is simulated. Figure 2 shows the evolution of the 5D longitudinal profile flow field of the butterfly valve at the 10°, 30°, 45°, 60° and 90° opening angles during the opening of the butterfly valve from 0° to 90°. It can be seen from the velocity streamline diagram that when the butterfly valve opening  $\alpha$  is 10°, two vortices of upper and lower in opposite rotation directions are formed behind the valve. The upper vortex rotates counterclockwise, opposite to the rotation direction of the butterfly valve; the lower vortex rotates clockwise, in the same direction as the butterfly valve. The upper and lower vortices together affect the flow field behind the valve. When the butterfly valve opening  $\alpha$  is 30°, the upper vortex gradually weakens, the flow field is dominated by the lower vortex, and the influence range becomes smaller than before. When the butterfly valve opening  $\alpha$  is 45°, the flow field vortex immediately behind the butterfly valve disappears, and a small amount of velocity streamline deflects, but does not affect the overall flow field. When the butterfly valve opening  $\alpha$  are 60° and 90°, the flow field behind the valve changes only with the change of valve plate angle. As the angle increases, the speed orientation change is more gradual.



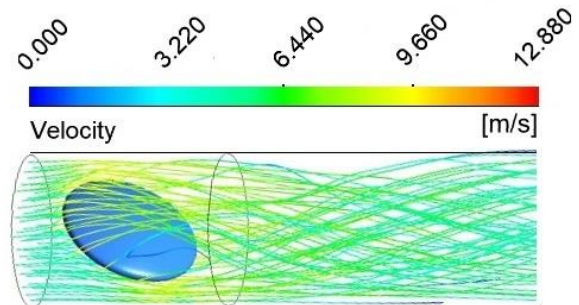
(a)  $\alpha=10$



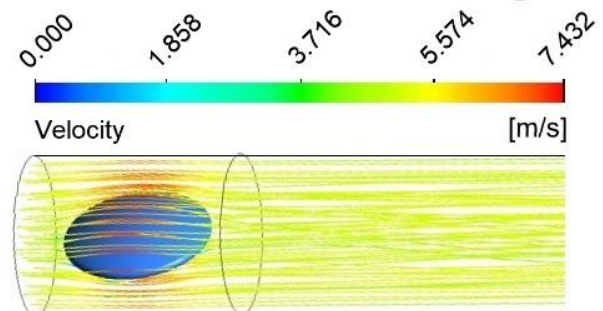
(b)  $\alpha=30^\circ$



(c)  $\alpha=45^\circ$



(d)  $\alpha=60^\circ$

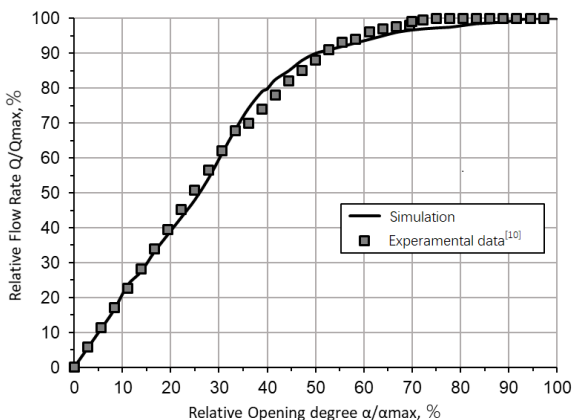


(e)  $\alpha=90^\circ$

**Figure 2:** Flow diagram of the flow field downstream of the butterfly valve at  $H=2.5m$  and different opening degrees

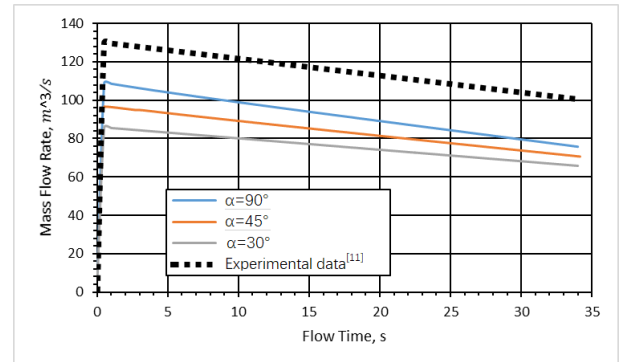
#### 4.2 Flow characteristics

Figure 3 is the calculation result of the flow rate changing with the opening degree of the butterfly valve at the head of  $H=2.5\text{m}$ . It can be seen from the figure that there is a nonlinear function relationship between the valve opening and the flow rate. Because the butterfly valve is not added with a seal when modeling, the flow rate has reached 90% when the opening is  $\alpha=45^\circ$ . During the opening changes from  $25^\circ$  to  $45^\circ$ , the flow rate and the valve opening degree have a fast opening flow characteristic (i.e., a quadratic relationship). While when the opening of the butterfly valve is changed from  $0^\circ$  to  $25^\circ$ , the flow rate and the valve opening are linearly increased rapidly, which is consistent with the trend of flow characteristics obtained by Song Hanwu<sup>[10]</sup> et al. based on actual experiments on the medium pressure butterfly valve.



**Figure 3:** Flow and opening curve of the butterfly valve

For a cylindrical water tank with a height of 3m and a diameter of  $D=1.5\text{m}$ , Figure 4 shows the simulation results of the relationship between the flow rate and the time when the butterfly valve keeps the valve opening degree constant, that is, at  $\alpha=90^\circ$ ,  $45^\circ$ , and  $30^\circ$  free outflows and the flow drops. This is consistent with the flow-time function proposed by Zhao Xueduan<sup>[11]</sup> et al., as shown in (5).



**Figure 4:** Flow rate versus time curve when the butterfly valve degree is constant

$$Q_1(t) = -\frac{\pi}{2} a D^2 t + \frac{\pi}{4} D^2 b \quad (5)$$

Where,  $a$  and  $b$  are constants related to the structure of the device, as shown in Table 2.

**Table 2:** Values of  $a$  and  $b$  under different valve opening degrees

Valve opening degree	$a$	$b$
90	0.281	61.681
45	0.228	54.721
30	0.168	48.55

Exact solution formula based on the complete venting time of the nozzle outlet container

$$T = \frac{8A}{\mu_j \pi d^2 \sqrt{2g}} \sqrt{H} \quad (6)$$

Where,  $A$  is the cross-sectional area of the variable head water tank;  $d$  is the diameter of the test pipeline;  $\mu_j=0.8$  is the flow coefficient of the variable head water tank. It can be calculated that when the butterfly valve opening degree  $\alpha=90^\circ$ , the complete venting time of the head water tank is  $T=95.3734\text{s}$ , and the numerical simulation result is about  $96.214\text{s}$ . It can be seen that the simulation results are basically consistent with the exact solution.

#### 4.3 Flow resistance characteristics

Under ideal conditions, the opening and closing process of the butterfly valve directly affects the flow resistance coefficient of the butterfly valve, which in turn affects the overcurrent capability of the butterfly valve. Therefore, it is helpful to adjust the flow rate by obtaining the flow resistance coefficient corresponding to the opening degree. Figure 5 is a graph showing the flow resistance coefficient of a butterfly valve under different opening degrees. It can be seen from the figure that the flow resistance coefficient is inversely

proportional to the valve opening. With the increase of the opening degree, the flow resistance coefficient tends to decrease. This is consistent with the hydraulics<sup>[12]</sup> theoretical value and the experimental data of Guan Honger<sup>[13]</sup>.

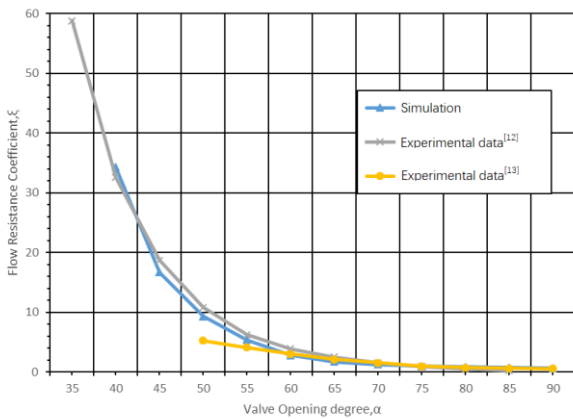


**Figure 5:** Flow resistance coefficient at different opening degrees

#### 4.4 Establishment of control functions

According to the simulation calculation, the corresponding flow resistance coefficient of the butterfly valve opening at 90°, 45°, 30°, setting of the corresponding back pressure, numerical simulation of the relationship between water level and flow when D=1.5m and cylinder water level drops from 3m to 1m is shown in Figure 6. It is particularly noted that due to the narrow water head range, the relationship between the water level and the flow rate is linear when water level is below 2.98 m. Experimental data<sup>[12]</sup>

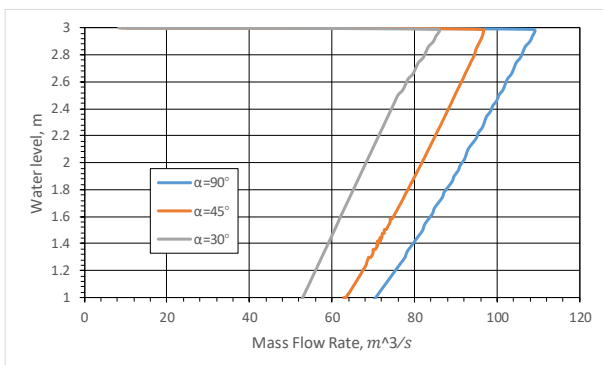


**Figure 6:** Curve of water height and variable heads flow under various opening conditions

Based on the relationship between the flow resistance coefficient and the opening degree of the butterfly valve and the relationship between the flow rate and the water level at a fixed opening, the curve of the valve opening degree and the water level under the constant flow rate can be obtained, as shown in Fig. 7.

level height under the constant flow rate can be obtained, as shown in Fig. 7.

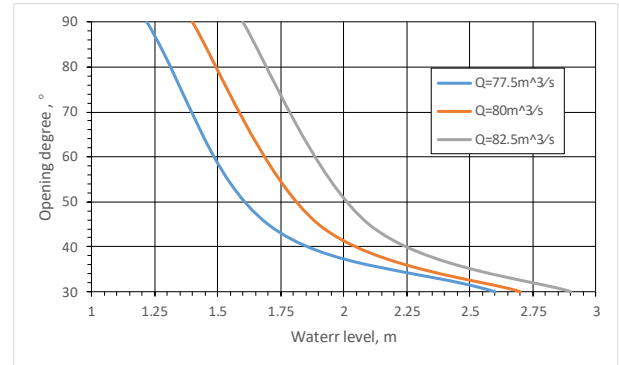


**Figure 7:** Curve of valve opening and water level

According to Figure 7, under constant flow, the butterfly valve opening and the water level are approximately inversely related, and the mathematical expression is shown in Equation 7:

$$\alpha = \frac{W}{H} \quad (7)$$

Where W is a parameter related to the structure of the device and the height of the water level, as shown in Table 3.

**Table 3:** W values at different water levels and valve openings when constant flow is 80m<sup>3</sup>/s

Water level	Butterfly valve opening	W
2.7	30	81
1.9	45	85.5
1.4	90	126

Experiments show that using the control function to open-loop control the butterfly valve ( Q = 80 m<sup>3</sup>/s, 77.5 m<sup>3</sup>/s, 82.5 m<sup>3</sup>/s ), the control accuracy of flow fluctuation less than 1% can be obtained.

#### 4. Conclusion

In this paper, a three-dimensional numerical model of the butterfly valve pipeline is established for the butterfly valve in the standard variable heads device. Combined with the dynamic grid technology, through the three-dimensional numerical simulation of the opening process of a butterfly valve, the flow vector diagram of the butterfly valve under different opening degrees, the relationship curve between the flow rate and the opening angle of the butterfly valve and the relationship curve between the flow rate and time under full opening condition of the butterfly valve are obtained. At the same time, the butterfly valve control function of the variable head device to

ensure the flow fluctuation less than 1% control accuracy is also discussed.

## References

- [1] Shi Jiabao. Application of large diameter hydraulic control butterfly valve in minjiang river water transfer project [J]. *Water Technology*, 2012(2): 22-24.
- [2] Cui B, Lin Z, Zhu Z, et al. Influence of opening and closing process of ball valve on external performance and internal flow characteristics [J]. *Experimental Thermal & Fluid Science*, 2016, 80:193-202.
- [3] Leutwyler Z, Dalton C. A CFD study of the flow field, resultant force, and aerodynamic torque on a symmetric disk butterfly valve in a compressible fluid [J]. *Journal of Pressure Vessel Technology*, 2008,130(2): 021302.
- [4] Shen Yang, Jin Xiaohong, Yang Ke. Three-dimensional flow field simulation of the butterfly valve and the solution of valve plate driving torque [J]. *Chinese Science and Technology Papers*, 2013, 8(8): 820-823.
- [5] Huang C D, Kim R H. Three-dimensional analysis of partially open butterfly valve flow [J]. *Transactions of the ASME*, 1996, 118:562-568.
- [6] Henderson A D, Sargison J E, Walker G J, et al. A numerical study of the flow through a safety butterfly valve in a hydro-electric power scheme [C]. *16th Australasian Fluid Mechanics Conference*, 2007.
- [7] Yang Zhixian, Yu Na, Mao Weiping, et al. Numerical simulation and flow characteristics analysis of flow field of central butterfly valve [J]. *Hydraulic & Pneumatics*, 2016(1): 95-99.
- [8] Youngchul P, Song X. Numerical analysis of large diameter butterfly valve [M]. *Advances in Computational Algorithms and Data Analysis*. Springer Netherlands, 2009:349-363.
- [9] Toro A D, Johnson M C, Spall R E. Computational fluid dynamics investigation of butterfly valve performance factors [J]. *Journal American Science and Technology*, 2012, 26(9): 2799-2806.
- [10] Song Hanwu, Wu Rongfang. Experimental study on flow and resistance characteristics of butterfly valves [J]. *Power Generation Equipment*, 1995(2): 3-4.
- [11] Zhao Xueduan, Zheng Ronggen. Numerical analysis of standard variable head and big flow system [J]. *Journal of University of Shanghai for Science and Technology*, 2011(1):1-10.
- [12] Wu Chigong. *Hydraulics* [M]. Beijing: Higher Education Press, 2003.
- [13] Guan Honger. Numerical simulation of internal flow field and structural static analysis of butterfly valve and multi-plate valve [D]. Liaoning: Northeastern University, 2010.

# On two-phase flow models for Coriolis flowmeters

Xiao-Zhang ZHANG <sup>1</sup>

<sup>1</sup> Tsinghua University, Beijing, P R China  
E-mail: zhangxzh@tsinghua.edu.cn

## Abstract

This paper reviews main previous works on the models of Coriolis flowmeter behaviour in two-phase flow. By experiment of bubble flow in vertical pipe with/without external vibration, some useful phenomena were observed. A general solution was obtained to the dynamic equation of a bubble motion. Some comments were given to the prediction of measurement errors by Coriolis flowmeters. Main points are: In most cases bubble shape is not sphere, but flat. Flat bubbles will be easy to move along a non-straight orbit, this causes transverse motion of the bubble. The transverse motion of bubbles are in a random way. Finally, this self-induced transverse vibration will affect the measurement of density and flowrate by a Coriolis flowmeter. It may be an intrinsic error source which is hard to eliminate. The paper also gives standard deviation and uncertainty of the random vibration in the experiment with various gas flowrate.

## 1. Introduction

A Coriolis flowmeter measures flowrate by force. It is considered as 'real' mass flowmeter [1]. Late in last century, people started to pay attention to behaviour of Coriolis flowmeters under multiphase flows [2]. In 2003, Hemp and Hoi gave a 'bubble model' [3]. Later Hemp and Kutin (2006) commented that 'compressibility change' would happen when liquid was mixed with gas [4]. Others also tried to model the behaviour of Coriolis flowmeters under multiphase. Weistain in his Ph D thesis [5] focused on 'decoupling' problem, which was defined as slipping of gas from liquid in the mixture. He concluded that smaller bubbles and external vibration would help to reduce measurement error; Gysling (2007) gave an aero-elastic model [6], and declared that acoustic speed of mixture could be used to correct the result by the flowmeter; Basse (2016) studied damping of the flowmeters due to 'decoupling'. He concluded that for small bubble and small void fraction, the damping was proportional to the void-fraction [8]. Liu et al (2001), instead used neural network technology to obtain better readings for the flowmeter [7].

The 'bubble model' assumes small size of bubble, no interaction between bubbles, small vibration amplitude, as well as no change in diameter ('solid bubble'). Based on these assumptions and by classic fluid mechanics [9], it is deduced that a quantity of liquid equivalent to a half of the bubble

volume will move with the bubble. This part of liquid is called as 'added mass' (or induced mass) of the bubble.

Further deduction using the 'added mass', it is concluded that, if a liquid with bubbles is doing vibration, the bubble's speed or acceleration is three times as that of the liquid. The 'bubble model' leads to measurement errors of a Coriolis flowmeter for water-gas two-phase flow as:

$$E_\rho = -3\alpha \quad E_{\dot{m}} = -\frac{2\alpha}{1-\alpha}$$

where  $E_\rho$  is the percentage error of two-phase density,  $E_{\dot{m}}$  is the percentage error of two-phase flowrate,  $\alpha$  is the void fraction:

$$\alpha = \frac{\text{gas volume}}{\text{water volume} + \text{gas volume}}$$

There are researchers doing experiments to look at the ability of Coriolis flowmeters to measure multiphase flows. A summary of some measurement errors by Coriolis flowmeters is given in Table 1:

**Table 1** Errors of Coriolis flowmeter in multiphase flow (Test data)

Author	Coriolis meter installation	Fluids	Void fraction	Max. Error
Skea and Hall	Straight, Curved	Oil+N2	6% N <sub>2</sub>	-15%
		Water	9% N <sub>2</sub> Max.	+5% 0.3%(small)

	3 others	in oil, Oil in water	15%	
<b>Wang et al</b>	Vertical	Liquid and gas	0~70%	-16%~2%
	Horizontal	CO <sub>2</sub>		-4%~14%
<b>Michael et al</b>	normal	High viscous oil	0~90%	±2%
		N <sub>2</sub>		±5%
<b>Liu et al</b>	U type	air, water	0~35%	0~25%
<b>B B Tao et al</b>	U type, horizontal	Gas, water	0~25%	2%~22%
<b>Weinstein</b>	U type, up/down	Gas, water	0~8%	Up: -15%, down: 12%

It shows that Coriolis flowmeters experience accuracy problem in multiphase flows. The questions are: Is it because we have not good models for the flowmeters? Or because certain intrinsic property of the flowmeters? Further investigation is thus still needed.

## 2. Experiment observation

We have undertaken some experiments. The goal was to observe the bubble behaviours for studying model for Coriolis flowmeter under two-phase flow.

Experimental system includes a Perspex tube vertically set, with a bearing on bottom and an elastic support on top, an electromagnetic exciter to make the tube vibration around an axis through the bearing. Air is pressed into the water in the tube from the bottom, with a control of the air flowrate. Bubbles moving upward the top of the tube are pictured using high speed camera. Vibration of the pipe is measured by eddy-current displacement sensor.

Since photos taken by high speed camera are in large numbers, only two typical photos are shown in Figure 1. The left is bubbles rising in a state pipe, while the right is bubbles rising with external excitation.

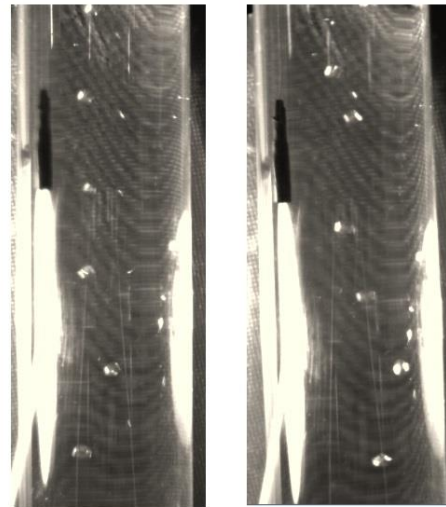


**Figure 1:** Rising bubbles without (left) and with (right) external excitation

By comparing many pictures taken by camera, difference of bubble behaviours with and without tube vibration is observed. Main phenomena are as follows:

1. The shape of the bubbles observed is not in sphere, rather is a flat one or even disk like. Diameter of the bubbles are 1~3 mm, which is within most industry cases. This would leads to increase of the 'added mass'.
2. These flat bubbles change their orientation while moving upward in non-straight orbits. This is self-induced under no external vibration. In the observation, the flat faces seem always point to the motion direction.
3. Difference of bubble speeds between tube vibrating and non-vibrating states is not obvious in the experiment. Exciting frequency is between 2~40Hz, with maximum amplitude from 1 mm to 0.1mm depending on the frequency.
4. A bubble flowing in water itself will induce random vibration. The vibration has a certain relation with void fraction of the air. It is linear for small void fraction.

An explanation for above phenomena is as bellow: When a bubble moves relatively to fluid, it carries a part of front fluid with it ('added mass'). The resistance of this part of fluid makes the bubble become flat. A flat bubble experiences different resistances in different directions. So the bubble tends to move in side direction where resistance is

smaller rather than in front direction. Here is transverse motion. But transverse motion in turn carries the fluid in side direction with bubble. Due to the resistance, the bubble changes its shape to have the flat face pointing to the new direction. This change of motion direction depends on balance of forces on the bubble. Occurrence time is random.

### 3. On theoretical model

To predict the behavior of a Coriolis flowmeter in two-phase flow, we need a model to predict bubbles' behavior. For this, model similar to previous references is used but with some changes of terms. We firstly consider a gas bubble (of size in industry cases) in a vertical water pipe up flow under transverse vibration. Mass of the air is neglected compared with water. Rather, added mass is considered [9][10]. Transverse motion for a bubble in this case can be equated as:

$$m_{in} \frac{d^2x}{dt^2} + c \frac{d(x-y)}{dt} = m_w y_0 \omega^2 e^{i\omega t} \quad (1)$$

where  $m_{in}$  is called 'added mass' of the bubble,  $m_w$  is the mass of water in same volume of the bubble,  $c$  is the damping caused by relative motion (slipping) of  $m_{in}$  in water,  $x$  is the absolute displacement of the bubble,  $y$  is the displacement of the fluid. It is supposed being the same as that of the pipe. The pipe is doing harmonic transverse motion with an angular frequency of  $\omega$ , with amplitude of  $y_0$ .

The solution of Equation (1) is:

$$x(t) = x(0) + v(0) \frac{m_{in}}{c} \left(1 - e^{-\frac{c}{m_{in}}t}\right) + x_0 e^{i\omega t + i\varphi} \quad (2)$$

where  $x(0)$  and  $v(0)$  are transverse displacement and transverse velocity at  $t=0$  respectively. The time  $t=0$  should be the moment when transverse velocity caused by the bubble itself becomes non-zero. In observed phenomenon 2, bubbles will do transverse motion randomly,  $x(0)$  and  $v(0)$  seem being random too.

The steady state solution of  $x(t)$  has a form of

$$x(t) = x_0 e^{i\omega t + i\varphi} \quad (3)$$

$$\text{with } \text{tg}\varphi = \frac{(m_{in} + m_w)c\omega}{m_{in}m_w\omega^2 - c^2} \quad (4)$$

$$x_0 = y_0 \frac{\sqrt{(m_{in} + m_w)^2(c\omega)^2 + (m_{in}m_w\omega^2 - c^2)^2}}{m_{in}^2\omega^2 + c^2} \quad (5)$$

where  $x_0$  and  $y_0$  are the magnitudes of bubble and pipe displacements respectively. In the extreme case of  $c=0$ ,  $\varphi$  will be 0, and  $x_0 = y_0 \frac{m_w}{m_{in}}$ . For solid spherical gas bubble where 'added mass' is 1/2 mass of bubble volume with water,  $x_0=2y_0$ . In the experiment, we only observed oblate gas bubble. If we take the 'added mass' as 0.7~0.95 times of water of the bubble volume as for oblate bubble [10], then  $x_0=(1.4\sim 1.05)y_0$ . It seemed closer to what we got from experiment. If the 'added mass' is the same as the fluid mass in the bubble volume,  $m_{in}=m_w$ , then  $x_0=y_0$ . This is the case of no bubble.

Equations (2) to (5) are usually used to estimate errors in density and flowrate measurement. However, in observed phenomenon 4, there is another force of  $f(t,\alpha)$ , which caused by bubble random motion. It is a random force as well. If we look at Equation (2), we find the second term is non-zero as long as there is transverse random motion of a bubble. The random property of  $v(0)$  makes it hard to predict  $x(t)$ . However, we are able to measure the vibrations of a pipe with bubble flow but without external excitation. A typical vibration is seen in Figure 2, where as a comparison, vibration of the pipe with water only under external excitation is also plotted.

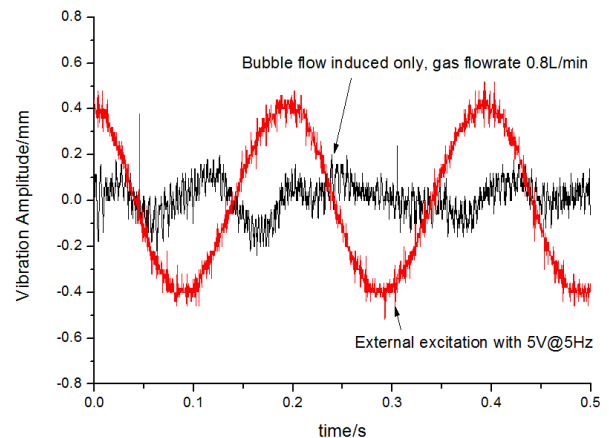


**Figure 2:** Bubble induced vibration compared with external excited vibration

Standard deviation of the bubble induced random vibration are given in Table 2 for various gas flowrates.

**Table 2:** Standard deviation of bubble flow induced vibration

Gas flowrate(L/min)	0.4	0.8	1.2	1.6
Standard deviation with uncertainty	0.053 ±0.003	0.083 ±0.002	0.148 ±0.035	0.235 ±0.067

From Table 2 we can see that, as gas flowrate becomes larger, the uncertainty of standards deviation becomes larger as well. The relation of the standard deviation with the void fraction of gas has a similarity to pipe damping in bubble flow [11].

So if we are to estimate the measurement errors of a Coriolis flowmeter, the error caused by bubble's random transverse motion needs to be considered. Since the random force seemed not be able to predicted, it may cause intrinsic measurement error in Coriolis flowmeters unless we can eliminate it.

#### 4. Summary

We undertook experiment of bubble flow in water in a vertical pipe. Some interesting phenomena were observed. These help us to study further the existing models for a Coriolis flowmeter under water-air two-phase flow. We found there are a few things need to re-consider:

1. Solid sphere bubble model needs to be changed. By this, the 'added mass' will be more than half of the bubble volume.
2. After assigning the 'added mass' for the bubbles, damping would be the viscous friction of the liquid to the 'added mass'. Here boundary layer theory would work.
3. By solving the dynamic equation of a bubble in transverse vibration fluid. Expression of the bubble motion was obtained. It includes terms for transient state for bubbles, which relates to self-induced random transverse motion of bubbles
4. There is a random force caused by random motion of bubbles. The effect may be measured but hard to predict by models. Random force may cause an intrinsic error on Coriolis flowmeter in two-phase flow.

#### References

- [1] Baker RC. Flow measurement handbook : Cambridge University Press; 2016
- [2] Wang T, Baker RC, Coriolis flowmeters: a review of developments over the past 20 years, and an assessment of the state of the art and likely future directions, Flow Meas. Instrum. 40 (2014) 99–123.

- [3] Hemp J and Yeung H. 2003. Coriolis meter in two phase condition, Computer and Control Engineering. 14:36-36.
- [4] Hemp J, Kutin J. Theory of errors in Coriolis flowmeter readings due to compressibility of the fluid being metered. Flow Meas. Instrum. 2006;17:359–69.
- [5] Weinstein JA, The Motion of Bubbles and Particles in Oscillating Liquids with Applications to Multiphase Flow in Coriolis Meters, University of Colorado, Boulder, Colorado, USA, 2008.
- [6] Gysling D L, An aeroelastic model of Coriolis mass and density meters operating on aerated mixtures , Flow. Meas. Instrum. 2007;18: 69-77.
- [7] Liu RP, Fuent MJ, Henry MP, Duta MD. A neural network to correct mass flow errors caused by two-phase flow in a digital Coriolis mass flowmeter. Flow. Meas. Instrum. 2001;12:23–63.
- [8] Basse NT. Coriolis flowmeter damping for two-phase flow due to decoupling , Flow. Meas. Instrum. 2016;52:40-52.
- [9] Landau LD, Lifshitz EM. Fluid mechanics. 2nd ed. Pergamon Press; 1987
- [10] Brennen C E: Fundamentals of Multiphase Flows, Cambridge University Press, 2005
- [11] Charreton C et al: Two-phase damping for internal flow: Physical mechanism and effect of excitation parameters, J. Fluids and Structures, 56(2015);56-74

# 2D and 3D numerical simulation results of vortex flowmeter under nonideal installation conditions

W. L. Chen<sup>1,2</sup>, J. Mu<sup>2</sup>,

<sup>1</sup> Lanzhou University, No. 222, tianshui south road, chengguan district, Lanzhou , China

<sup>2</sup> Xinjiang Institute of Measurement & Testing Technology, Urumqi, China

E-mail: chenwl16@lzu.edu.cn

---

## Abstract

An air test line of 50mm diameter was used in experiments covering two kinds of straight pipe length, and the numerical simulation results of vortex shedding frequency, which originated from the ANSYS FLUENT analysis results, were proved to be highly consistent with the experimental results. Based on this comparison, flow field simulation studies, including 13 pipe conditions, were carried out to establish the effect of upstream and downstream elbow fittings on the performance of the vortex flowmeter. The results indicated that the influences of the upstream straight pipe length were more obvious than the downstream straight pipe length. When there was an upstream elbow, the frequency value was greatly reduced, and the maximum error was -60.62%. The closer the elbow was to the vortex generator, the larger the decrease. The downstream elbows had a relatively small influence on the measurement results, and the maximum error was -13.23%. Considering the asymmetry of the 2D pipeline, the 3D simulations of part of the pipeline condition were further executed. The differences between 2D and 3D calculation results were analyzed, and the application value of different simulation results was explored.

---

## 1. Introduction

Since the development of the vortex flowmeter in the late 1960s, it has developed very rapidly and can be applied to liquid, gas and steam. It is a relatively advanced and ideal flow meter. However, the vortex flowmeter is still a developing flowmeter, and its theoretical basis and practical experience are relatively lacking. Therefore, it is still necessary to do a lot of basic research on the vortex flowmeter to avoid some unexpected problems in the actual use process[1].

The vortex flowmeter has certain requirements on the length of the straight pipe section and the roughness of the pipe wall during use. The calibration results and the stability of the flow rate depend on the length of the upstream and downstream straight pipe sections and the composition of the throttle components. And the vortex flowmeter can maintain the corresponding accuracy only if it meets the corresponding requirements[2]. The upstream elbow will cause an asymmetrical swirling flow in the pipeline, and the existence of the vortex will affect the pressure distribution near the wall of the pressure tap, which will affect the metering results of the flowmeter[3]. The University of Surrey in the United Kingdom and the British National Engineering Laboratory[2], the National Institute of Metrology of Japan[4], and Zheng Dandan of

Tianjin University[5], etc., respectively, carried out experimental studies in the measurement performance of vortex flowmeters under different installation conditions. The actual flow experiments can obtain the specific measurement results under certain conditions, but the change and characteristics of the internal flow field of the pipeline cannot be observed.

Using the numerical simulation method to study the fluid flow field can observe the change of the flow field in real time, which has a strong guiding significance for studying the specific characteristics of the flow field. In recent years, many scholars have used computer simulation to conduct a lot of research on the characteristics of vortex flowmeters[6-9].

For vortex flowmeters, the length of the straight pipe section is insufficient or there is a bend in the upstream and downstream close distance, etc., which will obviously affect the measurement results, leading to a significant reduction in measurement accuracy and even affecting the accuracy of the trade handover. However, in the actual installation process, due to site restrictions or unreasonable pre-engineering design, the actual installation conditions often fail to meet the requirements. In this paper, numerical simulation was used to study the influence of non-standard installation conditions on the

measurement results and internal flow field of vortex flowmeter after verifying the feasibility of the simulation method, and the related reasons were analyzed.

## 2. Measuring principle of vortex flowmeter

The vortex flowmeter uses the principle of fluid vibration to measure the flow. Under certain flow conditions, a part of the kinetic energy of the fluid is converted into vibration, and the vibration frequency has a certain proportional relationship with the flow velocity (fluid flow).

A non-streamlined vortex generator is placed in a direction perpendicular to the flow direction of the measured medium. When the fluid flows through the vortex generator, two rows of regular vortices are alternately separated and released on the rear sides of the body-facing surface. The vortex street generation process and flow measurement process are shown in Figure 1.

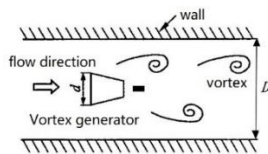


**Figure 1:** Schematic diagram of vortex generation process and flow measurement.

The average flow velocity  $v$  of the fluid in the pipeline and the vortex shedding frequency  $f$  satisfied Equation (1):

$$v = \frac{f \cdot m \cdot d}{S_t} \quad (1)$$

In the Equation,

$v$ - Flow rate of the measured fluid, m/s;

$f$ - Vortex shedding frequency, Hz;

$m$ - The ratio of the sum of the arched flow areas on both sides of the vortex body to the cross-section of the pipe;

$d$ - The width of the intercepting surface of the vortex generator, m;

$S_t$ - Strouhal number.

In a certain Reynolds number range,  $S_t$  can be regarded as a constant, and the vortex flow sensor measures the fluid flow rate by detecting the vortex frequency  $f$ , and then obtains the flow value.

## 3. Simulation of vortex flowmeter flow field

### 3.1 Simulation model establishment and computational condition setting

ANSYS ICEM was used to build geometric model of the corresponding pipeline and then divided the grid. The model was divided into three types: the upstream and downstream were straight pipe sections, the upstream had a single 90° elbow, and the downstream had a single 90° elbow. The dimensions of the vortex generator were shown in Fig. 2. The schematic diagram of the designed simulation pipeline was shown in Fig. 3. The diameter of the pipeline ( $D$ ) was 50mm, while  $n$  was a variable which indicated the length of different pipelines. The monitoring parameter was the static pressure at 0.7  $d$  ( $d$ : the width of the inlet surface of the vortex body) after the vortex generator.

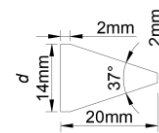


**Figure 2:** The size of vortex generator.

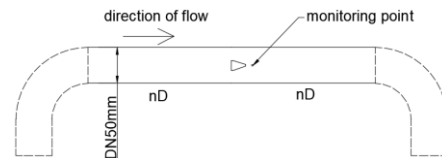


**Figure 3:** Design schematic diagram of the pipeline.

### 3.2 Comparison of experimental results with simulation results

In order to confirm the feasibility of the research method, an air test line of 50mm diameter was used in experiments covering two kinds of straight pipe length. Experiments were carried out on the critical flow venturi nozzle method gas flow standard device (negative pressure method) of Xinjiang Metrology and Testing Institute. The device information was as follows:  $U_{rel}=0.25\%$  ( $k=2$ ), the flow range was (0.1-15000)  $m^3/h$ . The experimental equipment adopted the piezoelectric vortex flowmeter commonly used in industry, the diameter was DN50 mm, the size of the vortex generator was the same as that of the simulation, and the calibration accuracy of the vortex flowmeter was  $\pm 1.5\%$ . Two experimental pipeline conditions were selected, which were upstream10D-downstream10D and upstream5D-downstream10D, respectively. The experimental conditions were basically the same as those defined by simulation.

**Table 1:** Relative error between 2D simulation data and experimental data. (%)

Pipeline condition	5m/s	10m/s	20m/s	30m/s
upstream10D-downstream10D	-6.27	-3.93	-3.48	2.33
upstream 5D-downstream10D	-8.78	-5.49	4.69	2.89

Table 1 showed the error between the simulation data and the experimental data, it showed that the two were closed to each other and the maximum error was -8.78%, which indicates that the flow field simulation applied by FLUENT could truly reflect the frequency of vortex shedding under actual conditions. The simulation results were credible. Therefore, it was also feasible to use FLUENT numerical simulation to study the flow field characteristics of vortex flowmeters under different installation conditions.

### 3.3 Simulation results analysis

The inlet flow rates of the air medium were adjusted to 5m/s, 10m/s, 20m/s, and 30m/s, respectively. After a certain number of steps, the waveform appeared periodically, as shown in Fig. 4a. The frequency of vortex shedding and the corresponding signal strength (Fig. 4b) were obtained by applying Fourier transform (FFT) to the pressure curve.

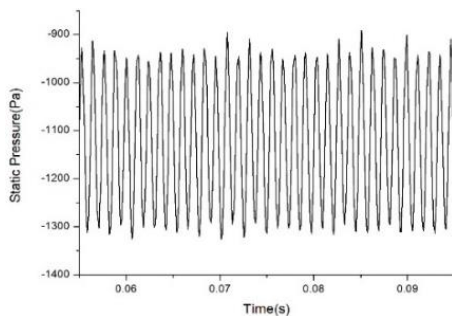


**Figure 4 a.** Waveform of static pressure at the monitoring point as a function of time period.

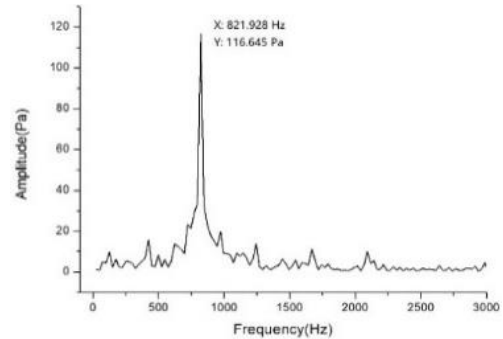


**Figure 4 b.** The frequency value and amplitude (ie, signal strength) obtained by the FFT processing of the waveform of the periodic variation.

For different inlet velocities, the distribution of vortex, velocity field and pressure field in the pipeline were similar. The difference was only the vortex shedding frequency  $f$  and amplitude. In Fig. 5, the calculation results were obtained when the length of the pipeline was upstream 10D -downstream 10D and the air velocity was 30m/s. It showed the vortex shedding in a certain period after the vortex generator. The vortices on both sides of the body alternately formed and fallen off, and the direction was opposite. The vortex intensity gradually decreased with the fluid flow.

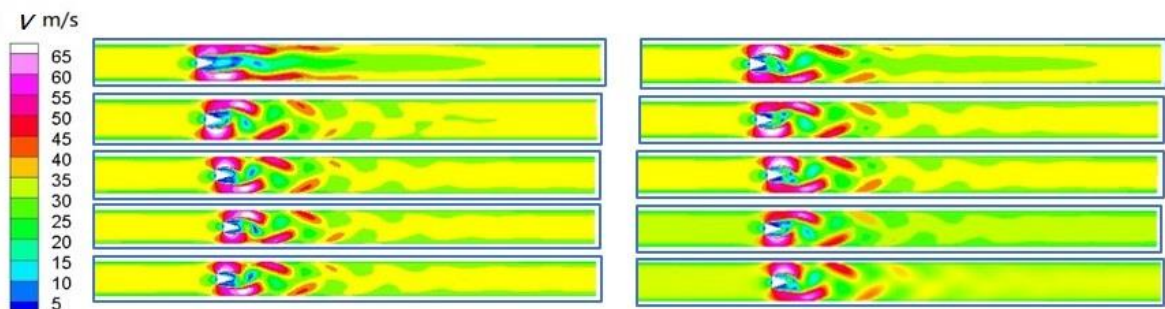


**Figure 5:** Vortex formation and shedding process during fluid flow

## 4. Analysis of simulation results under different pipeline conditions

Based on the above feasibility analysis, the flow field characteristics of the vortex flowmeter were analyzed at the upstream and downstream straight pipe section, the upstream elbows, the downstream elbows, respectively.

### 4.1 Both upstream and downstream were straight pipelines

The upstream and downstream were straight pipelines, including upstream10D-downstream10D, upstream5D-downstream10D, upstream5D-downstream3D, upstream3D-downstream1D, upstream1D-downstream1D, these five situations. The specific calculation results were shown in Fig. 6. It can be seen from the calculation results that as the length of the straight pipe section was shortened, the frequency value decreased, and the decrease of the upstream length of the straight pipe section had a more obvious effect on the results.

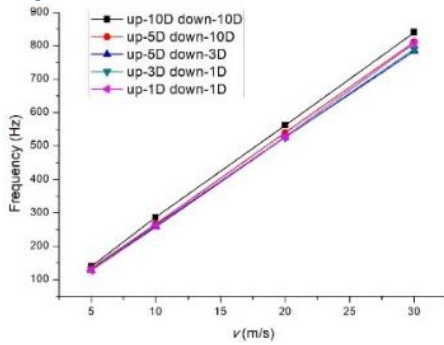


**Figure 6:** Calculation results corresponding to straight pipe sections of different lengths.

#### 4.2 There was a single 90° elbow upstream.

The effect of upstream distance was measured by changing the straight pipe length (between the upstream fitting and the flowmeter) from 1D to 40D, and all the length of the downstream straight pipe section was 5D. The data of the upstream10D-downstream 10D was used as a reference. The calculation results under various pipeline conditions were shown in Fig. 7.

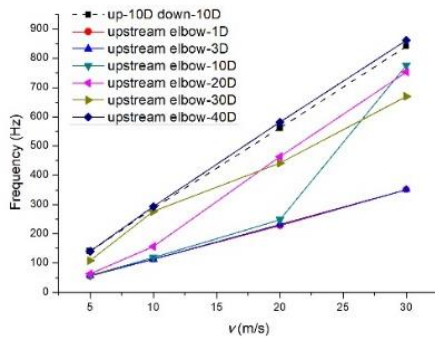


**Figure 7:** Calculation results corresponding to the front straight pipe length of different lengths of upstream elbow.

It could be seen that the shorter the length of the straight pipe section when there was an upstream elbow, and the closer the elbow was to the vortex generating body, the smaller the frequency value was, while the smaller the flow value in the pipe was. As the length of the straight pipe section increased, the frequency value gradually increased. If the upstream length of the straight pipe section was increased to 40D, the calculation result was close to the result when the straight pipe section was enough. It means that in the actual use, if the front end has a 90° elbow, the length of the front straight pipe section must not be lower than 40D. The frequency errors under each pipeline conditions were shown in Table 2.

**Table 2:** Relative error of simulation results with an upstream elbow (%)

Pipeline condition	5 m/s	10 m/s	20 m/s	30 m/s
--------------------	-------	--------	--------	--------

upstream1Delbow	-59.98	-60.36	-59.37	-58.22
upstream3Delbow	-58.10	-60.62	-58.69	-58.27
upstream10Delbow	-58.61	-58.42	-55.81	-7.69
upstream20Delbow	-54.06	-45.27	-17.40	-10.38
upstream30Delbow	-22.19	-3.61	-21.43	-20.33
upstream40Delbow	0.26	2.15	3.46	2.51

The flow field characteristics of upstream-1D-elbow while the velocity of 30m/s were taken as an example to analyse the relevant flow field characteristics. It could be seen from the pressure cloud diagram (Fig. 8a) that, due to the presence of the elbow, the pressure distribution of the fluid on both sides of the pipe wall was uneven, the outside pressure increased, and the inner pressure decreased, while the inner side even formed a cavity when the flow velocity increases. The velocity vector diagram (Fig. 8b) showed the overall flow of the fluid in the pipe, where the pressure was low and the flow velocity was fast, the velocity vector density was high.

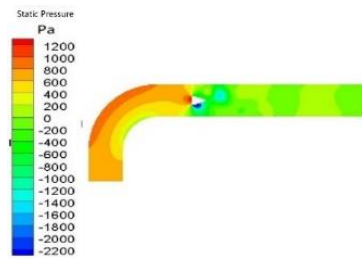


**Figure 8 a:** Pressure cloud diagram.



**Figure 8 b:** Velocity vector diagram.

The velocity cloud diagram (Fig. 9) fully reflected the influence of uneven pressure on both sides of the pipe wall: the outer side of the pipe wall had a higher pressure, the vortex fallen off faster, and the inner side was slower due to the lower pressure, resulting in a slower vortex shedding. The frequency of alternating vortex shedding on both sides of the body was reduced.

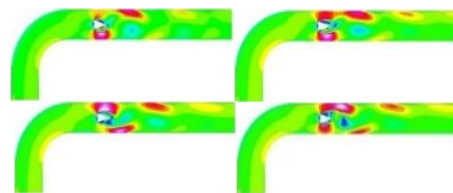


**Figure 9:** Velocity cloud diagram with elbow upstream.

#### 4.3 There was a single 90° elbow downstream.

The downstream had a 90° elbow, including upstream10D-downstream5D elbow, upstream10D-downstream1D elbow, upstream1D-downstream5D elbow, upstream1D-downstream1D elbow, these four situations. The calculation results were shown in Figure 9. The frequency error was shown in Table 3.

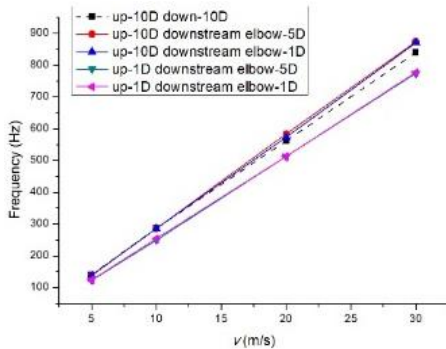


**Figure 9:** Calculation results corresponding to the straight pipe length of different lengths of downstream elbow.

It could be seen from the calculation results that when the upstream straight pipe length was 10D, the downstream elbow had less influence on the calculation results, and the maximum error was only 4.01%; but when the upstream straight pipe length was only 1D, the influence of downstream elbow was more significant, and the error was expanded to -13.23%. Therefore, if there was downstream elbow in the actual use, the length of the downstream straight pipe should not be shorter than 5D, to ensure the measurement accuracy to a certain extent.

**Table 3:** Relative error of simulation results with a downstream elbow (%)

Pipeline condition	5 m/s	10 m/s	20 m/s	30 m/s
Upstream10D-downstream5Delbow	-0.76	-0.48	3.88	4.01
Upstream10D-downstream1Delbow	-1.44	-0.55	2.05	3.68
Upstream1D-downstream5Delbow	-12.05	-13.23	-8.82	-7.85
Upstream1D-downstream1Delbow	-11.44	-11.65	-8.74	-7.53

As can be seen from the velocity cloud diagram (Fig. 10), In contrast to the upstream elbow, when there was a downstream elbow, the vortex on the inside of the pipe fallen off faster, and the outside was relatively slower. The frequency of pressure change slowed down, lead to the calculation result was also lower, which was consistent with the actual situation.

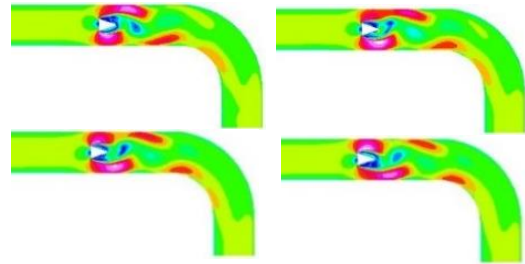


**Figure 10:** Velocity cloud diagram with elbow downstream.

## 5. Simulation results of 3D model.

Considering the asymmetry of the 2D pipeline, the 3D simulations of part of pipeline conditions were further executed. The 3D model of vortex flowmeter was shown in Fig. 11a. The geometric model was divided into different regions, which had different kind of mesh generation as shown in Fig. 11b.

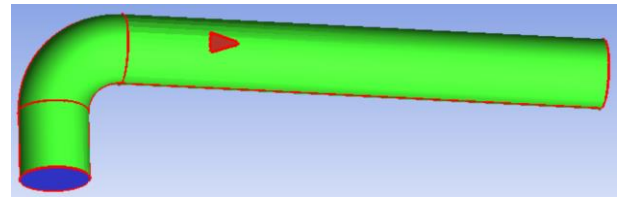


**Figure 11a:** The 3D model of vortex flowmeter.

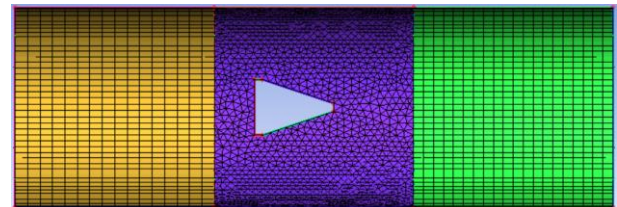


**Figure 11b:** The mesh generation of vortex flowmeter.

Table 4 showed the error between the 3D simulated data and the experimental data, and the results were compared with those obtained in 2D. It showed that the 3D simulation data were closer to the experimental data than 2D. This was because 3D models were more realistic.

**Table 4:** Relative error between simulation data and experimental data (%)

Pipeline condition	5 m/s	10 m/s	20 m/s	30 m/s
upstream10D-downstream10D (2D)	-6.27	-3.93	-3.48	2.33
upstream10D-downstream10D (3D)	-3.88	-2.34	-2.34	4.86
upstream 5D-downstream10D (2D)	-8.78	-5.49	4.69	2.89
upstream 5D-downstream10D (3D)	-4.72	-3.71	4.78	3.12

The results of different simulation methods under different pipeline conditions were shown in Table 5.

**Table 5:** Comparative results between 2D and 3D simulation data (Hz)

Pipeline condition	5 m/s		10 m/s		20 m/s		30 m/s	
	2D	3D	2D	3D	2D	3D	2D	3D
Upstream 10D-downstream 10D	139.86	143.44	287.03	291.79	561.64	568.24	840.03	860.76
Upstream 5D-downstream 10D	134.66	140.65	266.88	271.90	539.98	540.43	811.64	813.45
Upstream 10D elbow-downstream 5D	57.89	62.41	119.36	120.86	248.18	250.12	775.45	404.77
Upstream 40D elbow-downstream 5D	140.22	141.39	293.21	295.43	581.05	588.92	861.12	863.79
Upstream 1D-downstream 5D elbow	123.01	118.41	249.06	237.98	512.09	482.91	774.12	734.67

## 6. Conclusion

To sum up, the feasibility of numerical simulation method was verified by experiments in this paper, and the influence of different pipeline conditions on the output of frequency value was studied. The specific conclusions were as follows:

1. When the upstream and downstream straight pipe lengths were insufficient, the shorter the straight pipe length was, the smaller the output frequency value was, and the corresponding calculated flow rate would be smaller. The reduction of the upstream straight pipe length had a more obvious impact on the results;
2. When there was a single upstream 90 ° elbow, the frequency value dropped dramatically. The closer the elbow was to the vortex body, the greater the reduction. When the length of the upstream straight pipe section was 40D, the calculation result was close to that when the upstream and downstream straight pipe sections were enough.
3. When the upstream straight pipe length was 10D, which met the installation requirements, the downstream 90 ° elbow had little effect on the calculation results. However, when the upstream straight pipe length was only 1D, the influence of downstream elbow was more significant, and the maximum error expanded to -13.23%.
4. The 3D simulation data was much closer to the experimental data than 2D, this was owing to 3D models were more realistic. The velocity distribution in the 3D pipeline was closer to the real situation.

For more pipeline conditions, including non-fully open gate valves upstream of the pipeline or elbows in different planes, the measurement results of vortex flowmeter and changes in internal flow field are the next research content.

## References

- [1] Venugopal A, Agrawal A, Prabhu S V. Review on vortex flowmeter—Designer perspective[J]. *Sensors and Actuators A: Physical*, **170**: 8-23, 2011.
- [2] Mottram R C. Vortex flowmeters — Installation effects[J]. *Flow Measurement & Instrumentation*, **2**: 56-60, 1991.
- [3] Singh R K, Singh S N, Seshadri V. CFD prediction of the effects of the upstream elbow fittings on the performance of cone flowmeters[J]. *Flow Measurement and Instrumentation*, **21**: 88-97, 2010.
- [4] Takamoto M, Utsumi H, Watanabe N, et al. Installation effects on vortex shedding flowmeters[J]. *Flow Measurement & Instrumentation*, **4**: 277-285, 1993.
- [5] Zheng D D, Tang X H, Zhang T. Impact of Upstream Single Bend and Gate Valve on the Measurement Performance of Vortex Flowmeters[J]. *Journal of Tianjin University(Science and Technology)*, **44**: 1124-1130, 2011.
- [6] Chen D S, Cui B L, Zhu Z C. Numerical simulation of the effect of upstream swirling flow on swirl meter performance[J]. *Journal of thermal science*, **27**: 117-124, 2018.
- [7] Ford C L, Winroth P M, Alfredsson P H. Vortex-meter Design: The Influence of Shedding-body Geometry on Shedding Characteristics[J]. *Flow Measurement & Instrumentation*, **59**: S0955598617301875, 2018.
- [8] Yagmur S, Dogan S, Aksoy M H, et al. Comparison of flow characteristics around an equilateral triangular cylinder via PIV and Large Eddy Simulation methods[J]. *Flow Measurement & Instrumentation*, **55**: 23-36, 2017.
- [9] Chen J L. Frequency characteristics of a vortex flowmeter in various inlet velocity profiles[J]. *Advances in Mechanical Engineering*, **9**: 1687814017690507, 2017.

# The Theoretical Analysis and Waviness Profile Measurement for the Discharge Coefficient of Sonic Nozzles

Peijuan Cao<sup>1</sup>, Chao Wang<sup>1</sup>, Chunhui Li<sup>2</sup>, Hongbing Ding<sup>1</sup>

<sup>1</sup>Tianjin Key Laboratory of Process Measurement and Control, School of Electrical and Information Engineering, Tianjin University, Tianjin 300072, China

<sup>2</sup>National Institute of Metrology (NIM), Beijing 100029, China

E-mail (corresponding author): wangchao@tju.edu.cn

---

## Abstract

To improve the measurement accuracy of sonic nozzle, the theoretical analysis and waviness profile measurement for the discharge coefficient of sonic nozzles were conducted. The theoretical discharge coefficient used a correlation model that accounts for both viscous effects due to the boundary layer along the nozzle wall ( $C_{d,1}$ ), and the axisymmetric sonic line in the core region ( $C_{d,2}$ ). Firstly, the inner surface coordinates of one sonic nozzle with nominal throat diameter of 7.45 mm were measured by CMM of NIM, including the throat diameter  $d$  and curvature radius  $R_c$ . The curve profile, roundness and waviness of the overall and local geometric contours are evaluated by using the data of CMM and the perfect evaluation criteria about nozzle profile were proposed. Lastly, the  $R_c$  was used in calculating the theoretical discharge coefficients,  $C_{d,th}$ , while the  $d$  was used in calculating the experimental discharge coefficients,  $C_{d,exp}$ . The results showed the overall consistency between  $C_{d,exp}$  and  $C_{d,th}$  is better than 0.11% in the range of Reynolds number from  $4.45 \times 10^5$  to  $1.26 \times 10^6$ .

---

## 1. Introduction

The sonic nozzle (SN) standard facilities were established in many countries for precise measurement and control of the gas flow, especially for natural gas, because the natural gas is more and more widely used as the clear energy. The crucial parameter of SN is discharge coefficient, which defined as a dimensionless ratio of the actual mass flow-rate to the ideal mass flow-rate. When the SN is used as the transfer standard for flow measurement, it is necessary to obtain the discharge coefficient through actual calibration or theoretical calculation.

Many of the pioneering works for SN were investigated during the 1960s and 1980s, when numerous theoretical flow models were proposed for predicting the discharge coefficient of SN. The throat diameter  $d$  and the inlet curvature radius  $R_c$  are the key geometric parameters to calculate the experimental discharge coefficient  $C_{d,exp}$  and theoretical discharge coefficient  $C_{d,th}$ . The value of  $C_{d,exp}$  is usually calibrated by the primary gas flow standard facility (e.g. pVTt or Mt facility) with the expanded uncertainty of 0.05%~0.10% ( $k=2$ ). However, the primary standard facility has many inconveniences, such as long waiting time, limited flow rate range and so on. In order to avoid these shortcomings, the  $C_{d,th}$  is predicted by theoretical formula to realize the direct measurement of gas flow [1]-[7].

In 2005, the latest edition of ISO 9300 standard clearly specifies the geometry of SN. As shown in Fig.1, the ideal contour of SN is composed of a standard section and a diffusion section, and the arc section is tangent with diffuser section at point B, while the diffuser angle  $\theta$  is within ( $2.5^\circ \sim 6.0^\circ$ ). The profile transition between the standard section and the diffusion section is smooth, burr-free. In fact, it is difficult to meet the requirement of very low surface roughness for normally machined nozzles, especially for the entrance section. For the normally machined nozzles, it machined by a lathe and surface polished to achieve the desired smoothness of surface roughness less than  $1.5 \times 10^{-5}d$ , conforming to specification of ISO 9300. Unfortunately, in the process of polishing, the original ideal shape will be changed. Therefore, it is necessary to measure the geometrical profile of the SN in order to improve the prediction and experimental accuracy of the  $C_{d,th}$  and  $C_{d,exp}$ .

In this study, the variation of the discharge coefficient of SN is analysed when the flow is in the laminar boundary layer. Firstly, the coordinate measuring machine (CMM) was used to measure the contour profile of sonic nozzles with  $d=7.45$  mm, and corresponding the evaluation criterion was established, including curve profile, roundness and waviness for the whole and local contours. Finally, the  $C_{d,exp}$  calibrated by actual throat diameter  $d$  are employed to verify the  $C_{d,th}$  calculated by curvature radius  $R_c$ , which the  $C_{d,exp}$  was obtained at two pVTt facility in National Institute

of Metrology of China (NIM). When the geometric profile of the nozzle meets the requirements of the evaluation criteria, the theoretical model can be used to accurately predict the discharge coefficient within the uncertainty of less than 0.1%.

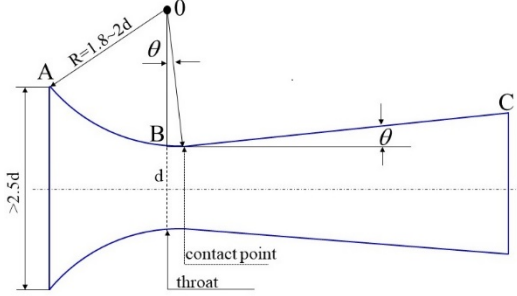


Figure 1: Effect of the parameters on the  $C_{d,th1}$ .

## 2. Discharge coefficient of SN

### 2.1 The theoretical discharge coefficients

As early as 1960s to 1980s, several theoretical or semi-empirical formulas for discharge coefficient have been proposed. In general, the theoretical discharge coefficient ( $1-C_d$ ) will be divided into three parts: viscous discharge coefficient ( $1-C_{d,1}$ ), inviscid discharge coefficient ( $1-C_{d,2}$ ) and virial discharge coefficient ( $1-C_{d,3}$ ) to obtain accurate flow rate. When the appropriate gas and flow conditions are selected (i.e. dry air without eddy current and near ambient temperature), the value of ( $1-C_{d,3}$ ) is very small and can be neglected.

For ( $1-C_{d,2}$ ), in 1959, Hall firstly calculated the maximum boundary layer displacement thickness as for a semi-infinite plate with zero longitudinal pressure gradient by equating the boundary layer of SN to a uniform circular tube with length  $L$  and ignoring the transverse curvature of the boundary layer. Unfortunately, the maximum boundary layer displacement thickness was obtained directly from the boundary layer theory of plate, which leads to a lower accuracy of calculation. Up to 1962, He further analysed the effect of multi-dimensional feature of transonic flow and used a perturbation series expansion in powers of  $1/R$  ( $R=2R_c/d$ ) to solve the steady, irrotational, axisymmetric, compressible flow equation in the transonic regime, and ulteriorly proposed the formula of the inviscid discharge coefficient, as seen Equation (1) as an example. Remarkably, for sufficiently small  $R$ , Hall's solution yields nonphysical results, predicting negative values of the inviscid discharge coefficient. In 1969, Kliegel and Levine found an error in Hall's original solution, and provided a modification, as shown in Equation (2), with a difference of about 0.06% before and after correction. In addition, they extended and improved Hall's work for inviscid discharge coefficient by using a perturbation series solution expanded about  $1/(1+R)$  that converges for all values of  $R$ , seen the Equation (3).

$$(1-C_{d,2}) = \frac{\gamma+1}{(2R_c/d)^2} \left( \frac{1}{96} - \frac{8\gamma+21}{4608(2R_c/d)} + \frac{754\gamma^2+1971\gamma+2007}{552960(2R_c/d)^2} \right) \quad (1)$$

$$(1-C_{d,2})_{mo} = \frac{\gamma+1}{(2R_c/d)^2} \left( \frac{1}{96} - \frac{8\gamma+21}{2304(2R_c/d)} + \frac{754\gamma^2+2123\gamma+2553}{552960(2R_c/d)^2} \right) \quad (2)$$

$$(1-C_{d,2})_{KL} = \frac{\gamma+1}{(1+2R_c/d)^2} \left( \frac{1}{96} - \frac{8\gamma-27}{2304(1+2R_c/d)} + \frac{754\gamma^2-757\gamma+3633}{276480(1+2R_c/d)^2} \right) \quad (3)$$

For ( $1-C_{d,1}$ ), in 1971, Geropp independently developed an equation of axisymmetric compressible boundary layer under adiabatic conditions by using the similarity transformations, and obtained the accurate analytical solution of the ( $1-C_{d,1}$ ) for the laminar flow boundary layer of SN, as shown in Equation (4). Then, in 1987, under the  $\Delta T_w \neq 0$  and  $Pr \neq 1$ , Geropp also put forward ( $1-C_{d,1}$ ) with wall heat transfer, and it is defined by Equation (5).

$$(1-C_{d,1}) = \frac{4 \left( \frac{\gamma+1}{2} \right)^{\frac{1}{2(\gamma-1)}}}{\sqrt{Re \cdot m}} \left( 3\sqrt{2} - 2\sqrt{3} + \frac{\gamma-1}{\sqrt{3}} \right), \Delta T_w = 0, Pr = 1 \quad (4)$$

$$(1-C_{d,1})_{he} = \frac{4\sqrt{6}b^{1/2} \left( \frac{\gamma+1}{2} \right)^{\frac{1}{2(\gamma-1)}}}{\sqrt{Re \cdot m}} \left\{ \left( 1 + \frac{m_T}{m} \sqrt{Pr} \right) \cdot \left( \sqrt{3 + \frac{3m_T}{2m}} - \sqrt{2 + \frac{3m_T}{2m}} \right) + \frac{(\gamma-1)\sqrt{Pr}}{6} \sqrt{2 + \frac{3m_T}{2m}} \right\}, \Delta T_w \neq 0, Pr \neq 1 \quad (5)$$

### 2.2 The experimental discharge coefficients

On of assuming a one-dimensional isentropic flow of an ideal gas, the ideal mass flow  $q_{mi}$  through the sonic nozzle, can be expressed as,

$$q_{mi} = \frac{AC_* p_0}{\sqrt{(R_u/M)T_0}} \quad (6)$$

Where,  $A$  is the area of throat;  $m^2$ ,  $C_*$  is the critical flow function;  $p_0$  is the stagnation pressure, Pa;  $T_0$  is the stagnation temperature, K;  $R_u$  is the universal gas constant, J/kmol/K;  $M$  is the molecular mass, kg/kmol.

The  $C_{d,exp}$  describes this difference between the real mass flow  $q_{mr}$  and the ideal mass flow,

$$C_{d,exp} = \frac{q_{mr}}{q_{mi}} \quad (7)$$

## 3. Evaluation criterion of contour

Under adiabatic conditions, it shows that the change of  $C_{d,th1}$  is less than 0.08% with the throat diameter changes by 3.0% for different throat diameters nozzles. The smaller the throat diameter, the greater the relative variation of  $C_{d,th1}$  is. In this experiment, the relative change of  $C_{d,th1}$  was less than 0.01% when the change of throat diameter was 0.5% for the nozzle with  $d=7.45$  mm. In addition, it can be seen that the  $C_{d,exp}$  is proportional to the square of diameter based on Equation (6) and Equation (7). When the uncertainty of throat diameter is 0.05%, the uncertainty of  $C_{d,exp}$  will be 0.1%. Obviously, the accurate value of throat

diameter  $d$  is more important for calculating  $C_{d,exp}$ , which has been verified by experimental data.

Based on Hall-Geropp theory with adiabatic, the effect of  $R_c$  on  $C_{d,th1}$  can be obtained. It found that the  $C_{d,th1}$  decreases with the increase of  $R_c$ . When the  $R_c$  changes by 1.5d%, the change of  $C_{d,th}$  is less than 0.02%. Furthermore, it can also be seen that the larger the throat diameter, the weaker the dependence of  $C_{d,th1}$  on  $R_c$  is, which can tolerate greater uncertainty. The uncertainty of  $R_c$  of 10% or less was acceptable to ensure that the uncertainty of predicted discharge coefficient was less than 0.01% for the nozzle of  $d=7.45$  mm.

Besides, the waviness profile of the nozzle also needs to be evaluated. The waviness profile is expressed as a kind of uneven surface which is larger than mean roughness  $R_a$  and smaller than the error of curve profile. It is an intermediate geometry error between micro and macro error. Therefore, the maximum height of waviness profile near the throat  $w_t$ , should be  $1.5 \times 10^{-5}d < w_t < 0.1d$ .

Based on above analysis and ISO 9300 standard, the deviations of the contour parameters are listed as follows, a) The inlet diameter should differ not more than  $\pm 0.001d$  from the ideal toroidal form; b) The  $R_c$  should be within  $1.8d$  to  $2.2d$ ; c) The deviation of curve contour between the actual and the ideal at the location of front and back throat of 1 mm should be less than  $\pm 0.005d$  and the deviation of the rest should not exceed  $\pm 0.1d$ . d) The maximum height of waviness profile near the throat  $w_t$ , should be  $1.5 \times 10^{-5}d < w_t < 0.1d$ .

#### 4. Experimental facility and measurement scheme

##### 4.1 The details of experimental apparatus

The nozzles were tested by two pVTt gas flow standard facilities constructed in 1986 and 2014 respectively at NIM, China. One apparatus with the expanded uncertainty of 0.10%~0.20% ( $k=2$ ) is used to calibrate the discharge coefficient of SN with the flow rates range from 1 m<sup>3</sup>/h to 1138 m<sup>3</sup>/h at the stagnation pressure of 0.1 MPa. Another apparatus based on the positive pressure method had been constructed as shown in Fig.3. This pVTt facility utilizes a dry compressed air to calibrate the discharge coefficients of sonic nozzles covering flow range extending from 0.019 kg/h to 1367 kg/h, and the stagnation pressure range from 0.1 MPa to 2.5 MPa. The expanded uncertainty of apparatus could be 0.06% ( $k=2$ ), while the expanded uncertainty of discharge coefficient of calibrated SN was 0.08% ( $k=2$ ) [8]-[9].

In this study, the nozzles with nominal throat diameter of  $d=7.45$  mm,  $R_c=2d$ , diffusion angle of 4° and total length of 48.5 mm are measured and analysed.

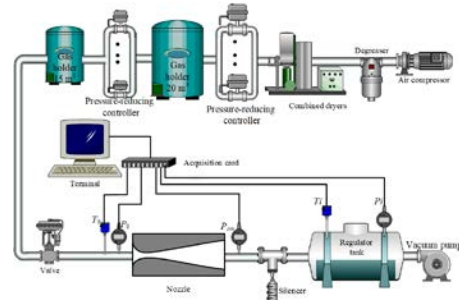


Figure 2: The positive pressure method pVTt facility

The geometry profile of the  $d=7.45$  mm nozzle is measured by using a Leitz 3D<sup>d</sup> coordinate measurement machine (CMM). The standard uncertainty ( $k=1$ ) of length measurements made using this CMM is  $(0.6+l/600)$  μm where the length dimension of  $l$  is in millimetres. The motion range of a CMM is 1200mm×1000mm×700mm. The expanded uncertainty of the throat diameter measurement is estimated to be 1 μm ( $k=2$ ). This machine is housed in a temperature controlled environment that is maintained at  $(20 \pm 0.01)$  °C to provide thermal stability. The diameter of the probe selected in this measurement is 3 mm.



Figure 3: The CMM and ruby probing

##### 4.2 The measurement method

A large number of profile data of nozzles are collected by CMM, instead of throat radius and curvature radius calculated by relative position of finite points, so the profile of SN can be evaluated comprehensively. Both  $d$  and  $R_c$  are indirectly determined by ruby probe of CMM along the circumference of various cross sections and measuring contours along different azimuthal planes of symmetry. The measurement steps are as follows,

- Firstly, Cartesian coordinate system is established with nozzle entrance section and axis of nozzle as coordinate Z axis.
- At each cross section, CMM measurements were taken spaced 30 degrees apart. Each of the eight angles corresponds to a curve along the SN wall that spans from the entrance to the throat, and the measurement step of each arc was 30 μm. These four curves on the axis are used to calculate the  $R_c$ .
- Based on 12 arcs, the approximate position of the smallest circle is found. A total of 25 concentric

circles of each circle about 40 point are generated before and after this position, with an axial interval of 20  $\mu\text{m}$  and a measuring length of 0.5 mm. Least squares regression is used to find the best-fit curve and the average diameter. These diameter at the zero slope location of this fit is taken to be the  $d$ .

Due to the restriction of measuring rod of CMM, the longest measuring distance of the axis is - 23 mm. In addition, the data measured by CMM is the coordinate value of the probe centre and not the coordinate value of the actual contact point between the probe and the nozzle, so the probe compensation should be carried out, which is corrected according to the normal vector direction of the curve where the point is located.

## 5. Multi-dimensional contour analysis of SN

### 5.1 Measurement results of the SN contour

The centre of entrance section and the axis direction of nozzle are taken as coordinate origin and Z axis, respectively. Then along the direction of Z axis for the nozzle of  $d=7.45$  mm, 12 arcs are measured at intervals of 30 degree, as shown in Fig.4. These twelve curves well reflect the contour of the SN, and are convenient for calculating its radius of curvature and throat diameter. However, these 12 curves do not compensate for the probe of CMM.

In order to accurately capture the physical dimension of SN, four curves of  $z_1$ ,  $z_4$ ,  $z_7$  and  $z_{10}$  are measured repeatedly, and can be corrected according to the probe and eccentricity error of the coordinate machine. The results of the four corrected curves are summarized as shown in Fig.5. As can be seen from Fig.5, these four corrected curves are scattered near the throat of SN due to slightly higher surface roughness caused by the processing method.

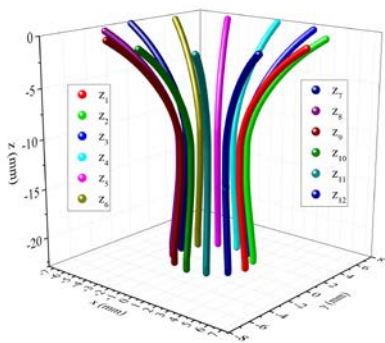


Figure 4: 12 curves of this nozzle.

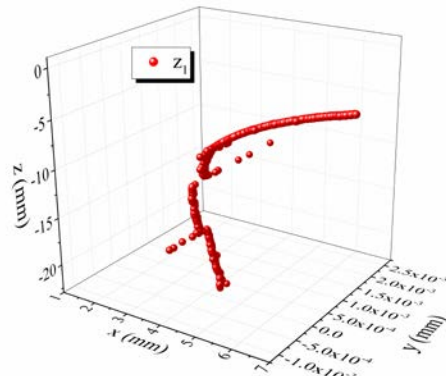
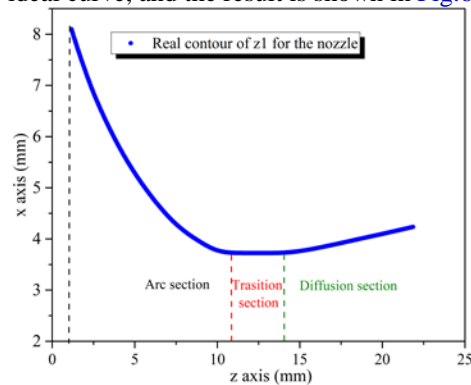


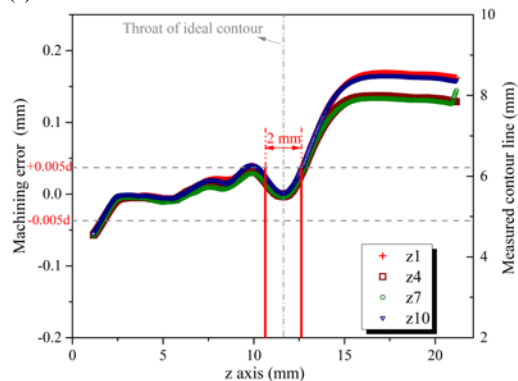
Figure 5:  $z_1$  corrected curve of SN.

### 5.2 Analysis of the SN contour

In order to accurately evaluate whether the contour of SN meets the requirements, it is necessary to analyse the deviation of curves profile and roundness. The three-dimensional curve measured is transformed into two-dimensional curve and compared with the ideal profile, and the comparison result for  $z_1$  curve is shown in Fig.6 (a). From the Fig.6 (a), the contour around the throat is more like a cylindrical nozzle, and the smallest diameter is located near Z axis of -12.32 mm. Moreover, using the results of these four modified curves, the error of the curve profile is analysed which is expressed as the minimum distance from the each measured points to the ideal curve, and the result is shown in Fig.6 (b).



(a) The measured results of  $z_1$  curve.



(b) The error of curve contour of  $z_1$ ,  $z_4$ ,  $z_7$  and  $z_{10}$ .

Figure 6: Sketch of whole curves profile for  $d=7.45$ mm nozzle.

It can be seen from the Fig.6 that the line profile error at the entrance and exit is large caused by the angle of attack of the processing probe and the wall angle error. However, it has been proved that the contour in the diffuser  $0.1d$  behind the throat has no influence on the discharge coefficient [10]. From the Fig.6, the maximum curve contour error of this nozzle is  $0.233 \text{ mm} < 0.1d$  mm. The local line profile error of the front and back 1 mm of the throat is smaller, within the required range of  $< 0.005d$ , which meets the requirements. Therefore, it mainly selected the measuring results at position of less than 1 mm before and after the throat to calculate the  $d$ , while it selected the results within 8 mm before throat to calculate the  $R_c$ .

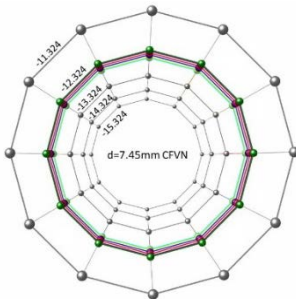


Figure 7: Roundness at five axial positions for  $d=7.45$ mm nozzle.

Fig.7 shows cross sectional views of the  $d=7.45$  mm SN at different axial distances upstream and downstream of the throat location, according to the 12 points measured 30 degrees apart at each axial location. The figure shows that this nozzle is essentially circular. In addition, the degree of roundness is evaluated by the minimum area method, as shown in Table 1. From Table 1, it can be seen that the maximum degree of roundness is  $5.11 \mu\text{m}$  for this nozzle and is less than  $\pm 0.001d$ , which meets the requirements of roundness stipulated in ISO 9300 standard.

Table 1: Roundness of SN at different axial positions.

Number	Axial position (mm)	Degree of roundness ( $\mu\text{m}$ )
1	-10.324	5.09
2	-11.324	4.74
3	-12.224	5.06
4	-12.324	4.62
5	-12.424	4.69
6	-12.524	4.92
7	-13.324	5.11
8	-14.324	3.33
9	-15.324	4.09

The contour of sonic nozzle not only needs to meet the requirements of curve profile and roundness, but also needs to meet the waviness requirements. The waviness near the throat of this nozzle is shown in Fig.8, and the sampling length  $l_w = 1.36$  mm. Within the sampling length, the maximum height of the waviness profile is  $0.61 \mu\text{m}$ , which is significantly less than the error of

curve profile and roundness and larger than the surface roughness of the normally machined nozzle of  $1.5 \times 10^{-5}d$ .

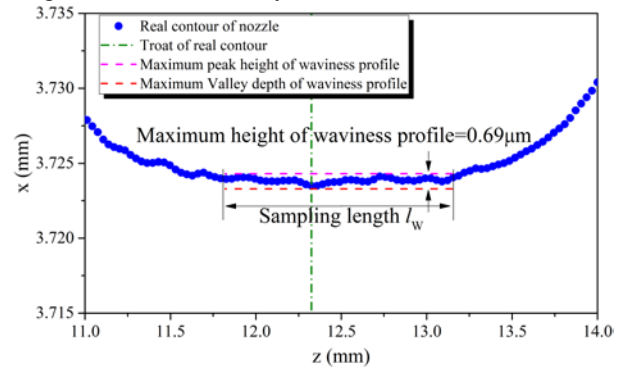


Figure 8: Waviness near the throat for  $z_1$  curve.

In conclusion, the whole contour of the nozzle with nominal throat diameter of 7.45 mm meets the geometric requirements. In addition, it found that the throat is located nearly Z axis of  $-12.32$  mm.

### 5.3 Measurement results of $d$ and $R_c$

Based on the above analysis, the position of the throat is about  $-12.324$  mm on Z axis. Therefore, a total of 25 concentric circles were generated before and after this position, with an axial interval of  $20 \mu\text{m}$  and a measuring length of  $0.5$  mm. Least squares regression is used to find the best-fit curve to calculate the average diameter. The  $d=7.451$  mm at Z axis of  $-12.1537$  mm with the zero slope of fitting curve at this location, as shown in Fig.9. The difference between the fitting result and the measured minimum pipe diameter is  $0.38 \mu\text{m}$ , i.e.  $0.005\%$ , and its influence on the discharge coefficient is less than  $0.01\%$ , which can be neglected.

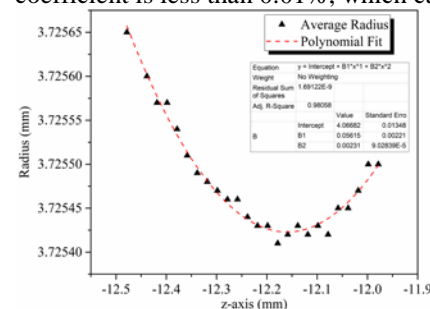


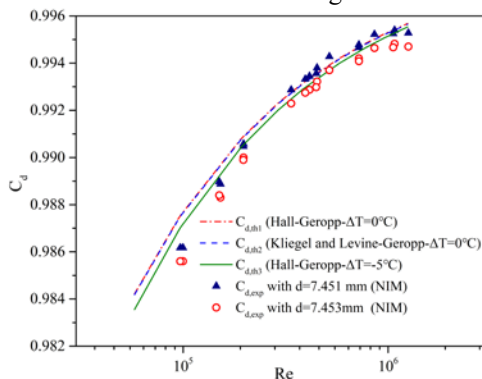
Figure 9: Fit curve of these average radius measurements.

In differential geometry, the reciprocal of curvature is the curvature radius, that is,  $R_c = 1/K$ . Taking the minimum diameter (or theoretical minimum diameter) as the throat diameter, 106 points of total of 717 measuring points were selected with 3 mm in front of the throat diameter to calculate the curvature radius.

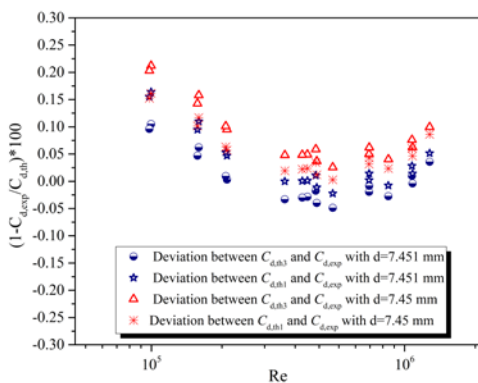
The mean curvature radius is  $14.800$  mm by fitting different curves. The difference of curvature radius between fitting and nominal curvature radius is  $0.106$  mm, i.e.  $0.71\%$ , which is far less than the requirement of  $10\%$ .

## 6. Comparison of $C_{d,th}$ with $C_{d,exp}$

Based on the  $d=7.451$  mm, the  $C_{d,exp}$  were calibrated on two sets of pVTt gas flow standard facilities, while the  $C_{d,th}$  of different models were calculated based on the  $R_c=14.800$  mm. The  $C_{d,th}$  is determined by combining Geropp's adiabatic and heat transfer viscous model in laminar boundary layer with modified Hall's inviscid model. The  $C_{d,th3}=(1-C_{d,2})_{mo}*(1-C_{d,1})_{he}$  for this SN agreed with  $C_{d,exp}$  to better than 0.11% with  $Pr=0.703$ ,  $\Delta T=T_w-T_0=-5^\circ C$  ( $T_w$  is wall temperature of nozzle) and  $\gamma=1.4$ , while the overall agreement between  $C_{d,th1}=(1-C_{d,2})_{mo}*(1-C_{d,1})$  and  $C_{d,exp}$  was better than 0.16% with  $Pr=1$ ,  $\Delta T=0^\circ C$  and  $\gamma=1.4$ , as shown in Fig.10. The measurement Reynolds number  $Re$  ranged from  $4.45 \times 10^5$  to  $1.26 \times 10^6$ , thus the boundary layer at the throat is limited only in laminar. Based on Fig.10, it can be seen that the deviation between  $C_{d,th}$  and  $C_{d,exp}$  increases with the decrease of Reynolds number. Moreover, it can also be seen that the difference between  $(1-C_{d,2})$  and  $(1-C_{d,2})_{KL}$  is no more than 0.03%, while the difference between  $(1-C_{d,2})_{mo}$  and  $(1-C_{d,2})_{KL}$  is less than 0.003%, which is basically the same. In the experimental measurement process, the stagnation temperature  $T_0$  can be stabilized at  $20^\circ C$  for a long time.



(a)  $C_{d,th}$  and  $C_{d,exp}$  based on the real and nominal  $d$ .



(b) Deviation between  $C_{d,th}$  and  $C_{d,exp}$ .

**Figure 10:** Comparison between  $C_{d,th}$  and  $C_{d,exp}$ .

## 7. Conclusion

The  $d$  and  $R_c$  for a sonic nozzle with nominal throat diameter of 7.45 mm were measured by a CMM to calculate the  $C_{d,exp}$  and  $C_{d,th}$ , and corresponding geometric evaluation criteria were established, including curve profile, roundness and waviness. In the range of  $Re$  ( $4.45 \times 10^5 \sim 1.26 \times 10^6$ ), the consistency between the  $C_{d,exp}$  and the  $C_{d,th3}$  was better than 0.11%.

The reliability of the theoretical model of discharge coefficient is verified by comparing the experimental data. Therefore, the theoretical model can be used to predict the discharge coefficient instead of the measured value, when nozzle contour satisfies the requirements of geometry evaluation criteria. In addition, the theoretical discharge coefficient model will not be accurate enough in small  $Re$ , and should receive more attentions.

## References

- [1] B.S. Stratford, The calculation of the discharge coefficient of profiled choked nozzles and the optimum profile for absolute air flow measurement, *Journal of the Royal Aeronautical Society*, 1964, 68 (640), 237-245.
- [2] S.P. Tang et al., Experimental determination of the discharge coefficients for critical flow through an axisymmetric nozzle, *AIAA Journal*, 1978, 41-46.
- [3] D. Geropp, Laminare grenzsichten in ebenen und rotationssymmetrischen lavalduesen, *Deutsche luft und raumfahrt forschungsbericht*, 1971, 71-90.
- [4] I.M. Hall, Transonic flow in two-dimensional and axially-symmetric nozzles, *Quarterly Journal of Mechanics and Applied Mathematics*, 1962, 15 (4) 487-508.
- [5] B.T. Arnberg, et al., Discharge coefficient correlations for circular-arc Venturi flowmeters at critical (sonic) flow, *Journal of Fluids Engineering*, 1974, 111-123.
- [6] M. Ishibashi, M. Takamoto, Discharge coefficient of critical nozzles machined by super-accurate lathes, *Proceedings of National Conference of Standards Laboratories*, New Mexico, 1998.
- [7] W.F. Seidl, Primary calibration of the Boeing 18 kg/s airflow calibration transfer standard, *Proceedings of International Symposium on Fluid Flow Measurement*, 1986, pp. 80-96.
- [8] CH Li, LS Cui, C Wang, The new pVTt facility in NIM. *FLOMEKO*, Pair, France, 2013.
- [9] CH Li, LS Cui, C Wang. The uncertainty analysis and capability verification for the high pressure pVTt gas flow facility of NIM. *FLOMEKO*, Sydney, Australia, 2016.
- [10] M Ishibashi, M Takamoto. Theoretical discharge coefficient of a critical circular-arc nozzle with laminar boundary layer and its verification by measurements using super-accurate nozzles. *Flow Measurement & Instrumentation*, 2000, 11(4):305-313.

---

# Pitot based on mean square error algorithm for gas-liquid flow gas flow measurement

Yu Gu<sup>1</sup>, HanSheng Ye<sup>2</sup>, ZhongJun Han<sup>3</sup>, Feng Chao<sup>4</sup>

*<sup>1</sup>HeFei Comate Smart Sensor co.,LTD, Floor 2,building D2,Innovation industrial park, No 800 Wangjiang west Road, HeFei,Anhui,China*

*<sup>2</sup>HeFei Comate Smart Sensor co.,LTD, HeFei, China*

*<sup>3</sup>HeFei Comate Smart Sensor co.,LTD, HeFei, China*

*<sup>4</sup>HeFei Comate Smart Sensor co.,LTD, HeFei, China*

*E-mail: yehsheng@comatemeter.com*

---

## Abstract

Pitot tube has the advantages of small pressure loss, cost economical, compact size, easy to carry, install and measure., which make It suitable for the flow measurement of medium and large diameter pipes, and flow velocity and velocity distribution measurement at any point in air duct, water pipe and mine. However, when measuring the mixed phase fluid of gas and liquid, the pitot tube will have abnormal fluctuations in the flow measurement with the passage of time, and the measurement result would be far from the actual flow rate.

Gas-liquid mixed phase fluid is widely used in industrial production. Because gas phase fluid can be compressed, and there is shifting between gas and liquid phases, and the two-phase interface is complex and variable, the flow measurement of gas-liquid mixed phase flow is very difficult. In actual measurement, there could be condense liquid slowly formed on the inner wall of the pressure tapping hole of the pitot tube. As the amount of the condense water increase, due to the effect of liquid surface tension. attracted by internal molecules, the liquid surface molecules have a tendency to be pulled inside. As time goes by, there will be more and more water drops, and once it reached to a certain amount, the water drops will form a water film. Once the water film is formed, the pressure tapping hole of the pitot tube is divided into the measuring side and the actual flow side by the water film, and the measuring side cannot correctly respond to the change of the flow rate any more, and therefore cause inaccurate measurement.

Based on the analysis of the feature of the flow profile of gas-liquid mixed-phase fluid and the data of the forming of water film, we propose a method of recognizing the abnormal data caused by the water fluid in a gas-liquid mixed-phase fluid base on the square error algorithm. We add a two-way solenoid valve to the front and rear pressure holes of the pitot tube. Under normal circumstances, the solenoid valve is closed. Once the algorithm recognizes the abnormal data, it opens the pressure-receiving hole by controlling the small solenoid valve built in the pitot tube, and the positive pressure or negative pressure of the gas-liquid mixed phase flow destroys the formation of the water film.

## 1. Background

In most gas measurement applications, pitot tube flow meters are widely used because of its low pressure drop, convenient installation and high accuracy. If there is water vapor contained in the gas to be measured, there will be condensate water in the form of liquid drop generated on the inner wall of the pressure tapping hole of the pitot tube. As the amount of the water increases, a water diaphragm will be generated on the inner wall. And once the diaphragm is generated, the pitot pressure tapping tube will be divided into measurement side and real flow side by the water diaphragm. The measurement side can not measure the real pressure anymore, and the flow meter will measure incorrectly due to this cause.

In order to overcome the influence of liquid impurities in gas-liquid mixed phase fluid on gas flow measurement, this paper provides a pitot tube flowmeter based on mean square error algorithm for gas-liquid mixed phase fluid flow measurement.

## 2. Technical goals

### 2.1 *Analysis of the influence of gas-liquid mixed phase fluid on measurement*

The pitot tube of this paper uses  $\varnothing 11$  probes. The inner diameter of the two capillaries for measuring total pressure and static pressure in the probe is  $\varnothing 3$ . The diameter of the capillary and the probe are thinner and can be used in pipe from DN25 to DN450. It causes less pressure loss in the pipe and can be hot tapping installed. The two capillaries in the pitot tube flowmeter are used to measure the total dynamic pressure and static pressure of the fluid in the pipeline. When measuring the gas-liquid mixed phase fluid, the water vapor will condense into water droplets on the two pressure tapping holes of the pitot tube. Due to the presence of surface tension of liquid, the molecules on the surface of the liquid are pulled towards inside by the gravity of the internal molecules. As time goes by, more and more water droplets will be formed and a water diaphragm will be formed afterwards when there is a certain amount of water droplet. According to the capillary condensation phenomenon, the water diaphragm will be a concave liquid surface in the capillary of the pitot tube. Please refer to the illustration (Figure 1) below about the water diaphragm inside the capillary.

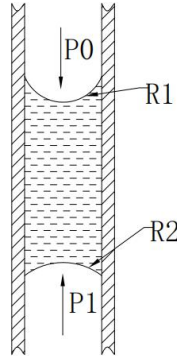


**Figure 1:** Schematic diagram of water diaphragm in capillary

Due to the surface tension and gravity of liquid, the pressure  $P_0$  at the upper side of the water diaphragm and the pressure  $P_1$  below it must be unequal. If the pressure inside the pipe is in dynamic equilibrium at this time, the relationship between  $P_0$  and  $P_1$  is as follows:

$$P_0 + \rho gh + 2 \frac{\alpha}{R_1} = P_1 + 2 \frac{\alpha}{R_2} \quad (1)$$

$$\Delta P = P_1 - P_0 = 2\alpha \left( \frac{1}{R_1} - \frac{1}{R_2} \right) + \rho gh \quad (2)$$

In the formula:

$\rho$  : Air density;

$g$  : Gravitational acceleration;

$h$  : Height of water diaphragm;

$\alpha$  : Water tension coefficient,  $7.28 \times 10^{-2} \text{ N/m}$ ;

$R_1$  : Curvature radius of upper side concave surface;

$R_2$  : Curvature Radius of lower side concave surface;

From Equation 2 we can tell that the pressure difference between the upper and lower side of the water diaphragm is caused by the gravity of water and the additional pressure caused by the different Curvature radius of the upper and lower side of the water diaphragm.

Assuming that a 10 mm thick water diaphragm is produced during the measurement, and the

curvature radius of the upper side and lower side of the water diaphragm are 3mm and 5 mm, as illustrated in figure 2:

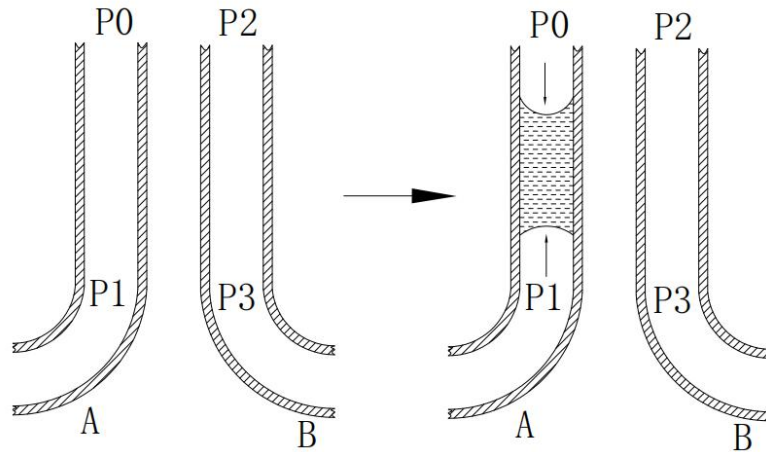


**Figure 2: Schematic diagram of the forming of water diaphragm**

The delta pressure measured by the differential pressure pitot tube flow meter before the forming of the water diaphragm:

$$P_m = P_0 - P_2 \quad (3)$$

$$P_0 = P_1 \quad (4)$$

$$P_2 = P_3 \quad (5)$$

$$P_m = P_1 - P_3 \quad (6)$$

In the formula:

$P_m$  : Differential pressure value collected by pitot tube;

$P_0$  : Upper side pressure of total pressure capillary;

$P_2$  : Upper side pressure of static pressure capillary;

$P_1$  : Lower side pressure of total pressure capillary;

$P_3$  : Lower side pressure of static pressure capillary;

---

Since the total pressure and the static pressure capillary are connected:

After the forming of the water diaphragm , the differential pressure value measured by the differential pressure pitot tube flowmeter:

$$P'_m = P'_0 - P_2 \quad (7)$$

$$P'_m = P_m - \Delta P \quad (8)$$

In the formula:

$P'_m$  : The differential pressure value collected by the pitot tube flowmeter after the forming of the water diaphragm;

According to the calculation formula (5), we can tell that the differential pressure value collected by the pitot tube flow meter after the forming of the water diaphragm in the total pressure capillary will be smaller than the value from normal measurement. and will be on the contrary if the water diaphragm formed in the static pressure capillary

The formula of calculating the flow velocity from the differential pressure of a pitot tube flow meter

$$v = K\sqrt{2\Delta P/\rho} \quad (9)$$

In the formula:

$v$  : Actual velocity in pipeline;

$K$  : Pitot tube coefficient, 0.65;

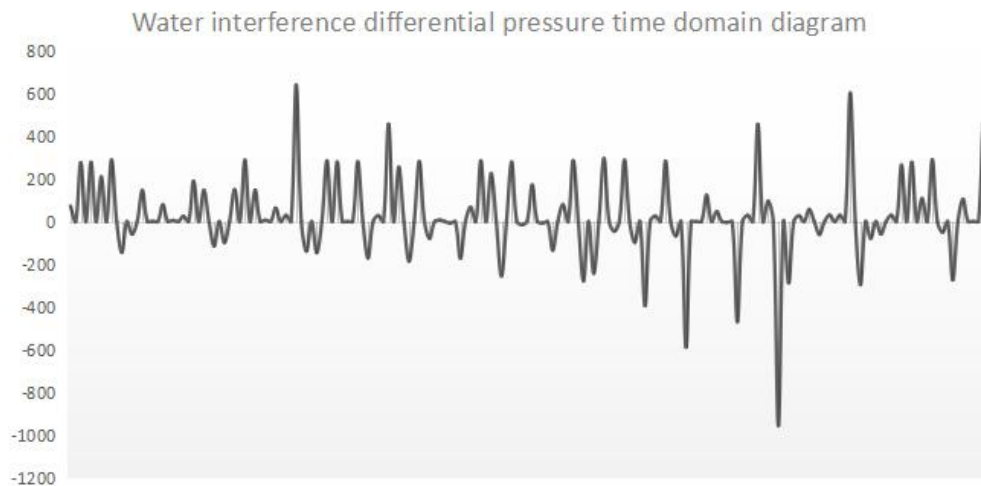
$\Delta P$  : Differential pressure value collected by pitot tube;

$\rho$  : Actual density value of the air.

If the gas-liquid mixed phase fluid in the pipeline runs at a velocity of 10 m/s, the differential pressure value obtained by the pitot tube calculated according to the calculation formula (6) will be 98.2 Pa. Say the thickness of the total pressure capillary water diaphragm is 10 mm. and the Curvature radius of the lower and upper side of water diaphragm are 5mm and 3mm,  $\Delta P$  will be about 120Pa according to the calculation formula (2), thus the differential pressure value collected by the pitot tube at this moment is -21.8Pa. If the water diaphragm is in the static pressure capillary, the differential pressure collected by pitot tube will be 218.2 Pa.

Based on these data, we can tell that the water diaphragm causes the pitot flow meter unable to measure the flow rate correctly.

The analysis above is based on the data of a single water diaphragm under a stable condition. But in a real measurement process, multiple of water diaphragms may be generated in the capillary, the thickness of the water diaphragm will be continuously increasing until the equilibrium state is broken, and some of the water diaphragms begins to slide down from the capillary until it reaches to a new balance. The following graphic shows the time-domain diagram of the differential pressure in two experiments on a normal pitot tube flow meter made in a 100mm inner diameter circular pipe with 7.8 barG pressure and 8 Nm<sup>3</sup>/min flow rate with interference of water.



When there is no water, the data is stable at around 285.7 with less fluctuates. When there is water, the differential pressure data is disorderly without pattern, sometimes even a negative value. After a long period of experiments and analyzing on the formation of water interference and the impact of water interference on differential pressure collection, we reached to a water interference identification algorithm.

Algorithm 1: In normal use, the gas in the pipeline will not flow backward, so there should not be negative differential pressure value. Once the negative differential pressure occurs in the pipeline with a pipe pressure larger than 0.1Mpa, it can be judged as water interference.

Algorithm 2: Calculate the maximum variation threshold of the differential pressure in the pipeline according to the differential pressure value at the moment and the response characteristic of the differential pressure sensing diaphragm. If the variation goes beyond threshold, it can be judged as water interference.

---

Algorithm 3: During a period of operation, although there is no negative differential pressure value, and the variation is within the set threshold, We can calculate the mean square error of the differential pressure value in the period , and check if the mean square error is beyond set threshold to judge if there is water interference.

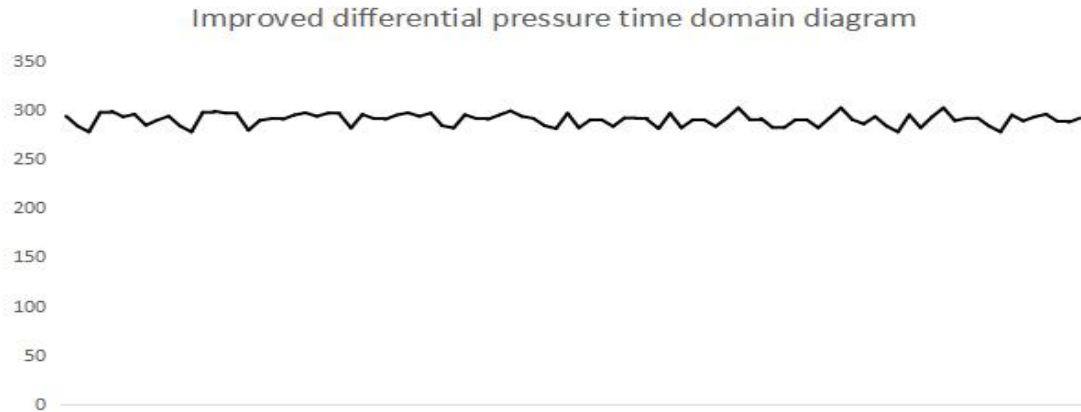
Algorithm 4: In order to ensure the of the reading displayed normally, define a set of damping arrays for flow rate calculation. Only normal differential pressure data determined by Algorithm 1, Algorithm 2, and Algorithm 3 can be put in the damping array and used in the calculation of the displayed flow rate.

## *2.2 Deal with the interference of gas-liquid mixed phase fluid on the flow rate measurement*

The technical solution adopted in this paper is to add dual-pass solenoid valve in both total pressure and static pressure capillary. The solenoid valve is initially and defaulted to be closed, and we know that the total pressure and static pressure capillaries are connected with the differential pressure pizoes. When the solenoid valves are open, the total pressure and static pressure capillaries connect with atmosphere. Control the open/close of the solenoid valve in a pulsing blowing method, to blow the condensate water droplet and water diaphragm in the capillaries. After the blowing process, the solenoid valve will return to initiating status of closed.

Install this kind of pitot tube flow meter in a air flowing pipeline which contains huge amount of water, and once the water diaphragm is formed, the water interference identification algorithms will work. Once a water interference is found according to the algorithms, the solenoid valves in the capillaries will be on and its closing/opening will be controlled under a pulse blowing method. In this method the valves will be opened for 3 seconds and closed for 1 seconds for 5 rounds, so the water diaphragm will be blow away. During the blowing process, the flow rate will be calculated according to historical differential pressure value. The differential pressure value 3 seconds after the blowing will be used in flow rate calculation .

Following charts show the experimental results of using the Pitot flowmeter of the present invention in a circular pipe with a inner diameter of 100 mm, under 0.78MPa, with a flow rate of 8 Nm<sup>3</sup> /min :



From the analysis chart ,we can tell that the differential pressure value fluctuates around 289.9, and the data is stable with no negative value. This invention can ensure a stable measurement with an accuracy of  $\pm 1\% \text{ RD} \pm 0.5\% \text{ FS}$  in a tough condition where the normal pitot tube can't measure properly.

This paper present a solution for measuring the gas flow rate in a gas-liquid mixed phase fluid. If the liquid in the fluid gasifies , the density of the gas will change and the flow rate measured by the pitot tube flow meter will differ from the real flow rate a lot. Thus our solution only applies to condition in which the density of the gas in the gas-liquid mixed phase fluid is stable

### References

- [1]Wuchang Cai. New flowmeter test instrument,Chemical Industry Press,November 2006
- [2]John David Anderson,Fundamentals of Aerodynamics,24(3): 69-71 September 2012

# A Method for Maintaining Accuracy of Ultrasonic Gas Flow Meters Calibrated on Air at Atmospheric Pressure when Measuring Natural Gas at High Pressure

A. Stetsenko, V. Naumenko

A. Stetsenko, [andrii.energo@gmail.com](mailto:andrii.energo@gmail.com), Olten, Switzerland  
V. Naumenko, [naumenko@energo.kh.ua](mailto:naumenko@energo.kh.ua), Kharkiv, Ukraine

---

## Abstract

With the increase in the requirements for the accuracy of measurement in the commercial accounting of natural gas, the issue of initial calibration and periodic verification of measuring instruments in conditions as close as possible to actual working conditions is relevant and commonly discussed among professionals. This issue also applies to ultrasonic gas meters. Despite the general tendency to calibrate (verify) ultrasonic gas meters at operating conditions, this requirement is not always appropriate. First of all, this is due to the high cost of calibration services and the insufficiently developed network of accredited calibration laboratories. The issue of determining the rules and criteria for justifying the need to calibrate ultrasonic gas meters at operating conditions remains extremely concurrent.

---

## 1. Statement of the problem

The major issues of metrological support of ultrasonic gas meters are the following:

1. Adequacy of calibration and verification of ultrasonic gas meters using "air" at atmospheric pressure as medium as compared to the use of "natural gas" at working pressure as medium for calibration.

The requirement of meters calibration and verification in conditions that are as close as possible to working ones is necessary, but not always optimal, because of the high technical, time and financial expenditures required to carry out this calibration (verification). Therefore, an evaluation of the results of comparing the calibration characteristics of meters obtained in air at atmospheric pressure and on natural gas at high pressure is a crucial task.

2. Insufficiently developed metrology infrastructure - currently there is just a small number of calibration labs working on natural gas at high pressure.

3. The normative base that regulates the calibration of meters in different environments and pressures is not developed - currently there are no compulsory normative documents regulating

compulsory testing on the working medium, as well as documents defining the criteria for selecting the medium and pressure for verification of ultrasonic gas meters.

## 2. Analysis of recent researches and publication

Analysis of the main international and state regulatory documents, as well as industry standards, demonstrates the lack of a unified approach to the requirements for determining the working environment and pressure when calibrating and periodical verification of ultrasonic gas meters [1-4].

The requirements for testing, calibration and verification of ultrasonic meters, depending on the class of their accuracy and the parameters of the working environment, are either contradictory or recommendatory in nature.

For example, paragraph 13.1.3 of OIML R 137 1&2 specifies the necessity to test the meters under the conditions closest to the operating ones. However, there are no specific criteria for choosing a decision on the verification conditions. Moreover, it is possible to carry out verification on the type of gas that is different from the operating one, according to the decision of the authorized bodies, and this can add the subjective human factor.

Statistical analysis of the existing regulatory documents (Table 1) shows, that meters of class 0.5 and 1.0 having maximum permissible error in the range of  $\pm 0,5-1,0\%$  for flow range  $Q_t < Q < Q_{max}$  are most common and are used in international classifications.

Table 1 — Classification of gas meters in accordance value of with maximum permissible error (MPE)

Class	MPE $Q_{min} < Q < Q_t$ , %	MPE $Q_t < Q < Q_{max}$ %	AGA Report №9	ISO 170891:2010	OIML R 137-1&2	Directive 2004/22/EC (MID)	RGazprom 5.13 - 2010
0,3	$\pm 0,6$	$\pm 0,3$					X
0,5	$\pm 1,0$	$\pm 0,5$			X		X
0,7	$\pm 1,0$	$\pm 0,7$					X
	$\pm 1,4 > 12''$	$\pm 0,7 > 12''$	X				X
	$\pm 1,4 > 12''$ ; $\pm 1,4 < 12''$	$\pm 0,7 > 12''$ ; $\pm 1,0 < 12''$		X			X
1,0	$\pm 2,0$	$\pm 1,0$			X	X	X
	$\pm 1,4 < 12''$	$\pm 1,0 < 12''$	X				X
1,5	$\pm 3,0$	$\pm 1,5$			X	X	
	$\pm 2,0 > 12''$ ; $\pm 2,0 < 12''$	$\pm 1,0 > 12''$ ; $\pm 1,5 < 12''$		X			

According to regional regulatory requirements, these classes of meters are the basic ones for commercial accounting of natural gas, and calibration (verification) on natural gas at operating pressure is objectively related either to the limitation of technical capabilities or to high time and financial expenses.

Paramount issues are the following:

- for meters of what accuracy class it is required to perform calibration on natural gas, and for which it is not compulsory?
- whether it is possible to confirm the metrological parameters of ultrasonic gas meters of class 0.5; 0.7 and 1.0 in the range  $Q_t < Q < Q_{max}$  under operating conditions after calibrating them in air at atmospheric pressure?

For example, the official calibration schemes approved in the territory of the CIS countries do not currently require verification (calibration) of ultrasonic meters on natural gas and working pressure [5,6]. The specified official reference to the verification of ultrasonic gas meters on natural gas is described in the corporate Recommendations of the "OAO Gazprom" Organization that regulate the calibration of high-precision ultrasonic meters with MPE no more than

0.35% with "natural gas" as verification medium and the pressure closest to the working one, and verification of the meters of class 1,0 - in air at atmospheric pressure [7].

European regulations allow the meter to be calibrated at an operating pressure of up to 6 bar in air at atmospheric pressure. At the same time, meters designed for operation at pressures above 6 bar must be calibrated in conditions as close as possible to working ones [8].

The question of the possibility of replacing the verification conditions and the criteria for making a decision remains open.

### 3. The aim of the research

As a rule, meters are calibrated and calibrated on calibration stands using air as measured medium at a pressure close to atmospheric pressure, while later they are used to account for natural gas at a higher pressure. As a result, the question arises of the correctness of such metrological procedures from the point of view of the actual error of the meter at operating conditions.

Until recently, there was little or no detailed research into the discrepancies that arise when verifying counters or gas flow meters using air, which is a medium that replaces the working environment of such devices-natural gas.

This is due in particular to the following:

- a small number of verification stands operating on natural gas at high pressures;
- a poorly developed regulatory framework that does not clearly define the criterion - which meters need to be calibrated on air at atmospheric pressure and which ones should be calibrated on medium and pressure corresponding to the operating conditions.
- the use of air instead of natural gas simplifies the design of test facilities, reduces their cost and significantly reduces the safety requirements for their operation.

It is believed that such a replacement is not only permissible, but also expedient. In support of this, the following arguments are presented:

- when checking, it is not necessary to determine the density of the working medium;
- full safety of verification process is guaranteed;
- consistent repeatability of verification results is ensured, since gas meters calibrated in air at zero overpressure and operating on gas at completely different pressures initially have a stable

conversion factor (a constant ratio of the output signal to the flow of air or gas passing through the instrument). This ensures reliable convergence of readings for different media and operating conditions. Otherwise, since in the gas measurement unit, in addition to the volumetric flow, it is still necessary to measure the temperature and pressure of the gas, even in the absence of the necessary stability of the conversion coefficient, it is always possible for the device to linearize its static characteristic during its calibration. And when moving to real operating conditions, also make the appropriate adjustments, calculating the Reynolds number ( $Re$ ) for each measurement case. Moreover, modern microelectronics can solve even more complex problems at relatively low costs.

Though the above arguments sound convincing, there are restrictions which apply. The problem of repeatability of the results discussed above can be solved in principle, but it is necessary to fully formulate the applicable conditions, and this has not been feasible so far. The point is that when the gas flows through the pipeline, and especially when it is expanded or compressed (as happens, for example, when the pipeline has bends or any obstacles in the flow and the medium goes around the flow), complex aerodynamic and thermodynamic processes take place. Accordingly, the flow depends not only on the value of Reynolds number  $Re$ , but also on the values of other aerodynamic and thermodynamic coefficients, in particular, the values of Strouhal number ( $St$ ), Nusselt number ( $Nu$ ) and Froude number ( $Fr$ ). And it has generally not been possible to carry out flow correction taking into account these values, because, firstly, there is insufficient experimental data, and secondly, in order to determine these values, we need at least continuous information on the composition of the gas, which is absent in most of the cases of installation of gas meters.

Thus, the feasibility of replacing natural gas with air for calibration can only be judged by analyzing in detail and confirming in practice the effect of such a replacement on the course of the processes that occur when verifying meters with the help of test rigs, and also during their operation in real conditions.

#### 4. The main material

There are quite a large number of sources regulating the requirements for calibration of turbine and rotary gas meters, as well as data on comparative tests of these meters under different

conditions [9-12]. Manufacturers of turbine and rotary gas meters, as a rule, measure meters both in air at atmospheric pressure and on natural gas for various pressures. The results of the calibration show the deviations of the characteristics of these meters for different values of the pressures of the medium being measured and the type of this medium.

At present, there is little information available on similar tests of ultrasonic meters. This information is either kept secret by manufacturers, or it is not available at all.

In order to determine the feasibility of conducting a primary (periodic) calibration at operating conditions of USGM of class 0.5; 0.7 and 1.0, an experimental study of two-channel and four-channel ultrasonic gas meters Energoflow GFE was carried out within the framework of the test program for compliance with the requirements and recommendations of the Directive 2014/32 / EC (MID) and OIML R 137-1 & 2.

When designing the instruments, an algorithm was used that made it possible to implement a mathematical model of calculations that maximally takes into account the dynamic processes in the measured flow. This solution allows calibrating the meters on air at atmospheric pressure, after which, by entering into the electronic unit the parameters of the working medium that correspond to the actual operating conditions of the meter (natural gas parameters, operating temperature and pressure ranges), keeps the measurement error in permissible range at operating conditions for various media and at different pressures.

The results of consequent verification of meters on natural gas at pressure of 4.0; 20.0 and 30.0 bar in the FORCE Technology laboratory (Denmark) and testing facilities of RMA (Germany) laboratory after initial calibration in air at atmospheric pressure demonstrated that these modifications of the meters confirm to the corresponding accuracy class of 0.5; 0.7 and 1.0 in the range  $Q_t < Q < Q_{max}$  according to OIML R 137-1 & 2 and MID 2014/32 / EU, respectively (Figures 1, 2).

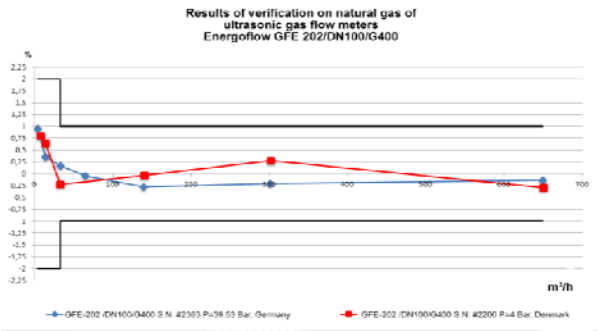


Figure 1 – Energoflow GFE 202 error curve

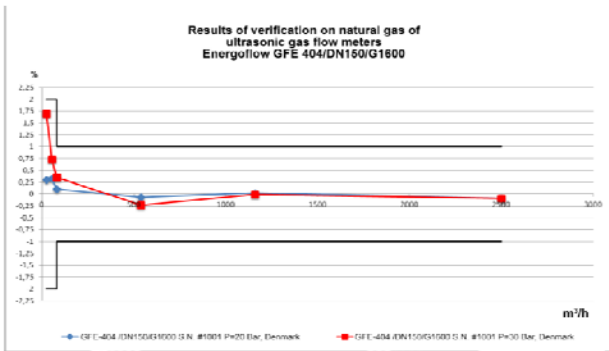


Figure 2 – Energoflow GFE 404 error curve

Particular attention should be paid to the Energoflow GFE 202 and Energoflow GFE 404 testing carried out to assess their conformity with the requirements of the MID 2014/32/EU Directive. These tests were conducted by representatives of PTB (Germany). The main types of tests are confirmation of the metrological characteristics on natural gas and at high pressure in conditions of strong disturbance of the flow caused by local resistances of the following configurations: "two bends in different planes", "two bends in different planes with the addition of a half pipe area plate (half-moon opening)" at different lengths of straight pipe runs and meter orientations. These tests were carried out at the testing facilities of RMA (Germany) laboratory.

Tests results (Figs. 3-7) confirmed the Energoflow GFE 202 and Energoflow GFE 404 compliance with the requirements of OIML R 137-1 & 2 and MID 2014/32 / EU.

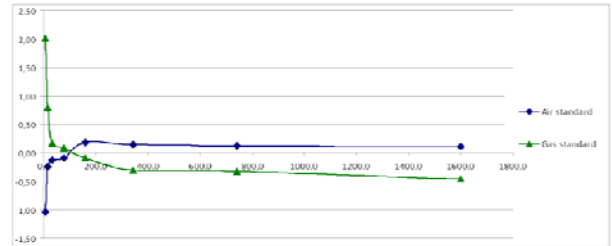


Figure 3 - Test results of the Energoflow GFE 202 at RMA calibration facilities (standard conditions, air, natural gas)



Figure 4 - Test results of the Energoflow GFE 202 at RMA calibration facilities (two bends in different planes, air, natural gas)

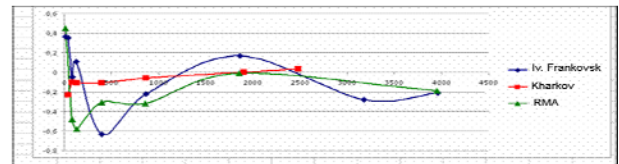


Figure 5 - Comparative results of Energoflow GFE 202 tests on different mediums and at various pressures

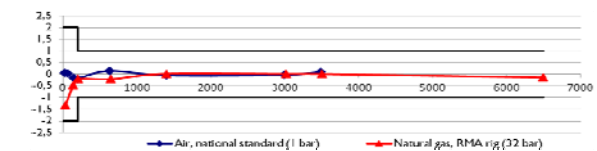
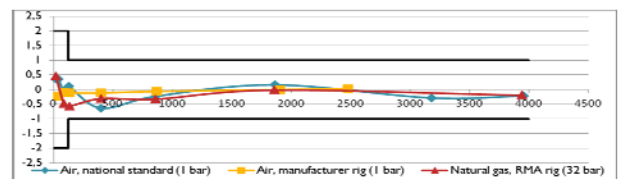


Figure 6 (a, b) - Test results of Energoflow GFE 404 at RMA calibration facilities (standard conditions, air, natural gas)

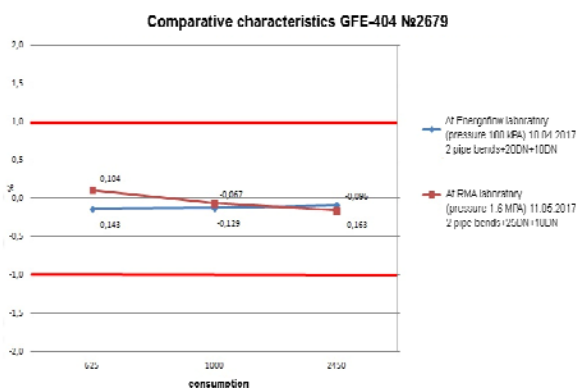


Figure 7 – Test results of Energoflow GFE 404 at RMA calibration facilities (two bends in different planes + half-moon opening, air, natural gas)

## 5. Conclusions

Considering the above, during the tests, Energoflow AG developed and checked an algorithm that enables to implement the mathematical model of calculations, maximally takes into account the dynamic processes in the flow to be measured. This solution allows for calibrating the meters on air at atmospheric pressure, and then, by entering in the electronics unit the parameters of the operating medium, which correspond to the real conditions of meter operation (parameters of natural gas, operating temperature and pressure ranges), to maintain the permissible values of errors in working conditions on different mediums and at various pressures.

1. Ultrasonic gas meters Energoflow GFE 202 and Energoflow GFE 404 showed good stable results in all types of tests and for different working mediums.

2. Despite the general tendency for calibration (verification) of ultrasonic gas meters under working conditions, this requirement is not always appropriate. Due to a significant reduction in the cost of calibration and associated transport costs during periodic maintenance, the proposed algorithm enables to expand the possibilities of using ultrasonic gas meters after calibration on air for natural gas measurement without additional calibration at process pressure on natural gas.

3. The obtained results open prospects for further research and improvement of technologies of ultrasonic gas meters in order to accumulate statistics of test results and the possibility of approving the described methodology at the regulatory level.

4. As a result of tests carried out jointly with PTB, MID certificate No. DE-16-MI002-PTB008, Revision 3 for Energoflow GFE202 and Energoflow GFE404 was obtained and report of class 0.5 according to OIML R137 1&2, section 5.3.2. for Energoflow GFE404 was issued.

## References

- [1] Measuring Instruments Directive 2004/22/EC of the European Parliament and of the Council.
- [2] OIML R 137-1&2:2012 Gas Meters - Part 1-2.
- [3] ISO 17089-1:2010 Measurement of fluid flow in closed conduits - Ultrasonic meters for gas.
- [4] AGA Report No. 9. Measurement of Gas by Multipath Ultrasonic Meters.
- [5] DSTU 3383: 2006 Metrology. State verification scheme for means of measuring volume and volume of gas consumption.
- [6] GOST 8.324-2002, State system for ensuring the uniformity of measurements. Gas meters. Verification procedure.
- [7] Recommendations of OAO Gazprom, R Gazprom 5.13-2010 Ensuring the uniformity of measurements. Organization and procedure of verification and calibration of ultrasonic gas flow converters in OAO Gazprom.
- [8] Calibration Certificate № 9.8-14664-4 dated 11-08-2015 and № 9.8-14665-2 dated 06-08-2015, Force Technology.
- [9] Dyakowska E., Jastrzębska R., Stańczak P.: Czy konieczne jest wzorcowanie gazomierzy turbinowych przy przewidywanym ciśnieniu roboczym?. *Pomiary, Automatyka, Robotyka*, 1, 1998, s. 30-33.
- [10] R. Richards and D. Bertels iMeter the Netherlands, Test Benches for Calibrating Custody Transfer Gas Meter, Paper for CII New Delhi Februari 2007.
- [11] Paul W. Tang, Calibration of turbine gas meter by matching Reynolds number and density.
- [12] EN 12480:2015 Gas meters. Rotary displacement gas meters.
- [13] EN 12261:2002 Gas meters. Turbine gas meters.

# Development of an optical measurement method for “sampled” micro-volumes and nano-flow rates

F.Ogheard<sup>1</sup>, P.Cassette<sup>2</sup>, A.W.Boudaoud<sup>3</sup>

<sup>1</sup>CETIAT, Domaine scientifique de la Doua, 25 avenue des Arts, 69100 Villeurbanne Cedex, France

<sup>2</sup>CEA, LIST, Laboratoire National Henri Becquerel, 91191 Gif sur Yvette cedex, France

<sup>3</sup>Sorbonne Université, 21 rue de l'École de médecine, 75006 Paris, France

E-mail (corresponding author): florestan.ogheard@cetiat.fr

---

## Abstract

Radiopharmaceuticals used in nuclear medicine for therapy or diagnosis (molecular imaging, PETscan, scintigraphy) are characterized in terms of volume activity before injection to patients. The current measurement process relies on dose calibrators which have to be calibrated by transfer standards, traceable to primary standards. For very short half-life radionuclides (few minutes), the metrological traceability can only be assured through an on-site calibration with primary standards. However, until now, there is no primary system for the direct measurement of such high activity radioactive solutions. This study presents the sub-system under development for the measurement of a sampled volume of the order of one microliter with an associated relative target standard uncertainty of 1 %.

This article focuses on the volume measurement method development and its validation by comparison to the gravimetric method.

The paper, in a first part, describes the developed method and the associated hardware and software. The authors have chosen a non-contact optical method implemented by a microscope camera and associated optics in front of a transparent capillary.

The second part of the paper describes the measurement process. Several image processing steps are described and the traceability to dimensional units are presented.

Finally, the paper presents some validation results by comparison to a gravimetric measurement, including repeatability and accuracy tests. Further development and improvements, necessary for the finalization of the prototype and the measurement of nano-flow rates are discussed.

---

## 1. Introduction

### 1.1 General context

Low liquid flow rates, typically below  $1 \text{ l.h}^{-1}$ , are present in a growing number of applications. For example, precise dosing in pharmaceuticals, chemical or food industries, microfluidics and its applications, therapeutical treatments, fuel and additives injections in automotive industry. All of these applications require dedicated measurement methods and instruments, given the increased amount of complexity of Physics underlying flows at such scales. Indeed, the flows of liquids at these flow rates are subject to additional influence parameters, such as evaporation, surface tension variations, adsorption, etc.

Since the beginning of the 2010s, some national reference laboratories in flow metrology, including

the CETIAT, have reference calibration benches. Most of these laboratories allow the measurement of flow rates down to a few microliters per hour.

However, below this threshold, metrological traceability to the International System of Units (SI) becomes difficult due to the lack of flow references.

### 1.2 Context at CETIAT

CETIAT's Liquid Flow Measurement Laboratory is the national reference laboratory, associated with the National Laboratory for Metrology and Testing (LNE) for the development of the "liquid flow" standard for water. Until 2012, the LNE-CETIAT was able to perform flow rates calibrations for flow rates ranging from  $8 \text{ l.h}^{-1}$  to  $36 \text{ m}^3.\text{h}^{-1}$ . This laboratory provides the best uncertainties in France for this physical quantity.

In 2012, the laboratory extended its capabilities and inaugurated a new calibration and testing platform for the generation and measurement of a micro-liquid flow over a range of flow rates from 1 ml.h<sup>-1</sup> to 10 l.h<sup>-1</sup> [1,2]. This platform, dedicated to calibrations and tests of measuring devices used in the pharmaceutical, medical, fine chemicals and analysis fields, is unique in the world because of its technical and metrological capabilities. It has been accredited by COFRAC (French accreditation body) for calibrating liquid flow meters. Moreover, LNE-CETIAT micro-flow facility has been used to metrologically assess drug delivery devices such as syringe pumps, in the scope of the European Joint Research Project "Metrology for Drug Delivery" funded by the EURAMET EMPIR program and the French Metrology [3]. The following figures 1 & 2 present a diagram and a picture of the French micro flow standard at LNE-CETIAT.

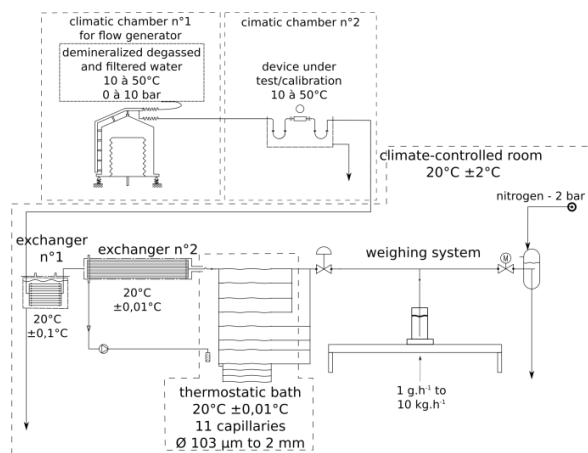


Figure 1: diagram of LNE-CETIAT micro flow facility



Figure 2: picture of LNE-CETIAT micro flow facility inside the climate-controlled room

### 1.3 A specific need for sampled micro-volume traceability: radiopharmaceuticals volume activity measurements

Radiopharmaceuticals are pharmaceutical drugs containing radioisotopes. They can be used as diagnostic or therapeutic agents [4-9].

The activity measurement of a radiopharmaceutical solution can be realized using several methods depending on the properties of the radionuclide in question (Its physical state, type of decay, etc.). These measurements can be primary or secondary. The latter ones are generally performed in an ionization chamber. This kind of devices requires a prior calibration consisting of the determination of the calibration factor, which ensures the conversion of the ionization current's intensity to a measured activity. This factor depends on many parameters e.g. the used source's geometry (syringe or vial), the chamber's environment, etc. Hence, a calibration factor is valid only for defined conditions and the calibration of the device in an accredited laboratory should be performed under identical or at least closest conditions to the ones in the medical service where the radiopharmaceuticals are prepared. Primary measurements of the activity of radioactive solutions emitting beta or alpha radiation are mainly performed using liquid scintillators. For this method, a preparation of radioactive primary solutions, by mixing the dissolved radionuclides with a scintillator, is necessary. For certain short-lived radionuclides used for PET in a medical service, for example <sup>11</sup>C (20 minutes) or <sup>15</sup>O (2 minutes), it is very difficult to route the radioactive solution for a primary calibration in the laboratory. This calibration must therefore be done on site. In the case where the primary measurement system is transportable, there is also a need to implement the specific material for the preparation of primary sources (e.g. precision microbalance), which is difficult to adapt to the operating constraints of a nuclear medicine service. A major technological breakthrough would be then to perform these measurements on site, with primary methods and without the need for source preparation.

In this context, this research project aims to develop an autonomous measuring device that can be used in situ by producers and radiopharmaceuticals users (radioisotope production centers for medical use and nuclear medicine services), and allowing the direct measurement of radiopharmaceuticals activity, without manipulation of the radioactive solution. The device consists of a volume sampling system, an optical sampled volume measuring system, and an activity measurement system. The solutions

usually have a high specific activity (up to 25 MBq/g for injectable solutions and a few tens to a few hundreds GBq/cm<sup>3</sup> at the end of production and during the synthesis of the MRP), the final system must allow measurement without manipulation of radioactive solution, in order to limit the maximum dose induced to operators and ensuring the maintenance of the sterility of the solution [10,11].

## 2. Description of the system

As part of the development of its volume sampling system, LNE-CETIAT had to address three main points: (1) Reducing the sampled volume, in order to reduce the total activity and thus, facilitating the measurements, (2) Improving the volume measurement accuracy, (3) Limiting the manipulation of radioactive solutions. LNHB, on its side, developed an innovative activity measurement system dedicated to radiopharmaceuticals.

### 2.1 Sampling and measurement system

The following figures 3 & 4 describe the sampling and measurement system.

The system developed at LNE-CETIAT is composed of (see figure 4):

A: Mako G507B camera with Optem 70XL zoom, piloted by R&D Vision HIRIS software and dedicated image processing script

B: Zaber (x and z axis, horizontal plan) positioning stage used to center the capillary in the image

C: Hilgenberg 0620 fused silica (quartz glass) capillary, length 15 cm, inner diameter 1 mm, outer diameter 1.2 mm

D: vial of radiopharmaceutical solution

E: Sartorius weighing scale used for the validation, measurement range 20 g, resolution 1 µg

F: Dinolite USB camera focused on liquid level in the vial

G: 25x25 mm white backlight

H: Zaber (y axis) translation stage to move the capillary up and down

I: Cetoni Nemesys syringe pump

J: ILS 100 µl syringe

K: Cetoni 3-way valve

L: stainless steel pipe 2 mm pipe, insulated

M: activity measurement system developed by LNHB, not described in this paper.

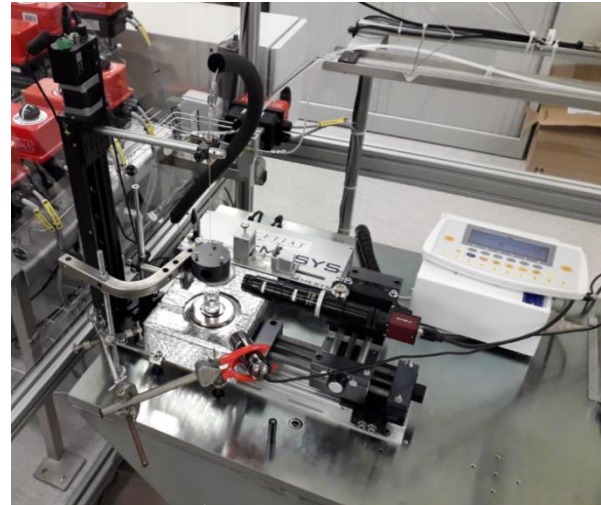


**Figure 3:** picture of the sampling and measurement system developed at LNE-CETIAT

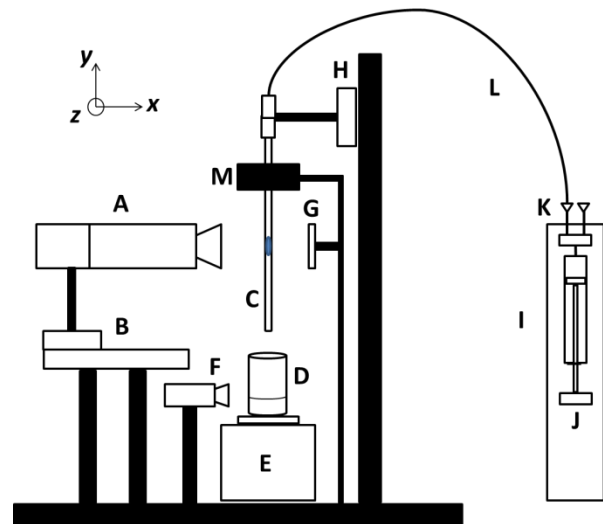


**Figure 4:** schematic of the sampling and measurement system developed at LNE-CETIAT

### 2.2 Sampling and measurement process

Using a translation stage (H), a clean and empty capillary (C) is moved toward a vial (A) containing the radiopharmaceutical solution to be calibrated (note that the weighing scale (E) is only used for validation). An USB camera (F) is used to check that the capillary end is flush with the surface: this is detected by moving the capillary downward until a liquid bridge is created. Then, the capillary is immersed of a known depth: typically, for a sampled volume of 1 µl, the immersion depth is 1 mm. The capillary is then moved upward in order to break contact with the liquid and until the sampled volume appears in the image acquired by the camera (A). The syringe pump (I) is used in sucking mode to move the sampled volume a few millimeters away from the capillary end so that it is

defined by two meniscus. The figure 5 below shows the volume in position to be measured.

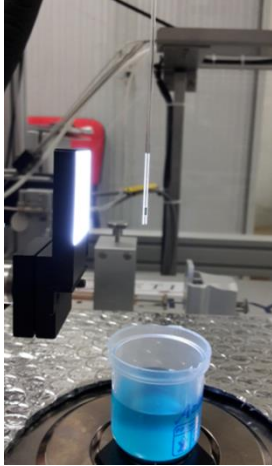


**Figure 5:** microvolume positioned to be measured

The figure 6 below shows the micro-volume as imaged and measured by the developed system.

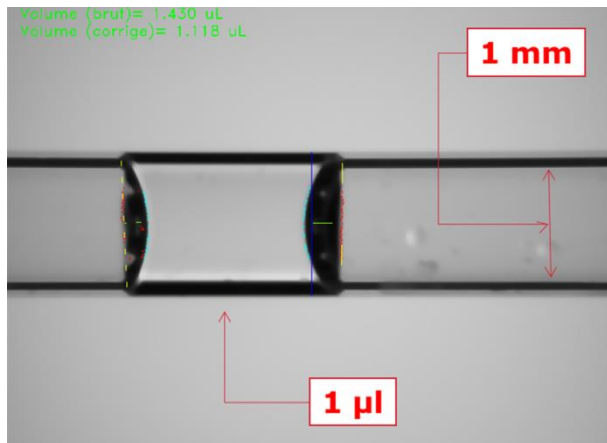


**Figure 6:** micro-volume as imaged and measured by the developed system

From the image acquired by the camera, several steps are required in order to measure a representative and accurate volume. Using the R&D VISION HIRIS software, a dedicated script, programmed by R&D VISION to fit LNE-CETIAT's goals, performed the steps described and illustrated in the figure 7.

The image processing script only requires the inner and outer diameters as an input, and detects, measures and corrects the raw cylindrical volume formed by the meniscus edges. Several corrections, described in the following chapter, can then be applied.

Step	Description	Input	Output
Edge detection	Oriented gradient calculation to detect horizontal borders		
Lines extraction	sharpening and detection hough line		
External edges extraction	external drop edges detection		
Spatial calibration	Minimum distance between borders calculation Zoom factor calculation relative to external diameter		
Vertical edges detection	Scan through image height to find left and right edges		
Internal edges detection	Scan through image height to find left and right edges		
External edges fitting	Linear fit on edges and minimum distance between lines calculation		
Meniscus height detection	Circular fit of internal points Finding maximum distance between edges and circles Calculation of local radius		
Volumes calculation	Raw volume calculation : $V_b = \pi \cdot r^2 \cdot D$ Spherical edges calculation $V_{cn} = \frac{1}{6} \cdot \pi \cdot H_n \cdot (3A_n^2 + H_n^2)$ Corrected volume calculation $V_c = V_b - V_{c1} - V_{c2}$		

**Figure 7:** image processing steps required to measure the sampled micro-volume

When a corrected volume has been measured and time-stamped by the image processing script, the capillary is translated (using stage H) upward to the activity measurement system (M) of the known distance between central focal point acquired by the camera (A) and the center of the activity measurement system.

Finally, after a few tens of seconds required to measure the activity, the capillary is translated downward, with its end inside the radiopharmaceutical vial, and the microvolume is expelled to the vial using the syringe pump in pushing mode.

The whole sampling, volume & activity measurement duration takes less than 5 minutes. The capillary being the only wetted part, it is replaced by new one for each measurement.

### 2.3 Traceability

Traceability of the measurement process is ensured by the use of a calibrated Olympus OB-M transmitted light object micrometer. Using the HIRIS software, the camera is directly calibrated so that the pixel size is known. The figures 8 & 9 illustrate the camera calibration process.



Figure 8: imaging of a micrometer object for camera calibration

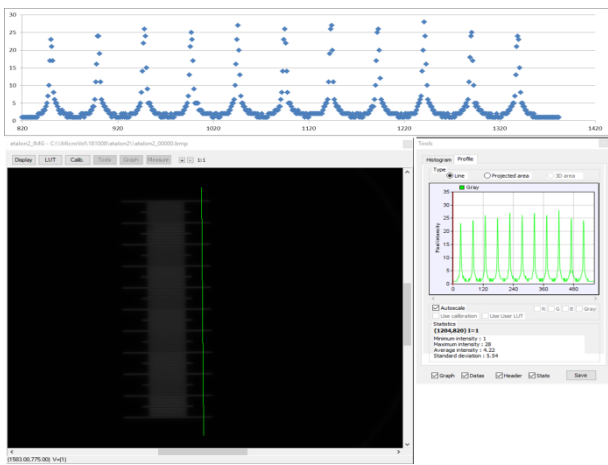


Figure 9: camera calibration using a micrometer object. Up: pixel intensity profile, Down: imaged micrometer object

When the camera is calibrated, it is then used to measure the inner and outer capillary diameter (in a location close to the image sampled volume) as the distance between edges in the intensity profiles, as illustrated in the figure 10 below.

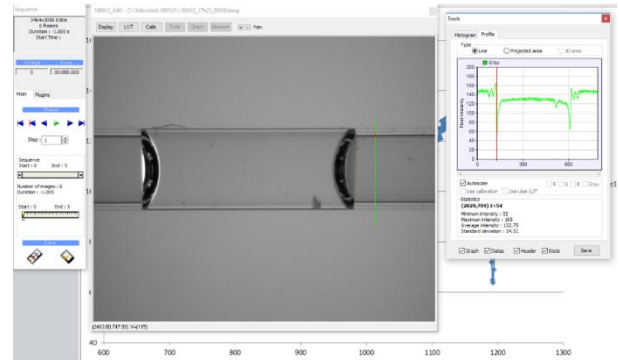


Figure 10: capillary imaging and intensity profile used for inner and outer diameter measurement

## 3. Results and discussion

### 3.1 Repeatability

In order to assess the repeatability of the measurement process, for 0.2 and 1  $\mu\text{l}$  volume has been imaged and measured for different positions in the image, with voluntary eccentricity from left to right in the image. The figures 11 and 12 and table 1 below present the results obtained.

Capillary inner diameter (mm)	Position in image (pixel)	raw volume ( $\mu\text{l}$ )	corrected volume ( $\mu\text{l}$ )
1	340	1,101	0,928
1	485	1,086	0,944
1	628	1,089	0,933
1	771	1,088	0,930
1	916	1,083	0,927
1	1057	1,088	0,930
1	1210	1,089	0,930
1	1355	1,085	0,929
1	1496	1,086	0,928
1	1646	1,087	0,927
1	1792	1,085	0,934
1	1923	1,101	0,954
1	2078	1,089	0,939
1	2216	1,067	0,892

Figure 11: example of the volume eccentricity effect in the raw and corrected volume measured for a 1  $\mu\text{l}$  sampled volume

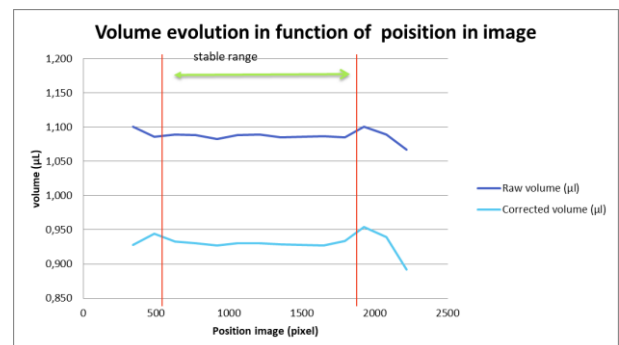
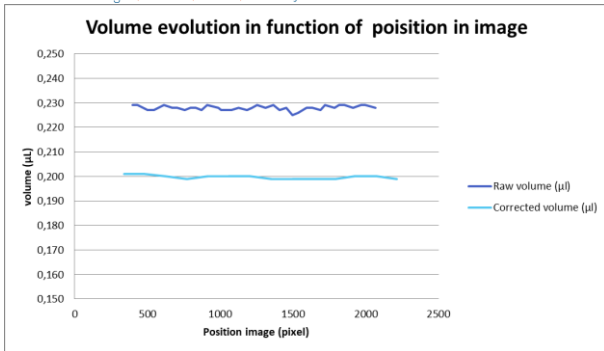


Figure 12: volume measurement evolution in function of position in image for repeatability measurements of 1  $\mu\text{l}$  sampled volume



**Figure 13:** volume measurement evolution in function of position in image for repeatability measurements of 0.2 µl sampled volume

Capillary (mm)	Mean raw volume (µL)	Mean corrected volume (µL)	raw SD (µL)	Corrected SD (µL)	Rel. Corrected SD (µL)
1	1,087	0,930	0,002	0,002	0,26%
0,5	0,228	0,199	0,001	0,001	0,47%

**Table 1:** repeatability measurements results

The position repeatability results obtained show that in a reasonably wide area in the image, the relative standard deviation for 0.2 and 1 µl volume measurements are respectively 0.5 % and 0.3 %.

### 3.2 Accuracy

In order to assess the accuracy of the measurement process, the volume obtained by the optical method, i.e. by image processing and traceability to length unit, has been compared to gravimetric measurement using the calibrated weighing scale (E). Using a vial filled with physiological serum (liquid having physico-chemical properties close to radiopharmaceutical solutions), the weighed mass has been monitored during the sampling process described in chapter 2. The Gravimetric Regression Method (GRM) described by Liang et al. in [12], the reference sampled mass and volume has been determined with 0.1 % accuracy for a 1 µl sampled volume. The figures below illustrate the evolution of the weighed mass during the sampling process.

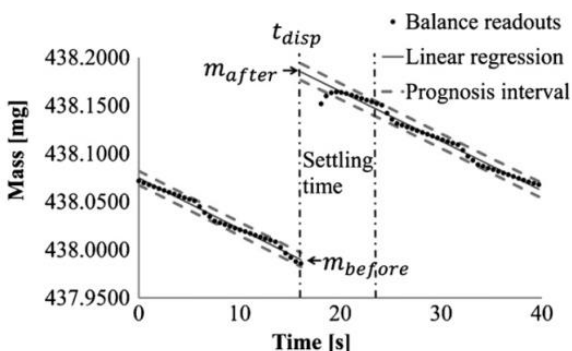


**Figure 14:** Gravimetric Regression Method as illustrated in [12]

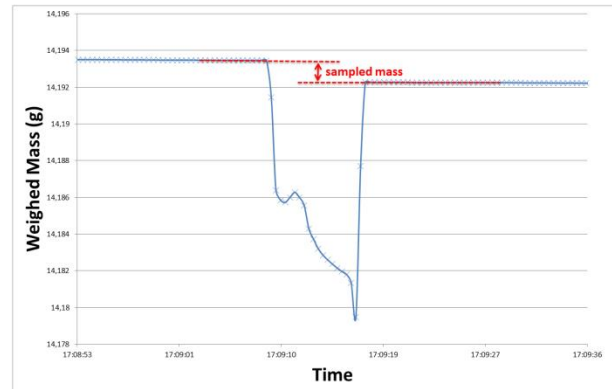


**Figure 15:** weighed mass during the sampling process of 1 µl

The GRM method applied here consists of (1) modelling of liquid evaporation before and after sampling, (2) calculation of average deviation between modelled mass curves, (3) conversion of sampled mass to volume using physiological serum density measured by a calibrated Anton Paar DMA5000 densitometer.

The deviation between the measured volume by the optical method and the gravimetric method is comprised between 0.2 % and 0.4 % for three measurements under productivity conditions for 1 µl sampled volumes.

## 4. Future developments

### 4.1 Capillary inner diameter measurement

As seen above, the measurement of a sampled micro-volume depends on the given outer and inner diameters of the capillary. The outer diameter can be determined with a 0.1 % relative accuracy from the intensity profile and the calibration of the camera. The inner diameter's measurement using the same method is, however, more subtle. In fact, refraction produces a pattern of shadows and bright regions on the transparent tube, preventing us from discerning the exact position of the inner diameter [13]. Other non-destructive measuring methods have then to be explored. We can mention among others, high spatial resolution X-Ray imaging techniques, like the Micro-Computed Tomography which is largely used in biology for 3D visualization of morphological structures [14] or the method using X-ray synchrotron radiation [15]. Another possibility would be to use an optical method in which the capillary is photographed using a digital camera and the focus is adjusted in such a way to produce, under certain conditions, two prominent light cusps. These cusps appear on the capillary as bright lines. The internal one corresponds to an apparent inner diameter from which the real diameter can be deduced using a mathematical equation [13]. Another way of

overcoming completely this problem would be to use a microfluidics chip in which droplets of the radioactive solution are generated using a given geometry [16] (Flow focusing, T-Junction, Co-flow focusing, etc.). In the case where the droplets do not occupy the whole section of the microfluidics channel, the value of the inner diameter is no longer necessary and the volume of the droplets can be measured simply by the optical method and a given software: Automated Droplet Measurement (ADM) [17], Droplet Morphometry and Velocimetry (DMV) [18], etc.

#### 4.2 Optical distortion corrections

Objects inside cylindrical capillaries appear distorted when viewed from the outside, due to the refraction of the light passing through media of different refractive indices. Figure 6 shows meniscus unrealistically extended into the tube's external wall. Another alteration that may appear on a digital image is the one caused by the radial lens distortion of a camera device. Such optical distortions may cause significant errors in geometrical measurements using optical observations. The measurement of the sampled micro-volume by the R&D VISION HIRIS software can be made more precise by introducing corrections in the computer program. A method proposed by Lowe and Kutt for correcting the meniscus profile by a point-by-point spatial position correction can be used [19,20]. Also, many ways for

overcoming the lens distortion limitation exist, including camera calibration methods and distortion corrections using analytical models and computer programs [21-26].

#### 4.3 nano-volumes measurements

The validation of the volume measurement system has been performed down to a 200 nl sampled volume (in a 500 µm inner diameter transparent capillary) with an associated relative standard uncertainty of 1%. The system described in this article is currently being upgraded with a motorized zoom so that volumes down to one nano-liter will be measured with a similar target uncertainty. The optics including the motorized zoom will be able to image a field of 2.3x1.7 mm (450 µm depth of field) down to 0.4x0.3 mm (42 µm depth of field). The figure below shows an example of a nanoliter sampled volume imaged with the current system in a 100 µm inner diameter capillary.

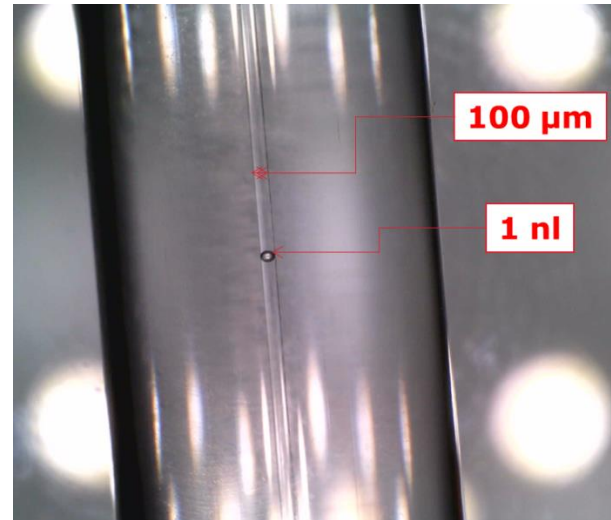


**Figure 16:** 1 nl sampled volume in a 100 µm inner diameter capillary imaged with LNE-CETIAT current system

#### 4.4 flow measurements

Feasibility of low flow measurements using an optical system to track the displacement of a meniscus in a transparent capillary has already been demonstrated [27]. Using the same method, LNE-CETIAT aims at measuring flow rates down to 1 nl/h in small transparent capillaries of 100 µm inner diameter or less. A few changes in the image processing process, will allow to measure the position (in µm) of the imaged meniscus in two successive time-stamped pictures, so that the average measured volumetric flow rate  $Q$  can be expressed as

$$Q = \frac{\Delta x}{\Delta t} \pi R^2$$

With  $\Delta x$  the displacement of the meniscus,  $\Delta t$  the difference in seconds between two successive time-stamped pictures, and  $R$  the capillary inner diameter radius.

### 5. Conclusion

In order to improve accuracy and traceability of radiopharmaceuticals volume activity measurements, LNE-CETIAT has developed a non contact micro-volume sampling and measurement system. Using on-the-shelf parts and a dedicated image processing algorithm, the system has been validated for sampled micro-volumes of 0.2 and 1 µl with relative standard uncertainty of 1 %. Future developments will allow this system to measure volumes down to 1 nl and flow rates down to 1 nl/h.

## 6. Acknowledgements

This work has been performed thanks to a French Metrology national funding piloted by LNE-DRST, and in collaboration with Laboratoire National Henri Becquerel (LNHB). Future developments will be funded in the scope of the Joint Research Project "Metrology For Drug Delivery 2", funded by the EURAMET EMPIR program of the European Union and the French Metrology funding piloted by LNE-DRST.

## References

- [1] F. Ogheard et al, *Recent improvements of the French liquid micro-flow reference facility*, Measurement Science and Technology, Volume 29, Number 2, Congrès International de Métrologie, CIM 2017
- [2] F. Ogheard, *Validation d'un banc d'étalonnage primaire en microdébitmétrie liquide et application aux dispositifs médicaux de perfusion*, REVUE FRANÇAISE DE MÉTROLOGIE n°42, Volume 2016-2
- [3] [www.drugmetrology.com](http://www.drugmetrology.com)
- [4] L DeNardo, *Treatment of Non-Hodgkin's Lymphoma (NHL) With Radiolabeled Antibodies (mAbs)*, Seminars in nuclear medicine, 35,2005.
- [5] T. Krishnamurthy et al, *Radioiodine I-131 therapy in the management of thyroid cancer. A prospective study*, Cancer. 40, 1977.
- [6] Kendall-Taylor et al, *Ablative radioiodine therapy for hyperthyroidism: Long term follow up study*, British medical journal (Clinical research ed.). 289. 361-3, 1984.
- [7] Alauddin et al, *Positron emission tomography (PET) imaging with (18)F-based radiotracers*, American journal of nuclear medicine and molecular imaging. 2. 55-76, 2012
- [8] D Neirinckx et al, *Technetium-99m d,l-HM-PAO: A new radiopharmaceutical for SPECT imaging of regional cerebral blood perfusion. Journal of nuclear medicine: official publication*, Society of Nuclear Medicine. 28. 191-202, 1987
- [9] Maddahi et al, *Myocardial perfusion imaging with technetium-99m sestamibi SPECT in the evaluation of coronary artery disease*, The American journal of cardiology. 66, 1990
- [10] Guide d'utilisation et de contrôle qualité des activimètres. NT LNHB 2006/033 - Juin 2006.
- [11] Amiot, Marie-Noëlle, RAPPORT CEA-R-6383 – Marie-Noëlle AMIOT «MESURES ET SIMULATIONS EN MÉTROLOGIE DE LA MESURE D'ACTIVITÉ PAR SCINTILLATION LIQUIDE ET CHAMBRE D'IONISATION PRESSURISÉE», 2014
- [12] Liang et al., *Novel gravimetric measurement technique for quantitative volume calibration in the sub-microliter range*, Meas. Sci. Technol. 24 (2013) 025301 (10pp)
- [13] N Hobeika et al, *Help from a Hindrance: Using Astigmatism in Round Capillaries to Study Contact Angles and Wetting Layers*, Langmuir: the ACS journal of surfaces and colloids. 33, 2017
- [14] Du Plessis et al, *Laboratory X-ray micro-computed tomography: a user guideline for biological Samples*, GigaScience, 6, 2017
- [15] Kwon Soonmu et al, *Precise measurement of inner diameter of mono-capillary optic using X-ray imaging technique*, Journal of X-Ray Science and Technology. 26, 2017
- [16] C Baroud et al, *Dynamics of microfluidic droplets*. Lab on a chip. 10. 2032-45, 2010
- [17] Chong et al, *Automated droplet measurement (ADM): an enhanced video processing software for rapid droplet measurements*, Microfluidics and Nanofluidics. 20, 2016.
- [18] A Basu, *Droplet morphometry and velocimetry (DMV): A video processing software for time-resolved, label-free tracking of droplet parameters*, Lab on a chip. 13, 2013.
- [19] M. Lowe et al, *Refraction through cylindrical tubes*, Experiments in fluids 13, 1992
- [20] Darzi et al, *Optical distortion correction of a liquid-gas interface and contact angle in cylindrical tubes*. Physics of Fluids. 29, 2017
- [21] B Prescott et al, *Line-Based Correction of Radial Lens Distortion*, CVGIP: Graphical Model and Image Processing, 59. 39-47, 1997
- [22] Grompone von Gioi et al, *Towards high-precision lens distortion correction*, 4237-4240, 2010
- [23] R Hartley et al, *Parameter-Free Radial Distortion Correction with Center of Distortion Estimation*, IEEE transactions on pattern analysis and machine intelligence, 29, 1309-21. 2007
- [24] J Jedlička et al, *CORRECTION OF RADIAL DISTORTION IN DIGITAL IMAGES*, 2007
- [25] A Wang et al, *A Simple Method of Radial Distortion Correction with Centre of Distortion Estimation*, Journal of Mathematical Imaging and Vision. 35. 165-172, 2009
- [26] R Cucchiara et al, *A Hough transform-based method for radial lens distortion correction*, 2003
- [27] Ahrens et al, *An experimental setup for traceable measurement and calibration of liquid flow rates down to 5 nl/min*, Biomed. Eng.-Biomed. Tech. 2015; 60(4): 337–345

# Development and uncertainty evaluation of gas flow standard facility with adjustable working temperature

Chaojian Tao<sup>1</sup>, Youyi Pan<sup>2</sup>, Liqiong Huang<sup>3</sup>, Yong Wang<sup>4</sup>, Shouyang Zhang<sup>5</sup>, Guofen Yang<sup>6</sup>, Zubao Chen<sup>7</sup>

<sup>1,2,3,5,6,7</sup>Tancy Instrument Group Co.,Ltd, No. 198 Hualian Rd., Cangnan industrial zone, Wenzhou City, China

<sup>4</sup>Goldcard Smart Group Co.,Ltd, Hangzhou, China

E-mail (corresponding author): taocj@tancy.com

---

## Abstract

To study a gas standard facility by master meter method, a master meter flow range is 10 to 250 m<sup>3</sup>/h, DN80. With one large-capacity temperature chamber, and the meter under test (MUT) places in the temperature chamber. The temperature chamber can be adjusted to a temperature range of -25 to 55 °C, and the temperature is stable when the test flow reaches a maximum of 250 m<sup>3</sup>/h. The master meter is placed in a room temperature environment, and a heat exchange is installed between the master meter and the MUT. The facility can be used to calibrate increasingly growing gas flow meters such as gas turbine meters, gas rotary meters, gas ultrasonic meters, and the like. In particular, it is possible to carry out research on the measurement performance change of a gas flow meter under different temperature environments. The facility adopts a Duo-rotary meter as master meter, and uses a non-fixed point method to correct the error of the master meter by the polyline method. To carry out the temperature stability test and measurement uncertainty evaluation on the facility. The facility was evaluated for uncertainty using the *ISO/IEC GUIDE 83-3:2008 GUM* method and the result was  $U_{rel} = 0.29\%$  ( $k = 2$ ). Tested with an actual working flow meter, the facility meets the requirements of the relative extended uncertainty of the design, and as an innovation, it will promote the temperature performance test level of gas flow standard facility technology.

- 
- **Keywords:** Master meter method, Gas flow standard facility, Meter under test (MUT), Adjustable temperature, Evaluation of measurement uncertainty

## 1. Introduction

The gas flow standard facility is used for the verification or calibration of the gas flow meter, and is an important device for the transmission and traceability of the quantity.

In 2018, global natural gas consumption was about 3.86 trillion cubic meters, a growth rate of 5.3%. Natural gas development has led to a significant increase in the use of gas flow meters. In general, the natural gas station requires an accuracy class of 0.5, and the accuracy class of the flow meter commonly used by urban natural gas industrial and commercial users is 1.0, and the usage is several hundred times that of the station. The gas flow facility device bears the periodic verification or calibration of the gas flow meter, and its resource allocation and the importance of technical performance indicators are self-evident.

At present, the gas flow standard facilities, in addition to a small number of primary standard facilities, the widely used gas flow standard facilities expanded uncertainty is usually 0.2% to 0.33% ( $k=2$ ), used to verify accuracy class 1.0 gas flow meter<sup>[1]</sup>. Usually, the facility is placed in a laboratory room temperature environment, so that it is impossible to evaluate the metering performance of the MUT at different work temperatures. Based on this, the gas flow standard facilities with adjustable ambient temperature of the study can provide a new idea.

## 2. facility composition and workflow

The gas flow standard facility of this study is mainly composed of temperature chamber system, MUT workbench and straight pipe section, heat exchanger, master meter, gas source, timer, computer control and data acquisition and processing system (see Figure 1 and Figure 2). The facility in this study adopts the

negative pressure method, and the flow range is (10-250) m<sup>3</sup>/h. For economic considerations, one MUT workbench and the straight pipe section is DN80, which can be used for the flow meter of DN80 and below to perform verification or calibration. The device has an expanded uncertainty of 0.29% and can be used to calibrate or calibrate accuracy class 1.0 meter with pulse output type or a field read type gas meter such as gas turbine meter, gas rotary meter, a gas swirling vortex meter, a gas ultrasonic meter, etc. .

Build an temperature chamber to place MUT inside it, to adjust the work temperature of the meter. According to the OIML R137<sup>[2]</sup>, EN 12261<sup>[3]</sup> and EN 12480<sup>[4]</sup> standards, The work temperature of meter is in common use -25 °C ~ 55 °C, and there is sufficient temperature control ability to ensure that the temperature does not exceed ± 0.5 °C in each test of the test maximum flow. The downstream pipeline of the MUT is wrapped with insulation material and connected to the heat exchanger. The heat exchanger is connected to the master meter through the pipeline. The test flow is controlled by the variable-frequency drive to control the blower speed and the ball valve opening. The PLC collects the temperature and the pressure signal of the MUT and the master meter. Through the comparison of the flow rate of the MUT and the master meter, the indication error and repeatability of the MUT are obtained. The following two types of MUT are available for this study:

- 1) A flow meter that only displays the mechanical counter to display the volume;
- 2) The output pulse frequency is related to the flow rate of the rotating part.

The following describes the second type of flowmeter to be tested, and defines the number of pulses per unit volume as the meter factor *K*.

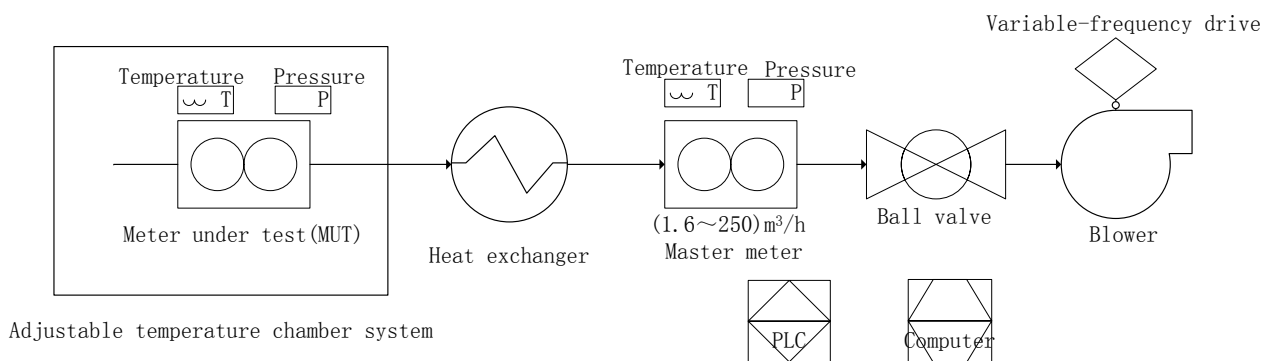


Figure 1: Device block diagram

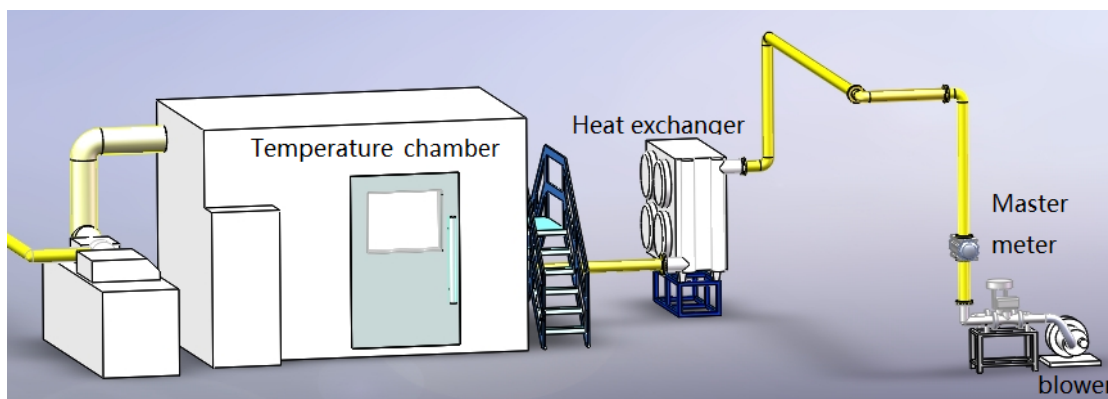
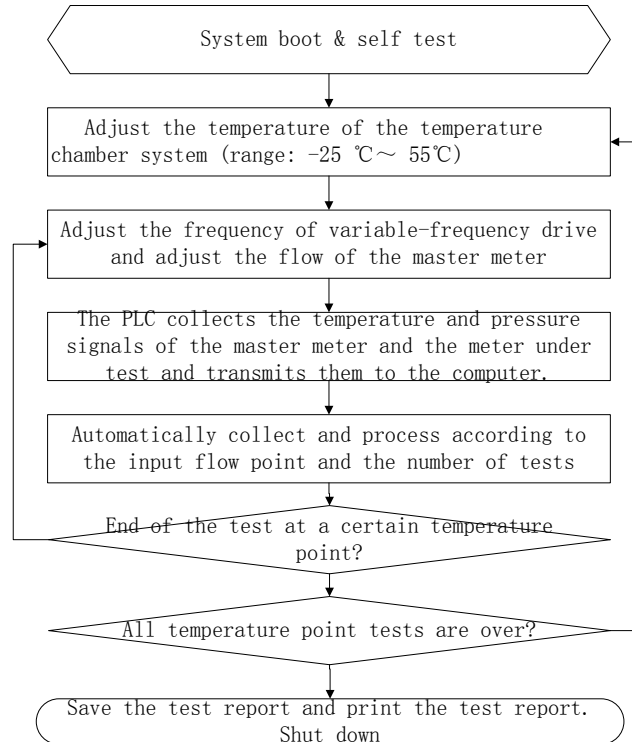


Figure 2: Device schematic

The computer system controls the temperature of the temperature chamber to be stable and maintains the flow of the blower through the variable-frequency drive and the adjustment of the opening degree of the ball valve. At the same time, the PLC in the system collects the temperature and pressure signals of the master

meter and the MUT and transmits them to the computer system for processing. The computer system completes the verification process and saves, outputs the verification or calibration results. The process is shown in Figure 3.



**Figure 3: workflow chart**

### 3. Working principle mathematical model

The master meter and the MUT are operated in series. At this time, the meter factor of a single verification for each flow point is calculated as follows <sup>[5][6]</sup>:

$$Q_s = N_s / K_s \quad (1)$$

$$Q_m = N_m / K_m \quad (2)$$

$$Q_m = Q_s \times \frac{273.15 + t_m}{273.15 + t_s} \times \frac{p_s}{p_m} \times \frac{z_m}{z_s} \quad (3)$$

$$K_m = \frac{N_m}{Q_m} = \frac{N_m}{Q_s} \times \frac{273.15 + t_s}{273.15 + t_m} \times \frac{p_m}{p_s} \times \frac{z_s}{z_m} \quad (4)$$

where

$K_s, K_m$  — respectively, the meter factor of the master meter and the MUT,  $(\text{m}^3)^{-1}$  or  $\text{L}^{-1}$ ;

$N_s, N_m$  - respectively, the number of pulses of the master meter and the MUT;

$Q_s, Q_m$  - respectively, the cumulative flow of the master meter and the MUT,  $\text{m}^3$  or  $\text{L}$ .

$T_s, t_m$  — respectively, the temperature of the gas at the master meter and the MUT, °C;

$P_s, p_m$  — respectively, the absolute pressure of the gas at the master meter and the MUT, Pa or kPa;

$Z_s, Z_m$  — respectively, the gas compression factor at the master meter and the MUT.

Because the master meter is not-fixed use, the curve is corrected by the polyline method, and the instantaneous flow rate flowing through the master meter is  $q$ , which has the following relationship:

$$K_s = K_{s,i} + \frac{q - q_i}{q_{i+1} - q_i} \times (K_{s,i+1} - K_i) \quad (5)$$

#### 4. Measurement uncertainty evaluation <sup>[7][8][9][10]</sup>

The uncertainty of the facility is shown in Table 1.

**Table 1:** Uncertainty analysis of gas flow standard device

No.	Symbol	Source	Standard uncertainty of input quantity $u_r(x_i)/\%$	Sensitivity coefficient $c_r(x_i)$	$ c_r(x_i)u_r(x_i) /\%$
1	$V_s$	calibration master meter device	0.1	-1	0.1
2	$K1$	master meter meter factor repeatability	0.010	1	0.010
3	$K2$	master meter interpolated meter factor	0.001	1	0.001
4	$T_s$	master meter temperature measurement	0.039	1	0.039
5	$T_m$	Checked table temperature measurement	0.046	-1	0.046
6	$P_s$	master meter pressure measurement	0.058	-1	0.058
7	$pm$	Pressure measurement at the checklist	0.058	1	0.058
8	$t$	timer	0.003	1	0.003

The combined standard uncertainty is 0.143%; the expanded uncertainty is 0.29%,  $k=2$

##### 4.1 Calibration Master meter Device Standard Uncertainty

The expanded uncertainty of the flow standard facility used to calibrate the master meter, therefore

$$u_r(V_s) = U_r(V_s) / k = 0.1\% \quad (6)$$

##### 4.2 Master meter Standard Uncertainty

Considering that the master meter factor of the master meter is 5820.74, the indication error of 10 m<sup>3</sup>/h or less in the calibration data is large, so (10 -250) m<sup>3</sup>/h is used. The calibration results are shown in Table 2, and the Bessel equation is used to calculate the repeatability. The standard uncertainty calculation formula of the interpolation algorithm is

$$u_{r,2}(K) = \frac{1}{\sqrt{3}} \times \left| \frac{K_{i+1} - k_i}{K_{i+1} + k_i} \right| \quad (7)$$

**Table 2:** Master meter Meter Coefficient Calculation and Uncertainty Analysis

flow/ m <sup>3</sup> h <sup>-1</sup>	Average meter factor/ m <sup>-1</sup>	Repeatability $u_{r,1}(K) / \%$	Interpolation $u_{r,2}(K) / \%$
250	5836.65	0.006	0.0005
160	5826.17	0.006	0.0002
100	5822.68	0.006	0.0002
65	5819.38	0.006	0.0003
40	5825.01	0.006	0.0008
25	5809.87	0.006	0.0002
16	5806.19	0.010	0.0008
10	5821.52	0.006	0.0014

#### 4.3 Master meter Temperature Measurement Standard Uncertainty

The standard temperature transmitter is -10 °C to 50 °C, the MPE is ± 0.2 °C, the master meter temperature is about 20 °C, according to the rectangular distribution, the standard uncertainty brought by the temperature transmitter is

$$u_r(T_s) = \frac{1}{\sqrt{3}} \times \frac{0.2}{273.15 + 20} = 0.039\% \quad (8)$$

#### 4.4 Uncertainty of temperature measurement standard at the MUT

The temperature transmitter at the meter is -50 °C to 100 °C, the MPE is ± 0.2 °C, the temperature range of the MUT is -25 °C to 55 °C, according to the rectangular distribution, the temperature transmitter with The maximum standard uncertainty is

$$u_r(T_s) = \frac{1}{\sqrt{3}} \times \frac{0.2}{273.15 - 25} = 0.046\% \quad (9)$$

#### 4.5 Uncertainty of pressure measurement standard at master meter and checklist

The pressure transmitter has an accuracy rating of 0.1, distributed in a rectangular shape.

$$u_r(p_s) = \frac{0.1\%}{\sqrt{3}} = 0.058\% \quad (10)$$

$$u_r(p_m) = \frac{0.1\%}{\sqrt{3}} = 0.058\% \quad (11)$$

#### 4.6 Timer Standard Uncertainty

The crystal oscillator adopts 12MHz, considering the crystal oscillator 8 hour stability, crystal resolution, timer interval, timer resolution, etc. The standard uncertainty is

$$u_r(t) = 0.003\%$$

## 5 Test and test data analysis

#### 5.1 Temperature stability test at the MUT workbench in the temperature chamber and master meter

According to JJG 1037-2008 *Verification regulation for turbine flowmeter*, the gas temperature change shall not exceed 0.5 °C at each flow point. In the temperature chamber, 6 temperature sensors are distributed for temperature measurement (see Figure 3), and the master meter is measured by temperature transmitter. The performance test data is shown in Table 3, Table 4, Table 5.

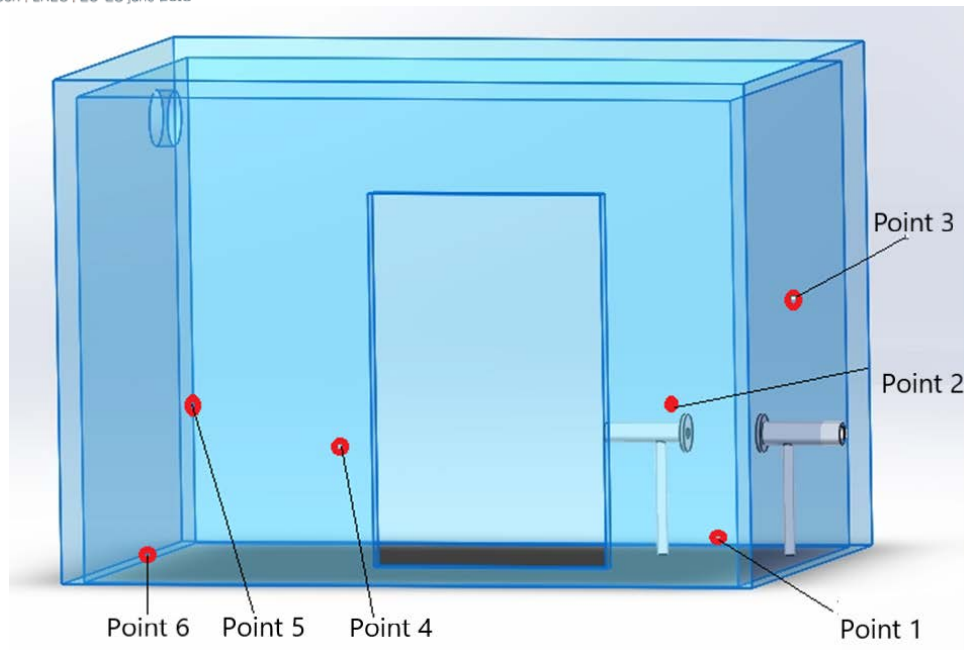


Figure 3: Distribution of 6 temperature sensors in the temperature compartment to measure temperature

Table 3: The temperature value of each test point when set the temperature chamber temperature is 55 °C

Time	Point 1	Point 2	Point 3	Point 4	Point 5	Point 6	MUT temperature	Mater meter temperature
	Average/max. deviation							
5 min	55.1/0.4	55.2/0.4	55.3/0.5	55.2/0.4	55.3/0.4	54.9/0.4	55.0/0.4	20.8/0.2
5 min	55.2/0.4	55.3/0.4	55.5/0.4	55.2/0.5	55.4/0.4	54.8/0.4	55.1/0.4	20.8/0.1
5 min	55.3/0.4	55.5/0.5	55.4/0.5	55.3/0.4	55.3/0.4	55.0/0.4	55.0/0.4	20.8/0.2

Table 4: The temperature value of each test point when set the temperature chamber temperature is 20 °C

Time	Point 1	Point 2	Point 3	Point 4	Point 5	Point 6	MUT temperature	Mater meter temperature
	Average/max. deviation							
5min	20.1/0.2	20.3/0.2	20.4/0.2	20.5/0.2	20.2/0.2	19.8/0.2	20.1/0.2	20.8/0.2
5min	20.2/0.3	20.4/0.3	20.3/0.3	20.5/0.3	20.1/0.4	19.9/0.2	20.1/0.3	20.7/0.2
5min	20.2/0.2	20.5/0.3	20.5/0.2	20.4/0.2	20.2/0.3	19.8/0.3	20.1/0.3	20.7/0.2

Table 5: The temperature value of each test point when set the temperature chamber temperature is -25 °C

time	Point 1	Point 2	Point 3	Point 4	Point 5	Point 6	MUT temperature	Mater meter temperature
	Average/max. deviation							
5min	-24.8/0.3	-24.6/0.3	-24.5/0.4	-24.5/0.4	-24.3/0.4	-24.8/0.4	-24.8/0.3	20.6/0.3
5min	-24.7/0.4	-24.7/0.4	-24.6/0.4	-24.5/0.2	-24.4/0.4	-24.5/0.3	-24.6/0.4	20.7/0.3
5min	-24.8/0.4	-24.5/0.4	-24.7/0.3	-24.6/0.3	-24.2/0.3	-24.8/0.2	-24.7/0.3	20.6/0.3

From the experimental data, the temperature stability requirements are met.

### *5.2 Calibration test on the tested form*

A gas rotary meter was selected for testing, and the test was carried out according to JJG 633-2005 *Verification regulation for gas displacement meters*. The test results are as Table 6, Table 7, Table 8. The test results show that the facility design meets the expected technical indicators<sup>[11]</sup>.

**Table 6: Test data for the MUT when the temperature of the temperature chamber is 55 °C**

Flow point (m <sup>3</sup> /h)	Flowrate (m <sup>3</sup> /h)	Vs (m <sup>3</sup> )	t (s)	MUT Pulses	MUT p <sub>m</sub> (kPa)	MUT T <sub>m</sub> (°C)	Master meter p <sub>s</sub> (kPa)	Master meter T <sub>s</sub> (°C)	K (1/m <sup>3</sup> )	Ave. K (1/m <sup>3</sup> )	Error %	Repeatability %
250	252.21	4.523	60.00	123984	99.27	56.31	96.76	25.79	27414.65	27400.52	0.32	0.20
	252.25	4.516	60.00	123943	99.14	56.22	96.71	25.79	27448.04			
	252.26	4.532	60.00	123888	99.18	56.66	96.79	26.02	27338.87			
62.5	62.28	1.145	60.00	31177	99.84	56.09	99.78	25.53	27233.05	27227.93	-0.32	0.02
	62.27	1.145	60.00	31179	99.90	56.60	99.71	25.58	27222.80			
	62.25	1.145	60.00	31173	99.91	56.30	99.73	25.46	27227.94			
25	25.26	0.466	60.00	12800	100.01	56.67	99.95	24.94	27448.52	27448.74	0.49	0.14
	25.26	0.467	60.00	12804	99.95	56.74	99.89	24.87	27411.55			
	25.25	0.466	60.00	12807	100.07	56.51	99.95	24.71	27486.15			
20	19.94	0.370	60.00	10130	99.81	56.31	100.02	24.31	27392.91	27434.14	0.44	0.14
	19.92	0.368	60.00	10118	100.05	56.61	99.96	24.49	27464.98			
	19.90	0.368	60.00	10113	99.95	56.57	99.93	24.28	27444.53			
12.5	12.32	0.228	60.00	6260	99.83	56.83	99.90	24.04	27413.06	27381.39	0.25	0.10
	12.29	0.228	60.00	6245	99.84	56.62	99.98	24.08	27361.20			
	12.31	0.228	60.00	6248	99.84	56.73	99.96	24.14	27369.91			

**Table 7:** Test data for the MUT when the temperature of the temperature chamber is 21.5 °C

Flow point (m <sup>3</sup> /h)	Flowrate (m <sup>3</sup> /h)	Vs (m <sup>3</sup> )	t (s)	MUT Pulses	MUT p <sub>m</sub> (kPa)	MUT T <sub>m</sub> (°C)	Master meter p <sub>s</sub> (kPa)	Master meter T <sub>s</sub> (°C)	K (1/m <sup>3</sup> )	Ave. K (1/m <sup>3</sup> )	Error %	Repeatability %
250	247.11	4.056	60.00	111838	99.27	22.33	97.07	19.28	27575.28	27513.52	0.37	0.26
	247.12	4.072	60.00	112092	99.04	22.35	96.95	19.28	27529.97			
	247.11	4.087	60.00	112124	98.99	22.36	97.11	19.19	27435.30			
62.5	62.47	1.048	60.00	28637	99.85	22.03	99.69	19.65	27333.32	27308.98	-0.37	0.19
	62.48	1.051	60.00	28637	99.76	21.79	99.85	19.49	27248.51			
	62.45	1.046	60.00	28616	99.93	22.24	99.71	19.65	27345.10			
25	25.27	0.425	60.00	11681	99.91	21.82	99.90	19.53	27501.47	27495.30	0.31	0.13
	25.27	0.425	60.00	11680	99.79	21.76	99.91	19.50	27458.19			
	25.26	0.424	60.00	11674	100.05	21.86	99.96	19.70	27526.24			
20	20.10	0.338	60.00	9291	100.08	21.74	99.91	19.68	27521.02	27497.11	0.31	0.10
	20.10	0.338	60.00	9288	99.77	21.50	99.91	19.56	27467.13			
	20.08	0.338	60.00	9283	100.07	21.40	99.97	19.65	27503.19			
12.5	12.35	0.208	60.00	5700	100.10	21.50	100.09	19.86	27437.25	27439.11	0.10	0.13
	12.34	0.208	60.00	5693	99.99	21.73	99.96	19.73	27403.99			
	12.34	0.207	60.00	5695	100.08	21.48	100.03	19.62	27476.09			

**Table 8: Test data for the UMT when the temperature of the temperature chamber is -25 °C**

Flow point (m <sup>3</sup> /h)	Flowrate (m <sup>3</sup> /h)	Vs (m <sup>3</sup> )	t (s)	MUT Pulses	MUT p <sub>m</sub> (kPa)	MUT T <sub>m</sub> (°C)	Master meter p <sub>s</sub> (kPa)	Master meter T <sub>s</sub> (°C)	K (1/m <sup>3</sup> )	Ave. K (1/m <sup>3</sup> )	Error %	Repeatability %
250	247.90	3.424	60.00	94049	99.17	-22.56	97.22	23.83	27469.23	27464.41	0.14	0.29
	247.85	3.414	60.00	94038	99.29	-22.52	97.07	23.80	27542.04			
	247.85	3.434	60.00	94033	99.40	-22.60	97.36	23.95	27381.95			
62.5	62.33	0.873	60.00	23884	99.99	-23.53	99.84	23.73	27355.22	27387.05	-0.14	0.13
	62.37	0.871	60.00	23895	100.02	-22.77	99.73	23.95	27427.04			
	62.32	0.872	60.00	23877	100.06	-22.94	99.73	23.95	27378.90			
25	25.27	0.355	60.00	9744	100.08	-23.03	99.94	23.85	27472.89	27438.47	0.05	0.11
	25.26	0.355	60.00	9736	99.88	-23.07	100.00	23.77	27423.54			
	25.24	0.355	60.00	9726	100.00	-23.40	100.05	23.77	27418.98			
20	19.96	0.280	60.00	7692	99.98	-23.88	99.90	23.70	27481.05	27446.90	0.08	0.18
	19.94	0.281	60.00	7685	99.74	-23.64	99.97	23.75	27391.65			
	19.94	0.280	60.00	7685	99.98	-23.42	99.93	23.82	27468.00			
12.5	12.54	0.176	60.01	4807	100.06	-23.71	100.06	23.89	27264.71	27270.49	-0.57	0.03
	12.54	0.176	59.99	4807	100.00	-23.36	99.92	23.88	27281.22			
	12.53	0.176	60.00	4802	99.88	-23.53	99.94	23.79	27265.53			

## 6 conclusion

Through the system mechanical design, electrical design, software design and test verification, the technical indicators meet the extended uncertainty of 0.29% ( $k=2$ ) standard surface gas flow standard device, which can be used for the 1.0-level gas flow with pulse frequency output. The test is performed and calibrated, and the flowmeter to be tested can be placed at different temperatures to verify its temperature adaptability. In view of the large investment required to build the temperature compartment, the device is an attempt, the maximum flow rate only reaches 250m<sup>3</sup>/h, and the verification or calibration caliber is not more than DN80. At the same time, it provides a new idea for gas flow metering test equipment.

## References

- [1] JJG 2064—2017 *Verification scheme of measuring instruments for gas flow* [S]. (Beijing, China Quality Inspection Press), 2017.
- [2] OIML R137-1&2:2012 *Gas meters Part 1: Metrological and technical requirements, Part 2: Metrological controls and performance tests*[S].
- [3] EN 12261:2002/A1:2006 *Gas meters — Turbine gas meters*[S].Brussels. CEN,2006.
- [4] EN 12480:2015 *Gas meters — Rotary displacement gas meters*[S].Brussels. CEN,2015.
- [5] JJG 633—2005 *Verification regulation for gas displacement meters*[S] . (Beijing, China metrology press), 2005.
- [6] JJG 1037—2008 *Verification regulation for turbine flowmeter* [S] . (Beijing, China metrology press), 2008.
- [7] Wang Chi, *Uncertainty analysis of flow measurement* [M], (Beijing, China metrology press), 2002.
- [8] GB/T 27759—2011/ISO 5168:2005 *Measurement of fluid flow — Procedures for the evaluation of uncertainties* [S], (Beijing, China standard press), 2011.
- [9] JJG 1059.1—2012 *Evaluation and expression of uncertainty in measurement*[S]. (Beijing, China Quality Inspection Press), 2013.
- [10] ISO/IEC GUIDE 98-3:2008 *Uncertainty of measurement—Part 3: Guide to the expression of uncertainty in measurement*[S].
- [11] JJG 643—2003 *Verification Regulation of Flow Standard Facilities by Master Metr Method*[S], (Beijing, China metrology press), 2003.

# The Impact of Geometric Parameters of a S-type Pitot tube on the Flow Velocity Measurement at Smoke-stacks

W. Kang<sup>1</sup>, D. T. Nguyen<sup>2</sup>, Y-M. Choi<sup>1</sup>, S-H. Lee<sup>1</sup>

<sup>1</sup>Korea Research Institute of Standards and Science, Daejeon, Republic of Korea

<sup>2</sup>University of Science and Technology, Daejeon, Republic of Korea

E-mail (corresponding author): woong.kang@kriss.re.kr

## Abstract

In the monitoring of greenhouse gas emission from industrial smoke-stacks, the most common device used to measure the stack gas velocity is the S-type Pitot tube in South Korea, which is used to estimate the volumetric flow rate by what is termed the Continuous Emission Monitoring System (CEMS). The S-type Pitot tube installed in the stack is inevitably affected during velocity measurements by velocity changes, yaw and pitch angle misalignments due to the harsh environments. Various geometries of the S-type Pitot tube can affect the characteristics of the S-type Pitot tube coefficients, including the degree of sensitivity to velocity changes and yaw and pitch yaw angle misalignments. Nevertheless, there are no detailed guidelines pertaining to the S-type Pitot tube geometry considering accurate and reliable measurements in the ISO, EPA and ASTM international standards. In the present study, S-type Pitot tubes with various geometric parameters, in this case the distance between the impact and wake orifices and the bending angle of the orifices, were manufactured by a 3D printer. Wind tunnel experiments were conducted in the Korea Research Institute of Standards and Science (KRIS) air speed standard system to determine the optimal geometry of an S-type Pitot tube for the accuracy velocity measurements in actual smokestacks which undergo velocity changes and yaw and pitch angle misalignments. Particle image velocimetry was also used to understand the flow phenomena around an S-type Pitot tube under various geometric and misalignment conditions by means of qualitative visualization.

## 1. Introduction

GHG emission estimates have been based on an activity-based method (i.e., fuel consumption and emission factors) and on Continuous Emission Monitoring System (CEMS) in the energy sector. The CEMS approach directly measures GHG emissions by monitoring GHG concentrations and volumetric flow rates at the stack. According to the U.S. Environmental Protection Agency (EPA) [1], The CEM method involves estimating the concentrations and flow rates of gas emissions at the stack via following Equation (1).

$$E = \sum_{i=1}^N E_{5min,i} = \sum_{i=1}^N \left( x_{5min,i} \times Q_{5min,i} \times \frac{M_{gas}}{MV} \right) \quad (1)$$

where  $E_{5min,i}$  is the 5-min accumulated emission of the  $i^{\text{th}}$  measurement (kg),  $x_{5min,i}$  is the 5-min averaged concentration of the  $i^{\text{th}}$  measurement (% or ppm).  $Q_{5min,i}$  is the 5-min accumulated volumetric flow of the  $i^{\text{th}}$  measurement ( $\text{m}^3$ ). The 5-min accumulated volumetric flow rate can be calculated with following Equation (2).

$$Q_{5min} = V \times \frac{\pi D^2}{4} \times \frac{P_s}{760} \times \frac{273.15}{T} \times (1 - x_w) \times 300 \quad (2)$$

where,  $Q$  is the dry gas flow rate ( $\text{m}^3$ ),  $V$  is the gas velocity (m/s),  $D$  is the stack diameter (m),  $P_s$  is the static pressure (mmHg),  $T$  is the emission gas temperature (K), and  $x_w$  is the water content of the emission gas. The S-type Pitot tube (Stauscheibe or reverse) is most commonly used in the stacks to measure the gas velocity in South Korea.

The S-type Pitot tube was designed to measure the flow velocity for industrial stacks in high-dust environments, as cited in the EPA [2] and ISO standards [3]. This tube design has large pressure orifices and strong tubes, as shown in Figure 1. The flow velocity can be obtained by measuring the differential pressure between the impact orifice and the wake orifice based on the Bernoulli equation. The S-type Pitot tube coefficient ( $C_p$ ) is used to calculate the flow velocity by measuring the differential pressure with the S-type Pitot tube, as in the following Equation (3).

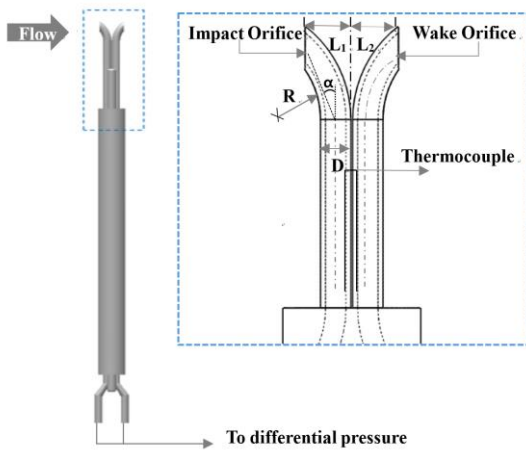


**Figure 1:** Configuration and definitions of the geometric parameters for the S-type Pitot tube.

$$V = C_p \times \sqrt{\frac{2\Delta P}{\rho}} \quad (3)$$

where  $\Delta P$  is the differential pressure (Pa) between the impact and the wake orifices and  $\rho$  is the density of the emission gas ( $\text{kg}/\text{m}^3$ ).

The S-type Pitot tube is usually installed and inserted in stacks which operate in harsh environments, such as those with tall stack heights and high gas temperatures, as shown in Figure 2. Therefore, it is difficult to observe the inside of the stack and verify the precise installation of an S-type Pitot tube. Accordingly, misalignments, such as yaw angle rotation, can occur during the installation of the S-type Pitot tube from outside of the stack [4]. As the diameter of the stack increases, the sampling point positions for measuring velocity distributions in the stack should increase according to the EPA method [2,3]. Since the inserted length of the S-type Pitot tube also increases, a pitch angle misalignment of the S-type Pitot tube can arise due to the deflection of the tube in stacks with large diameters.

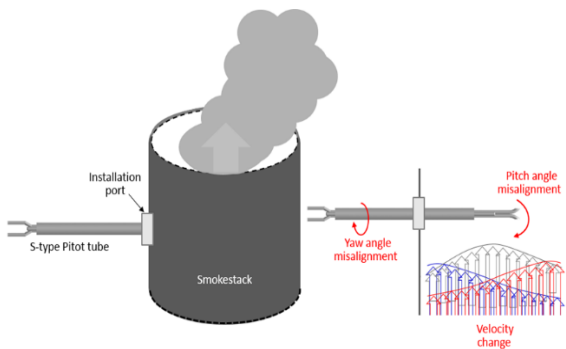


**Figure 2:** Installation effect of the S-type Pitot tube in the stack.

**Table 1:** Specifications parameters of an S-type Pitot tube recommended in the international standards

Parameter	ASTM D3796	ISO10780	EPA Method 2
D	-	4 mm to 10 mm	4.8 mm to 9.5 mm
$\alpha$	45°	-	-
$L=L_1=L_2$	9.52 mm	1.05D to 10D	1.05D to 1.5D

This would affect not only the velocity change but also the yaw and pitch angle flow to the S-type Pitot tube installed in the stack. Hence, an S-type Pitot tube installed in the stack is inevitably affected during velocity measurements by the velocity change, yaw and pitch angle misalignments due to the reasons described above (Figure 2).

If the geometry of the S-type Pitot tube is less sensitive to changes in the flow velocity and to yaw and pitch angle misalignments, flow velocity measurements by S-type Pitot tubes in the stack can be more accurate. From the international documents related to S-type Pitot tubes, specifically ISO, ASTM and EPA [3,5,6], the geometric parameters of S-type Pitot tubes, in this case the external diameter, the half of distance between the impact and wake orifices ( $L$ ), and the bending angle of the orifices ( $\alpha$ ), as shown in Figure 1, are defined and described in Table 1. However, the values of geometric parameters are described differently in the documents, specifically the range of the distance between the two orifices ( $L$ ) and the bending angles ( $\alpha$ ) of orifices. Various geometries of S-type Pitot tubes can affect the characteristics of the S-type Pitot tube coefficients, including the sensitivity to velocity changes and pitch and yaw angle misalignments. However, there are no detailed guidelines for S-type Pitot tube geometries considering accurate and reliable measurement characteristics in the international standards.

The main objective of the present study is to determine the optimal geometry of an S-type Pitot tube for accurate and reliable velocity measurements in an actual stack considering velocity changes and yaw and pitch angle misalignments. To this end, S-type Pitot tubes with various geometric parameters, in this case the distance ( $L$ ) and the bending angle ( $\alpha$ ) of the orifices, were manufactured by a 3D printer. Wind tunnel experiments were conducted in KRIS air speed standard system to determine the effects of the geometric parameters on the S-type Pitot tube coefficients with change in the velocity and yaw and pitch angles. Particle image velocimetry was also utilized to understand the flow phenomena around an S-type Pitot tube under various geometric and misalignment conditions by means of qualitative visualizations.

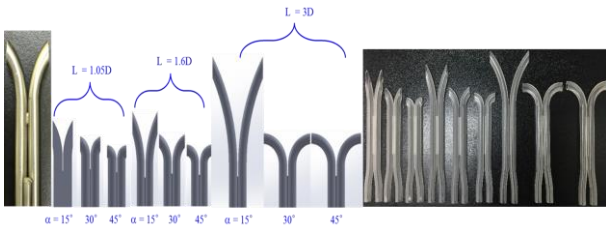


**Figure 3:** 3D printed S-type Pitot tube models with various geometric parameters.

## 2. Experimental method and apparatus

### 2.1 Geometric Parameters of the S-type Pitot tubes

In order to investigate the effects of the geometry of an S-type Pitot tube on the accuracy of flow velocity measurements in the stack, the various geometric parameters of the S-type Pitot tube were designed. In the present study, the values of the half of distance between the impact and wake orifices,  $L$ , were set to  $1.05D$ ,  $1.6D$  and  $3D$ . The used S-type Pitot tube in KRISS has  $30^\circ$  as the bending angle ( $\alpha$ ), which differs from the bending angle of  $45^\circ$  described in ASTM. The three different bending angle,  $15^\circ$ ,  $30^\circ$  and  $45^\circ$  were selected for S-type Pitot tube models. Each combination consisted of S-type Pitot tube models with these three distances ( $L=1.05D$ ,  $1.6D$  and  $3D$ ) and with bending angles  $\alpha$  of  $15^\circ$ ,  $30^\circ$  and  $45^\circ$ , as shown in Figure 3. To manufacture the designed S-type Pitot tube models with various geometric parameters, a 3D printer, which relies on a stereo lithography method, was used in the Daejeon Techno-Park with an ATOMm-4000 3D Printer.

### 2.2 Experimental in a wind tunnel system

To evaluate the effect of a change in the velocity and the yaw and pitch angle misalignments on the manufactured S-type Pitot tube models, wind tunnel tests were conducted in the subsonic open-circuit wind tunnel of KRISS, which was used as national air speed standards, as shown in Figure 4. The dimensions of the test section were 900 mm (width)  $\times$  900 mm (height)  $\times$  6000 mm (length). The inlet velocities were varied from 2 m/s to 16 m/s. The turbulent intensity in the test section is less than 0.5 %. The expanded uncertainty levels ( $U$ ) of the flow velocity measurements in the KRISS wind tunnel standards system is less than 1.1 % from 2 – 5 m/s and 0.6 % from 5 – 15 m/s at the 95 % confidence level. The experimental setup was arranged as shown in Figure 4, and all of the data were acquired automatically by the LabVIEW program. Additionally, to alter the yaw and pitch angle of the S-type Pitot tube, a rotating device was installed at the top of the test section.

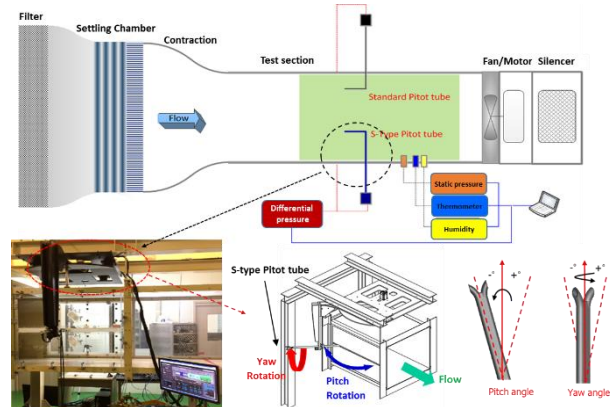


**Figure 4:** Experimental set-up of the S-type Pitot tube models in the KRISS wind tunnel.

With this rotating device, the yaw angles could change from  $-180^\circ$  to  $+180^\circ$  at an interval of  $1^\circ$ , while the pitch angles could change from  $-45^\circ$  to  $+45^\circ$  at  $5^\circ$  intervals. In addition to experiments in the wind tunnel system, to understand the flow phenomena around the S-type Pitot tube models when the velocity, yaw and pitch angle change, qualitative visualization experiments were also conducted using a particle image velocimetry (PIV) system. A laser light sheet was produced by a time-resolved laser that delivered 20mJ of energy per pulse at 1kHz. Tracer particles in the flow fields were seeded by a seeding generator. Particle images were captured by a 50mm lens (Zeiss) and a 12-bit high-speed camera (SpeedSense M310) at 1280  $\times$  800 pixels. The field of view was 150 mm  $\times$  100 mm. For each geometry of the S-type Pitot tube models, 5000 instantaneous PIV images were acquired using Dynamic Studio (Dantec Dynamics).

## 3. Results and discussions

### 3.1 The effect of the velocity changes on the S-type Pitot tube coefficients

To investigate the effects of the geometries of the S-type Pitot tube models on the S-type Pitot tube coefficients when the incoming velocity at the orifice of the S-type Pitot tube changes, wind tunnel experiments with S-type Pitot tubes were conducted at a velocity range of 2 to 15 m/s. The upper part of Figure 5 shows the distribution of the S-type Pitot tube coefficients with respect to velocity changes for  $L=1.6D$  and  $\alpha=15^\circ$ ,  $30^\circ$  and  $45^\circ$ . In particular, the distribution of the S-type Pitot tube coefficients with  $L=1.6D$  and  $\alpha=45^\circ$  has large coefficients when the incoming velocity increases as compared to when  $\alpha=15^\circ$  and  $30^\circ$  despite the identical distance ( $L$ ) between the two orifices. To understand this result, the flow phenomena around the S-type Pitot tube

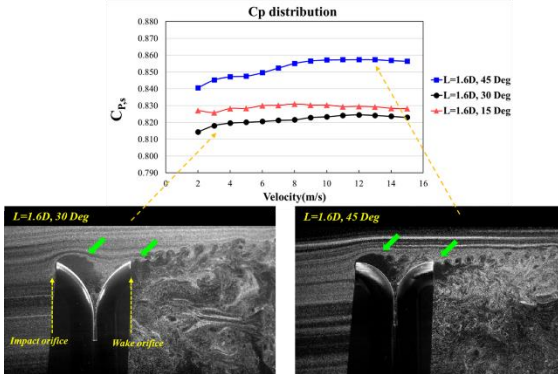


**Figure 5:** Distribution of S-type Pitot tube coefficients and flow visualization by PIV when  $L=1.6D$  and  $\alpha=15^\circ, 30^\circ$  and  $45^\circ$ .

models with  $L=1.6D$ ,  $\alpha=30^\circ$  and  $45^\circ$  were investigated by PIV measurements, as shown in the bottom of Figure 5. Due to complicated geometry between the impact and wake orifices, the separated flows were developed to a vortical structure behind the impact orifices. For the case of  $L=1.6D$  and  $\alpha=30^\circ$ , the separated flow develops to the vortical structures behind the impact and the wake orifices of the model. In contrast, in the case of  $L=1.6D$  and  $\alpha=45^\circ$ , downstream separated flows from wake orifice were less developed than when  $\alpha=30^\circ$  due to short distance between two orifices and a gradual change of curved shape. Accordingly, the lower pressure distribution was presented around the wake orifice. It causes the S-type Pitot tube coefficients for the case of  $L=1.6D$  and  $\alpha=45^\circ$  decreased as shown in the upper part of Figure 5.

In the flow phenomena between the two orifices of the S-type Pitot tube models in Figure 5, it can be seen that the actual contact distance of the flow between the two orifices is more important than the distance  $L$  as defined above when determining the S-type Pitot tube coefficients with respect to velocity changes. Therefore, the actual contact distance of the flow between the impact and wake orifice was introduced to examine the effects of the geometries of the S-type Pitot tube models on the S-type Pitot tube coefficients. In the present study, it was termed an effective length,  $eL$ , as shown in Figure 6.

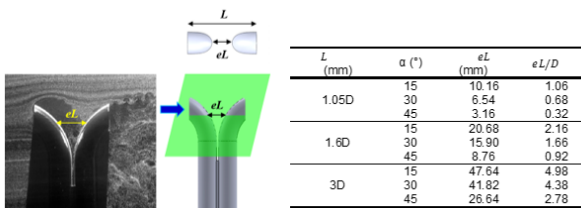


**Figure 6:** Definition of the effective length ( $eL$ ) of the S-type Pitot tube.

As shown in Figure 6, the normalized effective length ( $eL/D$ ) when  $L=1.6D$  and  $\alpha=45^\circ$  is shortest among all model with the same distance of  $L=1.6D$ . This indicates that the interference between the impact and wake orifice in the separated flow were stronger than in the other models with longer effective lengths.

Since the S-type Pitot tube as utilized in the stack uses the average value of the S-type Pitot tube coefficients within the velocity ranges, the more constant the coefficient within the entire range of velocity changes is, the more accurate the velocity measurements can be achieved. This can be determined by the standard deviation of the coefficients with respect to the change in the velocity. In addition, the recommended value of S-type Pitot tube coefficient, 0.84 was described in ISO 10780 [3]. Accordingly, the uncertainty due to S-type Pitot tube coefficients with respect of incoming velocity change can be assessed by Equation (4).

$$u_{C_p} = \sqrt{\sigma_{C_p}^2 + \frac{(C_p - 0.84)^2}{2\sqrt{3}}} \quad (4)$$

Figure 7 shows the uncertainty of S-type Pitot tube coefficients with respect to the normalized effective length ( $eL/D$ ) for all nine S-type Pitot tube models, which calculated by Equation (4). It is interesting to note that uncertainty of the S-type Pitot tube coefficients decreases as the effective length increases. This implies that S-type Pitot tube models with long effective lengths have more constant distributions of the S-type Pitot tube coefficients with respect to velocity changes. When the effective length ( $eL/D$ ) is larger than 0.8 in the Figure 7, the S-type Pitot tube models have lower uncertainty level that ISO's recommended value. It means that we can suggest geometric parameter of S-type Pitot tube, in this case, the effective length range for the constant distribution of S-type Pitot tube coefficients with respect to incoming velocity.

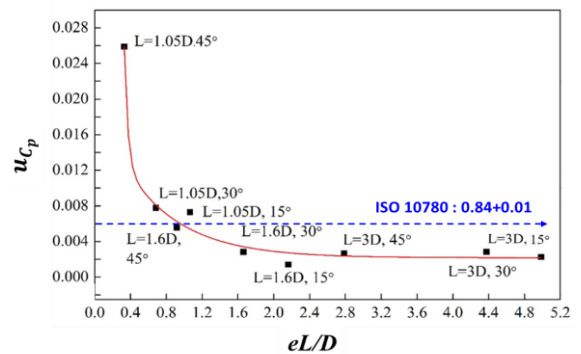


**Figure 7:** Uncertainty of S-type Pitot tube coefficients with respect to normalized effective length.

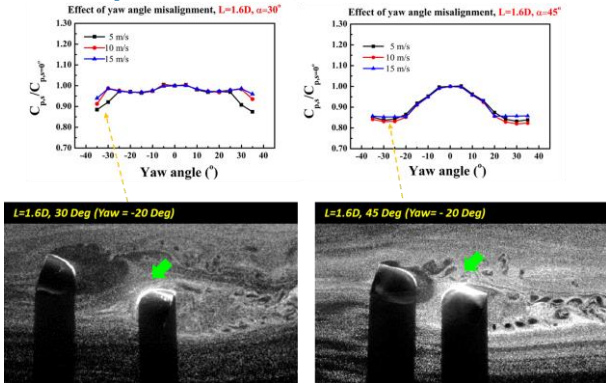


**Figure 8:** Distribution of S-type Pitot tube coefficients and flow visualization by PIV when  $L=1.6D$  with yaw angle change.

### 3.2 The effect of yaw and pitch angle misalignments on the S-type Pitot tube coefficients

To elucidate the effect of the geometries of the S-type Pitot tube models on the S-type Pitot tube coefficients under the yaw and pitch angle misalignments, wind tunnel experiments were conducted with various geometries of the S-type Pitot tube models. The yaw and pitch angle ranges varied from  $-35^\circ$  to  $+35^\circ$  within a velocity range of 2 to 15 m/s.

When  $L=1.6D$ ,  $\alpha=30^\circ$  and  $45^\circ$ , the distributions of the S-type Pitot tube coefficients were considerably different, as shown in the upper part of Figure 8. PIV measurements were conducted for the flow phenomena around the S-type Pitot tube models with  $L=1.6D$ ,  $\alpha=30^\circ$  and  $45^\circ$  with yaw angle misalignment of  $-20^\circ$ . The lower and right part of Figure 8 shows that the separated flows from the surface of the impact orifices interfere with vortical structures separated from the wake orifice when  $L=1.6D$  and  $\alpha=45^\circ$ . This causes the pressure distributions near the wake orifice to drop sharply. Thus, the normalized coefficient values of the model with  $L=1.6D$  and  $\alpha=45^\circ$  tended to decline dramatically upon yaw angle misalignments. On the other hand, in the case of  $L=1.6D$  and  $\alpha=30^\circ$ , there is no interference between the separated flows from the impact orifice and the flows near the wake orifice due to the long distance between the two orifices. It is interesting to note that the actual contact distance of the flow between the two orifices is also an important parameter when determining the effect of yaw angle misalignments.

To quantify the effects of the geometry of the S-type Pitot tube models on the S-type Pitot tube coefficients during yaw angle misalignments, an error index,  $I_{yaw\ error}$ , was defined by using the ratio of area between yaw normalized curve and curve at  $yaw=0^\circ$ . It is determined by the Equation (5).

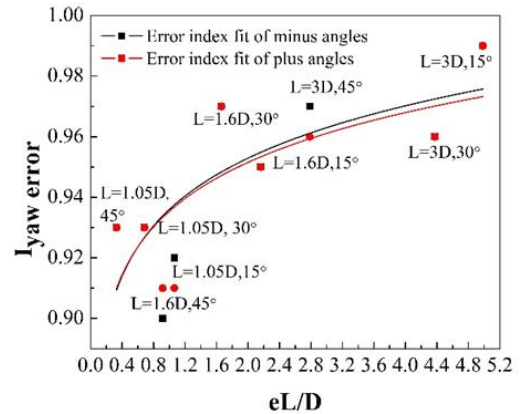


**Figure 9:** Yaw angle misalignment error indexes of S-type Pitot tube models with various geometries.

$$I_{yaw\ error} = \frac{\text{Area of yaw normalized curve}}{\text{Area of curve at } yaw=0^\circ} \quad (5)$$

Area of yaw normalized curve is the area under the curve for the normalized S-type Pitot tube coefficients with respect to the yaw angle misalignment. Area of curve at  $yaw=0^\circ$  is the area under the curve for the normalized S-type Pitot tube coefficients with no yaw angle misalignment, which is  $C_{p,s}/C_{p,s}=0^\circ$ . When error index,  $I_{yaw\ error}$ , closed to the 1, it indicates that the S-type Pitot tube models were less affected by the yaw angle misalignments.

Figure 9 shows the error index of yaw angle misalignments,  $I_{yaw\ error}$ , for S-type Pitot tube models with various geometric parameters. The positive and negative yaw angles show almost similar tendency as shown in the error index fit of all S-type Pitot tube models. It is interesting to note that the error index of the S-type Pitot tube models becomes close to 1 as the normalized effective length,  $eL/D$ , increases. This means that S-type Pitot tube models with long effective lengths are less affected by the yaw angle misalignments.

Unlike yaw angle misalignment, the S-type Pitot tube coefficients when negative and positive pitch angle misalignments are not symmetric. Therefore, in the case of negative pitch angle misalignments, the error index,  $I_{pitch\ error}$  is smaller than 1. On the other hand, in the case of positive pitch angle misalignments, the error index is larger than 1. When error index,  $I_{pitch\ error}$ , closed to the 1, it means that the S-type Pitot tube models were less affected by the pitch angle misalignments. Figure 10 shows the error indexes of pitch angle misalignments for S-type Pitot tube models with various geometric parameters. It is interesting to note that the effective length of S-type Pitot tube coefficients were not correlated with the error index, which shows similar values of error indexes except for small effective length,  $eL/D < 0.1$  in the negative pitch angle.

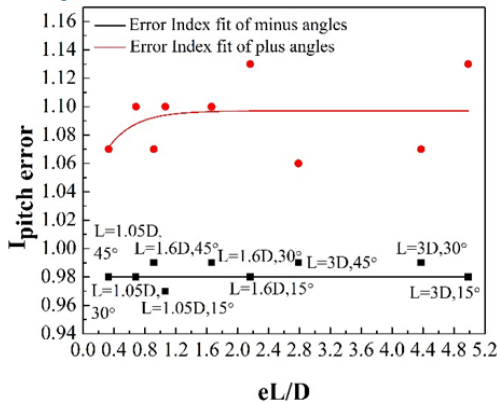


**Figure 10:** Pitch angle misalignment error index of S-type Pitot tube models with various geometries.

#### 4. Conclusion

The main objective of the present study is to determine the optimal geometry of an S-type Pitot tube so as to improve the accuracy of velocity measurements in actual smokestacks which undergo velocity changes and yaw and pitch angle misalignments. The wind tunnel experiments and PIV measurements for the S-type Pitot tube coefficients of models with various geometries show that the distributions of the coefficients with respect to incoming velocity are related to certain flow phenomena, in this case separated flows and vortical structures around the impact and wake orifices. An S-type Pitot tube coefficient with a long effective length,  $eL/D$  has more constant distributions of the S-type Pitot tube coefficients and lower uncertainty when the velocity changes from 2 m/s to 15 m/s. Therefore, we can suggest geometric parameter, in this case, the effective length range for the constant distribution of S-type Pitot tube coefficients with respect to incoming velocity.

The distributions of S-type Pitot tube coefficients upon yaw and pitch angle misalignments differed depending on the combination of geometric parameters for the distance ( $L$ ) and the bending angle ( $\alpha$ ). The actual contact distance of the flow between the two orifices, effective length is also an important parameter when determining the effects of yaw angle misalignments, similar to the effects of velocity changes. The error index,  $I_{yaw\ error}$  for yaw angle misalignments shows that S-type Pitot tube models with long effective lengths are less affected by yaw angle misalignments. However, the use of S-type Pitot tube with long distance length is impractical due to the hole size in the smoke-stack for installing S-type Pitot tube. Therefore, we can suggest the certain effective length of S-type Pitot tube considering both the sensitivity to yaw angle misalignment and the practical use in the smoke-stack. On the other hand, the S-type Pitot tube coefficients were mostly insensitive to the both of positive and negative pitch angle misalignments

regardless of the velocity and geometry of the various models. The error index for pitch angle misalignment shows that the S-type Pitot tube coefficients were not correlated with the effective length given the similar value of error indexes except for small effective length,  $eL/D < 0.1$  in the negative pitch angle.

#### References

- [1] U.S. Environmental Protection Agency, *Greenhouse Gas Reporting Program 40 CFR 98.30 Subpart C*, 2013
- [2] U.S. Environmental Protection Agency, *Determination of stack gas velocity and volumetric flow rate (type S Pitot tube), EPA method 2*, 2000
- [3] ISO 10780: *Stationary source emissions – Measurement of velocity and volume flowrate of gas streams in ducts*, 1994
- [4] Kang W, Trang N D, Lee S H, Choi H M, Shim J S, Jang H S, Choi Y M, “Experimental and numerical investigations of the factors affecting the S-type Pitot tube coefficients” *Flow Meas. Instrum.*, 44, 11-18, 2015.
- [5] U.S. Environmental Protection Agency, *Determination of stack gas velocity and volumetric flow rate (type S Pitot tube). US Environmental Protection Agency, Part 60 Appendix A, Method 2*, 1971.
- [6] ASTM D3796-90: *Standard practice for calibration of Type S Pitot tube*, 2004.

# Pitometry as a validation tool for water flow measurement in large diameter pipelines

Nilson Massami Taira<sup>1</sup>, Kazuto Kawakita<sup>1</sup>, Valmir Ruiz<sup>1</sup>

<sup>1</sup> IPT-Instituto de Pesquisas Tecnológicas  
Av. Prof. Almeida Prado 532 CEP 05508-901 São Paulo/SP Brazil  
nmtaira@ipt.br, kawakita@ipt.br, valmir@ipt.br

---

## Abstract

Accurate measurement of water flow rates in large diameter pipelines is a challenge for water companies that need to produce, transport and distribute increasing quantities of water. To a large extent, this challenge results from the impossibility of recalibration of the flow meters within the periodicity established in the metrological regulations since the removal of a large flow meter from its site of operation in the field and its dispatch to a calibration laboratory is in most cases technically and economically impracticable. As a result of this scenario, the article presents the pitometry technique as an interesting alternative to solve problems related to the validation of water flow measurements performed by flow measurement systems installed in large pipelines. The technique is based on the determination of the water flow rate by mapping the velocity profile of the water flow inside the pipe using Cole type Pitot tubes. The water flow rate is determined in a cross section of the pipe located near and in series to the flowmeter to be evaluated. Based on the results obtained in a great number of water flow measurements already performed by applying the pitometry technique in large diameter pipelines in the field, it is possible to conclude that this methodology is perfectly applicable in the validation of the performance of flow meters installed in these conduits solving satisfactorily the issues related to its operation.

---

## 1. Introduction

Due to technical and economic reasons, the accurate measurement of water flow rates in large diameter pipelines is a challenge for water supply companies that everyday need to produce, transport and distribute increasing quantities of this product. It is also an incitement for manufacturers of flowmeters that are requested to offer solutions to this progressively challenging metrological demand.

In the last decades, based on the development of sensors, electronic signal processors and software, it has been possible to witness the emergence of new water flow measurement technologies for these applications such as the widely used electromagnetic full bore meters, the ultrasonic transit time flowmeters and the electromagnetic and thermal insertion meters that are proposed to replace the former differential pressure meters such as the well-known Venturi tube and its several constructive variations. These developments have been induced by the need for automation and control of water flow measurement processes associated with the requirement for improving the reliability of flow measurement results.

Despite the natural process of modernization of the flow measurement systems used by the water companies, what has happened in practice is a series of issues arising from the application of these new technologies in such situations. Notably, the following topics deserve mention:

- the issue of recalibration of the flowmeters within the periodicity established in metrological regulations still remains unresolved. The removal of a large full-bore diameter flowmeter from its site of operation in the field and its dispatch to a calibration laboratory is in most cases technically and economically impracticable;
- the signal acquisition and treatment systems in these meters use proprietary electronics and software that are difficult to be audited and validated from the perspective of legal metrology, jeopardizing the transparency and reliability of flow measurement results;
- due to the large dimensions of the conduit, some types of flowmeters use the technique of sampling flow velocities only at a specific point in the pipe cross-

section or only in one or two paths through the flow, inferring the water flow rate based on that flow velocity sample, simply neglecting the possibility of occurrence of flows with asymmetric velocity profiles or with the presence of flow swirl;

- the criteria considered by users in the implementation of a water measurement system in large pipelines often consider only the costs of the initial investment, without assessing the costs of operating the meter, without guaranteeing the availability of spare parts and technical assistance services and without ensuring the metrological traceability of measurement results during the many years of meter operation.

## 2. Pitometry technique

Considering the worrying issues presented previously, the Fluid Flow Laboratory of IPT-Instituto de Pesquisas Tecnológicas, a technological research institute in Brazil, developed a methodology for measuring water flow in large conduits based on the fundamental technique of pitometry and using the Cole type Pitot tube for mapping the flow velocity profiles in the pipes.

### 2.1 Cole type Pitot tube

Basically, the Cole type Pitot tube is a differential pressure probe designed by Edward Cole around 1896 [1] and is composed of two parallel tubes of approximately 6 mm outside diameter, bent at a 90° angle and oppositely oriented at the ends. The Cole type Pitot tube is shown in Figure 1.

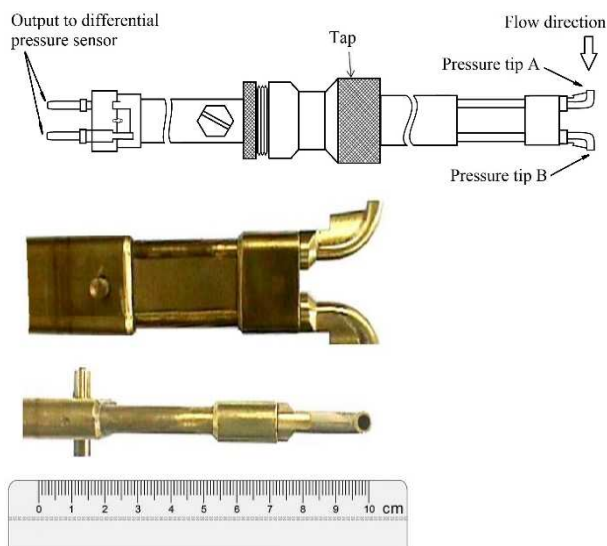


Figure 1: The Cole type Pitot tube.

One pressure tip is in the front position to the flow path of the liquid and the other in the opposite position. The front tip to the flow (tip A) measures the total pressure and the other (tip B) measures the pressure of the wake

flow, defining a differential pressure signal measured by pressure transducers and that is proportional to the square of the flow rate of the liquid.

As shown in Figure 2, in the measurement of water flow rates in large pipes it is common to use a modified Cole-type Pitot tube which has a safety pin located in between the tips to protect them from possible damage caused by their impact against the internal wall of the pipe during insertion of the probe.



Figure 2: Photograph of a modified Cole type Pitot tube with a safety pin in between the tips.

### 2.2 Cole type Pitot tube calibration

At IPT, the Cole type Pitot tubes are calibrated using an aerodynamic wind tunnel as shown in Figure 3.

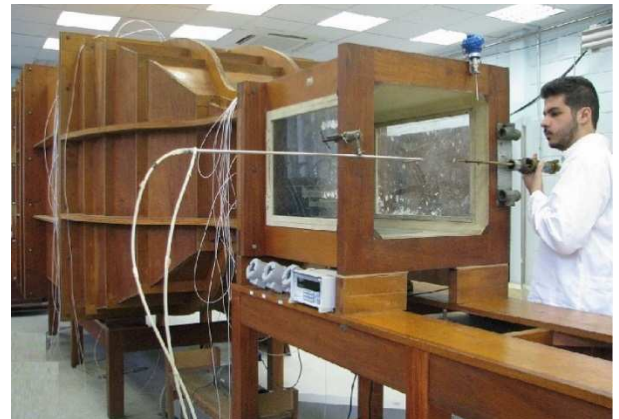


Figure 3: Calibration of Cole type Pitot tube in the aerodynamic wind tunnel at IPT Fluid Flow Laboratory.

Tests conducted at IPT using a wind tunnel and a large towing tank showed that Cole type Pitot tubes can be calibrated in air flows and used in water flows, provided that the Reynolds number similarity is respected [2].

During calibration, the Cole type Pitot tube is positioned at the central area of the wind tunnel discharge section, avoiding the regions near its internal walls. A conventional L-type Pitot-static tube is used as a reference air velocity probe. Both Pitot tubes are connected to pressure transducers and two rising sequences of points consisting of ten air flow velocities between 5 m/s and 36 m/s are compared. Based on Reynolds numbers similarity, where

$$Re_{water} = Re_{air} \quad (1)$$

these air flow velocity limits correspond to water flow velocities of 0.3 m/s and 2.4 m/s, respectively.

The mean calibration coefficient recommended by the literature for conventional Cole type Pitot tubes, including corrections, is 0.8696 [2]. Figure 4 presents a set of measurements that are commonly used by water utility companies in Brazil [3]. This figure shows the dependence of calibration coefficient ( $C_c$ ) of the Cole type Pitot tube to the flow Reynolds number. The Reynolds number is defined as:

$$Re = \frac{V L}{\nu} \quad (2)$$

where  $V$  is the fluid flow velocity in m/s,  $L$  is a characteristic length, here fixed as 1 m,  $\nu = 1.004 \times 10^{-6} \text{ m}^2/\text{s}$  is the kinematic viscosity of water at 20 °C.

The results shown in Figure 4 for  $5 \times 10^5 \leq Re \leq 3 \times 10^6$ , correspond to a water flow velocity range of  $0.5 \text{ m/s} \leq V \leq 3.0 \text{ m/s}$ . In this velocity range, the calibration coefficient of the Cole type Pitot tube varies between 0.883 for 0.5 m/s and 0.861 for 3.0 m/s with a mean value of 0.867.

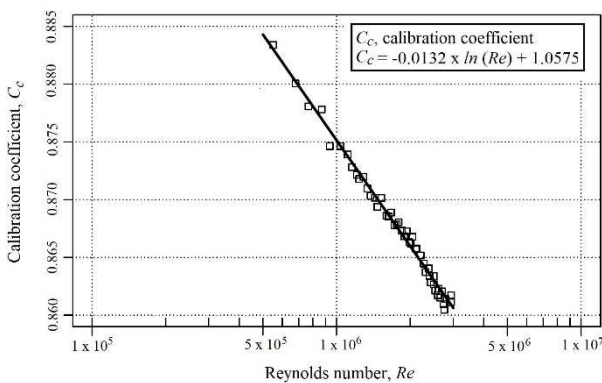


**Figure 4:** Reynolds number dependence of calibration coefficient ( $C_c$ ) of Cole type Pitot tubes according to reference [3].

The calibration coefficient of the Cole type Pitot tube is obtained using the following equation:

$$C_c = C_s \sqrt{\left( \frac{\Delta P_s}{\Delta P_c} \right)} \quad (3)$$

where  $C_s = 0.997$  is the calibration coefficient of the L-type Pitot-static tube used as a standard [4],  $\Delta P_s$  and  $\Delta P_c$  are, respectively, the differential pressures obtained by the L-type Pitot-static tube and Cole type Pitot tube.

### 2.3 Flow velocity profile

For the determination of the water flow rate, the guidance of the technical standard ISO 3966 [5] is

followed for the calculation of the mean flow velocity in the cross section of the pipe using Cole-type Pitot tube and the *log-linear* method for the mapping of the flow velocities at eleven points distributed along the conduit measuring diameter.

In Figures 5 and 6, respectively, the pitometry taps are shown in the outside perimeter of the pipe and the eleven measurement positions along the measuring diameter with respect to the reference dimension  $h$ , whose numbering starts at the point of the traverse closest to the tap and ends at the diametrically opposite point.

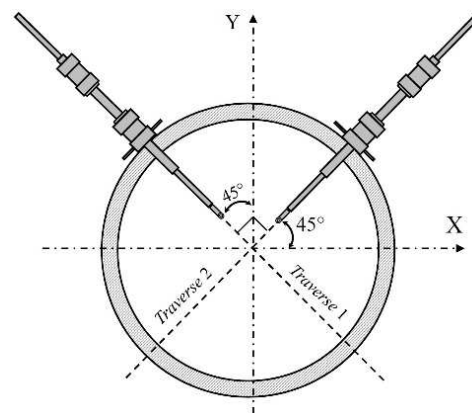


**Figure 5:** Position of the taps for mapping the flow velocity profile along two diameters arranged perpendicularly to each other.

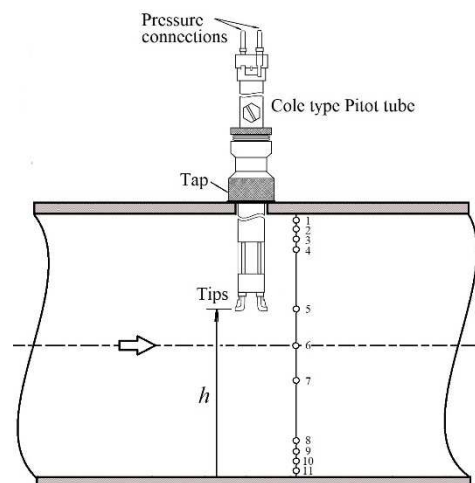


**Figure 6:** Positions of velocity measurement points along the traverse.

Figure 7 shows an example of water flow velocity profile including the eleven velocity measurement points.

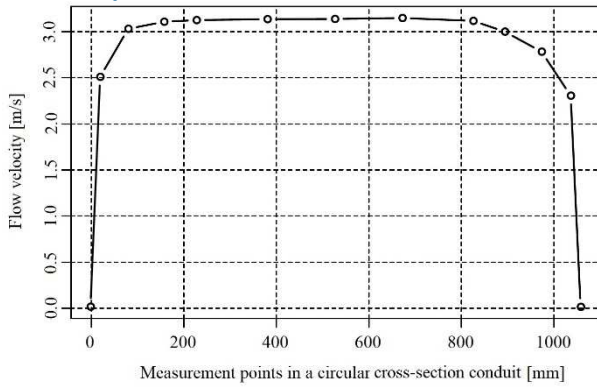


**Figure 7:** Water flow velocity profile determined by mapping the flow velocities at eleven points along the conduit measuring diameter.

#### 2.4 Volumetric flow rate calculation

The volumetric flow rate of water ( $Q$ ) in the conduit is calculated as a function of the average flow velocity ( $\bar{V}$ ) in the measuring section and the internal cross-sectional area ( $S$ ) of the measurement location. That is:

$$Q = \bar{V} \cdot S \quad (4)$$

where:

$$\bar{V} = C_c \cdot \frac{\sum_{i=1}^n \sqrt{\frac{2 \cdot \Delta P_i}{\rho_o}}}{n} \quad (5)$$

and:

$C_c$  calibration coefficient of the Cole type Pitot tube;

$\Delta P_i$  differential pressure measured at each point of the velocity mapping, disregarding the central point on the pipe axis (point 6);

$\rho_o$  water density under measurement conditions, considered equal to  $\rho_{o,25^\circ C} = 997,043 \text{ kg/m}^3$ .

The volumetric water flow rate can also be calculated from the flow velocity at the central point in the measurement section ( $V_C$ ), the average velocity factor ( $VF$ ) and the internal cross-sectional area of the measurement site ( $S$ ). That is:

$$Q = VF \cdot V_C \cdot S \quad (6)$$

where:

$VF = \frac{\sum_i^n \sqrt{\Delta P_i}}{n \sqrt{\Delta P_c}}$  is the mean velocity calculation factor, particular of the flow and valid exclusively for the specific pipe, with its singularities near upstream and downstream of the pitometric station and characteristic Reynolds number range. This is an empirical correlation for the calculation of the integral of

Karman's law (law of power);

$\Delta P_c$  is the differential pressure measured with the Pitot Cole tube at the central point in the axis of the pipe.

#### 2.5 Instrumentation scheme

The methodology developed and applied by IPT allows the monitoring of the signal of a flow meter present in series in the same pipeline during the process of mapping the velocity profile, as shown in Figure 8. This makes it possible to simultaneously perform the calibration of the flowmeter and make corrections of possible flow fluctuations that may occur during measurements.

Figure 8 shows the instrumentation scheme used for the mapping of flow velocity profiles established in the measurement section of the pipe.

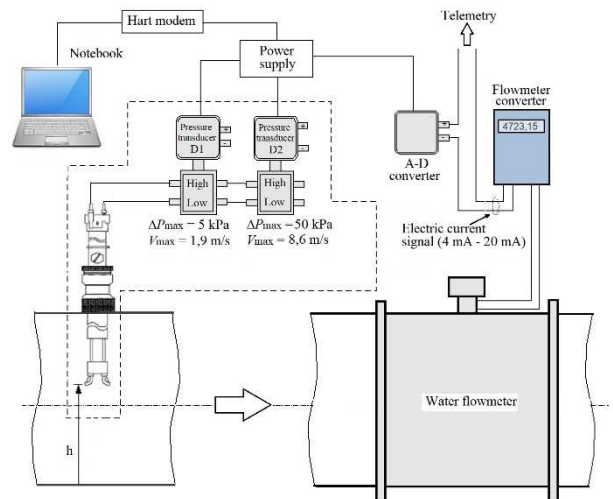


**Figure 8:** Scheme of the instrumentation used for the mapping of flow velocity profiles using the pitometry technique.

### 3. Case study

To illustrate the application of the method of water flow measurement by pitometry technique in large diameter pipelines, a case study involving the calibration of a water flow measurement system is presented below.

#### 3.1 Description of the installation

Figure 9 shows the scheme of a water pumping station which operates with two axial hydraulic pumps of same size in parallel. In the discharge pipeline of 2232 mm internal diameter, made in steel, there is installed a dual path transit time ultrasonic flowmeter with two pairs of transducers which needed to have its metrological performance evaluated.

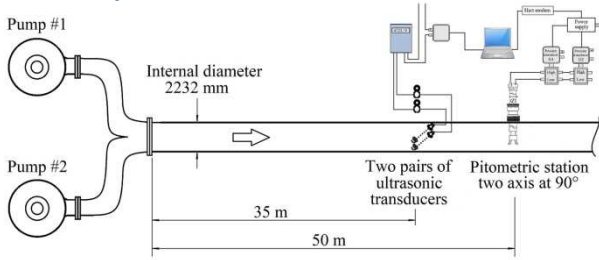


**Figure 9:** Sketch of the pumping station discharge pipeline, indicating the installation locations of the ultrasonic flow meter transducers and the pitometric station.

The water flow measurements were performed by applying the pitometry technique using two Cole type Pitot tubes mounted perpendicularly to each other and transversely to the longitudinal axis of the conduit through two special insertion connections, commonly known as taps.

To perform the calibration of the indication of the ultrasonic flow meter of the pumping station, in parallel to the measurement of water flow rate with Pitot tubes, the data acquisition of the flow rate indication of the ultrasonic meter was performed. For that, a data logger was installed in series at the output of the electrical signal (4 mA to 20 mA) of the ultrasonic meter sent to the supervisory system installed in the control room of the pumping station.

In the following items, the results obtained in the survey of the flow velocity profiles, the pump flow monitoring and the ultrasonic meter calibration are presented.

**3.2 Results of flow velocity profiles mapping**

Figures 10 and 11 show the graphs of the instantaneous flow rates measured with the pitometry technique, in two 90° diameters, and the flow rates indicated by the ultrasonic meter during the measurements performed in the pumping station discharge pipeline, respectively, only with the pump #1 in operation and with the pumps #1 and #2 in parallel.

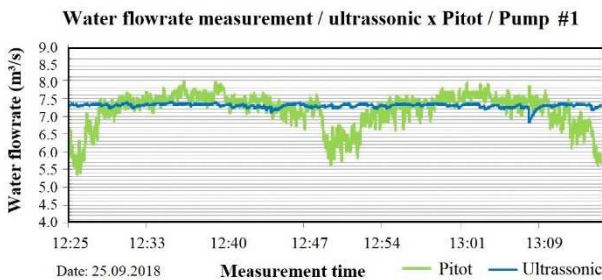


**Figure 10:** Water flow rates measured by the ultrasonic meter versus pitometry, only with the pump #1 in operation.

**Water flowrate measurement / ultrasonic x Pitot / Pumps #1 // #2**

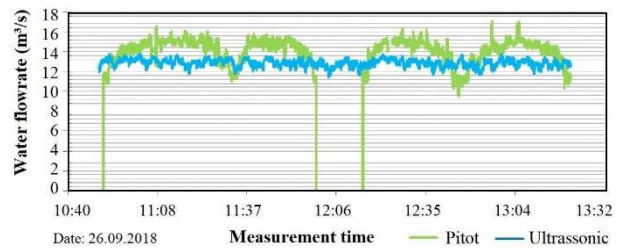


**Figure 11:** Water flow rates measured by the ultrasonic meter versus pitometry, with pumps #1 and #2 operating in parallel.

Figures 12 and 13 show the results sheets of the pitometry mapping performed on the discharge pipe of the pumping station, respectively, for the case of operation only with pump # 1 and for pumps # 1 and # 2 operating in parallel.

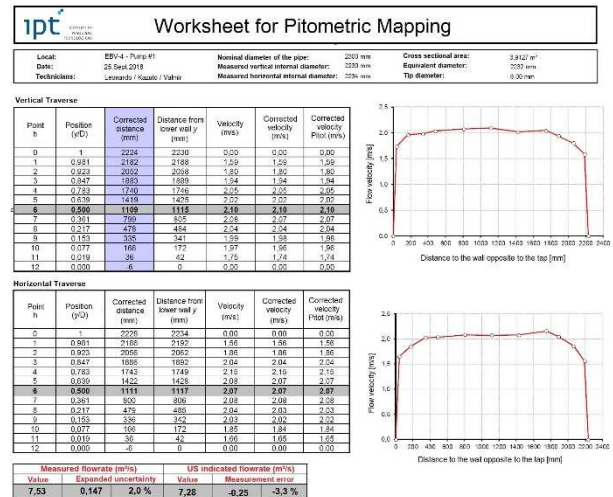


**Figure 12:** Pitometric data and flow velocity profiles in the discharge pipeline of the pumping station operating only with pump #1.

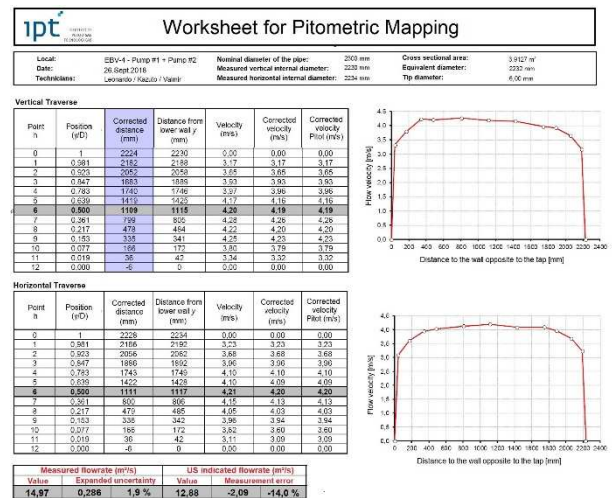


**Figure 13:** Pitometric data and flow velocity profiles in the discharge pipeline of the pumping station operating with pumps #1 and #2 in parallel.

Figure 14 shows the measurement errors determined in the calibration of the ultrasonic flow meter at the two-pump station operating flow rates.

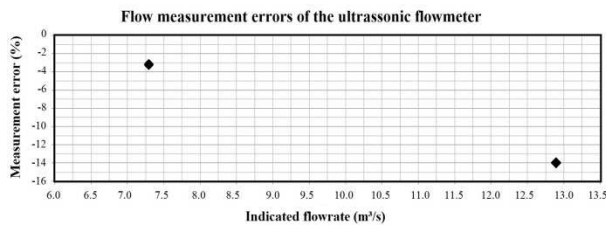


**Figure 14:** Flow measurement errors presented by the ultrasonic meter.

The information and data of the measured parameters recorded during the measurements indicated that the uncertainties associated with the measured values were of the order of 2.0 % of the water flow rate measured by means of the pitometry technique, which is fully compatible with the conditions and difficulties resulting from the measurement of water flow in the field in a large conduit.

#### 4. Conclusion

Based on the good results obtained in a large number of applications in closed conduits of raw and treated water together with water production, transportation and distribution companies, the fundamental and auditable technique of pitometry has shown to be a quite appropriate tool for validation of water flow measurement in large diameter pipelines. That is, the pitometry technique allows recalibration of the flow meters within the periodicity established in the metrological regulations without the need to removal the flow meter from its field operation site. In addition, it is not necessary to know and dominate the acquisition and signal processing technology used by these meters since the end result of the measurement system as a whole is validated to ensure the reliability of flow measurement results. Likewise, the effects of installing the meter, the conditions of the water flow in the conduit and sampling the flow velocity only at a specific point in the cross section of the tube (in the case of point velocity meters) or only in one or two trajectories through the flow (in the case of transit time ultrasonic meters) are solved. Finally, the metrological traceability of measurement results can be guaranteed during the many years of meter operation. However, although the uncertainties associated with the results of the measurements performed by applying the pitometry technique are greater when compared to those obtained in calibrations of water flow meters in a laboratory test bench, they can be improved with the technical standardization of the shape and dimensions of the Pitot tubes, by improvement of the calibration methods of the

probes and by using techniques of mathematical modelling of the flow.

#### References

- [1] Cole Edward.S. and Cole E.Shaw *Pitot Tubes in Large Pipes* Transactions of the A.S.M.E., New York, N.Y., August 1939, p. 465–560.
- [2] Espirito Santo G, Taira N M and Santos C 2004 *Comparison of calibration of pitot tubes in a wind-tunnel, towing tank and pipe*. Private Communication at IPT of results not published.
- [3] CETESB Sao Paulo *Manual de pitometria*.
- [4] ISO/IEC 61400 2005 *Wind turbine generator systems – part 12: Wind turbine power performance testing*, annex f.
- [5] ISO 3966:2008 *Measurement of fluid flow in closed conduits - velocity area method using pitot static tubes*. This standard was last reviewed and confirmed in 2012.

# Study on Application of Wet Gas Metering Technology in Shale Gas Measurement

Qiang Zhang<sup>1-2</sup>, Dingfa Liu<sup>1-2</sup>,

<sup>1</sup> Research Institute of Natural Gas Technology, Southwest Oil & Gasfield Company, Petrochina, Tianyan Road 218# Huayang town, Chengdu, China

<sup>2</sup> Chengdu Verification Branch of National Oil & Gas Large Flowrate Measurement Station, Chengdu, China  
E-mail: zhangq07@petrochina.com.cn

## Abstract

The application of wet gas flow meter at shale gas wellhead is of great significance to reduce the investment and operation cost of shale gas extraction. The flow conditions at the wellhead of shale gas and the technical measuring principles of the current wet gas flow meters are briefly analyzed in this paper. A wet gas flow meter was tested on the wet gas flow test facility, and the performance of the wet gas flow meter with the correlation model developed with the air and water as test medium is studied, which is helpful to optimize the wet gas metering process design of shale gas wellhead and to improve the wet gas metering technology. The research shows that the measurement principle of the current wet gas flow meters are workable, however, the wet gas correlations of the wet gas flow meter must be calibrated with wet natural gas according to the working conditions.

## 1. Introduction

In natural gas industry, the production of natural gas from a well is always accompanied by the water and hydrocarbon. This unprocessed output from gas well is called wet gas, and it is a particular subset of gas and liquid two phase flow. Now, there is no unanimous definition of wet gas in industry, various methods have been used to define and even to classify the wet gas, and it is most commonly defined as when the Lockhart-Martinelli parameter is less than or equal to 0.3[1]. Because of the presence of liquid in the gas flow, single phase gas flow meters fail to work or even damaged when expose to wet gas flows. Now the wet gas flow is measured applying separation technology in most cases in China.

## 2. Flow conditions of shale Gas wellhead and the demand of wet gas flow metering

Compared with the conventional natural gas extraction, there is no water or light hydrocarbon output produced from the shale gas reservoir. However, in the process of shale gas exploitation, unconventional hydraulic fracturing technology is used to stimulate the reservoir, quantities of fracturing fluid is injected into the reservoir. As a result, a large amount of fracturing fluid

accompanied in the shale gas in the process of shale gas extraction. The exploitation of shale gas can generally be divided into four stages according to the wellhead working conditions: drainage exploitation stage, early exploitation stage, middle exploitation stage and late exploitation stage, as it shown in talbe1.

**Table 1:** Working condition features of shale gas wellhead

Production Stage	Period	Wellhead Pressure (MPa)	Gas Production Rate ( $10^4 \text{Nm}^3/\text{d}$ )	Liquid Output Rate ( $\text{m}^3/\text{d}$ )
drainage exploitation stage	0-45day	40 \ 26	25	200-500
early exploitation stage	46day-8month	26 \ 10	10-15	20-200
	8-10month	10 \ 7	10	10-20
	11month-3year	7 \ 2	10 \ 5	1-10
middle exploitation stage	4year-5year	2 \ 1	5 \ 1.5	0.5-1
late exploitation stage	5 year later	1	$\leq 1.5$	$\leq 0.5$

As can be seen from the table, the gas production, liquid output and the wellhead pressure of shale gas gradually decrease as the extraction time increases. Compared with conventional gas production exploitation, wellhead production of shale gas decline more rapidly, most of the

wellhead production decline about 40% in the first year. Therefore, it is necessary to monitor the shale gas production to get the reservoir information and to evaluate the gas well production capacity, which is essential for the optimization of gas field extraction plans and production decision.

The wet gas can be measured apply separation or non-separation method. The separation method is a traditional technology that recognized by most people, however this method is high cost and low efficient as it requires a complex process pipe system and in most cases the flow of each well is separated and metered alternatively. Compared with the separation technology, the non-separation method or wet gas meter technology can greatly reduce the investment cost and improve the metering efficiency by monitor the well production of each well at the wellhead directly, however the technical maturity of wet gas metering technology has yet need to be tested and verified. Currently, in order to monitor the wellhead output production of shale gas, each wellhead of shale gas on the production platform is equipped with an individual separator and flow measuring meters, which is an expensive investment. The best solution for the shale gas wellhead production measurement is using the wet gas meter whose accuracy could meet the requirement. In this paper, a wet gas meter was tested on the wet gas flow test facility at Chengdu Verification Branch of National large flow rate measurement station, the performance of the wet gas flow meter with the correlation model developed with the air and water as test medium at low pressure is studied, which is helpful to optimize the wet gas metering process design of shale gas wellhead and to improve the wet gas metering technology.

### **3. Basic principles and technical features of current wet gas flow meters**

The wet gas flow meter technology is a new metering technology developed based on single phase flow meters with correlation model in recent few decades. The core of the wet gas flow meter is using the wet gas correlation model created based on large amount experiment data to correct the meter bias caused by the liquid in the gas flow.[2] Most of the available wet gas meters are based on some sort of differential pressure device with wet gas correlations and incorporate some other technologies to determine the liquid fraction of wet gas flow.[3] The metering principles of the most current wet gas meters can generally be summarized into two kinds. One is to use the liquid fraction detecting technology such as gamma ray

device or microwave technology to measure the liquid fraction directly and provide this measured liquid fraction information to the correlation models to calculate the gas and liquid flow rates of wet gas flow. The other kind is to use two different gas meters in series, which provide the same flow rate for dry gas but each meter has a different wet gas performance when liquid is present, and use the difference of two meters responses to the wet gas flow conditions to determine the liquid fraction of wet gas flow and then calculate both the gas and liquid flow rates by the correlation models.[4] It is obvious that the gas and liquid flow metering accuracy of wet gas flow meters totally depends on the correlation models.

### **4. Wet gas flow meter test**

#### *4.1 Wet gas flow test facility and the test method*

In order to study the performance of wet gas flow meter at the conditions of wet natural gas flow, a wet gas flow meter was tested at the wet gas test facility of Chengdu Verification Branch of National oil and gas large flow rate measurement station of China. This facility is designed for gas-liquid two phase flow studies consisting of water and natural gas. The schematic diagram of the wet gas test facility of CVB is shown figure1. This facility is mainly composed of gas and liquid reference meters, liquid pump injection and regulation system, gas-liquid two phase flow test section and gas-liquid separation system. The gas used for the wet gas facility comes from a high pressure pipeline. The gas reference meter is a high accuracy ultrasonic flow meter which measures the natural gas flow before mixing. The natural gas after is measured by the ultrasonic flow meter and then flows into the test section where the liquid phase is injected and mixed. The flow rate of the liquid is well regulated by the liquid pump injection and regulation system. A 0.5 inch and a 1 inch Coriolis mass flow meters work as liquid reference meters on the liquid injection line to measure the liquid flow rate. The natural gas drives the liquid through the test section and then flow into the gas-liquid separation system where the gas and liquid is separated. The liquid returned via the separator to the water tank and re-circulated by the liquid pump. The separated natural gas after test is discharged into a low pressure pipeline. The test pressure range of the wet gas test facility is from 15bar to 40bar, the gas flow test range is from 8m<sup>3</sup>/h to 650m<sup>3</sup>/h, and the liquid flow test range is from 0 to 8m<sup>3</sup>/h.

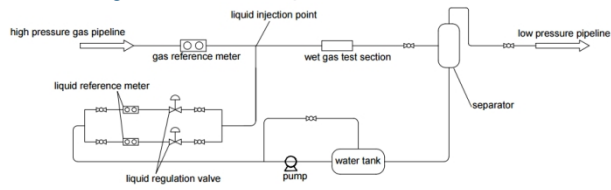


**Figure 1:** Schematic diagram of CVB wet gas test facility



**Figure 2:** Wet gas test facility of CVB

According to the flow conditions of wellhead shale gas and the metering range of wet gas flow meter, the experimental test matrix was determined as follows, the test pressure is 22bar, the gas flow rate ranges from 36m<sup>3</sup>/h to 130 m<sup>3</sup>/h, the Lockhart-Martinelli parameter ranges from 0 to 0.25, the detailed test conditions are shown in table2.

**Table 2:** Wet gas flow meter test point

Gas flow rate	36 m <sup>3</sup> /h	72m <sup>3</sup> /h	108m <sup>3</sup> /h	130m <sup>3</sup> /h
Liquid flow rate (m <sup>3</sup> /h)	0	0	0	0
	0.19	0.36	0.52	0.74
	0.38	0.71	1.06	1.43
	0.74	1.44	2.16	2.88
	1.1	2.20	3.23	4.49

In the test process, at each gas flow test conditions, the performance of wet gas flow meter at single-phase dry gas is first tested as the base reference for the wet gas flow test. After the dry gas test, the liquid is gradually injected into the natural gas flow from less to more to conduct the wet gas flow test. Figure3 shows the tested wet gas flow meter.



**Figure 3:** Wet gas flow meter under test

#### 4.2 The test result and analysis

The gas phase test result of wet gas flow test is shown figure4, and the liquid phase test result is shown is figure5. It can be seen from figure4, for the gas flow rate of 72m<sup>3</sup>/h and 108m<sup>3</sup>/h, the wet gas flow meter has a decent gas flow measurement result, the relative errors of gas phase flow is approximately within 3%. However, for the other two gas flow rates test condition of 36m<sup>3</sup>/h and 130m<sup>3</sup>/h, the gas flow rates measurement of the wet gas flow meter shows obvious positive error except the dry gas test point, and the error increases as the liquid hold up increase which indicated by L-M parameter. The maximum error of gas flow measured by the wet gas flow meter within the test range is 11%. The liquid phase flow measurement results of the wet gas flow meter shows negative error, which means that the liquid flow rates measured by the wet gas flow meter are obvious lower than that measured by the liquid reference meter, and the liquid measurement error of this wet gas flow meter increases as the L-M parameter increases, which has similar trend with the gas flow measurement error. The maximum liquid measurement error at test condition is -37%.

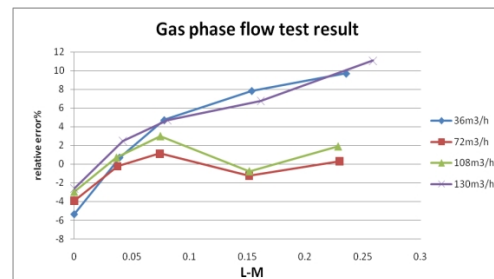


**Figure 4:** Gas phase flow test result

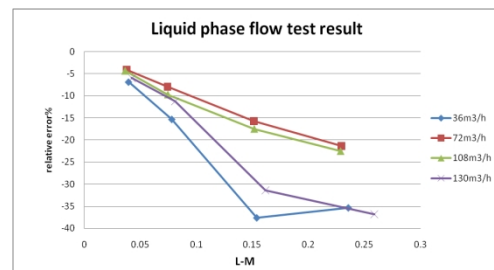


**Figure 5:** Liquid phase flow test result

As can be seen from the test results, the performance of wet gas flow meter shows the following three features. First, the gas and liquid flow measurement error is related to the liquid hold up of wet gas flow, the higher the liquid holdup of

wet gas flow is, the greater the error will be, and this feature is caused by the metering principles of wet gas flow meter, the measurement of wet gas flow meter relies on the correlation models and the metering algorithm. The correlation model of wet gas flow meter is a complex function that describes the relationship between the wet gas correction factors and liquid holdup and other influential factors. When there is a deviation of the correlation model, the deviation must be shown as a systematic deviation related to liquid holdup and other influential factors such as gas flow rate, gas density, therefore measurement error of wet gas flow meter increase as the liquid holdup of wet gas flow increases. And this is also the main reason why it is more difficult to measure the wet gas flow when the liquid holdup is higher using wet gas flow meters. Second, the gas flow error and liquid flow error of wet gas flow meter are in opposite directions, and this feature of wet gas flow meter is also associated with the metering principle and algorithm the meter, the measurement algorithm of wet gas flow meter firstly analyzes and measures the liquid holdup or liquid fraction of wet gas flow, and then measures the gas flow rate according to the measured liquid fraction and the correlation model. When the measured liquid fraction is smaller than the true value, the correction factor or the over-reading calculated by the liquid fraction and correlation model will also be smaller than the true value, and this will result a higher gas flow rate measurement and cause a positive error of gas flow, and vice versa. Third, the single phase dry gas flow measurement accuracy of wet gas flow meter is lower than that of single phase gas flow meter, this is because the metering algorithm of wet gas flow meter take the dry gas as the wet gas to measure and measures the liquid content first and then the gas flow, the measurement of the gas phase flow includes the measurement result of the liquid phase flow, and the measurement accuracy is lower than that of the simple dry gas measurement using single phase dry gas flow meter.

The above is the direct brief analysis of the test results. The essential reason for the measurement deviation of wet gas flow meter is that the correlation model deviate in the wet natural gas flow, the correlation model of the wet gas flow meter under this test was obtained by data fitting of the data tested with air and water as test medium at the pressure range from 5bar to 15bar. Due to the complexity of wet gas flow, the correlation metering model of current wet gas flow meter is a semi-empirical mathematical model, which is obtained by data fitting, therefore the application

scope of the correlations are strictly limited. The current technical reports and related research papers show that the wet gas correlation model will produce uncertain deviation when the wet gas conditions extrapolate the limits of the data range that used to create the correlation model. It can be seen from this study, due to the great difference between the low pressure wet air flow and the flow of high pressure wet natural gas, the correlation models developed with air and water as test medium can not be directly used at wet natural gas flow conditions. When this type of wet gas flow meter used in wet natural gas, the correlation model of the meter must be modified and re-calibrated using wet natural gas test data.

#### 4.3 Wet gas flow meter test after correlation calibration

The wet gas flow meter was tested again after the correlation model was re-calibrated according to the previous wet natural gas test data. The range of the re-test flow condition is consistent with the range of the calibration data, which means the re-test was carried out according to the working condition range of table2. The gas and liquid flow measurement test result after the wet gas meter correlation model calibrated are shown in figure6 and figure7.

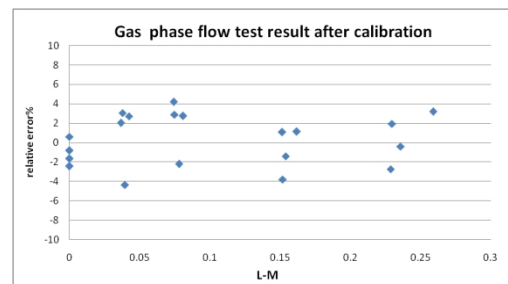


Figure 6: Gas phase flow test result after calibration

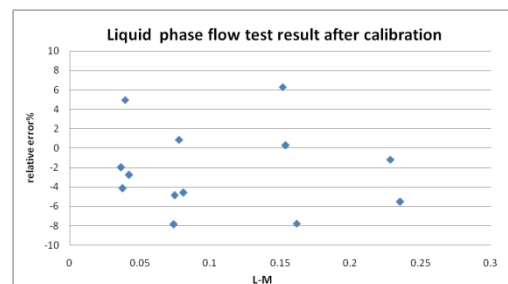


Figure 7: Liquid phase flow test result after calibration

It can be seen from figure6 and figure7 that the gas and liquid flow metering accuracy of the wet

gas flow meter have significantly improved after the correlation model. The gas phase flow rate measurement errors are within the scope between plus and minus 4% and the liquid phase flow rate measurement errors are within the scope between plus and minus 10%. If this wet gas measurement accuracy can be achieved at the wellhead, this wet gas meter can meet the needs of production and management of wellhead metering.

## 5. Conclusions and Suggestions

It can be seen from the performance test and re-test after calibration that the metering principles and methods of the current wet gas flow meters are workable, however the wet gas correlations of the wet gas flow meter must be re-calibrated with wet natural gas according to the working conditions. There would be an uncertain deviation when the wet gas flow meters that calibrated using air and water at low pressure are directly used at wet natural gas flow, which can not meet the needs of field measurement. Considering this technical feature of current wet gas flow meter, using wet natural gas to calibrate the correlation models according to the flow conditions of wellhead is the necessary mean to ensure the accuracy of wet gas flow meter at the field wellhead. Therefore, the wet gas flow meter should be calibrated under the flow condition as close as possible to the site it will be used.

The wellhead flow conditions of shale gas changes regularly, as the extraction time increase, the wellhead gas pressure and flow rate of shale gas gradually decreases, and the liquid fluid contained in the gas flow gradually decreases as well. According to the analysis of the measuring principles of wet gas flow meters, the difficulty of wet gas measurement reduces as the liquid fraction of wet gas flow decrease. And there is no hydrocarbon contained in the output of shale gas, the components of the gas and liquid of shale gas output are relatively fixed and simple, it is a particular simple case of gas-water two phase flow. Therefore, it is possible to mimic most of flow conditions of shale gas wellhead by wet gas test facility and establish the correlation models for the wet shale gas. The test envelop of the wet gas facility CVB built can cover the flow conditions of shale gas wellhead one year after it put into operation. The next step of wet gas natural gas measurement technology research on shale gas flow should make full use of this wet gas facility to carry out the following several aspects of research work in stages. First, to establish the wet gas correlation model in the test range of the wet gas

facility apply wet gas flow test of the facility, and then carry out the shale gas wellhead field test with the flow conditions in the range of the correlations have tested to study the field adaptability of wet gas correlations in the tested ranges and gradually improve the measuring accuracy and adaptability of wet gas correlations, which is helpful to ensure the field metering accuracy of the correlations within the envelope of wet gas test facility. Second, to study the performance of the correlations when extrapolate the flow conditions out of the test range of wet gas facility, to expand the applicable scope of the correlation model. Third, to update the pressure and liquid holdup test range of current wet gas test facility to enhance the test ability that could cover a wider range of test conditions and could able to mimic most of the flow conditions of shale gas wellhead.

## References

- [1] Lockhart R. W. and Martinelli R. C., "Proposed Correlation of Data for Isothermal Two Phase, Two Component Flow in Pipes", Chem. Eng. Prog., Jan. 1949, Vol. 45, No. 1., pp. 39-48
- [2] ISO TR12748: *Natural Gas – Wet gas flow measurement in natural gas operations*, 2015.
- [3] DeBoom R. J., Husan Z. D, *Wet Gas Flowmetering Guideline*. ASME MFC-19G-2008. New York, The American society of Mechanical Engineers, 2008
- [4] Steven R., "Horizontally installed cone differential pressure meter wet gas flow performance", *Journal of Flow Measurement and Instrumentation*, Volume 20, Issues 4-5, August-October 2009, Pages 152-167

# Modeling of the Flow Comparator as Calibration Device for High Pressure Natural Gas Flow Metering in Modelica

S. Singh<sup>1</sup>, G. Schmitz<sup>1</sup>, Bodo Mickan<sup>2</sup>

<sup>1</sup> Institute for Engineering Thermodynamics, Hamburg University of Technology (TUHH), Hamburg, Germany

<sup>2</sup> Physikalisch-Technische Bundesanstalt, Braunschweig, Germany

E-mail (corresponding author): [sukhwinder.singh@tuhh.de](mailto:sukhwinder.singh@tuhh.de)

## Abstract

The German national metrological institute, Physikalisch-Technische Bundesanstalt, is developing a new concept for volumetric primary standard to calibrate high pressure gas flow meters. The TUHH is supporting these R&D activities with its competence to elaborate computational models for detailed analysis of complex electromechanical systems including fluid flow aspects. The new primary standard is called Flow Comparator and uses an actively driven piston prover to measure the gas flow rate using the time the piston needs to displace a defined enclosed volume of gas in a cylinder. In Modelica a computational model is developed to investigate the Flow Comparator's dynamic behaviour and interaction with the other components in the loop. Furthermore, it allows to gather detailed information about pressure and temperature development at arbitrary chosen locations in the system with high time resolution. The validation of the developed model shows good compliance with measured piston velocity and differential pressure at the piston. The model is used to optimize the frequency inverter's control voltage trajectory to increase the available measuring time.

## Nomenclature

$a, b, c$	fitting parameters
$f$	relative deviation
$h$	enthalpy
$m$	mass
$p$	pressure
$s$	position
$t$	time
$u$	internal energy
$u_s$	voltage
$v$	velocity
$A$	area
$F$	force
$L$	inductance
$R$	resistance
$Q$	end effect factor
$\dot{Q}$	heat flow
$V$	volume
$\dot{V}$	volume flow rate
$\Delta$	difference
$\omega_r$	electric frequency
$\psi_r$	induced part flux
$\rho$	density
$\tau_m$	polar pitch
$\zeta$	pressure loss coefficient

## 1. Introduction

Natural gas is one of the most frequently used energy carriers worldwide and is usually transported in high pressure pipelines or as liquefied natural gas in tank vessels. For the trade with natural gas the uncertainty of high-pressure natural gas flow meters is of major importance. The uncertainty depends on the calibration chain and increases with each step. At the top of the calibration chain is the primary standard for high pressure natural gas flow metering. It is a High-Pressure Piston Prover, which is installed and operated at the calibration facility for gas meters pigsar™ in Dorsten, Germany [1,2,3]. The HPPP can be operated with inlet pressures up to 90 bar and flow rates up to 480 m<sup>3</sup>/h [3].

Due to the increasing size and flow rates of the gas flow meters and the limited operation range of the current national standard, a new concept for calibrating gas flow meters is being developed, the Flow Comparator (FC). For preliminary tests and to investigate the controllability and the usable flow rate a prototype under atmospheric conditions is used. The Flow Comparator prototype in closed loop configuration is shown in Figure 1.



**Figure 1:** Picture of the Flow Comparator prototype in closed loop configuration

## 2. Experimental Setup

The two main components of the Flow Comparator are a piston within a cylinder. The cylinder has two layers, one with magnetic properties and the other one acts as an electrical conductor. Furthermore, the piston has an integrated stator core with windings. Together the piston and the cylinder act as an asynchronous linear induction motor (LIM). The electrical power for the LIM is supplied with a cable connected to the piston. The acting force on the piston is controlled by a frequency inverter whose voltage and frequency can be controlled.

A simplified scheme of the experimental setup is shown in Figure 2. The piston has an integrated check valve to limited the pressure drop across the piston. Further more the differential pressure at the piston is measured. A specified leakage in the piston with a flow sensor measures the fluid flowing through it. The measurement and calibration are therefore based on the comparator principle [4]. As transfer standard a turbine meter (TM) is used. The temperature and pressure are measured at the turbine meter. The position of the piston is measured using a distance measuring equipment (DME). The ambient temperature and pressure as well as the temperature and pressure downstream of the cylinder are measured.

A fan is used to set the volume flow rate through the experimental setup. Due to the limited fan control accuracy the bypass valve 1 is installed. It is used to control the set volume flow rate with higher accuracy.

At the beginning the volume flow rate is set by the fan and the opening of valve 1. Valve 2 is open and the flow is bypassing the cylinder to achieve stationary conditions in the loop. When stationary conditions are obtained for a defined time the piston moves slowly upstream. At the starting point the

piston is accelerated downstream until the piston velocity is the same as the fluid velocity and Valve 2 is closed. The measurement phase starts when the piston reaches the defined velocity. The volume flow rate can be calculated as shown in Equation 1.

$$\dot{V}_{FC} = \frac{V_{FC}}{\Delta_{FC} t} \quad (1)$$

During the measurement phase the discrete pulses of the turbine meter are counted. The volume flow rate indicated by the turbine meter can be calculated using the discrete pulses per time span and a proportionality factor known from previous calibration or from manufacturer specifications. The result of the calibration is the relative deviation  $f$  of the real volume flow rate to the indicated volume flow rate at certain volume flow rate and pressure. The relative deviation  $f$  is calculated as stated in equation 2.

$$f = \frac{\dot{V}_{TM}^c - \dot{V}_{FC}^c}{\dot{V}_{FC}^c} \quad (2)$$

The calibration accuracy of the Flow Comparator can be improved by applying corrections methods based on the measured data of the integrated sensors in the piston. In the ideal scenario the piston velocity is the same as the fluid flow velocity for the entire measurement phase and the differential pressure and the velocity across the piston would be zero. But in the experimental setup small differences of the piston velocity to the fluid velocity occur. The first correction method is based on the differential pressure across the piston. A non-zero differential pressure at the piston results into a leakage around the piston. A relationship between the differential pressure and the leakage can be derived by appropriate experiments and can be used to correct the volume displaced by the piston. The relationship is shown in Equation 3.

$$\dot{V}_{leak,\Delta p} = a\Delta p \quad (3)$$

The correction method based on the differential pressure is practical for relatively high leakage flows. For smaller leakage flows the integrated flow velocity sensor is used. The relationship between indicated velocity by the flow sensor and leakage flow is shown in Equation 4.

$$\dot{V}_{leak,v} = bv^2 + cv \quad (4)$$

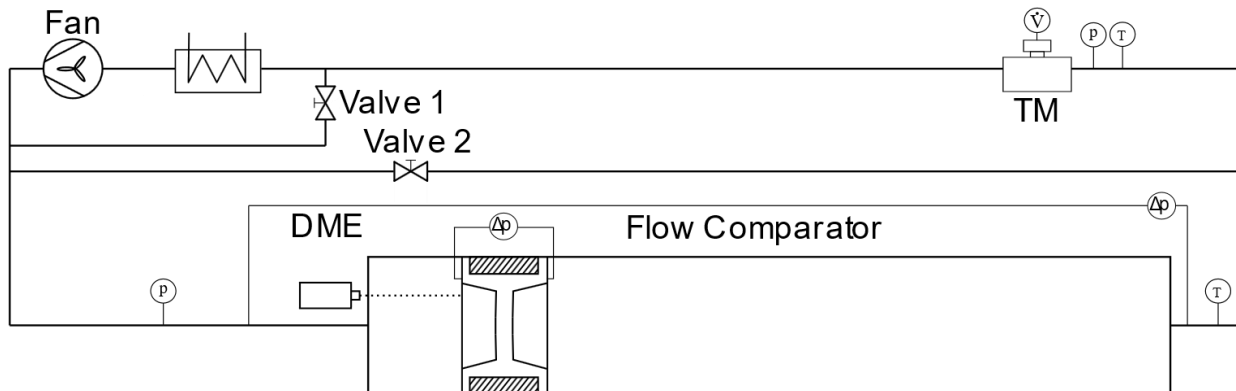


Figure 2: Scheme of the experimental setup with the Flow Comparator in closed-loop configuration

### 3. Modelica

Modelica is an object-oriented, non-proprietary and equation-based language to conveniently model components of different physical domains which can be connected to model complex physical systems. The models are described by differential, algebraic and discrete equations. The first specification for the Modelica language was released in 1997. It is developed by the non-profit Modelica Association. The Modelica Association is also responsible for the development of the opensource Modelica Standard Library (MSL) which contains about 1600 model components and 1350 functions from many domains [5].

Several components of the MSL containing equations of different physical domains, e.g. fluid flow, thermodynamics, tribology and electrical engineering could be used in the developed model to describe the Flow Comparator's dynamic behavior. The components are easily reusable due to the equation-based and object-oriented modelling approach. The media model used in the models can be easily exchanged allowing to test the model with atmospheric air as well as high pressure natural gas.

Furthermore, the equation-based modelling minimizes the error of rearranging equations and increases the readability of the written code. The physical equations are transformed and rearranged automatically by a compiler into a mathematical equation system which is solved with an algorithm. The symbolic index reduction as well as the solving of the equation system is usually executed by a simulation tool. The simulation environment used to develop and evaluate the Flow Comparator model in Modelica is Dymola® 2019.

### 4. Model description

A graphical representation of the developed model is shown in Figure 3. The assumptions used in the model are [6]:

- pressure losses are proportional to the dynamic pressure
- one dimensional gas flow
- adiabatic system
- neglect of potential energy
- heat transfer can be neglected in comparison to the convective energy transport

The model extension of the model presented in [7] and therefore the bypass is neglected in the first modelling approach.

In the model, the measuring cylinder is divided into one volume upstream of the piston and one volume downstream of the piston. The enclosed gas volumes of the measuring pipe depend on the position of the piston and change with piston movement. The measuring pipe volumes can store mass  $m$ , internal energy  $m \cdot u$  and momentum  $m \cdot v$  as described in Equation 5-7.

$$\frac{dm}{dt} = \dot{m}_i + \dot{m}_{i+1} \quad (5)$$

$$\begin{aligned} \frac{d}{dt} mu = & \dot{m}_i \left( h_i + \frac{v_i^2}{2} \right) + \dot{m}_{i+1} \left( h_{i+1} + \frac{v_{i+1}^2}{2} \right) \quad (6) \\ & + \dot{V}_i \left( \frac{p_{i+1} - p_i + p_{f,i+1} - p_{f,i}}{2} \right) \\ & + \dot{Q}_i \end{aligned}$$

$$\begin{aligned} \frac{d}{dt} mv = & \dot{m}_i |v_i| + \dot{m}_{i+1} |v_{i+1}| \quad (7) \\ & - A(p_{i+1} - p_i) - A(p_{f,i+1} - p_{f,i}) \end{aligned}$$

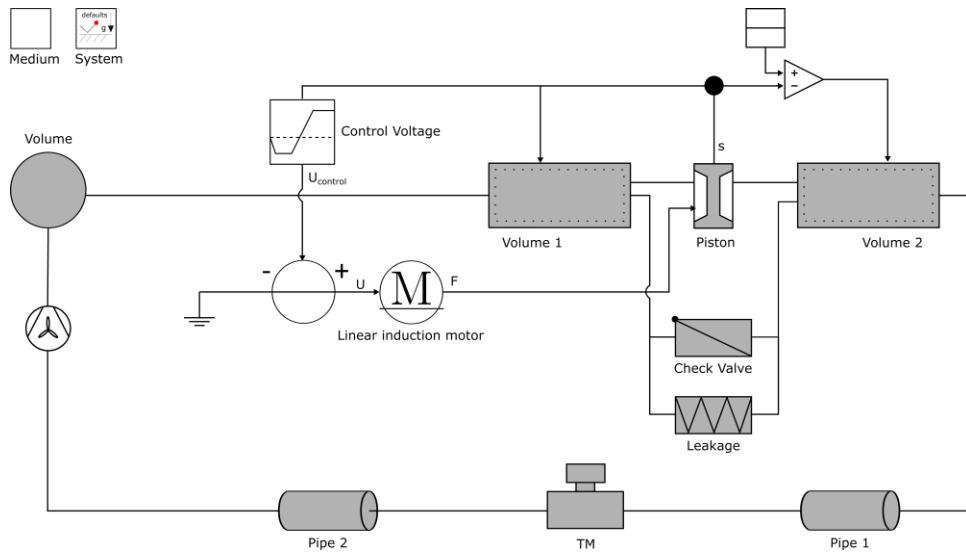


**Figure 3:** Graphical representation of the computational model

In direction of the fluid flow a spatial discretisation is applied to resolve the fluid flow in the measuring cylinder with higher accuracy. For this the finite volume method with the staggered grid approach is used. In a staggered grid the scalar variables are located in the control volume centre while the velocity and momentum variables are stored on the cell faces. The pressure loss is calculated using a wall friction model from the MSL. A heat port is included in the model which can be connected to a heat port of another model. This could be the environment or the piston. The heat flow is calculated based on the heat transfer model of the MSL.

The piston's motion is determined by Equation 8.

$$m_p \ddot{s}_p = p_1 A_p - p_2 A_p - F_{F,P} - F_{F,C} + F_{LIM} \quad (8)$$

The friction  $F_{F,P}$  is calculated using a constant roll resistance coefficient  $c_R$ . The resistance due to the connection cable  $F_{F,C}$  depends on the position and is calculated using the weight of the connection cable.

The movement of the piston is controlled by the force induced by the linear induction motor. The LIM is modelled using the space-vector equivalent circuit shown in Figure 4. The main differences to the equivalent circuit of a rotatory induction motor is the transversal branch. These are the eddy current resistance and the magnetizing inductance. The differences occur due to the end effect phenomenon in a LIM which influences the magnetizing inductance and the resistance. This is taken into

effect by the so-called end effect factor  $Q$  which is defined in Equation 9 [8].

$$Q = \frac{\tau_m R_r}{(L_m + L_{\sigma r})v} \quad (9)$$

The end effects increase with the air-gap thickness (results in higher leakage inductance) as well as with higher machine speed and reduces with increasing inductor length [8]. The magnetizing inductance and the resistance vary with the term  $f(Q)$ :

$$f(Q) = \frac{1 - e^{-Q}}{Q} \quad (10)$$

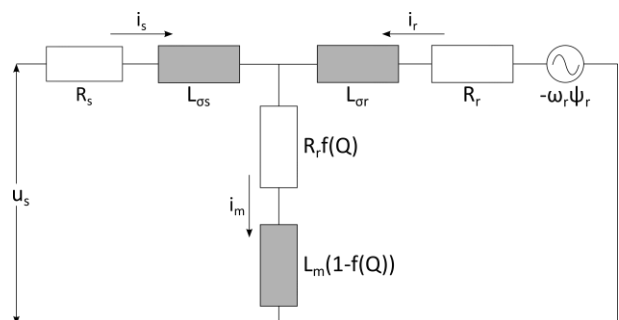


**Figure 4:** Space-vector equivalent circuit of the LIM

The control voltage depends on the position of the piston and changes sign and value at the starting position. It has a specified stopping time  $t_s$  and rising time  $t_r$ . The frequency inverter uses the control voltage and a constant  $U/f$  characteristic to determine the voltage for the LIM.

The turbine meter uses a constant pressure loss coefficient  $\zeta_{TM}$  to model the pressure loss occurring in the turbine meter. Furthermore, the model uses a relationship between indicated volume flow rate and real volume flow rate as described in [9].

The pipes are modelled using the DynamicPipe model of the MSL. The model uses balance equations for the mass  $m$ , the momentum  $m \cdot v$  and the internal energy  $m \cdot u$ .

## 5. Validation

The accuracy of the Flow Comparator model is highly relevant for the prediction of the dynamic behavior and interaction of the closed-loop system. It is affected by the aforementioned general assumptions, the accuracy of the given LIM parameters, the assumptions for the friction force, and further simplifications.

Experiments are conducted as described in Section 2 and the measurement data is used for model validation. The model is only validated for the part of the experiment where the piston moves forward and the actual calibration of the meter under test is executed. For the experiment and the simulation, the same control voltage trajectory is used to validate the model of the LIM and the frequency inverter.

In Figure 5 the measured and simulated piston velocity for three different control voltages is shown. For all control voltages the simulation has a lower acceleration than the measurement during the starting phase. After the piston accelerates to the velocity linked with the used control voltage, the simulation and measurement data have a similar value for all control voltages. Also, the decrease in piston velocity due to the increasing resistance force of connection cable shows a similar behavior in simulation and measurement.

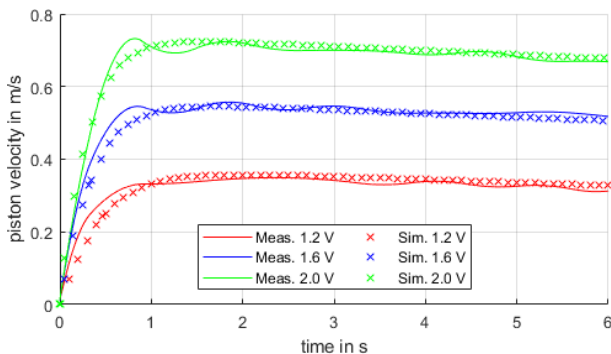


**Figure 5:** Comparison of the piston velocity over the time in the model and measured data for different control voltages at zero volume flow rate

The piston velocity as well as the differential pressure at the piston for a volume flow rate of  $\dot{V} = 100 \text{ m}^3/\text{h}$  is shown in Figure 6. The frequency inverter control voltage is set to achieve zero differential at the piston. The simulation is done with the same control voltage. Overall a good accordance of measurement data and simulation is achieved. But the differential pressure at the start of the measurement phase differs in measurement and simulation. This is due to the missing bypass in the simulation and therefore the differential pressure starts with a negative value. Furthermore, in the simulation the differential pressure at the piston increases little more than in the measurement data. A similar behavior is observable for the piston velocity as it decreases faster in the simulation than in the measurement.

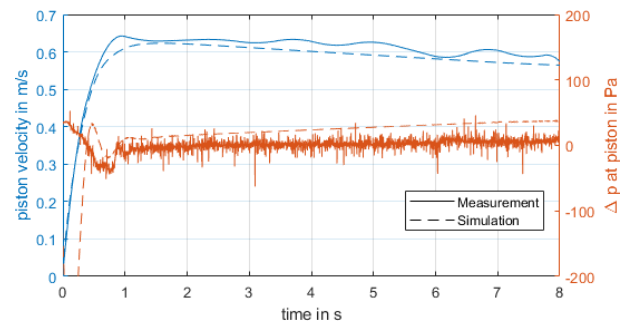


**Figure 6:** Comparison of velocity and differential pressure at the piston for a volume flow rate of  $\dot{V} = 100 \text{ m}^3/\text{h}$  and a control voltage of 1.8 V

## 6. Optimization

The model is used to optimize the control voltage trajectory of the frequency inverter to achieve maximum available measuring time with zero differential pressure at the piston. For this the trajectory in Figure 7 is applied to the model. It has an overshoot of control voltage at the beginning and an increasing slope during the measuring phase to offset the connection cable resistance.

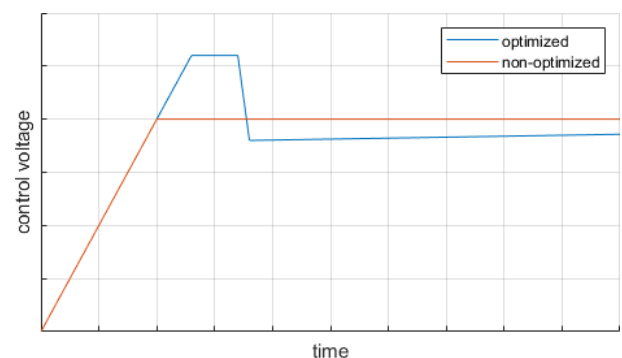


**Figure 7:** Exemplary control voltage trajectories for non-optimized and optimized case

In Figure 8 the simulation result for the optimized and non-optimized control voltage trajectory is shown. The piston velocity is lower in the optimized case and remains at an almost constant value throughout the simulation. The overshoot in control voltage also appears in the piston velocity. Due to this, the differential pressure initially decreases more than in the non-optimized case. But after the decrease the differential pressure in the optimized simulation decreases to zero and stays at that value for remaining simulation.

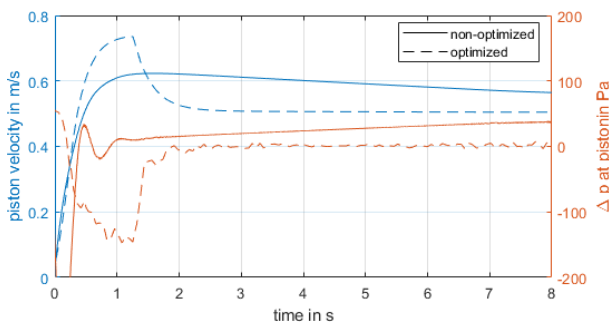


**Figure 8:** Comparison of velocity and differential pressure at the piston for a volume flow rate of  $\dot{V} = 100 \text{ m}^3/\text{h}$  with optimized and non-optimized frequency inverter control voltage trajectory

## 7. Conclusion

The Flow Comparator in loop configuration is modelled using the modelling language Modelica®. The implemented model is successfully validated against measurement data of the actual flow comparator prototype. As application example a simple optimization of the control voltage trajectory to maximize the available measuring time is conducted. This result of optimization will allow to extend the upper limits of flow rate usable for calibrations. Furthermore, the possibility to gather detailed information about pressure and temperature development at arbitrary chosen locations in the system with high time resolution enables much better and more reliable statements about the accuracy of flow rate measurement with this system.

The model of the linear induction motor describes the electromechanical interaction. In future work, it will be essential to extend the model by heat transfer from the motor components to the gas to complete the modelling of the overall thermodynamic performance of the piston prover.

Furthermore, the bypass needs to be considered in the model. This would allow the model to be used for actual predictions of the Flow Comparator in loop configuration with the desired event sequence.

Also, the friction force of the piston needs to be measured more accurately. This includes the position depending friction force, the velocity depending friction force as well as the increase of counter force due to connection cable weight. Based on this a more detailed optimization approach can be used to counteract small deviations which would affect a uniform piston velocity.

## References

- [1] G. Schmitz and A. Aschenbrenner. „Experience with a Piston Prover as the new primary Standard of the Federal Republic of Germany in High-Pressure Gas Metering.“ Proceedings of the 18th World Gas Conference.
- [2] Physikalisch-Technische Bundesanstalt PTB. Prüfschein der Rohrprüfstrecke. 1991.
- [3] Physikalisch-Technische Bundesanstalt PTB. PTB Mitteilungen. Special Issue Volume 119 no.1, 2009.
- [4] B. Mickan and R. Kramer: Evaluation of two new volumetric primary standards for gas volume established by PTB, 7th International Symposium on Fluid Flow Measurement (ISFFM) 2009, Anchorage, Alaska.
- [5] The Modelica Association, Modelica Language <https://modelica.org/>
- [6] M. von der Heyde, G. Schmitz and B. Mickan. Modeling of the German National Standard for High Pressure Natural Gas Flow Metering in Modelica. In Proceedings of the 11th International Modelica Conference, Versailles, France, September 21-23, 2015.
- [7] S. Singh, G. Schmitz and B. Mickan "Modeling of the Flow Comparator Prototype as New Primary Standard for High Pressure Natural Gas Flow Metering" in Proceedings of the 13th International Modelica Conference, Regensburg, Germany.
- [8] Sung, Jeong-Hyoun and Kwanghee Nam. „A new approach to vector control for a linear induction motor considering end effects.“ Conference Record of the 1999 IEEE Industry Applications Conference, 3-7 Oct. 1999, Phoenix, AZ, USA.
- [9] B. Mickan, R. Kramer, and V. Strunck. Transient response of turbine flow meters during the application at a high pressure piston prover. In 15th Flow Measurement Conference (FLOMEKO). Linköping University Electronic Press, 2010.

# Investigations on pressure dependence of Coriolis Mass Flow Meters used at Hydrogen Refuelling Stations

O. Büker<sup>1,\*</sup>, K. Stolt<sup>1</sup>

<sup>1</sup>RISE Research Institute of Sweden, Brinellgatan 4, 504 62 Borås, Sweden

\*E-mail (corresponding author): [oliver.buker@ri.se](mailto:oliver.buker@ri.se)

---

## Abstract

In the framework of the ongoing EMPIR JRP 16ENG01 “Metrology for Hydrogen Vehicles” a main task is to investigate the influence of pressure on the measurement accuracy of Coriolis Mass Flow Meters (CFM) used at Hydrogen Refueling Stations (HRS). At HRS hydrogen is transferred at very high and changing pressures with simultaneously varying flow rates and temperatures. It is clearly very difficult for CMFs to achieve the later expected legal requirements in relation to the demand for accurate mass flow measurement at the measurement conditions at HRS. It was observed, mainly due to the very dynamic filling process, that the accuracy of mass flow measurement at different pressure ranges is too inaccurate. Particularly at higher pressures it was found out that especially short refuelling time causes significant measurement deviations. On this background it can be concluded that the medium pressure has a great impact on the mass flow measurement accuracy. To gain a deeper understanding of this matter RISE has built a unique high-pressure test facility. With the aid of this newly developed test rig it is possible to calibrate CFMs over a wide pressure and flow range with water and base oils as test medium. The test rig allows calibration measurements under the conditions prevailing at 70 MPa HRS regarding mass flows (up to 3.6 kg min<sup>-1</sup>) and pressures (up to 87.5 MPa).

---

## 1. Introduction

To achieve the 2050 long-term goal of reduction of greenhouse gas emissions by 80-95% compared to the 1990 level, both the utilization of renewable and carbon-free energy carriers and the energy efficiency need to increase substantially over the next decades. This is particularly important for the transport sector which accounts at present for around 60% of the global oil consumption. To achieve these long-term climate objectives, the future of transport necessarily lies in the complete replacement of currently prevailing fossil fuels and electrification by renewables with zero emissions.

In general, electromobility is understood as electric drive with a power supply from a rechargeable battery. However, fuel cell electric vehicles (FCEV) are also used for electromobility, whereby the fuel cell (FC) is used as an energy converter and the energy store is a hydrogen tank. In a hydrogen-powered vehicle the compressed gaseous hydrogen (CGH<sub>2</sub>) is stored at high pressure (up to 70 MPa) in the tank. By separation of energy storage and energy converter significantly higher energy densities and thus ranges are possible.

The refuelling of a 70 MPa CGH<sub>2</sub> vehicle at a hydrogen refuelling station (HRS) is completed within a few minutes. From high-pressure intermediate storages (e.g. 44 MPa and 95 MPa) the hydrogen is filled via pressure drop (overflow) into the vehicle tank. A passenger car with a typically tank capacity of around 5 kg can be filled in around 3 min according to SAE J2601. While refuelling, the hydrogen and thus the vehicle tank is heated significantly. To avoid this the so-called cold filling procedure is used. In this case the hydrogen is pre-cooled (down to -40 °C) before filling, e.g. with liquid nitrogen.

For monitoring the amount of hydrogen dispensed into the vehicle at an HRS, a robust and accurate flow meter is required that can operate over a variety of flow and temperature ranges and pressures up to 87.5 MPa. OIML R 139-1 provides accuracy requirements for flow measurement of GCH<sub>2</sub>. The measurement of mass flow is typically performed using Coriolis Mass Flow Meters (CFM). CFMs measure, in contrast to many other methods, directly the mass flow independent of fluid properties, and are generally not very sensitive to changes in viscosity, temperature, and pressure.

## 2. Scope of application

Almost all HRS meet the requirements according to the SAE J2601 fueling protocol (see **Table 1**). The SAE standardizes the fueling process by defining limits for the relevant refueling parameters.

**Table 1: 70 MPa Hydrogen Fueling Specification**

Parameter	Limit
Min. gas temperature (pre-cooling)	-40 °C
Max. gas temperature (tank)	+85 °C
Ambient temperature	-40 °C to +50 °C
Min. tank storage capacity	2 kg
Max. tank storage capacity	10 kg
Min. pressure (tank)	0.5 MPa
Max. pressure (tank) => $1.25 \cdot 700$ MPa	87.5 MPa
Max. flow rate	60 g/s (3.6 kg/min)

A typical 70 MPa HRS consists of high-pressure storage tanks at different pressure levels, a compressor (e.g. diaphragm compressor, ionic compressor) to fill the high-pressure storage tanks or directly the vehicle tank, a heat exchanger (pre-cooler, refrigeration unit) and a dispenser which controls the flow into the vehicle tank. At fast filling the dispenser controls the flow in such a way, that fast filling of 5 kg hydrogen in 3 min (or 7 kg in 5 min, respectively) can be achieved. To avoid tank overheating during the filling process, due to rapid compression of the gas, the pressurized hydrogen is cooled down to -40 °C by the heat exchanger on its way from the high-pressure storage tank to the dispenser. But that also means the pressure in the vehicle tank exceeds 70 MPa (up to 87.5 MPa) at the end of the fast fill process to ensure a filling at 70 MPa after cooling down.

### 2.1 Refueling process at HRS

The sequence of operation of a refueling process is standardized. SAE J2601 states requirements for temperatures and the speed of fueling, specified by Average Pressure Ramp Rate, APRR (comparable with Constant Pressure Ramp Rate, CPRR) during the hydrogen refueling process. Compliance with this standard ensures fast and safe refueling. Before the actual refueling, the connections, e.g. between dispenser nozzle and vehicle tank are automatically checked by the system. Subsequently, the pressure in the vehicle tank and its volume is determined by an initial pressure pulse (pressure surge). Based on these values the temperature curve (expected gas heating), the target pressure and the APRR for a complete filling

are calculated. The APRR depends on the vehicles tank pressure and temperature, pre-cooling temperature and the ambient temperature. In accordance to SAE J2601 there are two ways to calculate the APRR. The classical way (lookup table method) is based on tables which specify the APRR for the given vehicle tank storage capacity, initial tank pressure, station type (station pressure and delivery temperature), ambient temperature and communication capability between vehicle and dispenser. The newly developed second way (MC formula method) works relatively similar. In contrast to the lookup table method the MC formula calculates a Dynamic Pressure Ramp Rate (DPRR) using adaptive feedforward control based on the measurement of pressure and temperature at the dispenser. Here, the pressure target is continuously and dynamically calculated in order to minimize the fueling time. For both methods all parameters are checked during refueling to monitor that they are consistent with the fueling protocol. When the vehicle is filled to the target pressure the refueling process is stopped and the nozzle can be disconnected from the vehicle.

### 2.2 Flow measurement at HRS

At HRS hydrogen is transferred at very high and changing pressures, varying flow velocities (very low to very high) and varying temperatures but the mass flow measurement must be extremely accurate. As it can be seen, these conditions are not trivial and not many flow meters are eligible. It is generally expected that CFMs are well suited for refuelling with continuously variable pressures and temperatures. The CFM measures the mass flow directly and the integrated value is used as basis for the billing of the H<sub>2</sub> supplied. There are mainly two different approaches for the installation of the flow meter (CFM). The CFM can either be installed before or after the pre-cooler. This implies the CFM measures the hydrogen mass flow at ambient conditions (at around 20 °C) or at a temperature of around -40 °C. In both cases the zero-point of the CFM is set once, namely during commissioning at the planned operating temperature, e.g. at -40 °C.

## 3. High-pressure test facility

### 3.1 Measurement principle

The measurement principle (see **Figure 1**) of the flow facility is based on the master meter method with flying start-and-stop. In this context a pair of two CFMs measures simultaneously, where one CFM is installed, as device under test (DUT), at the high-

pressure site and the other CFM, as reference meter (master meter), at the low-pressure site. Afterwards, the positions of the CFMs are exchanged. Both CFMs were previously calibrated at low-pressure using one of the national standard flow facilities at RISE (Research Institutes of Sweden).

### 3.2 Operating principle

From one of the selected storage tanks (200 L and 1000 L, filled with deionized and filtered water) the water is delivered to the high-pressure pump (PARKER AHL66-2D series) (passing two filters). The outlet pressure of the pressure pump (see **Figure 2**) is controlled by compressed air using a 1" pressure regulator in a range from 0 to 100 psi (0 to 7 bar) which corresponds to 0 to 13300 psi (0 to 913 bar) in the liquid line.



**Figure 1: Measurement set-up (high-pressure test facility) equipped with two CFMs from HEINRICHS.**

The compressed air is delivered by house connection but for higher pressures a diesel-powered air compressor (Ingersoll Rand 7/41+, air flow 4000 L/min at 7 bar, max. air pressure 8.6 bar) was used. A compressed air tank (volume 270 m<sup>3</sup>, max. pressure 11 bar, TIDAN-VERKEN AB) is filled in order to provide a regular supply of compressed

air for the high-pressure pump. Downstream the air passes an air dryer (HANKISON SPX series) and a compressed air filter (HANKISON HF series). The high-pressure pump is connected by an 800 mm long DN 10 high-pressure hose (spiralized steel reinforced polymer hose, CEJN) in order to prevent a possible vibration transmission from the pump to the high-pressure test facility.

By use of a needle valve the undesired fluctuations in pressure due to the piston movement are damped. Directly after the first elbow, another needle valve is installed using a tee connection (bypass line). At the beginning the bypass line is used to get rid of air bubbles in the first part of the high-pressure site. The pressure before the CFM at the high-pressure site (DUT) can be set by means of a pressure regulator (TESCOM 54-2000 series) in the range from 1500 to 15000 psi (100 to 1000 bar). The pressure before and after the DUT is measured by means of two pressure transmitters (KELLER Leo 3) in the range from 0 to 1000 bar.



**Figure 2: High-pressure pump PARKER AHL66-2D series.**

To ensure an accurate detection of the zero-point, the DUT is installed between two completely leak-tight on-off ball valves, for symmetrical reasons, both with the same distance from the CFM. It is advisable to reduce the pressure in several steps to avoid an excessive pressure drop. For this reason, two further pressure regulators (TESCOM 54-2000 series) in the range from 1500 to 15000 psi (100 to 1000 bar) and 500 to 6000 psi (35 to 400 bar), respectively were installed. The pressure after these pressure regulators is measured by means of two pressure transmitters (KELLER Leo 3) in a range from 0 to 700 bar and 0 to 300 bar, respectively. The pressure upstream the reference meter (CFM at the low-pressure site) can be set by another pressure regulator (TESCOM 54-2000

series) in the range from 5 to 500 psi (0.35 to 35 bar) and measured by another pressure transmitter (KELLER Leo 3) in the range from 0 to 10 bara. In the normal case, the inlet pressure of the CFM used as reference meter is set to 5 bar, the pressure the CFM was calibrated at the national standard flow facilities. With the needle valve behind the reference CFM the flow rate is adjusted. All the pipework of the high-pressure facility has an outer diameter of 0.375" (9.5 mm) and an inner diameter of 0.203" (5.2 mm) using mainly 3/8" MP (medium pressure) C&T (cone and thread) connections. For the data acquisition a DAQ system developed by RISE (own hardware and software) has been used. The DAQ system provides four input channels for temperature, eight input channels for current and four input channels for pulse and frequency measurement (double-time chronometry). For each measurement point the line pressure was logged as 4-20 mA signal from the five pressure transmitters (KELLER Leo 3), the temperature from both CFMs as 4-20 mA passive current output and the finally the passive pulse/frequency output also from both CFMs.

#### 4. Measurement results

##### 4.1 Devices under test

There are not many high-pressure CFMs on the market. The devices (see **Table 2**) of the three leading manufacturers (outside Asia) will be investigated in the EMPIR project. For this reason, the manufacturers have provided some devices as in-kind contribution to the project.

**Table 2: Overview of the investigated CFMs**

Manufacturer	Sensor	Transmitter
RHEONIK	RHM04	RHE27
HEINRICHS	TM SH	UMC4
KEM KÜPPERS	TCHM0450	TCE8000

A higher line pressure leads in general to a stiffer measuring tube resulting in an underestimated mass flow rate. This effect is in general greater for larger size CFM and in theory negligible for very small flow meters. Also, most manufacturers state that the actual hydrogen temperature, and not the pressure, is one of the most important factors affecting the measurement accuracy. High pressures, however, present problems with the currently available flow meters. It is anticipated that CFMs do not achieve the necessary accuracies at higher pressures, and it can be assumed that particularly short refuelling time causes significant measurement deviations. Some manufacturers provide pressure compensation by manual input of FLOMEKO 2019, Lisbon, Portugal

the operating pressure (stable condition) or the possibility for real time compensation by adding an external pressure sensor to measure the actual pressure (unstable condition).

##### 4.2 Measurements at low-pressure

Before the actual high-pressure measurements each individual CFM was separately calibrated with water as test medium at a temperature of 20 °C and an inlet pressure of around 5 bar by using one of the national standard flow facilities at RISE (Vattenmätkänk 7, VM7), see **Figure 3**.



**Figure 3: DUT calibrated at low pressure (HEINRICHS CFM).**

For these measurements the (mass) frequency and pulse output was used. Before the flow calibration was performed, a zero-point adjustment of the DUT was carried out at the actual pressure (5 bar) and temperature (20 °C) conditions. After setting the new zero-point the pulses (while the low flow cut-off is shut off and without flow) were logged for 5 minutes to check how well the (automatic) zero-point setting performs.

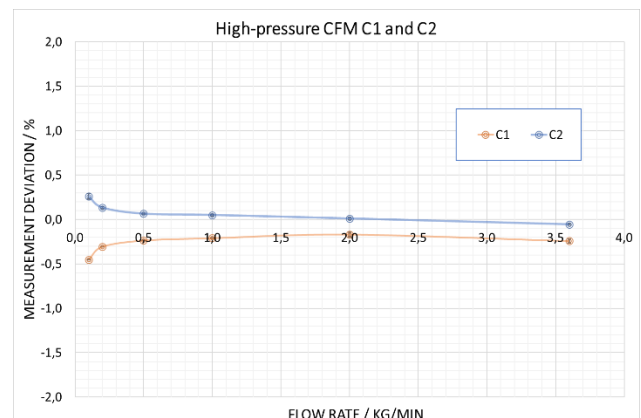


**Figure 4: Measurement results for one of the three CFM pairs (C1 and C2) at low-pressure calibration.**

The low-pressure calibration was performed at six different flow points (0.1 kg/min, 0.2 kg/min, 0.5 kg/min, 1.0 kg/min, 2.0 kg/min and 3.6 kg/min). For each flow point tested four repeated measurements were carried out, that means a total of 5 repetitions. The measurement results are shown in **Figure 4**.

#### 4.3 Measurements at high-pressure

After the low-pressure calibration measurements were conducted in water (5 bar inlet pressure) one meter was used as reference meter at the low-pressure side (5 bar) and one meter as DUT at the high-pressure side (up to 850 bar). A generic test matrix regarding mass flow rates and pressures has been prepared. Initially, the mass flow rates were selected to cover the full operating range for a 70 MPa HRS (typically 3.6 kg/min). In sum, measurements were performed at the same six flow rates as for the low-pressure calibration at six different pressures (10 MPa, 25 MPa, 40 MPa, 55 MPa, 70 MPa and 85 MPa). Due to the limitations of the high-pressure pump the maximum mass flow rate at 55 MPa and 70 MPa (65 MPa) was 2.0 kg/min, and at 85 MPa (80 MPa) 1.0 kg/min respectively.

For the high-pressure testing we used the same zero-points as for the low-pressure calibrations. That means the flow meters were installed without setting a new zero-point. As it can be seen in **Figure 1**, the measurement setup the CFMs are installed in series with stiff metal pipe connections in between. In theory, vibrations from one CFM could be transferred to the other CFM via the pipework but also via the table. This would result in interference and erroneous mass flow rate measurements. To prevent vibration transmission through the table a wooden table was chosen, and shock absorbent rubber were placed under the CFMs connections. However, before the actual measurements were performed, we checked for crosstalk effects since we were not sure in all cases whether the CFMs worked at different driving frequencies. For this reason, the pulses obtain during zero flow (closed on-off ball valves upstream and downstream of each CFM) were compared for a certain period (e.g. 5 min) in case when both meters were supplied with power and in case when only one CFM was supplied with power. In addition, the same procedure was repeated at a constant flow rate. Here the totalized mass counter for one CFM was logged and compared for a certain period for the cases when the other CFM was switched on and off, respectively.

From the measurement result (see **Figure 5**) one could assume that there is a dependence of the flow rate measurement from the pressure. With increasing pressure, the measurement deviation is decreasing. However, attention should be drawn to the fact, not shown in **Figure 5**, that with increasing pressure also the temperature, especially for the reference meter at the low-pressure side, is increasing.

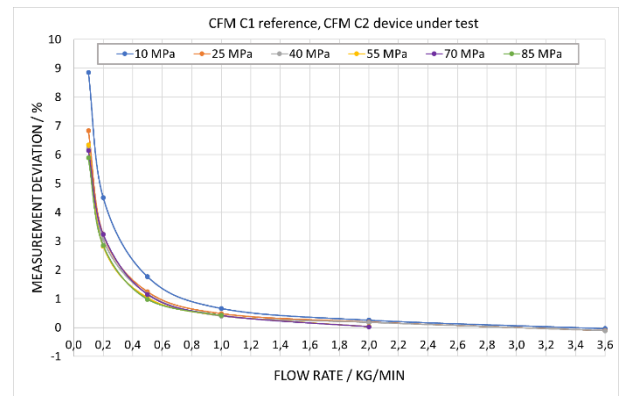


**Figure 5: Measurement results at high-pressure for one of the flow meter pair (CFM C1 as reference, CFM C2 DUT).**

It is particularly interesting to note that the temperature was quite stable at a certain pressure level during the measurements at different flow rates. But the temperature increased with increasing pressure values. Another effect was that the temperature at the place of the reference meter was depending on the compressed air supply. The compressed air supply was changed for higher pressures (usually after 400/550 MPa tests) from the house connection to the diesel-powered air compressor but some measurements (e.g. at 400 MPa) were performed with both configurations. Hereby it was established that the way of compressed air supply has an influence on the medium temperature at the place of the reference meter. The temperature measured at the place of the reference meter had, in some cases, a difference of up to 5 K depending on the compressed air was delivered by house connection or the diesel-powered air compressor (lower temperature). At the end in can be summarized that the temperature difference between 10 MPa and 85 MPa measurements was up to around 12 K (worst case) and that the measurement results need to be corrected regarding temperature to determine the pressure dependence of the mass flow rate. However, the desired correction regarding temperature requires more low-pressure calibrations in the temperature range of 20 °C to at least 30 °C.

## 5. Conclusion

A novel high-pressure flow test facility was built at RISE. With this facility it is possible to investigate the pressure dependence of Coriolis Mass Flow Meter (CFM) in a pressure range from 10 MPa to 85 MPa at flow rates in a range from 0.1 kg/min to 3.6 kg/min. Measurements were performed with CFMs from three different manufacturers. The achieved measurement results for one of in total three investigated pairs of high-pressure CFMs have been discussed. Summarized, it was shown that the conceived measurement setup works well. The only negative aspect is that the temperature at the place of the reference meter rises with increasing the inline pressure. Up to now low-pressure calibration were only performed at a temperature of 20 °C. However, it is possible to correct for the temperature effect and hence to separate the temperature and pressure effect, but this can only be achieved by additional traceable low-pressure calibration measurements at slightly elevated temperatures (e.g. up to 30 °C). In the next step additional low-pressure calibrations in a temperature range of 20 °C to 30 °C are planned for all CMFs. Afterwards, the obtained high-pressure data will be corrected regarding temperature. The overall objective is to publish a complete data set regarding the influence of pressure on the mass flow measurement accuracy for all three CFMs of the different brands.

## Acknowledgement

This paper was written under the Joint Research Project EMPIR Metrology for hydrogen vehicles (“MetroHyVe”) which is supported by the European Metrology Programme for Innovation and Research (EMPIR). The EMPIR initiative is co-funded by the European Union’s Horizon 2020 research and innovation programme and the EMPIR participating states.

## References

- [1] OIML R 137-1:2012 (E), *Gas meters – Part 1: Metrological and technical requirements*, International Organization of Legal Metrology, 2014.
- [2] OIML R 139-1:2014 (E), *Compressed Gaseous Fuel Measuring Systems for Vehicles – Part 1: Metrological and technical requirements*, International Organization of Legal Metrology, 2014
- [3] Measuring Instruments Directive (MID) 2014/32/EU Annex IV (MI-002), *Gas meters and volume conversion devices*, 2014
- [4] SAE J2601:2016, *Fueling Protocols for Light Duty Gaseous Hydrogen Surface Vehicles*, 2016.

# Discharge coefficients of CFVN predicted for high Reynolds numbers based on Low-*Re*-calibration

B.Mickan<sup>1</sup>

<sup>1</sup>Physikalisch-Technische Bundesanstalt, Bundesallee 100, D-38116 Braunschweig, Germany  
E-mail (corresponding author): bodo.mickan@ptb.de

## Abstract

In 2016, PTB introduced a function for the representation of the discharge coefficient  $c_D$  of critical flow venturi nozzles (CFVN) (versus the Reynolds number  $Re$ ) what covers the operating range with laminar boundary layers and with turbulent boundary layers as well. It contains the parameters  $a$  for the impact of the core flow,  $b_{lam}$  for the  $Re$ -dependency in case of laminar and  $b_{turb}$  in case of turbulent boundary layers. These parameters are not independent to each other but have the fixed relation of  $b_{turb} = 0.003654b_{lam}^{1.736}$ .

Furthermore, the parameter  $a$  and the parameter  $b_{lam}$  are both direct functions of the local curvature radius  $R_{c,throat}$  of the nozzle at the throat. These relationships to  $R_{c,throat}$  are described by theoretical models. Consequently, the overall dependency of the discharge coefficient  $c_D$  on Reynolds number  $Re$  can be derived from only one parameter.

The paper describes how the relationships mentioned above can be used to extrapolate the calibration values of a CFVN determined with atmospheric air to high pressure gas flow applications covering a Reynolds range of about 1:60. It is shown in detail by examples and the reliability is demonstrated by comparison data for low and high pressure of 33 nozzles. Finally, aspects of preconditions for such extrapolation and uncertainties will be discussed.

## 1. Introduction

### 1.1 Motivation and idea

In 2016, a functionality for the discharge coefficient  $c_D$  versus Reynolds number were successfully introduced to cover the operating of critical nozzles with laminar as well as turbulent boundary layers using only three parameters [1]. The outcome of this extended analysis of inter comparison data using this functionality as the base for LS-fitting indicated that there were only small differences left to the measured data in the order of 0.1 % and lower. With this, the question raised up if it is possible to use only the data at low Reynolds numbers (e.g. the measurements with air at atmospheric conditions) for such parameter determination and to use the functionality to get a reliable extrapolation to the high Reynolds numbers even to the range above  $Re \geq 2 \cdot 10^6$ .

The data for atmospheric air usually do not cover a wider range of Reynolds numbers but have to be considered approximately as a single point measurement, therefore it was necessary in a first

step to make further effort in the mathematical model to reduce the number of free parameters down to one. Nevertheless, it can be demonstrated here on the data base containing 33 different nozzles that this approach is reasonable.

### 1.2 Mathematical Model

The discharge coefficient of a sonic nozzle can be described as a combination of two independent displacement effects. At one side we have the effect of the two dimensional core flow  $c_{D,TwoDim}$  and on the other side the displacement effect of the boundary layer  $c_{D,BoundLayer}$ :

$$c_D = c_{D,TwoDim} \cdot c_{D,BoundLayer} \quad (1)$$

The displacement effect of the boundary layer can be described as a reduction of the geometrical cross section area  $A_{geom}$  by the complete area covered by the displacement thickness  $\delta_1$  of the layer:

$$c_{D,BoundLayer} = \frac{A_{geom} - A_{BoundLayer}}{A_{geom}} = \left(1 - 2 \frac{\delta_1}{d}\right)^2 \quad (2)$$

Replacing  $c_{D,TwoDim}$  with the parameter  $a$ , the discharge coefficient can be expressed as:

$$c_D = a \left(1 - 2 \frac{\delta_1}{d}\right)^2 \approx a - \frac{\delta_1}{d} = a - \frac{b}{Re^n} \quad (3)$$

The dependency on Reynolds number  $Re$  is different for laminar and turbulent boundary layers, expressed by different values of the exponent  $n$  in Equation (3):

$$\begin{aligned} c_{D,lam} &= a - b_{lam} Re^{-0.5} \text{ for laminar BL} \\ c_{D,turb} &= a - b_{turb} Re^{-0.139} \text{ for turbulent BL} \end{aligned} \quad (4)$$

For the parameters  $a$  and  $b_{lam}$ , there are theoretical solutions available, for a e.g. the solution of Kliegel [2] and for  $b_{lam}$  the solution of Geropp [3][4]. For both, these theoretical approaches provide the solution in dependency on the curvature radius of the nozzle at the throat  $R_{C,throat}$  as a common parameter. So, for the parameter  $a$  yield:

$$\begin{aligned} a &= 1 - a_2 + a_3 - a_4 \quad (5) \\ \text{with} \quad a_2 &= \frac{\kappa+1}{96(2R_{C,throat}+1)^2} \\ a_3 &= \frac{2304(2R_{C,throat}+1)^3}{(\kappa+1)(754\kappa^2-757\kappa+3633)} \\ a_4 &= \frac{276480(2R_{C,throat}+1)^4}{(\kappa+1)(754\kappa^2-757\kappa+3633)} \end{aligned}$$

And for the parameter  $b$ :

$$b_{lam} = G \cdot R_{C,throat}^{0.25} \quad (6)$$

For our purpose to reduce the number of free parameters we use the fact that the theoretical approaches for parameter  $a$  and  $b_{lam}$  are based both on the curvature radius  $R_{C,throat}$  at the throat. The real curvature radius determining these parameters probably differs from  $R_{C,throat}$ , but we assume that it is for both the same (virtual) curvature Radius  $R_{C,virt}$ . Finally, only the parameter  $b_{lam}$  remains as a free parameter and the other are linked to it via the relationships of Equations (5)(7) and (8)

$$R_{C,virt} = \left(\frac{b_{lam}}{G}\right)^4 \quad (7)$$

$$\begin{aligned} b_{lam} &\xrightarrow{(7)} R_{C,virt} \xrightarrow{(5)} a \\ b_{turb} &= 0.003654 b_{lam}^{1.736} \end{aligned} \quad (8)$$

Both, the parameter  $a$  [Equation (5)] and the factor  $G$  depend on the isentropic exponent  $\kappa$  of the gas. Furthermore, the factor  $G$  is a function of the Prandtl number and the wall temperature (rsp. the difference between wall and gas). With this, we have dependencies of the  $c_D$ -values not only on

Reynolds number but also slightly on the gas properties. Although we already know that the relationship given by Geropp [4] for the factor  $G$  in Equation (6) is not totally satisfying (see also[5][6]), we keep this here for our approach in same way as it was discussed in [1].

It is appropriate to bridge the laminar and turbulent boundary layer transition with one function shown by Equation (9) for the whole Reynolds range by means of a transition function given by the two weighing terms  $s_{lam}$  and  $s_{turb}$ . The parameter  $Re_{tr}$  defines the middle point of the transition and  $k_u$  the "sharpness" of the transition (the larger  $k_u$ , the more "sudden" the transition occurs).

$$\begin{aligned} c_D &= s_{lam} \cdot c_{D,lam} + s_{turb} \cdot c_{D,turb} \quad (9) \\ \text{with} \quad s_{lam} &= 0.5 \left\{ 1 - \tanh \left[ k_u \log \left( \frac{Re}{Re_{tr}} \right) \right] \right\} \\ s_{turb} &= 1 - s_{lam} \end{aligned}$$

For the investigation here in this paper we fix the values arbitrarily to  $k_u = 5.5$  and  $Re_{tr} = 1.25 \cdot 10^6$ . It is based on all the experience in the past and we will discuss later what conclusion we can derive from this. With these values, the range of transition between laminar and turbulent boundary layers is expected to occur between approximately  $Re = 7 \cdot 10^5$  and  $Re = 2.5 \cdot 10^6$ , see also Figure 1.

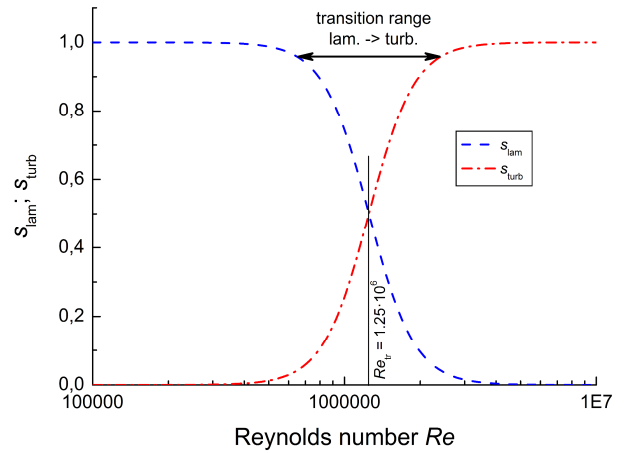


**Figure 1:** Weighing factors  $s_{lam}$  and  $s_{turb}$  to model the transition from laminar to turbulent boundary layers in dependency on Reynolds number  $Re$ .

All the relations given by Equations (4) to (9) and the pre-setting of  $k_u$  as well as  $Re_{tr}$  provide our base to adopt  $b_{lam}$  as the only free parameter and to get the overall functionality for the discharge coefficient from low to high Reynolds numbers.

## 2. Data evaluation

### 2.1 Data base

There are many information on calibration from the past years available in the data base of PTB. For the best proof of our approach in this paper, we choose all nozzles with the constrains that the highest Reynolds number shall be above  $Re \geq 2.5 \cdot 10^6$  to reach the region of turbulent boundary layers based on our measurement capabilities. Consequently, the throat diameter shall be at least 3.8 mm. Finally, data of 33 nozzles have been chosen. Their main specifications are listed in Table 1.

All nozzles are in principle designed based on the ISO 9300. The diameters ranges from 3.8 mm to 46.6 mm and the design curvature radius (normalised with the throat diameter) is  $R_{C,design} = 1$  for seven nozzles and  $R_{C,design} = 2$  for 24 nozzles. One nozzle has  $R_{C,design} = 2.5$  and one is a cylindrical nozzle.

In Table 1, there is the Reynolds number  $Re_0$  given what is achieved for the nozzles when operated with air at 100 kPa. Additionally, we noted in Table 1 the minimum and maximum of expanded uncertainties of the flow rate measurements in the range of Reynolds numbers for  $Re/Re_0 \geq 8$ . This is the range where we have data gathered with natural gas based on the traceability of PTB for high pressure natural gas.

Beside the data with high pressure natural gas based on PTB traceability, there are some nozzles where also other data are available. Nozzles #15, #21 and #33 were used in inter comparison in the year 2015 and LNE-LADG as well as NIM provided data based on high pressure air. The data and related information are already published in [1]. Nozzle #32 was used in an inter comparison between NIST, LNE-LADG and PTB in 2005 [7]. Hence, for this we have additionally data with nitrogen and air. Finally, the nozzles #11, #19 and #26 have been calibrated with high pressure nitrogen on customer site [8].

The diameters of all nozzles listed in Table 1 have been measured by means of 3D-CMM at PTB, an accredited laboratory or one of the other partners in the inter comparisons mentioned above. We claim an expanded uncertainty of 3  $\mu$ m for the diameter. This value is based on the comparison of repeated measurements of 9 sonic nozzles (with  $d_{throat}$  from 5 to 10 mm) with long time difference.

**Table 1:** Main information on data base.

Noz. Nr.	$d_{throat}$ in mm	$R_{C,design}$	$Re_0$ (100 kPa, air)	for $Re/Re_0 \geq 8$ ; $k = 2$	
				$U_{Q,min,rel}$	$U_{Q,max,rel}$
1	7,098	1	9,20E4	0,07%	0,15%
2	10,780	1	1,40E5	0,16%	0,16%
3	15,250	1	1,98E5	0,16%	0,16%
4	21,320	1	2,76E5	0,16%	0,16%
5	26,950	1	3,49E5	0,16%	0,16%
6	34,280	1	4,45E5	0,16%	0,16%
7	46,560	1	6,04E5	0,16%	0,16%
8	3,808	2	4,94E4	0,07%	0,15%
9	3,893	2	5,05E4	0,15%	0,15%
10	3,897	2	5,05E4	0,19%	0,24%
11	3,903	2	5,06E4	0,15%	0,15%
12	4,331	2	5,62E4	0,19%	0,20%
13	4,344	2	5,63E4	0,19%	0,22%
14	4,938	2	6,40E4	0,12%	0,12%
15	4,945	2	6,41E4	0,08%	0,14%
16	5,486	2	7,11E4	0,19%	0,25%
17	5,492	2	7,12E4	0,18%	0,23%
18	6,142	2	7,96E4	0,08%	0,12%
19	6,657	2	8,63E4	0,15%	0,15%
20	6,987	2	9,06E4	0,17%	0,19%
21	6,988	2	9,06E4	0,08%	0,14%
22	7,027	2	9,11E4	0,07%	0,15%
23	7,453	2	9,66E4	0,07%	0,15%
24	7,768	2	1,01E5	0,08%	0,12%
25	9,911	2	1,29E5	0,12%	0,12%
26	11,258	2	1,46E5	0,15%	0,15%
27	12,293	2	1,59E5	0,16%	0,18%
28	15,478	2	2,01E5	0,10%	0,12%
29	19,376	2	2,51E5	0,10%	0,12%
30	24,551	2	3,18E5	0,10%	0,12%
31	31,253	2	4,05E5	0,12%	0,12%
32	25,400	2,5	3,29E5	0,18%	0,19%
33	10,000	cylindr.	1,30E5	0,07%	0,13%

### 2.2 Illustration of approach for two nozzles

In Figure 2 there are all the single measurement data shown for the nozzles #1 and #22 of Table 1. Both have similar diameter of about 7 mm but different design curvature radius:  $R_{C,design} = 1$  for nozzle #1 and  $R_{C,design} = 2$  for nozzle #22. The real local curvature radii are shown in Figure 3 based on the dimensional measurements with 3D-CMM.

For the determination of the parameter  $b_{lam}$ , only the values of discharge coefficients  $c_D$  measured at Reynolds numbers below  $Re = 10^5$  were used. They are indicated with dark blue colour. All other data with air are shown in light blue and those with natural gas in red.

The first step is the calculation of the Likelihood-function for the measured  $c_D$ -values depending on the parameter  $b_{lam}$ . The base for this is the function of  $c_D$  depending on  $b_{lam}$  according Equation (5) and (7). The result for our two exemplary nozzles is shown in Figure 4 at the Reynolds number  $Re = 9.1 \cdot 10^4$ . The corresponding measured values  $c_{D,measured}$  are shown as well. For each point at the

curve of  $c_D(b_{lam}, Re = 9.1 \cdot 10^4)$  we get a distance to the  $c_{D,meas}$  and taking the uncertainty of  $c_{D,meas}$  into account we get the likelihood  $L(c_{D,meas}|b_{lam})$  of this  $c_{D,meas}$  if a specific  $b_{lam}$  is given.

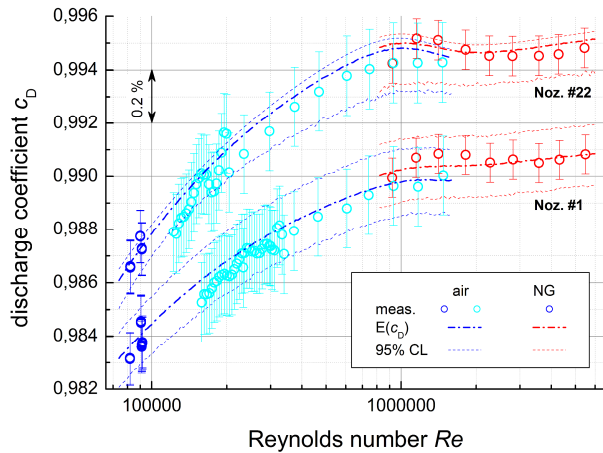


**Figure 2:** Exemplary data of two nozzles with the designed throat curvature radii  $R_{C,design} = 1$  (#1) and  $R_{C,design} = 2$  (#22), see also Table 1.

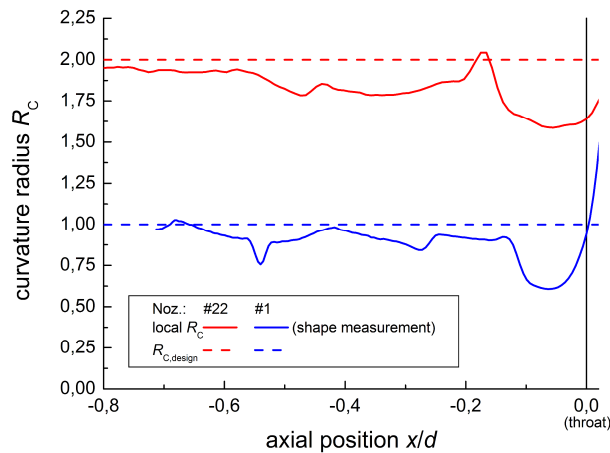


**Figure 3:** Local curvature radii  $R_C$  of the nozzles #1 and #22 in the inlet section upstream to the throat ( $x/d \leq 0$ ) based on dimensional shape measurements.

In Figure 5, there are the final Likelihood functions given for nozzles #1 and #22. Please note that this is already the Likelihood for all data  $c_{D,meas}$  with  $Re < 10^5$  (see Figure 2).

As you can see in Figure 5, the outcome of the Likelihood function can be asymmetric and may have also a separated second peak (here for nozzle #1). This means that there would be also a second but totally different value for  $b_{lam}$  what would fit to the measured  $c_D$ -values. To exclude such ranges, we need to include further information in the sense of a prior probability  $p_{prior}(b_{lam})$ . We can apply the

basic Bayesian formulation between Likelihood, prior and posterior as given in Equation (10):

$$p(b_{lam}|c_{D,meas}) \sim L(c_{D,meas}|b_{lam}) \cdot p_{prior}(b_{lam}) \quad (10)$$

In our case, we make only use of priors with  $p_{prior}(b_{lam}) = \text{const.}$  for all  $b_{lam}$  within  $0 \leq b_{lam} \leq b_{lam,max}$ . The  $b_{lam,max}$  can be derived from the information about the design curvature radius  $R_{C,design}$  or the local values of  $R_C$  out of shape measurements, e.g.  $b_{lam,max} = 2.9 R_{C,max}^{0.25}$  with  $R_{C,max} = 2 \cdot R_{C,design}$ . E.g., in the case of nozzle #1 we get  $b_{lam,max} = 3.5$ . With such prior we introduce of course restrictions to the quality of the nozzles shape so that overall the local shape curvature radius shall not be larger than two times of the designed value. Looking to Figure 3, this restriction seems reasonable and not very strong.

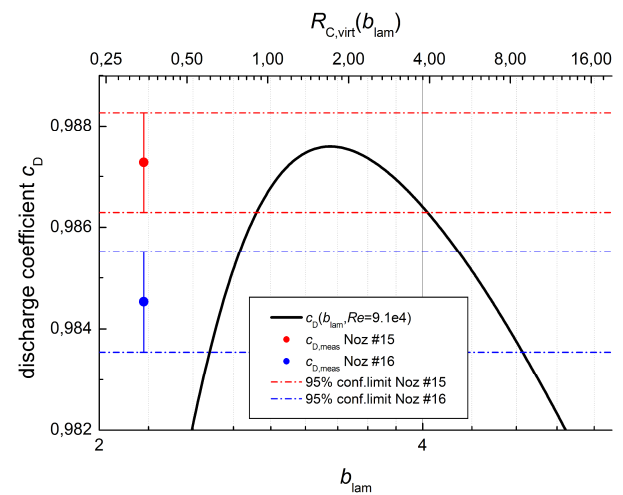


**Figure 4:**  $c_D$  as a function depending on  $b_{lam}$  for  $Re = 9.1 \cdot 10^4$  compared to the measured  $c_D$ -values for nozzle #1 and #22.

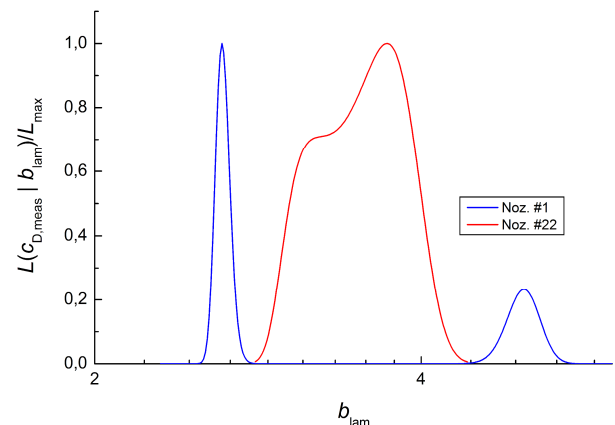


**Figure 5:** Likelihood of measured  $c_D$ -values for all data  $Re \leq 10^5$  in Figure 2.

With the probability density  $p(b_{lam}|c_{D,meas})$  we can determine in the next step the related probability density of (predicted)  $c_{D}$ -values for any other Reynolds number using a Monte Carlo approach. We generate (e.g.) 10.000 random numbers  $z$  equally distributed in the range  $[0,1)$  and transform these numbers using the inverse probability function  $P^{-1}(b_{lam}|c_{D,meas})$  to get the set of random  $b_{lam,i}$  with the probability density  $p(b_{lam}|c_{D,meas})$ . For all these  $b_{lam,i}$  the  $c_{D,extrapol,i}$  at the intended Reynolds number(s) are calculated. We use the expectation value  $E(c_{D,extrapol,i})$  for the final predicted value. Looking to Figure 2, it can be obtained that the outcome for  $c_{D,extrapol,i}$  can be significantly asymmetric (nozzle #22) and the 95%-confidence limits are asymmetric to the expectation value.

### 2.3 Results

The straight forward check of our approach is the comparison of the extrapolated  $c_{D,extrapol}$  with all the data measured at pressures  $\geq 110$  kPa which were not used for the parameter determination. In Figure 6 we plotted the differences

$$\Delta_{c_D} = c_{D,meas} - c_{D,extrapol} \quad (11)$$

versus the Reynolds number  $Re$ . The same data are shown in Figure 7 plotted versus the ratio of Reynolds numbers  $Re/Re_0$  (for  $Re_0$  see Table 1).

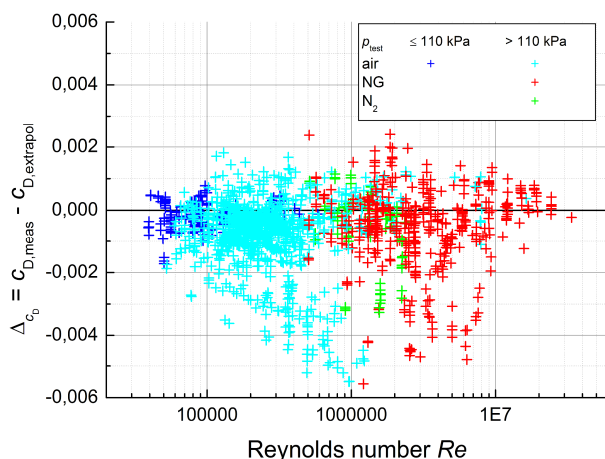


**Figure 6:** Differences  $\Delta_{cD}$  of the measured discharge coefficients  $c_{D,meas}$  to the extrapolated  $c_{D,extrapol}$  in dependency on the Reynolds number.

The histogram in Figure 8 summarizes all data with  $Re/Re_0 \geq 8$  for the evaluation of extrapolation because in this range the data origin mainly from the traceability for high pressure natural gas at PTB. This traceability is independent to the traceability for low pressure air.

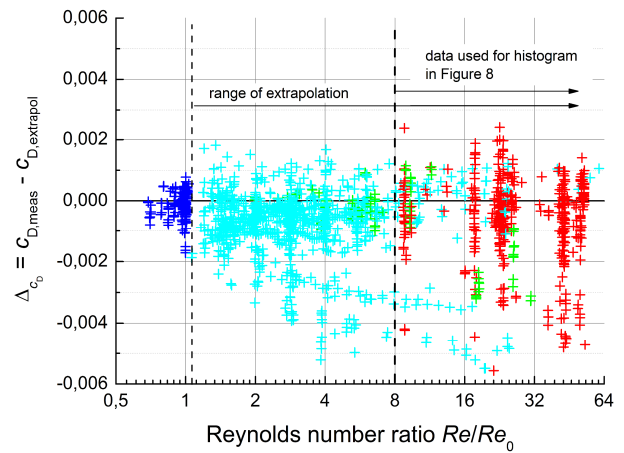


**Figure 7:** Differences  $\Delta_{cD}$  of the measured discharge coefficients  $c_{D,meas}$  to the extrapolated  $c_{D,extrapol}$  in dependency on the ratio of Reynolds numbers  $Re/Re_0$  (for  $Re_0$  see Table 1).

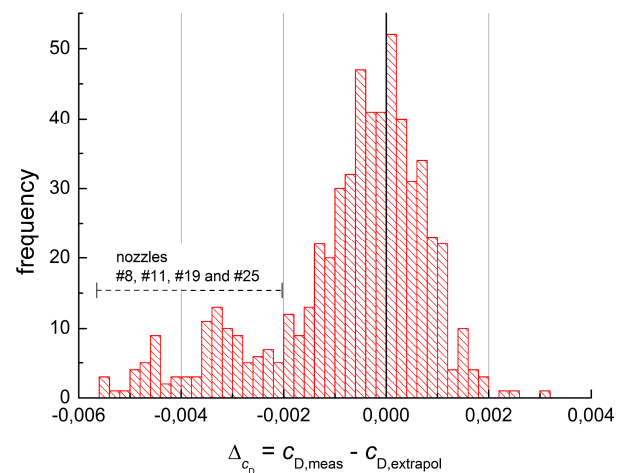


**Figure 8:** Histogram of differences  $\Delta_{cD}$  for the ratio of Reynolds numbers  $Re/Re_0 \geq 8$  (for  $Re_0$  see Table 1).

The differences  $\Delta_{cD}$  are almost within  $\pm 0.002$ , i.e.  $\pm 0.2\%$  of  $c_D$ . The values significantly outside of this limit can be allocated to four nozzles (#8, #11, #19 and #25) and are tending to negative deviations (means that the measured values are below the extrapolated).

The more detailed evaluation for each nozzle is using the value 0.002 as a normalisation factor for the single  $\Delta_{cD}$ . All values belonging to one nozzle are summarised to a mean value  $\Delta_{cD,mean}$  and are shown in Figure 9 and Figure 10. The error bars are the doubled standard deviation of the data set for each nozzle.

In Figure 9, the  $\Delta_{cD,mean}$  are plotted versus the nominal diameter of the nozzles and it can be obtained that there is no significant tendency visible

except that the scatter seems to be little larger for the smaller diameters. As mentioned above, most of data exceeding the limit 0.002 can be assigned to the nozzles #8, #11, #19 and #25.

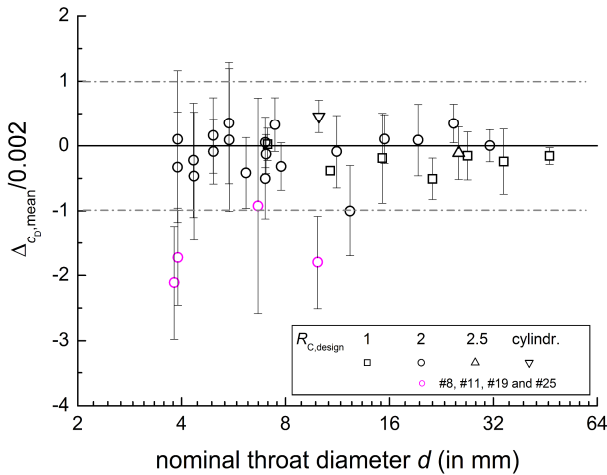


**Figure 9:** Histogram of normalised mean differences  $\Delta c_{D,mean}$  for each nozzle and ratio of Reynolds numbers  $Re/Re_0 \geq 8$  plotted versus the nominal diameter of the nozzles.

In Figure 10, same data as in Figure 9 are plotted versus the virtual curvature Radius  $R_{C,virt}$  of the nozzles. Here, a slight tendency can be detected that the  $\Delta c_{D,mean}$  are little lower for small  $R_{C,virt}$  than for large  $R_{C,virt}$ . But this trend is not yet strong significant as the regression coefficient for a linear trend versus the log-scale of the diagram is 0.7 only.

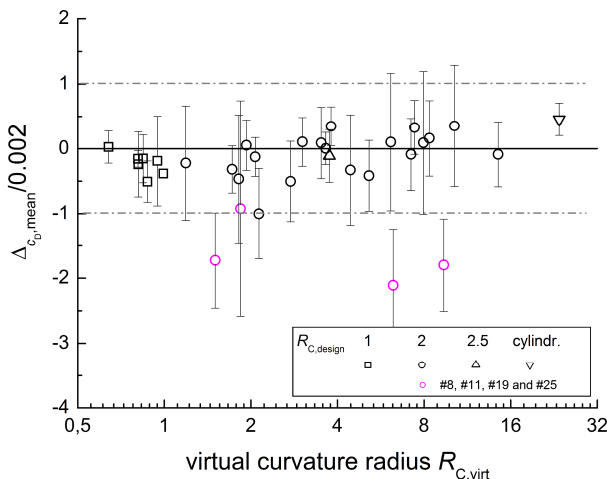


**Figure 10:** Histogram of normalised mean differences  $\Delta c_{D,mean}$  for each nozzle and ratio of Reynolds numbers  $Re/Re_0 \geq 8$  plotted versus the resulting virtual curvature Radius  $R_{C,virt}$  of the nozzles.

In Table 2, some main results are summarized for all nozzles. Beside the virtual curvature radius  $R_{C,virt}$  and the normalised mean differences  $\Delta c_{D,mean}$ ,

minimal and maximal standard uncertainty of the extrapolated  $c_D$ -values in the range for  $Re/Re_0 \geq 8$  are given. These standard uncertainties are within 0.02 % and 0.09 % except for the two nozzles #12 and #13. Please note that the probability density of the extrapolated  $c_D$ -values can be asymmetric so that a simple coverage factor cannot be applied in all cases to get the 95% coverage interval.

**Table 2:** Main results of the extrapolation.

Noz. Nr.	$R_{C,virt}$	$\Delta c_{D,mean} / 0.002$	for $Re/Re_0 \geq 8; k = 1$	
			$u_{extrapol,min}$	$u_{extrapol,max}$
1	0,64	0,02	0,06%	0,06%
2	0,99	-0,38	0,07%	0,08%
3	0,95	-0,19	0,06%	0,06%
4	0,87	-0,51	0,06%	0,06%
5	0,84	-0,15	0,06%	0,06%
6	0,81	-0,24	0,06%	0,06%
7	0,81	-0,16	0,06%	0,06%
8	6,24	-2,11	0,02%	0,04%
9	4,44	-0,33	0,02%	0,04%
10	6,13	0,10	0,02%	0,04%
11	1,50	-1,72	0,07%	0,08%
12	1,19	-0,22	0,14%	0,16%
13	1,81	-0,47	0,17%	0,21%
14	8,34	0,16	0,02%	0,05%
15	14,47	-0,09	0,02%	0,05%
16	10,20	0,35	0,02%	0,04%
17	7,96	0,09	0,02%	0,04%
18	5,15	-0,42	0,02%	0,04%
19	1,84	-0,92	0,04%	0,05%
20	2,75	-0,50	0,05%	0,07%
21	1,93	0,05	0,04%	0,06%
22	2,07	-0,13	0,04%	0,05%
23	7,41	0,33	0,02%	0,04%
24	1,72	-0,32	0,05%	0,06%
25	9,36	-1,80	0,03%	0,04%
26	7,20	-0,09	0,03%	0,04%
27	2,13	-1,00	0,02%	0,02%
28	3,02	0,11	0,05%	0,06%
29	3,51	0,09	0,06%	0,06%
30	3,80	0,35	0,06%	0,07%
31	3,64	0,00	0,05%	0,06%
32	3,75	-0,11	0,03%	0,04%
33	23,60	0,46	0,06%	0,09%

### 3. Discussion of the results

The main outcome of the results is that our extrapolation of  $c_D$  based on the measurements with low pressure air is in close agreement within 0.2% with the measured values even in the high Reynolds number range above  $Re/Re_0 \geq 8$ . Only the values of four out of 33 nozzles were detected as real outliers. Ignoring these outliers, there is no dependency of the agreement on the scale of extrapolation ( $Re/Re_0$ ), see Figure 7.

The outliers can be explained at one hand with a very strong variance of the local curvature radius in the inlet of the nozzles. This e.g. the case for nozzles #19 what has a high peak in the curvature radius short before the throat (documented in [8]).

On the other hand, our approach to link the  $b_{lam}$  with  $b_{turb}$  via Equation (8) can be applied only for hydraulic smooth surfaces in the nozzles. In cases of significant roughness this relation will not apply what can be concluded from publication dealing with rough nozzles [9]. A significant roughness would also explain that the measured values for the outliers tend to be lower than the extrapolated values.

The data base contains a wide range of nozzles shapes with four different design curvature radii (see Table 1). The real shape of the nozzles close to the throat is even wider distributed what can be concluded from the resulting virtual curvature radius with values  $0.64 \leq R_{C,virt} \leq 23.6$ .

The approach of the extrapolation is based on the assumption that the virtual curvature Radius  $R_{C,virt}$  is a constant all over the Reynolds number range investigated. This can be assumed for nozzles larger than a minimum size (i.e. above a minimum Reynolds number) but it is a simplification what will be not valid anymore for small nozzles (see for this e.g. [6]). Such additional dependency might be also the reason for the slight trend of the  $\Delta_{cD,mean}$  versus the  $R_{C,virt}$ .

The mathematical model for the overall function of  $c_D(Re)$  introduced above in section 1.2 contains the arbitrary values for  $k_u = 5.5$  and  $Re_{tr} = 1.25 \cdot 10^6$ . When looking to Figure 6, we can obtain that there is no significant enlargement of the  $\Delta_{cD}$  in the range of  $7 \cdot 10^5 \leq Re \leq 2.5 \cdot 10^6$ , so that these values are again confirmed as reasonable empirical values to model the transition region using Equation (9) for a wide variety of nozzles.

The standard uncertainties of the measured  $c_D$ -values at high Reynolds numbers are typically in the order of 0.06 to 0.08 % (see Table 1, note that the table provides the expanded uncertainties with  $k = 2$ ). This is the same level as we got for the extrapolated values (Table 2). The empirical limit of 0.2 % out of the histogram in Figure 8 (excluding the outliers and interpreted as a 95%-confidence level) is in good agreement with the combination of both the experimental and extrapolated uncertainty. Therefore, we can conclude that the uncertainty derived from the extrapolation process is reliable.

#### 4. Conclusion

We presented a mathematical model for the functionality of the discharge coefficient  $c_D$  versus Reynolds number covering laminar and turbulent FLOMEKO 2019, Lisbon, Portugal

boundary layers as well. It contains only one free parameter  $b_{lam}$  what can be determined therefore using the  $c_D$ -values measured in a narrowed range of Reynolds numbers with atmospheric air.

The outcome of this fitted model has been used for wide ranged extrapolation up to a factor of 60 in the Reynolds number. It was compared against a large dataset of experimental  $c_D$ -values of 33 nozzles. The agreement between experimental and extrapolated values were almost within 0.2 % for 29 of the 33 nozzles what confirms the reliability of the model and the related extrapolation. This agreement is independent to the design curvature radius as well as the resulting virtual curvature radius and covers a wide range of nozzles shapes.

Therefore, we could demonstrate that it is possible to extrapolate low pressure calibrations of sonic nozzles to high pressure application range with a reasonable uncertainty so that we can use such sonic nozzles to underfeed our traceability for high pressure gas additionally with a link to our low-pressure traceability chain.

The approach can be extended in two directions. First, the parameter determination should be applied to experimental values out of a larger range of Reynolds numbers. The larger the  $Re$ -range the more precisely the parameters can be determined. With such extended  $Re$ -range for parameter fitting, we can introduce also the throat diameter as a free parameter in the mathematical model.

Second, it is promising to refine the Bayesian approach in Equation (10), specifically when we will adopt also the diameter to the experimental data. A more specific formulation of the prior knowledge about the curvature radius and its impact to the parameter  $b_{lam}$  as well as the throat diameter gathered by dimensional measurements will enhance the reliability of such extrapolation.

#### References

- [1] Mickan, B., Vallet, J.-P., Li, C., Wright, J.: *Extended data analysis of bilateral comparisons with air and natural gas up to 5 MPa*, FLOMEKO 2016, Sydney, Australia, September 26-29, 2016
- [2] Kliegel, J. R., Levine, J. N.: *Transonic Flow in Small Throat Radius of Curvature Nozzles*, AIAA Journal Vol 7, nr. 7, 1969, pp. 1375 - 1378
- [3] Geropp, D., *Laminare Grenzschichten in ebenen und rotationssymmetrischen*

*Lavalduessen*, Deutsche Luft- und Raumfahrt, Forschungsbericht 71-90, 1971.

- [4] Geropp, D., *Laminare Grenzschichten in Überschalldüsen*, Deutsche Luft- und Raumfahrt, Forschungsbericht 01 TM 8603-AK/PA 1, 1987.
- [5] Wright, J. et al, *Thermal Effects on Critical Flow Venturis*, Proceedings of 9<sup>th</sup> International Symposium on Fluid Flow Measurement, Arlington, Virginia, 2015.
- [6] Mickan, B. et al, *Systematic investigations of cylindrical nozzles acc. ISO 9300 down to throat diameters of 125  $\mu$ m*, Proceedings of 10<sup>th</sup> International Symposium on Fluid Flow Measurement, Queretaro, Mexico, 2018.
- [7] Mickan, B., Kramer R., Dopheide D., Hotze, H.-J., Hinze, H.-M., Johnson, A., Wright, J., Vallet, J.-P., *Comparisons by PTB, NIST, And LNE-LADG in Air and Natural Gas with Critical Venturi Nozzles agree within 0.05 %*, Proceedings of 6<sup>th</sup> International Symposium on Fluid Flow Measurement, Queretaro, Mexico, 2006.
- [8] Mickan, B., Kramer, R., *Experiences With Sonic Nozzles Used For Different Gases And Wide Range Of Pressure And Temperature Conditions*, Proceedings of 7<sup>th</sup> International Symposium on Fluid Flow Measurement, Anchorage, Alaska, 2009.
- [9] Lambert, M.-A. et al., *Numerical and Experimental Investigations on the Shape and Roughness of Cylindrical Critical Flow Venturi Nozzles (CFVN)*, Proceedings of 10<sup>th</sup> International Symposium on Fluid Flow Measurement, Queretaro, Mexico, 2018.

# Cyclonic stack flow measurement uncertainties and impact on annualised mass emission measurements

M.D. Schakel<sup>1</sup>, M. Workamp<sup>1</sup>, J. Geršl<sup>2</sup>

<sup>1</sup>VSL, Thijssseweg 11, 2626 JA, Delft, The Netherlands

<sup>2</sup>Czech Metrology Institute, Okružní 31, 63800 Brno, Czech Republic

E-mail (corresponding author): mschakel@vsl.nl

---

## Abstract

Measurements of emissions of air pollutants are typically performed in accordance with CEN standards, which are being referred to as Standard Reference Methods. To determine emissions of air pollutants, concentration and flow measurements need to be performed within the stack. Standard EN ISO 16911-1 is employed as the Standard Reference Method for flow measurements. We perform validation measurements for this method in narrow stacks with cyclonic flows. To traceably determine the uncertainty of cyclonic flow in realistic field conditions, we use a stack simulator. We use a traceably calibrated wind tunnel to provide the stack with a well-defined input flow. We perform velocity measurements with a traceably calibrated L-Pitot tube in a stack simulator with two configurations: one with a straight stack entrance, the other with an elbow just before the stack entrance. In both cases, we measure the velocity at planes at several hydraulic diameters downstream from the stack entrance, namely 3, 4, 5, 6, and 7 diameters downstream of the stack entrance. We also characterize the velocity profile at the stack entrance. We show that in both configurations, the flow profile deviates significantly from fully developed turbulent pipe flow, even at 7 diameters downstream of the stack entrance. In case of cyclonic flow, the effect is more pronounced. Future work will focus on comparing the flow measurements with computational fluid dynamics modelling to gain further insight into the additional flow measurement uncertainty.

---

## 1. Introduction

Pollutants are becoming an increasingly large environmental and health hazard. Recently, new European legislation has been introduced to continue to drive down emissions, containing increasingly stringent emission limit values. Emission limits are enforced by measurements, legally required to adhere to CEN standards, typically being referred to as Standard Reference Methods. Standard EN ISO 16911-1 is employed as the Standard Reference Method for flow measurements [1]. This standard also refers to EN 15259 [2] which sets requirements for measurement sections and sites, including requirements for the measurement plane when determining the average velocity from a grid of point flow measurements (e.g. using a Pitot tube).

One of these requirements is that the “measurement plane shall be situated in a section of the waste gas duct (stack etc.) where homogenous flow conditions and concentrations can be expected”, for which it is noted that this

requirement is generally fulfilled in a section of a duct with at least five hydraulic diameters of straight duct upstream of the sampling plane and two hydraulic diameters downstream, if this section is of constant shape and free of any disturbances. However, the field validation trials for EN ISO 16911-1 were carried out at plants with no significant cyclonic flow [3]. Cyclonic flow (turbulent flow with a significant amount of swirl) may arise when a flow is making consecutive turns, such as an elbow before a stack entrance. Part of the EN ISO 16911-1 requirements is thus poorly validated in stacks with cyclonic flow, although the standard does provide a velocity correction formula which accounts for the tangential component of non-axial flow in case of significant swirl (swirl angle >15°).

We perform experiments in a narrow stack simulator to investigate the effect of flow disturbances on emission measurements. The stack has two configurations, one with a straight entrance via a T-junction, while the other has an additional elbow, which generates swirl in the vertical stack. We show that in both cases, the flow profile deviates

significantly from a fully developed profile, even at seven hydraulic diameters downstream of the T-junction. Future work will combine computational fluid dynamics (CFD) simulations with our measurements to gain additional insight to emission measurement uncertainties.

## 2. Experimental

We perform experiments in a stack simulator. The stack is a vertical pipe with a diameter of 0.2034 m. The stack has a blunt closed bottom, and the flow enters the stack through a T-piece, of which the horizontal tube is connected to a traceably calibrated wind tunnel via a cone-shaped connector. We use the stack simulator in two configurations: one with a straight stack entrance, the other with an elbow just before the stack entrance. For an overview of the two configurations of the stack simulator, see Figure 1.

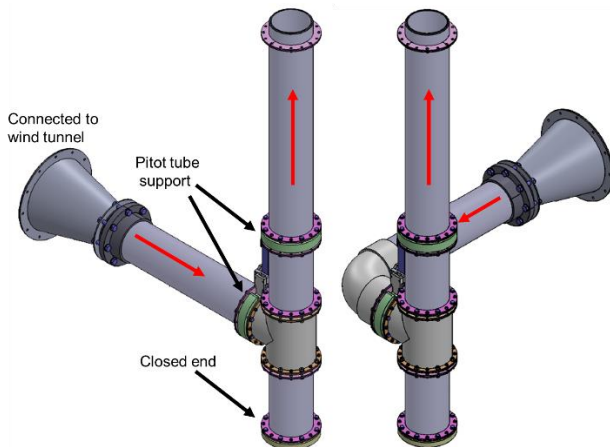


**Figure 1:** Overview of the two configurations of the stack simulator. Red arrows indicate the flow direction. Green parts represent the mounting ring of the Pitot tube support (Figure 2).

We use a traceably calibrated L-Pitot tube (AIRFLOW developments, UK) to perform the velocity measurements. The Pitot tube is held in place using a specially designed support, equipped with a hand-controlled linear stage (Mitutoyo, Prod. Nr. 539-803) with a digital readout, allowing to precisely position the Pitot tube at various radial positions in the stack. The Pitot tube support is mounted to a ring of which there are two in our stack simulator (Figure 2). For an overview of the Pitot tube support holder and mounting ring, see Figure 2.

The mountings rings are made such that, after loosening the bolts holding it in place, the ring is freely rotatable, allowing measurement at different measurement lines without disassembling the stack

simulator. The mounting rings are placed in two positions: one at the entrance of the T-junction, the other in the stack downstream of the T-junction. By using variable lengths of pipe, the latter was placed at 3, 4, 5, 6, or 7 diameters downstream of the stack entrance. As we use only one Pitot tube but two mounting rings, the hole for the Pitot tube on the mounting ring that is not in use, is sealed with a plug that sits flush with the inner surface of the ring.

We perform experiments at two different volumetric flow rates  $Q$  corresponding to bulk velocities  $v_{bulk} = Q/A$  of 5.0 and 10.0 m/s, where  $A$  is the cross-sectional area. Due to the use of the calibrated wind tunnel, the expanded uncertainty in  $Q$  does not exceed 0.15%.

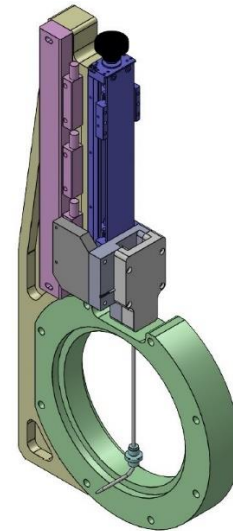


**Figure 2:** Overview of the Pitot tube support and mounting ring.

## 3. Uncertainty sources

### 3.1 Uncertainty of the velocity measurements

The axial velocity in the stack is measured using an L-Pitot tube, traceably calibrated in a wind tunnel. As we are interested in the velocity profile, we compute the non-dimensional axial velocity  $v_z^* = v_{measured}^*/v_{bulk}^*$ , at standard laboratory conditions (denoted by asterisks). The uncertainty in the average non-dimensional velocity  $\bar{v}_z^*$  has several uncertainty sources including:

- Pitot tube constant
- diameter of the pipe
- differential pressure
- atmospheric pressure
- temperature
- volumetric flow rate

We measure the velocity three times so that the uncertainty related to repeatability is also estimated.

### 3.2 Uncertainty in radial position of the Pitot tube

We determine the radial position of the Pitot tube using the digital readout of the linear stage. The uncertainty in the (radial) position of the Pitot tube originates from various sources. The largest uncertainty sources are:

- Play between the pipe and the mounting ring
- Imperfections in the straightness of the Pitot tube
- Definition of the zero point (i.e. the position at which the Pitot hits the wall)

The uncertainty related to the accuracy of the linear stage is negligible. Note that there's also an uncertainty in the angle of the Pitot tube support, which is estimated at 3 degrees ( $k=2$ ).

## 4. Results & Discussion

We characterize the flow by measuring the average non-dimensional axial velocity  $\bar{v}_z^*$  at measuring planes spaced 3, 4, 5, 6, and 7 hydraulic diameters downstream of the stack entrance. At each plane, we measure the velocity in two perpendicular measurement lines (x- and y-axes), corresponding to four different positions/angles of the Pitot tube mounting ring (the centre of the stack is sampled four times). Measurement points are chosen such that the distances from the wall are spaced logarithmically, see Figure 3.

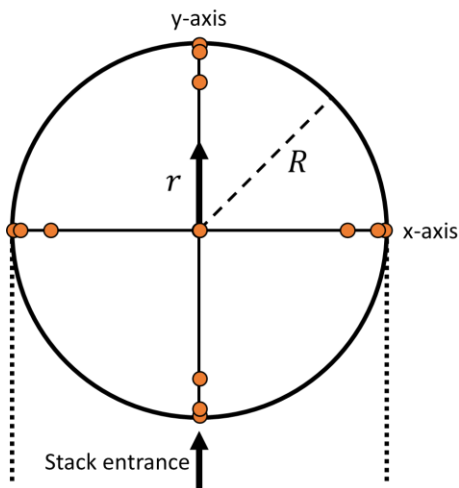


**Figure 3:** Top view of the measurement plane. The y-axis is parallel to the axis of the stack entrance. The radial position of measurement point is denoted by  $r$  while the tube radius is given by  $R$ . Orange points denote the measurement positions.

In Figure 4 we plot the results of the input profile measurements, for the case with a straight entrance (a) and with an elbow before the entrance (b). In the first case, the profile is very flat, in agreement with our expectations, as the stack is connected to our

wind tunnel which generates a flat profile. A relatively small effect can be observed: the measurements along the y-axis are slightly asymmetric. This agrees with expectations as well because the stack is closed at the bottom while it is open at the top. For the case with the elbow just before the entrance, we observe a very asymmetric profile, as a result of the bend. In agreement with expectations, the velocity is decreased in the section of duct directly after the inside of the elbow, while the outside has increased velocity.

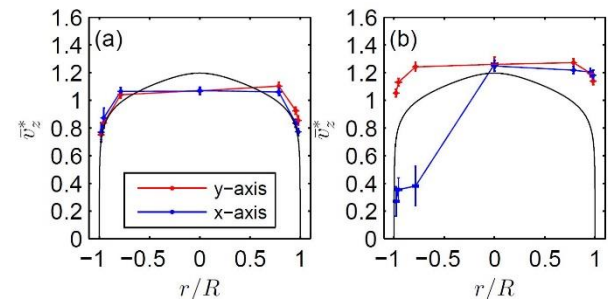


**Figure 4:** Average non-dimensional axial velocity  $\bar{v}_z^*$  as a function of  $r/R$ , for a stack with a straight entrance (a) and a stack with an elbow before the entrance (b), measured at the entrance of the T-junction. Solid black lines represent the Gersten-Herwig reference profile for fully developed turbulent pipe flow [6]. For these inlet measurements, the x-axis is along the horizontal line and the y-axis along the vertical line passing through the origin.

In Figure 5 we plot the results of measurements at 3, 5 and 7 hydraulic diameters downstream of the stack entrance, using  $v_{bulk} = 10.0$  m/s. Results at 5.0 m/s display similar trends (not shown). In the stack with the straight entrance, at 3 diameters downstream (Figure 5a), there's a large velocity depression at the side of the stack entrance, while at the opposite side the velocity is increased, in agreement to simulations of bigger stacks [5]. When looking further downstream (Figure 5b+c), the flow slowly becomes more axially symmetric, and approaches the reference profile for fully developed turbulent pipe flow as given by Gersten [6]. However, even at 7 hydraulic diameters downstream (Figure 5c), deviations from the reference profile exist. It is noteworthy that the profile does have a strong resemblance to the input profile (Figure 4a) at this plane.

In the case of the elbow before the stack entrance (Figure 5d-f) we observe highly asymmetric flow profiles. The flow profile remains highly asymmetric, even at 7 hydraulic diameters downstream of the T-junction (Figure 5f). The flow profile deviates significantly from the reference profile, as well the input profile, suggesting cyclonic effects could constitute a significant uncertainty source in mass emission measurements.

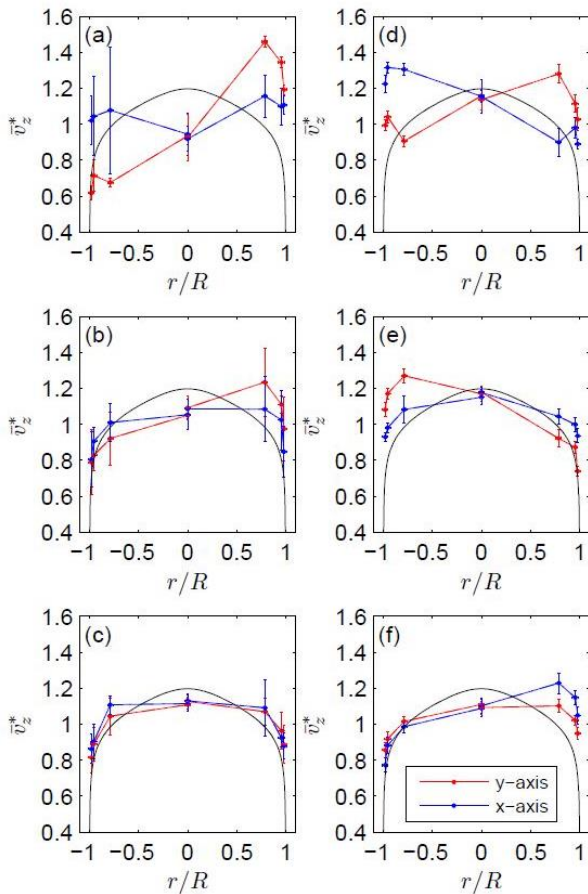


**Figure 5:** Average non-dimensional axial velocity  $\bar{v}_z^*$  as a function of  $r/R$ , for a stack with a straight entrance (a-c) and a stack with an elbow before the entrance (d-f) at 3 (a+d), 5 (b+e) and 7 (c+f) diameters downstream of the T-junction. All data shown was recorded at  $v_{bulk} = 10.0$  m/s. Legend in (f) applies to all panels. Solid black lines represent the Gersten-Herwig reference profile for fully developed turbulent pipe flow [6].

## 5. Conclusions

We develop a stack simulator to measure velocity profiles in narrow stacks using an L-Pitot tube. We present results of measurements in two configurations: one with a straight stack entrance and one with an elbow. The standard [2] suggests that 5 hydraulic diameters downstream of a flow disturbance, the flow can be considered “homogenous”. We show that for our narrow stack simulator, the flow profile deviates from the velocity profile at the stack entrance and the reference profile for fully developed pipe flow, even at 7 hydraulic diameters downstream of the flow disturbance. The deviations are larger for the configuration with the elbow before the stack entrance, which generates cyclonic flow. These findings suggest that cyclonic flow not only increases the error of the flow rate measurement according to [1, 2] by presence of transversal velocity components and their impact on

measurement error of a Pitot tube, but also by slower decrease with downstream pipe length of flow asymmetry introduced by the T-junction of the supply pipe. Future work will focus on determining the error of the Standard Reference Method [1] in conditions of cyclonic flow by direct comparison of the flow rate standard of VSL with flow rate measurements in the stack model according to [1, 2]. The measurement data from the stack model will be used to validate a CFD model providing a detailed computed velocity field in the stack which will be further utilised to predict the SRM error for various types of Pitot tubes with different swirl angle dependencies.

## 6. Acknowledgement

This research has received funding from the European Metrology Programme for Innovation and Research (EMPIR) under grant 16ENV08 IMPRESS II.

## References

- [1] ISO 16911-1: *Stationary source emissions – Manual and automatic determination of velocity and volume flow rate in ducts – Part 1: Manual reference method*, 2013.
- [2] EN 15259: *Air quality – Measurement of stationary source emissions – Requirements for measurement sections and sites and for the measurement objective, plan and report*, 2007.
- [3] Dimopoulos C, Robinson R A, Coleman M D, “Mass emissions and carbon trading: a critical review of available reference methods for industrial stack flow measurements”, *Accreditation and Quality Assurance*, **22**, pp. 161-165, 2017.
- [4] Bailey S C, Hultmark M, Monty J P, Alfredsson P H, Chong M S, Duncan R D, Fransson J H, Hutchins N, Marusic I, McKeon B J, Nagib H M, “Obtaining accurate mean velocity measurements in high Reynolds number turbulent boundary layers using Pitot tubes”, *Journal of Fluid Mechanics*, **715**, pp. 642-670, 2013.
- [5] Geršl J, Knotek S, Belligoli Z, Dwight R P, Robinson, R A and Coleman M D, “Flow rate measurement in stacks with cyclonic flow– Error estimations using CFD modelling”, *Measurement*, **129**, pp.167-183, 2018.
- [6] Gersten K, “Fully Developed Turbulent Pipe Flow”. In: *Fluid Mechanics of Flow Metering* (Berlin, Heidelberg, Springer), 2005.

# Air and Nitrogen Testing of Coriolis Flow Meters Designed for Hydrogen Refuelling Stations

M. MacDonald<sup>1</sup>, M. de Huu<sup>2</sup>,  
R. Maury<sup>3</sup>, W. Kang<sup>4</sup>

<sup>1</sup>NEL, East Kilbride, Glasgow, United Kingdom

<sup>2</sup>Federal Institute of Metrology (METAS), Bern, Switzerland

<sup>3</sup>CESAME-EXADEBIT SA, Poitiers, France

<sup>4</sup>Korea Research Institute of Standards and Science (KRISS), Daejeon, South Korea

E-mail (corresponding author): [mmacdonald@tuvnel.com](mailto:mmacdonald@tuvnel.com)

---

## Abstract

The performance of Coriolis flow meters designed for use in hydrogen refuelling stations was evaluated in air and nitrogen by several National Metrology Institutes and Designated Institutes. Three meters were tested by members of the MetroHyVe consortium; NEL, METAS and CESAME EXADEBIT. A fourth meter was tested separately by KRISS and there was found to be a significant overlap in the test conditions and results from each experimental programme.

A wide range of conditions were tested overall, with gas flow rates ranging from 0.05 to 3.8 kg/min and pressures ranging from 10 to more than 40 bar. The densities encountered using air and nitrogen ranged from 11.5 to more than 52 kg/m<sup>3</sup> (equivalent to hydrogen at approximately 125 bar and 875 bar respectively). There was also some investigation of the influence of temperature on flow meter performance, with selected points tested at temperatures as low as -40°C. The effect of pressure was studied separately using water and is presented in another paper.

When the flow meters were operated within the manufacturer's recommended flow rate ranges, errors were generally within  $\pm 1\%$ . For some of the meters tested, errors approached  $\pm 0.5\%$ .

---

## 1. Introduction

To support its use as a low carbon transport fuel, an extensive infrastructure for hydrogen-powered vehicles is currently in development in many countries worldwide. However, the hydrogen industry cannot yet meet the measurement requirements of legislation surrounding the use of hydrogen fuel, due to a lack of methods and standards.

A European Metrology Programme for Innovation and Research (EMPIR) Joint Research Project was launched to address the metrological challenges associated with hydrogen vehicles and refuelling stations [1].

Work package 1 of the "Metrology for Hydrogen Vehicles" (MetroHyVe) JRP aims to establish a traceability chain for hydrogen flow metering in fuel cell vehicle refuelling applications.

The conditions which meters must operate at for this application are challenging from a flow metrology perspective. Hydrogen refuelling stations operate across a wide range of temperatures (-40°C to 85°C) and pressures (up to 875 bar) in accordance with the worldwide accepted standard SAE J2601 [2].

Researchers have previously addressed this challenge by developing primary and secondary flow standards for hydrogen at pressures of up to 350 bar [3][4]. Within the MetroHyVe project, several portable gravimetric standards have been developed for verifying the measurements at hydrogen refuelling stations at pressures of up to 700 bar.

These are all important steps in establishing a traceability chain for flow metrology in hydrogen vehicle refuelling. However in the longer term, it may prove more practical and cost effective to

evaluate the flow measurements of hydrogen refuelling stations using a master meter.

Currently, there are no independent, traceable flow laboratories where flow meters can be calibrated with hydrogen across an appropriate range of pressures, temperatures and flow rates. An alternative approach is being investigated, which is the subject of this paper.

This involves using alternative fluids to hydrogen to perform type approval testing and to characterise the behaviour of mass flow meters under high pressure. If proven to be a success, flow laboratories will be able to use these new methods to perform type approval testing under safer conditions than using hydrogen at up to 875 bar.

The performance of three Coriolis mass flow meters developed for hydrogen refuelling applications was evaluated using air and nitrogen by three members of the MetroHyVe consortium; NEL, METAS and CESAME EXADEBIT. Test conditions were selected such that the densities and mass flow rates established in this test programme were broadly representative of those in field conditions.

The effect of temperature on meter performance was investigated by METAS during the same test programme. The effect of pressure on meter performance was studied separately using water and results will be presented in another paper.

Complementary research has been carried out by KRISS, who tested a fourth meter with air. The conditions tested by KRISS partially overlap with those tested by the MetroHyVe partners and extend the overall range of data collected to higher flow rates and lower pressures.

Results of the testing carried out by NEL, METAS, CESAME EXADEBIT and KRISS are presented in this paper.

## 2. Flow Meters Tested

A total of 4 flow meters were tested. All were Coriolis type flow meters currently used in hydrogen refuelling stations. Table 1 shows which flow meters were tested at each laboratory.

Meters A, B and C were loaned to the MetroHyVe project, each from a different manufacturer. Meters A and B were each tested by NEL, CESAME EXADEBIT and METAS. Meter C was tested by NEL only.

Meter D was purchased and tested by KRISS.

**Table 1:** Flow meters tested by each laboratory

	NEL	METAS	CESAME EXADEBIT	KRISS
Meter A	x	x	x	
Meter B	x	x	x	
Meter C	x			
Meter D				x

## 2. Test Matrices

### 2.1 MetroHyVe

A test matrix was devised by the MetroHyVe partners using mass flow rates representative of those encountered in a hydrogen refuelling station. Temperatures and pressures were selected so that tests could be conducted at densities of 23 and 46 kg/m<sup>3</sup>, equivalent to hydrogen at 350 and 700 bar.

Table 2 shows the generic test matrix prepared for the nitrogen and air tests conducted by NEL, METAS and CESAME EXADEBIT. In practice, each laboratory deviated from this matrix to some extent.

**Table 2:** MetroHyVe Test Matrix.

Pressure (bar)	Temperature (°C)	Density (kg/m <sup>3</sup> )	Mass Flow Rate (kg/min)
40	20	46.26	0.05
40	20	46.26	0.1
40	20	46.26	0.25
40	20	46.26	0.5
40	20	46.26	0.75
40	20	46.26	1
40	20	46.26	1.25
40	20	46.26	1.5
40	20	46.26	1.75
40	20	46.26	2
20	20	23.08	0.05
20	20	23.09	0.1
20	20	23.09	0.25
20	20	23.09	0.5
20	20	23.09	0.75
20	20	23.09	1

Flowrates were initially selected to cover the operating ranges of the tested flow meters up to 3.6 kg/min, the maximum flow rate specified by the SAE J2601 for light duty vehicles [2]. However, it was discovered that at this flow rate, pressure drop through each of the tested flow meters would be excessive.

At a meter inlet pressure of 40 bar and flow rate of 3.6 kg/min, the pressure drop with nitrogen would be more than 10 bar, or 25% of the inlet pressure. This would result in a significant density shift

through the flow meter, which could not be considered representative of field conditions. Although the flow meters can incur large pressure drops in a hydrogen refuelling station, the ratio of differential pressure to meter inlet pressure would be much lower.

The flow meter manufacturers recommended a maximum flow rate of 2 kg/min for testing with air or nitrogen at 40 bar. This advice was followed and a maximum flow rate of 1 kg/min was selected for testing at 20 bar to achieve the same maximum velocity.

A minimum flow rate of 0.05 kg/min was selected. This was based on the lowest flow rate specified from the data sheets of all of the flow meters, although the meters loaned to the MetroHyVe project were previously calibrated by the manufacturers at higher minimum flow rates.

All three meters were calibrated by the manufacturers using water. Two of the meters were calibrated to a minimum flow rate of 0.2 kg/min, one meter was calibrated to a minimum of 0.5 kg/min.

### 2.2 NEL and CESAME EXADEBIT

Testing conducted by NEL and CESAME EXADEBIT followed the matrix shown in Table 2 with some minor deviations. Both NEL and CESAME EXADEBIT added test points to demonstrate consistency at the cross-over points of the reference flow devices used. CESAME EXADEBIT also added intermediate flow rates for the testing at 20 bar.

### 2.3 METAS

METAS tested at 20°C and -40°C to investigate the effect of temperature on meter performance. Flow rates were selected from the matrix shown in Table 2, but test conditions at 1.25 and 1.75 kg/min were skipped.

The heat exchangers used incurred a large pressure drop, so METAS were not able to test at the same pressures as NEL and CESAME EXADEBIT for every flow rate.

At low flow rates, the METAS tests were conducted at three pressures and two temperatures:

- 20°C, 34 bar up to 0.55 kg/min
- 20°C, 20 bar up to 0.55 kg/min
- -40°C, 31 bar up to 0.55 kg/min

To reach flow rates higher than 0.55 kg/min, the inlet pressure had to be increased. The maximum pressure tested was 88 bar.

### 2.4 KRISS

Table 3 shows the conditions tested by KRISS.

Compared to the ranges tested in the MetroHyVe project, KRISS tested at higher minimum and maximum flow rates and at lower minimum pressure and gas density.

The maximum flow rate tested was 3.76 kg/min at 40 bar, compared to 2 kg/min in the MetroHyVe project. The conditions tested by KRISS therefore included the maximum flowrate of 3.6 kg/min stipulated by the SAE J2601 standard [2], and higher velocities than those recommended by the flow meter manufacturers to the MetroHyVe partners.

**Table 3:** KRISS Test Matrix.

Pressure (bar)	Temperature (°C)	Density (kg/m <sup>3</sup> )	Mass Flow Rate (kg/min)
10	20	11.53	0.23
10	20	11.53	0.23
10	20	11.53	0.23
10	20	11.53	0.45
10	20	11.53	0.45
10	20	11.53	0.45
10	20	11.53	0.92
10	20	11.53	0.92
10	20	11.53	0.92
20	20	23.09	0.44
20	20	23.09	0.44
20	20	23.09	0.44
20	20	23.09	0.89
20	20	23.09	0.89
20	20	23.09	0.89
20	20	23.09	1.82
20	20	23.09	1.82
20	20	23.09	1.82
30	20	34.67	0.66
30	20	34.67	0.66
30	20	34.67	0.66
30	20	34.67	1.36
30	20	34.67	1.36
30	20	34.67	1.36
30	20	34.67	2.75
30	20	34.67	2.75
30	20	34.67	2.75
40	20	46.26	0.87
40	20	46.26	0.87
40	20	46.26	0.87
40	20	46.26	1.78
40	20	46.26	1.78
40	20	46.26	1.78
40	20	46.26	3.76
40	20	46.26	3.76
40	20	46.26	3.76

### 3. Flow Laboratories

#### 3.1 NEL

Meters A, B and C were tested in the NEL High Pressure Gas Flow Facility. They were installed in the 1" vent line of the flow facility. The large diameter piping upstream of the vent line served as a reservoir of pressurised nitrogen, which could be pre-heated to provide stable, near ambient temperatures at the meter under test.

An installation diagram is shown in Figure 1.

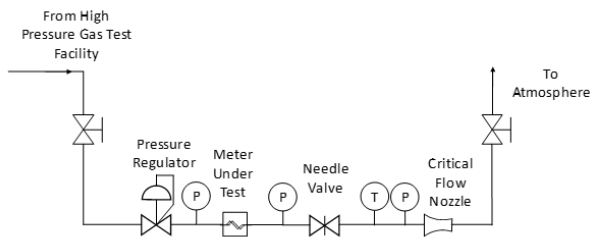


**Figure 1:** NEL Test Installation

The meter inlet pressure was set using a pressure regulator. Flow rates were controlled using a needle valve installed downstream of the test meter. Reference mass flow rates were determined using a range of critical flow nozzles installed further downstream and the nozzle outlet piping was open to atmosphere. The expanded uncertainty of the reference mass flow rate measurement is  $\pm 0.3\%$  at 95% confidence.

No heat exchanger was installed in the test section. Gas was heated upstream of the test installation to compensate for temperature drop across the pressure regulator. The internal temperature measurements of the Coriolis meters were logged, and temperatures were close to ambient for the full range of test conditions.

A temperature probe and pressure transmitter with traceable calibrations were installed at the inlet to the critical flow nozzle holder. Test points were logged only once stability was achieved for these instruments. Pressure was also measured at the outlet of the test meter.

#### 3.2 CESAME EXADEBIT

Meters A and B were tested in the CESAME EXADEBIT "M1" High Pressure Gas Flow Facility. The test rig uses dry air and operates at up to 45 bar. Very high volumetric flow rates can be achieved at low pressure, up to 5000 Nm<sup>3</sup>/hr. Critical flow nozzles are used for reference flow

rate determination, these are traceable to the CESAME EXADEBIT primary standard PVTt test rig. The measurement uncertainty of the reference nozzles ranges from  $\pm 0.2$  to  $\pm 0.3\%$  at 95% confidence.

An installation diagram is shown in Figure 2. The test meters were installed upstream of the reference critical flow nozzles. Gas was supplied at high pressure from the M1 flow facility. Flow control valves upstream and downstream of the test meter were used to set the required pressure and flow rate.

No heat exchanger was installed. Gas was provided at ambient temperature. The internal temperature measurements of the Coriolis meters were logged and were always close to ambient.

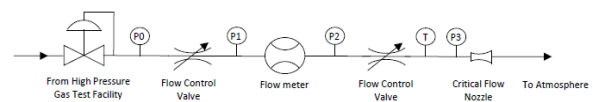


**Figure 2:** CESAME EXADEBIT Test Installation

#### 3.3 METAS

Meters A and B were installed in the METAS "Mobile Normale" Gas Flow Facility. The test rig used nitrogen delivered from a 600 L bundle at 300 bar(a). A pressure-reducing valve reduced the pressure down to 100 bar(a). The installation diagram is shown in Figure 3.

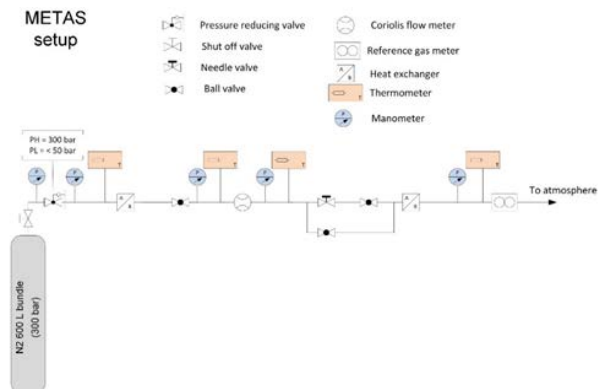


**Figure 3:** METAS "Mobile Normale" Gas Flow Facility

The test meters were installed between two heat exchangers. A heat exchanger upstream of the flow meter set the meter inlet temperature to either  $-40^{\circ}\text{C}$  or  $20^{\circ}\text{C}$ . A heat exchanger downstream of the flow meter stabilised the gas temperature to ambient temperature conditions before the gas entered the METAS reference flow meters. These are rotary type flow meters with an expanded

measurement uncertainty of  $\pm 0.3\%$  at 95% confidence.

Flow rates were controlled using a needle valve installed downstream of the test meter. Temperature probes and pressure transmitters with traceable calibrations were installed at the inlet and outlet of the test meter and at the inlet of the reference gas meter. Test points were logged only once stability was achieved for these instruments.

### 3.4 KRISS

Meter D was tested at the high pressure gas flow standard system of KRISS. As shown in Figure 4, this is a blow-down type of flow facility, consisting of two compressors, a 52.4 m<sup>3</sup> storage tank, temperature control loop and two control valves. Steady air flows are generated at pressures ranging from 0.1 to 5 MPa.

The maximum flow rate achievable is 10 000 m<sup>3</sup>/h at standard conditions (101 325 Pa and 293.15 K). Flow meters can be calibrated either against ISO 9300 sonic nozzles or the gravimetric primary standard consisting of a weighing tank and a fast-acting diverter. The expanded uncertainty of the primary standard is  $\pm 0.18\%$  at 95% confidence.

The test meter was installed at the position between the 2<sup>nd</sup> pressure control valves and sonic nozzles. In this study, nozzles with throat diameters of 1.4 mm, 2mm and 2.9 mm were used for the calibration of the Coriolis flow meter depending on the working pressure and flow-range.

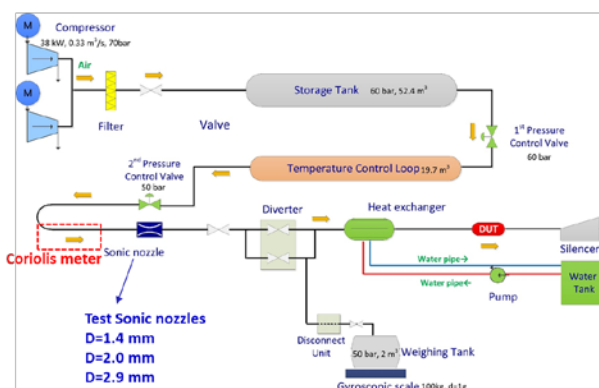


Figure 4: KRISS Test Installation

## 3. Test Results

### 2.1 NEL

Meters A, B and C were tested at NEL.

The results for Meter A are shown in Figure 5. Errors ranged from -1.26 to -0.09%. The largest error occurred at 39 bar(g) and 0.75 kg/min. All other results were within  $\pm 1\%$ . The average error was -0.54% and average repeatability was  $\pm 0.024\%$ .

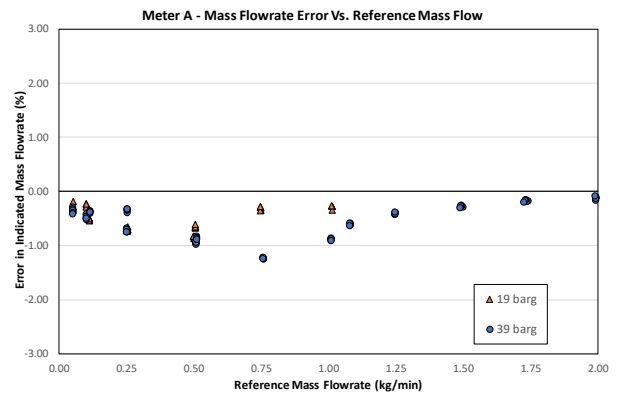


Figure 5: NEL Testing Meter A Results

The results for Meter B are shown in Figure 6. Errors ranged from -3.05 to 0.52%. The device performance was linear for most of the tested flow rates. Large negative errors occurred at low flow rates. At flow rates above 0.25 kg/min, errors were within  $\pm 1\%$ , most were within  $\pm 0.5\%$ . The average repeatability was  $\pm 0.06\%$ .

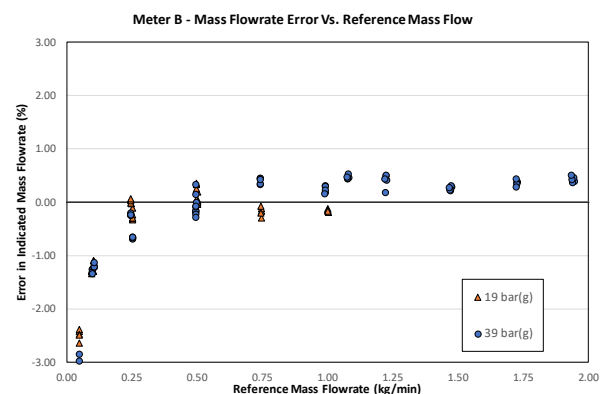
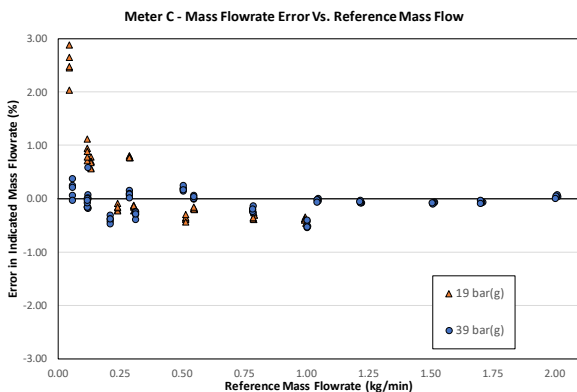


Figure 6: NEL Testing Meter B Results

The results for Meter C are shown in Figure 7. Errors ranged from -0.54 to 2.89%. The device performance was linear for most of the tested flow rates. Large positive errors occurred at low flow rates. At flow rates above 0.25 kg/min, errors were within  $\pm 1\%$ , most were within  $\pm 0.5\%$ . The average repeatability was  $\pm 0.065\%$ .



**Figure 7:** NEL Testing Meter C Results

## 2.2 CESAME EXADEBIT

Meter A and Meter B were tested at CESAME EXADEBIT.

The results for Meter A are shown in Figure 8. The performance of Meter A followed a similar trend to what was observed at NEL. Errors ranged from -1.18 to 0.41%. The largest error occurred at 39 bar(g) and 0.05 kg/min. The average error was -0.26% and average repeatability was  $\pm 0.04\%$ .

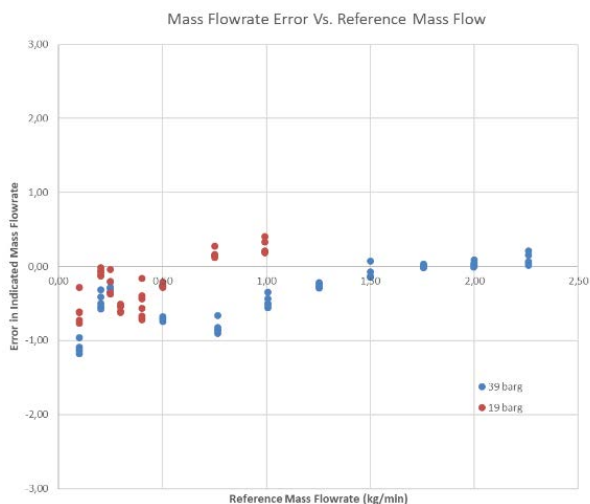


**Figure 8:** CESAME EXADEBIT Testing Meter A Results

The results for Meter B are shown in Figure 9. The performance of Meter B followed a similar trend to what was observed at NEL, but there appeared to be an overall offset of approximately -0.7%. Errors ranged from -2.16 to -0.49%. The device performance was linear for most of the tested flow rates. Errors were increasingly negative as flow rates decreased.

The largest error occurred at 39 bar(g) and 0.05 kg/min. The average error was -1.05% and average repeatability was  $\pm 0.06\%$ .

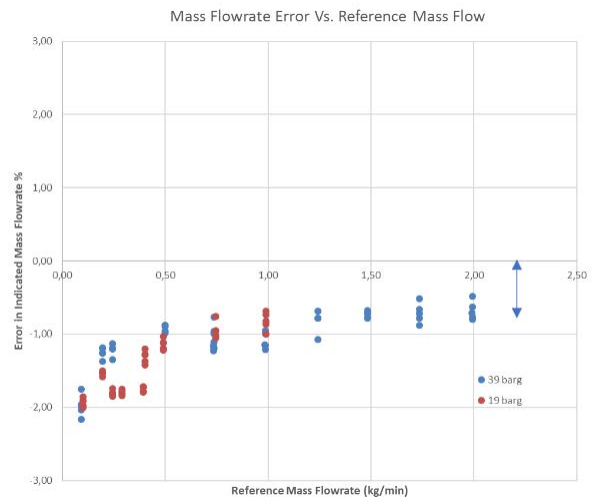


**Figure 9:** CESAME EXADEBIT Testing Meter B Results

## 2.3 METAS

Meter A and Meter B were tested at METAS.

The results for Meter A are shown in Figure 10. The largest errors occurred at flow rates of less than 0.2 kg/min. For flow rates above 0.4 kg/min, the average error was -0.8%.

Temperature appeared to have an influence on meter performance, but only at low flow rates. Larger errors and a greater spread of results occurred for the data collected at -40°C, but only at flow rates less than 0.4 kg/min. No clear inlet pressure dependence was observed.

At 20°C, repeatability was good,  $\pm 0.08\%$  at the lowest flow rate.

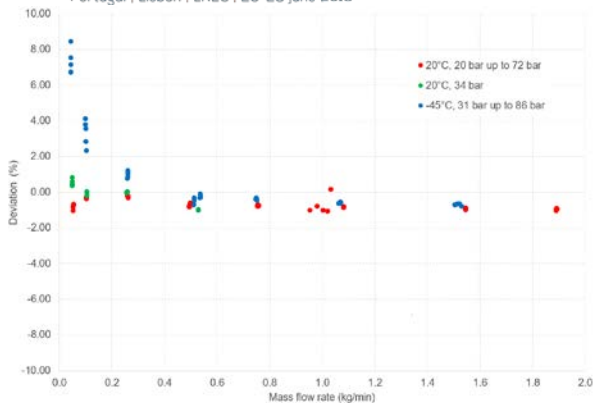


**Figure 10:** METAS Testing Meter A Results

The results for Meter B are shown in Figure 11.

Average error was 0.6% at flow rates less than 0.6 kg/min. Average errors decreased at higher flow rates to approximately 0.2% at 2 kg/min.

Larger errors occurred for the data collected at -40°C, errors were positive at flow rates less than 0.2 kg/min. Above 0.2 kg/min, errors for the low temperature data were negative, from -0.5% at 0.5 kg/min to -1% at 2 kg/min.

At 20°C, repeatability was good,  $\pm 0.1\%$  at the lowest flow rate.

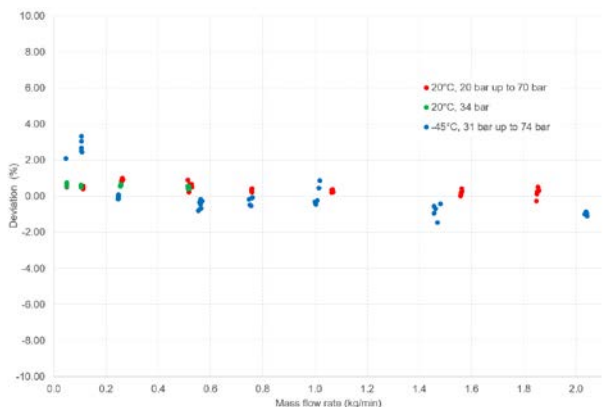


**Figure 11:** METAS Testing Meter B Results

## 2.4 KRISS

Meter D was tested at KRISS. The results are shown in Figure 12.

The meter was tested at four pressures, 10, 20, 30 and 40 bar. Errors ranged from -3.4 to 1.22 %. The largest errors occurred at flow rates below 0.5 kg/min. Above 0.5 kg/min, the meter performance was approximately linear and average error was FLOMEKO 2019, Lisbon, Portugal

0.12%. Errors exceed  $\pm 1\%$  for only a single data point in this range.

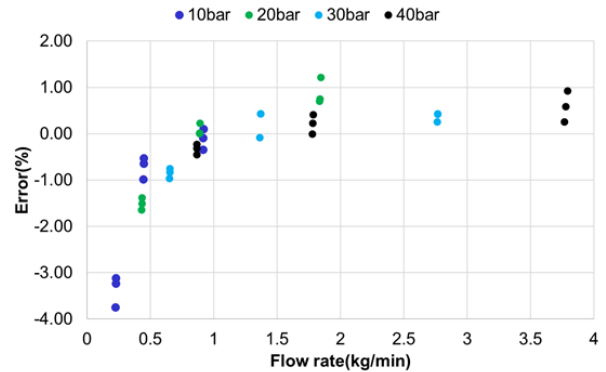


**Figure 12:** KRISS Testing Meter D Results

## 7. Conclusion

For most of the meters tested, the largest errors occurred at low flow rates. This is typical behaviour for Coriolis meters used at the low end of their operating range.

When the meters were operated at moderate to high flow rates, errors were typically within  $\pm 1\%$ . Linearity in this range was typically within  $\pm 0.5\%$ .

The meters tested were previously calibrated by their manufacturers with water. This shows the potential for calibrating meters with substitute fluids, considering the differences in density and viscosity between water and nitrogen, and the relatively low errors in the collected data.

One potential limitation of calibrating meters with substitute fluids such as nitrogen is that there will be a greater relative shift in density through the meter compared to operating with hydrogen at the same mass flow rate and inlet density. For this reason, the maximum flow rates tested in the MetroHyVe project were restricted. However, this restriction was not applied to the tests carried out at KRISS, and an influence of fluid velocity on meter performance was not observed.

An influence of temperature on meter performance was observed. Larger errors and a wider spread of results were observed when testing at -40°C. This effect was more pronounced at low flow rates.

For most of the data collected, pressure did not appear to have an influence on meter performance. At specific flowrates, differences were observed for data collected at different pressures, but an overall trend was not observed.

When installed in a hydrogen refuelling station, the meters will be subjected to a much wider range of pressures, so it is still necessary to investigate the influence of pressures up to 875 bar on meter performance. The effect of pressure up to 700 has been investigated separately within the MetroHyVe project using water.

## References

- [1] MetroHyVe. *Metrology for Hydrogen Vehicles*. [Online] <http://www.metrohyve.eu/> March 2019.
- [2] SAE J2601: *Fueling Protocols for Light Duty Gaseous Hydrogen Surface Vehicles*, SAE International, 2014.
- [3] Pope, J.G. and Wright, J.D., Hydrogen Field Test Standard: "Laboratory and Field Performance", *Flow Measurement and Instrumentation*, Vol. 46, 2015
- [4] Morioka, T., Ito, M., Fujikawa, S., Ishibashi, M., Nakao, S., "Development and evaluation of the calibration facility for high-pressure hydrogen gas flowmeters", *Flow Measurement and Instrumentation*, Vol. 39, 2014

# Augmented Intelligence Applied to Natural Gas Ultrasonic Measurement

E. Hanks, C. O'Neill

CEESmaRT, 1170 Hwy 51, Ponchatoula LA 70454, USA  
ehanks@ceesmart.com, coneill@ceesmart.com

## Abstract

We hear a great deal in the news about how Artificial Intelligence and the Internet of Things (IoT) is changing our lives, and how it will transform businesses across the globe. It's likely your business is already using some form of intelligence technology today. Research shows that on average nearly 80% of analysts' time is spent collecting and gathering data, while less than 20% of their time is spent analysing and communicating results to stakeholders. This paper explores the extent to which the application of Augmented Intelligence developed from continuously collected metering diagnostics can automate measurement analysis. The paper analyses the results of applying augmented intelligence methods to natural gas ultrasonic metering systems. The paper demonstrates that integrating augmented intelligence techniques into operations improves efficiency by 1) lowering the operator's time to resolve measurement issues, 2) lowering the number of adverse events 3) allowing for a greater focus on problematic stations. The result is that operators lowered their exposure to measurement error. The analysis indicates a steadily decreasing exposure to measurement error risk over time. After 4 years of implementation, the augmented intelligence methods were reducing risk by 1.3 Bcf/year (\$4M at \$3/Mscf) per 100 meter sites.

## 1. Introduction

Augmented Intelligence and Internet of Things are here and advancing business processes across the globe. It is estimated that by 2020, there will be around 30 billion IOT connected devices. These IOT devices generate vast amounts of data that can be difficult to effectively or efficiently understand. That's where augmented intelligence comes into play. Augmented Intelligence helps humans and machines come together to solve complex issues, reduce costs and achieve safer, faster results in a multitude of industries. In today's market, your business requires real-time awareness and data that AI provides, in turn, providing you with improved results and advanced decision making.

## 2. Time Spent on Data Analysis

Augmented intelligence systems make analysis more efficient and accurate by automating much of the work and decisions that analyst routinely perform. Figure 1 below illustrates current research breaking down how data analysts spend their time. The table shows that analyst spend less than 20% identifying insights and communicating these insights with stakeholders. They spend over 80% of their time gathering, cleaning, visualizing, selecting and applying analysis techniques.

Effective augmented intelligence automates much of this work [1].

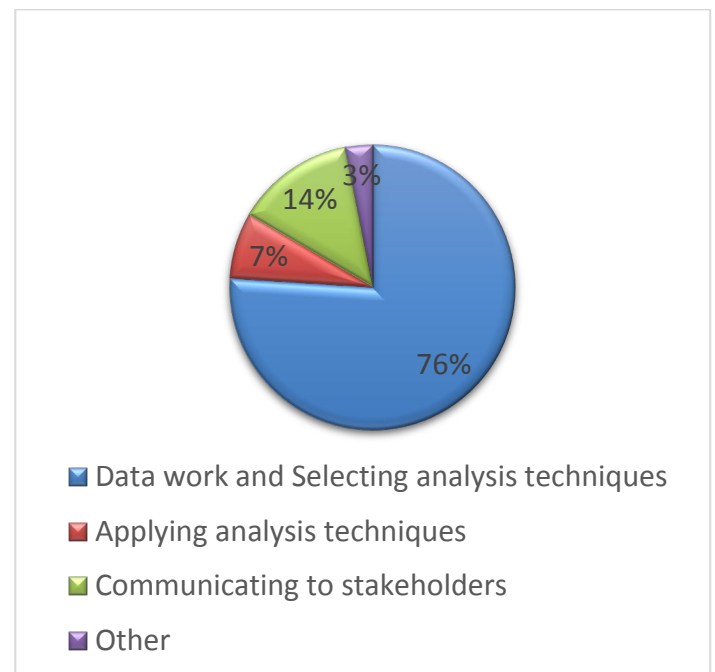


Figure 1: Time Data Analyst Spend on Job Task

### 3. Current State of Practical Machine Learning

News articles on augmented, or artificial, Intelligence tend to focus on cutting edge research using advance machine learning techniques such as Neural Networking and Deep Learning. However, current research shows that the most common techniques implemented by today's analysts are more mundane such as Regression and Time Series Analysis, Decision Trees, Rules, Visualization, Statistics, and Clustering [2]. Figure 2 illustrates the findings.

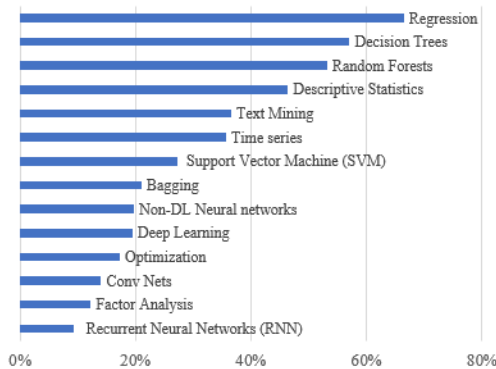


Figure 2: Respondents use of machine learning techniques [2]

Modern natural gas ultrasonic metering equipment produce tremendous amounts of diagnostic data. The question is, can current machine learning techniques be applied to the diagnostics to make measurement analysis more efficient?

### 4. Analysis of Augmented Intelligence Methods

This paper analyzes results from four years of augmented intelligence methods applied to natural gas ultrasonic metering systems. The data set from CEESmaRT includes a diverse array of metering equipment (meter sizes, brands, and geometries; flow computer brands; chromatograph brands; temperature and pressure transmitters; etc.).

The data was normalized to express the results per 100 meter stations. Of the total events detected by the augmented intelligence:

- 46% of the events detected included sufficient diagnostics information to estimate an error and provide maintenance recommendations, such as replacement of ultrasonic meter transducers, meter cleaning and/or removing debris from in front of the flow conditioners, or various flow computer, chromatograph,

pressure and temperature transmitter failures. Uncertainty estimates were developed from data sets collected at an ISO 17025 laboratory [3].

- 52% of the events detected contained sufficient information to identify preventative maintenance or non-critical equipment failures that did not cause an appreciable increase in uncertainty such as degradation in a ultrasonic meter transducer performance, ultrasonic noise effecting the meter, chromatographs in hold mode or not auto-calibrating, and pressure or transducer drift.
- 2% of the events detected identified a problem, but the failure was such that there was not sufficient diagnostic information to reasonably estimate an error or an increase in uncertainty such as total equipment failures.

The events were divided into 5 major categories: 1) UFM transducer and electronics issues, 2) Flow Computer issues, 3) Contamination and/or debris in the meter tube, 4) Pressure and Temperature measurement issues, and 5) Chromatograph issues. Figure 3 illustrates the average results for the entire four-year period.

Issue	% of sites	Events per Year	Resolution days (avg)	Impact (Mscf)
USM Transducers & Electronics	21%	37	70	608,734
Flow Computer	7%	8	38	375,681
USM Dirty/Debris	13%	21	78	164,070
P&T Transmitters	9%	12	46	73,188
Chromatographs	30%	44	49	170,950
	55%	123	59	1,854,556

Figure 3: Average Event Detection Results

For each of the categories the table illustrates the percentage of sites where an event was detected, the average number of events, the average time required to resolve an event, and the impact of the event (error or increased uncertainty given in units of Mscf).

#### 4.1 Analysis of Response Time

For the four-year period, the number of days it took to correct an issue averaged 59 days. This response time includes several factors: 1) prioritizing the event, 2) ordering parts as needed, 3) scheduling the equipment and resources need to perform the work, 4) and making operational arrangements to perform the work, for example scheduling a shutdown for maintenance.

Figure 4 below shows that over the four-year period, the response time decreased by 34%. The result suggests continual improvement as operators learn to trust and use augmented intelligence.

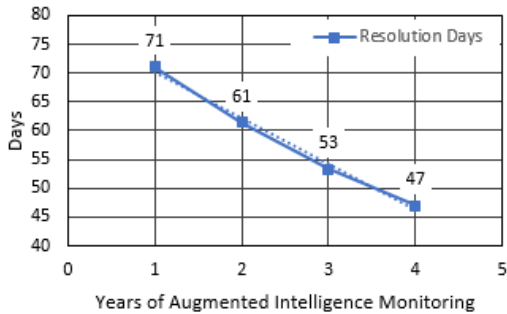


Figure 4: Average Response Time Per Year

#### 4.2 Analysis of the Detected Events

Over the same four-year period, on average 123 events were detected per year. Figure 5 below illustrates the trend over the four-year period.

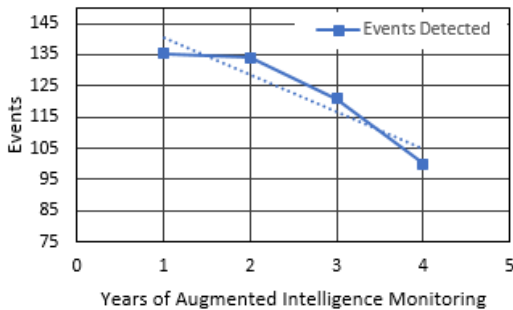


Figure 5: Average Number of Events Per Year

Like the resolution time, the trend also decreased (26% over the period), again suggesting that continued use and familiarity with the augmented intelligence had a positive impact on measurement operations.

The analysis also showed that the percentage of sites where augmented intelligence detected issues decreased by 44% over the four-year period. Figure 6 below illustrates the trend.

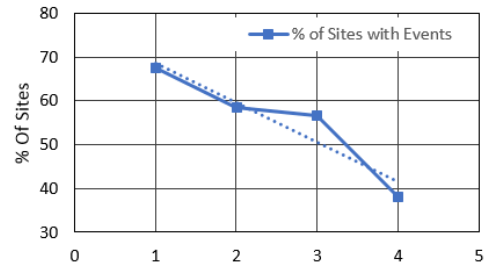


Figure 6: Average Number of Sites with Events Per Year

Combining the previous two findings shows that over time the events are concentrated at particular sites, allowing operation teams to focus their resources on problematic sites. Figure 7 below illustrates this. Over the four-year period the number of events per year at sites with an event increased by 30% (on average from 2 to 3 events per year).

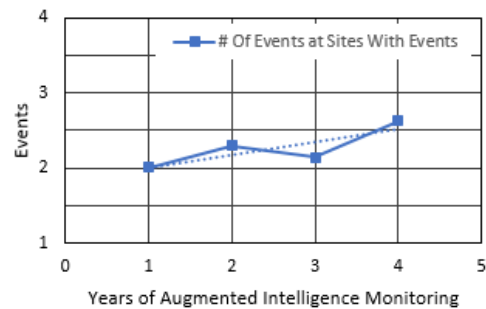


Figure 7: Average Number of Events at Sites with Identified Events

#### 4.3 Analysis of the Impact

Thus far, the analysis shows that as augmented intelligence methods are trusted and integrated into operations, the results are:

- A decrease in event resolution time.
- A decrease in the number of events.
- A greater focus on problematic stations.

Figure 8 below illustrates the final impact of augmented intelligence. The downward trend shows that the operator's exposure to measurement risk.

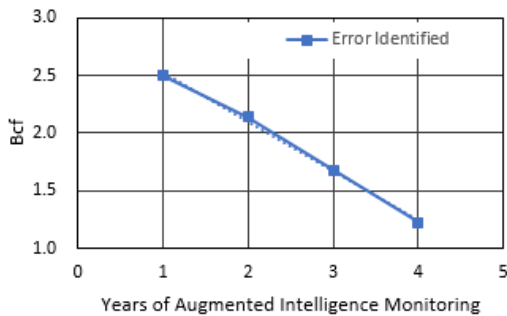


**Figure 8:** Impact of augmented intelligence.

Figure 8 shows that in the initial year of the implementation of augmented intelligence monitoring, 2.5 Bcf of error were identified. By year 4 the amount had been reduced to 1.2 Bcf. Therefore, in year 4 the augmented intelligence methods reduced measurement error exposure by 1.3 Bcf (\$4M at \$3/Mscf).

## 5. Conclusion

The analysis shows that application of augmented intelligence can significantly improve the efficiency of measurement analysis. The analysis shows that as operators integrate these techniques into their operations, they lower the number of measurement events, decrease the resolution time, and can focus their resources on problematic sites, resulting in a reduction in exposure to lost and unaccounted for gas. The analysis indicates a steadily decreasing exposure to measurement error risk over time. After 4 years of implementation, the augmented intelligence methods were reducing risk by 1.3 Bcf/year (\$4M at \$3/Mscf) per 100 meter sites.

## References

- [1] Bob Hayes, Business over Broadway, <http://businessoverbroadway.com/2019/02/19/how-do-data-professionals-spend-their-time-on-data-science-projects/>
- [2] Gregory Piatetsky, KDnuggets, <https://www.kdnuggets.com/2017/12/top-data-science-machine-learning-methods.html>
- [3] Randy Miller, Ed Hanks, "A History Of Naffmc Installation Effects Testing Including Current Testing"

# Best Practices for Proving Coriolis Meters with Small Volume Provers

M. Buttler<sup>1</sup>

<sup>1</sup>Emerson, 7070 Winchester Circle, Boulder, CO, 80301, USA  
E-mail: Marc.Buttler@Emerson.com

---

## Abstract

Coriolis meters have many advantages for mass flow and volumetric measurement in a wide variety of applications. Inherent reliability, linearity, and stable meter factor (MF) on a wide variety of products make them an ideal choice for pipeline transfer. With the recent introduction of high flow rate meters, Coriolis technology can now be used in line sizes up to 16". Custody transfer of products is very common in these large pipelines; in many applications contractual requirements dictate that meters be proved in situ periodically to ensure accurate measurement over time and/or product changes.

Traditionally, large pipe provers have been employed at metering stations. The overall size of a pipe prover and the maintenance costs of the complex four-way valve integral to a bi-directional pipe prover can be a concern. Small volume "piston-type" provers are becoming more common because they have a much smaller foot-print and reduced maintenance costs. Even the largest small volume provers are small (as much as 10 times smaller) compared to pipe provers of similar flow capacity. Small volume provers tend to perturb the flow rate when the piston launches. Because the measuring volume of a small volume prover is so much smaller, this rate change caused by the operation of the prover becomes an integral part of the proving cycle that is measured by the metering device.

Proper sizing of a small volume prover to pair with a Coriolis meter(s) can result in greater proving efficiency, optimum prover size, and reduced maintenance on the prover. This selection and pairing process is especially important when using small volume provers to prove high-precision, high-flowrate Coriolis meters. Data collected to validate Coriolis meter performance with small volume provers in lab testing and field proving has been analyzed to determine which procedural and design factors yield the best results. This analysis has resulted in the development of the concept called "Total Prove Time" (TPT).

In addition, proving methods that apply incremental uncertainty analysis to determine when proving is completed will afford operators the opportunity to attain even greater efficiency. This method of proving involves continuing to collect runs until the repeatability that is equivalent to a meter factor random uncertainty of better than  $\pm 0.027\%$  has been reached. This method is outlined in the American Petroleum Industry (API) Manual of Petroleum Measurement Standards (MPMS) Chapter 4.8, Second Edition, Operation of Proving Systems, Annex A, Evaluating Meter Proving Data.

The TPT concept is simple to apply and useful for selecting a small volume prover and Coriolis meter to achieve maximum freedom of choice between prover size selection and operational trade-offs including wear and tear. Diagnostic tools for enhancing overall measurement systems design, troubleshooting, and assessing future pipeline capacity expansions are another benefit that have resulted from this research.

---

## 1. Introduction

Proper sizing of a meter prover and flow meter(s) can result in greater proving efficiency, minimum prover size and cost for stationary provers, and reduced wear and tear on the prover. This selection process is exceptionally important when using small volume provers to prove high-precision, high-flowrate meters. Data collected to validate Coriolis meter performance with small volume provers in lab testing and field proving has been analyzed to determine which procedural and design factors yield the best results. This analysis has resulted in the development of the concept called “Total Prove Time” (TPT). The TPT concept is a useful tool for pairing a small volume prover with a high-precision, high-flowrate meter to achieve maximum freedom of choice between prover size selection and operational trade-offs including wear and tear.

In addition, proving methods that apply incremental uncertainty analysis to determine when proving is completed will afford operators the opportunity to attain even greater efficiency. This method of proving involves continuing to collect runs until the repeatability that is equivalent to a meter factor random uncertainty of better than  $\pm 0.027\%$  has been reached. This method is outlined in the *American Petroleum Industry (API) Manual of Petroleum Measurement Standards (MPMS) Chapter 4.8, Second Edition, Operation of Proving Systems, Annex A, Evaluating Meter Proving Data*.

## 2. Basics of Meter Proving

There are three main reasons to prove meters:

- To make the meter measure accurately using a traceable Meter Factor.
- To determine how much different process conditions affect the Meter Factor.
- To assess the proving data as a diagnostic of meter health.

Meter proving establishes a Meter Factor (MF) that reflects the accuracy performance of the meter under actual application conditions and with the actual fluid(s) that are being metered. The MF is determined by how the meter indicates flow compared to a traceable flow measurement field reference standard. The MF is applied to future measurements so that the meter indications will reflect traceability to the prover. Proving must be done on an ongoing basis to establish the MF over time for those metering technologies that may drift due to meter wear.

It is important to prove a meter at all the different conditions that it will see in service. If different flow rates will occur, proving should occur at each flow rate. If different fluid products will be metered, as in multi-product pipelines, proving should be done with each fluid. Proving at all conditions and on all fluids will reveal whether or not the MF will be the same or different as conditions change. If the MF changes as conditions change, it will be necessary to apply an array of different Meter Factors to apply the correct one for current conditions each time the conditions change.

Analysis of meter proving data patterns can provide indications of when a meter may need repair or replacement. For example, if the repeatability of the proving data should suddenly become more erratic, or if an uncharacteristically large shift in the average MF compared to the last proving should occur, this would normally be a good indicator that the meter should be thoroughly inspected and/or refurbished.

Two important metrics are applied to judge the quality of proving results:

- Repeatability
- Reproducibility

Repeatability is a measure of short-term variability in the proving data from each proving event. Repeatability performance is critical because it is used during proving to decide whether the prove has been successful or has failed to comply with the minimum standards as defined by industry standards such as the *American Petroleum Institute Manual of Petroleum Measurement Standards Chapter 4.8 (API MPMS Ch. 4.8) Operation of Proving Systems, Second Edition*.

API MPMS Ch. 4.8 prescribes several different methods that can be applied to assess the repeatability of proving data. All are designed to ensure that the uncertainty of the average meter factor that is the result will be 0.027% or better. If repeatability fails, it is common practice to discard the data and start over with a new proving attempt.

Reproducibility is the long-term stability and variation of the Meter Factors that were found for a meter resulting from a long series of proving events over time. Reproducibility is also critical because it is the best indication of how accurately the meter is measuring product during all the time that it is in service between proving events. If the MF that results changes from one proving event to the next, this should be a concern because this indicates that

the true measurement accuracy may also be varying considerably on an ongoing basis.

The variation in MF from one prove to the next (i.e., reproducibility) is typically not used to decide whether to reject any one set of proving data in the same way that the repeatability is used. However, many meter operators will define limits on the reproducibility variation that will result in action being taken, such as meter inspection and/or replacement if the MF value varies by too much from one prove to the next.

The reproducibility is also the only indicator of how wear and tear over time may be affecting the meter measurement accuracy. The repeatability will not reveal this because it is based entirely on a set of data that is all collected over a relatively short period of time (i.e., one proving event).

Proving methods fall into two main categories and several sub-categories:

- Fixed-volume static provers
- Fixed-volume dynamic provers
  - Ball / Pipe conventional provers
    - Bi-directional
    - Uni-directional
  - Compact/Small-volume provers
- Master meter provers
  - Volume meter (e.g., PD, turbine)
  - Coriolis meter (for mass and/or volume)

An example of a small volume prover is shown in Figure 1. The subject of this study focuses on fixed-volume dynamic provers and how they interact and perform with high-precision, high-flowrate meters while proving.

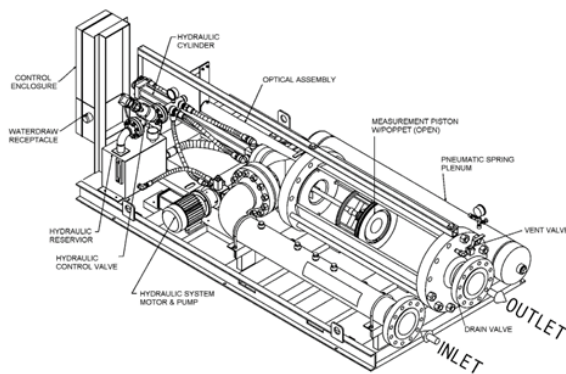


**Figure 1:** Small Volume Prover [1].

By their nature, fixed-volume dynamic provers are constrained to collecting data only during each pass of the displacer (i.e., the ball or the piston). Furthermore, as the flow rate becomes higher, the time that it takes for each pass of the displacer in a fixed-volume prover gets shorter and shorter as shown in Figure 2. It is the statistical analysis of this type of data that is of greatest interest here.

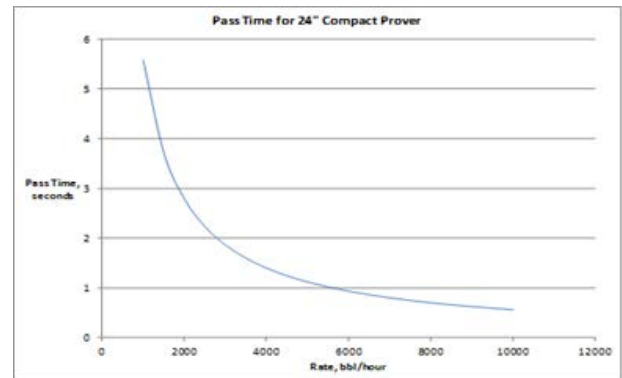


**Figure 2:** Pass Time vs. Flow Rate [1].

Proving with a master meter is not constrained by a fixed volume. Because the size of each proving run can be made as long or as short as desired with a master meter proving system, the fundamental concerns of this study do not apply.

### 3. Importance of Meter Response Speed with Small Volume Provers

Proving can present many challenges. The flow rate and other conditions must remain stable to ensure good repeatability. However, it is often quite possible that the proving equipment may cause unintended instability in the flow rate. For example, if a proving sphere is over-inflated, this can result in jittery flow as the ball slides past the walls of the pipe prover. Even more commonly, a small volume prover can cause a sudden change in the hydraulic resistance of the prover system when the poppet valve in the displacer closes to launch a proving pass. This change in the pressure drop across the displacer can result in a sudden change in the flow rate through the entire system, including the meter.

Meters must have sufficient speed of response to be able to prove successfully in situations where the flow rate is unstable during proving runs. Figure 3 shows an example of sufficient meter speed of response. In this case, the indicated rate has caught up to the true flow rate prior to the displacer reaching the first detector switch D1, so all the data collected between the two detector switches D1 and D2 is valid because it represents a period while the meter is indicating the true flow.

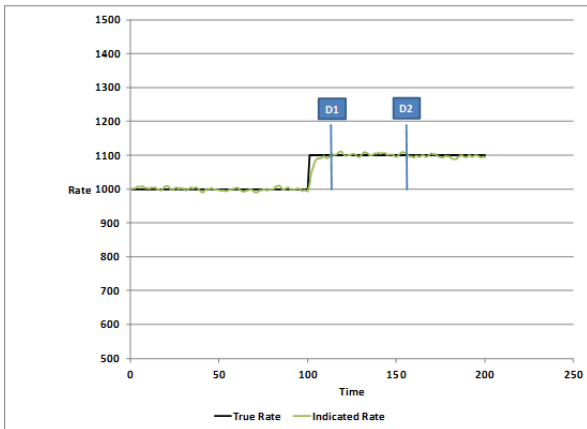


**Figure 3:** Sufficient Speed of Response [1].

Conversely, Figure 4 shows an example where the meter has insufficient speed of response. In this case, the indicated rate is still approaching the true flow rate as the displacer reaches the first detector switch D1. The total volume indicated by the meter for the period when the displacer is between the two detector switches D1 and D2 will be missing a small amount that is equal to the difference between the true flow rate and the indicated rate for the time that it takes for the meter indication to catch up to the true flow rate.

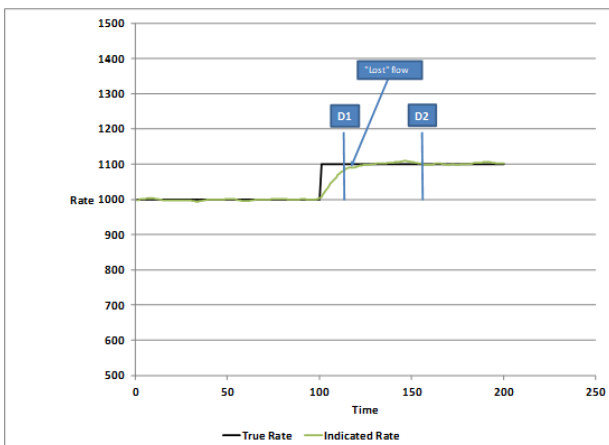


**Figure 4:** Insufficient Speed of Response [1].

The speed of response that will be required depends on the time that it takes for the displacer to reach the first detector switch D1 after it has been launched. This time and the related volume are known as the “pre-run” of the prover.

Mechanical meters (e.g., PD, turbine) have speed of response that is dependent on the inertial damping which will determine how quickly the angular momentum of the mass of the rotating elements of the meter can respond to changes in the flow rate.

Coriolis and Ultrasonic meters output manufactured pulses that are produced by microprocessor electronics to represent the measured flow. These manufactured pulses are subject to the response rate of the meter electronics signal processing speed and any additional delay selected by electronic filtering/damping settings. Electronic filtering/damping settings in these types of devices should be set to respond as fast as possible for proving applications. However, this will lead to the flow indication being noisier. Noisier flow indication can lead to repeatability issues if the prover pass time gets shorter due to a smaller prover size and/or an increasing flow rate.

#### 4. Prior Meter Testing

Prior studies on this subject [1] have analyzed data collected with small volume provers together with large Coriolis meters in both laboratory and field environments. Some of this earlier work was done to establish good estimates for the noise levels of flow meter indication as a function of flow rate and meter size.

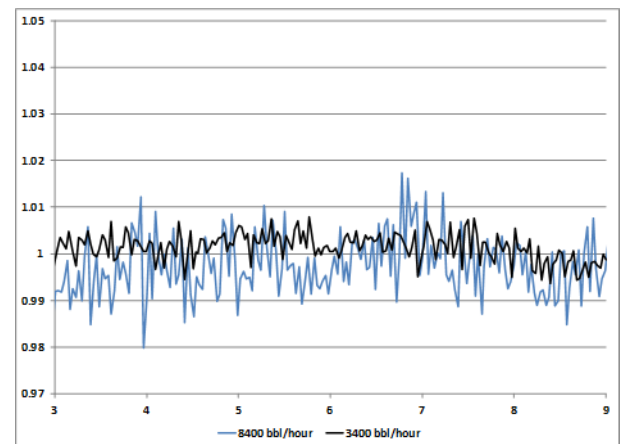


**Figure 5:** Normalized Noise Levels and Increasing Flow Rate [1].

These estimates have demonstrated that the normalized flow indication as shown in Figure 5 will consistently have an increasing noise level as the flow rate increases. A good correlation has been observed between the velocity of the fluid passing through the meter’s flow tubes and the noise level of the flow indication when the meter damping is set for the fastest possible speed of response.

#### 5. Estimated Minimum Total Prove Time (TPT) and Prover Sizing

The uncertainty of the average of the flow total output by a meter during the period of a single pass of a prover displacer is a function of the time

duration of that prover pass and the standard deviation of the meter flow indication noise. This relationship is shown in equation (1) where  $\sigma$  is the standard deviation of the flow indication, and  $n_{pass}$  is effective number of flow readings computed by the meter in the time that it takes for the displacer to pass between the two detector switches, which is also the time interval during which pulses from the meter are being counted.

$$U_{pass} = \frac{2\sigma}{\sqrt{n_{pass}}} \quad (1)$$

The uncertainty of the meter factor that results from a proving event is equal to the uncertainty of the average of the meter factors from all the runs taken. The uncertainty of each run was estimated by equation (1). One way to estimate the combined uncertainty of the average meter factor from a proving event is shown in equation (2) where  $n_{prove}$  is the effective number of flow readings for each pass ( $n_{pass}$ ) times the total number of passes taken for the prove.

$$U_{prove} = \frac{2\sigma}{\sqrt{n_{prove}}} \quad (2)$$

Together, equations (1) and (2) illustrate that the uncertainty of the average Meter Factor from a proving can be related to two factors:

- The noise level of the indicated flow output, and
- The total amount of time that data is collected from the meter.

The noise level of the indicated flow signal can be predicted from experience and testing at different flow rates through different flow meter sizes and geometries. With these predicted noise levels, it becomes possible to construct a model for predicting the minimum amount to total data collection time that may be needed to achieve the 0.027% uncertainty for the MF that is the goal of proving, as described in API MPMS Ch. 4.8. This total amount of accumulated time for data collection during a prove is referred to as Total Prove Time (TPT) and is defined in equation (3).

$$TPT = \frac{\text{Base Prover Volume (BPV)}}{\text{Flow Rate}} \times (\text{\# of runs}) \times (\text{\# of passes per run}) \quad (3)$$

With TPT defined in this way, it becomes possible to state the estimated minimum TPT that will be required to pass API requirements and thus achieve 0.027% MF uncertainty. It is important to note that estimated minimum TPT values are based on the anticipated flow indication noise levels observed during past experiences and testing, and that these numbers are conservative. In applications where the flow noise is less than the norms observed in the past, it may be possible to meet API repeatability requirements with less TPT than was estimated.

There are two methods whereby an estimated minimum required TPT could be used to help size the flow meter and the prover to work well together in a measurement system. The first method is to start by settling on a total number of passes that will be taken during proving and then calculate the Base Prover Volume (BPV) that will be needed to pass repeatability 95% of the time with that number of passes. This relationship is shown in equation (4).

$$BPV = \frac{TPT \times \text{Flow Rate}}{(\text{\# of runs}) \times (\text{\# of passes per run})} \quad (4)$$

The second method is to start by selecting a desired prover size and then use that to calculate the total number of passes that will be needed to pass repeatability at that flow rate with a prover of that size using equation (5).

$$(\text{Total \# of passes}) = TPT \times \frac{\text{Flow Rate}}{(BPV)} \quad (5)$$

Once the total number of passes is known, this will either be equal to the total number of runs in the case where each run will consist of a single pass, or the total number of runs that will be needed can be determined by dividing the total number of passes needed by the number of passes that will be averaged per run.

The estimated minimum TPT can also be used as a troubleshooting tool when a measurement system is having problems passing repeatability consistently. By comparing the TPT that is actually being accumulated during a prove during the current process to the estimated minimum TPT stated by the manufacturer, it is possible to gauge how close these two values are to each other. If the actual TPT is close to the estimated minimum TPT, then it is likely that the meter will start passing repeatability by simply adding as many additional passes as it will take to accumulate the estimated minimum TPT. If, however these two values are very far apart, this will be a strong indication that either a larger meter size or a larger prover size or both will be needed to improve the situation.

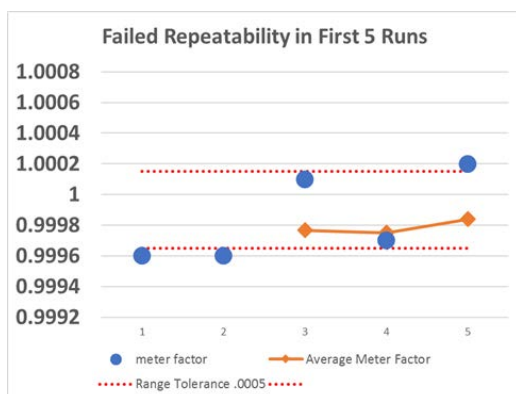
There are four key points to consider related to these conclusions about the relationship between flow rate, meter size, and TPT:

- A larger prover (BPV) means that, for a given flow rate, the time for each pass of the prover, and thus  $n_{pass}$ , will be greater, so fewer passes should be needed to reach  $n_{prove}$  and to pass repeatability requirements.
- More passes will mean that  $n_{pass}$  can be less, so a smaller prover (BPV) could be possible to use successfully.
- More passes can be added without changing the number of runs per prove if you average multiple passes per run, as explained in API MPMS Ch. 4.8.
- For any given flow rate, a larger meter size will result in a lower velocity flowing through the meter flow tubes and a lower noise level in the flow output, so less TPT should be required. In this way, increasing the meter size could open the door to successful proving with a smaller prover and/or fewer passes than would otherwise be needed.

## 6. Incremental Uncertainty Analysis for Proving Efficiency

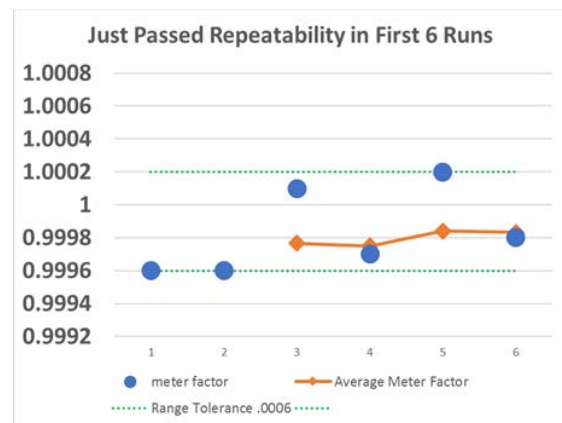
We have seen how each additional run added to a set of proving data has the potential of turning a meter proving that is failing to meet repeatability requirements into a successful proving with a MF uncertainty of 0.027% or better.

Figure 6 shows an example set of five proving runs. These are failing repeatability because the difference between the maximum and the minimum Meter Factors exceeds the tolerance of 0.0005 (0.05%) taken from API MPMS Ch. 4.8 for a MF uncertainty of 0.027%. In fact, the uncertainty of the average MF according to equation (2) would be 0.032% in this case.



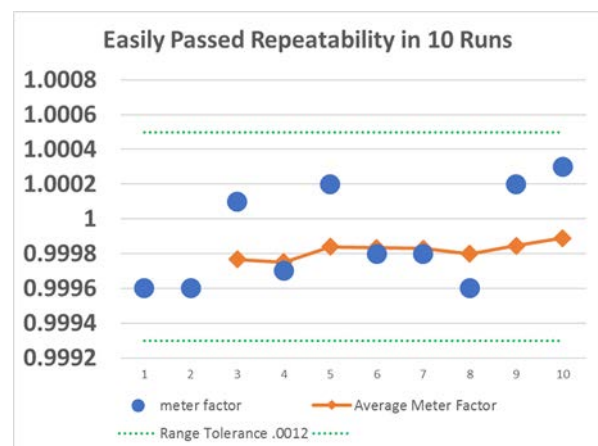
**Figure 6:** Failing Repeatability with 5 Runs [2].  
FLOMEKO 2019, Lisbon, Portugal

The same set of five proving runs will pass with the addition of just one additional run as shown in Figure 7. Although the addition of the sixth run has not changed the value of the difference between the maximum and the minimum Meter Factors because this new point falls between those two previous extremes, the result has changed because the tolerance from API MPMS Ch. 4.8 for six data points is now 0.0006 (0.06%). This new wider tolerance still results in the target uncertainty for the average MF of better than 0.027% because the additional run has reduced the uncertainty of the average. In this case, the uncertainty of the average MF according to equation (2) would be 0.025% because of the additional point that was added.



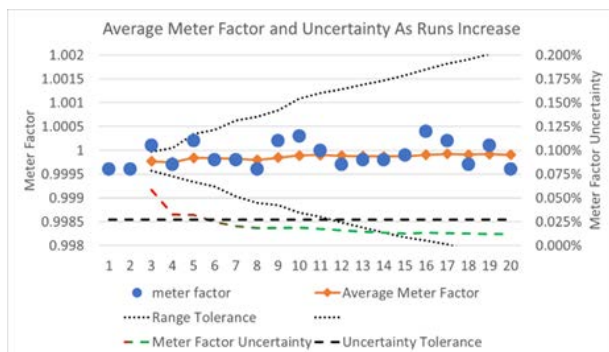
**Figure 7:** Passing Repeatability with 6 Runs [2].

Figure 8 shows that, with another additional four runs, making a total of ten runs for the prove, the meter passes the repeatability requirements easily because the tolerance from API MPMS Ch. 4.8 to meet a MF uncertainty of 0.027% or better with a set of 10 runs is a difference between the maximum and the minimum Meter Factors not to exceed 0.0012 (0.12%). The uncertainty of the average MF in this case, according to equation (2) would be 0.019%.



**Figure 8:** Passing Repeatability Easily with 10 Runs [2].

In Figure 9, the increasing Range Tolerance from API MPMS Ch. 4.8 is shown as expanding while the number of runs increases up to 20. Similarly, the uncertainty of the MF average according to equation (2) continues to decrease as more runs are added until it drops below 0.027% uncertainty. Although the uncertainty of the average MF continues to drop as more runs are added, it is worth noting that the actual average MF value itself changes only negligibly after the first six runs.



**Figure 9:** Tolerances and Uncertainty with 20 Runs [2].

A proving method that makes use of the incremental improvement to the average MF uncertainty that comes with each additional point would help to improve efficiency and minimize wear and tear on provers during operation. The basis of the method would be to avoid deciding how many runs or passes to take prior to proving, but instead just continue taking one more run until you reach the point where the 0.027% target uncertainty for the average MF has been reached. This approach would bring three benefits compared to a method that commits to a fixed number of passes and/or runs in advance of proving.

- It will always eventually achieve the target 0.027% average MF uncertainty.
- It will achieve the target uncertainty with the minimum number of passes, saving time and wear on the prover by eliminating unnecessary additional runs.
- It will avoid unnecessary additional runs and wasted data that happens when proving fails to meet repeatability and the process is started over at the beginning.

## 7. Conclusion

Meter proving is an essential function in some systems used for critical custody transfer and fiscal measurements. Selecting the right equipment and operating and maintaining it properly will enable good traceable measurements with the smallest possible uncertainty. The response speed of the meter and the size of the prover are important variables to consider in system design and operation.

Collecting more data while proving reduces the uncertainty of the Meter Factor. Repeatability during proving is a good measure to ascertain the uncertainty of the meter factor. By using a flexible approach in determining the number of runs to take, the optimum balance between proving efficiency, maintenance costs, and capital cost of equipment can be reached.

## References

- [1] T. Patten, "Proving Coriolis Meters with Small Volume Provers", *34<sup>th</sup> International North Sea Flow Measurement Workshop*, 2016.
- [2] M. Buttler, "Pairing Small Volume Provers with High-Precision, High-Flowrate Meters", *North Sea Flow Measurement Workshop*, 2018.

# Redefinition of standard equation for discharge coefficient of throat-tapped flow nozzle

Noriyuki Furuichi<sup>1</sup>, Yoshiya Terao<sup>1</sup>

<sup>1</sup>National Institute of Advanced Industrial Science and Technology, National Metrology Institute of Japan, 1-1-1, Umezono, Tsukuba, Japan  
E-mail (corresponding author): furuichi.noriyuki@aist.go.jp

## Abstract

Throat-tapped flow nozzle, which is widely used in power plants, are examined for several geometric parameters, throat-tap and upstream-tap diameter, surface roughness of nozzle and so on. It is found that the largest influence factor is the throat-tap diameter. According to the experimental result, new equations for the throat-tapped flow nozzle are proposed. All experimental discharge coefficient is within  $\pm 0.5\%$  of the proposed equations.

## 1. Introduction

Throat-tapped flow nozzle which is one of differential pressure flow meter is widely used in electric power plant. For example, ASME PTC 6 [1] requires using the throat-tapped flow nozzle to evaluate the steam turbine in fire power plant. Furthermore, the throat-tapped flow nozzle is used in nuclear power plant to manage a thermal output. Thus, the role of the throat-tapped flow nozzle is very important for electric power plants.

The standard equation for discharge coefficient of the throat-tapped flow nozzle is defined in ASME PTC 6 and PTC 19.5 as following,

$$C_{PTC6} = k_t - \frac{0.185}{Re_d^{0.2}} \left( 1 - \frac{361239}{Re_d} \right)^{0.8} \quad (1)$$

where,  $Re_d$  is Reynolds number based on a diameter of the throat area of the nozzle. The nominal value of the first term of the right-hand side is 1.0054. ASME PTC 6 requires that  $k_t$  is decided by the fitting of actual calibration data and it satisfies the range;  $1.0029 < k_t < 1.0079$ . This means that the discharge coefficient obtained by the actual calibration should be within  $\pm 0.25\%$  from Eq.(1) with  $k_t=1.0054$ . However, we obtained over ranged experimental discharge coefficients in past examinations [2],[3]. In Fig. 1, the experimental discharge coefficients,  $C_x$  given by authors [2] and

Reader-Harris et al.[3] are shown. This figure indicates the following two issues. The first is the influence of the diameter of the throat-tap;  $d_t$ . The discharge coefficient increases with the diameter of the throat-tap. ASME PTC 6 defines that Eq. (1) is available for  $d_t = 3.125 - 6.25$  mm. The difference between each throat-tap is 1.5% at maximum and it is not small to ignore the influence of the diameter of the throat-tap.

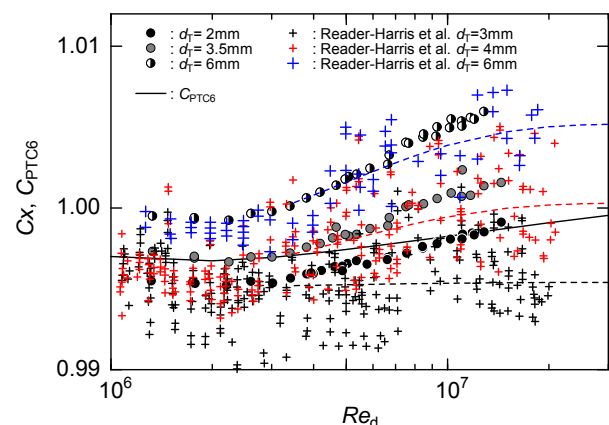


Figure 1: Discharge coefficients for throat-tapped flow nozzle by Furuichi et al. [2] and Reader-Harris et al [3].

The second issue is the experimental result of the discharge coefficient for high Reynolds number region. The increasing ratio of the discharge coefficient with Reynolds number is larger than Eq.(1). Consequently, the experimental discharge coefficient is largely deviated from Eq.(1) for larger

tap diameter, although it is within 0.25% for low Reynolds number region. The throat-tapped flow nozzle is generally used in power plants and the Reynolds number is up to  $10^7$ . This large difference at high Reynolds number region should be noticed with carefully.

According to the experimental results, we have proposed new equation of the discharge coefficient of throat-tapped flow nozzle in the previous reports [4]. In this paper, additional experimental results for the throat-tapped flow nozzle are presented and proposed the final equation of the discharge coefficient. As mentioned in previous, authors have been done many researches for the throat-tapped flow nozzle [2],[4]-[6]. This paper is a summary of these research works.

## 2. Experiments

The cut model of the throat-tapped flow nozzle is shown in Fig. 2. The parameters influenced to the discharge coefficient are throat diameter;  $d$ , pipe diameter;  $D$ , throat-tap diameter;  $d_t$ , upstream-tap diameter;  $d_u$  and surface roughness. In the series of the experiments, we examined for many nozzles with different geometric parameters shown in Table 1.

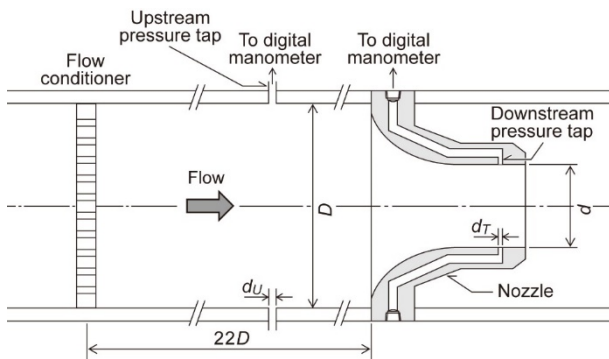


**Figure 2:** Schematic of throat-tapped flow nozzle.

**Table 1:** Parameters of examined throat-tapped flow nozzle.

Pipe diameter $D$ (mm)	100, 200, 350	
Throat diameter $d$ (mm)	50, 99, 165	
Diameter ratio $\beta$	app. 0.5	
Throat-tap diameter $d_t$ (mm)	2, 3.5, 4, 5, 6, 7	
$d_t/d$	0.012 – 0.1	
Upstream-tap diameter $d_u$ (mm)	2, 4, 5	
Surface roughness	$Ra$ ( $\mu\text{m}$ )	0.10, 0.80
	$Rt$ ( $\mu\text{m}$ )	0.60, 2.5

All experiments were carried out using the national standard of flow rate of water in NMIJ. The uncertainty of flow rate is different each experiment and it is from 0.040% to 0.10%. The uncertainty of the discharge coefficient is from 0.080% to 0.12% for all experiments.

## 3. Results

### 3.1 Influence of throat-tap diameter and $d_t/d$

The discharge coefficients for different  $d_t/d$  are shown in Fig. 3.  $C_{PTC6}$  is calculated from Eq.(1) with  $k_t=1.0054$ . We have examined three throat-tapped flow nozzles with different throat diameter,  $d$  as shown in Table 1. As mentioned in the introduction, the discharge coefficient increases with the size of the throat-tap diameter. This phenomenon, namely tap effect, is caused by the secondary flow in the pressure tap. The physical background of the tap effect has been clarified well in the previous papers [4][5]. From the results shown in Fig. 3, the discharge coefficient of the throat-tapped flow nozzle is influenced by the parameter  $d_t/d$ , namely dimensionless tap diameter. The discharge coefficients for  $d_t/d = 0.035, 0.036, 0.040$  are almost same although the throat diameter and tap diameter are different each other. From this result, the equation for the discharge coefficient of the throat-tapped flow nozzle should be included the parameter,  $d_t/d$ .

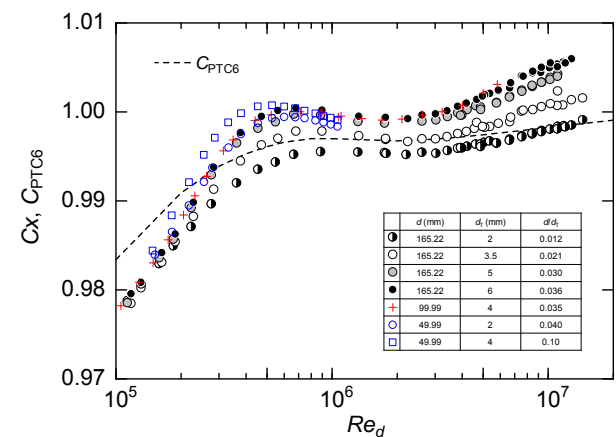


**Figure 3:** Discharge coefficients for different size of throat diameter  $d$  and throat-tap diameter  $d_t$ .

### 3.2 Influence of upstream-tap diameter

In generally, the measured pressure using wall pressure tap is larger than true pressure because of the tap effect [7]. Consequently, the differential pressure increases with increasing the throat-tap diameter and decreases with upstream-tap diameter. The discharge coefficients for different

upstream-tap diameter are shown in Fig. 4. The result shown in Fig.4 supports this phenomenon. The discharge coefficients for  $d_U=2$  mm are larger than  $d_U=5$  mm. However, the difference between two upstream-tap diameters is 0.02% at most. The uncertainty of the discharge coefficient is estimated to be 0.08% in this experiment. Therefore, it can be concluded that the influence of the upstream-tap diameter to the discharge coefficient is negligibly small.

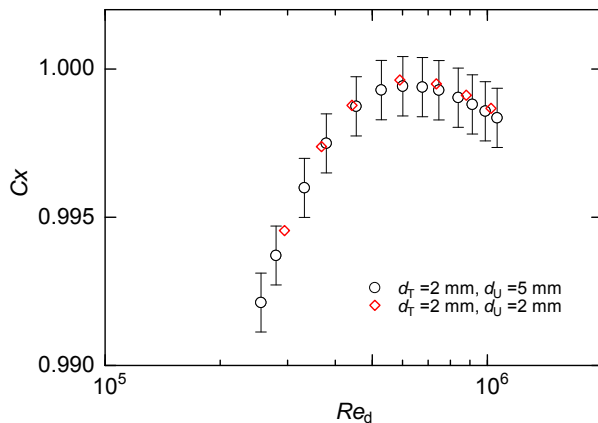


**Figure 4:** Influence of upstream-tap diameter.

### 3.3 Influence of roughness of surface

The discharge coefficient might be a function of the development of the boundary layer in the nozzle. Equation (1) is obtained by the theory of the boundary layer development by Murdock et al [8]. In this analysis, the surface finish of the nozzle is assumed to be hydraulic smooth. To satisfy the hydraulic smooth surface, the larger Reynolds number is, the smaller roughness required is. The relation between the required surface roughness and Reynolds number is following [9].

$$\frac{k_s}{d} < \frac{10\sqrt{2}}{Re_d\sqrt{\lambda}} \quad (2)$$

Where,  $k_s$  is the height of surface roughness,  $\nu$  is the kinematic viscosity and  $\lambda$  is the friction factor. If the roughness does not satisfy this requirement, the thickness of the boundary layer on the throat-tap is larger than the hydraulic smooth surface. Figure 5 gives the results for different roughness of the nozzle. The mean roughness of R1 is  $Ra=0.10$   $\mu\text{m}$  and R2 is  $0.80$   $\mu\text{m}$ . Both roughness value satisfy Eq.(2) for examined Reynolds number range, however the discharge coefficient is clearly influenced by the roughness at higher Reynolds number region,  $Re_d > 7 \times 10^7$ . In here, when  $Rt$ , which is the maximum roughness, is used instead FLOMEKO 2019, Lisbon, Portugal

of  $Ra$  in Eq.(2), the critical Reynolds number for R2 is  $Re_d \approx 7 \times 10^7$ . To evaluate the roughness of the nozzle, the relation between  $Rt$  and Reynolds number is better. It should be noted that the influence of the roughness is not related to the throat-tap diameter.

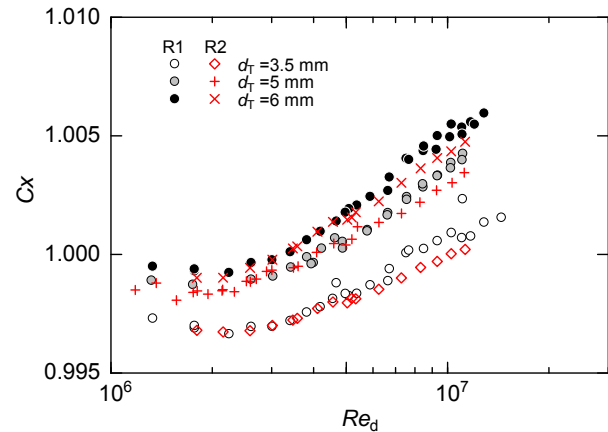


**Figure 5:** Influence of surface roughness of the nozzle

### 3.4 Influence of flow conditioner

ASME PTC6 requires to install the flow conditioner at upstream of the flow nozzle as shown in Fig. 2. The Mitsubishi type flow conditioner, which is plate type one, is installed at  $22D$  upstream in the experiments presented above sections. The flow conditioner is useful to eliminate the influence the upstream flow condition, however it induces generally large pressure loss. In this section, the influence of the flow conditioner is examined in terms of the necessity of it.

The examinations with the flow conditioner, without the flow conditioner, and with a half-moon plate were carried out. The half-moon plate is to simulate the downstream flow field of a single elbow. The pipe layouts for the experiments are shown in Fig. 6. The flow conditioner is installed downstream of the DN600 pipe with  $20D$  and the reducer to DN400 pipe. In the same position, the half-moon plate is installed instead of the flow conditioner. The discharge coefficients for each examination are shown in Fig. 7. From the comparison between with and without the flow conditioner, the discharge coefficient is not influenced by the flow conditioner in this pipe layout. Since the straight pipe section and reducer is installed at upstream of the flow conditioner, the velocity profile in there might be well developed and axisymmetric. Therefore, to disturb the flow field, the half-moon plate was installed in the same position of the flow conditioner and measured the discharge coefficient. The result is deviated app.

0.06% from the result without the half-moon plate. This deviation might not be large compared with the measurement uncertainty. When the upstream length is over than  $22D$ , the influence of the upstream condition appears to be not necessary to consider. This is reasonably equivalent with the requirement of straight pipe in ISO-5167.

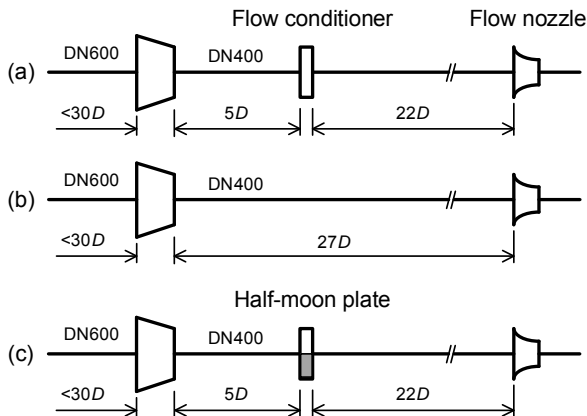


Figure 6: Pipe layouts.

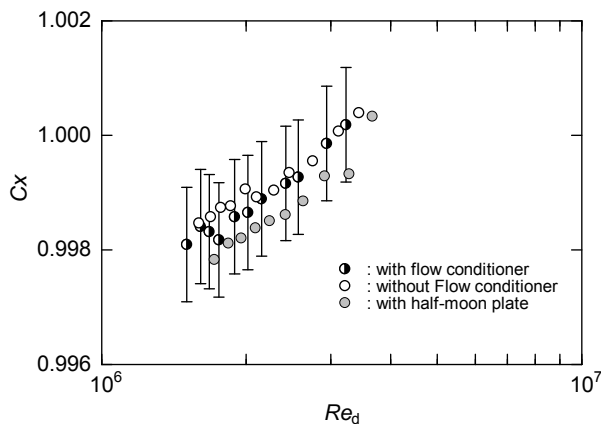


Figure 7: Influence of flow conditioner.

#### 4. Discussion

We have already established the equations of discharge coefficient as the function of Reynolds number and  $d_t/d$  by combining the theoretical and experimental analysis [4]. As shown in Fig. 3, the discharge coefficient is clearly related to dimensionless throat-tap diameter. If the flow nozzle is manufactured correctly, the discharge coefficient should exhibit a theoretical or semi-empirical curve when plotted against the Reynolds number. This is important to confirm the extrapolation of the discharge coefficient. However, sometimes we face to the different results depending of manufacturing procedure. Figure 8 FLOMEKO 2019, Lisbon, Portugal

shows the example which does not lie on the result in Fig.3 and the proposed equations. Furthermore, the result in Fig. 8 is clearly strange for the tap effect. The discharge coefficient should increase with the throat tap diameter, however it increases as  $d_t = 5, 6, 4,$  and  $7$  mm at  $Re_d = 1.0 \times 10^6$ . Although the reason of this result is not clear, but it might depend on the manufacturing finish of the throat tap. Therefore, the equation of the discharge coefficient for general use should be defined to cover such inconsistent data.

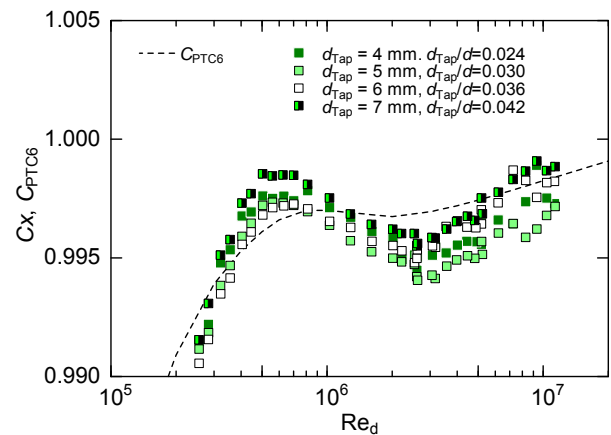


Figure 8: Experimental results of another throat-tapped flow nozzle.

The discharge coefficients obtained in the series of the experiments are plotted in Fig. 9. The all results for the parameters in shown in Table 1 are shown in there. We have done wide range of Reynolds number, from  $Re_d = 5 \times 10^5$  to  $1.4 \times 10^7$ . In the figure, Eq.(1) of ASME PTC6 with  $\pm 0.25\%$  criteria is also shown. The behaviour of the experimental discharge coefficients is not so different from ASME equation, however, many of data is outside of the  $\pm 0.25\%$  criteria, especially at high Reynolds number region. Since ordinal Reynolds number is up to  $Re_d = 10^7$  in most of plants, the equation for the discharge coefficients should be re-considered according those experimental data.

We propose the following new equations to give the discharge coefficient of the throat-tapped flow nozzle,

$$C_{P-1} = 1.0042 - \frac{8.41}{Re_d^{0.5}} \quad \text{for } Re_d < 1.3 \times 10^5 \quad (3)$$

$$C_{P-2} = 0.9558 - \frac{8.41}{Re_d^{0.5}} + 0.00492 \ln(Re_d) \quad \text{for } 1.3 \times 10^5 < Re_d < 4.0 \times 10^5 \quad (4)$$

$$C_{P-3} = 1.0090 - \frac{8.41}{Re_d^{0.5}} \quad \text{for } 4.0 \times 10^5 < Re_d < 8.0 \times 10^5 \quad (5)$$

$$C_{P-4} = 1.0090 - \frac{0.255}{Re_d^{0.2}} \left(1 - \frac{400000}{Re_d}\right)^{0.8} \quad \text{for } 8.0 \times 10^5 < Re_d < 3.0 \times 10^6 \quad (6)$$

$$C_{P-5} = 0.9823 - \frac{0.255}{Re_d^{0.2}} \left(1 - \frac{400000}{Re_d}\right)^{0.8} + 0.0018 \ln(Re_d) \quad \text{for } 3.0 \times 10^6 < Re_d \quad (7)$$

These equations are given by substitute  $d_T/d=0.24$  for the proposed equation in the previous paper [4]. The proposed equations are shown in Fig. 9. All experimental discharge coefficients are within  $\pm 0.5\%$  of the proposed equations.

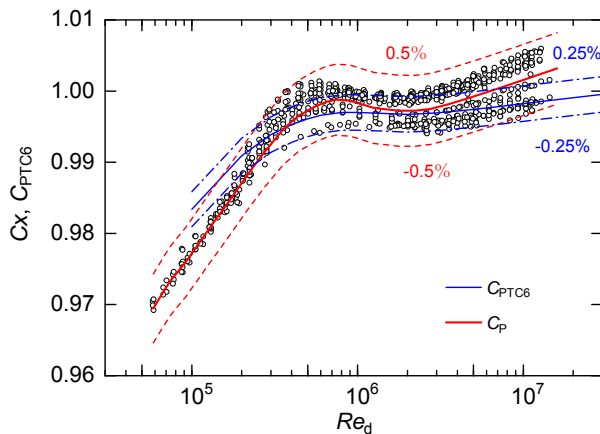


Figure 9: Examined data and proposed equation.

## 5. Conclusion

This paper presents experimental discharge coefficient for the several geometric parameters; throat-tap diameter, upstream-tap diameter, roughness of surface of nozzle and flow conditioner. The most influence parameter for the discharge coefficient is throat-tap diameter and the influence of the other parameters is generally negligible small. According to this result, new equations of the discharge coefficient for the throat-tapped flow nozzle is proposed. Although they are separated for five Reynolds number range, all experimental data in NMIJ is within  $\pm 0.5\%$  of them.

## References

[1] ASME PTC6, 2004, "Steam Turbines, Performance Test Codes".

- [2] Furuichi, N., Cheong, K.H., Terao, Y., Nakao S., Fujita K., Shibuya, K., "New Discharge Coefficient of Throat Tap Nozzle Based on ASME Performance Test Code 6 for Reynolds Number From  $2.4 \times 10^5$  to  $1.4 \times 10^7$ ", *Journal of Fluid Engineering*, **136(1)**, 011105, doi:10.1115/1.4025513, 2013
- [3] Reader-Harris, M., Gibson, j., Hodges, D., Nicholson, I.G., Rushworth, R., "The performance of flow nozzles at high Reynolds number", *Proceedings of FLOMEKO 14 (Johannesburg, South Africa)*, 2007
- [4] Furuichi, N., Terao, Y., Nakao, S., Fujita, K., Shibuya, K., "Further investigation of discharge coefficient for PTC 6 flow nozzle in high Reynolds number", *Journal of Engineering for Gas Turbines and Power*, **138**, 041605-1-11, 2016
- [5] (9) Furuichi, N., Terao, Y., "Static pressure measurement error at a wall tap of a flow nozzle for a wide range of Reynolds number", *Flow Measurement and Instrumentation*, **46**, pp.103-111, 2015
- [6] Furuichi, N., Cordova, L., Lederer, T., Terao Y., "Comparison of high temperature and high Reynolds number water flows between PTB and NMIJ", *Flow Measurement and Instrumentation*, **52**, pp.157-162, 2016
- [7] Shaw, R., 1960, "The influence of hole dimensions on static pressure measurement", *J. Fluid Mech.*, **7**, pp.550–564, 1960
- [8] Murdock, J.W., Keyser, D.R., "Theoretical basis for extrapolation of calibration data of PTC 6 throat tap nozzles", *Transactions of the ASME, Journal of Engineering for Gas Turbines and Power*, **113**, pp.228-232, 1991
- [9] Schlichting, H., Gersten, K., "Boundary layer theory, 8th revised and enlarged edition", Springer, 2000

# Development of clamp-on type thermal mass flow meter using near infrared absorption method for micro flow applications

S. H. Lee<sup>1</sup>, S. Park<sup>1</sup>, W. Kang<sup>1</sup>

<sup>1</sup>Division of Physical Metrology, Korea Research Institute of Standards and Science, 267 Gajeong-ro, Yuseong-Gu, Daejeon 34113, South Korea  
E-mail (corresponding author): seokhwan.lee@kriss.re.kr

---

## Abstract

We have developed a portable device, based on this infrared absorption method, that can measure in-situ micro flow rates from 0.2 to 20 mL/min using a simple diode laser and a photo detector. A 1450 nm laser absorbed in water was irradiated to form a hot spot and the temperature was measured upstream and downstream of the hot spot. Two diode lasers and two photodetectors were used to measure the water temperature in the tube upstream and downstream of the hot spot. The amount of laser diode light from 1550 nm to 1650 nm wavelength absorbed by the water varied with the temperature of the water. The flow rate was measured by the temperature difference obtained by the diode laser absorption upstream and downstream of the hot spot. The temperature difference measured upstream and downstream decreased exponentially with increasing flow rate. Thus, it was confirmed that the flow rate can be measured through the temperature difference gauged using a simple diode laser set. This method is used for various applications including biomedical and chemical processing without causing any contamination owing to the flow meter installation.

---

## 1. Introduction

The measurement and control of liquid micro flow rates is important in several processes, such as medical drug injection, semiconductor manufacturing processes, and chemical processes. Recently, many researchers have developed various methods for measuring micro flow rates. Coriolis flowmeters and thermal mass flowmeters are typically used for measuring micro flow rates. Coriolis flowmeters measure extremely low flow rates (maximum flow rate: 5 g/h) with extremely high accuracy ( $\pm 0.2\%$ ). However, they exhibit a few limitations, such as high cost and pressure resistance. Thermal mass flowmeters have relatively low flow measurement accuracy (10%). Despite these drawbacks, Coriolis flowmeters and thermal mass flowmeters are widely used in industry [1].

In addition, there is an increasing demand in the industry for approaches that allow in-situ flow rates to be measured without pipeline cutting and fluid contamination. As coriolis flowmeters and thermal mass flowmeters cannot measure in-situ flow rates, techniques for measuring the flow rate in-situ without cutting the piping are being developed, such as the use of ultrasonic waves. Ultrasonic

flowmeters use the clamp on type method to measure the flow rate by irradiating ultrasonic waves outside of a pipe for in situ measurement. However, measuring low flow rates with ultrasonic flowmeters is challenging because the signal intensity reduces as the flow velocity reduces.

Laser-based techniques for the measurement of flow rates have several advantages, such as remote, nonintrusive, in situ, spatial, and temporally precise measurement[2-5]. Laser Doppler velocimetry (LDV) uses the Doppler shift in a laser beam to measure the velocity of particle seeded fluid flows[6; 7]. Particle image velocimetry (PIV) measures the flow velocity field by capturing two images of seeding particles in the fluid with a time gap. Although several LDV and PIV have been applied to measure flow velocity, they require particle seeding. Recently, techniques for measuring the flow field without the seeding of particles were developed by using fluorescence and Raman scattering [3; 4; 8]. To overcome the disadvantages associated with using particles for measuring flow, different dyes were used as markers [9]. A non-intrusive measurement technique based on spontaneous Raman imaging was proposed to investigate microscale flow structures[8] and spray flow[3].

Specifically, near-infrared (NIR) spectroscopy is a conventional method for measuring the molecular composition of a substance using a vibrational molecular band [12]. Water exhibits several absorption bands in the NIR region, and the spectral shape of each band varies with respect to temperature. The absorption band of water (O-H band,  $\nu_1+\nu_3$ ) shifts to a shorter wavelength with increases in temperature [13]. Additionally, NIR spectroscopy is used for water temperature measurement in channels with sizes in the range of micrometers [10]. The water temperature in a microchannel was visualized by using the NIR absorption method with a high resolution (0.2 K) [11]. The NIR absorption method exhibits high potential in terms of measuring the flow rate. Recently, the technique was proposed for measuring micro flow rates by our group [12]. The flow rate is measured by irradiating water with an IR laser to heat it, and then measuring the water temperature by using FTNIR (Fourier transform near infrared). However, the FTNIR used to measure the near infrared absorption spectrum in that study was bulky and expensive, which would have made its application to industrial sites challenging. There is a need for an in-situ micro flowmeter that can be applied to industrial fields. Moreover, the development of low cost, small, and stable laser diodes has made it possible to simplify the infrared absorption technique. Studies have been performed to measure the flow velocity using tunable diode laser absorption spectroscopy, but this can only be applied to high speed flow [13]. However, no studies have been performed to measure micro flow rates using diode lasers.

In this study, a new technique for measuring micro flow rates using small chip diode lasers was developed. The NIR laser heats a tiny spot in a transparent polymer tube through a lens. The water temperatures upstream and the downstream of the heated point were measured by the laser diode absorption method. The theoretical heat transfer was analyzed through a simulation of the temperature profile for different flow rates. The temperature difference measured by the laser diode upstream and downstream of the heated point was used to measure the micro flow rate. The micro flow rate measurement accuracy and measurement range were determined according to the laser's energy and temperature measurement positions. The calibration curve for the temperature difference and the reference flow rate were obtained with a flow rate in the range of 0.2–20 mL/h. Thus, we confirmed that the laser diode absorption method can measure micro flow rates in the 0.2–20 mL/h range in-situ with high accuracy.

## 2. Experiment

Figures 1 (a) and (b) show the experimental setup for the laser diode (LD)-based thermal mass flowmeter and a magnification of the measurement position, respectively. The deionized (DI) water was sent to the LD flowmeter and the balance through an IV set tube commonly used in the hospital. The internal diameter of the IV set tube was 3 mm, and an optical transparency of 0.3  $\mu\text{m}$  to 3  $\mu\text{m}$  in the near infrared region. The flow was generated by air pressure using a pressure controller (Elve flow, OB1) and controlled from 0.2 to 20 mL/h using a mass flow controller (MFC, Bronkhorst M12). The reference flow rate was obtained using a micro balance (Mettler-Toledo, XPE 206 DR) with an evaporation trap. To obtain the reference flow rate using the balance, we calculated the measurement uncertainty of the balance with respect to buoyancy, evaporation, and accuracy of the balance. The detailed uncertainty calculation can be found in [14].

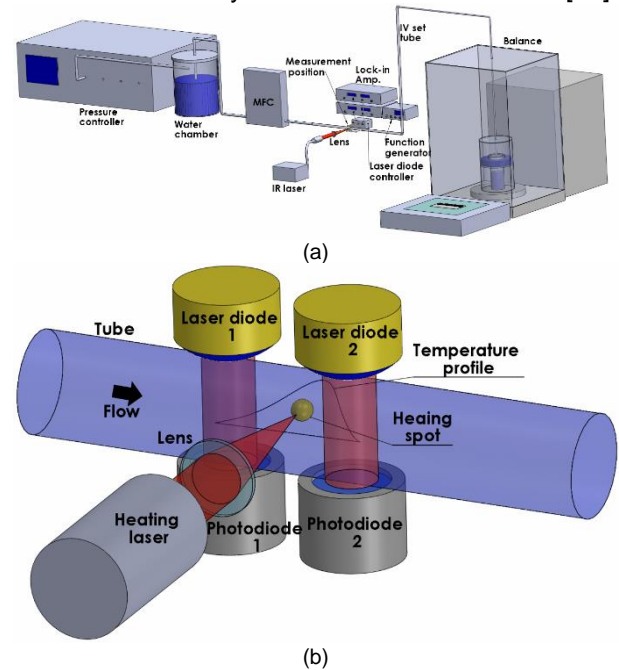


**Figure 1:** (a) Experimental setup for the laser diode-based micro flowmeter; (b) magnification of the measurement position shown in Fig. 1 (a)

The LD flowmeter consists of a heating laser (CNI, 1450 nm  $\pm$ 15 nm), two diode lasers (Thorlabs, LED1600L) for emitting light, and two photodetectors (Roithner Laser Technik, LAPD-1-09-17-TO46) for receiving light. The light emitted by the heating laser with a 1450 nm wavelength was absorbed by the water owing to the vibration ( $\nu_{\text{th}}$ ) [15]. The heating laser was focused on the center of the IV set tube through a lens (50 mm focal length). The water was heated at a tiny spot region

by the focused laser with a spot diameter of 12.5  $\mu\text{m}$ . To measure the temperature of water upstream and downstream of the heated spot, two diode lasers emitting light at a wavelength of 1550 nm to 1650 nm, and two photodetectors measuring light at 900 nm to 1700 nm were used. Near infrared light was collimated through a lens in front of the laser diode, and the light absorbed by the water in the tube was measured with a photodetector. Two lock-in amplifiers (SR530, Stanford Research Systems) were used to amplify the water absorption signal of the laser diode. The noise of the absorption signal was minimized by synchronizing the laser diode and photodetector with the signal generated by the function generator. The distance between the two laser diodes and photodetector pairs was 10 mm. The distance between the optimized upstream measurement point and the heated spot was 1 mm.

### 3. Results

#### 2.1 Temperature measurement using the NIR absorption method

In this study, the flow rate was measured using the temperature difference upstream and downstream of the heated spot by measuring the temperature under in-situ conditions. The principle of measuring the temperature under in-situ conditions was based on the fact that the absorption spectrum of NIR changes according to the temperature [11]. Figure 2 shows the absorption spectra according to the temperature (20, 30, 40, 50, and 60 oC) measured with Fourier transform near infrared (FTNIR) spectroscopy. When the temperature of water increases, the absorption intensity at wavelengths from 1400 nm to 1450 nm increases, and the absorption at wavelengths from 1500 nm to 1700 nm decreases. If we obtain the absorption intensity from 1500 nm to 1700 nm, we can measure the temperature of water under in-situ conditions. Therefore, we irradiated the light from 1550 to 1650 nm with a laser diode on the tube, and measured the light transmittance using a photodetector on the other side. Figure 3 shows the transmission intensity signal from the laser diode with various reference temperatures. When the reference temperature increases, the transmission intensity increases as shown in Fig. 3. This is because, as the temperature increases, the amount of light absorbed by the water decreases, thereby increasing the amount of light transmitted. The relationship between the reference temperature and the transmission intensity is a quadratic function, which depends on the characteristics of the measurement sensor. Using this temperature calibration curve, a quantitative temperature can be

obtained under in-situ conditions through a laser diode

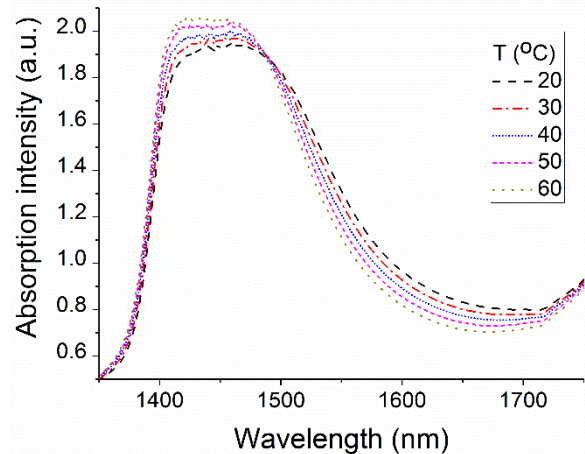


**Figure 2:** Absorption spectra according to the temperature (20, 30, 40, 50, and 60 °C) measured with FTNIR.

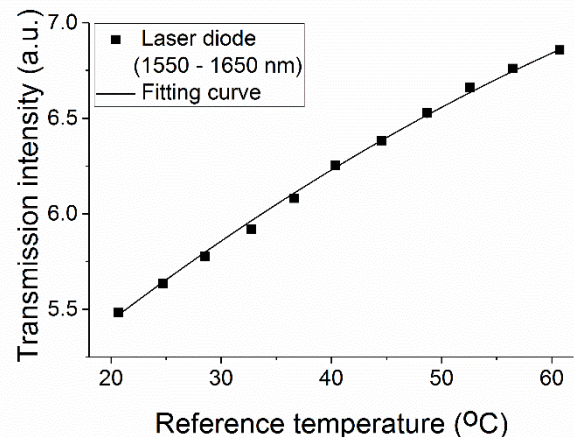
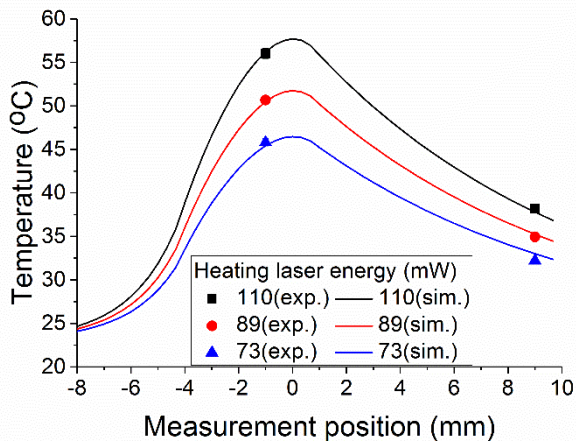


**Figure 3:** Variation in the transmission intensity signal from the laser diode with reference temperature

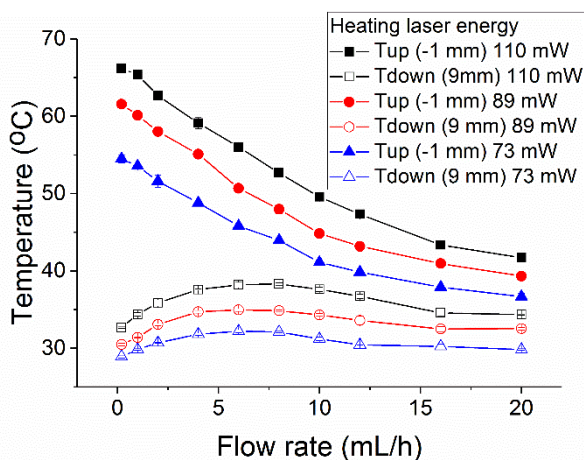
#### 3.2 Analysis of the laser diode flowmeter for different heating laser energies

The energy of the heating laser is one of the important parameters of the laser diode-based micro flowmeter. Therefore, we changed the heating laser's energy to analyze how the laser energy affects the flow measurement in this study. Figure 4 shows a comparison of temperature profiles between the experimental and simulation results of the 73, 89, and 110 mW heating laser energy cases at a 6 mL/h flow rate. This figure shows that the simulation results were well matched with the experimental results. When the heating laser energy increases, the maximum temperature increases up to more than 55 °C. The maximum temperature difference between the laser energy of

73 mW and 110 mW is about 10 °C. Upstream of the heated spot, the slope of the curve between the temperature and the measurement positions increases with increasing heating laser energy, and downstream of the heated spot, the slope of the curve is almost constant for different heating laser energies.



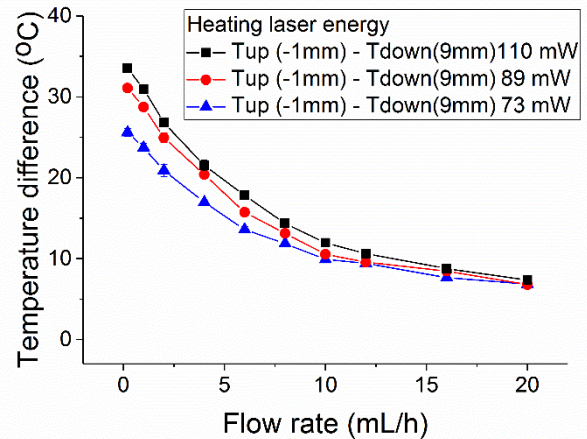
**Figure 4:** Comparison of temperature profiles between the experimental and simulation results of 73, 89, and 110 mW heating laser energy cases at 6 mL/h flow rate.



**Figure 5:** Temperatures at two measuring positions (upstream : -1 mm, downstream : 9 mm) according to the flow rates for different heating laser energies (73, 89, and 110 mW)

Figure 5 shows the temperatures at two measuring positions (upstream : -1 mm, downstream : 9 mm) according to the flow rates for different heating laser energies (73, 89, and 110 mW). When the flow rate increases, the temperature upstream of the heated spot decreases, and there is little change in the temperature downstream of the heated spot for each of the heating laser energy cases. As the heating laser energy decreases, the temperature curve according to the flow rate at each position is shifted downward. Therefore, the measured temperatures upstream and downstream of the FLOMEKO 2019, Lisbon, Portugal

heated spot do not overlap when the flow rate is high.



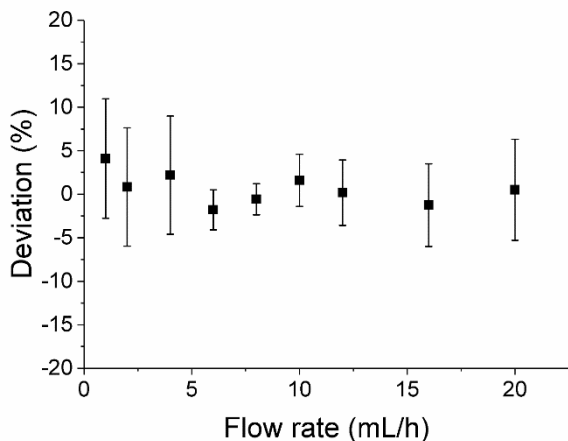
**Figure 6:** Temperatures difference according to the flow rates for different heating laser energies (73, 89, and 110 mW)

Figure 6 shows the temperature difference according to the flow rates for different heating laser energies (73, 89, and 110 mW). The temperature difference decreases exponentially as the flow rate increases. Moreover, as the heating laser energy decreases, the slope of the temperature curve decreases. This means that the higher the heating laser energy, the better the accuracy of the flow measurement. However, at low heating laser energies (73 mW), the temperature difference is maintained at a high flow rate range even though the accuracy of the flow measurement is low. Furthermore, the low heating laser energy (73 mW) has an operating temperature that is about 10 °C lower than that of the high heating laser energy (110 mW), which may be advantageous for applications involving biofluids that are easily destroyed by heat. The lowest flow rate measured in this study is 0.2 mL/h, but if the laser energy is controlled, lower flow rates can be measured in the future. As the accuracy of the flow measurement is drastically improved as the flow rate is lowered, the flowmeter can be used for accurate micro flow measurement.

#### 4. Uncertainty analysis

The Figure 7 shows the deviations in the LD flowmeter readings according to the flow rate with measurement uncertainty. When the flow rate increases, the deviation approaches zero. However, the measurement uncertainty decreases as the flow rate increases and then increases again. This is because the slope of the temperature difference according to the flow rate is lowered at a high flow rate, and the measurement accuracy is lowered.

Thus, the maximum measurement uncertainty was 6.8% at a 1 mL/h flow rate, and the minimum measurement uncertainty was 1.78% at 8 mL/h. However, these values vary with the measurement positions and the energies of the heating laser used to determine the optimal flow rate range. The performance of the LD flowmeter developed in this study was confirmed to be close to that of a commercial thermal mass flowmeter (10%, full scale). Using the laser diode-based flowmeter developed in this study, it is possible to measure flow rate in-situ without injecting contaminants such as particles for measurement without cutting piping. In addition, it can be manufactured in a miniaturized form at a low cost, and thus, it can be used for multi-drug infusion analysis, and semiconductor process monitoring, etc.



**Figure 7:** Deviations in laser diode-based flowmeter according to the flow rate with measurement uncertainty

## 5. Conclusion

We have developed a laser diode-based flowmeter based on this infrared absorption method that can measure in-situ micro flow rates from 0.2 to 20 mL/min using a simple diode laser and a photo detector. The amount of laser diode light from 1550 nm to 1650 nm absorbed by the water varied with the temperature of the water. The calibration curve of the infrared light transmission intensity through the water at various temperatures of the water was obtained. A 1450 nm laser absorbed in water was irradiated to form a heated spot at 0 mm, and the temperature was measured upstream and downstream of the heated spot. Two diode lasers and two photodetectors were used to measure the water temperature in the tube upstream and downstream of the heated spot. The flow rate was measured by the temperature difference obtained by two diode lasers and photodetectors upstream

and downstream of the heated spot. We measured the temperature profile of the flow rate by changing the heating laser energy upstream and downstream of the heated spot, and compared the obtained values with the simulation results. As the flow rate increased, the temperature profile shifted downstream, and the measured temperature upstream and downstream were analyzed according to the flow rate. The temperature difference measured upstream and downstream decreased exponentially with increasing flow rate, and it was confirmed that quantitative measurement could be made using this calibration curve. Increasing the energy of the heating laser also improved the measurement accuracy in the lower flow range. The developed flowmeter was calibrated by the gravimetric method, and the maximum measurement uncertainty was 6.8%, which is similar to that of the conventional commercial contact thermal mass flowmeter. The lowest flow measurement uncertainty was 1.78% at a flow rate of 8 mL/h. Thus, it was confirmed that the flow rate can be measured through the temperature difference gauged using a simple diode laser set. The diode laser-based flowmeter developed in this study has the following advantages:

1. The flow rate can be measured non-contact without the need to inject additional particles.
  2. We can measure the flow rate in-situ without cutting the pipe.
  3. We can set the flow measurement range by adjusting the heating laser energy and the measuring position.
  4. It is possible to measure the flow rate with high flow measurement accuracy in the low flow rate range.
  5. It can be manufactured in a small size at low price; thus, it is easy to mass produce.
- Owing to these advantages, this method can be used in various processes, including biomedical and chemical processes, without causing any contamination owing to the flowmeter installation.

## References

- [1] Nguyen, N. "Micromachined flow sensors—a review," *Flow measurement and Instrumentation* Vol. 8, No. 1, 1997, pp. 7-16.
- [2] Toloui, M., and Hong, J. "High fidelity digital inline holographic method for 3D flow measurements," *Optics Express* Vol. 23, No. 21, pp. 27159-27173, 2015.
- [3] Braeuer, A., Engel, S. R., Dowy, S., Luther, S., Goldlücke, J., and Leipertz, A. "Raman mixture composition and flow velocity imaging with high repetition rates," *Optics*

- Express Vol. 18, No. 24, pp. 24579-24587, 2010.
- [4] Garbe, C. S., Roetmann, K., Beushausen, V., and Jähne, B. "An optical flow MTV based technique for measuring microfluidic flow in the presence of diffusion and Taylor dispersion," *Experiments in Fluids* Vol. 44, No. 3, pp. 439-450, 2008.
- [5] Olsen, M., and Adrian, R. "Out-of-focus effects on particle image visibility and correlation in microscopic particle image velocimetry," *Experiments in fluids* Vol. 29, No. 1, pp. S166-S174, 2000.
- [6] Mickan, B., and Strunck, V. "A primary standard for the volume flow rate of natural gas under high pressure based on laser Doppler velocimetry," *Metrologia* Vol. 51, No. 5, pp. 459, 2014.
- [7] Dopheide, D., Taux, G., and Krey, E. "Development of a new fundamental measuring technique for the accurate measurement of gas flowrates by means of laser Doppler anemometry," *Metrologia* Vol. 27, No. 2, pp. 65, 1990.
- [8] Takahashi, M., Furukawa, T., Sato, Y., and Hishida, K. "Non-intrusive velocity measurement of millichannel flow by spontaneous Raman imaging," *Journal of Thermal Science and Technology* Vol. 7, No. 3, pp. 406-413, 2012.
- [9] Koochesfahani, M. M., and Nocera, D. G. "Molecular tagging velocimetry," *Handbook of experimental fluid dynamics*, pp. 362-382, 2007.
- [10] Siesler, H. W., Ozaki, Y., Kawata, S., and Heise, H. M. *Near-infrared spectroscopy: principles, instruments, applications*: John Wiley & Sons, 2008.
- [11] Kakuta, N., Fukuhara, Y., Kondo, K., Arimoto, H., and Yamada, Y. "Temperature imaging of water in a microchannel using thermal sensitivity of near-infrared absorption," *Lab on a Chip* Vol. 11, No. 20, pp. 3479-3486, 2011.
- [12] Lee, S. H., Lee, J., Chun, S., and Kang, W. "In situ measurement of micro flow rate using near infrared absorption method," *Optics express* Vol. 26, No. 13, pp. 17078-17091, 2018.
- [13] Strand, C., and Hanson, R. "Thermometry and velocimetry in supersonic flows via scanned wavelength-modulation absorption spectroscopy," 47th AIAA/ASME/SAE/ASEE Joint Propulsion Conference & Exhibit. 2011, p. 5600.
- [14] Lee, S. H., Kang, W., and Chun, S. "Dynamic behavior analysis of drug delivery devices using a dynamic gravimetric method," *Flow Measurement and Instrumentation*, 2018.
- [15] Libnau, F. O., Kvalheim, O. M., Christy, A. A., and Toft, J. "Spectra of water in the near-and mid-infrared region," *Vibrational spectroscopy* Vol. 7, No. 3, pp. 243-254, 1994.

# Measurement of hydrocarbon liquid flow rate using volumetric and gravimetric methods: comparison between KRISS and PTB hydrocarbon standard systems

S. H. Lee<sup>1</sup>, M. Link<sup>2</sup>, B.-R. Yoon<sup>1</sup>, E. Frahm<sup>2</sup>

<sup>1</sup>*Division of Physical Metrology, Korea Research Institute of Standards and Science, 267 Gajeong-ro, Yuseong-Gu, Daejeon 34113, South Korea*

<sup>2</sup>*Department Liquid Flow, Physikalisch-Technische Bundesanstalt, 100 Bundesallee, Braunschweig 38116, Germany*

*E-mail (corresponding author): enrico.frahm@ptb.de*

---

## Abstract

In this study, the hydrocarbon liquid flow rate was measured using both volumetric and gravimetric methods. Both methods are representative reference techniques for measuring the hydrocarbon flow rate. The volumetric method uses a calibrated volume tank, while the gravimetric method is based on a calibrated balance. Using these two methods, which have different traceability systems, a Coriolis flowmeter was calibrated under comparable flow conditions. The deviation and uncertainty of the flow measurement results obtained from the volumetric and gravimetric methods were analyzed.

The study included the calibration of a 1000 L reference volumetric tank at the PTB hydrocarbon facility by using two different approaches: a filling method and a gravimetric method. For the filling method, a 100 L reference volume pipette was installed above the volume tank. A balance system under the 1000 L tank was used to calibrate the tank based on the gravimetric method. The uncertainties of the filling and gravimetric methods were 325.18 ml and 171.39 ml ( $k=2$ ), respectively, and the maximum difference between these methods was 78.06 ml. Thus, the calibration values of both methods were found to agree with each other within the estimated uncertainties.

For the final comparison, a Coriolis flowmeter was calibrated using the 1000 L volume tank at the PTB flow facility. The diameter of the pipeline was 80 mm and the flow rate ranged from 13.68 t/h to 54.81 t/h. A balance reference was used at the hydrocarbon flow systems of KRISS. Since the fluid properties (density and viscosity) used at the two institutes are different, the flow measurements were compared based on the Reynolds number to compensate for these fluid properties. The calibration values of the Coriolis flowmeter at KRISS and PTB were 0.21–0.23% ( $U=0.08\%$ ,  $k=2$ ) and 0.18–0.24% ( $U=0.05\%$ ,  $k=2$ ), respectively, for an  $Re$  number range between 35,000 and 145,000. The results from the gravimetric method in KRISS matched very well with the results from the volumetric at PTB, within the estimated uncertainties. Thus, we confirmed that the hydrocarbon flow standard systems of KRISS and PTB have traceability when using the volumetric and gravimetric methods in the given range of  $Re$  number. The procedure and results of the volume tank calibration at the PTB hydrocarbon facility will be given during the presentation. In addition, the results of the flow comparison between PTB and KRISS will be presented to demonstrate the traceability of both hydrocarbon laboratories.

---

## 1. Introduction

Both volumetric and gravimetric methods are representative standard methods for measuring the flow rate. The volumetric method uses calibrated volume tanks, while the gravimetric method uses a calibrated balance. The volumetric method can measure the volume flow rate without the need to convert the mass flow rate into the volume flow rate;

however, the measurement accuracy is highly dependent on the changes in temperature.

In general, when calibrating a volume tank, the gravimetric method has a lower uncertainty than the volumetric method [1]. Both volumetric and gravimetric methods show consistent results within the uncertainty range during flow rate measurement [2]. However, previous studies have compared the volumetric and gravimetric methods separately using different facilities.

In this study, we performed the calibration of a volume tank by using both volumetric and gravimetric methods simultaneously in the same facility. Also, the hydrocarbon flow system was compared using the volumetric method of PTB and gravimetric method of KRISS.

## 2. Experiment

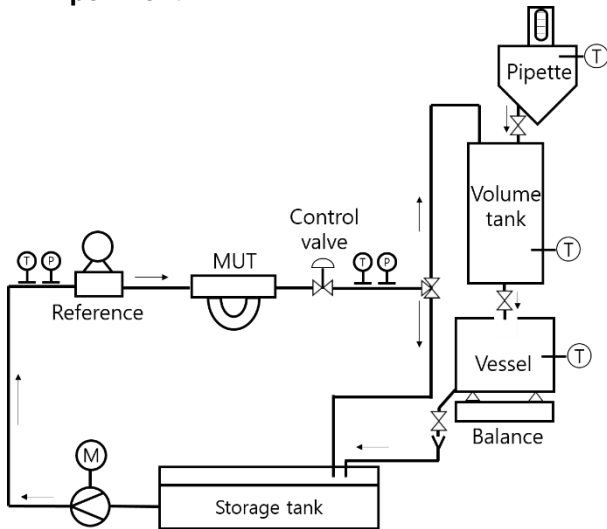


**Figure 1:** Schematic of measurement setup using volumetric and gravimetric methods.

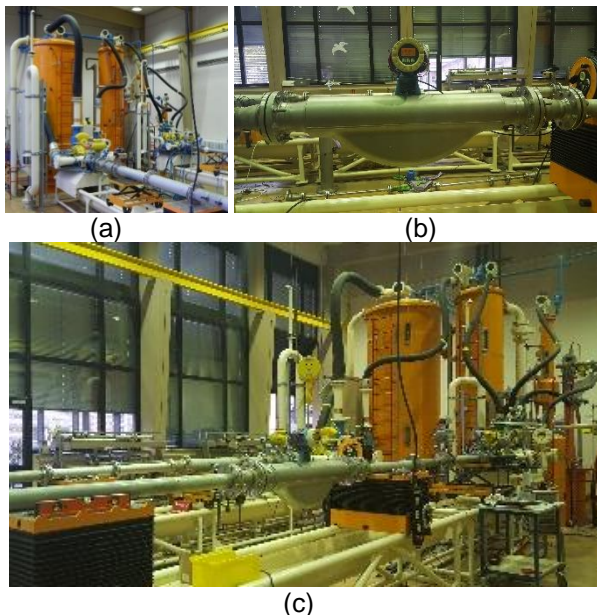


**Figure 2** (a) hydrocarbon flow calibration rig, (b) Coriolis flowmeter DN 100, and (c) hydrocarbon flow calibration rig with flowmeter installed in PTB

Figure 1 shows the schematic of the hydrocarbon flow rate measurement setup using volumetric and gravimetric methods.

A 1000 L volume tank was used for flowrate measurement and a 100 L reference volume tank and the calibrated balance were used simultaneously to calibrate the volume tank. A Coriolis flowmeter (Endress + Hauser, 83F1H) with a diameter of 100 mm was used to compare the PTB and KRISS hydrocarbon flow facilities. Figure 2(c) shows the installation of the flowmeter on the 80 mm pipeline of the PTB hydrocarbon flow facility.

## 3. Calibration of the volume tank at the hydrocarbon facility at PTB

The Department of Liquid Flow at PTB operates a test facility for the calibration of flow meters in the range between 0.6 m<sup>3</sup>/h and 120 m<sup>3</sup>/h. The test fluid is white spirit. The test facility has four separate volume tanks with capacities of 5000 L, 1000 L, 200 L, and 100 L. For the final filling stage of the tanks, the liquid level can be detected by manual meniscus reading. Additionally, in the 1000 L tank, the liquid level is measured gradually by using a magnetostriction displacement sensor. For traceable gravimetric calibrations of flow meters, a balance system with a maximum weight of 500 kg is also installed.

In this section, we evaluate the proven uncertainty of the facility (0.05 %, k = 2) by performing a recalibration of the 1000 L volumetric standard tank. Through a comparison between gravimetric and volumetric methods, the best practical procedure is determined and discussed.

The calibration procedures for the gravimetric method and volumetric method are based on the EURAMET guidelines “cg-19” [1] and “cg-21” [2], respectively. For the volumetric calibration, the filling method was applied using a 100 L traceable pipette and a 5 L pipette. For the gravimetric method, a specially installed high-resolution balance system (max. weight: 100 kg, resolution: 1 g) was used.

### 3.1 Calibration of the volume tank using volumetric method

We calibrated the 1000 L volume tank with five individual measurements by using a 100 L reference pipette for liquid levels lower than 2200 mm. For the upper part of the volume tank, a higher resolution was required. For that purpose, a 5 L pipette was used for liquid levels between 2000 mm and 2650 mm. In principle, the calibration procedure was based on the calibration guidelines of a standard capacity measure using a volumetric method [3]. For the calibration of one 1000 L tank, all single 100 L and 5 L pipette fillings were summed up.

The mathematical expression of the calibrated volume  $V_{T,vol}$  is given by equation (1). The final

approach of the calibration was to obtain a continuous function for the relation between the liquid level and tank volume. For that purpose, separate linear models for each linear level range were fit to the five individual calibration curves. The difference between the calibrated and modelled values gives the uncertainty of  $V_{Approx}$ .

$$V_{T,vol} = V_0[1 - \gamma_{RS}(T_{ORS} - T_{RS}) + \beta(T_{VT} - T_{RS}) + \gamma_{VT}(T_0 - T_{VT})] + \delta V_{men} + \delta V_{rep} + \delta V_{approx} + \delta V_{add} \quad (1)$$

Here,

- $V_0$  Volume of reference standard in L
- $T_{ORS}$  Water temperature of reference standard in the volume certificate in °C
- $T_{RS}$  Water temperature of reference standard in °C
- $T_0$  Reference temperature of volume tank in °C
- $T_{VT}$  Water temperature of the volume tank in °C
- $\gamma_{RS}$  Coefficient of cubical thermal expansion of reference standard material in °C<sup>-1</sup>
- $\gamma_{VT}$  Coefficient of cubical thermal expansion of volume tank material in °C<sup>-1</sup>
- $\beta$  Coefficient of cubical thermal expansion for water in °C<sup>-1</sup>
- $\delta V_{men}$  Meniscus reading in L
- $\delta V_{rep}$  Measurement repeatability in L
- $\delta V_{approx}$  Approx. function in L
- $\delta V_{add}$  Additional factors in L

Table 2 presents the main results of the uncertainty budget for the volume tank using the volumetric method. The measurement uncertainty was estimated to be 0.325 L ( $k = 2$ ). The main input parameters for the budget are the approximation function (52.8%), the calibration of reference pipette (31.0%) and the additional parameters (15.8%) such as evaporation, water loss, and air bubbles. The volume of the reference standard was estimated to be 1025.085 L for calibration and modelled with 1024.919 L. The deviation of 0.166 L between both values was less than the estimated measurement uncertainty of the volumetric method that was used.

**Table 2:** Results of uncertainty calculation for volume tank calculation using volumetric method

Standard uncertainty component $u(x_i)$	Source of uncertainty	Uncertainty $u_i(V_0) =  c_i  u(x_i)$
$u(V_0)$	Volume of the RS	9.06E-02 (L)
$u(T_{RS})$	Water temperature of RS	5.86E-03 (L)
$u(T_{VT})$	Water temperature of volume tank	1.19E-03 (L)

$u(\gamma_{RS})$	Coefficient of cubical thermal expansion of the RS	2.23E-04 (L)
$u(\delta VT)$	Coefficient of cubical thermal expansion of volume tank	3.12E-04 (L)
$u(\delta V_{men})$	Meniscus reading of the RS	7.22E-04 (L)
$u(\delta V_{rep})$	Measurement repeatability	8.99E-03 (L)
$u(\delta V_{approx})$	Approximation function	1.18E-01 (L)
$u(\delta V_{add})$	Additional factors	6.47E-02 (L)
$U_{T,vol}$	$U(V_{T,vol})$ 3.25E-01 L ( $k = 2$ )	

### 3.2 Calibration of the volume tank using gravimetric method

In addition to the previously described volumetric method, we calibrated the same 1000 L tank by using a high-resolution reference balance (max weight = 100 kg). The calibration procedure is described in the determination guidelines of uncertainty in gravimetric volume calibration [4]. Further, for the calibration of one 1000 L tank, the 100 kg balance tank was filled 10 times in a row to obtain a summed up value of the total 1000 L tank volume. The mathematical expression for the calibrated volume  $V_{T,Mass}$  is given in equation (2). Based on a previous approach, a function for the relation between the liquid level and tank volume was derived. The difference between the calibrated and modelled values also gives an uncertainty of  $V_{Approx}$ .

$$V_{T,Mass} = m \frac{1}{\rho_W - \rho_A} \left(1 - \frac{\rho_A}{\rho_B}\right) [1 - \gamma_{VT}(T_{VT} - T_0)] + \delta V_{rep} + \delta V_{approx} + \delta V_{add} \quad (2)$$

Here,

- $m$  Weighing result in kg
- $\rho_W$  Liquid density in kg/m<sup>3</sup>, at calibration temperature
- $\rho_A$  Air density in kg/m<sup>3</sup>
- $\rho_B$  Density of mass pieces during balance calibration = 7900 kg/m<sup>3</sup>
- $\gamma_{VT}$  Coefficient of cubical thermal expansion of volume tank material in °C<sup>-1</sup>
- $T_0$  Reference temperature of volume tank in °C
- $T_{VT}$  Water temperature of the volume tank in °C
- $\delta V_{rep}$  Measurement repeatability in L
- $\delta V_{approx}$  Approx. function in L
- $\delta V_{add}$  Additional factors in L

Table 3 shows the uncertainty budget for volume tank calculation using the gravimetric method. The measurement uncertainty was 0.171 L ( $k = 2$ ). The main input parameters for the budget are the approximation function (34.4%), the repeatability of the calibrations (19.8%) and the additional

parameters (45.7%) such as evaporation, water loss, and air bubbles. The volume of the reference standard was 1004.193 L, and the modelled volume at the same liquid level was also 1004.193 L. Thus, we confirmed that the volumes calculated using both volumetric and gravimetric methods were well matched with the reference standard under measurement uncertainty.

**Table 3:** Results of uncertainty budget for volume tank calculation using gravimetric method

Standard uncertainty component $u(x_i)$	Source of uncertainty	Uncertainty $u_i(V_0) =  c_i  u(x_i)$
$u(m)$	Balance reading	3.44E-06 (L)
$u(T_{VT})$	Water temperature of volume tank	2.43E-07 (L)
$\rho_W$	Density fluid	3.02E-06 (L)
$\rho_A$	Density Air	2.53E-08 (L)
$\rho_B$	Density mass pieces	1.12E-07 (L)
$u(\delta VT)$	Coefficient of cubical thermal expansion of volume tank	1.34E-07 (L)
$u(\delta V_{rep})$	Measurement repeatability	3.82E-02 (L)
$u(\delta V_{approx})$	Approximation function	5.02E-02 (L)
$u(\delta V_{add})$	Additional factors	5.80E-02 (L)
$U_{T,Mass}$	$U(V_{T,Mass}) 1.71E-01 L (k = 2)$	

### 3.3 Comparison of volumetric and gravimetric methods

The aim of the study was to estimate a liquid-level dependent function for the volume of a 1000 L tank by comparing two different calibration methods. The results summarized in Table 4 show that the uncertainty of the gravimetric method is nearly half of that of the filling method.

For using the investigated functions, only the linear level ranges of the 1000 L tank were relevant (Figure 2). On comparing these three ranges (Table 4 and Figure 3), the best agreement between the volume and the gravimetric model was found for the upper linear level. Here, the observed variation between both models was 78.06 mL, which is fully covered by the uncertainty of both methods.

**Table 4:** Summarized results of uncertainty budget for volume tank calculation using gravimetric and filling method

	$u (k = 1)$		$u (k = 2)$	
	ml	%	ml	%
Filling method	162.59	0.016	325.18	0.031
Gravimetric method	85.69	0.008	171.39	0.016

**Table 4:** Summarized results of uncertainty budget for volume tank calculation using gravimetric and filling method

Linear range of liquid level in mm	Differences between both models		
	Min in mL	Max in mL	Mean in mL
160 ... 950	8.66	237.79	109.46
2000 ... 2200	242.92	497.70	370.31
2450 ... 2650	5.68	78.06	29.88

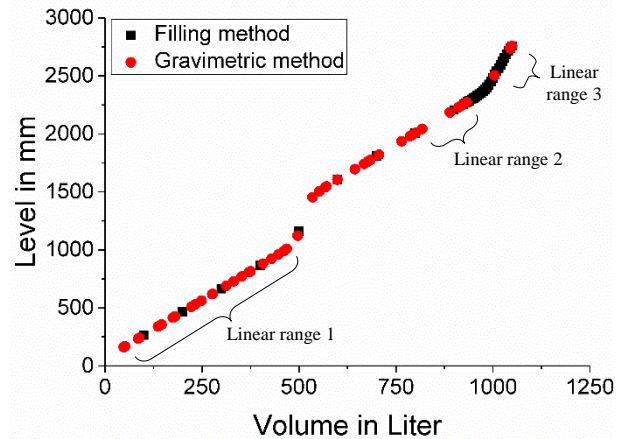


**Figure 2** Calibrated volume at reference temperature using filling and gravimetric methods. The linear level ranges are marked.

## 4. Comparison of hydrocarbon facilities between KRISS and PTB

The hydrocarbon flow rate was measured and compared with the results of the volumetric method from PTB and the gravimetric method from KRISS. The density and viscosity of the hydrocarbon used by PTB and KRISS are summarized in Table 5. Since PTB and KRISS use fluids with different densities and viscosities, the difference in fluid properties is compensated by using the Re number. The mass and volume flow rates of PTB and KRISS according to the Re number used are shown in Table 6.

Figure 3 shows the measured deviations from PTB and KRISS according to the Re number. The deviations measured in PTB and KRISS show good agreement within the uncertainty range ( $U_{PTB} = 0.05$ ,  $U_{KRIS} = 0.08$ ). The En values were found to be less than 1 in the measured Re numbers of PTB and KRISS (Table 6).

**Table 5:** Fluid properties of water and hydrocarbon

20 °C, 1 atm	Density (kg/m <sup>3</sup> )	Viscosity (cP)
Water	1000	0.001
Hydrocarbon in PTB	784.816	0.00135
Hydrocarbon in KRISS	805.37	0.00295

**Table 6:** Uncertainty budget for volume tank calculation using volumetric method

Re. number	KRISS flowrate		PTB flowrate		En number
	t/h	m <sup>3</sup> /h	t/h	m <sup>3</sup> /h	
3.59E+04	30	37.25	13.69	17.45	0.32
7.18E+04	60	74.50	27.39	34.90	0.37
1.08E+05	90	111.75	41.08	52.35	0.37
1.44E+05	120	149.00	54.78	69.80	0.27

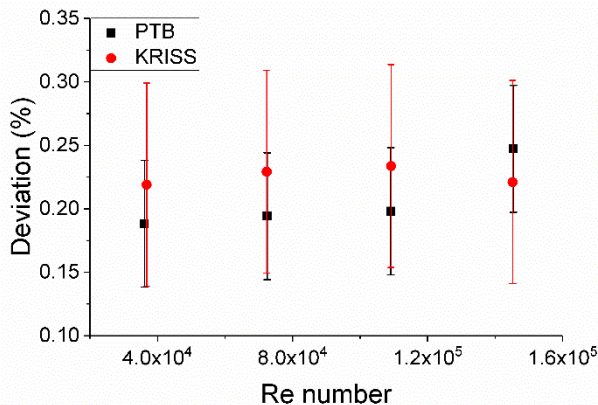


**Figure 3:** Comparison of hydrocarbon facilities between KRISS and PTB

## 7. Conclusion

In this study, we used the volumetric and gravimetric methods simultaneously to measure the hydrocarbon flow rate. A 1000 L volume tank was calibrated by both a filling method using a standard volume tank and a gravimetric method using a calibrated balance. The maximum difference between the filling method and the gravimetric method was 78.06 ml. In addition, we compared the hydrocarbon flow facilities of PTB with the volume tank and that of KRISS using the gravimetric method. The Re number was used to compensate for the density and viscosity differences in the working fluid. The calibration values of the Coriolis flowmeter in KRISS and PTB were 0.21–0.23% ( $U=0.08\%$ ,  $k=2$ ) and 0.18–0.24% ( $U=0.05\%$ ,  $k=2$ ), respectively, for an Re number range between 35,000 and 145,000. The results from the gravimetric method at KRISS matched very well with the results from the volumetric method at PTB, within the estimated uncertainties. Thus, we confirmed that the hydrocarbon flow standard systems of KRISS and PTB have traceability when using the volumetric and gravimetric methods in the given range of Re number.

## References

- [1] EURAMET project no. 1157: Inter-comparison of a 1000 L proving tank, 2013.
- [2] Wongthep P, Leetang K and Chinarak T, “The case study of water flow measurement comparison in the range of 12-120 L/min”, *Journal of Physics: Conf. Series*, **Vol.** 1144 pp 012077, 2018.
- [3] EURAMET cg-21: Guidelines on the calibration of standard capacity measures using the volumetric method, 2013.
- [4] EURAMET cg-19: Guidelines on the determination of uncertainty in gravimetric volume calibration, 2012.

# Uncertainty Evaluation of Stack Flowrate Measurement with S-Type Pitot Tube by Monte Carlo Method

D.T. Nguyen<sup>1</sup>, W.Kang<sup>2</sup>, Y.M.Choi<sup>2</sup>, S.H.Lee<sup>2</sup>, Y.M.Choi<sup>2</sup>

<sup>1</sup>University of Science and Technology, 217 Gajeong-ro, Yuseong-gu, Daejeon, Republic of Korea;  
<sup>2</sup>Korea Research Institute of Standards and Science, 267 Gajeong-ro, Yuseong-gu, Republic of Korea  
E-mail: [trangnd@kriss.re.kr](mailto:trangnd@kriss.re.kr); [trangnd@vmi.gov.vn](mailto:trangnd@vmi.gov.vn)

---

## Abstract

In order to attempt to mitigate the climate change, efforts to reduce the quantity of carbon emissions by actively seeking CO<sub>2</sub> trading and carefully control the liability of the emission test monitoring system from the industrial factories are a current issue. Therefore, the quality of greenhouse gas (GHG) emissions measurement with a proper uncertainty needs to be firstly considered. Currently, GHG emissions are estimated by a continuous emission measurement (CEM). The U.S Environmental Protection Agency (EPA), has classified the measurement of GHG emissions by the CEM as the highest quality Tier IV with lowest uncertainty level. Relating to accuracy of the CEM, both knowledge of the uncertainty contributions on GHG concentrations and volumetric flow rates are necessary for achieving a credible result. In order to accurately evaluate the uncertainty of the CEM method, flow rate measurements in the stack as well as GHGs concentration measurements by gas analyzer are crucial due to various uncertainty factors. In this study, we concentrate on finding measurand inputs and their uncertainty estimates that affect volumetric flow rates in a heat and power generation plant. Both the law of propagation method and Monte Carlo method (MCM) are used to evaluate the uncertainty of the flow rate measurement in order to minimize the numerical approximation of the partial derivatives of the complex model with respect to the every input. Consequently, the result of MCM is consistent with the result that by the law of propagation of uncertainty. The relative expanded uncertainties at 95% confidence level with coverage factor  $k=2$  are 528.1 m<sup>3</sup> and 527.2 m<sup>3</sup>, respectively.

---

## 1. Introduction

The increased GHG emissions such as CO<sub>2</sub>, CH<sub>4</sub> and N<sub>2</sub>O from the fossil fuel combustion causes the global warming phenomena by increasing average global temperature. The Inter-governmental Panel on Climate Change (IPCC)'s fifth assessment report described a global temperature rise of 0.89°C from 1901-2012 and a total anthropogenic radiation change of 2.29 W/m<sup>2</sup> [1]. Under the United Nations Framework Convention on Climate Change (UNFCCC), all countries are required to reduce greenhouse gas (GHG) emission for mitigating climate change. Korea GHG emission trading scheme has been implemented since January 2015 in accordance with the act on the allocation and trading of GHGs emission permits, which is the first nationwide cap and trade program in operation in Asia. The IPCC has developed practical guidelines for national inventories of GHGs emissions in different sectors such as energy, industrial process, agriculture and waste from economic activities [2]. The energy supply in the energy sector is an important source of GHG emissions as it contributes 25.9% of the global GHG emissions. Therefore, it is essential to properly estimate GHG emissions from the energy supply for mitigating climate change. In order to

reduce GHG emission, accurate and reliable GHG emission estimate with proper uncertainties should be carried out. GHGs emission estimate have been based on an activity-based method (i.e., fuel consumption and emission factor) and a continuous emission measurement (CEM). The CEM directly measures GHG emission through monitoring GHG concentrations and volumetric flow rate at a stack. In the U.S Environmental Protection Agency (EPA) [3], GHG emission by the CEM was classified as a highest quality Tier IV with lowest uncertainty level. Even though activity-based method for estimating GHG emission has been adopting in the Korea emission trade scheme, the CEM method should be examined for improving the quality of GHG emission inventories and trading. For evaluating an accurate uncertainty of CEM method, flow rate measurements in the stack as well as GHGs concentration measurements by gas analyzer are crucial due to various uncertainty factors [4]. The main objective of the present study is to evaluate the uncertainties in the stack gas flow rate measurement for the CEM method. To achieve this, continuous flowrate measurement were conducted with a S-type Pitot tube in a heat and power generation plant. The average flowrate were calculated with a flow velocity, a density, water content and a cross-sectional

area. Associated uncertainties of accumulated stack flowrate were calculated by propagating the uncertainties of input variables. Besides, Monte Carlo Method was also used to evaluate the uncertainty of flow rate measurement. This method can minimize the numerical approximation of the partial derivatives of the complex model with respect to the every input.

## 2. On site CEM method

According to the U.S.EPA [3], the amount of GHG emission can be determined by the fuel consumption measurements, the measured carbon dioxide concentration percent by the volume of the fuel and the total amount of exhaust volume flow rate from stack. However, CEMS method is mostly used in the power plants and industrial factories in order to estimate GHG emissions by equation (1):

$$E = \sum_{i=1}^N E_{5min,i} = \sum_{i=1}^N \left( x_{5min,i} \times Q_{5min,i} \times \frac{M_{gas}}{MV} \right) \quad (1)$$

where  $E_{5min,i}$  is the emission accumulated every 5 minutes of the  $i$ th measurement [% or ppm],  $Q_{5min,i}$  is the dried volumetric flow accumulated of the  $i$ th measurement [ $m^3$ ],  $M_{gas}$  is the molar mass of an emission gas,  $MV$  is the molar volume of ideal gas, and  $N$  is the total number of estimated emissions every five minutes. The 5-min accumulated volumetric gas flow rate can be calculated with the following equation:

$$Q_{5min} = \bar{V} \times \frac{\pi D^2}{4} \times \frac{P_s}{760} \times \frac{273.15}{T} \times (1 - x_w) \times t \quad (2)$$

where  $Q_{5min}$  is a 5-minute accumulated volumetric dry gas flow [ $m^3$ ],  $\bar{V}$  is an averaged gas flow velocity [ $m/s$ ],  $D$  is the stack diameter [ $m$ ],  $P_s$  is the static pressure [ $mmHg$ ],  $T$  is emission gas temperature [ $K$ ],  $t = 300$  [ $s$ ], and  $x_w$  is the water content [%] in the emission gas.

To measure the gas flow velocity in the stack, the types of flow meter are used as: 3-D Pitot tubes (DAT and sphere), averaging Pitot tubes, ultrasonic flowmeters, S-type Pitot tubes, and thermal flowmeters. But, the S-type Pitot tubes are the most commonly used in Korea, accounting for 56%. So, in this study, an S-type Pitot tube was selected in order to do the flow velocity measurements for CEMS. With a rigid body and two large pressure orifices, the S-type Pitot tube is suitable for measuring the flow velocity in high-dust environments [5,6]. The flow velocity can be obtained by measuring the differential pressure between the impact orifice and the wake orifice based on the Bernoulli equation. The S-type Pitot tube coefficient ( $C_p$ ) is used to calculate the flow velocity by measuring the differential pressure with the S-type Pitot tube, as in the following equation (3):

FLOMEKO 2019, Lisbon, Portugal

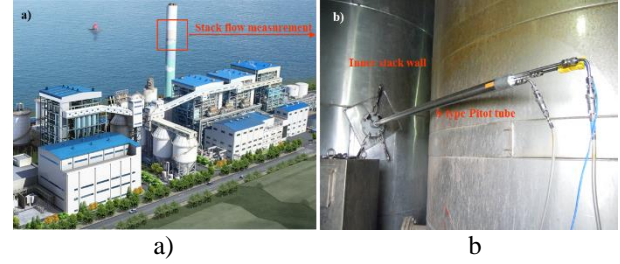


**Figure 1:** a) combined heat and power generation plant; b) Installation of the S-type Pitot tube in the wall of the stack

$$V_s = C_p \times \sqrt{\frac{2\Delta P}{\rho}} \quad (3)$$

where  $\Delta P$  is the differential pressure [ $Pa$ ] between the impact and the wake orifices and  $\rho$  is the density of the emission gas [ $kg/m^3$ ].

All flowrate measurements were conducted in a stack in the combined heat and power plant located in the western region of South Korea, as shown in figure 1. The flow rate measurement system of this company was connected to the national tele-metering system (TMS) for monitoring stack emissions reporting the 5-minute accumulated volumetric flow to the national TMS using equation (2).

## 3. Uncertainty evaluation of the gas flow measurement in the stack

### 3.1. Uncertainty evaluation by GUM

The mathematical model equation for the 5-minute accumulated volume flowrate measurement can be expressed as equation (2). Assuming that the input measurements were mutually independent, according to the ISO Guide [7], equation (2) can be expressed as the following uncertainty propagation using the Taylor series approximation.

$$u_c^2(Q_{5min}) = c_{\bar{V}}^2 u^2(\bar{V}) + c_D^2 u^2(D) + c_T^2 u^2(T) + c_{P_s}^2 u^2(P_s) + c_{(1-x_w)}^2 u^2(1 - x_w) \quad (4)$$

where  $c_{\bar{V}}$ ,  $c_D$ ,  $c_T$ ,  $c_{P_s}$ , and  $c_{(1-x_w)}$  are the sensitivity coefficients obtained by the partial differentiation of equation (2) with respect to each variable.  $u(\bar{V})$ ,  $u(D)$ ,  $u(T)$ ,  $u(P_s)$ , and  $u(1 - x_w)$  are the standard uncertainty of each of the variable.  $u_c(Q_{5min})$  is the combined uncertainty of  $Q_{5min}$ . Type A uncertainty is calculated with a standard deviation from the repeated experiment data of each variable. Type B uncertainty comes from flow calibration certification of instruments, fundamental constant or experience of experts. The sensitivity coefficient of each variable are as follows:

$$c_{\bar{V}} = \frac{\partial Q}{\partial \bar{V}} = \frac{\pi D^2}{4} \times \frac{P_s}{760} \times \frac{273.15}{T} \times (1 - x_w) \times 300$$

$$c_D = \frac{\partial Q}{\partial D} = \bar{V} \times \frac{\pi D}{2} \times \frac{P_s}{760} \times \frac{273.15}{T} \times (1 - x_w) \times 300$$

$$c_{P_s} = \frac{\partial Q}{\partial P_s} = \bar{V} \times \frac{\pi D^2}{4} \times \frac{1}{760} \times \frac{273.15}{T} \times (1 - x_w) \times 300$$

$$c_T = \frac{\partial Q}{\partial T} = -\bar{V} \times \frac{\pi D^2}{4} \times \frac{P_s}{760} \times \frac{273.15}{T^2} \times (1 - x_w) \times 300$$

$$c_{(1-x_w)} = \frac{\partial Q}{\partial (1-x_w)} = \bar{V} \times \frac{\pi D^2}{4} \times \frac{P_s}{760} \times \frac{273.15}{T} \times 300 \quad (5)$$

The combined standard uncertainty of the volumetric flow rate can be expressed as a relative form by dividing the square of flow rate and substituting sensitivity coefficients as following equation (6)

$$\frac{u_c^2(Q)}{Q^2} = \frac{u^2(\bar{V})}{\bar{V}^2} + 4 \frac{u^2(D)}{D^2} + \frac{u^2(P_s)}{P_s^2} + \frac{u^2(T)}{T^2} + \frac{u^2(1-x_w)}{(1-x_w)^2} \quad (6)$$

In the on-site energy plant, an S-type Pitot tube installed in the stack is typically fixed in a certain position. The measured velocity in a certain position has difference with the integrated average flow velocity of multi-points in the measuring plane of the cross section. Therefore, when installing an S-type Pitot tube in the stack wall, it is important to determine the best position to obtain a measured velocity that is close to the averaged velocity in the stack.

$$\bar{V} = V_s + \Delta V \quad (7)$$

$\bar{V}$  is the average velocity value calculated with the measured velocity distribution.  $V_s$  is the measured velocity value in a certain position fixed in the stack which can be calculated by equation (3) when using S-type Pitot tube.  $\Delta V$  is difference between averaged velocity and measured velocity of fixed position. The number of traverse points in the cross section of the stack are determined by EPA method [5] and ISO [6].

$$u^2(\bar{V}) = u^2(V_s + \Delta V) = u^2\left(C_P \sqrt{\frac{2\Delta P}{\rho}} + \Delta V\right) \quad (8)$$

$$u^2(\bar{V}) = c_{C_P}^2 u^2(C_P) + c_{\Delta P}^2 u^2(\Delta P) + c_{\rho}^2 u^2(\rho) + c_{\Delta V}^2 u^2(\Delta V) \quad (9)$$

$$c_{C_P} = \frac{\partial \bar{V}}{\partial C_P} = \sqrt{\frac{2\Delta P}{\rho}}$$

$$c_{\Delta P} = \frac{\partial \bar{V}}{\partial \Delta P} = \frac{1}{2} C_P \sqrt{\frac{2}{\rho \Delta P}}$$

$$c_{\rho} = \frac{\partial \bar{V}}{\partial \rho} = -\frac{1}{2} C_P \sqrt{\frac{2\Delta P}{\rho^3}}$$

$$c_{\Delta V} = \frac{\partial \bar{V}}{\partial \Delta V} = 1 \quad (10)$$

A typical S-type Pitot tube coefficient is known to be approximately 0.85 according to the ISO [6]. However, for the accurate and reliable velocity measurement, both a specific coefficient and its associated uncertainty,  $u(C_P)$ , need to be determined for each Pitot tube by a national metrology institute or accredited calibration laboratory. In the present study, the coefficient of the Pitot tube calibrated in the Korea Environment Corporation (KECO) was 0.826.  $u(C_P)$  in the KECO calibration was 0.55%. The uncertainty of the different velocity,  $u(\Delta V)$  was determined by 1.54%. The uncertainty of the different pressure,  $u(\Delta P)$  was 1.91%.

Moreover, the density of emission gas ( $\rho$ ) can be determined by estimating a weighted average density based on the concentration of major gas components ( $N_2$ ,  $CO_2$ ,  $O_2$ ,  $Ar$ ,  $H_2O$ ) in the emission gas from the stack as in the following equation 11:

$$\rho = \frac{(x_{CO_2} \times 44 + x_{O_2} \times 32 + x_{Ar} \times 39.94 + x_{N_2} \times 28 + x_{H_2O} \times 18) \times 100}{22.4} \quad (11)$$

The concentration measurements of  $N_2$ ,  $CO_2$ ,  $O_2$ ,  $Ar$  and  $H_2O$  obtained by ULTRAMAT6 gas analyzers were used to estimate a weighted average density of emission gas at 760 mmHg and 0°C. The uncertainty of the gas emission,  $u(\rho)$  including the difference between the weighted average value and the fixed value used in the stack was determined as 1.1%.

The water content can be calculated by condensed moisture in the impinger and volume flow rate in the dry gas meter according to EPA method 4 [8], which can be expressed as equation 12:

$$x_w = \frac{\frac{22.4}{18} m_a}{Q_m \times \frac{273.15}{T_m} \times \frac{P_m}{760} + \frac{22.4}{18} m_a} \quad (12)$$

where  $m_a$  is the measured mass of moisture in the impinge (g/min),  $Q_m$  is the dry gas volume measured by the dry gas meter (L/min),  $P_m$  is absolute pressure at the dry gas meter (mmHg),  $T_m$  is absolute temperature (K). In the present study, a continuous weighing method with balance was applied to the uncertainty evaluation of water contents and flow rate. The water mass out of a cold condenser prior gas analyzer and flow meter were measured every 10 seconds, and were found to be about

**Table 1:** Uncertainty budget of volumetric flow rate measurements at 14.5 m/s

Component	Value	Unit	Standard Uncertainty (%)		Sensitivity coefficient, $c_i$	Uncertainty contribution, $u_i \times c_i$ (%)	
			Type A	Type B			
$C_p$	0.826	-	-	0.55	1	0.55	
$\Delta P$	136.4	Pa	0.54	1.78	0.5	0.68	
$\rho$	0.885	kg/m <sup>3</sup>	0.0054	1.12	0.5	0.53	
$D$	2500	mm	-	0.23	2	0.46	
$P_s$	756	mmHg	0.0019	0.15	1	0.13	
$T$	409	K	0.0048	0.14	1	0.25	
$1 - x_w$	91.5	%	0.0016	0.16	1	0.30	
$\bar{V}$	14.5	m/s	-	1.54	1	1.54	
$Q$	12972.5	m <sup>3</sup> /min					
Combined uncertainty of the flow rate measurement, $u_C$ =						2.03%	
with 95% confidence level, $k$ =						2	
Relative expanded uncertainty, $U$ =						4.1%	

0.292 g/min. The dry gas passing through the condenser was measured using a flow meter. The uncertainty of the water content,  $u(1 - x_w)$  including the difference between the sampling value and the theoretical value of fuel coal used in the energy plant was determined by 0.16%. On the other hand, the uncertainty of the static pressure,  $u(P_s)$  was 0.15%. The uncertainty of the temperature,  $u(T)$  was 0.14%. And the uncertainty of the stack diameter,  $u(D)$  was 0.23%. From all these values, the relative expanded uncertainty of the 5 minutes accumulated volumetric flow rate in Table 1 was estimated about 4.1% (or 527.2 m<sup>3</sup>),  $k=2$  with a 95% confident level.

### 3.2. Uncertainty evaluation by GUM

MCM performs a random draw from prescribed probability distribution for each input parameter and the corresponding value of output parameter will be formed by the known functional relationship. Also, during doing random sampling from the probability density function of the input quantities, MCM provides the probability distribution of the output and the coverage interval [9,10]. To do MCM for evaluating uncertainty of the volumetric flow rate, simplifying equation (2) in order to have a general overview regarding the all input variables that will be taken part into the Monte Carlo propagation simulation procedure as follows:

$$Q_{5min} = f(\bar{V}, D, P_s, T, x_w) \quad (13)$$

As assuming in 3.1, all input quantities in equation (13) had no relationship with each other. Therefore, no multivariate probability density function was required in this sampling procedure. It means that the 5-minutes accumulated volumetric flowrate and its uncertainty were only estimated by random sampling from the predefined probability distributions associated with each input as Table 2. The values of  $\bar{V}$  were randomly drawn from equation (3), (7), (11) and the values of  $x_w$

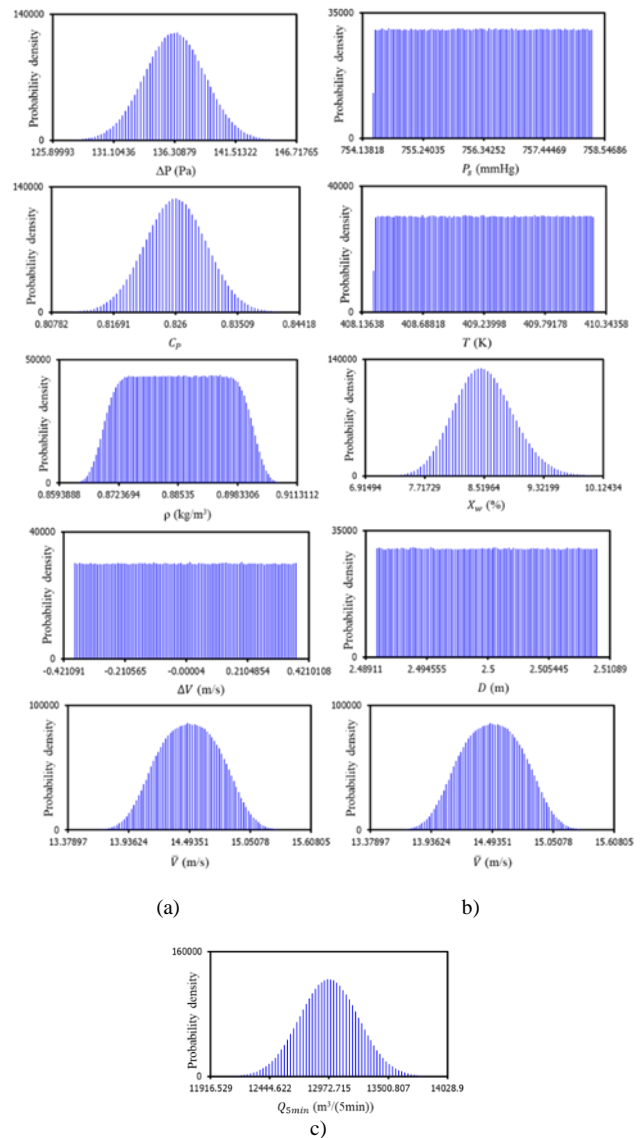


**Figure 2:** a) Random sequences for  $\bar{V}$ ; b) and c) Random sequences for  $Q_{5min}$

**Table 2:** The input quantities and the probability density function assigned to them

Input $x$	Units	$\bar{x}$	Probability density function	Uncertainty $u(x)$
$P_s$	mmHg	756	Rectangular	1.154
$T$	K	409	Rectangular	0.577
$x_w$	%	8.5	Normal	0.40
$D$	m	2.5	Rectangular	0.0058
$\bar{V}$	m/s	14.5	Normal	0.278

were randomly drawn from equation (12). Random sequences are graphed in figure 2. The number of Monte Carlo trials,  $M$  deliver the shape of the probability distribution for the output quantity as well as the coverage probability required and a value of  $M=10^6$  was suggested to give a 95% coverage interval for the output quantity [9]. So, with this choice of  $M$ , the result of MCM was  $Q_{5min} = 12972.7 \text{ m}^3$  and  $U_{MCM}(Q_{5min}) = 528.1 \text{ m}^3$ . These value are quite close to the results implemented by GUM ( $Q_{5min} = 12972.5 \text{ m}^3$ ) and  $U_{GUM}(Q_{5min}) = 527.2 \text{ m}^3$ ). The difference of two estimation of uncertainties is 0.17%. The framework of this simulation was based on the Microsoft Excel and Microsoft Visual Basic for Application.

#### 4. Conclusions

The Monte Carlo Method produces the results having no big difference from GUM method, the difference of 0.17%. It also commits to simplify the calculation and show graphically how the effect of input quantities on the distribution shape of output. Hence, MCM is well suited for uncertainty estimation when the functional relationship is complex as this study.

#### References

[1] Intergovernmental Panel on Climate Change Fifth Assessment Report, Climate Change 2013: The Physical Science Basis, 2013.

[2] Intergovernmental Panel on Climate Change, Guidelines for National Greenhouse Gas Inventories, 2006.

[3] U.S. Environmental Protection Agency, Greenhouse Gas Reporting Program 40 CFR 98.30 Subpart C, 2013.

[4] Lee, S. I., Choi, Y.M., Woo, J. C., Kang, W. and Jung, J. S., Estimating and Comparing Greenhouse Gas Emissions with Their Uncertainties Using Different Methods, Journal of the Air & Waste Management Association, 64(10), 2014.

[5] U.S. Environmental Protection Agency, Determination of Stack Gas Velocity and Volumetric Flow rate (Type S Pitot tube) EPA method 2, 2000.

[6] ISO, Stationary Source Emissions – Measurement of Velocity and Volume Flowrate of Gas Streams in Ducts, ISO 10780, 1994.

[7] JCGM, Evaluation of measurement data - Guide to the expression the uncertainty in measurement, JCGM 100, 2008

[8] U.S. Environmental Protection Agency, Determination of Moisture Content in Stack Gases EPA method 4, 2000

[9] JCGM, Guide to the expression of uncertainty in measurement – Propagation of distributions using Monte Carlo method. JCGM 101, 2008

[10] I.Farrance, R. Frenkel “Uncertainty in Measurement: A review of Monte Carlo simulation using Microsoft Excel for the calculation of uncertainties through functional relationships, including uncertainties in empirically derived constant”, Clean Biochem Rev, 2014.

# Comparison of calibrations of wind speed meters with a large blockage effect

J. Geršl<sup>1</sup>, P. Busche<sup>2</sup>, M. de Huu<sup>3</sup>, D. Pachinger<sup>4</sup>, H. Müller<sup>5</sup>, K. Hölper<sup>6</sup>,  
A. Bertašienė<sup>7</sup>, M. Vilbaste<sup>8</sup>, I. Care<sup>9</sup>, H. Kaykısızlı<sup>10</sup>, L. Maar<sup>11</sup>, S. Haack<sup>12</sup>

<sup>1</sup>Czech Metrology Institute, Okružní 31, 63800 Brno, Czech Republic

<sup>2</sup>Deutsche WindGuard Wind Tunnel Services GmbH, Varel, Germany

<sup>3</sup>Federal Institute of Metrology METAS, Wabern, Switzerland

<sup>4</sup>BEV/E+E, Engerwitzdorf, Austria

<sup>5</sup>Physikalisch Technische Bundesanstalt, Braunschweig, Germany

<sup>6</sup>Westenberg Engineering, Köln, Germany

<sup>7</sup>Lithuanian Energy Institute, Kaunas, Lithuania

<sup>8</sup>Testing centre, University of Tartu, Tartu, Estonia

<sup>9</sup>CETIAT, Villeurbanne, France

<sup>10</sup>TÜBİTAK UME, Gebze / Kocaeli, Turkey

<sup>11</sup>Czech Hydrometeorological Institute, Prague, Czech Republic

<sup>12</sup>Danish Technological Institute, Aarhus, Denmark

E-mail (corresponding author): jgersl@cmi.cz

---

## Abstract

In this paper we report on the first results of EURAMET project no. 1431 which was initiated in 2017 with a goal to experimentally determine systematic deviations of calibration results of vane and cup anemometers due to various boundary conditions in different wind tunnels especially in wind tunnels with open test section where theoretical models are missing. For that purpose 3 vane anemometers and 2 cup anemometers of various dimensions have been calibrated in 14 wind tunnels with various types and sizes of test sections ranging from 15 cm to 100 cm in diameter. This paper provides the first look to calibration data from the recently completed measurements. On top of that, velocity disturbance fields in front of the 5 tested anemometers have been measured in order to avoid mixing of the effect of boundary conditions with other source of deviations due to placing a reference meter to an area influenced by a meter under test. The velocity disturbance fields reported in this paper can be useful for all air speed calibration laboratories giving an idea how large these deviations can be and what is the optimal position and distance of a reference meter.

---

## 1. Introduction

When an anemometer is calibrated in a wind tunnel the velocity indication of the meter is influenced by flow conditions at a boundary of a test section of the wind tunnel leading to the so called blockage effect. The larger is the meter compared to the test section diameter the more significant the blockage effect is. The effect also depends on a type of the test section (open or closed) and on a type of the anemometer tested. Moreover, it is desirable to place a reference anemometer to a position where the velocity field is not significantly influenced by the meter under test which may not be possible for large meters leading to another source of systematic errors in anemometer calibrations [1, 2]. These effects were observed also in inter-laboratory comparisons of wind-speed calibration

laboratories and in [3] it was concluded that the results of the comparisons indicate a need for more attention to blockage effects during air speed calibrations and their effect on air speed uncertainty statements.

To make the calibration results from various wind tunnels comparable they should be corrected to values corresponding to certain standardized boundary conditions – e.g. to free stream conditions assuming an infinite asymptotically homogeneous velocity field with reference velocity given by the velocity at infinity (far enough from the anemometer). Or at least the size of such correction should be estimated and included in the uncertainty budget.

A theory of velocity corrections of measurements in wind tunnels with closed measurement section to the free stream conditions was developed by Glauert [4] and further extended by Mikkelsen and Sørensen [5]. Their

theory for closed measuring sections is reviewed and extended to open measuring sections in [6] or in the monograph [7]. This theory is suitable for horizontal axis wind turbines (vane anemometers) and it contains some simplifying assumptions and therefore its experimental validation is necessary.

In standards the blockage effect is addressed e.g. in [8] where a relative uncertainty contribution of 1/4 of the blockage ratio for closed measuring sections and 1/16 of the blockage ratio for open measuring sections is recommended in case of cup anemometer calibrations with Pitot tube as a reference, the blockage ratio being the ratio of the area of the anemometer projected to a plane perpendicular to the flow and the cross sectional area of the test section of a wind tunnel. For closed measuring sections use of the Maskell theorem [9] is recommended. Otherwise we are not aware of quantitative recommendations for blockage corrections or uncertainties. To eliminate these uncertainties the standards [8, 10] recommend not to exceed the blockage ratio of 10 % for wind tunnels with an open test section and 5 % for wind tunnels with a closed test section. The standard [11] recommends not to exceed 5 % in general. Experimental investigation of influence of the blockage effect to cup anemometer calibrations can be found e.g. in [12].

In this paper we report on the first results of the EURAMET project no. 1431. The final goal of this project is to experimentally determine the blockage effect corrections for vane and cup anemometers especially in case of wind tunnels with open test section. Such wind tunnels are widely used by calibration laboratories but the known correction models mostly apply to wind tunnels with closed test section. Mathematical modelling of processes at a boundary of air stream in open test sections is challenging [6].

Three vane anemometers and two cup anemometers of various sizes have been calibrated in 12 laboratories providing 14 wind tunnels with test sections of various types and sizes in a time period from November 2017 to March 2019. To separate the effect of boundary conditions from the effect of placing the reference meter to an area influenced by the meter under test the velocity fields in front of the 5 anemometers have been measured in a wind tunnel of the pilot laboratory (CMI). The measurements have been finished recently and the data analysis is in progress. This paper provides a first look and discussion of the measured data.

In Sections 2 and 3 of this paper we present details of the 14 participating wind tunnels and of the 5 used transfer standards. In Section 4 we show maps of the measured velocity disturbance fields in front of the transfer standards together with positions of the reference meters in the participating wind tunnels and we discuss their impact to systematic deviations between the participants. In Section 5 we present calibration curves of the 5 anemometers in the 14 wind

tunnels and in Section 6 we discuss the results, draw conclusions and plan a future work.

## 2. Participating wind tunnels

The laboratories participating in the EURAMET project no. 1431 are (order according to a time of calibration): Czech Metrology Institute (CZ), BEV/E+E (AT), Physikalisch Technische Bundesanstalt (DE), Deutsche WindGuard Wind Tunnel Services (DE), Westenberg Engineering (DE), Lithuanian Energy Institute (LT), Testing centre - University of Tartu (EST), CETIAT (FR), Federal Institute of Metrology METAS (CH), TÜBİTAK UME (TR), Czech Hydrometeorological Institute (CZ), Danish Technological Institute (DK) (see also Figure 1).



**Figure 1:** Map of the participating laboratories.

**Table 1:** Overview of the participating wind tunnels.

wind tunnel no.	wind tunnel type	test section type	nozzle shape	nozzle diameter /width (cm)
1	closed	open	square	100
2	open	box	circular	80
3	closed	open	rectang.	50 x 60
4	closed	open	circular	45
5	closed	box	circular	40
6	closed	open	circular	32
7	open	box	circular	31.5
8	closed	box	circular	25.5
9	closed	open	circular	25.5
10	open	box	circular	15.2
11	closed	closed	rectang.	74 x 49
12	closed	closed	square	51
13	open	closed	square	50
14	closed	closed	circular	40

An overview of parameters of the wind tunnels participating in the project is in Table 1. The wind tunnels are numbered according to the size of their test section from the largest to the smallest. First the wind tunnels with open test section or a test section bounded

by a box are listed (1-10) and then the wind tunnels with closed test section follow (11-14). By closed test section we mean a test section which is bounded by walls surrounding a space with the same cross-sectional area as the outlet nozzle of the wind tunnel, i.e. the walls are continuous prolongation of the nozzle. By a test section bounded by a box we mean a test section which is bounded by walls enclosing a space with a larger cross-sectional area than the area of the nozzle, i.e. the box is wider than the nozzle. This is a typical setup for open (Eiffel) type wind tunnels and there can be a large variety of dimensions of the box. By open test section we mean an unbounded test section. There can be other variants with slight deviations from the above definitions. E.g. the wind tunnel no. 1 has a wall (only) at the bottom and the wind tunnel no. 11 has three walls missing the bottom one.

### 3. Transfer standards

The following anemometers have been circulated among the participating laboratories:

- 1) Vane anemometer Schiltknecht MiniAir20 with the probe Macro; propeller diameter including frame 8.5 cm (Figure 2 top)
- 2) Vane anemometer Testo 0635 9340 with measuring unit Testo 445; propeller diameter including frame 10.7 cm (Figure 2 bottom)
- 3) Vane anemometer RM Young Gill Propeller MODEL 27106D/F; propeller diameter 20 cm; no frame (Figure 3)
- 4) Cup anemometer Vaisala WAA151; cup diameter 5.3 cm; propeller diameter 18.2 cm (Figure 4 right)
- 5) Cup anemometer Thies First Class Advanced type 4.3351.10.000; cup diameter 8 cm; propeller diameter 24 cm (Figure 4 left)



Figure 2: Anemometers Schiltknecht (top) and Testo (bottom).

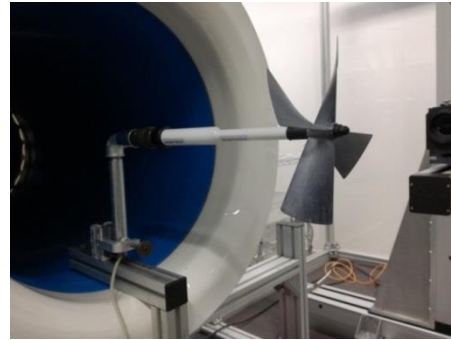


Figure 3: Anemometer RM Young Gill Propeller.



Figure 4: Anemometers Thies (left) and Vaisala (right).

The blockage ratio of an anemometer in a wind tunnel is determined as ratio of projected cross-sectional area of a cup wheel or propeller, sensor and support apparatus to the total area of a nozzle of the wind tunnel. The approximate blockage ratios of the 5 anemometers in the 14 wind tunnels are summarised in Table 2. Also wind tunnels exceeding the recommendations of [8, 10] on the blockage ratio, i.e. 10 % for open test sections and 5 % for closed test sections, are included in order to obtain more visible systematic deviations due to the blockage effect.

Table 2: Blockage ratios of the transfer standards.

wind tunnel	test sect.	vane Schilt.	vane Testo	vane RM Y.	cup Vais.	cup Thie.
		blockage ratio (%)				
1	open or box	0.57	0.90	1.3	1.4	2.2
2		1.1	1.8	2.5	2.8	4.4
3		1.9	3.0	4.2	4.7	7.4
4		3.6	5.7	7.9	8.9	13
5		4.5	7.2	10	9.8	16
6		7.1	11	x	11	22
7		7.3	12	16	12	23
8		11	18	25	18	35
9		11	18	x	x	x
10		31	50	x	x	x
11	closed	1.6	2.5	3.5	3.9	6.1
12		2.2	3.5	4.8	5.4	8.5
13		2.3	3.6	5.0	5.7	8.9
14		4.5	7.2	10	11	x

#### 4. Velocity disturbance fields

In order to find the systematic deviations in calibration results due to boundary conditions in a test section of a wind tunnel it is necessary to have other sources of systematic deviations under control. One such possible source is the influence of a tested anemometer to the velocity field in a position where a reference anemometer is placed. Therefore, the velocity fields in front of the 5 tested anemometers have been measured in the wind tunnel of Czech Metrology Institute (CMI) for all velocities for which the calibrations have been performed (see Section 5) and maps of distribution of the reference meter positions of the participating laboratories have been created. The velocity fields in front of the anemometers may differ in different wind tunnels so the maps presented here, obtained in the wind tunnel of CMI, give just an estimate of a size of the effect of reference meter position.

The velocity fields have been measured with LDA placed on a 3D traversing system. Only the velocity component along the axis of the test section has been measured. The graphs presented here shows a velocity disturbance caused by the tested meter which is determined as a difference of the velocity field with the anemometer installed minus a velocity field measured in an empty test section. Since there can be a small unknown offset between the measurements with and without the anemometer the velocity disturbance fields are determined up to this offset and therefore the isolines in the plots are not provided with values. The step of the isolines is 0.2 % of a nominal velocity in all the plots Figure 5-11. This step is unaffected by the offset and therefore the plots show gradients of the velocity disturbance field and enable to determine velocity differences between the positions of the reference meters of the participants and also enable to determine an area in front of a meter where the influence of the meter is negligible by looking for a negligible gradients of the velocity disturbance field.

In Figures 5-7 the velocity disturbance fields in front of the vane anemometers are shown for the maximal velocities in which the anemometers have been calibrated (12 m/s for Testo and 20 m/s for Schiltknecht and RM Young). The fields were measured in a horizontal plane in a height of the centre of the anemometer's propeller in a grid of points with a step of 2 cm in both axial and transversal directions corresponding to the grid nodes in the plots. The flow direction in the plots is from bottom to the top (it is a top view of the horizontal plane), the bottom line being 2.5 cm behind the wind tunnel nozzle which is circular with a diameter of 45 cm. The width of the depicted area is 40 cm with axis of the test section in the middle, however, for the vane anemometers only a half of the plane was measured and the second half is mirrored assuming an axial symmetry of the meters and the flow.

The tested anemometers are depicted as the grey blocks above the upper line. The projection of the anemometer shape is rectangular since this is a top view.

In Figures 8-11 the velocity disturbance fields in front of the cup anemometers are shown for the maximal velocity 20 m/s. The flow around the cup anemometers is not axially symmetric as in case of the vane anemometers and therefore it is not sufficient to measure the velocity field just in a horizontal half-plane. The Figures 8 and 10 again show the velocity disturbance field in a horizontal plane in a height of the centre of the anemometer's propeller with a difference that the whole plane was measured (no mirrored half-plane) and we can see the flow asymmetry in the measured field. The Figures 9 and 11 then show the velocity disturbance field in a vertical plane given by the axis of the wind tunnel test section and rotation axis of the anemometer. Only a half-plane above the propeller centre was measured since nobody place the reference meter below - in front of the anemometer body. In this case the flow direction is from left to right and again the left-most line of the grid is placed 2.5 cm behind the wind tunnel nozzle. The grid step is 2 cm as in all other plots.

The velocity disturbance fields for lower velocities, expressed in a relative way as percentage of a nominal velocity, look very similar to the ones for the maximal velocities depicted here. The fields for different velocities have been compared at the axis of the test section and slightly larger gradients have been observed only for the lowest velocity 0.5 m/s and for some of the meters (RM Young and Schiltknecht). Relative fluctuations of the velocity at the grid points are larger for lower velocities giving not so clear contours in the plots.

The positions of the reference anemometers of the particular laboratories are depicted as the red dots which are numbered according to the wind tunnel numbering introduced in the Table 1. The wind tunnel 5 is not included since the reference meter is placed 1.5 m in front of the meter under test. The wind tunnel 10 is not included since it uses a differential pressure measurement at the wind tunnel nozzle as a reference. The wind tunnel 14 is not included since the geometry data have not been submitted yet to the pilot laboratory. The reference meters of the wind tunnels 2 and 11 are placed 8 cm and 5 cm behind the right-most line of the plots. In case of the vane anemometers the positions of the reference meters which are not placed in the horizontal plane at the level of anemometer centre has been rotated and depicted in this plane taking the axial symmetry into account.

Discussion of the measured velocity disturbance fields is postponed to the Sections 5 and 6.

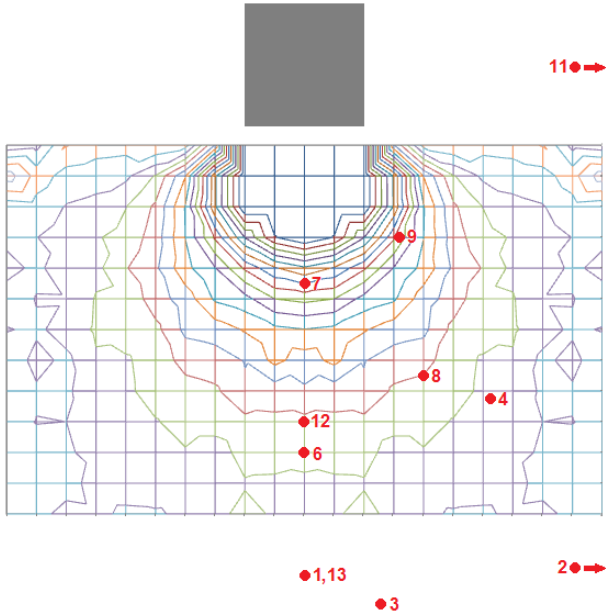


**Figure 5:** Velocity disturbance field, Schiltknecht, 20 m/s, isolines with step 0.2 % of 20 m/s (further explanation in the text).

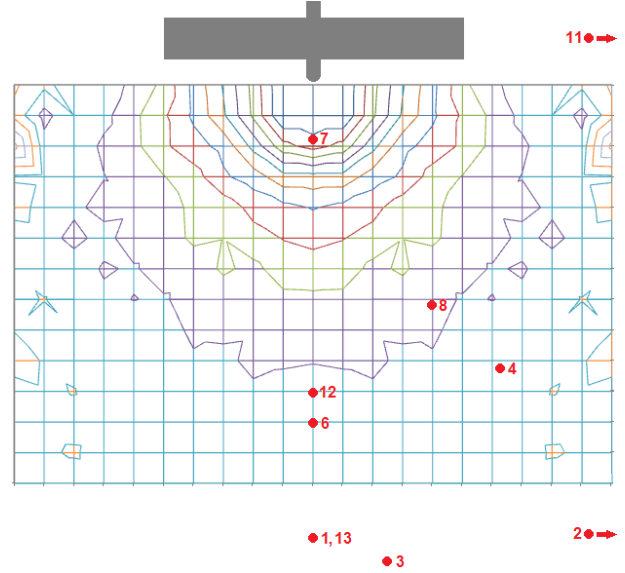


**Figure 7:** Velocity disturbance field, RM Young, 20 m/s, isolines with step 0.2 % of 20 m/s (further explanation in the text).

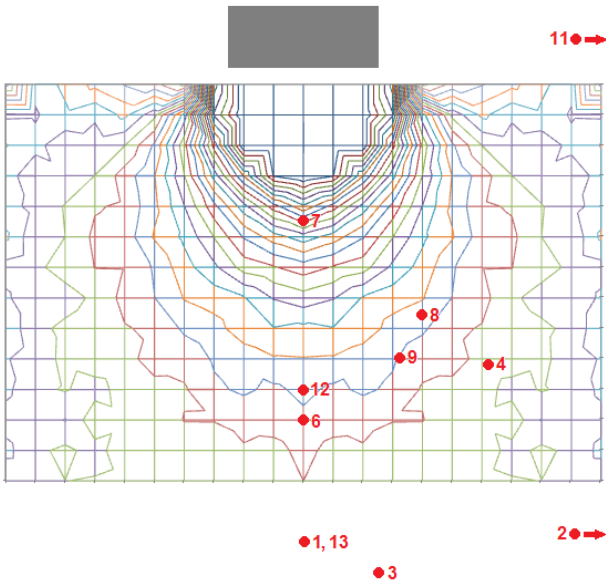


**Figure 6:** Velocity disturbance field, Testo, 12 m/s, isolines with step 0.2 % of 12 m/s (further explanation in the text).

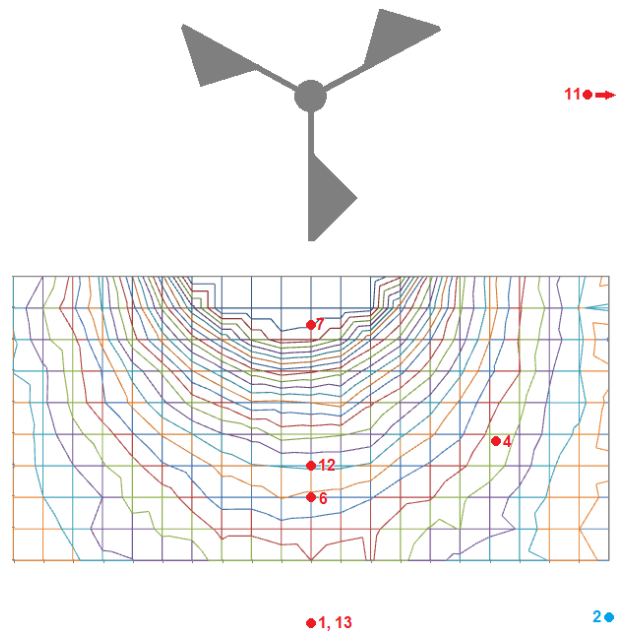


**Figure 8:** Velocity disturbance field in horizontal plane, Vaisala, 20 m/s, isolines with step 0.2 % of 20 m/s; the blue dot is 20 cm out of the plane towards the reader (further explanation in the text).

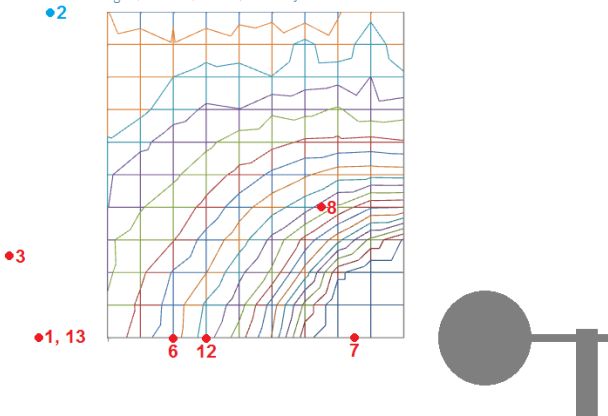


**Figure 9:** Velocity disturbance field in vertical plane, Vaisala, 20 m/s, isolines with step 0.2 % of 20 m/s; the blue dot is 20 cm out of the plane towards the reader (further explanation in the text).

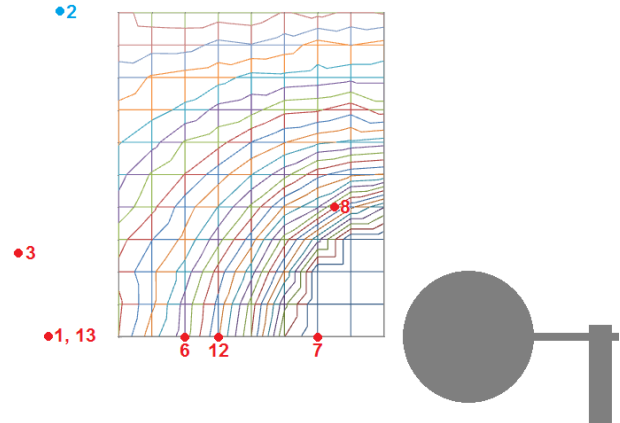


**Figure 11:** Velocity disturbance field in vertical plane, Thies, 20 m/s, isolines with step 0.2 % of 20 m/s; the blue dot is 20 cm out of the plane towards the reader (further explanation in the text).

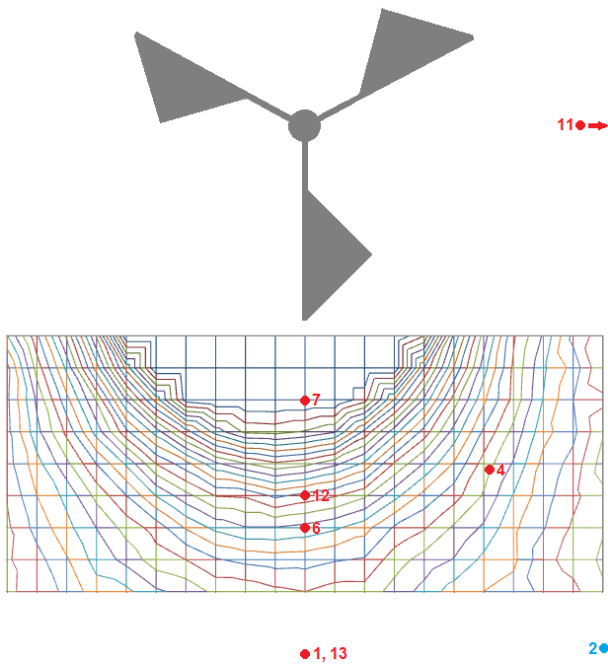


**Figure 10:** Velocity disturbance field in horizontal plane, Thies, 20 m/s, isolines with step 0.2 % of 20 m/s; the blue dot is 20 cm out of the plane towards the reader (further explanation in the text).

## 5. Calibration results

The anemometers Schiltknecht, RM Young and Thies have been calibrated in velocity points 0.5, 2, 5, 8, 12 and 20 m/s. In case of the anemometer Testo the 20 m/s was skipped since the meter has a range up to 15 m/s. For the anemometer Vaisala the 0.5 m/s was replaced by 1 m/s because of the starting threshold of the meter. The same mounting pipes have been used in all the laboratories. Each laboratory used its usual calibration procedure. During the measurement campaign (Nov 2017 – Mar 2019) all the meters have been calibrated

6 times in the pilot lab (CMI) to evaluate the stability of the meters.

In Figures 12-16 the error curves of the 5 anemometers in the 14 wind tunnels are shown. The  $v_M$  axis displays a velocity indicated by a meter under test. The  $E$  axis displays the error of a meter, i.e.  $E = v_M - v_{ref}$  with  $v_{ref}$  being a reference velocity. An error curve obtained in a particular wind tunnel has the number of the wind tunnel as defined in the Table 1. The curves drawn by a full line belong to wind tunnels satisfying the criteria of [8, 10] on the blockage ratio, i.e. less than 10 % for open test sections and less than 5 % for closed test sections. For test sections bounded by a box the 10 % criterion was used. The curves drawn by a dashed line belong to wind tunnels which exceed these limits. Uncertainty bars are not included for all the error curves in the Figures 12-16, however, for each velocity there is a pair of lines showing stability of the meter and typical expanded uncertainty of the calibrations. The span of the first line from a pair is given as difference between maximal and minimal error of the meter obtained during the six repeated calibrations in the pilot laboratory (CMI). The span of the second line from a pair is given as median of all expanded uncertainty intervals as reported by the participating laboratories. Only the span of the lines plays a role. The position of the lines in the plots has just a graphical justification.

In the Figure 12 with error curves of the smallest vane anemometer Schiltknecht we see a group of error curves at lower error values and then several curves above them. The shift of the wind tunnels 7 and 9 to the larger error values can be explained by the close position of the reference meter (see Figure 5). The shift of 5, 13 and 14 is probably caused by a different kind of systematic error. The shift of 13 and 14 to the larger error values repeats also for the other meters.

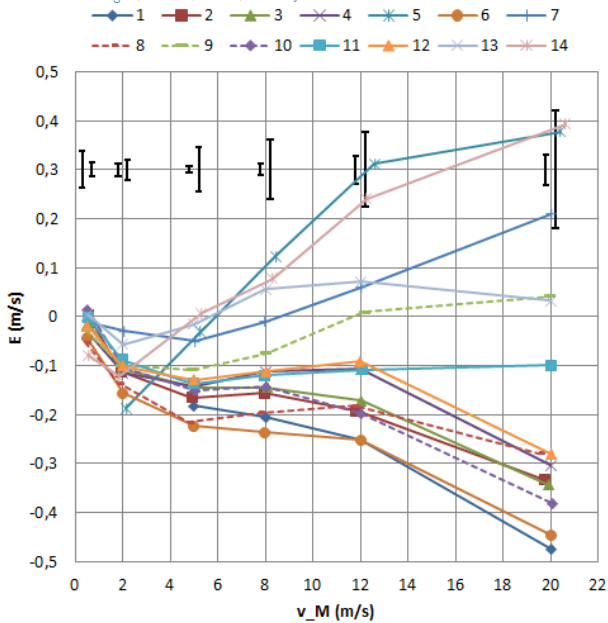


**Figure 12:** Error curves – vane anemometer Schiltknecht; for explanation of the graphical elements see the text.

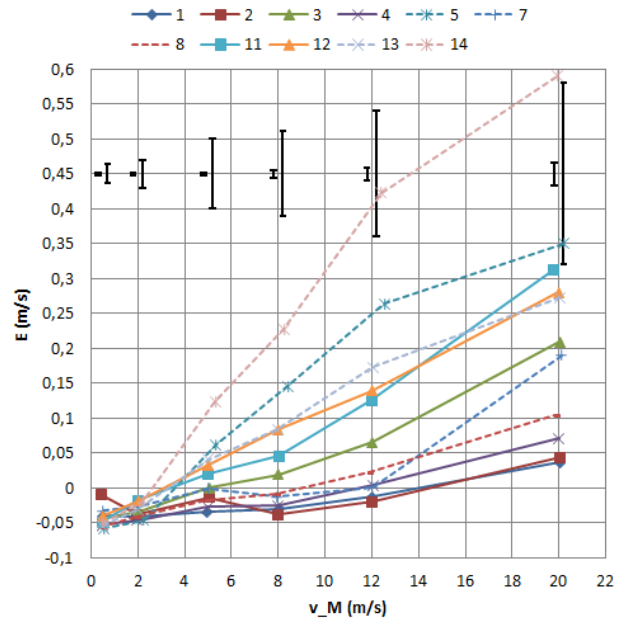


**Figure 14:** Error curves – vane anemometer RM Young; for explanation of the graphical elements see the text.

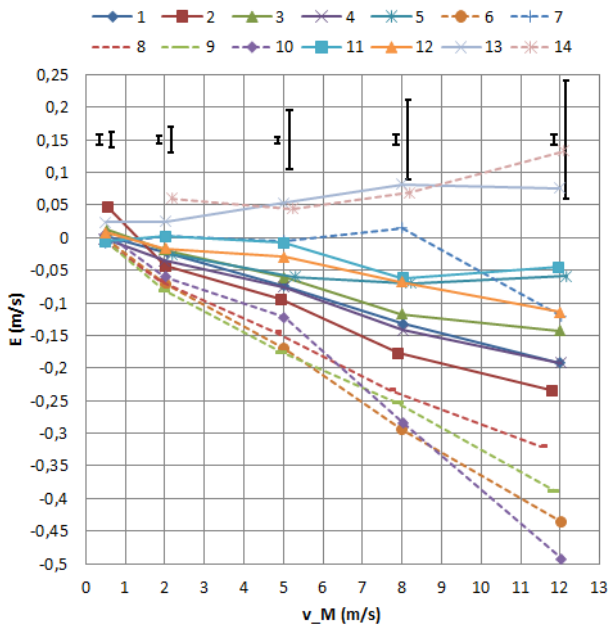


**Figure 13:** Error curves – vane anemometer Testo; for explanation of the graphical elements see the text.

In the Figure 13 with error curves of the midsize vane anemometer Testo we can see the error curves of the small wind tunnels (dashed lines) grouped at lower error values with exception of the wind tunnels 7 and 14 mentioned already above. The wind tunnel 9 in this case has the reference position shifted by 10 cm further from the MUT (see Figure 6) so the shift to the larger error values does not occur. The error curves of the larger

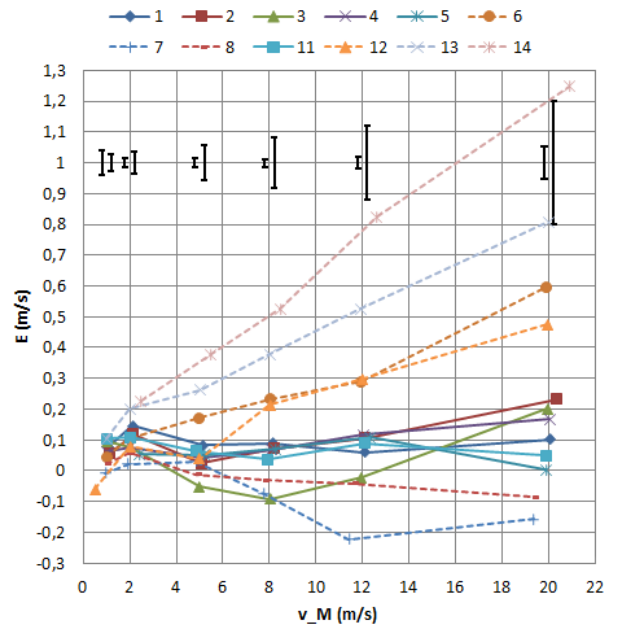


**Figure 15:** Error curves – cup anemometer Vaisala; for explanation of the graphical elements see the text.

wind tunnels (full lines) are grouped in the middle except no. 13 which is shifted similarly as for the Schiltknecht vane anemometer.

In the Figure 14 with error curves of the largest vane anemometer RM Young Gill Propeller we see quite good agreement between the error curves besides the curve 14 which is deviated also for the other meters. We

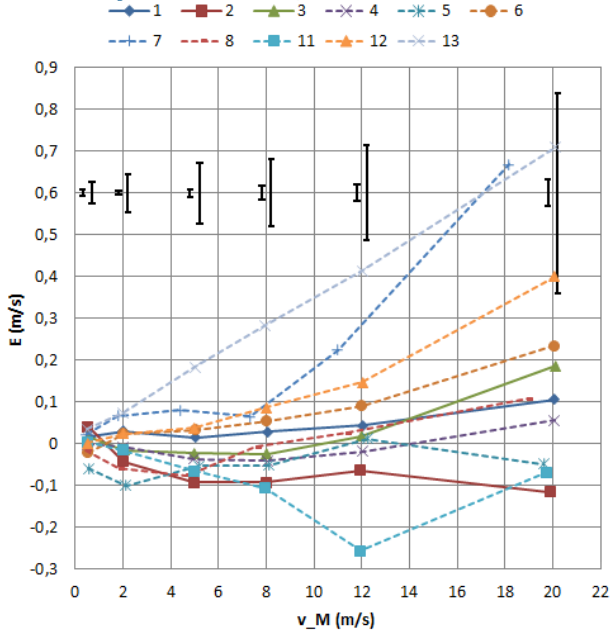


**Figure 16:** Error curves – cup anemometer Thies; for explanation of the graphical elements see the text.

cannot see a clear distinction between smaller wind tunnels (dashed lines) and larger wind tunnels (full lines). The reason could be that in spite of the large size of the meter the interaction with air stream is not so strong as follows from the Figure 7.

In the Figure 15 with error curves of the smaller cup anemometer Vaisala we can see a clear grouping of the curves belonging to the large wind tunnels (full lines) and the curves of the smaller wind tunnels (dashed lines) scattered around them. Similar behaviour can be seen also in the Figure 16 with the error curves of the larger cup anemometer Thies.

## 6. Discussion and conclusions

From the measured velocity disturbance fields (Figures 5-11) we see that the velocity gradients in front of the anemometers strongly depend not only on the anemometer size but also on the anemometer construction. The lowest influence was observed for the 20 cm vane anemometer RM Young Gill Propeller (see Figure 7) even if it has the blockage ratio which is the largest from the vane anemometers and comparable to the blockage ratio of the smaller cup anemometer Vaisala. The smaller vane anemometers Schiltknecht and Testo have a frame around their propellers which is not moving and stops the air causing the larger influence in front of the meters (see Figures 5 and 6). For the vane anemometers one can conclude that most of the wind tunnels have a reference meter in an area where the velocity gradient causes systematic deviations of a few tenths of percent between the labs which may FLOMEKO 2019, Lisbon, Portugal

be a significant value compared to typical uncertainty values, however, in most cases it is not a leading uncertainty component.

On the other hand for cup anemometers the velocity gradients in front of the meters are larger (see Figures 8-11). Even the largest wind tunnels in the project do not place their reference meter to a position with negligible velocity gradient and the systematic deviations between the labs due to the velocity gradient can exceed 1 % and therefore the velocity gradient becomes one of the dominant uncertainty sources.

Therefore, if we want to investigate the effect of boundary conditions in a wind tunnel and we want to avoid mixing with other effects like this effect of velocity gradient in front of a meter, it seems, that for the vane anemometers in this project it will be viable but for the cup anemometers it will be challenging.

Besides the velocity disturbance in front of the meters the calibration data (Figures 12-16) are influenced by various kinds of other systematic errors mixing with the effect of test section boundary conditions. Therefore, to achieve the goal of this project, also the other systematic deviations must be understood or compensated.

A compensation of additive errors not depending on a meter size could be realised by subtracting errors of two anemometers – one of them being small with a negligible blockage effect. For that purpose also a thermal anemometer Airflow TA440 was calibrated in all wind tunnels but because of its bad stability and other sources of systematic deviations (pressure setting, contamination) the data from this meter probably cannot be used for the compensation and we do not report the data from this meter here. Instead of the thermal anemometer additional measurements with a small vane anemometer with propeller diameter 22 mm have been planned.

We hope that further data analysis together with additional measurements will lead to visible trends in the anemometers' errors depending on a wind tunnel size.

Even if this project is not a classical inter-comparison and validation of uncertainty statements is not its primary purpose we can use the obtained data also for this.

In Table 3 a statistics of lab to lab equivalence degrees is shown. The equivalence degree between a lab 1 and a lab 2 is calculated as

$$En = \frac{|E_1 - E_2|}{\sqrt{U_1^2 + U_2^2 + D^2}} \quad (1)$$

where  $E_1$ ,  $E_2$  are errors of the labs,  $U_1$ ,  $U_2$  are their expanded uncertainties and  $D$  is a contribution of instability of a meter given as the difference between maximal and minimal error obtained during the

6 repeated calibrations at CMI. The equivalence degrees have been calculated for all pairs of wind tunnels and the percentage of “successful” values not exceeding 1 is shown in the Table 3. The percentage is calculated for two wind tunnel sets – one set containing all the wind tunnels performing the calibration (rows denoted “all”), second containing only the wind tunnels satisfying the recommendation of [8, 10] on maximal blockage ratio (rows denoted “large”). In the column denoted “no. wts” an amount of the wind tunnels contained in the particular sets is shown.

**Table 3:** Statistics of lab to lab equivalence degrees  $\leq 1$ . For explanation see the text.

meter	wt.set	v (m/s) no. wts	0.5	2	5	8	12	20
			% En $\leq 1$					
Sch.	all	14	99	64	53	49	47	49
	large	11	98	53	47	42	38	45
Tes.	all	14	88	58	51	51	47	
	large	8	81	93	75	71	68	
RM.	all	11	76	100	69	56	51	64
	large	6	73	100	93	80	87	80
Vai.	all	12	84	59	64	50	56	58
	large	6	87	67	80	73	93	93
Thi.	all	11	69	62	73	75	69	67
	large	3	67	67	67	67	100	67

For the meters Testo, RM Young and Vaisala we see that excluding the “small” wind tunnels significantly improves the percentage of  $En \leq 1$  which indicates underestimated uncertainties of the “small” wind tunnels. On the other hand the results of the smallest vane anemometer Schiltknecht show poor percentage of  $En \leq 1$  not depending on wind tunnel size indicating that significant part of the observed systematic deviations has an origin different than the blockage effect.

In any case the first look to the results of this project gives evidence that there is a work to be done in the uncertainty budgets for calibrations of vane and cup anemometers.

### Acknowledgements

This work has been supported by technical development grants no. UTR 17601501, 18601501, 19601501 provided by the Czech Ministry of Industry and Trade.

### References

[1] Care I and Arenas M, “On the impact of anemometer size on the velocity field in a closed wind tunnel”, *Flow Measurement and Instrumentation*, **44**, 2-10, 2015.  
[2] Sluše J, “Influence of blockage effect on measurement by vane anemometers”, in *EPJ Web of Conferences*, **143**, 02110, 2017.

[3] Müller H, “Final report on EURAMET project No. 827: LDA-based intercomparison of anemometers”, *Metrologia*, **50**, Technical Supplement, 2013.  
[4] Glauert H, *Airplane Propellers, Aerodynamic Theory*, edited by Durand W F (New York, Dover), 1963, Chap. 7, Div. L  
[5] Mikkelsen R and Sørensen J N, “Modelling of Wind Tunnel Blockage”, in *Proceedings of the 2002 Global Windpower Conference and Exhibition* [CD-ROM], www.ewea.org.  
[6] Sørensen J N, Shen W Z and Mikkelsen R, “Wall Correction Model for Wind Tunnels with Open Test Section”, *AIAA Journal*, **44**, No. 8, August 2006.  
[7] Sørensen J N, *General Momentum Theory for Horizontal Axis Wind Turbines* (Springer), 2016  
[8] EN 61400-12-1: *Wind turbines – Part 12-1: Power performance measurements of electricity producing wind turbines, Annex F*, 2005.  
[9] Maskell E C, “A Theory of the Blockage Effects on Bluff Bodies and Stalled Wings in a Closed Wind Tunnel”, *Aeronautical Research Council Reports and Memoranda no. 3400*, 1963.  
[10] ISO 17713-1: *Meteorology – Wind measurements – Part 1: Wind tunnel test methods for rotating anemometer performance*, 2007.  
[11] ASTM D 5096-02: *Standard Test Method for Determining the Performance of a Cup Anemometer or Propeller Anemometer*, 2017.  
[12] Westermann D, Balaesque N and Busche P, “Systematic deviation of the anemometer calibration due to geometrical interference”, *Report of Deutsche WindGuard Wind Tunnel Services GmbH*, 2011.

# Experimental Analysis of Influencing Factors on Flow Stability of Water Flow Facilities

T. Meng<sup>1</sup>, C. Xing<sup>1</sup>, B. Wu<sup>2</sup>, C. Wang<sup>1</sup>, H. C. Shi<sup>3</sup>, X. P. Li<sup>1</sup>

<sup>1</sup>National Institute of Metrology, mengt@nim.ac.cn, Beijing, P. R. China

<sup>2</sup>Guangzhou Institute of Energy Testing, Guangzhou, P. R. China

<sup>3</sup>Beijing University of Chemical Technology, Beijing, P. R. China

E-mail (corresponding author): mengt@nim.ac.cn

---

## Abstract

Because the flow fluctuation can cause the deviation of flow measurement, flow stabilizing methods are used in the most of the flow metering facilities. Two common flow stabilizing methods of water flow facilities are tested by a new flow stability measurement system which is consisted by a flowmeter and a pressure sensor. The amplitude of fluctuation can be measured by flowmeter, and the frequency of fluctuation can be obtained by FFT (Fast Fourier Transform) analysis of the pressure signal. The direction of fluctuation source can be distinguished by correlation analysis of pressure and flow signals. Based on this method, the characteristics of the fluctuation source can be obtained by experiments under different flow rate and pipe pressure.

An obvious fluctuation signal with a frequency of about 1.5Hz had been found in a test for a flow facility with a buffer tank. The amplitude of fluctuation increases with the decrease of flow rate. When the flow rate is less than 1/10 of the rated flow rate of the pump, the amplitude of fluctuation is about 1%. It is shown that the high frequency fluctuation produced by the pump can be effectively isolated by the buffer tank, but the low frequency fluctuation can be caused by the pump when it worked in a low efficiency range.

In another set of experiments, a flow facility with a constant head water tank and a buffer tank was tested, and two flow stabilizing methods were directly compared and analysed. The test results of the two methods are close under the similar working flow rate and pressure. And if it is under different operating conditions, the amplitude of fluctuation is closely related to the opening of the regulating valve which is installed downstream of the test bench. The fluctuation amplitude increases with the decrease of the valve opening. When the valve opening is less than 30%, the fluctuation amplitude is about 0.5%. Further, it is obtained that the cavitations is caused by the excessive local pressure loss of the regulating valve is the main reason of the fluctuation for the facility with constant head water tank.

In summary, the buffer tank and the constant head water tank are both effective methods for stabilizing flow, and the optimal stabilization effect can be obtained by setting a reasonable range of operation for the pump and the regulating valve.

Keyword: Flow Stability, Water Flow Facility, Buffer Tank, FFT, Correlation Analysis

---

## 1. Introduction

Flow stability is an important technical index of flow standard facilities. In recent years, with the decrease of uncertainty of flow facility, the influence of flow instability on the flow meter calibration process has been gaining increasing attention. For example, the study of Dr. Engel<sup>[1]</sup>, J. Berrebi<sup>[2]</sup> and others have shown that the fluctuation of the flow not only affects the accuracy of water flow facility itself, but also may bring a large uncertainty to the calibration results. Due to the non-linearity or sampling error of various types of flowmeters, J. Berrebi *et al.*<sup>[3]</sup> pointed out in the

study of ultrasonic flow meter that the effect has far exceeded its maximum permissible error. Therefore, it is of great significance to find out the causes of the fluctuation for improving the calibration capability and decreasing the uncertainty.

The buffer tank and the high constant water head tank are two kinds of methods for stabilizing flow widely used in the water flow facilities, the actual effect of them was studied by the experiments in this paper. In the previous study, Meng *et al.*<sup>[4]</sup> proposed a flow stability evaluation method based on flow-pressure correlation analysis, which was applied to measure the amplitude and frequency of

flow fluctuation in this study. It was given that the main causes of the fluctuation and the improvement methods of the water flow facilities.

## 2. Measurement of flow stability

The flow stability measurement system is shown in Fig. 1, which is composed of a pressure sensor and a flow meter in series.

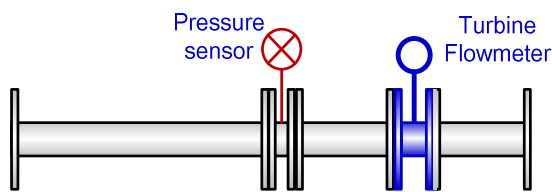


Figure 1: The flow stability test system

According to previous studies<sup>[4]</sup>, the amplitude of flow fluctuation can be represented by the dispersion degree of the flow signal tested by the flow meter, as shown in formula (1).

$$D_q = \sqrt{\frac{\sum_{i=1}^N (q_i - \bar{q})^2}{N}} / \bar{q} \quad (1)$$

Where,  $q_i$  is the value given by flowmeter in a single flow measurement ( $i=1,2,\dots, N$ ), and  $\bar{q}$  is the mean of  $q_i$  in one test.

By performing FFT (Fast Fourier Transform) analysis on the pressure signal, the frequency characteristic of the flow fluctuation can be obtained. The correlation between pressure signals and flow signals can be used to analyse the direction of fluctuations source, as shown in formula (2).

$$r_{qp} = \frac{\sum_{n=1}^N q(n)p(n+m)}{\sigma_q \sigma_p} \quad (2)$$

where  $\sigma_q^2$  and  $\sigma_p^2$  are the variances of the flow and pressure measurements, respectively;  $q(n)$  is the  $n$ th measured value of the flow signal,  $p(n)$  is the  $n$ th measured value of the pressure signal,  $n = 1, 2, \dots, N$ . Because of the difference in the response speed between the flowmeter and pressure sensor,  $m$  is the delay between them. When the pressure signal and flow signal show obvious positive correlation ( $0.3 < r_{qp} < 1$ ), it indicates that the main wave source comes from the upstream of the measurement point; When there is a significant negative correlation between the two signals ( $-1 < r_{qp} < -0.3$ ), it means that the main source of fluctuations comes from the downstream of the measurement point.

In the experiments of this paper, the turbine flow meter with good signal quality and high sampling frequency is selected in the measurement system<sup>[5]</sup>, as well as the high-frequency response pressure sensor with sampling frequency up to 2kHz, which can detect the flow fluctuation signal in a wide range of frequency.

## 3. Experiment on buffer tank method

### 3.1 Experimental facility and scheme

The experiment was carried out on an hot and cold water flow facility (1# facility). That facility is mainly used to measure or calibrate the flow meter and heat meter in the diameter range of DN80 ~ DN400, and its relative uncertainty can reach 0.04% ( $k=2$ )<sup>[6]</sup>, which is currently recognized as one of the most advanced water flow facilities in the world. A centrifugal buffer tank is installed between the pumps and the test pipeline to eliminate bubbles in the water and reduce flow fluctuation caused by the pumps. The process chart of the 1# facility is shown in Fig. 2.

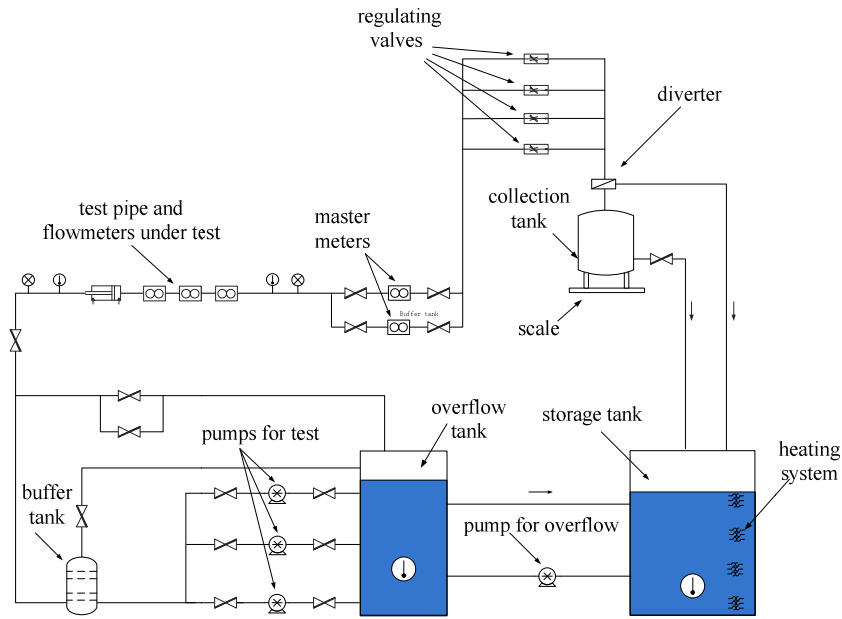


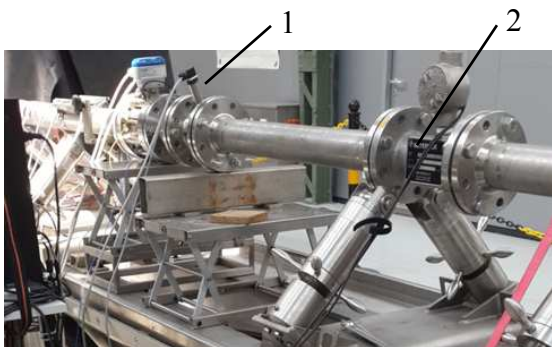
Figure 2: The schematic diagram of 1# facility

The experiment was done on the pipe diameter of DN80. According to the measuring range of the turbine flow meter, the experimental flow range was (15~120) m<sup>3</sup>/h, and the outlet pressure of the test pipe was (0.1~0.2) MPa. The experiment began from 15m<sup>3</sup>/h, and the flow increased by about 10m<sup>3</sup>/h each time. The experimental results were summarized in Table 1.

61	0.10	--	0.49
71	0.09	--	0.56
80	0.09	--	0.39
90	0.09	--	0.38
100	0.08	--	0.33
109	0.09	--	0.23
120	0.08	--	0.25

### 3.2 Experimental results analysis of 1# facility

It can be seen from Table 1 that the main fluctuation frequency measured by the pressure sensor was low, and the sampling rate of the turbine flowmeter was high enough to measure fluctuation amplitude. The flow fluctuation amplitude showed a trend of rapid decrease with the increase of flowrate, as shown in Fig. 4.



1--Pressure Sensor; 2--Turbine Flowmeter

Figure 3: Experimental photos on 1# facility

Table 1: Summary of flow stability test results of 1# facility

Flow Rate (m <sup>3</sup> /h)	Flow Fluctuation Amplitude (%)	Flow Fluctuation Frequency (Hz)	Correlation Coefficient
15	1.36	1.45	0.70
20	0.95	1.48	0.77
30	0.34	1.61	0.77
40	0.18	1.73	0.68
50	0.13	1.91	0.61

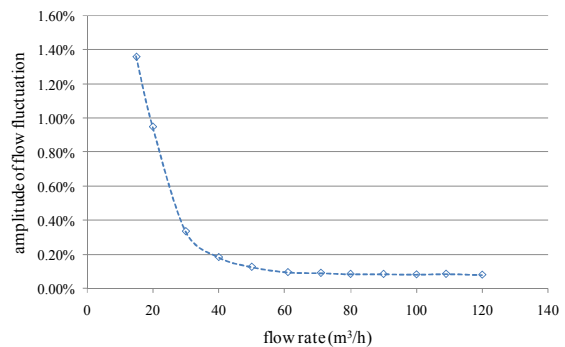
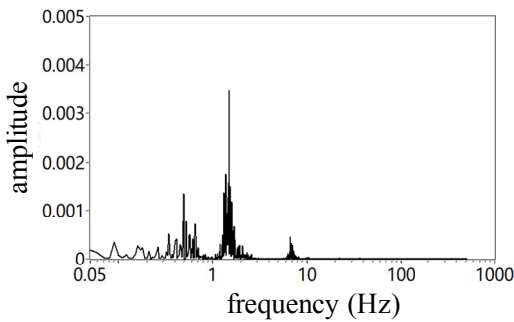


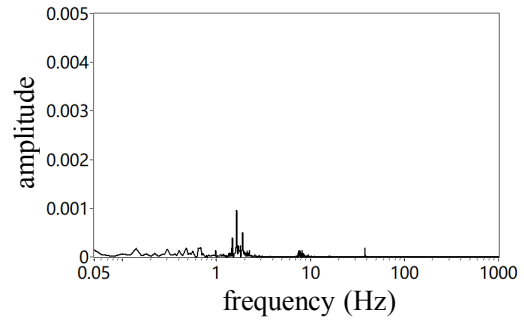
Figure 4: Variation curve of flow fluctuation amplitude with pipe flowrate in 1# facility

In the low flow rate area, the flow fluctuation of the facility was obvious. Within the flow range of (15~20) m<sup>3</sup>/h, the flow fluctuation amplitude was about 1%. After the flow rate exceeded 40m<sup>3</sup>/h, the fluctuation amplitude was less than 0.2%, which indicated that the facility entered a relatively stable working area. With the further increase of the flow rate, the corresponding fluctuation amplitude also continues to decrease. When the flow rate exceeded 50m<sup>3</sup>/h, the relative fluctuation amplitude gradually reduced to 0.08%~0.10%.

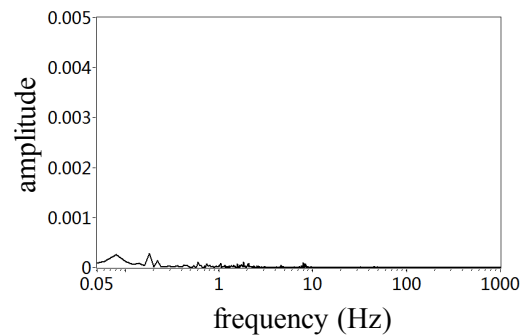
In terms of the characteristics of fluctuation frequency, the main fluctuation frequency was about 1.5Hz in the low-flow rate area, as shown in Fig. 5. However, when the flow rate is greater than 60m<sup>3</sup>/h, there was no obvious characteristic frequency. In order to analyze and find out the causes of fluctuations, the research work was focused on the range of (15~50) m<sup>3</sup>/h.



(a) flow rate,  $q=15\text{m}^3/\text{h}$



(b) flow rate,  $q=40\text{m}^3/\text{h}$



(c) flow rate,  $q=60\text{m}^3/\text{h}$

**Figure 5:** FFT spectrum analysis results of pressure sensor in 1# facility

Within this flow range, it was an obvious positive correlation ( $0.6 < r_{pq} < 0.8$ ) between flow and pressure, and it can be inferred that the fluctuation source mainly was at the upstream of the measurement system. In Fig. 6, the pump operating curve was overlaid with Fig. 4 for comparing the fluctuation amplitude with the performance of the pump.

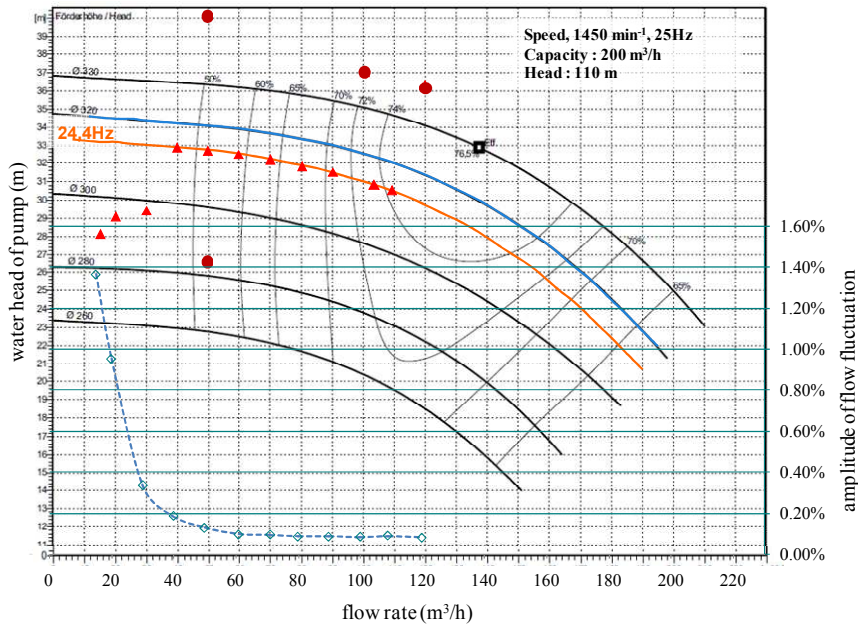


**Figure 6:** The comparison of pump operating curve with flow fluctuation amplitude

In Fig. 6, the orange curve was the operating curve of the pump at 24.4Hz, the red triangle represented the experimental points, and most of the experimental flow rate in Table 1 were fixed at this frequency. In order to verify the correlation between pump frequency and flow stability, comparative experiments were carried out with different pump frequency at some flow rate which were marked with dark red dots. The dotted blue line was the curve of flow fluctuation amplitude with flow change in Fig. 4, and the experimental points were marked with hollow diamond. For instance, three experiments were done at the pump frequency of 21.2Hz, 24.4Hz and 27.7Hz at same flow rate of 50m<sup>3</sup>/h. The results were shown in Table 2:

**Table 2:** The comparison of measurement results under 50m<sup>3</sup>/h and different pump frequency

Water Pump Frequency (Hz)	Flow Fluctuation Amplitude (%)	Flow Fluctuation Frequency (Hz)
21.2	0.11	1.9
24.4	0.13	1.9
27.7	0.14	2.0

Seen from Table 2, the variation of amplitude and frequency between 3 experiments were very small, and they did not have obvious correlation. There were several efficiency curves of pump marked with thin dotted lines in Fig. 6, which was provided by the manufacturer, and the efficiency percentage was marked on the curve. For example, the best working point of this type of pump is flow rate of FLOMEKO 2019, Lisbon, Portugal

130m<sup>3</sup>/h at outlet water head of around 31m, and the efficiency value can reach 76.5% which gradually decreases along the working curve to both sides. Generally, the higher the working efficiency of the pump is, the more stable it is. It can be found in Fig. 6 that the flow stability got worse as the pump efficiency got lower, even the efficiency was lower than 50%. That pump was smallest one of this facility, but it was too big to being used at low flow rate range in these experiments. In order to improve the facility, the flow fluctuation amplitude can be reduced by adding a low flow rate pump or using a small constant head water tank.

Based on above experimental results, a good flow stability can be get by installing a well-designed buffer tank. There were no obvious high-frequency fluctuation that was detected, so it can be seen that the high-frequency pulsation generated by pumps can be effectively isolated by the buffer tank. But its effect on the low-frequency pulsation is limited. In addition, it was found that the unstable operation of the pump in the low efficiency area is the main factor causing the flow fluctuation.

#### 4. Experiment on facility with high constant water head tank

##### 4.1 Experimental facility and scheme

In order to further research the effect of different methods to stabilize flow in the water flow facilities, the experiments were carried out on a set of facility

(2# facility) with high constant water head tank. The process flow chart of the facility is shown in

Fig. 7.

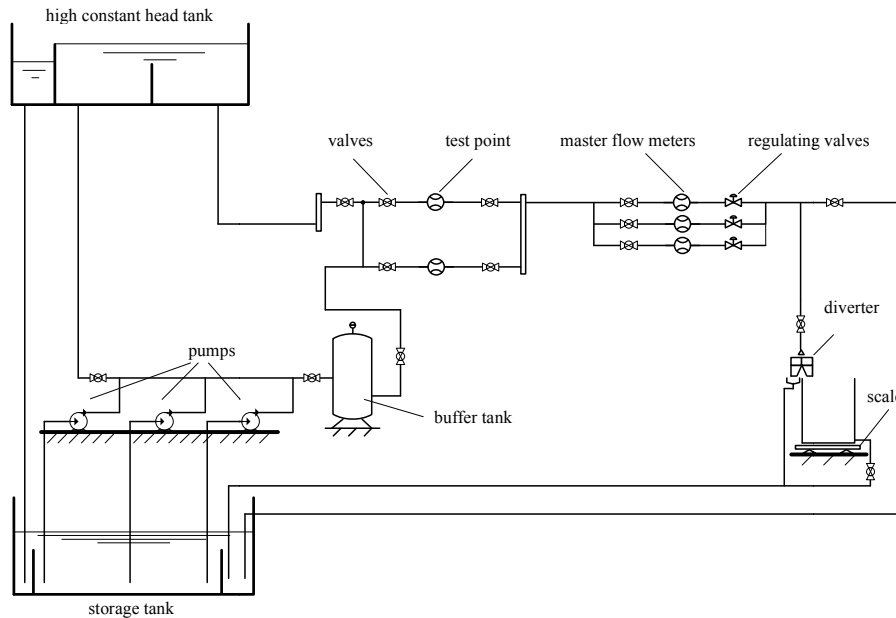


Figure 7: Schematic diagram of 2# facility

The flow range of 2# facility is  $(0.01\sim 200)\text{m}^3/\text{h}$ , the best measurement uncertainty is 0.05% ( $k=2$ ), and the maximum experimental pipe diameter is DN100. A characteristic of the facility is that it has two different methods for flow stabilization: (1) High constant water head tank. Because the pump flow is kept larger than the experimental flow, the pressure at the pipeline inlet is constant. This method is generally considered to be the most effective way to stabilize flow at present. However, since the inlet pressure cannot be adjusted, the flow adjustment can only be through the regulating valves installed at downstream of the test bench. (2) Buffer tank. This method is similar to 1# facility. Compared with the constant water head tank, this method can adjust the flow and pressure of the pipeline simultaneously by changing the frequency of the pump and the opening of valve. It is more flexible in use and the cost is much lower than that of the constant water head tank.

In this experiment, the diameter of the test pipeline

was DN100. The regulating valve VT1 of this pipeline was a linear ball valve, and its flow adjustment range was  $(30\sim 200)\text{m}^3/\text{h}$ . For easy to compare 2 kinds of flow stabilizing methods, the test flow range was  $(30\sim 120)\text{m}^3/\text{h}$ . The experiments were divided into four groups, and the experimental conditions and purposes were as follows: The first group H-01~H-03, mainly tested the stability flow of high constant water head tank; The second group, H-04~H-06, used the buffer tank to stabilize the flow. For comparing with first group, the flow and pressure pipeline of two groups were similar; The third group of H-07~H-08 and the fourth group of H-09~H-10 experiments still used the buffer tank to stabilize the flow. By adjusting the opening of the valve VT1, the high-pressure experiment with the pipeline pressure of about 300kPa and the low-pressure experiment with the valve fully open were respectively carried out to observe the change of flow stability. The results of 4 groups were shown in Table 3.

**Table 3:** Comparison of the results of two pressure stabilizing methods

Experimental Group	Experiment Number	Stabilizing Pressure Method and Working Condition	Flow Rate (m <sup>3</sup> /h)	Fluctuation Amplitude (%)	Pipeline Pressure (kPa)	Valve Opening (%)
Group 1	H-01	constant head tank	30	0.52	175	28
	H-02		50	0.36	171	40
	H-03		120	0.22	143	70
Group 2	H-04	buffer tank, mid-pressure	30	0.50	175	29
	H-05		50	0.38	172	40
	H-06		120	0.22	164	66
Group 3	H-07	buffer tank, high-pressure	50	0.47	299	31
	H-08		120	0.31	289	54
Group 4	H-09	buffer tank, low-pressure	50	0.20	39	100
	H-10		120	0.18	99	100

#### 4.2 Experimental results analysis of 2# facility

According to the data in Table 3, the variation of flow fluctuation amplitude with flow rate was shown in Fig. 8.

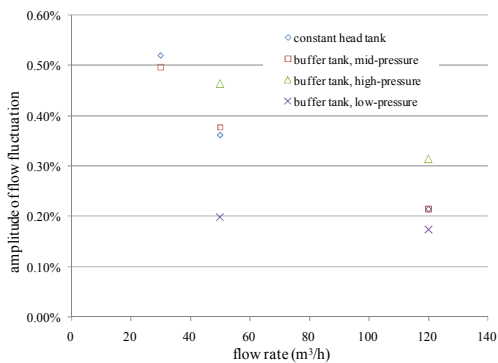
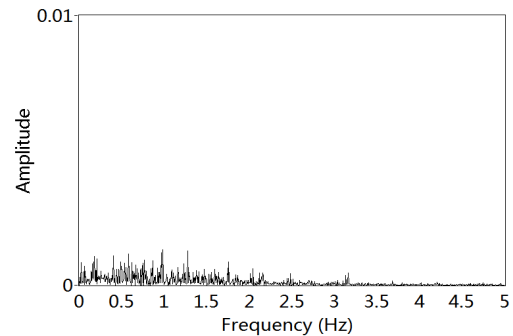
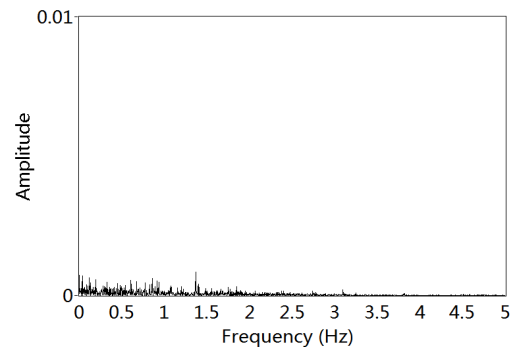


**Figure 8:** The relationship between flow fluctuation amplitude and flow rate of 2# facility

Compared with the result of group 1 and group 2, it can be found that the fluctuation amplitude of the two stabilizing flow methods were very close at different flow rate. In addition, at the low flow rate of 30m<sup>3</sup>/h, the facility had the worst stability and the fluctuation amplitudes were more than 0.5%. However, in the FFT power spectrum of pressure signal (as shown in Fig. 9), no obvious characteristic frequency was found, and only some weak signals were found around 1Hz.



(a) experiment H-01 (water tower)



(b) experiment H-04 (buffer tank)

**Figure 9:** The spectrum analysis of experiment in 2# facility

In the correlation analysis of pressure and flow signals, it was found that there was a significant negative correlation between them, as shown in Fig. 10. It can be inferred that the fluctuation source mainly at downstream of the measuring point.

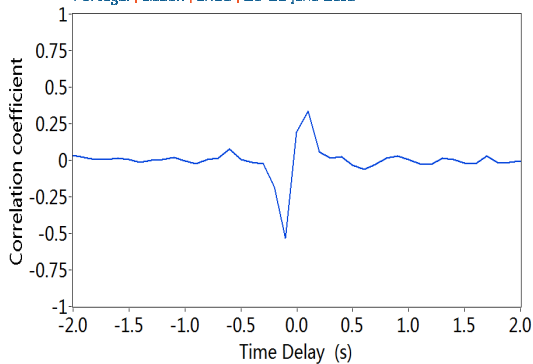


**Figure 10:** P2-TFM correlation curve of experimental H-07 in 2# facility

According to the downstream pipeline condition and the observation on field, when the VT1 valve had a small opening, for example less than 50%, the noise at VT1 valve increased evidently. Therefore, it can be judged that the excessive pressure loss led to cavitation at VT1 valve and flow fluctuation. Fig. 11 showed the variation of flow fluctuation amplitude with valve opening which also came from Table 3.

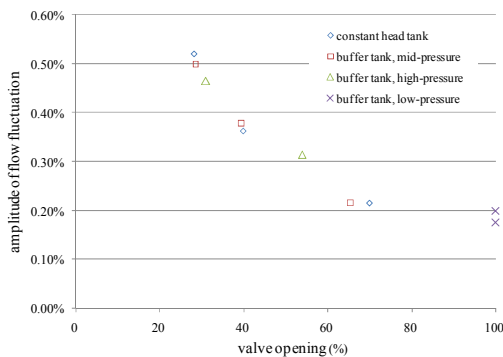


**Figure 11:** The relation between flow fluctuation amplitude and the opening of regulating valve in the 2# facility

In Fig. 11, the flow fluctuation amplitude decreased monotonically with the increase of valve opening, and the correlation coefficient of the two reached -0.92, showing a strong negative correlation. However, the experimental results of group 3 and group 4 at the same flow rate had a large dispersion in Fig. 8, which was obviously different from the distribution rule in Fig. 4, and the reasons were fully explained in Fig. 11.

The above experimental results showed that the well-designed buffer tank can achieve a stabilizing flow effect similar to that of the constant head water tank. When the regulating valve VT1

maintains a large opening, the flow fluctuation amplitude is always kept at a good level of 0.2%. The cavitation phenomenon caused by excessive pressure loss was the major cause of flow fluctuation. Therefore, in the design of the water flow facility, it is necessary to make a reasonable planning for the type selection of the regulating valve and its operating range, so as to avoid adjustment ratio too large.

## 5. Conclusion

The amplitude and frequency of flow fluctuation are not only the technical indicators to represent the flow stability of the facility, through the analysis of the direction of the fluctuation source and the change rule of flow stability at different working conditions (flowrate, pressure, pump operating parameters), the causes of the fluctuation can be effectively found.

Through the experimental study of two sets of facilities with different flow stabilization methods, it was found that they both had good isolation effect on the shaft frequency and blade frequency pulsation generated by the pump with relatively high frequency. However, for flow facilities with the buffer tank, working in low-efficiency areas of pumps should be avoided; and for facilities with the high constant water head tank, the reasonable regulating valve groups should be designed to avoid excessive local pressure loss, so as to obtain good flow stability.

## References

- [1] Engel R, Baade H J, Quantifying impacts on the measurement uncertainty in flow calibration arising from dynamic flow effects. *Flow Measurement & Instrumentation*, 44(2014):51-60.
- [2] Berrebi J, Deventer J V, Delsing J, Reducing the flow measurement error caused by pulsations in flows. *Flow Measurement & Instrumentation*, 15(2004):311-315.
- [3] Berrebi J, Martinsson P E, Willatzen M, et al., Ultrasonic flow metering errors due to pulsating flow. *Flow Measurement & Instrumentation*, 15(2004):179-185.
- [4] Tao Meng, Shangchun Fan, Chi Wang, Huichao Shi, Xiaopeng Li. A flow stability evaluation method based on flow-pressure correlation. *Flow Measurement & Instrumentation*, 2018(64): 155 - 163.
- [5] Tao Meng, C Koglin, K Richter, T Lederer, C Wang. Comparison of Test Methods for Measuring Flow Stability. *Proc. Flomeko2016*,



18<sup>th</sup> International Flow Measurement Conference

Portugal | Lisbon | LNEC | 26-28 June 2019

Sydney, Australia, 26-29 Sep, 2016: B.10.3-1-  
B.10.3-6

- [6] Tawackolian K, Bükér O, Hogendoorn J, et al. Calibration of an ultrasonic flow meter for hot water. *Flow Measurement & Instrumentation*, 2013, 30(30):166-173.
- [7] Ledderer T, Mathies N, Rose J, et al. New test facility for large water flowrates up to 1000 m<sup>3</sup>/h in a temperature range between 3°C and 90°C at PTB- Berlin. *Flomeko2009*, 2009.

# Novel calibration facility for water flow with large temperature span

A.K. Niemann<sup>1</sup>, S. Haack<sup>1</sup>, J. Frederiksen<sup>1</sup>

<sup>1</sup> Danish Technological Institute, Aarhus, Denmark  
E-mail (corresponding author) Anders K. Niemann: [aknn@dti.dk](mailto:aknn@dti.dk)

## Abstract

Danish Technological Institute (DTI) is extending the flowrate of the existing flow rig up to 1.000 m<sup>3</sup>/h in the temperature span from 4 – 85 °C and pipe dimension up to DN400, and thereby become a unique calibration facility. The new test rig will serve as the national primary standard for the field of water flow measurement and thereby replacing the current at DTI.

From 0.5 – 500 m<sup>3</sup>/h the test rig is based on gravimetric principle using a diverter principle. From 500 – 1000 m<sup>3</sup>/h the test rig is based on reference flow metering. The reference flow meters will consist of two high precision Coriolis flowmeters mounted in parallel. The reference flowmeters are placed in the same circuit as the gravimetric system. This setup allows for calibration of each reference flowmeter against the gravimetric method without dismantling the meters. This ensures low uncertainties and traceability to a primary standard and possibility to participate in international inter-comparisons.

The new flow rig will be highly digitalized with a high degree of automation. Communication with flowmeters under test will be flexible with both conventional analogue interfaces but also through industrial communication standards.

## 1. Introduction

There is a demand for calibration facilities with high flow combined with the possibility for use at different temperatures. This combination is the motivation for development of a new flow test rig at the Danish Technological Institute.

The new test rig is built upon the existing test rig, which is based on the gravimetric principle. The existing flow facility consist of three different test rigs covering an accredited flow range from 5 L/h up to 500 m<sup>3</sup>/h. Each test rig has its own diverter, weighing tank, and scale. Calibrations can be performed in a temperature range from 4 °C up to 85 °C.

The revamped test rig will be able to cover flows up to 1000 m<sup>3</sup>/h in DN400 pipes and with the option of 1 bar pressure difference across the test section (across a DUT) at the maximum flow rate. This enables the test facility also to be used for measuring  $k_v$  values and test of different types of valves e.g. regulation valves.

The temperature range will be the same as for the existing test rigs, 4 °C up to 85 °C.

The test rig will also be suited for dynamic flow measurement e.g. to assess the performance of domestic water meters under dynamic load changes.

DTI is partner in the EMPIR (European Metrology Programme in Innovation and Research) project METROWAMET [1], where assessment of dynamic performance of domestic water flow meters is one of the major aims of work packages 1. Hereby potential future test requirements will be integrated into both the test rig and the data acquisition system.

## 2. Reference flow metering

### 2.1 Reference flow metering

Traceability for flow rates above 500 m<sup>3</sup>/h is realised through reference flow metering with two DN200 coriolis flow meters. The maximum flow rate of 1000 m<sup>3</sup>/h is covered by mounting the two flow meters in parallel and splitting the flow in two with 500 m<sup>3</sup>/h as maximum flow rate for each meter, se figure 1.

In order to get a very low uncertainty state-of-the-art coriolis flow meters were chosen. These flow meters have a high accuracy in a very large flow range, see figure 2 below, and they are very stable. The stated accuracy is 0.05 % of the actual flowrate from 800 m<sup>3</sup>/h down to a flow rate of 28 m<sup>3</sup>/h.

The traceability of the reference flow meters is realised by calibrate them against the existing accredited gravimetric system. A very huge advantage is, that the flow meters can be calibrated separately without dismantling them. This means that they can be calibrated

in situ against the gravimetric standard on the large test rig.

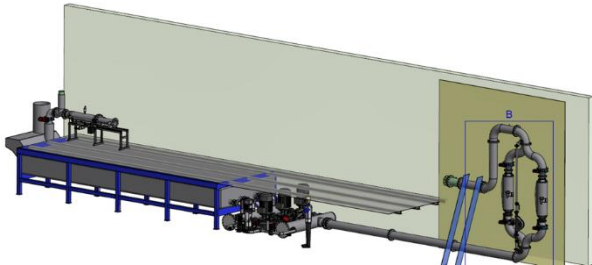


Figure 1, Three-dimensional view of the new test rig with the parallel reference flowmeter system shown on the right side of the figure.

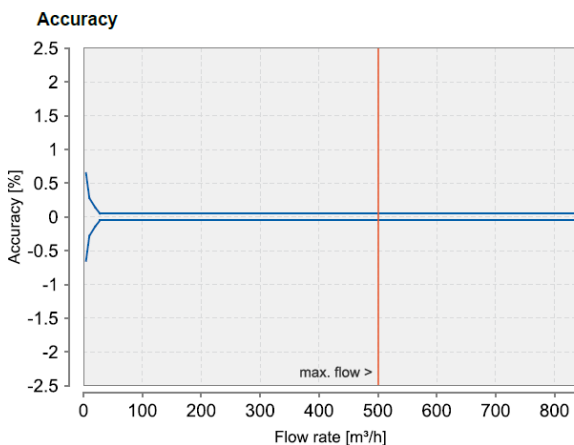


Figure 2, the graph shows the expected accuracy of the Coriolis flow meter as stated by the manufacture.

To cover low flow rates with reference flow meters a third reference flow meter is also installed. This flow meter covers the range down to 1.8 m<sup>3</sup>/h with a stated accuracy of 0.05 % of the actual flowrate.

The uncertainty of the existing gravimetric system is 0.05 % and the uncertainty of the reference metering system is expected to be in the size of 0.2 %.

### 2.1 Pumping system

In order to deliver a flow rate of 1000 m<sup>3</sup>/h three 55 kW pumps are installed. The large power of the pump is necessary as the pressure loss across the Coriolis reference flow meters have a size of approximately 1 bar at a flowrate of 500 m<sup>3</sup>/h. At the maximum flowrate (1000 m<sup>3</sup>/h) the flow is split in two at the parallel reference meter system and the flow through each meter is therefore 500 m<sup>3</sup>/h. The pressure loss in the piping system is estimated to 2.5 bar and with the required differential pressure capacity of 1 bar across the DUT, the total differential pressure, which the three pumps should be able to maintain is 4.5 bar. Beside the three

pumps a smaller pump is installed in order to adjust the flow to specific flow rate within narrow limits. All pumps are equipped with frequency converters and can be controlled through the new automatized system explained in the next section.

### 3. Digitalization

The revamped test rigs will be full automated and data acquisition from both measurement equipment mounted to run the test rigs and from DUTs will be digitalized and collected through network cables and stored in a database. Calibration certificates can then be generated automatically from the stored measurement data ensuring that errors arising from manual handling of data can be avoided. All measurement conditions such as humidity, air temperature, water temperature etc. will also be collected and stored together with calibration data from the DUT and from the reference meter or from the gravimetric system.

The automation of the test rig is realized through a Programmable Logic Controller (PLC) system and an industrial PC installed with a SCADA (Supervisory Control And Data Acquisition) software to run the PLC system. All valves will be quipped with actuators, so that they can be controlled through the SCADA system. All pumps can also be controlled and regulated through this system. Moreover there will be a regulation system to sustain a specific predefined flow rate.

The user can control the test rig through a client computer installed with client software. Standard calibration procedures are stored in the system and contains the overall setup for the system e.g. valve settings, data acquisition, target flow rates, duration of test etc. New procedures can be built from scratch or upon existing produces and stored.

Communication with flowmeters under test will be flexible with both conventional analogue interfaces but also through industrial communication standards e.g. ModBus. The control software will include possibilities to setup automatically test protocols which can be associated with the unique ID for the device under test and thereby reducing risk of setup-error between test. The test data from both reference test rig and device under test will be stored in a database for generating certificates and for temporal comparison of performance of device.

### 4. Dynamic flow patterns

As DTI participate in the METROWAMET project it is a demand that the new test rig should also be suited to perform dynamic measurement as it is stated in the project protocol., that it is necessary to have test rigs and protocols available for the verification of domestic water meters under dynamic load changes. Beside this the rig

must meet at minimum the specifications of OIML R49 (Section 4 “Metrological Requirements”). This dynamic ability is realised by installing a fast response weighing system consisting of load cells, load cell amplifier and fast acquiring data acquisition system.

## **5. Conclusion**

At the time of writing the test rig is not finish and no tests has been performed. Consequently, there is still a lot of work to do to claim the CMCs (calibration and measurement capability) of the reference system and to get all the automatized calibration procedures to work. Issuing certificates based on data in a database by a push of a button is also left to do. Dynamic measurement is also an area that still needs a lot of investigation, however, together with a couple of other Metrology Institutes across Europe we are working together to solve this task and are very confident that we will succeed.

## **References**

- [1] <https://www.ptb.de/empir2018/metrowamet/the-project/>

# Hydrogen refuelling station calibration with a traceable gravimetric standard

R. Maury<sup>1</sup>, C. Auclercq<sup>1</sup>, C. Devilliers<sup>2</sup>

<sup>1</sup>CESAME-EXADEBIT SA, Poitiers, France

<sup>2</sup>AIR LIQUIDE, Sassenage, France

E-mail (corresponding author): [r.maury@cesame-exadebit.fr](mailto:r.maury@cesame-exadebit.fr)

---

## Abstract

Of all alternatives to gasoline fuels, hydrogen offers the greatest long-term potential to radically reduce many problems inherent in transportation fuel use. Hydrogen vehicles have zero tailpipe emissions and are very efficient. If it is made from renewable sources, nuclear power, or fossil sources with carbon emissions captured and sequestered, hydrogen use on a global scale could produce nearly zero greenhouse gas emissions and greatly reduce emissions of air pollutants. The aim of this work is to realise a traceability chain for hydrogen flow metering in the range typical for fuelling application in a wide pressure range with pressures up to 875 bar (for Hydrogen Refuelling Station HRS with Nominal Working Pressure of 700 bar) and temperature changes from -40 °C (pre-cooling) to 85 °C (maximum allowed vehicle tank temperature) in accordance with the worldwide accepted standard SAE J2601. Several HRS have been tested in Europe (France, Netherlands and Germany) and the results show a good repeatability for all tests. This demonstrates that the testing equipment works well in real conditions. Depending on the configuration of installation, some systematic errors have been detected and explained. Errors observed for the stations of Configuration 1 can be explained by the difference of pressure, at beginning and end of the fuelling, in the piping between the CFM and the dispenser: the longer the distance, the bigger the errors. For Configuration 2, as this distance is very short, the error is negligible.

---

## 1. Introduction

We observe air quality issues in our cities. It is not only about CO<sub>2</sub> but also about NO<sub>x</sub>, SO<sub>x</sub> and particulate matter. These are much smaller particles that enter the bloodstream and are at the root of the cause of many deceases in big urban agglomerations. It is therefore important to tackle one of the main causes of these issues at city but also rural level: the transport sector.

Amongst the major objectives of the European Union, the decarbonization of transportation has a significant role. Reducing transport related greenhouse gases emissions through both Energy efficiency improvements and increased usage of Clean Alternative technologies (powertrain, fuels) is considered as critical. With 25% of the GHG emissions attributable to transport, and the requirement to reduce them by 95% by 2050, there is no other way than to opt for massive electrification of transport, spurred by introduction of renewables, including both battery electric vehicles and fuel cell electric vehicles which complement each other.

Without efficient electric power drive systems such as fuel cells the long-term climate goals cannot be achieved.

Of all alternatives to gasoline fuels, hydrogen offers the greatest long-term potential to radically reduce many problems inherent in transportation fuel use. For example, hydrogen could enhance energy security and reduce dependence on imported oil, since it can be made by water electrolysis from various primary energy sources, including natural gas, coal, biomass, and wastes, and renewables. Also, hydrogen vehicles have zero tailpipe emissions and are very efficient. If it is made from renewable sources, nuclear power, or fossil sources with carbon emissions captured and sequestered, hydrogen use on a global scale could produce nearly zero greenhouse gas emissions and greatly reduce emissions of air pollutants.

In many countries, there is increasing support for the development of a large hydrogen infrastructure as a measure to reduce greenhouse gas emissions. This includes a network of hydrogen refuelling stations (HRS), which is necessary to enable the

widespread adoption of hydrogen fuel cell vehicles. However, the industry faces the dilemma that they are required to meet measurement requirements set by legislation that cannot currently be followed due to the lack of available methods and standards. In the EMPIR Metrology for Hydrogen Vehicles (MetroHyVe) project, this is addressed through the development of gravimetric standards for field verification; as well as an investigation into the use of substitute fluids for laboratory calibration of flow meters.

The aim of this work is to realise a traceability chain for hydrogen flow metering in the range typical for fuelling application in a wide pressure range with pressures up to 875 bar (for HRS with NWP of 700 bar) and temperature changes from -40 °C (pre-cooling) to 85 °C (maximum allowed vehicle tank temperature) in accordance with the worldwide accepted standard SAE J2601 [1].

## 2. Basic operating principle of a HRS station

### 2.1 Basic principle and listing of the component

The refuelling station system boundary starts at the hydrogen supply source and ends with the inlet to the vehicle's tank. The hydrogen can be supplied to a refuelling station in either gaseous or liquid form. The components that are part of the refuelling station vary and are dictated by the physical form of supplied hydrogen (i.e., gaseous or liquid) and the working pressure of the vehicle's tank. Most automakers have agreed to adopt a 700bar vehicle storage system. The primary goal of a refuelling station is to refuel vehicles to a 100% state of charge (SOC) throughout the station's daily operations.

The hydrogen station is usually composed of a low-pressure storage (200bar), a low-mid pressure compressor, some mid/high pressure storage, a booster compression for high pressure, a precooling and dispensing device. All these components are shown in Figure 1 below.

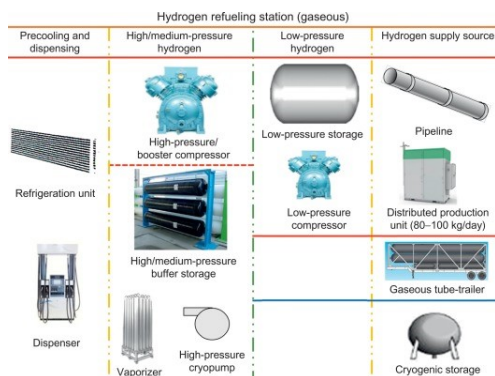


**Figure 1:** Hydrogen refuelling station components.  
FLOMEKO 2019, Lisbon, Portugal

The OIML R139 [2] describes a Hydrogen Refuelling Station as a measuring system which should include at least:

- meter;
- pressure and/or flow control device;
- emergency power supply;
- transfer point;
- gas piping;
- zero-setting device.

The Figure 2 (from OIML R139 [\*]) shows the constituents of a typical compressed fuel measuring system for vehicles.

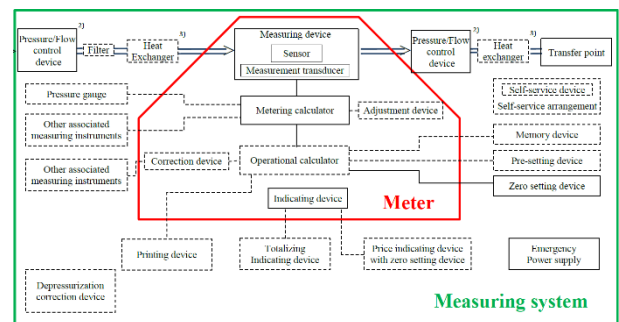


**Figure 2:** Constituents of a typical compressed gaseous fuel measuring system for vehicles.

The measuring system may also be provided with the following other ancillary and additional devices:

- calculator;
- associated measuring instruments;
- pressure gauge;
- digital indicating device;
- self-service arrangement;
- pre-setting device;
- memory device;
- price indicating device;
- printing device;
- heat exchanging device
- other ancillary and additional devices.

The “devices” listed above can be designated as a “typical” configuration of a measuring system.

### 2.2 Potential sources of error in the mass measurement

Within the framework of the EMPIR project (METROHYVE), an extensive list of uncertainty sources and measurement errors will be given and sorted out by their influence on the calculation of the hydrogen mass displayed by the dispenser (see Table 1).

**Table 1:** List of potential uncertainty sources and their impact on the uncertainty budget

Main Uncertainty Sources	
<b>Mass flow rate from Coriolis meter</b>	<b>1</b>
<b>Pressure measurements</b> (in particular those closest to flow meter/dead volume/fuel transfer point) Pressure measurements may be used for pressure corrections to the flow meter and for calculating the density of hydrogen in the dead volume to allow the mass to be determined.	<b>2</b>
<b>Temperature measurements</b> (in particular those closest to flow meter/dead volume/fuel transfer point) Temperature measurements may be used for temperature corrections to the flow meter and for calculating the density of hydrogen in the dead volume to allow the mass to be determined.	<b>3</b>
<b>Depressurisation of fuel hose &amp; dead volume</b> connecting volume between flow meter and fuel nozzle (generally in hose)	<b>4</b>
<b>Position of flow meter</b> (this will affect the dead volume)	<b>5</b>
<b>Hydrogen density equation</b>	<b>6</b>
<b>System repeatability</b>	<b>7</b>
<b>System reproducibility</b>	<b>8</b>
<b>Minimum Measurable Quantity</b>	<b>9</b>

Explanation on each source:

#### 1-Mass flow rate from Coriolis flow meter:

The rapid variation in temperatures / pressure can affect stress and torsion on the meter and might modify the meter accuracy / performance.

- The CFM manual (tested) states that the temperature variation shall be no more than 1°C per second.
- During the pulse initial phase, literature suggests large errors can be expected. Is the pulse measurable for the CFM?

The zero adjustment must be done once before type approval or periodic verification but how reliable is it if conditions evolve significantly?

#### 2-pressure measurements:

A pressure measurement will be required for 'dead volume' gas density calculations and correction. Literature suggests that drift of the pressure sensors can be a significant issue.

#### 3-Temperature measurements:

A temperature measurement will be required for 'dead volume' gas density calculations.

#### 4-Depressurisation of fuel hose & dead volume:

Dead volume is the volume between the flow meter and the point of transfer into the vehicle (fuel nozzle at the end of the hose mainly). The mass dispensed into a vehicle is the mass measured by the flow meter minus the mass in the dead volume (generally refuelling hose) at the end of a fill (assuming there was no gas mass in the dead volume to begin with). If hydrogen was present in the dead volume at the start of the fill, the mass dispensed into a vehicle is the mass measured by the flow meter minus the difference in mass in the dead volume at the end of the fill and start of the fill. The design of the system shall ensure that the measured quantity is delivered. Figure 3 shows what is usually vented in a HRS.

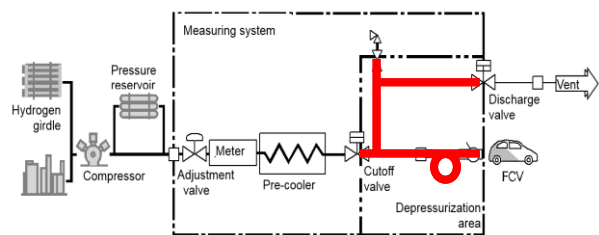


**Figure 3:** Depressurization in a HRS

The size of the dead volume is therefore required. As a rough approximation, for an 8mm inner diameter (typical 9/16" medium pressure tubing ID) hose that is 5m long, the maximum mass of hydrogen in the dead volume should be approximately 10g (assuming a gas density of ~40 kg/m<sup>3</sup> at 700 bar and 20 °C). The depressurization takes also into account the piping length from the hose to the flow meter.

It has been reported by end users that the vented quantity is generally between 10g and 50g. Since storage masses for cars generally vary from 1 kg (being the minimum quantity) to 5 kg. Fill masses are therefore likely within this range, the dead volume mass can correspond up to 1% of the tank's mass capacity.

As mentioned, pressure and temperature measurements close to the dead volume are required to calculate the density, and therefore the mass of hydrogen in the dead volume. Uncertainty in this could therefore be a significant contributor to the overall uncertainty.

### 5-Position of the meter:

Flow meter position is important as the further away it is from the point of transfer into the vehicle, the larger the mass of hydrogen that is measured by the flow meter that is not actually dispensed into the vehicle (dead volume).

The meter location can have a large influence if it is mounted before or after the heat exchanger. Depending of the position, the flow meter can have a relatively stable temperature during the fuelling in the warm area (before the heat exchanger) or experience a rapid temperature variation at the beginning of the fuelling when hydrogen at ambient temperature is replaced by cooled hydrogen after it went through the heat exchanger. In both case, pressure variations are always present.

### 3. Test protocol for HRS calibration (on-site) and primary gravimetric standard (by Air Liquide).

#### 3.1 Definition of the testing protocol based on the OIML R139 requirements

This work has been done within the framework of two European project: the METROHYVE project (Empir EURAMET) and the FCH-JU program (N° FCH / OP / CONTRACT 196: "Development of a Metering Protocol for Hydrogen Refuelling Stations").

The objective of this study is to define, in agreement with European national metrological institutes, a structured approach for accelerating the certification of metering systems for HRS in Europe. This certification is required for invoicing hydrogen at Hydrogen refuelling Stations (HRS) to the public. In the European countries where the roll-out of the hydrogen infrastructure has started (for instance, in Germany), the authorities require a prompt implementation of metering systems compliant with national regulation; without such certified metering systems, the construction of new stations could be stopped in the coming years.

For this reason, it was critical to define a temporary certification process for HRS before a revised version of OIML R139 is issued. Even if this revision was expected for beginning of 2019, it will take time to change the legislation in each European country.

For accuracy tests, it has been decided to perform a new test on-site. The tests are more severe than

the proposed tests in the OIML R139 since it is requested to perform:

1. Full fillings: 20-700 bar → 2 times
2. Partial fillings 20-350 bar → 1 time
3. Partial fillings 350-700 bar → 1 time
4. Filling at Minimal Measured Quantity (MMQ = 1 kg) → 4 times with several initial pressures.

The acceptance criteria are the following for this test campaign:

1. Class 2 for future station (i.e. MPE=2% and 4% at MMQ)
2. Class 4 for existing station (i.e. MPE=4% and 8% at MMQ).

The Figure 4 presents the test protocol

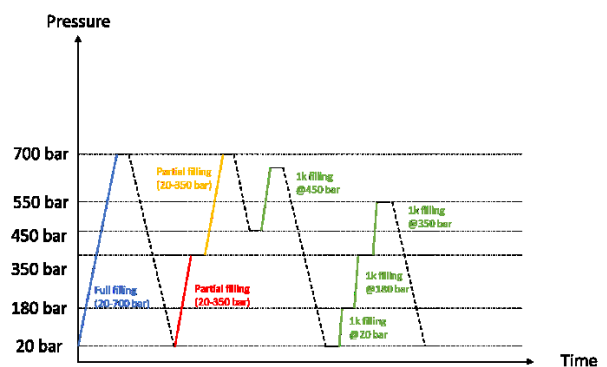


Figure 4: Test protocol

This test protocol should be repeated at least three times to assess the repeatability of the measurements.

#### 3.2 Description of the primary gravimetric standard

The primary standard has been developed by Air Liquide with the support of LNE-LADG. Air Liquide received a PTB certification for the "Usage for the conformity assessment and verification for legal metrology purposes".

The gravimetric calibration device is measuring standard which is designed as a compact, mobile reference measuring system. This standard serves for measuring the amount of hydrogen filled into a tank at hydrogen refuelling stations according to the SAE J2601 protocol.

The primary standard consists in a hydrogen tank (type IV) with an inner volume of 104 L which is mounted on a frame. The mass of the tank including

the mass of the frame for mounting the vessel, the piping and gas containing devices (valves, manometer etc.) can be measured before and after the filling process with the installed precision scale (Mettler PKB989-CC150).

This enable the determination of the mass difference and hence the amount of fuel gas. The balance is carried out with explosion protection measures (ATEX zone 2).

For protection against wind forces and the influences connected with them, the primary standard is installed in a vehicle trailer with closable openings inclusive a massive and openable trailer roof. For different steps of operation, the roof and the openings may be used. A pneumatic lifting device serves for applying and removing the load onto the precision scale. This allows installing the balance below the frame with the vessel at the place of use as well as removing the scale for transport.

The Figure 5 presents two pictures of the primary standard developed by Air Liquide (in collaboration with LNE-LADG).



**Figure 5:** Pictures of the reference measuring system for hydrogen refuelling station

The primary standard measures the mass difference of a vessel before and after the filling by a hydrogen refuelling station. At the beginning of the measurements, this means before the first filling, the precision balance may be tarred. Else the mass of the empty tank including frame may be addressed before the measurements. The results are given in kg. The resolution of the display is 0,2 g.

The standard allows to use either nitrogen or hydrogen from 20 to 875 bar. The gas temperature range should be maintained between -40 and 40°C.

### 3.3 Uncertainty budget assessment of the primary gravimetric standard

In the OIML R139, there is two class of maximum permissible error defined, class 2 and class 4. The MPE for the measuring system are 2 and 4% respectively. The MPE are doubled at the MMQ.

An uncertainty budget assessment of the primary standard has been carried out by LNE-LADG, PTB and NMi certin for different mass of hydrogen (from 1kg to 4 kg). The main uncertainty sources have been identified as the following:

- Buoyancy (stability of air density at the beginning of the fuelling, vessel expansion)
- Short time drift of the scale (temperature effect, wind)
- Water condensation
- Repeatability of measurements
- Connection / disconnection influence
- Non-linearity of the scale
- Zero stability after depressurization

The primary standard is under the requirements (1/5 of MPE) for all the range of hydrogen mass for a class 1.5.

#### 4. Results from on-site measurements with the primary traceable gravimetric standards.

In this chapter, the description of the experiments in several hydrogen refuelling stations will be detailed.

##### 4.1 Selection of HRS

The purpose was to involve a statistically significant sample of HRS in Europe, representing a minimum of 3 members States. This has been transferred to 3 main requirements for the selection.

1. All technologies and / or specificities should be tested
2. HRS from different manufacturers in Europe
3. HRS in operation in minimum three different countries of the EU.

Based on these criteria, the following HRS were selected (see Table 2 below).

**Table 2:** List of HRS tested in the protocol and main characteristics

LOCATION		CHARACTERISTICS
Country	City	
Germany	HRS1	Short distance between CFM (in the station) and the dispenser
	HRS2	long distance between CFM (in the station) and the dispenser
	HRS3	Compressed gas
	HRS4	Cryo pump (cold area)
	HRS5	Compressed gas (CFM in dispenser)
France	HRS6	--
Netherlands	HRS7	--

The Figure 6 presents the different hydrogen station environment.



**Figure 6:** Pictures of HRS tested in the program

##### 4.2 Description of testing protocol for each HRS

The time needed to perform the protocol is approximatively 4 days. The first day, 2 or 3 hours are needed to the installation of the primary standard and the hydrogen venting system. The trailer must not move for the whole test campaign to avoid any levelling adjustment. The Hydrogen Refuelling Station must be accessible for car filings. The scale must be powered up for 1h30 before starting any measurements.

The calibration of the scale is done each day with reference weight (30 minutes) by following the procedure detailed below (see Figure 7).

- Check zero-point stability during 5 min
- Put the balance below the frame (and fix it)
- 1/ Check the resolution with the 20g weight: it must be exactly the value (a deviation of +/- 0,2g is accepted)

2/ Check the sensitivity with reference weight: 0,5Kg or 1Kg (depending on the MMQ value, 2Kg / 4Kg. At least two times for each weight. Compare the results with the mass. Maximum deviation shall be inside 1/5 of the uncertainty budget (in grams). Check hysteresis:

- ◆ Put 0,5Kg (or 1Kg), then remove
- ◆ Put 2Kg, then remove
- ◆ Put 4Kg, then remove
- ◆ Put 4Kg again, then remove
- ◆ Put 2 Kg, then remove
- ◆ Put 0,5Kg (or 1Kg), then remove
- ◆ Put 0,5Kg (or 1Kg) again, then remove



**Figure 7:** Calibrated weights handled cautiously with gloves

This verification was done at the full range of the scale, i.e. when the empty cylinder was already in place onto the scale. Scale deviation was recorded and removed to the mass measurement for each day. The linear regression calculated (see Figure 8) is subtracted to each mass measured the same day of the scale verification.

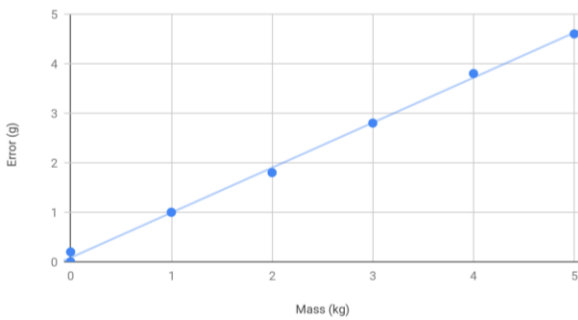


**Figure 8:** Example of scale deviation

### 4.3 Description of HRS configuration

Over the 7 HRS tested, it came out that HRS measuring systems can be divided into two main configurations:

- Configuration 1: where the CFM is installed in the container, and not in the dispenser (see Figure 9).

**Advantages:** the flowmeter remains always under pressure and is exposed to stable gas temperature conditions (ambient temperature).

**Disadvantages:** the distance between the container and the dispenser generates some errors.

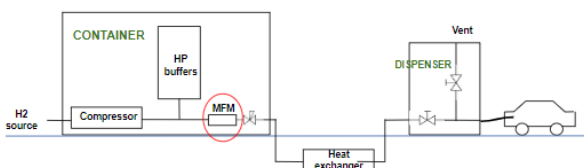


**Figure 9:** Illustration of configuration1, where the CFM is located in the main container

- Configuration 2: where the CFM is installed in the dispenser, close to the break-away device (see Figure 10).

**Advantages:** The error is minimized due to the short distance between the CFM and the transfer point.

**Disadvantages:** the flowmeter is subjected to big variation of pressure (from 0 to 875 bar) and temperature (from ambient to -40°C in less than 30 seconds) → *more severe operating conditions.*

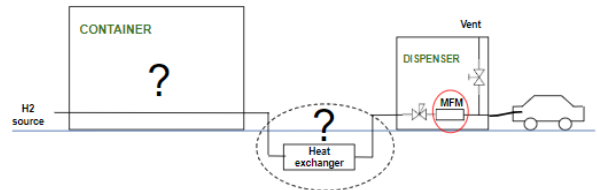


**Figure 10:** illustration of configuration 2, where the CFM is located in the dispenser

### 4.4 Results for accuracy tests – configuration 1 (HRS 1 to 5)

The Figure 11 to Figure 15 present the summary of all the tests realized in the week (see Figure 4 for reminder).

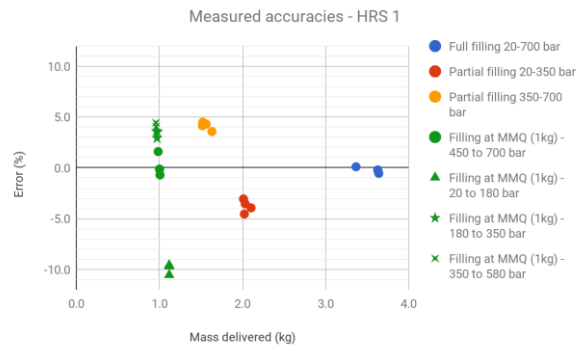


**Figure 11:** Results of accuracy tests in HR1.

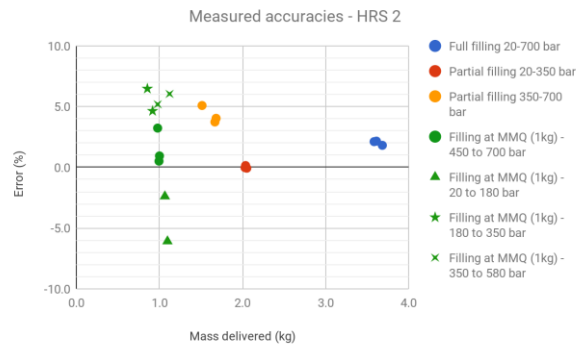


**Figure 12:** Results of accuracy tests in HR2.

These results show a positive shift of test results. According to OIML R139, an adjustment is authorized on the meter to center results around 0. This adjustment could be done with the transmitter of the flowmeter but has not been implemented yet on site. A manual correction was brought to the test results afterwards, by subtracting the mean error value of full fillings tests to all results.

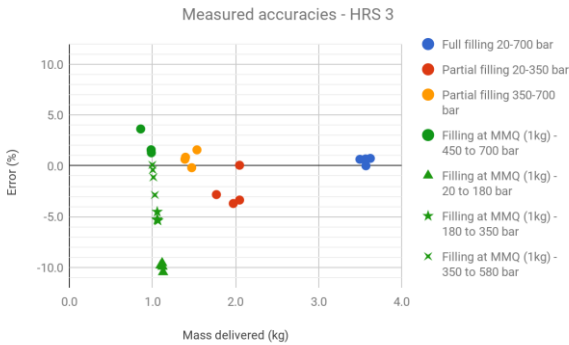


Figure 13: Results of accuracy tests in HR3.

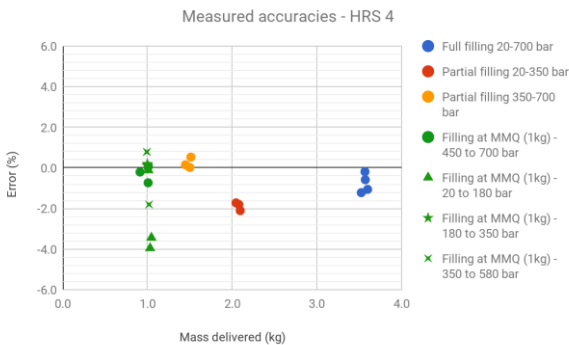


Figure 14: Results of accuracy tests in HR4.

Here again, a negative shift of 1% is observed. A manual correction was brought to the test results afterwards, by subtracting the mean error value of Full fillings tests to all results.

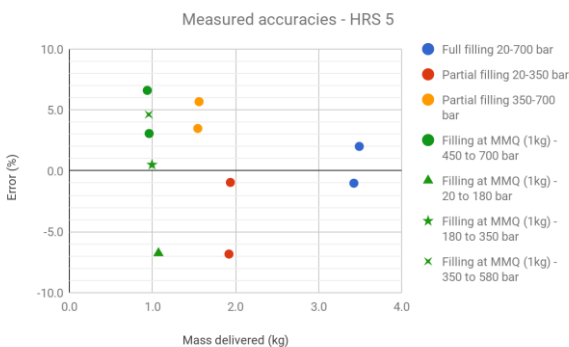


Figure 15: Results of accuracy tests in HR5.

A non-negligible scatter has been observed on this station. But the tendency of tests results looks similar to previous HRS.

#### 4.5 Results for accuracy tests – configuration 2 (HRS 6 to 7)

The to present the summary of all the tests realized in the week (see Figure 4 for reminder).

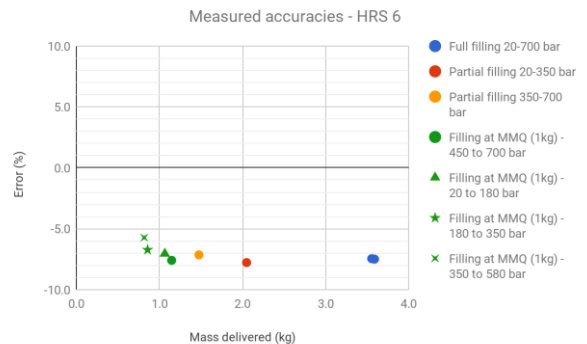


Figure 16: Results of accuracy tests in HR6.

In this case, a significant negative deviation was observed (around -7,5%). This error is too significant to be attributed to a simple adjustment of the CFM. It has been explained afterwards by the HRS manufacturer, but no more information was given. Therefore, it has been manually corrected afterwards, to give the following results

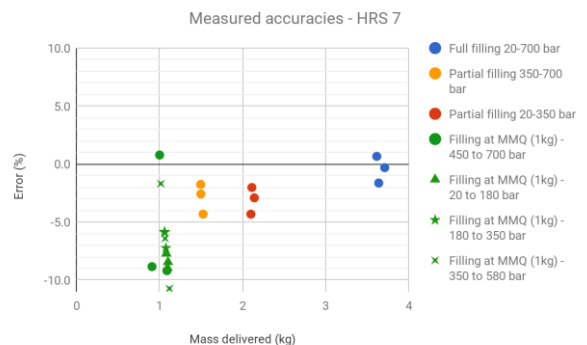


Figure 17: Results of accuracy tests in HR7.

Pretty large repeatability errors have been observed in that case (more dispersion). A constant negative deviation is noticed. Information was given by the HRS operator that a correction is done for the vented H2 quantity, but with no more details.

#### 4.6 Analysis of the accuracy tests

From all the figures presented in the section 4.5, the mean value has been calculated for each station and for each type of tests (see below).

**Table 3:** Summary table of tests results for all HRS tested, per type of tests

	Configuration 1				
	HRS1	HRS2	HRS3	HRS4	HRS5
Full filling 20-700 bar	-0.24%	0.00%	0.52%	0.00%	0.50%
Partial filling 20-350 (*)	-3.77%	-2.01%	-2.46%	-1.11%	-3.89%
Partial filling 350-700	4.13%	2.26%	0.72%	1.00%	4.58%
Filling at MMQ 450-700	0.16%	-0.47%	2.02%	0.47%	4.84%
Filling at MMQ 20-180 (*)	-9.94%	-6.26%	-9.95%	-1.74%	-6.75%
Filling at MMQ 180-350 (*)	3.36%	3.53%	-5.12%	0.91%	0.51%
Filling at MMQ 350-580 (*)	3.78%	3.59%	-1.07%	0.69%	4.62%
	Configuration 2				
	HRS6 (*)	HRS7			
Full filling 20-700 bar	0.00%	-0.42%			
Partial filling 20-350 (*)	-0.30%	-3.08%			
Partial filling 350-700	0.33%	-2.88%			
Filling at MMQ 450-700	-0.12%	-5.75%			
Filling at MMQ 20-180 (*)	0.43%	-8.37%			
Filling at MMQ 180-350 (*)	0.74%	-6.32%			
Filling at MMQ 350-580 (*)	1.74%	-6.28%			

#### Legend:

**Green value:** all values are within the limits (MPE)

**Orange value:** mean value is within the limits (or very close to the limits), but some single values are out of the limits (MPE)

**Red value:** all values are out of the limits (MPE)

(\*) single value (not mean value)

(\*) test out of OIML R139:2018 scope

Tests results can be summarized as follow:

**Configuration 1:** The same tendency was observed for all HRS of Configuration 1 (**HRS 1 to 5**):

- Very good accuracy for Full filling tests (from 20 to 700 bar): Error close to zero, and very repeatable
- Negative deviation for Partial filling tests (from 20 bar to 350 bar)

- Positive deviation for Partial filling tests (from 350 bar to 700 bar)
- Variable deviation for 1 kg fillings (MMQ) depending on the initial pressure in the tank

#### Configuration 2:

- **HRS 6:** After adjustment of test results, the accuracy looks very good (close to 0% for most of tests, and < 2% for one test condition).
- **HRS 7:** No clear conclusion / tendency without further explanations from the HRS manufacturer on the measuring system.

#### Reminder:

With the new version of OIML R139:2018 for HRS besides accuracy class 1.5, also accuracy class 2 and 4 are allowed. Herewith for HRS the MPE for accuracy class 2 and 4 are respectively 2 and 4 % for type approval, initial and subsequent verifications. For existing HRS (in service inspection), the MPE are respectively 3 and 5 %. For fillings at MMQ (1 kg), the MPE is twice the mentioned MPE. For example, for an existing HRS with accuracy class 4 during an in-service inspection, the MPE for fillings at MMQ (1 kg) is 10 %. See full details in OIML R139-1:2018 paragraph 5.2.

#### 4.7 Explanation of the accuracy tests results: influence of distance between CFM and dispenser

##### Configuration 1:

For HRS of Configuration 1, a systematic deviation (either positive or negative) was observed for partial fillings:

##### Partial filling - from 20 to 350 bar:

**Negative deviation** means that the quantity of hydrogen delivered to the customer is higher than the quantity invoiced (i.e. counted):  $m_{delivered} > m_{invoiced}$

##### Partial filling - from 350 to 700 bar:

**Positive deviation** means that the quantity of hydrogen invoiced to the customer (i.e. counted) is higher than the quantity really delivered:  $m_{delivered} < m_{invoiced}$

In analyzing in more details, the test results, it comes out that errors observed for HRS (**Configuration 1**) can be explained by the distance between the CFM and the dispenser: the longer the distance (i.e. bigger the volume), the bigger the errors.

Indeed, at beginning of the test, the line between the CFM and the dispenser is full of hydrogen at a certain pressure, called **P1** (see Figure 18 ).

- This pressure depends on the end pressure of the previous filling (independent of the customer).
- This quantity is not counted by the CFM (because already in the pipe at beginning of the transaction) and given to the customer.

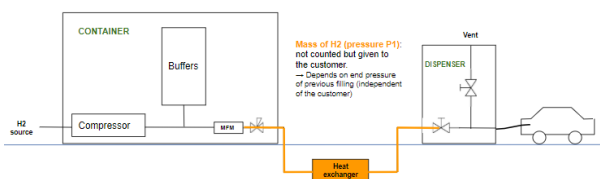


**Figure 18:** Schematic diagram of a HRS – situation before fuelling

At end of the test, this same line is full of hydrogen at a certain pressure, called **P2** (see Figure 19).

- This pressure depends on the end pressure of the ongoing filling (during transaction): end pressure is given by the filling protocol (and depends on filling conditions - AUTOMATIC stop). But the customer can at any time stop the filling by himself (STOP button).
- This quantity is counted by the CFM but not transferred into the customer vehicle.

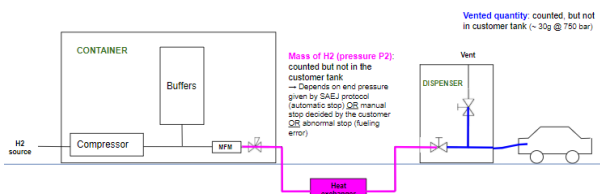


**Figure 19:** Schematic diagram of a HRS – situation at the end of fuelling

If **P1 ~ P2**, then the customer pays exactly the quantity delivered in his tank: the quantity of hydrogen initially present in the pipe (delivered but not counted) is **replaced by the same quantity** at end of the fuelling (counted, but not delivered).

If **P1 > P2**, then the customer gets **more** hydrogen than the quantity invoiced: the quantity of hydrogen initially present in the pipe (delivered but not counted) is replaced by a **lower** quantity at end of the fuelling (counted, but not delivered) → **Negative deviation**.

If **P1 < P2**, then the customer gets **less** hydrogen than the quantity invoiced: the quantity of hydrogen initially present in the pipe (delivered but not counted) is replaced by a **higher** quantity at end of the fuelling (counted, but not delivered) → **Positive deviation**.

#### Application to the tests performed:

##### **Full fillings** (from 20 to 700 bar):

- These tests were performed right after the previous filling which ended at 700 bar. So, pressure in the line between CFM and dispenser is around 700 bar (**P1**)
- End pressure was around 700 bar. So, pressure in the line between CFM and dispenser is around 700 bar (**P2**)
- So **P1 ~ P2**. That is why the found error is **close to zero**.

##### **Partial filling** (from 20 to 350 bar):

- These tests were performed right after the previous filling which ended at 700 bar. So, pressure in the line between CFM and dispenser is around 700 bar (**P1**)
- End pressure was around 350 bar. So, pressure in the line between CFM and dispenser is around 350 bar (**P2**)
- So **P1 > P2**. That is why the found error is **negative**.

##### **Partial filling** (from 350 to 700 bar):

- These tests were performed right after the previous filling which ended at 350 bar. So, pressure in the line between CFM and dispenser is around 350 bar (**P1**)

- End pressure was around 700 bar. So, pressure in the line between CFM and dispenser is around 700 bar (P2)
- So  $P1 < P2$ . That is why the found error is **positive**.

#### Filling of 1 kg (MMQ) (from 450 to 700 bar):

- These tests were performed right after the previous filling which ended at 700 bar. So, pressure in the line between CFM and dispenser is around 700 bar (P1)
- End pressure was around 700 bar. So, pressure in the line between CFM and dispenser is around 700 bar (P2)
- So  $P1 \sim P2$ . That is why the found error **close to zero**.

#### Filling of 1 kg (MMQ) (from 20 to 180 bar):

- These tests were performed right after the previous filling which ended at 700 bar. So, pressure in the line between CFM and dispenser is around 700 bar (P1)
- End pressure was around 180 bar. So, pressure in the line between CFM and dispenser is around 180 bar (P2)
- So  $P1 > P2$ . That is why the found error is **negative**.

Note: deviations are much important for 1 kg fillings, as the reference mass is small.

#### Filling of 1 kg (MMQ) (from 180 to 350 bar):

- These tests were performed right after the previous filling which ended at 180 bar. So, pressure in the line between CFM and dispenser is around 180 bar (P1)
- End pressure was around 350 bar. So, pressure in the line between CFM and dispenser is around 350 bar (P2)
- So  $P1 < P2$ . That is why the found error is **negative**.

#### Filling of 1 kg (MMQ) (from 350 to 580 bar):

- These tests were performed right after the previous filling which ended at 350 bar. So, pressure in the line between CFM and dispenser is around 350 bar (P1)
- End pressure was around 580 bar. So, pressure in the line between CFM and dispenser is around 580 bar (P2)

- So  $P1 < P2$ . That is why the found error is **negative**.

By consequent, it appears that **the longer the distance (i.e. the bigger the volume), the bigger the errors**. Knowing precisely the pressure and the volume of the pipe between the CFM and the nozzle, it must be possible to correct the systematic error due to HRS configuration.

#### Configuration 2:

In case of **Configuration 2** (when the CFM is located in the dispenser), the distance between the CFM and the nozzle is very small (almost negligible): the CFM counts exactly the quantity delivered to the vehicle (no “buffer volume” as in Configuration 1), except the vented quantity which must be subtracted.

That is why errors were very good on HRS 6 (after adjustment), and close to zero whatever the type of test.



## 7. Conclusion

Test results are presented in this report. For Configuration 1, it showed mainly:

- A very good accuracy for Full filling tests (from 20 to 700 bar): Error close to zero, and very repeatable
- A negative deviation for Partial filling tests (from 20 bar to 350 bar): around -2 to -4%
- A positive deviation for Partial filling tests (from 350 bar to 700 bar): around +2 to 4%
- A variable deviation for 1 kg fillings (MMQ) depending on the initial pressure in the tank: Error close to zero from some of them, and error up to -10% in specific test conditions.

For Configuration 2, accuracy looked much better, especially for one HRS which showed found errors close to zero, whatever the type of test performs.

Based on these results, the following conclusions can be drawn:

- A good repeatability was observed for all tests. This demonstrates that the testing equipment works well in real conditions.
- Errors observed for the stations of Configuration 1 can be explained by the difference of pressure, at beginning and end of the fueling, in the piping between the CFM and the dispenser: the longer the distance, the bigger the errors. For Configuration 2, as this distance is very short, the error is negligible.

## 8. Acknowledgement

*“The information and views set out in this report are those of the author(s) and do not necessarily reflect the official opinion of the FCH 2 JU. The FCH 2 JU does not guarantee the accuracy of the data included in this study. Neither the FCH 2 JU nor any person acting on the FCH 2 JU’s behalf may be held responsible for the use which may be made of the information contained therein.”*

*“This project has received funding from the EMPIR programme co-financed by the Participating States and from the European Union’s Horizon 2020 research and innovation programme”*

## References

- [1] SAE J2601 – 2014 – Fuelling Protocols for light Duty Gaseous Hydrogen Surface Vehicles.
- [2] OIML R139 – 2018 – Compressed gaseous fuel measuring systems for vehicles.

# Investigations on pressure dependence of Coriolis Mass Flow Meters used at Hydrogen Refuelling Stations

O. Büker<sup>1,\*</sup>, K. Stolt<sup>1</sup>

<sup>1</sup>RISE Research Institute of Sweden, Brinellgatan 4, 504 62 Borås, Sweden

\*E-mail (corresponding author): [oliver.buker@ri.se](mailto:oliver.buker@ri.se)

---

## Abstract

In the framework of the ongoing EMPIR JRP 16ENG01 “Metrology for Hydrogen Vehicles” a main task is to investigate the influence of pressure on the measurement accuracy of Coriolis Mass Flow Meters (CFM) used at Hydrogen Refueling Stations (HRS). At HRS hydrogen is transferred at very high and changing pressures with simultaneously varying flow rates and temperatures. It is clearly very difficult for CMFs to achieve the later expected legal requirements in relation to the demand for accurate mass flow measurement at the measurement conditions at HRS. It was observed, mainly due to the very dynamic filling process, that the accuracy of mass flow measurement at different pressure ranges is too inaccurate. Particularly at higher pressures it was found out that especially short refuelling time causes significant measurement deviations. On this background it can be concluded that the medium pressure has a great impact on the mass flow measurement accuracy. To gain a deeper understanding of this matter RISE has built a unique high-pressure test facility. With the aid of this newly developed test rig it is possible to calibrate CFMs over a wide pressure and flow range with water and base oils as test medium. The test rig allows calibration measurements under the conditions prevailing at 70 MPa HRS regarding mass flows (up to 3.6 kg min<sup>-1</sup>) and pressures (up to 87.5 MPa).

---

## 1. Introduction

To achieve the 2050 long-term goal of reduction of greenhouse gas emissions by 80-95% compared to the 1990 level, both the utilization of renewable and carbon-free energy carriers and the energy efficiency need to increase substantially over the next decades. This is particularly important for the transport sector which accounts at present for around 60% of the global oil consumption. To achieve these long-term climate objectives, the future of transport necessarily lies in the complete replacement of currently prevailing fossil fuels and electrification by renewables with zero emissions.

In general, electromobility is understood as electric drive with a power supply from a rechargeable battery. However, fuel cell electric vehicles (FCEV) are also used for electromobility, whereby the fuel cell (FC) is used as an energy converter and the energy store is a hydrogen tank. In a hydrogen-powered vehicle the compressed gaseous hydrogen (CGH<sub>2</sub>) is stored at high pressure (up to 70 MPa) in the tank. By separation of energy storage and energy converter significantly higher energy densities and thus ranges are possible.

The refuelling of a 70 MPa CGH<sub>2</sub> vehicle at a hydrogen refuelling station (HRS) is completed within a few minutes. From high-pressure intermediate storages (e.g. 44 MPa and 95 MPa) the hydrogen is filled via pressure drop (overflow) into the vehicle tank. A passenger car with a typically tank capacity of around 5 kg can be filled in around 3 min according to SAE J2601. While refuelling, the hydrogen and thus the vehicle tank is heated significantly. To avoid this the so-called cold filling procedure is used. In this case the hydrogen is pre-cooled (down to -40 °C) before filling, e.g. with liquid nitrogen.

For monitoring the amount of hydrogen dispensed into the vehicle at an HRS, a robust and accurate flow meter is required that can operate over a variety of flow and temperature ranges and pressures up to 87.5 MPa. OIML R 139-1 provides accuracy requirements for flow measurement of GCH<sub>2</sub>. The measurement of mass flow is typically performed using Coriolis Mass Flow Meters (CFM). CFMs measure, in contrast to many other methods, directly the mass flow independent of fluid properties, and are generally not very sensitive to changes in viscosity, temperature, and pressure.

## 2. Scope of application

Almost all HRS meet the requirements according to the SAE J2601 fueling protocol (see **Table 1**). The SAE standardizes the fueling process by defining limits for the relevant refueling parameters.

**Table 1: 70 MPa Hydrogen Fueling Specification**

Parameter	Limit
Min. gas temperature (pre-cooling)	-40 °C
Max. gas temperature (tank)	+85 °C
Ambient temperature	-40 °C to +50 °C
Min. tank storage capacity	2 kg
Max. tank storage capacity	10 kg
Min. pressure (tank)	0.5 MPa
Max. pressure (tank) => $1.25 \cdot 700$ MPa	87.5 MPa
Max. flow rate	60 g/s (3.6 kg/min)

A typical 70 MPa HRS consists of high-pressure storage tanks at different pressure levels, a compressor (e.g. diaphragm compressor, ionic compressor) to fill the high-pressure storage tanks or directly the vehicle tank, a heat exchanger (pre-cooler, refrigeration unit) and a dispenser which controls the flow into the vehicle tank. At fast filling the dispenser controls the flow in such a way, that fast filling of 5 kg hydrogen in 3 min (or 7 kg in 5 min, respectively) can be achieved. To avoid tank overheating during the filling process, due to rapid compression of the gas, the pressurized hydrogen is cooled down to -40 °C by the heat exchanger on its way from the high-pressure storage tank to the dispenser. But that also means the pressure in the vehicle tank exceeds 70 MPa (up to 87.5 MPa) at the end of the fast fill process to ensure a filling at 70 MPa after cooling down.

### 2.1 Refueling process at HRS

The sequence of operation of a refueling process is standardized. SAE J2601 states requirements for temperatures and the speed of fueling, specified by Average Pressure Ramp Rate, APRR (comparable with Constant Pressure Ramp Rate, CPRR) during the hydrogen refueling process. Compliance with this standard ensures fast and safe refueling. Before the actual refueling, the connections, e.g. between dispenser nozzle and vehicle tank are automatically checked by the system. Subsequently, the pressure in the vehicle tank and its volume is determined by an initial pressure pulse (pressure surge). Based on these values the temperature curve (expected gas heating), the target pressure and the APRR for a complete filling

are calculated. The APRR depends on the vehicles tank pressure and temperature, pre-cooling temperature and the ambient temperature. In accordance to SAE J2601 there are two ways to calculate the APRR. The classical way (lookup table method) is based on tables which specify the APRR for the given vehicle tank storage capacity, initial tank pressure, station type (station pressure and delivery temperature), ambient temperature and communication capability between vehicle and dispenser. The newly developed second way (MC formula method) works relatively similar. In contrast to the lookup table method the MC formula calculates a Dynamic Pressure Ramp Rate (DPRR) using adaptive feedforward control based on the measurement of pressure and temperature at the dispenser. Here, the pressure target is continuously and dynamically calculated in order to minimize the fueling time. For both methods all parameters are checked during refueling to monitor that they are consistent with the fueling protocol. When the vehicle is filled to the target pressure the refueling process is stopped and the nozzle can be disconnected from the vehicle.

### 2.2 Flow measurement at HRS

At HRS hydrogen is transferred at very high and changing pressures, varying flow velocities (very low to very high) and varying temperatures but the mass flow measurement must be extremely accurate. As it can be seen, these conditions are not trivial and not many flow meters are eligible. It is generally expected that CFMs are well suited for refuelling with continuously variable pressures and temperatures. The CFM measures the mass flow directly and the integrated value is used as basis for the billing of the H<sub>2</sub> supplied. There are mainly two different approaches for the installation of the flow meter (CFM). The CFM can either be installed before or after the pre-cooler. This implies the CFM measures the hydrogen mass flow at ambient conditions (at around 20 °C) or at a temperature of around -40 °C. In both cases the zero-point of the CFM is set once, namely during commissioning at the planned operating temperature, e.g. at -40 °C.

## 3. High-pressure test facility

### 3.1 Measurement principle

The measurement principle (see **Figure 1**) of the flow facility is based on the master meter method with flying start-and-stop. In this context a pair of two CFMs measures simultaneously, where one CFM is installed, as device under test (DUT), at the high-

pressure site and the other CFM, as reference meter (master meter), at the low-pressure site. Afterwards, the positions of the CFMs are exchanged. Both CFMs were previously calibrated at low-pressure using one of the national standard flow facilities at RISE (Research Institutes of Sweden).

### 3.2 Operating principle

From one of the selected storage tanks (200 L and 1000 L, filled with deionized and filtered water) the water is delivered to the high-pressure pump (PARKER AHL66-2D series) (passing two filters). The outlet pressure of the pressure pump (see **Figure 2**) is controlled by compressed air using a 1" pressure regulator in a range from 0 to 100 psi (0 to 7 bar) which corresponds to 0 to 13300 psi (0 to 913 bar) in the liquid line.



**Figure 1: Measurement set-up (high-pressure test facility) equipped with two CFMs from HEINRICHS.**

The compressed air is delivered by house connection but for higher pressures a diesel-powered air compressor (Ingersoll Rand 7/41+, air flow 4000 L/min at 7 bar, max. air pressure 8.6 bar) was used. A compressed air tank (volume 270 m<sup>3</sup>, max. pressure 11 bar, TIDAN-VERKEN AB) is filled in order to provide a regular supply of compressed

air for the high-pressure pump. Downstream the air passes an air dryer (HANKISON SPX series) and a compressed air filter (HANKISON HF series). The high-pressure pump is connected by an 800 mm long DN 10 high-pressure hose (spiralized steel reinforced polymer hose, CEJN) in order to prevent a possible vibration transmission from the pump to the high-pressure test facility.

By use of a needle valve the undesired fluctuations in pressure due to the piston movement are damped. Directly after the first elbow, another needle valve is installed using a tee connection (bypass line). At the beginning the bypass line is used to get rid of air bubbles in the first part of the high-pressure site. The pressure before the CFM at the high-pressure site (DUT) can be set by means of a pressure regulator (TESCOM 54-2000 series) in the range from 1500 to 15000 psi (100 to 1000 bar). The pressure before and after the DUT is measured by means of two pressure transmitters (KELLER Leo 3) in the range from 0 to 1000 bar.



**Figure 2: High-pressure pump PARKER AHL66-2D series.**

To ensure an accurate detection of the zero-point, the DUT is installed between two completely leak-tight on-off ball valves, for symmetrical reasons, both with the same distance from the CFM. It is advisable to reduce the pressure in several steps to avoid an excessive pressure drop. For this reason, two further pressure regulators (TESCOM 54-2000 series) in the range from 1500 to 15000 psi (100 to 1000 bar) and 500 to 6000 psi (35 to 400 bar), respectively were installed. The pressure after these pressure regulators is measured by means of two pressure transmitters (KELLER Leo 3) in a range from 0 to 700 bar and 0 to 300 bar, respectively. The pressure upstream the reference meter (CFM at the low-pressure site) can be set by another pressure regulator (TESCOM 54-2000

series) in the range from 5 to 500 psi (0.35 to 35 bar) and measured by another pressure transmitter (KELLER Leo 3) in the range from 0 to 10 bara. In the normal case, the inlet pressure of the CFM used as reference meter is set to 5 bar, the pressure the CFM was calibrated at the national standard flow facilities. With the needle valve behind the reference CFM the flow rate is adjusted. All the pipework of the high-pressure facility has an outer diameter of 0.375" (9.5 mm) and an inner diameter of 0.203" (5.2 mm) using mainly 3/8" MP (medium pressure) C&T (cone and thread) connections. For the data acquisition a DAQ system developed by RISE (own hardware and software) has been used. The DAQ system provides four input channels for temperature, eight input channels for current and four input channels for pulse and frequency measurement (double-time chronometry). For each measurement point the line pressure was logged as 4-20 mA signal from the five pressure transmitters (KELLER Leo 3), the temperature from both CFMs as 4-20 mA passive current output and the finally the passive pulse/frequency output also from both CFMs.

## 4. Measurement results

### 4.1 Devices under test

There are not many high-pressure CFMs on the market. The devices (see **Table 2**) of the three leading manufacturers (outside Asia) will be investigated in the EMPIR project. For this reason, the manufacturers have provided some devices as in-kind contribution to the project.

**Table 2: Overview of the investigated CFMs**

Manufacturer	Sensor	Transmitter
RHEONIK	RHM04	RHE27
HEINRICHS	TM SH	UMC4
KEM KÜPPERS	TCHM0450	TCE8000

A higher line pressure leads in general to a stiffer measuring tube resulting in an underestimated mass flow rate. This effect is in general greater for larger size CFM and in theory negligible for very small flow meters. Also, most manufacturers state that the actual hydrogen temperature, and not the pressure, is one of the most important factors affecting the measurement accuracy. High pressures, however, present problems with the currently available flow meters. It is anticipated that CFMs do not achieve the necessary accuracies at higher pressures, and it can be assumed that particularly short refuelling time causes significant measurement deviations. Some manufacturers provide pressure compensation by manual input of FLOMEKO 2019, Lisbon, Portugal

the operating pressure (stable condition) or the possibility for real time compensation by adding an external pressure sensor to measure the actual pressure (unstable condition).

### 4.2 Measurements at low-pressure

Before the actual high-pressure measurements each individual CFM was separately calibrated with water as test medium at a temperature of 20 °C and an inlet pressure of around 5 bar by using one of the national standard flow facilities at RISE (Vattenmätkänk 7, VM7), see **Figure 3**.



**Figure 3: DUT calibrated at low pressure (HEINRICHS CFM).**

For these measurements the (mass) frequency and pulse output was used. Before the flow calibration was performed, a zero-point adjustment of the DUT was carried out at the actual pressure (5 bar) and temperature (20 °C) conditions. After setting the new zero-point the pulses (while the low flow cut-off is shut off and without flow) were logged for 5 minutes to check how well the (automatic) zero-point setting performs.

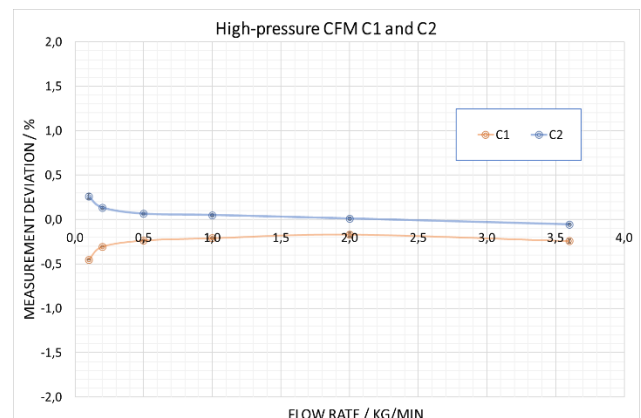


**Figure 4: Measurement results for one of the three CFM pairs (C1 and C2) at low-pressure calibration.**

The low-pressure calibration was performed at six different flow points (0.1 kg/min, 0.2 kg/min, 0.5 kg/min, 1.0 kg/min, 2.0 kg/min and 3.6 kg/min). For each flow point tested four repeated measurements were carried out, that means a total of 5 repetitions. The measurement results are shown in **Figure 4**.

#### 4.3 Measurements at high-pressure

After the low-pressure calibration measurements were conducted in water (5 bar inlet pressure) one meter was used as reference meter at the low-pressure side (5 bar) and one meter as DUT at the high-pressure side (up to 850 bar). A generic test matrix regarding mass flow rates and pressures has been prepared. Initially, the mass flow rates were selected to cover the full operating range for a 70 MPa HRS (typically 3.6 kg/min). In sum, measurements were performed at the same six flow rates as for the low-pressure calibration at six different pressures (10 MPa, 25 MPa, 40 MPa, 55 MPa, 70 MPa and 85 MPa). Due to the limitations of the high-pressure pump the maximum mass flow rate at 55 MPa and 70 MPa (65 MPa) was 2.0 kg/min, and at 85 MPa (80 MPa) 1.0 kg/min respectively.

For the high-pressure testing we used the same zero-points as for the low-pressure calibrations. That means the flow meters were installed without setting a new zero-point. As it can be seen in **Figure 1**, the measurement setup the CFMs are installed in series with stiff metal pipe connections in between. In theory, vibrations from one CFM could be transferred to the other CFM via the pipework but also via the table. This would result in interference and erroneous mass flow rate measurements. To prevent vibration transmission through the table a wooden table was chosen, and shock absorbent rubber were placed under the CFMs connections. However, before the actual measurements were performed, we checked for crosstalk effects since we were not sure in all cases whether the CFMs worked at different driving frequencies. For this reason, the pulses obtain during zero flow (closed on-off ball valves upstream and downstream of each CFM) were compared for a certain period (e.g. 5 min) in case when both meters were supplied with power and in case when only one CFM was supplied with power. In addition, the same procedure was repeated at a constant flow rate. Here the totalized mass counter for one CFM was logged and compared for a certain period for the cases when the other CFM was switched on and off, respectively.

From the measurement result (see **Figure 5**) one could assume that there is a dependence of the flow rate measurement from the pressure. With increasing pressure, the measurement deviation is decreasing. However, attention should be drawn to the fact, not shown in **Figure 5**, that with increasing pressure also the temperature, especially for the reference meter at the low-pressure side, is increasing.

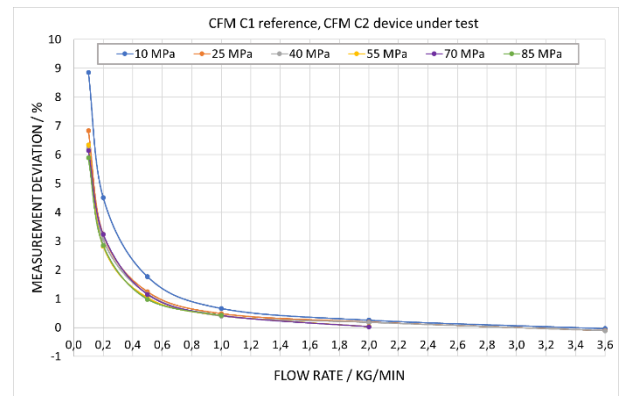


**Figure 5: Measurement results at high-pressure for one of the flow meter pair (CFM C1 as reference, CFM C2 DUT).**

It is particularly interesting to note that the temperature was quite stable at a certain pressure level during the measurements at different flow rates. But the temperature increased with increasing pressure values. Another effect was that the temperature at the place of the reference meter was depending on the compressed air supply. The compressed air supply was changed for higher pressures (usually after 400/550 MPa tests) from the house connection to the diesel-powered air compressor but some measurements (e.g. at 400 MPa) were performed with both configurations. Hereby it was established that the way of compressed air supply has an influence on the medium temperature at the place of the reference meter. The temperature measured at the place of the reference meter had, in some cases, a difference of up to 5 K depending on the compressed air was delivered by house connection or the diesel-powered air compressor (lower temperature). At the end in can be summarized that the temperature difference between 10 MPa and 85 MPa measurements was up to around 12 K (worst case) and that the measurement results need to be corrected regarding temperature to determine the pressure dependence of the mass flow rate. However, the desired correction regarding temperature requires more low-pressure calibrations in the temperature range of 20 °C to at least 30 °C.

## 5. Conclusion

A novel high-pressure flow test facility was built at RISE. With this facility it is possible to investigate the pressure dependence of Coriolis Mass Flow Meter (CFM) in a pressure range from 10 MPa to 85 MPa at flow rates in a range from 0.1 kg/min to 3.6 kg/min. Measurements were performed with CFMs from three different manufacturers. The achieved measurement results for one of in total three investigated pairs of high-pressure CFMs have been discussed. Summarized, it was shown that the conceived measurement setup works well. The only negative aspect is that the temperature at the place of the reference meter rises with increasing the inline pressure. Up to now low-pressure calibration were only performed at a temperature of 20 °C. However, it is possible to correct for the temperature effect and hence to separate the temperature and pressure effect, but this can only be achieved by additional traceable low-pressure calibration measurements at slightly elevated temperatures (e.g. up to 30 °C). In the next step additional low-pressure calibrations in a temperature range of 20 °C to 30 °C are planned for all CMFs. Afterwards, the obtained high-pressure data will be corrected regarding temperature. The overall objective is to publish a complete data set regarding the influence of pressure on the mass flow measurement accuracy for all three CFMs of the different brands.

## Acknowledgement

This paper was written under the Joint Research Project EMPIR Metrology for hydrogen vehicles (“MetroHyVe”) which is supported by the European Metrology Programme for Innovation and Research (EMPIR). The EMPIR initiative is co-funded by the European Union’s Horizon 2020 research and innovation programme and the EMPIR participating states.

## References

- [1] OIML R 137-1:2012 (E), *Gas meters – Part 1: Metrological and technical requirements*, International Organization of Legal Metrology, 2014.
- [2] OIML R 139-1:2014 (E), *Compressed Gaseous Fuel Measuring Systems for Vehicles – Part 1: Metrological and technical requirements*, International Organization of Legal Metrology, 2014
- [3] Measuring Instruments Directive (MID) 2014/32/EU Annex IV (MI-002), *Gas meters and volume conversion devices*, 2014
- [4] SAE J2601:2016, *Fueling Protocols for Light Duty Gaseous Hydrogen Surface Vehicles*, 2016.

# Bistatic wind lidar system for traceable wind vector measurements with high spatial and temporal resolution

S. Oertel, M. Eggert, C. Gutmuths, P. Wilhelm, H. Müller, and H. Többen

Physikalisch-Technische Bundesanstalt, Dept 1.4: Gas Flow, 38116 Braunschweig, Germany  
E-mail (corresponding author): stefan.oertel@ptb.de

## Abstract

Wind lidar systems have become a cost-efficient alternative to wind met masts in the recent years to measure and monitor the wind velocity in many applications in the fields of wind energy and meteorology. Conventional wind lidar systems work according to the monostatic measurement principle that is inherently accompanied by a spatial and temporal averaging procedure. This averaging procedure complicates the traceability of such systems as the uncertainty of the measured wind velocity depends on the homogeneity of the investigated wind fields. In contrast, the wind lidar system presented here works according to a bistatic measurement principle that measures the velocity vector of single aerosols in a spatially highly resolved measurement volume in heights from 5 m to 250 m with a resolution of about 0.1 m/s. The novel system has the potential for traceable wind speed measurements in homogeneous as well as in inhomogeneous wind fields as was proven by comparison measurements with a wind met mast. At PTB, the aim is to use the bistatic wind lidar as a traceable reference standard to calibrate other remote sensing devices, necessitating an in-depth validation of the bistatic lidar system and its measurement uncertainty. To this end, a new, specially designed wind tunnel with a laser Doppler anemometer (LDA) as flow velocity reference has been built up to validate the bistatic lidar in detail. First validation measurements in the velocity range from 4 m/s to 16 m/s are presented, showing an average deviation between the bistatic lidar and the LDA of 0.37 %.

## 1. Introduction

Wind met masts with cup anemometers are currently the most precise wind speed measuring devices for traceable wind speed measurements as they are necessary, for example, for the site assessment of prospective wind farms in the field of wind energy [1]. However, tall masts covering hub heights of modern wind turbines of more than 100 m are very expensive and will exceed mechanical and financial limits at future hub heights [2]. In the recent years, ground-based wind speed remote sensing by means of conventional monostatic wind lidar (light detection and ranging) systems has become an efficient measurement technique to supplement and extend wind met mast measurements [3]. The monostatic measurement principle (see Figure 1) utilized by conventional wind lidars is based on a common transmitting and receiving beam that is tilted in different directions to measure the complete wind vector. Due to the large measurement volume determined by the tilt angle this technique is inherently accompanied by a spatial and temporal averaging procedure. Provided that the wind field is almost homogeneous within the measurement volume, these systems deliver reliable measurement results [4]. However, leaving flat terrain

and having to consider the inhomogeneous wind conditions that predominate on complex terrain, significant errors for the wind speed measured arise and can be on the order of 10 % [5].

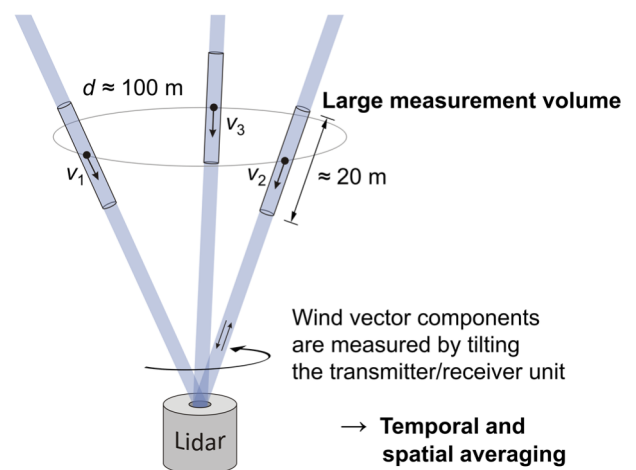
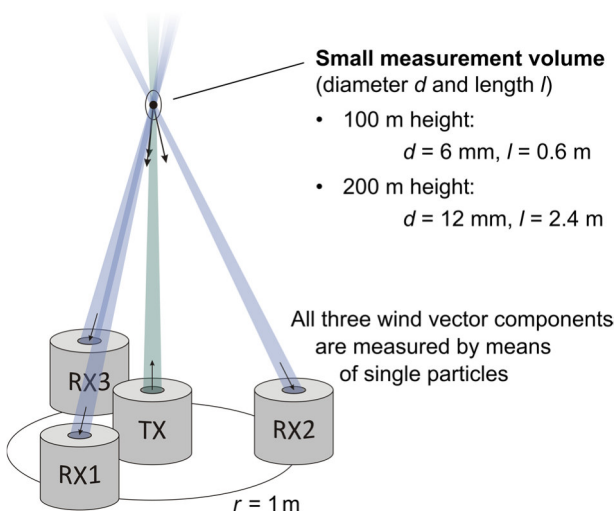


Figure 1: Conventional monostatic measurement principle

The new three-component fiber laser-based wind lidar sensor developed by the Physikalisch-Technische Bundesanstalt (PTB) uses one transmitting unit and three receiving units to measure the velocity vector of single aerosols in a spatially highly resolved measurement volume (with diameter  $d$  and length  $l$ ) in heights from 5 m ( $d = 300 \mu\text{m}$ ,  $l = 2 \text{ mm}$ ) to 250 m ( $d = 14 \text{ mm}$ ,  $l = 4 \text{ m}$ ) with a resolution of about 0.1 m/s (see Figure 2). Detailed comparison measurements with a 135 m high wind met mast and a conventional lidar system have proven that the high spatial and temporal resolution of the new, so-called bistatic lidar leads to a reduced measurement uncertainty compared to conventional lidar systems [6, 7]. Furthermore, the comparison demonstrated that the deviation between the bistatic lidar and the wind met mast lies well within the measurement uncertainty of the cup anemometers of the wind met mast for both homogeneous and inhomogeneous wind fields. Thus, the novel system has the potential for traceable wind speed measurements in flat as well as in complex terrain. At PTB, the aim is to use the bistatic wind lidar as a traceable reference standard to calibrate other remote sensing devices, necessitating an in-depth validation of the bistatic lidar system and its measurement uncertainty. To this end, a new, specially designed wind tunnel with a laser Doppler anemometer (LDA) as flow velocity reference has been erected on a platform at a height of 8 m; this allows the new wind lidar to be positioned below the wind tunnel test section to be validated in detail for wind vector measurements that are traceable to the SI units. First validation measurements within the wind tunnel test section at seven different velocities in the velocity regime from 4 m/s to 16 m/s are presented, showing an average deviation between the bistatic lidar system and the LDA of 0.37 %.



**Figure 2:** Bistatic measurement principle consisting of one transmitting unit TX (green beam) and three receiving units RX (blue beams)

## 2. Setup

Similar to monostatic lidar systems, the bistatic system designed by the Physikalisch-Technische Bundesanstalt (PTB) comprises a narrow bandwidth ( $< 1 \text{ kHz}$ ) master laser with a wavelength of 1550 nm, an acousto-optic modulator (AOM) for signal conditioning and a high-power (up to 30 W), erbium-doped fiber amplifier (EDFA) to generate the laser light transmission (Figure 3a). However, in contrast to monostatic systems, which typically use a common transmitting and receiving unit and an optical circulator to separate the received scattering light, the bistatic system is based on one transmitter and three discrete, spatially separated receivers. The receivers are positioned at a radius of 1 m around the transmitter to ensure both sufficient particle-scattering light intensity (quasi-backward direction) and sufficient resolution for the determination of the horizontal velocity component. Three heterodyne receivers convert the particle scattering light (three receiving beams) after the generation of optical beat signals into three electrical signals by differential photodetectors (PD). The transmitter beam as well as the beams of the three receivers are focused into a small measuring volume by the use of motor-controlled lenses and mirrors (see Figure 3b), forming Gaussian beams with a diameter of about 35 mm at the lenses and thereby centering the beam waists in the measuring volume.

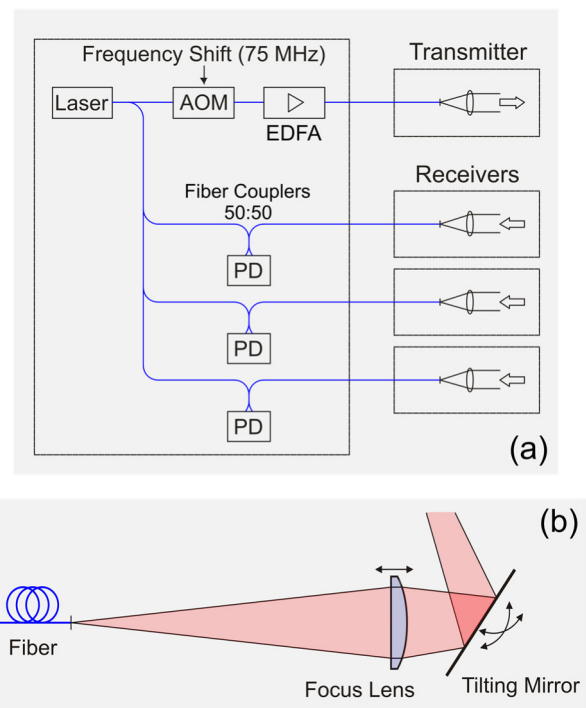


**Figure 3:** (a) Block diagram of the bistatic lidar system. (b) Sketch of the transmitter and receiver optics.

The resulting measuring volume is locally highly resolved and depends on the measuring distance. Typical measurement volume dimensions calculated according to Gaussian beam optics are shown in Figure 2. An optical phase delay measurement and correlation techniques between the three detection channels are applied to ensure that wind vector measurements are based on the scattering light from the same particles in the selected measuring distance between 5 m and 250 m. To ensure a mobile operation with stable working conditions in the field, especially with respect to requirements on the mechanical setup and the optoelectronics, the bistatic lidar system has been enclosed in an air-conditioned housing unit mounted on a trailer (Figure 4 and 5).



**Figure 4:** Optical installation inside the PTB lidar (opened trailer housing).

### 3. Wind tunnel test facility

A wind tunnel test facility (WTTF) was built up in the metrological Competence Center for Wind Energy (CCW) at PTB to analyze and investigate the bistatic wind lidar, its reliability and its measurement uncertainty in controllable and well-defined flow fields with a precise flow velocity reference traceable to the SI units. The specially designed wind tunnel from Deutsche WindGuard Wind Tunnel Services GmbH is erected on a platform at a height of 8 m enabling the bistatic lidar system to be positioned below the test section of the wind tunnel (Figure 5). The wind tunnel has an open test section 0.75 m in length with a cross-sectional area of 0.5 m x 0.5 m and a flow velocity range of 1 to 30 m/s. In the relevant part of the test section that is used for validation measurements of the bistatic lidar system, i.e., in the core of the flow field, the turbulence level is for all flow velocities below 0.35 % and the homogeneity of the flow field is 0.01 % per cm. An LDA 1-D fp50-unshift from Intelligent Laser Applications (ILA) R&D GmbH with a measurement uncertainty of 0.18 %, with the type being identical to an LDA used as transfer standard in the CIPM key comparison of air speed CCM.FF-K3.2011 [8], serves as a reference standard for the flow velocity within the wind tunnel test section. A more

detailed description and characterization of the wind tunnel can be found in [7].



**Figure 5:** Bistatic PTB lidar (opened trailer housing) positioned below the test section of the wind tunnel test facility.

### 4. Validation measurements

For all comparison measurements between the bistatic PTB lidar and the LDA reference standard in the wind tunnel both the lidar measurement volume ( $d = 400 \mu\text{m}$ ,  $l = 4 \text{ mm}$ ) and the LDA measurement volume ( $d = 300 \mu\text{m}$ ,  $l = 2.5 \text{ mm}$ ) resided – perpendicular to each other – within the same volume of about  $1 \text{ cm}^3$  in the core of the wind tunnel flow field, i.e., the sector of the test section with high homogeneity and low turbulence level. Figure 6 depicts the results of a long-term comparison lasting 3 h with the  $z$  component of the lidar system pointing along the flow field direction. For data analysis the raw data were averaged over time intervals (averaging time  $\Delta t$ ) from 0.1 to 600 s. The resulting mean values were further used to calculate the standard deviations  $\sigma$  for each averaging time. The red ( $\sigma_{\text{Lidar},z}$ ) and the black ( $\sigma_{\text{LDA}}$ ) line in Figure 6 show the result of this data evaluation for the lidar system (relevant  $z$  component) and the LDA, respectively. A lower signal-to-noise ratio in addition to a lower data rate of the lidar system leads to higher standard deviations of the lidar system compared to the LDA which are, however, well within the same order of magnitude. For long averaging

times both standard deviations reach the same asymptotic value caused by a long-term drift of the wind tunnel of about 0.003 m/s per 1 h. Figure 6 also shows the standard deviations of the two other vector components ( $\sigma_{\text{Lidar},x}$  and  $\sigma_{\text{Lidar},y}$ ) measured by the lidar system and, additionally, the mean values  $v_{\text{mean}}$  of the measured flow velocities averaged over the complete long-term measurement (3 h). The deviation between the lidar system ( $v_{z,\text{mean}}$ ) and the LDA ( $v_{\text{LDA},\text{mean}}$ ) for this single measurement is about 0.005 %.

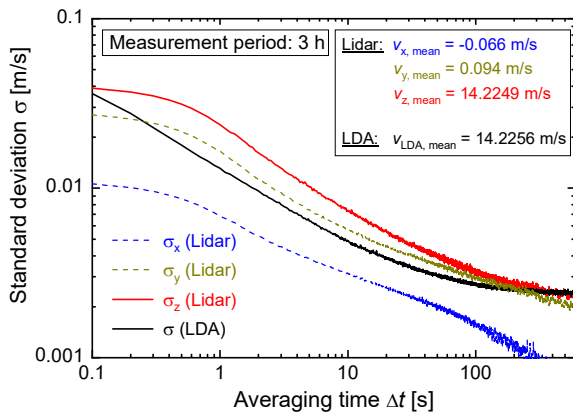


**Figure 6:** Long-term comparison measurement of the PTB lidar and the LDA.

A comparison of the lidar system with the LDA in the WTTF in the velocity range from 4 to 16 m/s is shown in Figure 7. For all measurements the measurement time was 1 h with an averaging time  $\Delta t$  of 1 s. The blue circles are the mean velocities measured by the lidar system referred to the LDA whereby the red line is the identity. More interesting, the squares show the mean deviations of the PTB lidar that are in the complete velocity range well below 0.5 %. The magenta-colored square at 10 m/s is a measurement at which the lidar system was rotated about 90° with respect to the other measurements. Both values at 10 m/s (black and magenta) are within both measured standard deviations demonstrating a consistent result regarding the measurement geometry of the lidar system. The average mean deviation (dashed line) of all measurements is  $0.37 \% \pm 0.06 \%$  indicating a small systematic error that is supposed to arise from an inaccuracy in the determination of the measurement height of the lidar system within the wind tunnel test section. Further extensive measurements with the WTTF will be performed in the future especially with an improved and more accurate measurement height determination to investigate and validate the PTB lidar and its accuracy.

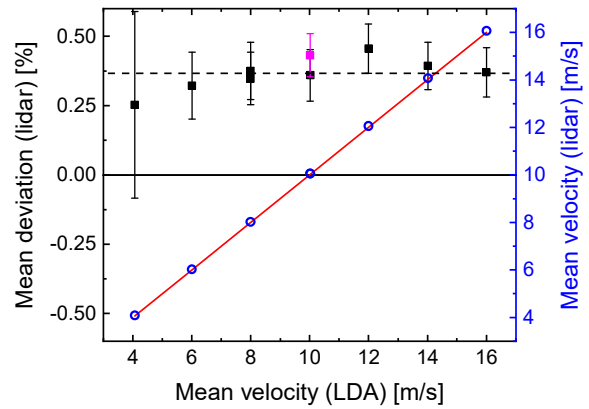


**Figure 7:** Comparison of the PTB lidar with WTTF reference (LDA).

## 5. Conclusion

A new three-component fiber laser-based bistatic wind lidar system constructed at the Physikalisch-Technische Bundesanstalt (PTB) enables traceable wind velocity measurements in heights from 5 m to 250 m. Due to the bistatic setup of the system the PTB wind lidar offers a high spatial and temporal resolution resulting in a reduced measurement uncertainty compared to conventional monostatic wind lidar systems and a potential application for traceable wind velocity measurements in flat as well as in complex terrain. For a detailed analysis and validation of the PTB wind lidar as a new reference standard for other wind speed remote sensing devices a new wind tunnel test facility (WTTF) was built up at the PTB that enables the measurement uncertainty of the bistatic wind lidar system to be determined quantitatively in controllable and well-defined flow fields. First comparison measurements show a measurement behavior of the lidar system comparable with the LDA of the WTTF concerning the evolution of the standard deviation during long-term measurements. Furthermore, the average deviation of the lidar system in the flow velocity range from 4 m/s to 16 m/s was determined to be  $0.37 \% \pm 0.06 \%$  and is for all measured flow velocities below 0.5 %.

## References

- [1] IEC 61400-12-1, Edition 2.0: *Wind energy generation systems – Part 12-1: Power performance measurements of electricity producing wind turbines*, 2017.
- [2] Emeis, S., Harris, M., and Banta, R. M., “Boundary-layer anemometry by optical remote sensing for wind energy applications”, *Meteorol. Z.*, **16**, 337–347, 2007.
- [3] Albers, A., Janssen, A. W., and Mander, J., “How to gain acceptance for lidar measurements”, available at: <https://www.windguard.de/veroeffentlichungen.html> (last access: 4 January 2019), 2010.

- [4] Gottschall, J., Courtney, M. S., Wagner, R., Jørgensen, H. E., and Antoniou, I., “LiDAR profilers in the context of wind energy – A verification procedure for traceable measurements”, *Wind Energy*, **15**, 147–159, 2012.
- [5] Bingöl, F., Mann, J., and Foussekis, D., “Conically scanning lidar error in complex terrain”, *Meteorol. Z.*, **18**, 189–195, 2009.
- [6] Eggert, M., Gutmuths, C., Müller, H., and Többen, H., „Time resolved wind vector comparison measurements between the PTB Lidar transfer standard and a 135 m wind met mast”, in *Proc. Experimentelle Strömungsmechanik* (German Association for Laser Anemometry, Karlsruhe), 3.1 – 3.7, 2016.
- [7] Oertel, S., Eggert, M., Gutmuths, C., Wilhelm, P., Müller, H., and Többen, H., "Validation of three-component wind lidar sensor for traceable highly resolved wind vector measurements", *J. Sens. Sens. Syst.*, **8**, 9–17, 2019.
- [8] Müller, H., Caré, I., Lucas, P., Pachinger, D., Kurihara, N., Lishui, C., Su, C.-M., Shinder, I., and Spazzini, P. G., “CCM.FF-K3.2011: Final report for the CIPM key comparison of air speed, 0.5 m/s to 40 m/s”, *Metrologia*, **54**, 07013, 2017

# A novel calibration of the Large Piston Prover at INRIM

**E. Audrito<sup>1</sup>, F. Bertiglia<sup>1</sup>, M. Bisi<sup>1</sup>, C. Francese<sup>1</sup>, G. La Piana<sup>1</sup>, A. Piccato<sup>1</sup>,  
M. Santiano<sup>1</sup>, P.G. Spazzini<sup>1</sup>**

<sup>1</sup>INRIM, Strada delle Cacce, 91, Torino, Italy  
E-mail (corresponding author): a.piccato@inrim.it

---

## Abstract

INRIM realizes its flow rate standard using three distinct facilities, aimed at measuring different flow rate ranges; in particular, for the larger flow range (10-2600 L/min) a piston of 1000 mm nominal diameter and 1200 mm nominal stroke is used. The traceability of the standard is obtained through dimensional calibration of the piston, regarding both the piston size and its stroke.

The first calibration of the machine was performed at its initial installation. Even if most of the relevant documentation about this first calibration is not available, INRIM realized a procedure similar to the old one and performed measurements to renovate the first facility calibration. The present paper will dedicate special attention to the description of the measurement chain used for the calibration of the piston in its own siege. Moreover, the method for the transfer of traceability from the length standard to the measurement of the piston diameter will be discussed; it should be noted that the dimensional study is not completed yet, because the first set of measurements described in the present work, evidenced the criticalities of the procedure adopted in the past. For this aim, a further measurement campaign will be carried out in order to minimize the uncertainty associated to the dimensional measurement of the piston and of its displacement. Finally, the results of first dimensional evaluation will be presented alongside.

---

## 1. Introduction

Measurement of gas flow rates is a field whose importance is growing due to the need for accurate calibration of mass flow meters with various FSR (Full Scale Range), that have an increasingly wide field of application (e.g. for dynamical gas mixing, aerospace applications, etc.).

For intermediate flow ranges, a robust and reliable technology is the piston prover volumetric method, since it allows to provide a carefully controlled flow of gas; its accurate measurement requires a reliable and precise knowledge of the relationship between delivered volume and piston movement, the possibility to precisely measure the gas temperature and pressure, and the possibility of using high purity gases for the tests.

INRIM has operated the MEGAS bell prover for several years now [1]. This test rig allows measurements of flow rates lower ranging between 1 and 2400 L/min with uncertainties of the order of 0.05% due to several technological features which include a very accurate piston machining, reduced movement friction, accurate measurement of the piston movement and of the gas thermodynamic conditions, and temperature stabilization of the ambient. Though, the main requirement for the measurement is still an accurate calibration of the

volume of the piston as a function of its movement, which can be obtained through measurement of the local diameter; in this paper, the dimensional method employed at INRIM for this task is described alongside with the presentation of results obtained during the last measurements.

## 2. MEGAS design and capabilities

### 2.1 MEGAS design

The MEGAS test rig (Figure 1) was designed as a high-performance piston prover for gas flow; within volumetric calibration machines, the piston prover design is intrinsically more accurate than the bell prover design since it requires an accurate machining of the exterior diameter of a piston instead of the interior diameter of a bell and allows therefore lower uncertainties. Of course, this is true provided all other terms of the uncertainty budget are kept low enough. The prover here described includes a stainless steel hollow piston with nominal diameter of 1 m and nominal length of 1.6 m, which moves within a cylindrical chamber also built in stainless steel; the system is provided with a pressure probe allowing the measurement of its internal pressure and twelve platinum resistance thermometers (PT100), placed on the inner wall of the cylinder at different heights in order to measure

the average temperature of the test gas inside the machine and to detect possible vertical thermal gradients. The piston is moved by a screw (10 mm pitch) actuated by an electrical motor controlled by a digital driver and connected to a gear box with variable ratio; it is thus possible to obtain a wide range of stably controlled piston speeds.

The measurement of the gas flow is performed by measuring the movement of the piston by a high resolution encoder (18000 steps per revolution) and the flow time by a quartz clock. The gas flow is then obtained by means of the mass equation balance. This method computes the gas flow by evaluating the initial mass of gas present inside the cylinder (which can be obtained from the initial thermodynamic conditions and an evaluation of the initial volume) and the final mass of gas (obtained from the final thermodynamic conditions and the final volume). The method thus implicitly keeps into account the variations of thermodynamic conditions. More importantly, it can be shown that, if the variations of thermodynamic conditions are not large, the sensitivity coefficient of the uncertainty associated to the initial volume is very small, therefore it is not required to have an accurate evaluation of this quantity; on the other hand, the accuracy on the volume variation is one of the main components in the determination of the final uncertainty, therefore all details of the machine were designed with the aim of increasing this accuracy. In particular, the piston was carefully machined to have a shape very close to a perfect cylinder and the thickness of its wall is large enough to ensure a very high rigidity, thus a remarkable stability, as will be shown in the results section. Additionally, the distance between the piston and the inner walls of the chamber is of 40 mm to reduce the dead volume.

In order to reduce temperature variations, the test rig is placed within a temperature-conditioned room where the temperature is stable within 0.1 K (during a typical measurement time) and with small vertical temperature gradients. The ambient pressure and the relative humidity of the room are monitored by means of a TESTO instrument.

### 2.2 MEGAS capabilities

The test rig presented in subsection 2.1 has a maximum flow rate capability of 2400 L/min (which corresponds to 144 m<sup>3</sup>/h), which can be obtained by completing a full stroke of the piston in 30 s, while the minimum flow rate that can be obtained is of the order of 1 L/min. The uncertainty of the flow rate, evaluated based on the previous calibration of the system, is of 0.05%.

The machine in its present status can work as a gas provider running at constant speed, although

future developments of the motor control system are forecast to render it possible to work as a gas acceptor and to run at variable speed to maintain constant pressure inside the cylinder in order to expand its calibration possibilities



**Figure 1:** MEGAS; the piston (yellow arrow) and the chamber (white arrow).

### 3. MEGAS calibration procedure

The MEGAS calibration takes into account the geometrical characteristics of the MEGAS piston, the displacement and the translation time of piston inside the MEGAS chamber (see Figure 1).

The total volume of the piston has to be evaluated in order to compute the mean volume variation during the piston translation. The piston is not removable from the chamber, and its sizes of about 1 m of diameter and 1.6 m of length do not allow its geometrical evaluation by means of the measurement facilities allowable at INRIM (as for example the Coordinate Measurement Machine property of the Institute). For these two reasons the relevant geometrical characteristics of the piston were evaluated in situ.

A linear encoder system was used for the diameter evaluation whereas the vertical translation of the piston was measured by a traceable interferometer. The two systems and their placement are described in detail in the following section.

An appropriately designed bar (Figure 2), traceable to the length standard, was used as a reference for the piston diameter measurement. The reference bar is made of stainless steel with two parallel faces at the tips and a nominal length of 1 m; the rectangular faces are machined to reduce the surface roughness and to grant an accurate parallelism between each other. The body of the bar is designed to allow its positioning on the top of

the piston taking into account the footprint of the central screw. The bar length is traceable to the length standard by means of a calibration report. According to the calibration report, the bar length was evaluated in two different positions on the tip faces: in the central point of the rectangular faces and in a peripheral position. For the current measurements the mean value of the two calibrated lengths has been considered:

$$\bar{l}_{ref} = 999.255 \text{ mm} \pm 5 \text{ } \mu\text{m}.$$



**Figure 2:** The reference bar and an enlargement showing the tip face.

The evaluation process of the piston diameter consists in the dimensional scanning of six couple of generatrices positioned at an angle of 30° from each other and a seventh couple of generatrices (Ref) positioned as shown in Figure 3. This test configuration has been repeated according to the first calibration procedure conducted on the MEGAS in order to compare present results with those obtained in the past.

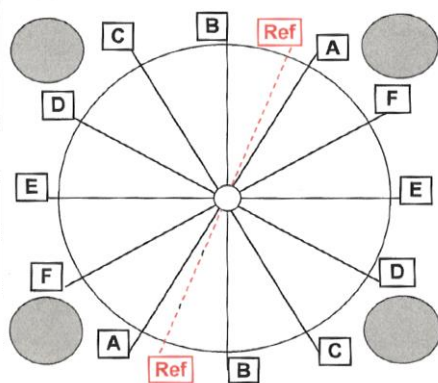


**Figure 3:** sketch of the top view of the piston. Letters indicate the seven positions investigated. Notice that the Ref (in red) indicates the last configuration investigated and not the reference bar.

The scanning procedure was conducted with two calibrated linear encoders positioned as described in section 4. A platinum resistance thermometer

(PRT) was positioned on the reference bar in order to monitor the thermal conditions of the bar reference during scanning measures.

The piston is about 1.6 m long and the two end-of-strokes of the piston run cover 1.3 m of total length. For the diameter evaluation a portion of the piston height, called *working length*, of about 0.8 m centred with respect to the middle section of the piston, has been considered.

The piston displacement has been evaluated by means of an interferometer aligned to the piston axis. The acquisition of the interferometer was synchronous with that of the linear encoder system. The interferometer setup and its positioning is described in section 4.

The measurement procedure followed for the seven couple of generatrices is the following: The linear encoders are positioned in the configuration A according to the scheme shown in Figure 3.

The piston is positioned in its lower position and the reference bar is placed on top of the piston; after an appropriate waiting time for thermal effect stabilization caused by the operator intervention, the linear encoders are set on the reference parallel tip faces (see Figure 4). The initial reference value  $\Delta l_{ref1}$  is thus acquired, then the piston is positioned at its lower end-of-stroke and the scanning procedure of the first couple of generatrices started. The piston is stopped at its higher end-of-stroke and the scanning procedure is repeated downward.

The generatrix scanning (upward and downward) is thus repeated six times obtaining seven repetitions totally. Finally the final reference value  $\Delta l_{ref2}$  is acquired again by the two linear encoder on the reference bar that was kept in the same position for the whole scanning procedure. The acquisition of this last reference value complete the scanning procedure of one couple of generatrices.

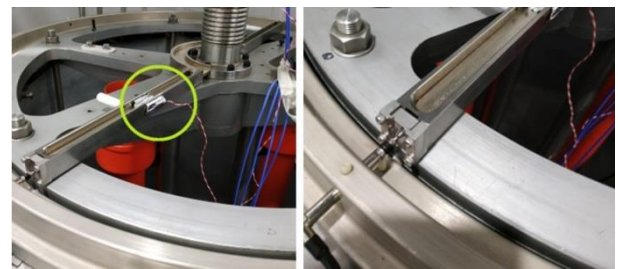


**Figure 4:** on the left: reference bar placed on the top of the piston and PRT on the reference bar (green circle); on the right: linear encoder positioned on a reference tip face.

At the end of the first scan (configuration A), the linear encoders are rotated around the piston axis according to the proposed scheme (Fig. 4) and the scanning procedure is repeated for the remaining six positions (B, C, D, E, F and Ref).

The acquisition of the interferometer, measuring the piston displacement, was set synchronous with the linear encoder system. Ambient conditions (pressure, temperature and humidity) have been acquired during the whole measurement campaign in order to evaluate the proper correction for air refractivity.

The analyses of measures are described in results subsection 5.

#### 4. Measurement chain for calibration

Details of the measurement chains designed for the MEGAS calibration are described in this subsection in order to detail the measuring procedure in the previous section.

##### 4.1 linear encoder system

Two linear encoders TESATRONIC TT60 have been used to evaluate the mean value of the piston diameter. The TT60 measurement range is 5 mm with a resolution of 0.1  $\mu\text{m}$ . A stainless steel ring was opportunely designed to place the two linear encoder stems in correspondence to the piston diameter (Figure 5).

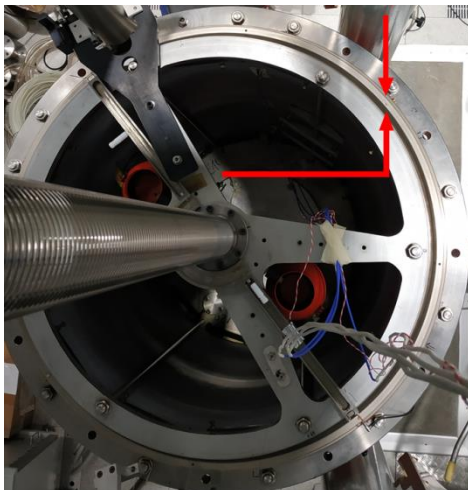


**Figure 5:** red arrows indicate the ring for the linear encoder positioning.

The ring is placed on the O-ring between the chamber and the piston after removing a ring made of Teflon for dust protection. The ring is transversally holed in order to insert the two linear encoder stems in correspondence to a ring FLOMEKO 2019, Lisbon, Portugal

diameter. The stems are thus locked to the ring structure by means of two clamping grains made of Teflon (Figure 4).

For this first measurement campaign the ring has not been fixed during the scanning procedure but it is expected to consider the use of a fixing system for future measures. The linear encoders were positioned in the seven configurations described in the previous section (Figure 3) by turning the ring around the piston axis.

The measure of each couple of generatrices was conducted at a piston speed of about 6.5 mm/s; the acquisition time for every generatrix was about 197 s, corresponding to 1295 output samples.

##### 4.2 interferometer

An AGILENT 5518A interferometer was placed under the MEGAS chamber on the floor (Figure 6). The laser alignment was difficult because, in spite what happens usually, it was not possible to move the corner cube (CC), which was fixed to the piston bottom surface inside the MEGAS chamber. As a consequence of this measurement system configuration, the alignment of the Laser to the movement axis had to be performed with two mirrors (M1 and M2), with a not favourable optical leverage. The alignment was checked with a four-quadrant detectors in order to keep the cosine error below  $10^{-8}$ . The interferometer acquisition was synchronous with the linear encoder system resulting in about 1 output sample every millimetre of piston stroke.

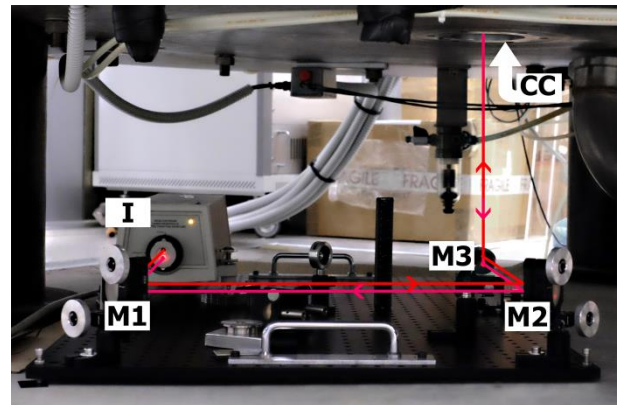


**Figure 6:** red arrows indicate the laser path. I: interferometer; M1, M2, M3: mirrors; CC: corner cube positioned on the piston (not visible in figure).

##### 4.3 thermometric sensors

The temperature of the piston was measured by placing four platinum resistance thermometers (PRT - Pt100 1/3 Din) inside it.

Four PRTs have been positioned in the inner surface of the piston in correspondence of the two generatrices A (fig. 4) and in particular: one

thermometer was placed in the middle of a generatrix, whereas three thermometers are placed respectively in the centre and about 0.5 upward and 0.5 m downward with respect to the centre of the specular generatrix. This thermometer placement allowed to evaluate thermal stability over time and to monitor the temperature gradient along the axis and the central diameter of the piston.

A fifth additional PRT has been placed on the reference bar to evaluate its thermal stability (Figure 3).

All PRTs are connected to a KEITHLEY 6 ½ Digit digital multimeter mod. 2700 via a 20-channel scanner card. This thermometric chain was calibrated at INRiM, in a range from 18 °C to 22 °C with a final expanded uncertainty of 0.01 °C.

The commercial software ExcelLink by KEITHLEY was used for acquisition. Every thermometer temperature has been acquired in series during all the scanning procedure every 2 seconds.

In addition to these five thermometers, placed specially for MEGAS facility calibration, twelve PT100 calibrated probes, are placed on the inner surface of the chamber containing the piston at different heights. This last thermometric chain is a permanent component of the MEGAS measurement chain and it is used to monitor the temperature gradients of the test gas inside the facility and to detect vertical thermal gradients in the piston chamber.

## 5. Measurement results

In this section the first measurement results are shown.

First, the linear encoders measures have been analysed for the evaluation of the pistons diameter as a function of the generatrices.

The following Equation (1) has been applied:

$$d_{i(genA)} = \Delta l_{i(genA)} - \bar{l}_{ref(genA)} + \bar{l}_{ref} \quad (1)$$

Where:

$d_{i(genA)}$  is the i-th diameter with linear encoders positioned in the A configuration (generatrix A, Figure 3).

$\Delta l_{i(genA)}$  is the i-th linear encoders output (generatrix A).

$\bar{l}_{ref(genA)}$  is the mean value of  $\Delta l_{ref1}$  and  $\Delta l_{ref2}$  (see section 3)

$\bar{l}_{ref}$  is the calibrated mean length of the reference bar (see section 3).

The equation 1 is representative for the case of linear encoder in the configuration A (Figure 3); the

same equation is used for all the seven configurations (A, B, C, D, E, F and Ref.)

Then the mean diameters of the piston, taking into account the seven couple of generatrices scanned seven times each, has been evaluated; the resulting curve trends are shown in Figure 7.

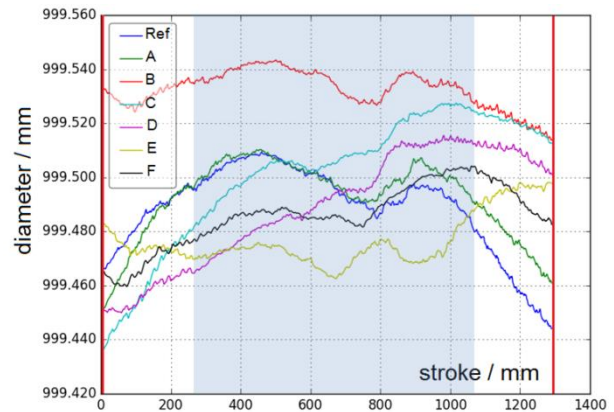


**Figure 7:** mean diameters as a function of the seven generatrices. Red lines: end-of-strokes; blue zone: working length.

The less regular trend evidenced by the acquisition at the ends of the piston are out of the working zone, therefore the higher dispersion of the curves in these zones does not contribute to the mean diameters dispersion. Taking into account the working zone (between 265 mm to 1063 mm in Figure 7) the mean diameter curves show a dispersion of values between 999.46 mm to 999.54 mm. This result shows a larger dispersion with respect to the first MEGAS calibration [1], when a dispersion between 999.50 mm to 999.53 mm at 20 °C in a working length of 1 m was found.

In Table 1 the mean values of each diameter curves as a function of the generatrix positions are shown.

**Table 1:** diameters mean values and associated standard deviations as a function of generatrices.

Generatrix	stroke		working length	
	Mean / mm	$\sigma$ / mm	Mean / mm	$\sigma$ / mm
Ref	999.489	0.016	999.498	0.007
A	999.492	0.014	999.501	0.005
B	999.532	0.007	999.536	0.005
C	999.501	0.024	999.508	0.012
D	999.489	0.021	999.493	0.015
E	999.477	0.009	999.472	0.005
F	999.486	0.011	999.489	0.007

As a final evaluation, the mean diameter of the piston has been computed taking into account all the repeated acquisition along the seven generatrices. Table 2 summarizes this last result.

**Table 2:** mean diameter of the piston as a function of the investigated zone.

	Mean / mm	$\sigma$ / mm
<b>stroke</b>	999.495	0.024
<b>working length</b>	999.500	0.021

The PRT on the bar evidenced a temperature variation of the order of 0.05 K. The same order of temperature variation was registered by the four PRT placed on the inner surface of the piston. Taking into account the coefficient of thermal expansion of stainless steel (of the order of 10 ppm/K) and the acquired temperature variations, it is reasonable to neglect the thermal expansion of the reference bar and of the piston in the final mean diameter computation.

As regards the piston displacement measure, a mean displacement of the piston has been evaluated to be  $(0.5555 \pm 0.0006) \mu\text{m}/\text{step}$ .

Figure 8 and Figure 9 show, respectively, the displacement of the piston as acquired by the interferometer between two consecutive sampling points (corresponding to 1 mm), and a closer view of the first 100 points, showing a periodic variation with a period equal to the 10 mm screw pitch.

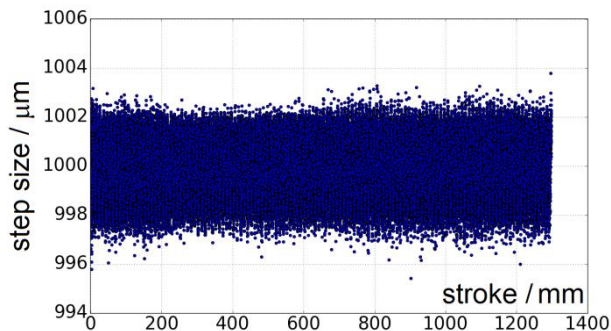


**Figure 8:** displacement between two consecutive interferometer sampling points.

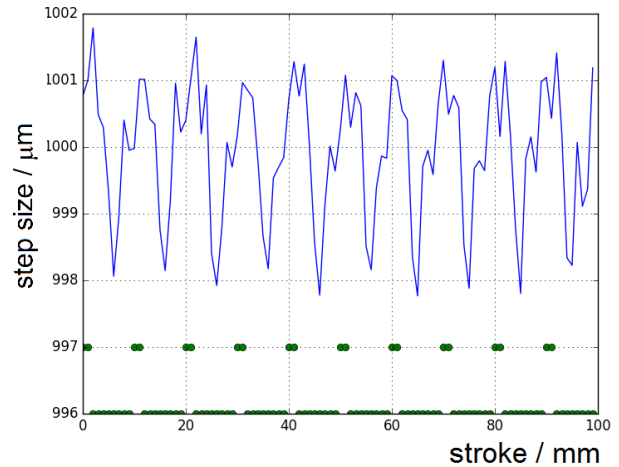


**Figure 9:** close-up of Figure 8.

We anticipate the result of the mean volume increment obtainable by moving the piston by one single step:

$$V_{\text{step}} = (4.358 \pm 0.005) \times 10^{-7} \text{ m}^3/\text{step},$$

corresponding to  $(0.4358 \pm 0.0005) \text{ mL}/\text{step}$ .

## 6. Conclusion

The dimensional investigation of the test volume at the MEGAS confirmed the values of the previous calibration and, at the same time, evidenced some criticality in the measurements procedure. The measures of piston diameters and displacements will be repeated. In particular, the displacement evaluation need to be investigated more deeply as this measure influences the volume uncertainty budget considerably. A review of the interior piston structure could be evaluated in order to reduce the dispersion of displacement measures and will be discussed in a future work.

## References

- [1] G. Cignolo, A. Rivetti, G. Martini, F. Alasia, G. Birello, G. La Piana, "The National Standard Gas Prover of the IMGC-CNR", in *Flomeko 2000, Salvador (Brazil) Proc.*, 5-9 June, 2000

# The inter-comparison of air speed from 2 m/s to 40 m/s by Pitot static tubes

Y.M. Choi<sup>1</sup>, N.D. Trang<sup>2</sup>, W. Kang<sup>1</sup>, Y. Terao<sup>3</sup>, N. Kurihara<sup>3</sup>, A. Iwai<sup>3</sup>, T. Funaki<sup>3</sup>,  
S.H. Bak<sup>4</sup>, C.S. Yoo<sup>4</sup>, Y.T. Kwon<sup>4</sup>

<sup>1</sup>Korea Research Institute of Standards and Science, 267 Gajeong-ro, Daejeon, Republic of Korea

<sup>2</sup>University of Science and Technology, 217 Gajeong-ro, Daejeon, Republic of Korea

<sup>3</sup>National Institute of Advanced Industrial Science and Technology (AIST), National Metrology Institute of Japan, Tsukuba Central 3, Umezono 1-1-1, Tsukuba, Ibaraki 305-8563, Japan

<sup>4</sup>HCT Co., Ltd, 74 Seoicheon-ro 578, Icheon, Gyeonggi-do, Republic of Korea

E-mail: ymchoi@kriss.re.kr

---

## Abstract

The Mutual Recognition Arrangement (MRA) is framed by the International Committee of Weights and Measures in order to establish the degree of equivalence of national measurement standards via the key comparisons as well as the inter-comparisons of measurements. Based on this objective, the current work was performed in order to determine the degrees of equivalence among three laboratories in Korea Research Institute of Standards and Science (KRISS), National Metrology Institute of Japan (NMIJ) and HCT company for air speed over the range from 2 m/s to 40 m/s. In this inter-comparison of air speed, two AMCA type Pitot static tubes were considered as artifacts. The reference value (RV) and its uncertainty was calculated from all measurement results reported by the participants. The normalized deviations,  $E_r$ -number, were mostly smaller than 1. Consequently, the results of participants were mutually consistent.

---

## 1. Introduction

This inter-comparison has been performed between three laboratories including KRISS, NMIJ and HCT in which KRISS played the role of a pilot. Because it takes role of the national metrology laboratory, Gas Flow Standards Group in NMIJ undertakes the function of developing, maintaining and disseminating the national primary standards of gas flow and air speed in Japan. In addition, NMIJ proved their calibration and measurement capabilities of air speed up to 40 m/s by participating in the key comparisons of International Committee for Weights and Measures as well as that of Asia Pacific Metrology Programme as: CCM.FF-K3 [1], [2] and APMP.M.FF-K3 [3]. Similar to the gas flow group in NMIJ, fluid flow group in KRISS is the national laboratory in Republic of Korea. KRISS gives the traceability of liquid flow, gas flow and air speed and performs the research for developing the flow measurement technology. The equivalence of their calibration and measurement capabilities of air speed up to 16 m/s is also published in APMP.M.FF-K3 [3]. HCT is one of the six laboratories accredited by Korea Laboratory Accreditation Scheme (KOLAS) in air speed field and their air speed standard system has the range up to 40 m/s. HCT supplies the calibration and testing services for the industry. The main purpose of this

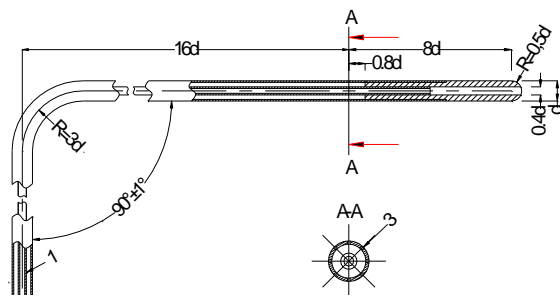
research is to determine the degree of equivalence between three laboratories at the air speed of 2 m/s and 40 m/s. In order to carry out this inter-comparison, three laboratories have calibrated two AMCA type Pitot tubes over the range from 2 m/s to 40 m/s. In advance, the inter-comparison was performed by KRISS and HCT, however, the measuring range of their system is different. The maximum speed of KRISS is 16 m/s and HCT's system is 55 m/s. And NMIJ can measure the air speed up to 90 m/s [4], so NMIJ was invited to ensure this inter-comparison cover the range from 2 m/s to 40 m/s. The arrangement as well as the expression of the inter-comparison result was partly based on the Guidelines of Measurement comparisons in the CIPM MRA [5].

## 2. Experimental and analysis methods

### 2.1. Artifacts used in the comparison measurement

There are three types of Pitot static tube recommended in the international standard, ISO 3966 [6] as: AMCA type, NPL type, and CETIAT type. AMCA type is popularly used in the industry. Therefore, in this inter-comparison, two AMCA Pitot tubes were used as the artifacts. The first AMCA Pitot tube (PT1) is produced by United Sensor Company. This has the specifications as the following: the outer diameter  $d$  is 2.4 mm, the axis of

stem is  $nd = 10d$  from plane of static-pressure holes, and the distance from tip of nose to static-pressure holes is  $4d$ . The second AMCA Pitot tube (PT2) is manufactured by Airflow Company. Its geometric parameters following: the outer diameter  $d$  is equal to 4.7 mm, the axis of stem is  $nd = 11d$  from plane of static-pressure holes, and the distance from tip of nose to static-pressure holes is  $6.6d$ . Meanwhile, these parameters suggested in the international standard are  $nd = 16d$  and  $8d$ , respectively [6]. Two artifacts are illustrated in Figure 1.



(a) ISO 3966, specification of AMCA Pitot tube



(b) PT1

(c) PT2

**Figure 1:** AMCA Pitot tubes

In order to measure the dynamic pressure of the artifacts in this research, a Furness micro manometer FCO510 with working ranges of (0-20) Pa and (20-200) Pa for velocity measurements below 20 m/s and an Yokogawa differential pressure gauge for velocity measurements above 20 m/s at NMIJ. At KRISS, two precise MKS differential pressure gauges with a working range of (2-200) Pa were used. Meanwhile, at HCT, the same Furness micro manometers FCO510 as at NMIJ was used for velocity measurements below 20 m/s and another Furness micro manometer with working ranges of (0-2000) Pa and (2000-20000) Pa was used for velocity measurements above 20 m/s.

### 2.2. Medium wind tunnel system in NMIJ

The medium air speed standard system in NMIJ consists of a Gottingen type wind tunnel in which the test section area is  $0.4 \text{ m} \times 0.4 \text{ m}$ , the working range is from 1.3 m/s to 40 m/s as shown in Figure 3, the maximum turbulent intensity in the test section is 0.03%. The working standard for the wind tunnel is ultrasonic anemometer mounted on the wall of the test section. The anemometer is calibrated by using an LDA system, which has been calibrated against a rotating disc [7]. The expanded uncertainty values of the NMIJ air speed

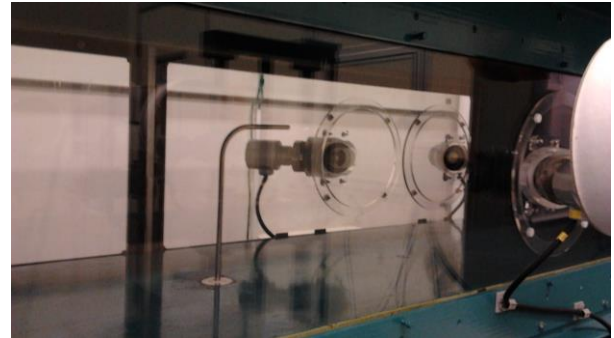


**Figure 2:** Air speed system in NMIJ

standard system is  $[0.297 + 0.27/(v^2 - 0.77v)] \%$  from 1.3 m/s to 27.5 m/s and  $[-0.0001185v^3 + 0.01157v^2 - 0.3677v + 4.124] \%$  from 27.5 m/s to 40 m/s [1].

### 2.3. Air speed system in KRISS

The air speed standard system in KRISS used for calibrating the two Pitot tubes includes: a subsonic open-circuit wind tunnel in which the test section area is  $0.9 \text{ m} \times 0.9 \text{ m}$ , the working range is from 2 m/s to 16 m/s as shown Figure 3, and the maximum turbulent intensity in the test section is 0.4%; the reference is a standard NPL Pitot tube and other instruments are two precise MKS differential pressure gauges with a working range of (2-200) Pa for velocity measurements. The expanded uncertainty values of the KRISS standard air speed system is 1.1% from 2 m/s to 5 m/s and 0.6% from 5 m/s to 16 m/s [8].



**Figure 3:** Air speed system in KRISS

### 2.4. Air speed system in HCT

The air speed standard system in HCT consists of a Gottingen wind tunnel having the specifications as the following: the diameter of jet outlet is 255 mm; the length of working section is 320 mm, the working range covers from 0.1 m/s to 55 m/s, and the maximum turbulent intensity in the test section is 0.7%; the reference is an Fp50 LDA system manufactured by ILA company with: beam distance is 45 mm, wavelength is 561 nm. This LDA was calibrated by the National Metrology Institute of Germany (PTB) and its expanded uncertainty is 0.22%. The measurement setup was arranged on the HCT system as shown in Figure 4 and the expanded uncertainty values of the air speed standard system in HCT is 0.44%.

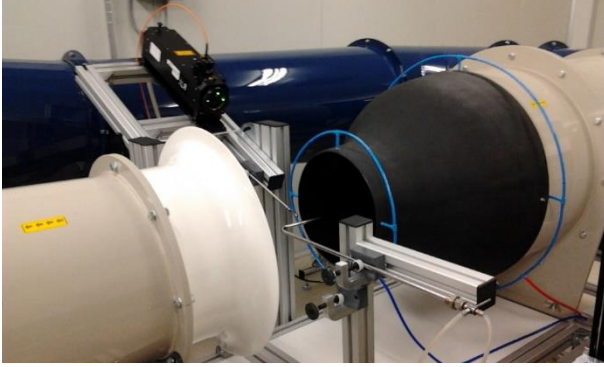


**Figure 4:** Air speed system in HCT

### 2.5. Method of measurement and analysis

The calibration of two artifacts was performed by the participants at ambient condition at 10 velocities from 2 m/s to 40 m/s and the two artifacts were completely and separately calibrated. At each velocity, five repeated measurements were recorded in order to calculate the velocity conversion factor  $K$  according to the following equation:

$$K = \frac{V_{ref}}{V_{DUT}} \quad (1)$$

Where,  $V_{ref}$  [m/s] is the reference velocity measured by the participant,  $V_{DUT}$  [m/s] is the velocity read by the artifacts [2].

Based on the data of  $K$  given by the participants, the degree of equivalence of the measurement would be analysed according to the procedure A proposed by Cox [9], [10]. The reference value  $K_{RV}$  is considered as a best estimate of the measurand and determined by the weighted mean of the measurements as the equation (2):

$$K_{RV} = \frac{\frac{K_{KRIS}}{u^2(K_{KRIS})} + \frac{K_{NMIJ}}{u^2(K_{NMIJ})} + \frac{K_{HCT}}{u^2(K_{HCT})}}{\frac{1}{u^2(K_{KRIS})} + \frac{1}{u^2(K_{NMIJ})} + \frac{1}{u^2(K_{HCT})}} \quad (2)$$

where  $K_{KRIS}$ ,  $K_{NMIJ}$  and  $K_{HCT}$  are the values of the velocity conversion factor;  $u_{KRIS}$ ,  $u_{NMIJ}$  and  $u_{HCT}$  are the standard uncertainty.

And the standard uncertainty of  $K_{RV}$  is equal to:

$$u(K_{RV}) = \frac{1}{\frac{1}{u^2(K_{KRIS})} + \frac{1}{u^2(K_{NMIJ})} + \frac{1}{u^2(K_{HCT})}} \quad (3)$$

Then, all results obtained from participants are tested an overall consistency if a chi-squared test satisfies the equation (4) and (5)

$$\chi_{obs}^2 = \frac{(K_{KRIS}-RV)^2}{u^2(K_{KRIS})} + \frac{(K_{NMIJ}-RV)^2}{u^2(K_{NMIJ})} + \frac{(K_{HCT}-RV)^2}{u^2(K_{HCT})} \quad (4)$$

$$Pr\{\chi^2(v) > \chi_{obs}^2\} > 0.05 \quad (5)$$

In addition, the degree of equivalence  $d$  of each participant displays the deviation from the  $K_{RV}$  at each velocity point and it has the expanded uncertainty at 95% level of confidence as the following:

$$d = K - K_{RV} \quad (6)$$

$$U(d) = 2u(d) \quad (7)$$

where  $u(d)$  is given by  $u^2(d) = u^2(K) - u^2(K_{RV})$ .

Moreover, the consistency of the participants is indicated by normalized deviations  $E_n$  and a value of  $|E_n| < 1$  is supposed to show the consistency.

$$E_n = \frac{d}{U(d)} \quad (8)$$

## 3. Results and discussions

### 3.1. Measurement results of PT1

The values of  $K$  determined by the participants for PT1 are illustrated in Figure 5 and Figure 6. The results show the consistency between the participants. By using the reciprocals of the squares of the combined standard uncertainties attached to these factors,  $K_{RV}$  of the PT1 were determined according to the equation (2). Simultaneously, applying a chi-squared test to do an overall consistency checking of all data. The results obtained were shown in Table 1 and Figure 5. In general, all  $K$  measured by participant lie within the uncertainty of the  $K_{RV}$  even though, there was a certain scatter of the  $K$  values at 2 m/s. This scatter might come from the measurement ability of the differential pressure sensor. But, the normalized deviation values  $E_n$  of each participant are all smaller than 1 as shown in Figure 7. This proclaims a consistency between the results of three participants

**Table 1:** Results of the consistency test for PT1

$V_{nom}$ (m/s)	$K_{RV}$	$U(K_{RV})$	$\chi^2_{obs}$	n-1	Test $\chi^2_{0.05, n-1}$	Result
2	1.0027	0.0028	1.352	2	5.991	Pass
5	0.9966	0.0013	0.807	2	5.991	Pass
7	0.9965	0.0012	0.811	2	5.991	Pass
10	0.9962	0.0011	1.377	2	5.991	Pass
15	0.9960	0.0011	1.063	2	5.991	Pass
20	0.9987	0.0013	1.815	1	3.841	Pass
25	0.9989	0.0012	0.276	1	3.841	Pass
30	0.9983	0.0013	0.132	1	3.841	Pass
35	0.9972	0.0014	0.206	1	3.841	Pass
40	0.9958	0.0013	0.570	1	3.841	Pass

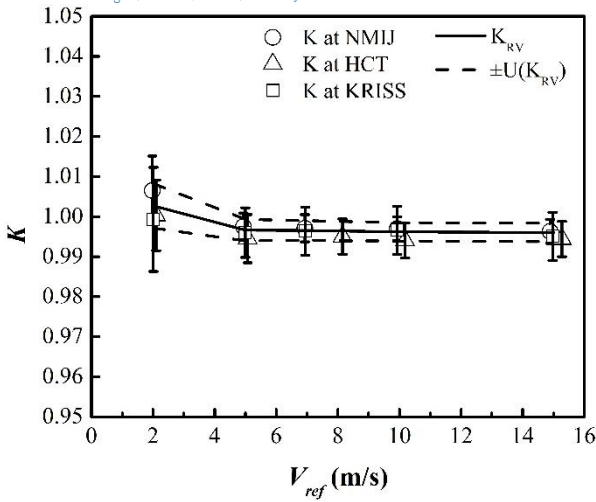


Figure 5:  $K$  for PT1 from 2 m/s to 15 m/s

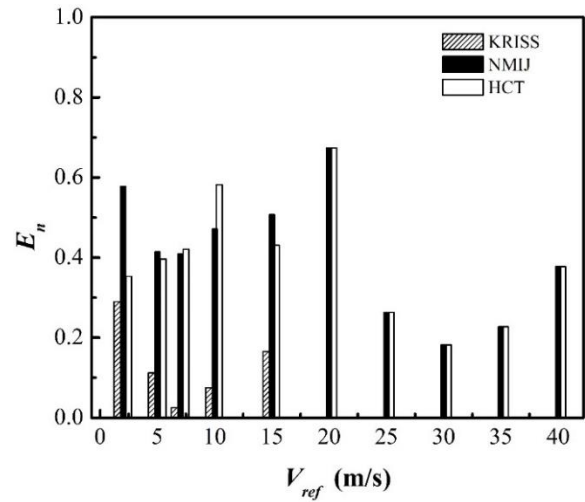


Figure 7:  $E_n$  number for PT1

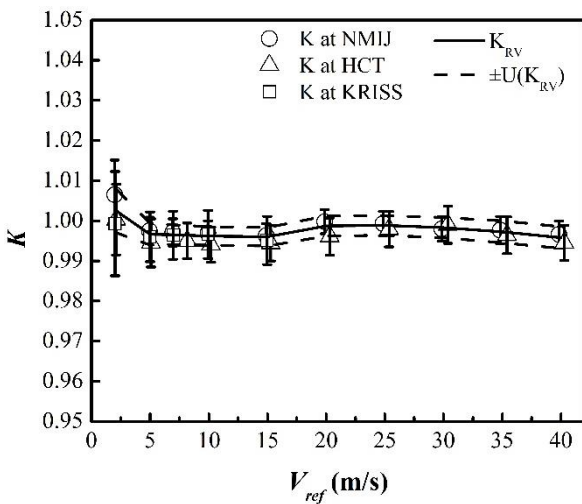


Figure 6:  $K$  for PT1 from 2 m/s to 40 m/s

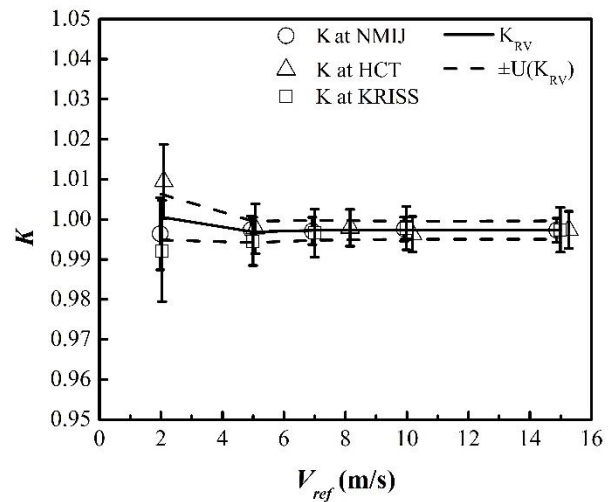


Figure 8:  $K$  for PT2 from 2 m/s to 15 m/s

### 3.2. Measurement results of PT2

Applying the same calculating procedure for the PT2, the value of  $K$  and  $K_{RV}$  were followed the equation (1) and (2). The velocity conversion factors were determined by the participants for PT2 summarized on Figure 8 and Figure 9.

At 2 m/s, the calibration result of KRISS and HCT scattered from  $K_{RV}$  over its expanded uncertainty. However, at the most of all velocities, the results are on the  $RV$  trend and homologous to each other. Consequently, the normalized deviation values  $E_n$  of each participant are mostly smaller than 1 and a high consistency between the results of three participants is shown in Figure 10. The result of an overall consistency check of all data for PT2 was listed in Table 2.

Table 2: Results of the consistency test for PT2

$V_{nom}$ (m/s)	$K_{RV}$	$U(K_{RV})$	$\chi^2_{obs}$	n-1	Test $\chi^2_{0.05, n-1}$	Result
2	1.0006	0.0029	6.435	2	5.991	Pass
5	0.9969	0.0013	0.793	2	5.991	Pass
7	0.9972	0.0012	0.135	2	5.991	Pass
10	0.9973	0.0011	0.281	2	5.991	Pass
15	0.9973	0.0011	0.002	2	5.991	Pass
20	1.0003	0.0013	0.585	1	3.841	Pass
25	1.0001	0.0012	0.317	1	3.841	Pass
30	0.9999	0.0012	0.408	1	3.841	Pass
35	0.9996	0.0013	0.063	1	3.841	Pass
40	0.9981	0.0014	0.020	1	3.841	Pass

In summary, the scattering of  $K$  and their uncertainty are getting larger at 2 m/s. To make clear the reason, the Youden graphical diagnose was applied for comparing precision and bias amongst participants [11], [12].

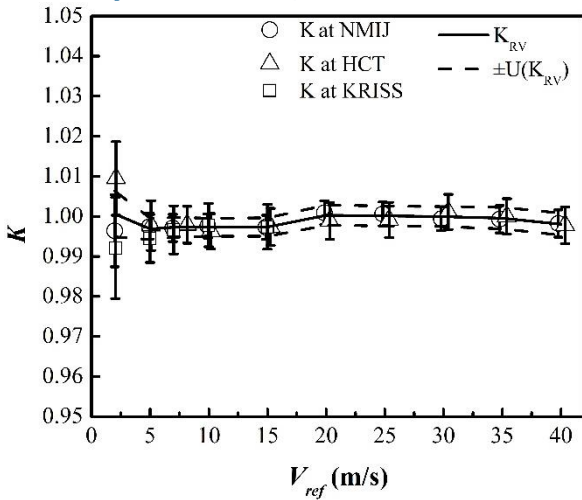


Figure 9:  $K$  for PT2 from 2 m/s to 40 m/s

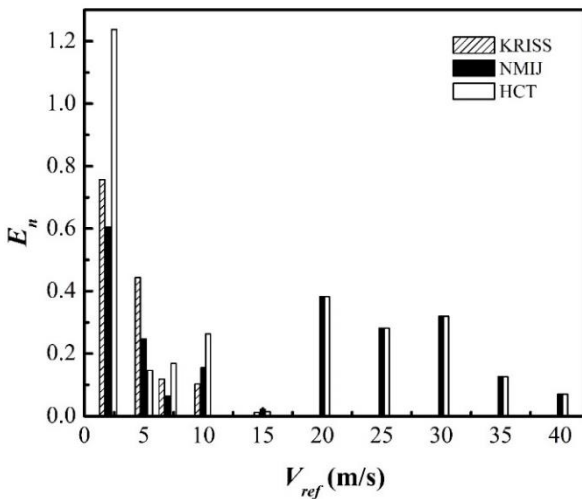


Figure 10:  $E_n$  number for PT2

In the Youden plot, the results of PT1 and PT2 are two axes of graph. The center of Youden circle is the intersection of median lines of PT1 and PT2. The random components are the distances from the each measurement point to the 45 degree line. The radius of this circle is the multiplication of the standard deviation of the random components and 2.45 [11]. Figure 11 & 12 show that all measurement results of participants randomly scattered within the circle. This result implies that there are no systematic errors in this inter-comparison. At the 2 m/s, the big variation of  $K$  between participants makes random components large so they make the radius of the circle large, as shown in Figure 11. The random effect at 2 m/s possibly comes from the measurement limit of the different pressure gauges and the turbulent intensity in the test section of participants is different. But, at the 5 m/s, all measurement point are close to the circle center and lie almost on the 45 degree line.

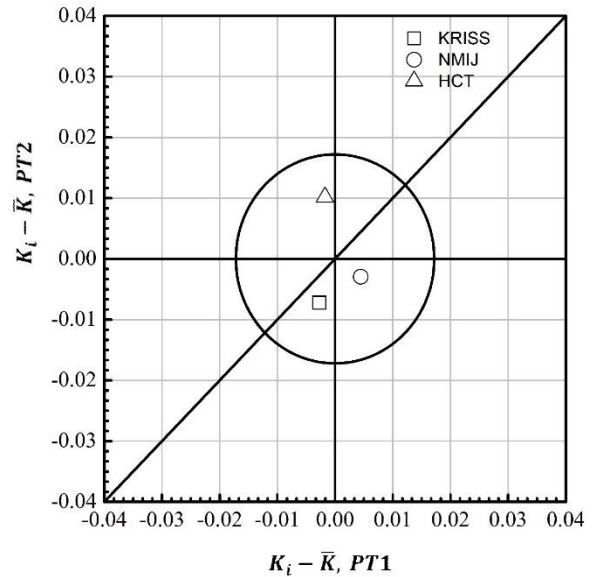


Figure 11: Youden plot at 2 m/s

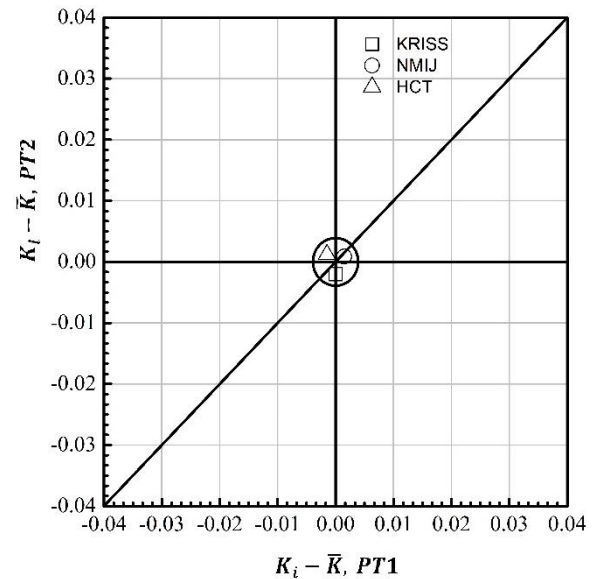


Figure 12: Youden plot at 5 m/s

So, the random errors and the radius of circle reduces. It means the random effect at 2 m/s is larger than 5 m/s. This means the all results have high precision and good agreement more than at 2 m/s. Similarly, at the velocity range over than 5 m/s, the measurement data are located within the narrow band of  $K_{RV}$  uncertainties. The random effect seems not to have significant contribution to the measurement results.

#### 4. Conclusions

In this inter-comparison, three participants, KRISS, NMIJ and HCT had the experiments at the velocity from

2 m/s to 15 m/s and NMIJ and HCT had the experiments for the velocity above 15 m/s up to 40 m/s. The conclusions drawn from this work are as follows:

1. At the velocity smaller and equal to 2 m/s, the quality of measurement of Pitot tubes has quite big influence with the random effect of measurement.
2. Both PT1 and PT2 showed the good performance at the velocity larger than 5 m/s.
3. The calibration results obtained from the participant has a high consistency because the degrees of equivalence and the normalized deviations  $E_n$  are mostly smaller than

## References

- [1] "CCM.FF-K3.2011 CIPM - Key Comparison of Air Speed, 0.5 m/s to 40 m/s. Final Report", 2011.
- [2] "Final Report on the CIPM Air Speed Key Comparison (CCM.FF-K3.2011)", 2007.
- [3] "APMP.M.FF-K3: Final Report on APMP Air Speed Key Comparison", 2010.
- [4] A.Iwai, T. Funaki, N. Kurihara and Y. Terao, "Establishment of a National Primary Standard for Air Speed up to 90 m/s at NMIJ", Flomeko 2016.
- [5] Guidelines for CIPM key comparisons, March 1999 (Revised in October 2003)
- [6] ISO 3966:2008 Measurement of fluid flow in closed conduit - Velocity area method using Pitot static tube, 2008.
- [7] Kurihara. N, Terao. Y, Nakao. S, and Takamoto. M, "Uncertainty of Laser Doppler Velocimeter calibration for air speed standard" Transactions of the Japan Society of Mechanical Engineers series B, vol. 71.
- [8] Woong Kang, Nguyen Doan Trang, Saeng Hee Lee, Hae Man Choi, Yong Moon Choi, "Experimental and numerical investigations of the factors affecting the S-type Pitot tube coefficient", Flow Measurement and Instrumentation, vol 44, 2014.
- [9] M. G. Cox, "The evaluation of key comparison data," Metrologia vol. 39, 2002.
- [10] G. M. Cox, "The evaluation of key comparison data: determining the largest consistent subset," Metrologia, vol. 44, 2007.
- [11] W.J.Youden, "Graphical Diagnosis of Interlaboratory Test Results", Industrial Quality Control, Vol. XV, No.11, May 1959
- [12] Jan Gersl, Libor Lojek, "Inter-comparison of water flow standards using electromagnetic flowmeters", Euramet project No.1046, Brno, July 2011.

# Numerical simulation, validation, and analysis of two-phase slug flow in large horizontal pipes

S. Schmelter<sup>1</sup>, M. Olbrich<sup>1,2</sup>, E. Schmeyer<sup>1</sup>, and M. Bär<sup>1</sup>

<sup>1</sup>Physikalisch-Technische Bundesanstalt (PTB), Abbestr. 2-12, 10587 Berlin, Germany

<sup>2</sup>Institute of Fluid Dynamics and Technical Acoustics, Technische Universität Berlin, Müller-Breslau-Straße 8, 10623 Berlin, Germany

E-mail (corresponding author): [sonja.schmelter@ptb.de](mailto:sonja.schmelter@ptb.de)

---

## Abstract

Multiphase flow, especially two-phase gas-liquid flow, is of great importance for a variety of applications and industrial processes, for example in the nuclear, chemical, or oil and gas industries. In this contribution, we present simulation results for gas-liquid slug flow in large horizontal pipes. Six test cases with different oil, water, and gas flow rates are considered, which cover a wide range of different slug flows. The numerical predictions are validated by comparison with experimental data obtained from video observations, which have been recorded at NEL as part of the European research project “Multiphase flow metrology in oil and gas production”. The relative error of the mean liquid level between experiment and simulation is less than 10.8 per cent for all but one test cases. Furthermore, a frequency analysis is performed. The single-sided amplitude spectrum as well as the smoothed power spectral density are calculated. For both, experimental and simulation data, one observes an increase of the dominant frequencies if the ratio of liquid and gas superficial velocity is increased.

---

## 1. Introduction

One central issue in subsea oil and gas production is the evaluation and reduction of uncertainty in multiphase flow measurement. While for single-phase flow metrology there exists a well-established reference network with norms and standards, such a network is lacking for multiphase flow metrology. This leads to a high level of uncertainty in multiphase flow measurement systems reaching up to 20 per cent [1].

The main objective of the European research projects “Multiphase flow metrology in oil and gas production” (MultiFlowMet I) and “Multiphase flow reference metrology” (MultiFlowMet II) is to reduce this level of uncertainty. Therefore, a comprehensive experimental intercomparison on multiphase flow is conducted on one hand. On the other hand, the process of flow pattern formation as well as the quantitative influence of relevant flow condition parameters are studied by computational fluid dynamics (CFD). The great advantage of CFD is that it gives insight into areas that are hardly accessible by experiments. Therefore, simulations can help to understand flow

pattern formation as well as their influence on the measurement process. However, before CFD simulations can be used for predicting flows, they need to be validated first.

In this contribution, we present simulation results for two-phase slug flow in horizontal pipes, which have been investigated during the MutliFlowMet I project. The numerical predictions are validated by comparison with experimental data obtained from video recordings at NEL.

The paper is organized as follows. Section 2 gives a description of the considered geometry as well as of the material properties and superficial velocities of the investigated test cases. Furthermore, the numerical modeling is shortly summarized. In Section 3, the simulation results are compared with experimental data. First, the mean value and standard deviation of the liquid level are considered. Second, a frequency analysis is performed. Finally, conclusions are drawn in Section 4.

## 2. Multiphase flow simulation

In the following, we present simulation results for six test cases with different oil, water, and gas flow rates, see Table 1, which were all classified as slug flow in the corresponding experiments.

**Table 1:** Superficial velocities of the considered test cases.

Name of test point	Superficial velocities in m/s		
	Nitrogen	Paraflex oil	Brine water
TP 01	7.063	0.294	-
TP 03	1.399	1.144	-
TP 05	0.545	1.635	-
TP 77	7.063	-	0.294
TP 79	1.399	-	1.144
TP 81	0.545	-	1.635

The material parameters of the different fluids are summarized in Table 2.

**Table 2:** Material parameters of the different fluids.

	Nitrogen	Paraflex oil	Brine water
Density in $\text{kg} \cdot \text{m}^{-3}$	10.8	815.8	1011
Viscosity in $\text{Pa} \cdot \text{s}$	$1.75 \cdot 10^{-5}$	$7.84 \cdot 10^{-3}$	$8.82 \cdot 10^{-4}$

The multiphase flow simulations were performed using the commercial CFD solver ANSYS FLUENT. The interface between the different phases was modeled by the volume of fluid (VOF) method [2], which was applied within a mixture model. An unsteady RANS (Reynolds-averaged Navier-Stokes) approach was used for turbulence modeling. The  $k-\omega$ -SST (shear stress transport) model [3] was applied because it allows the inclusion of turbulence damping. Turbulence damping is required if there are high velocity gradients at the interface between the different phases to model such flows correctly [4, 5]. Further details about the numerical modeling can be found in [6].

Figure 1 shows the resulting flow pattern for one of the nitrogen-oil test cases (TP 03, see Table 1). It displays the simulated gas volume fraction in a longitudinal section through the middle of the pipe

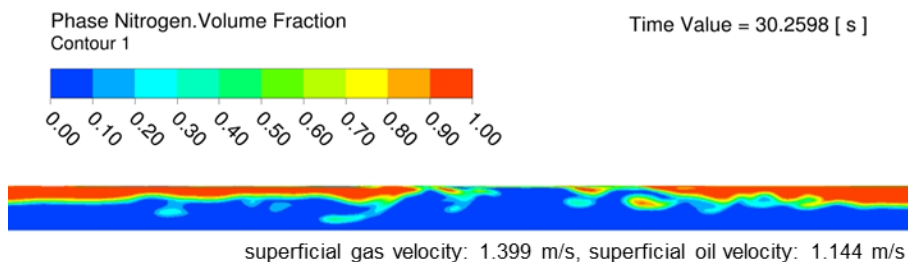


**Figure 1:** Slug flow observed for one of the test cases (TP 03) after ca. 30 seconds. The picture shows ca. 2 meter of the longitudinal section through the middle of the pipe.

after ca. 30 seconds. One observes slug flow, which is in accordance with the pattern recorded in the corresponding experiment.

## 3. Comparison with experimental data

The numerical predictions are validated by comparison with experimental data obtained from video observations, which have been recorded at NEL during the MultiFlowMet I project. For the quantitative evaluation of the experimental observations, a tool for video analysis has been implemented [7], which extracts the liquid level over time from the recorded video observations.

Since the pipe wall has a thickness of several millimeters, the light rays inside and outside the pipe are displaced relative to each other. This leads to a distortion of the observed liquid level. To account for this, the liquid level has been corrected using Snell's law together with basic formulas for the height of a circular segment in geometry, see [8].

Furthermore, due to the installation of the viewing section, the recorded videos do not show the whole inner pipe. Only 94 per cent of the inner diameter are visible in the experimental observations, whereas the lowest and highest 3 per cent of the pipe cannot be seen because of tie bars. Since in general we cannot decide whether the unseen area is covered with liquid or not, we decided to use only the visible part for the comparison with the CFD results. To obtain a reasonable comparison between experiment and simulation, we "reduced" the simulation results in the same way. This means that we consider only the (inner) 94 per cent of the pipe for the analysis shown in the following subsections.

### 3.1 Liquid level

In the following, we compare the mean value and standard deviation of the liquid level derived from the experimental video observations with the corresponding data from CFD.

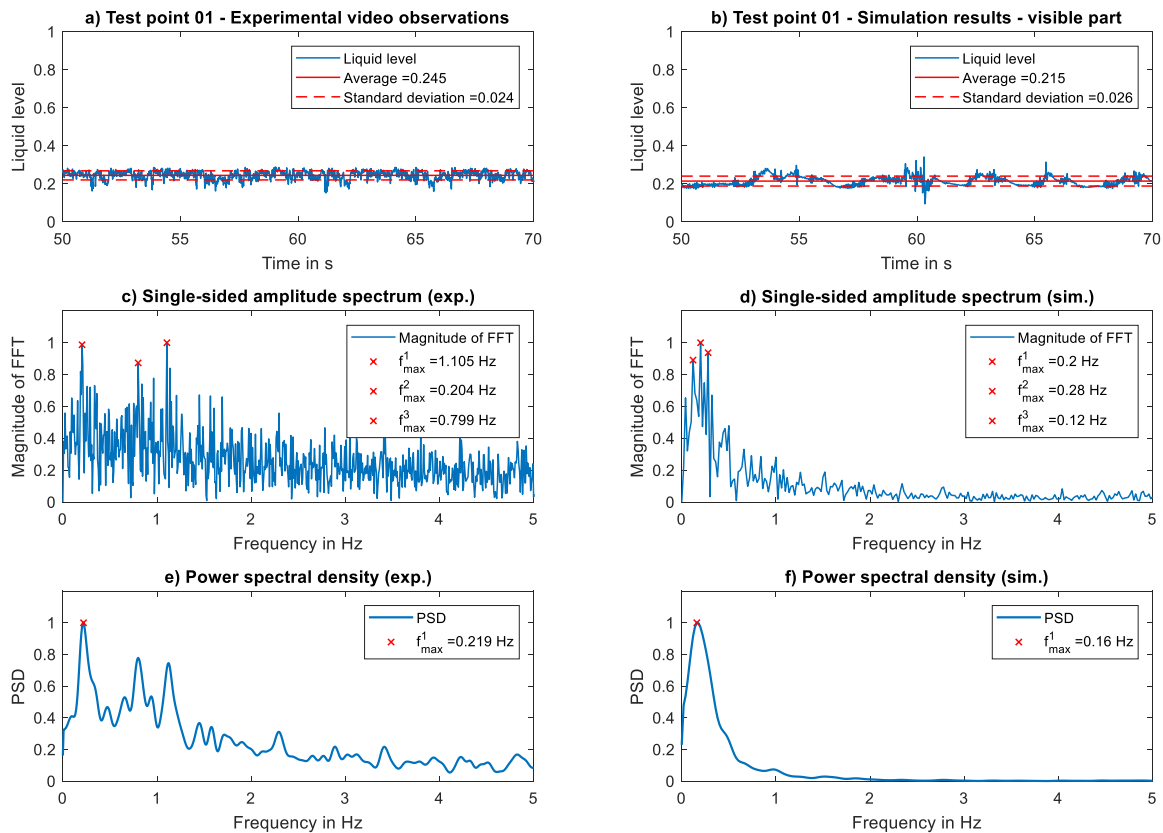


**Figure 2:** Comparison of the extracted liquid level (mean value  $\pm$  standard deviation), its single-sided amplitude spectrum obtained by FFT as well as its smoothed PSD (pictures on the left) with the corresponding data from CFD (pictures on the right) for TP 01.

While the mean value gives an impression of the general proportion of liquid in the pipe, the standard deviation describes how much this value changes. A higher standard deviation implies larger fluctuations in the distribution of the phases, for example due to higher waves or more slugs.

Note that it does not make sense to directly compare the extracted experimental versus the computed liquid level at one fixed point in time. The reason for this is that slug flow is intermittent. Therefore, only statistical data should be compared.

Figure 2 a) shows the liquid level over time that has been extracted from the experimental video observation of one of the nitrogen-oil test cases (TP 01, see Table 1). Note that, for better illustration, only 20 seconds of the recorded time interval are displayed in the figure. However, the mean value and standard deviation stated in the

legend nevertheless represent the mean value and standard deviation for all data recorded. Figure 2 b) shows the corresponding data from CFD. One observes good agreement for both, the mean value as well as the standard deviation of the liquid level.

Figure 3 a)+b) show the same analysis for a nitrogen-water test case (TP 81, see Table 1). This test case has a much lower gas and a much higher liquid superficial velocity leading to a higher liquid level and more slugs than in the previous test case. A comparison between the liquid level extracted from the video observations with the one from the CFD simulation shows good agreement. However, the standard deviation of the simulated liquid level is much smaller than in the experiment. One reason might be the larger time step size used in the evaluation of the simulation data (because the flow field was saved only every 100 time steps).

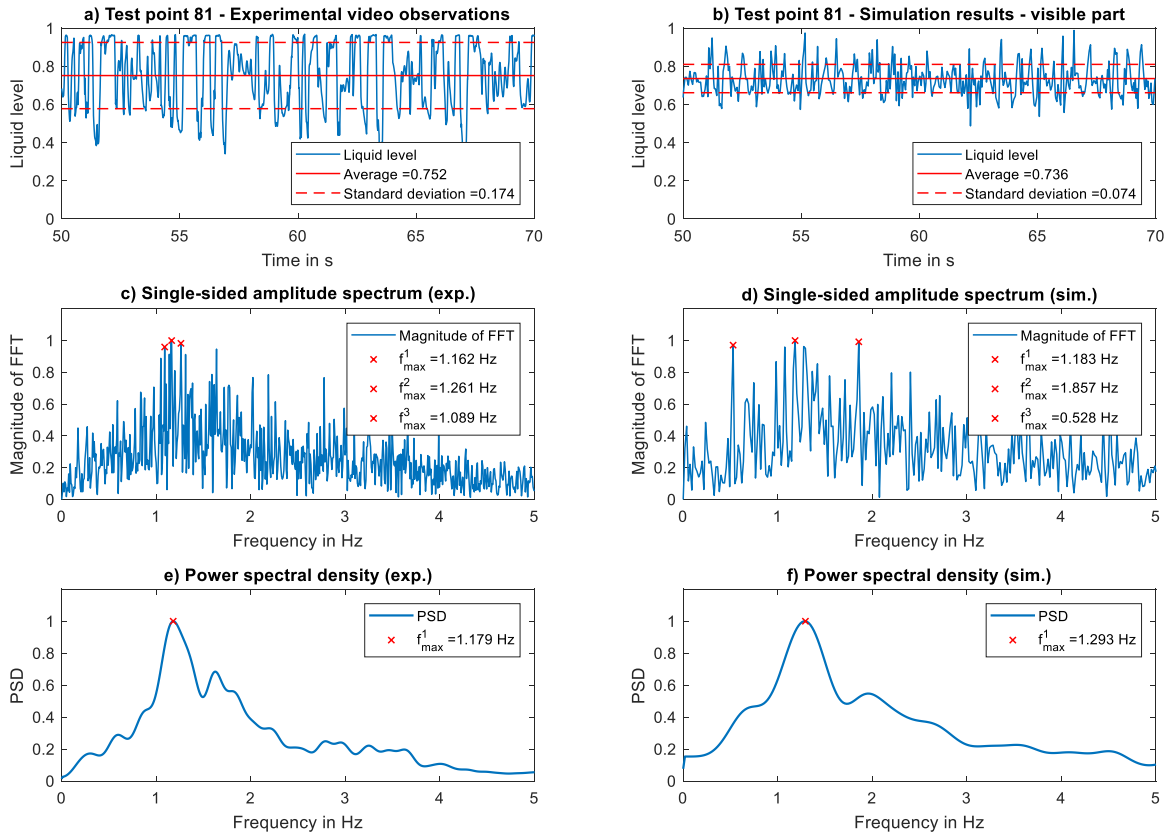


**Figure 3:** Comparison of the extracted liquid level (mean value  $\pm$  standard deviation), its single-sided amplitude spectrum obtained by FFT as well as its smoothed PSD (pictures on the left) with the corresponding data from CFD (pictures on the right) for TP 81.

In Figure 4, the mean value and standard deviation of the experimental liquid level are compared to the corresponding simulation results for all six considered slug flow test cases, see Table 1. One observes that a higher liquid superficial velocity

leads, as expected, to a higher liquid level in the pipe. Except for one case (TP77), the relative error of the mean liquid level between experiment and simulation is less than 10.8 per cent.

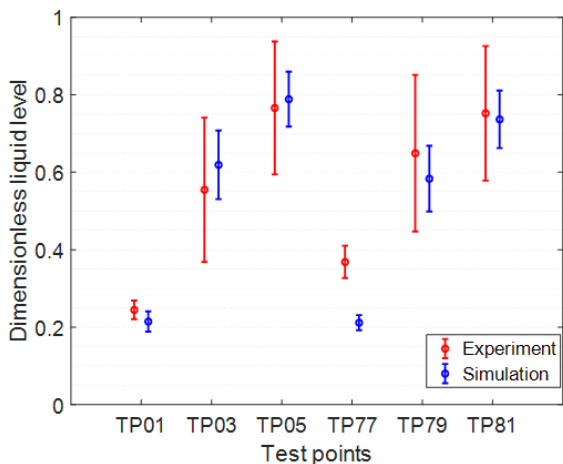


**Figure 4:** Comparison of the liquid level (mean  $\pm$  standard deviation) extracted from experimental video observations (red) and simulation results (blue).

### 3.2 Frequency analysis

A classical parameter for distinguishing different slug flow cases from each other is the so-called slug frequency, i.e., the number of slugs occurring in a certain time interval. In theory, one would say that there is a slug if the pipe is fully filled with liquid at a certain position. In practice, however, slugs usually contain some gas (e.g., in the form of bubbles), which means that even in the core of the slug the liquid level might not be equal to one. This means that a threshold for the liquid level needs to be defined, above which a slug is counted. However, inspecting different slug flow cases shows that such a threshold is not universal.

Therefore, we use a frequency analysis instead. We apply the fast Fourier transform (FFT) to both, experimental and simulation data, and compare the resulting frequencies as well as the peaks in the corresponding smoothed power spectral

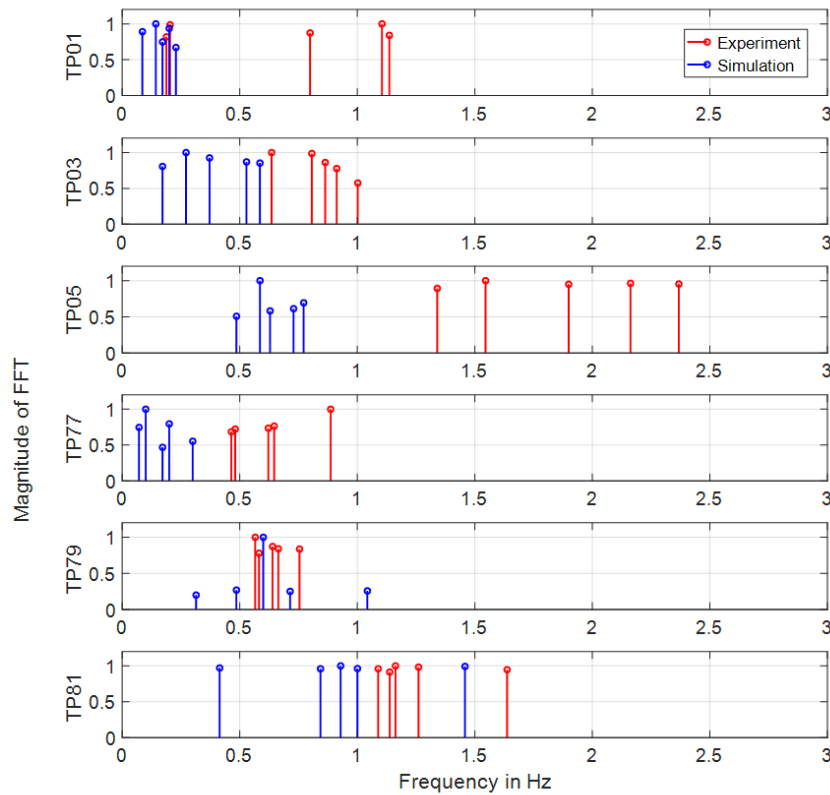


**Figure 5:** Comparison of the five most dominant frequencies from experimental video observations (red) and simulation data (blue).

density (PSD). Even though the frequencies identified by FFT do not necessarily represent the slug frequency, they nevertheless provide a quantitative description of the dynamics of the slug flow. Hence, they can be used for comparison between experiment and simulation.

Figure 2 c)+d) show the (normalized) single-sided amplitude spectra of experimental and simulation data, respectively, for the nitrogen-oil test case TP01 (see Table 1). For the simulated liquid level, the most dominant frequencies are all around 0.2 Hz. This value can also be found as one of the most dominant frequencies in the FFT of the experimental liquid level. However, in the experiment, the amplitude spectrum has further peaks around 0.8 and 1.1 Hz. This can also be seen in the smoothed PSD, see Figure 2 e)+f), which has been calculated using the Matlab function `pwelch`.

The same analysis (FFT and PSD) is shown in Figure 3 c)+d) and e)+f), respectively, for the nitrogen-water test case TP 81, see Table 1. For this test case, the three most dominant frequencies of the FFT are centered around ca. 1.2 Hz in both, experiment and simulation. This is also reflected by the peak in the PSD, which is ca. 1.2 Hz in the FLOMEKO 2019, Lisbon, Portugal

experiment and ca. 1.3 Hz in the corresponding simulation.

Figure 5 displays the five most dominant frequencies of the FFT spectrum for all test cases, see Table 1. The experimental data is shown in red, the simulation data in blue. Note that the amplitudes of the FFT spectra have been normalized to one in all cases. In general, the observed frequencies in the simulation are lower than in the experiment. On the other hand, the increase of the frequencies with higher superficial liquid velocity can be seen in both, experiment and simulation. For one case (TP 79), the dominant frequency of approximately 0.7 Hz observed in the experiment is reproduced almost exactly by the numerical simulation. In other cases (TP 01, TP 03, and TP 81) at least some of the dominant frequencies observed in the experiment can also be found in the simulation.

#### 4. Conclusion

In this paper, we presented simulation results for different slug flow test cases. The numerical predictions have been compared with experimental data obtained from video observations, which have

been recorded at NEL during the MultiFlowMet I project. The relative error of the mean liquid level between experiment and simulation is less than 10.8 per cent for all but one test cases.

Furthermore, a frequency analysis has been performed. The single-sided amplitude spectrum as well as the smoothed PSD have been calculated for both, experimental and simulation data. Even though the observed slug frequency (which can be determined by counting slugs, for example) usually cannot directly be identified with the highest frequencies obtained by FFT, neither in the experiment nor in the simulation, these frequencies provide a quantitative description of the dynamics of the slug flow. For both, experiment and simulation, one observes an increase of the dominant frequencies if the ratio of liquid and gas superficial velocity is increased.

However, for a better comparison between experiment and simulation, further analysis is necessary. Methods like proper orthogonal decomposition (POD) [9,10] can be applied to identify typical structures in the flow that are characteristic for a specific pattern. Simulation data can then be validated by comparison with experimental data with respect to these relevant structures. Furthermore, commonly used flow pattern categories can be changed or extended according to the identified characteristics.

### Acknowledgements

This work was supported through the Joint Research Project “Multiphase flow reference metrology”. This project has received funding from the EMPIR programme co-financed by the Participating States and from the European Union’s Horizon 2020 research and innovation programme.

The authors would like to thank Terri Leonard and Marc MacDonald from NEL, who provided the experimental video observations.

### References

- [1] EURAMET Publishable JRP Report for ENG58 “MultiFlowMet – Multiphase Flow Metrology in the Oil and Gas Sector”, available from [https://www.euramet.org/Media/docs/EMRP/JRP/JRP\\_Summaries\\_2013/Energy\\_JRPs/ENG58\\_Publishable\\_JRP\\_Summary.pdf](https://www.euramet.org/Media/docs/EMRP/JRP/JRP_Summaries_2013/Energy_JRPs/ENG58_Publishable_JRP_Summary.pdf), 2017.
- [2] Hirt C W, Nichols B D, “Volume of fluid (VOF) method for the dynamics of free boundaries”, *J. Comput. Phys.*, **39**, 201-225, 1981.
- [3] Menter F R, “Two-equation eddy-viscosity turbulence models for engineering applications”, *AIAA J.*, **32**, 1598-1605, 1993.
- [4] Frank T, “Numerical simulation of slug flow regime for an air-water two phase flow in horizontal pipes”, in *11<sup>th</sup> International Topical Meeting on Nuclear Reactor Thermal-Hydraulics (NURETH-11)*, Avignon, France, October 2005.
- [5] Egorov Y, “Validation of CFD codes with PTS-relevant test cases”, *EVOL-ECORA-D07*, 2004.
- [6] Fiebach A, Schmeier E, Knotek S, Schmelter S, “Numerical simulation of multiphase flow in a vertically mounted Venturi flow meter”, in *17<sup>th</sup> International Flow Measurement Conference (FLOMEKO)*, Sydney, Australia, September 2016.
- [7] Olbrich M, Schmeier E, Riazzy L, Oberleithner K, Bär M, Schmelter S, “Validation of simulations in multiphase flow metrology by comparison with experimental video observations”, *Journal of Physics: Conference Series*, **1065**, 092015, 2018.
- [8] Schmelter S, Olbrich M, Schmeier E, Bär M, “Validation of multiphase flow simulations by comparison with experimental video observations”, in *North Sea Flow Measurement Workshop*, Aberdeen, Scotland, October 2018.
- [9] Lumley J L, *Stochastic tools in turbulence* (New York, Academic Press, Inc.), 1970.
- [10] Sirovich L, “Turbulence and the dynamics of coherent structures: Part I: Coherent Structures”, *Quarterly of Applied Mathematics*, **45**, 561-571, 1987.

# Uncertainty Analysis for Multiphase Flow: A Case Study for Horizontal Air-Water Flow Experiments

Felipe Jaloretto<sup>1,2</sup>, Marcelo Souza de Castro<sup>2</sup>

<sup>1</sup>*IPT – Instituto de Pesquisas Tecnológicas do Estado de São Paulo S.A., São Paulo, Brazil - Av. Prof. Almeida Prado 532 CEP 05508-901 São Paulo / SP Brasil*

<sup>2</sup>*Department of Energy, School of Mechanical Engineering, University of Campinas, Campinas, Brazil  
E-mail: [felipej@ipt.br](mailto:felipej@ipt.br), [mcastro@fem.unicamp.br](mailto:mcastro@fem.unicamp.br)*

---

## Abstract

This work describes the procedure used to define the measurements uncertainties of experiments in horizontal air-water two-phase flow performed in order to identify influences due to pipe diameter. These experiments were performed with 4 different pipe diameters, always using the same test section length, therefore varying the length-by-diameter (L/D) ratio. Several parameters were measured, such as fluid flow, pressure, temperature and pressure drop; other parameters were calculated, such as the superficial velocities of each fluid, as well as their respective properties. The main parameters studied were the flow patterns for different velocity configurations and the two-phase pressure drop to be used for model improvement, thus the importance of uncertainties analysis. The sources of uncertainty were defined, detailed, systematically studied and quantified. The flow maps with its uncertainties could show the regions a pattern can be defined, and the plots of two-phase pressure drop variation with diameter validated the homogeneous model as a good approach to calculate pressure drop

---

## 1. Introduction

Correctly quantifying the superficial velocities of each fluid, their respective properties, as well as the pressures involved in multiphase flow experiments are very important for the qualification of the results. The uncertainty definition of each measured or calculated result should show the boundaries within which the comparison between results, whether by repetition of the same experiment or in comparison with others, can be performed with a certain degree of confidence. However, in general, a few studies describing the methodology for calculating uncertainties in multiphase experiments are available, although this kind of studies usually shows the uncertainty calculated in their presented results.

An example of a study that sought to identify and quantify the sources of uncertainty arising from multiphase processes, focusing the analysis on energy market demands, especially in the oil and gas industry, is the "Characterization of Confidence in Multiphase Flow Predictions" [1]. In that study the authors emphasize the importance of uncertainties quantifying for the design of multiphase systems, as well as to analyze a

systematic method of propagation of uncertainty in deterministic multiphase models and to briefly review some of the tools available to perform each step. They also notes that the uncertainties in multiphase models are not always considered in the available studies, and observes that important variables such as fluid properties and flow characteristics are often not considered as a source of uncertainty.

The work of Pereyra *et al.* [2], also focusing on the oil and gas industry, present a methodology for comparing the results of prediction models of flow patterns, using as an example the one proposed by Barnea, D. [3], with results obtained experimentally and available in databases. In it the confidence level of the models relative to the experimental is quantified by the success fraction of the prediction in relation to the realized one.

In the definition of the uncertainties involved in the present study results, a description of the Brazilian version of the "Guide to the expression of uncertainty in measurement: evaluation of measurement data" is given by describing that "the purpose of a measurement is to determine the value of the measurand, that is, the value of the

particular quantity to be measured." ([4], p.4) and that "... In general, the result of a measurement is only an approximation or estimate of the value of the measurand and thus is complete only when accompanied by a statement of the uncertainty of that estimate" ([4], p.4). Thus, it is necessary to define what are the measurands whose values are necessary in the quantification of some physical quantity, and their respective standard uncertainties, to finally determine the expanded uncertainty of that physical quantity under study.

This work aims to show the uncertainty calculations for the velocity and pressure results of horizontal air-water two-phase flow experiments. The experiments have been made to study the influence of pipe diameter [5] and this article intends to analyse the uncertainty of the results applying a simple, but systematic, methodology presented by Brazilian guide to the expression of uncertainty in measurements [4].

## 2. Experimental facilities and procedures

The experiments were performed at the Experimental Laboratory of Petroleum (LabPetro) of the Center for Petroleum Studies (CEPETRO) at University of Campinas (UNICAMP), and at the Flow Measurement Laboratory (LV) of the Center for Mechanical, Electrical and Fluid Flow Metrology (CTMetro) at Technological Research Institute (IPT). Four setups were built, each one with different pipe inner diameters: 27.75 mm, 53.55 mm, 82.25 mm and 106.47 mm. All of them were built with a fixed test section length of 12 m, resulting in experiments with 432, 224, 146 and 113 diameters of length (L/D), respectively. Pressure drop were measured with the upstream tap at 9.0 m from the test section inlet and 2.5 m apart from the downstream one. A visualization section was installed at the end of the test section. Tap water and compressed air were the working fluids. A schematic draw of experimental setups is shown in Figure 1.

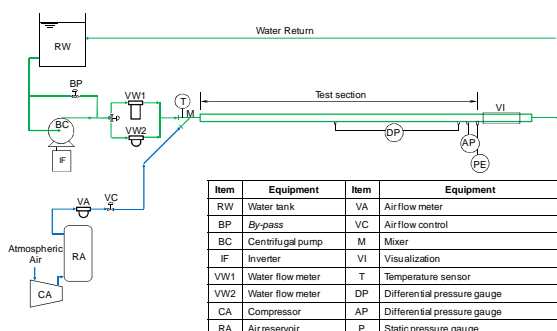


**Figure 1:** Scheme of the experimental setup. FLOMEKO 2019, Lisbon, Portugal

Flow patterns classification was done by visual observation and statistical analysis of pressure signature on time (further details of this statistical analysis can be found in reference [5]). The test procedure was made in two steps: the first one with water single-phase flow, aiming to validate the pressure sensor; and the second were the tests with two-phase air-water flows. The first step was done daily before the two-phase flow tests to validate the results of pressure drop in comparison with established theoretical models and was named validation step. After validation, the tests with two-phase flow could get, and they were performed with a fixed water superficial velocity for which the air superficial velocity could be varied.

All the superficial velocities combinations were executed three times, in ascending, descending and ascending order, to neutralize hysteresis effects and evaluate the setups reproducibility, with an acquisition time of about 2 minutes, in addition to obtaining statistically relevant data.

A total of 397 experimental data points were obtained to investigate mainly pressure drop and build the flow maps. Each data point were repeated three times. Table 1 summarizes the ranges of air ( $j_2$ ) and water ( $j_1$ ) superficial velocities, besides with the total points and the flow patterns obtained for each experimental setup.

**Table 1:** Ranges of superficial velocities studied for each setup.

D (mm)	$j_1$ (m/s) (water)	$j_2$ (m/s) (air)	Flow Pattern	Nr. of Points
27.75	0.04 to 6.37	0.30 to 15.87	SS, WS, EB, S, B, A	120
53.55	0.05 to 2.12	0.25 to 4.32	WS, EB, S	70
82.25	0.02 to 0.76	0.11 to 1.94	SS, WS, EB, S	129
106.47	0.10 to 3.72	0.10 to 1.02	SS, WS, EB, S, B	78

## 3. Uncertainties

For each physical quantity measured, or calculated, on the experiments, the way to define its uncertainty had 11 steps:

1. Define physical quantity;
2. Define a physical model of the quantity to be measured;
3. Define a mathematical model of the quantity;
4. Identify the sources of uncertainty in the measurement;
5. Organizing the sources of uncertainty and look for cause and effect relations;
6. Quantify the variability of each source;
7. Reduce to standard uncertainty;

8. Determining combined standard uncertainty;
9. Look for correlated input quantities;
10. Define reliability;
11. Determining expanded uncertainty.

### 3.1 Physical quantities

The physical quantities are those that the experiments seek to determine. Fluid velocities were calculated, and pressures were measured. There are:

- superficial velocities of each fluid;
- two-phase and single phase (water) pressure drop.

To do so, the following quantities were measured:

- mass flow rate of each fluid;
- water temperature;
- static pressure of the mixture;
- single and two-phase pressure drop.

Thus, the superficial velocities of each fluid were calculated from: the measurements of flow, static pressure, water temperature and area of the pipe section. The velocity uncertainty of each fluid will be composed of these variables.

The uncertainties of the single and two-phase pressure drop measurements were compounded by the calibration results of the instruments used, or the uncertainty reported by the manufacturer, and the reproducibility of each result.

### 3.2 Physical models

The respective physical models to be considered for each physical quantity are:

- superficial velocity of each fluid:
  - steady state flow;
  - the fluids are considered incompressible;
  - variations on the density of each fluid does not influence the flow measurement;
  - the pipe has constant section area along the entire test line;
  - the measured temperature and static pressure influences the calculated result of the air superficial velocity, as it influences the value of its density, although the variations do not characterize compressibility effects.
- two-phase pressure drop:
  - the constant relative roughness of the pipe;
  - the constant diameter of the pipe;
  - the gravitational acceleration is constant;
  - constant static pressure in the point of measurement for each experiment;

### 3.3 Mathematical models

The mathematical models directly influence the velocities results. For superficial velocities, air density and pipe areas, the mathematical models are:

$$j_1 = \frac{W_1}{\rho_1 A} \quad (1)$$

$$j_2 = \frac{W_2}{\rho_2 A} = \frac{W_2}{\frac{P_{est} A}{RT}} = \frac{W_2 RT}{P_{est} A} \quad (2)$$

$$\rho_2 = \frac{P_{atm} + P_{est}}{RT} \quad (3)$$

$$A = \frac{\pi D^2}{4} \quad (4)$$

### 3.4 Sources of uncertainty in the measurement

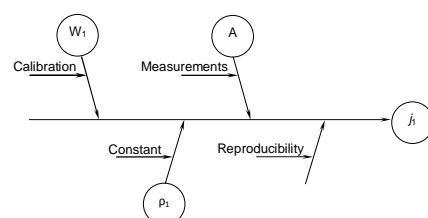
The following sources of uncertainty are considered:

- uncertainty of calibrated instruments: experimental standard deviation of the mean; or the worst uncertainty result of calibration certificate, when available;
- manufacturer specification uncertainties of the instruments, when calibration results are not available;
- uncertainty in temperature and static pressure measurements: for the gas component of the mixture, both the uncertainty of the calibration and the local fluctuation of the variables;
- reproducibility uncertainty: once the velocity and two-phase pressure drop will be presented in average values, it is the experimental standard deviation of the mean of the three measurements taken each time the setup repeats a given test;
- uncertainty in considering atmospheric pressure and water density constants for some experiments;
- uncertainty of the pipe diameter measurements.

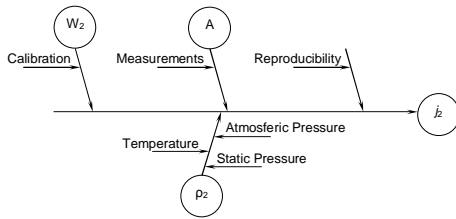
### 3.5 Organizing the sources

Organizing sources on cause and effect diagrams for better understanding their influence:

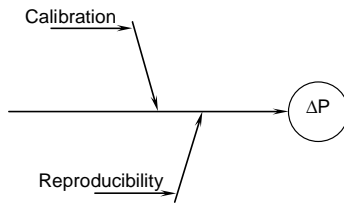
- superficial velocities:
  - water:



- air:



- pressure drop:



### 3.6 Quantifying and reduce each source

- uncertainty of water and air flow (considering infinite degrees of freedom and normal probability distribution):

$$u(W_i) = \frac{U(W_i)}{k} \quad (5)$$

- pressure drop, static pressure and temperature (considering infinite degrees of freedom and normal probability distribution):

$$u(\Delta P) = \frac{U(\Delta P)}{k} \quad (6)$$

$$u(P_{est}) = \frac{U(P_{est})}{k} \quad (7)$$

$$u_1(T) = \frac{U(T)}{k} \quad (8)$$

$$u_2(T) = \frac{\sigma_T}{\sqrt{n-1}} \quad (9)$$

The uncertainty of the static pressure fluctuation is not considered, since this fluctuation is expected for the different flow patterns, when in two-phase flow. In addition, fluctuating temperature during measurement is also a source of uncertainty in its measurement. Thus, for temperature:

$$u^2(T) = \sum_{z=1}^2 u_z^2(T) \quad (10)$$

- pipe diameter uncertainty:
  - method uncertainty (with triangular distribution and 50 degrees of freedom):

$$u_1(D) = \frac{\text{Assigned value}}{\sqrt{6}} \quad (11)$$

- uncertainty from the resolution of reference instrument (with rectangular distribution and infinite degrees of freedom):

$$u_2(D) = \frac{\text{Resolution}}{2\sqrt{3}} \quad (12)$$

- uncertainty of the reference instrument calibration (with normal distribution and infinite degrees of freedom):

$$u_3(D) = \frac{U(\text{Reference})}{2} \quad (13)$$

- uncertainty of the measurements (with normal distribution and degrees of freedom being the number of samples minus 1):

$$u_4(D) = s(\bar{D}) = \frac{s(D_j)}{\sqrt{n}} \quad (14)$$

The uncertainty values of pipe areas will be mathematically defined from the calculated uncertainties of each pipe diameter:

$$u^2(D) = \sum_{z=1}^4 u_z^2(D) \quad (15)$$

- water density uncertainty:
  - at LabPetro (for rectangular distribution and infinite degrees of freedom):

$$u(\rho_1) = \frac{\rho_{1max} - \rho_{1min}}{\sqrt{12}} \quad (16)$$

- at IPT (for triangular distribution and infinite degrees of freedom):

$$u(\rho_1) = \frac{\rho_{1max} - \rho_{1min}}{\sqrt{24}} \quad (17)$$

- atmospheric pressure uncertainty:
  - for LabPetro tests the atmospheric pressure was verified on a specific website that measures it on that region [6] (for rectangular distribution and infinite degrees of freedom):

$$u(P_{atm}) = \frac{P_{atmmax} - P_{atmmin}}{\sqrt{12}} \quad (18)$$

- at IPT, with the uncertainty of barometric pressure gauge (normal distribution) and the local fluctuation (rectangular distribution) for infinite degrees of freedom:

$$u_1(P_{atm}) = \frac{U(P_{atm})}{k} \quad (19)$$

$$u_2(P_{atm}) = \frac{P_{atmmax} - P_{atmmin}}{\sqrt{12}} \quad (20)$$

And so:

$$u^2(P_{atm}) = \sum_{z=1}^2 u_z^2(P_{atm}) \quad (21)$$

- reproducibility of values, by the experimental standard deviation of the mean (with normal distribution and degrees of freedom corresponding to the number of sample minus 1), for pressure drop and superficial velocity:

$$u(R\Delta P) = s(\overline{\Delta P}) = \frac{s(\Delta P_z)}{\sqrt{n}} \quad (22)$$

$$u(Rj_i) = s(\bar{j}_i) = \frac{s(j_i)}{\sqrt{n}} \quad (23)$$

### 3.7 Determining combined standard uncertainty

- Combined standard uncertainty of area:

$$u_c(A) = \sqrt{[c_A \cdot u(D)]^2} = \sqrt{\left[\frac{\partial A}{\partial D} \cdot u(D)\right]^2} \quad (24)$$

- Combined standard uncertainty of air density

$$u_c(\rho_2) = \sqrt{\left[\frac{\partial \rho_2}{\partial P_{atm}} \cdot u(P_{atm})\right]^2 + \left[\frac{\partial \rho_2}{\partial P_{est}} \cdot u(P_{est})\right]^2 + \left[\frac{\partial \rho_2}{\partial T} \cdot u(T)\right]^2} \quad (25)$$

- Combined standard uncertainty of air superficial velocity

$$u_c(j_2) = \sqrt{\left[\frac{\partial j_2}{\partial W_2} \cdot u(W_2)\right]^2 + \left[\frac{\partial j_2}{\partial A} \cdot u_c(A)\right]^2 + \left[\frac{\partial j_2}{\partial \rho_2} \cdot u_c(\rho_2)\right]^2 + u(Rj_2)^2} \quad (26)$$

- Combined standard uncertainty of water superficial velocity

$$u_c(j_1) = \sqrt{\left[\frac{\partial j_1}{\partial W_1} \cdot u(W_1)\right]^2 + \left[\frac{\partial j_1}{\partial A} \cdot u_c(A)\right]^2 + \left[\frac{\partial j_1}{\partial \rho_1} \cdot u(\rho_1)\right]^2 + u(Rj_1)^2} \quad (27)$$

- Combined standard uncertainty of pressure drop

$$u_c(\Delta P) = \sqrt{u(\Delta P)^2 + u(R\Delta P)^2} \quad (28)$$

### 3.8 Correlated input quantities

It was considered in the present work that the physical quantities are independent. Thus, they are not correlated with each other.

### 3.9 Reliability

The expanded uncertainty of measurement,  $U$ , is stated as the combined standard uncertainty multiplied by the coverage factor  $k$ , which for a distribution  $t$  with  $\nu_{eff}$  (effective degrees of freedom) corresponds to a coverage probability of approximately 95%. The expanded uncertainty will be:

$$U = k \cdot u_c \quad (29)$$

- Coverage factor  
In accordance with [4].

- Effective degrees of freedom  
From the Welch-Satterthwaite equation:

$$\nu_{ef} = \frac{u_c^4(y)}{\sum_{i=1}^N \frac{u_i^4(y)}{\nu_i}} \quad (30)$$

## 4. Results

Flow pattern maps for each different setup show regions of different flow patterns for the experiments. Figure 2 to Figure 5 shows the maps, with their respective uncertainties for each velocity.

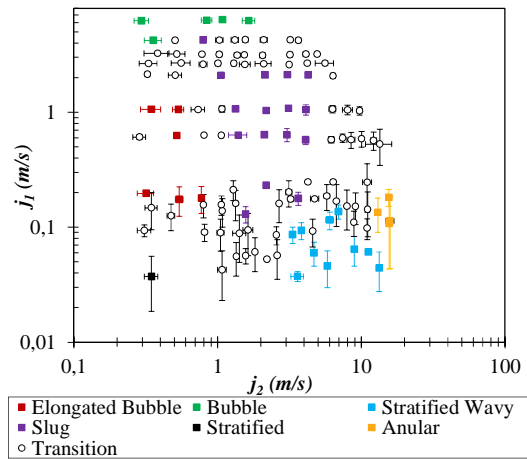


**Figure 2:** Flow pattern map for 27.75 mm inner diameter.

Also, the uncertainties for one and two-phase pressure drop were calculated. From the measured two-phase pressure drop, its variation with diameter, for homogeneous model, was proposed in the form shown in Equation 31. For each setup velocities and fluid properties, shown in the graphs from Figure 6 to Figure 8, the pressure drop was calculated, in addition to the uncertainty of the calculation, and the results were plotted together.

$$-\left(\frac{dP}{dx}\right) = \frac{2}{d} f \rho j^2 = (0.092 \mu_m^{0.2} \rho_m^{0.8} j^{1.8}) d^{-1.2} \quad (31)$$

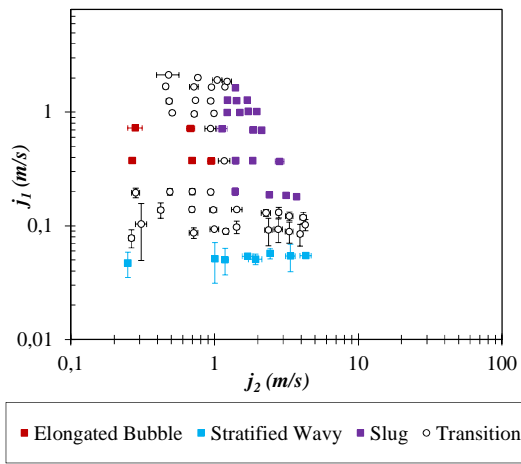


**Figure 3:** Flow pattern map for 53.55 mm inner diameter.

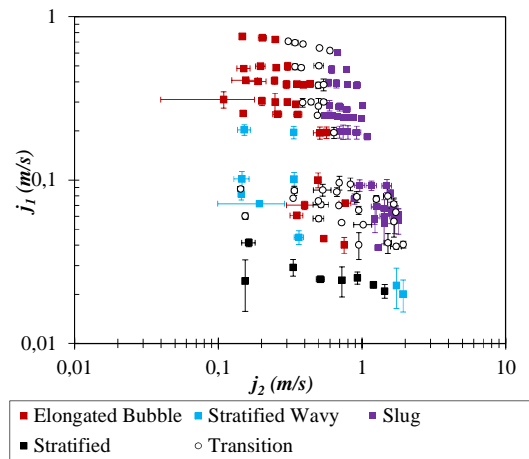


**Figure 4:** Flow pattern map for 82.25 mm inner diameter.

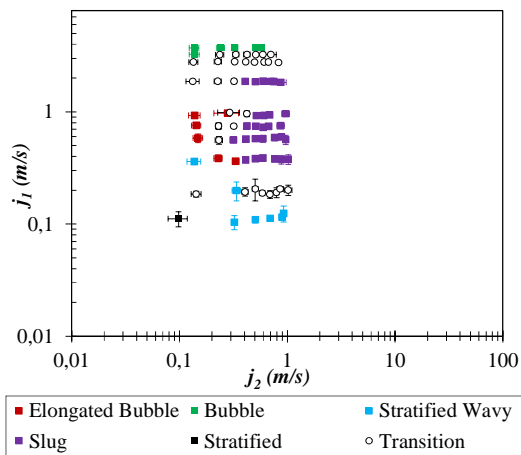


**Figure 5:** Flow pattern map for 106.47 mm inner diameter.

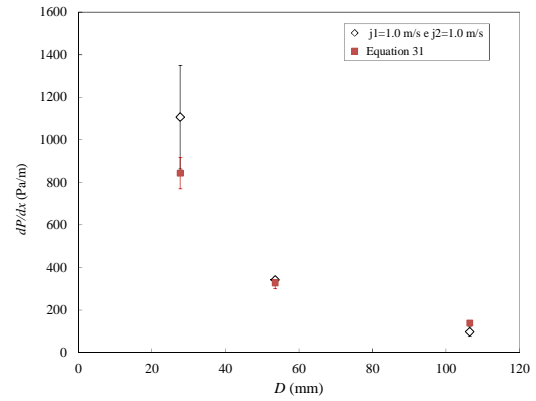


**Figure 6:** Two-phase measured pressure drop versus diameter, compared with calculated and its uncertainties, for  $j_1=1.0 \text{ m/s}$

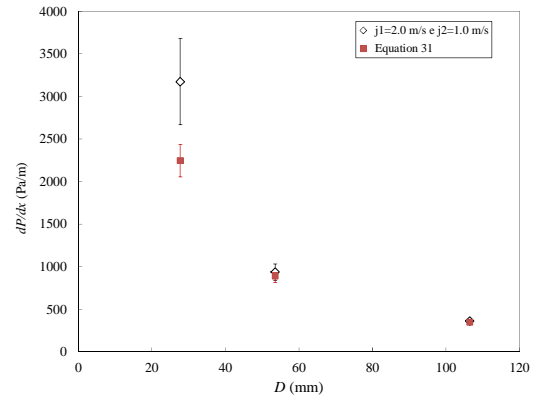


**Figure 7:** Two-phase measured pressure drop versus diameter, compared with calculated and its uncertainties, for  $j_1=2.0 \text{ m/s}$

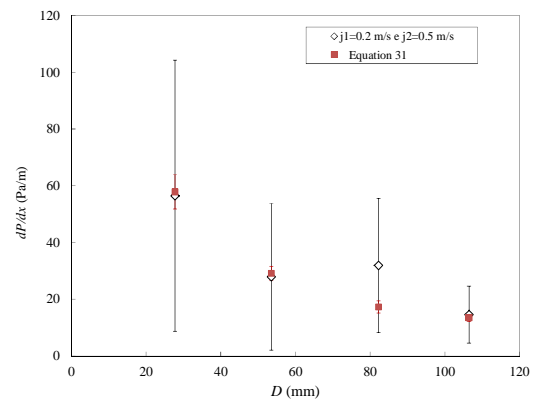


**Figure 8:** Two-phase measured pressure drop versus diameter, compared with calculated and its uncertainties, for  $j_1=0.2 \text{ m/s}$

## 5. Conclusion

From the analysis of the flow pattern maps proposed, it is possible to locate certain set of water-air velocities in a specified region or near other one. As the uncertainties in the maps are just

for superficial velocities, it can help understand regions of flow pattern transitions.

The variability of pressure drop results gave a better idea of how known are the process studied, or the experimental setup, and focus the conclusions for original study that aimed to understand the diameter influence on two-phase air-water flows. The two-phase pressure drop variation with diameter validated the homogeneous model as a good approach to calculate pressure drop when it is considered the uncertainties of both measured and calculated.

Consider the reproducibility of the results as a source of uncertainty, repeating each experiment in each setup three times, improves the quantification of the final uncertainties because it considers the possibility of new tests being performed, thus showing the capacity of the bench setups on reproduce the measured results.

### Acknowledgments

The authors would like to acknowledge IPT, ALFA Research Group and all of its contributors for the support and suggestions.

### Symbols and nomenclature

#### Latin Characters

$A$	Annular flow pattern; pipe section area
$B$	Bubble flow pattern
$D$	Pipe diameter
$EB$	Elongated bubble flow pattern
$f$	Friction factor
$j$	Superficial velocity
$J$	Mixture velocity
$k$	Coverage factor
$n$	Number of samples
$P_{atm}$	Atmospheric pressure
$P_{est}$	Static pressure
$R$	Gas constant (287,053 J.kg <sup>-1</sup> .K <sup>-1</sup> )
$S$	Slug flow pattern
$s$	Biased estimator of standard deviation
$SS$	Stratified smooth flow pattern
$T$	Temperature
$u$	Standard uncertainty
$U$	Expanded uncertainty
$u_c$	Combined standard uncertainty
$V_{eff}$	Degrees of freedom
$W$	Mass flow rate
$WS$	Wavy stratified flow pattern
$y$	Refers to a general physical quantity

#### Greek Characters

$\Delta P$	Pressure drop
$\mu_m$	Mixture viscosity
$\rho; \rho_m$	Density; mixture density
$\sigma$	Standard deviation

#### Superscripts and subscripts

1,2	1 refers do water; 2 refers to air
$i$	Refers to water or air (1 or 2)
$j$	Number of samples
$z$	Number of samples

### References

- [1] S. Cremaschi, G. E. Kouba, and H. J. Subramani, "Characterization of Confidence in Multiphase Flow Predictions," *Energy & Fuels*, vol. 26, no. 7, pp. 4034–4045, Jul. 2012.
- [2] E. Pereyra, C. Torres, R. Mohan, L. Gomez, G. Kouba, and O. Shoham, "A methodology and database to quantify the confidence level of methods for gas–liquid two-phase flow pattern prediction," *Chem. Eng. Res. Des.*, vol. 90, no. 4, pp. 507–513, Apr. 2012.
- [3] D. Barnea, "A unified model for predicting transitions for the whole pipe inclinations," *Int. J. Multiph. Flow*, vol. 13, no. 1, pp. 1–12, 1987.
- [4] INMETRO, *Guia para a expressão de incerteza de medição: avaliação de dados de medição*. Rio de Janeiro: Tradução de: Evaluation of measurement data: guide to the expression of uncertainty in measurement., 2012.
- [5] F. J. da SILVA, "Study of the pipe diameter effect on horizontal air-water two-phase flow," Universidade Estadual de Campinas, 2018.
- [6] "Cepagri". Available: <https://www.cpa.unicamp.br/index.html>.

# Identification of coherent structures in horizontal slug flow

M. Olbrich<sup>1,2</sup>, E. Schmeyer<sup>1</sup>, M. Bär<sup>1</sup>, M. Sieber<sup>2</sup>, K. Oberleithner<sup>2</sup> and S. Schmelter<sup>1</sup>

<sup>1</sup> *Physikalisch-Technische Bundesanstalt (PTB), Abbestr. 2–12, 10587 Berlin, Germany.*

<sup>2</sup> *Institute of Fluid Dynamics and Technical Acoustics, Technische Universität Berlin, Müller-Breslau-Straße 8, 10623 Berlin, Germany.  
E-mail (corresponding author): marc.olbrich@ptb.de*

---

## Abstract

Multiphase flow measurement devices are significantly affected by the occurring flow pattern, such as, e.g., slug flow, leading to large uncertainties. In this context, the slug flow pattern in horizontal pipes is investigated with the aim of finding a statistical characterization of the structures in space and time. For this, two different instances of slug flow are analyzed with a snapshot proper orthogonal decomposition and an additional mode coupling algorithm, which provides an energy-ranked mode basis of the underlying coherent structures. For the considered flows, the most energetic mode pair has been identified with the corresponding slugging structures. Thereby, the temporal and spatial information of these mode pairs enables a statistical characterization of the slugs. In this context, a length scale, a dominant frequency, and an energy representation of the slugging structures is obtained from this method.

---

## 1. Introduction

One central aim in multiphase flow metrology is to evaluate and reduce the large uncertainty in multiphase flow metering that reaches up to 20% in the oil and gas industries [11]. For this, the flow pattern in horizontal pipes is of special interest since multiphase flow measurement devices can significantly be affected by liquid slugs and the induced pressure fluctuations and vibrations. Therefore, the process of flow pattern formation is investigated.

In this contribution, we focus on the analysis of horizontal slug flow by means of snapshot proper orthogonal decomposition (snapshot POD), see, e.g., [1,2,4], with an additional mode coupling algorithm, as proposed in [4]. The snapshot POD extracts an energy-ranked mode basis of the coherent structures from the flow data with the aim of representing the relevant flow phenomena (e.g., slugs) by a few elements of the mode basis. This method is applied to spatially and temporally resolved data.

At first, we analyze data obtained from the CFD simulation of an air-water slug flow test case, for

which the slugs occur at a fixed frequency of 1 Hz [6]. Furthermore, the snapshot POD analysis is applied to data from experimental video observations of a nitrogen - brine water slug flow.

Since the flow pattern is characterized by the distribution of the different phases in the pipe, time-resolved phase volume fraction fields from CFD, as well as gray intensity fields from video observations are used for this analysis.

In both slug flows, the most energetic mode pair from snapshot POD provides a statistical characterization of the slugging structures through their temporal and spatial information.

## 2. Data analysis methodology

### 2.1 Snapshot proper orthogonal decomposition

The snapshot proper orthogonal decomposition (snapshot POD) is a modal decomposition and often used for the identification and characterization of coherent structures in turbulent flows, see, e.g., [1,2,3,4,5].

For the analysis of coherent structures in the slug flow regime, the snapshot POD is applied to spatially and temporally resolved data of this flow pattern. For this, let  $g(x,y,t)$  be a snapshot

sequence of a two-dimensional scalar field. Then, the data is decomposed as follows

$$\begin{aligned} g(x, y, t) &= \bar{g}(x, y) + g'(x, y, t) \\ &= \bar{g}(x, y) + \sum_i a_i(t) \phi_i(x, y), \end{aligned} \quad (1)$$

where  $\bar{g}$  denotes the time-averaged data field,  $g'$  the corresponding fluctuations,  $a_i$  the temporal coefficients and  $\phi_i$  the spatial modes. Furthermore,  $a_i$  and  $\phi_i$  can be obtained from an eigenvalue decomposition of the correlation matrix of the fluctuations  $g'$  as follows. Let  $G \in \mathbb{R}^{M \times N}$  be the matrix of the rearranged fluctuations of the snapshot sequence  $g'$  with  $M$  rows and  $N$  columns, where  $M$  denotes the number of spatial points and  $N$  denotes the number of snapshots. Here, all spatial points of the  $i$ -th snapshot are arranged in the  $i$ -th column of  $G$ . Then  $a_i$  and  $\phi_i$  are obtained from the eigenvalue decomposition of  $R := \frac{1}{N} G^T G$ :

$$R v_i = \lambda_i v_i, \quad i = 1, \dots, N, \text{ with } \lambda_1 \geq \dots \geq \lambda_N \geq 0. \quad (2)$$

Here, the temporal coefficient  $a_i$  is given by the scaled eigenvector  $v_i$  with respect to the eigenvalue  $\lambda_i$  as,

$$a_i(t) := \sqrt{N \lambda_i} v_i \quad (3)$$

and the spatial mode  $\phi_i$  is given as

$$\phi_i(x, y) := \frac{1}{N \lambda_i} \sum_{k=1}^N a_i(t_k) g'(x, y, t_k) \quad (4)$$

for  $i = 1, \dots, N$ . In the context of fluid dynamics, a temporal coefficient  $a_i(t)$  (Equation (3)) can be interpreted as the dynamical behaviour of an underlying coherent structure of the flow field. The corresponding eigenvalue provides a measure of the energy of this coherent structure. The spatial mode  $\phi_i(x, y)$  (Equation (4)) can then be understood as a weighted time-average of the considered flow field fluctuations, weighted with the corresponding dynamics and energy. This provides spatial information of the underlying coherent structure. Further details can be found in [1,2,3,4].

## 2.2 Mode-coupling algorithm

Since the dynamics of periodic structures can be described by a pair of modes, the mode-coupling algorithm proposed in [4] is used in addition. Related modes are identified by the spectral similarity of their temporal coefficients, which accounts for modes that are shifted by a quarter period. The mode coupling is computed by an additional eigenvalue decomposition

$$A c_i = \mu_i c_i \quad (5)$$

$$\text{with } A := \begin{bmatrix} a_1^2 & \dots & a_N^2 \\ \vdots & \ddots & \vdots \\ a_1^N & \dots & a_N^N \end{bmatrix}^T \cdot \left( \begin{bmatrix} a_1^1 & \dots & a_N^1 \\ \vdots & \ddots & \vdots \\ a_1^{N-1} & \dots & a_N^{N-1} \end{bmatrix} \right)^+,$$

where  $a_i^k$  denotes  $k$ -th entry of  $i$ -th temporal coefficient  $a_i$  and  $(\cdot)^+$  denotes the Moore-Penrose pseudo inverse of the corresponding matrix. Note that this is a dynamic mode decomposition (DMD) on the temporal coefficients. The similarity measure of the temporal coefficients  $a_i$  and  $a_j$  is given by

$$H_{i,j} := \text{Im} \left( \sum_{k=1}^N c_k^i \overline{c_k^j} \text{sgn}(\text{Im}(\mu_k)) \right), \quad (6)$$

where  $\overline{c_k^j}$  denotes the complex conjugate of  $c_k^j$ ,  $\text{Im}$  the imaginary part and  $\text{sgn}$  the sign function. The matrix  $H$  is also called *harmonic correlation matrix*. The indices of the coupled modes are then given by the indices of the maximal entries of  $H$ , since it indicates the temporal coefficients with the highest spectral similarity. The dominant frequency  $f$  of an identified mode pair  $(a_i, a_j)$  (equivalently denoted by  $(\phi_i, \phi_j)$ ) is then derived from the corresponding eigenvalue  $\mu_k$  (Equation (5)) by

$$f = \frac{\text{Im}(\ln(\mu_k))}{2\pi}. \quad (7)$$

To determine the combined energy content of the mode pair  $(a_i, a_j)$  the corresponding eigenvalues of the modal decomposition (see Equation (2)) are summarized as

$$E = \frac{\lambda_i + \lambda_j}{\sum_{l=1}^N \lambda_l}. \quad (8)$$

Note that  $E$  represents the energy distribution in terms of a discrete time signal. It can only be identified with a physical energy if  $g$  has appropriate physical units. For details see [4].

## 3. Data of horizontal slug flow

For the analysis of horizontal slug flow with snapshot POD, two different types of slug flow data are considered.

At first, phase volume fraction fields, obtained from the CFD simulation of a periodic air-water slug flow, are used. Because of its periodicity, this flow is suitable for testing the applicability of snapshot POD.

Second, the method is applied to video observations of an experimental nitrogen-brine water slug flow.

### 3.1 CFD simulation of periodic air-water slug flow

The simulation of an air-water slug flow through a horizontal pipe with an inner diameter of  $D = 0.054$  m and a length of  $L = 8$  m, was adopted from [6]. The fluid properties and superficial velocities of this flow are given in Table 1.

**Table 1:** Fluid properties and superficial vel. for CFD.

	water	air
density in $\frac{\text{kg}}{\text{m}^3}$	998.2	1.225
dyn. viscosity in $\text{Pa} \cdot \text{s}$	$1.003 \cdot 10^{-3}$	$1.789 \cdot 10^{-5}$
superficial vel. in $\frac{\text{m}}{\text{s}}$	1.0	1.0

For the computation, the pipe was discretized as an O-grid consisting of about 1.1 million nodes (45 nodes in radial, 104 nodes in angular, and 685 nodes in longitudinal direction).

To generate a periodic formation of slugs in the pipe, a time-dependent sinusoidal displacement of the vertical position of the air-water interface is applied to this flow as introduced in [6]. For this, the inlet is initialized with equally distributed phases in the inlet cross section, such that the lower half of the cross section is filled with water and the upper half is filled with air (see Figure 1). The initial condition is obtained from the vertical position of the interface  $\tilde{y}_{int}$  by

$$\tilde{y}_{int}(x, t = 0) = \frac{D}{4} \sin\left(2\pi \frac{4x}{L}\right) + \frac{D}{2}, \quad (9)$$

where  $t$  denotes the time and  $x$  the spatial component in flow direction (see Figure 1). The time-dependent vertical position of the interface at the inlet is then given by

$$\tilde{y}_{int}(x = 0, t) = \frac{D}{4} \sin\left(2\pi \frac{v4t}{L}\right) + \frac{D}{2}, \quad (10)$$

where  $v = 2 \frac{\text{m}}{\text{s}}$  denotes the inlet gas or liquid velocity. This perturbation leads to a periodical slug formation in the pipe of 1 Hz (see Figure 2).

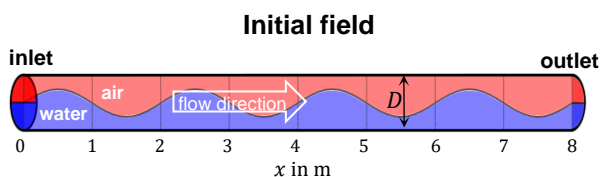


**Figure 1:** Illustration of the initial field (not to scale).

Furthermore, a no-slip boundary condition at the walls of the pipe and a pressure outlet boundary condition was set.

The CFD simulation was performed in ANSYS FLUENT [10]. For this, an unsteady Reynolds-averaged Navier-Stokes (URANS) approach with the  $k-\omega$ -SST turbulence model was chosen [8].

To model the gas-liquid interface the volume of fluid (VOF) method was applied within a mixture model [12]. In addition, turbulence damping was included to model such flows with high velocity gradients at the interface correctly [10]. The space and time discretization schemes are chosen as in [12].

In Figure 2, a snapshot of the gas volume fraction field  $\alpha_{air}(x, y, t)$  from a longitudinal section of the pipe at  $t = 70.86$  s is depicted. Here, the time-dependent interface displacement at the inlet is visible along the first meters of the pipe. Further downstream the water slugs are formed.

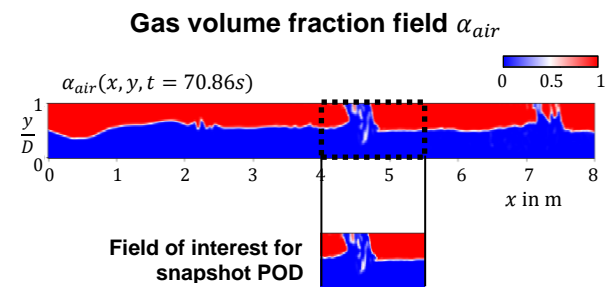


**Figure 2:** Snapshot of gas volume fraction field from a longitudinal pipe section at  $t = 70.86$  s with exposed field of interest (not to scale).

To analyze the fully developed slug flow from the simulations with snapshot POD, the gas volume fraction field data is collected from a longitudinal section of a 1.5 m long pipe segment at 4 – 5.5 m (see Figure 2). To ensure that numerical effects from the initialization do not affect the flow field anymore and the simulated flow is well developed, the snapshot sequence is collected in a time interval of 10 s from 70 s to 80 s with a sample rate of 100 Hz (see Figure 3).

### 3.2 Experimental slug flow

The considered experiment of a horizontal gas-liquid slug flow was performed by TUV SUD NEL. The experimental setup consists of a straight horizontal pipe with an inner diameter of  $D = 0.0972$  m and a length of  $100D$ , followed by a Perspex viewing section with a length of  $0.5$  m, where the slug flow was recorded from aside by a high-speed camera with a frame rate of 240 fps. This section is followed by a right bend and a vertical measurement configuration [11], but this is of minor interest, since the slugging structures in the

horizontal pipe are investigated. The fluid properties and superficial velocities are listed in Table 2.

**Table 2:** Fluid properties and superficial vel. for experiment.

	Brine water	nitrogen
density in $\frac{\text{kg}}{\text{m}^3}$	1011	10.8
dyn. viscosity in $\text{Pa} \cdot \text{s}$	$8.82 \cdot 10^{-4}$	$1.75 \cdot 10^{-5}$
superficial vel. in $\frac{\text{m}}{\text{s}}$	0.545	1.635

To obtain a scalar field representation of the multidimensional RGB-frames from the video, the grayscale is extracted. A snapshot sequence of this grayscale frames for a time interval of 50 s is then used for the analysis with snapshot POD (see Figure 3).

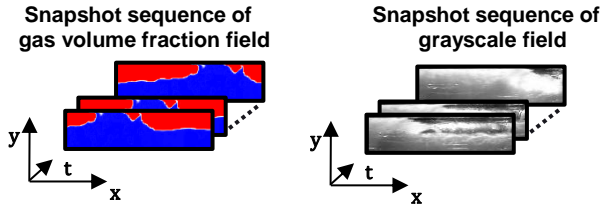


**Figure 3:** Illustration of snapshot sequences from CFD data (left) and grayscale frames of experimental videos (right).

## 4. Results

In this chapter, the results of the snapshot POD analysis of the flow field data from CFD and experimental video observations are presented. Since this work focuses on a statistical characterization of the slugging structures, only the relevant results are selected. For both data sets, the coherent structures, represented by the most energetic mode pair can be identified with the slugging structures of the corresponding slug flow. Hence, this mode pair provides spatial and temporal parameters for a characterization of the slugging structures.

### 4.1 Results for CFD data

In Figure 4, the most energetic mode pair of the air-water slug flow from CFD, as well as the corresponding temporal coefficients and the time-averaged gas volume fraction field are depicted as result of the analysis with snapshot POD. In addition, the vertical position of the gas-liquid interface (liquid level) over time and the averaged slugging structure are also given for validation. The liquid level was extracted from the snapshot sequence at  $x = 15D$  with the method of tracking the gas-liquid interface described in [13]. The averaged slugging structure was obtained from the mean of all snapshots with a slug (at centered position).

FLOMEKO 2019, Lisbon, Portugal

### Snapshot POD results for CFD data

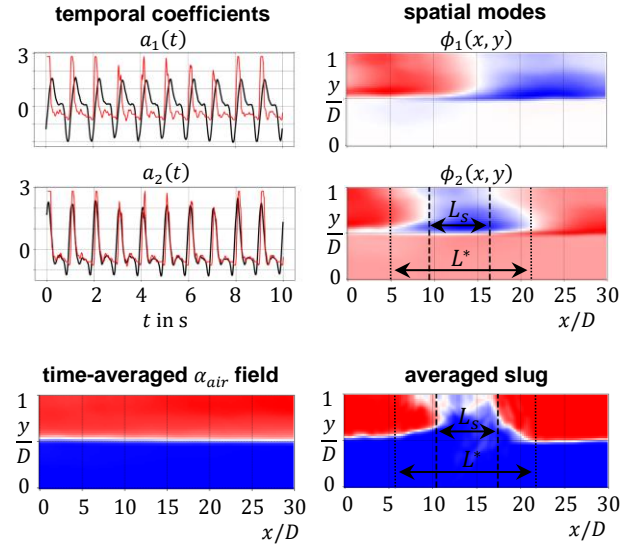


**Figure 4:** Most energetic mode pair ( $\phi_1, \phi_2$ ) with corresponding temporal coefficients  $a_1, a_2$  (—) from snapshot POD in comparison with liquid level over time (—), the averaged slug and the time-averaged gas volume fraction field  $\bar{\alpha}_{air}$ , obtained from CFD data. In addition, the derived length scales  $L_s, L^*$  are given. Note that  $a_1, a_2$  and the liquid level are depicted in standard score, respectively. Drawings not to scale.

This mode pair is identified with the averaged slugging structure of the corresponding air-water slug flow, since the temporal coefficients coincides with the liquid level, especially in width and periodicity of the peaks. Note that  $a_1$  is shifted to  $a_2$  as stated in Chapter 2. Furthermore, the frequency of the coupled mode pair ( $\phi_1, \phi_2$ ) of 1 Hz (see Equation (8)) is equal to the frequency of slug occurrence of the periodic slug flow. The structure displayed in the spatial mode  $\phi_2(x, y)$  is interpreted as the averaged slugging structure. This can be verified by the averaged slug, which is also depicted in Figure 4. From that, the slug body length  $L_s$  can be derived [14, 15, 16]. This length scale and the slug frequency  $f$  provide parameters for a statistical characterization of the slug flow.

Furthermore, an additional length scale  $L^*$  can be obtained as proposed in [15]. For this the transitional velocity of a slug  $v_s$  is multiplied with the time interval of a slug  $\Delta t_s$  passing by at one point, i.e.:

$$L^* = v_s \cdot \Delta t_s. \quad (11)$$

Based on the unit cell model [14] and the considered specific rectangular shape of a slug, this length scale is often used for the calculation of the slug body length, see [15]. But for slugs, which deviate much in their shape from the unit cell model, this identification is not obvious. Since on strongly tilted

slugging structures as in Figure 4, it is not clear to determine a unique time of a slug front and a slug tail. Nevertheless, the length scale  $L^*$  can be obtained from the liquid level over time or rather the temporal coefficient  $a_2$  under knowledge of  $v_s$ , since it depends only on temporal information and a velocity. Therefore, a complete peak in between two local minima of the liquid level over time is considered as one slug. Then, the obtained length scale  $L^*$  provides an information of the length of the complete structure, and not just the inner part of the slug body. To determine  $L^*$ , average parameters are considered, since a statistical characterization is sought. For this, the averaged translational velocity of the slugs is obtained by a cross correlation of a column of the dataset at  $x_1 = 0D$  and  $x_2 = 30D$  over time. Since the distance is known, the average velocity of the slugs is then derived by the shift of the data obtained by the (unique) maximum of the cross-correlation function. This procedure is adopted from the PIV-measurement technique, see, e.g., [17]. This leads to an average translational velocity  $\bar{v}_s = 2.63 \frac{m}{s}$  of the slugging structures.

Since the temporal coefficient  $a_2$  represents the dynamics of the liquid level, the time interval of a slug  $\Delta t_s$  can be approximated by the width of the associated peak from zero to zero. Taking the mean of all these intervals, the average time interval  $\bar{\Delta t}_s = 0.31 s$  can be derived. This results in a length scale for the averaged slugging structure of about  $L^* = 16 D$  which also matches the length of the

**Table 3:** Parameters for statistical characterization of air-water slug flow from CFD data.

<b>Coupled energy content <math>E</math> of mode pair <math>(\phi_1, \phi_2)</math></b> (see Equation (8))	46.6 %
<b>Frequency <math>f</math> of mode pair <math>(\phi_1, \phi_2)</math></b> (see Equation (7)) (Identified with slugging frequency)	1 Hz
<b>Averaged slug body length <math>L_s</math></b>	$7 D$
<b>Averaged structure length <math>L^*</math></b>	$16 D$

average slugging structure shown in  $\phi_2$  and the averaged slug (see Figure 4). The parameters for a statistical characterization of the slugs obtained from analysis with snapshot POD are summarized in Table 3.

#### 4.2 Results for experimental data

In Figure 5, the most energetic mode pair of the experimental nitrogen - brine water slug flow, as well as the corresponding temporal coefficients are depicted as result of the analysis with snapshot POD. Analogously to Figure 4, the liquid level over time, obtained from the experimental video observations with the same method as mentioned in

Section 4.1, see [13], is plotted for comparison. Since a snapshot sequence of grayscale fields are analyzed, the modal decomposition accounts for the changes in the gray intensities. For the considered flow, the brine water shows higher gray intensities than the transparent nitrogen in front of the dark background. But the highest gray intensities appear at the gas-liquid interface, due to reflection at the liquid surface. Hence, the spatial modes show coherent structures of the flow in terms of gray intensities, but with a highlighted gas-liquid interface.

#### Snapshot POD results for experimental data

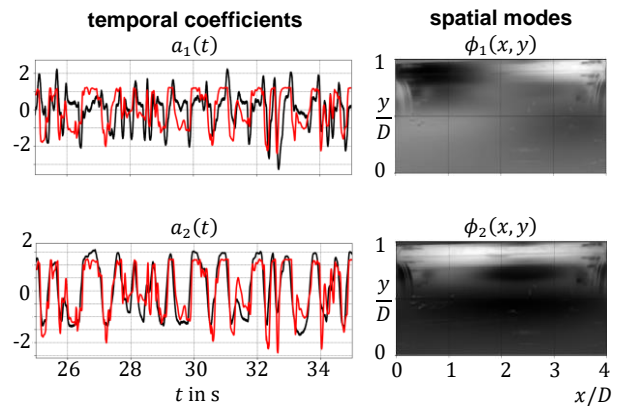


**Figure 5:** Most energetic mode pair  $(\phi_1, \phi_2)$  with corresponding temporal coefficients  $a_1, a_2$  (—) from snapshot POD in comparison with liquid level over time (—). Note that  $a_1, a_2$  and the liquid level are depicted in standard score for a 10 s time interval [25 s, 35 s], respectively. Drawing of  $\phi_1, \phi_2$  not to scale.

The depicted mode pair (see Figure 5) is also identified with the averaged slugging structure because of the clear similarity of the liquid level with the corresponding temporal coefficients and the shape of the spatial modes. Since the gas-liquid interface in  $\phi_2$  occupies the complete length of the field of view, it can be deduced, that the average slug is at least as long as the field of view. Therefore, an average slug body length scale  $L_s$  cannot be derived from the spatial mode. Nevertheless, the length scale  $L^* = 7.6 D$  can be derived from the temporal coefficient  $a_2$ . For this, the averaged translational velocity  $\bar{v}_s = 2.85 \frac{m}{s}$  and the averaged time interval  $\bar{\Delta t}_s = 0.26 s$  are obtained as explained before in Section 4.1. Furthermore, the dominant frequency  $f$  and the energy content  $E$  of the selected mode pair is also provided by snapshot POD analysis. These parameters can be used for a statistical characterization of the slugging structures and are summarized in Table 4. Note that the dominant frequency  $f = 1.4 Hz$  agrees with the averaged frequency of slug occurrence, where the

number of counted slugs (72) is divided by the length of the considered time interval (50 s).

**Table 4:** Parameters for statistical characterization of nitrogen – brine water slug flow from experimental data.

<b>Coupled energy content <math>E</math> of mode pair <math>(\phi_1, \phi_2)</math></b> (see Equation (8))	55.9 %
<b>Frequency <math>f</math> of mode pair <math>(\phi_1, \phi_2)</math></b> (see Equation (7)) (Identified with slugging frequency)	1.4 Hz
<b>Averaged structure length <math>L'</math></b>	7.6 $D$

#### 4. Conclusion

To characterize the structures of two different slug flows statistically, an analysis with snapshot POD was performed and validated. For both examples, the most energetic mode pair was identified with the slugging structures and used for their characterization in space and time. Altogether, the snapshot POD with an additional mode coupling algorithm is a valid tool for the identification of coherent structures in horizontal slug flow and enables a quantitative characterization of the occurring liquid slugs by their temporal and spatial information.

#### Acknowledgements

This work was supported through the Joint Research Project "Multiphase flow reference metrology". This project has received funding from the EMPIR programme co-financed by the Participating States and from the European Union's Horizon 2020 research and innovation programme. The authors would like to thank Terri Leonard and Marc MacDonald from TUV SUD NEL, who provided the experimental video observations.

#### References

- [1] Taira K, Brunton S L, Dawson S T M, Rowley C W, Colonius T, McKeon B J, Schmidt O T, Gordeyev S, Theofilis V and Ukeiley L S. "Modal Analysis of Fluid Flows: An Overview", *AIAA Journal*, **Vol. 55**, pp. 4013-4041, 2017.
- [2] Holmes P, Lumley J L, Berkooz G. *Turbulence, coherent structures, dynamical systems and symmetry*. Cambridge University Press, 1996.
- [3] Sirovich L, "Turbulence and the dynamics of coherent structures. Part I: Coherent structures", *Quart. Appl. Math.*, **Vol. 45**, pp. 561-571.1987.
- [4] Sieber M, Paschereit C, Oberleithner K. "Spectral proper orthogonal decomposition". *Journal of Fluid Mechanics*, **Vol. 792**, pp. 798-828, 2016.
- [5] Polanski J, Wang M. "Proper orthogonal decomposition as a technique for identifying two-phase flow pattern based on electrical impedance tomography", *Flow Measurement and Instrumentation*, **Vol. 53**, pp. 126-132, 2016.
- [6] Frank T, "Numerical simulation of slug flow regime for an air-water two phase flow in horizontal pipes", in: *The 11th International Topical Meeting on Nuclear Reactor Thermal-Hydraulics (NURETH-11)*, Avignon, France.
- [7] Fluent Inc., *Fluent User's Guide 16.0*, 2015.
- [8] Menter F R, "Two-equation eddy-viscosity turbulence models for engineering applications", *AIAA J*, **Vol. 32**, pp. 1598–1605, 1993.
- [9] Hirt C W, Nichols B D, "Volume of fluid method for the dynamics of free boundaries", *Journal of Computational Physics*, **Vol. 39**, pp. 201–225, 1981.
- [10] Egorov Y, "Validation of CFD codes with PTS-relevant test cases", EVOL-ECORA-D07, 2004.
- [11] *Final Publishable JRP Report Multiphase flow metrology in oil and gas production (ENG58)*, Euramet, 2018.
- [12] Fiebach A, Schmeyer E, Knotek S, Schmelter S, "Numerical simulation of multiphase flow in a vertically mounted Venturi flow meter", in: *Proceedings of FLOMEKO*, 2016.
- [13] Olbrich M, Schmeyer E, Riazly L, Oberleithner K, Bär M, Schmelter S. "Validation of simulations in multiphase flow metrology by comparison with experimental video observations", *IOP Conf. Series: Journal of Physics: Conf. Series*, **Vol. 1065**, 2018.
- [14] Taitel Y, Barnea D, "A consistent approach for calculating pressure drop in inclined slug flow", *Chem. Eng. Sci.*, **Vol. 45**, pp. 1199-1206, 1990.
- [15] Al-Kayiem H H, Mohammed A O, Al-Hashimy Z I, Time R W, "Statistical assessment of experimental observation on the slug body length and slug translational velocity in a horizontal pipe", *International Journal of Heat and Mass Transfer*, **Vol. 105**, pp. 252-260, 2017.
- [16] Baba Y D, Aliyu A M, Archibong A E, Abdulkadir M, Lao L, Yeung H, "Slug length for high viscosity oil-gas flow in horizontal pipes: Experiments and prediction", *Journal of Petroleum Science and Engineering*, **Vol. 165**, pp. 397-411, 2018.
- [17] Brossard C, Monnier J-C, Barricau P, Vandernoot F-X, Le Sant Y, Champagnat F, Le Besnerais G, "Principles and Applications of Particle Image Velocimetry", *AerospaceLab Journal*, 2009.

# Combining three independent traceability chains for high-pressure gas flow in Germany

Jos van der Grinten and Bodo Mickan

Physikalisch-Technische Bundesanstalt, Braunschweig, Germany  
E-mail (corresponding author): jos.v.grinten@ptb.de

## Abstract

Currently all measurement capabilities for high-pressure gas flows in Germany are based on a single traceability chain. However, there are three primary standards available that can be made traceable without mutual dependencies. In this study PTB investigates the benefits of combining three independent traceability chains. The applied method is identical to the harmonization of the high-pressure cubic metre of natural gas [1]. For two G1000 transfer reference meters the measurement uncertainty decreases from 0.110% to 0.089%. For the working standards the CMCs decrease from 0.156% and 0.175% to 0.142% and 0.163% respectively. When only two chains are used the CMCs of the working standards improve with approximately 0.01%. More scenarios are explored. The development of a new primary standard with a CMC of 0.10% has the potential to improve the CMCs of the working standards with approximately 0.02%.

## 1. Introduction

The concept of the harmonized cubic metre of high-pressure natural gas has been in use for 20 years. This harmonized reference value is obtained by combining several independent traceability chains from different countries. Last year the underlying key comparison procedure and the data processing methods were updated and published [1].

The reduction obtained in the measurement uncertainty was the motivation for PTB to study whether this method can also be applied to currently available references that can be made independently traceable. These references are located at the pigsar calibration facility in Dorsten and have the following independent traceability sources:

- a High-Pressure Piston Prover (HPPP), which is directly traceable to length;
- Critical Flow Venturi Nozzles (CFVN), traceable to PTB's airflow facilities in Braunschweig;
- a Laser-Doppler Anemometer (LDA), traceable to a rotating disk that provides a reference velocity.

## 2. Operating ranges

Figure 1 gives a schematic overview of the current pigsar calibration facility. After entering the station inlet, the natural gas is first cleaned in a cartridge filter and then preheated. During the calibration, the preheater also controls the temperature. Between the heater and the pressure regulator two safety

shut-off valves protect the test facility against excess pressure. Downstream of the pressure regulator the gas flow is divided into a gas stream which is used for calibration and an internal bypass stream. The flowrate is controlled further downstream in both gas flows, shortly before they join up again ahead of the station outlet. The piping configuration was optimized such that gas volume between the working standards and the test meters is reduced to the minimum, which minimizes the line-pack effect. The gas meters to be calibrated, including upstream and downstream straight lengths provided by the customer, can be installed on a total of six test meter runs with a length of up to 22 m.

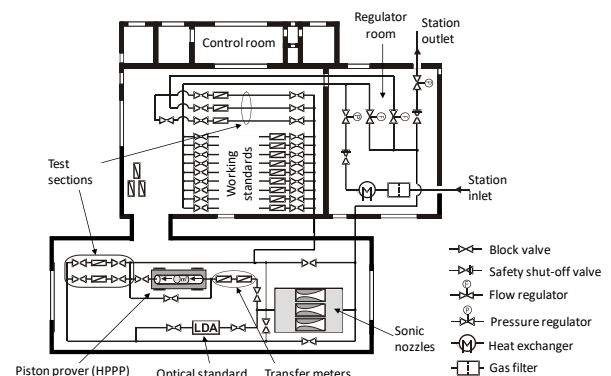


Figure 1: Schematic view of the current pigsar facility.

The PTB test installations (piston prover HPPP, optical standard, transfer meters, sonic nozzles), shown in the bottom part of Figure 1 are permanently integrated into the pigsar piping system in a separate metering room. The High-Pressure Piston Prover (HPPP) is described in [2], the sonic nozzles (CFVN) in [3] and the optical LDA standard in [4]. Their measurement capabilities are listed in Table 1.

**Table 1:** Operating ranges of primary standards.

	HPPP	CFVN	LDA
Pressure [bar]	8 – 50	8 – 50	8 – 50
Flowrate [m <sup>3</sup> /h]	3 – 480	3 – 1600	3 – 1600
CMC	0.065%	0.15%	0.21%

The CMC is the Calibration and Measurement Capability, i.e. the best expanded uncertainty ( $k=2$ ) that can be routinely achieved for a well repeatable meter under test. The CMC of the piston prover [5] is smaller than the CMCs of the other devices. However, its operating range is smaller.

### 3. Combining traceability chains

The three independent traceability chains are graphically depicted in Figure 2. The two G1000 Transfer Reference Meters are calibrated in series up to 1600 m<sup>3</sup>/h. The piston prover can only be used up to 480 m<sup>3</sup>/h. For that reason, first two G250 secondary references are calibrated, which are used to calibrate four G250 working standards up to 400 m<sup>3</sup>/h each. With the four working standards the G1000 meters can be calibrated. This so-called bootstrapping process is performed at 16 bar and 50 bar. Later in the paper the left, middle and right traceability chains in Figure 2 will be denoted as traceability chain 1, 2 and 3, respectively.

The uncertainty  $U_{TRM}$  of the G1000 transfer meter is calculated according to [1] using the uncertainties  $U_i$  ( $i = 1..3$ ) of the individual traceability chains

$$\frac{1}{U_{TRM}^2} = \frac{1}{U_1^2} + \frac{1}{U_2^2} + \frac{1}{U_3^2} \quad (1)$$

which results in  $U_{TRM} = 0.082\%$ . As the three traceability chains will produce slightly different values for the deviation an additional uncertainty of 0.05% ( $k=2$ ) for the reproducibility is taken for each meter. As the two meters are calibrated in series the additional uncertainty of the average is  $\sqrt{(0.05^2+0.05^2)}/2$ , which results in an overall uncertainty of the transfer standards of 0.089% shown at the bottom of Figure 2.

The uncertainty of the transfer standard based on a single traceability chain is 0.110% [6]. So, at this

level an absolute uncertainty improvement of 0.021% is achieved.

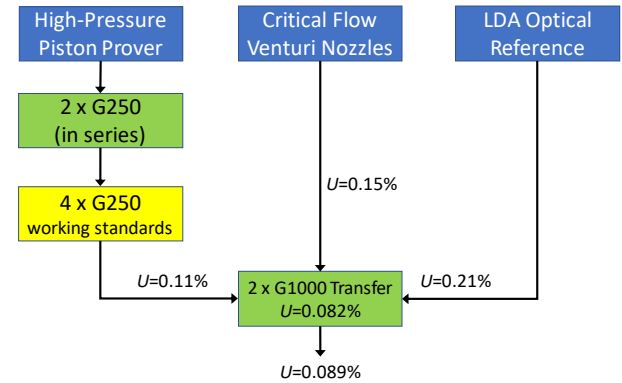


**Figure 2:** Effect on the final uncertainty for the unit of volume flowrate provided by the transfer package based on calibrations with three independent sources of traceability. The combined uncertainty is determined according to [1]. Finally, for the uncertainty of the transfer package, a reproducibility of 0.05 % is considered for each of the two G1000 transfer meters calibrated in series.

### 4. Traceability benefits

How will the rest of the traceability chain benefit from the improved uncertainty of the G1000 TRMs? The traceability chain is schematically depicted in Figure 4. The two G1000 TRMs are used to calibrate four parallel working standards (yellow). These are used to calibrate a new TRM up to 6500 m<sup>3</sup>/h, which will be used to calibrate the working standards (orange) of pigsar's new closed-loop calibration facility CLP. With these working standards another TRM or MuT can be calibrated.

The calculation of the uncertainties in the entire traceability chain is performed using the method in a previous study [6]. In order to simplify the calculations, the uncertainty contributions have been subdivided in three categories: traceability, process conditions and repeatability. During all traceability steps the same type of instruments are used, of which the uncertainties are practically equal. This means that a single uncertainty value can be assigned to all process-based uncertainty contributions together. As some of the process parameters are mutually dependent, the model was programmed into a Monte Carlo Simulator [7]. The result is that the expanded ( $k=2$ ) uncertainty of all process variables together equals 0.056%. The uncertainty of the MuT due to repeatability of successive measurements is evaluated to be 0.01%.

The evaluation of the uncertainties of the entire traceability chain is depicted in Figure 3. The process starts with the uncertainty of the two G1000

TRMs, shown in the column total. The repeatability and process uncertainties are shown in the columns Type A and Type B, respectively. Subsequently, the uncertainties of all traceability steps are added by root-sum-square summation. In this picture the transfer meters and MuT are at the same level because they are calibrated by the same references. However, in order to achieve the CMC an experience-based additional uncertainty for the long-term stability of 0.075% needs to be added. The CMCs are shown in the rightmost column of Figure 3. The values based on three parallel traceability chains are shown in bold. In italic the CMC values are shown that are based on a single traceability chain. The absolute CMC improvement at the third level in Figure 3 is 0.015% and at the last step 0.012%.

		Type A	Type B	Total	Stability	CMC
Long-term stability for turbine gasmeters						0.075%
TRM	2 x	8" G1000 TM		0.089%	↓	
Process				0.056%	↓	
References	4 x //	8" G1000 TM	0.01%	→ 0.106%	↓	
Process				0.056%	↓	
TRM / MuT	2 x	16" G6500 TM	MuT 0.01%	→ 0.120%	↓	<b>0.141%</b> <i>0.156%</i>
Process				0.056%	↓	
References CLP	3 x //	20" G6500 TM	0.01%	→ 0.133%	↓	
Process				0.056%	↓	
TRM / MuT		Transfer	MuT 0.01%	→ 0.144%	↓	<b>0.163%</b> <i>0.175%</i>

**Figure 3:** Evaluation of the CMCs ( $k = 2$ ) of pigsa's current (yellow) and new CLP (orange) working standards, based on three independent traceability chains from Figure 2. All uncertainties are added by root-sum-square summation. The boxed value of 0.075% is the additional uncertainty for the long-term stability of the turbine gasmeters and is used to evaluate the CMC at the transfer meter level. The CMC values based on the current single traceability chain are displayed in italic.

## 5. Discussion

After the previous exercise the question rises how many independent traceability chains you want to use in practice and what is the optimum CMC for a standard.

In Table 2 the achievable CMCs of the two G1000 TRMs and the CMCs of the working standards are shown for different combinations of traceability chains. The results for the single traceability chain 1 (row 1, below the header) and the combination of three chains 1, 2 and 3 (row 3) are the same as shown in Figure 3. The LDA optical standard has a much higher CMC than the other two. Omitting this chain results in an uncertainty that is 0.006% higher for the TRMs and 0.004% and 0.003% higher CMCs for the working standards. As uncertainties of a

laboratory's measurement capability are generally represented by two decimals, this change is hardly visible.

**Table 2:** Comparison of achievable uncertainties of the two G1000 TRMs and CMCs of working standards in Figure 3 for combinations of different independent traceability chains shown in the leftmost column. Chain 1 – 3 are the HPPP, CFVN and LDA shown in Figure 2, respectively. Chain 4 is introduced as a new standard under development with a CMC of 0.10% [6].

Traceability combination	U(2x G1000)	CMC WS2	CMC WS3
	≤ 1600 m <sup>3</sup> /h	≤ 6500 m <sup>3</sup> /h	≤ 21000 m <sup>3</sup> /h
1 – – –	0.110%	0.156%	0.175%
1 2 – –	0.095%	0.146%	0.166%
1 2 3 –	0.089%	0.142%	0.163%
1 – – 4	0.082%	0.137%	0.159%
1 2 – 4	0.075%	0.133%	0.156%
1 2 3 4	0.072%	0.132%	0.154%

Theoretically, several traceability chains with equal measurement uncertainties will result in the lowest combined measurement uncertainty. For this reason, we introduced a fourth traceability chain with a CMC of 0.10% in Table 2. Combination of the first and the fourth traceability chain (Table 2, row 4 below header) results in a lower uncertainty than the three parallel traceability chains 1, 2 and 3.

In row 5 of Table 2 the CFVNs are added. Combination of chains 1, 2 and 4 results in uncertainties that are approximately 0.02% better than the single traceability chain. Four parallel chains result in uncertainties that are approximately 0.002% better than the previous combination. The improvement is only one tenth of the previous improvement, which makes the additional efforts costly.

In this study several traceability chains have been combined at a flowrate level of 1600 m<sup>3</sup>/h maximum. If the two G6500 TRMs could be calibrated at a level of 6500 m<sup>3</sup>/h with an additional traceability chain with an uncertainty equal to the present traceability chain, and using the same method that leads to Figure 3, a CMC of 0.151% can be achieved for the working standards up to 21000 m<sup>3</sup>/h. This value is better than any of the CMCs listed in the righthand column of Table 2. So it makes sense to combine traceability chains at the flowrate level where meters are calibrated for application in the field. However, the difference with the combination of chains 1, 2 and 4 is 0.005%, a value that does not justify the additional work to build a second independent traceability chain up to flowrates of 6500 m<sup>3</sup>/h. In addition, these flowrates are also covered by international cooperation on the harmonized cubic metre [1].

In the EuReGa framework of international cooperation an intercomparison between primary standards

has been performed [8],[9] with flowrates up to 400 m<sup>3</sup>/h. Combination of two primary standards results in an uncertainty reduction of less than 0.005% for the two G250 in the first traceability chain. Due to additional uncertainty sources, this benefit will disappear further down the traceability chain.

## 6. Conclusion

From this study the following conclusions can be derived.

- Combining PTB's present three parallel independent traceability chains results in better CMCs for transfer reference meters (TRMs) and working standards. Compared to the present single traceability chain. The improvement is 0.021% for the two G1000 travelling reference meters and 0.014% and 0.012% for the working standards.
- The LDA optical standard is the traceability chain with the highest CMC. If this standard is omitted, the two remaining chains obtain CMCs of the working standards that are 0.009% and 0.010% better than the CMC values obtained with a single traceability chain. Using two traceability chains is a consideration as CMCs are generally published in two digits.
- Combining a new primary standard with an uncertainty of 0.10% with the present traceability chain will lead to an uncertainty reduction of almost 0.03% for the TRMs and almost 0.02% for the working standards.

## Abbreviations and symbols

CFVN	Critical Flow Venturi Nozzle
CLP	Closed Loop pigsar, pigsar's new calibration facility, which is currently under construction
CMC	Calibration and Measurement Capability, i.e. the best expanded uncertainty ( $k=2$ ) that can be routinely achieved for a well repeatable meter under test
HPPP	High-Pressure Piston Prover
LDA	Laser Doppler Anemometry
MuT	Meter under Test
TRM	Transfer Reference Meter

### Latin symbols

$k$	coverage factor	[-]
$U$	expanded uncertainty	[-]

### Index

$TRM$	Transfer Reference Meter
1, 2, 3	first, second and third traceability chain

## References

- [1] Jos van der Grinten, Henri Foulon, Arnthor Gunnarsson, Bodo Mickan, "[Reducing measurement uncertainties of high-pressure gas flow calibrations by using reference values based on multiple independent traceability chains](#)", *Technisches Messen*, **85**(12), pp 754-763, 2018.
- [2] B. Mickan, R. Kramer, H. Müller and V. Strunck, D. Vieth, H.-M. Hinze, "[Highest Precision for Gas Meter Calibration Worldwide: The High Pressure Gas Calibration Facility Pigsar™ with Optimized Uncertainty](#)", Proceedings of 7<sup>th</sup> International Symposium on Fluid Flow Measurement, Anchorage, Alaska, 2009.
- [3] B. Mickan, "Discharge coefficients of CFVN predicted for high Reynolds numbers based on Low-Re-calibration", 18<sup>th</sup> International Flow Measurement Conference, FLOMEKO, 26-28 June 2019, Lisbon, Portugal.
- [4] B. Mickan and V. Strunck, "A primary standard for the volume flow rate of natural gas under high pressure based on laser Doppler velocimetry", *Metrologia*, **51**(5), pp 459-475, 2014. doi:10.1088/0026-1394/51/5/459
- [5] BIPM KCDB, [https://kcdb.bipm.org/appendixC/country\\_list\\_search.asp?CountSelected=DE&sservice=M/FF.9.2](https://kcdb.bipm.org/appendixC/country_list_search.asp?CountSelected=DE&sservice=M/FF.9.2)
- [6] Jos van der Grinten, Detlef Vieth and Bodo Mickan, "The new Closed Loop pigsar high-pressure gas flow calibration facility and its projected CMC", 36<sup>th</sup> International North Sea Flow Measurement Workshop, Aberdeen, 22 – 24 October 2018.
- [7] Jos van der Grinten, Detlef Vieth and Bodo Mickan, "[Der neue Closed Loop pigsar und dessen projektierte Messunsicherheit – The new Closed Loop pigsar calibration facility and its design uncertainty](#)", 9. Workshop Gasmengenmessung – Gasanlagen – Gas-technik, 7 – 8 March 2018, Rheine, Germany, pp 155-170.
- [8] Jos van der Grinten, Arnthor Gunnarsson, Mijndert van der Beek and Bodo Mickan, "Intercomparison of primary high pressure flow standards", Euramet F1301, 2019, <https://tinyurl.com/y39lx5ud>
- [9] Arnthor Gunnarsson, Jos van der Grinten, Mijndert van der Beek, Bodo Mickan, "Primary Piston Prover Intercomparison Between PTB, VSL and FORCE Technology", 18<sup>th</sup> International Flow Measurement Conference, FLOMEKO, 26-28 June 2019, Lisbon, Portugal.

# Flow Instability Evaluation at the NMISA Gas Flow Laboratory

**D. Jonker, W. M. Dlamini, R. M. Molefe**

NMISA – National Metrology Institute of South Africa, [djonker@nmisa.org](mailto:djonker@nmisa.org), Pretoria, South Africa  
E-mail (corresponding author): [djonker@nmisa.org](mailto:djonker@nmisa.org)

---

## Abstract

Interlaboratory comparison and verification measurements performed in the Gas Flow Laboratory indicated stability problems in the flow ranges below 50 mL/min and above 30 L/min. Initially the stability problems in the low flow range below 50 mL/min were attributed to the flow cell used as reference standard. The unstable measurements above 30 L/min were attributed to the lack of sufficient pressure drop in the flow path from the gas cylinder to the measuring point. However, further measurements performed indicated that this might not be the cause of the instabilities experienced. To further investigate the matter, a second reference standard was acquired, and the flow path was lengthened and equipped with more pressure regulators to ensure better pressure control and a larger pressure drop. This paper discusses the methods to determine the causes of the instability, the measurements performed, analysis of the measurement results and measures implemented to eliminate further problems.

This paper includes a discussion of the possible flow instability generated by the insertion of thermistors in the flow path to perform temperature measurements of volume flow devices. The Flow Laboratory regularly receives volumetric flow devices and to calculate standardised flow conditions, it is necessary to measure the gas temperature and pressure at the unit under test (UUT) location. Emphasis is given to the determination of the immersion depth and measurement position of the temperature sensor in the flow path to ensure no, or negligible, disturbances in the gas flow path.

---

## 1. Introduction

The National Metrology Institute of South Africa (NMISA), is mandated to provide measurement traceability to the South African industry. The NMISA Gas Flow Laboratory is ISO/IEC 17025 accredited for volume gas flow measurements in the flow range 5 mL/min to 50 000 mL/min.

Interlaboratory comparison and intermediate check measurements performed in the flow ranges 5 mL/min to 50 mL/min and 40 000 mL/min up to 50 000 mL/min have indicated unstable behaviour resulting in  $E_n$  values greater than one and reference standards deviating with more than the calculated measurement uncertainty [1]. Possible causes for this flow instability were identified and measurements were performed to investigate and solve these instabilities.

As the laboratory receives numerous volumetric flow devices (bubble flow meters) for calibration, temperature and pressure measurements at the

flow device's location must be performed to enable standard flow condition calculations. Measurements were performed with the thermistor positioned in the flow path at the inlet and the outlet of the unit under test to determine the best location for these measurements. Measurements were performed with the unit under test positioned to the outlet of the reference standard.

## 2. The NMISA Gas Flow Laboratory

The Gas Flow Laboratory is part of the Physical Metrology group of NMISA. Gas flow (volume gas flow) calibration services are offered in the flow range 5 mL/min to 50 000 mL/min. The laboratory is ISO/IEC 17025 accredited since March 2017. Nitrogen gas is used as the calibration medium. Typical instruments received for calibration include mass flow controllers, mass flow meters, bubble flow meters and rotameters.

The Flow Laboratory is equipped with two secondary reference gas flow standards as

highest-level standards, a Bios ML-800 positive displacement piston prover and Fluke molbloc-L laminar flow elements (LFE). As the laboratory is not equipped with a primary gas flow standard, the secondary reference standards are calibrated by National Metrology Institutes with relevant calibration and measurement capabilities (CMCs) in the BIPM key comparison database (KCDB). Traceability to international standards is therefore imported from these National Metrology Institutes [1].

### 3. Flow instability evaluation

The flow ranges 5 mL/min to 50 mL/min and 40 000 mL/min to 50 000 mL/min were investigated.

#### 3.1 Flow range 5 mL/min to 50 mL/min

Currently the NMISA Gas Flow Laboratory is ISO/IEC 17025 accredited to perform measurements in the flow range 5 mL/min to 50 mL/min with a CMC value of 2% of reading. The measurements performed in this flow range indicate unstable behaviour.

Reference standards and equipment used in this flow range are:

- a) Two piston prover flow cells, ML-800-3 (50 sccm) and ML-800-10 (500 sccm)
- b) Two molbloc-L laminar flow elements, 5E1-VCR-V-Q (50 sccm) and 1E2-VCR-V-Q (100 sccm)
- c) 50 sccm mass flow controllers

Possible causes of the instability in this flow range were identified as:

- a) Stability of the reference standard
- b) Flow disturbances in the gas flow stream
- c) Tubing – length and diameter
- d) Moisture entering the flow line
- e) Restrictions (valves or adapters) in the flow line
- f) Environmental conditions
- g) Pressure drop over flow path
- h) Stabilization time
- i) Cleanliness of flow medium

Currently, the stability of the piston prover low flow cell, ML-800-3 (50 sccm), is suspected as being the main cause of the instability problem in this flow range. Since acquiring this flow cell, it has been sent back to the manufacturer twice because of malfunction (sticky piston) and instability problems. Communication with the manufacturer resulted in advice regarding filtration in the flow path. It seems the filter in place prior to the flow cell to ensure clean (contamination free) nitrogen

entering the flow cell and to smooth out flow fluctuations has a price. Stabilization time is long. What is long? The laboratory's calibration procedures prescribe a stabilization time of at least one hour before performing calibrations. As the calibration procedures prescribe four sets of measurements (ten readings per measurement set) per calibration point, a longer than one-hour stabilization time may cause the calibration of an instrument run over more than one day.

The Gas Flow Laboratory has been renovated to lengthen the flow path from the gas cylinder to the inlet of the unit under test. Lengthening the flow path includes using multiple stages pressure regulators to improve stabilization of the gas flow and implement a more sufficient pressure drop – 600 kPa to 500/400 kPa to 400/300 kPa. Before renovating the laboratory, ¼" tubing of approximately 1,5 meters was used to directly connect the outlet of the nitrogen gas cylinder to the inlet of the measuring path. The laboratory layout with lengthened flow path is shown in Figure 1.



Figure 1: Laboratory layout.

Intermediate checks between similar and overlapping flow cells and laminar flow elements were performed to investigate the flow instability in this flow range. Firstly, piston prover flow cells and laminar flow elements of the same flow ranges were compared – 50 sccm: ML-800-3 against 5E1-VCR-V-Q and 500 sccm: ML-800-10 against 5E2-VCR-V-Q. Thereafter the two flow cells ML-800-3 (50 sccm) and ML-800-10 (500 sccm) were compared to the 1E2-VCR-V-Q (100 sccm) laminar flow element [3].

Tables 1 to 6 report intermediate check results between different reference standards.

**Table 1:** Reference standards: LFE 5E1-VCR-V-Q (S/N 7029) versus ML-800-3 (S/N 128014).

Reference Value (Bios)	Indicated Value (LFE)	Correction	Expanded Uncertainty (k=2)	Meet Acceptance Criteria
mL/min	mL/min	mL/min	mL/min	
5.182	5.177	0.005	0.020	Yes
15.150	15.084	0.066	0.110	Yes
25.145	25.157	-0.012	0.165	Yes
30.042	30.150	-0.108	0.190	Yes
39.688	40.061	-0.373	0.172	No
48.953	49.437	-0.484	0.207	No

**Table 2:** Reference standards: LFE 5E2-VCR-V-Q (S/N 7030) versus ML-800-10 (S/N 135209).

Reference Value (Bios)	Indicated Value (LFE)	Correction	Expanded Uncertainty (k=2)	Meet Acceptance Criteria
mL/min	mL/min	mL/min	mL/min	
6.030	6.064	-0.034	0.043	Yes
50.444	50.527	-0.084	0.151	Yes
149.767	149.897	-0.130	0.414	Yes
250.001	250.272	-0.271	0.673	Yes
299.658	299.965	-0.307	0.795	Yes
399.407	399.826	-0.420	1.056	Yes
498.464	498.880	-0.416	1.315	Yes

**Table 3:** Reference standards: LFE 1E2-VCR-V-Q (S/N 7481) versus ML-800-3 (S/N 128014).

Reference Value (LFE)	Indicated Value (Bios)	Correction	Expanded Uncertainty (k=2)	Meet Acceptance Criteria
mL/min	mL/min	mL/min	mL/min	
5.478	5.491	-0.012	0.016	Yes
14.999	15.052	-0.053	0.043	No
25.205	25.282	-0.077	0.106	Yes
30.710	30.840	-0.130	0.099	No
40.494	40.654	-0.160	0.110	No
49.438	49.643	-0.205	0.123	No

**Table 4:** Reference standards: LFE 1E2-VCR-V-Q (S/N 7481) versus ML-800-10 (S/N 135209).

Reference Value (LFE)	Indicated Value (Bios)	Correction	Expanded Uncertainty (k=2)	Meet Acceptance Criteria
mL/min	mL/min	mL/min	mL/min	
5.375	5.388	-0.013	0.015	Yes
14.902	14.920	-0.018	0.028	Yes
25.114	25.137	-0.023	0.044	Yes
30.623	30.640	-0.017	0.055	Yes
40.412	40.425	-0.013	0.072	Yes
49.363	49.375	-0.012	0.088	Yes

**Table 5:** Reference standards: LFE 1E2-VCR-V-Q (S/N 7481) versus ML-800-3 (S/N 128014).

Reference Value (LFE)	Indicated Value (Bios)	Correction	Expanded Uncertainty (k=2)	Meet Acceptance Criteria
mL/min	mL/min	mL/min	mL/min	
5.478	5.491	-0.012	0.023	Yes
14.999	15.052	-0.053	0.085	Yes
25.205	25.282	-0.077	0.282	Yes
30.710	30.840	-0.130	0.234	Yes
40.494	40.654	-0.160	0.248	Yes
49.438	49.643	-0.205	0.247	Yes

**Table 6:** Reference standards: LFE 1E2-VCR-V-Q (S/N 7481) versus ML-800-10 (S/N 135209).

Reference Value (LFE)	Indicated Value (Bios)	Correction	Expanded Uncertainty (k=2)	Meet Acceptance Criteria
mL/min	mL/min	mL/min	mL/min	
5.375	5.388	-0.013	0.019	Yes
14.902	14.920	-0.018	0.035	Yes
25.114	25.137	-0.023	0.047	Yes
30.623	30.640	-0.017	0.060	Yes
40.412	40.425	-0.013	0.075	Yes
49.363	49.375	-0.012	0.098	Yes

Table 1 reports measurements with the two reference standards deviating from one another more than the calculated measurement uncertainty at flow rates 40 mL/min and above. Table 2 indicates reference standards complying with the acceptance criteria in the flow range up to 50 mL/min. Table 3 shows measurement results with four out of six measurement points where the reference standards deviated more than the calculated measurement uncertainty. Table 1 and Table 3 report measurements with the ML-800-3 flow cell as one of the two comparing reference

standards. Table 4 to Table 6 report measurements with the acceptance criteria for intermediate checks met.

Table 3 to Table 6 indicate results for measurements performed comparing the ML-800-3 and ML-800-10 flow cells against the same laminar flow element, 1E2-VCR-V-Q, at the same measurement points over the flow range 5 mL/min to 50 mL/min. However, the measurement uncertainty for the measurements in Table 3 and Table 4 were calculated evaluating the repeatability of the error using the standard deviation of the mean and in Table 5 and Table 6 evaluating the repeatability of the error based on maximum deviation, using the standard deviation value instead of the standard deviation of the mean.

The ML-800-10 flow cell complied with the acceptance criteria irrespective of how the repeatability of the error is evaluated in the uncertainty measurement evaluation or against which other reference standard it is compared to. The ML-800-3 flow cell complied only where the repeatability of the error was treated based on maximum deviation, using the standard deviation value and not the standard deviation of the mean - only complying when the measurement uncertainties have been increased.

**3.2 Flow range 40 000 mL/min to 50 000 mL/min**  
Currently the NMISA Gas Flow Laboratory is ISO/IEC 17025 accredited to perform measurements in the flow range 40 000 mL/min to 50 000 mL/min with a CMC value of 0,5% of reading. The measurements performed in this flow range indicate unstable behavior.

Reference standards and equipment used in this flow range:

- a) One piston prover flow cell, ML-800-44 (50 SLM)
- b) One molbloc-L laminar flow element, 3E4-VCR-V-Q (50 SLM)
- c) 50 SLM mass flow controller

Of all the possible causes of instability, insufficient pressure drop over the flow path has been identified as being the main cause of the instability problem in this flow range.

Again, intermediate checks between similar and overlapping flow cells and laminar flow elements were performed to investigate the flow instability in this flow range. Firstly, the piston prover flow cell and laminar flow element of the same flow range

were compared – 50 SLM: ML-800-44 against 3E4-VCR-V-Q. Thereafter the two flow cells, ML-800-44 (50 SLM) and ML-800-75 (100 SLM) were compared.

Tables 7 to 8 report intermediate check results between the different reference standards.

**Table 7:** Reference standards: LFE 3E4-VCR-V-Q (S/N 7028) versus ML-800-44 (S/N 128098).

Reference Value (Bios)	Indicated Value (LFE)	Correction	Expanded Uncertainty (k=2)	Meet Acceptance Criteria
mL/min	mL/min	mL/min	mL/min	
534.06	542.25	-8.19	20.57	Yes
5028.22	5036.06	-7.84	23.54	Yes
15053.53	15061.14	-7.61	45.24	Yes
25008.40	25006.61	1.79	66.27	Yes
30037.83	30041.92	-4.09	69.27	Yes
40007.98	40000.79	7.18	94.72	Yes
49272.40	49255.09	17.31	115.00	Yes

**Table 8:** Reference standards: ML-800-44 (S/N 128098) versus ML-800-75 (S/N 136463).

Reference Value (ML-800-44)	Indicated Value (ML-800-75)	Correction	Expanded Uncertainty (k=2)	Meet Acceptance Criteria
mL/min	mL/min	mL/min	mL/min	
15154.85	15133.83	21.02	35.24	Yes
25042.28	24979.90	62.38	69.27	Yes
30154.23	30084.93	69.30	93.93	Yes
40205.38	40017.05	188.32	130.21	No
47642.75	47463.08	179.68	259.41	Yes

Table 7 and Table 8 report measurements performed with the lengthened flow path using multiple stages pressure regulators inducing a pressure drop from 600 kPa to 300 kPa.

Table 7 reports intermediate checks performed in the flow range 500 mL/min to 50 000 mL/min which indicated good agreement between the two reference standards, the ML-800-44 flow cell and the 3E4-VCR-V-Q laminar flow element. Deviations between the two reference standards agree within the calculated measurement uncertainty.

An alternative method was used to check measurement results above 10 000 mL/min. Two flow cells, ML-800-44 and ML-800-75, with overlapping flow ranges, were used to perform the measurements being reported in Table 8. At 40 000 mL/min the acceptance criteria were not met.

#### 4. Temperature and pressure measurements at the location of the unit under test

To calibrate volume flow meters, the NMISA Gas Flow Laboratory measures the temperature and pressure of the gas in the flow path at the location of the UUT to enable standard flow condition calculations. A reference thermometer (thermistor) and barometer are used respectively [2].

To determine the preferred position for measuring the temperature and pressure, measurements were performed with the thermistor positioned to the inlet and to the outlet of the unit under test. The unit under test (piston prover) was connected to the outlet of the reference standard (laminar flow element); the outlet of the unit under test was open to atmosphere. A ¼” union cross adapter is used for the connection of the thermistor and barometer. As the flow path is only a ¼” in width, there is no other option than to position the thermistor in the middle of the connector.

Figures 2 and 3 show the calibration setup with the thermistor and barometer connected to the inlet of the unit under test.



**Figure 2:** Thermistor and barometer connected to the inlet of the unit under test.



**Figure 3:** Thermistor and barometer connected to the inlet of the unit under test.

Table 9 reports calibration results with the thermistor connected to the inlet of the unit under test.

**Table 9:** Thermistor positioned at the inlet of unit under test.

Flow values are standardised to a reference temperature of 0 °C and reference pressure of 101.325 kPa				
UNIT UNDER TEST		Reference Flow Rate (mL/min)	Correction (Standardised Flow Rate) (mL/min)	Expanded Uncertainty (k=2) (mL/min)
Volumetric Flow Rate (mL/min)	Calculated Standardised Flow Rate (mL/min)			
639.736	508.183	505.691	-2.492	1.539
1270.918	1008.986	1004.486	-4.500	2.631
1904.123	1509.965	1504.523	-5.442	2.877

Figures 4 and 5 show the calibration setup with the thermistor and barometer connected to the outlet of the unit under test.



**Figure 4:** Thermistor and barometer connected to the outlet of the unit under test.



**Figure 5:** Thermistor and barometer connected to the outlet of the unit under test.

Table 10 reports calibration results with the thermistor connected to the outlet of the unit under test.

**Table 10:** Thermistor positioned at the outlet of unit under test.

Flow values are standardised to a reference temperature of 0 °C and reference pressure of 101.325 kPa				
UNIT UNDER TEST		Reference Flow Rate (mL/min)	Correction (Standardised Flow Rate) (mL/min)	Expanded Uncertainty (k=2) (mL/min)
Volumetric Flow Rate (mL/min)	Calculated Standardised Flow Rate (mL/min)			
635.981	505.952	504.738	-1.214	0.965
1264.635	1005.602	1003.919	-1.683	1.778
1894.333	1505.862	1504.006	-1.856	2.829

The correction values differ between the inlet and outlet measurement positions with more than the calculated measurement uncertainty. For volumetric instruments like bubble flow meters the temperature and pressure measurements can only be measured at the inlet of the instrument.

## 5. Conclusion

From the measurements performed, it can be concluded that the behaviour of the ML-800-3 flow cell is indeed the cause of  $E_n$  values larger than one and reference standards deviations exceeding the calculated measurement uncertainty in the low flow range. It is recommended that one more set of measurements is performed in the flow range 5 mL/min to 50 mL/min to assign the reason for the instability behaviour in this flow range to the ML-800-3 flow cell. This set of measurements will compare the two molbloc-L laminar flow elements; 5E1-VCR-V-Q and 1E2-VCR-V-Q, thus the

50 sccm laminar flow element against the 100 sccm laminar flow element over this flow range.

The measurement results in the flow range above 40 000 mL/min showed satisfactory results. However, it is recommended that measurements are again performed in this flow range with the two reference standards, ML-800-44 flow cell and 3E4-VCR-V-Q laminar flow element. As these two reference standards are currently the only available instruments for the flow range up to 50 000 mL/min, it is recommended that measurements are performed using a needle valve to control the flow rate instead of a mass flow controller.

More measurements must be performed to investigate the unit under test temperature and pressure measurement location. These measurements must also be performed using the piston prover as reference standard where instruments are positioned in line with the reference standard.

## References

- [1] Jonker D, Högström R, Dlamini M W, “Bilateral Comparison between NMISA and VTT-MIKES – Part of the NMISA Flow Laboratory Journey to Accreditation”, in *Flomeko 2016 Conference Proc.*, 2016.
- [2] Dlamini M, Jonker D, Molefe M R, “Volume Flow Rate vs Standardised (Mass) Flow Rate in Gas Flow Measurements”, in *Test and Measurement 2018 Conference and Workshop Conference Proc.*, 2018.
- [3] NMISA Internal Report, NMISA-18-00246: *Flow Instability Evaluation – 5 mL/min to 50 mL/min & 40 L/min to 50 L/min*, 2019.

# Cavitating Herschel Venturi nozzle test rig

H. Warnecke<sup>1</sup>, C. Kroner<sup>2</sup>, D. Schumann<sup>2</sup>, J. Tränckner<sup>3</sup>

<sup>1</sup>*Physikalisch-Technische Bundesanstalt, Heiko.Warnecke@ptb.de, Braunschweig, Germany*

<sup>2</sup>*Physikalisch-Technische Bundesanstalt, Braunschweig, Germany*

<sup>3</sup>*University of Rostock, Rostock, Germany*

*E-mail (corresponding author): Heiko.Warnecke@ptb.de*

---

## Abstract

Cavitation is a phenomenon, which is typically associated with negative effects, for example damage at propellers in water. However, there are various applications in which cavitation is exploited advantageously such as injection nozzles in diesel engines or cleaning with an ultrasonic bath. A new application is the deployment of cavitating nozzles in liquid flow measurements. The novelty of the application means from a metrological point of view the requirement to analyse potential influencing factors on the measurement quality in-depth. These comprise among others the installation conditions of the nozzles in a test rig or the additivity of flows when more than one nozzle is used. Furthermore, comprehensive insights into cavitation processes for different liquids are desirable with the view on a broad range of cavitation nozzle applications in liquid flow measurements.

First investigations are carried out for different fluids including liquid mixtures such as white spirits. A detailed analysis of the pressure measurement in front and at the back of the nozzles gives further information about how fast the flow rate changes and about the cavitation process itself. This is of relevance for a possible application, in which flow rate profiles are used to assess flow meter performance under dynamic loads. Such load profiles e.g. serve as input for a test rig with cavitation nozzles to assess the performance of domestic water meters.

---

## 1. Introduction

Cavitation occurs if a liquid pressure is lower than the local vapour pressure and a gaseous saturated steam volume is formed. The appearance of this cavitation ranges from single bubbles to stable cavitation layers. In case of a nozzle throat, the cavitation layer is a cylindrical skirt around the liquid flow. On the one hand this cavitation is a disadvantage in applications, where the gas bubbles collapse and cause damage to structural components for instance at propellers. On the other hand, cavitation is exploited in ultrasonic cleaning baths, wastewater treatment and to homogenize suspended particles in colloidal liquids. Another application of cavitation is the use in flow metrology. Known from gas flow measurements with critical flow venturi nozzles (CFVN) the concept of a stable and reproducible mass flow is transferred to liquid flows deploying cavitation nozzles.

In first experiments nozzles are installed in a test rig with water as liquid. The measurements proves the feasibility of using nozzles as liquid flow controlling device [2],[3]. The experiments are performed with toroidal gas nozzles

referred to ISO: 9300 [1]. Furthermore, numerical investigations by Brinkhorst [4] show that the deployment of Herschel Venturi nozzles instead of toroidal Venturi nozzles leads to an improved flow stability. The difference between the nozzle typ is a cylindrical throat in the Herschel Venturi nozzle and the difference of stability is on the order of one magnitude.

Another aspect affecting flow stability is related to the ratio of upstream and downstream pressure. To ensure that cavitation occurs, the ratio of downstream to upstream pressure needs to be below 0.75 [3]. For all measurements presented in the paper the ratio is less than 0.6. This is well below the critical value of 0.75. Above this value cavitation inception, and thereby the flow, becomes unstable [3]. The basics can be described by Bernoulli's principle. If the pressure of the liquid drops below the local vapour pressure, cavitation begins in the nozzle throat and a further decrease of the liquid pressure is not possible. In this case the flow is regulated by the absolute upstream pressure and depends on that stability. Thus, it became clear that monitoring the pressure at temporally higher resolution and more precise as previously, would provide a deeper insight into the

performance of the cavitating nozzles. Therefore, four pressure sensors are installed as shown in Figure 1, with two sensors measuring the upstream pressure and two the downstream pressure. The time resolution of the pressure sensor with temporally higher resolution is about 100 ms and the resolution of the precise pressure sensor in amplitude is on the order of 1 mbar.

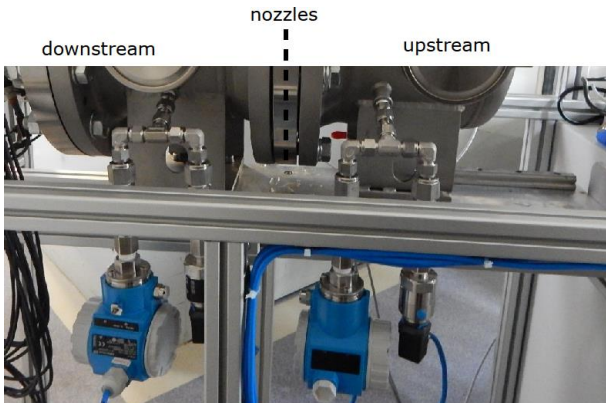


**Figure 1:** Pressure sensors upstream and downstream of the cavitating nozzles.

## 2. Single and multiple nozzle flows

In a first step the individual Herschel Venturi nozzles are characterised in a single holder by water flow measurements on a known test rig with different upstream pressures from 2 bar to 5 bar. Afterwards the six nozzles are installed in a cavitation nozzle apparatus added to the test rig and the characterization repeated for the whole ensemble. Following this, the flow rate for cases with multiple nozzles open simultaneously is investigated.

For the experiments six nozzles with a nominal throat diameter of 0.74 mm, 1.4 mm and 2.6 mm are selected (Table 1) to enable the relevant flow rates of a load profile, discussed in section 4. With different nozzles of the same nominal diameter the reproducibility of the nozzle manufacture can be assessed by flow rate measurements. The flow rates for the individual nozzles cover a range from 37 l/h to 588 l/h and are measured at a liquid temperature near ambient temperature of 22 °C with a maximum deviation of 2 °C. The mean variation of the temperature within one flow rate measurement is  $\pm 0.1$  °C.

**Table 1:** Diameter  $d$  of the nozzle throats, flow rate  $Q$  at pressure  $p$  and the slope  $b$  of the flow against upstream pressure.

Nozzle nr. $i$	Diameter $d$ mm $\pm 1 \mu\text{m}$	Upstream pressure $p$ bar $\pm 0.01$ bar	Flow $Q$ l/h $\pm 0.1 \%$	Slope $b$ l/h/bar
1	0.740	3.999	42.69	$5.4 \pm 0.2$
2	0.738	3.996	42.65	$5.4 \pm 0.2$
3	1.396	4.005	151.80	$19.2 \pm 0.4$
4	1.397	4.005	152.40	$19.5 \pm 0.5$
5	1.393	4.004	154.50	$19.5 \pm 0.5$
6	2.601	4.013	527.80	$71.0 \pm 1.4$

The function of the cavitating nozzle apparatus is the simultaneous use of multiple nozzles to extend the range of generated flow rates up to the combined flow of six nozzles. The complete experimental setup is shown schematically in Figure 2. It consists of a conventional mass flow test rig in which a cavitation nozzle apparatus is integrated. As consumption is typically determined as volume flow, mass flow is converted to volume flow using the current medium's density and then considered in these investigations.

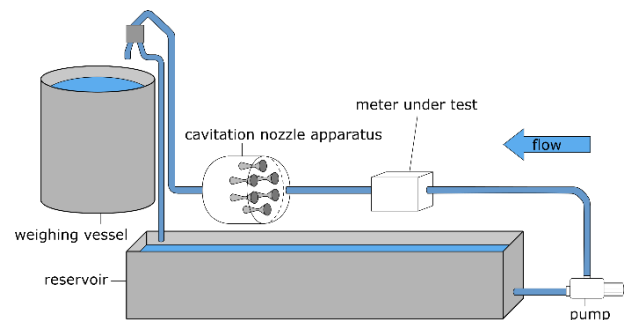


**Figure 2:** Schematic drawing of the test rig in the set-up.

### 2.1 Flow generated by individual Herschel Venturi nozzles

The correlation between flow rate and upstream pressure for each nozzle is important to know for an estimate of the flow generated by multiple nozzles, as higher flow rates (e.g. 1000 l/h) cause a relevant decrease (0.06 bar) in pressure. To describe the relation between flow rate and upstream pressure a regression line is fitted to the measurement data. An example for the regression is shown for nozzle 6 (Table 1) in Figure 3 at the top and is summarised for the other nozzles at the bottom. The expanded measurement uncertainty of the test rig is 0.1 % and the standard deviation for most flow rate measurements is less than 0.1 %. An exception are the two measurements with an upstream pressure below 3 bar, when nozzle 6 is characterised. The error bars for the measurement with these nozzles are shown in Figure 3 (top).

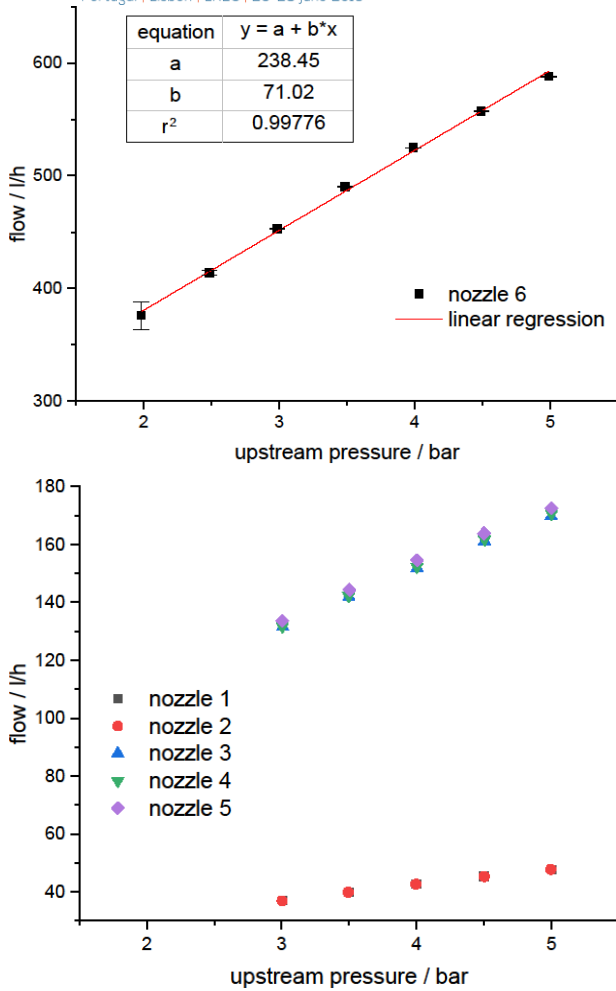


**Figure 3:** Flow rate against absolute upstream pressure, with different Y-axis. Top: Nozzle 6 and fitted regression line with correlation coefficient  $r^2$ . Bottom: 5 different nozzles with a diameter of 0.74 mm and 1.4 mm, regression values in Table 1.

The slope  $b$  of the regression line is determined for each nozzle from the experimental data plotted in Figures 3. The values are summarised in the last column of Table 1 and quantify the above-mentioned flow rate dependency of the upstream pressure for the nozzles. With this relation a reduction of the upstream pressure mean variation directly leads to a more stable flow rate of the nozzle. There is no significant difference in the correlation between upstream pressure and flow rate for nozzles with the same diameter. A linear relationship exists between the flow rate of nozzles with different diameter and the slope  $b$ .

## 2.2 Multiple nozzle flow

After the characterisation of the individual nozzles these are set into the cavitation nozzle apparatus to generate multiple nozzle flows. As the pressure sensor in the single nozzle holder is mounted closer to the individual

measured nozzle than in the test rig, the correlation between upstream pressure and flow rate is investigated in the single nozzle holder. To take the different installation conditions into account, the characterization of the individual nozzles is repeated. Because the position of the pressure sensors is about 70 mm further upstream in the test rig than in the single nozzle holder the flow rates had a significant offset. With the flow rate determined in the test rig at an upstream pressure of  $4 \pm 0.01$  bar the theoretical flow of two or more nozzles is calculated as the sum  $Q_{theo,j}$  of the individual flow rates  $Q_i$ , corrected for the decrease in pressure due to higher flow rates, according to equation (1)

$$Q_{theo,j} = \sum_i (Q_i + (p_j - p_i) * b_i) \quad (1)$$

with:

$b_i$ : calculated slope of each nozzle

$p_i$ : upstream pressure of single nozzle flow

$p_j$ : upstream pressure of multiple nozzle flow.

The relative deviation of the flow rate for the different nozzle combinations is calculated from equation (2) and given in Table 2

$$rel. dev. = \frac{Q_{exp} - Q_{theo}}{Q_{theo}} \quad (2)$$

**Table 2:** Nozzle addition, calculated and measured flows.

Combined nozzles nr.	Calculated flow $Q_{theo}$ l/h	Measured flow $Q_{exp}$ l/h	Rel. dev. %
1+2	85.40	85.34	-0.071
1+3	194.57	194.51	-0.031
1+2+3	237.25	237.15	-0.040
3+4	303.48	303.49	0.004
1+3+4	346.16	346.15	-0.002
1+2+3+4	388.86	388.79	-0.018
3+4+5	456.54	456.56	0.005
1+3+4+5	498.89	498.88	-0.002
1+2+3+4+5	541.78	541.59	-0.037
1+6	570.59	570.29	-0.053
1+2+6	612.82	612.37	-0.074
3+6	679.11	678.69	-0.062
1+3+6	721.01	720.58	-0.060
1+2+3+6	763.03	762.45	-0.077
3+4+6	829.08	828.63	-0.055
1+3+4+6	870.89	870.48	-0.047
1+2+3+4+6	913.73	913.20	-0.058
3+4+5+6	980.32	979.99	-0.034
1+3+4+5+6	1022.94	1022.33	-0.060
1+2+3+4+5+6	1064.63	1063.74	-0.084

The results of the simultaneously cavitating nozzles are displayed in Figure 4 as relative deviation of the measured and the calculated flow rates. The error bars contain the overall uncertainty of the test rig (0.1 %) and the standard deviation of the measurements. The calculated flow rate based on the single nozzle measurements is accurate to 0.01 % in comparison with

the flow rate measurement at multiple nozzle operation. This result confirmed the assumption that the flow rate of multiple nozzles can be calculated using single nozzle flow rates, when the absolute upstream pressure and the correlation between upstream pressure and flow rate are known. Except for two measurements the deviation is negative but within the error. This could indicate a further upstream pressure loss between the pressure sensor and the nozzle holder, which is not included in the calculations. A comprehensive upstream pressure measurement would provide an insight into the pressure distribution that has a direct proportional influence on the flow rate of the nozzle.

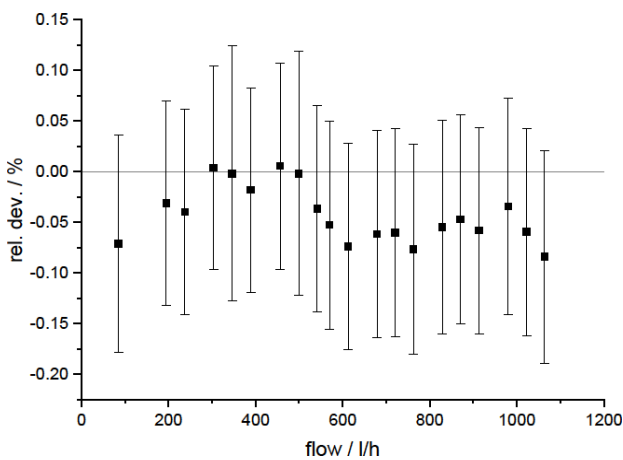


**Figure 4:** Relative deviation of calculated and measured nozzle flow rates against calculated flow rates. Ascending order as Table 2.

### 3. Different liquids

To understand the cavitation phenomenon in liquids it is necessary to investigate other liquids than water as well. One of the most frequently used liquids in flow applications is fuel. The typical substitute white spirit is used for the cavitation nozzle flow analysis. A second commonly used liquid in many applications is cleaner solvent. These two liquids are accessible easily and have different vapour pressure curves than water. This is expected to cause a different cavitation layer and flow rates. Furthermore, there is a potential for effects due to the different constituents that make up the liquid. As presented by Keller [6] the cavitation inception especially depends on the presence of nuclei and their size in a liquid.

For the investigations with different liquids nozzle 2 (Table 1) with a diameter of 0.74 mm is set in a second test rig for white spirits and the flow rate is measured against a gravimetric standard. Furthermore, the flow rate of nozzle 2 is measured in a third test rig operating with a cleaner solvent called Haku, which has a similar density to that of the white spirit (Table 3). The set-up of the two FLOMEKO 2019, Lisbon, Portugal

other test rigs is analogue to the first test rig run with water and single nozzle holder, described in Figure 2. The experiments are also done with the same temperature at  $22\text{ }^{\circ}\text{C} \pm 2\text{ }^{\circ}\text{C}$  and an opened downstream outlet. Due to the different densities of the liquids it is reasonable to compare the mass flow in this section.

**Table 3:** Liquids used for flow measurements with cavitating nozzles and the physical properties density, vapour pressure and kinematic viscosity measured at  $20\text{ }^{\circ}\text{C}$ .

Medium	Principal constituents	Density g/cm <sup>3</sup>	Vapour pressure mbar	Viscosity mm <sup>2</sup> /s
White spirit	Hydrocarbon, C10 – C13, n-Alkane, iso-Alkane, cyclic compound	0.785	0.5	1.2
Haku 1025-310	Hydrocarbon, C11 – C14, iso-Alkane, cyclic compound	0.761	0.6	1.3
Water	Tap water	0.998	23.4	1.0

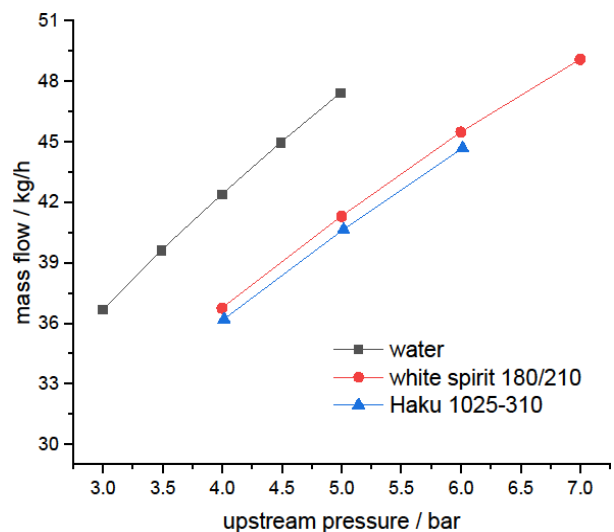


**Figure 5:** Nozzle diameter 0.74 mm; mass flow against upstream pressure for water, white spirit and a cleaner solvent, called Haku 1025-310.

The measurements for the different liquids water, white spirit and cleaner solvent are shown in Figure 5. The expanded measurement uncertainty ( $k = 2$ ) of the test rig for white spirits is 0.05 % and 0.3 % for the cleaner solvent test rig. The standard deviation of the measurement carried out with water (about 0.01 kg/h) is the same as the standard deviation associated with the cleaner solvent (about 0.01 kg/h). The standard deviation of the measurement with white spirit is about 0.05 kg/h because of a lower number of measurement points, but in

the same order of magnitude. There is a significant difference between the flow rate measurements using water, white spirit and cleaner solvent. The white spirit and the cleaner solvent have a comparable mass flow and the same slope of  $4.2 \pm 0.2$  l/h/bar, determined by linear regression. The difference in the flow measurements between water and white spirit is investigated for a second nozzle (2.6 mm in diameter as nozzle 6) and plotted in Figure 6. The flow rate of white spirit is about 13 % (0.74 mm diameter nozzle) less than the flow rate of water, 12 % less respectively for the nozzle with a 2.6 mm diameter.

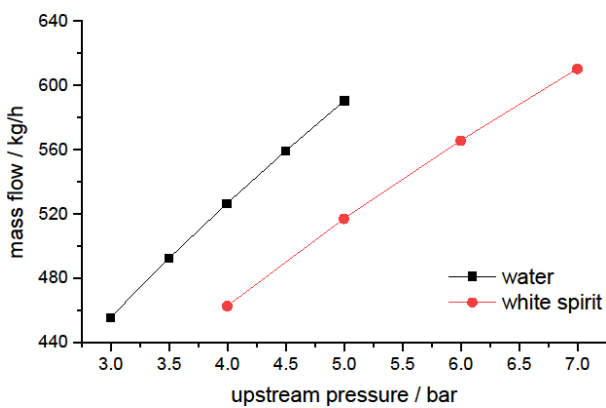


Figure 6: Nozzle diameter 2.6 mm; mass flow of water and white spirit.

For a nozzle diameter of 1.4 mm and two liquids the flow is shown against the upstream pressure in Figure 7. The offset between the two liquids is on the same order of magnitude as the flow difference of the nozzles with 0.74 mm and 2.6 mm and increases with the flow rate. Potential effects on this offset could have been caused by different vapour pressure curves or different suspended particle concentrations in the liquids. Thus, with cavitating nozzles, a stable flow rate could also be realised with the liquid mixtures in addition to water.

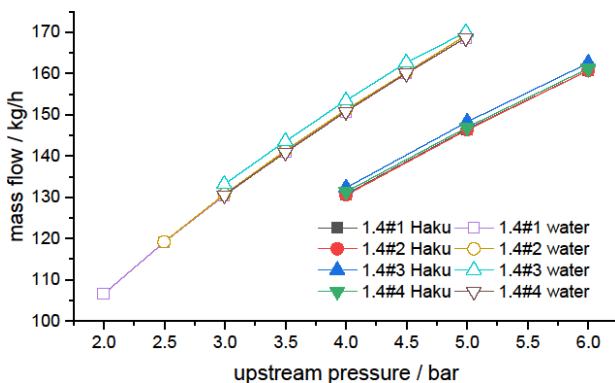


Figure 7: Flow measurement of four different nozzles, same nominal diameter 1.4 mm and two liquids (water and cleaner solvent Haku).

#### 4. Generating load profiles

With the Herschel Venturi nozzles integrated in a water test rig fast flow rate changes (about 100 ms) and a wide range of flow rates ( $10$  l/h -  $10^4$  l/h) could be realised, to generate load profiles close to actual consumption profiles [2]. These are current investigations about the water meter calibration procedure in which load profiles are needed. Based on a model profile load changes are generated with the test rig. The diagram in Figure 8 (top) shows the modelled profile in black as well as the generated flow rates in red. The profile in red considers the fact, that with the current setup 23 different flow rates can be generated. To verify the flow rates and the transitions, the weighing signal is recorded with a sampling rate of 2 Hz and a resolution of 1 g. The pressure variations are monitored with a sampling rate of 5 Hz and a resolution of 0.1 mbar. The third profile shown in blue in Figure 8 (top) is the flow rate calculated from the slope of the dynamic weighing values for each step of the load profile. The flow rate determined from the balance values in general fits with the generated flow rate, except for the time between about 90 s to 135 s. This discrepancy is caused by a controller failure, which results in one nozzle not opening as intended. Within the performance characteristics of the dynamic balance measurement technique there is no significant difference between the profile generated in the test rig and the balance measured profile.

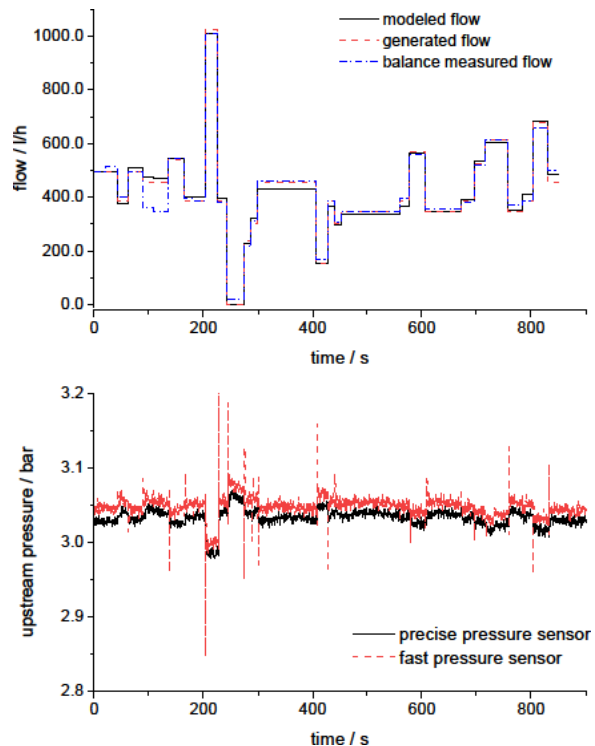


Figure 8: Top: model, generated and balance measured load profile; bottom: upstream pressure response of two different pressure sensors.

To investigate the quality of the flow rate change, the upstream pressure is measured with two different sensors as illustrated in Figure 8 (bottom). The offset between the two sensors before calibration is retained for better readability of the data. Both pressure sensors show peaks concurring with changes in the flow rate. In Figure 9 an enlarged section of the upstream pressure and the dynamic balance value is shown. The maximum amplitude measured with the fast pressure sensor is up to 7 % above the average pressure. The pressure excursion lasts about 1 s, but no influence on the balance signal and thereby the flow rate at the sampling rate of 500 ms is seen. Within the scope of the dynamic balance measurement technique there is no significant difference between the profile to be generated in the test rig and the profile measured by the balance. Consequentially, the dynamic balance signal can be used to verify the flow rates during a load profile generation

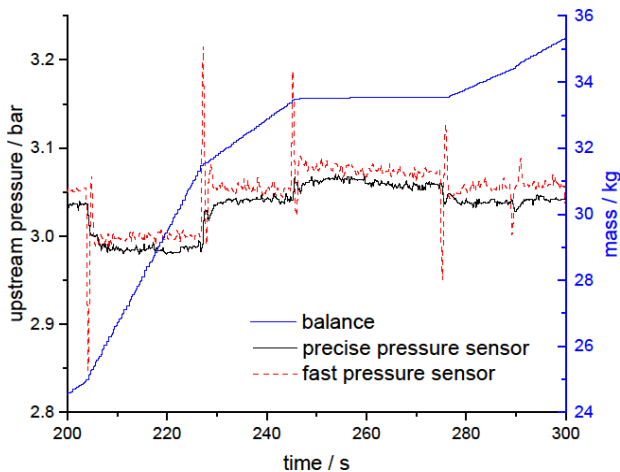


Figure 9: Upstream pressure peaks and mass measured by balance.

## 5. Conclusions

The experimental results presented in this paper show, that the flow rates of the individual nozzles simply sum up to the expected total flow rate, which is demonstrated based on the flow rates measured with six cavitating Herschel Venturi nozzles at the same time (Table 2). As expected, the flow rate decreases with upstream pressure loss. That could be corrected in case of a sufficiently known correlation between upstream pressure and flow rate.

Furthermore, a constant mass flow can be generated with different liquids, including liquid mixtures. The white spirit and the cleaner solvent in contrast to water have different flow rates for an identical upstream pressure (Figure 5). This difference is likely caused by different cavitation layer thicknesses in the nozzles. Apart from the vapour pressure other medium dependent properties

such as viscosity, density or compressibility could also affect the cavitation in the nozzle and thereby the flow measurement. This requires further investigations.

By an ensemble of Herschel Venturi nozzles load profiles can be generated. The values of the balance indicate an instantaneous flow rate change, whereas the upstream pressure sensors record a pressure pulse that takes about 1 s. This is caused by closing and opening the nozzles and could have an influence on the cavitation layer and thereby the flow rates at that time. The effect on the flow rate is temporally below the current detection limit of the balance. These experiments are a first step to understand the phenomenon of a stable flow in cavitating Herschel Venturi nozzles and their application in a test rig and could serve as basis for future research.

## 6. Acknowledgement

This research is supported by the TransMeT project “Prüfung von Wasserzählern unter realitätsnahen Bedingungen”, which is carried out in cooperation between the Physikalisch-Technische Bundesanstalt and Verband der deutschen Wasser- und Wärmezählerindustrie (VDDW).

## References

- [1] ISO 9300: *Measurement of gas flow by means of critical flow Venturi nozzles*, 2005.
- [2] Schumann D, Wendt G, Tränckner J, “Development of a calibration process for water meters close to real word conditions”, in *FLOMEKO*, 2016.
- [3] Schumann D, Kroner C, “Using Cavitation Metrologically”, in *ISFFM Publications*, 2018.
- [4] Brinkhorst S, *Numerische und experimentelle Untersuchung zur metrologischen Nutzung von kavitierenden Venturi-Düsen*, dissertation, 2017.
- [5] Korth A, Martin T, (2016): “Aktualisierung von Verbrauchsganglinien für Haushalte, öffentliche Gebäude und Kleingewerbe sowie Entwicklung eines Modells zur Simulation des Wasserbedarfs”, DVGW-Forschungsvorhaben W-10-01-11, unpublished
- [6] Keller A, “cavitation scale effects – empirically found relations and the correlation of cavitation number and hydrodynamic coefficients“, in *CaltechCONF*, 2001

# Experimental Investigation to Measure the Natural Flow by Gas Laser Doppler Laser Doppler Velocimetry

Chen Hui-yu<sup>1</sup>, Cui Li-shui<sup>2</sup>

1. Chengdu Branch of National Station of Petroleum and Natural Gas Flow, [chhy@petrochina.com.cn](mailto:chhy@petrochina.com.cn), Chengdu, China

2. National Institute of Metrology, [cuilis@nim.ac.cn](mailto:cuilis@nim.ac.cn), Beijing, China;

---

## Abstract:

In order to solving the natural gas flow measurement problem about measuring flow under the complicated conditions and the measurement traceability of large diameter instruments, a set of optical natural gas flow metering devices based on Laser Doppler Velocimetry was established, translating the traditional flow volume measurement into pipeline section velocity field measurement to achieve the accurate measurement of natural gas flow. Results show that: the facility can achieve 1.45Mpa, 500m<sup>3</sup>/h the largest experiment measuring ability and the expanded uncertainty was 1.42% ( $k=2$ ); The relative deviation between the experimental results and the standard flow based on the ultrasonic flowmeter was 0.09%~2.93%; The results verify the feasibility of optical method measuring natural gas flow, and the established experiment system can be used for broader flow range of the research of high pressure natural gas flow measurement.

## Key words:

Metrology; Laser Doppler velocimeter; Natural gas; Flowrate measurement

---

## 1. Introduction

In recent years, with the continuous growth of natural gas trade, the accuracy of flow measurement is very important, and the accuracy of gas flow measurement is closely related to the calibration technology. For a long time, the field real - flow calibration of large diameter flowmeter is a difficult problem. Secondly, there are differences between physical parameters and gas composition parameters of natural gas, working conditions on the measurement site are different and installation conditions of flowmeter are relatively complicated, so that not only measurement errors are increased, but also increase the difficulty of real flow calibration of the large-diameter flowmeter. At present, the world's metrology experts are committed to solving the above problems, improve the natural gas flow measurement level<sup>[1]</sup>.

In order to solve the problems of natural gas flow measurement under complicated working conditions and traceability of large-caliber meter value and to promote the unification of measurement values of natural gas flow in China, Chengdu Branch of National Oil & Gas Large Flowrate Measurement Station (CVB) and National Institute of Metrology (NIM) established a set of natural gas flow metering device by optical method in 2015. The device adopted a laser Doppler velocimeter as a standard device to achieve a maximum experimental measurement capacity of 1.45 MPa and 500 m<sup>3</sup>/h, with an expanded uncertainty of 1.42% ( $k=2$ ). In this paper, the

analysis of the establishment of the device and the traceability of value were analyzed, This paper focuses on the establishment of the analytical device and quantity value traceability, and verifies the feasibility of the optical method for measuring natural gas flow by comparing the flow measurement results with the verification flow meter (an ultrasonic flow meter).

## 2. Establishment of natural gas flow metering device

### 2.1 Working principles

The flow is the amount of fluid flowing through the cross section of the pipeline or the open channel per unit time, i.e. the integral of the flow velocity over the flow cross section<sup>[2]</sup>. Due to the fluidity of the fluid, the movements of various units in each part of the fluid are not necessarily the same, but the relationship between the flow velocity and the flow can be established once flow velocity distribution on the flow cross section is accurately obtained, thereby realizing the measurement of the flow from flow velocity.

Hot-wire anemometer (HWA), particle image velocimeter (PIV) and laser Doppler velocimeter (LDV) are the main methods of measuring flow velocity at present. Compared with HWA and PIV, LDV has greater potential and advantages in measurement of a wide dynamic range of velocity at high spatial resolution. This is a non-intrusive, point-by-point method of measurement. At present, the resolution of LDV to measure the position in the

fluid pipeline has been very accurate. [3 ~ 4].

The working principle of LDV is shown in Figure 1. The measurement principle is explained with the fringe model: Two coherent Gaussian beams are intersected in air to form a measuring body in the intersection area and form alternately dark and bright interference fringes in the measuring body. When the scattered particles following the fluid pass through the measuring body, the Doppler frequency of the light intensity signal of the scattered particles is related to the motion speed of the particles:

$$v_{LDV} = \frac{\lambda}{2 \sin(\theta/2)} f \quad (1)$$

Where  $\lambda$  stood for wavelength of emitted light,  $\theta$  stood for included angle between two beams of coherent light, and  $f$  stood for Doppler frequency.

In formula (1),  $\frac{\lambda}{2 \sin(\theta/2)}$  characterizes the spacing between interference fringes in the measuring body, and  $f$  characterizes the transition time that the scattered particles pass through the measuring body.

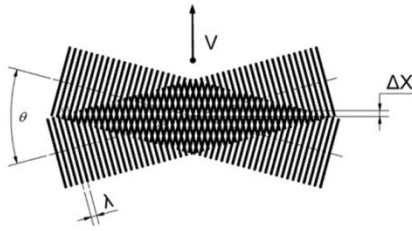


Figure 1: Working Principle Diagram of LDV

## 2.2 Composition of device

The natural gas flow metering device by optical method mainly consisted of a standard device, a window section, a particle source, a check meter, etc. The gas source came from the main pipeline of natural gas from CVB. The principle diagram of the device was shown in Figure 2.

The standard device is the key equipment of the device, which provides the standard measurement velocity. The standard device mainly including a laser Doppler velocimeter output power 150 mw, wavelength 532 nm), The LDV equipment includes one probe for 1D and one probe for 2D, and 1 set of lens with focal lengths of 250 mm and 400 mm respectively.

Due to the high requirement of light transmittance when LDV is used to measure pipeline velocity, it is not possible to directly measure natural gas pipeline, so it is necessary to set the measurement window section. The measurement window is a transparent round pipe of plexiglass (L= 500mm). The diameter

of the pipe in the measurement window is the same as that of the natural gas pipe being measured, so as to avoid the influence of disturbance caused by the change of pipe diameter on the flow field.

The particle source provides the standard tracer particle for the experiment, and was located at 30D upstream of the window section. The particle source mainly included a pressure Laskin particle generator, dioctyl sebacate (DEHS) particle liquid and nitrogen source. Nitrogen source pressure is higher than natural gas pipeline pressure..

By considering that the feasibility of measuring natural gas flow by optical method needed to be compared with traditional and reliable flow measuring methods, the device was provided with a DN 100 ultrasonic flowmeter which was adopted as a check table.

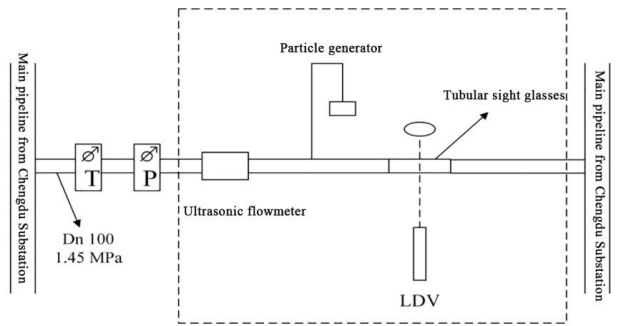


Figure 2: Structural Sketch of optical method gas flow facility

## 2.3 Calibration of LDV

In order to realize the traceability of measurement and ensure the reliability of the results, the value of the optical natural gas flow metering devices needed to be traced to the national measurement standard. a set of optical method gas flow facility Therefore, the actual value of fringe spacing in the measuring and distribution should be obtained through calibration. As an effective tool, turntable was widely used in calibration research through LDV. PTB of Germany, NIST of the United States and NMIJ of Japan have established their own turntable measurement systems respectively [6].

NIM has also established a turntable measurement system, which can be traced to the two basic quantities of length and time. Its technical parameters were shown in Table 1. Based on the above system, the LDV device of CVB was used to calibrate with a speed range of 1 m/s~25 m/s. The physical diagram and results were shown in Fig. 3 and Table 2. The calibration results showed that the maximum error between the measured value of LDV standard device and the indicating value of the standard value was 0.343%. The LDV was calibrated by PTB at the factory while being delivered, and the relative deviation between the

two calibrations was 0.11%, which also verifies the accuracy of the above calibration results.

**Table 1:** Technical Parameters of NIM Turntable Measurement System

Name	Parameters
Diameter of turntable	200.2848 mm
Range of linear velocity	(0.1~35) m/s
Diameter of tungsten filament	5μm

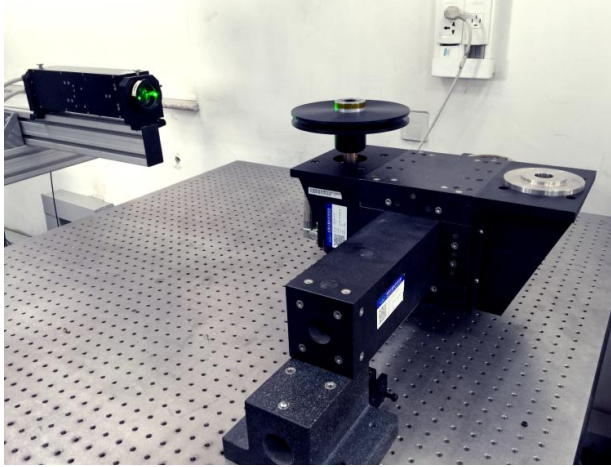


**Figure 3:** LDV of CVB for NIM Turntable System Calibration

**Table 2:** (1~25)m/s LDV fringe spacing in NIM measurement results (Green Light λ=532nm)

Doppler frequency [Hz]	NIM fringe spacing [μm]	Standard velocity [m/s]	LDV velocity [m/s]	Indicating value error [%]
2.257E+05	4.655	1.051	1.054	0.337
1.123E+06	4.668	5.253	5.248	-0.109
2.251E+06	4.668	10.507	10.515	0.076
3.365E+06	4.668	15.760	15.717	-0.275
4.514E+06	4.668	21.014	21.086	0.343
5.627E+06	4.668	26.267	26.285	0.068
Average error	0.073%			

#### 2.4 Uncertainty

By considering comprehensively, the uncertainty composition of the optical natural gas flow metering devices was as follows:

$$u_r(Q) = \left\{ \begin{array}{l} u_{rel}^2(V_{LDV}) + u_{rel}^2(T) + u_{rel}^2(P) \\ + u_{rel}^2(Q_{center}) + u_{rel}^2(Q_{boundary}) + u_{rel}^2(V_p) \end{array} \right\}^{0.5} \quad (5)$$

Where,  $u_{rel}(V_{LDV})$  is standard uncertainty of single point flow velocity measured by LDV;  $u_{rel}(P)$  is standard uncertainty of pressure measurement;  $u_{rel}(T)$  is uncertainty of temperature measurement;  $u_{rel}(Q_{center})$  is standard uncertainty of flow integral of core area;  $u_{rel}(Q_{boundary})$  is standard uncertainty of flow integral of boundary layer of pipeline wall;

$u_{rel}(V_p)$  stood for repeatability of flow velocity measurement at single point. Therefore, the uncertainty sources of optical natural gas flow metering devices are shown in table 3

**Table 3:** List of Uncertainty of optical natural gas flow metering devices

S/N	Symbol	Source	$c_r(x_i)$ [1]	$u_r(x_i)$ [%]	$u_r(x_i) \cdot c_r(x_i)$ [%]
1	$u_{rel}(V_{LDV})$	Flow velocity at single point of LDV measurement	1	0.15	0.15
2	$u_{rel}(P)$	Pressure measurement	1	0.1	0.1
3	$u_{rel}(T)$	Temperature measurement	1	0.1	0.1
4	$u_{rel}(Q_{center})$	Flowrate integral of core area	1	0.3	0.3
5	$u_{rel}(Q_{boundary})$	Flowrate integral of boundary layer of pipeline wall	1	0.6	0.6
6	$u_{rel}(V_p)$	Measurement of repeatability	1	0.1	0.1
Combined standard uncertainty $u_r(Q_{EMUT})=0.71\%$					
Expanded uncertainty $U_r(Q_{EMUT})=1.42\%$ ( $k=2$ )					

### 3. Experimental results and analysis

During the experiment, the natural gas flow was adjusted by a flow regulating device. The flow field of nation gas flowrate was measured at 100 m<sup>3</sup>/h, 300 m<sup>3</sup>/h, 400 m<sup>3</sup>/h and 500 m<sup>3</sup>/h in pipe. The measuring points are selected in the radial section of the pipe, the center of the section is taken as the origin of the measuring point coordinates, and 5mm is taken as the distance between the measuring points. The distribution diagram is shown in figure 4. The LDV is fixed on a coordinate frame, and the origin of the measuring area is positioned with a tape measure and a coordinate frame. After the gas flow is stabilized, the measurement is carried out, and 20 particles are sampled at each measuring point.

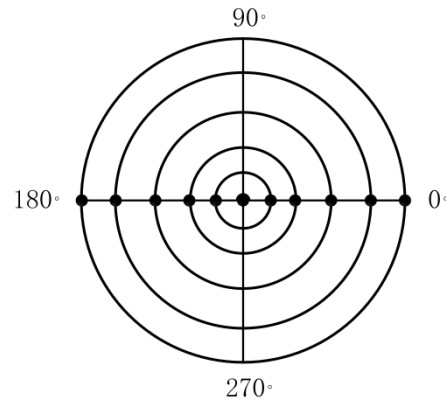


**Figure 4:** Distribution Diagram of LDV Measuring Points

#### 3.1 Following feature of particles

According to the measurement principle of LDV, the

value measured by LDV is not the velocity of the fluid, but the velocity of the scattered particles in the flow field. The following problem of particles must be considered first in experiments. The common particle following property is generally solved by BBO equation. Based on the calculation results of the BBO equation, we calculated the particle following in the experiment, and the calculation results are shown in table 4. In the experiment, we use particles with a diameter of  $5\mu\text{m}$  to obtain relatively good follow-through to the fluid.

**Table 4** Solution of BBO Equation for Following Features of Particles with Different Particle Sizes

$d_p$ [ $\mu\text{m}$ ]	$\omega$ [ $l$ ]	$V_p/V_f$ [ $l$ ]	$T$ [ms]
0.50	130941.58	1.000000000000	0.000001
0.76	130941.58	1.000000000000	0.000002
1.01	130941.58	1.000000000000	0.000004
2.02	130941.58	0.999999999999	0.000016
4.00	130941.58	0.999999999418	0.000062
5.00	130941.58	0.999999997816	0.000097
6.00	130941.58	0.999999993551	0.000140
7.00	130941.58	0.999999983869	0.000190
8.00	130941.58	0.999999964278	0.000249
9.00	130941.58	0.999999927930	0.000315
10.00	130941.58	0.999999864912	0.000389
20.00	130941.58	0.999991505834	0.001554

### 3.2 Distribution of Axial Velocity at Section of Pipeline

In Fig. 5-8,  $v$  stood for the average velocity at the measuring point, and  $x$  stood for the radial distance from the measuring point to the center of the section. It could be seen that the axial velocity at the section of the pipeline was within the range of  $X=-50$  to  $X=-45$  and  $X=45$  to  $X=50$ , i.e. there was a window period of measurement at the edge of the pipeline wall. With the increase of pipeline flow, the window period of measurement was expanded to  $X=40$ . The axial velocity was not symmetrically distributed at the axis of the section, but in a " ~ " shape, and it gradually developed into an irregular " S" shape. The degree of irregularity was proportional to the flow.

It showed that the flow measurement in circular tube was easily affected by turbulence intensity and boundary layer. There were three main reasons. 1. The size of the particle was close to that of the boundary layer. The internal velocity gradient was large, and the following features of the particles were decreased, so that the number of particles were influenced; 2. In actual flow, the thickness of the boundary layers on both sides of the pipeline wall were not completely equal, and the energy exchange between the boundary layer and the core area was changed while the flow position was changed along the pipeline; 3. The particles were added to the pipeline under high pressure on single side, which belonged to the problem of impact jet flow perpendicular to the mainstream direction. This

certainly disturbed the asymmetric distribution of number of the particles and the turbulence intensity of the mainstream.

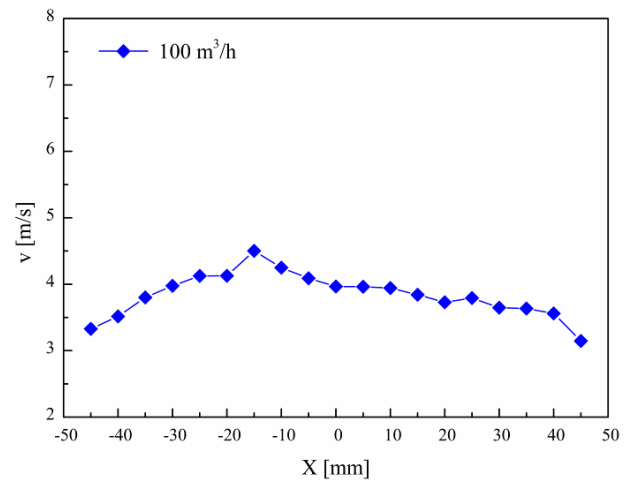


**Figure 5:** Distribution of Axial Velocity at Radial Section of Pipeline under  $Q=100\text{ m}^3/\text{h}$

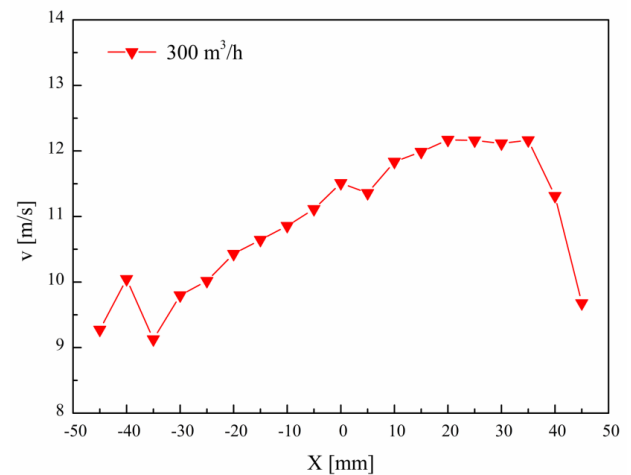


**Figure 6:** Distribution of Axial Velocity at Radial Section of Pipeline under  $Q=300\text{ m}^3/\text{h}$

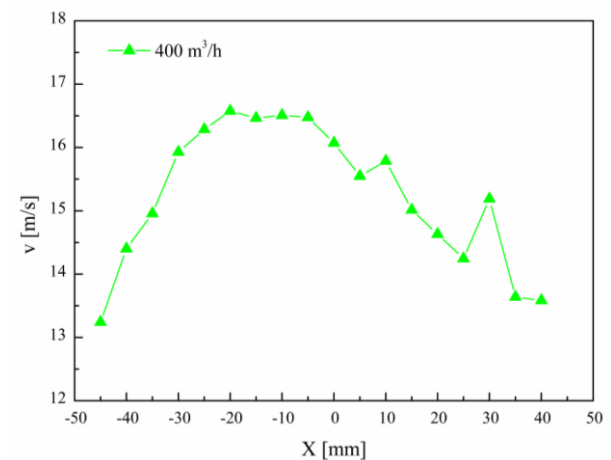


**Figure 7:** Distribution of Axial Velocity at Radial Section of Pipeline under  $Q=400\text{ m}^3/\text{h}$

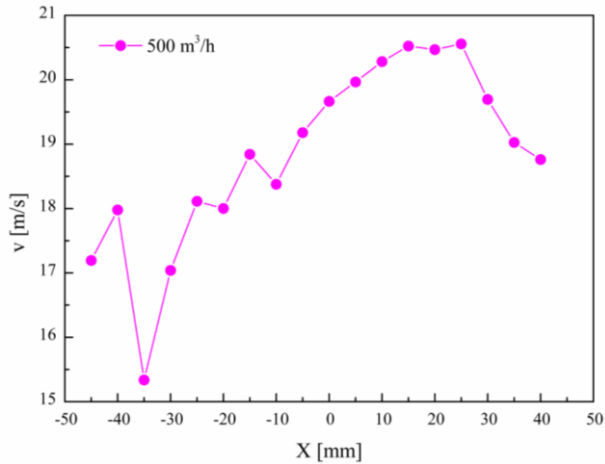


**Figure 8:** Distribution of Axial Velocity at Radial Section of Pipeline under  $Q=500 \text{ m}^3/\text{h}$

### 3.3 Establishment of relationship between flow velocity and flowrate

Based on the above-mentioned distribution of axial flow velocity, the flow velocity was converted into the flow in an integral manner, so as to obtain flow of the pipeline.

According to fluid dynamics theory, pipeline fluid included two parts: core area and boundary layer.

Therefore, total flow  $Q_{total}$  was equal to the sum of the flow in the core area,  $Q_{centre}$  and the flow in the boundary layer  $Q_{boundary}$ , i.e.  $Q_{total} = Q_{boundary} + Q_{centre}$ . By considering the asymmetric flow of the measured fluid, we considered on both sides based on the center of the pipeline section which adopted as

benchmark, i.e.  $Q_{total} = Q_{total\_plus} + Q_{total\_minus}$ . The distribution of flow velocity obtained at under different flow rates was treated as shown in Fig. 9.

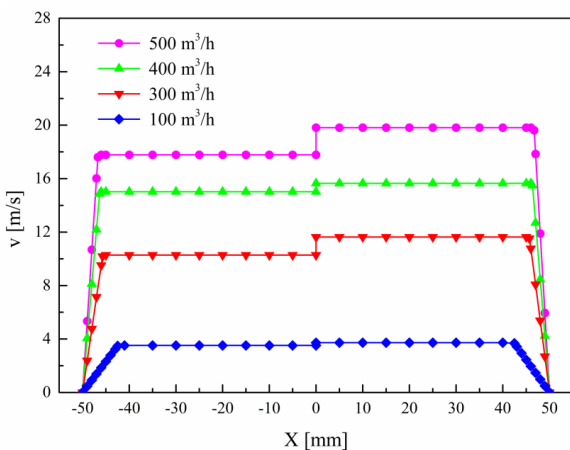


**Figure 9:** Measuring Results of Flow Velocity Treated at Different Flow Rates

Based on the measurement results of the flow velocity at the section of the pipeline processed in Fig. 6, the volume flow obtained at measured flow

section by integration was compared with the standard flow of the ultrasonic flowmeter as shown in Table 6. By considering that the window section was connected with the ultrasonic flowmeter through a straight pipeline section and the distance was short, the changes of pressure and temperature could be ignored. Therefore, the indicated volume flow of ultrasonic flowmeter could be directly compared with the integral flow based on LDV. It could be seen that the maximum deviation between the flow rates was -0.81% except that the deviation between the two was -2.93% at  $100 \text{ m}^3/\text{h}$ . This verified the feasibility of measuring natural gas flow by optical method.

**Table 6:** Correspondence of Measured Natural Gas Flow Rate and Standard Flow Rate Based on LDV

Flow point	Stepping direction	Average velocity in core area	Integral flow	Total integral flow	Standard flow	Indicating value error
Q ( $\text{m}^3/\text{h}$ )	/	m/s	$\text{m}^3/\text{h}$	$\text{m}^3/\text{h}$	$\text{m}^3/\text{h}$	%
100	Negative direction	3.52	42.64	87.71	90.36	-2.93
	Positive direction	3.72	45.07			
300	Negative direction	10.28	133.25	284.00	286.32	-0.81
	Positive direction	11.63	150.75			
400	Negative direction	15.02	197.17	402.62	402.25	0.09
	Positive direction	15.65	205.44			
500	Negative direction	19.81	261.99	497.14	499.45	-0.46

## 4. Conclusions

Chengdu Branch of National Oil & Gas Large Flowrate Measurement Station and National Institute of Metrology (NIM) established a set of natural gas flow metering device by optical method in 2015. In this paper, the establishment of the device and the traceability of value were emphatically analyzed, and experiments were carried out. Conclusions were as follows:

- 1) The natural gas flow metering device by optical method adopted the laser Doppler velocimeter as the standard device to achieve a maximum experimental measurement capacity of 1.45 MPa and  $500 \text{ m}^3/\text{h}$ , with an expanded uncertainty of 1.42% ( $k=2$ ).
- 2) The feasibility of measuring natural gas flow by optical method was preliminarily verified through experiments. The established experimental devices could be used for the research on measurement of natural gas flow within a wider flow range.
- 3) Measurement in circular tube was easily influenced by turbulence intensity and boundary

layer, but the measurement reliability of the above method could be improved by reducing turbulence intensity and increasing the number of particles.

#### **[References]**

- [1] B Mikan, V Strunck. A Primary Standard for the Volume Flow Rate of Natural Gas Under High Pressure Based on Laser Doppler Velocimetry [J]. *Metrologia*. 2014(51): 459–475.
- [2] Edited by Su Yanxun and Yang Youtao, Flow Detection Technology, China Quality Inspection Press, 2012
- [3] Bayer C, Shirai K, Buttner L, Czarske J. Measurement of acceleration and multiple velocity

components using a laser Doppler velocity profile sensor [J]. *Meas. Sci. Technol.* 2008(19).

- [4] J. Czarske, L. Buttner, T. Razik, H.Muller. Boundary Layer Velocity Measurements by a Laser Doppler Profile Sensor with Micrometer Spatial Resolution [J]. *Measurement Science and Technology* 2002(13): 1979–1989.

- [5] P. C. Miles. Geometry of the fringe field formed in the intersection of two Gaussian beams [J], 1996, 30(35), 5887-5895

- [6] Yoshiya Terao, Yong Moon Choi, Mikhail Gutkin, Wu Jian, Iosif Shinder and Cheng-Tsair Yang. Final report on the APMP air speed key comparison(APMP.M.FF-K3) [J]. *Metrologia*, 2010, 47(7), 88-94

# Effects of inclination of a clearance-sealed piston prover on the leakage flow rate

G. Bobovnik, J. Kutin

University of Ljubljana, Faculty of Mechanical Engineering, Laboratory of Measurements in Process  
Engineering, Aškerčeva 6, Ljubljana, Slovenia  
E-mail: gregor.bobovnik@fs.uni-lj

## Abstract

The leakage flow rate represents one of the most important contributions to the uncertainty of the measured gas flow rate at the bottom limit of the measuring range in a clearance-sealed piston prover. In order to successfully minimize its uncertainty contribution, it is necessary to understand the effects related to the reproducibility of the piston's travelling path relative to the cylinder and to the ability to position the piston prover in the ideal vertical position. The paper deals with an experimental study of the leakage flow rate in the inclined piston prover. The test results show that the leakage flow rate slightly increases with the inclination of the flow cell and that the leakage flow rate is correlated to the pressure inside the flow cell of the piston prover. The results indicate that such relationship could also be applied for predicting the leakage flow rate in a non-inclined piston prover.

## 1. Introduction

Piston provers are widely used volumetric primary standards in gas flow metering [1-3]. The general principle of operation is based on determining the time interval needed for a piston to pass a known volume of gas at a defined pressure and temperature. The proposed study deals with a clearance-sealed realization of the piston prover, (Figure 1), i.e., the seal in the flow cell is realized by a small clearance of the order of 10  $\mu\text{m}$  between the piston and the cylinder.

The piston prover consists of the base and the flow cell containing the travelling piston. The piston is made of a graphite composite and the cylinder is made of borosilicate glass. The passage of the piston is detected by infrared light emitters and sensors. The flow cell also contains the temperature and gauge pressure sensors that are positioned at the entrance to the cylinder. The base holds the computer, the timebase clock and the barometric pressure sensor. The measurement model for the mass and volume flow rate of the piston prover under study can be expressed as

$$\begin{aligned} q_m &= \rho(P_a, T) q_v(P_a, T), \\ q_v(P_a, T) &= \left( \frac{V_m^*}{\Delta t} + q_{v,l} \right) \varepsilon_\rho, \end{aligned} \quad (1)$$

where  $\rho(P_a, T)$  stands for gas density at atmospheric pressure  $P_a$  and time-averaged gas temperature in the piston prover  $T$ , and  $V_m^*$  is the effective measuring volume of the gas collected by the piston prover in the measuring interval  $\Delta t$ . The leakage flow through the clearance between the piston and the cylinder  $q_{v,l}$  represents only the Poiseuille component, whereas the Couette component is taken into account when determining the effective measuring volume. The density correction factor  $\varepsilon_\rho$  [4] accounts for the variations in the density of the gas relative to  $\rho(P_a, T)$ .

The Poiseuille leakage flow component is driven by a pressure difference on the piston. Considering that the relative pressure difference  $\Delta p/P_a$  and the relative piston-cylinder clearance  $\delta/D$  are relatively small, and that the piston is quiescent in the central position within the cylinder, the Poiseuille leakage volume flow rate can be written as:

$$q_{v,l} = \frac{\pi D \delta^3}{12 \mu} \frac{\Delta p}{H} \quad (2)$$

where  $D$  is the piston diameter,  $H$  is the piston height and  $\mu$  is the gas dynamic viscosity. However, the piston position within the cylinder significantly influences the resulting leakage flow rate. For the quiescent piston in its extreme eccentric position,

the Poiseuille leakage volume flow rate is 2.5 times higher than the one resulting from Equation (2). Because the actual travelling position of the piston is unknown, the leakage flow rate has to be determined experimentally.

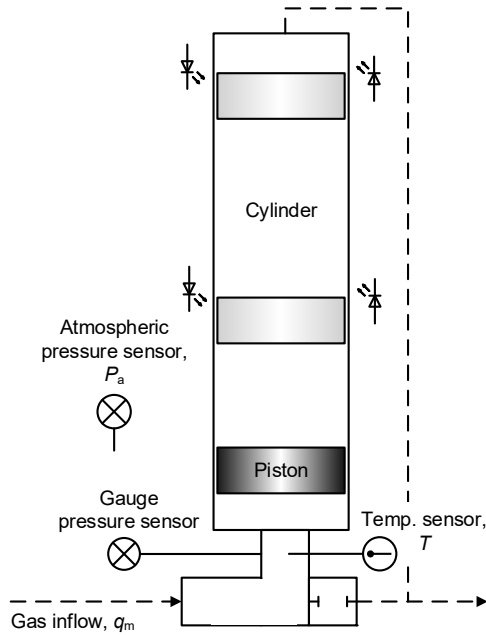


**Figure 1:** Schematic representation of the piston prover

Our previous study [5] showed that the determination of the leakage flow rate represents one of the most important contributions to the uncertainty of the measured flow rate at the lower limit of the measuring range. In order to successfully minimize its uncertainty contribution, it is vital to understand all important effects contributing to the leakage flow rate. It was presented in [6] that the systematic effects related to the gas viscosity (temperature of the gas, type of the gas) can be successfully corrected. On the other hand, the effects related to the reproducibility of the piston's travelling path relative to the cylinder and to our ability to position the piston prover in the ideal vertical position remain significant. In order to minimize them, the present experimental study focuses on understanding, interpretation and correction of these effects.

The tests with the intention to determine the Poiseuille leakage flow rate and the pressures inside the inclined flow cell were carried out by using the dynamic summation method. Tests were made for different supply air mass flow rates and different inclinations of the piston prover. To ensure that the results are not influenced by viscosity variations the

piston prover was placed into a climate chamber, where stable temperature conditions were assured.

## 2. Measurement method

The dynamic summation method [6] is used to measure the leakage flow rate  $q_{v,l}$  during the operation of a piston prover. The gas is supplied from two stable flow sources to two parallel flow branches, each restricted by a valve, which reunite before the inlet to the piston prover. During the measurement the uncorrected readings of the piston prover are recorded by setting  $q_{v,l}$  in (1) to zero. So the actual mass flow rate ( $q_m$ ) is the sum of the uncorrected reading of the piston prover ( $q_m^*$ ) and the leakage mass flow rate through the piston cylinder clearance ( $q_{m,l}$ ). The mass flow rate is consecutively measured from each flow source separately ( $q_{m1}$ ,  $q_{m2}$ ) by closing the valve in the other branch, as well as from both flow sources simultaneously ( $q_{m1+m2}$ ). By closing a valve in a particular branch the gas is diverted to the surroundings. Assuming that all mass flow rate sources remain stable during the measurement, the following holds true:

$$\begin{aligned} q_{m1+m2}^* + q_{m,l} &= q_{m1}^* + q_{m,l} + q_{m2}^* + q_{m,l} \Rightarrow \\ q_{m,l} &= q_{m1+m2}^* - q_{m1}^* - q_{m2}^* \end{aligned} \quad (3)$$

Finally, the leakage volume flow rate as defined in the measurement model of the piston prover in Equation (1) is calculated as  $q_{v,l} = q_{m,l} / \rho \varepsilon_\rho$ , where  $\rho$  and  $\varepsilon_\rho$  are taken as the average values during the measurement.

Using the following sequence of measured flow rates:  $q_{m1}$ ,  $q_{m1+m2}$ ,  $q_{m2}$ ,  $q_{m1+m2}$  ..., multiple values of leakage flow rate ( $q_{v,l,i}$ ) are obtained. The mean leakage flow rate and the experimental standard deviation of the mean (ESDM) for  $N$  successive measurement results are estimated by [7]:

$$\begin{aligned} q_{v,l} &= \frac{1}{N} \sum_{i=1}^N q_{v,l,i}, \\ s(q_{v,l}) &= \sqrt{\frac{s^2(q_{v,l,i})}{N} \left( 1 + \frac{2(N-1)\hat{R}}{N} \right)}, \end{aligned} \quad (4)$$

where  $s(q_{v,l,i})$  is the experimental standard deviation given by

$$s(q_{v,l,i}) = \sqrt{\frac{1}{N-1} \sum_{j=1}^N (q_{v,l,j} - q_{v,l})^2}, \quad (5)$$

and  $\hat{R}$  is the sample autocorrelation between the two successive leakage flow rates given by

$$\hat{R} = \frac{\sum_{j=1}^{N-1} (q_{v,l,j} - q_{v,l})(q_{v,l,j+1} - q_{v,l})}{\sum_{j=1}^N (q_{v,l,j} - q_{v,l})^2}. \quad (6)$$

The calculation considers that the two successive leakage flow rates are correlated, because they share one common measured flow rate ( $q_{m1}$  or  $q_{m2}$ ).

### 3. Measurement system

The leakage flow rate was measured for the piston prover (Sierra Instruments, Cal=Trak SL-800 with flow cell SL-800-10, flow range: 0.0012 g/min to 0.6 g/min). A detailed scheme of the experimental setup is shown in Figure 2.

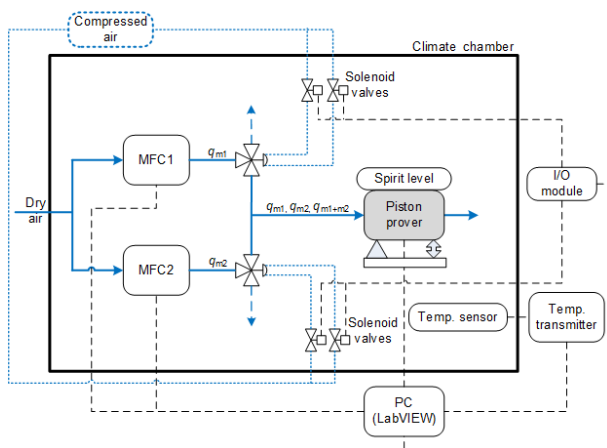


**Figure 2:** Measuring system

Two mass flow controllers (Bronkhorst F-201CV, full scale value: 13 mg/min) were used for stable flow sources. Downstream of the flow source each branch is restricted by a 3-way valve, enabling the piston prover to measure the flow rate from each source separately or from both sources simultaneously. The 3-way valve is equipped with a double-acting pneumatic actuator, the position of which is controlled using two on/off solenoid valves.

In order to control the temperature conditions and to ensure the temperature stability during the tests, the entire measuring system is placed into a climate chamber (Kambič KK-340 CHLT, stability: 0.1°C). The ambient temperature in the chamber is measured with a Pt100-based measuring system (Tetratec 624T 379 + PicoTech PT-104, expanded uncertainty: 0.15 K). The inclination of the piston

prover from vertical is regulated by using the inflatable bellows as schematically shown in Figure 3. The inclination of the piston prover was measured using a digital spirit level (Laserliner, DigiLevel Plus 25, resolution: 0.1°). The adjustment of the inclination was made from outside the chamber and the angle value displayed on the spirit level was monitored by using the camera positioned inside the climate chamber.

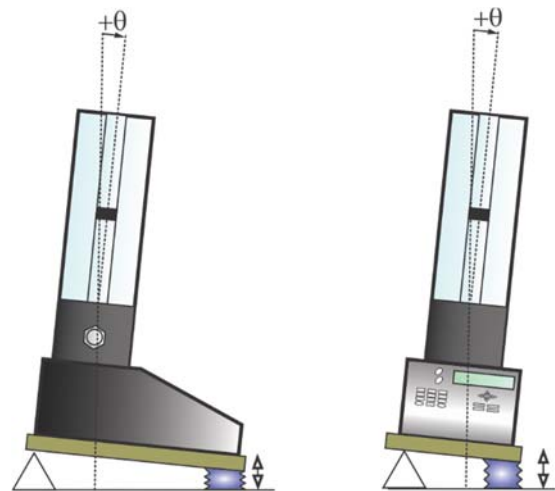


**Figure 3:** Inclination of the piston prover in the direction of positive angle  $\theta$ : a) back and forth, b) right and left.

The tests were carried out with dry air. The air properties were calculated using the REFPROP database [8] for a given air temperature in the flow cell and at ambient pressure. Both quantities were measured by using the piston prover's internal sensors, having expanded uncertainties of 0.15 K for the temperature and 0.055 kPa for the ambient pressure. The gauge pressure at the beginning and at the end of the measuring stroke in the flow cell was measured by the integrated pressure sensor having the expanded uncertainty of 1%.

The tests were, with the exception of the inclination adjustment and the temperature regulation of the climate chamber, fully automatized, by using a control program prepared with LabVIEW software (National Instruments, Ver.10.0.).

### 4. Test results

The tests were carried for different inclinations of the piston prover. The inclination of the piston was changed in two different directions (back and forth, right and left) in the following direction: 0° → 5° → 0° → -5° → 0° in four steps between the indicated values. At the end of the cycle some repetitions were made at random points. The mass flow rate

supplied to the piston was equal to the 50% of the full scale of the mass flow controllers ( $q_{m1} = q_{m2} \approx 6.3$  mg/min), except for the piston prover's ideal vertical position ( $0^\circ$ ) at which some measurements were also made at different air supply mass flow rates with mass flow controllers set to 25% and 100% of their full scale. For a single test, the mean leakage flow rate,  $q_{v,l}$ , and its ESDM,  $s(q_{v,l})$ , are based on  $N = 10$  consecutively measured values of the leakage flow rate.

During the tests the temperature at the inlet of the piston prover was equal to  $(22,2 \pm 0,1)$  °C and the ambient pressure was  $(98,2 \pm 0,6)$  kPa. Hence, the air viscosity changed by less than 0.03% during the experiments.

Figure 4 shows the variation of the leakage flow rate with the angle and the direction of the inclination. The results show a slight increase of the leakage flow rate at higher angles of inclination. The average leakage flow rate at  $0^\circ$  equals about 0.233 ml/min, which is about 23% of the minimum flow rate measured with the flow cell. The standard deviation of the measured values at  $0^\circ$  equals  $1.2 \cdot 10^{-3}$  ml/min. The measured leakage flow rates show large scattering for all angles of inclination, which indicates additional influences to the reproducibility of the leakage flow rate, e.g. variations of the piston travelling path, and stability of the mass flow controllers. One can notice that the minimum leakage flow rates are observed at  $\theta$  of about  $1.2^\circ$ , which could be related to non-alignment of the measuring cylinder inside the flow cell.

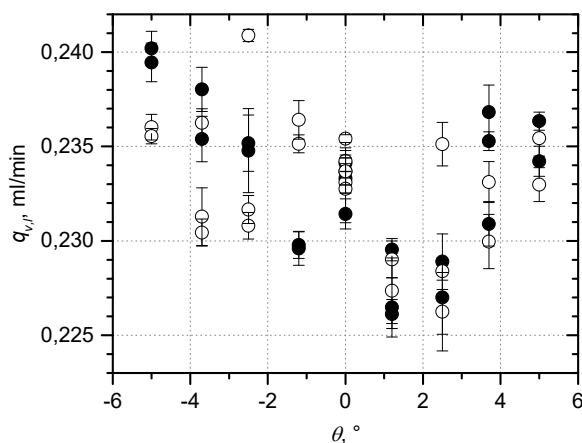


**Figure 4:** Leakage flow rates at different angles of inclinations of the piston prover (direction: ● - back and forth, ○ - right and left)

To observe if there is any trend of  $q_{v,l}$  with the magnitude of inclination, the same data as in Figure 4 are in Figure 5 presented relative to  $|\theta|$ .

The data show slight increase of the average value of  $q_{v,l}$  with  $|\theta|$ . The linear approximation function predicts an increase in  $q_{v,l}$  of about 1.6% for relative change of the inclination of  $5^\circ$ . This estimate is influenced by a large scatter of data and slightly different number of measuring points at each  $\theta$ .

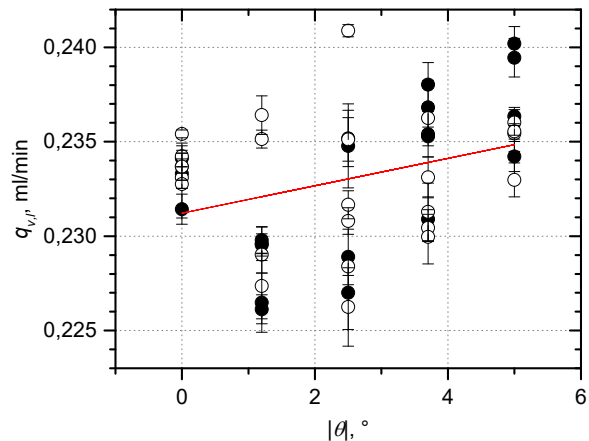


**Figure 5:** Variation of leakage flow rates for different absolute angles of inclinations of the piston (direction: ● - back and forth, ○ - right and left)

Figures 4 and 5 show that all measured flow rates are within the interval of  $\pm 3\%$ , which indicates that the average travelling path of the piston during the measurement stroke remains more or less similar for all measuring points; i.e., note that if the piston travelling path is changed from its central to its extreme eccentric position the leakage flow rate would increase for about 2.5-times. When the flow cell is tilted the most (for  $5^\circ$ ) the piston is almost certainly touching the cylinder wall (i.e. sliding along the cylinder wall), which means that it remains in a very similar position also in all other cases.

If we assume that the piston relative position and gas viscosity are relatively constant, then the leakage flow rate could be linked to the variations of the pressure difference acting on the piston. The magnitude of the pressure difference is influenced by the weight of the piston and the friction force acting on the piston. In this case the pressure difference ( $\Delta p_\theta$ ) at  $\theta$  relative to the pressure difference ( $\Delta p_0$ ) at  $0^\circ$  can be given as:

$$\frac{\Delta p_\theta}{\Delta p_0} = \cos|\theta| + k_f \sin|\theta|, \quad (7)$$

where the terms on the right-hand of the equation represent the variation of the gravity force and the friction force, respectively. Taking into account that the friction coefficient  $k_f$  between the piston and the

cylinder wall is about 0.2 (this value was provided by the manufacturer of the piston-cylinder assembly), the relative increase of pressure for  $\theta = 5^\circ$  equals 1.3%, which is close to the estimated increase of the leakage flow rate in Figure 5.

This assumption can be verified by investigating the monitored gauge pressure inside the flow cell. Because the outlet of the flow cell is opened to the ambient, the gauge pressure in the flow cell represents the pressure difference acting on the piston. The integrated sensor does not measure the pressure continuously during the measurement stroke, but only outputs its values at the beginning ( $p_1$ ) and at the end ( $p_2$ ) of the stroke.

During the leakage flow test  $M = 2N + 1$  individual measurement have to be made to obtain  $N$  measurement values of the leakage flow rate (see Section 2). Figure 6 shows the variation of the pressure values  $p_{1,i}$ ,  $p_{2,i}$  and their mean value  $p_{m,i} = (p_{1,i} + p_{2,i})/2$  for each individual measurement  $i$  during the leakage flow test performed at  $\theta = 0^\circ$  and  $q_{m1} = q_{m2} \approx 6.3$  mg/min. Note that the odd measurements represent pressures obtained for the supplied mass flow rate equal to  $q_{m1}$  (or  $q_{m2}$ ) and the even measurements for  $q_{m1+2} \approx 2q_{m1}$ . We can see that the pressures change during the test but without influence of the measured mass flow rate. It is also clear that there is no permanent correlation between  $p_1$  and  $p_2$ ;  $p_1$  can be smaller, greater or equal to  $p_2$  for a given measurement. Therefore, the average ( $p$ ) of all measured pressures  $p_1$  and  $p_2$  is selected as the pressure parameter characterizing the test:

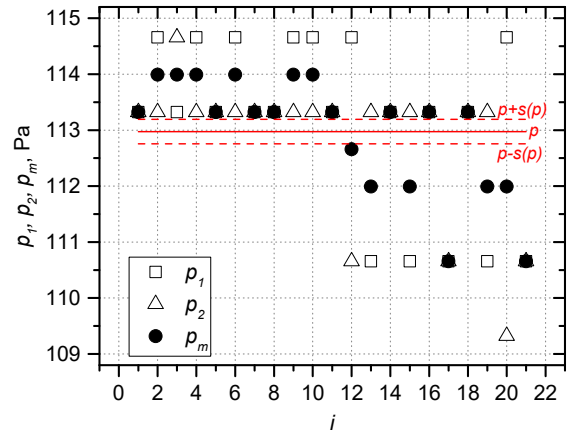
$$p = \frac{1}{M} \sum_{i=1}^M \frac{p_{1,i} + p_{2,i}}{2}, \quad (8)$$

with its experimental standard deviation of mean given by:

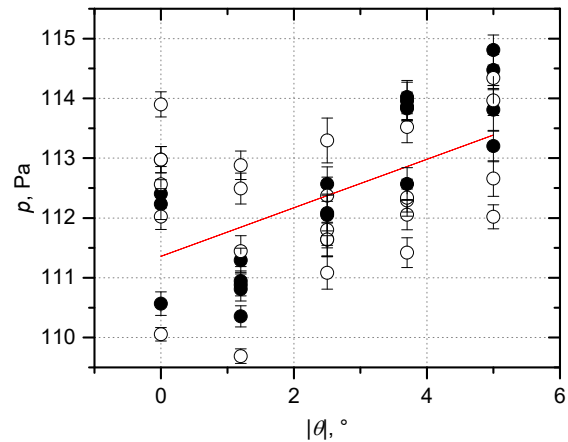
$$s(p) = \frac{1}{2} \sqrt{\frac{s^2(p_{1,i}) + s^2(p_{2,i})}{M}}. \quad (9)$$

Figure 7 shows how the mean pressure  $p$  changes with the absolute angle of inclination (the results are obtained for the same tests used to measure  $q_{v,i}$  in Figures 4 & 5). Despite the relatively large scatter at any given angle of inclination, the increase of the average value of  $p$  at higher angles is clearly visible. The linear fit of pressure values predicts the relative change of pressure at  $5^\circ$  of about 1.8%. The results show that the increase of the average pressure in

the flow cell is of the same order as the estimated increase of the leakage flow rate. The estimated increase of pressure (leakage flow rate) agrees well with the theoretical prediction from Equation (7).



**Figure 6:** Characteristic pressures  $p_1$ ,  $p_2$ ,  $p_m$  and  $p$  ( $\theta = 0^\circ$  and  $q_{m1} = q_{m2} \approx 6.3$  mg/min)



**Figure 7:** Mean pressures for different absolute angle of inclinations of the piston prover (direction: ● - back and forth, ○ - right and left)

The actual correlation between the leakage flow rate and the mean gauge pressure in the flow cell is presented in Figure 8. The increase of the leakage flow rate with pressure was approximated with linear function, which shows that the ratio  $q_{v,i}/p$  remains approximately constant, which confirms our previous observations. Figure 8 also proves some correlation between  $q_{v,i}$  and  $p$  for a non-inclined flow cell (those results are denoted with black points).

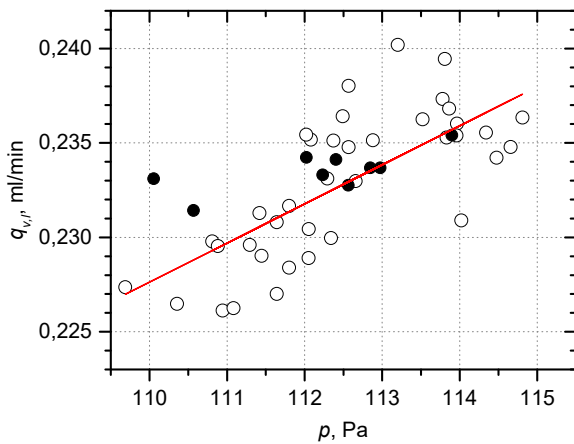


**Figure 8:** Correlation between the leakage flow rate and the mean pressure (● – measurements at  $\theta = 0^\circ$ ).

## 7. Conclusion

The presented analysis shows that the leakage flow rate in the inclined clearance-sealed piston prover could be related to the increased friction and therewith to the increased pressure in the flow cell. The results indicate that such relationship could also be used for leakage flow rate prediction in non-inclined flow cell. This would lead to the decrease of the uncertainty of the leakage flow rate related to the repeatability of the travelling path of the cylinder and to the ability to position the flow cell in the ideal vertical position.

The main drawback of the current study is the fact that the pressure inside the flow cell was measured only at the beginning and at the end of the measurement stroke. Monitoring the pressure inside the flow cell during the entire stroke, which would require the use of an external dynamic pressure sensor, would result in a more adequate mean value of the pressure during the measurement stroke. The observed variations of the pressure during the measurement stroke would also provide some additional information about travelling path of the piston.

The tests are also planned for other flow cells with the measuring range up to 50 l/min, in order to research the possibilities of a broader applicability of the current findings.

## References

[1] Wright J D, Mattingly G E, Nakao S, Yokoi Y, Takamoto M “International comparison of a NIST primary standard with an NRLM transfer

standard for small mass flow rates of nitrogen gas”, *Metrologia*, **35**, 211–221, 1998.

- [2] Berg R F, Cignolo G, “NIST–IMGC comparison of gas flows below one litre per minute”, *Metrologia* **40**, 154–158, 2003.
- [3] Berg R F, Gooding T, Vest R E “Constant pressure primary flow standard for gas flows from  $0.01 \text{ cm}^3 \text{ min}^{-1}$  to  $100 \text{ cm}^3 \text{ min}^{-1}$  ( $0.007\text{--}74 \mu\text{mol s}^{-1}$ )”, *Flow Meas. Instrum.*, **35**, 84–91, 2014.
- [4] Kutin J, Bobovnik G and Bajsić I, “Dynamic pressure corrections in a clearance-sealed piston prover for gas flow measurements”, *Metrologia*, **50**, 66–72, 2013.
- [5] Bobovnik G, Kutin J, Bajsić I “Uncertainty analysis of gas flow measurements using clearance-sealed piston provers in the range from  $0.0012 \text{ g min}^{-1}$  to  $60 \text{ g min}^{-1}$ ”, *Metrologia*, **53**, 1061–1068, 2016.
- [6] Bobovnik G, Kutin J, “Experimental identification and correction of the leakage flow effects in a clearance-sealed piston prover”, *Metrologia*, **53**, 1061–1068, 2016.
- [7] Zhang N F, “Calculation of the uncertainty of the mean of autocorrelated measurements”, *Metrologia*, **43**, S276–S281, 2006.
- [8] Lemmon E W, Huber M L, McLinden M O, *NIST Reference Fluid Thermodynamic and Transport Properties—REFPROP Version 9.0* (Gaithersburg, MD: National Institute of Standards and Technology), 2010.

# PVTt primary flow standard for small gas flow rates

U. Primožič, G. Bobovnik, J. Kutin

University of Ljubljana, Faculty of Mechanical Engineering, Laboratory of Measurements in Process Engineering,  
Aškerčeva 6, SI-1000 Ljubljana, Slovenia  
E-mail (J. Kutin): joze.kutin@fs.uni-lj.si

## Abstract

A PVTt primary flow standard operates on the principle of determining the change of density of the measured gas in the tank of a known volume and the corresponding time interval. The PVTt standard presented in this paper is based on the diverter-operated flying start and finish method. It contains the gas collection tank that is constructed as a dismountable assembly, which enables determining its internal volume by dimensional measurements. The standard is designed for the flow range from 0.12 mg/min to 12 mg/min and it achieves the relative expanded measurement uncertainty between 0.12% and 0.24%. We performed a comparison of the realized PVTt flow standard with the piston-prover flow standard for flow rates above 1.2 mg/min, and the results were found successful in view of normalized errors,  $E_n$ .

## 1. Introduction

The general principle of the operation of a pressure, volume, temperature, and time (PVTt) primary gas flow standard is based on determining the change of density of the measured gas in the tank of a known volume and the corresponding time interval [1–4]. The measured gas flow can be collected in the measuring tank (increase of gas density) or generated from the measuring tank (decrease of gas density). The PVTt standards usually operate in the flying start-and-finish method, which assure nearly constant flow rate through the device under test. This method can be designed with static or dynamic measurements of the fluid density.

This paper deals with the realization of the PVTt primary gas flow standard, which is based on the static (diverter-operated) flying start-and-finish method. The system is designed for the volume flow rates between 0.1 cm<sup>3</sup>/min and 10 cm<sup>3</sup>/min at standard gas conditions; i.e., for the mass flow rates of the air-like gas between 0.12 mg/min and 12 mg/min. The core of the standard is the collection measuring tank, which is constructed as a dismountable assembly, so that its internal volume can be determined directly by dimensional measurements. The metrological characteristics of the realized PVTt standard were compared with the piston prover gas flow standard, but so far only for flow rates above 1.2 mg/min, which is the minimum flow limit of the employed piston prover.

The paper is organized as follows: Section 2 presents a configuration of the measurement system of the PVTt flow standard; Section 3 discusses main contributions to

the measurement uncertainty and evaluates the expanded uncertainty of the measured mass flow rate; and Section 4 introduces the results of a comparison between the PVTt standard and the piston prover.

## 2. Measurement system

A top view of the realized PVTt flow standard is presented in Figure 1.

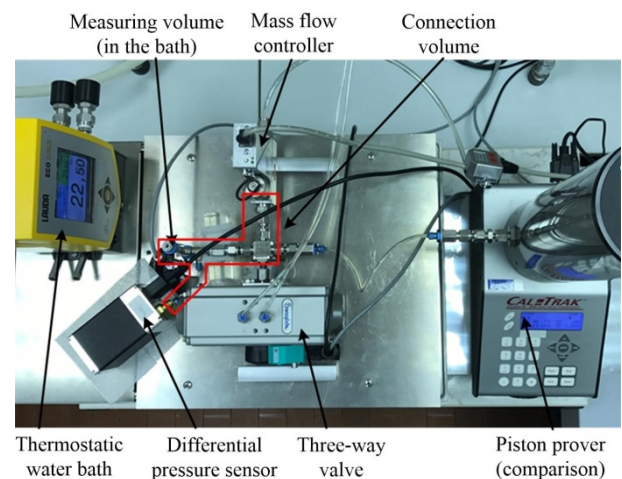


Figure 1: Top view photo of the PVTt measurement system.

The main part of the collection volume is the stainless steel cylindrical tank of about 100 cm<sup>3</sup>, which is placed into the thermostatic water bath (Lauda ECO Gold) and is for that reason not visible in this photo. The PVTt standard requires a stable mass flow rate of the measured gas, which is ensured by the thermal flow

controller (Bronkhorst F-201CV). The gas flow is diverted into or out of the collection tank by the three-way valve positioned downstream of the flow controller. The valve is equipped with a double-acting pneumatic actuator, the position of which is controlled by using solenoid valves. An electrical output of the valve position sensor is used to trigger the measurement of the time interval, which is performed by the DAQ board (National Instruments USB-6341).

The filling of the tank starts at the ambient pressure conditions and finishes when the gauge pressure reaches the target value. The gauge pressure is measured by the differential pressure sensor positioned at the entrance to the tank (Mensor CPT6100), and the ambient pressure is measured by the absolute pressure sensor (Mensor CPG2500). Temperature is measured by the resistance temperature sensor positioned in the tank wall (TetraTec WIT-S + PicoTech, PT-104). Gas density is calculated for the stationary conditions before and after the filling stage by using the REFPROP fluid properties database [5]. The maximum pressure in the collection volume is limited by the upper range limit of the gauge pressure sensor that is 2500 Pa.

The PVTt standard is automated by using a LabVIEW acquisition and programming environment.

### 3. Measurement model and uncertainty

The mass flow reading of the presented PVTt gas flow standard is calculated by the following measurement model:

$$q_m = \frac{V\Delta\rho}{\Delta t}, \quad (1)$$

where  $V$  is the collection volume,  $\Delta t$  is the effective collection time interval, and  $\Delta\rho = \rho_2 - \rho_1$  is the difference of gas densities in the collection volume after and before the filling stage.

The measuring volume of the gas  $V$  is the whole gas collection volume downstream of the mass flow controller and can be written as a sum of the volume of the tank  $V_e$  and the connection (dead) volume  $V_d$  between the mass flow controller and the tank including the internal volume of the gauge pressure sensor; i.e.,  $V = V_e + V_d$ . The internal volume of the tank was determined by traceable dimensional measurements of the internal diameter and length. The connection volume was measured by the gas expansion method using the tank as the reference volume. The tank and connection volumes are  $V_e = 99.6928 \text{ cm}^3$  and  $V_d = 7.5738 \text{ cm}^3$ , respectively, so the total measuring volume equals  $V = 107.2666 \text{ cm}^3$ . The relative standard uncertainty of the

measuring volume is estimated to  $u(V)/V = 4.0 \cdot 10^{-4}$ . The largest contribution represents the uncertainty of the connection volume, estimated as experimental standard deviation of the measurement results.

The effective collection time interval  $\Delta t$  is determined as a sum of the time interval measured by the DAQ board  $\Delta t_m$  and the diverter correction time  $\Delta t_d$ . The diverter correction was determined at different flow rates by approximately following the procedure in [6]. If the constant mass flow rate is measured for two different collection times, we assume:

$$q_m = \frac{V\Delta\rho_1}{\Delta t_{m,1} + \Delta t_d} = \frac{\Delta\rho_2}{\Delta t_{m,2} + \Delta t_d}, \quad (2)$$

therefore the diverter correction time can be estimated as:

$$\Delta t_d = \frac{\Delta\rho_1\Delta t_{m,2} - \Delta\rho_2\Delta t_{m,1}}{\Delta\rho_2 - \Delta\rho_1}. \quad (3)$$

The average value of the diverter correction time is  $\Delta t_d = 0.533 \text{ s}$  and its standard measurement uncertainty, estimated as experimental standard deviation of the results, is  $u(\Delta t_d) = 0.015 \text{ s}$ . The standard uncertainty of the effective time interval  $u(\Delta t)$  is calculated as the root-sum-square of  $u(\Delta t_d)$  and the standard uncertainty of the measured time interval  $u(\Delta t_m)$ , where the latter is estimated to  $u(\Delta t_m) = 3 \cdot 10^{-5} \Delta t_m$ .

Gas density is determined by using the REFPROP database for the selected gas and the time-averaged measured values of the absolute pressure (calculated as a sum of the ambient pressure and the gauge pressure) and the temperature. The relative standard measurement uncertainty of the density change is estimated as:

$$\frac{u(\Delta\rho)}{\Delta\rho} = \sqrt{\left(\frac{u(\Delta p)}{\Delta p}\right)^2 + \left(\frac{u(T)}{T}\right)^2 + \left(\frac{u(M/Z)}{M/Z}\right)^2}, \quad (4)$$

where  $u(\Delta p) = 0.5 \text{ Pa}$  is the standard measurement uncertainty of the pressure change,  $u(T) = 0.1 \text{ K}$  is the standard measurement uncertainty of the temperature, and  $u(M/Z)$  considers uncertainties of the gas composition and the density model (for the dry air used in measurements in this paper the last term in Eq. (4) is estimated to  $2 \cdot 10^{-4}$ ).

Furthermore, leak testing was performed for the collection volume using the pressure decay method. The leakage mass flow rate was found to not exceed  $q_{m,l} = 1.2 \cdot 10^{-4} \text{ mg/min}$ , therefore,  $u(q_{m,l}) = q_{m,l}/\sqrt{3}$ .

The relative combined standard measurement uncertainty of the mass flow rate is evaluated as:

$$\frac{u(q_m)}{q_m} = \sqrt{\left(\frac{u(V)}{V}\right)^2 + \left(\frac{u(\Delta t)}{\Delta t}\right)^2 + \left(\frac{u(\Delta \rho)}{\Delta \rho}\right)^2 + \left(\frac{u(q_{m,l})}{q_m}\right)^2} \quad (5)$$

Finally, the expanded measurement uncertainty of the mass flow rate measured by the PVTt standard is estimated as:

$$U(q_m) = k u(q_m), \quad (6)$$

using the coverage factor  $k$  for 95.45% confidence interval of a  $t$ -distribution with effective degrees of freedom obtained from the Welch-Satterthwaite formula [7]. Finite degrees of freedom were considered for uncertainty components associated with the connection-volume and correction-time measurements.

Figure 2 shows the relative expanded measurement uncertainty of the mass flow rate,  $U_r(q_m) = U(q_m)/q_m$ , for the pressure changes of 2500 Pa and 1000 Pa. The corresponding time interval is nearly 1600 s at 0.12 mg/min and nearly 16 s at 12 mg/min for the 2500 Pa pressure change, and it is 2.5-times lower for the 1000 Pa pressure change.

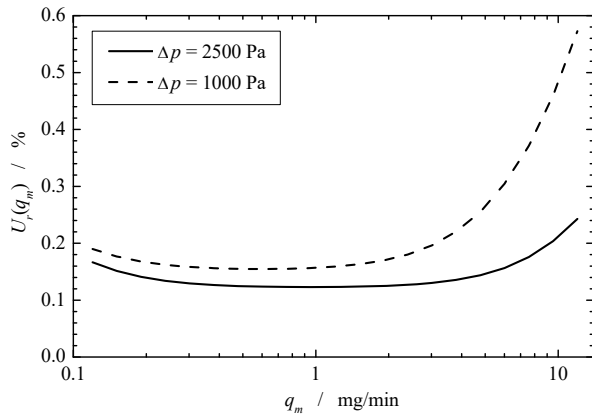


**Figure 2:** Variation of the relative expanded measurement uncertainty with the mass flow rate of dry air for two different pressure changes.

For the maximum pressure change of 2500 Pa the expanded uncertainty varies from 0.12% to 0.24% of the measured mass flow rate. The largest contributions to the uncertainty are associated with the leakage effects at the smallest flow rates and the time-interval measurements at the highest flow rates. The volume and temperature measurements are the largest contributions to uncertainty for the intermediate flow rates. For the pressure change of 1000 Pa the expanded uncertainty increases to the values between 0.15% and 0.57% of the measured mass flow rate. Such an increase is the result FLOMEKO 2019, Lisbon, Portugal

of relatively larger effects related to the pressure and time measurements.

#### 4. Comparison results

The realized PVTt gas flow standard was tested by comparison with the piston prover gas flow standard (Sierra Instruments Cal=Trak SL-800), which has the flow range between 1.2 mg/min and 600 mg/min and the expanded measurement uncertainty of  $U(q_m) = 0.015 \text{ mg/min} + 2.5 \cdot 10^{-4} q_m$  [8]. Because of the minimum flow limit of the employed piston prover, we performed a comparison in the flow range of 1.2 mg/min to 12 mg/min. The piston prover was connected to a free port of the three-way diverter valve of the PVTt standard. The measurements were carried out alternately with both flow standard and were repeated three times at each flow rate of dry air. The PVTt standard was used with the collection time corresponding nearly to the maximum pressure change of 2500 Pa.

Figure 3 shows relative deviations between the mass flow readings of the PVTt system and the piston prover (index “PP”),

$$e_r = \frac{q_{m,PVTt} - q_{m,PP}}{q_{m,PP}}, \quad (7)$$

and the relative expanded uncertainties associated with measurements by both standards,  $U_r(q_{m,PVTt})$  and  $U_r(q_{m,PP})$ . The observed relative deviations are within  $\pm 0.19\%$  for the largest four flow rates and within  $\pm 0.41\%$  for the smallest two flow rates. In all cases the deviations do not exceed the expanded uncertainty of the piston prover.

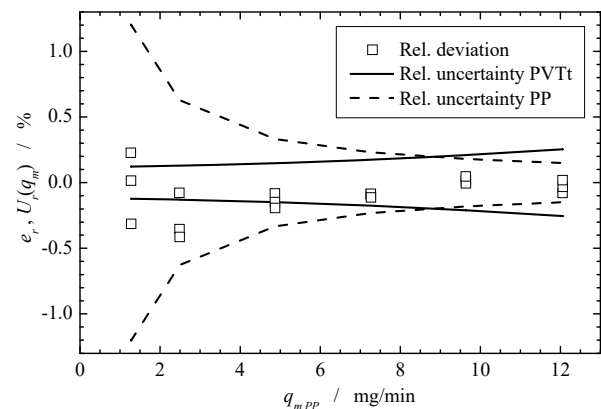


**Figure 3:** Relative deviations between the mass flow readings of the PVTt standard and the piston prover, and relative expanded uncertainties associated with both standards.

The comparison results are also evaluated in terms of normalized errors:

$$E_n = \frac{q_{m,PVTt} - q_{m,PP}}{\sqrt{U(q_{m,PVTt})^2 + U(q_{m,PP})^2}} \quad (1)$$

As shown in Figure 4, the normalized errors lie between  $-0.65$  and  $0.19$ . Because all  $E_n$  values are within the  $\pm 1$  range, the comparison results can be considered as statistically satisfactory. At least at higher flow rates, where the uncertainties of both standards are of the same order of magnitude, these results can be considered as a confirmation of metrological characteristics of the realized PVTt gas flow standard.

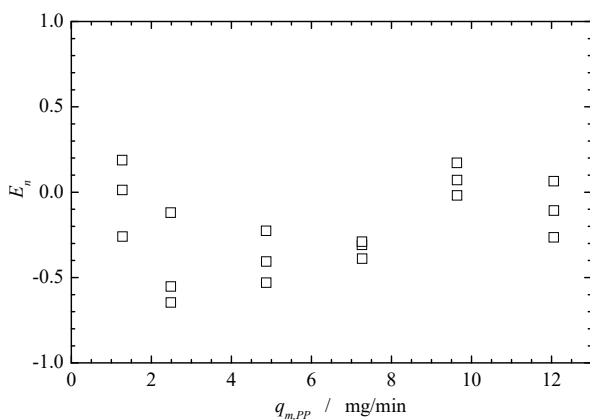


**Figure 4:** Results of a comparison between the PVTt system and the piston prover in terms of normalized errors.

## 5. Conclusions

The aim of this paper was to present a realization of the PVTt primary flow standard, which is based on the diverter-operated flying start-and-finish method. The standard is designed for the flow range of  $0.12$  mg/min to  $12$  mg/min and it achieves the relative expanded measurement uncertainty between  $0.12\%$  and  $0.24\%$  when used with the maximum pressure change of about  $2500$  Pa. The largest contributions to the measurement uncertainty are associated with the leakage effects at the smallest flow rates and the time-interval measurements at the highest flow rates. The volume and temperature measurements are the largest contributions to measurement uncertainty for the intermediate flow rates.

The metrological characteristics of the realized PVTt standard were compared with the piston prover gas flow standard, but so far only for flow rates above  $1.2$  mg/min, which is the minimum flow limit of the employed piston prover. The comparison results evaluated in terms of normalized errors are found to be statistically satisfactory, with  $E_n$  values between  $-0.65$  and  $0.19$ . Nevertheless, one should bear in mind that the uncertainties of the piston prover are relatively large at its minimum flow limit.

## References

- [1] Wright J D, Johnson A N, Moldover M R, Kline G M, *Gas flowmeter calibrations with the 34 L and 677 L PVTt standards* (Gaithersburg, MD: NIST), 2003.
- [2] Nakao S, “Development of the PVTt system for very low gas flow rates”, *Flow Measurement and Instrumentation* 17 (2006) pp. 193-200.
- [3] Morgado I, Legras J C, Clodic D, “Primary standard for the calibration of refrigerant leak flow rates”, *Metrologia* 47 (2010) pp. 135-145.
- [4] Levine P D, “A new approach to gas flow calibration”, *Measurement* 43 (2010) pp. 1644-1648.
- [5] Lemmon E W, Huber M L and McLinden M O, *NIST Reference Fluid Thermodynamic and Transport Properties – REFPROP Version 9.0* (Gaithersburg, MD: NIST), 2010.
- [6] ISO 4185: *Measurement of liquid flow in closed conduits – Weighing method*, 1980.
- [7] JCGM 100: *Evaluation of Measurement Data – Guide to the Expression of Uncertainty in Measurement*, 2008.
- [8] Bobovnik G, Kutin J, Bajsić I, “Uncertainty analysis of gas flow measurements using clearance-sealed piston provers in the range from  $0.0012$  g min<sup>-1</sup> to  $60$  g min<sup>-1</sup>”, *Metrologia* 53 (2016) pp. 1061–1068.

# Liquid level detection in standard capacity measures with computer vision

T. Mušič, G. Bobovnik, J. Kutin

University of Ljubljana, Faculty of Mechanical Engineering, Laboratory of Measurements in Process Engineering, Aškerčeva 6, SI-1000 Ljubljana, Slovenia  
E-mail (T. Mušič): [maticko.music@gmail.com](mailto:maticko.music@gmail.com)

## Abstract

The article presents a computer vision system for liquid level detection in standard capacity measures that can be used for automating measurements or performing them in inaccessible places. The developed computer vision system consists of a digital camera and a computer program in the LabVIEW environment. The acquired images are processed and corrected for different distortions (parallax, lens and tilt distortion). By using the edge detection method, liquid level is detected and corrected for all distortions. The computer vision system was tested using water in a laboratory environment on the standard capacity measure with a nominal capacity of 100 l. The measurement results acquired with the automated computer vision system were compared with the readings made by an operator and the agreement is found to be satisfactory.

## 1. Introduction

Standard capacity measures are commonly used volume standards for testing measuring systems for liquids other than water. A typical standard capacity measure has a transparent neck with scale marks corresponding to its nominal capacity, and to the volumes below and above the nominal capacity [1]. Liquid level detection and obtaining readings from the measuring scale can often be difficult due to the location of the capacity measure or to the nature of the measured liquid. The purpose of this paper is to present a computer vision system that automatically detects the liquid level and reads the volume from the capacity measure. If we want to use this system as a substitution for a human operator, it has to achieve or surpass the accuracy of manual reading. This has been tested by making measurements by computer vision and then comparing them to the ones taken by an operator.

The developed computer vision system consists of a digital camera and a computer program in the LabVIEW environment. Figure 1 show the measuring system with the camera and the capacity measure under test. The acquired images are processed and corrected for different distortions. After all image corrections are done, liquid level is detected using edge detection. Although the accuracy of the system can be compared with the accuracy of a human, it is very susceptible to lightning conditions.



Figure 1: Measuring system for liquid level detection and reading from the measuring scale of the capacity measure.

## 2. Image corrections

### 2.1 Parallax

The first distortion effect is parallax that causes a shift of the liquid level's apparent position in the background regarding the measuring scale positioned in the foreground. It occurs due to the distance between the liquid and the measuring scale. Therefore, when the liquid level is not in line with the central axis of the camera, the measurement error occurs. In order to avoid this, the camera should be moved, so it can be constantly in line with the liquid level, or the corrections should be performed after the reading is taken [2].

In standard capacity measures the glass is often thick relative to the gap between the measuring scale and the fluid. This means that a different amount of parallax that occurs in the glass due to a different angle of light is significant enough and cannot be neglected. Consequently, parallax correction is done in two steps, firstly, correcting for the distance between measuring scale and glass,  $d$ , and, secondly, by correcting for the thickness of the glass,  $s$  (Figure 2). When viewing from angle  $\alpha$ , an error of  $h_1$  is made. Red line represents where the liquid level would be seen, if there was no glass. Green line represents the true path of the light from the liquid level to the camera.

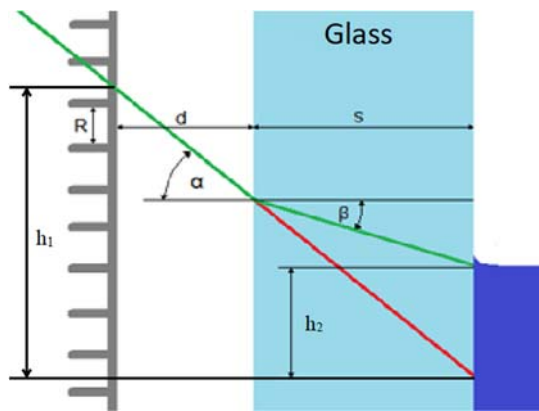


**Figure 2:** Schematic representation of the parallax effect when viewing from angle  $\alpha$ .

### 2.2 Lens distortion

Lens distortion is present in every lens, some of it appears due to the manufacturing errors and imperfections, other distortions are consequences of physical properties of light. There are many types of lens distortion, but for our purposes we will focus on the ones that change ratios of an image, barrel and pincushion distortion (Figure 3). Barrel distortion is common with wide angle lenses. Image magnification decreases with the distance and we get images that appear to be mapped around the barrel. With pincushion distortion it is the other way around, image magnification increases further from the center of the image. Most lenses have a combination of those effects [3].

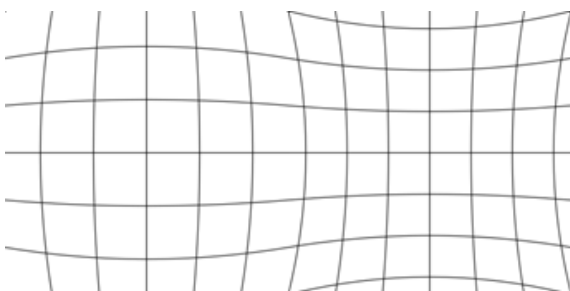


**Figure 3:** Barrel (left) and pincushion (right) distortion

To get the information about the lens distortion a calibration is needed before the first measurement, the results of which are then used for all subsequent measurements to properly correct the image. The majority of image correction models are based on polynomial corrections. We must be aware that the true lens distortion cannot be fully described by some function, because of the small random defects in lens that are caused by manufacturing and physical properties of a light, so all distortions are merely approximations. In our case we only need to correct the image in a narrow band (where the measuring scale and liquid level are located), therefore we will perform lens correction only in one dimension using cubic polynomial.

First, we must make sure that camera plane is parallel to the plane of measuring scale. Because we will perform correction only in one dimension, it is preferable that the measuring scale is in the centre of the image. Positions of measuring scale marks are read and cubic polynomial is approximated through them. We can say that the image is not distorted at the center, how far from the center of an image we can neglect distortion depends on the camera and the lens we are using. After choosing our distortion “free” zone, we approximate linear function through the points in this zone. Subtracting cubic and linear functions will result in function that describes how pixels are shifted when we move from the center.

### 2.3 Tilt of the camera

When trying to do measurements from an image, it is important that ratios between objects in the image match ones in the real world. After correcting the lens distortion, the camera should work as mirroring through a point. Therefore, all ratios should be preserved as long as planes (in our case the measuring scale and the camera sensor) are parallel.

But sometimes this cannot be achieved; therefore we have to make another correction for camera tilt. Based on trigonometry we can get a relation that describes how the angle of camera effects distribution of the mirrored points:

$$L = \frac{\tan\left(\arctan\left(\frac{r}{f}\right) - \gamma\right)s}{R} + LS, \quad (1)$$

where  $L$  is the value of the scale,  $r$  is the read position of a liquid level (distance from the centre of an image),  $f$  is the focal length of the camera in pixel units,  $\gamma$  is the camera angle,  $s$  is the distance between the camera and the measuring scale,  $R$  is the distance between the individual lines of the measuring scale.  $LS$  stands for a possible shift of the measuring scale, if for instance a zero is not the first read line of the scale.

### 3. Liquid level detection and reading

Before its first use, a camera must be calibrated and some basic information about setup must be known, the distance between the camera and the fluid; e.g., the distance between the fluid and the measuring scale, and the distance between individual scale marks. If for some reason distance between the camera and the measuring scale cannot be obtained, or when it is not constant, information about the field of view can be used instead.

Detection and reading is done in few steps; firstly, the measuring scale is detected either by using pattern recognition or by using the predefined area (marked by red lines in Figure 4) if the camera is not expected to move. Next, all scale marks are read along the green line in Figure 4. Every mark line is detected at the upper and the lower bound, and these points are used for calculation of the line's centreline. For small distances (only a few pixels), we can assume both points are equally distorted. After the positions of all mark lines are determined, lens correction is performed (using previously obtained correction), after which the function for tilt distortion is approximated over the corrected points and the camera angle is determined.

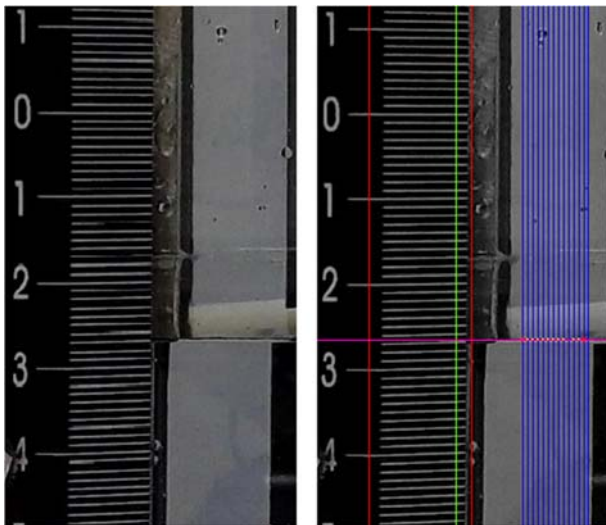


**Figure 4:** Measuring scale and liquid level; raw image (left) and processed image (right).

Simultaneously, liquid level is detected using the edge detection procedure. Edge detection is carried out on multiple vertical lines across the fluid area (blue lines in Figure 4), so that discrete air bubbles or droplets that might be present in the area do not influence the results. When the height of the liquid level is determined (purple line in Figure 4), it is corrected for the lens distortion. Then the angle between the liquid level and the horizontal plane is determined, using information about the camera setup and the camera angle. This is then used to make corrections for the parallax effect.

### 4. Testing and results

Images were captured using a standard web camera (Razer, Kiyō). The computer vision system was tested in a laboratory environment on the standard capacity measure with the nominal capacity of 100 l using water. Although the developed system is intended for measurements of liquids other than water, water was chosen as a testing medium to take up the challenge of level detection of more transparent liquids. Figure 4 shows an example of the captured image of the measuring scale in its raw (left) and processed form (right). The scale interval represents 10 ml, which is equal to 0.01% of the nominal capacity (one scale interval is approximately 1 mm).

The standard capacity measure was gradually filled with the water. Readings were taken for different liquid levels (from -0.7% to 0.7% of the nominal capacity) by the operator and the computer vision system. The maximum error of the reading of the liquid level by an operator is estimated to not to exceed one scale interval. Figure 5 shows the deviation between the results read by the computer vision system and the operator for different liquid levels in % of the nominal capacity.

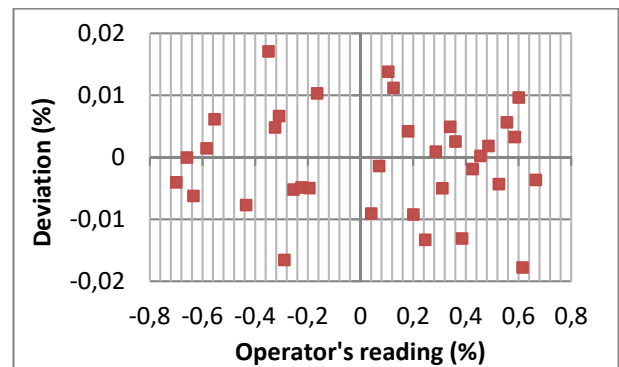


**Figure 5:** Deviations between the readings by the computer vision system and the operator for different liquid levels.

It is evident that the measurement deviations do not exceed 0.02%, which is satisfying considering the scale resolution. When using standard capacity measures in legal metrology, the target expanded uncertainty is of the order of 0.1%, so the achieved quality of readings can be considered acceptable for such applications.

Nevertheless, the system still struggles when lightning conditions are poor or when they change constantly. Nevertheless, since we were using water as a test liquid, detection of the liquid level was more difficult and more dependent on lightning than in case of coloured fluids. Figure 6 shows an example of the captured image of the measuring scale for diesel fuel (other capacity measure as in the presented tests). It is evident that a much

clearer edge of the liquid level can be obtained, which decreases the lighting effects.

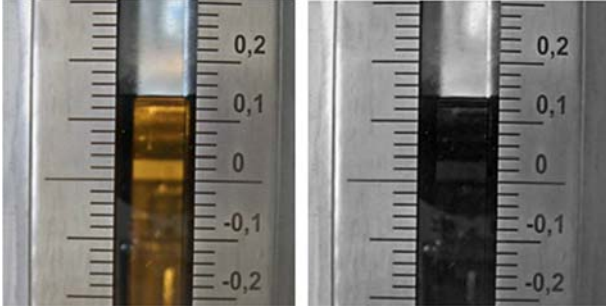


**Figure 6:** Image of the capacity measure scale for diesel fuel; raw image (left) and monochrome image (right).

## 5. Conclusion

The computer vision system was tested in a laboratory environment on the standard capacity measure with the nominal capacity of 100 l using water. The measurement results obtained with the computer vision system show relatively small deviations from the readings made by the operator ( $< 0.02\%$  of the nominal capacity). We anticipate that with proper lightning the automated measurements can be at least as accurate as the manual ones. Therefore, the developed measuring system has a potential for inexpensive and nonintrusive automation of standard capacity measures that are used for calibration and verification of the measuring system for fuels or other liquids.

## References

- [1] OIML R120: *Standard capacity measures for testing measuring systems for liquids other than water*, 2010.
- [2] Szeliski, R., *Computer Vision: Algorithms and Applications* (Springer), 2010.
- [3] Hornberg, Alexander., *Handbook of Machine Vision* (Wiley-VCH-Verl.), 2011.

# Vertically installed Venturi tubes for wet-gas flow measurement: possible improvements to ISO/TR 11583 to extend its range of applicability

E. M. Graham<sup>1</sup>, M. Reader-Harris<sup>1</sup>, G. Chinello<sup>1</sup>, K. Harkins<sup>1</sup>, N. Bowman<sup>1</sup>, L. Wales<sup>1</sup>

<sup>1</sup>NEL, Scottish Enterprise Technology Park, East Kilbride, UK  
E-mail (corresponding author): [emmelyn.graham@tuv-sud.co.uk](mailto:emmelyn.graham@tuv-sud.co.uk)

---

## Abstract

Venturi tubes are commonly used for wet-gas flow measurement, and the majority of commercial wet-gas flow meters generally include a Venturi tube installed vertically with embedded secondary instrumentation. The presence of the liquid causes an increase in the measured differential pressure and results in the Venturi tube over-reading the actual amount of gas passing through the meter. Most of the research in the literature is focused on the investigation of the over-reading for horizontally oriented Venturi tubes, thus limiting the development of over-reading correlations for vertical installation. An experimental campaign was recently conducted at the National Engineering Laboratory (NEL) high-pressure wet-gas loop, where three Venturi tubes of the same nominal diameter (4") but different throat to inlet diameter ratio (0.4, 0.6, 0.75) were tested, installed vertically after a blind tee. The results of this experimental campaign are presented in this paper and the effects of various parameters (line pressure, gas Froude number, diameter ratio) on the over-reading are briefly discussed. It is shown that the over-reading correlation included in the ISO/TR 11583:2012 and developed for horizontally oriented Venturis, is not applicable to vertically oriented Venturis. However, if modified, the correlation included in the ISO/TR 11583 is capable of meeting its stated uncertainty limits for the experimental data presented here for vertically installed Venturis.

---

## 1. Introduction

Venturi tubes are one of the most common types of device used worldwide for wet-gas flow measurement as they are a simple, robust and cost-effective flow meter. They also form the main component in the majority of commercial wet-gas and multiphase flow meters. Major oil and gas operators acknowledge that more accurate measurement of wet-gas and multiphase flows can be used to increase production. Hence there is a drive to improve the accuracy and increase the use of this technology.

The presence of the liquid in the gas phase causes an increase in the measured differential pressure and results in the Venturi tube over-reading the actual amount of gas passing through the meter. This over-reading is usually 'corrected' using available correlations derived from the experimental data to determine the actual gas mass flowrate.

The equations used for correcting the Venturi tube over-reading included in ISO/TR 11583:2012 [1] were developed for 2-phase one-liquid-component wet-gas flows in horizontal installation. The majority of research

and the development of corrections for using Venturis in wet-gas flows are for horizontal installations. Research on vertical Venturis has been conducted by [2], which developed a correlation for a non-standard Venturi tube at low pressure. Experimental and modelling work on vertically downward oriented Venturis has been conducted by [3]–[6]. Experiments and modelling for vertically upward oriented Venturis at high pressure have been conducted by [7].

The high-pressure wet-gas flow measurement facility at NEL was used to collect new data for 4-inch (DN 100) Venturi tubes with a diameter ratio from 0.4 to 0.75 installed in a vertical orientation. This data was used to assess the robustness of the correlation for horizontal installation in ISO/TR 11583 and to give insight on the development of corrections for vertical installation. The results provided further evidence that the correlation in ISO/TR 11583 is not appropriate for vertical installations and that ISO/TR 11583 correlation must be modified to reduce the measurement uncertainty. The uncorrected wet-gas data resulted in flow measurement errors of over 60%; using the ISO/TR 11583 correlation reduced this to less than 13%, which is over four times the uncertainty of 3% quoted in ISO/TR 11583. Using new correction

factors for vertical installation reduced the uncertainty to less than 3%.

In section 2 some relevant definitions for wet-gas flow are briefly reported, and in section 3 the ISO/TR 11583 correlation is reported. Section 4 shows the experimental set-up and tests conditions, while in section 5 the experimental results are discussed. In section 6 conclusions are drawn and plans for future research are presented.

## 2. Definitions of Wet-Gas Flow

For this research, wet-gas flow is defined as the flow of gas and liquids with a Lockhart-Martinelli parameter,  $X$ , in the range  $0 < X \leq 0.3$ .

The Lockhart-Martinelli parameter is defined as

$$X = \frac{m_{liq}}{m_{gas}} \sqrt{\frac{\rho_{l,gas}}{\rho_{liq}}} \quad (1)$$

where  $m_{liq}$  and  $m_{gas}$  are the mass flow rates of the liquid and gas phase respectively and  $\rho_{liq}$  and  $\rho_{gas}$  are the densities of the liquid and gas phase respectively. In this work the density of the gas phase is that at the upstream pressure tapping,  $\rho_{l,gas}$ .

The gas densimetric Froude number,  $Fr_{gas}$ , is a dimensionless number directly proportional to the gas velocity. It is defined as the square root of the ratio of the gas inertia if it flowed alone to the gravitational force on the liquid phase.

Gas densimetric Froude number,

$$Fr_{gas} = \frac{v_{gas}}{\sqrt{gD}} \sqrt{\frac{\rho_{l,gas}}{\rho_{liq} - \rho_{l,gas}}} \quad (2)$$

where  $v_{gas}$  is the superficial gas velocity,  $g$  is the acceleration due to gravity and  $D$  is the pipe internal diameter.

The superficial gas velocity is given by

$$v_{gas} = \frac{m_{gas}}{\rho_{l,gas} A} \quad (3)$$

where  $A$  is the pipe area.

The gas-to-liquid density ratio,  $DR$ , is defined as

$$DR = \frac{\rho_{l,gas}}{\rho_{liq}} \quad (4)$$

The corrected gas mass flowrate,  $m_{gas}$ , is given by

$$m_{gas} = \frac{EA_d C \varepsilon_{wet} \sqrt{2 \rho_{l,gas} \Delta p_{wet}}}{\phi} \quad (5)$$

where  $E$  is the velocity of approach factor defined in equation (6),  $A_d$  is the Venturi-tube throat area,  $C$  is the discharge coefficient,  $\varepsilon_{wet}$  is the gas expansibility in wet-gas conditions,  $\Delta p_{wet}$  is the actual (wet-gas) differential pressure and  $\phi$  is the wet-gas over-reading or correction.  $\varepsilon_{wet}$  was determined from ISO 5167-4 [8] using the actual value of the pressure ratio.

The velocity of approach factor,  $E$ , is defined as

$$E = \frac{1}{\sqrt{1 - \beta^4}} \quad (6)$$

where  $\beta$  is the diameter ratio of the Venturi tube (diameter at throat divided by diameter of pipe).

## 3. ISO/TR 11583 correlations for Venturi Tubes

The wet-gas discharge coefficient is derived using the following equation

$$C = 1 - 0.0463 e^{-0.05 Fr_{gas,th}} \min\left(1, \sqrt{\frac{X}{0.016}}\right) \quad (7)$$

where the throat Froude number ( $Fr_{gas,th}$ ) is calculated as

$$Fr_{gas,th} = \frac{Fr_{gas}}{\beta^{2.5}} \quad (8)$$

The over-reading is

$$\phi = \sqrt{1 + C_{Ch} X + X^2} \quad (9)$$

where  $C_{Ch}$  accounts for the density ratio and is given by the following equation

$$C_{Ch} = \left( \frac{\rho_{liq}}{\rho_{l,gas}} \right)^n + \left( \frac{\rho_{l,gas}}{\rho_{liq}} \right)^n \quad (10)$$

The value of  $n$  is determined by

$$n = \max(0.583 - 0.18\beta^2 - 0.578e^{-0.8Fr_{gas}/H}, 0.392 - 0.18\beta^2) \quad (11)$$

where  $H$  is a parameter to account for the effect of the liquid properties on the over-reading.  $H = 1$  for liquid hydrocarbon,  $H = 1.35$  for water at ambient temperature and  $H = 0.79$  for liquid water in wet-steam flow (hence at elevated temperatures). The ISO/TR 11583 correlation in its original form is restricted to one-liquid-component flows only. However, later research showed that for oil/water mixtures the parameter  $H$  can be obtained by knowing the water cut and linearly interpolating  $H$  between 1 and 1.35 [9]. Further improvement may be obtained with another simple equation for  $H$  [10].

The correlation can be used to determine the gas mass flowrate under the following conditions

$$0.4 \leq \beta \leq 0.75$$

$$0 < X \leq 0.3$$

$$3 < Fr_{gas,th}$$

$$0.02 < \rho_{l,gas}/\rho_{liq}$$

$$D \geq 50 \text{ mm}$$

with an uncertainty of

$$\begin{cases} 3\% \text{ for } X \leq 0.15 \\ 2.5\% \text{ for } 0.15 < X \leq 0.3 \end{cases}$$

if the Lockhart-Martinelli is known without error [1][11].

#### 4. Experimental Test Set-Up

Three 4-inch Venturi meters with diameter ratios  $\beta$  equal to 0.4, 0.6 and 0.75 (convergent angle  $21^\circ$  and divergent angle  $7.5^\circ$ ) were installed in a vertical upward orientation directly after a blind-tee in NEL's high-pressure wet-gas flow measurement facility. Figure 1 and Figure 2 show photographs of the experimental set-up. Gas (nitrogen) and oil (kerosene substitute Exxsol D80) flow rates were varied to obtain gas densimetric Froude numbers ( $Fr_g$ ) between 1 and 5.5 across a range of Lockhart-Martinelli parameters ( $X = 0$  to 0.3). The conditions tested are shown in Table 1. The line pressure was varied between 15 and 60 barg.

**Table 1:** Test Conditions.

Venturi diameter ratio, $\beta$ (-)	Line Pressure (barg)	Gas Froude number, $Fr_g$ (-)	Density Ratio, $DR$ (-)
0.4	15	1, 2, 2.5	0.023
	30	1.5, 2, 3	0.046
	60	1.5, 3, 4	0.088
0.6	15	1.5, 2.5, 3	0.024
0.75	15	2, 3, 4, 5	0.025
	30	1.5, 4, 5	0.044
	60	2, 5, 5	0.088



**Figure 1:** Photograph of the Venturi setup and instrumentation.

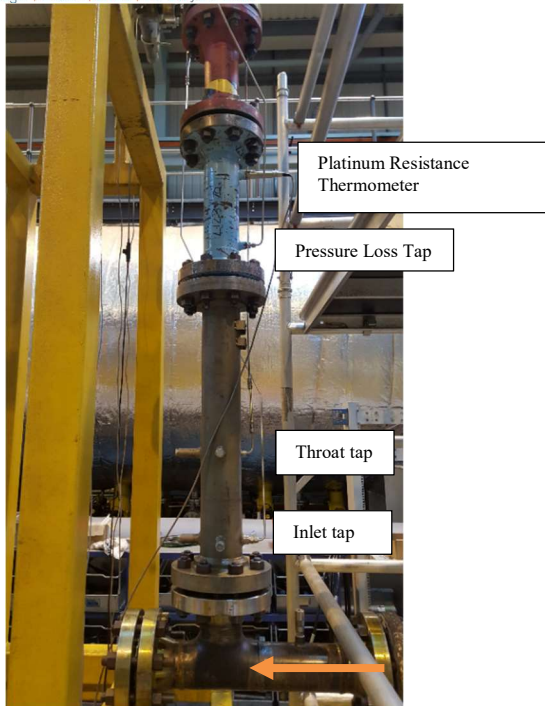


Figure 2: Photograph of the Venturi setup.

**5. Results**

The equations in ISO/TR 11583 were developed to correct the gas reading of horizontally installed Venturi tubes subjected to wet gas flows. Figure 3 shows the errors when using the ISO/TR 11583 correlation with the new data collected for vertical Venturi tubes. The error increases for increasing Lockhart-Martinelli values and a maximum error of approx. 13% is found at  $X \approx 0.3$ , which is over four times higher than the 3% uncertainty quoted in ISO/TR 11583.

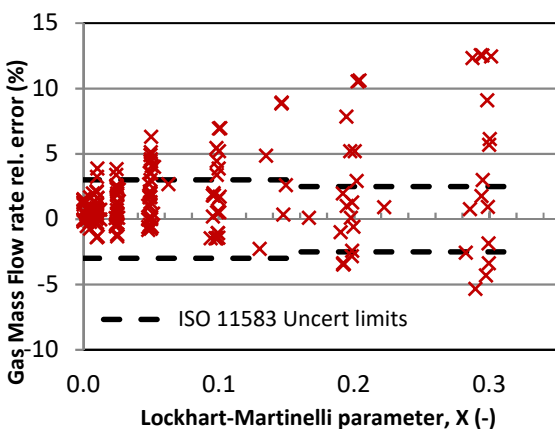


Figure 3: Relative error in gas mass flow rate obtained when applying the ISO/TR 11583 correlation to the present experimental data for vertically oriented Venturi tubes.

For Venturi tubes installed horizontally the gas Froude number has a substantial impact on the meter over-reading; above a gas Froude number of approx. 1.5, as the gas Froude number increases the over-reading increases reaching a constant maximum value at high gas Froude number. This effect is accounted for in both Equations (7) and (11) used respectively to determine the value of the wet gas discharge coefficient and the value of the  $n$ -exponent. Instead, for Venturi tubes installed in a vertical orientation, the gas Froude number seems to have much less impact on the meter over-reading, see also [12]. For example, Figure 4 shows the over-reading for the  $\beta=0.4$  Venturi tube at a single line pressure of 30 barg (DR=0.046) but varying the gas Froude number. It can be seen that the over-reading values are approximately the same. This effect was noted in all the data sets presented here.

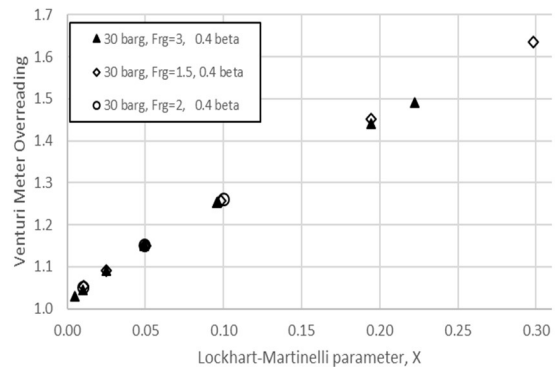


Figure 4: Over-reading for  $\beta=0.4$  Venturi at 30 barg (density ratio 0.046) tested at three gas Froude numbers (Frg = 1.5, 2, 3).

For comparison Figure 5 shows some of the data from Figure 4 plotted together with some data previously collected with the same  $\beta=0.4$  Venturi tube at the same line pressure of 30 barg (DR=0.046) but installed in a horizontal orientation. This show that the effect of the gas Froude number on the meter over-reading is almost negligible when the Venturi is installed vertically in comparison with when it is installed horizontally.

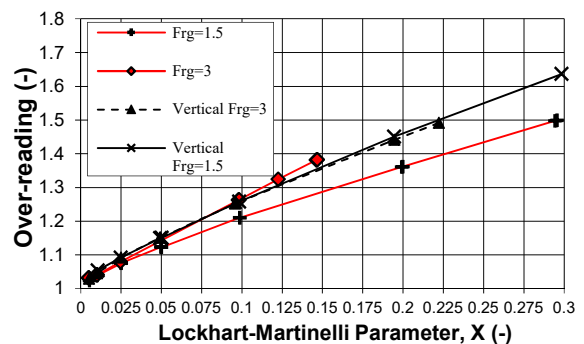
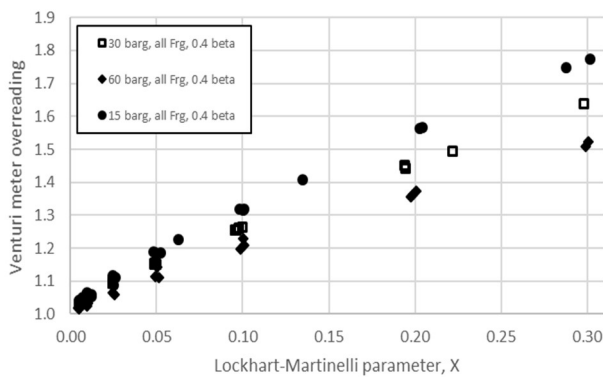


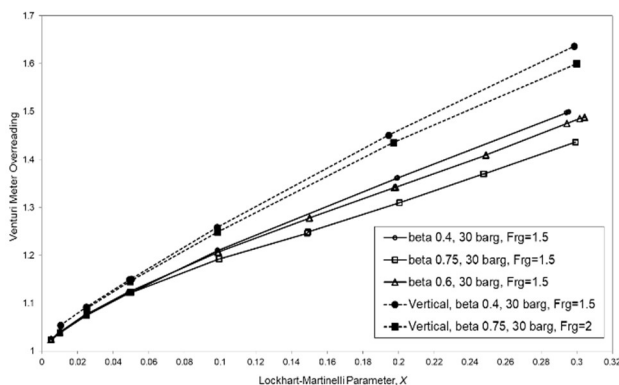
Figure 5: Over-reading for  $\beta=0.4$  Venturi at 30 barg (density ratio 0.046) in a horizontal orientation (red curves) and vertical orientation (black curves) as a function of the gas Froude number.

Figure 6 shows all the data for the vertically installed Venturi tube with diameter ratio 0.4. This shows that the density ratio (i.e. gas pressure) does still have a significant effect on the meter over-reading for vertically installed Venturi tubes.



**Figure 6:** Over-reading for vertically installed  $\beta=0.4$  Venturi at all pressures and gas Froude numbers.

The diameter ratio  $\beta$  of the Venturi does still have a significant impact on the over-reading. Figure 7 shows the over-reading data for horizontal and vertical Venturi tubes with diameter ratios from 0.4 to 0.75 at 30 barg and similar gas Froude numbers,  $Fr_{gas} \approx 1.5$ . This shows that the over-reading is more sensitive to the diameter ratio  $\beta$  when installed horizontally than vertically, but that the diameter ratio still has an effect for vertically installed Venturis.



**Figure 7:** Over-reading for vertically installed  $\beta=0.4$  and  $\beta=0.75$  Venturi tubes, and for  $\beta=0.4, 0.6, 0.75$  horizontally installed Venturi tubes at 30 barg line pressure and gas Froude numbers approx. equal to 1.5.

Because the gas Froude number has a negligible effect on the over-reading of vertically installed Venturi tubes, then a single value of the  $n$ -exponent can be fitted for each diameter ratio. The effect of the gas pressure (i.e. density ratio) is considered accounted for by the density ratio in Equation 7. Table 2 shows the derived values of the  $n$ -exponent for each Venturi tube.

**Table 2:** Fitted values of the  $n$ -exponent for each Venturi.

Venturi diameter ratio	Fitted value of $n$
Beta 0.4	0.503
Beta 0.6	0.478
Beta 0.75	0.425

The  $n$ -exponent values were obtained by minimizing the root-mean-square error of the gas mass flow rate for each diameter ratio, over all the tested conditions for the Venturi diameter ratio  $\beta$ . Figure 8 shows the relative error in the gas mass flow rate using the values of  $n$  from Table 2 and using the wet-gas discharge coefficient given by Equation 7. This shows that the gas mass flow rate can be corrected to within 3% (99.4% coverage factor) by fitting the  $n$ -exponent as a function of the diameter ratio.

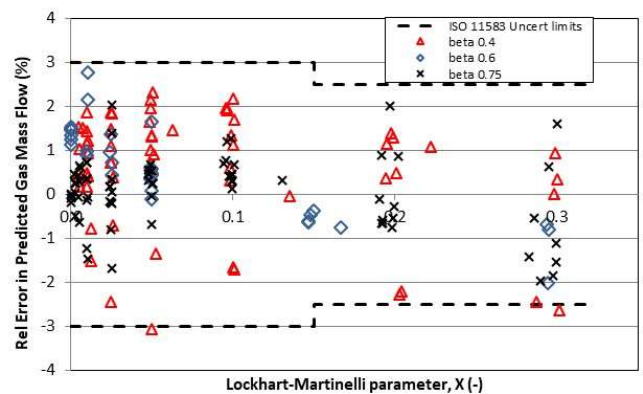


**Figure 8:** Errors when using new fitted values of the  $n$ -exponent for each Venturi and using wet-gas discharge coefficient from ISO/TR 11583:2012.

Figure 9 compares the errors when using the dry-gas discharge coefficient and re-fitted values of the  $n$ -exponent, against using the wet-gas discharge coefficient and the fitted values for  $n$  in table 2. This shows that the wet-gas discharge coefficient derived for horizontal Venturi tubes provides a robust fit also to the vertical Venturi data and significantly reduces the errors compared with using the dry-gas discharge coefficient.

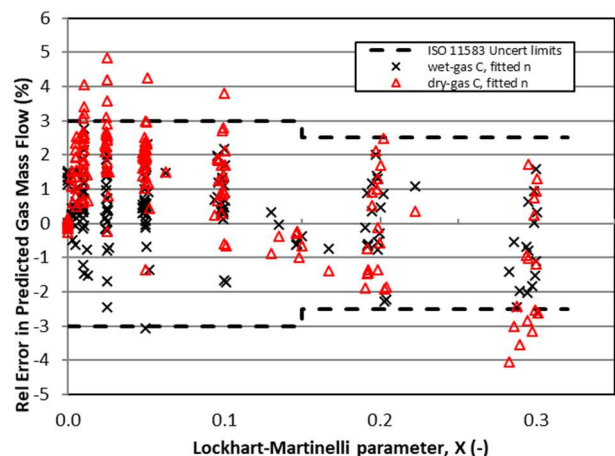


**Figure 9:** Comparison of errors when using values of  $n$  for each Venturi and using wet-gas discharge coefficient from ISO 11583 and the dry-gas discharge coefficient.

## 6. Conclusion

New experimental results were obtained at the National Engineering Laboratory for three different Venturi tubes of 4" nominal diameter but different diameter ratio (0.4, 0.6, 0.75) installed vertically and subject to wet-gas flow. The results confirm that the over-reading is not significantly affected by the gas Froude number when the Venturi is installed vertically, as previously found by [5]. The over-reading was found still largely affected by the line pressure. The results show that the Venturi's diameter ratio has a smaller impact on the over-reading than for horizontally installed Venturis. However, the diameter ratio was found still to have a significant effect on the over-reading. Present results confirm that the ISO/TR 11583 over-reading correlation cannot be employed directly for Venturi tubes installed vertically. However, if the  $n$ -exponent is fitted as a function of the diameter ratio and the wet-gas discharge coefficient included in ISO/TR 11583 is used, then the gas mass flow rate can be predicted within  $\pm 3\%$  error.

A larger and extended experimental dataset is needed to draw further conclusions and to develop a suitable over-reading correlation for vertically installed Venturi tubes. It is thus planned to conduct further research with the aim of forming the basis on which the current wet-gas standards/best practice will be updated to cover a wider range of installations for Venturi tubes.

## Acknowledgements

The work described in the paper was carried out as part of the National Measurement System's Engineering and Flow Programme, under the sponsorship of the United Kingdom Department for Business, Energy and Industrial Strategy.

## References

- [1] ISO/TR 11583:2012, *Measurement of wet gas flow by means of pressure differential devices inserted in circular cross-section conduits*. Geneva, International Organization for Standardization, 2012.
- [2] L. Xu, W. Zhou, and X. Li, "Wet gas flow modeling for a vertically mounted Venturi meter," *Meas. Sci. Technol.*, vol. 23, no. 4, pp. 1–9, 2012.
- [3] A. Lupeau, B. Platet, P. Gajan, A. Strzelecki, J. Escande, and J. P. Couput, "Influence of the presence of an upstream annular liquid film on the wet gas flow measured by a Venturi in a downward vertical configuration," *Flow Meas. Instrum.*, vol. 18, no. 1, pp. 1–11, 2007.
- [4] G. Salque, J. P. Couput, P. Gajan, A. Strzelecki, and J. Fabre, "New correction method for wet gas flow metering based on two phase flow modelling: Validation on industrial Air/Oil/Water tests at low and high pressure," in *26th International North Sea Flow Measurement Workshop*, 2008, pp. 331–348.
- [5] G. Salque, P. Gajan, A. Strzelecki, J. P. Couput, and L. El-Hima, "Atomisation rate and gas/liquid interactions in a pipe and a venturi: Influence of the physical properties of the liquid film," *Int. J. Multiph. Flow*, vol. 51, pp. 87–100, 2013.
- [6] P. Gajan, G. Salque, J. P. Couput, and J. Berthiaud, "Experimental analysis of the behaviour of a Venturi meter submitted to an upstream air/oil annular liquid film," *Flow Meas. Instrum.*, vol. 33, pp. 160–167, 2013.
- [7] H. R. E. van Maanen and H. de Leeuw, "Modelling of Wet Gas flow in Venturi Meters to Predict the Differential Pressure," in *34th International North Sea Flow Measurement Workshop*, 2016, no. October.
- [8] ISO 5167-4:2003, *Measurement of fluid flow by means of pressure differential devices inserted in circular cross-section conduits running full — Part 4: Venturi tubes*. Geneva, International Organization for Standardization, 2003.
- [9] E. Graham *et al.*, "Impact of Using ISO / TR 11583 for a Venturi Tube in 3-Phase Wet-Gas Conditions," in *33rd International North Sea Flow Measurement Workshop*, 2015.
- [10] M. Reader-Harris, E. Graham, and C. Forsyth, "Testing ISO/TR 11583 outside its range of applicability: areas of possible improvements," in *European Flow Measurement Workshop (Powerpoint only)*, 2017.
- [11] M. Reader-Harris, *Orifice Plates and Venturi Tubes*. Cham: Springer International Publishing, 2015.
- [12] E. Graham, M. Reader-Harris, D. Hodges, R. Hone, A. Barrie, and N. Ramsay, "Performance of a Vertically Installed Venturi tube in Wet - Gas Conditions," in *32nd International North Sea Flow Measurement Workshop*, 2014.

# Assessment of allocation systems: combining Data Validation & Reconciliation scheme and PVT simulations

Dr. D. van Putten<sup>1</sup>, L.H. van Luijk<sup>1</sup>,  
Dr. H.J.Riezebos<sup>1</sup>, B.Tinge<sup>1</sup>)

<sup>1</sup>DNV GL, Energieweg 17, NL-9743AN Groningen, the Netherlands  
E-mail (corresponding author): [Henk.Riezebos@dnvgl.com](mailto:Henk.Riezebos@dnvgl.com)

---

## Abstract

For increasingly complex production systems, the traditional allocation processes appear to be less suitable and an alternative methodology is required. An assessment was carried out on a large wet gas allocation system containing more than 120 wells. The assessment was based on an approach that combines the Data Validation and Reconciliation (DVR) methodology and process simulations to accurately calculate the reconciliation factors applied to each well. It was found that the current imbalance and the allocation method complies with requirements stated in the agreement between stakeholders. The assessment provided much insight in the sensitivity of the overall gas balance and provides prioritization of the improvements to minimize the imbalance. A more balanced allocation system leads to a fairer division of the accrued revenues.

---

## 1. Introduction

Allocation methods are applied in the oil and gas industry to compensate for the imbalance in measurement systems. Reconciliation of the measured values is possible if redundancy in the measurements is present. Different approaches to resolve this imbalance are designed [1] and the choice of the allocation method depends on the agreement between the stakeholders.

The need for more fair allocation methodologies is increasing nowadays due to the fact that accurate metering at every relevant element of a production process is either very expensive or physically (near to) impossible, taking into account recent trends such as deepwater field development, use of subsea production systems, enhanced oil recovery and tie-backs of pipelines from smaller fields. This leads to the sharing of production or transport facilities and meters for different wells, which in turn leads to more complex allocation systems [5].

The industry is driving towards more efficient operation which leads to more small field tie-ins in existing allocation systems. The same cost efficiency may lead to the choice of the operator to omit metering or use alternatives like virtual flow metering [4].

Also, more small-size operating companies are buying (depleting) fields from larger operating companies, leading to more stakeholders in an

allocation system. Change in the allocation procedure, the number of stakeholders or the operating conditions in an allocation system, requires an assessment on the procedures in place to critically evaluate the impact on the stakeholders such as Finance, Operations and Reservoir Engineers.

For increasingly complex production systems, the traditional allocation processes appear to be less suitable and an alternative methodology is required..

## 2. Allocation systems

A general allocation system is outlined in Figure 2 1. The allocation system is divided into three measurement stages: wells, well head platforms (WHP) and the custody transfer (CT) location. In case of a general multiphase flow measurement system, the gas, oil and water flow rate is measured. In Figure 2 1, these flows are evaluated in terms of the measured mass flows  $\hat{m}_k$ , where  $k = g, o, w$  indicating the phase **g**as, **o**il and **w**ater respectively. The allocated mass flows after reconciliation will be denoted by  $\dot{m}_k$ . The reason for taking the mass flows is to take into account interphase mass transfer within the entire allocation system as will be explained in section 4. In general, each measurement is taken at different thermodynamic conditions, i.e. at different

pressures and temperatures. The change in thermodynamic conditions is indicated by the valves in Figure 2 1.

The measurements at the CT location are typically considered as exact, meaning no uncertainty or bias is attributed to that measurement. Therefore, these measurements are equal to their reconciled values.

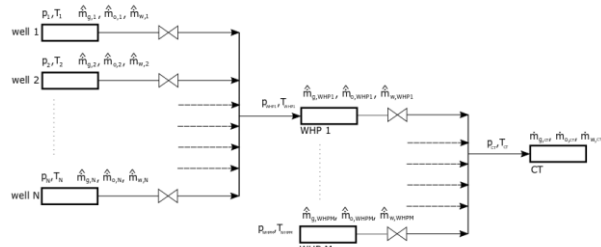


**Figure 2-1:** Schematic representation of a subsection of an allocation system with N wells feeding into a well head platform. A total of M well head platforms feed into the custody transfer location

The most common allocation methods used in the industry are By-Difference (BD), Pro-Rata (PR) and Uncertainty Based (UB) allocation or a combination of these methods. These methods are commonly evaluated in terms of standard volume flow rates, indicated by  $Q_k$ . In the proceeding sections these methods will be elaborated for a simple two-stage allocation system with N wells for phase measurement  $Q_k$  at standard conditions, as outlined in Figure 2.2. The advantages and disadvantages of the allocation methodologies are briefly described.

All allocation methods rely on the concept of redundancy in measurements. The most common type is spatial redundancy in which multiple measurements are measured again in a combined stream, as depicted in Figure 2 1 where multiple well measurements are measured at the well head platform as a combined stream. The redundancy of an allocation system is defined as the number of measurements plus the number of constraints (balance equations) minus the number of unknowns. In the example just mentioned, the redundancy is one and the system is called over-determined.

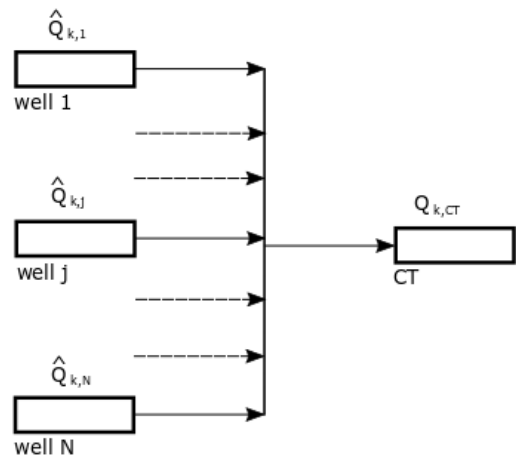


**Figure 2-2:** Schematic representation of a two-stage allocation system.

### 2.1 Allocation By difference

The By-Difference (BD) allocation method attributes the imbalance of the allocation system to one of the well measurements. Considering the allocation system in Figure 2 2 and applying the BD allocation method to the measurement of well j, results in the mathematical procedure

$$\begin{aligned} Q_{k,i} &= \hat{Q}_{k,i}, \forall i \neq j \\ Q_{k,j} &= Q_{k,CT} - \sum_{i \neq j} \hat{Q}_{k,i} \end{aligned} \quad (1)$$

where the hat indicates the measurement value and the value without hat the reconciled value. The resulting relative uncertainty of the measurement of well j, denoted by  $u^*(Q_{k,j})$ , can be calculated if the relative uncertainties of the other measurements are known and is given by

$$u^*(Q_{k,j}) = \sqrt{\left[ \frac{Q_{k,CT}}{\hat{Q}_{k,j}} u^*(Q_{k,CT}) \right]^2 + \sum_{i \neq j} \left[ \frac{Q_{k,i}}{\hat{Q}_{k,j}} u^*(Q_{k,i}) \right]^2} \quad (2)$$

It is clear from equation (2) that the uncertainty of well j increases when the value of  $Q_{k,j}$  is small compared to the other wells. In specific applications, this method may be appropriate, e.g. in systems where the well with significantly larger flow rate is reconciled and the smaller flow rates are unaltered. In general, the method requires knowledge about the measurements and expected performance. Moreover, for a system as depicted in Figure 2 2 the redundancy is equal to zero,

resulting in the assumption that the measurement of all wells, except well  $j$ , are exact.

### 2.2 Allocation Pro rata

The Pro-Rata (PR) allocation method divides the imbalance of the allocation system to each well proportional to the value of  $Q_{k,j}$  and can be mathematically expressed as

$$I = Q_{k,CT} - \sum_i \hat{Q}_{k,i}, \quad \alpha_j = \frac{\hat{Q}_{k,j}}{\sum_i \hat{Q}_{k,i}} \quad (3)$$

$$Q_{k,j} = \hat{Q}_{k,j} + \alpha_j I,$$

where  $I$  is the allocation imbalance and is the allocation factor of well  $j$ . The resulting relative uncertainty of the measurement of well  $j$  is given by

$$u^*(Q_{k,j}) = \sqrt{u^*(Q_{k,CT})^2 + \left[ \left( 1 - \frac{\hat{Q}_{k,j}}{\hat{Q}_{k,i}} \right) u^*(\hat{Q}_{k,j}) \right]^2 + \sum_{i \neq j} \left[ -\frac{\hat{Q}_{k,i}}{\hat{Q}_{k,i}} u^*(\hat{Q}_{k,i}) \right]^2}, \quad \hat{Q}_{k,i} = \sum_i \hat{Q}_{k,i} \quad (4)$$

The PR method distributes the imbalance over all measurements and treats all measurements similarly. Therefore, PR allocation assumes that the measurement uncertainties and biases are equal. It also requires that all input streams are measured.

### 2.3 Allocation based on uncertainty

To account for the differences in measurement uncertainty, the Uncertainty-Based (UB) allocation can be applied. The method relies on proper estimates of the absolute uncertainties, denoted by

$$u(\hat{Q}_{k,j}) = \hat{Q}_{k,j} u^*(\hat{Q}_{k,j}) \text{ of the measurements in}$$

terms of their variance, i.e.  $u(\hat{Q}_{k,j})^2$ . The

allocation method has a similar structure as equation (3), however the allocation factor is evaluated as

$$\alpha_j = \frac{u(\hat{Q}_{k,j})^2}{u(Q_{k,i})^2 + \sum_i u(\hat{Q}_{k,i})^2} + \frac{\hat{Q}_{k,j}}{\hat{Q}_{k,i}} \frac{u(Q_{k,i})^2}{u(Q_{k,i})^2 + \sum_i u(\hat{Q}_{k,i})^2} \quad (5)$$

The UB method distinguishes the reconciliation factor based on the absolute uncertainties. Since the absolute uncertainty is proportional to the measured value and its relative uncertainty, the UB method can be considered as a relative uncertainty scaled PR allocation. For a two-stage allocation

system the method can be implemented as outlined in equation (5), however, the application to a multistage allocation system as depicted in Figure 2-1 is not straightforward [1]. The UB method does not consider the dependencies of the streams between the different stages and therefore at the intermediate stage, the combined stream is not corrected.

### 3. Data Validation and Reconciliation

The Data Validation and Reconciliation (DVR) method is based on a minimization condition that corrects the initial measured mass flows  $\hat{m}_{k,j}$  to an allocated value  $\dot{m}_{k,j}$  taking into account the measurement uncertainty of  $\hat{m}_{k,j}$ , see e.g. [6]. The absolute measurement uncertainty is often written in terms of the standard deviation, denoted as  $\sigma_{k,j}$ . DVR minimizes the total required scaled correction to the original measured value that is still able to compensate the imbalance of the allocation system. Mathematically, this results in the minimization of the cost function by means of the least squares method

$$F(\hat{\mathbf{m}}_k, \dot{\mathbf{m}}_k, \boldsymbol{\sigma}_k) = \sum_j \left( \frac{\dot{m}_{k,j} - \hat{m}_{k,j}}{\sigma_j} \right)^2 \quad (6)$$

Subject to the balance condition:

$$\dot{m}_{k,CT} = \sum_j f_j \dot{m}_{k,j} \quad (7)$$

The bold symbols in equation (6) represent the vector notation of all measurements, i.e.

$$\dot{\mathbf{m}}_k = (\dot{m}_{k,1}, \dot{m}_{k,2}, \dots, \dot{m}_{k,N})^T$$

The parameter accounts for the interphase mass transfer from well  $j$  and its interaction with the other wells that feed into the same CT stream. As an example, in a gas allocation system  $k=g$ , part of the gas flow at the CT location can be attributed to degassing of condensate produced from well  $j$ . Also, the composition of other wells may influence the mass flow of well  $j$  that arrives at the CT location. Formally, this can be expressed as:

$$f_j = 1 + \frac{\sum_p \dot{m}_{p \leftrightarrow k, i \rightarrow j}}{\dot{m}_{k,j}} \quad (8)$$

where  $p$  is the phase which is in interaction with phase  $k$ , typically these are the gas and oil/condensate phases. In a multi-stage allocation process, multiple mass balance conditions may be present. Solving equations (7) and (8) simultaneously results in the solution for the allocated mass flow rates.

In the DVR analysis, the well measurements can be assessed by means of the so-called penalty factor, defined by

$$z_j = \frac{|\dot{m}_{k,j} - \hat{m}_{k,j}|}{\sigma_j} < 1.98 \quad (9)$$

where the factor 1.98 is related to the 95% confidence interval. Using the definition of the

reconciliation factor  $r_j$  leads to the equivalent expression for the penalty factor

$$z_j = \frac{|r_j - 1|}{\sigma_j^*}, \quad r_j = \frac{\dot{m}_{k,j}}{\hat{m}_{k,j}} \quad (10)$$

where  $\sigma_j^*$  is the relative standard deviation of measurement  $j$ .

#### 4. Process modelling

The schematic allocation system in Figure 2 1 is modelled in the process simulation tool HYSYS [2]. This tool calculates the mass balance on component level, i.e. for each individual species in the flow and is used widely in the oil and gas industry. The mass flow of each phase is not conserved since the condensate phase may evaporate or the gas may condensate due to changes in external conditions. To account for this, HYSYS solves the phase equilibrium problem by a multi-stage flash calculation for each stream from the conditions at the well,  $(p_j, T_j)$ , to the custody transfer location,  $(p_{CT}, T_{CT})$ .

At each well the gas, oil and water phases are in equilibrium at the measurement location. The input from the field may be limited or partly incorrect. Errors in the composition will directly lead to interphase mass transfer, causing an imbalance in the simulation. Therefore, it is mandatory to pre-condition the gas, oil and water flow rates.

The use of HYSYS has the advantage that all PVT data is available at all stages in the allocation system and can be checked with the configuration of the metering systems.

#### 5 Application to wet gas allocation system

The DVR allocation method combined with the process modelling was employed to assess a large wet gas allocation system in the Malaysia-Thai Joint Development Area, see Figure 5 1. This wet gas allocation system is operated by Carigali Hess and consists of 12 different fields with more than 120 wells connected to 6 well head platforms. The total gas allocation process of these fields is based on BD and PR allocation methods and is described in the Production Measurement and Allocation Procedure (PMAP), see [3]. A BD allocation is performed between the custody transfer measurement and the well head platforms, the subsequent well allocation is done by means of PR allocation. The measurements on the wells are performed by Venturi flow meters with a wet gas correction algorithm.

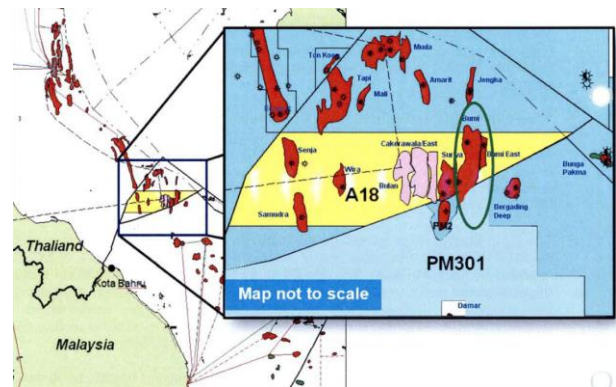


Figure 5-1: Malaysia-Thai joint development area.

The agreement between the different stakeholders demands a global reconciliation factor of the gas production between 0.9 and 1.1, see equation (7). This also means that in the current allocation procedure the BD allocation of the well head platforms could be well outside this specification, however, no requirement has been defined per well.

The application of the DVR methodology requires the definition of the uncertainties of the wet gas Venturi measurements. The uncertainty of these wet gas measurements depends on the choice of correction model, calibration uncertainty of the measurements, range of operation, fluid composition and wetness conditions. These conditions differed greatly per well, resulting in estimated relative uncertainties of the well measurements between 2 and 9%.

## 5.1 Results

The anonymized results for the reconciliation factors of the DVR allocation and the current allocation method for each well are shown in Figure 5 2 for a one-month period in October and November 2017.

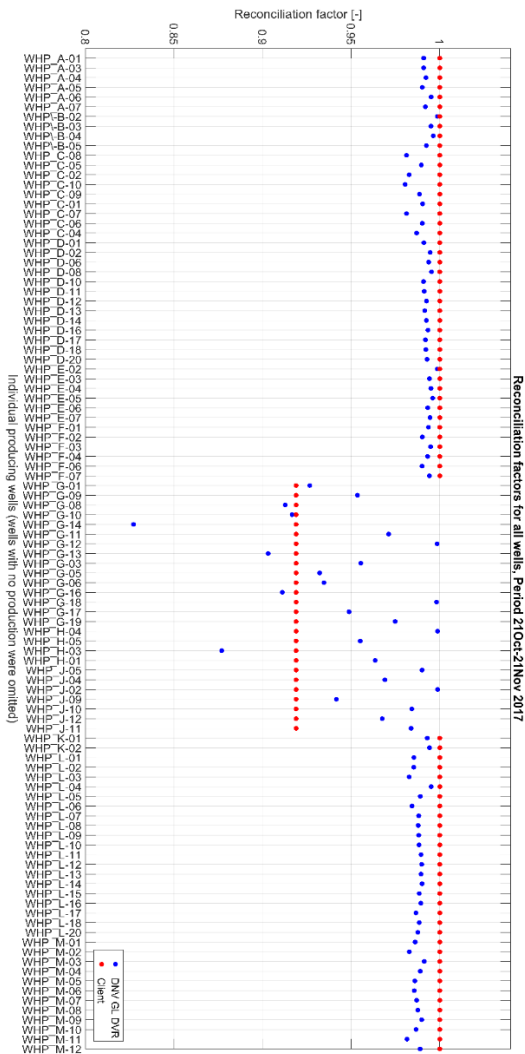


**Figure 5-2 : Anonymized results of the gas reconciliation factors: Current allocation method (red) and DVR method (blue)**

It is observed that the wet gas Venturi measurements over-predict the total flow leading to a negative imbalance. The current method produces, by definition, a reconciliation factor of 1 for the well head platforms that are unaffected by the BD allocation procedure. Also, the wells that are corrected (WHP\_G/H/J) all have the same reconciliation factor.

The solution of the DVR allocation method shows that most wells, that were assigned a reconciliation factor of 1 in the current allocation method, have a

DVR reconciliation factor of within 2% to their original value.

The wells connected to the WHP\_G/H/J platforms show more variability. This is mainly due to the differences in the combination of the production rate and relative uncertainty of the measurement. Since DVR is an uncertainty-based allocation method, the absolute uncertainty of the measurement determines the reconciliation factor. In general, the wells with high production volumes have a higher reconciliation factor, and therefore more of the imbalance of the allocation system is assigned to these wells. The sources of uncertainty differ per well as state in the introduction of Section 5.

To isolate the effect of the flow rate, the reconciliation factor can be plotted as a function of the relative sensitivity factor. This parameter is defined as

$$S_j = \frac{\dot{m}_{g,j}}{\dot{m}_{g,CT}} \frac{\partial \dot{m}_{g,CT}}{\partial \dot{m}_{g,j}} = f_j \frac{\dot{m}_{g,j}}{\dot{m}_{g,CT}} \quad (11)$$

The results are given in Figure 5 3. If the relative uncertainties of all the wells would be equal, the graph would show all dots on a straight line where the value of the relative uncertainty determines the slope. The clear outliers are the malperforming wells in the allocation system and it is observed that some of the wells will be reconciled with a lower factor than others. However, this does not directly imply that these well measurement are performing out of specification. This depends on the estimated uncertainty and wells with a reconciliation factor that differs significantly from 1 could still be within their expected uncertainty. On the other hand, these wells are bringing imbalance to the allocation system and therefore should be addressed, although they could perform according to specification. Therefore, Figure 5 3 indicates which measurements to improve to minimize the gas imbalance of the allocation system.

To assess the well measurements the penalty factor can be plotted for the wells that do not satisfy equation (9), see Figure 5 4. Some of the wells that distort the balance in the allocation system also show a large penalty factor, e.g. WHP\_G-14. Other wells perform relatively well in the allocation system, e.g. WHP\_J-09 compared to WHP\_G-05/06, whilst the penalty factor of WHP\_J-09 is higher than WHP\_G-05/06. Therefore, Figure 5 4 indicates which well measurements are not performing according to its specification and need further investigation.

It is clear from this case study that WHP\_G-14 and WHP\_H-03 are both malperforming in the

allocation system and the cause can be related to a malperforming wet gas flow meter.

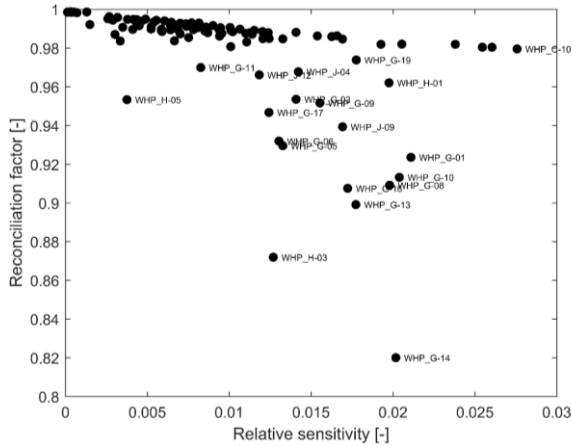


Figure 0-1 : Reconciliation factor of each well as function of the sensitivity parameter

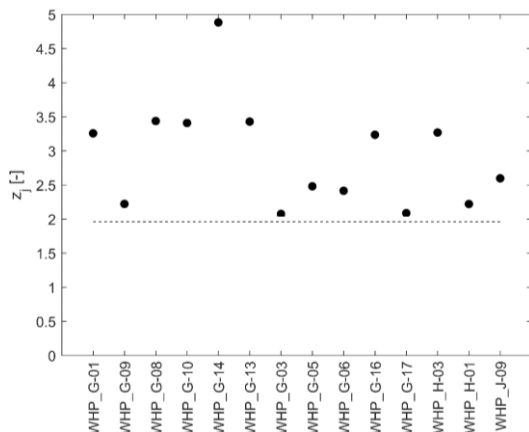


Figure 0-2 : Penalty factor of well measurements with a value not complying with equation Error! Reference source not found.

## 6. Conclusion

An assessment was carried out on a large wet gas allocation system of Carigali Hess containing more than 120 wells. The assessment was based on an approach that combines the Data Validation and Reconciliation (DVR) methodology and process simulations in HYSYS to accurately calculate the reconciliation factors applied to each well. It was found that the current imbalance and the allocation method complies with requirements stated in the agreement between stakeholders.

The DVR calculation indicated that the imbalance of the allocation system can be improved by further investigating the well measurements on two specific wells. The method also provided penalty factors on the well measurements that indicate that

the wet gas Venturi meters are not performing according to their specification.

The assessment of the allocation system provided much insight in the sensitivity of the overall gas balance and provides prioritization of the improvements to minimize the imbalance. A more balanced allocation system leads to a fairer division of the accrued revenues from the Malaysia-Thai Joint Development Area.

## References

- [1] A. Amin, Using Measurement Uncertainty in Production Allocation. Upstream Production Measurement Forum (2016)
- [2] <http://home.aspentech.com/en/products/engineering/aspens-hysys..>
- [3] Carigali Hess, Production Measurement and Allocation Procedure (PMAP) 2012.
- [4] J.P. Couput, N. Laiani and V. Richon, *Operational experience with virtual flow measurement technology* North-Sea Flow Measurement Workshop (2017).
- [5] A. Johnsen and A.M. Dahl, Maria to Kristin allocation from project to operation, a real life experience Hydrocarbon Management Workshop (2018).
- [6] S. Narasimhan and C. Jordache, *Data Reconciliation & Gross Error Detection* (Gulf Publishing Company, Houston, 2000)

# A Low Reynolds Number Discharge Coefficient Equation for Critical Flow Venturis and the Effects of Inlet Radius

B. W. Sims<sup>1</sup>, J. A. Brandt<sup>2</sup>, R. J. McKee<sup>3</sup>

<sup>1,2</sup>Flow Systems Inc, 220 Bunyan Avenue, Berthoud, USA

<sup>3</sup>Robert McKee Engineering, Everett, USA

E-mail: [bsims@flowsystemsinc.com](mailto:bsims@flowsystemsinc.com)

---

## Abstract

The discharge coefficient,  $C_d$ , for a Critical Flow Venturi Nozzle (CFVN) corrects the theoretical mass flow to the actual mass flow at measured inlet conditions. The theoretical mass flow is calculated using 1-D isentropic theory and does not account for the subsonic boundary layer along the CFVN wall. For a precisely known throat area,  $C_d$  must be less than unity due to this boundary layer. Theory predicts that the geometry of the inlet to a CFVN will affect the boundary layer and therefore effect the  $C_d$ . This effect on  $C_d$  becomes more significant for smaller CFVNs which are operated at lower Reynolds Numbers. The international standard, ISO 9300 [1], for toroidal CFVNs allows inlet curvature to vary from 1.8 to 2.2 times the throat diameter,  $d$ , but limits the use of the Empirical  $C_d$ -Reynolds Number equation to Reynolds Numbers above 21000. Low Reynold's Number calibration data for hundreds of small CFVNs with  $2d$  inlet curvature will be used to generate an Empirical  $C_d$ -Reynolds Number equation. This paper will also present the results of testing multiple CFVNs with varying inlet curvature at low Reynolds Numbers. These results will be used to examine the specific  $C_d$  sensitivity to this geometric component and determine if more stringent inlet curvature requirements are necessary for low Reynolds number CFVN applications. The Empirical  $C_d$ -Reynolds Number equation, along with additional inlet curvature guidelines will be presented as a method for calculating actual mass flow through a CFVN when the Reynolds Number is below the minimum value at which the ISO 9300 [1] equation can be applied.

---

## 1. Introduction

The theoretical mass flow for a CFVN is calculated using 1-D isentropic theory and does not account for the subsonic boundary or the curvature of the flow profile within the CFVN. The discharge coefficient ( $C_d$ ) for a CFVN corrects the theoretical mass flow to the actual mass flow. Theory predicts that the geometry of the inlet to a CFVN will affect the boundary layer and possible other aspects of flow and therefore effect the  $C_d$  [2]. This effect on  $C_d$  becomes more significant for smaller CFVNs which are operated at lower Reynolds Numbers ( $Re$ ). The international standard, ISO 9300 [1], provides an Empirical  $C_d$ - $Re$  equation to Reynolds Numbers above 21000. Below this  $Re$  limit there is not a  $C_d$  equation available for calculating mas flow through a CFVN or for performing sizing calculation on CFVNs. There is a need for a low  $Re$  Empirical Equation for use below the lower limit of the ISO 9300 [1] equation. Additionally, the inlet curvature requirements from ISO 9300 [1] of 1.8-2.2 times the throat diameter ( $1.8d$ - $2.2d$ ) need to be evaluated for low  $Re$  applications.

## 2. Low Reynolds Empirical Equation

Calibration data taken over 5 years from 184 toroidal throat critical flow venturis was gathered in order to generate a low  $Re$  empirical discharge  $C_d$  equation that could be used below the lower limit of the ISO 9300 [1] equation. The CFVNs varied in nominal throat diameter from 0.28mm to 2.36mm. They were all designed per the geometry guidelines in ISO 9300 [1] with nominal inlet curvature of 2 times their throat diameters ( $2d$ ) and conical diffusers. All calibration data had uncertainties on  $C_d$  ( $k=2$ ) of 0.2% or less. The 3613 total calibration points can be seen in Figure 1. The large scatter in the  $C_d$  values is due to the calibration method where a "nominal" throat diameter is used during data processing rather than a precise value. With this method the difference between the true throat diameter and the "nominal" throat diameter is then accounted for in the calibration  $C_d$  and as long as the same nominal value used during calibration is used during operation the value is correlated and no additional uncertainty needs to be included.

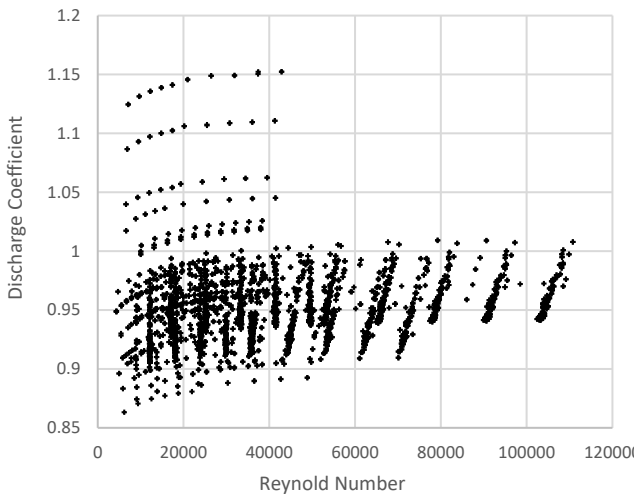


**Figure 1:** Calibration data from 184 CFVNs.

In order to generate an empirical equation based on this data the results needed be adjusted to correct for the difference between the nominal and actual throat diameters. In order to do this the calibration Cd-Re values must be compared against known Cd-Re values and the variation used to adjust the nominal throat diameter to a true throat diameter. Only calibrations that included Cd data within and below the ISO 9300 [1] equation Re limits was used. This allowed the points within the limits to be used to correct the throat diameter. The corrected throat diameter was then used to reprocess the calibration points below the ISO 9300 [1] limit while maintaining the curvature of the calibration fit. With the throat diameters corrected the calibration data collapses as seen in Figure 2.

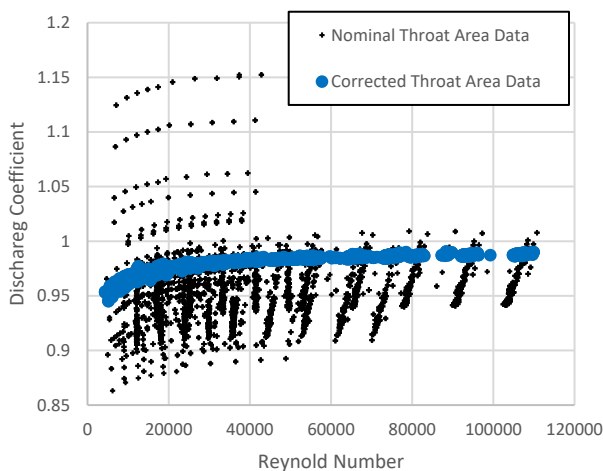


**Figure 2:** Calibration data from 184 CFVNs with the throat area corrected

The corrected calibration data was then compared to the extrapolated ISO 9300 [1] below the minimum Re of 21000 to see how well it represents the corrected data. Figure 3 displays the results and shows that when extrapolated, the ISO 9300 [1] equation over predicts Cd by 0.5-1.0% and a new equation should be generated.

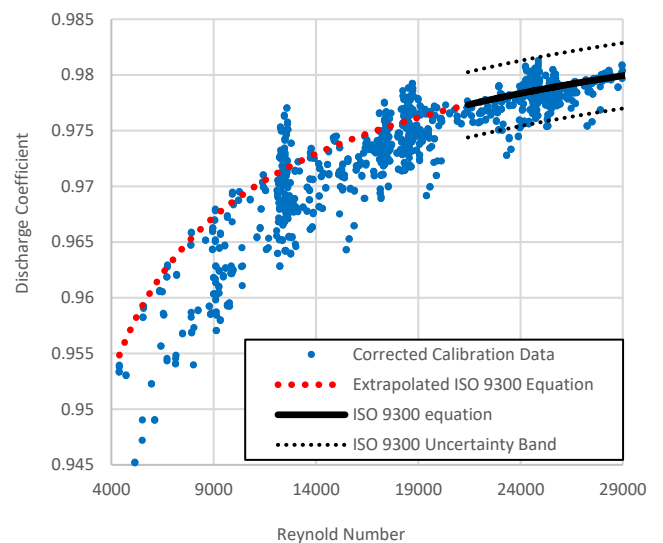


**Figure 3:** Extrapolated ISO 9300 Equation

To generate a best fit equation for the corrected calibration data the Cd values were plotted against  $Re^{-0.5}$  which partially linearize the results as shown in Figure 4.

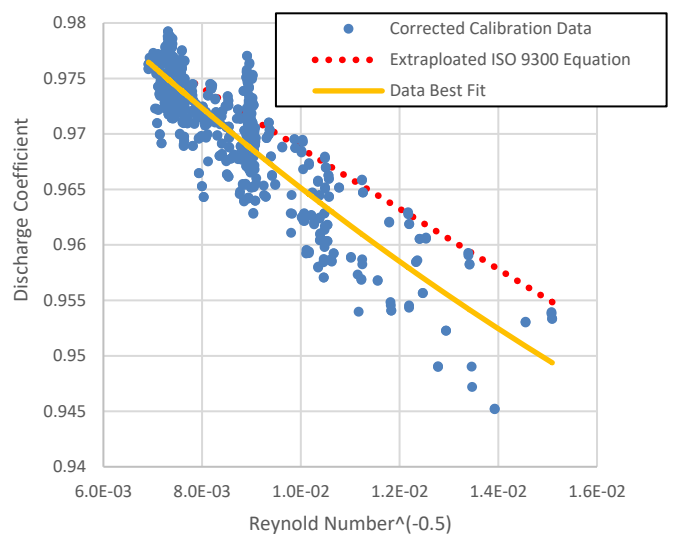


**Figure 4:** Best fit of corrected calibration data

The plot provides the best fit Equation 1 for the corrected calibration data.

$$Cd = 1.0068 - 4.8720 \times Re^{-0.5} + 70.895 \times Re^{-1}$$

with a range of  $7000 \leq Re \leq 21000$

**Equation 1:** Low Re Empirical Cd Equation with Re limits

Due to the sparse data at very low Reynold Numbers the equation bounds were limited. It was decided to bound the equation by excluding the lowest 4% of the data and setting a minimum Re range of 7000. With the high concentration of data at the higher Reynold Number range no reduction in the upper bound was necessary and the equation can be used up to the ISO 9300 [1] Re limit of 21000.

In order for the new equation to be properly applied, an associated uncertainty needs to be provided. Three primary components were used to conservatively calculate the uncertainty in the empirical Cd equation. The first uncertainty component  $U_c$ , is due to the uncertainty Cd from the original 184 CFVN calibrations. All the calibration Cd values had established uncertainties less than 0.2% so that value was conservatively used for all data points. The next uncertainty component  $U_d$ , comes from the throat diameter correction. This correction was based on the ISO 9300 Cd equations which has a published uncertainty of 0.3%. The final uncertainty component  $U_f$ , is established from the residuals from the curve fit and the corrected data. In order to determine this, a +/- band on the curve fit line was establish to bound 95% calibration data. The three-primary uncertainty components were then combined using the Root-Sum-Squared method show by Equation 2.

$$U = [U_c^2 + U_d^2 + U_f^2]^{-0.5}$$

**Equation 2:** Uncertainty of Empirical Cd Equation

The resulting combined uncertainty of the equation was 0.65% ( $k=2$ ). The corrected data, curve fit, and uncertainty band can be seen in Figure 5.

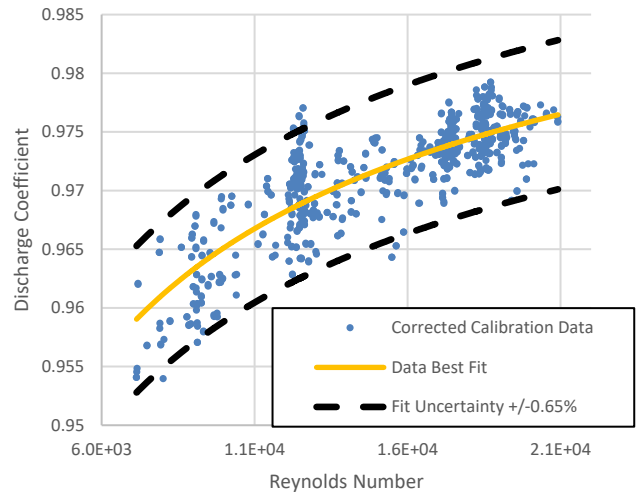


**Figure 5:** Empirical Cd Curve Fit with uncertainty bands

### 3. Inlet Curvature Effects on Cd

The corrected calibration data collapsed and provided a useful low Re empirical equation but there was still significant scatter in the data. It was hypothesized that while the inlet radius of the all the CFVNs was nominally 2 times the throat diameter, due to the difficulty of machining CFVNs with throats as small as 0.28mm, the true inlet radius may deviate significantly from nominal. In order to determine if variations in actual inlet curvature would invalidate the equation or were the primary cause of the scatter, 8 new 1.47mm throat CFVNs were manufactured and calibrated. Two each with 1.5d, 1.8d, 2.2d, and 2.5d inlet radius CFVNs shown in Picture 1.



**Picture 1:** CFVNs with varying inlet curvature.

The calibration results for these CFVNs are shown in Figure 6 and 7 and compared to the empirical Cd equation.

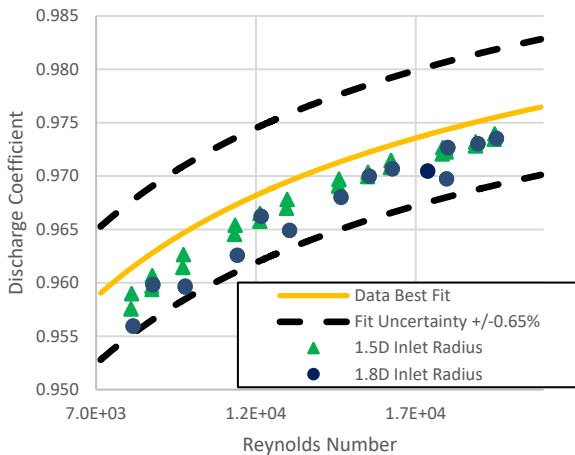


**Figure 6:** 1.5D and 1.8D Inlet Curvature

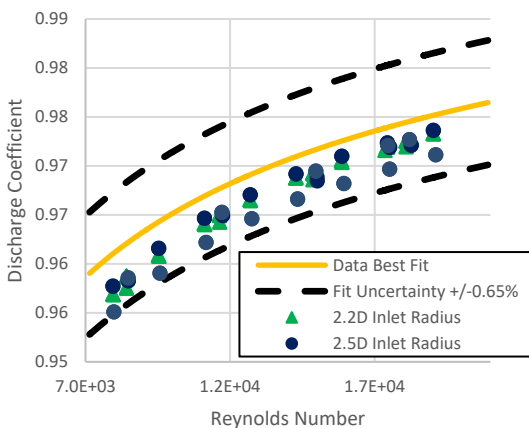


**Figure 7:** 2.2D and 2.5D Inlet Curvature

The results from calibrating the 1.5d, 1.8d, 2.2d and 2.5d inlet curvature CFVNs show Cd values consistently low but within the uncertainty expectations of the empirical equation. This is an unexpected result as theory predicts that the 1.5d and 1.8d inlet curvature should result in higher Cd values than 2d CFVNs as shown by the theoretical CFV flow models developed by Johnson and Wright [2]. The Johnson and Wright [2] model predicts that below a Re of 150,000 a decreased inlet curvature results in larger Cd values. These results suggest that the Low Re number scatter is due to a factor other than inlet curvature. Manufacturing variations in surface finish or the transition from the inlet curvature to the diffuser cone are other possible causes of this scatter. The results do however show that data taken from with inlet curvature from 1.5D

to 2.5D falls within the uncertainty expectations of the empirical Cd equation allowing reduced curvature restriction than the ISO 9300 [1] equation.

#### 4. Conclusion

Calibration data was collected from 184 CFVNs in order to determine an Empirical Cd-Re curve fit that could be used below the ISO 9300 [1] equation minimum Reynolds Number of 21000. All the calibrations included data within the ISO 9300 [1] range which was used for throat diameter corrections from nominal to actual.

The following equation was established:

$$Cd = 1.0068 - 4.8720 \times Re^{-0.5} + 70.895 \times Re^{-1}$$

with a range of  $7000 \leq Re \leq 21000$  and an uncertainty of 0.65% ( $k = 2$ )

**Equation 3:** Low Re Empirical Cd Equation with Re limits and Uncertainty

The equation is valid for toroidal throat CFVNs built per the ISO 9300 requirements and seems to allow for an inlet curvature range as wide as 1.5d to 2.5d.

This equation can be used as a more accurate tool for sizing low Reynold number CFVNs than extrapolating the ISO 9300 equation. It can also be combined with a standard throat measuring dimensional technique such as pin gauges to provide a Cd\*A value for higher uncertainty flow rate calculations. As an example; for a 5mm throat CFVN using a +0.00/-0.02 mm gauge pin set and the developed empirical equation an uncertainty in Cd\*A of approximately 1.2% ( $k=2$ ) is achievable. Further research into the effects of manufacturing techniques on low Re CFVN Cds could be used to further reduce the scatter and uncertainty in the Empirical Cd equation.

#### References

- [1] ISO, Measurement of Gas Flow by Means of Critical Flow Venturi Nozzles, ISO 9300, 1st edition, 1990, 2nd edition, 2005.
- [2] Johnson, A., and Wright, J., "Comparison Between Theoretical CFV Flow Models and NIST's Primary Flow Data in the Laminar, Turbulent, and Transition Flow Regimes", Journal of Fluids Engineering, Vol 130, 071202-1 through -11, 2008.

# Design and Performance of Water Flow Velocity Calibration Facility

Heming Hu<sup>1</sup>, Yuan Liu<sup>1</sup>, Zhigang Wang<sup>2</sup>, Zeyu Guo<sup>1</sup>, Yunlong Zhu<sup>1</sup>

1. National Institute of Metrology, Beijing 100029, China;

2. China Institute of Water Resources and Hydropower Research, Beijing 100038, China;

E-mail: huhm@nim.ac.cn

**Abstract:** Current meters are used for flow velocity measurement in river and ocean. Accurate measurements need accurate calibrations. There are more than ten tow tank facility in China providing water velocity calibration, and all of them are ~100 m long concrete tank with no clear uncertainty budget, especially there is not a thorough understanding of the water movements in the tow tank. We have built a small tow tank which is 8 m long, 1.2 m wide and 1.2 m high with a cart running speed of 0.01m/s~1m/s. It was made of transparent glass and was possible to use optical instruments to investigate the background flow field that might compromise calibration results. In order to test the performance of flow velocity calibration facility, Micro ADV produced by Sontek was employed to make a test, and the results showed that the calibrated results for ADV using flow velocity calibration facility proposed in this article agreed well with the manufacture's declaration for accuracy and USGS's conclusions. In addition, SNR (signal-noise ratio) of MicroADV was also analysed and related to the concentration of particles in water body. The performances verified that the flow velocity calibration facility was effective and could be used to conduct further analysis of current meters.

**Key words:** flow velocity, flow velocity calibration facility, open channel, MicroADV

## 1 Introduction

Flow velocity is an important hydraulic index in various flows. How to determine it have been a focus for a long time. Various of current meters have been developed to determine the key velocities, for example electromagnetic current meters, ultrasonic current meters, ADVs, and widely used rotating current meters (GB/T11826, 2002, Yao 2012, Voulgaris & Trowbridge 1998, Hurther & Lemmin, 2001, Parsheh et al. 2010, Jiang et al. 2010, Xiao et al. 2002). However, subject to the measuring mechanism, nearly all types of current meters couldn't perform perfectly with no errors. For example, the rotating current meters perform badly in the cases with ultra-low velocities where the effective signals are seriously overwhelmed by errors. ADVs will give good flow velocity measurements only if enough particles exist in the measured flow.

Therefore the current meters should be pre-calibrated before used. Traditionally, the calibration facility for current meters are a specially constructed long flume (mostly>100m) in earth. A cart is mounted over the flume and its speed can be set according to requirements. When needed to be calibrated, the current meters can be fixed on the cart and move together with the cart. Comparing the

cart's speeds and the current meter's indications can clearly show the performance of the current meter, and the adjusting curve can also be provided. However, the traditional calibration facility can't give elaborated illustrations of the interaction of current meter and the tested flows. And the influences of water quality, abundance of particles, background velocities are also not easy to be obtained. Thus in this paper, a new flow velocity calibration facility was designed and constructed. And its performance would be testified by Micro ADV, a kind of widely used ADV current meters produced by Sontek (Sontek/YSI, 2001).

As is known, the noise is existing during the whole measuring procedure, and its influences couldn't be ignored. Many researchers have done lots of researches (He 2013, Marc & Beat 2012, Yan et al. 2017), however, how to reduce the disturbance of noise to achieve a higher accuracy has not reached an agreement. In addition, USGS organized a comparison tests of ADV in global in 2013. The tested revealed that background velocity, rod shape and size, vibration, concentration of tracer particles would probably affect the calibration results. And the accuracy should be re-verified when the flow velocity was low (0.01~0.1m/s)

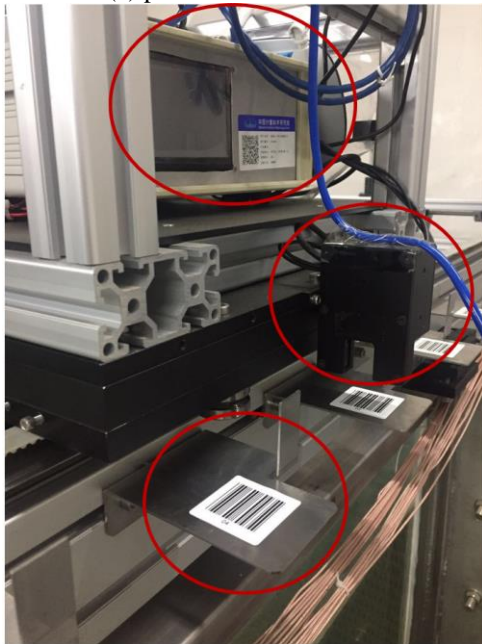
## 2 Design of water flow velocity calibration facility

### 2.1 Composition and Function

The main part of the flow velocity calibration facility was the flume, which was shown in Fig.1. It was 8m×1.2m×1.2m (length × width × depth). The frame of the flume was made of stainless steel. The glass was arranged inside the frame in order for a convenience for visual observation. As the velocity of cart could be easily determined, thus the standard flow velocity was simulated by a moving cart velocity relative to the still water. The rails, on which the cart runs, were mounted on the top of both sidewalls. The designed cart velocities were 0.01m/s~1m/s. When conducting calibration, the current meter should be fixed to the cart. The current meter holder was made to be a 1m-long cylindrical iron pole with the diameter being 0.02m. The cylindrical shape could well decrease the disturbances produced by itself. In addition, the current meter holder was made with fillets, which was also beneficial to reduce the self-influence.



(a) photos of the tow tank



(b) cart speed measurement system

Fig.1 Flume in flow velocity calibration facility

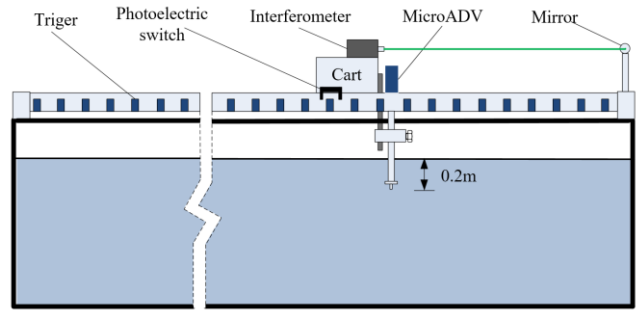


Fig.2 Sketch of cart speed system

### 2.2 Cart Speed

Reliability of flow velocity calibration facility depends on the accuracy of cart speeds. In this flow velocity calibration facility, two sets of cart speed measuring devices were mounted, and one device was Laser Interferometer and the other was Photoelectric Trigger, which were shown in Fig.2. In both devices, the measurements of distance and time were the key. The Laser Interferometer occupied a linear resolution of 0.01μm when measuring the displacements of the cart. The time measurement was conducted by a timer/counter developed by National Institute of Metrology of China. And the relative errors of timing was within 0.01%. The Photoelectric Trigger also referred to the determination of interval of neighboring trigger elements and responding time, and the tested results were shown in Fig.3.

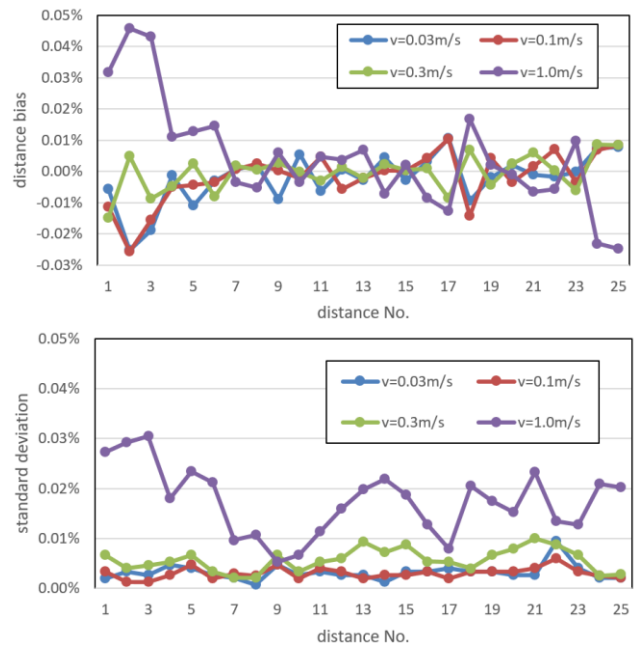


Fig.3 Interval calibration of baffles at different speeds

In this flow velocity calibration facility, photo-electronic components were used. They need different responding times when triggered at different cart speeds. And the responding times increased with increasing cart speeds. In

all tested cases, the responding time was restricted within 10 $\mu$ s. If the cart velocity was slow, the responding time could minimized to being within 4 $\mu$ s. Subjected to the responding time, the intervals between neighboring triggers also varied depending on the cart speeds. In the 4 tested cases, the calibrated result at the case when the cart speed was 1.0m/s was more largely deviated from the true value.

Table 1 showed the measuring stability of two cart speed measuring ways. When Laser Interferometer was employed, the relative standard errors decreased with the increasing cart speed. The reason is that the sampled data tended to be less when the cart speed increased at the same sample frequency. If the sample frequency was adjusted, the measuring stability would be changed, namely measuring stability would get worse with increasing sample frequency. When Photoelectric Trigger was used, the quantity of the sampled data would be the same as the quantity of the trigger components was a constant. However, due to the influence of the responding time, the measuring stability of Photoelectric Trigger also performed worse with the increasing cart speed. As for the sample frequency, Chinese national standard makes a recommendation. When the cart speed is slower than 0.2m/s, the speed measuring unit is recommended as 10s, or the speed measuring unit should take the value of 1s.

Table 1 Speed stability of two speed measuring methods

Velocity measuring way	Nominal cart speed (m s <sup>-1</sup> )	Actually cart speed (m s <sup>-1</sup> )	Relative standard deviation (%)
Cart speed measuring by Laser Interferometer	0.03	0.03008	1.33
	0.10	0.10016	0.46
	0.30	0.30012	0.29
	1.00	1.00078	0.63
Cart speed measuring by Photoelectric Trigger	0.03	0.03008	0.06
	0.10	0.10015	0.06
	0.30	0.2999	0.20
	1.00	1.00049	0.66

### 2.3 Background velocity

Background velocity could undoubtedly influence the cart speed as well as the flow velocity measuring. Commonly, it is advisable to conduct physical model tests with large time intervals when no disturbances are introduced. In this section, two typical cases were chosen to reflect the influences of background velocity.

Where the cart speed was 0.3m/s, it was observed that during the towing process, the velocity component of Y direction (X is the traveling direction and Y is the vertical direction of X) fluctuated between -0.01m/s~0.03s/s, and the water body tended to be stable after the waiting time of nearly 2min. It could be seen that the velocity deviation

caused by the background velocity couldn't be ignored in the precise measurements.

### 3 Performance of flow velocity calibration facility

In this section, SonTek MicroADV was employed to make a calibration test. The accuracy of Micro ADV is declared as  $\pm 1\%$  and greater than 2.5mm/s.

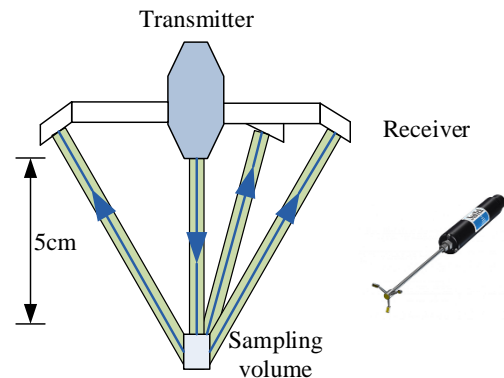


Fig.4 Sontek 16M MicroADV

In this section, 6 typical cart speeds, namely 0.01m/s, 0.03m/s, 0.05m/s, 0.1m/s, 0.3m/s and 1.0m/s, were chosen, and the tested results were shown in Fig.4. Clearly, the measuring error almost exceeded 10% when the cart speed was 0.01m/s while the measuring error was within 1% when the cart speed increased to over 0.1m/s, which agreed well with the manufacture's accuracy declaration.

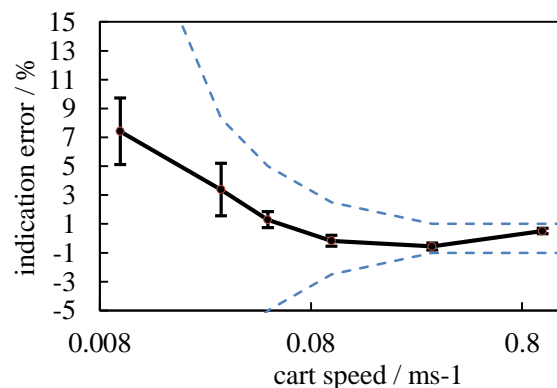


Fig.5 Performance of flow velocity calibrated facility

In addition, USGS have conducted similar experiments. The calibrated current meter chosen was ADV produced by OTT in Germany. The tested results showed that the measuring error was as large as 6% when the cart speed was 0.05m/s. However, when the cart speed increased to 0.4m/s, the measuring error was decreased to within  $\pm 1\%$ . In a word, the measuring results of this paper also agreed well with USGS.

From the analysis and comparisons above, it could be concluded that the flow velocity calibrating facility was effective. Besides, this facility can also help us make

further analysis of the current meter. As was known, the signal strengths were closely related with the concentration of particles in water body. If the water body was too clean, the strength of the effective signal might be at the same with or lower than the noise level, inducing velocity measuring unsuccessfully. Herein, the signal strengths would be analyzed further, and the results were shown in Fig.7 and Fig.8.

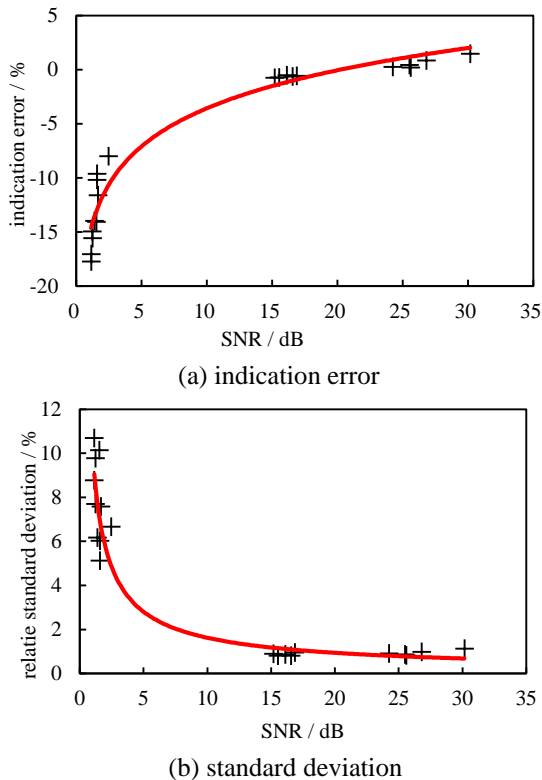


Fig.6 performance of MicroADV under different SNR

Clearly, as the signal strength increased, the relative standard deviations decreased in an exponential form while the velocity indication errors increased in a logarithmic form. When SNR of Micro ADV was smaller than 5dB, the relative standard deviation of velocity would exceed 10% and the velocity indication errors would be smaller than -15%. When SNR increased to above than 15dB through increasing the concentration of particles, the velocity measurement would be much more stable, and the relative standard deviation decreased to be within 1%. The velocity indication errors would also be smaller than 2%. After investigation, it was found that the settlement of particles was the main reason to influence the velocity measurement quality. Through observation in still water, the settling velocity of particles were in the range of 0.15cm/s~0.30cm/s. When the particles continued settling till SNR were smaller than 5dB, ADV would fail in velocity measuring. However, the signal strength would not be linear with the concentration of particles. In fact, as the concentration of particles continued increasing, the signal strength would be first increased and then reversed

to decrease. The concentration was 0.3% ~ 0.5% when the signal strength got reversed.

#### 4 Conclusions and future work

Current meters are used for flow velocity measurement in river and ocean. Accurate measurements need accurate calibrations. In this paper, a flow velocity calibration facility was established. In this facility, the flow velocity measuring was instead of cart traveling speed's measuring. Laser Interferometer and Photoelectric Trigger were employed to conduct the measurement of distances while a self-designed timer/counter was employed to conduct time determination. And then the cart's velocity could be easily obtained.

In order to test the performance of flow velocity calibration facility, Micro ADV was employed to make a test, and the results showed that the calibrated results for ADV using this facility agreed well with the manufacture's declaration for accuracy. In addition, USGS also made similar conclusions. The performances showed that the flow velocity calibration facility was effective. Besides, the flow velocity calibration facility could also be used to conduct further analysis about the relationship between SNR and the concentration. The results showed that SNR being larger than 15dB could make stable velocity measurement. However, SNR was not linear related with the concentration of particles, and too large concentrations might decrease the effective signal strength.

In the future, we are planning to add a dynamic calibration system to extend its maximum velocity. It will use a pump and a nozzle (outlet diameter is 200mm) to generate a submerged jet with a top-hat velocity profile as testing region. We are planning to test small current meter using LDV as reference from 0.3 m/s to 3 m/s.

#### Acknowledgments

This paper is currently supported by The National Key R&D Program of China (project/subject SN. 2017YFC 0405705).

#### References

- [1] GB/T11826-2002, Rotating Current Meter[S]. (in Chinese)
- [2] HE Qifeng, Research on the Applicability of Acoustic Doppler Velocimeter[D]. Beijing : Tsinghua University,2013. (in Chinese)
- [3] Hurther D, Lemmin U. A Correction Method for Turbulence Measurements with a 3D Acoustic Doppler Velocity Profiler[J]. Journal of Atmospheric & Oceanic Technology, 2001,

- 18(3):446-458.
- [4] JIANG Songyan, GAO Wei, LUO Gong. Analysis on Calibration of Acoustic Doppler Current Meter [J]. *Water Resources Information*, 2010.4: 54-56. (in Chinese)
- [5] Marc de Huu , Beat Wuthrich. Gravity wave effects on the calibration uncertainty of hydrometric current meters[C]. IGHEM, Trondheim, Norway 2012.
- [6] Parsheh M, Sotiropoulos F, Porté-gel F. Estimation of Power Spectra of Acoustic-Doppler Velocimetry Data Contaminated with Intermittent Spikes[J]. *Journal of Hydraulic Engineering*, 2010, 136(6):368-378.
- [7] SonTek/YSI, Inc. Acoustic Doppler Velocimeter Principles of Operation[Z]. 2001
- [8] Voulgaris G, Trowbridge J H. Evaluation of the Acoustic Doppler Velocimeter (ADV) for Turbulence Measurements\*[J]. *Journal of Atmospheric & Oceanic Technology*, 1998, 15(15):272-289.
- [9] YAN Song, WU Hao, SUN Dapeng, et al. Application of Acoustic Doppler Velocimetry in Flume Flow Experiment [J]. *Research and Exploration in Laboratory* 2017.36(5): 9-13. (in Chinese)
- [10] YAO Yongxi. Calibration Method Comparison of Rotating Element Current Meters in China and Other Countries[J]. *Hydrology*, 2012(3):1-5. (in Chinese)

# Calibration of Microfluidic Flow Meters

Y. Liu<sup>1</sup>, X. Feng<sup>1</sup>, Y. Yao<sup>1</sup>, L. Lei<sup>2</sup>, P. Zhao<sup>2</sup>, T. Meng<sup>3</sup>, L.J. Huang<sup>1</sup>

<sup>1</sup>Siargo Ltd., 3100 De La Cruz Boulevard, Suite 210, Santa Clara, California 95054 USA

<sup>2</sup>National Institute of Measurement and Testing Technology, Chengdu 610021, China

<sup>3</sup>National Institute of Metrology, Beijing 100029, China

E-mail: Liji@Siargo.com

---

## Abstract

Calibration of a microfluidic meter is conventionally done with a precision reference such as a high accurate balance or a precise syringe pump system. These processes normally are very time consuming and are not the feasible approaches for high volume flow meter manufacture. In this paper, we will discuss the comparison of the calibration options of the thermal time-of-flight microfluidic meter including the precise syringe system, balance and Coriolis flow meter. The flow range of the meter covers from 20 $\mu$ L/min to 400mL/min. The comparison of the metrology features and the procedure of each system is discussed. Further, for the hygienic sensitive applications, the liquid calibration often leads to concerns for the cleaning procedure after the calibration. Comparison of the calibration with the calculated values and DI water and the conversion between the fluids is also discussed.

---

## 1. Introduction

In recent years, demands for the precision flow rate measurement in microfluidic applications become more and more pronounced. Examples are the applications in drug delivery, DNA sequence analyser, liquid analytical instrumentation (such as HPLC), pharmaceutical equipment and monitoring of the physiological fluid in medical intensive care units. For these applications, traditional Coriolis mass flow meters or thermal calorimetric sensors are often too expensive and manufacture of those products in high volume is also not feasible. As of today, there is still no suitable products that can meet the market demands. Although a couple of companies are offering microfluidic flow sensor products for evaluation [1,2,3], but these products are still having a very high cost while the performances are not as desired.

The current available products targeting for high volume applications are made of three different measurement principles. The MEMS Coriolis mass flow sensors were initially proposed for the drug infusion applications, but it had a very complicated manufacture process and in a foreseeable time it could not reduce the manufacture cost for the disposable options. The MEMS calorimetric sensors have a path for the cost-effective sensor chips, and is also proposed for drug infusions but the required package makes the final product yield and cost

problematic for the high-volume production. Another microfluidic flow rate product with energy dispersion approach was also having a high manufacture cost, and therefore the desired high-volume applications are not feasible.

For medical and/or pharmaceutical applications, while the precision of the products is required, these applications also ask the products to be disposable to avoid cross contamination since the cleaning is very challenge within the tiny microfluidic flow channels. In a previous report [4], the authors proposed a micromachined thermal time-of-flight sensing technology aiming to provide the desired performance of large dynamic range with a high accuracy. While the performance could meet the current market requirements, the cost is critically dependent on the manufacture of such, in particular the time-consuming calibration process to maintain the desired accuracy. For the thermal time-of-flight sensing technology with the micromachined chips, the distances between the thermal source and the sensing element is well defined and known once the design is fixed. In theory, if the thermal time-of-flight sensing can be well established, the flow speed can be readily calculated by a precise measurement of the time lag for the thermal register travelled at the known distances. However, in reality other thermal effects could not be completely eliminated, a calibration shall still be required. In this paper, we discuss the various calibration approaches and the

correlations between the calibration data and the theoretical values.

## 2. The design of the thermal time-of-flight flow meter

Figure 1 shows the design and final formality of the thermal time-of-flight flow meter LF6000 for microfluidics. The products have two models. The differences of these two models are the sensing chips on which the distances between the microheater and the sensors are different. One of the sensor chips with the shorter distances among the microheater and sensing elements measures the flow rate from 20 $\mu$ L/min to 3 mL/min, while another with longer distances measures from 2 mL/min to 400mL/min.

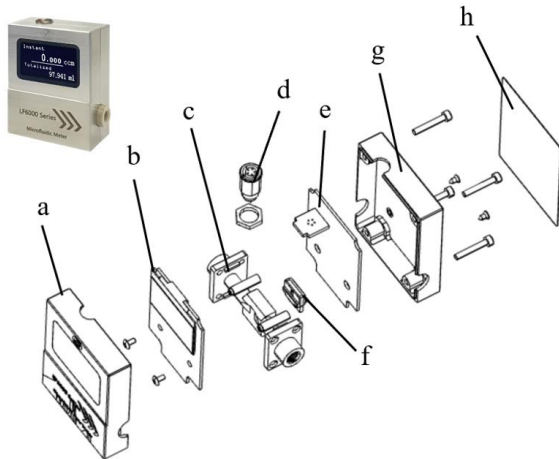


**Figure 1:** The explosive view of the thermal time-of-flight flow meter for microfluidics. The insert photo is the actual product, LF6000. a – the front cover; b – the OLED display; c – the flow channel with ¼ - 28 standard connectors; d – the interface connector; e – control electronics on PCB; f – MEMS sensor assembly; g – back cover and h – product plate/label.

In the explosive view shown above in Figure 1, the meter was made with stainless steel cover for both front- and backside. The OLED display presents a clear view even with a strong light. The flow channel as designed has a venturi type of structure and has a pressure rating of 10 MPa, and the flow channel materials was moulded PEEK which provide a wide spectrum of fluid compatibility. The connectors at the both end of the flow channel are the standard ¼"-28 UNF fittings providing each tubing for the measurements. The MEMS flow sensor chip was moulded into a polypropylene flow channel base where the surface was made flat and aligned with the channel while the sensor connection was isolated by the moulding materials from the flow channel. The meter's control electronics provide all signal processing as well as data interface that are provides a variety of options including the default

I<sup>2</sup>C and Bluetooth LE. Customers can request most of the common interfaces such as RS485, IO-Link and voltage output. The meter provides a default 100:1 dynamic range and the product is also available for customization.

The moulded flow channel is completely separated from the control electronics and other parts of the meter making the disposable option is possibility from the material cost of view. However, to ensure the accuracy of the performance, each of the meter is currently required to be calibrated. The selection of a calibration process is dependent on the required dynamic range and accuracy which could be quite time consuming. The calibration process contributes the major cost of the product. Hence for a high volume but cost-effective microfluidic flow sensing product, optimization of the calibration process is critical.

## 3. Calibration approaches and setups

For the calibration of a microfluidic sensing products, there are a few approaches are currently available and those can be readily applied. Among these approaches, precision syringe pumps and balances are commonly are accepted as the reference standards. Using a high precision Coriolis mass flow meter is also justified as the Coriolis has the needed precisions for a calibration.

### 3.1 Calibration with syringe pump and balance

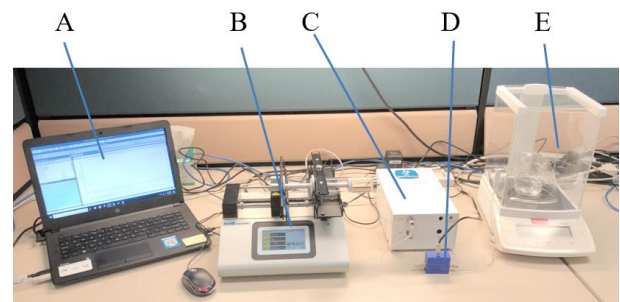


**Figure 2:** The calibration setup with a precise syringe pump and a precise balance. A – the calibration control system with software and connections to all references; B – reference syringe pump; C – degasser; D – the flow meter to be calibrated and E – the precise balance.

Figure 2 is a simple yet conventional calibration setup for microfluidic flow meters. The reference meter shown in the picture is a precise syringe pump by KD Scientific, Legato 210 dual syringe infusion/withdraw pump. It has an accuracy of  $\pm 0.35\%$  for a volume of 0.5 $\mu$ L to 140mL providing a capability of measuring 3.06 $\mu$ L/min to 215.8mL/min. It also has a maximum step rate of 26 $\mu$ sec/ $\mu$ step which allows a smooth delivery of the fluid. Another reference is to utilize the precise balance system

that can weight the fluid at the exit assuming a continuous and no dead volume in the flow path. The balance shown in the setup is a Sartorius CPA225D that can measure up to 220g (220mL for water). It has a precision of 0.01mg or 0.01 $\mu$ L for water as well. Both these two reference meters are equipped with digital interfaces that are readily connected to a computer in which a software developed in house can simultaneously read the data from the two references as well as from the meters to be calibrated.

It is critical to ensure the flow path is air bubble free during the calibration as the compression or expansion of the air would create unexpected uncertainties which would prevent the measurement from establishing the repeatability which is the base for an accurate calibration. In the system shown in Figure 2, a degasser made by Biotech, DEGASI PREP+ is placed in the calibration ring to ensure the air bubbles are not present during calibration. This model of degasser has multiple channels and each channel has a capability of handling 70mL/min with the degassing efficiency about 85% at about 10ml/min. It also has a very low pressure drop of 0.0226 kPa/ml/min.

### 3.2 Calibration with Coriolis flow meters

The precise syringe pumps have been widely used as a reference for microfluidic system, but it is not the ideal one for manufacture of a flow sensor as the syringe volume is limited and continuation of operation would have been frequent interrupted. For example, a full syringe in above system could only calibrate about 5 flow sensors with a full scale of 50mL/min. Therefore, alternative approaches shall be preferred.

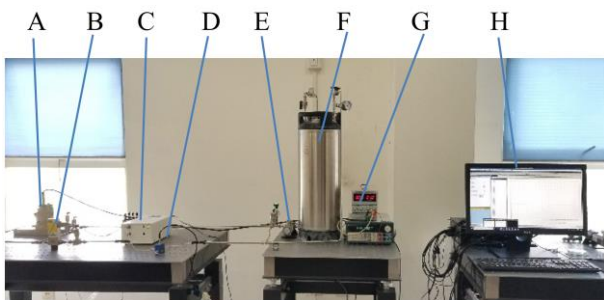


**Figure 3:** The calibration setup using a standard flow meter as a reference. A – the reference Coriolis mass flow meter by Bronkhorst; B – line pressure gauge; C – degasser; D – the flow meter to be calibrated; E – system pump; F – pressurized water tank; G – power sources and H – the data acquisition system.

Figure 3 shows the calibration system using a Coriolis mass flow meter as the reference standard. In this system, the reference Coriolis mass flow meter was manufactured by Bronkhorst, model

M14V14I. This meter has a nominal uncertainty of  $\pm(0.2\% \text{Reading} + 6\text{g/hr})$  but the actual uncertainty per calibration was  $\pm 0.06\%$  at 5.3 bar gauge pressure at 20°C with water when the ambient was at 101.6kPa. The calibration water density was 998.5 kg/m<sup>3</sup>. The cycling of the water was supplied by a magnetically coupled gear pump that delivers a maximum flow rate of 3kg/hr. As the Coriolis mass flow meter is sensitive to the vibration, an optical table was used to support the system as shown in the figure. The line pressure before the product to be calibrated was about 0.05 bar, which was monitored during the calibration by a pressure gauge that is also made by Bronkhorst, the model is P520C with a rated accuracy of  $\pm 0.5\%$ FS.

The degasser is the same as that used in the syringe pump calibration system as discussed earlier, and the water tank has a volume of 18.9L with a water filter.

The advantage of the Coriolis mass flow meter system is that the calibration medium is cycled continuously without the needs of change the supply as it does in the syringe pump calibration system. Hence it is more efficient for the volume manufacture.

### 3.3 Calibration procedures

Calibration of a microfluidic sensor is nontrivial as the susceptibility of various components of the system with respect to the variation in system pressure. Several discussions about the calibration procedures [5.6] have addressed the system stability and proximity of the sensor performance. One of the key issues is to ensure the flow path is free of obstacles since the channel size is very much limited in size. To ensure the performance, the system is normally flushing with the fluid medium to be calibrated until a stable condition is reached and air bubble degasser was working for a reasonable time frame. Then start the actual initiation of the calibration process.

For the calibration with the syringe plus the precise balance system, as the product with the full scale flow ranges of a few 10s of millilitre per minute are the ranges for most of the calibration discussed in this paper, the evaporation would not contribute to any measurement uncertainties, therefore the enclosure protection for evaporation would not be necessary for the current discussed flow range. However, for reducing the droplet impact to the balance, the water cup set on the balance was pre-loaded with water that allows the pipe exit to be immersed into the water in the cup.

The thermal time-of-flight sensor products to be calibrated were dried with nitrogen before connected to the system. This is to ensure that there would not be any residues which could create wetted separations or interfaces inside the small flow channels. The computer with the software, which is digitally connected to both the syringe pump and the balance, is controlling the calibration process via the data recording sequences. When the products to be calibrated is connected and no leakage is registered in the whole microfluidic line system, the calibration is then ready to start. For the syringe pump plus balance calibration system, the calibration will start by running the syringe pump at the full-scale flowrate in order to establish a completely filled flow path which is further confirmed after the data were received from the output of the balance, the calibration data acquisition shall start after waiting for about 30 sec for system to be stabilized. For the same reason, the same waiting time applied to the Coriolis mass flow meter calibration system.

#### 4. Calibration and verification

In the one-dimensional proximity, the change of the temperature  $T$  with time  $t$  in the flow direction  $x$  can be expressed as below,

$$\frac{\partial T}{\partial t} = D \left( \frac{\partial^2 T}{\partial x^2} \right) - V_x \left( \frac{\partial T}{\partial x} \right) \quad (1)$$

where  $D$  represents the fluid properties and  $V_x$  is the fluid velocity. Therefore, in the current one sensor approach, the measurement shall be flow medium dependent. Since the medium properties will not be changing within the interested working conditions, the calibration in theory can be converted to different medium with water calibration. To completely make the measurement independent on flow medium, at least two sensors will be required on the same sensor chip.

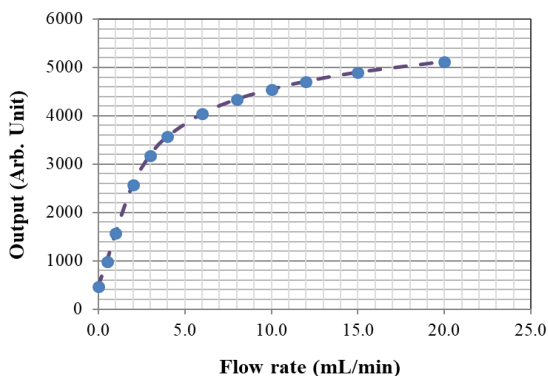


**Figure 4:** The calibration curve using the phase shift (time lag) sensing with the syringe pump calibration system.

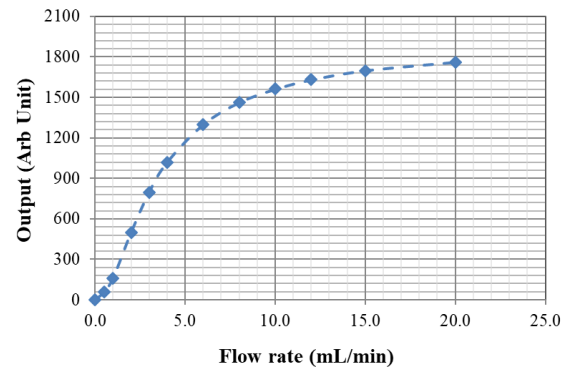


**Figure 5:** The calibration curve using the amplitude (calorimetric) sensing with the syringe pump calibration system.

Figure 4 and 5 show the calibration curves from the phase shift (time lag) and the amplitude (calorimetric) that were acquired simultaneously from the thermal time-of-flight microfluidic sensing product LF6000. The data shown in the figures were both taken from the syringe pump system where the balance and syringe data were correlated to each other with excellent linearity ( $R^2=1$ ) and a deviation within  $\pm 0.25\%$ . During the calibration, the reference flow rates were from the set points of the syringe pump and the corresponding voltages were acquired from the product. The time lag (Figure 4) can be fitted with a polynomial while the calorimetric output is hardly fitted with the same approach. The amplitude curve then fitted with a sampling function and converted into a lookup table (LUT).

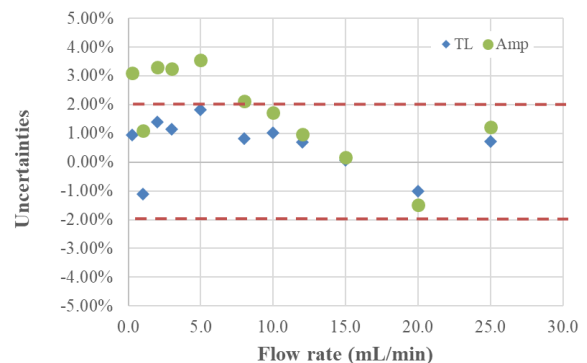


**Figure 6:** The verification data using the syringe pump system showing that the time lag measurement yielded a higher accuracy as compared to those with amplitude data.

Figure 6 compares the performance of the calibration based on the time lag and amplitude, respectively. The verification data were acquired again from the syringe pump system. The performance using the time lag data calibration is clearly better over those with the amplitude data, in particular at the low flow rate regime. In the dynamic range of 100:1 (25 to 0.25mL/min), a  $\pm 2.0\%$  reading accuracy can be achieved based on

the verification. The linearity is not as desired but there could be some additional data acquisition procedure improvement including the data sampling and average algorithm.

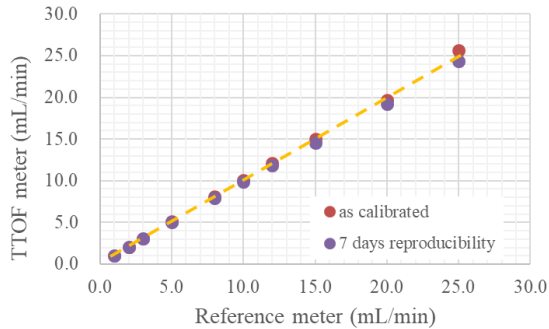


**Figure 7:** The reproducibility data using the syringe pump system with the time lag measurement.

Figure 7 shows the reproducibility tests where it was found that unlike the traditional thermal mass flow performance, the reproducibility of this tested meter was better at the low flowrate. The deviations observed at the high flow could be due to the fact that the calibration curve reached its flatness where instability would be more likely. Therefore, in this particular flow channel design, the flow rate specifications would be better moving to a lower flowrate regime.

## 5. System correlations

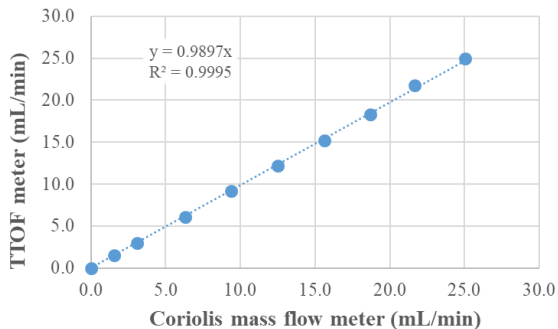


**Figure 8:** The reproducibility data using the syringe pump system with the time lag measurement.

As discussed above, the syringe-balance system could be accurate and easier for a larger dynamic range test, but it is not suitable for a volume production. The Coriolis mass flow meter system will be much more efficient for the production. As the pressure drop is very low for the products as well as the calibration system discussed (not including the pressure drop across the Coriolis mass flow meter), the Coriolis mass flow meter calibration system can achieve multiple sensor calibration while for the syringe pump it is difficult. It was estimated the

efficiency would be about 10x with the current configurations. Figure 8 shows the verification data for a thermal time-of-flight LF6000 meter that was first calibrated with the syringe-balance system and then verified with the Coriolis mass flow meter system. The results show an excellent linearity with a deviation of -2.1% with the regression. This value is marginally larger than that for the achieved product accuracy, but can be easily corrected once the true value is established. Additional work to identify the sources for the system deviations were in process as of this report is completed.

## 7. Concluding remarks

This paper discussed the two calibration systems for microfluidic flow metering products. The syringe-balance calibration system could be accurate and easy to adjust the calibration dynamic range but it is not efficient for volume manufacture. The Coriolis mass flow meter calibration system has the necessary accuracy and is much more efficient for the volume manufacture. Correlations of these two systems were well established and further work for eliminating the system deviations is in progress.

## References

- [1] Tanaka Y et al., "Micro flow sensor for microreactor" *J. Yokogawa Technology*, **V52**, 145, 2008.
- [2] Smith R et al., "A MEMS-based Coriolis mass flow sensor for industrial applications", *IEEE Transactions on Industrial Electronics*, **Vol 56**, 2009.
- [3] Mayer F, Harberil AM, "Method and device for measuring the flow of a fluid", US Patent 6763710, July 20, 2004.
- [4] Yao Y, "MEMS thermal time-of-flight flow meter", 15<sup>th</sup> International Flow Measurement Conference, October 13, 2010, Taipei.
- [5] Yamasaki Y et al., "Method and apparatus for testing liquid flow meter", US Patent Application 2017/0052056, February 23, 2017.
- [6] Lewis D, "Flow sensor calibration methods and apparatus", US Patent 7055366, June 6, 2006.

# Uncertainty of SO<sub>2</sub> measurements in dryers due to water droplet and water film condensation

S. Knotek<sup>1</sup>, J. Geršl<sup>1</sup>, A. Paták<sup>2</sup>

<sup>1</sup>Czech Metrology Institute, Brno, Czech Republic

<sup>2</sup>Institute of Scientific Instruments of the Czech Academy of Sciences, Brno, Czech Republic

E-mail (corresponding author): sknotek@cmi.cz

## Abstract

The article presents the modeling of SO<sub>2</sub> diffusion into water droplet and water film which arise in dryers by condensation or evaporation in dependence on physical and chemical conditions. The motivation of the modeling is the attempt to quantify the SO<sub>2</sub> losses in drying during sampling of emissions. The basic processes of gaseous substances dissolution into liquid are discussed theoretically and quantitative results of computer computations are presented.

## 1. Introduction

The SO<sub>2</sub> pollution of air has a significant impact on health of the population in long-term as well as in short-term period [1]. Since most of the atmospheric SO<sub>2</sub> is produced by industrial processes, the accurate measurement of emissions is needed.

Nowadays, the Standard Reference Methods (SRMs) used for measuring of emissions are based on laboratory analysis of solution which is received by dissolution of stack gas passing through a series of glass impingers filled with H<sub>2</sub>O<sub>2</sub>(aq). Thus, the concentration of SO<sub>2</sub> in stack gas is related to the amount of corresponding sulphate. Since this attitude contributes to the uncertainty of the measurement, needs other calibrations and also does not allow automated monitoring of emissions, other attitudes are being sought. One of the possible measuring approaches with required uncertainty are portable automated measuring systems (P-AMSs), see Figure 1. However, these P-AMSs are able to measure only filtered and dried stack gas. Since the sulfur dioxide is soluble in water, the amount of SO<sub>2</sub> removed from stack air during process of drying should be described. The aim of this article is an attempt to summarize an appropriate mathematical model.

## 2. Theoretical background

Two basic phenomena need to be taken into account in modeling of removing gaseous substances during drying process. Since the gas is dissolved in liquid water, the condensation processes are needed to be described in dependence on the physical and geometrical conditions. Once the microscopic liquid phase of water occurs in the dryer (in form of water film or water droplet), the

transfer of gaseous soluble species into water is driven by diffusion processes simultaneously with the continuing condensation of water.



**Figure 1:** Portable gas conditioning unit. Taken from [2].

The dropwise or filmwise condensation of water can proceed simultaneously or one of the process can prevail. The dropwise condensation obviously occurs in atmosphere on nucleus of dust, while the filmwise condensation prevails on hydrophilic surfaces with temperature under the saturation temperature (in multicomponent vapor called dew point). Both processes are supposed to proceed in dryers of P-AMSs since small nucleus can probably still occur in filtered stack gas and the gas cooler inside P-AMSs, see the scheme in Figure 2, is based on subcooling of glass walls to defined temperature deeply under the saturation temperature. Thus, both of the condensation processes are outlined in following paragraphs.

### 2.1. Droplet growth by condensation

The mathematical description of droplet growth is studied in theory of aerosols, e.g. in [3].

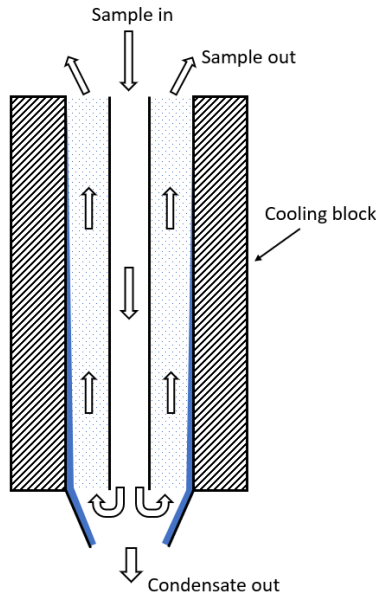


**Figure 2:** Schemes of the condensation in dryer.

The condensation processes in humid air depends on the saturation ratio (multiplied by 100% known as relative humidity) of the partial pressure of water vapor to the saturation vapor pressure

$$S_R = \frac{p}{p_s} \quad (1)$$

The saturation water vapor pressure for a plane liquid surface is given by empirical formula

$$p_s = \exp\left(16.7 - \frac{4060}{T - 37}\right) \quad (2)$$

where  $T$  is the absolute temperature in K and  $p_s$  is the saturation pressure in kPa.

In case of the planar surface water begins to condense if  $S_R = 1$ . However, the saturation ratio, called the Kelvin ratio  $K_R$ , in case of microscopic water droplets is given by the Kelvin or Thomson-Gibbs equation

$$K_R = \frac{p_d}{p_s} = \exp\left(\frac{4\gamma M}{\rho R T d}\right) \quad (3)$$

where  $\gamma$ ,  $M$ ,  $\rho$  and  $R$  are the surface tension, molecular weight, density of the liquid and universal gas constant, respectively,  $p_d$  is partial pressure at the surface of the droplet with diameter  $d$ . Since the argument of exponential function in (3) is always positive, the right-hand side of (3) is always bigger than one. It means that for the equilibrium state (droplet diameter remains the

same) the saturation ratio needs to be bigger than for flat surface. This is caused by the strongly curved surface from which molecules escape easier than from flat surface. According to the formula, the smaller diameter of the droplet the bigger partial pressure is needed for the equilibrium state. Theoretically saturation ratio of 220 would be needed for the growth of an individual molecule. However in reality, the droplet growth starts from the cluster of several molecules which are established due to van der Waals forces. From the other direction, the saturation ratio is close to unity for droplet diameter bigger than  $0.1 \mu\text{m}$  ( $K_R = 1.044$  for  $d = 0.05 \mu\text{m}$  at 293 K).

Once a stable nucleus of droplet is established, i.e. the diameter of nucleus is bigger than  $d$  given by formula (3) for a given saturation ratio (or reversely saturation ratio is bigger than  $K_R$  given by formula (3) for a given nucleus diameter), the droplet begins to growth. In [3] two formulae in dependence on the current diameter are derived. When the droplet diameter is less than gas mean free path,  $\lambda$ , the formula has the form

$$\frac{d(d_p)}{dt} = \frac{2M\alpha(p_\infty - p_d)}{\rho N_A \sqrt{2\pi m k T}} \quad \text{for } d_p < \lambda \quad (4)$$

where  $\alpha$  is accommodation coefficient,  $p_\infty$  is partial pressure far from the droplet surface,  $p_d$  is partial pressure of vapor at the droplet surface given by Kelvin equation (3),  $N_A$  is Avogadro constant,  $m = M/N_A$  is mass of vapor molecule and  $k = 1.3806485 \cdot 10^{-23}$  is Boltzmann constant.

In case the droplet is bigger than mean free path, the formula becomes

$$\frac{d(d_p)}{dt} = \frac{4DM}{R\rho d_p} \left(\frac{p_\infty}{T_\infty} - \frac{p_d}{T_d}\right) \phi \quad \text{for } d_p > \lambda \quad (5)$$

where  $D$  is diffusion coefficient of water vapor,  $\phi$  is the Fuchs correction factor significant for particles less than  $1\mu\text{m}$ ,  $p_d$  is vapor partial pressure near the droplet surface which can be calculated by formula (3) and finally the droplet temperature  $T_d$  can be computed using ambient temperature  $T_\infty$  by

$$T_d = T_\infty + \frac{(6.65 + 0.345T_\infty + 0.0031T_\infty^2)(S_R - 1)}{1 + (0.082 + 0.00782T_\infty)S_R} \quad (6)$$

where  $T_\infty$  in ratio needs to be in  $^\circ\text{C}$ .

Since gas mean free path is quite small in comparison to final droplet diameters, the amount of dissolved  $\text{SO}_2$  is not affected by the initial droplet growth described by equation (4). Moreover, since the expected final droplet

diameters are much bigger than 1  $\mu\text{m}$ , we will approximate the droplet growth by eq. (5) for  $\phi = 1$ . After integration of (5) we get the prescription for droplet diameter in time by

$$d_p(t) = \sqrt{\frac{8DM}{R\rho} \left( \frac{p_\infty}{T_\infty} - \frac{p_d}{T_d} \right) (t - t^0) + (d_p^0)^2} \quad (7)$$

where  $d_p^0$  is initial droplet diameter in time  $t^0$ . Temporal evolution of droplet diameter for different relative humidity can be seen in Figure 3.

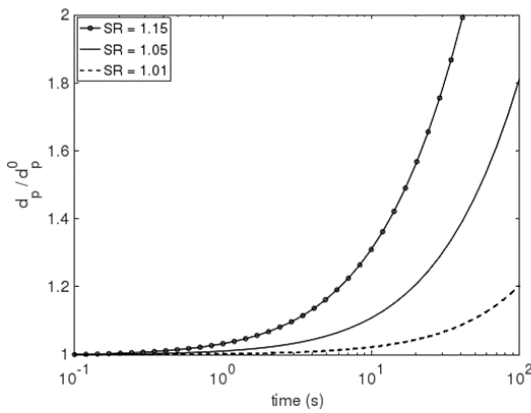


**Figure 3:** Temporal evolution of the droplet diameter in dependence on the saturation ratio (relative humidity).

## 2.2 Liquid film condensation

The liquid film occurs in case when a saturated or superheated vapor is located near the object (wall) that has the temperature lower than the corresponding saturation temperature. Authors in [4] distinguish heterogeneous nucleation which occurs at the solid-liquid interface and homogeneous nucleation which is the name for the case when growing droplet occurs entirely in the supercooled water as was described in the previous paragraph. In case of heterogeneous nucleation, the wettable surface leads to the filmwise condensation while the hydrophobic surface leads to the dropwise condensation, see Figure 4. Supposing that the glass of the cooler in P-AMSs is hydrophilic, we will focus in the next text on the filmwise condensation.

The classical analysis of laminar film on inclined or vertical wall is known from Nusselt (1916). Since the film covers whole surface, the condensation process is pushed by the heat transfer between the vapor and wall. Following from the Fourier's Law and supposing some assumptions (laminar flow, stagnant liquid vapor, smooth liquid film surface, etc. see [4]), the following formula (8) for liquid film thickness,  $\delta$ , can be derived.

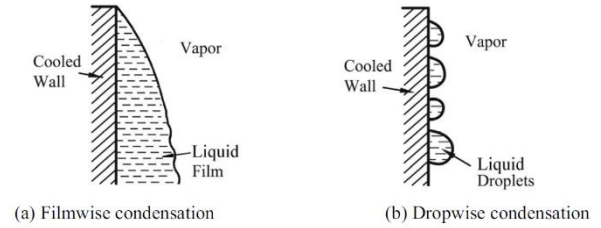


**Figure 4:** Heterogeneous condensation. Taken from [4].

$$\delta(x) = \left( \frac{4k_l\mu_l x \Delta T}{\rho_l(\rho_l - \rho_v)g h_{lv}} \right)^{1/4} \quad (8)$$

where  $k_l$  is thermal conductivity of the liquid,  $\mu_l$  and  $\rho_l$  are dynamic liquid viscosity and liquid density,  $\rho_v$  is vapor density,  $x$  is coordinate in the wall direction and  $h_{lv}$  is latent heat of the liquid-vapor phase change.

As was mentioned above, the Nusselt theory has been derived for laminar flow regime and the vertical configuration. However, as the condensation proceeds, more and more liquid flows down due to gravity and becomes unstable. At first small waves are established on the liquid film surface and if the wall is long enough, the irregular waves called ripples can appear and the turbulent regime can be achieved. Unfortunately, no standardized theory has been approved for unstable regimes and the numerical attitudes are often need to be used.

The flow regime can be determined using the Reynolds number defined in [4] as

$$Re = \frac{4\rho_l(\rho_l - \rho_v)g\delta^3}{3\mu_l^2} \quad (9)$$

The flow regime changes from laminar to wavy around  $Re=30$  and becomes turbulent for approximately  $Re=1800$  [4].

Note that in the previous text it was assumed that the vapor is stagnant. As follows from the design of P-AMSs, the film is supposed to flow downward due to gravity, while stack gas is flowing upward through the cooler, see Figure 2. We speak about countercurrent vapor flow and the motion of gas needs to be taken into account. Authors in [4] show that a nonlinear system of governing equations is derived if a shear stress from vapor motion is supposed on the liquid film interface. The corresponding mechanistic models are outlined in [5], [6] or [7]. Numerical implementation using finite volume methods can be found in [8] or [9].

Other attitude is based on the theory of heat exchanger design, see e.g. in [10]. In this case the reverse value of the overall heat transfer coefficient,  $\bar{h}$ , is found as the sum of the heat resistances for the appropriate heat exchanger. From the heat and mass balance the amount of condensate can be estimated. However, since the liquid film becomes thicker with increasing condensation and the flow regime can change along the wall, the division into several zones should be taken into account in this attitude.

### 2.3 Effect of noncondensable gas

Near the liquid film exists a boundary layer in which the partial pressure of the condensable vapor decreases from  $p_{v\infty}$  far from the interface to  $p_{v\delta}$  at the interface. On the other hand, the partial pressure of the noncondensable gas increases according to Dalton's law of partial pressure.

$$p = \sum p_i \quad (10)$$

Since the partial pressure of the condensable gas decreases, the corresponding saturation temperature decreases as well and hence the temperature at the gas-liquid interface,  $T_\delta$ , can be much lower than in case of pure vapor. According to [4], in case of small inert gas content, this temperature can be computed using equation (11), where  $h_g$  and  $h_l$  are heat transfer coefficients in gas and liquid phase, respectively.

$$T_\delta - T_w = \frac{h_g}{h_l} \left[ \frac{h_{lv}}{c_{pg}} \ln \frac{p - p_{v\delta}}{p - p_{v\infty}} \right] \quad (11)$$

### 2.4 Mass transfer through gas-liquid interface

According to the *Henry's law* in form

$$n_l = H^{cp} p_i \quad (12)$$

the concentration of a species in the aqueous phase,  $n_l$ , is proportional to the partial pressure of this matter in the gas phase,  $p_i$ .  $H^{cp}$  is the *Henry's law constant* in  $\text{mol} \cdot \text{m}^{-3} \cdot \text{Pa}^{-1}$ . Note that there are several other definitions of Henry's law constant. The dimensionless form is given by

$$H^{cc} = \frac{n_l}{n_g} \quad (13)$$

The conversion between  $H^{cc}$  and  $H^{cp}$  for ideal gas is

$$H^{cc} = H^{cp} R T \quad (14)$$

where  $R$  is the universal gas constant.

Due to this limitation of maximal concentration in liquid, the solution through the interface is not continuous as it is for example in the problem of heat conduction which is represented by the same differential equation. The dependence of Henry's law constant on temperature can be extrapolated from a single data point applying van't Hoff equation by formula

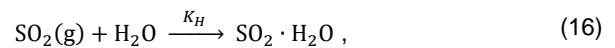
$$H(T) = H^0 \exp \left[ -\frac{\Delta h}{R} \left( \frac{1}{T} - \frac{1}{T^0} \right) \right] \quad (15)$$

where  $H^0$  is Henry's law constant in temperature  $T^0$  and  $\Delta h$  is enthalpy change due to transport of soluble gas substance into liquid. The dependence of Henry's law constant on temperature and independence on pressure have been confirmed in [11]. The values of Henry's law constant for different substances and water as solvent can be found in [12].

The ratio of molecules absorbed through the gas-liquid interface to the number of molecules which hit the liquid surface is given by the *mass accommodation coefficient*,  $\alpha$ . As has been shown in [13] using the comparison of characteristic times of different processes, the droplet surface is saturated faster than equilibrium state can be established due to diffusion. This leads to the re-evaporation of some molecules from interface and the resulting ratio of absorbed molecules can be described using the mass accommodation coefficient. The experimental measurements of mass accommodation coefficient of  $\text{SO}_2$  at the air-water interface are presented in [13] and [14]. The authors report measurements of  $\alpha = (6.0 \pm 0.8) \cdot 10^{-2}$  at 298 K and  $\alpha = (5.4 \pm 0.6) \cdot 10^{-2}$  at 295 K, respectively.

### 2.5 Physical and chemical processes in liquid phase

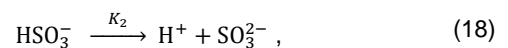
Experimental observations in [13] show that the mass accommodation coefficient is strongly dependent on pH and real solubility at the droplet surface. For considering of these dependencies, the chemical processes in liquid need to be taken into account. According to [15], the following chemical reactions occur if  $\text{SO}_2$  is dissolved in water



$$\text{where } K_H = \frac{[\text{SO}_2 \cdot \text{H}_2\text{O}]}{p_{\text{SO}_2}}$$



$$\text{where } K_1 = \frac{[\text{H}^+][\text{HSO}_3^-]}{[\text{SO}_2 \cdot \text{H}_2\text{O}]}$$



$$\text{where } K_2 = \frac{[\text{H}^+][\text{SO}_3^{2-}]}{[\text{HSO}_3^-]}.$$

Note that  $[\cdot]$  represents the concentration,  $K_H$  is the Henry's constant  $H^{cp}$ ,  $K_1$  and  $K_2$  are the first and the second dissociation constants. The total concentration of the dissolved sulfur with oxidation number four can be calculated as the sum

$$[S(IV)] = [SO_2 \cdot H_2O] + [HSO_3^-] + [SO_3^{2-}] \quad (19)$$

Following the considerations in previous paragraph, the equilibrium state of the sulfur dioxide concentration inside the droplet can be expressed by

$$n_l = H_{S(IV)}^{cp,*} p_{SO_2}, \quad (20)$$

where  $H_{SO_2}^{cp,*}$  is the effective Henry's constant computed by formula

$$H_{S(IV)}^{cp,*} = H_{SO_2}^{cp} \left( 1 + \frac{K_1}{[H^+]} + \frac{K_1 K_2}{[H^+]^2} \right), \quad (21)$$

where concentration  $[H^+]$  is connected with pH scale by

$$pH = -\log[H^+], \quad (22)$$

where  $[H^+]$  needs to be in mol/dm<sup>3</sup>.

Note that neglecting the second dissociation term  $[SO_3^{2-}]$  which has very low concentration, the effective Henry's law constant can be expressed using substitution of (14) and (15) into (19) by

$$H_{S(IV)}^{cp,*} = K_H + \sqrt{\frac{K_H K_1}{p_{SO_2}}} \quad (23)$$

As well as the Henry's law constant also the dissociation constants are dependent on temperature. According to experimental data, authors in [16] proposed correlations

$$\ln K_H = -\frac{3715.2}{T} + 16.765 \quad (24)$$

$$\ln K_1 = \frac{1447.1}{T} - 9.11 \quad (25)$$

Using equation (23) and formulas (24-25) authors of [16] derived equation for total concentration of sulfur dioxide absorbed in water in dependence on temperature, see formula (26). The corresponding concentration of SO<sub>2</sub> which can be absorbed from air with initial concentration of 0.01 ppm in dependence on temperature can be seen in Figure 5.

$$[S(IV)] = 2.407 \cdot 10^{-6} \cdot \left[ 0.0218 \cdot \exp\left(\frac{3715.2}{T}\right) p + \exp\left(\frac{2581.1}{T}\right) p^{0.5} \right] \quad (26)$$

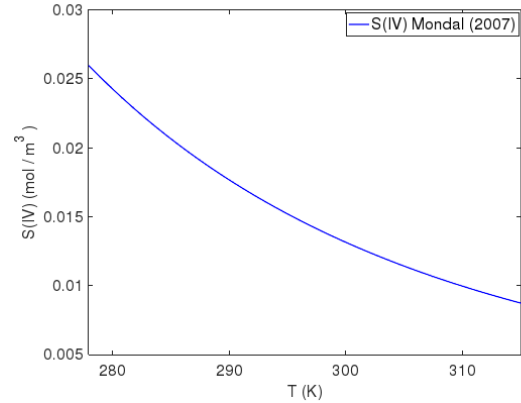


**Figure 5:** Total SO<sub>2</sub> absorbed in water in dependence on temperature. Initial SO<sub>2</sub> concentration in air 0.01ppm.

## 2.6 Diffusion

The diffusion processes are described by equation

$$\frac{\partial n(x, t)}{\partial t} = \frac{\partial}{\partial x} \left( D \frac{\partial n(x, t)}{\partial x} \right) \quad (27)$$

where  $n(x, t)$  is concentration in position  $x$  and time  $t$  and  $D$  is the diffusion coefficient. Since the studied phenomenon needs to be solved as coupled system for both phases, the system of two coupled diffusion equations for constant diffusion coefficients takes the form

$$\frac{\partial n_g(x, t)}{\partial t} = D_g \frac{\partial^2 n_g(x, t)}{\partial x^2} \quad (28)$$

$$\frac{\partial n_l(x, t)}{\partial t} = D_l \frac{\partial^2 n_l(x, t)}{\partial x^2} \quad (29)$$

The dependence of diffusion coefficient of SO<sub>2</sub> in water on temperature and pH is presented in [17]. The influence on temperature is given by

$$D_l = -1.21 \cdot 1010^{-3} + 4.33 \cdot 10^{-6} \cdot T \quad (30)$$

Analytical solutions of equations (28) and (29) for different geometrical configurations and different boundary conditions are given in [18]. However, the presented suitable solutions do not take into account the Henry's law which limits the maximal concentration of

dissolved substance in liquid and the mass accommodation coefficient which defines the fraction of molecules entering through the gas-liquid interface. The boundary conditions which take into account the Henry's Law and accommodation coefficient are presented in [19] by forms

$$-D_g \frac{\partial}{\partial x} n_g(x_i, t) = \frac{\alpha \bar{v}}{4} \left( n_g(x_i, t) - \frac{n_l(x_i, t)}{H^{cc}} \right), \quad (31)$$

$$-D_l \frac{\partial}{\partial x} n_l(x_i, t) = \frac{\alpha \bar{v}}{4} \left( n_g(x_i, t) - \frac{n_l(x_i, t)}{H^{cc}} \right), \quad (32)$$

where  $x_i$  is the location of the gas-liquid interface and  $\bar{v}=300$  m/s is mean thermal velocity of  $\text{SO}_2$  as given by [20].

### 3. Solution notes

Fairly comprehensive attitude to the modeling of soluble gas transport into large droplets during evaporation and condensation is presented in [15] and [21]. Rather complex numerical solution of the presented differential equations with moving boundaries led to the idea of using the tool based on finite element (FEM) or finite volume method (FVM) using Fluent [22]. The attitude with global heat transfer coefficient computed using correlation of Nusselt dimensionless numbers is used in [23]. Although some research articles can be found for each of the aforementioned phenomena, there is a lack of studies dealing with the analysis of  $\text{SO}_2$  in dryers of P-AMS type as well as with analysis of gas dissolution in simultaneously condensing liquid.

Since number of different processes (convection, diffusion, chemical reactions, moving gas-liquid interface etc.) makes the solution quite complex from its nature, the problem seems to be still not well implemented in modern tools for computational fluid dynamic. Thus, the step by step written mathematical model seems to be needed. However, regarding to the geometry and physical configuration of the supposed dryer, the estimate of maximal concentrations can be done separately using model of diffusion into the growing droplet and into the condensing film. In case of droplet the simultaneous simulation of diffusion and droplet growth need to be done. The results using FEM tool are presented in Figures 6. The model is based on equations (28-29) with boundary conditions (31-32) prescribed on gas-liquid interface. The mass accommodation coefficient is set to 0.054, the effective Henry's law constant is computed using (23) where dissociation constants  $K_H$  and  $K_1$  are taken from [16], see formula (24-25). The droplet growth is defined by formula (7) where droplet temperature is prescribed by

formula (6), vapor partial pressure is computed by equation (3) and saturation pressure is given by (2).

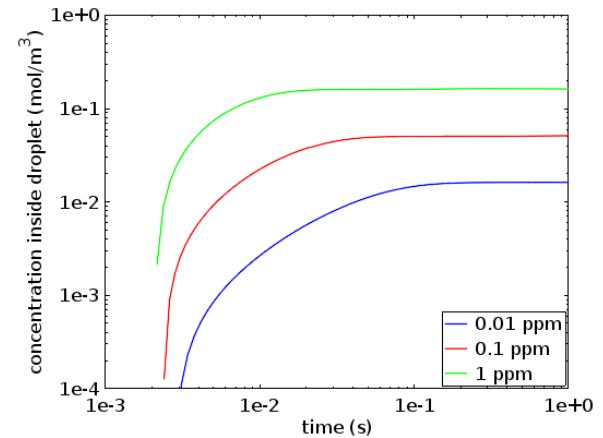


**Figure 6:** Concentration of  $\text{SO}_2$  in growing droplet during time for different values of  $\text{SO}_2$  concentration in air with relative humidity equal to 101% and temperature 20°C.

The figure 6 shows the concentration of  $\text{SO}_2$  in growing droplet in dependence on the relative humidity. Depending on the initial concentration of  $\text{SO}_2$  in gas, the time needed to reach the maximal concentration, which is given by formula (26), ranges between 0.02 and 0.2s. Regarding the dimensions of condensation tubes in P-AMSs (diameter of the tube from 6mm, height from 125 mm) and flow velocity of sampled air, we can suppose, that the maximal concentration can be reached before the droplet is attached to the liquid film on the wall. On the other hand, the droplets are established only in case the relative humidity is bigger than 100%. In other cases, the condensation on the cooled wall with temperature 5°C is predominant for the drying processes in the dryer. Hence, the modeling of liquid film formation due to condensation and corresponding  $\text{SO}_2$  dissolution is important for total amount of dissolved  $\text{SO}_2$ .

In contrast to the growing droplet, in case of the condensing liquid film, the corresponding analysis can be done for a given film thickness, if we can suppose that in process of measurement a stagnant liquid film is established. Hence, although the stationary liquid film thickness can be taken into account, the mathematical models suffer from other complications such as the modeling of interfacial friction or liquid velocity on the film surface in case of moving vapor in dryer when the formula (8) cannot be used. Authors in [6] note two effects of increasing vapor flow on the heat transfer. As can be supposed, the bigger interfacial shear stress leads to the decreasing of the film velocity and increasing film thickness. Bigger film thickness itself would lead

to bigger heat transfer resistance and decreasing condensation rate. However, the increasing interfacial shear stress influences the interfacial perturbations and leads the reinforcement of the turbulence in the liquid film. Bigger turbulence leads to increase of heat transfer. Both effects apply differently in dependence on the value of the film Reynolds number, thus the detailed analysis is needed.

In case of a typical P-AMS, the maximum gas volume flow rate is 150 NI/h. For a tube with diameter 6mm, this corresponds to gas velocity of about 0.4m/s and laminar flow regime. Supposing limited influence of this laminar flow on the liquid film, the classical Nusselt formula (8) can serve as a basic estimate of the liquid film thickness along the dryer and the liquid volume in which the gas can diffuse. Supposing the length of the dryer tube 0.15m with diameter 0.006m and standard physical properties of water, the film thickness using (8) equals about 0.1 mm for saturation temperature of about 290K. As in the case of water droplet, several FEM simulations have been done using the theoretical basis outlined in the previous chapter. The main difference was the stagnant interface between liquid and gas phase and resolution of convection using the assumptions of laminar flow regimes in both phases. The constant film thickness of 0.1mm have been defined along the 0.15m long dryer. Zero flux of SO<sub>2</sub> has been prescribed in the upper boundary of liquid film and on the wall. The boundary conditions (31-32) have been prescribed on the gas-liquid interface.

The resulting ratios of outlet to inlet SO<sub>2</sub> concentrations in gas for different average velocity of gas flow and different inlet concentrations can be read in Table 1.

**Table 1: SO<sub>2</sub> concentration after passing through the cooler with constant water film thickness. Resulting values are normalized to the initial concentration before entrance to the cooler.**

	$n_g^{SO_2} = 1 \text{ ppm}$	$n_g^{SO_2} = 10 \text{ ppm}$	$n_g^{SO_2} = 100 \text{ ppm}$
$U_g = 0.4 \text{ m/s}$	46.9 %	48.4 %	52.4 %
$U_g = 0.2 \text{ m/s}$	28.6 %	29.9 %	33.8 %
$U_g = 0.1 \text{ m/s}$	12.6 %	13.4 %	16.0 %

The resulting dependencies in Table 1 show that the SO<sub>2</sub> loses increase with decreasing gas velocity and decreasing SO<sub>2</sub> concentration in gas phase. The loses increase only slightly for lower inlet concentrations, while the dependence on the gas velocity is much more significant. This result is related to the fact, that in case of low gas velocity the dissolving species has more time to diffuse into the water film. Although, the tendencies just presented makes the physical sense, note that a more detailed numerical analysis is needed for credibility of quantitative results.

## 7. Conclusion

The article summarizes the mathematical models of the main processes crucial for the assessing of SO<sub>2</sub> loses during drying processes in P-AMSs. The models of droplet growing and liquid film formation during condensation have been presented on basis of theoretical as well as experimental findings published in literature. The molecular transport of condensable gas has been discussed with regards to the molecular processes on gas-liquid interface as well as with regards to chemical processes inside liquid. The governing equations of diffusion processes have been presented and the significant boundary condition has been defined using physical parameters from previous sections. The concentrations of SO<sub>2</sub> dissolved in one droplet have been computed using presented mathematical model of diffusion simultaneously with modeling of droplet growth. The average concentration of SO<sub>2</sub> in gas flow leaving the dryer has been simulated for stagnant film thickness, but as well as for droplet using aforementioned diffusion model based on Henry's law theory and chemical reactions connected with dissolution of SO<sub>2</sub> in water. Both cases have been implemented and simulated in FEM tool COMSOL Multiphysics®. From the comparison of resulting SO<sub>2</sub> concentrations at the inlet to the dryer and the final concentrations at the outlet from the dryer it follows that the SO<sub>2</sub> loses can be significant for the measurements using P-AMSs. However, more detailed numerical analysis and comparison with experimental findings should be done for validation of this conclusion.

## Acknowledgement

The author acknowledges the support received from the European Metrology Programme for Innovation and Research (EMPIR) through the Joint Research Project "Metrology for Sampling and Conditioning SO<sub>2</sub> Emissions from Stacks". The EMPIR is jointly funded by the European Commission and participating countries within Euramet and the European Union.

## References

- [1] F. Derriennic, S. Richardson, A. Mollie a J. Lellouch, „Short-term effect of sulphur dioxide pollution on mortality in two French cities,“ *International Journal of Epidemiology*, pp. 186-197, March 1989.
- [2] [Online]. Available: <http://www.learsiegler.com.au/suppliers/mc/PSS.html>. [16/5/2019].
- [3] W. C. Hinds, *Aerosol Technology*, New York: John Wiley & Sons, Inc., 1999.

- [4] A. Faghri a Y. Zhang, *Transport Phenomena in Multiphase Systems*, London: Academic Press, Elsevier Inc., 2006.
- [5] A. Faghri, „Turbulent Film Condensation in a Tube with Concurrent and Countercurrent Vapor Flow,“ v *AIAA/ASME 4th Joint Thermophysics and Heat Transfer Conference*, Boston, 1986.
- [6] S. Thumm, C. Philipp a U. Gross, „Film condensation of water in a vertical tube with countercurrent vapour flow,“ *International Journal of Heat and Mass Transfer* 44, pp. 4245-4256, 2001.
- [7] R. A. Seban a J. A. Hodgson, „Laminar film condensation in a tube with upward vapor flow,“ *International Journal of Heat and Mass Transfer*, Vol. 25, No. 9, pp. 1291-1300, 1982.
- [8] N. Samkhaniani a M. R. Ansari, „The evaluation of the diffuse interface method for phase change simulations using OpenFOAM,“ *Heat transfer - Asian Res*, pp. 1-31, 2017.
- [9] M. K. Groff, S. J. Ormiston a H. M. Soliman, „Numerical solution of film condensation from turbulent flow of vapor-gas mixtures in vertical tubes,“ *International Journal of Heat and Mass Transfer*, 50, pp. 3899-3912, 2007.
- [10] M. Nitché a R. O. Gbadamosi, *Heat exchanger design guide. A practical Guide for planning, Selecting and Design of Shell and Tube Exchangers*, London: Butterworth Heinemann, Elsevier, 2016.
- [11] N. Zhang, J. Zhang, Y. Zhang, J. Bai a X. Wei, „Solubility and Henry's law constant of sulfur dioxide in aqueous polyethylene glycol 300 solution at different temperatures and pressures,“ *Fluid Phase Equilibria*, 348, pp. 9-16, 2013.
- [12] R. Sander, „Compilation of Henry's law constants (version 4.0) for water as solvent,“ *Atmospheric Chemistry and Physics*, 15, pp. 4399-4981, 2015.
- [13] J. L. Ponche, C. George a P. Mirabel, „Mass Transfer at the Air/Water Interface: Mass Accommodation Coefficients of SO<sub>2</sub>, HNO<sub>3</sub>, NO<sub>2</sub> and NH<sub>3</sub>,“ *Journal of Atmospheric Chemistry*, 16, pp. 1-21, 1993.
- [14] J. A. Gardner, L. R. Watson, Y. G. Adewuyi, P. Davidovits, M. S. Zahniser, D. R. Worsnop a C. E. Kolb, „Measurement of the Mass Accommodation Coefficient of SO<sub>2</sub> (g) on Water Droplets,“ *Journal of Geophysical Research*, vol. 92, No. D9, pp. 10887-10895, 20 September 1987.
- [15] T. Elperin, A. Fominykh a B. Krasovitev, „Scavenging of soluble gases by evaporating and growing cloud droplets in the presence of aqueous-phase dissociation reaction,“ *Atmospheric Environment*, 42, pp. 3076-3086, 2008.
- [16] M. K. Mondal, „Experimental determination of dissociation constant, Henry's constant, heat of reactions, SO<sub>2</sub> absorbed and gas bubble-liquid interfacial area for dilute sulphur dioxide absorption into water,“ *Fluid Phase Equilibria*, 253, pp. 98-107, 2007.
- [17] A. Koliadima, J. Kapalos a L. Farmakis, „Diffusion Coefficients of SO<sub>2</sub> in Water and Partition Coefficient of SO<sub>2</sub> in Water-Air Interface at Different Temperature and pH Values,“ *Instrumentation Science & Technology*, 37:3, pp. 274-283, 21 April 2009.
- [18] J. Crank, *The Mathematics of Diffusion*, Oxford: Clarendon Press, 1975.
- [19] T. Huthwelker a T. Peter, „Analytical description of gas transport across an interface with coupled diffusion in two phases,“ *J. Chem. Phys*, 105, (4), pp. 1661-1667, 22 July 1996.
- [20] J. O. Hirschfelder, C. F. Curtiss a R. B. Bird, *Molecular Theory of Gases and Liquids*, New York: Wiley, 1954.
- [21] T. Elperin, A. Fominykh a B. Krasovitev, „Evaporation and Condensation of Large Droplets in the Presence of Inert Admixtures Containing Soluble Gas,“ *Journal of the Atmospheric Sciences*, pp. 983-995, March 2007.
- [22] M. P. Perujo, „Condensation of Water Vapor and Acid Mixtures from Exhaust Gases, PhD Thesis,“ Technische Universität Berlin, Berlin, 2004.
- [23] E. Serris, M. Cournil a J. Peultier, „Modeling and simulation of acid gas condensation in an industrial chimney,“ *International Journal of Chemical Reactor Engineering*, De Gruyter, p. pp.A39, 2009.
- [24] H. G. Maahs, „Sulfur-dioxide/water equilibria between 0° and 50°C. An examination of data at low concentrations,“ v *Heterogeneous Atmospheric Chemistry, Geophysical Monograph*, 26, S. D. R., Editor, Washington, D.C., Am. Geophys. Union, 1982, pp. 187-195.

# Factors influencing the quality of flow measurements in drinking water systems – lessons learned

M. A. Silva<sup>1,2</sup>, D. Loureiro<sup>1</sup>, A. S. Ribeiro<sup>1</sup>, C. Amado<sup>2</sup>

<sup>1</sup>National Laboratory for Civil Engineering, Avenida do Brasil, 101, 1700-066 Lisbon, Portugal

<sup>2</sup>CEMAT, Instituto Superior Técnico, Avenida Rovisco Pais 1, 1049-001 Lisbon, Portugal

E-mail (corresponding author): [mjsilva@lnec.pt](mailto:mjsilva@lnec.pt); [maria.jose.silva@tecnico.ulisboa.pt](mailto:maria.jose.silva@tecnico.ulisboa.pt)

---

## Abstract

The flow measurement is essential for drinking water network monitoring. A better knowledge about the flow that is abstracted or pumped to drinking water systems, transferred between water utilities or monitored at the entrance of the subsystems can be achieved through the flow measurement. Nevertheless, this is a topic insufficiently studied. The accuracy can be an excellent parameter to the analysis of the uncertainty sources impact on the measurements obtained from manufacturer's catalogues, and the contributions related with installation, data acquisition, transfer, storage and processing. To understand the influence of these factors in flow data, a set of flowmeters from six water utilities was selected and surveyed in this paper. This paper aims to explore a methodology to analyse the relationship between the uncertainty in daily flow patterns and influential factors. To run the analysis, a robust coefficient of variation was computed for each hour of the workday flow pattern. The most influential factors were: the direction of the flow measurement, year of installation and practices adopted for nominal diameter selection. Although the flow profiles and the elbows are considered in the literature as factors that influence the measurement, in this set of flowmeters, no influence was verified. This exploratory analysis allowed to point out factors related to flowmeter installation that have a significant impact on the quality of the flow measurements.

---

## 1. Introduction

The flow measurement has a major role in monitoring water supply systems, providing information about the flow that is abstracted or pumped to drinking water systems, transferred between water utilities or monitoring the entrance of subsystems. In the case of water that is transferred and billed between water utilities, flow measurement becomes a crucial factor for the confidence level between the different agents and the economic sustainability of the service. When flow measurement is used for network monitoring and control of water losses, data quality is needed to ensure that results from well-known approaches (e.g., water balance, minimum night flow analysis) are trustable [1]. However, the quality of flow measurement in water supply systems is a topic insufficiently studied both nationally and internationally [2].

In Portugal, the most relevant drinking water systems were built 20-30 years ago. The population growth projections that did not occur and the firefighting requirements lead to oversize the networks and the majority of existing flowmeters. In fact, in several water utilities, a common practice is still to adopt a flowmeter diameter of the same size of the network pipe diameter,

disregarding the flow pattern and flow velocity best practices for measurement.

An informative indicator to understand the factors that affect flow measurements (usually mentioned as uncertainty sources) and their impact on results is the measurement accuracy. However, the errors indicated in catalogues only mention part of the uncertainty sources that should be taken into account (associated with the measurement equipment). The uncertainty sources related to the installation, data acquisition, transfer, storage and processing are not indicated in the catalogue. Since the measurement inaccuracy is determined by the characteristics which are not in the ideal conditions, the observation of these characteristics is necessary to the study of the factors that influence the measurement. The flow profiles are one of the factors that should be considered [3], as well as the elbows influence, in the proximity of measurement locations, able to affect measurement because of disturbance produced in the flow profiles [4,5]. The effect of different combinations of T-junctions was studied in [4]. Moreover, in [6], the existence of elbows together with the orientation of the flowmeter was considered. These characteristics in an electromagnetic flowmeter may also include, e.g., non-compliance with sizing rules, interference of

electromagnetic fields, intrinsic noise, the resolution associated to the conversion analogic to digital and data processing [7]. This list should not be adopted for non-electromagnetic flowmeters, since different factors of influence are found, e.g., in an ultrasonic or insertion flowmeters [8-10]. In any case, it is evident that the uncertainty of measurement depends on many other factors besides the equipment calibration.

In this paper, a set of flowmeters in use in Portuguese water utilities was characterised to obtain information about adopted practices, characteristics of flowmeters and installation conditions. Data were collected through a survey, in the scope of a collaborative project yield in Portugal, involving 13 water utilities (iperdas.org). Collected data included technical characteristics of the flowmeter, procedures adopted for the quality control, characteristics of recorded information, installation and installation chamber characteristics.

This paper is organised as follows. In Section 2, a description of the survey sent to the water utilities is presented, as well as the methodology used to analyse these data. Section 3 is concerned with the results obtained. Conclusions of this study and future work are presented in Section 4.

## 2. Methodology

The survey used to collect the information used was divided into five sections: technical characteristics of the flowmeter; quality control of data acquisition, periodic calibration and intermediate verification; characteristics of the data recorded; installation conditions; and installation chamber layout. In addition, flow data was also requested. In the next subsections, a more detailed description of the survey applied is given.

### 2.1. Technical characteristics of the flowmeter

Technical characteristics include the type of equipment, nominal diameter (DN) of the flowmeter,  $Q_3/Q_1$  ratio, where  $Q_3$  is the permanent flow and  $Q_1$  the minimum flow [11], age, year of installation and condition (good, mean, bad). Moreover, the output mode of the data (analogic or digital) was also requested, as well as if the flowmeter is unidirectional or bidirectional.

### 2.2. Quality control in flowmeter acquisition, periodic calibration and intermediate verification

In this section, some questions about the flowmeters' calibration practices were surveyed. Examples are the prerequisite of a calibration certificate at the moment of the flowmeter acquisition, the existence of a calibration plan, maintenance and its execution and the periodicity of intermediate verification of parameters.

### 2.3. Characteristics of the data recorded

Information about the measured values that are recorded is needed, such as the type of value registered (i.e., instantaneous, mean or total value) in order to have a perception of the representativeness of the available data.

Furthermore, water utilities were asked about their control and treatment of data regarding the percentage of missing values and anomalous data.

### 2.4. Installation conditions

In terms of installation characteristics, the survey starts questioning how the diameter of the flowmeter is chosen, being the options the nominal diameter of the pipe or the mean velocity of flow. Different criteria are also possible to mention. The existence of established procedures to install flowmeters and requirements for technical qualification of persons responsible for installation and maintenance is also inquired. Other technical questions were made, concerning the practical conditions of installation:

- The existence of straight water pipe upstream and downstream of the flowmeter and the respective lengths;
- Levelling of the inlet and outlet pipes and the flowmeter;
- The existence of upstream and downstream valves and distances to the flowmeter;
- The existence of an upstream filter;
- The existence of electric or signal cables nearby.

Information about the water pipe where the flowmeter is installed was also collected, namely, the pipe material, its internal diameter, the pipe condition and the existence of reduction connections to the inlet pipe of the flowmeter. Characteristics related to the power supply and other characteristics specific for electromagnetic flowmeters are also relevant and, therefore, they were also part of the survey. Pulse emitter type, battery autonomy and recover capacity, protection against atmospheric discharges, ground connections of the meter and upstream and downstream connection pipes, and surrounding sources of electromagnetic radiation are some examples.

### 2.5. Installation chamber layout

The survey also inquired about the existence of some layout characteristics of the installation chamber, namely, access facilities, ventilation, drainage system, a system for flood detection, a system for intrusion detection, UPS/relief and switchboard.

### 2.6. Flow data

As mentioned previously, flow data recorded was requested. This allows studying the flow velocity and the volume measured in each flow velocity range. The flow time series was also analysed to characterise the flow range. These analyses are of great importance in order to

evaluate the suitability of the flowmeter and to reduce the effect of measurement errors and their uncertainties.

Firstly, a similar period of the flow data was selected from all the flowmeters and the time interval was uniformised. Secondly, flowmeters installed upstream of storage tanks were separated from the analysis because they have patterns that are guided by emptying/filling storage tanks rules. The remaining flowmeters, that are installed in distribution networks, were divided into groups according to the definition of the daily pattern: flow data with a regular daily pattern during the selected period, flow data with irregular patterns, and flow data with an intermediate behaviour. Lastly, in each group, the answers to the survey were analysed to understand if there is a connection between the factors under study and the uncertainty in the daily flow patterns. In order to measure this uncertainty, a robust version of the coefficient of variation of the flow was computed for each hour and flowmeter. Let be  $\mathbf{X}_t = \{X_{1t}, X_{2t}, \dots, X_{nt}\}$ , where  $X_{it}$  represents the value of the flow time series at time  $t$  of the working day  $i$  ( $i = 1, \dots, n; t = 0, \dots, 23$ ). The Robust Coefficient of Variation (RCV) is defined as:

$$RCV(t) = \frac{MAD(\mathbf{X}_t)}{|\text{Median}(\mathbf{X}_t)|} \quad (1)$$

where MAD is the Median Absolute Deviation, i.e.  $MAD(\mathbf{X}_t) = \text{Median}(|X_{it} - \text{Median}(\mathbf{X}_t)|)$ .

### 3. Results

Data from 25 flowmeters from six water utilities were analysed, 88% of which were electromagnetic flowmeters. The variability of DN is significant, with values in a range from 40 mm to 600 mm. However, the most typical DN was of 200 mm. The average age of the flowmeters was approximately equal to 10 years, though the average number of years they are installed is lower than ten years. The condition was indicated as good in 72% of the flowmeters and as average in 12%. The status of the remaining 12% is not known. Relative to the flow direction, 40% of these flowmeters were bidirectional. In metrological terms, the ratio  $Q_3/Q_1$  varied significantly, between 25 and 1 000, although this information is only available for 44% of flowmeters.

In terms of quality control applied to flowmeter acquisition, periodic calibration and intermediate verification, the number of answers was scarce. A calibration certificate at the moment of flowmeter' acquisition was required to 92% flowmeters of the 48% for which this information was available. Nevertheless, calibration plan, maintenance and intermediate verification only exist for 70% of the 40% flowmeters having this information available, with an interval of one or five years.

Regarding the type of measured value recorded, all 52% of flowmeters with answers make records of the total value, being that the only data recorded in only 23% of these flowmeters. The remaining 77% flowmeters also make records of the instantaneous value. Furthermore, the results showed that less than 20% of the water utilities control the flow data received (e.g., data synchronisation, control of the percentage of non-received and anomalous data), although 50% did not answer. This control is considered as critical to ensure data redundancy and to detect problems due to faults in the equipment or the communication systems. Furthermore, it is crucial to ensure that the data history is the most complete as possible (i.e., without missing values).

In terms of flowmeter selection and its installation, there is no information about the criteria used to select 32% flowmeters. In the other 68% of meters, the diameter of 65% was selected based on the diameter of the main. In addition to this criterion, only 18 % of flowmeters were selected also taking into account the consumption history. Only 24% of the flowmeters were selected taking into account the mean flow velocity expected. Not considering the flow conditions increases measurement errors and related uncertainties. Moreover, procedures for the flowmeter installation are not usual, such as requirements for technical qualification of the person responsible by the installation. Only one water utility indicated they have these procedures and requirements.

Considering the 76% of answers about the existence of straight water pipe upstream and downstream of the flowmeter, only 11% (respectively, 5%) of flowmeters do not have a straight water pipe upstream (respectively, downstream). This 5% of meters that do not have a straight water pipe downstream also do not have it upstream. The average length of the upstream straight water pipe is 1,16 m, while the average length of the downstream is 0,84 m. Considering the recommendations in [12], the length of the upstream straight water pipe should be at least five times the DN and the length of the downstream should be at least two times the DN. In practice, only 60% of the flowmeters have an upstream straight pipe of enough length, while 93% have a downstream straight pipe with the adequate length. Regarding the levelling of the inlet and outlet pipes and the flowmeter, all the water utilities that answered this question said that they are levelled. Moreover, almost all or even all water utilities pointed out that there are neither an upstream filter of the meter nor electric or signal cables nearby. Contrariwise, a metering valve upstream or downstream exists in 94% of the installations with answers with a median distance between it and the flowmeter of 1 m.

Regarding the material of network pipes, Figure 1 shows the percentages of types of water pipes material used. The

most typical is the cast iron, followed by the asbestos cement and the steel. The status of water pipe inside was indicated as good in almost all the flowmeters with an answer.

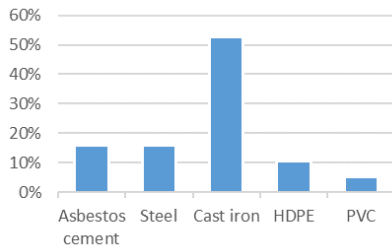


**Figure 1:** Material of water pipes (HDPE: High-density polyethylene; PVC: Polyvinyl chloride).

Questions about the characteristics related to the electric supply and specific for electromagnetic flowmeters were left blank for most of the cases.

For the analysis of the flow data, a screening was performed to select only the flowmeters with more than three weeks of data. This condition resulted in the selection of only 21 flowmeters, since the other four do not have at least three weeks of data. There is a significant number of flowmeters where the flow velocities are very low (below 0,25 m/s), generating large errors and uncertainties. In 38% of the flowmeters, the volume measured below 0,25 m/s was higher than 40%. Moreover, in 71% of the meters, the volume measured below 0,50 m/s was higher than 40%.

Since the flow data have different time interval steps and the biggest is 60 minutes (Table 1), the time step of all flow time series was uniformised for 60 minutes, allowing to perform a direct comparison of time series. Furthermore, the flow data have different time intervals, as can be seen in Table 1, and data can be available for three years or only for one month. Even when it is available for only one month, it can be different for different flowmeters. Thus, a selection of the time interval to be used in the analysis should be made, trying to harmonise as much as possible the data used. For data with only one month, all the data was considered, regardless of the month in question. For data with more months, June (of 2015, if possible) was the month selected, since it is one of the months more frequent. For flowmeters 17 and 18 and once June was not available, September was selected. The choice of September was made due to its similarity in terms of users' occupation and weather with June, in Portugal. Besides this, these two flowmeters were separated from the general analysis as they were associated with storage tank filling. Their behaviour is very different and cannot be compared with flow data measured in the middle of the network. Figure 2 shows a month of flow data from meter 17, associated FLOMEKO 2019, Lisbon, Portugal

with a storage tank filling. It is possible to observe that, in almost all month, the flow is equal to zero or a maximum closer to 200 m<sup>3</sup>/h. Although flowmeter 18 is also associated with a storage tank filling, its records show different behaviour. In this case, the flow does not frequently achieve the zero and the maximum values, varying in the middle results. This means that flowmeters associated with storage tanks filling should be analysed separately, due to the different parametrisations of the tanks.

**Table 1:** Basic characterisation of flow data from each flowmeter (time interval, time step and percentages of missing and null values).

Flow meter	Time interval	Time step (minutes)	Percentage of missing values	Percentage of null values
1	01/01/15 – 27/10/16	60	0,1%	2,4%
2	01/01/15 – 27/10/16	60	0,1%	0,0%
3	01/01/15 – 27/10/16	60	0,1%	0,0%
4	02/07/13 – 30/06/16	15	0,8%	0,0(7)%
5	02/07/13 – 30/06/16	15	0,0(6)%	0,0(2)%
6	02/07/13 – 30/06/16	15	3,7%	0,0%
7	01/01/15 – 31/12/15	15	0,0(2)%	0,0%
8	01/01/15 – 01/01/16	15	0,2%	0,0%
9	01/01/15 – 31/12/15	15	1,2%	0,0%
10	01/01/15 – 31/12/15	15	0,4%	0,0%
11	17/05/17 – 28/06/17	15	0,0%	0,7%
12	17/05/17 – 28/06/17	15	0,0%	0,1%
13	17/05/17 – 28/06/17	15	0,0%	0,1%
14	16/05/17 – 30/06/17	15	0,0%	0,9%
15	17/05/17 – 28/06/17	15	0,0%	0,0%
16	17/05/17 – 28/06/17	15	0,0%	2,2%
17	01/09/16 – 20/11/16	30	0,0%	26,0%
18	01/09/16 – 20/11/16	30	0,0%	1,7%
19	02/11/16 – 28/11/16	15	0,0%	0,0(4)%
20	01/11/16 – 29/11/16	15	9,1%	0,6%
21	01/08/16 – 31/08/16	15	0,0%	71,6%

The remaining 19 flowmeters are placed in the network and their behaviour should reproduce the water consumption of the associated network sector. Since there is a daily and weekly seasonality in the water consumption, all working days of the month under analysis were represented in the same graph to allow the

vision of the variation along the month. Weekends were not considered due to the small representativeness. Three groups of flowmeters were identified: the first one is constituted by eight flowmeters with a defined daily pattern (although the pattern can be different from meter to meter); the second one by five flowmeters with a daily pattern more or less defined, but with higher variation; and the last one constituted by six flowmeters with an irregular daily pattern. Figure 3 presents three examples of flowmeters, one from each of the groups, showing the differences between them. Although the flowmeter 1 has outliers, it presents a defined daily pattern with low variation and, consequently, it was included in the first group. The example of a flowmeter that was included in the second group is the 13<sup>th</sup> meter. A pattern is possible to identify with low values of consumption until 6/7 a.m., followed by an increase of values. Another increase of values occurs at 8/9 p.m. Although this flowmeter has a daily pattern, the variation in each time instant is more significant than in the flowmeter 1. Thus, it was considered in another group. The last group is constituted by flowmeters as the 19<sup>th</sup>, presented in Figure 3. In this case, there is no daily pattern.

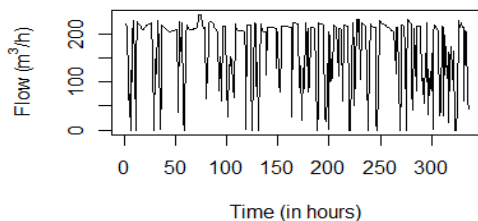


**Figure 2:** Example of flow data from a storage tank filling of one month.

For the analysis of the factors that influence the uncertainty, the RCV series of the working days was used together with the groups' division. Therefore, the factors that allow a good distinction between the groups are the factors that are influencing the uncertainty of these flowmeters. Flowmeter 21 was excluded from the analysis due to the observation of a high number of zeros that unable the computation of the RCV.

Figure 4 shows the RCV for each flow time series divided by the three groups (three plots) according to the direction of the flowmeter (bidirectional - red or unidirectional - green). A distinction is visible: the flowmeters with less variation are predominantly bidirectional, while the flowmeters with higher variation are predominantly unidirectional.

The same analysis was repeated for each question that was made in the survey. A relation was not obtained for almost all the factors. Although the flowmeters with higher variation were installed predominantly in 2016, it is believed that this relation is not general and is due to

the data used. The sample of flowmeters installed in older years may not be representative, while the number of flowmeters installed in 2016 is high. The practices used to select the meter DN also showed a relationship with the flow data variation. Meters with higher variation have DN's chosen based only on the pipe network DN, while flowmeters with lower variation have DN's chosen based on the mean velocity. Although the flow profiles and the elbows are considered as two factors that influence the measurement quality, in this study, no clear relation between them and the flow data was possible to establish.

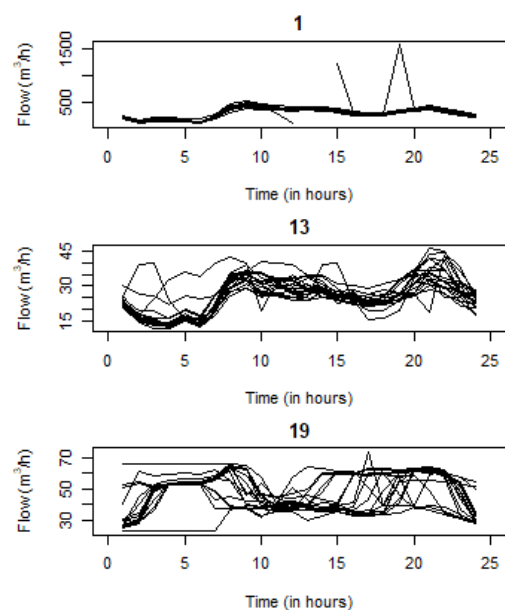


**Figure 3:** Examples flowmeters from each group (1 – defined daily pattern, 13 – defined daily pattern with more variation, 19 – irregular daily pattern).

#### 4. Conclusion

This paper aimed to explore a methodology to analyse the relationship between the uncertainty in daily flow patterns and influential factors. With this purpose, a set of flowmeters was studied in the context of a national project yield in Portugal. Each water utility answered a survey about the flowmeters selected, in terms of the technical characteristics of the flowmeter, the quality control, the data recorded, the installation characteristics and the flow data.

For an accurate comparison between the flowmeters, the flow data was normalised for a time interval step of one hour and one month was selected. When possible, the month selected was June. Two flowmeters were separated from the analysis, because they are placed before a storage tank and, therefore, the flow data reflects its filling. On the other side, the flowmeters placed in the middle of the network have daily and weekly seasonality. Thus, only the working days were considered, and the

flowmeters were divided into groups according to the definition of their daily patterns. Then, the RCV was computed for each hour of a day for each flowmeter. The analysis of the factors that influence the flow measurement quality was based on the analysis of the RCV. Three factors were identified as influence factors of the measurement quality: the direction of the flow in the flowmeter (unidirectional or bidirectional); the installation year; and the characteristics used to select the flowmeter' DN.

This exploratory analysis allows for understanding the practical impact on the quality of the flow measurements of some factors associated with the installation of flowmeters. The low rate of answers limited a more in-depth analysis. Furthermore, these results indicate that there is still a long way to go when it comes to flow measurement quality. In the future, a more in-depth study of each flowmeter will be done, through the modelling of the daily patterns. Then, the uncertainty in each time instant could be computed. Moreover, in the future, the effect of the time step in the uncertainty can also be analysed using the flow data with small time steps.

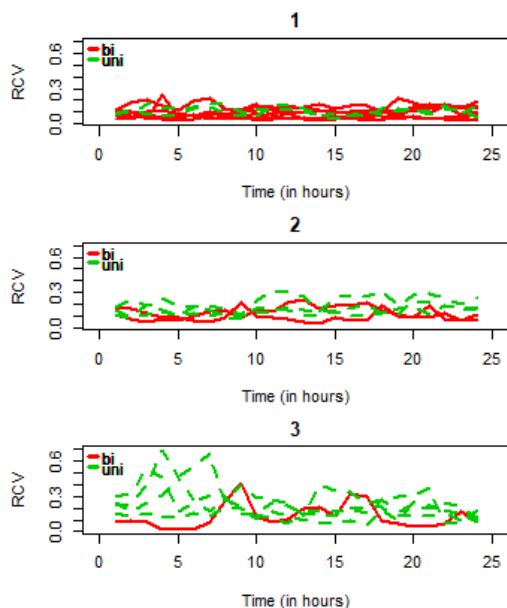


**Figure 4:** Robust coefficient of variation (RCV) for the three groups according to the flowmeter direction (legend, bi: bidirectional; uni: unidirectional).

### Acknowledgements

The authors acknowledge the water utilities involved in the project. The first author acknowledges the Fundação para a Ciência e Tecnologia (FCT), Portugal, for the PhD Grant SFRH/BD/131382/2017. The authors also acknowledge FCT for the project UID/Multi/04621/2019 of CEMAT/IST-ID, Center for Computational and

Stochastic Mathematics, Instituto Superior Técnico, ULisboa.

### References

- [1] Farley, M; Trow. S., *Losses in water distribution networks: A practitioner's guide to assessment, monitoring and control* (London, IWA Publishing), 2003.
- [2] Ribeiro, A. S.; Loureiro, D.; Martins, L.; Sousa, J. A.; Batista, E.; Dias, L.; Soares, A. C., "Measurement uncertainty of turbine flow meter calibration used in conformity assessment for water management", *Journal of Physics: Conference Series*, **1065**, 092006, 2018.
- [3] Wendt, G.; Jahn, T.; Hein, A., "Investigation of flow behaviour of water in pipes and inside water meters and characterization of the flow by dimensionless parameters", in *International Workshop on Water and Heat Meters*, 2013.
- [4] Mattingly, G.E.; Yeh, T. T., "Secondary flow effects due to several elbow configurations", in *ASME Fluid Measurement and Instrumentation Forum 1990*, 1990.
- [5] Mattingly, G. E.; Yeh, T. T., "Effects of pipe elbows and tube bundles on selected types of flow meters", *Flow Measurement and Instrumentation*, **2**, 4-13, 1991.
- [6] Weissenbrunner, A.; Fiebach, A.; Schmelter, S.; Bär, M.; Thamsen, P. U.; Lederer, T., "Simulation-based determination of systematic errors of flow meters due to uncertain inflow conditions", *Flow Measurement and Instrumentation*, **52**, 25-39, 2016.
- [7] Henriques, J. D.; Palma, J. C.; Ribeiro, A. S., *Medição de caudal em sistemas de abastecimento de água e de saneamento de águas residuais urbanas* (Lisbon, IRAR and LNEC), 2007.
- [8] Carlander, C.; Delsing, J., "Installation effects on an ultrasonic flow meter", in *FLOMEKO (ITF)*, 149-154, 1998.
- [9] Kelner, P. E., "Flow meter installation effects", *American School of Gas Measurement Technology*, 2009.
- [10] Shercliff, J. A., "Relation between the velocity profile and the sensitivity of electromagnetic flowmeters", *Journal of Applied Physics*, **25**, 817-818, 1954.
- [11] Directive 2004/22/CE of the European Parliament and of the Council of 31 March 2004 on measuring instruments.
- [12] ISO 20456, *Measurement of fluid flow in closed conduits - Guidance for the use of electromagnetic flowmeters for conductive liquids*, 2017.

# Water cut determination in co-current liquid-liquid flow using electrical capacitance metering

Y. Arellano<sup>1</sup>, A. Hunt<sup>2</sup>, O. Haas<sup>3</sup>, H. Ahmed<sup>3</sup>, and L. Ma<sup>2\*</sup>

<sup>1</sup> Fluids and Complex Systems Research Centre, Mile Lane, Coventry University, Coventry, UK

<sup>2</sup> iPhase Limited, Unit 7 Intec Business Park, Basingstoke, UK

<sup>3</sup> Research Institute For Future Transport and Cities, Coventry University, Coventry, UK

\*E-mail: luma@iphaseflow.com

---

## Abstract

Despite intensive research dedicated to multiphase flow measurement in the past decades, accuracy remains one of the key challenges in the oil and gas industry. The Multiphase flow of gas-liquid mixtures has been extensively addressed in the literature. However liquid-liquid flows, are intrinsically more complex and their hydrodynamics are not yet completely understood.

The present study investigates the capabilities of in-line tomography technologies for water cut determination in co-current immiscible liquid-liquid flows. The proposed experimental metering system operates by interrogating the imaging region contained by the pipe walls with a high-frequency alternating electric field. The experiments are conducted on the horizontal section of a flow rig of 100mm in diameter using synthetic oil and saline water as test fluids. Measurements of stratified flows from electric capacitance tomography are contrasted to measurements from an electrical capacitance meter. Measurements enable the computation of water cut in horizontal pipes for diverse flowrates. The results show for the first time the potential of using high frequency non-intrusive electric capacitance meters for oil-water flow measurement.

---

## 1 Introduction

Multiphase flows are present in a vast number of industrial processes, including the chemical, aeronautical, food, and petroleum industries. The oil and gas industry, in particular, has led the advances in multiphase flow measurements since its early implementation in oilfields in the late 1990s [1]. Accurate multiphase flow measurement in pipelines is of paramount importance throughout the oil and gas value chain. Multiphase liquid flows are present in a variety of process, particularly in the transport of currents downstream the separation vessels all the way through the storage and dehydration facilities. Fluids flowing through pipelines present a variety of flow structures which are inherently dependant on the rheological characteristics of the phases and the process conditions. Measurement of multiphase flow in pipes is largely affected by this spatial distribution of the flow structures [2]. The hydrodynamics of liquid-liquid flows are highly complex due to the low density and viscosity ratios, and the effect of the interfacial tension. This makes the pattern characterisation and hence accurate measurement of liquid-liquid flow challenging [3].

The present study focusses on the use of in-line measurement of segregated horizontal oil-water flows. Here, a combination of electrical capacitance techniques is presented. The metering systems infer the phase concentrations based on measurements of the dielectric properties of the fluid flow [4]. This work investigates the capabilities of the Electric Capacitance Tomography (ECT) for co-current immiscible liquid-liquid measurement. The measurements of the ECT are contrasted against single-pair electrode capacitance measurements.

Following the analysis of the experimental data, the influence of the volumetric fractions on the measurements is assessed. The correlation between the measurement and the phase distribution is presented here.

The remainder of the paper is organised as follows: section (2) describes the methodology of the study and describes the experimental facilities used for measurement of the single-phase flows as well as eleven multiphase oil-water mixtures. The results of

the experimental campaign are discussed in section (3). Section (4) derives the numerical expression for water cut computation from experimental electric capacitance measurements. Finally, a brief summary of the most relevant findings is presented in section (5).

## 2 Material and Methods

The experimental campaign accounted for metering of the flow dielectric properties by means of two meters. Details of the experimental facilities and metering devices is presented following.

### 2.1 Multiphase flow rig

Experiments were conducted at the iPhase multiphase flow loop in Basingstoke, UK, illustrated in Figure 1. The experimental loop comprises a recirculation rig that uses gravimetric separation of the fluids in continuous operation. The liquid flows are recirculated around the test facility using centrifugal pumps. The injection flows are controlled by an automated circuit led by turbine flow meters located at the separation vessel outlet. The three-phase gravity separator, with a capacity to segregate the water and oil phases, also serves as a liquid storage tank.

The horizontal experimental segment of 100mm diameter and 3m long (30D) contains a clear acrylic section that allows visualization of the flow prior metering. Experiments were conducted at controlled laboratory conditions at a temperature of 20°C. The working liquids used on the loop were Ultramax10 oil and saline water. The experimental matrix and flow conditions are summarised in Table 1.

**Table 1.** Conditions for experimental liquid-liquid flow measurement.

<b>Water cut (%)</b>	{0,25,30,35,40,45,50,55,60,65,70,75,100} ±2%
<b>Pressure (psig)</b>	3
<b>Temperature (°C)</b>	20
<b>Oil superficial velocity (m/s)</b>	0.11 – 0.32
<b>Water superficial velocity (m/s)</b>	0.11 – 0.32
<b>Oil type</b>	Exol Ultramax10
<b>Oil density (kg/m<sup>3</sup>)</b>	851
<b>Oil relative permittivity</b>	2.156 – 2.224
<b>Water conductivity (S/m)</b>	1.05



**Figure 1** Flow rig diagram showing the metering system on the horizontal test section.

### 2.2 Electrical Capacitance metering

Electric Capacitance Tomography (ECT) is a non-intrusive tomography technique that has been largely used for imaging and velocity measurement of non-conducting two-phase flows [4] [5]. ECT applications concerning the Oil and Gas Industry, have proved highly accurate in oil-gas metering [6] [7]. However, its use for conductive phases has been restricted to mixtures with low water cuts [8].

The principle of operation of ECT is based on the sensitivity of the electrodes to changes in the dielectric properties of the fluid contained within the imaging region. The difference between the permittivity of the fluids give rise to variations in the inter-electrode capacitance measurement. Hence, the measurements from the sensing electrodes are directly proportional to the distribution of the dielectric properties within the pipe.

The sensor array was arranged around the outside of the horizontal test section of the rig. ECT measures the capacitances between combinations of pairs of electrodes placed around the perimeter of the pipe. The meter comprised 16 electrodes arranged in two measurement planes of 8 sensors each. All unique capacitance pairs were measured yielding a full set of measurements. The calibration of the ECT meter used oil and air as reference fluids. When water is present the value of average mixture permittivity may exceed the calibration range, in which case simple extrapolation is used. Secluded single-pair electrode data was also collected for every test point. This allows to correlate the measured capacitance, relative permittivity, and the water cut, which as shown below, is key for high water contents.

The excitation signal used consisted of 24 V peak to peak square wave at a frequency of 2.5 MHz. The experimental setup of the sensor array is illustrated in Figure 2.

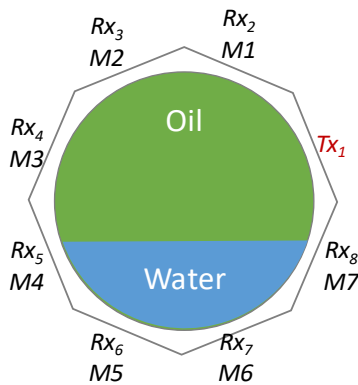


**Figure 2** Illustration of the experimental setup showing a transversal view of the sensor array around the pipe perimeter. Example positions of the transmitter (Tx) and receiving sensors (Rx) are shown for a given excitation mode.

### 3 Results

The calibration of the ECT system is restricted to low permittivity values from air and oil. Water flow through the meter is expected to affect the overall metering accuracy. To address this issue, the ECT measurements are contrasted to single-pair electric capacitance measurements. The results of the study are presented following.

The mean relative permittivity of single-phase flows and low water contents is plotted in Figure 3. The results show two clearly different levels of relative permittivity for single-phase flows, namely air and oil. As the water content increases in the oil-water flow from 25% to 35%, the measured relative permittivity also increases. As expected, the multiphase flow shows relative permittivities larger than the single-phase flows, with an increasing difference as the water cut increases.

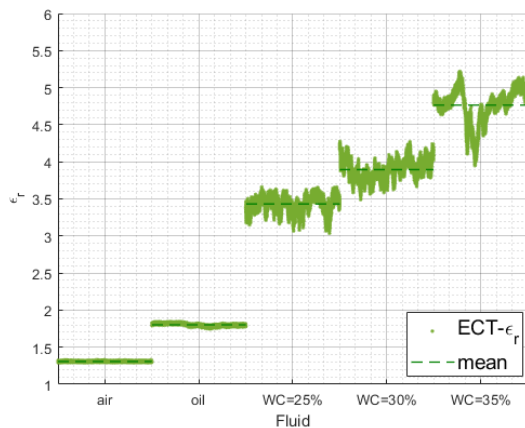
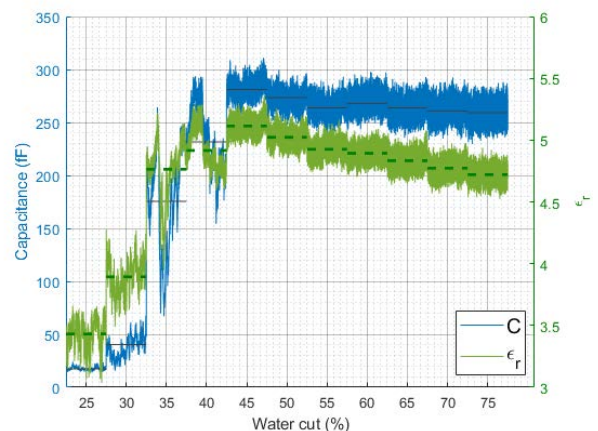


**Figure 3** Measurement of mean relative permittivity in the ROI for two single phase flows (air and oil,) and multiphase flow with low water cuts (25% to 35%)

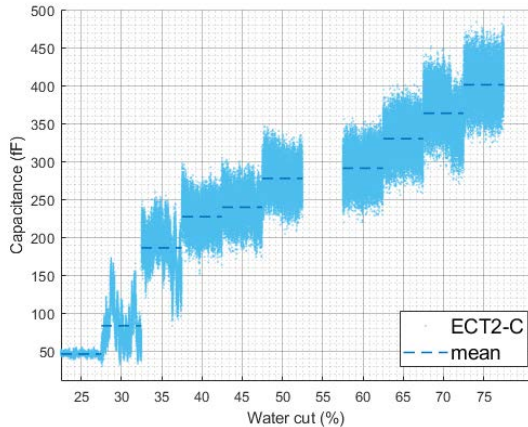
Figure 4 shows the mean relative permittivity of the oil-water multiphase flow within the imaging region and the induced capacitance between the electrode pair  $T_{x1}$ - $R_{x4}$  (M3) from the full ECT system (see Figure 2). The results show consistent trends between both measurements for varying water cuts. The increase in water volume, which holds a higher relative permittivity than oil, results in a higher overall mixture permittivity and hence in a larger inter-electrode capacitance for water cuts between 25% and 45%. Conversely, for water contents above 45%, the trend shifts and a slight decrease is evident as the water content continues to increase. The shift in trends suggests an inversion in the coupling mechanism of the electrodes as the conductive phase becomes dominant in the liquid-liquid mixture and the water level reaches the sensor pair  $T_{x1}$ - $R_{x4}$ .

Figure 5 shows the capacitance measurements from a selected single-pair electrode. The measurements were gathered at the top section of the pipe at 135 deg from the transmitting sensor (position M3). The two-channel electrical capacitance meter provides a consistent increase in capacitance with increasing water cut throughout all oil-water ratios. The capacitance measurements show improved signal to noise ratio with decreasing water content.

The full 8-sensor ECT provides a larger dynamic range for lower water cuts (25%-45%) but fails to accurately predict the relative permittivity when the conductive phase inundates the pipe cross-section in agreement with [8].



**Figure 4** Measurement from the full ECT system of mean relative permittivity in the ROI (green) and capacitance from electrode pair  $T_{x1}$ - $R_{x4}$  (blue) for various multiphase flows.



**Figure 5** Measured capacitance from a single-pair electrode located at the top of the pipe.

The difference seen in the measurements at high water cuts from both meters plotted in Figure 4 and Figure 5 can be attributed to the inherent signal compensation that occurs during the solution of the inverse problem of the full ECT system.

#### 4 Water cut prediction

The quasilinear trend of the single pair electrode measurement seen in Figure 5 allows back-computation of the water cut in the pipe. Through multiple regression analyses, the influence of the volumetric fractions on the mean measured capacitance was assessed by fitting the measured data with quadratic curves. The capacitance was determined to vary against the water content in the stratified flow a ratio given by Equation (1). The developed correlation describes over 96% of the variability of the measurement.

$$C_{M3} = [2931(WC) - 73570]^{\frac{1}{2}} \quad (1)$$

where  $C_{M3}$  is the capacitance in pF measured from the electrode pair  $T_{x1}-R_{x4}$  at the measurement position M3 (see Figure 2) and  $WC$  is the water volumetric fraction expressed in percentage.

The predicted water cut against the reference water flowrate is illustrated in Figure 6. Results show a significant linear relationship between predicted and reference values with an overall fitting inside the  $\pm 10\%$  deviation range.

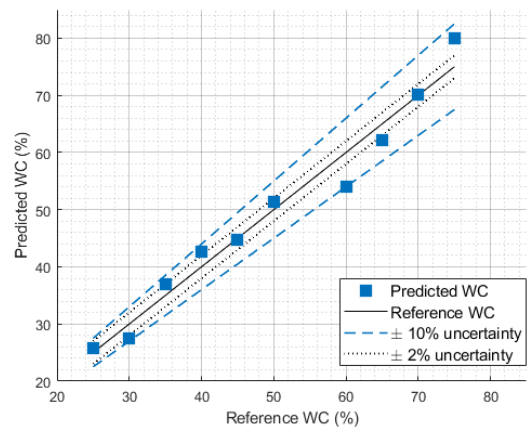


**Figure 6** Predicted water fraction against reference measurements showing data dispersion around linear trend.

#### 5 Conclusions

An 8-sensor ECT meter was used to measure oil-water flows in horizontal pipes. ECT was found to be able to recognise changes in liquid-liquid concentration for low water ratios.

The analysis of data from selected electrodes pairs indicated that electric capacitance meters are sensitive to changes in flow concentrations regardless of the conductive properties of one of the phases or its volumetric fraction. A correlation for water cut computation was developed from single-electrode pair measurements. The water cut predicted provides an uncertainty range below 10% over a spectrum of water cuts from 25% to 75%.

#### Acknowledgements

The authors would like to thank iPhase Ltd for allowing the use of their facilities and permission to publish the data.

#### References

- [1] G. Falcone and B. Harrison, "Forecast expects continued multiphase flowmeter growth," *Oil Gas J.*, vol. 109, no. 10, pp. 25–34, 2011.
- [2] R. Thorn, G. a Johansen, and B. T. Hjertaker, "Three-phase flow measurement in the petroleum industry," *Meas. Sci. Technol.*, vol. 24, pp. 1–17, 2012.
- [3] R. Ibarra, I. Zadrazil, C. N. Markides, and O. K. Matar, "TOWARDS A UNIVERSAL DIMENSIONLESS MAP OF FLOW

REGIME,” in *11th International Conference on Heat Transfer, Fluid Mechanics and Thermodynamics*, 2015.

- [4] M. Zhang, Y. Li, and M. Soleimani, “Experimental Study of Complex-valued ECT,” in *9th World Congress on Industrial Process Tomography*, 2018, pp. 19–24.
- [5] X. Zhu, P. Dong, and Z. Zhu, “Gas-solids Flow Measurement in Cyclone Dipleg by Dual-plane Electrical Capacitance Tomography Sensor,” pp. 203–209, 2018.
- [6] A. Hunt, L. A. Abdulkareem, and B. J. Azzopardi, “Measurement of Dynamic Properties of Vertical Gas-Liquid Flow,” *7th Int. Conf. Multiph. Flow*, pp. 1–10, 2010.
- [7] R. Yan and S. Mylvaganma, “Flow Regime Identification with Single Plane ECT Using Deep Learning,” in *9th World Congress on Industrial Process Tomography*, 2018, pp. 289–297.
- [8] A. Hunt, “Industrial Applications of High-speed Electrical Capacitance Tomography,” in *9th World Congress on Industrial Process Tomography*, 2018, pp. 857–864.

# Influence of disturbing part on measurement of the standard for cryogenic flow rate measurement using LDV

J. Sluse<sup>1</sup>

<sup>1</sup>*Czech Metrology Institute, Okružní 31, 638 00 Brno, Czech Republic  
E-mail (corresponding author): jsluse@cmi.cz*

---

## Abstract

Disturbing parts situated on upstream of the flowmeter have influence on inlet velocity field. This change on the inlet of the flowmeter may influence measurement accuracy of the flowmeter. The aim of this article is to determine influence of disturbing parts on the measurement. Typical disturbing part situated on upstream of the flowmeter is elbow, swirl, half-plate, valve etc. The influences will be determined the standard for cryogenic flow rate measurement using LDV which was developed for measurement of the flow rate of liquefied natural gas (LNG) and other cryogenic fluids. The measuring system is simplistically special type of Venturi tube. Principle of this system is measurement of velocity profile using laser doppler velocimeter (LDV) behind the nozzle where the velocity profile is flat. After that the flow rate is calculated from measured velocity profile and diameter of nozzle throat. The influence of disturbing part on accuracy of the measurement will be determined by using numerical simulation. The determination of rate of the influence will be carried out by comparison of numerical simulation with and without the disturbing part. The simulation will be carried out for several disturbing parts.

---

## 1. Introduction

The transportation of fuel is accompanied by measurement. The amount of fuel is measured on each unloading and loading point. But each measurement is done with some error and all errors between the first point of the chain (producer) and the last point of chain (customer) are cumulated. This difference means money that one side gets and the other side lose. The difference in measurement can be caused by quality of measurement (procedure, flowmeter etc.). The aim of all members of the transport chain is to reduce the error of measurement. One of several things which can have influence on measurement is disturbing parts. The aim of this article is determinate the influence of disturbing parts situated on upstream of the standard for cryogenic flow rate measurement using LDV on the measurement.

This research is a part of a project “Metrology for LNG” within the European Metrology Programme for Innovation and Research (EMPIR).

---

## 2. The standard for cryogenic flow rate measurement using LDV

The measuring system is equipment for measuring of cryogenics fluid flow rate using Laser Doppler Velocimetry technique. This system was developed by the CESAME Exadebit - company in France. The principle of this equipment is based on velocity measurement in one point behind the convergence nozzle and then calculation of the flow rate.

The first generation of that measuring system was tested in EMRP project LNG II and the results were published on FLOMEKO 2016 [1]. The partial part of project LNG II was optimization of the nozzle of flow metering system for liquefied natural gas. That optimization was one of more things which were used for development of second generation of measuring system. The simulations in this article were carried out with second generation of measuring system.

### 2.1 Introduction and geometry

The measuring system consists of front part (inlet part) where the medium is seeded by particles (bubbles or another spherical material). Then the fluid flows through the convergent nozzle to the

measuring space. For measurement by LDV it is necessary to make the equipment with windows or from transparent material. The measuring system (Figure 1) includes special cavities (Figure 2) with windows on the body of the measuring system. The medium continues to the divergent part of the nozzle and goes outside. For satisfactory accuracy of measurement and low uncertainty of the measurement it is convenient to create nearly flat velocity profile behind the nozzle throat (like piston velocity profile) to reduce the shear region influence on the mass flow rate calculation.

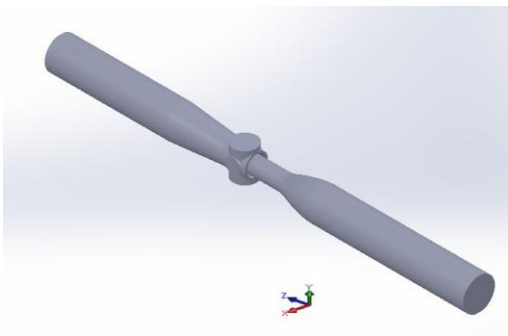


**Figure 1:** Internal part of the measuring system.

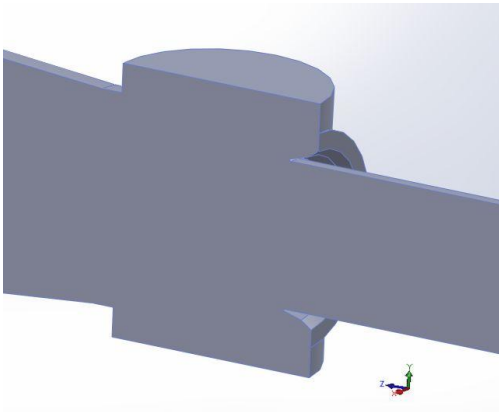


**Figure 2:** Internal part of measuring space.

The aim of this part of paper is to simulate the flow through the measuring system. The results will be used as unaffected flow in measuring system. It will be used for determination of influence of disturbing parts on the flow as well as on the measurement.

### 2.2 Mesh & boundary condition & simulation

Mesh has been created by using of capability of OpenFOAM called blockMesh and snappyHexMesh. The mesh includes coarse part in the core of the stream and refinement in the

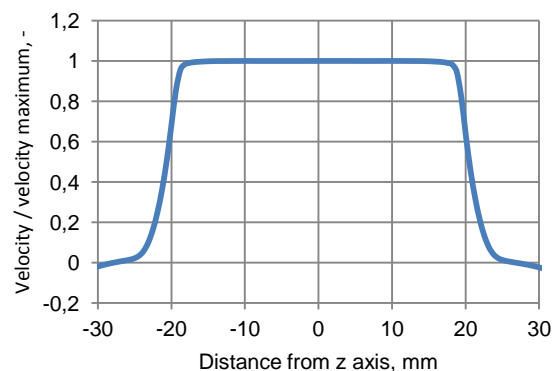
direction to the wall. It consists of hexahedral cells and the mesh quality fulfils the base condition for successful simulation.

The boundary conditions were predescribed on three patches – wall, inlet and outlet and for fluid. Fully developed profile was predescribed on inlet patch. The zero gradient of pressure was predescribed on patch outlet. The wall function was predescribed on patch wall.

The simulation was done only for air (pressure 10 bar). The numerical problem was solved as a steady, viscous, turbulent, incompressible flow by a simpleFoam solver with  $k-\omega$  SST turbulence model which was verified in the article [1]. Converged results were those results which had residuals lower than  $10^{-6}$  for velocity in z axis and  $10^{-5}$  for velocity in y and x axis.

### 2.3 Results

The simulation was carried out for velocity 2.5 m/s on inlet (fully developed profile). The velocity profile in measuring section is shown on Graph 1. It was generated from velocities in cells lying on a line which is identical to y axis and is situated 5 mm behind the nozzle. The vertical coordinates are given as velocities in the middle of the cell divided by maximal velocity of all cells on the line. The horizontal coordinates are distances from z axis. This profile will be used as unaffected velocity profile in measuring section. The velocity profile is constant in core of the stream and steeply decreases to zero near the cavities.



**Graph 1:** Velocity profile in measuring system without disturbing parts.

### 3. Disturbing parts

Disturbing parts are parts of pipelines which change character of flow, velocity profile or pressure drop.

### 3.1 U-bend

The U-bend consists of four elbows DN 80 connected together to shape U. The internal part of U-bend is shown on Figure 3. The U-bend is connected to measuring system on inlet part.

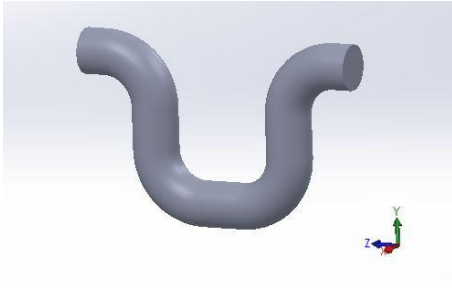


**Figure 3:** Internal part of U-bend.

The mesh has the same decomposition of cells as measuring system and it is figured on Figure 4. The setup of simulation was carried out as well as in measuring system – a steady, viscous, turbulent, incompressible flow simulated by a simpleFoam solver with  $k-\omega$  SST turbulence model.

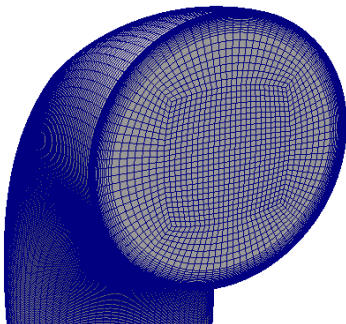


**Figure 4:** Decomposition of cells in U-bend.

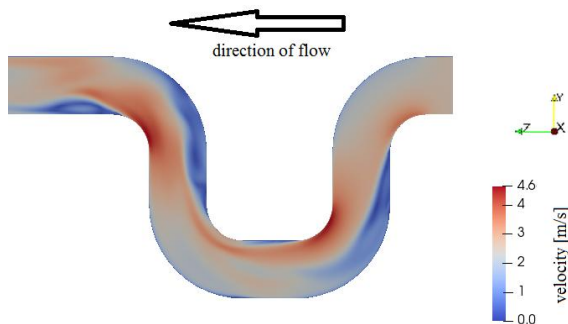
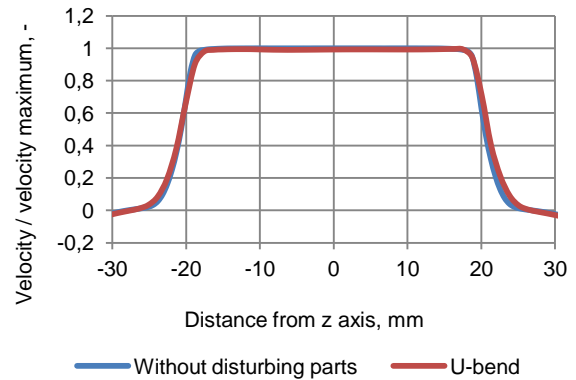


**Figure 5:** Decomposition of velocity in U-bend.

The decomposition of velocities in U-bend for inlet velocity 2.5 m/s (fully developed velocity profile) is figured on Figure 5. The velocity profile on outlet of

U-bend is not rotary symmetric. This changed profile enters into the measuring system. The flow is accelerated in the nozzle and flows into the measuring section. The velocity profile behind the nozzle is shown on Graph 2. For comparison, on the same graph there is depicted velocity profile from simulation without the U-bend.



**Graph 2:** Velocity profile in measuring system with and without U-bend.

The vertical coordinates are given as velocities in the middle of the cell divided by maximal velocity of all cells on the line in case without disturbing parts. The horizontal coordinates are distances from z axis. The differences between both curves are very small. The U-bend has negligible influence on the velocity profile.

### 3.2 Half plate

The half plate reduces flowing surface by 50 percent. Thickness of half plate is 50 mm. This disturbing part is also connected to measuring system on inlet part.

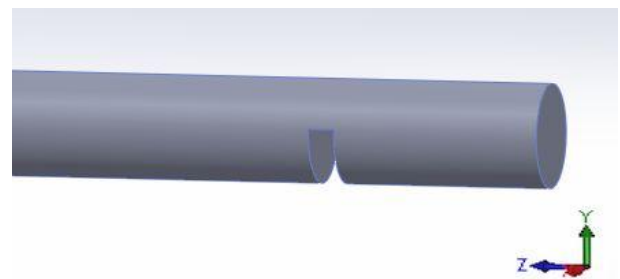


**Figure 6:** Internal part of half plate.

The mesh has same decomposition of cells as measuring system. The setup of simulation was carried out as well as in measuring system – a steady, viscous, turbulent, incompressible flow

simulated by a simpleFoam solver with  $k-\omega$  SST turbulence model.

The decomposition of velocities in half plate for inlet velocity 2.5 m/s (fully developed velocity profile) is figured on Figure 7. The half plate has significant influence on velocity profile. The velocities in cells lying under  $z$  axis are very high and below the  $z$  axis are low. This situation caused higher vorticity in section behind the half plate.

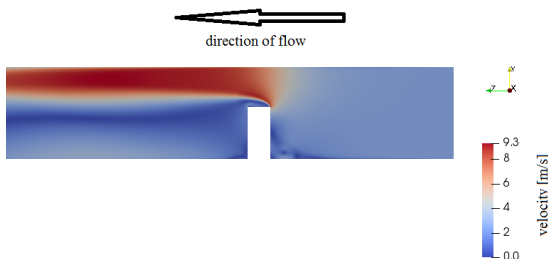
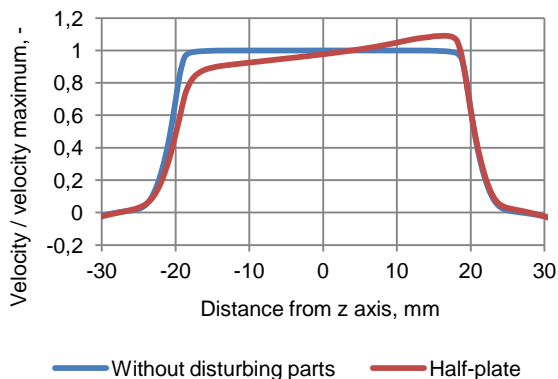


**Figure 7:** Decomposition of velocity in half plate.

The velocity in measuring section is shown on Graph 3. For comparison, on the same graph there is depicted velocity profile from simulation without the half plate.



**Graph 3:** Velocity profile in measuring system with and without half plate.

The vertical coordinates are given as velocities in the middle of the cell divided by maximal velocity of all cell on the line in case without disturbing parts. The horizontal coordinates are distances from  $z$  axis. The profile is very influenced by disturbing part. This type of disturbing element influences the measurement and it is necessary to use some stabilizing element or longer pipe for stabilization of flow.

#### 4. Conclusion and future work

In this article two types of disturbing parts namely U-bend and half plate were tested. Both of these were connected on upstream of measuring system. The simulations were carried out only for one flow rate (velocity). The results show that U-bend has negligible influence on the velocity profile in measuring section. That negligible influence can be reduced by longer pipe between measuring system and disturbing part. Half plate, on the contrary, very influences the velocity profile. The resulting velocity profile on the border of the stream is changed by more than 10% compared to velocity profile without disturbing parts.

Future work will consist of testing of more disturbing parts as elbow, swirl etc. For testing will be used more velocities and the test will be carried out also with liquefied natural gas. The simulation in this article will be used for verification with experimental data.

#### Acknowledgement

I would like to thank Remy Maury and CESAME Exadebit for their assistance with the simulation.

The author acknowledges the support received from the European Metrology Programme for Innovation and Research (EMPIR) through the Joint Research Project "Metrology for LNG". The EMPIR is jointly funded by the European Commission and participating countries within Euramet and the European Union.

#### References

- [1] J. Sluse, R. Maury, J. Gersl, A. Strzelecki, "Numerical simulation of flow metering system for liquefied natural gas", in *17<sup>th</sup> International Flow Measurement Conference, FLOMEKO 2016*.

# NEW PRIMARY STANDARD WITH PISTON PROVER FOR MICROFLOW OF LIQUIDS

Miroslava Benková<sup>1</sup>, František Schweitzer<sup>2</sup>,  
Miroslava Benková, Czech Metrology Institute, Czech republic  
František Schweitzer, JUSTUR, spol. s r.o., Slovak republic

*1mbenkova@cmi.cz, Czech Institute of Metrology, Okružní 31, Brno, Czech Republic*  
*2schweitzer@justur.sk, Justur, s.r.o., Dr. A. Schweitzer 194, Stara Tura, Slovakia*  
*E-mail (corresponding author): mbenkova@cmi.cz*

---

## Abstract

The Czech Metrology Institute continues in development of a method in the area of very small flows of liquid aimed at reducing uncertainties and expanding flow to lower values. The primary standard developed based on mass method has successfully been internationally compared and the results have shown data stability.

With increasing accuracy of flow meters on the market, requirements for reduction of uncertainty of primary or secondary standards are rising.

In case of very small flows, i.e. below 10 ml/h, some calibrations and subsequent result evaluations by means of the weighing method become a little complicated. With the aim to automate the calibration process as well as to reduce uncertainty of measurement and also enlarge the range to lower flows, an innovative primary standard with 200 mL micro piston prover has been developed. Long-term experience with development of a volumetric method using a similar type of piston prover with a special fluid displacement system in the area of the larger flows was applied.

The paper is focused on the presentation of the comparison of measurement results between the volumetric standard with the piston prover and gravimetric standard in one place. A detailed design of the new test equipment with integrated micro piston prover into the testing line is presented as well. Further, experimental measurements in very low flow rates (1 to 6,000) ml/h are described and evaluated. Achieved measurement uncertainties are also presented. The results show the benefits of the applied method.

---

## 1. Introduction

The Czech Metrology Institute uses for measurements in the area of microflow of liquids a gravimetric primary standard in the range of (10 to 6000) g/h. This standard was fully adapted for required conditions, proclaimed as the Czech national standard and successfully internationally compared within the EURAMET No. 1379 project with degree of equivalence ( $E_n$  value) in the range (0,09 to 0,38) for the range of flow (500 to 6000) g/h. For calibration of flow meters as infusion pump calibrators, peristaltic pumps, mass and volumetric flow meters or micro-injection pumps usually secondary mass standards are used in the same range. The reason is a more practical measurement even at the cost of a slight increase in measurement uncertainty. "More practical measurements" means elimination of certain effects that occur in the mass method, especially the impact of liquid evaporation, influence of changing temperature with the effect on

density in the calculation of the correct value and also the duration of particular measurements.

According to previous research, the negative effect of evaporation could be excluded by using liquids other than distilled water with lower evaporation ability. Unfortunately, a large number of calibrated devices are from the health sector and experience has shown the necessity of using clean, i.e. distilled water.

The use of secondary standards has its practical advantages at the installation of the meter or the measurement time, but also disadvantages in the form of heating up the meters and thus the increase of the temperature gradient, also the effect on the final value in form of density in the calibration of volumetric flow meters and especially the experience with calibration in zero position (zero calibration) are very important. The range of low flows is also limited.

For these reasons the Czech Metrology Institute has chosen the direction of development of a piston

standard, with the aim of reducing the measurement uncertainty while maintaining comfort during calibration. In this area, long term experience in the field of gas flow measurement using the volumetric method with a bell prover, in the field of development of piston standards used in testing equipment for verification of water meters has been used together with experience in the field of very small flow measurements.

Also in this work, the experience of a flow standard equipment manufacturer and the national metrology institute was commonly used.

The aim of the project was to design and produce a standard equipment based on a piston standard for calibration of flow meters in the field of small flows from 1 ml to 6000 ml.

## 2. Mass primary standard

With respect to the required accuracy and measuring range a balance with weighing range of 220 g with resolution of 0.1 mg was specified. The balance is placed on a separate base due to possible vibration from pumps. The equipment is controlled electronically and all necessary data are recorded directly into the PC. All data can be recorded in selected intervals to have an analysis of the entire measuring process.

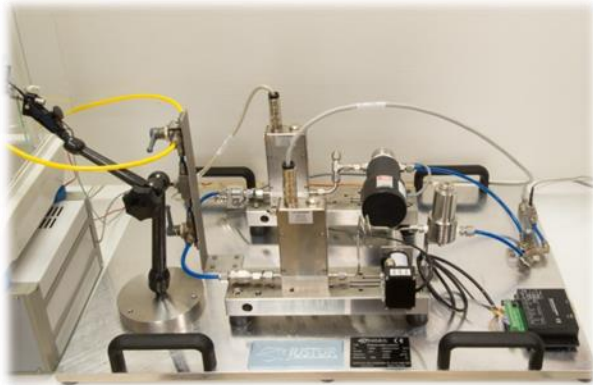


Figure 1: Mass primary standard.

The following measuring parameters and uncertainties were confirmed:

Table 1: Parameters of the standard for a very small liquid flows

Temperature (°C )	Prime Parameter
Measuring range:	(10 to 6 000) g/h (10 to 6 000) ml/h
Working pressure:	(140 – 340) Pa
Testing liquid:	distilled water
Water temperature:	(25 ± 5) °C

Expanded uncertainty (CMC) – mass flow	0,50 % for flow (10 to 30) g/h 0,15 % for flow (30 to 2000) g/h 0,20 % for flow (2000 to 6000) g/h
Expanded uncertainty (CMC) – volumetric flow	0,60 % for flow (10 to 30) ml/h 0,20 % for flow (30 to 2000) ml/h 0,25 % for flow (2000 to 6000) ml/h

## 3. Piston standard

### 3.1 Solution proposition

Several design issues have been addressed during the project:

- Designing the optimal piston diameter in relation to the required test flow range as well as volume required from 0,1 to 200 ml. An important question in this area was also the manufacturability in relation to the length of the piston, avoiding possible shape deformations as well as the possibility of admeasurement (gauging) in sufficient accuracy. For this reason, stainless steel 1.4404 (AISI316L) was chosen as the material for production of the very piston – made of a raw precision-drawn bar with cured surface without residual internal stress.
- By analysing various factors a nominal piston diameter of 35mm was defined, movement speed of the piston corresponding to a flow range from  $2,89 \times 10^{-4}$  mm/s to 1,73 mm/s.
- Another question was the motion screw, gearbox and servo drive. By optimizing particular parameters it was necessary to achieve a ratio of 1:2000. We chose a slack-free ball motion screw with a diameter of 12mm and a 5mm pitch of highest accuracy class IT1 with direct connection to the gearbox with servo drive via a preloaded pair of flanged nuts. A stage itself was the optimization of the servo drive motion control, setting and debugging of control parameters.
- An encoder for reading pulses with a resolution of 65536 pulses per revolution is solid attached to the screw, corresponding to a volume of  $1,002 \times 10^{-6}$  ml per 1 pulse.
- The piston itself moves along the ball runner block with high accuracy. The piston is sealed with a special set of gaskets consisting of a scraper, sealing („X“ type) and a guide ring, ensuring high level of tightness.
- The piston prover is positioned in an inclined position to enquire easier removal of eventual air bubbles.
- The equipment is equipped with a collecting water tank for displacement of the liquid, distilled water is used as standard, but the equipment also allows calibration with other liquids.

- The system is equipped with Pt100 temperature sensing with a diameter of 3mm and pressure sensing directly in the piston chamber.
- The equipment is controlled by software that allows to pre-define an amount of sequences in measurement points and various test types and methods, so that tests can run automatically at night without presence of the operator, while they can be changed or controlled remotely over remote access. All measured parameters are logged and it is possible to back evaluate particular variables, e.g. temperature stability in the piston prover, temperature stability in the room, pressure, various pulses etc.

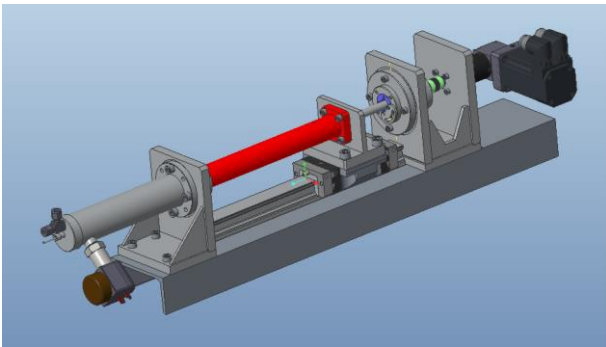


**Figure 2:** Designing of piston prover PP002.

### 3.2 Piston admeasurement

The admeasurement of the piston was done using a probe coordinate measuring machine type SIP CMM 5, with a measurement uncertainty of 0,001 mm. The initial concerns about the impact of roughness on the measurement have proved to be unfounded, since after polishing of the surface, roughness can't be determined by common means. The piston is clamped to the measuring machine where the centre of clamping will be the centre of the piston. Subsequently, radiuses (distance of the clamped centre and surface of the piston) are counted using the measuring machine's probe. Radiuses are counted on an imaginary line lying on the surface of the piston parallel to the axis of the piston, always at distances of 5 mm from each other. After reaching the end of the piston the piston is rotated by 45° and the measurement is repeated. The entire process is done in eight planes to measure radiuses at angles: 0°, 45°, 90°, 135°, 180°, 225°, 270° and 315°.

Due to the unevenness of the piston, as well as the possible deviation of the actual and selected piston centre, the individual radiuses in one plane of the admeasurement are not the same. Therefore, the cross-sectional area of the piston at the selected

point is calculated as a sum of partial areas (8 areas, each bordered by two adjacent radiuses).

We calculate one part of the surface  $\rho$  using the surface of the Archimedean screw:

$$\rho = \frac{\alpha_1 - \alpha_2}{6} * (r_1^2 + r_1 * r_2 + r_2^2)$$

after simplification (if delta alpha = 45°)

$$\rho = \frac{\pi/4}{6} * (r_1^2 + r_1 * r_2 + r_2^2)$$

Subsequently, the cutting area of the piston is calculated at one point of the measurement:

$$P = \sum_{i=1}^8 \rho_i$$

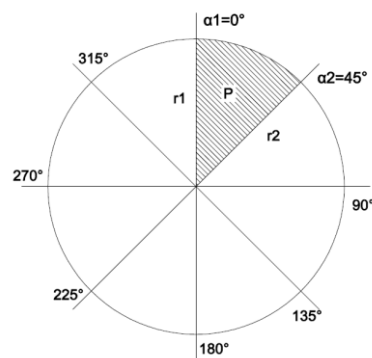


**Figure 3:** Piston admeasurement.

### 3.3 Measurement principles

The main purpose of the described standard equipment is to calibrate the largest possible range of meters. Therefore, the equipment has been designed to allow direct measurement of flow volume, volumetric as well as gravimetric, but also to calibrate the quantity of volumetric and gravimetric flow. Some meters have the ability to connect to automatic read out, some meters need to read manually. The control software and particular applied calculations have been adapted respectively.

When applying the mass method, the value of mass before and after the test from the meter is read by the control PC. The difference in mass values from the meter is compared to the mass value of water displaced from the piston (based on the volume, temperature and mass of distilled water).

When applying the Massflow method, the equipment is set to the desired flow rate. The system waits until the meter starts to indicate flow and settles within the selected tolerance. After

reaching it, the system starts to average the instantaneous mass flow (automatically, approximately every second). The test stops after the requested amount has flown. Subsequently, based on the average flow from the meter and the time of test it calculates mass and compares it repeatedly to the mass of water displaced from the piston based on volume, temperature and mass of distilled water.

In case the meter is connected with a volume output of flown amount or flow, a similar principle is applied - described as Volume and Volumeflow, whereby the flow volume from the piston is directly applied as the correct value.

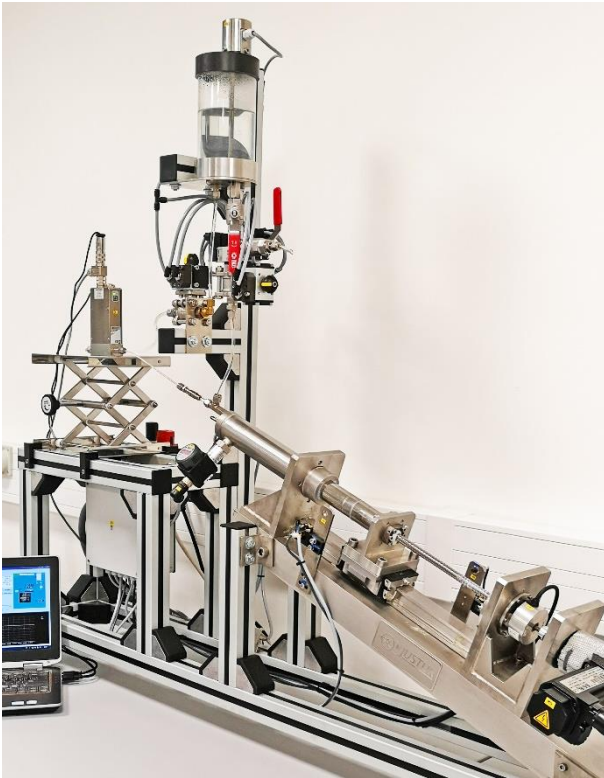


Figure 4: Piston prover standard PP002.

### 3.4 Measurement uncertainty

Following effects were considered by generation of mathematical models:

- Effect of water temperature change in the body of the piston. The component takes into account the effect of water temperature change  $\Delta t_P$  to the constant (not displaced during the course of the test) volume of water in the body of the piston prover. The change of this volume is not compensated by the application.
- Effect of pressure change to the volume of water in the body of the piston

- Effect of temperature change to the dimensions of the piston chamber shell
- Effect of temperature change to the dimensions of the piston body. The component takes into account the change in temperature of the piston body in between the start and the end of the test (i.e. storage effect). A correction of thermal volumetric expansion due to different temperature during the piston calibration and measurements is not included in this component.
- Effect of the final step size of the piston position sensor. The component takes into account the final step size of the incremental sensor for piston position at the start and end of the measurement.
- Effect of play of the mechanical connection of the helix with the piston. The component takes into account the play in between the helix and the piston body to the measured volume.
- Effect of thermal expansion of the helix. The component takes into account the change in dimension of the helix in longitudinal direction due to its thermal expansion, which affects the real longitudinal position of the piston body when measuring with the incremental sensor
- Effect of mechanical accuracy of the helix. The component takes into account the effect of the screw's production inaccuracy to the actual longitudinal position of the piston body when measuring with the incremental sensor.
- Effect of the piston's body calibration uncertainty
- Effect of water temperature difference in between the meter and standard. The component takes into account the effect of the change in density and hence of the volume flow in between the piston and the meter. The effect is compensated by the control program, so the source of uncertainty is the water temperature measurement by temperature sensors.
- Operating accuracy of the temperature sensor
- This component includes the measuring chain stability, including the temperature sensor and the analog-digital encoder.
- Effect of water pressure change in between the meter and the standard
- The component takes into account the effect of volume flow change in between the meter and the standard due to different water pressure. The control program compensates this value based on the mean value of pressures during the measurement, thus the source of uncertainty the determination of pressure by the sensors in the standard and in the meter.

- Pressure sensor operating accuracy. This component includes the stability of the measuring chain, including the pressure sensor and the analog-digital encoder.
- Pressure sensor calibration
- Effect of tubing expansion effect in between the meter and the standard

The following graph represents the overall expanded uncertainty of the equipment (k=2) depending on the testing flow and volume:

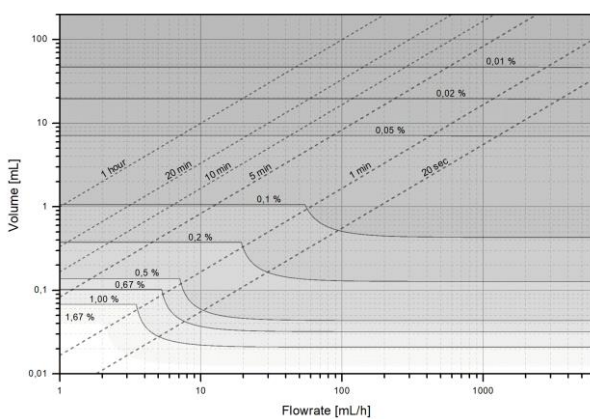


Figure 5: Expanded uncertainties values.

#### 4. Confirmation of metrology parameters

Parameters having a significant impact on the correct measured value have been monitored during the development of the piston. These are especially: accuracy of delivered quantity, temperature and flowrate. As the piston standard is a volumetric meter, the stability and accuracy of temperature measurement are significant factors. Measurements of temperature stability in the laboratory where the equipment was to be placed were conducted. Long-term measurements (10h) showed stability better than 0,07°C (Max-Min). Real measurements with the PP002 have shown a bigger temperature change during the measurement and were measured directly in the piston against the measurement in the laboratory, at the level of approx. 0,1°C. This fact is probably caused by heating up the water by mass flow meters, that were used for evaluation of results. However, such temperature fluctuations have very little effect on the resulting measurement uncertainty. The uncertainty contribution is at a level of 0,002% at a testing volume of 5ml.

##### 4.1 Comparative measurements with the reference standard meters

The functionality of the entire test equipment with a piston prover was inspected with reference mass flow meters Bronkhorst – CoriFlow (P1, P2, P3) linked to the primary standard with weighing scales described in the text bellow and also with production calibration. These measurements were performed in the range of (1 až 6000) g/h. The resulting values are mean values from 5 to 10 repeat measurements, standard deviations are shown at each point of flow.

The figure 6 shows the relative error values of P1 (mass meter CoriFlow) in the range 550 to 6000 g/h when measured by gravimetric method at Mass primary standard with weighing scale (red line) and by Piston prover using mass method described in 3.3. (blue and green lines). The blue line shows the results where zero setting was applied only at the beginning of whole run of tests comparing the green line with zero setting at each testing point.

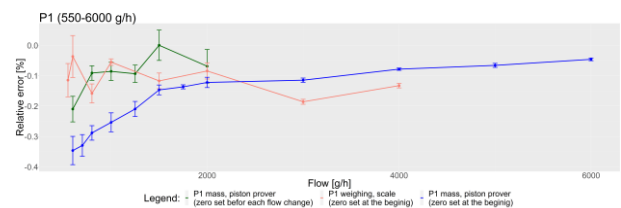


Figure 6: P1 (550-6000) g/h.

The figure 7 shows relative error values of P2 meter in the range 10 to 600 g/h. Here, all three methods - Piston prover Mass (green line), Piston prover Mass flow (blue line) and gravimetric method at Mass primary standard with weighing scale (red line) - were compared. This experiment showed a good continuity of individual measurements, especially in the range where the reference scale is very stable. Worse stability results have been shown in the Mass flow method, due shorter test times. This effect can be eliminated by optimization of test times.

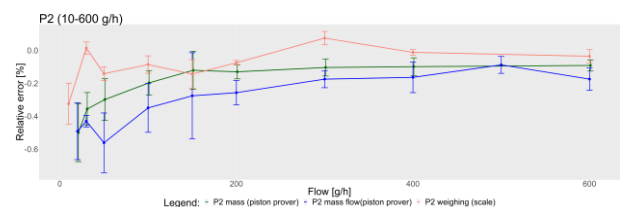
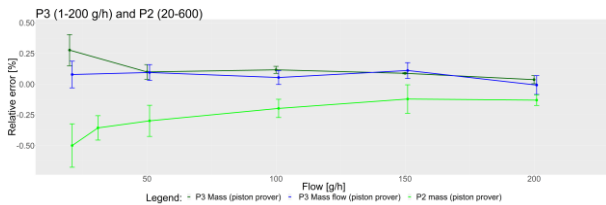


Figure 7: P2 (10-600) g/h.

The figure 8 shows the relative error values of both meters P2 and P3 in the common range (20 to 200) g/h measured by the piston standard. Here we can see P3 Mass (dark green line), P3 Mass flow (blue line)

line) and P2 Mass method (light green line) on one graph. This experiment showed a good continuity of the individual measurements, using different measurement methods.



**Figure 8:** P3 (1-200) g/h and P2 (20-600) g/h.

The figure 9 shows the relative error values in the lower range of P3 meter (1 to 20) g/h, whereby the upper range (20-200g / h) is shown in the Figure 8. Here, two (Mass - green line and Mass flow - blue line) measurement methods were compared. In this case the worst repeatability of Mass method measurements has been demonstrated.

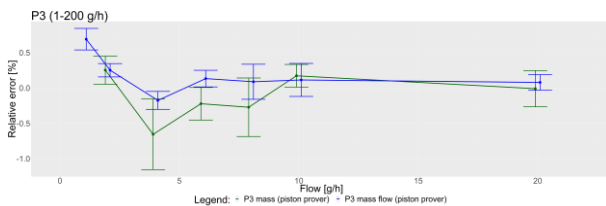


**Figure 9:** P3 (1-200) g/h.

## 6. Conclusion

Based on the presented results, it can be concluded that the chosen piston prover method for calibration of measuring instruments for a very small flows (1-6000) g/h could be considered with the expanded uncertainty less than (0,05 to 0,6)%.

The traceability chain was presented in [3].

Experimental measurements as well as practical experience to date have confirmed the original intention to implement a piston standard equipment for the use of flow meter calibrations in the area of very small flow rates while achieving high accuracy and stability of results, simple calibration, and minimizing equipment maintenance costs.

In the next period, a direct comparison of the piston to the scales is planned, thus avoiding the impact of the reference meters and further reduction of the up to now designated measurement uncertainty is expected.

The design of the equipment ensures long-term tightness stability with simple visual leak control and very high performance. Excluding some effects

such as temperature stability, flow stability, evaporation, etc. has a major effect on reducing partial uncertainties, which ultimately contributes to high accuracy and stability of measurement. The piston equipment allows calibration by a more methods, so the field of tested instruments is being extended.

## References

- [1] ILAC Policy for Uncertainty in Calibration, ILAC-P14:12/2010.
- [2] E.Batista, R.Patton, The selection of water property formulae for volume and flow calibration, 2007.
- [3] M. Benková, I. Mikulecký, PRIMARY STANDARD AND TRACEABILITY CHAIN FOR MICROFLOW OF LIQUIDS

# Structural condition monitoring of Coriolis flowmeters through stiffness measurement

Jingqiong Zhang<sup>1</sup>, Tao Wang<sup>2</sup>, Jinyu Liu<sup>1,2</sup>, Yong Yan<sup>1</sup>, Edward Jukes<sup>2</sup>

<sup>1</sup>*School of Engineering and Digital Arts, University of Kent, Canterbury, U.K.*

<sup>2</sup>*KROHNE Ltd, Wellingborough, U.K.*

*E-mail (corresponding author): jz233@kent.ac.uk*

---

## Abstract

Condition monitoring of an abrasive or erosive process is essential to give early warning of potential issues and ensure safe delivery of fluid material via pipeline transportation. As one of the solutions to direct mass flow measurement, Coriolis flowmeters provide highly accurate and repeatable measurements in single phase flow processes. In some multiphase flow processes containing solid particles, Coriolis flowmeters may not perform well or even fail due to erosive wear of the measuring tubes. This paper presents an in-situ technique to monitor the structural conditions of a Coriolis flowmeter by analyzing a stiffness related diagnostic parameter in order to validate measurements or prevent flowmeter failure.

This paper demonstrates the procedure to extract the stiffness related diagnostic parameter from a Coriolis flowmeter, on the basis of a mathematical model of the Coriolis oscillation system. With the aid of additional frequencies applied to the drive signal, the stiffness related diagnostic parameter of the measuring tubes is determined through frequency response analysis. This stiffness diagnostic parameter is linked to the physical stiffness of the measuring tubes by introducing a scaling factor. Furthermore, various vibration models, with different degrees of freedom and damping levels, are used to simulate the stiffness diagnostics in Coriolis flowmeters. The feasibility and repeatability of the proposed method are verified through computer simulation and experimental tests. The results show that the proposed method performs well in determining the stiffness related diagnostic parameter of a Coriolis flowmeter and hence the verification of its structural condition.

---

## 1. Introduction

Erosive wear results in severe problems in a wide range of processes, particularly in the oil, gas, mineral and metal mining industries. The solid particles in a transportation pipeline system may collide with the piping components such as pipe sections, pipe fittings, valves, flanges, flowmeters and other measurement devices. Consequently, wear problems will affect the operation, performance and service lifespan of such equipment and sometimes even lead to a failure of the whole piping system. It is therefore essential to develop techniques for the condition monitoring of abrasive and erosive processes such as slurry flows where wear problems may occur.

There has been considerable research in developing techniques for condition monitoring of slurry flow processes [1]. El-Alej et al. [2] demonstrated an active acoustic method to monitor sand transportation in sand-water flow. An electrical resistance tomography method, which can visualize the distribution of the sand phase, has been proposed by Faraj et al. [3]. Gao et al. [4] designed an ultrasonic sensing system to investigate the

interactions between sand particles and the pipe wall. However, the main effort of the previous work is devoted to measure and characterize sand particles in order to ensure smooth slurry transportation.

There have been some studies to examine the structural conditions of piping components such as a flowmeter. Through a series of erosive tests on three different types of flowmeters, measurement errors arising from wear problems, were reported in [5]. The performances of two Coriolis flowmeters from two different manufacturers along with a turbine meter and a venturi meter were compared through experimental tests. Some structural information, available from the diagnostic function of one Coriolis flowmeter's manufacturer, was also recorded and linked to erosive wear on the flowmeter. However, no detailed description of the diagnostic function was given. A photo of the erosion scars on the measuring tubes of a Coriolis flowmeter is shown in Figure 1. Investigations into Coriolis flowmeters of three main manufacturers [6-8] have indicated that they are all able to provide some diagnostic data to examine the structural condition of the flowmeter. Some manufacturers have already released this diagnostic

feature into their commercial products [6]. However, limited theoretical research and analytical work has been reported about this diagnostic method.



**Figure 1:** Photo of the eroded tubes of a twin bend-tube Coriolis flow meter [5].

This paper introduces a technique to assess the structural conditions of a Coriolis flowmeter. This method is non-intrusive and cost-effective, making it possible to judge if a flowmeter is eroded and if the measurement results are valid in an erosive environment. This paper firstly illustrates the close link between the stiffness parameter and the calibration of a Coriolis flowmeter, and then explains how to extract the stiffness related diagnostic data from the Coriolis oscillation system. In this paper, we conduct, for the first time, mathematical model based computer simulation to analyze the stiffness extraction process and identify the factors in stiffness determination from the theoretical point of view. The simulation under various sceneries, not only validates the feasibility of this method, but also investigates the influence of modal parameters on the stiffness extraction, such as, the effect of damping level and degrees of freedom. Additionally, experimental tests were conducted to assess the performance of the proposed technique.

## 2. Methodology

### 2.1 Working principle and calibration parameters of Coriolis flowmeters

Coriolis flowmeters provide highly accurate single phase mass flow measurement in a wide variety of liquid and gas applications. A typical Coriolis flowmeter consists of two measuring tubes (twin-tube). Along each measuring tube, a drive coil and magnet pair is positioned at the centre to generate a sinusoidal signal, whilst two electromagnetic sensors are placed at the inlet and outlet of the tube to receive motion signals. When the flow moves through the tube, the two signals are distorted by the Coriolis force, and hence, a time shift,  $\delta_t$ , is created between the signals. The mass flowrate of the flow  $Q_m$  is directly proportional to the time shift [10],

$$Q_m = P_C \delta_t \quad (1)$$

where  $P_C$  is the calibration parameter of the flowmeter, which is determined through a standard calibration process.

Basically, a Coriolis flowmeter continuously tracks the resonant frequency of a fundamental mode,  $f_r$ , which is often referred to as drive or working frequency. Benefiting from this, a Coriolis flowmeter is also capable of providing an independent measurement of the fluid density resulting from the effective vibrating mass,

$$\omega_{r1} = \sqrt{\frac{k_1}{m_1}} \quad (2)$$

Where  $m_1$  denotes the effective vibrating mass, comprising the mass of the empty tube as well as of the fluid in the tube,  $k_1$  represents the stiffness of the measuring tube, and  $\omega_{r1}$  is the angular resonant frequency of the measuring tube vibrating in its fundamental eigenmode.

With an external force ( $F$ ) applied on an object or a structure,  $k_1$  can be defined by the ratio of this force to the resulting displacement ( $\delta x_1$ ) under the same mode,

$$k_1 = \frac{F}{\delta x_1} \quad (3)$$

According to Equations (1) and (2), the constant or unchanged  $P_C$  and  $k_1$  are important for the performance of a Coriolis flowmeter. Over its service life, any changes in the calibration parameters from the original values, obtained from the manufacturer, may result in uncertainties in its specified measurement accuracy and repeatability. However, in an abrasive or corrosive process such as slurry flow, there is a risk that the measuring tubes may be eroded. If erosion occurs, the structural properties of the measuring tubes will change, giving rise to incorrect calibration parameters,  $P_C$  and  $k_1$ , and subsequently errors in the measurements of mass flowrate and density.

Erosion on a Coriolis flowmeter can be observed from the erosion scars on the tube surfaces. Since regular inspections of the internal surfaces of the measuring tubes are impractical to implement, it is desirable develop an online, in-situ monitoring technique to identify erosion. The physical parameter, *stiffness*, of a measuring tube, is a parameter related to its structural condition and also vital for the flowmeter calibration. It is hence of great importance to measure the stiffness of the measuring tube.

### 2.2 Mathematical model of Coriolis flowmeters

According to the working principle of a Coriolis flowmeter, a measuring tube can be modelled using a mass-spring-damper system. Assuming that all the components in the Coriolis oscillation system couple together and follow the same motion, a single measuring tube is simplified by a simplest single degree of freedom (SDOF) model, as shown in Figure 2.

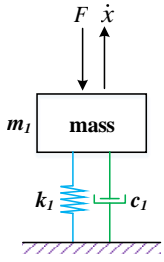


**Figure 2:** SDOF model of a measuring tube of a Coriolis flowmeter.

Here, the effective mass,  $m_1$ , is composed of the effective vibrating mass of a measuring tube and the fluid. The tube acts as the spring, described by the stiffness  $k_1$ . The energy loss, resulting from the interactions between the measuring tube and the environment and other sources, is quantified in terms of the viscous damping coefficient  $c_1$ . The transfer function of the external force and resulting velocity of the lumped mass is given,

$$G_{r1} = \frac{\dot{x}(s)}{F(s)} = \frac{s}{m_1 s^2 + c_1 s + k_1} \quad (4)$$

where  $F$  denotes the force actuated by the drive coil and  $x$  represents the displacement of the lumped mass.

By transferring Equation (4) to the frequency domain, the frequency response function (FRF) of the system is given by,

$$FRF_{phys} = \dot{H}(\omega) = \frac{\dot{x}(\omega)}{F(\omega)} = \frac{j\omega}{-m_1 \omega^2 + j c_1 \omega + k_1} \quad (5)$$

### 2.3 Extraction of stiffness related diagnostic data from frequency response data

Here, we introduce the stiffness related diagnostic parameter to indicate the structural condition of a Coriolis flowmeter. The stiffness related diagnostic parameter is obtained from frequency response of a Coriolis sensing system. In a Coriolis sensing system, the drive signal is proportional to the applied force  $F$ , and the sensor signal is proportional to velocity  $\dot{x}$ . As a result the relationship between the physical FRF data of the measuring tubes and the directly measured FRF data from a Coriolis sensing system can be quantified by a scaling constant,  $A_s$ ,

$$FRF_{meas} = \frac{V_{sensor}}{I_{drive}} = A_s FRF_{phys} \quad (6)$$

By substituting  $FRF_{phys}$  into Equation (6), the measured FRF data from a Coriolis sensing system is written as,

$$FRF_{meas} = \dot{H}_m(\omega) = A_s \dot{H}(\omega) = \frac{j A_s \omega}{-m_1 \omega^2 + j c_1 \omega + k_1} \quad (7)$$

In order to determine the stiffness  $k$ , Equation (7) is split up into the real and imaginary parts,

$$\begin{cases} \text{Re}\{FRF_{meas}(\omega)\} = \text{Re}\{\dot{H}_m(\omega)\} = \frac{A_s c_1 \omega^2}{(k_1 - m_1 \omega^2)^2 + (c_1 \omega)^2} \\ \text{Im}\{FRF_{meas}(\omega)\} = \text{Im}\{\dot{H}_m(\omega)\} = \frac{A_s \omega (k_1 - m_1 \omega^2)}{(k_1 - m_1 \omega^2)^2 + (c_1 \omega)^2} \end{cases} \quad (8)$$

Combining Equations (2) and (8), the stiffness related diagnostic parameter under the flowmeter's fundamental oscillation mode is solved as follows,

$$k_{diag} = \frac{k_1}{A_s} = \frac{\omega_{r1}^2 \omega_{an} \text{Im}\{\dot{H}'(\omega_{an})\}}{(\omega_{r1}^2 - \omega_{an}^2) |\dot{H}'(\omega_{an})|^2} \quad (n = 1, 2, \dots) \quad (9)$$

Where  $\omega_{r1}$  is the angular resonant frequency of the measuring tube vibrating in its first mode and  $\omega_{an}$  represents the additional frequencies, differing from  $\omega_{r1}$ , with the number  $n = 1, 2, \dots$

For the purpose of stiffness measurement, at least one additional frequency,  $f_{a1}$ , is required to apply into the excitation system, apart from the resonant frequency  $f_{r1}$ , according to Equation (9). More additional frequencies yield more stiffness related diagnostic values.

### 2.4 Implementation of stiffness diagnostics

Figure 3 depicts how to implement the stiffness measurement in a Coriolis flowmeter. The drive coil excites the tubes at its resonant frequency, which is determined by the phase control loop. Firstly, one or more additional frequencies are applied to the drive signal on purpose. Secondly, the vibration responses of the measuring tubes, which are induced by these additional frequencies, are collected from the sensor signals [13]. Then, based on quadrature demodulation, the original sensor signal is decomposed into several individual components in terms of frequencies. Next, those separated components in sensor signal corresponding to additional frequency  $f_a$ , are picked out to acquire FRF data,  $FRF_{meas}$ , based on Equation (6). Finally, the stiffness diagnostic value  $k_{diag}$  of the measuring tube is calculated from Equation (9). With reference to the factory baseline data from the manufacturer, the change in stiffness,  $\Delta k_p$ , is determined [6],

$$\Delta k_p = \frac{\Delta k}{k_0} = \frac{k_{diag-situ} - k_0}{k_0} 100\% \quad (10)$$

Where  $k_{diag-situ}$  is the stiffness related diagnostic result during the diagnosis performed by customer in situ, and  $k_0$  denotes the original factory baseline data, which is recorded during the calibration of the flowmeters under factory conditions.

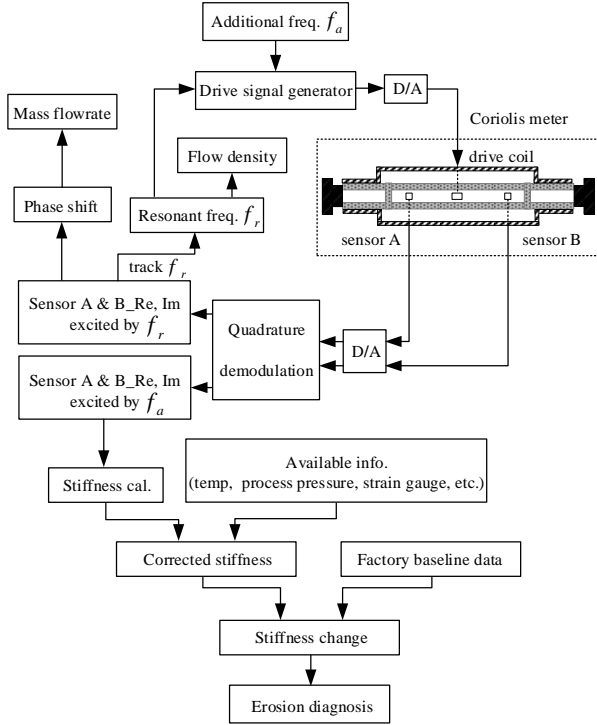


**Figure 3:** Implementation of stiffness measurement in a Coriolis flowmeter.

### 3. Simulation results and experimental validation

To validate the above theoretical analysis and evaluate the stiffness diagnostic method, analytical modelling and computational simulation were conducted using Simulink. With the aim to take the complexity of a real industrial process into account, we test various mass-spring-damper models.

#### 3.1 Simulation system

A measuring tube can be simplified by a vibration model, which is described by four key parameters, including the degrees of freedom, mass, stiffness and damping level. To investigate the effect of degrees of freedom on stiffness extraction, the simulation work begins with a simplest SDOF model. Then it is extended to a 3DOF (three-degree-of-freedom) model. Other modal parameters, namely *mass*, *stiffness* and *damping*, are set to proper values, estimated from the actual data of a commercial Coriolis flowmeter. The following calculations detail the relevant estimations, given in Equation (11). Since air is much lighter than water,  $m_{air}$  is neglected, to simplify the calculation. Likewise, we also assume that the effective vibrating mass simply equals to the mass of an empty tube plus that of the fluid.

$$\begin{cases} \omega_{r\_air} = \sqrt{\frac{k}{m_{tube}+m_{air}}} = \sqrt{\frac{k}{m_{tube}}} \\ \omega_{r\_water} = \sqrt{\frac{k}{m_{tube}+m_{water}}} = \sqrt{\frac{k}{m_{tube}+\rho_{water}A_{tube}L_{tube}}} \end{cases} \quad (11)$$

Where  $\omega_{r\_air}$  and  $\omega_{r\_water}$  represent the resonant frequencies when pure air and water flow through the tube, respectively.  $m_{tube}$  is the mass of the empty tube.  $m_{air}$  and  $m_{water}$  denote the mass of air and water inside the tube.  $m_{water}$  is determined by the water density  $\rho_{water}$  and the internal volume of the tube. With the known dimension data including the cross sectional area  $A_{tube}$  and the tube length  $L_{tube}$ ,  $m_{water}$  is estimated.

In this work, the numerical substitutions of  $\omega_{r\_air}$ ,  $\omega_{r\_water}$ ,  $A_{tube}$ , and  $L_{tube}$  are undertaken based on actual data of a DN50 Coriolis flowmeter (KROHNE OPTIMASS 6400 S50) under room temperature. Finally, the unknown stiffness  $k$  and  $m_{tube}$  are solved from Equation (11). The value of  $k$  is around  $2.4 \times 10^6$  N/m, which is used in the simulation. In terms of the low-pass filter for signal demodulation, a 16<sup>th</sup>-order Butterworth IIR filter is employed.

#### 3.2 Simulation results based on a SDOF model

A simplest SDOF model is established here. The undamped resonant frequency is assumed as 240 Hz, referred to the first working frequency of a DN50 Coriolis flowmeter mentioned above. The stiffness of the spring is supposed to be  $2.4 \times 10^6$  N/m, regarded as the reference  $k_{ref}$ . Based on the resonant frequency and stiffness values, the mass value is estimated from Equation (2), i.e. 1.0554 kg.

In order to explore the effect of damping on stiffness measurement, different damping levels are added to the model. Here the dimensionless Q factor [12] is used to characterize the damping levels in this work. Equation (12) gives the relevant calculation of Q factor. In the lightly damped case in this simulation, the Q factor is calculated to be 1592, and it is decreased to 159 in the heavily damped case.

$$Q = \frac{\omega_{r1}m_1}{c_1} \quad (12)$$

Different additional frequencies are applied into the drive signal one at a time, with frequency offset  $\Delta f = f_a - f_r = -10, -9, \dots, -3, +3, \dots, +10$  in Hz. In this way, 16 stiffness results are collected from the model, resulting from 16 different frequency locations respectively, which can imply the measurement repeatability and the influence of locations. To evaluate the stiffness diagnostic results, the absolute value of relative error (change)  $\mu_i$  is computed, corresponding to different frequency locations, through Equation (13). Then, with the aid of the 16 stiffness diagnostics, the mean value of the absolute relative error (change),  $\bar{\mu}_{ARE}$ , is calculated to evaluate the accuracy of this method, whilst the standard deviation  $\sigma_{ARE}$  is given to see the repeatability, according to Equation (14),

$$\mu_i = \left| \frac{k_{simu(i)} - k_{ref}}{k_{ref}} \right| 100\% \quad (i = 1, 2, \dots, 16) \quad (13)$$

$$\begin{cases} \bar{\mu}_{ARE} = \frac{\sum_{i=1}^{16} \mu_i}{16} \\ \sigma_{ARE} = \sqrt{\frac{\sum_{i=1}^{16} (\mu_i - \bar{\mu}_{ARE})^2}{15}} \end{cases} \quad (14)$$

Figure 4 shows the stiffness diagnostic results and the effect of different damping levels, based on a SDOF model. It can be seen that relative error (change) between the simulation results and theoretical reference values are quite small, although heavy damping levels can lead to relatively higher uncertainty. This small relative error (change) is caused by the applied Butterworth IIR filter during signal demodulation. The simulation results indicate that the stiffness diagnostic method is feasible with excellent accuracy and repeatability.

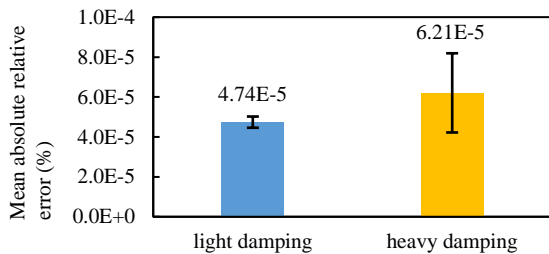


**Figure 4:** Effect of damping on stiffness measurement based on a SDOF model.

### 3.3 Simulation results based on a 3DOF model

A Coriolis oscillation system usually contains more than one degree of freedom in reality, depending on the involved specific processes. Viewing from the sensing system, we can divide a measuring tube into three concentrated elements. Among them, one element is assigned at the location of sensor A, with the lumped mass including the substitute part of empty tube part as well as the flow. Similarly, the other two elements are located near the drive coil and sensor B. Based on these substitutions, a tube can be assumed as a 3DOF system, as shown in Figure 5.

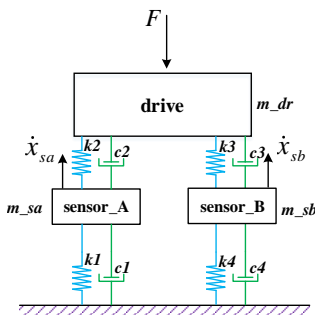


**Figure 5:** 3DOF model of the measuring tube of a Coriolis flowmeter.

The simulation system is rebuilt based on a 3DOF model. Drive signal was exerted upon the drive element, whilst

two sensor signals were picked up from sensor A and B respectively. The related modal parameters in this 3DOF model, the mass and spring stiffness, are set symmetrically with respect to the drive element. The theoretical calculations of undamped stiffness of the first oscillation mode were obtained as reference  $k_{ref\_sa}$  and  $k_{ref\_sb}$ , representing the factory baseline data. In the same way with previous work, 16 different frequencies were applied into the drive signal, with offset  $|\Delta f|$  from 3 Hz to 10 Hz, which yielded 16 pairs stiffness results,  $k_{simu\_sa(i)}$  and  $k_{simu\_sb(i)}$ , from sensor A and B, respectively.

Various damping levels were introduced in this 3DOF model to create the lightly damped and heavily damped cases. The resonant frequencies were determined by frequency sweep with an increment of 0.001 Hz. Figure 7 summarizes the stiffness diagnostic results based on a symmetric 3DOF model, which demonstrates the larger relative errors resulting from the change of damping levels. It is worth noting that, the heavy viscous damping can give rise to uncertainty in stiffness measurement, especially in a multi-degree-of-freedom (MDOF) system. The larger degrees of freedom, as well as the heavier damping levels, increase the measurement errors and uncertainties in the collected FRF data from a Coriolis sensing system, which may be affected by the adjacent vibration modes [9].

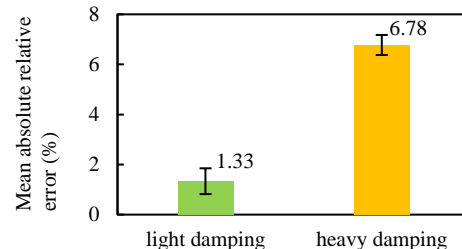


**Figure 6:** Effect of damping on stiffness measurement based on a symmetric 3DOF model.

By comparing the results in Figures 4 and 6, it can be found that, two modal parameters, the degrees of freedom and the damping levels, can affect the accuracy of stiffness measurement. Moreover, the locations of the applied additional frequencies may also cause measurement uncertainties, demonstrated by the larger standard deviation in the 3DOF case.

### 3.4 Experimental tests

With  $\pm 20$ Hz frequency offset, several tests were conducted on a DN50 Coriolis flowmeter (KROHNE OPTIMASS 6400) using tap water, under room temperature and different mass flowrates, 9t/h, 18t/h, 24t/h, 32t/h. The stiffness related diagnostic results are summarized in Figure 7. Each data point is produced

from the average values of five continuous stiffness diagnostic outputs. The maximum relative change in stiffness diagnostic results is within 0.2%, showing the good reproducibility of this method under room temperature and different mass flowrates.

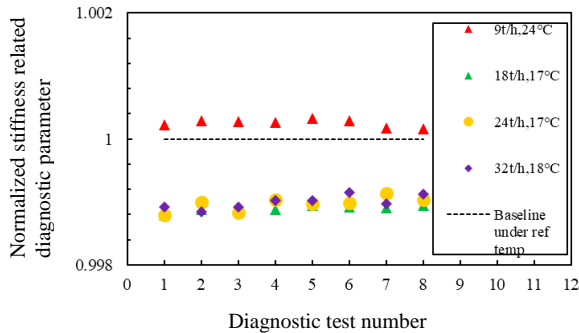


**Figure 7:** Normalized stiffness diagnostic results of a DN50 Coriolis flowmeter.

Moreover, according to the results in Figure 7, process temperature is a key factor in stiffness measurement. Temperature can not only affect the scaling constant,  $A_s$ , which is related to the drive coil and magnet units, but also influence the structural stiffness of the measuring tube. Since physical stiffness is linked to many process conditions, such as temperature, process pressure, and strain gauge [11], false alarms in stiffness diagnostics may occur when there are significant changes in process conditions.

#### 4. Conclusions

This paper provides an online in-situ method to identify the potential erosion on Coriolis flowmeters. The stiffness related diagnostic parameter is obtained to indicate the structural condition of Coriolis flowmeters, and it is proportional to the physical stiffness of the measuring tubes by a scaling factor. Based on the mathematical model of a Coriolis flowmeter, the computer simulation results have validated the feasibility of this stiffness diagnostic method. The theoretical analysis has illustrated that, two modal parameters, damping and degrees of freedom, can affect stiffness diagnostics in a Coriolis flowmeter. The larger degrees of freedom, as well as the heavier damping levels, increase the measurement errors and uncertainties in the diagnostic results, which explains the possibility of false alarms in stiffness diagnostics when the in-situ process and operation conditions deviates significantly from the factory conditions. Furthermore, experimental results obtained with a DN50 Coriolis flowmeter under room temperature have demonstrated the reproducibility of the stiffness diagnostic method with the maximum relative change in stiffness diagnostics within 0.2%.

#### References

- [1] K. J. Albion, L. Briens, C. Briens, and F. Berruti, "Multiphase flow measurement techniques for slurry transport," *Int. J. of Chem. Reac. Eng.*, vol. 9(1), 2011.
- [2] M. El-Alej, D. Mba, T. Yan, and M. Alsayh, "Identification of minimum transport condition for sand in two-phase flow using acoustic emission technology," *Appl. Acoust.* vol. 74(11), pp. 1266-1270. 2013.
- [3] Y. Faraj, M. Wang and J. Jia, "Automated Horizontal Slurry Flow Regime Recognition Using Statistical Analysis of the ERT Signal," *Procedia Engineering*, vol. 102, pp. 821-830, 2015.
- [4] G. Gao, R. Dang, A. Nouri, H. Jia, L. Li, X. Feng, and B. Dang, "Sand rate model and data processing method for non-intrusive ultrasonic sand monitoring in flow pipeline," *J. of Petro. Sci. Eng.*, vol.134, pp. 30-39, 2015.
- [5] T. Boussouara and J. P., "Assessment of erosion in flowmeters using performance and diagnostic data," 32th Int. North Sea Measurement Workshop, St Andrews, UK, Oct, 2014.
- [6] T. J. Cunningham and T. O'Banion, "Allow Smart Meter Verification to Reduce your Proving and Proof-Test Costs," 8th Int. Symposium on Fluid Flow Measurement (ISFFM), Micro Motion, 2012.
- [7] R. Baker, T. Wang, Y. Hussain and J. Woodhouse, "Method for Testing a Mass Flow Rate Meter," US 7603885B2, Oct, 2009.
- [8] E+H, flowmeters with Heartbeat Technology. Available on: <https://www.uk.endress.com/en/field-instruments-overview/product-highlights/heartbeat-technology-verification-monitoring>.
- [9] D.J. Ewins, "Modal Testing: Theory and Practice," Letchworth: Research studies press, 1984.
- [10] T. Wang and R. Baker, "Coriolis flowmeters: A review of developments over the past 20 years, and an assessment of the state of the art and likely future directions," *Flow Meas. Instrum.* vol. 40, pp. 99-123, 2014.
- [11] K. Kolahi, T. Schroder and H. Rock, "Model-based density measurement with Coriolis flowmeter," *IEEE Trans. Instrum. Meas.*, vol. 55(4), pp. 1258-1262, 2006.
- [12] J. W. Kunze, R. Storm and T. Wang, "Coriolis mass flow measurement with entrained gas," in *Proc. of Sensors and Measuring Systems*, 17th ITG/GMA Symposium, Nuremberg, Germany, Jun, 2014.
- [13] M. J. Rensing, A.T. Patten, T.J. Cunningham, and M.J. Bell, "Meter Electronics and Methods for Verification Diagnostics for a Flow Meter," US 0178738A1, Jul, 2011.

# Development of small weighing system for liquid micro-flow

R. Doihara, K. H. Cheong, T. Shimada, N. Furuichi

National Metrology Institute of Japan, AIST, 1-1-1 Umezono, Tsukuba, Japan  
E-mail (corresponding author): r-doihara@aist.go.jp

## Abstract

A prototype small weighing system for liquid micro-flow from 10 mL/min down to 1  $\mu$ L/min has been constructed. The calibration method was the static weighing with standing start and stop. The weighing system was set in a constant temperature and humidity chamber. At small flow rates, evaporation effect comes to be a significant error source. In order to reduce evaporation error, a detachable system between a weighing tank and a pipe line has been developed. The detachable device prevents pipeline tension to the weighing scale and is able to keep the pipeline closed while collection. Performance of the weighing system was evaluated by analysis of calibration factors to a syringe pump. At a preliminary test, the collected liquid was from 0.2 g to 2 g of water. In the preliminary test, the evaporation error was estimated to be below 0.1 % down to 2  $\mu$ L/min of water. The system is aiming to use at calibrations of liquid micro-flow meter for the semiconductor industry and the medical field.

## 1. Introduction

A purpose of this study is to minimize evaporation errors in weighing system. The goal is to reduce the evaporation error to less than 0.1% in the flow rate range from 1  $\mu$ L/min to 10 mL/min. For this goal, a detachable system between a weighing tank and a pipeline was developed. By using this mechanism, a calibration facility for micro flow sensors is constructed. By providing a means to evaluate micro flow sensors using this calibration system, we aim to contribute to the micro / nano technology, semiconductor industry, and medical fields.

NMIJ has expanded the range of flow standards to smaller flow rates to cope with fuel flow meters in automotive industry [1][2]. On the other, micro flow sensors are also used in semiconductor industry and medical fields. Upstream of the vaporizer for semiconductor equipment, a liquid mass flow meter measures and controls small flow rates (down to several  $\mu$ L/min) of various of liquids. In pharmaceutical and chemical industry, microflow chemical synthesis using microreactors instead of batch processes is being developed. Micro flow sensors and syringe pumps will play an important role in the flow chemical synthesis system.

The weighing method is the main calibration method for micro flow calibration. The syringe pump also needs to be calibrated using the weighing method. At micro

flow rates, the evaporation effect causes significant errors in the weighing method [2]. Several approaches can be used to reduce the evaporation error, including trapping evaporation with a saturated vapor atmosphere

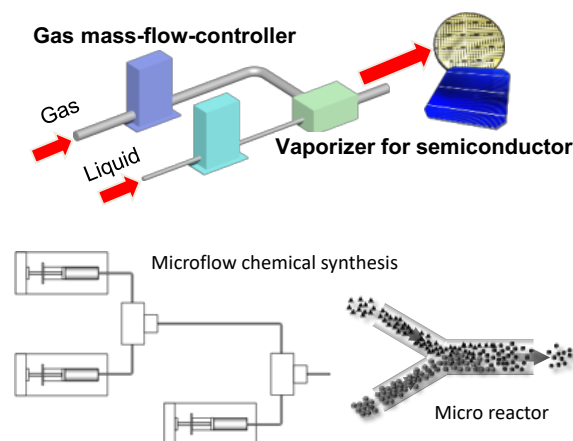
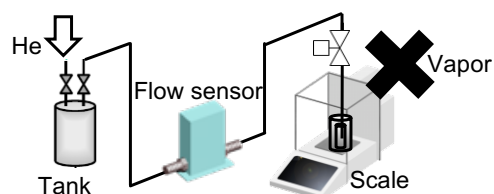


Figure 1: Micro flow sensors and devices.



(Error: Vaporization, Surface tension, Buoyancy)

Figure 2: Conventional weighing system.

[2-4] and applying a cover layer of a lower-density liquid [5,6], such as oil, which has a low vapor pressure.

In this study, a novel detachable device was adopted. A prototype small weighing system for liquid micro-flow from 10 mL/min down to 1  $\mu$ L/min has been developed. Preliminary test has been conducted to evaluate evaporation error. This paper reports the results.

## 2. Weighing system

### 2.1 Outline of calibration facility

The facility is set in a constant temperature (usually 23 deg. C) and humidity chamber. The calibration method is the static weighing with standing start and stop. The working liquid is water and can be collected up to 10 g at one calibration. The weighing scale has a resolution of 0.01 mg. To remove bubbles, an inline degasser equipped with a vacuum pump is installed in a circulation line. The flow is generated by a pressurized tank or syringe pump.

### 2.2 Weighing tank and detachable device

The weighing tank and the detachable device are shown in figure 3. The weighing tank is capped by a lid having an orifice sealed with elastomer. A needle-nozzle from a flow meter or syringe pump can penetrate the orifice. The needle-nozzle is fixed with a frame, and the weighing tank is moved up and down by a motor-controlled lift. The weighing tank is automatically connected and disconnected with the needle-nozzle by the motion of the lift. While the liquid is collected, evaporation from the weighing tank is prevented because of the orifice seal between the lid and the needle-nozzle. The air pushed out from inside the weighing tank is accumulated into an air bag. Then, after disconnected from the nozzle, the weighing tank is placed on a weighing scale at free from any tension.



**Figure 3:** Detachable system between the weighing tank and needle-nozzle.

### 2.3 Syringe pump as working standard

The syringe pump is shown in figure 4. The syringe pump can be used to calibrate a flow meter as a working standard. A portion of the syringe volume identified by the pulse address is calibrated by using the primary weighing system. The syringe pump is also used to drain the working liquid in the weighing tank. As a preliminary test to evaluate the evaporation effect, the pulse rate per volume of the syringe pump was calibrated at different flow rates. The syringe pump has a resolution of approximately 19,200 pulses per mL when using a 2.5 mL syringe. In case of 0.1 mL syringe, the syringe pulse factor is to be 480,000 (pulse/mL).

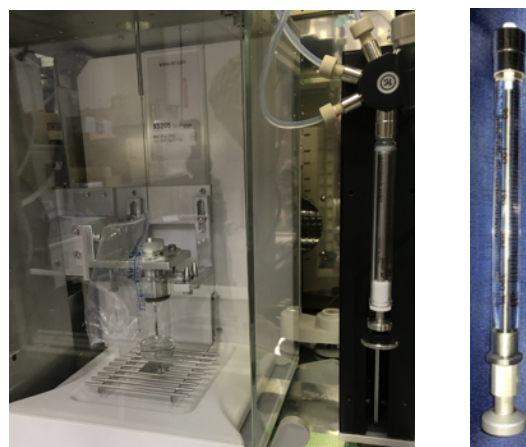


**Figure 4:** Syringe pump.

At this stage, the motor specification of the syringe pump is a stepping type, but the syringe pump will be replaced with a servomotor type to improve flow stability.

## 3. Results and discussion

### 3.1 Analysis model using calibrated syringe pulse factor

The syringe pulse factor is the reciprocal of the volume per stroke of the pulse in the calibration region of the cylinder. It is thought that the syringe pulse factor should be constant for different flow rates. However, the calibrated value could be change if the weighing system or syringe system have something error source. For instance, if the calibration system has an evaporation error, the syringe pulse factor increases as the flow rate decreases [2]. Of course, other errors might affect it. If air bubbles are generated in the connection pipe between the syringe and the weighing tank, the factor decreases as the flow rate decreases. Analytical models are plotted in figure 5. Assuming that the other errors are smaller than the evaporation error, the evaporation rates can be estimated by using fitting.

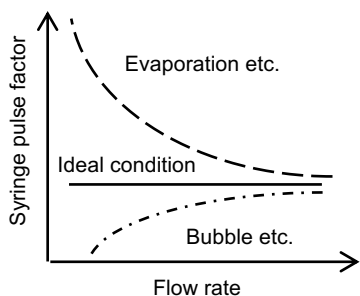


Figure 5: Analysis model using calibrated syringe pulse factor

### 3.2 Calibration result of 2.5 mL syringe

The syringe pulse factor is calibrated at different flow rates to evaluate the evaporation error of a weighing system equipped with the detachable mechanism. When a 2.5 mL syringe is attached to the pump actuator, the minimum flow is 25  $\mu\text{L}/\text{min}$ . At the minimum flow rate, the pump actuator creates a pulsating flow due to the nature of the stepping motor. It is not suitable for flow meter calibration, but there is no problem in evaluating evaporation effect.

Figure 6 shows the calibration factor for a 2.5 mL syringe. The small spread of the plot shows that the detachable mechanism has sufficient repeatability to a 2.0 g collected weight. It has been shown that evaporation is prevented as the calibrated factors do not change significantly for different flow rates.

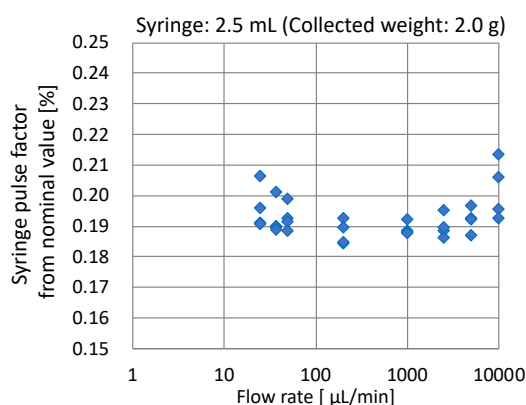


Figure 6: Calibration factor for 2.5 mL syringe.

### 3.2 Calibration result of 0.1 mL syringe

The installed syringe was replaced to a smaller size to investigate the evaporation effect at lower flow rates. For a 0.1 mL syringe, the minimum flow rate becomes 1  $\mu\text{L}/\text{min}$  and the collected weight is 0.08 g. Figure 7 shows the calibration factor for the 0.1 mL syringe. The

open vent condition (without the air bag) was also calibrated in order to confirm the phenomenon of evaporation error to the calibrated syringe pulse factor. The spread of the plot became large because the relative value of the repeatability of the detachable mechanism to the collected weight increased. For the sealed weighing tanks (normal condition), the calibration factor did not increase as the flow rate decreased. This means that this weighing system is not affected by evaporation down to 1  $\mu\text{L}/\text{min}$ . On the other hand, for the open vent case, the calibrated syringe pulse factor increased as the flow rate decreased, and the evaporation rate was estimated to be 4 nL/min to 8 nL/min.

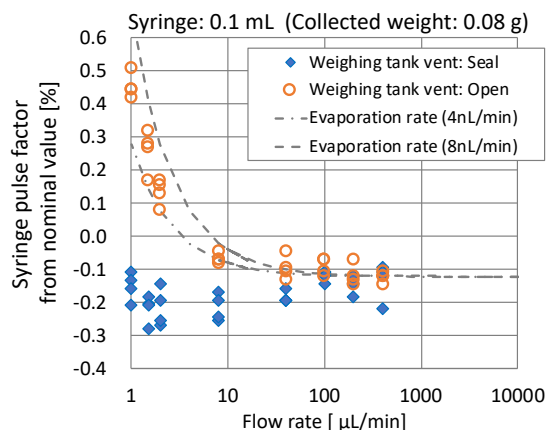


Figure 7: Calibration factor for 0.1 mL syringe.

## 7. Conclusion

A weighing system for liquid microflow from 10 mL/min to 1  $\mu\text{L}/\text{min}$  has been constructed. In order to prevent evaporation errors, a novel detachable system was adopted between the weighing tank and the pipeline. Two size of syringes (syringe pumps) have been calibrated using the weighing system. The ability of the detachable system has been confirmed by analysis of the syringe pulse factor. It was confirmed that the evaporation error was suppressed at flow rate down to 1  $\mu\text{L}/\text{min}$ .

## References

- [1] Doihara R, Shimada T, Cheong K.-H, Terao Y., "Liquid low-flow calibration rig using syringe pump and weighing tank system", Flow Measurement and Instrumentation 50, 90-101, 2016
- [2] Cheong K.-H, Doihara R, Shimada T, Terao Y., "Development of a gravimetric system using a conical rotating double-wing diverter for low

liquid flow rates”, Flow Measurement and Instrumentation 56, 1-13, 2017

- [3] David, C., Lecoffre, Y., Dupuy, J. L. and Claudel, P., Micro flow meters calibration test loop at CETIAT, In: Proceedings of the 3rd European conference on microfluidics, Heidelberg; 2012.
- [4] Bissig, H., Tschannen, M. and Huu., M., Micro-flow facility for traceability in steady and pulsating flow, Flow Measurement and Instrumentation 44 (2015) 34–42.
- [5] Melvad, C., Kruhne C. and Frederiksen J., Design considerations and initial validation of a liquid Microflow calibration setup using parallel operated syringe pumps, Meas. Sci. Technol. 21 (2010) 074004 (6pp)
- [6] Su, C.-M., Lin, W.-T. and Yang, C.-T., Flow Calibration system for micro-flowrate delivery and measurement, In: Proceedings of the NCSL International Workshop and Symposium; 2008

# Primary standard for liquid hydrocarbon at low flow rates using light oil, kerosene and industrial gasoline

K-H. Cheong<sup>1</sup>, R. Doihara<sup>2</sup>, N. Furuichi<sup>3</sup>, T. Shimada<sup>4</sup>, Y. Terao<sup>5</sup>

<sup>1-5</sup> National Metrology Institute of Japan, National Institute of Advanced Industrial Science and Technology (NMIJ, AIST), 1-1-1 Umezono, Tsukuba 305-8563, Japan.

E-mail (corresponding author): kh.cheong@aist.go.jp

---

## Abstract

Motivated by the need to establish a measurement traceability in engine fuel consumption for the industry (automobile, shipping and aviation) as well as in the household fuel metering and bio-fuel production (bio-fuel blending), NMIJ developed a primary standard for low liquid hydrocarbon flow rates that works on three common types of liquid fuels, namely light oil (diesel), kerosene and industrial gasoline (flash point over 40°C). To achieve a high calibration accuracy below 0.1 % which is needed by the industry, this primary standard adopted the gravimetric method performing static weighing with flying-start-and-finish as the calibration method. To cater to a wide flow range from 0.02 L/h to 100 L/h, the calibration facility operates on two gravimetric systems, one using a compactly designed conical rotating double-wing diverter for 1 L/h to 100 L/h and another using a pair of high-speed switching valves as a diverter for 0.02 L/h to 1 L/h. Features of each gravimetric system and its performance are highlighted in the paper. For validation of the calibration capability of the primary standard, uncertainty analysis as well as intra-comparisons with other facilities at NMIJ are also reported.

---

## 1. Introduction

Flow metering for liquid hydrocarbon at low flow rates is mainly applied to industrial practices such as measurement of engine fuel consumption in the automobile, shipping and aviation industry as well as metering of household fuel consumption and blending of bio-fuel with petrol. In particular, the race for achieving better fuel efficiency among the automakers is becoming highly competitive, urging the need for stricter monitoring of the accuracy and credibility of flow metering at engine test bench. This initiated the work to develop a calibration facility as a primary standard at National Metrology Institute of Japan (NMIJ) with the aim of establishing measurement traceability for low flow range encountered in the industrial practices mentioned above.

Flow range at engine test bench may span from few hundreds of L/h to as low as 0.02 L/h and flow metering instruments used at engine test bench such as radial piston positive displacement (PD) flowmeters have a high turndown ratio of over 1000:1 with the best accuracy claimed at about 0.1 %. This posed a huge challenge for us in

developing a calibration facility versatile enough to cater to the wide flow range with an uncertainty aimed at below 0.1 %. Primary standards at NMIJ had been providing calibration coverage from 0.1 m<sup>3</sup>/h to 300 m<sup>3</sup>/h. Hence a new facility was intended to expand the bottom limit (0.1 m<sup>3</sup>/h = 100 L/h) of the calibration coverage to the lowest flow rate of 0.02 L/h performed at engine test bench. We faced different challenges and problems in different flow ranges as we expanded the flow range downwards. Two different gravimetric diverting systems performing static weighing with flying-start-and-finish were newly designed: one is a compact conical rotating double-wing diverter [1] for the upper flow range (1 L/h~100 L/h) and another is a set of two instantaneous switching valves [2] for the lower flow range (0.02 L/h~1 L/h).

This paper presents the main features of the calibration facility incorporating the two gravimetric systems mentioned above in the succeeding section, followed by the uncertainty analysis and verification of the calibration capability of the facility through internal comparison.

## 2. Calibration facility

A 3D illustration of the facility is shown in Figure 1. The facility comprises three main sections, namely (a) flow generation section, (b) test section and (c) weighing section. The flow generation section consists of a storage tank, a magnetic gear pump, a heat exchanger and a header tank. The working fluid, either light oil, kerosene or industrial gasoline, is delivered into the flow loop by the magnetic gear pump whose revolution speed is variable. Temperature of the working fluid can be maintained at any value in the range of 15 °C ~35 °C. In the flow generation section, the flow circulates from the pump to the header tank and back to the storage tank. From the header tank, a portion of the working fluid is released into the test line. The header tank takes the role of stabilizing any pulsating flow as well as adjusting the fluid pressure.

The test section where DUTs (device under test) are mounted was built inside a thermostatic chamber for better stabilization of liquid temperature in the test line. Thermometer sensors and pressure transmitters are being set up upstream and downstream of each DUT.

The weighing section comprises two gravimetric systems, one using a 2 kg weighing scale (for 1 L/h~100 L/h) and the other using a 100 g weighing scale (for 0.02 L/h~1 L/h). Both gravimetric systems perform static weighing with flying-start-and-finish as the calibration method. Features of each gravimetric system are described in the following sections.

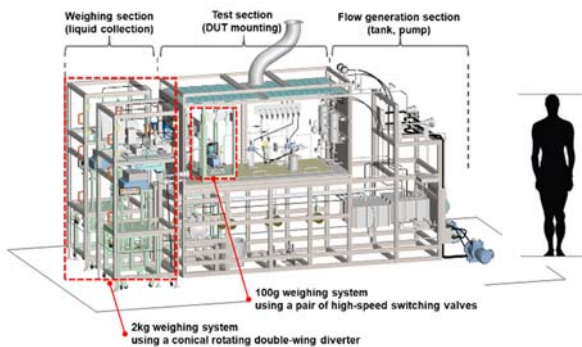


**Figure 1:** Calibration facility for low liquid hydrocarbon flow rates

### 2.1 Gravimetric system using a conical rotating double-wing diverter

As illustrated in Figure 2, this 2 kg weighing system comprises a conical rotating double-wing diverter (CRDWD), a rectangular weighing tank sitting on a weighing scale and a liquid discharge mechanism using a suction nozzle. The diverter takes the shape

of a conical structure with a small window (opening) on the cone surface and two wings protruding from both sides of the window. These two wings move in the same direction at constant speed across the liquid jet to perform symmetric diversion, a common characteristic with double-wing diverter. The diverter rotates in the same direction around the center axis of the cone which runs parallel to the liquid jet flowing vertically downward. The window leads the liquid jet into the weighing tank while the rest of the cone surface acts as the bypass sloping 'roof', letting the liquid to flow down its surface with little splashing and head towards the exit of the diverter box. The gravimetric system is being discussed in more details in [1].

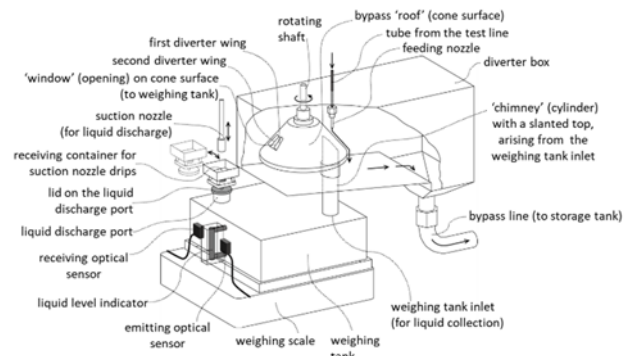


**Figure 2:** Gravimetric system using a conical rotating double-wing diverter

### 2.2 Gravimetric system using a pair of high-speed switching valves

As shown in Figure 3, this 100 g weighing system comprises the three main components of: i) a pair of switching valves as a flow diverter, ii) a weighing vessel enclosed in a chamber and iii) a liquid discharging mechanism with a bypass-cum-discharge bin. The pair of switching valves (of diaphragm type) is mounted on a flow module platform (a metal block inside which symmetrical flow channels are machined). Liquid from the DUT enters the module platform and passes through either one of the valves before exiting the module platform. We constructed two symmetrical (in terms of path configuration) flow paths with one departing from the module platform to the weighing vessel and the other to the bypass line. As a result, the flow rates going through either one of the flow paths will always be identical to maintain a constant flow rate passing through the DUT in conformity with the flying-start-and-stop (FSS) method. A detailed description of the gravimetric system is being made in [2].

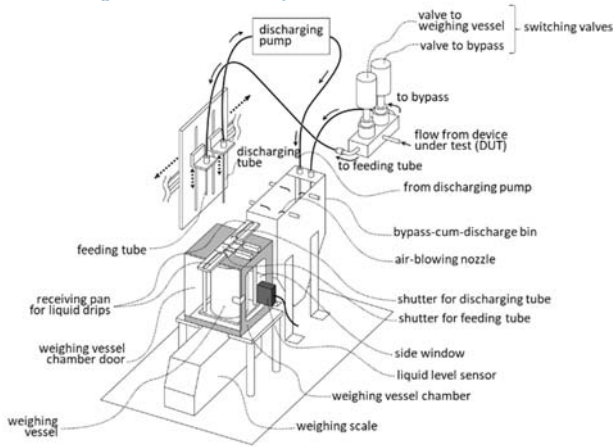


**Figure 3:** Gravimetric system using a pair of high-speed switching valves

### 3. Uncertainty analysis

Analysis of measurement uncertainty is based upon the following model equations; Equation (1) for mass flow rate and Equation (2) for volumetric flow rate.

$$K_{FM} = \frac{I_p}{(M_L + \Delta M_{LDV}) t_p} t_D \quad (1)$$

$$K_{FV} = \frac{I_p t_D \rho_{FM}}{1000 t_p (M_L + \Delta M_{LDV})} \quad (2)$$

- $K_{FM}$  : K-factor for mass flow rate (pulse/kg)  
 $K_{FV}$  : K-factor for volumetric flow rate (pulse/L)  
 $I_p$  : number of pulses totalized by the pulse counter over the duration of liquid collection (pulse)  
 $M_L$  : mass of liquid collected in the weighing vessel (kg)  
 $\rho_{FM}$  : liquid density in the flow meter (kg/m<sup>3</sup>)  
 $\Delta M_{LDV}$  : variation of liquid mass in the dead volume (volume between flow meter and the end of nozzle heading into the weighing vessel) over the duration of liquid collection (kg)  
 $t_D$  : liquid collection time for one run of calibration (s)  
 $t_p$  : time interval measured from the first rising edge of the pulse output of flowmeter detected right after the diverter trigger signal is 'on' to the first rising edge of the pulse output detected right after the diverter trigger signal is 'off' (s)

Thus, the relative combined standard uncertainty of K-factor for mass flow rate and volumetric flow rate are expressed as follows.

$$\left\{ \frac{u_c(K_{FM})}{K_{FM}} \right\}^2 = \left\{ \frac{u(I_p)}{I_p} \right\}^2 + \left\{ \frac{u(t_p)}{t_p} \right\}^2 + \left\{ \frac{u(t_D)}{t_D} \right\}^2 + \left\{ \frac{u(M_L)}{M_L} \right\}^2 + \left\{ \frac{u(\Delta M_{LDV})}{M_L} \right\}^2 \quad (3)$$

$$\left\{ \frac{u_c(K_{FV})}{K_{FV}} \right\}^2 = \left\{ \frac{u(I_p)}{I_p} \right\}^2 + \left\{ \frac{u(t_p)}{t_p} \right\}^2 + \left\{ \frac{u(t_D)}{t_D} \right\}^2 + \left\{ \frac{u(M_L)}{M_L} \right\}^2 + \left\{ \frac{u(\Delta M_{LDV})}{M_L} \right\}^2 + \left\{ \frac{u(\rho_{FM})}{\rho_{FM}} \right\}^2 \quad (4)$$

The terms on the right side of Equation (3) and Equation (4) represent uncertainties due to pulse count, measurement of time interval of pulse output, measurement of liquid collection time, measurement of liquid mass, variation of liquid mass in dead volume and estimate of liquid density in flow meter (Equation (4) only) respectively.

Uncertainty budget for the calibration flow range of 1 L/h ~ 100 L/h (2 kg weighing system) and 0.02 L/h ~ 1 L/h (100 g weighing system) are listed in Table 1 and Table 2 respectively. The values presented in Table 1 and Table 2 are all relative uncertainties for light oil, kerosene and industrial gasoline, respectively. The relative combined standard uncertainties given in Table 1 and Table 2 are meant for volumetric flow rate.

**Table 1:** Uncertainty budget for 1 L/h ~ 100 L/h using 2 kg weighing system

Uncertainty sources	Light oil	Kerosene	Industrial gasoline
Pulse count	8.2×10 <sup>-5</sup>	8.2×10 <sup>-5</sup>	8.2×10 <sup>-5</sup>
Time interval of pulse output	1.4×10 <sup>-5</sup>	1.4×10 <sup>-5</sup>	1.4×10 <sup>-5</sup>
Liquid collection time	8.1×10 <sup>-5</sup>	8.1×10 <sup>-5</sup>	8.1×10 <sup>-5</sup>
Measurement of liquid mass	3.3×10 <sup>-5</sup>	3.3×10 <sup>-5</sup>	3.3×10 <sup>-5</sup>
Dead volume effect	6.1×10 <sup>-6</sup>	6.4×10 <sup>-6</sup>	6.6×10 <sup>-6</sup>
Estimation of liquid density	2.6×10 <sup>-4</sup>	3.0×10 <sup>-4</sup>	3.2×10 <sup>-4</sup>
Relative combined standard uncertainty	2.8×10 <sup>-4</sup>	3.2×10 <sup>-4</sup>	3.4×10 <sup>-4</sup>

**Table 2:** Uncertainty budget for 0.02 L/h ~ 1 L/h using 100 g weighing system

Uncertainty sources	Light oil	Kerosene	Industrial gasoline
Pulse count	$8.2 \times 10^{-5}$	$8.2 \times 10^{-5}$	$8.2 \times 10^{-5}$
Time interval of pulse output	$1.4 \times 10^{-5}$	$1.4 \times 10^{-5}$	$1.4 \times 10^{-5}$
Liquid collection time	$8.1 \times 10^{-5}$	$8.1 \times 10^{-5}$	$8.1 \times 10^{-5}$
Measurement of liquid mass	$1.8 \times 10^{-4}$	$1.8 \times 10^{-4}$	$1.8 \times 10^{-4}$
Dead volume effect	$1.2 \times 10^{-4}$	$1.3 \times 10^{-4}$	$1.3 \times 10^{-4}$
Estimation of liquid density	$2.6 \times 10^{-4}$	$3.0 \times 10^{-4}$	$3.2 \times 10^{-4}$
Relative combined standard uncertainty	$3.5 \times 10^{-4}$	$3.8 \times 10^{-4}$	$4.0 \times 10^{-4}$

Comparing Table 1 and Table 2, estimation of liquid density is the largest uncertainty source in both flow ranges. However, in the flow range of 0.02 L/h ~ 1 L/h, measurement of liquid mass and dead volume effect show the same order of magnitude as estimation of liquid density in terms of uncertainty contribution. Here, how these two uncertainty sources gain importance is discussed.

One has to take note that the uncertainties shown in Table 1 and Table 2 are relative values. In 100 g weighing system, the reason for dead volume effect to become relatively larger is that the value is evaluated in relative to the smallest amount of liquid collection which is 10 g. 10 g of liquid collection is performed at 0.02 L/h and it takes about 40 minutes for one collection. To cut down the dead volume effect, the dead volume between the flow meter and the end of nozzle is made as small as possible and temperature variation of liquid in the dead volume is controlled and stabilized by placing the measurement setup in a thermostatic chamber. At 0.02 L/h, liquid temperature variation in dead volume was evaluated as  $\pm 0.025^\circ\text{C}$  in one hour duration.

On the other hand, contributing factors that cause the larger uncertainty of liquid mass measurement in the 100 g weighing system are liquid evaporation and leakage possibility. Industrial gasoline is the most evaporative among the three types of liquid. For safety reason and to reduce the evaporation error, the highest liquid temperature set for industrial gasoline is  $20^\circ\text{C}$  whereas light oil and kerosene are being operated up to  $35^\circ\text{C}$ . At  $20^\circ\text{C}$ , the evaporation rate of industrial gasoline was evaluated as 0.0015 g for a duration of 1 hour which equals to that of kerosene at  $35^\circ\text{C}$ . In relative to 10 g of liquid collection, this produces  $1.5 \times 10^{-4}$  in terms of uncertainty.

The second largest contributing factor to uncertainty of liquid mass measurement in the 100 g weighing system is undetectable leakage. Leakage amount can be so small that it cannot be detected by pressure variation. Yet this tiny amount is not negligible in relative to 10 g of liquid collection. In practice, leakage check is performed by monitoring the pressure and temperature variation for the longest time of liquid collection (40 minutes). During this period, variation of pressure and temperature has to be maintained within  $\pm 10$  kPa and  $\pm 0.01^\circ\text{C}$  respectively. In other words, leakage that is not detectable within  $\pm 10$  kPa and  $\pm 0.01^\circ\text{C}$  is treated as an uncertainty factor in liquid mass measurement and is estimated as  $1.0 \times 10^{-4}$  in relative to 10 g of liquid collection.

Uncertainty sources shown in Table 1 and Table 2 are all due to the calibration facility. Combined with the uncertainties due to flowmeter (DUT), the ultimate uncertainty of calibration is obtained in Table 3.

**Table 3:** Ultimate uncertainty of calibration

Flow range, Q (Weighing system)	Volumetric flowrate (%)	Mass flowrate (%)
1 L/h $\leq$ Q $\leq$ 100 L/h (2 kg weighing system)	LO: 0.029 <i>(0.058)</i>	LO, KE, IGA: 0.010 <i>(0.020)</i>
	KE: 0.032 <i>(0.064)</i>	
	IGA: 0.034 <i>(0.068)</i>	
0.02 L/h $\leq$ Q < 1 L/h (100 g weighing system)	LO: 0.036 <i>(0.072)</i>	LO, KE, IGA: 0.025 <i>(0.050)</i>
	KE: 0.039 <i>(0.078)</i>	
	IGA: 0.040 <i>(0.080)</i>	

Note: Calibration and measurement capability in italic; coverage factor,  $k=2$ ; LO: light oil, KE: kerosene, IGA: industrial gasoline.

#### 4. Validation of calibration and measurement capability (CMC) through intra-comparisons

To justify the calibration capability of the facility (hereafter, small oil flow facility), we performed intra-comparisons with other primary standard facilities (small water flow facility; medium oil flow facility) in NMIJ which are linked to international comparisons. Intra-comparisons using light oil and kerosene have been reported in previous papers [3, 4]. In this paper, we present the intra-comparison conducted between the small oil flow facility and the medium oil flow facility [5] using industrial gasoline.

Figure 4 shows the intra-comparison results between the small oil flow facility (2 kg weighing system) and the medium oil flow facility using industrial gasoline as the working liquid and a piston

type volumetric flow meter as the transfer standard. Difference of K-factors (shown in percentage in relative to the nominal K-factor) obtained from the two facilities is shown in the ordinate axis in Figure 4. The error bar indicates the expanded uncertainty of each facility. Overall the difference is within  $\pm 0.03\%$  which is within the expanded uncertainty of the facilities for volumetric flow rate calibration, hence providing supporting evidence for the calibration capability of the 2 kg weighing system of small oil flow facility.

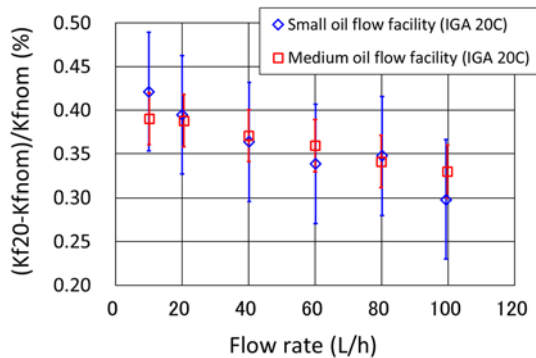


**Figure 4:** Intra-comparison between small oil flow facility and medium oil flow facility using industrial gasoline.

To justify the calibration capability of the 100 g weighing system of small oil flow facility, a comparison was conducted between the two weighing systems of 100 g and 2 kg over an overlapping flow range of 0.6 L/h  $\sim$  6 L/h using a volumetric flow meter as a transfer standard. As shown in Figure 5, the two weighing systems agree well within the expanded uncertainties of the facilities ( $E_n < 1$ ). Hence the calibration capability of the 100 g weighing system is justified. As such, the comparison results in Figures 4 and 5 provide supporting evidence that validates the overall calibration capability of the small oil flow facility.

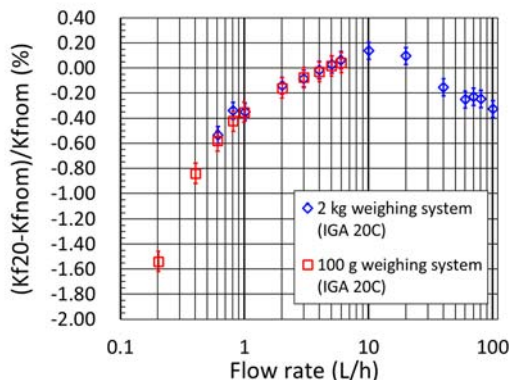


**Figure 5:** Comparison between 100 g weighing system and 2 kg weighing system within the small oil flow facility.

## 5. Summary and conclusions

To provide measurement traceability in engine fuel consumption for the industry (automobile, shipping and aviation) as well as in the household fuel metering and bio-fuel production (bio-fuel blending), NMIJ developed a primary standard for low liquid hydrocarbon flow rates that works on three common types of liquid fuels, namely light oil (diesel), kerosene and industrial gasoline.

The primary standard comprises two gravimetric systems, one using a 2 kg weighing scale with a conical rotating double-wing diverter in the flow range of 1 L/h  $\sim$  100 L/h, and the other using a 100 g weighing scale with a pair of high-speed switching valves as diverter in the flow range of 0.02 L/h  $\sim$  1 L/h. Calibration method of static weighing with flying-start-and-finish is performed in both gravimetric systems.

From the uncertainty analysis, the expanded uncertainty for calibration of the upper range of volumetric flow rates from 1 L/h  $\sim$  100 L/h by using the 2 kg weighing system is estimated at 0.058 %, 0.064 % and 0.068 % for light oil, kerosene and industrial gasoline respectively whereas the expanded uncertainty for the corresponding mass flow rates is estimated at 0.020 % for all working liquids. On the other hand, the expanded uncertainty for calibration of the lower range of volumetric flow rates from 0.02 L/h  $\sim$  1 L/h by using the 100 g weighing system is estimated at 0.072 %, 0.078 % and 0.080 % for light oil, kerosene and industrial gasoline respectively whereas the expanded uncertainty for the corresponding mass flow rates is estimated at 0.050 % for all working liquids.

Intra-comparisons with other primary standards in NMIJ that are linked to the international comparisons (CCM.FF.K1, CCM.FF.K2) show a good agreement between the facilities, hence justifying the CMC claimed by the primary standard (small oil flow facility) being discussed in this paper.

## References

- [1] K-H. Cheong, R. Doihara, T. Shimada, Y. Terao, "Development of a gravimetric system using a conical rotating double-wing diverter for low liquid flow rates", *Flow Measurement and Instrumentation*, Vol. 56, pp. 1-13, 2017.
- [2] K-H. Cheong, R. Doihara, T. Shimada, Y. Terao, "Gravimetric system using high-speed double switching valves for low liquid flow rates", *Measurement Science and Technology*, Vol. 29, 075304 (15 pp), 2018.

- [3] K-H. Cheong, R. Doihara, T. Shimada, Y. Terao, "Improvement to small hydrocarbon flow calibration facility at NMIJ", *Proceedings of 8th ISFFM 2012*.
- [4] K-H. Cheong, N. Furuichi, R. Doihara, T. Shimada, Y. Terao, "In-house comparison between small hydrocarbon flow facility and small water flow facility at NMIJ", *Proceedings of FLOMEKO 2013*.
- [5] R. Doihara, T. Shimada, K-H. Cheong, Y. Terao, "Evaluation of hydrocarbon flow standard facility equipped with double-wing diverter using four types of working liquids", *Metrologia*, Vol. 54, pp. 262-279, 2017.

# Turbulence Measurements With A New Two Components Ultrasonic Profiler

H. Guta<sup>1</sup>, S. Fischer<sup>2</sup>, D. Dufour<sup>2</sup>, M. Burckbuchler<sup>2</sup>, G. Fromant<sup>1</sup>

<sup>1</sup> *Laboratory of Geophysical and Industrial Flows, Grenoble, France*

<sup>2</sup> *UBERTONE, Strasbourg, France, info@ubertone.fr*

*E-mail (corresponding author): marie@ubertone.fr*

---

## Abstract

In the present paper, a data set of time-resolved two components velocity profile measurements under steady uniform turbulent rough clear water and sheet-flow are presented. The purpose of this campaign was to evaluate the performances of a commercial ADV, the *UB-Lab 2C* from the company Ubertone, by comparing it to a well-established instrument, the ACVP, developed by the LEGI. This measurement method provides quasi-instantaneous co-located two (2C) components velocity profiles, overcoming limitations of previously developed acoustic measurement methods, and allowing to resolve fine flow scale for the characterisation of turbulence statistics and turbulent processes.

Taking into account flow condition differences in the tilting flume with sediment pit, the results of this measurement campaign demonstrates the good performance of the commercial ADV compared to the ACVP, in clear water and sheet-flow. Its capabilities for time-resolved turbulence measurements are also supported by similar results described in the literature, namely, the significant reduction of Von Karman parameter in sediment-laden flows and the higher contributions of ejections in CW (and sweeps in SF) for the Reynolds shear stress. This suggests the potential of this acoustic system to analyse a wide range of hydrodynamic phenomena, both in rigid-bed and mobile-bed, in which turbulence plays a major role.

---

## 1. Introduction

Measuring velocity profiles in turbulent flows has always been of great theoretical and practical interest. It allows the statistical characterisation of turbulence and better understanding of processes such as sediment motion, closely related to the flow turbulence. A full agreement on how turbulent flows are affected by presence of particles is yet to be reached. An example is the modification of the well-known law of the wall, which has been the subject of analysis by several authors ([4], [14], [16]). All the studies report a reduction of the von Karman parameter in mobile-bed flows, however, the full description of these modifications according to the sediment-laden flow regime is not available. Another question lies in understanding the behaviour of turbulent bursting events. They are reported ([18], [13], [11], [5]) to be very important on the suspension dynamics.

Over the past two decades, the development of increasingly sophisticated measuring systems has enabled flow parameters to be obtained from acoustic technology. For example Acoustic Doppler Current Profilers (divergent beams on a multi-monostatic

configuration) or UVPs (single (1C) and multi-components velocity profilers), are able of reasonable to high temporal and spatial resolutions and have been increasingly used in the fields of research and environmental engineering. Yet, none of these devices allow to resolve sufficiently fine flow scales, preventing a proper characterization of turbulence statistics and turbulent processes. To overcome these limitations, ADVs (Acoustic Doppler Velocity Profilers) were developed to provide quasi-instantaneous co-located two (2C) to three (3C) components velocity profiles along the transmitter beam axis, using a multi-bistatic configuration. These devices were shown to resolve up to the Taylor microscale.

The study aims to display the performance of the UB-MES (a prototype of the *UB-Lab 2C* currently commercialised) in terms of mean flow properties and time-resolved turbulence measurements, focusing in the von Karman and turbulent bursting events modifications in sheet-flow.

The structure of the paper is as follows: in section 2 the experimental setup and flow conditions are presented. The mean flow properties and time-resolved turbulence

measurement results in clear water are presented and discussed in section 3. In section 4, the sheet flow results are presented. The turbulence measurement capabilities of UB-MES are summarised in section 5.

## 2. Methodology

### 2.1 Experimental setup

The experiments were carried out at the LEGI, using a 10 m long tilting flume, with 0.35 m width. Different slopes were set for clear water experiments and for sheet-flow experiments. For sheet flow experiments, the (rectangular) sediment pit, located at 5 m from the beginning of the channel is 3 x 0.11 m<sup>2</sup>, is initially filled with low density ( $\rho v=1192$  kg/m<sup>3</sup>) non-spherical plastic sediments (Poly-Methyl MethAcrylate) of median diameter  $d_p=3$  mm and the packed volumetric concentration is 0.55. The settling velocity  $w_s$  of the particles is 5.6 cm/s. The fixed bed is covered by glued particles, with the same properties as the sediments filled in the channel. For the clear water measurements, the fixed bed is placed in the sediment pit. For both conditions (clear water and sheet flow), a sluice gate at the downstream end and a by-pass at the upstream end allow to regulate the flow discharge.

### 2.2 Experimental protocol and flow properties

The sheet-flow experimental protocol from [16] was applied. The experiments are performed with no recirculation of the sediments. In such conditions, there is an initial transient phase, in which the bed erosion rate reaches its peak value, followed by a quasi-uniform phase of the flow, with a fairly steady bed erosion rate, which lasts about 30 s. The flow analysis is performed during this quasi-steady period, in which the flow is quasi-uniform. For better statistical convergence, the flow quantities are averaged over 4 experimental runs with ACVP and 5 experimental runs with UB-MES.

For clear water experiments, no particular protocol was implemented since the sediment pit was covered by fixed rough bed plates. It was only necessary to approach the uniform flow conditions for which the mean flow and turbulence properties are well known and described in the literature [13].

For both clear water and sheet-flow conditions, the flow was highly turbulent, hydraulically rough and subcritical (Table 1), as indicated by the high Reynolds number ( $Re = UH_f/\nu > 2000$ ), the high bed roughness Reynolds number ( $Re^* = u k_s/\nu > 70$ ) and the low Froude number ( $Fr = U/\sqrt{g H_f} < 1$ ).

**Table 1:** Sediment and flow properties in Clear water (CW) and Sheet-flow (SF)

	$S_0$ (%)	$u_*$ (cm/s)	$H_f$ (m)	$Q$ (m <sup>3</sup> /s)	$U$ (m/s)	Re	Fr
CW <sub>(ACVP)</sub>	0.375	5.7	0.12	28,9	0.69	$8 \times 10^4$	0.6

& UB-MES)

SF<sub>(ACVP)</sub> 0.5 4.3 0.135 28.8 0.59  $8 \times 10^4$  0.5

SF<sub>(UB-MES)</sub> 0.5 4.1 0.145 28.8 0.55  $8 \times 10^4$  0.5

$S_0$ : Slope of the channel;  $U$ : bulk mean velocity;  $H_f$ : water depth;  $\nu$ : kinematic viscosity of water;  $u_*$ : friction velocity;  $k_s$ : equivalent roughness ( $k_s=2.5 d_p$  for mobile bed experiments and  $k_s=3$  mm for clear water) and  $g$  is the gravitational acceleration.

### 2.3 ACVP and UB-MES

Several authors ([8], [7], [10], [16], [17], [3]) have successfully performed velocity, concentration and sediment flux measurements using the ACVP, and compared it to other measurement techniques.

The company Ubertone has recently developed a commercial version of the ACVP: the *UB-Lab 2C* whose prototype is named UB-MES in this paper. One of the major differences between the two systems is that, unlike the ACVP, the UB-MES is compact, low power and the embedded software runs autonomously. Consequently, it is limited in terms of continuous data flow load in opposition with the ACVP. For both acoustic systems, the carrier frequency was set to 1 MHz, with a pulse duration of 2  $\mu$ s allowing a vertical spatial resolution of 1.5 mm. The obtained time resolution for velocity measurements was 19 Hz.



**Figure 1:** Illustration of UB-MES (blue) and ACVP (red).

Figure 1 shows UB-MES prototype and ACVP. The same set of transducers was used with both systems, in order to compare the functioning of the systems solely in terms of electronics. It is possible to see that UB-MES is significantly compact in comparison with ACVP. This gives UB-MES an important advantage in terms of mobility. In contrast, for high time-space resolutions, ACVP provides a larger vertical profiling range.

### 2.4. Velocity measurement principle

The velocity profiling principle in both acoustic systems relies on the measurement of Doppler frequencies. By employing one emitter (that emits sound pulses at a given frequency) and two receivers (Figure 2), two Doppler frequencies along the common emitter axis can be measured. The streamwise velocity  $u$  and the flow normal velocity  $w$  are then obtained from the Doppler Shift frequencies (Equation 1 and 2)

$$u = \frac{c}{2f_0 \sin \alpha} (f_d^+ - f_d^-) \quad (1)$$

$$w = \frac{c}{2f_0(1 + \cos \alpha)} (f_d^+ + f_d^-) \quad (2)$$

where  $f_d^+$  and  $f_d^-$  are the Doppler frequencies obtained from the two receivers,  $f_0$  is the emitted frequency,  $c$  is the sound speed in water and  $\alpha$  is the angle between the emitter and receiver axis. The echo intensities are backscattered by air bubbles contained in the fluid, and by the suspended particles in case of sheet-flow.

### Local velocity decomposition

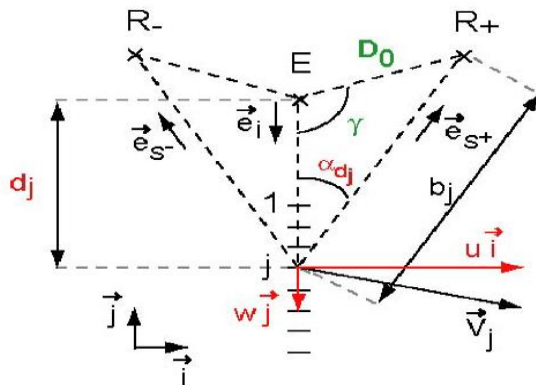


**Figure 2:** Configuration of the transducers, with one emitter E and two receivers R- and R+.

## 3. Results and Discussion - Clear Water (CW)

The first part of the analysis determines the fluid velocity measurement performances of the UB-MES prototype in terms of mean quantity and its fluctuations.

### 3.1 Mean velocity and velocity fluctuations

Figure 2 presents the streamwise mean velocity profiles measured by the ACVP and the UB-MES as functions of the bottom distance normalized by the water flow depth  $Hf$ .

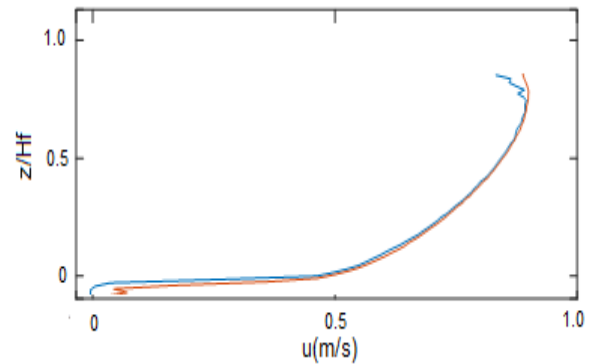


**Figure 2:** Mean velocity profile for UB-MES (blue) and ACVP (red)

As observed in Figure 2 the mean velocity profiles measured by ACVP and UB-MES under the same clear water flow conditions are in good agreement. In both systems, it can be found the typical logarithmic behaviour of the velocity profile. In the upper region of the flow, the flow is strongly disturbed by the presence of the box holding the sensors positioned at the free-surface height. In the near bed there is the effect of the rough sublayer.

The degree of velocity fluctuations generated by turbulent eddies can be described by turbulence intensities. Figure 3 shows the turbulence intensity profiles for the horizontal ( $u$ ) and vertical ( $w$ ) components as a function of the (normalized) distance to the wall. There is a very good agreement between the UB-MES and ACVP measurements on the entire vertical profile. The origin of the discrepancies in the near-bed and the upper region of the flow referred previously for the mean velocity measurements are also valid for turbulence intensities. The normalized mean turbulent intensities can be defined as:

$$u_{rms} = \frac{\sqrt{\overline{u'^2}}}{u_*} \quad (3)$$

$$w_{rms} = \frac{\sqrt{\overline{w'^2}}}{u_*} \quad (4)$$

where  $\overline{u'}$  and  $\overline{w'}$  denote the mean streamwise and the vertical velocity fluctuations, respectively. The measurements of turbulent intensities obtained by the two instruments reveal the same degree of anisotropy between the horizontal and vertical components, which is induced by the average friction exerted by the flow on the rigid rough bottom (sheared boundary layer on rough wall).

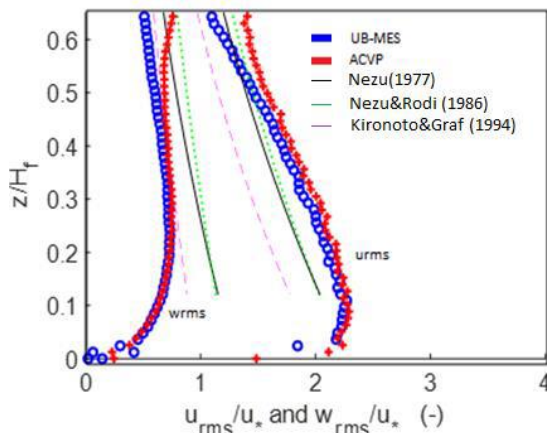


**Figure 3:** Normalized mean turbulence intensity profiles.

The values of the normalized intensities as well as the shapes of the associated profiles (Figure 4) are very similar to those found in the literature for rough open channel turbulent flows ([12], [13]), which can be estimated by the following formulas:

$$\frac{u_{rms}}{u_*} = B_u \exp(-C_u z) \quad (5)$$

$$\frac{w_{rms}}{w_*} = B_w \exp(-C_w z) \quad (6)$$

where the empirical parameters  $B_u$ ,  $B_w$ ,  $C_u$  and  $C_w$  have been proposed by several authors, and the resulting turbulence intensities are presented in Figure 3.

The mean relative differences between the measurements of mean velocity profiles and turbulence intensities with both systems are below 10%.

### 3.2 Turbulent bursting events

Turbulent bursting phenomenon and the resulting coherent structures are relevant in understating sediment entrainment process in turbulent flows. Turbulent bursting events can be quantified from conditional statistics of velocity fluctuations ([13], [6], [17]). This procedure allows to evaluate the total Reynolds shear stress at a given point as a sum of contributions from different bursting events, which are distinguished according to the quadrant in plane [9], and the respective threshold level  $H$ : outward interactions, ejections inward interactions and sweeps. The analysis of conditional statistics consists in fixing a threshold level that allows to exclude weak events (below the magnitude defined by the threshold level  $H$ ).

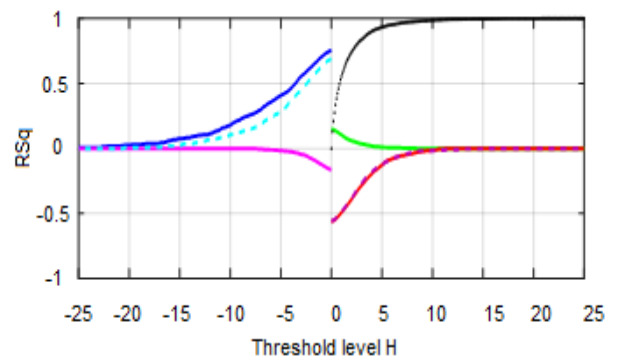


**Figure 4:** Quadrant threshold distribution of fractional contributions (RSq) to turbulent shear stress, at  $z/H_f=0.3$ , for UB-MES (solid lines) and for ACVP (dashed lines). blue=Sweeps, red=Ejections, green=Outward interactions and purple=Inward interactions.

Figure 4 displays the quadrant threshold distribution, in terms of fractional contribution (RSq) to the total Reynolds shear stress of different events (in colors), at a given vertical position ( $z/H_f=0.30$ ), as function of the threshold level  $H$ , for UB-MES (solid lines) and ACVP (dashed lines). The black line represents the proportion of events with lower magnitude than the magnitude at threshold level. As the threshold increases, only the stronger events are selected, thus the reduction in fractional contributions and an increase of excluded events is observed. It should be noted that from a given threshold level ( $H \sim 5$ ) only ejections and sweeps contribute for total Reynolds shear stress. Additionally, it can be observed that ejections are the bursting events with higher magnitude. As result, from the threshold level  $H \sim 10$ , only ejections are responsible for the Reynolds shear stress. This is true for both systems. These results are consistent with the literature ([13], [2]), who reported ejections as the main contributors to the turbulent shear stress in rigid-bed turbulent flows.

## 4. Results and Discussion – Sheet Flow (SF)

In this section, firstly, the mean velocity and mean turbulent shear stress, which result from streamwise and vertical velocity fluctuations in both systems are compared. Secondly, comparisons (in terms of von Karman parameter and turbulent bursting phenomenon) with clear water are established. The corresponding Shields number  $\theta$  was about 0.3 for both systems. The suspension number is  $w_s/u_* = 1.4$  and 1.3 for UB-MES and ACVP respectively.

### 4.1 Mean velocity and mean Reynolds shear stress profiles

Figure 5a displays the mean streamwise velocity profiles for ACVP (+) and UB-MES (o). The relative difference between UB-MES and ACVP increased with elevation up to 14% at the top of the profiles. Such

difference is attributed to different flow conditions, despite the same flow regime, as indicated by the same order of magnitude of the flow parameters.

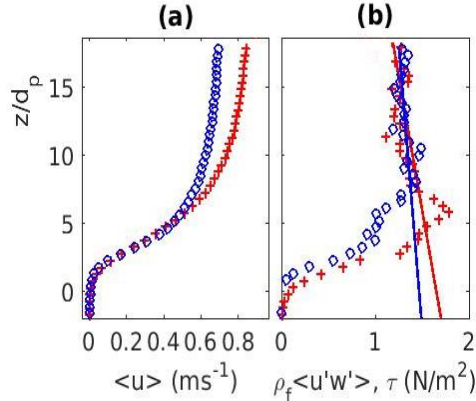


**Figure 5:** Mean profiles of streamwise velocity (a) and Reynolds shear stress (b), for UB-MES (blue, o) and ACVP (red, +).

The Reynolds shear stress profiles presented in Figure 5b show very similar order of magnitude for the two systems. Both profiles from ACVP and UB-MES display a quasi-linear behavior, indicating the uniform flow. The friction velocity, estimated based on the extrapolated Reynolds shear stress up to the bed interface, was about  $u^*=4.1$  cm/s for UB-MES and  $u^*=4.3$  cm/s for ACVP, which shows a good agreement between the systems.

#### 4.2 Reduction of Von Karman parameter in SF

Despite similarities with the clear water velocity distribution, the law of the wall cannot be directly applied in this flow conditions, as previously shown by [16]. One reason is the reduction of the von Karman parameter (equal to  $\kappa=0.41$  in clear water) in sediment-laden flows. Figure 6a shows the mean velocity profile and Figure 6b displays the mixing length. The mixing length can be estimated as follows [15]:

$$l = \frac{\sqrt{\tau/\rho_m}}{\left| \frac{du}{dz} \right|} \quad (3)$$

where  $\rho_m$  is the fluid specific mass,  $\tau$  is the total shear stress obtained from the extrapolation of the Reynolds shear stress profile. The slope of the linear fitting of the mixing length provides information regarding the von Karman parameter, which was  $\kappa=0.25$  for the UB-MES and  $\kappa=0.24$  for the ACVP. Thus, a good agreement is observed between both systems with respect to the vertical structure of the flow.

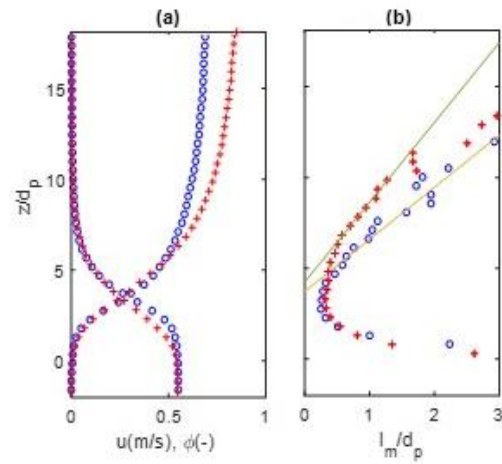


**Figure 6:** Mean velocity and concentration profiles (a) and mixing length (b); for UB-MES (blue, o) and ACVP (red, +).

#### 4.3 Turbulent bursting events

Figure 7 presents the quadrant threshold distribution for the shear stress using  $H=0$ . Sweeps are the predominant events in the near-bed region. A similar behaviour is observed for UB-MES and ACVP. This is in agreement with [13] who argued that in hydraulically rough flows, sweeps dominate over ejections, and with [1], who describes sweeps as the governing mechanism for bed-mobility.

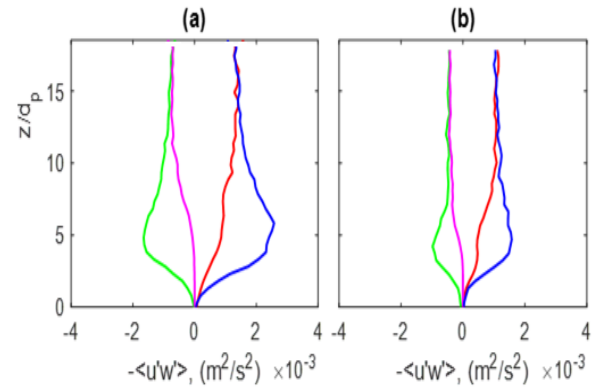


**Figure 7:** Quadrant threshold distribution for shear stress using  $H=0$  for ACVP (a) and for UB-MES (b). blue=sweeps, red=Ejections, green=Outward interactions and purple=Inward interactions

As sweeps are the strongest events, it suggests that they are the most important for sediment suspension, as described by [5]. They reported that strong coherent structures are important contributors of suspended sediment transport, and that they carry a significant part of vertical sediment flux. The observed differences between CW and SF in terms of coherent flow structures are a clear evidence of turbulence modifications in sediment-laden flows.

## 6. Conclusion

In the present study, it was showed that UB-MES (prototype of the *UB-Lab 2C*) displays a good performance in high-resolution two components velocity profiling, by comparing its measurements with reference measurements from ACVP. The relative difference in measurements of both systems remained below 10% in CW and 20% in SF. Regarding the sheet-flow, differences in the flow conditions were observed between the two systems, explaining the greater relative differences compared with clear water conditions.

The capabilities of the *UB-Lab 2C* for time-resolved turbulence measurements are supported by similar results described in the literature, namely, the significant reduction of Von Karman parameter in sediment-laden flows and the higher contributions of ejections in CW (and sweeps in SF) for the Reynolds shear stress. This suggests the potential of this acoustic system to analyse a wide range of hydrodynamic phenomena, both in rigid-bed and mobile-bed, in which turbulence plays a major role.

## Acknowledgment

The authors are grateful for the support of the French DGA through the ANR ASTRID program.

## References

- [1] Dey S, *Fluvial Hydrodynamics: Hydrodynamic and Sediment Transport Phenomena* (Springer Verlag Berlin Heidelberg), 2015.
- [2] Dey, S., and R. Das, “Gravel-bed hydrodynamics: Double-averaging approach”, *J. Hydraul. Eng.* 138(8), 707-725, 2012.
- [3] Fromant, G., Mieras, R.S., Revil-Baudard, T., Puleo, J. A., Hurther, D. & Chauchat, J. “On bed load and suspended load measurement performances in sheet-flows using acoustic and conductivity profilers”. *J. Geoph Res: Earth Surface*, 2018.
- [4] Gust G and Southard J B, “Effects of weak bed load on the universal law of the wall”. *J Geophys Res*, 88(C10):5939–5952, 1983
- [5] Hurther D and Lemmin U, “Turbulent particle flux and momentum flux statistics in suspension flow”, *Water Resour Res* 39(5):1139, 2003.
- [6] Hurther D., Lemmin U. & Terray E.A., “Turbulent transport in the outer region of rough-wall open-channel flows: the contribution of large coherent shear structures”, (LC3S) *J. Fluid Mech.*, 574, 465-493, 2007.
- [7] Hurther, D. & Thorne, P. D. “Suspension and near-bed load sediment transport processes above a migrating, sand-rippled bed under shoaling waves”. *J. Geophys. Res.: Oceans* 116, C07001, 2011.
- [8] Hurther D, Thorne P D, Bricault M, Lemmin U and Barnoud J M, “A multifrequency acoustic concentration and velocity profiler (ACVP) for boundary layer measurements of fine-scale flow and sediment transport processes”, *Coastal Engineering*. 58, 594–605, 2011.
- [9] Lu S S and Willmarth W W, “Measurements of the structure of the Reynolds stress in a turbulent boundary layer”. *J. Fluid Mech.* 60, 481-511, 1973.
- [10] Naqshband S, Ribberink J S, Hurther D and Hulscher S J M H. “Bed load and suspended load contributions to migrating sand dunes in equilibrium”, *Journal of Geophysical Research: Earth Surface* pp. n/a–n/a. 2014.
- [11] Nelson J, Shreve R L, McLean S R and Drake T G, “Role of near-bed turbulence structure in bed load transport and bed form mechanics”, *Water Resour Res* 31,2071–2086, 1995.
- [12] Nezu I Turbulent structure in open channel flow. PhD thesis, Kyoto University, Kyoto, 1977.
- [13] Nezu I. and Nakagawa H, Turbulence in *Open-channel Flows*. (Rotterdam, Balkema), 1993.
- [14] Nikora V I and Goring D G, “Effects of bed mobility on turbulence structure”, *NIWA internal report* number 48, National Institute of Water & Atmospheric Research (NIWA), Christchurch, 1999.
- [15] Prandtl, L. “Bericht über neuere Turbulenzforschung”. *Hydraulische Probleme* pp. 1–13, 1926.
- [16] Revil-Baudard T, Chauchat J, Hurther D. and Barraud P A, *Investigation of sheetflow processes based on novel acoustic high-resolution velocity and concentration measurements*. *J. Fluid Mech.* 767, 1–30, 2015.
- [17] Revil-Baudard T, Chauchat J, Hurther D and Eiff O A, “Turbulence modifications induced by the bed mobility in intense sediment-laden flows”, *J. Fluid Mech.*, 808, 469 - 484. 2016.
- [18] Thorne P D, Williams J J, Heathershaw A D, “In situ acoustic measurements of marine gravel threshold and transport”, *Sedimentology* 36(1):61–74. 1989.

# Deformations and volume changes due to moisture variations in heritage buildings - Use of NDT techniques

José Dias<sup>1</sup>, Luís Matias<sup>2</sup>,  
Maria Henriques<sup>3</sup>

<sup>1</sup>National Laboratory for Civil Engineering, Buildings Department, *mirandadias@lnec.pt, Lisboa*

<sup>2</sup>National Laboratory for Civil Engineering, Buildings Department

<sup>3</sup>National Laboratory for Civil Engineering, Concrete Dams Department

---

## Abstract

Elements of building envelope, during service life, are subjected to deformations and volume changes due to moisture variations, which can cause anomalies in the building, such as the cracking of facade walls and consequent rain penetration, with increase of their moisture content. In case of heritage buildings with structural concrete elements and infill masonry walls, when, besides moisture variations, other different causes can be hypothetically possible, it can be justifiable to investigate more profoundly the anomalies with the available NDT techniques. This study is related to the application of non-destructive testing (NDT) techniques, with a view to the evaluation of anomalies related to the presence and flow of moisture in masonry walls, notably through Ultrasound, Infrared Thermography (IRT) and Photogrammetry. These NDT techniques are used in the evaluation of masonry specimen with variable moisture content, subjected to compression test, before and after been tested, when cracking will be present.

---

## 1. Introduction

Elements of building envelope, during service life, are subjected to deformations and volume changes due to moisture variations, which can cause anomalies in the building, such as the cracking of facade walls and consequent rain penetration, with increase of their moisture content. In case of heritage buildings with structural concrete elements and infill masonry walls, when, besides moisture variations, other different causes can be hypothetically possible, it can be justifiable to investigate more profoundly the anomalies with the available NDT techniques. This study is related to the application of non-destructive testing (NDT) techniques, with a view to the evaluation of anomalies related to the presence and flow of moisture in masonry walls, notably through Ultrasound (US), Infrared Thermography (IRT) and Photogrammetry. These NDT techniques are used in the evaluation of masonry specimen with variable moisture content, subjected to compression test, before and after been tested, when cracking will be present. Here, the aim is to use NDT techniques to analyze the anomalies that can be attributed predominantly to deformations

due to moisture variations in masonry walls and structural elements; it refers to the buildings with reinforced concrete integral structure or with mixed structure of reinforced concrete and masonry.

## 2. Potential use of NDT to access movements in buildings masonry walls and concrete elements due to moisture variation and their consequent degradation

Many buildings suffer, during their use, from cracking of finishes, spalling of surfaces, which can affect, sometimes, in case of exterior finishes, their weathering characteristics, and permit substantial wetting or rain penetration, that, consequently, may lead to severe weakening of the structural building elements as deterioration progress. Often, the mechanisms responsible for such anomalies are usually associated with deformations in materials due to moisture content. As many common building materials have a porous structure and can absorb water more or less readily, the nature and magnitude of moisture deformations assume considerable importance [2] and is important to access, namely through NDT techniques. Moisture deformation is generally reversible, except in

materials such as concrete, mortars and plasters. To access the type of movements that is present in masonry, the use of NDT techniques can be explored, taking in due account the type of constituent material of the masonry and their possible variation in moisture content and in volume. IRT allows to relate observed situations of thermal inhomogeneity with an internal “picture” and state of the element, such as the characteristics of the materials as well as the occurrence in the wall renders of detachment, surface discontinuities and internal cracks and, particularly interesting for present analysis, the distribution of moisture on the masonry wall [5]. That distribution possibly can reveal zones with different moisture expansion rate.

In respect to the use of NDT in detection of moisture presence and its evolution, it should be noted that several factors might, however, restrict the use of thermography. The method of detection depends on the wall surface temperature changes due to water evaporation rate or to the change of thermal characteristics of the constituent materials [5]. The causes of deformations of building materials, elements and concrete structures may be due, to moisture content changes resulting in swelling or shrinkage, but also can be combined with other causes. In particular, can be combined to the following causes [2]: temperature changes resulting in expansions or contractions; chemical action in the presence of moist, air or water resulting in volume change, usually expansion; applied loads resulting in elastic and inelastic deformations.

When subjected to long-term loading, many building materials suffer supplementary deformation, which does not fully vanish when the loading is removed (deformation associated to creep, which is in relation to structural deflections for the particular case of concrete elements). Photogrammetry can possibly give the first information about this case, when this creep deflection, mainly occurring in beams or pavements, is visibly considered anomalous and, clearly, these deformations can be, mainly, attributed to creep and, with less importance, to the moisture deformations. Although it may not be possible, generally, to determine precisely the deformations or stresses due to moisture content changes, it is possible to access them approximately, in case this effect of creep can be neglected.

Cracking can, for example, occur when stresses are induced in materials by restraint to deformation

imposed. When the linkage to other building materials, in order to form a building element, restrains the materials, deformations from changes of moisture content may be restricted. Stresses may be induced, which, in certain cases, maintain the deformation controlled; but, in other cases, these stresses exceed the strength of the material, and the material can crack. Photogrammetry can explore in detail the apparent state of the surface of the building element, namely superficial defects associated to cracks [5].

For example, in the analysis of cracks in facades, both metric and interpretive photogrammetry should be used: the first because it enables measurements from photogrammetric products (measuring the length and aperture of a crack is an example); the second because it allows, using image processing techniques, the recognition and identification of relevant features on the surfaces [5]. Through the enhancement of some features one can extract information such as the type of anomalies related, in particular, to presence of moisture changes in concrete elements that accelerates their carbonation (cracking and delamination of concrete, and reinforcement corrosion) or in masonry walls (cracking, detachment of renders, degradation of the paintings, and presence of mould in the external surface of the facade).

## **2. Previous experimental tests for the evaluation of the variation of moisture in masonry wall specimen through ultrasound method**

Ultrasound tests have been used as a non-destructive inspection technique of not homogeneous materials, such as the masonry walls. The advantages of their use are the easy data acquisition and speed of operation. These tests can be used in detection of cracks or other discontinuities, as well as in the detection of significant variations in moisture content of masonry wall constituents and their rendering. Previously, ultrasound tests were performed to access their potential use for detection of significant variations in moisture content on a masonry wall specimen, which was primarily subjected to a test for the determination of the rainwater permeability [1].

Intended to record the evolution of ultrasonic velocity during the hardening of the rendering and to detect possible changes of that velocity after wetting one face of the wall, during the test, on different dates, measurements of ultrasound

velocity were carried out. A first measurement was made a week after the construction of this wall specimen; 2<sup>nd</sup> measurement was made before the test of rainwater permeability of that masonry wall. That test started about 1 month after the construction of the wall, and lasted for 48 hours; and a 3<sup>rd</sup> measurement was made few hours after the end of the of rainwater permeability test, during which the specimen was moistened. Direct and indirect measurements were made in a frame of points (see Figure 1) deployed on each face of specimen, as shown in Figure 2.

A global analysis of these results revealed that it was possible to register some dominant trends in the evolution of ultrasonic velocity values. It was noted that, in general, since the 1<sup>st</sup> week after the construction of the wall, the direct measurements values decreased, until they reach a minimum before the test. After being moistened during the rainwater permeability test, ultrasound measurements taken in the specimen afterwards the end of that test, a generalized rise of direct measurements values was registered. This allows launching the hypothesis that the ultrasound velocity in direct measurements of that type of specimen was sensitive to changes of moisture content of masonry renderings. As regards indirect measurements, although it was registered, generally, a decrease of the values from the 1<sup>st</sup> week until the date that the test was performed, however, no dominant trend was detected in the evolution of the values, after the humidification of the face (B) subject during the test.

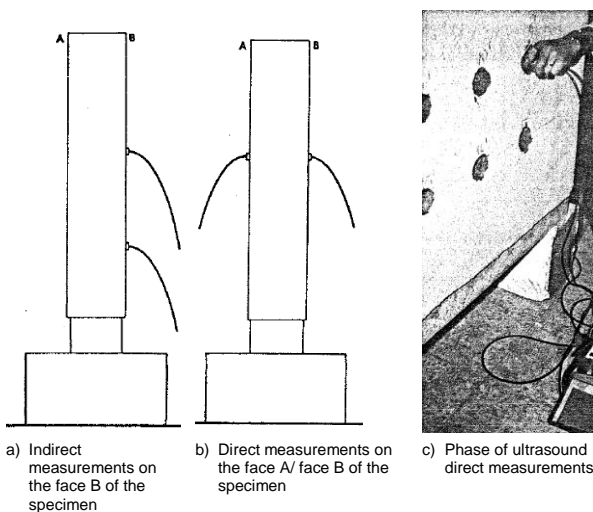


**Figure 1:** Indirect and direct measurements of ultrasound velocity on the face A and face B of the specimen, which was subjected to humidification during the rainwater permeability test

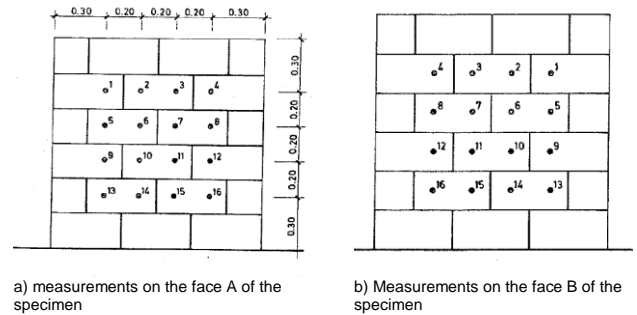


**Figure 2:** Schematic representation of the frame points for ultrasound measurements in the face A and Face B of the wall specimen.

Point	Direct measurements			Point	Indirect measurements		
	Ultrasound velocity (km/s)				Ultrasound velocity (km/s)		
	7 <sup>nd</sup> Day	29 <sup>nd</sup> Day	After Test		7 <sup>nd</sup> Day	29 <sup>nd</sup> Day	After Test
1 - 2	2.00	1.94	1.95	1 - 2	2.30	2.22	2.17
2 - 2	2.66	2.23	2.25	1 - 3	2.55	2.50	2.35
3 - 3	2.02	1.97	2.08	1 - 5	2.22	2.11	2.22
4 - 4	2.72	2.21	2.60	1 - 9	2.34	2.13	2.22
5 - 5	2.03	2.16	2.21	2 - 3	2.44	2.20	2.22
6 - 6	1.97	1.88	1.92	2 - 4	2.52	2.41	2.20
7 - 7	2.60	2.07	2.08	2 - 10	2.45	1.62	1.75
8 - 8	1.91	1.85	1.89	3 - 4	2.27	2.20	2.20
9 - 9	2.55	2.03	2.02	3 - 11	1.86	2.44	2.02
10 - 10	2.19	2.14	2.21	4 - 12	2.56	2.23	1.83
11 - 11	2.05	2.03	2.03	5 - 7	2.48	2.37	2.50
12 - 12	2.08	2.12	2.50	5 - 9	2.25	2.13	1.82
13 - 13	2.72	2.27	2.21	5 - 13	2.22	1.79	1.82
14 - 14	1.87	1.89	1.92	6 - 8	2.37	2.25	2.30
15 - 15	2.78	2.16	2.25	6 - 14	2.55	1.75	1.72
16 - 16	1.89	1.89	1.89	7 - 15	1.75	1.77	1.79
-	-	-	-	8 - 16	1.72	1.71	1.75
-	-	-	-	9 - 11	2.56	2.37	2.25
-	-	-	-	9 - 13	2.30	2.20	2.27
-	-	-	-	10 - 12	2.48	2.47	2.50
-	-	-	-	13 - 15	2.29	2.23	2.26
-	-	-	-	14 - 16	2.22	2.11	2.19

**Table 1:** Results of indirect and direct measurements of ultrasound velocity on the face A and face B of the wall specimen, one week after construction; 29 days after construction; and after the rainwater permeability test

### 3. Laboratory test

#### 3.1 General

To access the potential use of NDT techniques (US, IRT and Photogrammetry) in the detection and evaluation of the progression of cracking in masonry walls with variable moisture content, a compression test was made in a masonry specimen with variable moisture content.

Masonry specimen M1 was subjected to three loading phases of axial compression until it reached, in the third loading phase, a state of significant cracking, without reaching a global collapse. During the three loading phases, a combined use of NDT was used to assess the presence of cracking and of variable moisture content.

Specimen test M1 (Fig. 3) was built with massive ceramic blocks, which have average dimensions of approximately 213 mm (length) x 108 mm (thickness) x 60 mm (height), and cement mortar joints (cement sand ratio - 1: 4 / volumetric ratio).

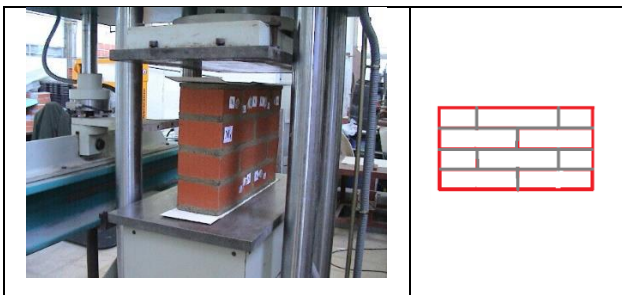


**Figure 3:** Specimen M1 before test (dimensions: 213 mm (length) x 108 mm (thickness) x 60 mm (height))

Initially, the specimen, in dry condition, was slightly loaded (pre-loaded correspondent to 10 kN of axial compression load), and then was discharged. Subsequently, the specimen was weighted (28830 g of weight), before going to a phase of complete immersion in water, during approximately 12 hours. After retiring from immersion, a thermographic analysis was made. And, the wet specimen was again weighted (30856 g of weight – increase of moisture content of 7.1% relatively to the previous weighting of the dry specimen), before subjected to a second loading phase, where a gradual axial compression load was applied, with loading steps of 10 kN (0.21 MPa), 20 kN (0.42 MPa), 40 kN (0.85 MPa), 60 kN (1.27 MPa), 80 kN (1.70 MPa), 100 kN (2.12 MPa), 120 kN (2.54 MPa), 140 kN (2.97 MPa), 180 kN (3.81 MPa), and 300 kN (6.36 MPa); then the loading phase was halted. The third loading phase was initiated 6 days after the previous loading phase, and, before the application of load, the specimen was again weighted (29457 g of weight – increase of moisture content of 2.1% relatively to the dry specimen, and decrease of 4.5% relatively to the previous weighting, after immersion)

In the third loading phase, a gradual axial compression load was applied, with loading steps of 10 kN (0.21MPa), 120 kN (2.54 MPa), 180 kN (3.81 MPa), 300 kN (6.36 MPa), 420 kN (8.90 MPa), 540 kN (11.44 MPa) and final load of 660 kN (13.98 MPa); then ended this loading phase. During the three loading phase, for each loading

step, after reaching the corresponded load, the specimen was discharged, and immediately after that discharge, the horizontal and vertical residual deformations were measured with alongameter (registering the residual deformations after load), Also, the ultrasound velocity measurements (direct and indirect measurements), and the acquisition of images of IRT and the photos were made during these tests breaks.

Then, after all NDT measurements were made, a new phase load was initiated. It was tried to find out, during the process of applying increasing axial load, the degree of sensitivity of each of these techniques in the detection and evaluation of the progression of cracking in masonry with variable moisture content.

### 3.2 Main results

The results of the measurement of deformations with alongameter in specimens show that the variation of horizontal (A1-A3; A2-A4: see reading points in Figure 10) and vertical (A2-A5; A3-A6: see reading points in Figure 10) residual deformations, measured after discharge of the specimen, in end of each load step, were generally correspondent to a gradual expansion of the specimen (Figures 4 to 5); and can detect, with the increase of load, the gradual progression of cracking (see signs of cracking in Figures 9 and 10, which could affect, especially, measurement dv1/A2-A6 and dh1/A1-A3), that occurred in final part (after the 420 kN (8.90 MPa) of load) of the 3<sup>rd</sup> loading phase.

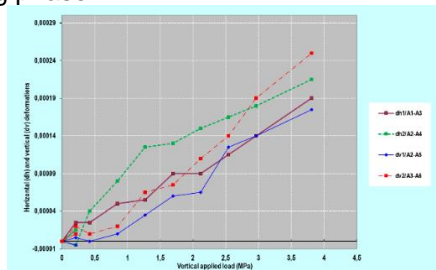


**Figure 4:** Deformations of the specimen M1 during 2nd loading phase for the vertical applied load

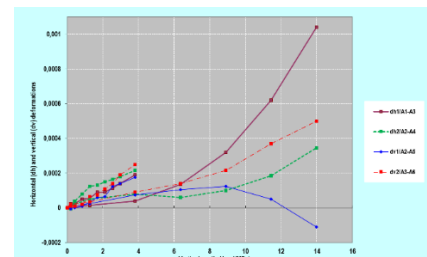


**Figure 5:** Deformations of the specimen M1 during the three loading phases for the applied load

Concerning the results of the application of ultrasound method in the specimen, the indirect

measurements show that, in the dry specimen, with the application of the first load step of 10 kN (1<sup>st</sup> loading phase), there was an increase of the ultrasound velocity measured after discharge of that load, relatively to the correspondent value for 0 kN, for all the measurements, namely horizontal (U1/U2 (path with no mortar joints); U3-U4 (path with one mortar joint) - see reading points in Figure 10) and vertical (U1/U3 and U2-U4 (path with three mortar joints) - see reading points in Figure 10) measurements. After the end of immersion of the specimen, the ultrasound velocity measured (indirect), for 0 kN, was significantly lesser than the correspondent value (for 0 kN) in the dry specimen - which indicates that the ultrasound velocity is sensible to the increase of moisture content (7.1% as was previously referred in 3.1). Subsequently, with the application of the first load step of 10 kN, in the 2<sup>nd</sup> loading phase, there was an increase of the ultrasound velocity measured after discharge of that load, for all the measurements, namely horizontal measurements (see Figure 6); in the direct measurements, similarly, a reduction of velocity value was observed, although only in U1/U1' and U4/U4', and it was less expressive than in indirect measurements (see Figure 7).

Furthermore, these results reveal an almost constant decrease of the values of the ultrasound velocity (indirect measurements) in the 2<sup>nd</sup> and 3<sup>rd</sup> loading phases (see Figures 6 to 9), more in the vertical than in horizontal measurements, due presumably to the number of joints covered by vertical measurement (three mortar joints), that are higher than in horizontal measurement (one mortar joint or no mortar joints). Moreover, due, likewise, to the same effect, horizontal measurements generally are higher than vertical; and, in horizontal measurements, the U1/U2 velocity values (path with no mortar joints) are higher than U3-U4 values (path with one mortar joint).

The results reveal a decrease of the values of direct measurements of the ultrasound velocity, for higher loads, in the 3<sup>rd</sup> loading phase, probably due to the correspondent increase of micro-cracks inside the ceramic blocks.

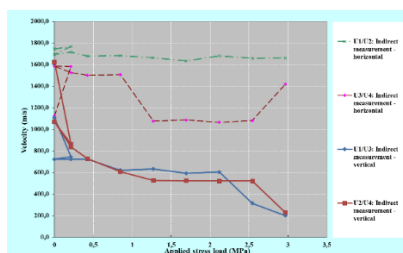


**Figure 6:** Ultrasound velocity (indirect measurements) of the specimen M1 during 1st loading and 2nd loading phase for the vertical applied load

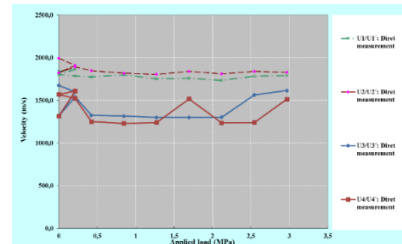


**Figure 7:** Ultrasound velocity (direct measurements) of the specimen M1 during 1st loading and 2nd loading phase for the vertical applied load

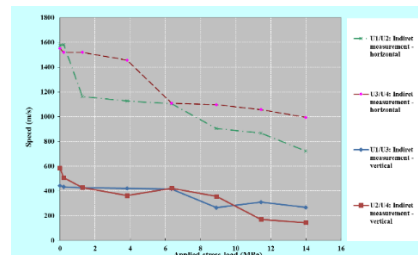


**Figure 8:** Ultrasounds indirect measurements of the specimen M1 during 3rd loading phase

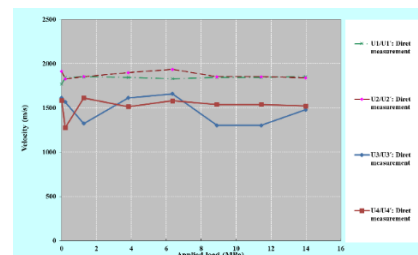


**Figure 9:** Ultrasound velocity (direct measurements) of the specimen M1 during 3rd loading phase

In addition, for the same level of loads, some of the ultrasound velocity values (indirect) measured, in the 3<sup>rd</sup> loading phase, are higher (horizontal: U1/U2 and U3-U4 values) others are lesser, than the correspondent values of 2<sup>nd</sup> loading phase, due presumably to the significant decrease of moisture content (4.5% as was previously referred in 3.1), 6 days after the end of the immersion of the specimen. In the 3<sup>rd</sup> loading phase, an expressive reduction of velocity values was observed, particularly, with the gradual progression of cracking (cracking that affect, especially, U1/U2 velocity values (indirect) and U1/U1' (direct)) that occurred in final part (after the 420 kN (8.90 MPa) of load) of that loading phase.

Concerning the use in this test of photogrammetry, to generate an orthomosaic (image that is the result of stitching several orthorectified images) with a pixel of 0.12 mm it was necessary to make the photo survey with a high quality digital camera. Several photos were taken from different locations in front of the surface, but all at the same distance (70 cm). Digital image processing was applied to enhance the cracks. On Figure 11-A is presented

the result of the enhancement applied to the gray-scale version of the image. Two types of edges can be detected. These were manually coloured in Figure 11-B. In red the cracks, only perceivable in the bricks since the mortar presents great variability in intensity (is a heterogenous area, mixing pixel whites, blacks and grays). In yellow, the borders between two different images used to create the orthomosaic. These borders, barely perceived in the original orthomosaic, were enhanced also.



**Figure 10:** Orthomosaic of the surface. Pixel size 0.12 mm

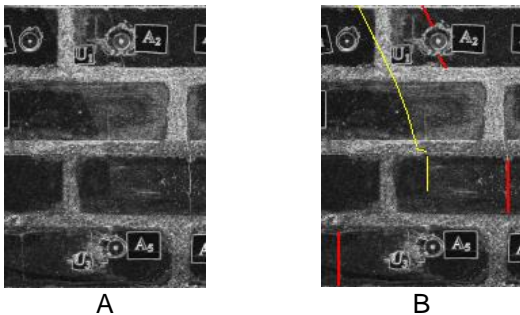


**Figure 11:** Detail of an image created by applying digital image processing tools to the orthomosaic (A). Edges coloured (B)

Concerning IRT analysis, Figure 11 shows a thermogram obtained some days after the last loading phase. The humidity content (2.1%) is still visible with IRT (cold central zone) but no cracks were detected.

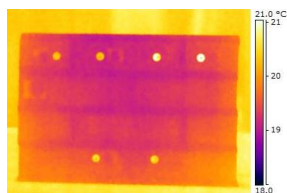


**Figure 11:** Test specimen thermogram after last loading phase

Figure 12 shows thermogram and photo of dry test specimen after a quick heating period (2 minutes). The heating of surface specimen allows, more clearly, to “see” the different materials of the specimen (Figures 11 and 12), but cannot detect obtained cracks. Increasing the heating period (30 minutes), IRT results indicate the same facts. However, it should be noted that visible cracks are very small.

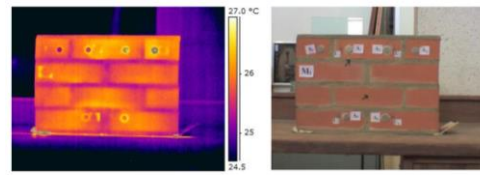


**Figure 12:** Test specimen thermogram and photo after heating (2 min)

#### 4. Conclusion

In this paper, a study was made related to the application of non-destructive testing (NDT) techniques, with a view to the evaluation of anomalies related to the presence and flow of moisture in masonry walls, notably through Ultrasound (US), Infrared Thermography (IRT) and Photogrammetry. These NDT techniques were used in the evaluation of masonry specimens with variable moisture content, subjected to compression tests. The results of test of the specimen M1 reveals that the ultrasound velocity is sensible to the increase of moisture content, and show a decrease of the values of the ultrasound velocity (indirect measurements), after wetting the specimen, and application of load in the 2<sup>nd</sup> and 3<sup>rd</sup> loading phases; also, reveals a reduction of the velocity values particularly, with the gradual progression of cracking. Concerning the use in this test of photogrammetry, digital image processing was applied to enhance the cracks, and two types of edges can be detected. IRT analysis allows the evaluation humidity state of test specimen and the identification of its constituent’s materials. No cracks were detected with this NDT technique. However, it should be noted that visible cracks are very small.

#### Acknowledgments

LNEC Planned Research Programme (P2I) for the period 2013-2020 (P2I Project “COREAP” – Service life, conservation and rehabilitation of walls of buildings with relevant patrimonial value”) has funded the present study. The assistance and help in the experimental tests of the Senior Technicians Deodato Sanches and Ari Reis and of the Lab Assistant Hugo Teixeira da Silva are gratefully acknowledged.

#### References

- [1] José Miranda Dias, “Caracterização experimental das paredes – Ensaios de isolamento sonoro e de estanquidade à água da chuva”. Technical Note 01/91 - NPC/DED, Lisboa, LNEC, February 1991.
- [2] M.C. Baker, “Thermal and Moisture Deformations in Building Materials”, Digest CBD-56, 1964.

- [3] Grimm, C. T. - Differential movement in composite load-bearing masonry walls. Journal of Structural Division Engineer, ASCE, No ST7, Proc. Paper 14666, pp.1277-1288, July 1977.
- [4] José Miranda Dias, Movements in masonry walls caused by temperature and moisture changes. Proceedings of 6th international masonry conference, pp. 86-94, 2002.
- [5] José Miranda Dias, Luís Matias, Maria João Henriques, Maria Sofia Ribeiro, Teresa O. Santos - Combined use of non-destructive methods for the survey of facades anomalies of heritage buildings with structural concrete elements. 7th International Conference on Engineering Surveying (INGEO2017), LNEC, October 2017.
- [6] José Miranda Dias, Luís Matias, Maria João Henriques, Maria Sofia Ribeiro, Sónia Raposo - NDT techniques for the analysis of anomalies related with durability - Heritage buildings with masonry walls and confining concrete elements. Congresso Betão Estrutural 2018 (BE2018), LNEC, November 2018.

# Model Study on the volume value of the gas discharged by high precision bell prover

XING Jing-fang<sup>1</sup>, LIU Chen-kui<sup>2</sup>, CHEN Shi-yan<sup>3</sup>, NIU Li-na<sup>4</sup>, ZHANG Da-peng<sup>5</sup>

<sup>1</sup>Institute of Metrology of Hebei Province, Shangzhuang Street, Luquan, Shijiazhuang, China

<sup>2-5</sup>Institute of Metrology of Hebei Province, Shijiazhuang, China

xjfhbjl@126.com

---

## Abstract

This paper is based on the 0.1 class 2000L standard bell prover of gas flow which is the provincial highest measurement standard established by our institute. The research subject of this device is from the provincial science and technology special project of hebei province. In this paper, the concept of volume coefficient is proposed for bell provers with different accuracy levels. The common mathematical model is analyzed and a new Fourier fitting mathematical model is proposed. The mathematical model of the inner volume of the bell prover is given by the definite integral principle. The actual volume value of the gas discharged from the bell prover is derived by analyzing the starting and stopping process of the bell. That is the volume of the bell corresponding to the distance translated downward by the height of the bell falling which is measured by the displacement measuring mechanism. It is pointed out that in calibrating high accuracy grade bell prover, the effective use segment and its lower volume segment should be calibrated as well.

---

## 1. Introduction

Bell prover gas flow standard device (hereinafter referred to as "bell prover") is a kind of metering standard equipment which is used to calibrate, calibrate and test the gas flow meter with gas as the medium. Many countries have studied and established it as a reference device for low-pressure gas flow. The main factor affecting the uncertainty of flow measurement of bell prover is the internal volume value. According to JJG165-2005 regulation, for devices with a volume of 500L or more, dimensional measurement is recommended. Measuring instruments of bell prover's diameter include: diameter ruler<sup>[1,2]</sup>, thickness meter, inside diameter micrometer<sup>[2]</sup>, laser tracker<sup>[2]</sup>, special device developed and so on, the height measuring instruments are: altimeter or steel ruler, encoder, laser interferometer<sup>[2]</sup>, grating ruler<sup>[3]</sup> and so on.

Diameter ruler, thickness gauge, steel ruler, as the conventional measuring instrument, it is mainly used for low accuracy level for the

calibration of bell. Laser tracker, laser interferometer, grating ruler and special device are convenient to measure the diameter of many heights, mainly used for the segmented calibration of bell prover with high accuracy. After calibrating the volume of the shield, the specific relationship between the inner diameter and the height of the shield was obtained. After calibrating the volume of the bell, the specific relationship between the inner diameter and the height of the bell is obtained, which is called the volume coefficient of the bell, with  $r = f(h)$ . The volume coefficient model is different between whole section calibration and section calibration

When the whole section of the bell is calibrated, the structure of the bell is considered to be an ideal cylinder. According to the verification rules, the inner radii of the upper, middle and lower sections are measured, the average radius  $\bar{r}_i$  ( $i$  is the number of measurements) was used as the measurement result take, and the volume coefficient is a constant, with  $f(h) = \bar{r}_i$ . The displacement measuring mechanism installed on the bell prover measures that the bell is lowered

from position  $h_{\text{begin}}$  to position  $h_{\text{end}}$ . Drop height difference is  $\Delta h = h_{\text{end}} - h_{\text{begin}}$ . The volume of gas discharged by the bell falling is the value of the internal volume of the bell within the range of this height difference, which is  $V = \pi f(h)^2 \cdot \Delta h$ . Because  $f(h)$  is the constant, the volume value of the gas discharged is only related to the height difference and has nothing to do with the starting and stopping position of the bell.

However, for high precision bell prover, the influence of processing accuracy and deformation during transportation on the inner volume of the bell prover should be considered. In this case, the radius values corresponding to different heights of the bell are inconsistent, so it is necessary to calibrate the bell piecewise to obtain the radius values in different height difference sections, and the volume coefficient is a piecewise function, as shown in formula (1):

$$f(h) = \begin{cases} \bar{r}_{1i}, & h_0 \leq h < h_1 \\ \bar{r}_{2i}, & h_1 \leq h < h_2 \\ \vdots & \\ \bar{r}_{ni}, & h_{n-1} \leq h < h_n \end{cases} \quad (1)$$

Where,  $h$  is the height of the bell,  $n$  is the number of segments, and  $i$  is the number of measurements within each segment.

By this time,  $V = \pi f(h)^2 \cdot (h_{\text{end}} - h_{\text{begin}})$ , It can be seen that the descending position of the bell should be considered when the bell is used in sections

In this method, the radius values of different heights of the bell are refined to a certain extent, but the radius values in each segment are still a constant, and the radius values of any heights are not given fundamentally. On this basis, a new calibration method is proposed, and a volume coefficient model in the form of continuous smooth function is established. The objective is to obtain the actual value of the volume of gas discharged at any height when the bell descends.

## 2. Establishment of the bell volume coefficient model

Taking the 0.1 class 2000L bell prover of Hebei Institute of Metrology Supervision and Inspection as an example, using Photography to measure the inner radius of the bell. The cross-section radius of 160 different heights at 11 mm intervals in the range of 1800 mm of axial height is

obtained and the two-dimensional array of heights and radius is formed, which is  $(h_i, r_i)$ ,  $i = 1, 2, \dots, 160$ . Matlab software was used for curve fitting of two-dimensional array [6]. After analysis and comparison of fitting error, it was determined to adopt eight-time Fourier fitting curve, that is, to obtain the function of inner diameter about standard height. Its mathematical model is shown in formula (2):

$$r = f(h) = a_0 + \sum_{k=1}^8 [a_k \cos(k\omega h) + b_k \sin(k\omega h)] \quad (2)$$

Where  $a_0, a_k, b_k$  are the Fourier coefficient,  $\omega$  is fundamental frequency. These parameters can be obtained by curve fitting. Its function curve and plot diagram of measured data are shown in figure 1.

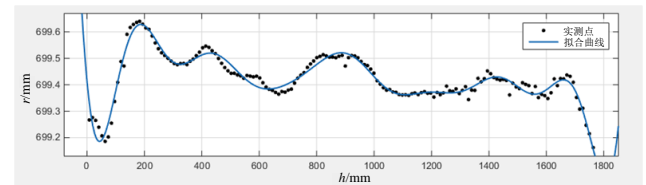


Figure 1 :comparison between fitting results and measured data

## 3. Calculation of the actual volume of gas discharged from the bell

The above volume coefficient model is a continuous function, which can be calculated by definite integral to obtain the gas volume at any height of the bell, as shown in formula (3):

$$V = \int_{h_1}^{h_2} \pi r^2 dh = \int_{h_1}^{h_2} \pi [f(h)]^2 dh \quad (3)$$

Where,  $h_1$  is the height value measured by the displacement measuring mechanism before the bell descends,  $h_2$  is the height value measured by the displacement measuring mechanism after the bell descends. The actual value of the volume of gas discharged at any point in the bell is calculated.

As shown in FIG. 2, the bell device has a liquid level balancing mechanism, which is characterized by the liquid level remaining unchanged during the bell descending process. Let the difference between the indicating position of the displacement measuring mechanism and the internal liquid level be  $h_c$ . The bell descends to discharge gas, the actual height corresponding to the volume of this gas is  $h'_1$  to  $h'_2$ , however, the height measured by the displacement measuring mechanism is  $h_1$  to  $h_2$ . The bell descends from initial position  $h_1$  to final position  $h_2$ , the volume

of the gas in the bell at the initial position is  $V_1$ , and at the termination position is  $V_2$ . Where,  $h'_1 = h_1 - h_c$ ,  $h'_2 = h_2 - h_c$ .

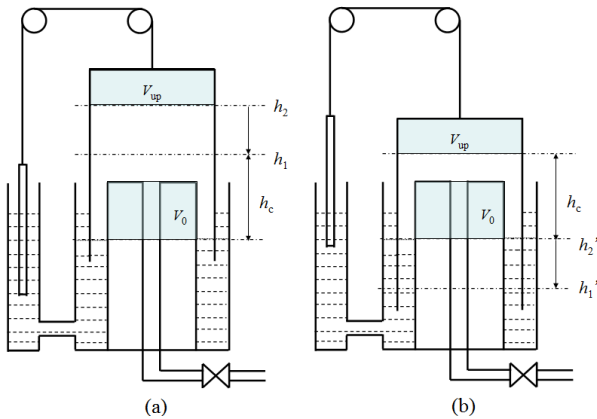


**Figure. 2:** Diagram of the corresponding heights of the volume of gas discharged when the bell prover

$$V_1 = V_{up} + \pi \int_{h_1}^{h_2} f^2(h)dh + \pi \int_{h'_1}^{h_1} f^2(h)dh - V_0 \quad (4)$$

$$V_2 = V_{up} + \pi \int_{h'_2}^{h_2} f^2(h)dh - V_0 \quad (5)$$

During this descent, the volume of the gas discharged from the bell is:

$$\begin{aligned} V_D &= V_1 - V_2 \\ &= \pi \int_{h_1}^{h_2} f^2(h)dh + \pi \int_{h'_1}^{h_1} f^2(h)dh - \pi \int_{h'_2}^{h_2} f^2(h)dh \\ &= \pi \int_{h_1}^{h_2} f^2(h)dh + \pi \int_{h'_2}^{h'_1} f^2(h)dh + \pi \int_{h'_1}^{h_1} f^2(h)dh \\ &\quad - \pi \int_{h'_2}^{h_2} f^2(h)dh - \pi \int_{h_1}^{h_2} f^2(h)dh \\ &= \pi \int_{h'_1}^{h'_2} f^2(h)dh = \pi \int_{h_1-h_c}^{h_2-h_c} f^2(h)dh \quad (6) \end{aligned}$$

It can be seen from this that the actual value of the gas volume corresponding to the falling height of the bell measured by the displacement measuring mechanism is the inner volume corresponding to the downward translation  $h_c$  at this height.

#### 4. Discussion and Conclusion

For the low precision bell prover, its volume coefficient is a constant and has nothing to do with the starting and stopping position of the bell. The radius difference between the effective use segment of the bell and the volume segment below it can be ignored and only the radius value of the effective use segment can be calibrated<sup>[7]</sup>. For the high precision bell prover, it can be seen from formula (6) that the volume value of the discharged gas is closely related to the starting and stopping position of the bell and the difference of the indicating position of the

displacement measuring mechanism and the internal liquid level. Similarly, the volume coefficient in the form of piecewise function has the same problem. In bell prover calibration, besides calibrating the effective usage section, the lower section should be also calibrated to obtain the complete data group, so that the  $f(h)$  containing  $h_c$  can be fitted effectively.

#### References

- [1] John D.Wright and George E.Mattingly.NIST Calibration Services for Gas Flow Meters Piston Prover and Bell Prover Gas Flow Facilities[R].Gaithersburg:National Institute of Standards and Technology,1998.
- [2] Li Xu, CUI Li-shui, MENG tao, et al. A new method for calibrating bell jar gas flow standard device based on dimension method [J]. Metrology technology,2008(9) : 42-45.
- [3] XING Jing-fang, BI Li-xin, NIU Li-na, et al. Uncertainty analysis of standard gas flow device with 0.1 class bell jar [J]. Metrology technology,2014(4) : 71-73.
- [4] LIU Yi-ping, SONG Jin, XU Yao, et al. Measurement method of internal volume of bell jar gas flow standard device [J]. Acta metrology sinica,2016,37(6):615-618.
- [5] GAN Xiao-chuan. Camera calibration and length measurement error calibration in digital close-range photogrammetry system [D]. Beijing: China institute of metrology,2012.
- [6] XIE De-you. Simulation model verification method based on curve fitting [J]. Journal of guizhou university (natural science edition),2014,31(4):18-20.
- [7] LIU Chen-kui,QU Hong-qiang, CHEN Shi-yan, et al. Study and establishment of the mathematical model of the standard volume of the bell prover [J]. Acta metrology sinica, 2008,39(6):874-877.
- [8] WANG Zi-he, FAN Zhen. Gas flow standard device: revised edition [M]. Beijing: China metrology press,2005:48-53.

# Performance study in fuel dispensers in the field of volume measurements

**E. Batista, M. Condeço, A. Almeida, J. Alves e Sousa, I.I Godinho**

*Instituto Português da Qualidade, I.P., Caparica, Portugal*

*E-mail: ebatista@ipq.pt*

---

## Abstract

Like any type of measuring instruments used for commercial transactions, fuel dispensers, commonly known as petrol pumps, are submitted to metrological control in order to assure consumer protection and provide society in general and citizens in particular the guarantee of accurate measurements, the verification being directly linked with the volume measurement of the delivered fuel.

In Portugal, the fuel dispenser approved under the MID is subject to metrological control in service taking into account its annual verification by the verification bodies, following the procedures defined by IPQ, according to specific national regulations.

Presently there are 45 000 hoses of the fuel dispensers in Portugal, verified by several verification bodies equally distributed in the national territory.

In order to evaluate the influence factors in volume error determination of fuel dispensers, a study using standard test measures of different type, materials and volume was designed and implemented. The uncertainty of the volume determination according to the GUM methodology was evaluated, considering different atmospheric conditions, volume variation over time, different fuel types and determination of error the in different types of standard test measures.

There was some difference in performance and error determination when using different standard test measures, but in all implemented tests, the maximum permissible error was not exceeded.

The results allowed simplifying the internal procedure while maintaining the accuracy of results.

---

## 1. Introduction

Metrological verification of some measuring instruments, such as petrol pumps (SMDCs), water meters, meters for liquids other than water, gas meters and fluid storage tanks is directly related to volume measurement.

In particular, with respect to SMDCs, it is necessary to use appropriate methods and standards for the determination of the volume of these measuring instruments subject to metrological control [2], [3], to guarantee the accuracy of the measurements.

The graduated standards capacity (RVG) measures between 2 L and 50 L, with removable scale, are the standards used in determining the volume of SMDCs. These measures have suffered over time a technical evolution evidenced both by a better resolution and by the type of material with which they are constructed.

The calibration of the RVG may be carried out by the gravimetric method, according to ISO 4787 [4], or by the volumetric method, using the procedure described in the EURAMET cg - 21 [5] guide, depending on the accuracy of the required measurement and uncertainty.

The SMDCs are subject to annual legal metrological control, carried out by entities recognized and qualified by the Portuguese Institute for Quality (IPQ), using calibrated volume standard measures and the IPQ Technical Procedure PT1039107501. The metrological control of these measuring instruments is defined in the Ordinance n.º 19/2007 [6], with a maximum permissible error (MPE) of 0,5 % for these instruments .

## 2. Experimental conditions and equipment

In this experimental study, a SMDC from ABA CODEISA was chosen with resolution of 0,01 L.

The tests were conducted in the south of Portugal, mainly in Almodôvar.

Three types of standard test measures were used to determine the error of the SMDC. Two types of RVG were made of carbon fiber - CFX (Fig.1a) and PWLite (Fig.1b) and one made of Stainless Steel (Fig.1c). The tests were performed at 20 L and 5 L.



**Figure 1:** a) on the left a CFX standard test measure, b) on the centre a PWLite measure and c) on the right a Stainless Steel measure.

The environment conditions of the tests are described in table 1.

**Table 1:** Environmental conditions of the tests

	May 2017	November 2017	January 2018
<b>Air temperature (°C)</b>	30	16	16
<b>Humidity (%)</b>	35	27	65
<b>Gasoline temperature (°C)</b>	25	20	16
<b>Diesel temperature (°C)</b>	25	22	17

## 5. Volume and uncertainty calculation

The equation used to determine volume of the SMDC at 20 °C is as follows:

$$V_{20} = V_t [1 + \gamma(20 - t)] \quad (1)$$

Where,  $\gamma$  is the coefficient of the cubic thermal expansion of the RVG and  $t$  is the temperature of the liquid test.

The uncertainty components associated with the volume determination of the fuel dispensers are:

- uncertainty of RVG;
- RVG resolution;
- SMDC resolution;
- uncertainty in reading the meniscus;
- liquid temperature;
- expansion of material of the RVG.

The uncertainty component with the greatest influence on the determination of the volume of SMDCs is the resolution of the measuring instrument (SMDC). In the case of PWLite and Stainless Steel equipment, the resolution of the RVG and the value of its calibration are also relevant.

## 6. Results

In order to verify the influence of factors such as environmental conditions (air temperature and humidity), fuel temperature, evaporation and fuel type in the measurement of volume of SMDC, were performed the following tests:

- determination of the SMDC error at different atmospheric conditions, in different months of the year (reproducibility);
- determination of the repeatability of the assay, with different types of RVG;
- determination of volume variation over time (evaporation study).

In the evaluation of results, a significant variation is considered if when comparing the obtained errors they are outside of the uncertainty of each test.

The error indicated in the following figures is obtained by the difference between the read value in the RVG scale and its nominal value.

For the repeatability values, each point corresponds to only one test.

### 6.1 Reproducibility tests results

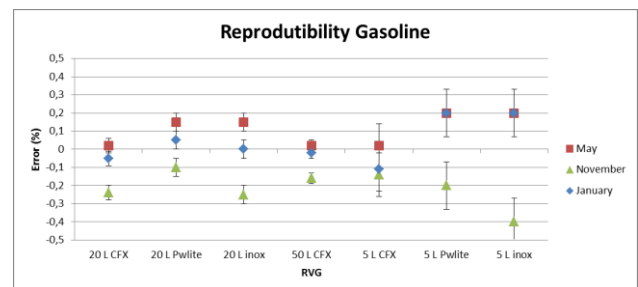


**Figure 2:** Reproducibility values for gasoline.

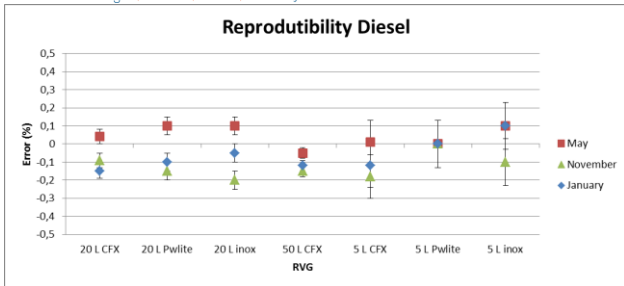


**Figure 3:** Reproducibility values for diesel

When analyzing the results it can be observed that the values obtained in November for gasoline are visibly lower than in other months since it was very windy, which caused a higher rate of evaporation and therefore a lower volume. With diesel, this effect is not so pronounced.

### 6.2 Repeatability tests

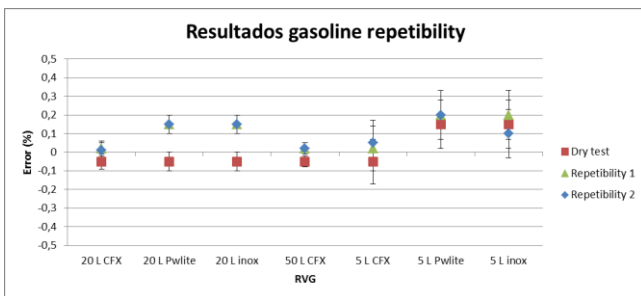


**Figure 4:** Repeatability values for gasoline

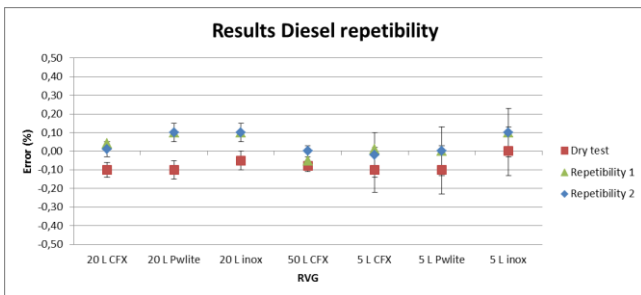


**Figure 5:** Repeatability values for diesel

From the previous figures, it can be verify that there is only some variation between the dry and the wet results obtained in the tests of the 20 L stainless steel and PwLite RVG. The consecutive repeatability tests with wet RVG do not show any variability in the results, for both diesel and gasoline.

### 6.3 Volume variation with time and temperature test (evaporation study)

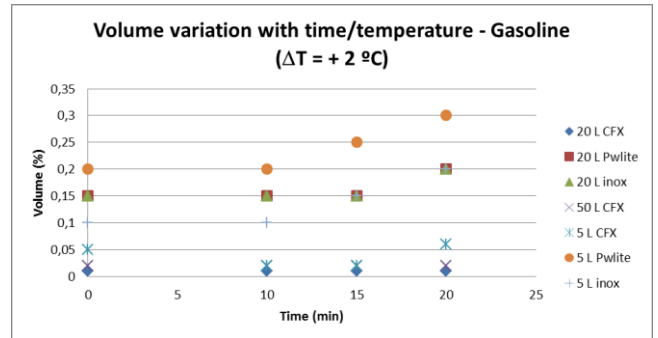


**Figure 6:** Volume variation with time and temperature for gasoline

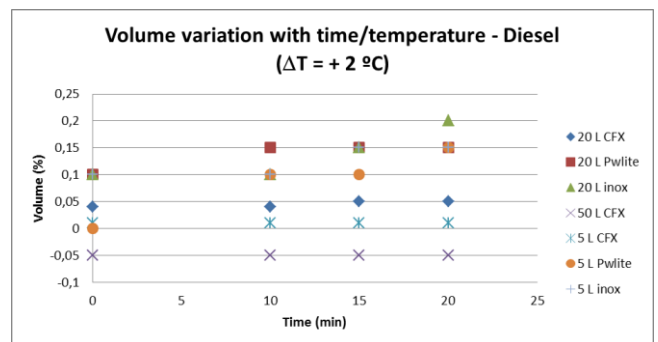


**Figure 7:** Volume variation with time and temperature for diesel

During the evaporation study for the two fuels, the liquid temperature increased by 2 °C in 20 minutes. There is also an increase in the volume of gasoline and diesel, especially in stainless steel and PwLite RVG, which is due to their open neck characteristics, which means that they are more subject to variations in atmospheric conditions. The fact is that an increase in volume with temperature results from the expansion of the liquid ( $0.0009 \text{ } ^\circ\text{C}^{-1}$ ) which is much higher than the expansion of the material ( $0.000001 \text{ } ^\circ\text{C}^{-1}$  for carbon fiber and  $0.000048 \text{ } ^\circ\text{C}^{-1}$  for stainless steel).

## 7. Conclusion

Several performance tests were affected on the same petrol pump, in different months, using standard test measures with different characteristics. The objective of this study was to verify the influence factors in the determination of volume that should be considered relevant in the metrological verification of SMDC.

By the analysis of the obtained results, it was verified that the RVG CFX is not affected by any change in the type of liquid used, temperature or test, dry or wet.

No significant differences were identified between consecutive repeatability tests in wet RVG, even with liquid temperature variations above 0,5 °C.

It was concluded that, for air temperature values between 16 °C and 30 °C and for humidity values between 27 % and 65 %, in no case the maximum permissible error of the SMDCs (0,5 %) was achieved and therefore no rejection of result was obtained.

In the evaporation test some variation in volume was observed, especially for gasoline in the stainless steel and PWLite RVG, which is due to their open neck characteristics. However, evaporation or condensation of liquid, where relevant, only occurs after 5 minutes (operator cannot be expected to wait 5 minutes to read the meniscus).

The study of volume variation over time revealed that in very windy situations the results obtained are much smaller. There are also some situations of increase or decrease of volume with temperature due to the expansion of the liquid, and in the case of diesel, the volume variation with the atmospheric conditions is not so significant.

It was also established that no case exceeded the maximum permissible error of the SMDC, 0,5 %, than meaning that the verified SMDC would be approved at any time of the year, regardless of the atmospheric conditions or RVG used.

## References

- [1] PT IPQ 1039107501-03, Metrological control- Petrol pumps.
- [2] Decree-Law n.º 291/90, of 20 of September.
- [3] Ordinance n.º 962/90, of 9 of October.
- [4] ISO 4787 (2011) - Laboratory glassware -- Volumetric instruments -- Methods for testing of capacity and for use.
- [5] Calibration Guide EURAMET cg - 21 - Guidelines on the Calibration of Standard Capacity Measures Using the Volumetric Method, version 1.0, 2013;
- [6] Ordinance n.º 19/2007, of 5 de January.

# Orifice Meter Diagnostics – Predicting the Magnitudes of Flow Prediction Biases

R Steven<sup>1</sup>, K Lewis<sup>2</sup>

<sup>1</sup>DP Diagnostics, Windsor, Colorado, USA

<sup>2</sup>DP Diagnostics, Windsor, Colorado, USA  
rsteven@dpdiagnostics.com

---

## Abstract

With most modern flow meters there is a drive to equip the meter with a comprehensive verification system driven by a diagnostic suite. A diagnostic suite is a collection of different individual diagnostic checks grouped together to collectively offer more information. The state of the art is to use these diagnostic suites to show if the meter has a problem, and if so then use diagnostic suite pattern recognition to try to identify the source of the problem. However, there is virtually no R&D published that goes on to then try and predict the associated flow prediction bias induced by that identified malfunction. One such orifice meter diagnostic suite (commonly called 'Prognosis') is based on pressure field analysis. In this paper the development of Prognosis to show a problem exists, identify the source of the problem, and **then** predict the associated flow prediction bias is discussed..

---

## 1 Introduction

This paper discusses the capabilities of an orifice meter verification system. The DP Diagnostics verification system (Prognosis) uses a downstream pressure tap (e.g. see Fig 1) to access the information contained within the meter's entire pressure field. An automated system states in real time when the meter has a problem, and then by use of pattern recognition states what that problem is, or short lists the possible problems. The system is now being developed to also estimate the associated flow prediction bias of various common orifice meter malfunctions in real time.

## 2. State of the Art of Flow Meter Verification Systems

Flow meter users ask three things from the developers of flow meter diagnostic suites: 1) will indicate when something is wrong? If so, 2) will it say what is wrong? And if so, 3) will it tell the operator the associated flow prediction bias? For state of the art flow meter diagnostic suites the answers are:



Fig 1. 8", Orifice Meter with Downstream Pressure Tap.

1) The diagnostic suite needs to have at least one diagnostic test that is sensitive to the specific problem, and the problem will have to be significant enough to cross that diagnostic test's sensitivity threshold. But yes, modern diagnostic suites will indicate

a problem exists for most common malfunctions.

2) A modern flow meter diagnostic suite produces multiple individual diagnostic test results. Collating them produces a diagnostic pattern. Abnormal diagnostic patterns can be matched to common malfunctions. However, the state of the art of such techniques tends to be rudimentary. Many flow meter diagnostic results are rather ambiguous. The state of the art of flow meter diagnostic technology is hand crafted (i.e. not artificial intelligence learned) heuristic diagnostic pattern recognition. The Prognosis orifice meter diagnostic system uses automated pattern recognition to supply a list of possible common malfunctions in order of their probability. Depending on the diagnostic pattern a specific malfunction or a short list of probable malfunctions are offered.

3) Automatically identifying a particular malfunction with any flow meter's diagnostic pattern is challenging. Little to nothing has been done on the follow on task of estimating the associated flow prediction bias for a predicted malfunction.

However, it has now been realised that such a system is possible for the orifice meter verification system. In practice, most flow meter malfunctions are caused by a relatively few common singular problems, and not combinations of complex rare problems. That is, it could be claimed that there is a Pareto Principle at work, i.e. an 80/20 rule, i.e. 80% of mis-measurements come from 20% of the possible malfunction sources.

On that point, an orifice meter verification system has now been developed that can identify specific single malfunction types, or short list a few single malfunction types that can cause specific diagnostic patterns, and then assign corresponding estimated flow prediction biases to each malfunction case.

### **3 Diagnostic Suite Constituent Parts**

*In order to learn more from flow meter diagnostics it is first necessary to learn more about flow meter diagnostics.*

Before reviewing and developing the orifice meter diagnostic suite it is first beneficial to consider some fundamental facts regarding the nature of diagnostic tests.

Lord Kelvin stated: *“When you can measure what you are speaking about, and express it in numbers, you know something about it, when you cannot express it in numbers, your knowledge is of a meager and unsatisfactory kind; it may be the beginning of knowledge, but you have scarcely, in your thoughts advanced to the stage of science.”*

That insight has consequences to flow meter diagnostic suites. Flow meter diagnostic results tend to be treated as qualitative subjective information, not quantitative objective information. Nevertheless, in reality most flow meter diagnostic suites contain an assortment of subjective and objective diagnostic tests.

An objective diagnostic check is where the diagnostic result is derived from comparison with physical law, and not just comparison with intuition, opinion, or some general rule of thumb set by experience. It compares a measureable diagnostic value to a baseline fixed by physical law, thereby creating a *quantitative* objective numerical result. You *“measure what you are speaking about, and express it in numbers, and you know something about it”*. It is a clear and precise diagnostic statement. Objective diagnostic tests are useful for both measuring *absolute* changes and monitoring *relative* changes in a system's performance.

A subjective diagnostic check is where the diagnostic result is not derived from comparison with physical law, but rather comparison with intuition, opinion, or some general rule of thumb set by experience. It compares a measureable diagnostic value to an arbitrary variable baseline. With a changeable / debatable baseline such diagnostic results are not truly expressible as meaningful numbers. The ambiguous nature of this baseline produces a *qualitative* subjective result. Such subjective results are perhaps “the beginning of knowledge”, and hence valuable, but all the same, the knowledge

is of a more meagre kind. It is an ambiguous and imprecise diagnostic statement open to various interpretations. Subjective diagnostic tests are therefore really only useful for monitoring *relative* changes in instrument performance.

Hence, objective diagnostic tests tend to be more powerful, i.e. more useful, than subjective diagnostic tests. That is, *not all diagnostic tests are created equal*. Some inherently contain more useful information than others. That is not to say that subjective diagnostic tests do not have their place. They certainly do. A subjective diagnostic test is far better than no diagnostic test, and an objective test coupled with a subjective test is more useful than an objective test alone. The more distinct separate pieces of information a diagnostic suite contains, the more unique the corresponding diagnostic pattern for each malfunction, and the more conducive to successful pattern recognition it is.

However, once a malfunction has been identified by such a diagnostic pattern, in order to make a defensible accurate estimate of the corresponding flow prediction bias you *must* use objective diagnostics. With objective diagnostics offering a quantifiable absolute precise measurement, they offer a portal to calculating an associated precise flow prediction bias. Subjective diagnostics offer only relative vague results, and hence there is no way to use them to make precise numerical predictions. Therefore, for a flow meter diagnostic suite to be successfully developed such that it can state flow prediction biases for malfunctions it identifies, it will need to use the *quantitative* objective results produced from objective diagnostics as the tools.

It is important to realize that it is not possible to directly jump from stating a malfunction type to predicting an associated flow prediction bias. There is seldom discussed *vital* middle step. In order to predict the flow prediction bias associated with an identified flow meter malfunction type, it isn't good enough to just identify the *type* of malfunction, you also have to *quantify the magnitude* of that malfunction. This is the essential middle

step and it is no trivial matter. In fact, this step is the most difficult in the whole process. After the flow meter diagnostic suite identifies the type of problem it must then accurately estimate the magnitude of that problem, i.e. express it in a quantifiable / measureable way. Only when the magnitude of the malfunction is expressible in numbers are you in a position to then make quantifiable predictions about its effects.

Finally, before reviewing the existing orifice meter diagnostics system and then developing it, it is necessary to make two further comments regarding the nature of objective diagnostic tests:

First, in practice no diagnostic test is *truly* objective. All measured values include instrumentation reading uncertainties. The stated instrument uncertainties are by their nature subjective. Hence, in practice even theoretically objective diagnostic tests have an element of subjectivity. Nevertheless, in practice this is not problematic. The influence on the theoretical objective results of the instrument uncertainties is small, and often trivial. There is still clearly two sets of diagnostic tests, i.e. objective tests based on the theory of physical law, and subjective tests that are not.

Secondly, calibrated diagnostic parameter values known to be reproducible from laboratory to the field can be used to practically create objective diagnostic tests. This is the application of a key axiom in science, paraphrased as: '*Whatever is true of everything we've seen here and now is true of everything everywhere in the future*'. If the same flow meter remains effectively physically unchanged, and the installation between the calibration and field application is effectively the same, then the flow meter's performance across the same calibration and field flow conditions should remain unchanged. Such calibration values are therefore valid baselines, and any measured change in performance is therefore, from a practical standpoint, an objective result. However, this is only true of *reproducible* calibration results. Due to inevitable various subtle installation and flow condition differences not all calibrated

parameters are reproducible in the field. Only calibration parameters that are truly reproducible, i.e. transferable to the field, can be used for objective diagnostic tests.

Let us now review the orifice meter diagnostic suite before applying these principles to the task of quantifying the magnitude of malfunctions, and thereby estimating the flow meter's associated flow prediction bias.

### 5. Orifice Meter Diagnostic Suite 'Prognosis' Composition Review

Figure 2 shows a simplified sketch of an orifice meter with instrumentation and the pressure field through the meter body. There is an extra (3<sup>rd</sup>) pressure port 6D downstream of the plate. As shown in Fig 2, this allows the reading of not just the traditional DP ( $\Delta P_t$ ), but also the recovered DP ( $\Delta P_r$ ), and the permanent pressure loss DP ( $\Delta P_{PPL}$ ). Traditional orifice meter installations only read a single 'traditional' DP,  $\Delta P_t$ . The extra information contained in the pressure field was traditionally ignored. The diagnostic system uses these three DPs to monitor the whole pressure field and extract significantly more information about the flow and meter performance than the traditional orifice meter system.

$$\Delta P_t = \Delta P_r + \Delta P_{PPL} \quad (1)$$

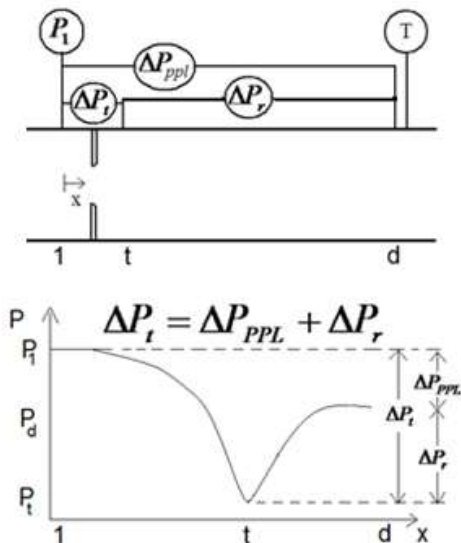


Fig 2. Orifice Meter with Instrumentation and Pressure Field Schematic.

Equation 1 (and Fig 2) shows the simplicity of the DP relationships. Any one of these three DPs can be inferred from the other two. The sum of the recovered and PPL DPs gives an inferred traditional  $\Delta P$  ( $\Delta P_{t,inf}$ ). This inferred traditional  $\Delta P_{t,inf}$  should equal the read value. However, there are uncertainties to each DP reading, and hence the allowable difference between the inferred and read  $\Delta P_t$  values is denoted as uncertainty  $\theta\%$ . The actual percentage difference is denoted as  $\delta\%$  (see equation 2).

$$\delta\% = ((\Delta P_{t,inf} - \Delta P_t) / \Delta P_t) * 100\% \quad (2)$$

*This is an objective diagnostic test based on a known physical reality, and not just intuition, opinion, or some general rule of thumb set by experience.*

Traditional / Primary Flow Equation:

$$m_t = \frac{A\beta^2}{\sqrt{1-\beta^4}} \varepsilon C_d \sqrt{2\rho\Delta P_t}, \pm x\% \quad (3)$$

Expansion Flow Equation:

$$m_r = \frac{A\beta^2}{\sqrt{1-\beta^4}} K_r \sqrt{2\rho\Delta P_r}, \pm y\% \quad (4)$$

PPL Flow Equation:

$$m_{ppl} = AK_{PPL} \sqrt{2\rho\Delta P_{PPL}}, \pm z\% \quad (5)$$

Traditionally, there is a single DP meter flow rate calculation based on the traditional (i.e. primary)  $\Delta P_t$  reading, i.e. equation 3. However, the additional two  $\Delta P$ s give two extra flow prediction calculations, i.e. the expansion meter based on the recovered  $\Delta P_r$  reading (equation 4) and PPL meter based on the  $\Delta P_{PPL}$  reading (equation 5). Note that  $m_t$ ,  $m_r$ , and  $m_{PPL}$  represent the traditional primary, expansion and PPL mass flow rate equation predictions respectively. The symbols  $\rho$  and  $\varepsilon$  represents the inlet fluid density and gas expansibility. Symbols  $A$  and  $\beta$  represent the inlet area and the beta respectively. Beta is a geometric constant for a given orifice meter, and is calculated by equation 6, where  $A_t$ ,  $d$ , and  $D$  denote the orifice area, orifice diameter and inlet diameter respectively.

$$\beta = \sqrt{A_t / A} = d / D \quad (6)$$

The terms  $C_d$ ,  $K_r$ , and  $K_{PPL}$  represent the discharge coefficient, the expansion coefficient, and the PPL coefficient respectively. Whereas these coefficients can be found by calibration, standard orifice meters tend to not be calibrated. Hence, they have to be derived from the standards. ISO 5167-2 [1] offers the Reader-Harris Gallagher (RHG) discharge coefficient prediction (see equation 7), which is a function of beta and Reynolds number (see equation 8) where  $\mu$  denotes fluid viscosity:

$$C_d = f(\beta, Re) \quad (7)$$

$$Re = 4m/\pi\mu D \quad (8)$$

ISO 5167 also offers a prediction for the Pressure Loss Ratio, 'PLR' (i.e. the ratio  $PLR = \Delta P_{PPL}/\Delta P_t$ ). This ISO equation links the orifice meter PLR to the beta and discharge coefficient, i.e.  $PLR = f(\beta, C_d)$ . However, this theoretical equation's assumptions become less valid as beta increases, and the discharge coefficient influence is known to be a second order effect. Hence, there are now  $PLR = f(\beta)$  data fits to predict the base line PLR:

$$PLR_{base} = f(\beta) \quad (9)$$

It can then be shown, that the expansion ( $K_r$ ) and PPL ( $K_{PPL}$ ) coefficients are derivable without calibration from the ISO  $C_d$  and selected PLR predictions, i.e.:

$$K_r = (\epsilon C_d) / \sqrt{1 - PLR_{base}} \quad (10)$$

$$K_{PPL} = (\beta^2 / \sqrt{1 - \beta^4}) \cdot ((\epsilon C_d) / \sqrt{1 - PLR_{base}}) \quad (11)$$

Orifice meters with a downstream pressure tap are in effect three flow meters. All three flow coefficients are considered reproducible in the field and can be used to produce objective tests. Furthermore, the physical law of conservation of mass dictates that these three mass flow rate predictions should be the same. Hence, the inter-comparison of any two of the three mass flow rate predictions is an objective diagnostic check. There are three pairs of flow rate predictions, hence three objective diagnostic tests.

Equations 12, 13, and 14 show the respective pair's flow rate comparison. Naturally these mass flow predictions have

associated uncertainties induced by DP reading, flow coefficient prediction uncertainties etc.. Let us introduce these uncertainties as  $x\%$ ,  $y\%$  &  $z\%$  for the traditional, expansion, and PPL meters respectively. By convention, a correctly operating meter will have no difference between any two flow equations greater than the root sum square of the two uncertainties. The maximum allowable difference between any two flow rate equations, i.e.  $\Phi\%$ ,  $\xi\%$ , and  $v\%$  is shown in equation set 15 thru 17.

Primary to PPL Meter Comparison :	
$\psi\% = [(m_{PPL} - m_i)/m_i] * 100\%$	(12)

Primary to Expansion Meter Comparison:	
$\lambda\% = [(m_r - m_i)/m_i] * 100\%$	(13)

PPL to Expansion Meter Comparison:	
$X\% = [(m_r - m_{PPL})/m_{PPL}] * 100\%$	(14)

Primary/PPL Meter allowable difference:	
$\Phi\% = \sqrt{(x\%^2) + (z\%^2)}$	(15)

Primary/Expansion Meter allowable difference:	
$\xi\% = \sqrt{(x\%^2) + (y\%^2)}$	(16)

Expansion/PPL Meters allowable difference:	
$v\% = \sqrt{(y\%^2) + (z\%^2)}$	(17)

Equation 1 can be re-written as equation 1a. Hence, for any given PLR there are corresponding Pressure Recovery Ratio ( $PRR = \Delta P_r / \Delta P_t$ ), and Recovered to PPL DP Ratio ( $RPR = \Delta P_r / \Delta P_{PPL}$ ) values. The PLR, and hence the PRR and RPR, are characteristics of any given DP meter. These DP Ratios can be found by calibration, but as orifice meters are not typically calibrated they can be found by use of the chosen  $PLR = f(\beta)$  relationship. That is, derive the correct 'baseline' PLR ( $PLR_{base}$ ) from equation 9 and then apply equations 18 and 19 to derive the corresponding  $PRR_{base}$  and  $RPR_{base}$  baselines respectively. These predictions of PLR, PRR, and RPR have assigned uncertainties of  $a\%$ ,  $b\%$ , and  $c\%$  respectively.

$$(\Delta P_r / \Delta P_t) + (\Delta P_{PPL} / \Delta P_t) = PLR + PRR = 1 \quad (1a)$$

$$PRR_{base} = 1 - PLR_{base} \quad (18)$$

$$RPR_{base} = (1 - PLR_{base}) / PLR_{base} \quad (19)$$

All three DP ratio predictions are based on historical massed orifice meter calibration PLR results, and are considered transferable from the laboratory to the field. Hence, *these DP ratio parameters produce objective diagnostic checks*. The measurable quantities  $\alpha\%$ ,  $\gamma\%$ , and  $\eta\%$  represent the quantifiable difference between measured and baseline DP ratios (see equations 20 thru 22).

PLR test: $\alpha\% = [(PLR_{read}/PLR_{base}) - 1] * 100\%$ (20)
PRR test: $\gamma\% = [(PRR_{read}/PRR_{base}) - 1] * 100\%$ (21)
RPR test: $\eta\% = [(RPR_{read}/RPR_{base}) - 1] * 100\%$ (22)

The DP meter diagnostic display is conducive for hand crafted heuristic diagnostic pattern recognition. These seven diagnostic checks can be denoted as four points on a graph.

For the $DP_t$ and $DP_{PPL}$ pair: $x_1 = \psi\%/\phi\%$ and $y_1 = \alpha\%/a\%$
For the $DP_t$ and $DP_r$ pair: $x_2 = \lambda\%/\xi\%$ and $y_2 = \gamma\%/b\%$
For the $DP_{PPL}$ and $DP_r$ pair: $x_3 = X\%/\nu\%$ and $y_3 = \eta\%/c\%$
For the $DP_t$ and $DP_{t,inf}$ pair: $x_4 = \delta\%/\theta\%$ and $y_4 = 0\%$

Table 1 shows the individual objective diagnostic test results within the suite that would or would not create a warning. Each of the seven diagnostic tests has *normalized data*, i.e. each diagnostic parameter percentage difference output is divided by the allowable percentage difference for that parameter.

Figure 3 shows the standard DP meter diagnostic suite display. Considering Table 1, with all seven diagnostic coordinates within the normalized diagnostic box ('NDB') no meter malfunction is found. But one or more diagnostic coordinate/s outside of the NDB indicates a warning. Furthermore, when a warning is shown, i.e. one or more point/s are outside the NDB, the position of all

four points set by the seven diagnostic coordinates, i.e. the 'diagnostic pattern', gives information to what the source of the problem is. Skelton [2] describes the methodology in considerably more detail.

DP Pair	No Warning	WARNING	No Warning	WARNING
$\Delta P_t$ & $\Delta P_{PPL}$	$-1 \leq x_1 \leq +1$	$-1 > x_1$ or $x_1 > +1$	$-1 \leq y_1 \leq +1$	$-1 > y_1$ or $y_1 > +1$
$\Delta P_t$ & $\Delta P_r$	$-1 \leq x_2 \leq +1$	$-1 > x_2$ or $x_2 > +1$	$-1 \leq y_2 \leq +1$	$-1 > y_2$ or $y_2 > +1$
$\Delta P_{PPL}$ & $\Delta P_r$	$-1 \leq x_3 \leq +1$	$-1 > x_3$ or $x_3 > +1$	$-1 \leq y_3 \leq +1$	$-1 > y_3$ or $y_3 > +1$
$\Delta P_{t,read}$ & $\Delta P_{t,inf}$	$-1 \leq x_4 \leq +1$	$-1 > x_4$ or $x_4 > +1$	N/A	N/A

Table 1. The DP Meter Diagnostic Results.

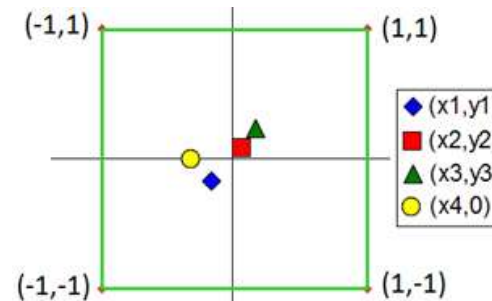


Fig 3. Normalized Diagnostic Box (NDB) Display.

These seven orifice meter objective quantifiable diagnostic tests could be described as constant parameter 'static' diagnostic tests, meaning the parameters used discount any small statistical dynamic variations and average them out. Such tests tend to be reproducible from calibration laboratory to field, and produce objective quantitative diagnostic tests. However, there are also subjective qualifiable diagnostic tests that could be described as variable parameter 'dynamic' statistical diagnostic tests, meaning the parameters used specifically monitor dynamic variations. Such tests tend not to be reproducible from calibration to field, and produce subjective qualitative diagnostic tests.

There is such a test for orifice meters, i.e. an 8<sup>th</sup> orifice meter diagnostic test. This test, the exacting analysis of the DP signal and corresponding diagnostic parameter dynamic behaviour, is a dynamic subjective diagnostic test where a variable parameter is monitored. It is described by Rabone et al [3]. In truth, there are multiple analytical techniques for monitoring dynamic behaviours, so it could be argued that there are multiple orifice meter subjective diagnostic tests, but we will consider them all under one umbrella term here.

Fluctuation of primary signals is not easily predictable by physical law, and such calibration data is not generally transferable from calibration laboratory to the field. Small installation peculiarities and the secondary flow conditions, e.g. flow pulsation from compressors, light pipe vibration, slight disturbance from upstream components etc., can vary these parameters in subtle unpredictable ways. Hence, this subjective diagnostic test is useful specifically for trending an in-service meter's instrumentation output over time only. It is not included in the orifice meter output display (Fig 3) but it is accounted for in the background pattern recognition capabilities.

Diagnostic Check	Type
PPL to Traditional Mass Flow Comparison ( $x_1$ )	objective
Recovered to Traditional Mass Flow Comparison ( $x_2$ )	objective
Recovered to PPL Mass Flow Comparison ( $x_3$ )	objective
PLR Shift from Calibrated Baseline ( $y_1$ )	objective
PRR Shift from Calibrated Baseline ( $y_2$ )	objective
RPR Shift from Calibrated Baseline ( $y_3$ )	objective
DP Summation Integrity Check( $x_4$ )	objective
DP Reading and DP Ratio Standard Deviation Shifts	subjective

Table 2. Orifice Meter Diagnostic Tests Objective / Subjective Designation.

Table 2 shows the eight orifice meter diagnostic tests. It is the diagnostic pattern produced by these eight tests that is used

for pattern recognition. For all there is only a single subjective diagnostic test in the diagnostic suite it is a very useful addition for pattern recognition. For example, wet gas flow, a blocked impulse line, and erroneous high orifice diameter keypad entry all produce the same *average* diagnostic pattern. However, this subjective test on the instrumentation dynamic behaviour separates the erroneous geometry from the other two possibilities. An erroneous geometry use has normal DP signal variation. However, the other two possibilities do not. The subjective diagnostic can then further separates the blocked impulse line and wet gas flow options. Wet gas flow causes short period / low amplitude  $\Delta P$  fluctuation, while a blocked impulse line causes long period / high amplitude  $\Delta P$  fluctuation. Figure 4 is a schematic pictorially showing the difference. Hence, the subjective diagnostic family of analytical tests is very useful indeed for pattern recognition.

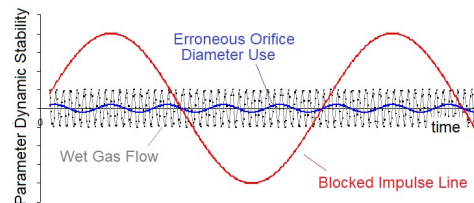


Fig 4. Orifice Meter Parameter Stability (Subjective Diagnostic Test) for Three Different Malfunction Sources.

A flow meter having eight diagnostic checks where seven are objective diagnostic checks is unusual. Other meter designs have more of an objective / subjective mixture in their respective diagnostic suites. As way of an example the Appendix shows such an analysis on the well documented ultrasonic meter diagnostic suite, where out of a total seven tests one is objective, two are arguably objective, and four are subjective. Nevertheless, as Aristotle stated "the whole is greater than the sum of its parts". We will see in Section 7 via worked examples that the sum of these orifice meter objective and subjective diagnostic tests together produce a diagnostic suite where the pattern recognition can identify a specific malfunction, or at least give a short list of a few possible malfunctions.

However, it is now time to discuss how such a system can be developed to not just indicate a problem exists, and suggest what that problem probably is, but also estimate the magnitude of that problem, and therefore what the associated flow prediction bias will therefore.

## 6. Estimating Flow Biases

Presently there are a few limited sporadic academic publications that discuss in a quantitative way how select orifice meter malfunctions affect the meters flow prediction. These publications show data on the graduating scale of a specific problem vs. the associated induced flow rate prediction bias. However, in order to use this information an orifice meter operator would need to know the meter has a malfunction, and what the specific type and severity of that malfunction was.

An orifice meter diagnostic system that could indicate something was wrong, then what specifically was wrong, and then what the magnitude of that malfunction was, and then estimate the corresponding flow prediction bias, would be beneficial. Such an automated system would mean the flow prediction bias could be estimated in real time with the meter in-situ, i.e. without the meter having to come off line for maintenance.

The combination of both objective and subjective diagnostic tests produce a diagnostic suite for which pattern recognition can be applied. For this task subjective diagnostics are valuable and useful. However, when moving on to *quantifying* the magnitude of an identified problem a quantifiable (i.e. an objective) diagnostic technique *must* be used.

Fig 5 shows how a meter diagnostic suite can estimate a malfunction's magnitude and associated flow prediction bias. For each common malfunction two relationships must be known. Firstly, for each malfunction, one or more of the quantifiable objective diagnostic test results must be relatable to the magnitude of that malfunction (see upper graph). Secondly, the magnitude of malfunction must be relatable to the flow prediction

bias (see lower graph). Then the objective test result is related to the flow prediction bias.

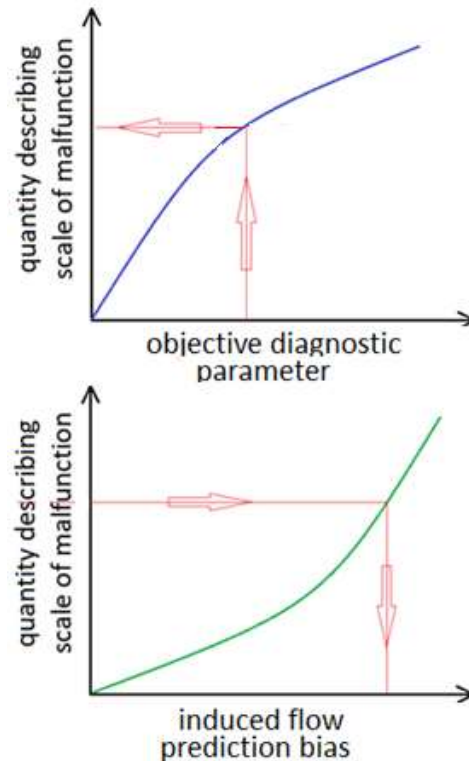


Fig 5. Diagnostic System Malfunction Magnitude and Associated Flow Prediction Bias Estimation.

DP Diagnostics has gathered various common malfunction orifice meter data from various laboratories, field tests, and actual service meters. DP Diagnostics has now developed the system to estimate the magnitude of various identified malfunctions and the corresponding flow prediction bias. The following worked examples help explain the concept, and the surprising simplicity of the method.

## 7. Worked Examples

### 7.1 Erroneous DP Readings

Fig 6 shows a serviceable 10", 0.46 $\beta$ , orifice meter. Fig 7 shows this meter's diagnostic display. A slight leak on the primary (DP<sub>1</sub>) DP transmitter's 5 way manifold equalization valve was then deliberately introduced.

Fig 8 shows the resulting diagnostic pattern. Traditionally a problem with the DP reading/s would go un-noticed, but the diagnostic suite now indicates a problem, and specifically indicates an erroneous primary (traditional) DP reading as the malfunction source. That is, one or more point/s outside the box indicates something is wrong. The  $x_4$  point shows the issue is with the DP transmitters. The remaining



Fig 6. 10", 0.46β Orifice Meter with an Installed Diagnostic System.

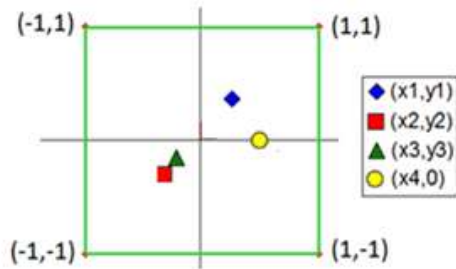


Fig 7. 10" Orifice Meter Diagnostic Result of Correctly Operating System.

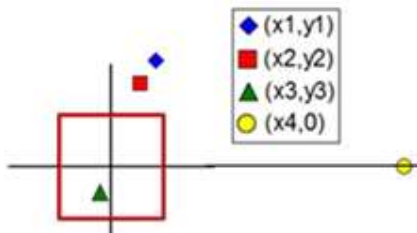


Fig 8. 10" Orifice Meter Diagnostic Result with Erroneous  $\Delta P_t$  Reading..

pattern shows  $(x_3, y_3)$ , i.e. the recovered and PPL DP readings, have no problem. The two points  $(x_1, y_1)$  and  $(x_2, y_2)$  are both outside the NDB and their communal DP transmitter is that reading the primary (traditional) DP. Hence this DP reading is erroneous. But how erroneous?

Select objective diagnostic  $x_4$  which is based on the physical relationship of the

three DPs as described by equation 1. The diagnostic pattern showed that  $\Delta P_r$  and  $\Delta P_{PPL}$  are trustworthy. Hence this objective diagnostic shows that the inferred  $\Delta P_{t,inf} = 64.56''WC$  is correct and can therefore be compared to the directly read (and known to be erroneous)  $\Delta P_t = 61.08''WC$ . Thus, the objective diagnostic test tells us that the direct  $\Delta P_t$  reading has a quantifiable -5.4% bias.

$$p\% = \left\{ \left( \frac{m_{t,bias}}{m_{t,correct}} \right) - 1 \right\} * 100\%$$

$$\approx \left\{ \sqrt{\frac{\Delta P_{t,read}}{\Delta P_{t,inf}}} - 1 \right\} * 100\% \quad (23)$$

Equation 23 shows the associated gas flow prediction bias ( $p\%$ ), calculation. In this example the bias is found to be -2.7%. Figs 9 and 10 show the relationship between the objective diagnostic 'x4' vs. Malfunction Quantity vs. Flow Prediction Bias.

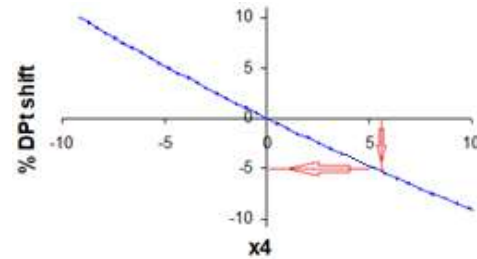


Fig 9. Meter Objective Diagnostic vs.  $\Delta P_t$  Reading Bias

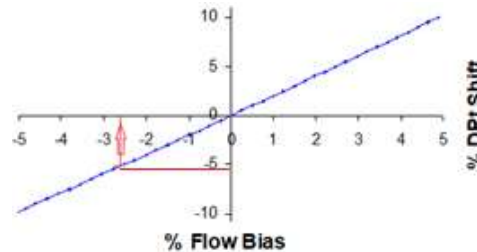


Fig 10.  $\Delta P_t$  Reading Bias vs. Flow Prediction Bias.

Alternatively, as the diagnostic pattern recognition has identified  $\Delta P_r$  and  $\Delta P_{PPL}$  as correctly read, the correct mass flow rates can be predicted by equations 4 and 5 respectively. This can be compared to

the meter's erroneous flow rate output to derive the bias  $\approx -2.7\%$ .

In this DP reading error example the problem is caused by a leaking valve on the DP transmitter manifold. However, the same principle holds for any source of DP reading error, e.g. when a DP transmitter is over-ranged (i.e. 'saturated'), drifting, wrongly calibrated, etc.

## 7.2 Erroneous Orifice Diameter

A potential problem with orifice meters is erroneous keypad entry geometries to the flow computer. Traditionally this goes unnoticed, but the use of an orifice meter diagnostic suite can now warn of a problem, and offers a short list of possible causes that includes 'erroneous orifice diameter'.

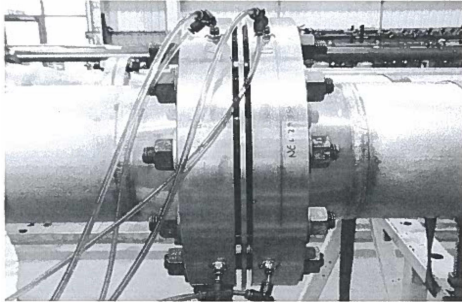


Fig 11. 4", 0.6 $\beta$  Orifice Meter

A 4", sch 40, 0.6 $\beta$  paddle plate orifice meter was tested at a water flow facility (see Fig 11). Inlet and orifice diameters were 4.026", and 2.416" respectively. Flow was 19.42 kg/s with  $DP_t = 51.54\text{kPa}$ ,  $DP_r = 18.75\text{kPa}$  and  $DP_{PPL} = 32.74\text{kPa}$ . This produced a read PLR of 0.6363, an ISO  $C_d$  prediction of 0.607, and a PLR baseline prediction of 0.635. The flow prediction and reference agreed to  $<0.5\%$ , i.e. the orifice meter was serviceable.

Consider the case where the orifice diameter was erroneously entered as 2.516". Fig 12 shows the diagnostic suite's response for the correct geometry. Fig 13 shows the response for the erroneous orifice diameter. The pattern is indicative of a few possible malfunction sources, but excludes all other malfunction sources. The DP integrity check  $x_4$  shows the DP readings are trustworthy. An

erroneous high orifice diameter entry is one of the few possible sources that can produce this diagnostic pattern.

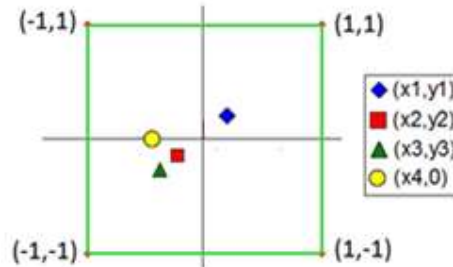


Fig 12. Correctly Operating Orifice Meter

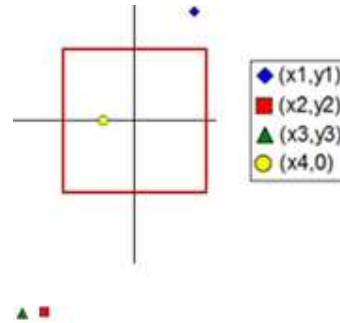


Fig 13. High Orifice Diameter Entry.

The keypad entered geometry suggests  $\beta = d/D = 2.516" / 4.026" = 0.625$ . Select objective diagnostic  $\alpha\%$ , i.e. predict the *actual* beta from the read PLR. As the DP integrity check  $x_4$  indicates the DPs are correct we can trust the read PLR. And the read PLR is in effect a measure of the actual beta, i.e. reverse equation 9.

$$\beta = d/D = f(PLR_{read}) = f(0.6363) = 0.6003$$

The resulting beta is 0.6003. Hence, the actual orifice diameter is estimated as:

$$d = D\beta = 4.026" * 0.6003 = 2.417"$$

The erroneous orifice diameter induced flow prediction bias ( $p\%$ ) can now be directly calculated, see equation 24.

$$p\% = \left\{ \left( \frac{m_{t,based}}{m_{t,correct}} \right) - 1 \right\} * 100\% \\ \approx \left\{ \left( \frac{\beta_{biased}}{\beta} \right)^2 \sqrt{\frac{1-\beta^4}{1-\beta_{biased}^4}} - 1 \right\} * 100\% \quad (24)$$

The erroneous beta is  $\beta_{biased} = 0.625$ , and the predicted beta is  $\beta_{biased} = 0.6004$ . In

this worked example for simplicity it is reasonably assumed that  $(\epsilon C_d)_{biased} \approx \epsilon C_d$ , however in practice flow computer

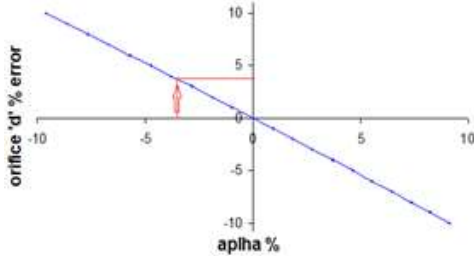


Fig 13. Objective Diagnostic vs. Orifice 'd' Bias. vs. Flow Prediction Bias.

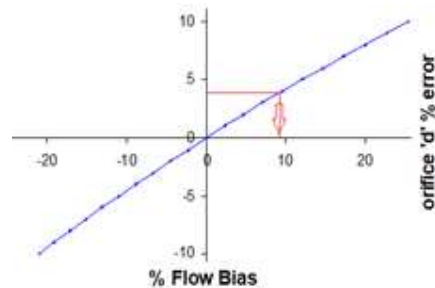


Fig 14. Orifice 'd' Bias. vs. Flow Prediction Bias.

software would also calculate this second order effect. Equation 24 therefore estimates the flow prediction bias ( $p\%$ ) induced by the erroneous orifice diameter as  $\approx +9.8\%$ . Fig 13 shows the objective diagnostic parameter  $\alpha\%$  being used to predict the magnitude of the source of the problem (i.e. the percentage bias in the orifice diameter). Fig 14 shows the resulting diameter bias being converted to an associated percentage flow prediction bias.

### 7.3 Worn Orifice Edge

An orifice plate should have a sharp perpendicular edge. Worn orifice plates cause the meter to have a negative flow prediction bias. Traditionally this went unnoticed, but use of diagnostic suite now warns of a problem, and offers a short list of possible causes that includes 'worn edge'.

A problem when discussing wear on an orifice plate is what quantifying parameter should be used? Wear is never the same on any two plates. However, modelling the wear as a symmetrical chamfer with height

$l$  depth ' $l$ ', i.e. as a wear height ( $l$ ) to orifice diameter ' $d$ ', ( $l/d$  ratio), see Figure 15,

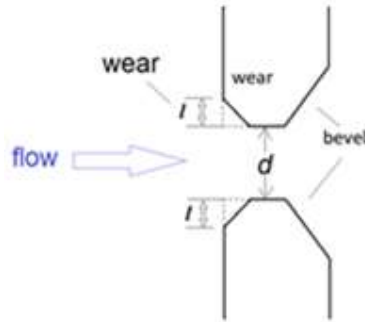


Fig 15. Modelling Orifice Plate Edge

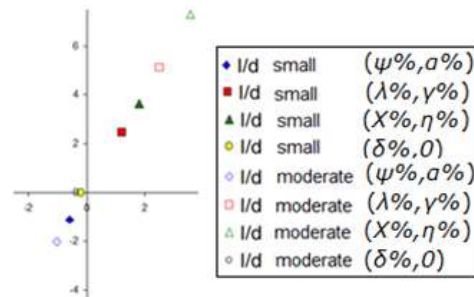


Fig 16. Sample Orifice Meter Diagnostic Data for Worn Edge.

gives reasonable predictive results. The small 3<sup>rd</sup> party public data set on the issue models wear as a smooth circular segment of radius ' $r$ ', i.e. ( $r/d$  ratio). Both models are approximate and in practice with  $r \approx l$  they are effectively equivalent.

Over several years DP Diagnostics tested plates in the laboratory and in the field with varying degrees of worn edge, e.g. see Figures 17 and 18. DP Diagnostics recorded the worn edge ( $l/d$ ) vs. objective diagnostic values vs. flow prediction bias ( $p\%$ ) data. Figure 16 shows the description of the edge wear and sample un-normalised diagnostic data.

Figure 16 show the un-normalized objective diagnostic results  $(\psi\%, \alpha\%)$ ,  $(\lambda\%, \gamma\%)$ ,  $(X\%, \eta\%)$ , and  $(\delta\%, 0)$ . Whereas the DP reading integrity check ( $\delta\%$ ) has no relationship with the edge wear, and nor should it, the other six objective diagnostic parameters do. In this case the RPR objective diagnostic check is the most sensitive, i.e.  $\eta\%$  vs.  $l/d$  value

(although the any of the six could be successfully used).



Fig 17. Filed Induced Wear on Edge.



Fig 18. Chamfered Lathe Induced Wear on Edge.

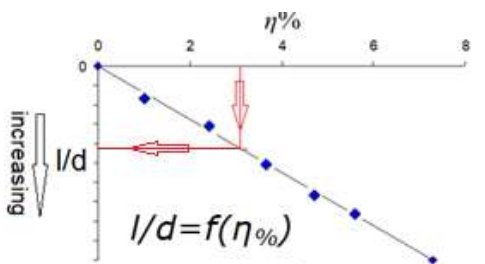


Fig 19. Objective Diagnostic vs. Amount of Edge Wear

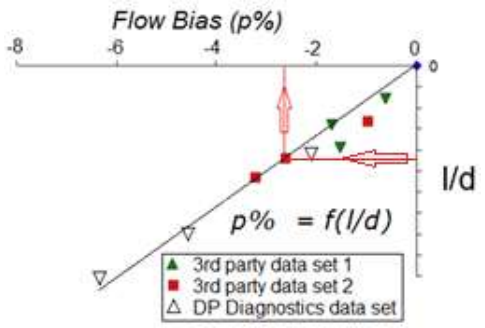


Fig 20. Amount of Edge Wear vs. Flow Prediction Bias.

Figure 19 shows orifice edge wear ( $l/d$ ) vs. measured objective diagnostic  $\eta\%$  data, with a data fit, i.e.  $l/d=f(\eta\%)$ . The last step of estimating the flow prediction bias ( $p\%$ ) for that edge wear estimation (i.e.  $l/d$ ) is through the published equations stating  $p\%=f(l/d)$ . Fig 21 shows the similarity of the DP Diagnostics data to the 3<sup>rd</sup> party data published by Reader-Harris [4].

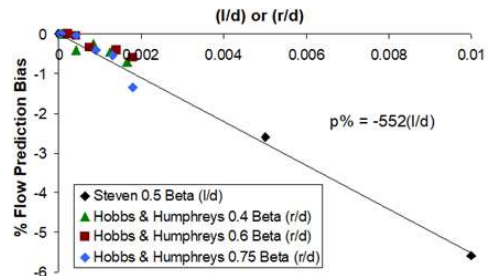


Fig 21. 3<sup>rd</sup> Party and DP Diagnostics Edge Wear vs. %Flow Prediction Bias ( $p\%$ ).

The existence of edge wear and associated flow prediction bias is unknown. Traditionally, such wear is only found once the meter is taken off-line for routine scheduled maintenance, and the magnitude of the wear then manually measured. Only then can the associated flow prediction bias can be estimated. However, with the use of these diagnostics whilst the meter remains on-line, a problem is noted, a worn edge is stated as one of a few possibilities, any trending in such wear can be actively monitored, and all that time, in real time, the system estimates the magnitude of the wear and the associated flow prediction bias.

7.4 Backwards / Reversed Orifice Plate

Many orifice plate designs are not symmetrical, they have a bevel on the back face (e.g. see Fig 22). A common operational mistake is to install the orifice plate backwards. This induces a significant negative flow prediction bias. Traditionally this went un-noticed, but the use of the diagnostic suite can warn of a problem, and 'backwards plate' is stated as the most probable reason for that particular diagnostic pattern.

The change from a correctly installed plate to a backwards plate is a change from one precise geometry to another. That is, for a



Fig 22. View of an Orifice Plate Back Face.

specific beta a backward plate always produces the same predictable step shift in all six diagnostic parameters (the seventh  $x_4$  being unaffected). The diagnostic pattern (inclusive of actual coordinates) is specific to backwards plates.

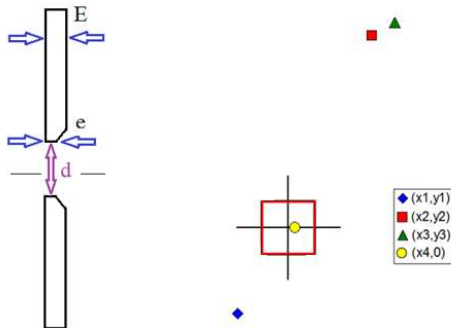


Fig 23. Sketch of Plate and Diagnostic Suite Reversed Plate Pattern.

There are various published calculation routines that estimate the flow prediction bias induced by a backwards plate. Reader-Harris [4] gives equations 25 and 26. The plate thickness ( $E$ ) and bevel thickness ( $e$ ) are required, but these are set geometries of the plate used and should therefore be available information in practice.

Researcher Witte suggests for  $e/E > 0.5$ :

$$p\% = -18.93 + 12.91\beta - 34.04 \frac{E}{D} - 8.9 \frac{e}{E} + 13.64 \left( \frac{e}{E} \right)^2 \quad (25)$$

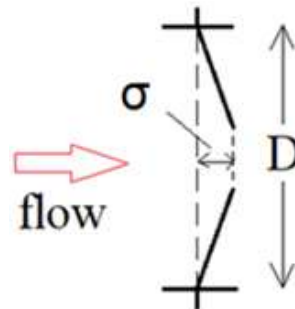
Researcher Reader-Harris suggests for  $e/E \leq 0.5$ :

$$p\% = -\left(17.2 - 10.4\beta^{2.5}\right) * \left(1 - \exp\left(\frac{-1270 \frac{(E-e)}{d}}{17.2 - 10.4\beta^{2.5}}\right)\right) \quad (26)$$

With the use of this diagnostic system whilst the meter remains on-line, a problem is immediately noted, the specific problem is suggested, and all that time, in real time, the system estimates the magnitude of the associated flow prediction bias.

### 7.5 Buckled / Warped / Bent Orifice Plates

An orifice plate should be perpendicular to the flow. Buckled (i.e. 'warped' / 'bent') orifice plates cause the meter to have a negative flow prediction bias. Traditionally this went un-noticed, but the use of the diagnostic suite can now warn of a problem, and offers a short list of possible causes that includes 'buckled plate'. Fig 24 shows the diagnostic result for a small and then moderate plate buckle.



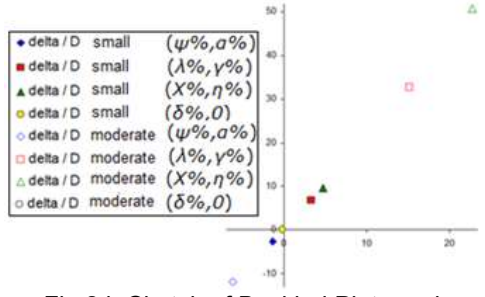


Fig 24. Sketch of Buckled Plate and Diagnostic Suite Buckled Plate Pattern.

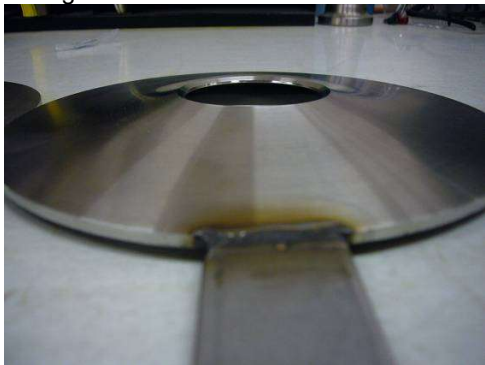


Fig 25. Moderately Buckled Plate.



Fig 26. Severely Buckled Plate.

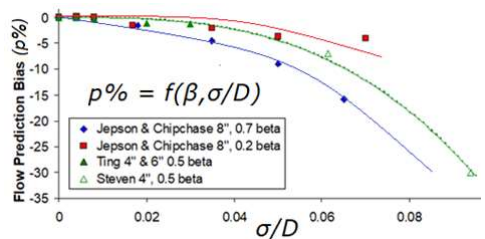


Fig 27. Buckle Magnitude vs. Flow Prediction Bias Data.

When discussing orifice plate buckling it is necessary to choose a parameter to quantify the magnitude of the buckle. Let us model the buckle as a symmetrical

buckle of depth 'sigma' to meter inlet diameter 'D', (i.e. a sigma/D ratio), see Figure 24.

Over several years DP Diagnostics tested buckled plates in laboratories with varying degrees of buckle, e.g. see Figs 25 & 26. This buckled plate magnitude (sigma/D) vs. flow prediction bias (p%) data is similar to the limited 3<sup>rd</sup> party data sets (see sample data in Figure 27). The buckle (sigma/D) vs. flow prediction bias (p%) relationship is somewhat beta dependent, but nevertheless it is possible to estimate the flow prediction bias for a known beta (beta) and known magnitude of buckle (sigma/D). DP Diagnostics recorded the buckle (sigma/D) vs. objective diagnostic values vs. flow prediction bias (p%) data.

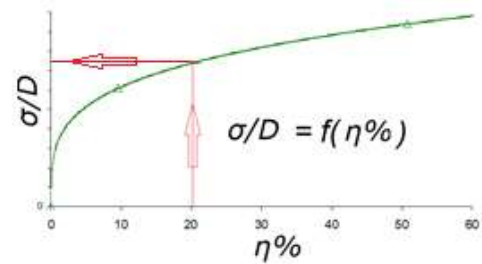


Fig 28. Objective Diagnostic Parameter (eta%) vs. Buckled Plate (sigma/D)

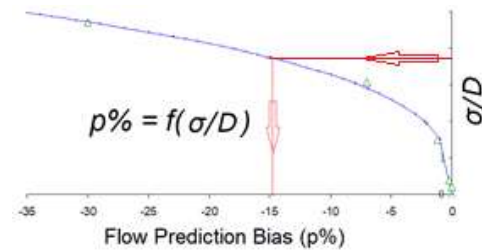


Fig 29. Buckled Plate (sigma/D) vs. Flow Prediction Bias (p%).

Fig 24 shows that various objective diagnostic checks have a relationship with the magnitude of a plate buckle. In this case the RPR objective diagnostic check is the most sensitive, i.e. eta% vs. sigma/D value (although the any of the six could be successfully used). Fig 28 shows, for a fixed beta, orifice plate diagnostic result eta% can be related to the buckle magnitude (sigma/D). Fig 29 shows that once the buckle magnitude is estimated the associated flow prediction bias can be predicted through the DP Diagnostics data fit p%=f(beta,sigma/D).

## 8. Further Developments

There are various different malfunction sources that afflict any given flow meter design. Some are communal to most flow meter designs, e.g. wet gas, inlet flow disturbance, erosion, contamination, instrument faults etc.. Others are specific to that meter design, e.g. for an orifice meter an orifice edge wear, buckled plate, backward plate etc. Some malfunction / problem sources are significantly simpler to quantify than others. A general rule is the less specific the malfunction term, the more challenging it is to quantify.

For example, 'orifice edge wear' is specific. It distinctly describes the change in shape of the square edge. A 'buckled plate' is specific. It distinctly describes the bowing of the plate. But, for example, 'contamination' or 'disturbed flow' are not specific. What is contaminated? The upstream and / or downstream meter run? The upstream and/or downstream surface of the plate? And what substance is the contaminant, solid or fluid? What sort of flow disturbance is there? Asymmetrical or swirl flow? And how is it asymmetrical, and if its swirling in what direction? Terms like 'contaminated' or 'disturbed' flow are too vague, too general to quantify. They are more of a group of issues than a specific issue.

Well defined specific meter malfunction sources, such as worn plate, buckled plate, etc., tend to have literature linking these quantifiable malfunctions to flow prediction biases. However, perhaps unsurprisingly, ill-defined, vague, non-specific meter malfunction sources, such as contamination and disturbed inlet flow, do not to have literature linking these unquantifiable malfunctions to flow prediction bias. Yes, there are published case studies where a given contamination or disturbance is recorded as having produced a given flow prediction bias. But this is of little use to predicting how the bias changes as the problem increases or decreases in severity. That is, such data offers little predictive power. The pertinent point is that for such undefined malfunction sources there is not surprisingly a *dearth of predictive equations*.

This limitation presently caps the capability of an orifice meter diagnostic system to estimate more types of problem's associated flow prediction biases. You first have to clarify a question before you can formulate a concise answer. That is, certain malfunction sources need to be better defined such that there is a quantifying parameter that can measure the magnitude of the problem. Only then is there a clear question, i.e. what effect does that specific magnitude of problem have on the flow prediction? This undoubtedly will mean breaking general vague terms into more precisely definable quantifiable sub-terms.

## 10. Conclusions

Flow meter verification systems (powered by diagnostic suites) are very useful aids for optimization of flow meter maintenance and operation. They are also useful for auditing and lost and unaccounted for product calculations. Whereas it is beneficial to have a generic warning stating something is wrong, heuristic pattern recognition now increases the benefit of the system by specifically stating what is wrong, or at least short listing the meter problems that could cause such a result.

All flow meter diagnostic suites consist of a set of individual diagnostic tests that are either objective or subjective tests. The combined set of these diagnostic tests can produce a revealing diagnostic pattern. However, it is specifically the objective tests alone that hold the key to estimating the identified malfunction's associated flow prediction bias. Once pattern recognition has isolated the type of malfunction, the objective tests can be used to estimate the magnitude of that malfunction, and from there the associated flow prediction bias can be estimated.

This principle has been developed by DP Diagnostics and proven on various different orifice meter malfunction data sets. Due to the 'nature of the beast' flow meter diagnostic suite technology is never complete, but just continually improved. Hence, although the system is not claimed to be perfect, it is now capable enough to

be of considerable practical usefulness.  
*And a technology does not need to work perfectly all of the time to be of considerable practical use most of the time.*

## **11. References**

1. International Standard Organisation, "Measurement of Fluid Flow by Means of Pressure Differential Devices, Inserted in Circular Cross Section Conduits Running Full", no. 5167-2.
2. Skelton M. et al, "Developments in the Self-Diagnostic Capabilities of Orifice Plate Meters", North Sea Flow Measurement Workshop, October 2010, UK.
3. Rabone J. et al "Advanced DP Meter Diagnostics – Developing Dynamic Pressure Field Monitoring (& Other Developments)", North Sea Flow Measurement Workshop, St Andrews, Scotland, UK, 2014.
4. Reader-Harris M. "Orifice Plates and Venturi Tubes", Published by Springer 2015, ISBN 978-3-319-16879-1.

# A Hybrid Wet Gas Meter Design for Marginal Fields

E Sanford<sup>1</sup>, K Igarashi<sup>2</sup>, R Steven<sup>3</sup>

<sup>1</sup>Vortek Instruments, Fredrick, Colorado, USA

<sup>2</sup>AZBIL, Fredrick, Colorado, USA

<sup>3</sup>DP Diagnostics, Windsor, Colorado, USA  
esanford@vortekinst.com

---

## Abstract

Combining different metering physical principles into one metering system offers various advantages. In this paper the advantages of producing a hybrid vortex and cone DP meter system is discussed. In single phase flow applications this hybrid meter produces a mass flow, volume flow, and fluid density predictions. In saturated steam and wet natural gas flow applications this hybrid meter can predict the two-phase flow quality, and total mass flow rate. The cone meter sub-system can also run the generic DP meter pressure field analysis diagnostic system 'Prognosis'.

---

## 1. Introduction

Natural gas onshore production is often from marginal wells. Such wells, or groups of wells, often produce wet natural gas through small pipes and therefore wet gas meters are desirable. However, most wet gas meter products are sophisticated, complex, and expensive systems largely aimed at offshore high productivity flows. They tend to be cost prohibitive for marginal well small pipe wet gas flows. Marginal field operation requires simpler, more cost effective, wet gas meter designs.

One simple wet gas meter design concept is use of two dissimilar gas meters in series. The two meter's different responses to wet gas flow are cross-referenced to produce a gas flow rate and liquid loading prediction. Such designs exist on the market, but they tend to use at least one specially designed meter and be expensive. This paper discusses a simple low cost two meters in series wet gas meter design. It pairs a vortex meter and a cone DP meter. It is developed from a single phase mass meter design.

## 2. A Single Phase Flow Mass Meter – A Hybrid Vortex and Cone DP Meter System

Direct mass flow metering means the metering of mass flow without the fluid density value being required from a source external to the meter. There are various ways of doing this, e.g. critical nozzle, Coriolis, and 'Boden' mass meter designs. Naturally, each of these physical principles have pros and cons. For example, critical nozzles operate with very clean gas flows only, and have

relatively high pressure loss. Coriolis meters have a large footprint and are relatively expensive.

The Boden mass flow meter design principle is simple, has a long history, is publicly available technology, but is not widely known. In 1956 Boden, an engineer in the aerospace industry, proposed pairing a density insensitive volume meter (e.g. a turbine meter) in series with a density sensitive volume meter (e.g. a Differential Pressure meter). The density insensitive meter predicts the fluid volume flow rate without knowledge of the fluid density being required. The volume flow through the adjacent density sensitive meter is therefore now known. A stand-alone DP meter requires the fluid density be supplied in order to predict the volume flow. However, the calculation can be reversed. With a known volume flow rate the DP meter equation predicts the fluid density. The mass flow prediction is simply the product of the predicted volume flow and density. This is the simplicity of the Boden principle.

However, with this Boden principle, the devil is in the detail. The idea more than half a century old, but only with the advent of modern computers is such a system industrially practical. But even then, few end users want two separate meters in series. That is potentially expensive, has a large footprint, and brings images of a contraption. A practical Boden mass meter design must be compact, effectively operate as a single entity, a simple hybrid design blending the two separate meter principles together. However, that's easier said than done. There are two significant problems for the designer:

a) A common limitation of different flow meter designs is that their performance is adversely affected by disturbed flow. It is therefore a challenge to find a combination of meters that can operate in close proximity to each other and not be adversely affected by each other's presence.

b) When two different metering principles are blended into one design, i.e. are placed together, it can become challenging to independently design the two sub-systems such that they operate across the same flow range. It is a requirement that the density sensitive and density insensitive meters have the same flow range if they are to be successfully paired.

Most early Boden mass meter designs failed to pass the development stage and make it to market as the designers either failed to recognize the importance of, or simply failed to accomplish, these two essential requirements. The VorCone™ meter is a Boden design hybrid vortex meter and cone DP meter that meets these two requirements. Figure 1 shows a sketch of the system. The vortex meter is a density insensitive volume meter. The cone DP meter is a density sensitive volume meter. Sanford et al [1] discusses the development in detail.

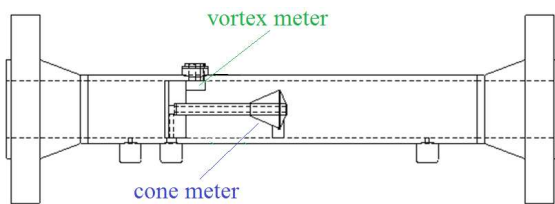


Fig 1. VorCone Meter Schematic

The vortex meter is upstream of the cone meter and receives the undisturbed inlet flow. The vortex meter performance is unaffected by the cone meter downstream. The cone meter assembly uses the vortex shedding bar as the cone meter support. The gusseted cone is set back such that the apex of the cone is downstream of the vortex shedding sensor. The cone element is positioned in the vortex meter's wake. However, the generic cone DP meter is renowned for its resistance to disturbed flows (e.g. see ISO 5167-5 [2]). Multiple prototypes tested over several years of development have honed the VorCone meter design such that the cone meter is also now shown to be unaffected by the close upstream proximity of the vortex meter.

$$Q_v = \frac{f}{K} \quad (1)$$

$$Q_v = \frac{A\beta^2}{\sqrt{1-\beta^4}} Y C_d \sqrt{\frac{2\Delta P}{\rho}} \quad (2)$$

$$\rho = 2\Delta P \left\{ \frac{KYC_d}{f} \frac{A\beta^2}{1-\beta^4} \right\}^2 \quad (3)$$

$$Q_m = \rho Q_v \quad (4)$$

The vortex meter predicts the volume flow rate ( $Q_v$ ) via equation 1, where 'f' is the vortex shedding frequency, and 'K' is the vortex meter factor. Equation 2 represents the cone DP meter volume flow rate equation. Note, A is the inlet area,  $\beta$  is the beta (i.e. cone size parameter), Y is expansibility (i.e. the correction for any density fluctuation through the meter),  $C_d$  is the cone 'discharge coefficient' meter factor,  $\Delta P$  is the differential pressure, and  $\rho$  is the fluid density. Substituting the volume flow prediction of equation 1 into equation 2 gives a density prediction (see equation 3). Mass flow is found from the volume flow rate and density prediction (see equation 4).

### 2.1 3" VorCone Meter Gas Flow Laboratory Test

Figure 2 shows a photograph looking downstream into a 3" gas VorCone meter. Figure 3 shows this meter under test in a CEESI gas calibration facility. Figures 4 & 5 show the cone and vortex meter sub-system independent calibration results. Figure 6 shows the gas mass, volume, and density predictions compared to the CEESI test facility references. The meter was tested with air flow at 810, 400, & 150 psia across a 10:1 flow range. The volume flow is predicted to 0.5%, the mass flow to 1%, and the density to 1.5% all at 95% confidence level.



Fig 2. 3" VorCone Meter.



Fig 3. 3" VorCone Meter Gas Tested at CEESI.

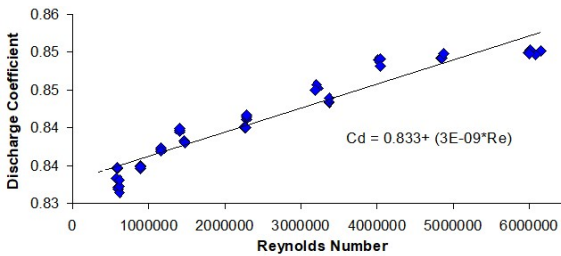


Fig 4. Cone Meter Sub-System Calibration of 3" VorCone Meter.

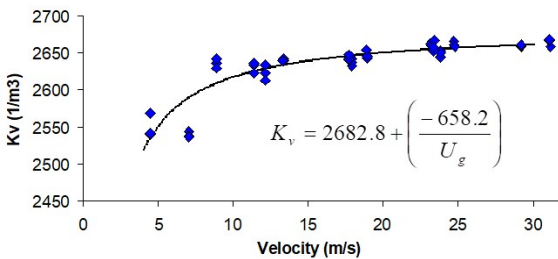


Fig 5. Vortex Meter Sub-System Calibration of 3" VorCone Meter.

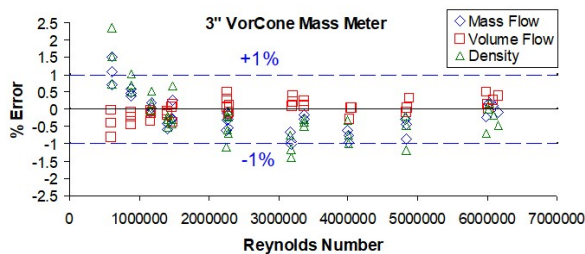


Fig 6. 3" VorCone Meter Gas Mass, Volume, and Density Prediction Results

## 2.2 4" Meter Liquid Laboratory & Field Tests

Oil is transported from some local well storage facilities by truck (e.g. Figure 10). The storage facility measures the oil quantity being loaded via

volume change in the storage tank. The truck has an independent check meter. The loading and unloading oil quantity must match between the truck flow meter and storage facility measurements. However, the oil density can change between batches. Hence, a mass meter is preferred on the truck. Sometimes Coriolis meters are used. However, with excessive vibration whilst the truck is in motion on unpaved surfaces, fluctuating flow rates while in operation, start / stop induced errors etc., the application is challenging for all meters designs. Under such adverse flow conditions the operator reported a typical mass flow uncertainty of approximately 1% from the Coriolis meters. Two 4" VorCone meters were tested.



Fig 7. Two 4" VorCone Meters Close Coupled For Bi-Directional Application Under Calibration at the CEESI Water Facility.

As the VorCone meter is unidirectional and the truck loads and unloads through a single pipeline two close coupled meters were installed, one for each direction. Figure 7 shows these meters during calibration in this configuration at the CEESI water flow facility. Figures 8 & 9 show the calibrations results. Both meters predicted the volume and mass flow rates to < 1% uncertainty and the density to < 1.5% uncertainty (at 95% confidence).

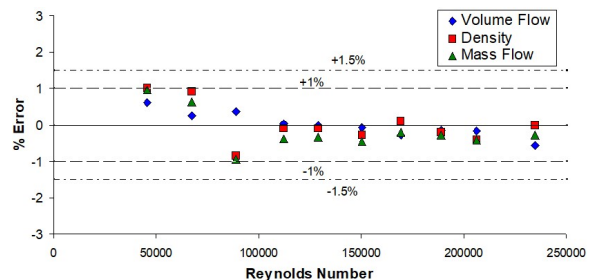


Fig 8. CEESI Water Flow Calibration Results From First 4" VorCone Meter.

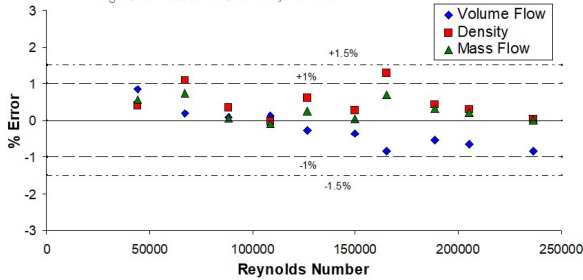


Fig 9. CEESI Water Flow Calibration Results From Second 4" VorCone Meter.



Fig 10. Truck with 4" VorCone Meters Installed.

Figures 10 and 11 show the truck and the installed meters respectively. These meters were used in multiple oil transfers. The data was recorded in batches (i.e. the run counter) that sum to the total batch quantity. As reported for the Coriolis meters there was a reasonable amount of scatter between run counts. Figure 12 shows the results with the authors estimated facility storage tank reference uncertainty of 0.5% error bars included. Both VorCone meters predicted the flow to 1% uncertainty. However, as with the Coriolis meter, the totalized oil quantity values for loading and unloading



Fig 11. Oil Truck Mounted 4" VorCone Meters

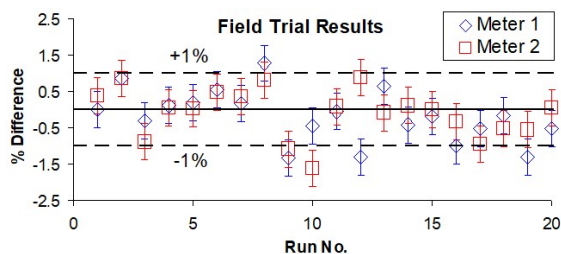


Fig 12. Truck 4" VorCone Meter Performances Compared to Facility Reference.

over the twenty runs showed good agreement with the facility references. Table 1 shows the facility volume reference vs. the meters loading & unloading totalized values. The volume difference between the facility references and the loading and unloading meters are -0.19% and -0.09% respectively. No zeroing / re-calibration was required in the field.

	Reference BBLs	Meter Under Test BBLs	% Difference of Total
Meter 1 Loading	4488.8	4480.4	-0.19
Meter 2 Unloading	4488.8	4484.6	-0.09

Table 1. Totalized Flow Rate Results.

### 3. Saturated Steam Flow

In 2015 an oil company investigated if the VorCone meter could be used in a 'heavy oil' field saturated steam injection application. The VorCone meter was used to predict the saturated steam quality ( $x$ ) and monitor for quality changes. Steam quality, sometimes called 'dryness fraction', is defined by equation 5, where  $m_g$  and  $m_l$  denote the mass flow of steam (i.e. steam vapor / gas) and liquid (i.e. water).

Saturated steam is the carrier mechanism to inject heat into the well to reduce the oil viscosity and make it easier to extract. Saturated steam is an expensive commodity,

$$x = \frac{m_g}{m_g + m_l} \quad (5)$$

$$Q_{v,Total} = f/K \quad (1a)$$

$$\rho_{hom} = 2\Delta P_{tp} \left\{ \frac{KYC_d}{f} \frac{A\beta^2}{1-\beta^4} \right\}^2 \quad (3a)$$

$$x = \frac{\rho_g(\rho_l - \rho_{hom})}{\rho_{hom}(\rho_l - \rho_g)} \quad (6)$$

requiring considerable fuel costs and boiler CAPEX and OPEX. There are application dependent optimum steam quality (i.e. heat injection) values. Too high a steam quality, and a needlessly excessive amount of heat is injected while possibly causing fouling of the pipe line. Too low a steam quality and there is not enough heat injected to

optimize the process. However, it is notoriously difficult to meter saturated steam quality.

Industries research into wet gas flow metering has found that the liquid dispersion in the gas phase strongly dictates the flow meter's reaction to its presence. (For example, see ASME MFC 19G [3]). For a given pressure and gas velocity a major factor dictating the liquid dispersion is known to be the liquid's surface tension. For horizontal flow, the higher the surface tension the more tendency for the liquid to flow as a separated phase at the base of the pipe. The lower the surface tension the more the tendency for the liquid to flow as droplets suspended in the gas flow, i.e. a mist flow. Mist flow approximates to a pseudo-single phase homogenous mixture.

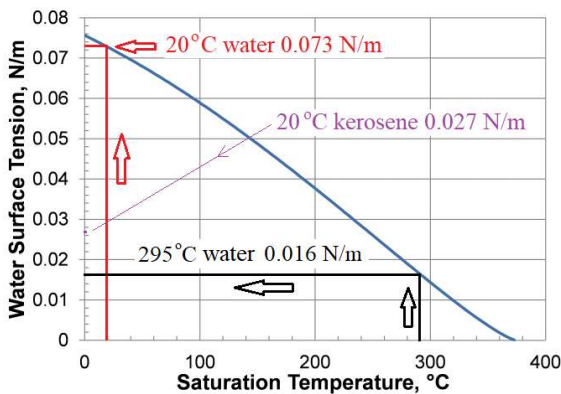


Fig 13. Fluid Surface Tensions

Saturated steam has  $x \leq 100\%$ , i.e. there is a mixture of steam / water (i.e. gas / liquid). Compared to wet natural gas at ambient temperatures saturated steam has a liquid phase (i.e. very hot water) with a very low surface tension. Figure 13 shows the approximate surface tension values for water and a light oil at 20°C, i.e. a typical wet natural gas production flow temperature. The water value is 0.073 N/m, the kerosene value is 0.027 N/m. Figure 13 also shows the surface tension of water at elevated temperatures. A saturated steam flow at 80 Bar / 295°C has a water surface tension of approximately 0.016 N/m, i.e. approximately five times less than the value at 20°C.

This facilitates the liquid being well dispersed in the steam vapor even at moderate gas velocities. Hence, if the local steam velocity is high the water and steam will be well mixed, and could be reasonably modelled as a homogenous mix. The meter itself further helps the mixing.

Hence, the vortex meter subsystem's volume flow prediction could be approximated to be the homogenous mix total volume ( $Q_{v,Total}$ ). The cone meter's DP produced by the two-phase flow mixture ( $\Delta P_{tp}$ ) could be approximated to be the DP produced by a homogenous 'pseudo-single phase' mixture. Hence, Equation 1a produces a total volume flow prediction, and Equation 3a then produces a homogenous density prediction. With measured pressure and temperature the 'steam tables' supply the steam ( $\rho_g$ ) and water ( $\rho_l$ ) densities. Therefore, Equation 6 predicts the steam quality.



Fig 14. 3" VorCone Meter Saturated Steam Field Installation.

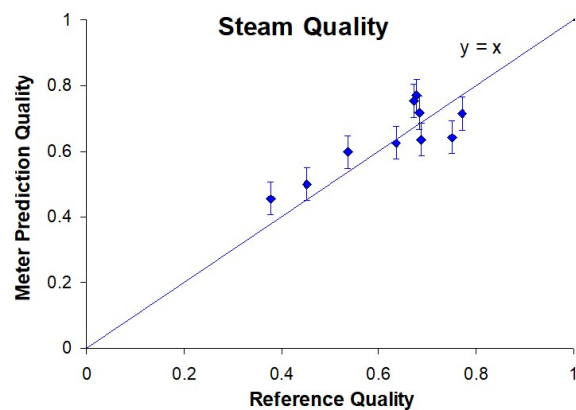


Fig 15. 3" VorCone Meter Saturated Steam Flow Quality Prediction Results.

Figure 14 shows a 2" VorCone meter during a heavy oil field saturated steam injection test. The saturated steam flow reference data was obtained from a downstream cyclone separator with single phase gas and liquid Coriolis meters at the outlets. Due to their nature field references are never as precise as laboratory references. It is estimated that due to the possibilities of imperfect separation and phase change after separation the field quality

reference uncertainty was 5%. Figure 15 shows the resulting VorCone meter's quality prediction vs. the field reference values (with associated reference uncertainty bars). Whereas the direct measurement of saturated steam quality is notoriously difficult the fully theoretical steam quality prediction agrees with the reference data (with 5% uncertainty) to less than 10% uncertainty (i.e.  $x\% \pm 10\%$ ). Furthermore, changes in steam quality is clearly correctly tracked.

The hydrocarbon production industry tends to describe liquid loading not by quality ( $x$ ), but by the 'Lockhart Martinelli' parameter ( $X_{LM}$ ), see equation 7. Therefore, for a predicted quality, and known gas and liquid density values, the Lockhart-Martinelli parameter is also predicted. The steam vapor / gas flow through the VorCone meter can now be predicted using a correction factor. ISO TR 12748 [4] offers a cone meter wet gas correlation shown here as Equation set 8 thru 11. Note,  $m_{g,App}$  is the 'apparent' gas mass flow predicted by the uncorrected meter, 'C' is the Chisholm coefficient, 'n' is the Chisholm exponent, 'g' is the gravitational constant, 'D' is the meter inlet diameter, and ' $Fr_g$ ' is the Froude number. The Froude number is a non-dimensional expression of the gas mass flow rate through the meter at set fluid densities. This equation set traditionally requires the liquid loading to be known from an external source, which the VorCone meter supplies. That is, for a predicted quality, i.e. predicted Lockhart Martinelli parameter, gas mass flow is solved by iteration of this equation set.

$$X_{LM} = \frac{m_l}{m_g} \sqrt{\frac{\rho_g}{\rho_l}} = \frac{1-x}{x} \sqrt{\frac{\rho_g}{\rho_l}} \quad (7)$$

$$m_g = \frac{m_{g,App}}{\sqrt{1 + CX_{LM} + X_{LM}^2}} \quad (8)$$

$$C = \left(\frac{\rho_g}{\rho_l}\right)^n + \left(\frac{\rho_l}{\rho_g}\right)^n \quad (9)$$

$$Fr_g = \frac{m_g}{\sqrt{gD}} \sqrt{\frac{1}{\rho_g(\rho_l - \rho_g)}} \quad (10)$$

$$n = \frac{1}{2} \left\{ 1 - \left( \frac{0.83}{1.14 \exp(0.31 Fr_g)} \right) \right\} \quad (11)$$

The percentage 'over-reading' (OR) is the steam / gas flow prediction positive percentage bias induced by the presence of the water / liquid. Figure 16 shows the uncorrected cone meter steam percentage over-reading (OR) when using the steam vapour density (from the pressure and temperature readings and the steam tables). Figure 16 also shows the effect of applying the wet gas correction methods, i.e. the results of using the VorCone meter's predicted quality (i.e. Lockhart-Martinelli parameter) with the ISO cone meter correction factor. Without correction the wetness of the steam can cause the steam vapor mass flow prediction to have > 30% over-reading. With the correction the steam vapour mass flow rate matches the reference data to < 5% uncertainty. As this is field data with relatively high reference uncertainties, it is very probable that laboratory data would show a significantly smaller steam vapor mass flow prediction uncertainty.

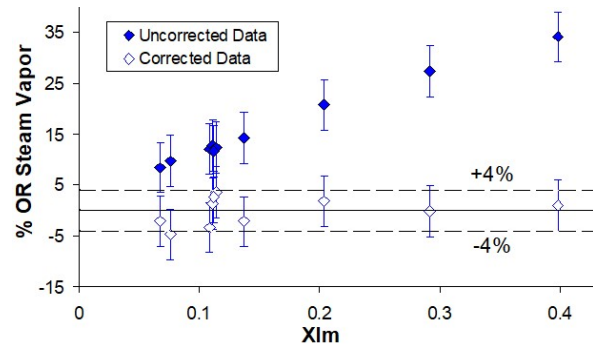


Fig 16. 2" VorCone Meter Saturated Steam Uncorrected and Corrected Steam Vapor Mass Flow Predictions.

Two 4" VorCone meters were subsequently installed at the outlet of a new steam boiler. There was no independent quality reference but the boiler was set to produce 75% steam quality. The meter read 73% steam quality.



Fig 17. 4" VorCone Meter Installed at Outlet of Steam Boiler set to Produce 75% Quality Steam.

#### 4. Wet Natural Gas Flow

A 4" to 3" reduced bore VorCone meter was tested at the CEESI wet natural gas flow facility (see Figure 18) with natural gas and kerosene flow at 35 Bar and ambient temperature. The kerosene at ambient temperature had a surface tension approximately 70% more than the field test's high temperature water (see Figure 13). It therefore takes more gas dynamic pressure to mix the kerosene than it does to mix hot water. That is, it takes a higher Froude number to produce a well-mixed gas / kerosene flow than a saturated steam flow. Therefore, this wet natural gas flow test is more challenging than the saturated steam flow test. A reduced bore design was used to increase the local gas velocity / Froude number at the meter.



Fig 18. 4" to 3" Reducer VorCone Meter at the CEESI Wet Gas Facility

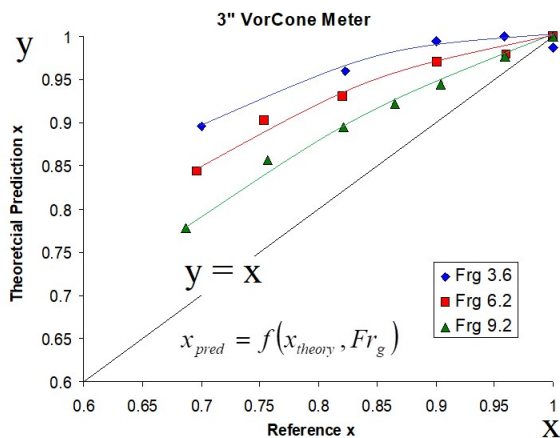


Fig 19. 3" VorCone Meter Theoretical Quality Prediction (No Fit) at the CEESI Wet Gas Facility.

Figure 19 shows the wet natural gas theoretical homogenous model quality prediction results for

the quality range tested of > 65%. For all three flow rates the quality prediction clearly tracks the reference correctly. The higher the Froude number (i.e. the faster the gas flow) the better mixed the phases are and the better the corresponding theoretical homogenous model quality prediction. The data can be data fitted to give a more precise quality prediction. Figure 20 shows such fitted curves (Equation 12) on the data, where the quality prediction ( $x_{pred}$ ) is related to the theoretical homogenous model steam prediction ( $x_{theory}$ ) and the gas densiometric Froude number (see Equation 10).

$$x_{pred} = f(x_{theory}, Fr_g) \quad \text{--- (12)}$$

The quality prediction ( $x_{pred}$ ) relationship with the gas densiometric Froude number ( $Fr_g$ ) means that the quality and gas mass flow rate predictions are found by an iteration of Equation 12 and Equation set 7 thru 11.

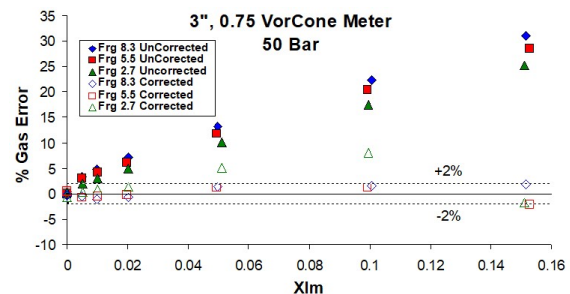


Fig 20. 4" to 3" Reducer VorCone Meter Uncorrected Cone Meter Over-Reading and with Correction Data Applied.

Figure 20 shows the VorCone meter's uncorrected gas flow rate prediction percentage error (or 'over-reading'), and the gas flow rate percentage bias after the correction factor has been applied. Across the liquid loading range tested (i.e.  $0 \leq X_{LM} \leq 0.15$  or  $65\% > x > 100\%$ ) for  $Fr_g > 5$  the gas flow rate was predicted to 2% uncertainty at a 95% confidence level. For slower flow, i.e.  $Fr_g < 5$ , where there was less mixing, the bias was somewhat higher. However, it is important to note that for most applications the minimum local gas densiometric Froude number at the inlet to the meter is controllable via the common meter practice of matching the applications flow condition range to a reduced bore meter design. For example, a reduction from 3" to 2" schedule 80 increases the gas densiometric Froude number by 2.74 times. For most applications, proper reduced bore meter design can guarantee an appropriate local gas densiometric Froude number range and therefore successful wet gas operation.

The unofficial benchmark performance for the sophisticated and complex wet gas flow meter products tends to be metering the gas flow to 5% uncertainty. The unofficial benchmark performance for single phase gas meter designs with published correction factors is to have a gas flow prediction uncertainty (for *precisely* known liquid flow rates) of 2%. However, in the field the supplied liquid flowrate prediction has a significant uncertainty (typically up to 10%). Therefore, the reality of using a gas meter with a wet gas correction is that the real gas flow rate prediction uncertainty ends up being about 5%. Hence, a simple single phase meter design that can predict the gas flow of a wet gas flow to <5% is a viable wet gas meter.

#### 5. An Additional VorCone Meter Liquid Loading Tracking Capability

The cone meter sub-system of the VorCone meter operates as a standard cone DP meter. Therefore, the proprietary DP meter verification system 'Prognosis<sup>TM</sup>' can be utilized. In wet gas / saturated steam flow applications Prognosis can give a second *independent* Lockhart Martinelli parameter / quality monitoring system, thereby giving liquid loading monitoring redundancy. The following text gives an over-view of the Prognosis methodology.

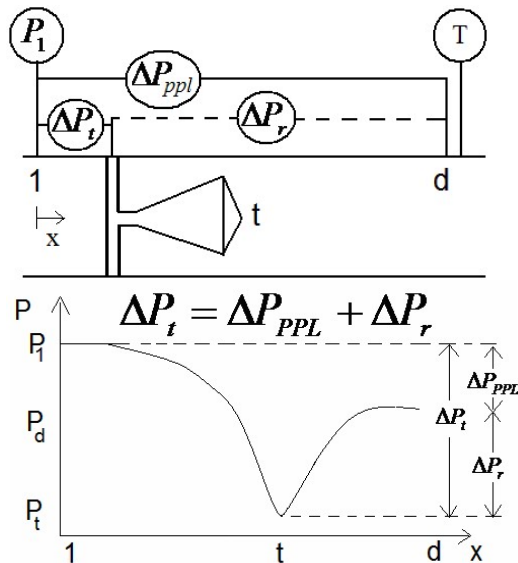


Figure 21. VorCone Meter with Instrumentation Sketch and Pressure Field Graph.

Figure 21 shows a sketch of a VorCone meter with a graph of the meter's pressure field. The meter has a third pressure tap downstream of the two traditional pressure ports. Note that the VorCone meter sketch of Figure 1 shows such a downstream pressure tapping, as do the FLOMEKO 2019, Lisbon, Portugal

photographs of VorCone meters shown in Figures 3, 14, & 17. The downstream tap allows three DPs to be read, i.e. the traditional ( $\Delta P_t$ ), recovered ( $\Delta P_r$ ) and permanent pressure loss ( $\Delta P_{PPL}$ ) DPs. These DPs are related by Equation 13. This relationship is a consequence of physical law and is therefore an objective diagnostic check on the health of the DPs read. The difference between the read  $\Delta P_t$  and the sum of the read  $\Delta P_r$  and  $\Delta P_{PPL}$  cannot exceed the combined DP reading uncertainties.

$$\text{DP Summation: } \Delta P_t = \Delta P_r + \Delta P_{PPL},$$

$$\text{Uncertainty } \pm \theta \% \quad (13)$$

Traditional flow calculation:

$$m = \frac{A\beta^2}{\sqrt{1-\beta^4}} YC_d \sqrt{2\rho_g \Delta P_t}, \text{uncert } \pm x\% \quad (14)$$

Expansion flow calculation:

$$m = \frac{A\beta^2}{\sqrt{1-\beta^4}} K_r \sqrt{2\rho \Delta P_r}, \text{uncert } \pm y\% \quad (15)$$

PPL flow calculation:

$$m = AK_{PPL} \sqrt{2\rho_g \Delta P_{PPL}}, \text{uncert } \pm z\% \quad (16)$$

Each of the three DPs can be independently used to meter a single phase flow rate, as shown in Equations 14, 15 & 16. Note  $K_r$  and  $K_{PPL}$  denote the 'expansion' coefficient and 'PPL' coefficient of the expansion and PPL flow rate prediction methods. The three DPs turn the VorCone meter from one stand-alone meter to effectively a primary DP meter with two check DP meters. The three flow rate predictions give three pairs of flow rate predictions for comparison. The difference between any two flow rate predictions cannot exceed the combined flow rate prediction uncertainties.

The three read DPs produce three pairs of DPs, i.e. three DP ratios. Such DP ratios of any generic DP meter are known to be characteristics of a DP meter. They do not change with changes in single phase flow conditions. The three DP ratio baselines are set during the VorCone meters calibration. Comparison of each found to expected (baseline) DP ratio produces three diagnostic checks. For each of the three DP ratios the difference between the found to expected (baseline) DP ratio cannot exceed the calibration baseline values uncertainties.

The three flow meter coefficients  $C_d$ ,  $K_r$ , &  $K_{PPL}$  and the three DP ratios are found during the standard calibration of the flow meter.

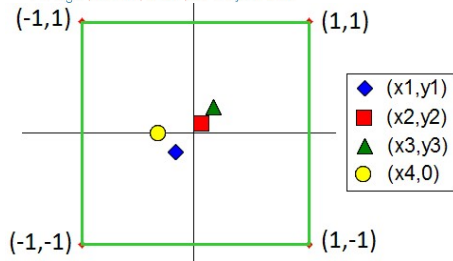


Fig 22. Diagnostic results

The seven diagnostic results are shown on a graph (Figure 22) as four co-ordinates  $(x_1, y_1)$ ,  $(x_2, y_2)$ ,  $(x_3, y_3)$  &  $(x_4, 0)$ . Note,  $x_4$  represents the DP reading integrity check. The three other 'x' values represent the three flow rate prediction comparisons. The three 'y' values represent the three DP ratio found to expected comparisons.

All points inside the box indicate a serviceable cone meter. One or more point/s outside the box represent/s a potential problem. The pattern of point distribution gives indications of possible problems. Two-phase flow, i.e. saturated steam ( $x < 100\%$ ) or wet natural gas ( $X_{LM} > 0$ ) produces a specific Prognosis pattern.

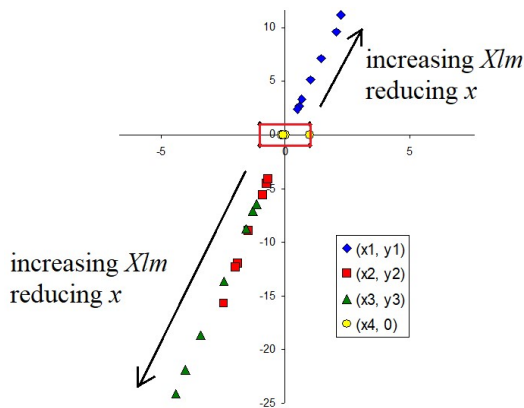


Fig 23. 3" VorCone Meter Prognosis Result at 35 Bar, 300 m<sup>3</sup>/hr

Figure 22 shows a typical Prognosis verification system result for the 3" VorCone meter tested with single phase natural gas at CEESI (see Figure 18). As required all points are inside the box indicating a fully serviceable correctly operating cone meter.

Figure 23 shows the subsequent Prognosis results when the 3" VorCone meter installed in the CEESI wet gas facility was subjected to varying liquid loading wet gas flows at the 35 bar, and 400 m<sup>3</sup>/hr. For display clarity, the abscissa (x) and ordinate (y) axes have been changed in scale relative to each other. Prognosis clearly indicates a problem, i.e. points are out the box. This is a typical Prognosis

wet gas flow pattern. Coordinate  $(x_1, y_1)$  is in the first quadrant, while  $(x_2, y_2)$  and  $(x_3, y_4)$  are in the third quadrant. The DP reading check, i.e.  $(x_4, 0)$  is unaffected by the presence of wet gas flow. As the liquid loading increases (i.e. the quality reduces / the Lockhart Martinelli parameter increases) the points diverge from the origin and the box, and vice versa. This is a method of tracking liquid loading that is independent of the primary VorCone meter method described in Sections 3 and 4.

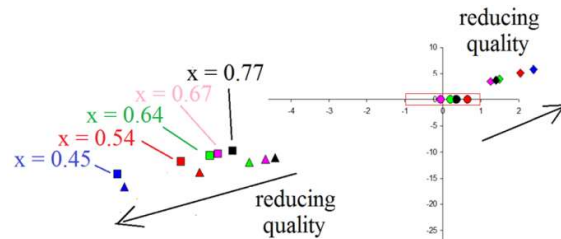


Figure 25. 2" VorCone Meter Prognosis Field Response to Changes in Saturated Steam Quality.

Figure 25 shows the 2" VorCone meter Prognosis response during the saturated steam injection oil field test (see Figure 14). During the test the quality was varied between 45% and 77%. Prognosis showed the flow was two-phase ( $x < 100\%$ ) and correctly tracked the changes in quality.

## 6. Conclusions

The VorCone meter is a hybrid vortex and cone DP meter. It is a Boden type single phase mass flow meter. The design has blended the two separate flow metering principles into one meter body such that the two meters do not have adverse effects on each other's performance. The VorCone meter has been shown with laboratory and field trials to be a capable single phase gas or liquid mass flow meter and densitometer. The VorCone meter can operate with the DP meter verification system Prognosis.

The VorCone meter can be used in the adverse flow conditions of saturated steam or wet natural gas flow. Moderate to high local gas velocities, that if necessary can be assured by an appropriate reduced bore meter design, allow the meter to track liquid loading using only theoretical principles. Reduced bore designs are common across many meter designs. Furthermore, a flow quality / liquid loading data fit allows the VorCone meter to predict the gas flow rate of a wet gas flow. The 3" VorCone meter tested at the CEESI wet gas facility predicted the gas flow to 2% uncertainty for a quality range of  $x > 65\%$ . This is industrially useful, as many steam quality meters / monitor designs only operate at  $x > 90\%$ .

Finally, the cone meter verification system 'Prognosis' can monitor the health of the cone meter sub-system in single phase flow, and can track changes in wet gas flow liquid loading independently of the main metering system liquid loading prediction method. This means that the VorCone meter has the rare feature of redundancy in liquid loading tracking methods.

## 7. References

1. Sanford E. et al "Gas Mass Flow Metering – An Alternative Approach" North Sea Flow measurement Workshop, Tonsberg, Norway, 2015
2. ISO 5167-5:2016 "Measurement of fluid flow by means of pressure differential devices inserted in circular cross-section conduits running full -- Part 5: Cone meters".
3. ASME MFC 2008 Report 19G "Wet Gas Metering".
4. ISO TR 12748 "Natural Gas –Wet Gas Flow Measurement in Operations".

# Statistical quality control method for automated water flow measurements in concrete dam foundation drainage systems

J. Mata<sup>1</sup>, L. Martins<sup>1</sup>, A. Tavares de Castro<sup>1</sup>, A. S. Ribeiro<sup>1</sup>

<sup>1</sup>LNEC – National Laboratory for Civil Engineering, Avenida do Brasil, 101, 1700-066 Lisbon, Portugal  
E-mail (corresponding author): [jmata@lnec.pt](mailto:jmata@lnec.pt)

---

## Abstract

Seepage through the foundation is a relevant condition for the structural assessment of concrete dams. The knowledge of the water flow measured in the drainage system installed to reduce the uplift pressure in a dam's foundation is, therefore, a main issue in the safety control of concrete dams. Monitoring systems include measuring devices to determine the water collected from drains and weirs in order to evaluate the amount of water that flows through the dam. In most large concrete dams, both manual and automated water flow measurements are possible.

This paper proposes a statistical quality control method for automatic measuring systems based on simultaneous manual water flow measurements and the knowledge of the corresponding measurement uncertainties. Experimental tests performed in a weir of a Portuguese concrete dam are described and paired water flow estimates and corresponding measurement uncertainties are presented and applied to the proposed method. The results of this study show that the method allows statistical quality control of automated water flow measurement systems applied in concrete dam drainage systems.

---

## 1. Introduction

The majority of recorded failures in concrete dams, not including issues related with appurtenant structures, are due to problems in the foundation, such as erosion and internal dissolving of rock masses, which often lead to a loss of strength and lack of shear resistance in weak planes of unfavorable direction [1].

Concrete dams are always founded in rock masses, characterized by a significant number on discontinuities or joints, which are very important for the mechanical and hydraulic behaviour of the foundation. Despite impermeabilization works done during construction in the foundations to minimize the water flow, leakage and seepage occur in all concrete dam foundations. The amount of water flow is a function of the reservoir level, watertightness of joints, foundation permeability, reservoir and ambient temperatures, and grout curtain or cutoff effectiveness [2].

Continued measurement of seepage can provide an indication of progressive dissolution or erosion in a dam foundation or abutment [3]. The types of measurement instruments used to monitor

seepage include weirs, flow meters and standard recipients [4].

In general, manual measurements of the water flow in the drainage system is obtained by an operator from the filling time measurement of a standard recipient with known volume. In this paper, this measurement system is denoted as Manual Data Acquisition System (MDAS).

Measurement estimates from MDAS are subjected to an in situ quality control procedure, being compared with previously defined threshold values. These control limits allow the detection of gross measurement errors and are established taking into account the measurement range and extreme values observed in prior records [5].

Many large concrete dams also operate with Automated Data Acquisition Systems (ADAS), which allow water flow measurements in weirs without direct human intervention [1,6,7]. This measurement system has the advantage of performing continuous measurements, being a fundamental tool for real time safety control of concrete dams. Therefore, a high level of confidence in the obtained automatic

measurements is required in order to perform a robust and reliable safety analysis, thus implying the need to adopt a periodic evaluation of ADAS metrological performance.

This evaluation is traditionally achieved by calibration of the measuring system in situ or in laboratory. However, in this case, it reveals to be a complex task since in situ calibration of ADAS lacks reference measurement standards with an acceptable accuracy, while laboratorial calibration is unpractical considering the need to temporarily remove the automatic measurement chain from the concrete dam.

Therefore, to provide traceability to the system, an alternative is proposed: the use of a statistical quality control method based on simultaneous water flow measurements by MDAS and ADAS, and the knowledge of measurement uncertainties found in both measurement methods (manual and automated).

In this paper the identification of uncertainty sources in both measurement methods for each input quantity is presented. The output quantity – water flow – measurement uncertainty is evaluated using the Guide to Expression of Uncertainty in Measurement (GUM) [8]. However, due to the recognizable non-linearity of the applied mathematical models, a Monte Carlo method (MCM) [9] is applied in order to validate the accuracy of the first order GUM approximation results of measurement uncertainty.

The proposed statistical quality control method is applied to experimental data obtained in a Portuguese concrete dam – the Alto Lindoso dam – where the MDAS and ADAS for water flow measurement coexist in three weirs. This study only focuses on results obtained from water flow measurements obtained from the weir named “Bica 1”. The described experimental procedures provided estimates for measurement uncertainty evaluation and statistical quality control analysis of a wide range of automated water flow measurements in concrete dams.

## 2. Water flow measurement in concrete dam drainage systems

### 2.1 Water flow measurement by Manual Data Acquisition System

In the MDAS, the water flow measurements in drains and weirs are performed using standard recipients with known volume. The filling time is FLOMEKO 2019, Lisbon, Portugal

manually measured with a stopwatch, thereby obtaining the water flow quantity by

$$Q = \frac{V}{t}, \quad (1)$$

where  $Q$  is the water flow (usually expressed in L/min),  $V$  is the recipient's volume and  $t$  is the recipient filling time.

The recipient choice, and consequently its volume, depends on the magnitude of the water flow observed in a particular drain or weir of the concrete dam. A commonly adopted empirical rule states that a recipient's filling time of less than 10 seconds is not recommended as it decreases the accuracy of the measurement results.

### 2.2 Water flow measurement by Automated Data Acquisition System

The water flow measurements by ADAS are usually done in weirs located inside the drainage gallery of the concrete dam.

In most concrete dams, the ADAS performs a level measurement using a brass or stainless steel V-notch weir with the following design and installation requirements (see Figure 1) [10]:  $0,05 \text{ m} \leq h \leq 0,6 \text{ m}$ ;  $25^\circ \leq \alpha \leq 100^\circ$ ;  $A \leq 0,10 \text{ m}$ ;  $h/A \leq 1,2$ ;  $H/L \leq 0,4$ ;  $L \geq 0,60 \text{ m}$ ; and  $2 \cdot B \geq 1,5 \cdot h$ .

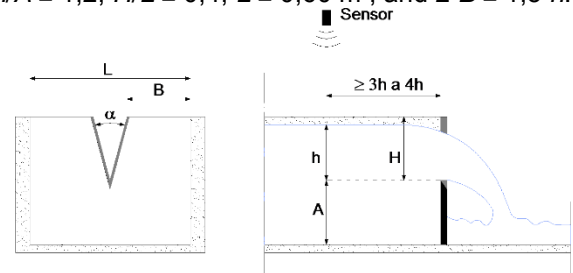


Figure 1: V-notch weir design and installation requirements.

In this type of weir (V-notch), and considering a uniform flow regime, a functional relationship between water level and flow can be established, allowing an indirect evaluation of the water flow. This mathematical relation is generally expressed by the Kindsvater-Shen formula [11]:

$$Q = \frac{8}{15} C_d \cdot \tan\left(\frac{\alpha}{2}\right) \cdot h_e^{\frac{5}{2}} \cdot \sqrt{2 \cdot g} \quad (2)$$

where  $Q$  is the water flow ( $\text{m}^3/\text{s}$ ),  $C_d$  is the discharge coefficient (dimensionless),  $\alpha$  is the V-notch angle (rad),  $g$  is the gravitational acceleration ( $\text{m}/\text{s}^2$ ),  $h_e = h + k_h$  is the effective head above the crest of the weir,  $h$  (m) is the total head, and  $k_h$  is a head correction factor that takes into

account surface tension and viscosity influence (m).

The system's measurement chain is composed of several elements, including an ultrasonic sensor to evaluate the water level in the weir basin and a computational unit where the measurement results are stored.

### 3. Statistical quality control method

The proposed quality control method of simultaneous ADAS and MDAS water flow measurements is supported in the statistical test of the estimate's difference of the population means,  $\Delta = \mu_{Q_{ADAS}} - \mu_{Q_{MDAS}}$ . For this purpose, two populations are considered (MDAS and ADAS measurements) with standard deviations,  $\sigma_{ADAS}$  and  $\sigma_{MDAS}$ , each one assumed equal to the correspondent value of the standard measurement uncertainties,  $u(Q_{ADAS})$  and,  $u(Q_{MDAS})$ , respectively.

The statistic is defined as the difference between sample means and the null hypothesis corresponds to zero difference between population means, so that the alternative hypothesis states that difference between population means is not zero,

$$\begin{aligned} H_0 : \mu_{Q_{ADAS}} - \mu_{Q_{MDAS}} &= 0 \\ H_A : \mu_{Q_{ADAS}} - \mu_{Q_{MDAS}} &\neq 0 \end{aligned} \quad (3)$$

In this study, it is assumed that both types of measurements follow Gaussian Probability Distribution Function (PDF), and that they are considered independent of each other.

Once the water flow quantity has a Gaussian PDF,  $Q \sim N(\mu_Q, \sigma_Q)$ , its mean value PDF corresponds  $\bar{Q} \sim N\left(\mu_Q, \frac{\sigma_Q}{n_Q}\right)$ , where  $n_Q$  corresponds to the sample dimension.

Hence, the statistical test,  $z$ , is given by

$$z = \frac{(\bar{Q}_{ADAS}) - (\bar{Q}_{MDAS}) - (\mu_{Q_{ADAS}} - \mu_{Q_{MDAS}})}{\sqrt{\frac{\sigma_{ADAS}^2}{n_{Q_{ADAS}}} + \frac{\sigma_{MDAS}^2}{n_{Q_{MDAS}}}}}, \quad (4)$$

and follows a Gaussian PDF, testing the equality of the two Gaussian population means,  $\mu_{Q_{ADAS}}$  and  $\mu_{Q_{MDAS}}$ , based upon independent random samples. The variance of a sample mean depends upon the sample size and the variance of the population from which the sample is selected. Consequently, the sizes of the two samples and the variances of the two populations will influence the comparison of the sample means.

If a significance level equal to 5 % ( $\alpha = 0,05$ ) is considered, the critical values of  $z$  are  $-1,96$  and  $+1,96$ . As a consequence, the decision rule is such that if  $z < -1,96$  or  $z > +1,96$ , the null hypothesis  $H_0$  is rejected.

### 4. The case study of the Alto Lindoso concrete dam

The proposed quality control method for automated water flow measurements was tested in the Alto Lindoso dam (see Fig. 2). Built in 1992, it is a double curvature concrete arch dam located in a symmetrical valley in the North of Portugal, and currently exploited by EDP (a Portuguese company for electricity production). It is 110 m high with a total crest length of 297 m, having three internal horizontal galleries and a drainage gallery close to its foundation.



Figure 2: The Alto Lindoso concrete dam.

All the water gotten from drains and leakages is collected in three weirs. Weir named "Bica 1" collects a portion of the water drained in the left bank.

MDAS are performed both in drains and weirs using a stopwatch and available standard recipients with volumes equal to 0,1 L, 0,25 L, 0,5 L, 1 L, 2 L, 5 L and 10 L. In addition, at the three weirs, ADAS measurements are also available through the use of ultrasonic sensors to evaluate the water flow.

The ADAS flow meters installed consider a V-notch angle of  $\pi/6$  rad. The output quantity - water flow - is obtained through the use of the Kindsvater-Shen formula (eq. 2) considering, as suggested by the equipment supplier, a head correction  $k_h$  equal to zero and a discharge coefficient  $C_d$  equal to 0,62.

The main metrological characteristics of the ultrasonic sensor for distance measurement installed at the Alto Lindoso concrete dam are: (i) water level measurement range up to 100 mm; (ii) linearity below 0,2 %; (iii) repeatability equal to 0,3 %.

MDAS water flow measurements recorded in weir “Bica 1” from January 2010 to March 2019 are presented in Fig. 3 (manual measurements were scheduled each two weeks and the time of the measurement was not recorded).

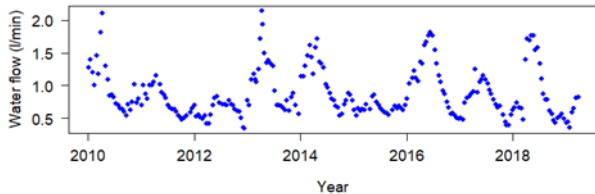


**Figure 3:** MDAS measurements in the weir Bica 1 (2010-2019).

#### 4.1 Measurement uncertainty evaluation

The following sections present the measurement uncertainty evaluation performed for the MDAS and ADAS. A first approach for uncertainty propagation for indirect measurement of water flow (see expressions 1 and 2) was done using the GUM method. The model obtained by the GUM method is easier to use than the model based on the MCM, as it requires less computational effort, and its implementation and use is simpler and more direct than the MCM. However, due to non-linearities, some representative MCM results were obtained in order to validate the GUM results. After being properly validated through the MCM, the model based on the GUM method can be adopted.

##### 4.1.1 Water flow measurement using MDAS

Two input quantities are measured when using the MDAS for indirect measurement of water flow: (i) the standard recipient volume; (ii) the corresponding filling time interval. In this study, the following probabilistic formulation is considered: (i) the nominal volume,  $V$  (L/min), of the standard recipient is assumed as the measurement estimate and a triangular PDF is adopted; this function is centred at the volume estimate and its variation limits are within  $\pm 2,5$  %, accounting for calibration and temperature uncertainty sources. The triangular PDF is adopted for uncertainty components since limit values for its dispersion are known but there isn't enough information to evaluate if it has a probabilistic gaussian behaviour; (ii) the main uncertainty sources of the filling time measurement,  $t$  (min), are considered to be the repeatability and the reproducibility related to the manual measurement through the use of a stopwatch; the PDF for this quantity is triangular and centred at the estimate obtained and variation limits are within  $\pm 0,75/60$  min.

The application of GUM's Uncertainty Propagation Law (correlation parameters are null) allows the expression of the MDAS water flow variance as

$$u^2(Q_{MDAS}) = \left(\frac{\partial Q}{\partial V}\right)^2 \cdot u^2(V) + \left(\frac{\partial Q}{\partial t}\right)^2 \cdot u^2(t), \quad (5)$$

where the sensitivity coefficients are equal to  $\frac{\partial Q}{\partial V} = \frac{1}{t}$  and  $\frac{\partial Q}{\partial t} = -\frac{V}{t^2}$ . Based on the above mentioned formulation, the input measurement standard uncertainties are  $u(V) = \frac{0,025}{\sqrt{6}} \cdot V$  and  $u(t) = \frac{0,75}{60\sqrt{6}}$  min. The 95 % expanded measurement uncertainty relative,  $\frac{U_{95\%}(Q_{MDAS})}{Q_{MDAS}}$ , is given by

$$\frac{U_{95\%}(Q_{MDAS})}{Q_{MDAS}} = 1,98 \cdot \sqrt{\frac{2,6 \cdot 10^{-5}}{t^2}} + 1,04 \cdot 10^{-4}, \quad (6)$$

with  $t$  (min). Based on the previous expression, Fig. 4 presents the estimate and 95 % relative expanded measurement uncertainty evolution according to filling time interval and recipient volume.

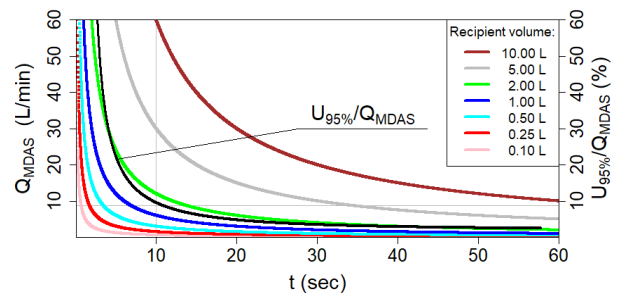


**Figure 4:** Water flow estimates and relative 95 % expanded uncertainty function of filling time interval and recipient volume.

Fig. 4 confirms the adequacy of the filling time interval rule which states that measurements should only be made with time intervals above 10 s in order to reduce measurement uncertainties. It is possible to observe that, in a filling time interval between 10 s and 60 s, the 95 % relative expanded measurement uncertainty related to the water flow reduces from, approximately, 6,5 % to 2,3 %.

##### 4.1.2 Water flow measurement using ADAS

According to expression (2), three different input quantities are required for ADAS water flow indirect measurement: (i) the discharge coefficient; (ii) the weir's V-notch angle; (iii) the water level above the weir's V-notch. The following probabilistic formulations are considered: (i) a discharge coefficient estimate equal to 0,62 is used in the

parameterisation of the water level measurement equipment; for this input quantity,  $C_d$ , a triangular PDF is considered, centred at the mentioned estimate with variation limits within  $\pm 0,01$ ; therefore, the related measurement standard uncertainty is given by  $u(C_d) = \frac{0,01}{\sqrt{6}}$ ; (ii) the nominal V-notch angle for weir “Bica 1”,  $\alpha$ , is equal to  $\pi/6$  rad; this value is used as the centre of a triangular probability distribution function with variation limits equal to  $\pm \pi/360$  rad, corresponding to a measurement standard uncertainty given by  $u(\alpha) = \frac{\pi}{360 \cdot \sqrt{6}}$  rad; (iii) the main uncertainty sources for the water level measurement,  $h$ , are the linearity and the repeatability related to the ultrasound measurement equipment, and the floatation on the water crest. The in situ experimental observation of the water floatation phenomenon allows representing its probabilistic behaviour by a Gaussian PDF, with a null central value and standard deviation equal to 1,5 mm. The combined standard uncertainty is equal to  $u(h) = \sqrt{1,3 \cdot 10^{-5} \cdot h^2 + 2,25 \cdot 10^{-6}}$  m. Using GUM's Uncertainty Propagation Law, an expression for the ADAS water flow variance can be obtained,

$$u^2(Q_{ADAS}) = \left(\frac{\partial Q}{\partial C_d}\right)^2 \cdot u^2(C_d) + \left(\frac{\partial Q}{\partial \alpha}\right)^2 \cdot u^2(\alpha) + \left(\frac{\partial Q}{\partial h}\right)^2 \cdot u^2(h), \quad (7)$$

where the sensitivity coefficients are the following,

$$\frac{\partial Q_{ADAS}}{\partial C_d} = \frac{8}{15} \cdot \tan\left(\frac{\alpha}{2}\right) \cdot h^{\frac{5}{2}} \cdot \sqrt{2 \cdot g}, \quad (8)$$

$$\frac{\partial Q_{ADAS}}{\partial \alpha} = \frac{4}{15} \cdot C_d \cdot \left(\tan^2\left(\frac{\alpha}{2}\right) + 1\right) \cdot h^{\frac{5}{2}} \cdot \sqrt{2 \cdot g}, \quad (9)$$

$$\frac{\partial Q_{ADAS}}{\partial h} = \frac{4}{3} \cdot C_d \cdot \tan\left(\frac{\alpha}{2}\right) \cdot h^{\frac{3}{2}} \cdot \sqrt{2 \cdot g}. \quad (10)$$

The development of the previous variance expression, supported in the discharge coefficient and V-notch angle estimates for weir “Bica 1”, allows writing the 95 % relative expanded measurement uncertainty as

$$\frac{U_{95\%}(Q_{ADAS})}{Q_{ADAS}} = 2,622 \cdot 10^{-2} \sqrt{1 + \frac{8,018 \cdot 10^{-2}}{h^2}}. \quad (11)$$

Based on this expression, Fig. 5 shows the absolute and 95 % relative expanded measurement uncertainty in a wide range of water flow measurements by ADAS.

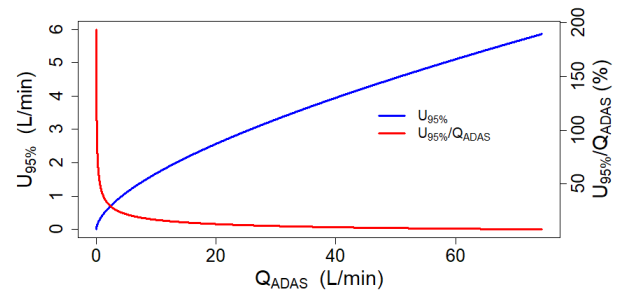


**Figure 5:** Absolute and relative expanded uncertainty (95 % confidence level) for ADAS water flow measurements.

For the case of the ADAS related to weir “Bica 1”, where the water level measurement range is between zero and 100 mm, the 95 % relative expanded measurement uncertainty of the water flow is close to 30 %, for a water flow near 2 L/min and converges to 8 % for higher water flow estimates. These results were validated by MCM for a wide range of water flow values (0,5 L/min, 1 L/min, 2 L/min, 5 L/min, 10 L/min, 20 L/min, 30 L/min, 40 L/min, 50 L/min and 60 L/min). The PDF, provided through the MCM, shows that the studied measurement range has a Gaussian shape.

#### 4.2 Experimental work

The main objective of the experimental work was to obtain simultaneous MDAS and ADAS water flow measurements in weir “Bica 1” in order to apply the proposed quality control method to a wide measurement interval. The first measurements were obtained under natural operational conditions of the dam (water flow values below 2 L/min). Artificial water flows were introduced in the weir in order to achieve high water flow values (up to 35 L/min).

The water flow measurement procedure by MDAS included a visual inspection of the weir to determine the existence of residues that could constitute obstacles to the water flow. Each water flow increment over the studied range was followed by a stabilization time interval of the water surface inside the weir before recording any measurement.

During the test, the ADAS was programmed to record measurements each minute. During this test, a total of approximately 350 measurements were made. The results are presented in Fig. 6. From the obtained results, pairs  $(Q_{MDAS}, Q_{ADAS})$  were selected based on the time of measurement. Fig. 7 shows good agreement between the pairs of water flow values as they can be located,

approximately, along an ideal straight line ( $Q_{MDAS} = Q_{ADAS}$ ).

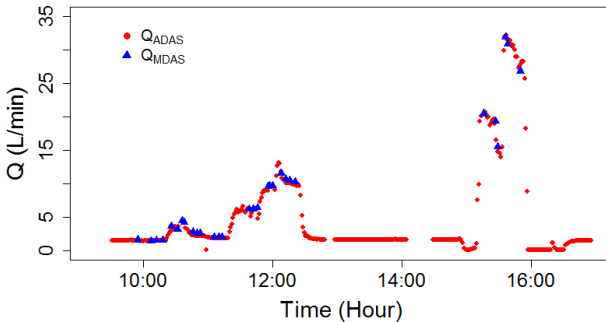


**Figure 6:** MDAS and ADAS flow measurements in weir Bica 1.

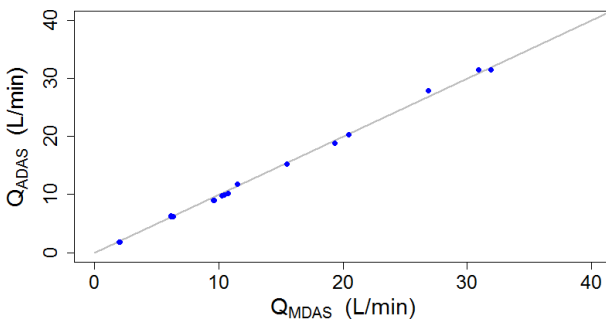


**Figure 7:** Paired water flow observations.

The statistical quality control method proposed is applied to the previously collected data to verify if there is evidence of rejection of the null hypothesis. The results presented an absolute  $z$  value minor than 0,75, whereby there is no evidence to reject the null hypothesis for a significance level equal to 5 %.

## 5. Final remarks

This study indicates that the ADAS device for water flow measurement in weir “Bica 1” at the Alto Lindoso dam has an acceptable metrological performance for the intended use, based on the experimental work activities.

Measurement uncertainties were also evaluated, showing that the MDAS has a 95 % relative expanded measurement uncertainty between 6,5 % and 2,3 %, considering filling time intervals between 10 s and 60 s. In the case of the ADAS, the relative expanded uncertainty obtained assumes high values (30 %) for the water flow near 2 L/min and converges to 8 % for higher water flow estimates.

The experimental activity regarding simultaneous measurements with MDAS and ADAS revealed

that a uniform water flow regime in the weir is critical for the accuracy of the automatic measurements since it affects the stability of the water surface and, consequently, the water level reading. Regular weir cleaning is recommended in order to improve the stability of the water flow and remove any residues on the water's surface, eliminating changes in its viscosity and superficial tension.

The proposed method is suitable to perform statistical quality control of automated water flow measurements by ADAS in concrete dams. However, to do so, it is recommended that ADAS measurements are obtained in a synchronized way with MDAS water flow measurements scheduled in a dam's observation plan.

## 6. Acknowledgements

The authors acknowledge the company EDP – Energias de Portugal who provided the data for the procedures addressed in this paper.

## References

- [1] ICOLD: *Guidelines for automated dam monitoring systems*, 1999.
- [2] Strom R W, Cunningham G, *et al*, Evaluation of concrete dam stability, <http://www.damsafety.org/media/Documents/DownloadableDocuments/TADS/EvaluationOfConcreteDamStability.pdf>.
- [3] ICOLD: *Lessons from dam incidents*, 1974.
- [4] ICOLD: *Monitoring of dams and their foundations*, 1988.
- [5] Ramos J M, *Concrete dam behaviour. Practical aspects* (Lisbon, LNEC), 2004.
- [6] ICOLD: *Automated dam monitoring systems - Guidelines and case histories*, 2000.
- [7] ASCE: *Guidelines for instrumentation and measurements for monitoring dam performance*, 2000.
- [8] JCGM 100: *Evaluation of measurement data. Guide to the expression of uncertainty in measurement*, 2008.
- [9] JCGM 101: *Evaluation of measurement data. Supplement 1 to the “Guide to the expression of uncertainty in measurement”. Propagation of distributions using a Monte Carlo method. Joint Committee for Guides in Metrology*, 2008.
- [10] Lencastre A, *General Hydraulics* (Lisbon, Armando Lencastre), 1996.
- [11] BSI: *Methods of Measurement of Liquid Flow in Open Channels. Weirs and Flumes. Method Using Thin-plate Weirs*, 1981.

# Initial Results on the Flow Dynamics of Household Water Consumption

B. Ünsal<sup>1</sup>, B. Akselli<sup>1</sup>,  
Ş. Sacı<sup>2</sup>, E. Aksel<sup>3</sup>

<sup>1</sup>TÜBİTAK UME (National Metrology Institute of Turkey)

<sup>1</sup>TÜBİTAK Gebze Yerleşkesi, Barış Mah. Dr. Zeki Acar Cad. No:1, 41470 Gebze, Kocaeli, Turkey

<sup>2</sup>TEKSAN, Çatalmeşe Mahallesi Reşadiye Caddesi 185. Sokak No:6 34794 Çekmeköy, İstanbul, Turkey

<sup>3</sup>ISU (Kocaeli Su ve Kanalizasyon gen. Müd.), Kocaeli, Turkey

E-mail (corresponding author): bulent.unsal@tubitak.gov.tr

---

## Abstract

Household water meters are tested/calibrated at steady flow conditions however, during their actual usage, flow conditions are not always steady and not so much known about the flow dynamics. The present paper reports about instantaneous flow rate measurements conducted at households to find out what kind of flow rate profiles exist through household meters. From these measurements, 3200 single water consumption events were extracted. Then each single event was analysed to obtain various information such as rise time, fall time, amplitude, event duration and consumed water volume. These results showed that the distributions of rise and fall times with respect to number of events are mostly around 100 to 300 ms. And more than 5% of the flow time, the meter is under dynamic flow conditions.

---

## 1. Introduction

According to OIML R49 [1] and ISO 4064 [2], water meters used for household consumption are tested/calibrated at constant flow rates in laboratory conditions. On the other hand, the measurements [3-5] conducted at households showed that water meters are exposed to highly changing flow rates. Furthermore, particles and inorganic composition [6-8] of the drinking water within distribution pipelines are also not considered by the present legal metrology requirements (e.g. type approval tests). A recently started EMPIR (European Metrology Programme for Innovation and Research) project called MetroWaMet (Metrology for Real-World Domestic Water Metering) [9] aims to establish a metrological infrastructure which will enable an integral characterization of domestic water meter performance close to real-world conditions and not at laboratory conditions as presently done. The present study was conducted within the MetroWaMet project to analyse flow dynamics of household water consumption.

In literature, there are several reports on measurement results conducted at households

and a brief summary of such studies can be found in [4, 5]. In these studies, the researchers are mostly interested in identifying consumption patterns to match with usage purpose. And develop algorithms to be used with smart meters, to provide detailed water consumption statistics to users and water distributors. Although some of these studies were done with high resolution meters at households, an analysis of flow dynamics were not made.

Schumann et. al [3] reports a summary of the results obtained from the measurements conducted at 300 households. In this study, no information was provided how the measurements were conducted and technical description of the flow meters used for the measurements (e.g. time resolution). And also time scales of the flow dynamics were not made. On the other hand, the authors provided some sample flow variations and probability distribution of flow rates.

The present paper reports about test measurements conducted at households to find out what kind of flow dynamics exist through household meters. For this aim, a special water meter was built together with electronics to reach

time resolution of up to 12 ms. Such time resolution was necessary in order to measure instantaneous changes accurately.

## 2. Measurements



**Figure 1:** Picture of the meter and electronic used for the measurements.

A standard meter was modified to obtain high time resolution which was 60 pulses/l. With this modified meter up to 12 ms time resolution was possible at 5040 l/h. Electronics were developed to read pulses and store the pulse data as shown in Fig. 1. This stand alone system was installed at four households just next to their actual meter. The battery shown Fig. 1 allowed to perform at least 6 days of uninterrupted measurement which can be extended by replacing the battery.

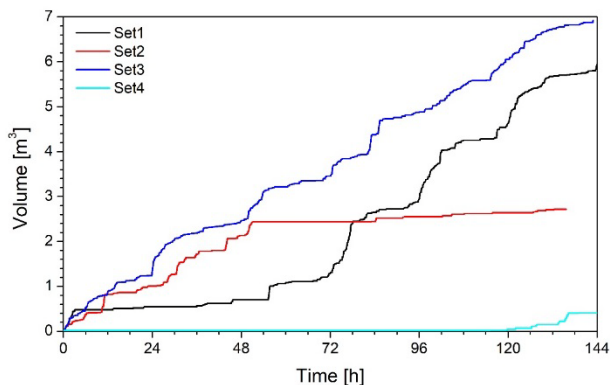


**Figure 2:** Raw data from four set of measurements.

Figure 2 shows the raw data from four sets of measurements conducted at four different households. As can be seen from the picture, during the measurements, two of the households (set2 and set4) were not occupied some of the time.

## 3. Results

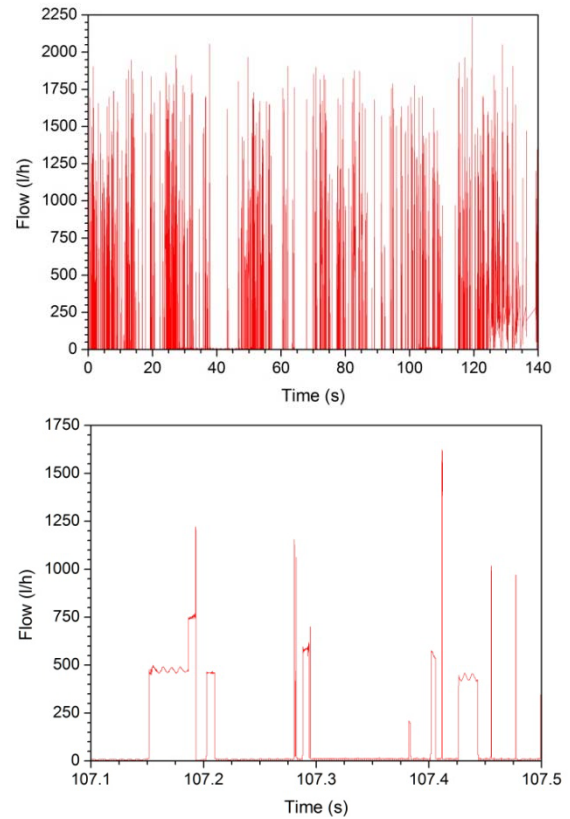


**Figure 3:** Flow rate variations samples.

The raw data shown in Fig. 1 were processed to obtain flow rate data and some samples are shown in Fig.1. This figure shows the complete instantaneous flow rate data of set1 and also a zoomed portion of the same data to see some of the events closely. As can be seen from these figures there are rapid flow rate changes which are occurring relatively short time intervals and these changes will be called as flow events.

In figure 4 some single flow event samples are shown. These events correspond to some certain water consumption activity and in literature there are various approaches to identify consumption activities from measured flow events, based on some known patterns, [4, 5]. In the present study aim is to characterise flow dynamics of household water consumption and hence the focus is given to characterise these events.

The extracted flow events can be grouped as single amplitude and multi amplitude events event as indicated in Fig. 4. For single amplitude events, below parameters can be defined for characterization as shown in Fig. 5;

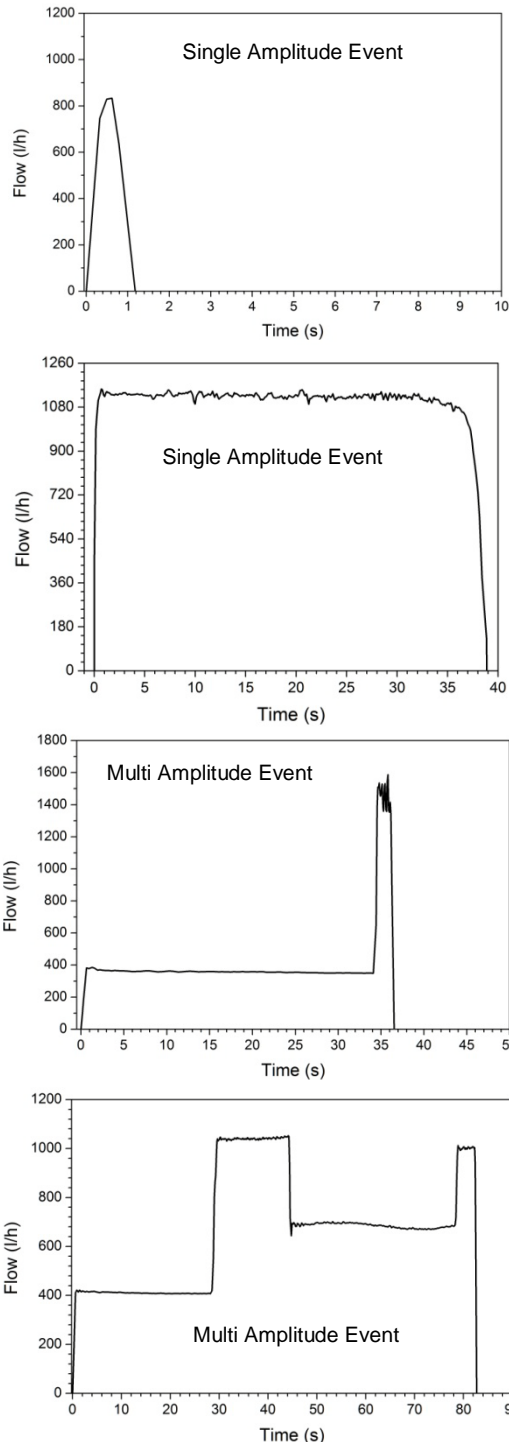


Figure 4: Flow event samples.

1. Event duration
2. Rise time
3. Fall time
4. Event volume
5. Rise volume
6. Fall volume
7. Amplitude

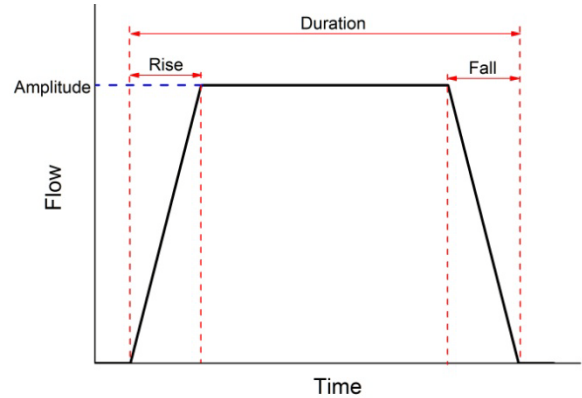


Figure 5: Characteristic parameters of a single amplitude event.

These parameters were analysed for each single event and there was 3200 events extracted from four set of measurements. A general summary of the results are given in table 1.

Table 1: Single event analysis results.

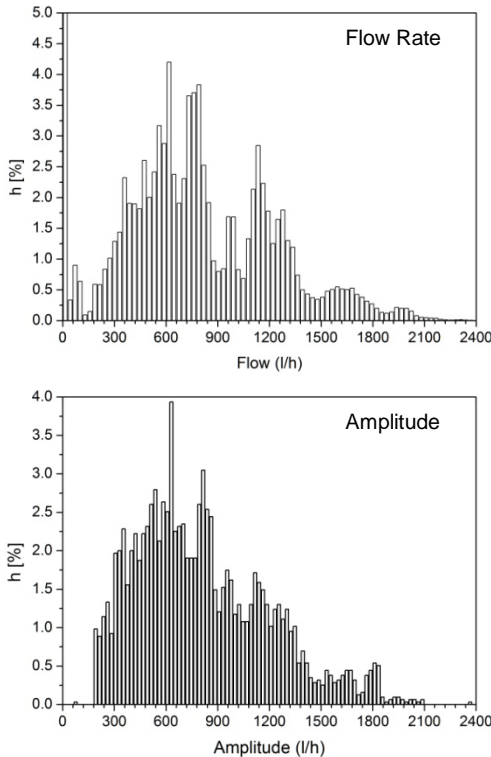
		Set1	Set2	Set3	Set4	Total
Events	#	893	565	1655	87	3200
Multi Amplitude Events	# - %	164 - 18.4	55 - 9.7	218 - 13.2	9 - 10.3	446 - 13.9
Volume (consumption)	m <sup>3</sup>	5.9	2.7	6.0	0.53	15.1
Duration	h	6.71	3.59	10.14	0.6	21.05
Total Rise Time	%	1.4	1.94	2.04	2.36	1.83
Total Fall Time	%	2.2	2.81	2.12	1.64	2.25
Total Rise Volume	%	1.24	2.18	2.28	2.8	1.87
Total Fall Volume	%	2.47	3.45	3.33	1.82	2.96
Volume / Event	l	6.63	4.71	3.62	6.06	4.72
Duration / Event	s	27.05	22.85	22.07	24.99	23.68
Rise Time / Event	s	0.379	0.443	0.450	0.590	0.433
Fall Time / Event	s	0.595	0.642	0.468	0.410	0.533

As given in table 1; 446 of the 3200 events are multi amplitude events which means around 86% of the events are single amplitude. The total flow duration is 21 hours and around 4% of the total time the flow rate is rising/falling. This means that 4% of the total flow time, the flow is unsteady. By considering multi amplitude events, the unsteady time could be more than 5% of the total flow time.

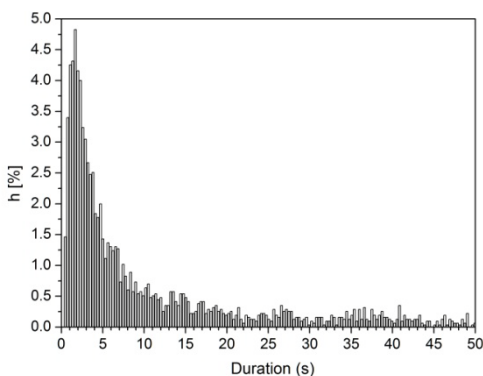
The total measured volume is around 15 m<sup>3</sup> and around 5% of this volume the flow rate is rising/falling. By considering multi amplitude events, the volume measured under unsteady conditions could be more than 6.5% of the total volume.

Table 1 also provides some average information for one event. Average volume is 4.7 l, duration is

23 s, rise time is 433 ms and fall time is 533 ms for one flow event.



**Figure 6:** Distribution of measured flow rates and extracted amplitudes.



**Figure 7:** Distribution of event durations.

Distribution of flow rates and amplitudes are given in Fig. 6. As the figure indicates flow rate varies mostly within 200 to 1800 l/h for both measured flow rate and flow event amplitudes. It is important to note that the maximum flow rate of the actual water meter for these households is 3125 l/h and nominal flow rate is 2500 l/h which are higher than required and these meters are tested/calibrated at these constant flow rate values.

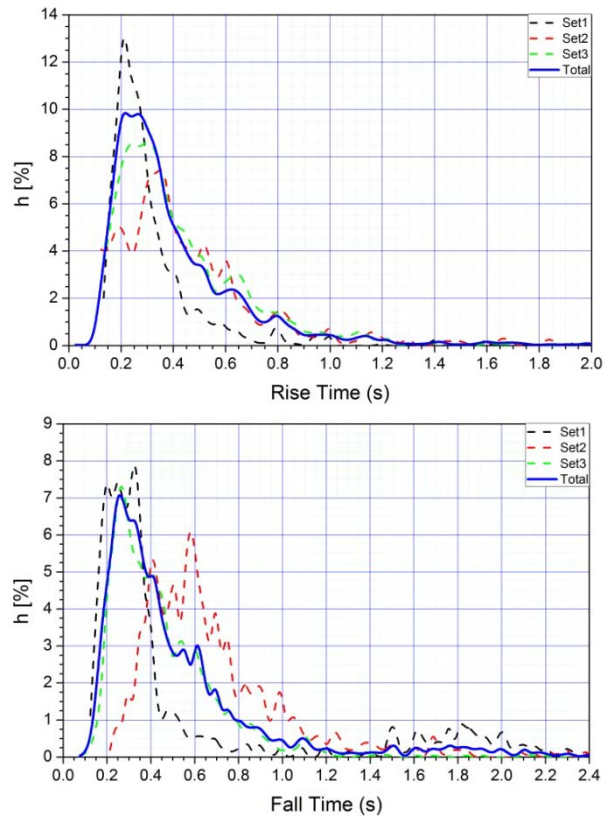


**Figure 8:** Distribution of rise and fall time.

Figure 7 shows the distribution of event durations. As the figure indicates important portion of the events are last less 10 seconds and the peak values are few seconds. Based on this figure; 46% of the events are having duration within 0.5 to 5 s. And 62% of them are having duration within 0.5 to 10 s.

Distribution rise and fall time for each set and also for the all extracted events are given in Fig. 8. There are some differences between the sets especially for fall time distribution. But it must be noted again that during the set2 measurement the house was not occupied every day. On the other hand, rise and fall time distributions are similar when the total distributions are considered. Both of the distributions are mostly within 0.1 to 1.2 s and the peak value is around 0.2 to 0.3 s.

It is interesting to know what fall and rise time values are important when flow duration and total volume are considered. In order to obtain this information, cross distributions were made as shown in Fig. 9. This figure indicates total events volume for the events with some certain rise time interval. Similar distributions were made for duration and the results are given in table 2 and 3.

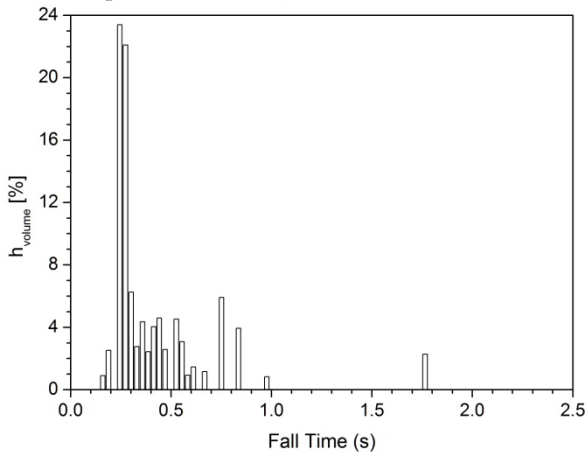


**Figure 9:** Cross distribution of fall time versus total events volume.

**Table 2:** Rise time intervals and corresponding distribution percentages.

Rise time interval [s]	h[%]	h <sub>duration</sub> [%]	h <sub>volume</sub> [%]
0.05–0.2	10.1	8.15	≈ 0.01
0.2–0.4	57.5	43.12	54.94
0.4–0.6	15.2	23.09	17.22
0.6–0.8	9.6	13.45	8.71
0.8–1	3.4	3.54	0.68
1–3.5	4.25	8.64	18.45

**Table 3:** Fall time intervals and corresponding distribution percentages.

Fall time interval [s]	h[%]	h <sub>duration</sub> [%]	h <sub>volume</sub> [%]
0.05–0.2	7.62	4.2	3.42
0.2–0.4	42.6	34.56	61.3
0.4–0.6	23.02	24.89	19.72
0.6–0.8	12.73	16.67	8.54
0.8–1	4.95	5.21	4.75
1–3.5	9.08	14.46	2.27

From the tables 2, 3 and figure 9, it is easy to conclude that rise and fall times of 0.2 to 0.6 s are mostly encountered with respect to total event duration and volume.

#### 4. Conclusions

Flow rate measurements were made at four households and each measurement was almost one week long. The processed data showed that there are two water end use events as single and multi amplitude. The total number of detected

events are 3200 and 14% of them are multi amplitude events.

For each event, an unsteady portion can be defined as rise time and fall time which are the durations where the flow rate reaches an amplitude from zero flow (rise time) and then after some flow time the flow rate becomes zero again (fall time) as indicated in Fig. 5. For all the events, this unsteady time is around 5% of the total flow duration and 6.5% of the total measured volume. These values are not small and it requires further investigations to check water meters performances under such unsteady conditions since presently the meters are not tested for that.

In order to test water meters for unsteady conditions, it is necessary to apply rise and fall times values. From the present measurements results, the events which correspond to 70 to 80% of the total volume are having rise and fall times within 0.2 to 0.6 s. Thus this suggests that the test-rigs for unsteady tests should be able to generate at least 0.2 s of rise and fall times within the amplitude/flow range given in Fig. 6.

#### Acknowledgement

The project MetroWaMet (Metrology for Real-World Domestic Water Metering) [9] is carried out with funding by the European Union under the EMPIR. The EMPIR is jointly funded by EURAMET (European Association of National Metrology Institutes) and the European Union.

#### References

- [1] OIML R 49, Water meters for cold potable water and hot water, 2013.
- [2] ISO 4064, Water meters for cold potable water and hot water, 2014.
- [3] D. Schumann, G. Wendt, J. Tränckner, “Development of a calibration process for water meters close to real world conditions”, FLOMEKO 2016, Sydney, Australia, September 26-29, 2016.
- [4] B. Ellert, F. Popowich, S. Makonin, “Appliance Water Disaggregation via Non-Intrusive Load Monitoring (NILM)”, EAI International Conference on Big Data and Analytics for Smart Cities (BigDASC) 2015.
- [5] K.A. Nguyen, H. Zhang, R.A. Stewart, “Development of an intelligent model to categorise residential water end use events”, Journal of Hydro-environment Research, ISSN1570-6443, 2013.

- [6] JHG. Vreeburg, D. Schippers, JQJC. Verberk, C. Van Dijk, "Impact of particles on sediment accumulation in a drinking water distribution system", *Water Res.*, 42(16), 4233-4242, 2008.
- [7] D. Banks, M. Birke, B. Flem, C. Reimann, "Inorganic chemical quality of European tap-water: 1. Distribution of parameters and regulatory compliance", *Appl. Geochem.*, 59, 200-210, 2015.
- [8] B. Flem, C. Reimann, M. Birke, D. Banks, P. Filzmoser, B. Frengstad, "Inorganic chemical quality of European tap-water: 2. Geographical distribution", *Appl. Geochem.*, 59, 211-224, 2015.
- [9] <https://www.ptb.de/empir2018/metrowamet/the-project/>

# Ultrasonic Flowmeter for flow rates below 100 l/h

R. Kramer<sup>1</sup>, T. Dietz<sup>2</sup>

<sup>1</sup> *Physikalisch-Technische Bundesanstalt, rainer.kramer@ptb.de, Braunschweig, Germany*

<sup>2</sup> *SICK Engineering GmbH, toralf.dietz@sick.de, Ottendorf-Okrilla Germany*

*rainer.kramer@ptb.de*

---

## Abstract

The paper describes an ultrasonic flow meter with an axial measuring path, which uses acoustic plane waves propagating through pipes with a sufficiently small diameter. The propagation of plane waves in a circular pipe depends on the pipe diameter and the wavelength of the acoustic signal. Therefore, the design of the meter has to consider the speed of sound for the gases intended to use, e.g. nitrogen, methane, hydrogen and any mixture of these. In order to measure low flow rates with small uncertainties, a great acoustic path length, i.e. a pipe with long length is advantageous. On the other hand, the signal attenuation increases proportionally with the length of the measuring pipe. The paper provides information about the basic conditions to reach plane waves in a pipe with small diameters.

The investigated prototype uses an inner pipe diameter of 4 mm and a path length of 320 mm. The ultrasonic transducers and the electronics are taken from a commercially available ultrasonic meter with two paths and a working frequency of 135 kHz. In this configuration, the signal quality is already very good with nitrogen under atmospheric conditions, but due to the acoustic attenuation, methane is only measurable with more than 2 bar absolute pressure. The results for nitrogen and methane show nearly linear behaviour over a flow range from 10 to 1,000 l/h. At the lower flow range of the meter the zero flow uncertainty is the limiting influence value. The prototype has shown stabilities of lower than  $q_z = 0.1$  l/h.

The meter may be used for quality assurance of test rigs such as checking small nozzles and as transfer standard for intercomparisons.

---

## 1. Introduction

For determining flow rates in pipes, various measurement principles are on the market. For flowrates below 100 l/h, the available kinds of meters are limited though. Laminar flow meters and thermal mass flow meter are usable, but both principles are sensitive to the composition of the gas. Diaphragm gas meters are used in very large numbers for such flow rate ranges, however, the long term stability and reproducibility is influenced by mechanical stress and purity of the gas. A rotary meter, which was developed for low flows, show a severe slope of the error curve at flow rates below  $Q = 100$  l/h already because of internal leakages and friction losses of the mechanics. Wet-test gas meters are not influenced by the type of gas if the solubility of the gas in the sealing liquid is negligible. Wet-test gas meters are able to provide uncertainties below  $U = 0.2$  %, but the handling is relative difficult.

Flow measurement in pipes based on the travel time of ultrasound signals by ultrasonic flow meters (USM) is mature technology for accurate and robust measurement

of gas quantities. Along with the high repeatability and high accuracy, ultrasonic technology has inherent features like negligible pressure loss and high rangeability. In addition, the measured speed of sound may be compared with the speed of sound calculated from pressure, temperature, and gas composition to check the mutual consistency of the four instruments involved. Further, the signal quality may be supervised during application.

## 2. Design of an USM for very small flow rates

### 2.1 Basic principle of an USM

Figure 1 illustrates the basic principle of an USM. Typically, at least two ultrasonic transducers, marked (A) and (B), are arranged in an angle  $\theta$  to the pipe axis. Hence, the direct line between the two transducers defines the measuring path of the length  $L$ . A signal pulse transmitted from a transducer travels with the speed of sound  $c$  of the fluid to the transducer located opposite.

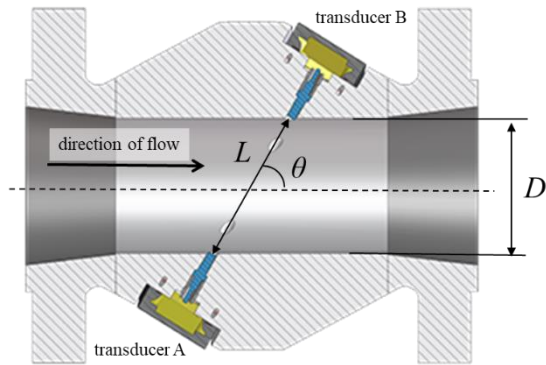


**Figure 1:** Basic arrangement of an ultrasonic measuring path

The signal pulse additionally accelerates when travelling with and decelerates when travelling against the flow. Thus, the flow measurement is derived from the measured signal travel time  $t_{AB}$  between the two transducers with the flow and  $t_{BA}$  against the flow.

$$t_{AB} = \frac{L}{c + v \cos \theta} \quad (1)$$

$$t_{BA} = \frac{L}{c - v \cos \theta} \quad (2)$$

Here, the time difference is a direct measure of the average flow velocity  $v_{path}$ , whereas the sum is a measure of the speed of sound along the acoustic path.

$$v_{path} = \frac{L}{2 \cos \theta} \left( \frac{1}{t_{AB}} - \frac{1}{t_{BA}} \right) \quad (3)$$

$$c_{path} = \frac{L}{2} \left( \frac{1}{t_{AB}} + \frac{1}{t_{BA}} \right) \quad (4)$$

To increase the accuracy for an arrangement shown in Figure 1, more than one measuring path is arranged over the cross-sectional area  $A$  of the pipe. Several of these multi-path layouts may be found e.g. in [1]. These layouts provide different path velocity information of different regions of the cross sectional area. The individual path velocity measurements are combined by a mathematical function, e.g. a weighted average, to yield an estimation of the average velocity  $v$  in the pipe. The volumetric flowrate  $q_v$  is obtained by multiplying the cross-sectional area  $A$  with the estimate of the average velocity  $v$ .

$$q_v = A \cdot v = 0.25 \cdot \pi \cdot D \cdot v \quad (5)$$

### 2.2 Design constraints for very small pipe diameters

Considering a flow velocity of approximately 30 m/s in the pipe at the maximum flowrate of e.g. 1,000 l/h results

in some millimeters pipe diameter only. On the other hand, the size of the ultrasonic transducer relates to its working frequency and cannot be scaled down proportionally to the pipe diameter. Obviously, the conventional USM design as shown in Figure 1 is not applicable here due to the space needed for the transducers in the pipe wall. Furthermore, the signal travel time will be excessively short for an accurate time measurement.

To cope with these challenges, the transducers A and B are aligned with the axis of the pipe, as Figure 2 shows. Thus, the diameter will no longer be a limiting factor for the path length.

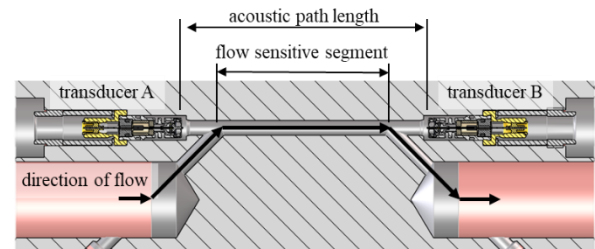


**Figure 2:** Axially arranged ultrasonic measuring path

The fluid flow is guided through the measuring path e.g. as Figure 2 shows or flows directly around the transducers before entering respective leaving the meter. The acoustic signal shall propagate along the pipe axis only, and the sound field shall cover the complete cross-sectional area without interference of the signal by reflected signals. In a cylindrical pipe, the fundamental wave mode, respective a plane wave fulfils these requirements. The front of a plane wave propagates equal to the speed of sound  $c$ . If higher wave modes are present as well, the propagation speed of the acoustic signal pulse will become slower than the speed of sound [2].

For a circular flow channel with the diameter  $D$  and a flow velocity  $v$ , the higher wave modes can propagate if the signal frequency is higher than the cut-on frequency of the respective wave mode [3]. For the 1<sup>st</sup>-order wave mode this cut-on frequency is given with Equation (6) below.

$$f_{cut-on} = \frac{1.84118}{\pi D} c \sqrt{1 - \left(\frac{v}{c}\right)^2} \quad (6)$$

### 2.2 Design of an USM for very low flow rates

For the presented prototype of an USM with an axial path, the transducers and electronics of a commercially available flow meter with two measuring paths and a working frequency of 135 kHz was used. The meter shall measure different gases at pressures up to 50 bar and a maximum flow rate of 1,500 l/h under measuring

conditions. Considering the different speed of sound for the different gases intended to use, with Equation (6), we can calculate the cut-on frequencies of the 1<sup>st</sup>-order mode in our meter as shown in Table 1 below.

**Table 1:**

	Nitrogen	Methan	Hydrogen
Speed of sound [m/s] @ 101kPa, 20°C	349,1	445,0	1304,1
f_cut-on [kHz], Di 4mm	51,1	65,2	191,1
Dmax_f(1,1) [mm]	1,5	1,9	5,7
qV <sub>max</sub> [l/h] @ 33m/s	214	348	2991

According to Equation (6), the propagation of higher wave modes may be prevented by reducing the pipe diameter and / or the signal frequency. Due to the fact that the available ultrasonic sensors and electronics define the signal frequency, only the pipe diameter might change. The dilemma here is the dramatically reduced maximum flow capacity when we will reduce the pipe diameter. With a pipe diameter of 1.5 mm, the maximum flow rate at 33 m/s velocity will be 214 l/h only. A higher flow velocity might be applicable if on one side the increasing pressure drop and on the other hand, the increasing flow induced acoustic noise will not limit the measurement setup.

Due to the various gases to measure and the possible maximum flowrate limitations, a compromise with a pipe diameter of 4 mm and a length of 322 mm for the acoustic path was chosen. Unfortunately, do we have to expect the propagation of higher wave modes for gases with lower speed of sound values than at Hydrogen.

Both measuring paths of the electronics were used with the option of getting two independent measuring channels. Hence, this offers the possibility to choose different path lengths and/or pipe diameters in a later phase of the project.

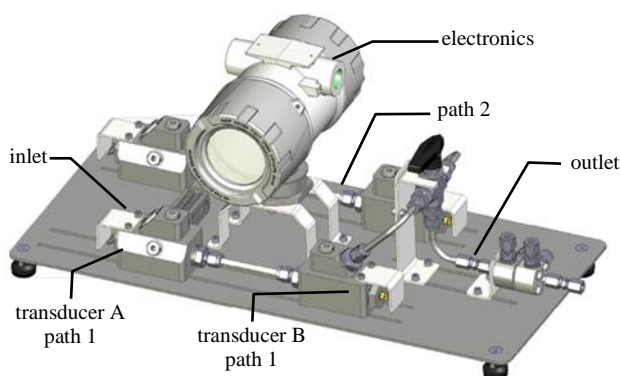


**Figure 3:** Flow meter with axially arranged ultrasonic measuring paths

Each transducer is mounted in a metal block with the gas in- / outlet, and a connection for the measuring channel. The measuring channel is made from a standard 6 mm stainless steel pipe with a wall thickness of 1 mm, resulting in the 4 mm diameter of the acoustic channel. Furthermore, each of the four mounting blocks provides connection ports for measuring the gas temperature and pressure.

### 3. Results of the USM with different gases

#### 3.2 Test setups

For investigating the capillary USM, a positive displacement meter (PD meter) and a mercury sealed piston prover (PP meter) were used. Figure 4 shows the error curve of the DP meter

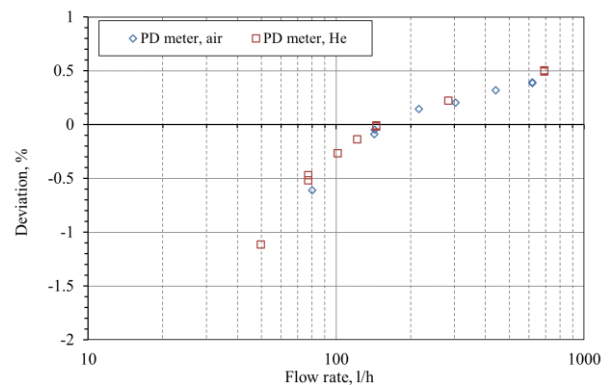


**Figure 4:** Error curve of the PD meter with nitrogen and helium at atmospheric conditions

The PD meter provides similar results for nitrogen and helium. For flows below 100 l/h, the reproducibility of the results decreases. As mentioned in chapter 1, this is because of increasing influences by friction and inner leakage.

In order to investigate the USM prototype for flow rates below 100 l/h at metering conditions  $p_{USM}$ , the mercury sealed piston provers (PP) of the flow laboratory at PTB were used.

Figure 5 shows the arrangement of the interferometer for determining the speed of the piston. The inner diameter of the glass cylinder is traceable by length and was calibrated by a coordinate measurement machine. The PP is not sensitive to the kind of gas as long as the mercury seal does not react with the gas. For inert gases this is the case.

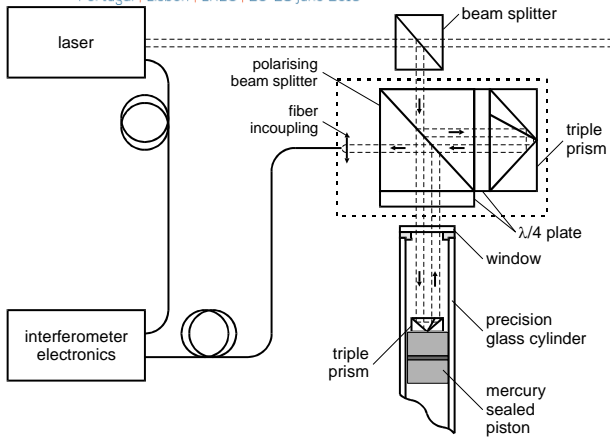


**Figure 5:** Interferometer system of the mercury sealed piston prover for gas independent flow determinations

### 3.1 Flow test results

The capillary USM was investigated with nitrogen and methane. As mentioned above, the methane measurements were carried out at a measuring pressure of  $p_{abs,USM} = 3$  bar only. For determining the measuring pressure, the port at the inlet was used. As long as the pressure drop is low in comparison to the measuring pressure, the results are independent of the port (inlet or outlet) used. The flow standards were always used at atmospheric conditions, that means for the 3 bar measurements downstream to the USM prototype, a needle valve was used for depressurisation of the gas.

The results with nitrogen at measuring pressure of 1 bar (atmospheric pressure) and 3 bar are plotted in Figure 6.

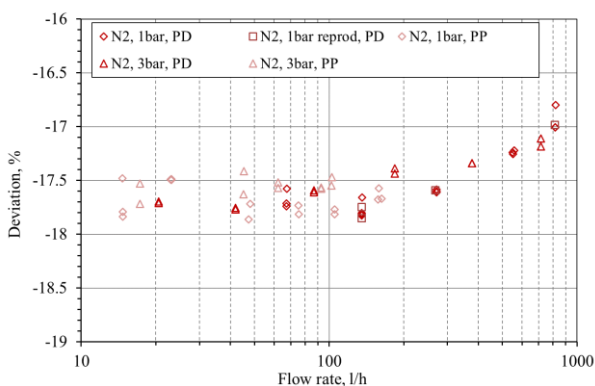


**Figure 6:** Results with nitrogen with  $p_{USM} \approx 1$  bar and  $p_{USM} \approx 3$  bar

The error curves measured by the two different flow standards are overlapping quite well. At higher flows the errors shift to plus.

The large bias of roughly  $E = -18\%$  is caused by the pipe sections near to the transducers which are flow dead zones. Nevertheless, these pipe sections contribute to the measured signal travel times.

Figure 7 shows the results with nitrogen and methane for a measuring pressure of 3 bar. The results of the two gases differ in average by approximately 0.5 %, but the error curves are quite constant for the whole flow rate range.

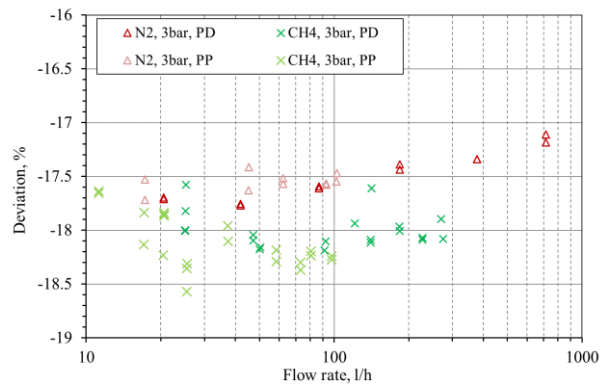


**Figure 6:** Results with nitrogen and methane ( $p_{USM} \approx 3$  bar)

During the measurements it was observed that the deviation of the meter in case of changing the kind of gas drifts over longer times (up to 30 min). This also concerns the measured speed of sound. The reason is the time needed to exchange the gas in the flow dead zones of the prototype. By changing the pressure in the meter, for instance by several 3bar / 1bar cycles, the exchange time may be reduced severely.

### 3.2 Speed of sound test results

Gas qualities of N5.0, respective 99.999% purity was used for the flow tests. The theoretical speed of sound of the gas at the actual conditions of pressure and temperature was calculated by means of the GERG-2008 [4] algorithm. Figure 8 shows the deviation of the measure speed of sound to the calculated theoretical value from gas type, pressure and temperature.

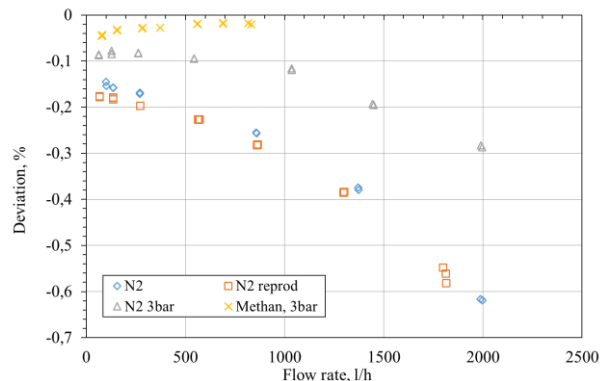


**Figure 8:** Speed of sound deviation from theoretical value

Surprisingly, the speed of sound has shown a strong flow rate dependency. The first attempt to correct this

dependency by taking into account the pressure drop over the length of measuring path turned out to be insufficient.

Much better results were achieved by considering the Mach-number and applying Equation (7) as correction factor.

$$c' = \frac{c}{\sqrt{1 - \left(\frac{v}{c}\right)^2}} \quad (7)$$

After correction by the Mach-number, the speed of sound deviation is better than 0.05% over the tested flow range (see Figure 9). Nevertheless, a difference between nitrogen and methane was observed, which might be caused by the expected propagation of higher acoustic wave modes in the measuring pipe.

Further tests with hydrogen are planned to investigate how the speed of sound measurement is influenced by the acoustic signal propagation on higher wave modes.

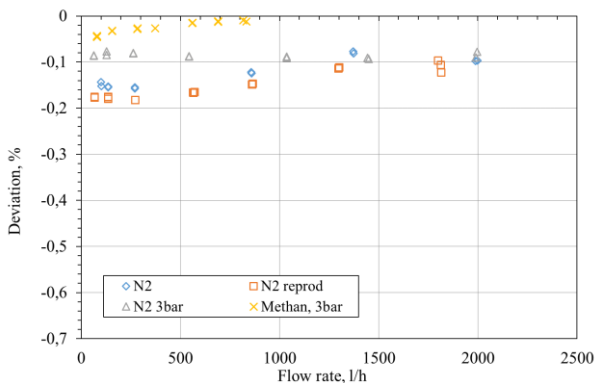


**Figure 9:** Speed of sound deviation from the theoretical value with correction factor applied

## 7. Conclusion

The investigated prototype has shown the applicability of a capillary USM for flow rate measurements. By an inner diameter of the used capillary of 4 mm and an acoustic frequency of the transducers of 135 kHz, a flow rate range down to 10 l/h was reached with different gases. The reproducibility of the meter deviation was mostly inside a range of 0.2 %. The results show a relatively small dependency of the error curve from the kind of gas in case of nitrogen and methane. The reasons for this dependency need to be investigated further. The flow velocity influenced severely the speed of sound detected by the USM, but a compensation based on the Mach-number led to deviations between measured and calculated SOS of lower than 0.05%.

It is planned to use the meter for inter comparisons and for the measurement of speed of sound for changing gas compositions.

## References

- [1] ISO 17089-1, *Measurement of fluid flow in closed conduits - Ultrasonic meters for gas -- Part 1: Meters for custody transfer and allocation measurement*, 2010
- [2] Ehrenfried K., *Strömungsakustik: Skript zur Vorlesung*, Berlin, Mensch und Buch Verlag, 2011
- [3] Möser M., *Technische Akustik*, Springer-Verlag Berlin Heidelberg, 2005
- [4] ISO 20765-2, *Natural gas -- Calculation of thermodynamic properties -- Part 2: Single-phase properties (gas, liquid, and dense fluid) for extended ranges of application*, 2015

# Establishment of an Ultra-High Accuracy 670 PVTt Gas Flow Primary Standard at NMIA

K. Chahine<sup>1</sup>, Z. Wang<sup>1</sup>,

<sup>1</sup>National Measurement Institute, 36 Bradfield Rd, Lindfield NSW 2070, Australia  
E-mail (corresponding author): [khaled.chahine@measurement.gov.au](mailto:khaled.chahine@measurement.gov.au)

---

## Abstract

A new PVTt standard for gas flow has been commissioned at NMIA, which relies on measurements of pressure, volume, temperature and time. The main aim of developing this new standard was to reduce the  $\pm 1000$  ppm ( $\pm 0.10\%$ ) uncertainty of measurements made with NMIA's bell and mercury-sealed piston provers. The uncertainty associated with measuring the mass flowrate using the new PVTt standard is estimated to be  $\pm 116$  ppm ( $\pm 0.012\%$ ), this significant improvement in uncertainty can be attributed to two reasons. Firstly, the volumes of existing provers at NMIA were measured to no better than  $\pm 400$  ppm, whereas the volume of the new PVTt standard has been determined gravimetrically using water with an uncertainty of  $\pm 80$  ppm. Secondly, existing provers are used in ambient air with a spatial temperature uniformity of 150 mK, while the new PVTt standard is immersed in a temperature controlled water tank with a temperature uniformity of 2 mK. In this paper, a description of the PVTt standard is presented. A comprehensive uncertainty analysis is also made and an example calibration is described.

---

## 1. Introduction

A 300 L bell prover and a set of 5 mercury-sealed piston provers are currently used at the National Measurement Institute Australia (NMIA) as primary standards for gas flowrates ranging from  $1 \text{ cc min}^{-1}$  to  $25 \text{ m}^3 \text{ h}^{-1}$  with a least uncertainty of  $\pm 0.10\%$  [1]. There are many advantages and disadvantages of using bell and mercury-sealed piston provers as primary flow standards and to state all of them is beyond the scope of this paper. However, some of the disadvantages are (1) safety concerns due to the use of mercury and oil as seals in these standards, (2) the limitation on using these standards for measurement with pressures higher than atmospheric due to the oil and mercury liquid seals, (3) difficulty in reducing the large spatial temperature non-uniformity in and around these standards while used in ambient air, which is currently assessed to be 150 mK, and (4) difficulty in determining the volumes of these provers to better than 400 ppm.

These bell and mercury-sealed piston provers are mainly used in the calibration of critical flow Venturi nozzles (CFVN). These CFVNs are then combined in parallel to be used in the calibration of other flow measuring devices for flowrates up to  $7000 \text{ m}^3 \text{ h}^{-1}$  (normalised at  $20^\circ\text{C}$  and  $101.3 \text{ kPa}$  conditions). The

current uncertainty associated with using these nozzle arrays is  $\pm 0.13\%$  ( $k = 2$ ). This measurement uncertainty is obtained from a two-tier build-up calibration that relies on existing provers to attain. NMIA is planning to expand its calibration services to include high pressure and high flow ranges in the near future while maintaining the competitive uncertainty needed to service the requirements of local industry. To establish measurement traceability of the planned high pressure facility, existing CFVN arrays will be used in the calibration of other CFVNs at higher upstream pressures. To achieve the needed uncertainty, a standard with a higher operating range of flowrates and pressures and reduced uncertainty is therefore needed.

A 670 L PVTt gas flow standard has recently been designed and constructed at NMIA. The aims of constructing this standard are to (1) replace the existing bell and mercury-sealed piston provers, (2) increase the range of flowrate up to  $120 \text{ kg h}^{-1}$ , and (3) improve the measurement uncertainties. This new standard is based on measurements of pressure, volume, temperature and time; hence the acronym PVTt.

In this paper, a description of the NMIA's PVTt standard is presented including the methodology

followed in its design. A measurement uncertainty analysis is also included.

## 2. The PVTt Standard

### 2.1 Design and Mode of Operation

Several national metrology institutes around the world employ PVTt standards for ultra-high accuracy measurements of gas flowrate [2,3,4]. At NMIA, a PVTt standard with a nominal volume of 670 L has been designed and constructed as an ultra-high accuracy gas flowrate standard. The design of the PVTt standard is based on the same principles adopted by other laboratories but with several significant improvements which will be described here.

The PVTt system consists of eight annular stainless steel cylinders connected together by a circular pipe, shown schematically in Figure 1.

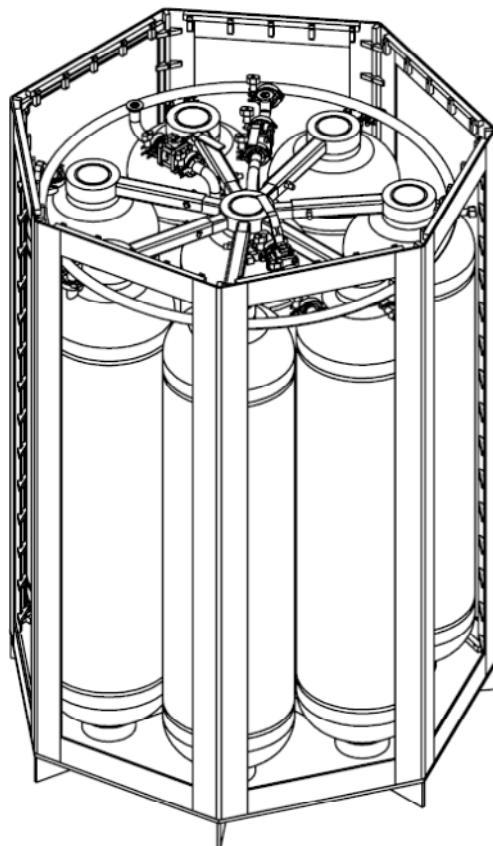


**Figure 1.** Schematic diagram of NMIA's PVTt standard.

A valve is used to separate the centre cylinder from the surrounding cylinders to enable two volume options with nominal values of 80 L or 670 L. The cylinders and connecting pipe-works are immersed vertically inside a tank filled with distilled water to FLOMEKO 2019, Lisbon, Portugal

achieve tight temperature uniformity and stability. NMIA's new design of annular cylinders allows heat transfer from the water to both the outer and inner stainless steel surfaces and then to the gas inside, hence reducing the time constant for transient heat transfer between the water and the gas. In addition, having all cylinders placed vertically inside the tank, as opposed to horizontally, improves the convective heat transfer along the cylinder surfaces and allows for faster stabilisation of the gas inside the cylinders.

A 3-way diverter valve with built-in limit switches is used to divert the flow from the DUT to the PVTt tank or from the DUT to atmosphere. The limit switches on the diverter valve are powered by a 24 Vdc signals that are used in conjunction with a high accuracy timer to record the time interval between the start and stop of gas flow into the PVTt tank. An example of the calibration setup of a CFVN using the PVTt standard is shown in Figure 2.

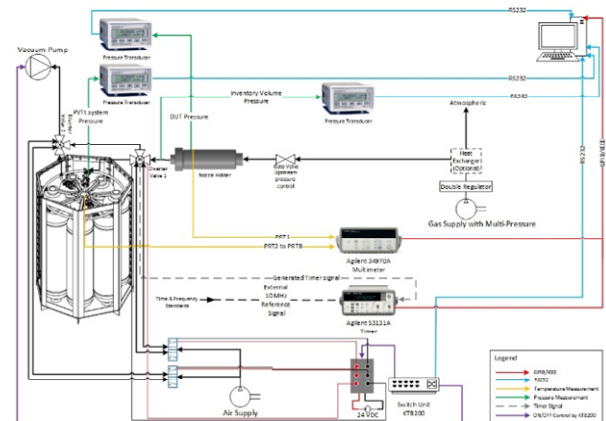


**Figure 2.** Setup for calibration of a critical flow Venturi nozzle using NMIA's PVTt standard.

The steps to conduct a measurement using the PVTt standard are: (1) evacuate the tank to the required pressure, (2) wait for the pressure and temperature to stabilise; it was observed that 30 minutes is sufficient, (3) record pressure and temperature of the tank at start conditions, (4) open the diverter valve so that the flow is from the DUT to the tank, (5) collect readings from the DUT; for a CFVN the collected readings are the upstream pressure and temperature (and relative humidity if using air), (6) close the diverter valve so that the flow is from the DUT to the atmosphere, (7) wait for the pressure and temperature to stabilise, and (8) record the pressure and temperature at end conditions.

The measurement procedure has been fully automated with a PC and custom software to minimise user errors and streamline data collection.

Usually, the measurements are conducted several times to establish a measure of their repeatability and reproducibility.

## 2.2 Volume Determination

The uncertainty of the tank volume is vital as it is a major component in the total uncertainty budget of the flowrate measurement. To minimise this component, the cylinders were designed to facilitate measuring their volumes gravimetrically using water. The volumes of the eight cylinders were measured individually with an uncertainty of  $\pm 80$  ppm. All plumbing inventories used to connect the cylinders together and to the device under test were also measured gravimetrically using water with an uncertainty of  $\pm 100$  ppm. The small volume of these inventories compared to that of the eight cylinders means that the effect of their uncertainty on the total volume uncertainty is minimal and a total uncertainty of the full volume can therefore be maintained at  $\pm 80$  ppm.

To validate the total volume measurement using the gravimetric method with water,  $V_{PVTt,water}$ , a second method using nitrogen gas was conducted. In this method, a known mass of nitrogen gas is deposited into the PVTt tank; this mass of nitrogen is discharged from a gas cylinder with its weight measured before and after by NMIAs chemical metrology group. Prior to depositing the nitrogen, the PVTt tank is evacuated to a very low pressure ( $<100$  Pa) then allowed to stabilise; stable pressure readings are a good indication of steady state conditions of the gas inside the PVTt tank. After depositing the nitrogen, the tank is allowed to stabilise again. Pressure inside the PVTt volume and water temperature are measured at steady state conditions before and after the deposition of nitrogen. Using these measurements, the volume of the PVTt standard,  $V_{PVTt,N_2}$ , is calculated using the following equation:

$$V_{PVTt,N_2} = \frac{m_{N_2}}{\rho_e - \rho_s} - V_{Inv,N_2} \quad (1)$$

where  $m_{N_2}$  is the measured mass of nitrogen deposited into the PVTt tank,  $\rho_s$  and  $\rho_e$  are the densities of nitrogen calculated from temperature and pressure measurements of the tank before and after depositing the nitrogen (e.g.: start and end), and  $V_{Inv,N_2}$  is the volume of the plumbing inventory used to connect the nitrogen cylinder to the PVTt tank.

As can be seen from Equation (1), the measurement uncertainty of  $V_{PVTt,N_2}$  is mainly influenced by (1) the uncertainty associated with measuring the mass of

the nitrogen,  $m_{N_2}$ , and (2) the uncertainty in calculating the nitrogen densities,  $\rho_e$  and  $\rho_s$ . The measurement uncertainty associated with  $m_{N_2}$  was determined by NMIAs chemical metrology group to be  $\pm 33$  ppm. The uncertainty associated with the densities are dominated by the uncertainty in the equation of state obtained from [5] to be  $\pm 100$  ppm (at 95% C.L.). On the other hand, the uncertainty contribution of  $V_{Inv,N_2}$  is considered to be negligible due to its small size (10 mL) when compared to the volume of the PVTt tank. In estimating the uncertainty in  $V_{PVTt,N_2}$ , a more conservative approach was adopted by considering all of its components to have non-correlated uncertainties. A value of  $(663.415 \text{ L} \pm 221 \text{ ppm})$  was obtained for  $V_{PVTt,N_2}$ . This value compares with  $V_{PVTt,water}$  of  $(663.358 \pm 80 \text{ ppm})$ . Both volume determinations are plotted in Figure 3 for easier comparison. A more comprehensive analysis of the volume measurement  $V_{PVTt,N_2}$  and its uncertainty is presented in [6].

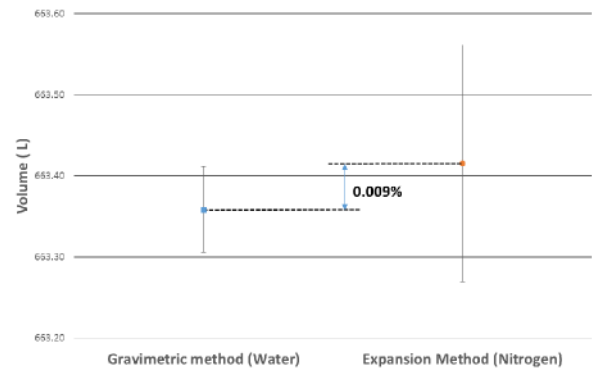


**Figure 3.** Comparison of the NMIAs PVTt tank volume measurements, with their error bars, using water and nitrogen.

As can be seen from Figure 3, measurements of the PVTt volume using water and nitrogen agree well within their estimated uncertainties. A difference of 90 ppm (or 0.009%) is observed with  $V_{PVTt,water}$  having lower uncertainty. Consequently, the value obtained from the gravimetric technique using water,  $V_{PVTt,water}$ , is used as the PVTt tank volume.

## 2.3 Water Tank Temperature Control

As mentioned before, the stability and uniformity of temperature of the gas inside the cylinders is a major source of uncertainty in the flowrate measured using the PVTt standard. To minimise this contribution, the PVTt tank is immersed inside a water tank maintained at fixed temperature. The temperature of the water tank is controlled by using 400-watt heater elements connected to a PID

controller with temperature read by an SPRT (Standard Platinum Resistance Thermometer) in its feedback loop. Dry air is bubbled throughout the water tank to (1) induce faster circulation and mixing of water hence increasing the convective heat transfer over the stainless steel surfaces of the cylinders, and (2) create cooling effect caused by the evaporation of water into the dry air, which is needed to act as a balance to the heater elements. Measurements of water temperature were recorded over a period of 15 hours and are plotted in Figure 4.

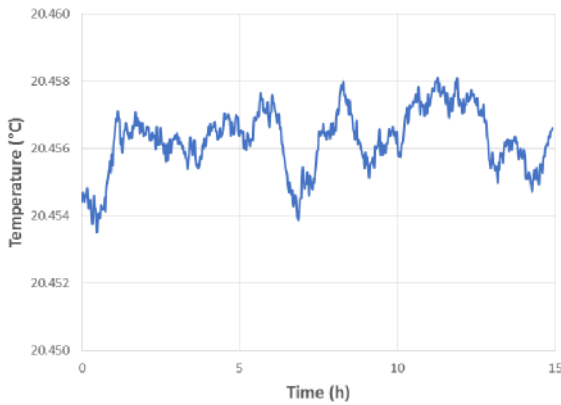


**Figure 4.** Plot of the NMIA's PVTt water tank temperature over a period of 15 hours.

As can be seen from Figure 4, the water temperature is stable within 2 mK with a standard deviation calculated to be 0.9 mK. In addition, seven PRTs placed at various positions inside the tank were used to assess the spatial temperature uniformity. Measurements conducted showed less than 2 mK of spatial temperature variation inside the water tank.

It can be concluded that the contribution of the temperature stability and uniformity to total uncertainty is negligible. This is a major improvement upon NMIA's existing standards, bell and mercury sealed piston provers, in which temperature stability and uniformity were a major source of their uncertainties.

### 3. Uncertainty Analysis

#### 3.1 Model of the Measurement

Using the principle of conservation of mass, the mass flowrate measured by the PVTt,  $Q_m$ , is calculated using the following equation:

$$Q_m = \frac{(m_{PVTt}^e - m_{PVTt}^s) + (m_{Inv}^e - m_{Inv}^s)}{t} \quad (2)$$

where  $m_{PVTt}^e$  is the mass of the gas inside the PVTt volume at end conditions,  $m_{PVTt}^s$  is the mass of the FLOMEKO 2019, Lisbon, Portugal

gas inside the PVTt volume at start conditions,  $m_{Inv}^e$  is the mass of gas inside the inventory volume at end conditions,  $m_{Inv}^s$  is the mass of the gas inside the inventory volume at start conditions, and  $t$  is the time between the start and end of gas collection. Using the relation between mass ( $m$ ), volume ( $V$ ) and density ( $\rho$ ), Equation (2) can be rewritten to give:

$$Q_m = \left[ \frac{V_{PVTt}(\rho_{PVTt}^e - \rho_{PVTt}^s) + V_{Inv}(\rho_{Inv}^e - \rho_{Inv}^s)}{t} \right] \quad (3)$$

where  $V_{Inv}$  is the inventory volume between the diverter valve and the DUT. Note that the superscripts in Equation (3),  $e$  and  $s$ , denote the end and start conditions. The densities,  $\rho_{PVTt}^e$  and  $\rho_{PVTt}^s$ , are calculated from measurements of pressure and temperature in the PVTt tank. On the other hand, the densities,  $\rho_{Inv}^e$  and  $\rho_{Inv}^s$ , are calculated from measurements of pressures and temperatures in the inventory volume.

#### 3.2 Uncertainty Analysis

The measurement uncertainty of  $Q_m$  can be determined based on the model given in Equation (3) using the root-sum-square of all its components with the assumption that these components are non-correlated. However, this may result in an overestimation of the total uncertainty as some of these components are fully or highly correlated. To calculate the uncertainty of a mathematical model,  $y$ , consisting of correlated components,  $x_i$  and  $x_j$ , the following equation can instead be used [7]:

$$u_c^2(y) = \sum_{i=1}^N c_i^2 u^2(x_i) + 2 \sum_{i=1}^{N-1} \sum_{j=i+1}^N c_i c_j u(x_i) u(x_j) r(x_i, x_j) \quad (4)$$

in which  $r(x_i, x_j)$  is the 'correlation coefficient' that expresses the degree of correlation between the input quantities,  $x_i$  and  $x_j$ . For a measurand with all of its components being non-correlated, the value of  $r(x_i, x_j)$  is 0. In this case Equation (4) is simplified to the root-sum-square of these components or simply the case of considering all uncertainty components to be non-correlated. On the other hand, for a model with fully correlated uncertainty components, the value of  $r(x_i, x_j)$  is either 1 or -1.

From Equation (3), the components  $V_{PVTt}$ ,  $V_{Inv}$  and  $t$  are obtained by various measurement methods and therefore considered to have non-correlated uncertainties, hence  $r(x_i, x_j) = 0$ . On the other hand, the two sets of densities,  $(\rho_{PVTt}^e, \rho_{PVTt}^s)$  and  $(\rho_{Inv}^e, \rho_{Inv}^s)$ , are calculated from measurements of

pressure and temperature in conjunction with a published equation of state [5]. It can be safely assumed that the measurement uncertainties for each set of densities are fully correlated since they are all measured using the same equipment and the same equation of state to calculate their values, hence  $r(x_i, x_j) = 1$ ; same concept work has been adopted by other researchers [2,3,4]. A more conservative approach is adopted herein by considering these densities to have highly correlated uncertainties with  $r(x_i, x_j) = 0.95$ .

It follows from the above that the uncertainty in  $Q_m$ , or  $u_{Q_m}$ , can be calculated using:

$$u_{Q_m} = \sqrt{\begin{aligned} & (c_{V_{PVTt}} u_{V_{PVTt}})^2 + (c_{\rho_{PVTt}^e} u_{\rho_{PVTt}^e})^2 + \\ & (c_{\rho_{PVTt}^s} u_{\rho_{PVTt}^s})^2 + (c_{V_{Inv}} u_{V_{Inv}})^2 + \\ & (c_{\rho_{Inv}^e} u_{\rho_{Inv}^e})^2 + (c_{\rho_{Inv}^s} u_{\rho_{Inv}^s})^2 + (c_t u_t)^2 \\ & + 2c_{\rho_{PVTt}^e} c_{\rho_{PVTt}^s} u_{\rho_{PVTt}^e} u_{\rho_{PVTt}^s} r(\rho_{PVTt}^e, \rho_{PVTt}^s) \\ & + 2c_{\rho_{Inv}^e} c_{\rho_{Inv}^s} u_{\rho_{Inv}^e} u_{\rho_{Inv}^s} r(\rho_{Inv}^e, \rho_{Inv}^s) \end{aligned}} \quad (5)$$

where the terms  $c$  and  $u$  are the corresponding sensitivity factors and uncertainty components of each term in Equation (3) respectively.

As can be deduced from Equation (5), it is expected that  $u_{Q_m}$  is minimised when the mass collected in the PVTt tank,  $(m_{PVTt}^e - m_{PVTt}^s)$ , is much larger than the inventory mass difference between the start and end of gas collection,  $(m_{Inv}^e - m_{Inv}^s)$ . The inventory volume was therefore designed to be as small as possible, less than 20 mL. This volume is measured to  $\pm 1\%$  (or  $\pm 0.2$  mL) equating to 0.3 ppm of  $V_{PVTt}$ . At the same time, having a small inventory volume reduces the effect of pressure variation on the mass of gas collected when switching the flow from the DUT to the PVTt tank.

### 3.3 Example Calibration

A CFVN with a nominal diameter of 2 mm was connected in series with the PVTt standard. The starting pressure in the PVTt tank was set to  $\sim 100$  Pa. Dry nitrogen, with a purity better than 99.999% produced by the boil-off of liquid nitrogen at NMIA cryogenic facility, was allowed to flow into the PVTt tank through the CFVN for a period of 420 s giving an end pressure of  $\sim 39$  kPa. The temperature of the tank's water was set to 20.450°C and this set point was maintained within  $\pm 0.9$  mK. Measurements of the PVTt tank pressures and water temperatures were recorded. These measurements were repeated seven times. Based on these values, a list of the uncertainty components associated with  $Q_m$  is given in Table 1. FLOMEKO 2019, Lisbon, Portugal

The uncertainties of  $Q_m$  at 66%,  $u_{Q_m}$ , and 95%,  $U_{Q_m}$ , Confidence Limits (C.L.) are also reported in the table; note 66% C.L. and 95% C.L. correspond to coverage factors of  $k = 1$  and  $k = 2$ .

**Table 1:** Uncertainty components associated with the measurement of  $Q_m$  using NMIA's PVTt standard for a given measurement scenario.

Gas used: dry nitrogen, N <sub>2</sub> Starting Pressure = 100 Pa, End Pressure = 39×10 <sup>3</sup> Pa Temperature = 20.450°C, $V_{PVTt} = 0.663\ 358$ m <sup>3</sup> , $V_{Inv} = 18 \times 10^{-6}$ m <sup>3</sup> , $t = 420$ s			
Components	$u$ (@1SD or $k=1$ )		Source
		ppm	
$V_{PVTt}$	27 mL	40	Cal report
$\rho_{PVTt}^e$			
Pressure	5 Pa	132	[6]
Temperature	6 mK	21	[6]
Equation	$2.2 \times 10^{-5}$ kg m <sup>-3</sup>	50	[5]
$\rho_{PVTt}^s$			
Pressure	5 Pa	131	[6]
Temperature	6 mK	0.06	[6]
Equation	$6.2 \times 10^{-8}$ kg m <sup>-3</sup>	0.2	[5]
$V_{Inv}$	0.18 mL	0.1	[6]
$\rho_{Inv}^e$			
Pressure	5 Pa	0.004	[6]
Temperature	6 mK	<0.001	[6]
Equation	$2.3 \times 10^{-5}$ kg m <sup>-3</sup>	0.002	[5]
$\rho_{Inv}^s$			
Pressure	5 Pa	0.004	[6]
Temperature	6 mK	<0.001	[6]
Equation	$2.3 \times 10^{-5}$ kg m <sup>-3</sup>	0.001	[5]
$t$	$5 \times 10^{-3}$ s	12	[6]
<i>if all uncertainties are non-correlated</i>			
$u_{Q_m} (k = 1, r = 0) = 182$ ppm			
Let $r = 0.95$ (highly correlated uncertainties)			
$u_{Q_m} (k = 1, r = 0.95) = 57.8$ ppm			
$U_{Q_m} (k = 2, r = 0.95) = 116$ ppm			

The reported pressure uncertainties in Table 1 are the results of combining (1) the calibration uncertainty of the pressure transducers used, (2) contribution from any hysteresis using these transducers, and (3) any fluctuation of pressure readings during measurements. Similarly, all temperature uncertainties reported are the results of combining (1) the calibration uncertainty of the PRTs used, and (2) uncertainties due to fluctuations of these temperature readings during measurements. On the other hand, the uncertainty associated with time measurement consists of (1) contribution from the high precision digital timer used, which has been calculated to be  $10^{-9}$  s (negligible), and (2) contribution from time delay caused by the mechanical switching of the diverter valve, which was measured as 5 ms [6].

Other measurement uncertainty components associated with the volume of the plumbing that connects the PVTt tank to various instruments and

the small volume of the tank not submerged in water are not listed in Table 1 due to their small size. The uncertainty contribution to  $U_{Q_m}$  associated with this plumbing volume is estimated to be <1 ppm [6].

On the other hand, the CFVN is calibrated by calculating a nozzle coefficient given by the following equation [8]:

$$N = \frac{Q_m}{\sqrt{\rho_N p_N}} \quad (6)$$

where  $\rho_N$  and  $p_N$  are the density and pressure of the dry nitrogen at the nozzle's upstream conditions respectively. The density is calculated from temperature and pressure measurements at upstream nozzle conditions [5]. The uncertainty is then calculated based on this mathematical model. Table 2 gives a list of uncertainty components associated with calculating  $N$ . The uncertainties of  $N$  at  $k=1$ ,  $u_N$ , and  $k=2$ ,  $U_N$ , are also included in the table.

**Table 2:** List of uncertainty components associated with the measurement of the CFVN's nozzle coefficient.

Components	$u$ (@1SD or $k=1$ )		Source
		ppm	
$Q_{m,STD}$	$3.9 \times 10^{-8} \text{ kg s}^{-1}$	58	Table 1
$\rho_N$			
Pressure	7.9 Pa	39	Combined
Temperature	4 mK	7	Combined
Equation	$5.9 \times 10^{-5} \text{ kg m}^{-3}$	25	[5]
$p_N$	7.9 Pa	39	Combined
Repeatability (7 trials)	$1.4 \times 10^{-10} \text{ m}^2$	15	Measured
$u_N(k=1, r=0) = 85.5 \text{ ppm}$			
$U_N(k=2, r=0) = 171 \text{ ppm}$			

From the table, the resultant uncertainty,  $u_N$  or  $U_N$ , is calculated based on the assumption that all uncertainty components are non-correlated ( $r=0$ ). It can also be noted that uncertainties of the mass flowrate and pressure are major contributors. The repeatability value of 15 ppm is the calculated standard error of the average of the seven measurements collected with a standard deviation of 40 ppm.

## Conclusions

Improvement of flowrate uncertainty associated with NMIA's bell and mercury-sealed piston provers has been achieved using the newly commissioned PVTt standard. The measurement uncertainty has been improved by almost a factor of 10, from 1000 ppm (or 0.10%) to 116 ppm. This improvement is mainly credited to (1) having a well determined volume with an uncertainty of  $\pm 80$  ppm, and (2) a volume with

stringent temperature control and uniformity of  $\pm 2$  mK.

Further improvements on the uncertainty of  $Q_m$  reported in Table 1, can be achieved by (1) reducing the measurement uncertainty associated with measuring the tank pressure by using more accurate transducers, and (2) conducting further investigations on increasing the correlation among various components from highly correlated,  $r=0.95$ , to fully correlated,  $r=1$ .

Improvements on the measurement uncertainty of calibrating a CFVN, reported in Table 2, can also be made by (1) employing better pressure transducers, and (2) placing the CFVN in a more uniform and better controlled temperature environment; for example inside a temperature controlled water tank.

Although a preliminary comparison with NMIA standards has shown good agreement with existing provers within the specified uncertainties [6], a formal comparison that involves other national measurement institutes around the world might be necessary to establish more confidence in the claimed measurement uncertainty using the NMIA PVTt standard.

## References

- [1] Chahine K, "Comparison of Low Pressure Gas Flow Standards", in Proceedings of FLOMEKO. Peebles, Scotland, NEL, 2005.
- [2] Wright J D *et al*, "Design and Uncertainty Analysis for a PVTt Gas Flow Standard", *Journal of Research of the National Institute of Standards and Technology*, **108**, 21-47, 2003.
- [3] Ishibashi M *et al*, "New System for the Pressurized Gas Flow Standard in Japan", in Proceedings of International Symposium on Fluid Flow Measurements, AGA, 1985.
- [4] Li C H *et al*, "The uncertainty analysis and capability verification for the high pressure pVTt gas flow facility of NIM", in Proceedings of FLOMEKO, Sydney, Australia, MSA, 2016.
- [5] Lemmon E W *et al*, "NIST Standard Reference Database 23: Reference Fluid Thermodynamic and Transport Properties-REFPROP", Version 9.1, National Institute of Standards and Technology, Standard Reference Data Program, Gaithersburg, USA, 2013.
- [6] Chahine K *et al*, "Measurement Report on the 670L PVTt Gas Flow Standard at NMIA". Internal Report at National Measurement Institute Australia, Ref. No. 19/010/433.0001, 2019.



18<sup>th</sup> International Flow Measurement Conference

Portugal | Lisbon | LNEC | 26-28 June 2019

- [7] Bentley R E, "Uncertainty in Measurement: The ISO Guide". Monograph 1: NMI Technology Transfer Series, 11<sup>th</sup> ed., National Measurement Institute, Australia, 2005.
- [8] Chahine K *et al*, "Evaluation of the Effect of Relative Humidity of Air on the Coefficients of Critical Flow Venturi Nozzles", in Proceedings of FLOMEKO 2013, Paris, France, 2013.

# Design and capability analysis of pure water calibrated TOF for ultrasonic level meter

Yuan Liu<sup>1</sup>, HeMing Hu<sup>1</sup>, Chi Wang<sup>1</sup>, Qisen Miao<sup>2</sup>, Hang Cui<sup>3</sup>,

<sup>1</sup>National Institute of Metrology of China, lyuan@nim.ac.cn, Beijing, China

<sup>2</sup>Hohai University, Nanjing, China

<sup>3</sup>China Jiliang University, Hangzhou, China

---

## Abstract

We will investigate the measuring principle of time-of-flight (TOF) ultrasonic level meter, related analysis and comparison of performance and modification method. Higher measuring precision of height at 0.1mm order of magnitude, and algorithm robustness in the case of weak surface movement, are expected. When using absolute transit time algorithm, the head of wave should be clear, by eliminate echo faster than that through main wave path. And in second trace echo case, ensure there are parts of two echo waves, can be located by theoretical arithmetic and waveform algorithm, have higher relevancy than 98%. In order to enhance the precision of ultrasonic level meter, a proper transit time algorithm will be selected and optimized. The systematic time deviation and delay, transit time in protective containment, cable delay and circuit running time, will be estimated, then adjusted in stable water. The speed of sound, to modify level results with high precision TOF, in objective experimental environment can be calibrated by manometer and thermometer, in pure water media, fluctuation of sound speed measured by ultrasonic apparatus and transfer from temperature is smaller than 0.01%. Finally, micrometer and pressure meter will be used, to compare and evaluate the precision, stability and linearity of level meter, in stable and moving water.

---

## 1. Introduction

Research of the water level with high accuracy and precision is fundamental to the application of acoustic systems and technologies in the flow rate measurement in open channel. Water level is can be illustrated by a variety of principles, including mechanical, optical, electromagnetic and ultrasonic methods, that have achieved certain progress on the water level measurement. The mechanical method mainly uses a buoy floater on the water to measure the distance between surface and a proper height. This distance can be obtained by sliding resistance, radar, digital camera or ruler, which is usually easily to implement, but limited by posture of the buoy. The ultrasonic time-of-flight method is physically related to speed of sound, much easier to use in complex situation and higher cost performance, that can be compared with manometer measurement<sup>[1]</sup>. There are several significant point to improve the capacity of ultrasonic water level measurement, including transmit signal optimization, chosen and utilization of echo, time-of-flight estimation, and received signal processing algorithm. Attenuation and reflection of ultrasonic wave can influence the signal quality used in measure apparatus<sup>[2]</sup>, thus

sensor and echo method used in different situation has to be chosen<sup>[3]</sup>. The lamb wave travel along the wall can be detected by ultrasonic sensor in water level bucket<sup>[4]</sup>. In case of principle of water level detection is essentially a kind of transit time sensing, most of method in ultrasonic time-of flight estimation can be applied to improve the resolution<sup>[5]</sup>. Digital filter can be used to remove the noise and interference in ultrasonic wave, many a time algorithm, such as Hilbert transformation and cross-correlation, is effective in different measuring apparatus<sup>[6-8]</sup>.

We discuss our results with respect to potential of ultrasonic time-of-flight sensor in length and water level measuring to produce stable and high precision apparatus. Then compare with length and manometer value, to analyze the linearity of it, the results present are restricted to NPT(normal pressure and temperature).

## 2. Apparatus and Principle

### 2.1 Stable water level

In order to illustrate the ability of ultrasonic level meter, assume it is used in still water. This apparatus was similar as the time-of-flight (TOF) speed meter, for laboratory use. Ultrasonic wave pulses are emitted from one side into water over a

distance of a few centimeters by a transducer and detected by the same element after reflection. The travel distance is then calculated from the measured travel times and sound speed of the pulses along the unknown sound path.

An extensive second trace echo technique approach is used, where sound pulses are emitted by the same transducer simultaneously in same directions into the liquid along paths of different length. Most system time delay source from waveform and processing circuit will be eliminate during additive operation of two transit time, in the case of two echo have nice correlations. A simple cross-correlation method is used to get the time difference, the range is fixed 1024 sample points at 16MHz sample rate, automatically, ultrasonic waveform is simplified to capture by threshold value method. The sensor need to be designed to make only one pure wave pack without long trail, reflection echo in the sensor has to be separated. The center frequency of the forced vibration is 1MHz, and thickness of protective layer is 1.47mm, stainless steel, shown in Fig 1. In this measuring application, a single transducer and a stainless steel reflector are used to generate and capture echo, take the place of water surface. Connecting structures are several pairs of stainless steel single end studs with different length from 50mm to 500mm, instead of water level. The length connection can't neither be too short, or the first echo may overlap with the other echo and noise, nor too long, or the connecting structures may be easily twisted a small angle, which make the reflection not straight enough to represent the water level. The environment are NPT, about 19°C in water. The total offset in experimental period is about 1°C, and expansion by heat and contraction by cold during this range is about 25nm~250nm, far less than water level accuracy requirement, and will not be taken consideration in this case.



**Fig 1:** Time of flight sensor with changeable echo path length

The sound speed we used is dependent on the real-time condition of liquid media. In this case, the liquid media is tap-water, it's assumed to pure water to simplify the process. Two thermometers with high-precision was set nearby the center of connecting structure's outer edge. Anton Paar MKT50 platinum wire resistance thermometer are used to record real-time temperature, with 0.001°C resolution. We will use IAPWS-95 polynomial

formulation<sup>[1]</sup> to transfer temperature to sound speed, which means resolution of temperature takes 3mm/s to sound speed, about 2 ppm deviation in theory, also enough for this apparatus. The temperature is between 18.9°C~19.9°C, its gradient characteristics can be described by the difference between two sensors, shown in Fig 2, in the range of [-0.0138,0.0259] ° C, about 39.7mK width.

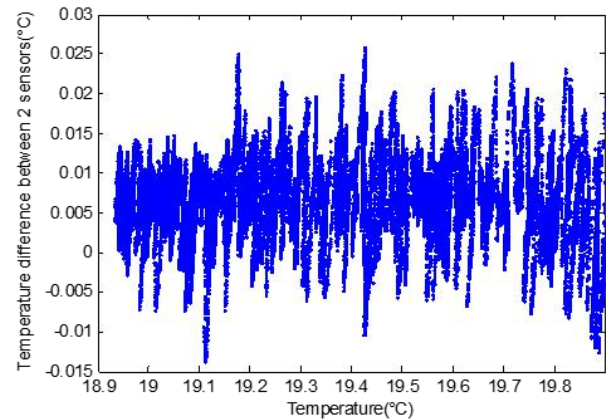


**Fig 2:** Temperature homogeneity between two thermometers in about 40 hours

The length between center of ultrasonic and reflector is the average observed value from a micrometer, which is enough resolution in water level measurement.

## 2.2 Unstable water level

Based on the illustration of ultrasonic sensor ability in stable length measurement, the unstable water level with small fluctuation will be taken into consideration. In this case, a liquid level measuring bucket with 150mm inner diameter, PVC hollow containment structure. The basic principle of this apparatus is to drive a series of ultrasonic waves to measure the transit time between sensor and almost static water level, depend on the real-time sound speed. Then the average distance between center of sensor and geometric center of water in bucket can be estimate by transit time and sound speed in same liquid environment.

Because of fluctuation of water level, each reflection path during short time will alterable in a certain extent. This may bring more uncontrollable factors if we choose second trace echo method. Ultrasonic echo from the water surface may not straight from sensor and water face, the second echo may meet the shell of pipe wall because of a certain beam width, which will change the transit path and received waveform. The time difference will contain more information on the reflection path, and distorted waveform will take more deviation to correlation method. So a single pulse echo method is used in this water level measurement, and an

easy waveform algorithm method is use to find a zero-crossing fitting point on the proper edge of waveform. In this case, system time delay from wave propagation in protect layer and measuring circuit will be counted in transit time, so a correction is necessary to calibrated by standard instruments.

A Yokohama MT210 digital manometer is used to record the pressure of water, with  $\pm 0.01\%$  accuracy declared. The results can be considered directly to represent height of water level, if there is a communicating vessels to connect liquid level measuring bucket and the manometer. A plastic hose is used as a connector on the bottom of bucket and manometer, and we tried different heights of manometer, in case of responds characteristics to measuring range. During the experiments, water level could be quantitative changed by add or draw off water in a proper short time, the results of manometer continuous record once in 1s through serial port. We observed that the gauge reading need a long time to reach steady state if we try to draw off water by steps, which may caused by water environment disturbance near the connector and influence the responds character of sensor in manometer. When we try to add water to bucket, there will be water droplets on the wall of pipe and slide down gradually, which will cause smaller than 0.1mm magnitude changes in few minutes, the display of manometer barely be disturbed during this process, so it is chose to make sure pressure as accurate as possible.

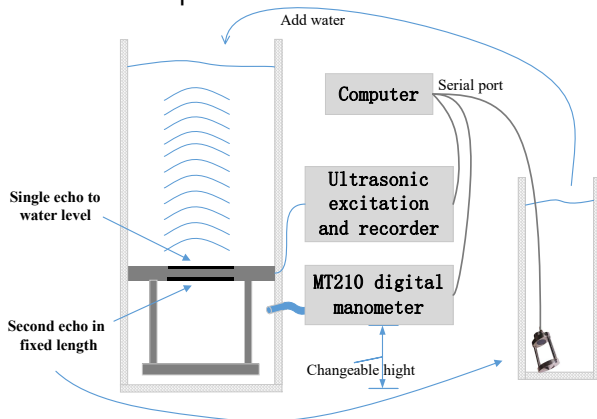


**Fig 3:** Measurement setup of ultrasonic level meter

We use a sound speed measuring application by second trace echo method, similar to the sensor used in stable water, see as Fig 1. The fluctuation and accuracy of ultrasonic speed meter will be illustrated by the experiments in section 2.1. The sound speed application is in the extra water bucket, where the water added to liquid level bucket from, all of this measuring process is happened in 1 hour, enclosed environment, so that,

the sound speed in two bucket can be considered the same, record synchronously with water level sensor and manometer. The measurement setup of water level, sound speed and manometer is shown in Fig 3.

### 3. Measurement results

#### 3.1 Ability of the sensor in steady state

We start the water level measurement in solution with fixed length reflection, between 50mm and 500mm, instead of still water surface, in section 2.1. Solution is measured in 2 days, with at least half hour in each length step. The thermometer on the both sides of ultrasonic measuring application can record the real-time temperature around sound path, and then transfer to sound speed. To account for variety and fluctuation of temperature and transit time, 30 continuous 60s data are chosen from each measuring step, randomly. The fluctuation of sound speed in each half hour is less than 0.01%, transfer from temperature, during 40 hours, is shown in Fig 4, the total offset of temperature is 1° C, much less than expectant of water level, can be considered as a steady state. The fluctuation of measured length is shown in Table 1, which is smaller than 0.01%, the trend is not monotonically with length, and get largest undulation at 200mm, about 15 $\mu$ m. The precision deviation measured from thermometer can be ignored.

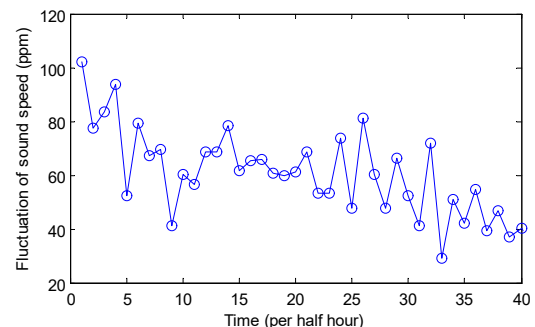


**Fig 4:** Fluctuation of sound speed calculated from thermometer by IAPWS-95(average value in each continuous 30mins during 40hours)

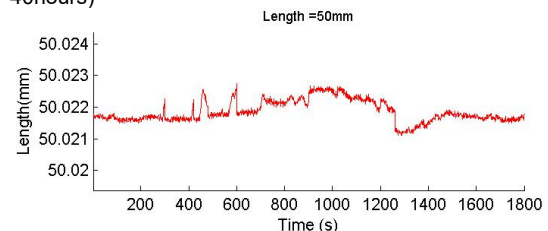


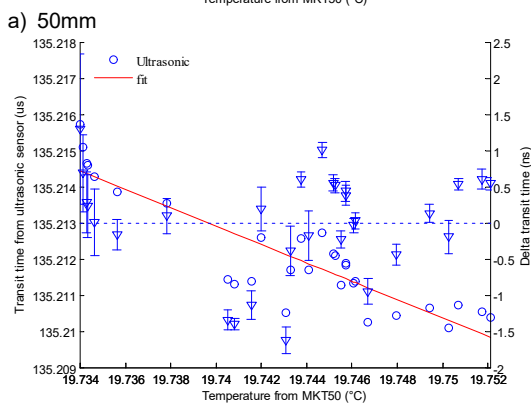
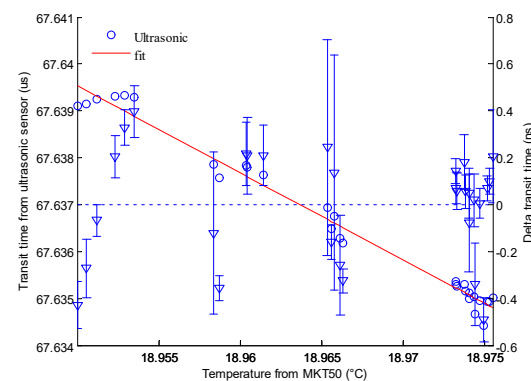
**Fig 5:** Length measured by ultrasonic sensor in random 30mins(when length is 50mm, display width is about 0.05% of nominal length)

Using tap water instead of pure water in a quite and close environment, we still relied on the

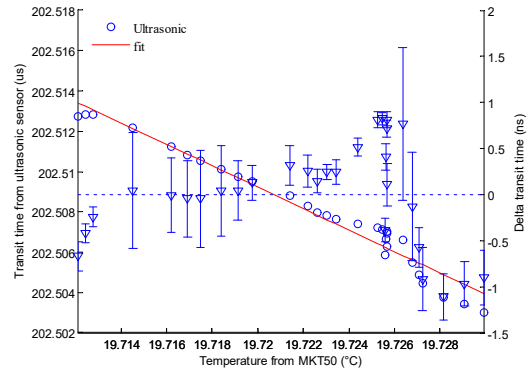
temperature to calculate the sound speed by IAPWS-95 polynomial formulation, which may make a unidirectional offset during 1 ° C variation range. Transit time is the direct measured value of ultrasonic sensor in 2.1 and 2.2 section, thus its characteristics is significant in water level measurement. The linearity and fluctuation of transit time in each 60s, measured by ultrasonic sensor and length, measured by micrometer, divided by real-time sound speed, is shown in Fig 6. The red straight full line is fitted curve of average temperature of each 60s and divided transit time in random 1800s, variation range of transit time is from 5ns to 50ns, increase with travel length of wave monotonically, approximately. The triangle shows the difference between measured ultrasonic transit time and fitted value, which means the linearity, and its whisker show the standard error of ultrasonic transit time in each 60s. Abscissa axis is average temperature of two thermometer in 60s. These will display the influence and changing rule of minor environmental differences.

**Table 1:** Fluctuation of ultrasonic sensor measurement in each length.

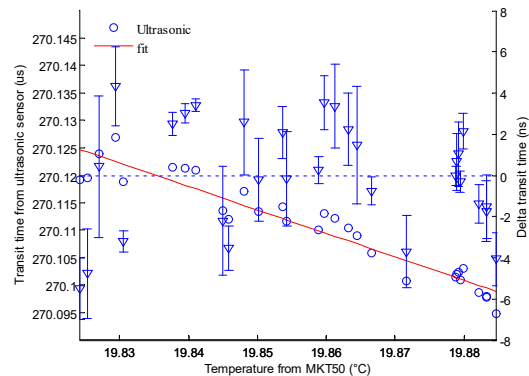
Nominal length (mm)	50	100	150	200	300	400	500
Fluctuation in 30mins(μm)	1.657	3.939	2.707	15.073	9.177	8.320	9.777
Relative fluctuation(ppm)	33.14	39.39	18.05	75.37	30.59	20.80	19.56



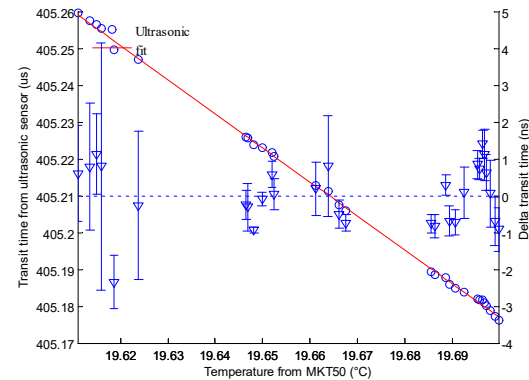
b) 100mm



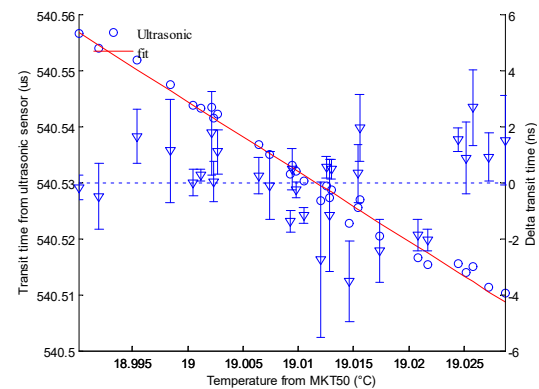
c) 150mm



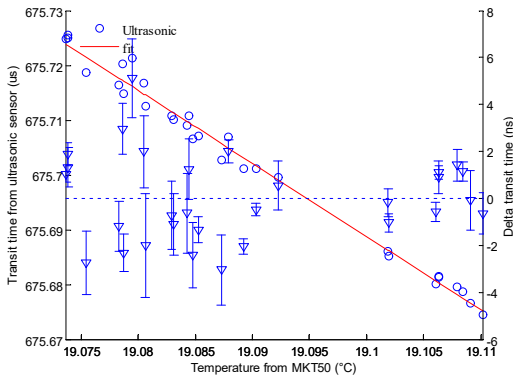
d) 200mm



e) 300mm



f) 400mm



g) 500mm

**Fig 6:** Linearity and fluctuation of ultrasonic time of flight sensor (each sample set contain 1min calculation, 30 sample sets are selected random)

The standard error shows similar law to fluctuation in Table 1, which means stability of transit time measurement is not monotonic to travel length of wave. Indication and linearity deviation of travel length can be seen in Table 2, the results measured by ultrasonic sensor is transit time multiplied real time sound speed. There is always about 0.5mm offset between two measured value, which may caused by steel protective layer. If the average offset is ignored or counted in system delay, the linearity between micrometer and ultrasonic sensor is smaller than 0.05mm. This can easier be seen in Fig 7, tendency of difference shows no obvious relationship with length, and the standard error of length is smaller than 5µm.

**Table 2:** Comparison of length between ultrasonic sensor and micrometer.

Nominal length (mm)	Average value by ultrasonic (mm)	Average value by micrometer (mm)	Indication error (mm)	Linearity deviation (µm)
50	50.022	49.432	0.590	26.644
100	100.163	99.652	0.511	-53.024
150	150.008	149.412	0.596	31.525
200	200.141	199.598	0.543	-22.037
300	300.123	299.546	0.577	10.903
400	399.798	399.205	0.593	25.980
500	499.860	499.312	0.548	-19.992

### 3.2 Liquid level measuring bucket

With the conclusion in section 3.1, water level can be measured in bucket. Where the sound speed application use the same setup as that for section 3.1, 50mm length, characteristics can be shown in Fig 6a, standard error of transit time is less than 0.5ns, about 7ppm in 60s.

Water level measurement is usually prospected in short period, thus we wait 5 to 10 min after adding water to the bucket for each step, till most water drop fall down to water surface and water calm

enough, 1min in each steady state is chosen. Experiments are repeated 3 times, with 3days and 1month interval to ensure the repeatability in a proper period. We record the sound speed in 100min, and rotate a proper angle, which is the gradient of temperature change, then the fluctuation is about 60ppm in the whole range (still lower than 0.01%).

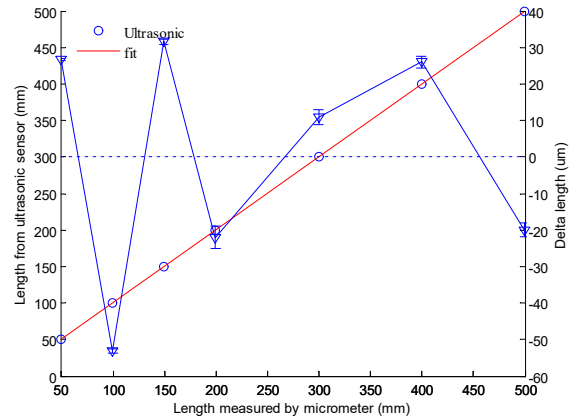


**Fig 7:** Linearity and standard error of ultrasonic time of flight sensor in random 1800s

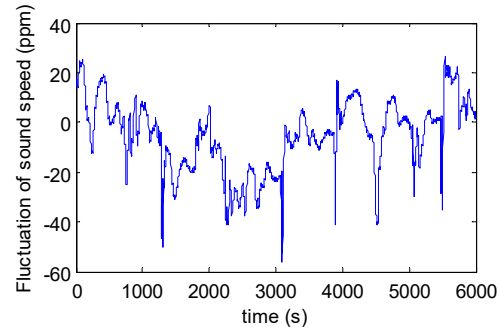
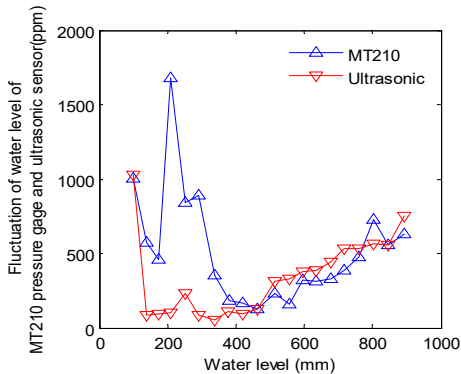


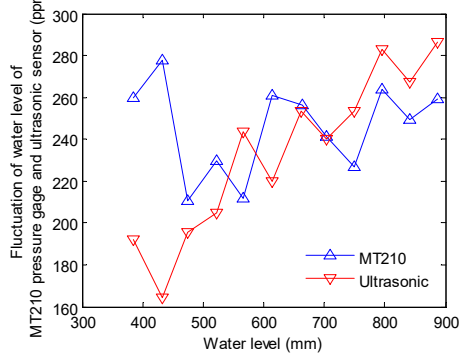
**Fig 8:** Fluctuation of sound speed without circumstantial change by rotation in the first experiment

In the first experiment, the manometer is set the close level with ultrasonic water level sensor, and second higher, the third lower, which will change the linear range of it. The fluctuation of manometer and ultrasonic sensor in each measuring step can be shown in Fig 9. Each of ultrasonic measured length need to add a system offset, including the altitude intercept of manometer and system time delay of ultrasonic sensor, the manometer results can be taken as standard value. The offset of each experiment is average difference in same setup. The fluctuation of manometer results increase slowly when water level is higher than 400mm, and lower than 0.05% in most situation, however undulate strenuous in low water level. The ultrasonic results shows monotonous increasing trend with waver level when higher than 20mm, and show a repeatability better than 0.01% in overlapping range (400mm~600mm).

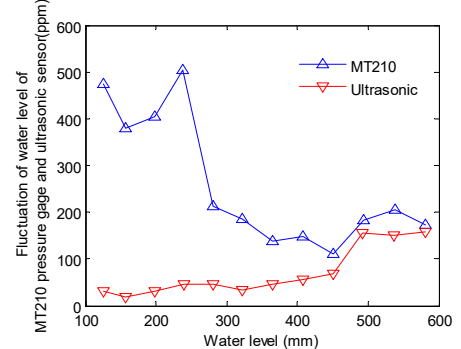
Fig 10 summarizes the ultrasonic measurement linearity which are also listed as an indication error relative to manometer in Table 3. Most linearity deviation is lower than 0.5mm, and most indication error is in  $\pm 0.5$  mm range, increasing with water level when height is higher than 100mm.



a) Exp.1



b) Exp.2



c) Exp.3

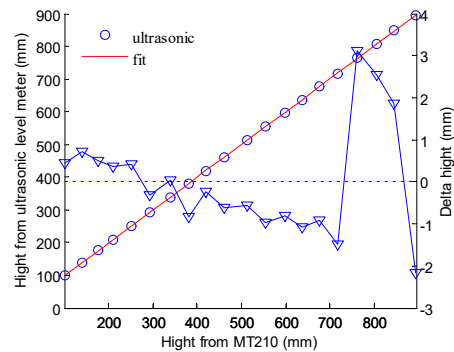
**Fig 9:** Fluctuation of water level measured by manometer and ultrasonic sensor

## 5. Conclusions

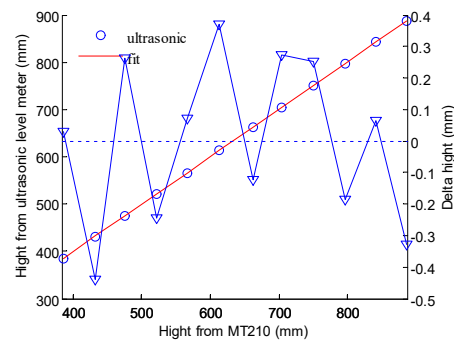
The primary intention of our analysis is to ensure the capabilities of the time-of-flight ultrasonic sensors as instruments for routine practice of in situ water level measurements. We make the results in this paper as the first step of a thorough application that demonstrates and substantiates the potential of time-of-flight sensors in flow research. With the fluctuation, linearity FLOMEKO 2019, Lisbon, Portugal

deviation and indication error of each component to obtain water level in still reflect surface and water surface, we can obviously find the fluctuation of ultrasonic time-of-flight sensor about 0.01%, increase monotonously in a effective measuring range larger than 20mm, and the linearity depends on the stability of contrastive standard apparatus. However, as the contrastive apparatus, such as manometer, show not stable enough responds in test, the indication error and linearity will be abnormal in part of range, yet still tendency toward monotony.

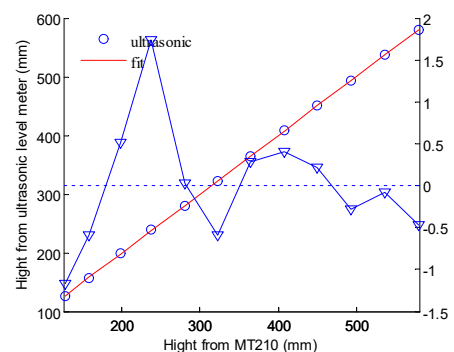
In the follow exploration, we will transfer the water level directly to length, then more precise measuring instrument can be used to evaluate the capacity of ultrasonic time-of-flight sensor



a) Exp.1



b) Exp.2



c) Exp.3

**Fig 10:** Linearity of water level measured by manometer and ultrasonic sensor

**Table 3:** Comparison of length between ultrasonic sensor and manometer from 3 repeating experiments.

Experiment time & No.	Average value by ultrasonic (mm)	Average value by manometer (mm)	Indication error (mm)	Linearity deviation ( $\mu\text{m}$ )
2019/1/29 1	99.668	98.874	-0.794	-185.402
	139.769	139.414	-0.355	190.910
	175.519	175.136	-0.383	107.305
	208.477	208.104	-0.373	65.673
	250.159	250.042	-0.117	255.707
	292.911	292.329	-0.582	-275.819
	338.750	338.660	-0.090	143.987
	379.617	378.872	-0.745	-574.835
	420.104	420.131	0.028	134.372
	461.754	461.601	-0.153	-111.944
	512.543	512.692	0.149	111.224
	554.878	554.806	-0.072	-176.398
	596.873	597.178	0.306	135.413
	635.435	635.659	0.224	-7.065
	676.400	676.961	0.561	266.127
	717.624	717.834	0.210	-149.021
760.489	761.122	0.634	206.926	
803.964	804.346	0.382	-112.846	
844.744	845.560	0.816	257.700	
893.881	894.234	0.354	-282.012	
2019/1/31 2	385.285	385.174	-0.111	30.231
	432.468	431.913	-0.555	-439.908
	475.066	475.237	0.172	262.282
	522.378	522.068	-0.310	-245.847
	566.034	566.064	0.031	70.132
	613.482	613.839	0.357	370.127
	662.837	662.730	-0.108	-122.585
	703.896	704.206	0.310	271.721
	749.915	750.231	0.316	251.736
	795.878	795.782	-0.097	-186.533
	841.984	842.165	0.181	65.000
886.768	886.583	-0.185	-326.357	
2019/3/4 3	126.297	125.184	-1.113	-1172.013
	157.708	157.168	-0.540	-590.613
	197.871	198.430	0.559	519.167
	237.584	239.351	1.768	1738.692
	280.661	280.708	0.047	29.803
	322.475	321.891	-0.583	-589.825
	364.851	365.127	0.277	281.714
	407.697	408.084	0.387	403.113
	450.151	450.338	0.187	215.206
	492.862	492.540	-0.321	-282.031
	537.425	537.293	-0.132	-80.906
580.832	580.297	-0.535	-472.307	

### Acknowledgement

This paper is currently supported by The National Key R&D Program of China (project/subject SN. 2017YFF0206303).

### References

- [1] Tilford C.-R.. The Speed of Sound in a Mercury Ultrasonic Interferometer Manometer [J]. metrologia, 1987, 24(3): 121-131.
- [2] Meribout,M.,Habli,et al.. A new ultrasonic-based device for accurate measurement of oil, emulsion, andwater levels in oil tanks [C]//Instrumentation and Measurement Technology Conference, 2004. IMTC 04.

Proceedings of the 21st IEEE, 2004: 1942-1947.

- [3] Meier Karsten,Kabelac Stephan. Speed of sound instrument for fluids with pressures up to 100MPa [J]. REVIEW OF SCIENTIFIC INSTRUMENTS, 2006, 77.
- [4] Sakharov V.E.,Kuznetsov S.A.,Zaitsev B.D.,et al. Liquid level sensor using ultrasonic Lamb waves[J]. Ultrasonics, 2003, 41(4): 319-322.
- [5] Villadangos José-Manuel,Ureña Jesús,García Juan-Jesús,et al. Measuring time-of-flight in an ultrasonic LPS system using generalized cross-correlation[J]. Sensors, 2011, 11(12): 10326-10342.
- [6] Gruber P,Odermatt P,Etterlin M, et al. The Detection of Cavitation in Hydraulic Machines By Use of Ultrasonic Signal Analysis [J]. Iop Conference Series: Earth and Environmental Science, 2014, 22(5).
- [7] Tresch T,Gruber P,Staubli T. Use of Hilbert Transform for Robustness Improvement of the Acoustic Method[C]//The 5th International Conference on Hydraulic Efficiency Measurement, Switzerland: [s.n.], 2004.
- [8] Tamim Noor-Shafiza-Mohd,Ghani Farid. Hilbert Transform of FFT Pruned Cross Correlation Function for Optimization in Time Delay Estimation[C]//Proceedings of the 2009 IEEE 9th Malaysia International Conference on Communications, 2009: 809-814.

# Measurement Uncertainties Estimation Introduced by the Diverter Into the Budget of Standard Uncertainties

R.A. Korneev<sup>1</sup>, A.R. Tukhvatullin<sup>1</sup>, V.A. Fafurin<sup>1</sup>, A.V. Shchelchkov<sup>1,2</sup>, A.I. Ataeva<sup>1</sup>

<sup>1</sup>Federal State Unitary Enterprise «All-Russian Research Institute of Flow Metering»,  
St. 2<sup>nd</sup> Azinskaya, 7a, Kazan, Republic of Tatarstan, Russian Federation, 420088

<sup>2</sup>Kazan National Research Technical University named after A. N. Tupolev - KAI,  
Karl Marx Street, 10, Kazan, Republic of Tatarstan, Russian Federation, 420011  
E-mail (corresponding author): [lexa\\_kzn@mail.ru](mailto:lexa_kzn@mail.ru)

---

## Abstract

An indirect method is presented for estimation standard measurement uncertainties included into a standard uncertainty budget by the diverter, reproducing units of mass and volume of fluid in a stream, mass and volumetric flow rates of a fluid.

---

## 1. Introduction

The review of literature sources on the actual topic of transferring units of mass and volume of liquid in the flow, mass and volume flow of liquid to the working standards of the 1st, 2nd and 3rd categories, which are used as calibration units with weighing devices, allowed to determine the list of main influencing factors on the budget of uncertainties. According to the recommendations of the standards [1-3], the accuracy of the static weighing method when calibrating the flow and quantity measuring instruments depends on the determination of water and air densities.

It is also necessary to pay attention that the pipeline and shut-off valves must be completely filled with a flow of moving liquid, and there must be no air or gas bubbles in the measuring line [3,4]. Not unimportant factor in the quality of the standard is a part of the measuring system that ensures the stability of the flow rate of liquid in the pipeline, for example, by maintaining a constant level in the pressure tank, or the use of proportional-integral-differential control, etc. V.P. Kargapol'tsev recommends in article [4] to complete the system that circulates the working fluid with low-noise circulation pumps with a low level of vibration threshold values. As a reference, it is recommended to use flow meters produced by the world's leading manufacturers, one of the functional advantages of which can be attributed to the stability of the readings in time. These recommendations will ensure satisfactory long-term operation of the

standard, and the transition process will fade over time.

It is necessary to discuss one of the requirements imposed on the calibration facilities, formulated in the article [4]: «... an important requirement is the compactness of the installation to exclude significant costs for the construction of new premises». This requirement enters into serious disagreement with the recommendations in the articles by W. Nunner [5], R. Koch [6], R.L. Webb [7], A. Shchelchkov [8] and monographs of L. Loitsyansky et al. [9], I. Idelchik [10] on the length of sections of hydrodynamic stabilization of fluid flow, on which the velocity profile after local resistance gradually changes to the normal stabilized flow profile. For example, in turbulent flow, the relative length of the rectilinear section is not less than 35-130 calibers, depending on the Reynolds number [9].

It should be noted that the requirement for compactness of installations mentioned in article [4] requires deep theoretical and empirical study. Consideration of this issue has a practical aspect. One of the requirements to ensure the declared metrological characteristics of the measuring instrument during the installation of the pipeline is the presence of straight sections of the pipeline of a certain length, in order to eliminate the factors that cause a change in the normal profile of the speed of the stabilized fluid flow.

Influential factor on the budget of uncertainty of the standard in transferring units of mass and volume of

fluid in the stream, the mass and volumetric flow of the fluid is the function of the diverter. When assessing the metrological characteristics of the majority of high-precision standards in the Russian Federation, only the time difference of the diverter operation is taken into account. Meanwhile, the researchers T. Shimada [11] and Rainer Engel [12], based on the results of optical Particle Image Velocimetry (PIV) experiments, demonstrated the presence of irregularity of the velocity profile and turbulent pulsations on the nozzle section of the diverter. The experimental studies of V. Fafurin, R. Korneev, A. Shchelchkov, etc., presented in the article [13], performed using the pneumometric method, also recorded significant differences in the profile of the liquid flow rates at the nozzle section of the diverter from the «ideal», determined by the average flow rate (Figure 1-2). For this reason, the mass  $M=M_{r2}+M'+M_{r2}$  (Figure 2), which differs from the calculated the mass  $M_{calc}=M_{r1}+M'+M_{r1}$  (Figure 1) by the magnitude of the mass  $M_d$  gets on the weight device for the time  $\tau$ . Here,  $M_{r1}$  and  $M_{r1}$  are the calculated masses of the fluid at the forward  $\tau_{forward}$  and reverse  $\tau_{reverse}$  the diverter stroke times.  $M_{r2}$  and  $M_{r2}$  are the experimental masses of the fluid at the forward  $\tau_{forward}$  and reverse  $\tau_{reverse}$  the diverter stroke times.

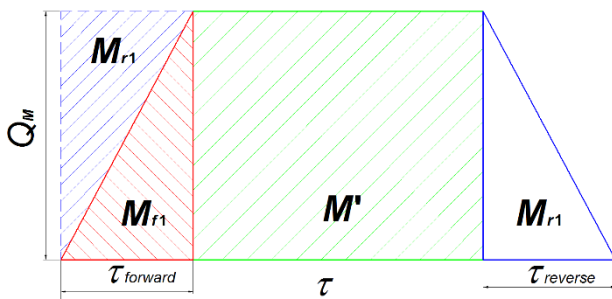


**Figure 1:** Theoretical timing diagram of the diverter operation.

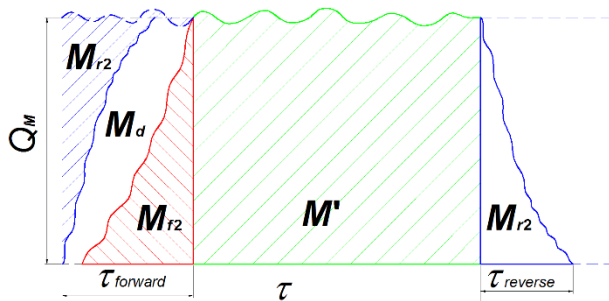


**Figure 2:** Experimental timing diagram of the diverter operation.

It should be noted that due to the design features of the diverter real standards, optical and pneumatic methods do not always allow to determine the local values of flow rates in the nozzle section. In this FLOMEKO 2019, Lisbon, Portugal

regard, there is a need to determine engineering approaches to assess the impact of factors introduced by the diverter in the budget of uncertainty of the standard in a wide range of design and operating parameters.

**The purpose of this article** is to test an indirect method for estimating standard measurement uncertainties introduced by the diverter to a standard uncertainty budget when reproducing units of mass and volume of liquid in a stream, mass and volume flow rates of a liquid.

## 2. Features of the method for conducting experiments to evaluate

Reproduction of units of mass and volume of liquid in the flow, mass and volume flow rate of the standard liquid is based on the static measurement of the mass of the working fluid entering the weighing device for a fixed interval of time, followed by the ejection force.

Filling degree and distribution of flow velocities (flow velocity profile) of the fluid in the slice (plane) of the diverter nozzle are factors that affect the metrological characteristics of the entire standard. It should be noted that the evaluation of standard measurement uncertainties caused by the operation of the standard diverter is also influenced by the following factors: asynchronous signals «start» – «stop» between the measuring controller of the standard and the testing flow meter; the difference in time and irregularity in the operation of the actuators of the diverter in «direct» and «reverse» strokes; pulsations (instability) fluid flow rate; leakage (overflow) and splashing of a jet of liquid when switching to the opposite drain [1-4,11-14].

Experimental studies for evaluation the standard uncertainty of the measurements made by the diverter, are made in the range of liquid mass flow rate  $Q_M=11,1-83,3$  kg/s (40-300 t/h) for weighting device, part of the experimental standard, the description of which is presented in [13]. Before starting the research, visually make sure that there are no effects in the diverter associated with splashing and overflowing.

According to the indirect method, to estimate the standard measurement uncertainties introduced by the reference diverter, it is necessary to select at least three points (modes) of mass flow  $Q$ , kg/s (t/h):  $Q_{Mmin}$ ,  $Q_{Mmax}$ , and the arithmetic mean of the sum of the largest and minimum mass  $Q_{Mavg}=0,5 \cdot (Q_{Mmin}+Q_{Mmax})$ . It is allowed to increase the number of flow points in the range. In studies,

the authors chose 8 mass flow points for a more complete and thorough study of the characteristics of the flow switch standard.

For each point (mode) of the mass flow, it is necessary to select at least five values of the measurement time interval  $\tau$  (s), during which the liquid enters the weighing device. Maximum value of  $\tau_1$  can be limited by the volume of the storage tank. Minimum value  $\tau_5$  is determined, including the lower range of sensitivity and discreteness of the weighing device, as well as due to the quality of the flow switch, and for each standard individually. It should be noted that in GOST R 8.909 - 2016 [1] and international standard ISO 4185 [3], minimum value of the measurement time interval is recommended  $\tau_5 \geq 30$  s. Intermediate values of time intervals are calculated in equal time intervals  $\tau_3 = 0,5 \cdot (\tau_1 + \tau_5)$ ,  $\tau_2 = 0,5 \cdot (\tau_1 + \tau_3)$ ,  $\tau_4 = 0,5 \cdot (\tau_3 + \tau_5)$ . For each value of the time interval  $\tau_i$  at a fixed flow rate mode is carried out at least eleven measurements. For each point weighing  $i$  write values measurement time  $\tau_i$ , mass of fluid  $M_i$  received in the storage container and liquid mass flow rate  $Q_{Mi}$ .

### 3. Features of the experimental data processing methodology

The initial data for processing measurement results are: a) density of the driving fluid  $\rho_f$ , kg/m<sup>3</sup>; b) the mass of the liquid according to the indications of the weighing device  $M$ , kg; the density of the environment  $\rho_a$ , kg/m<sup>3</sup>; the measurement time  $\tau$ , s. For one of the studied flow points (modes):

1) The arithmetic mean values of the basic values of the measurement equation are determined:

$$\bar{M}_j = \frac{1}{n} \sum_{i=1}^n M_{ji} \quad (1)$$

where  $M_{ji}$  – the mass value according to the weights, kg;  $\bar{M}_j$  – average mass value for 2, 3, ..., 10 and  $n$  measurements according to the weight device, kg;  $n$  – number of measurements ( $n \geq 11$ );  $i, j$  – indices of weighing point and series of measurements. The obtained data are used in the construction of graphical dependencies of the form  $M_{ji}=f(n)$  and  $\bar{M}_j=f(n)$  (example  $\bar{Q}_{Mj}=250$  t/h – Figure 3).

$$\bar{\tau}_j = \frac{1}{n} \sum_{i=1}^n \tau_{ji} \quad (2)$$

where  $\tau_{ji}$  – the value of time according to indications of the channel, s;  $\bar{\tau}_j$  – the arithmetic average of the time for 2, 3, ..., 10 and  $n$  measurements according to indications of the channel, s. The obtained data are used in the construction of graphic

dependencies  $\tau_i=f(n)$  and  $\bar{\tau}_j=f(n)$  (example  $\bar{Q}_{Mj}=250$  t/h – Figure 4).

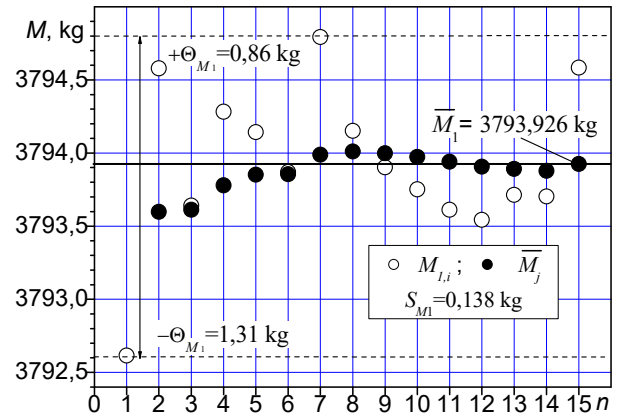


**Figure 3:** Graphic dependences of measurements quantities  $n$  on the basic value of the equation of measurement of mass values  $M$  according to the readings of the weighing device.

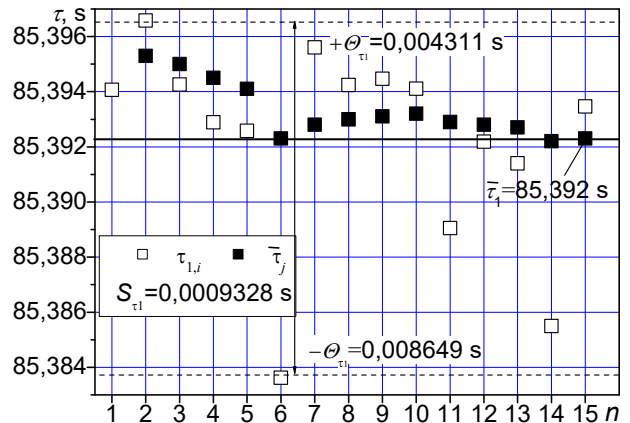


**Figure 3:** Graphic dependences of measurements quantities  $n$  on the basic value of the equation of measurement of time values of measurements according to the time channel  $\tau$ .

$$\bar{Q}_{Mj} = \frac{1}{n} \sum_{i=1}^n Q_{Mji} \quad (3)$$

where  $Q_{Mji}$  – the value of the mass flow, kg/s;  $\bar{Q}_{Mj}$  – the arithmetic mean value of the mass flow rate of at least 11 measurements, kg/s.

Graphic dependencies (Fig. 3-4) allow you visually justify the required number of measurements of basic quantities  $M_{ji}$  and  $\tau_{ji}$ . Further increase in the number of measurements of  $n$ , from the metrological and economic points of view is impractical, because the increase in the number of measurements of  $n > 11$  is self-similar.

2) For the set point (mode) of flow we determine ( $Q_{Mmin}$ ,  $Q_{Mavg}$ ,  $Q_{Mmax}$ ), the value of the liquid mass  $M_d$  that did not fall into the weight device due to the functional features by the diverter, flow control and automated system of measurement and control standard [1], kg:

a) we assume that value of the liquid mass for the first  $\bar{\tau}_{j1}$ , second  $\bar{\tau}_{j2}$ , ..., fifth  $\bar{\tau}_{j5}$  time values are  $M_{dji} = M_{d1j} = M_{d2j} = M_{d3j} = M_{d4j} = M_{d5j}$ ;

b) we assume that in the systems of equations (4-7) the mass flow value  $\bar{Q}_{M1}$  is «true».

$$1-2 \begin{cases} \bar{M}_{1j} = \bar{Q}_{M1j} \cdot \bar{\tau}_{1j} - M_{d1j} \\ \bar{M}_{2j} = \bar{Q}_{M2j} \cdot \bar{\tau}_{2j} - M_{d2j} \end{cases} \quad (4)$$

$$1-3 \begin{cases} \bar{M}_{1j} = \bar{Q}_{M1j} \cdot \bar{\tau}_{1j} - M_{d1j} \\ \bar{M}_{3j} = \bar{Q}_{M3j} \cdot \bar{\tau}_{3j} - M_{d3j} \end{cases} \quad (5)$$

$$1-4 \begin{cases} \bar{M}_{1j} = \bar{Q}_{M1j} \cdot \bar{\tau}_{1j} - M_{d1j} \\ \bar{M}_{4j} = \bar{Q}_{M4j} \cdot \bar{\tau}_{4j} - M_{d4j} \end{cases} \quad (6)$$

$$1-5 \begin{cases} \bar{M}_{1j} = \bar{Q}_{M1j} \cdot \bar{\tau}_{1j} - M_{d1j} \\ \bar{M}_{5j} = \bar{Q}_{M5j} \cdot \bar{\tau}_{5j} - M_{d5j} \end{cases} \quad (7)$$

The required value  $M_{dji}$  (8-11) is determined by substituting the mass flow  $\bar{Q}_{M1}$  into the second equation of system (4-7):

$$M_{d(1-2)j} = \bar{Q}_{M1j} \cdot \bar{\tau}_{2j} - \bar{M}_{2j} \quad (8)$$

$$M_{d(1-3)j} = \bar{Q}_{M1j} \cdot \bar{\tau}_{3j} - \bar{M}_{3j} \quad (9)$$

$$M_{d(1-4)j} = \bar{Q}_{M1j} \cdot \bar{\tau}_{4j} - \bar{M}_{4j} \quad (10)$$

$$M_{d(1-5)j} = \bar{Q}_{M1j} \cdot \bar{\tau}_{5j} - \bar{M}_{5j} \quad (11)$$

Similar actions are performed for systems of equations.

$$2-3 \begin{cases} \bar{M}_{2j} = \bar{Q}_{M2j} \cdot \bar{\tau}_{2j} - M_{d2j} \\ \bar{M}_{3j} = \bar{Q}_{M3j} \cdot \bar{\tau}_{3j} - M_{d3j} \end{cases} \quad (12)$$

$$2-4 \begin{cases} \bar{M}_{2j} = \bar{Q}_{M2j} \cdot \bar{\tau}_{2j} - M_{d2j} \\ \bar{M}_{4j} = \bar{Q}_{M4j} \cdot \bar{\tau}_{4j} - M_{d4j} \end{cases} \quad (13)$$

$$2-5 \begin{cases} \bar{M}_{2j} = \bar{Q}_{M2j} \cdot \bar{\tau}_{2j} - M_{d2j} \\ \bar{M}_{5j} = \bar{Q}_{M5j} \cdot \bar{\tau}_{5j} - M_{d5j} \end{cases} \quad (14)$$

$$3-4 \begin{cases} \bar{M}_{3j} = \bar{Q}_{M3j} \cdot \bar{\tau}_{3j} - M_{d3j} \\ \bar{M}_{4j} = \bar{Q}_{M4j} \cdot \bar{\tau}_{4j} - M_{d4j} \end{cases} \quad (15)$$

$$3-5 \begin{cases} \bar{M}_{3j} = \bar{Q}_{M3j} \cdot \bar{\tau}_{3j} - M_{d3j} \\ \bar{M}_{5j} = \bar{Q}_{M5j} \cdot \bar{\tau}_{5j} - M_{d5j} \end{cases} \quad (16)$$

$$4-5 \begin{cases} \bar{M}_{4j} = \bar{Q}_{M4j} \cdot \bar{\tau}_{4j} - M_{d4j} \\ \bar{M}_{5j} = \bar{Q}_{M5j} \cdot \bar{\tau}_{5j} - M_{d5j} \end{cases} \quad (17)$$

We assume that in systems of equations (12-14) «true» mass flow value –  $\bar{Q}_{M2}$ , for systems of equations (15-16) «true» mass flow value –  $\bar{Q}_{M3}$  and for (17) «true» mass flow value –  $\bar{Q}_{M4}$ .

$$M_{d(2-3)j} = \bar{Q}_{M2j} \cdot \bar{\tau}_{3j} - \bar{M}_{3j} \quad (18)$$

$$M_{d(2-4)j} = \bar{Q}_{M2j} \cdot \bar{\tau}_{4j} - \bar{M}_{4j} \quad (19)$$

$$M_{d(2-5)j} = \bar{Q}_{M2j} \cdot \bar{\tau}_{5j} - \bar{M}_{5j} \quad (20)$$

Unknown quantity  $M_{dji}$  (18-20) for other systems of equations are determined by substituting the second equation of each mass flow system  $\bar{Q}_{M2j}$  in (12-14).

$$M_{d(3-4)j} = \bar{Q}_{M3j} \cdot \bar{\tau}_{4j} - \bar{M}_{4j} \quad (21)$$

$$M_{d(3-5)j} = \bar{Q}_{M3j} \cdot \bar{\tau}_{5j} - \bar{M}_{5j} \quad (22)$$

Unknown quantity  $M_{dji}$  (21-22) for other systems of equations are determined by substituting the second equation of each mass flow system  $\bar{Q}_{M3j}$  in (15-16).

$$M_{d(4-5)j} = \bar{Q}_{M4j} \cdot \bar{\tau}_{5j} - \bar{M}_{5j} \quad (23)$$

Unknown quantity  $M_{dji}$  (23) for other systems of equations are determined by substituting the

second equation of each mass flow system and  $\bar{Q}_{M_{4j}}$  in (17).

3) Non-excluded systematic error of liquid mass which did not get into the weighing device, due to the functional features by the diverter, flow control and automated system of measurement and control of the standard [1], in  $j$  - point  $\Theta(M_d)_j$ , кг, determine:

$$\Theta(M_d)_j = \bar{M}_{dj} \quad (6)$$

$$\text{where } \bar{M}_{dj} = \frac{M_{d(1-2)j} + \dots + M_{d(2-3)j} + \dots + M_{d(4-5)j}}{10}$$

4) Standard deviation of liquid mass that did not get into the weighing device, due to the functional features by the diverter, flow control and automated system of measurement and control of the standard [1], in  $j$  - point  $S(M_d)_j$ , кг, determine:

$$S(M_d)_j = \sqrt{\frac{(M_{d(1-2)j} - \bar{M}_{dj})^2 + \dots + (M_{d(4-5)j} - \bar{M}_{dj})^2}{n \cdot (n-1)}} \quad (7)$$

Next, a quantitative comparison of non-excluded systematic error of liquid mass that did not fall into the weighing device due to the functional features of the diverter and flow control systems of the medium, as well as an automated system of measurement, control of the standard is made [1]  $\Theta(M_d)_j$  obtained by indirect method and experimental data of the authors [13], defined with the use of pneumometric method (Figure 5).

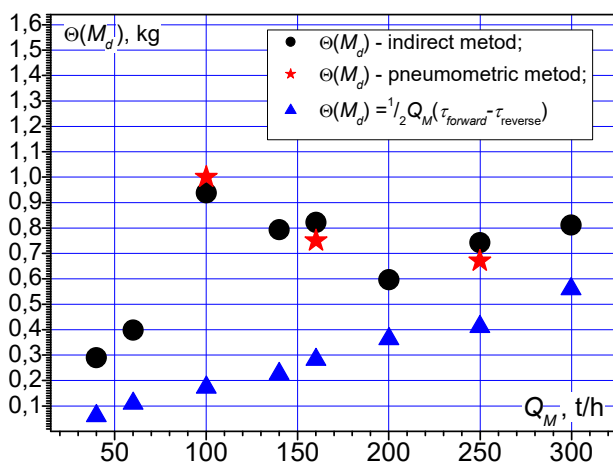


**Figure 5:** Non-excluded systematic error of missing liquid mass in the weighing device, determined by various methods.

Field research by an indirect method is presented in the range of fluid mass flow  $Q_M=11,1-83,3$  kg/s (40-300 t/h) for the weight device which is a part of the standard (with fixed geometry diverter nozzle). It should be noted that the results of the pneumometric method are obtained on the basis of measurements of flow velocity profiles on the nozzle section in the range of the mass flow rate  $Q_M=27,7-69,4$  kg/s (100-250 t/h). The results of the pneumometric method are indicated in the form of stars «★» (Figure 5). This method is difficult for wide application in real-life standards due to the design features of the diverters. The results of the indirect method are indicated in the form of circles «●» (Figure 5). There is a satisfactory agreement of results obtained by direct and indirect methods, which led to the conclusion about their reliability.

It should be recalled that in existing methods, the only influencing factor determining the characteristics of the diverter operation is the difference in the operation of the diverter actuators. Component values of non-excluded systematic error of liquid mass that did not get into the weighing device, due only to the time difference in the «forward» and «reverse» moves are indicated in the form of triangles «▲»(Figure 5), significantly lower than the values taking into account other influencing factors.

## 7. Conclusion

1) overall estimate of contributing factors of diverter on metrological characteristics of the standard by indirect method was conducted; 2) verification of the results of pneumometric and indirect methods, allowed to determine a rational method for assessing the impact of the diverter on the metrological characteristics of the standard units of liquid mass and volume in the flow, mass and volume flow rates; 3) testing of a rational method for assessing the contributing factors of the diverter (evaluation of standard measurement uncertainties).

It is necessary to take into account all standard uncertainty budget components introduced by the diverter, including the degree of filling and the distribution of flow rates of the fluid in the nozzle section (plane), asynchronous signals “start” – “stop” between the measuring controller of the standard with the flow meter under study, ripple fluid flow rate; as well as leaks (overflow) and splashing of a jet of liquid when switching to the opposite drain [1]. Therefore, the authors included in the developed standard method of transferring units of mass and volume of fluid in the flow, mass and

volumetric flow rates of liquid, indirect measurement method, developed for the first time an indirect method for estimating the maximum number of standard measurement uncertainties introduced by the standard of the diverter. This method does not require additional expensive equipment, performing complex numerical and experimental procedures, and is made without the involvement of well qualified personnel.

At present, the specialists of FGUP "VNIIR" are testing the standard method of transferring units of mass and volume of liquid in the flow, mass and volume flow of liquid on the standards located in Kazan, in order to determine the possibility of its wide application in the certification of working standards.

## References

- [1] GOST P 8.909-2016: State system for insuring the uniformity of measurements. Secondary standards of units of mass and volumetric flow rate, mass and volume of fluid. General metrological and technical requirements, 2016.
- [2] GOST R 8.608-2004 GSI: State system for ensuring the uniformity of measurements. Mountings for verification of instruments measuring the expenditure and volume of water by calibrating with transformers (meters) of expenditure and (or) volume of water. General metrological and technical requirements, 2004.
- [3] ISO 4185:1980: Measurement of liquid flow in closed conduits. Weighing method, 1980.
- [4] Kargapoltsev V P, «Requirements for pouring installations for flow meters - water meters and process fluids», *Oil and Gas Business*, **Vol. 1**, pp. 1-6, 2004.
- [5] Nunner W., «Warmeübergang und Druckabfall in rauchen Rohren», *VDI-Forschungsheft*, **Vol. 455**, pp. 5-39, 1956.
- [6] Koch R, «Druckverlust und Wärmeübergang bei verwirbelter Strömung», *VDI-Forschungsheft*, **Vol. 469**, pp. 44-49, 1958.
- [7] Webb R L, «Generalized heat transfer and friction correlations for tubes with repeated-rib roughness», *Int. J. of Heat and Mass Transfer*, **Vol. 15**, pp. 180-184, 1972.
- [8] Shchelchikov A, «Thermohydraulic characteristics of discretely rough tubes for the transitional flow regime», *Heat Transfer Research*, **Vol. 47**, pp. 545-557, 2016.
- [9] Loitsyansky L G, *Fluid and gas mechanics*, (Moscow, State. ed. Technical and theoretical lit.), 1950.
- [10] Idelchik I, *Handbook of hydraulic resistance* (Moscow, Mashinostroenie), 1992.
- [11] Shimada T, Oda S, Terao Y, Takamoto M, «Development of a new diverter system for liquid flow calibration facilities», *Flow Measurement and Instrumentation*, **Vol. 14**, pp. 89–96, 2003.
- [12] Rainer Engel, «Liquid Flowmeter Characteristics, Meter Calibration, Measurement Uncertainty and Traceability», *Conference Proc. COOMET comparison of National Standards for Liquid Flow* (PTB Braunschweig, Germany, 24 – 25 February), 2009.
- [13] .Korneev R A, Tukhvatullin A R, Fafurin V A, Shchelchikov AV, «Impact assessment of the flow switch on the metrological characteristics of the standard units of mass and liquid volume in the flow, mass and volume liquid flow», *Measurement Techniques*, **Vol. 4**, pp. 42–47, 2019.
- [14] Kosach N I, «Estimation of measurement uncertainty of fluid flow on standards», *Information processing systems*, **Vol. 6 (64)**, pp. 47-50, 2007.

# Performance of the LDA Volumetric Flow Rate Standard Under Severely Disturbed Flow Conditions

Felix Heitmann<sup>1</sup>, Jonas Steinbock and Markus Juling<sup>1</sup>

<sup>1</sup>Physikalisch-Technische Bundesanstalt, Abbestraße 2-12, 10587 Berlin, Germany  
felix.heitmann@ptb.de

---

## Abstract

In thermal power plants, flow meters are operated at high temperatures and pressures and often encounter disturbed flow profiles. This leads to an increased measurement uncertainty, which limits the safe operating range of flow rates and hence the plant's power output. Therefore, the laser optical flow rate standard (LFS) was developed. It is designed to allow the on-site calibration of industrial flow meters in power plants at high temperatures and pressures. It makes use of the metrologically traceable and non-invasive laser Doppler anemometry (LDA) to measure the velocity field simultaneously with two LDA systems. The volumetric flow rate is then determined by means of integration. Here, we present flow rate measurements for fully developed pipe flow and 6 pipe diameters downstream of a disturbance generator. The mean deviation in flow rate between the two LDA systems was 0.05 %, with a mean deviation from the gravimetric reference flow rate of 0.12 %. The highest deviations from the reference were 0.21 % and 0.31 %, for the two systems respectively.

---

## 1. Introduction

Industrial liquid flow rate meters are calibrated at test facilities which provide fully developed turbulent pipe flow, temperatures well below 100 °C and moderate pressures [1][2].

In contrast, water flow meters in power plants are operated at up to 400 °C and 300 bar.

Here, the fluid dynamic properties of water change drastically.

Further, the flow meter is deformed by the resulting thermal expansion and mechanical stress, changing the effective cross-sectional area.

Depending on the measurement principle, elevated temperatures will also affect the performance of the measurement equipment itself.

Due to space constraints, flow meters are often installed close to pipe bends and other instrumentation. This causes disturbed flow conditions inside the flow meters, resulting in deviations in the measured flow rate.

These factors aggregate to a measurement uncertainty in the field of around 2 % [3]. For operational safety, this limits the permissible range of flow rate and therefore the power output of the plant.

If the flow meters were to be calibrated in-situ, the factors mentioned above would be captured in the calibration process and therefore not be considered when determining the measurement uncertainty.

This, in turn, would lead to a major decrease in uncertainty of the flow rate and therefore allow the increase of the plant's power output.

A laser optical flow rate standard for high pressure natural gas was described by Mickan et al. [4]. The vastly different physical properties of water, however, require a very different design in many aspects.

LDA measurements for the determination of the flow rate in water were carried out by Müller et al. [5]. Yet, the design of the measurement setup prohibits the application at high temperatures and does not allow precise alignment of the LDA probe.

Thus, at the Physikalisch-Technische Bundesanstalt (PTB), a portable laser optical flow rate standard (LFS) was developed [3][6][7]. It employs the non-invasive and traceable laser-Doppler anemometry (LDA) for the point-wise measurement of the streamwise velocity. The flow field is approximated by spline (radial) and nearest-neighbor (azimuthal) interpolation between the measured points. The volumetric flow rate is

determined by integration of the flow field over the pipe's cross-sectional area.

In this contribution, following a brief description of the LFS measurement setup, we present volumetric flow rate measurements obtained with the LFS under heavily disturbed flow conditions and compare them to the undisturbed, fully developed turbulent flow case.

## 2. Experimental setup

### 2.1 Configuration of the LFS

Optical access to the flow is provided by an industrial stainless-steel sight glass fitting (DN 150, PN 40) equipped with two metal fused sight glasses (PN 40,  $T_{\max} = 280\text{ }^{\circ}\text{C}$ ) on opposing sides perpendicular to the direction of flow.

A short stainless-steel Venturi nozzle is installed inside the fitting, reducing the inner diameter from  $D_p = 158\text{ mm}$  at the inlet to  $75\text{ mm}$ . This quadruples the mean velocity and therefore greatly increases the obtainable LDA burst rate. Furthermore, the flow profile is flattened considerably as described by Steinbock et al. [8].

Downstream of the nozzle, a calibrated precision glass pipe ( $r = (37.518 \pm 0.008)\text{ mm}$ ) provides a well-defined cross section for the LDA measurements.

Pointwise velocity measurements are carried out simultaneously and independently by two cross beam LDA probes ( $P = 200\text{ mW}$ ) with wavelengths of  $532\text{ nm}$  and  $561\text{ nm}$ , respectively.

In water, the resulting measuring volume is approximately  $920\text{ }\mu\text{m}$  in length with a diameter of  $65\text{ }\mu\text{m}$  ( $1/e^2$ -criterion).

Each probe contains receiving optics that connect to a photomultiplier by multimode fiber optics.

As the two LDA probes are located on opposite sides of the optical access, each probe collects the forward scattered light from the other probe's measuring volume. This increases the obtainable LDA burst rate by a factor of 10 compared to operation in backward scattering mode.

The photomultiplier voltages are read out with a 12-bit digitizer and at least 10-fold oversampling of the LDA burst frequency.

The LDA probes are each mounted on a 6-axis hexapod positioning system. Besides traversing the LDA measuring volume over the pipe cross-section, they allow the precise alignment of the LDA probes to the glass pipe. A circumferential marking on the outer mantle of the glass pipe serves as a measurable reference of the pipe axis [3][9].

As the positioning system is not connected to the optical access pipe fitting, the alignment procedure is carried out before every measurement campaign. This physical separation between the potentially hot optical access and the positioning system allows the LFS to be used at high temperatures as the measurement systems is sensitive to temperature change.

When passing through the curved geometry of the glass pipe, the laser beams get refracted due to the difference in refractive indices. To place the measuring volumes at the desired positions inside the flow, numerical raytracing of the laser beams is performed individually for each positioning system and measuring position as described by Steinbock [6].

LDA measurements spanning the whole cross-section of the glass pipe are carried out at  $n_{\text{rad}} = 20$  radial paths each containing 15 points between the pipe center and  $0.99r$  (300 points in total). Hence, the last point is located at  $375\text{ }\mu\text{m}$  distance from the wall. Between the pipe center and  $0.8r$ , points are evenly placed at distances of  $0.1r$ . Beyond  $0.8r$ , 6 additional points are placed to minimize the error of the flow field integral [6].

This fine measurement grid allows the reconstruction even of strongly disturbed flow profiles and thereby the volumetric flow rate as later demonstrated.

Per point, LDA bursts are recorded until either a statistical uncertainty for the velocity of  $0.05\%$  ( $k = 1$ ) or a measurement time of  $45\text{ s}$  is reached.

### 2.2 Data processing

For the near-wall positions, where the measuring volume partially intersects with the wall, the effective position is calculated as the intensity centroid of the remaining measuring volume according to Steinbock et al. [10].

To correct for the LDA velocity bias, the  $n$  individual burst velocities  $w_i$  of each measurement point (MP) are weighted with their respective inverse velocity according to Equation 1 and 2 as proposed by McLaughlin and Tiederman [11]. This seems to be adequate because the measured streamwise velocity is dominant over the other velocity components in this setup.

$$\bar{w}_{\text{MP}} = \frac{\sum_{i=1}^n w_i * \xi_i}{\sum_{i=1}^n \xi_i} \quad (1)$$

$$\xi_i = |w_i|^{-1} \quad (2)$$

For each radial path, a cubic Hermite spline is used to approximate the flow profile between the measured points. From the outermost point to the wall, the velocity profile is completed by the logarithmic law of the wall and a linear approach for the viscous sublayer.

As the wall shear stress is unknown, it is chosen so that the law of the wall velocity profile connects to the last measured point.

The volumetric flow rate is then calculated according to Equation (3).

$$Q_{LDA} = \frac{2\pi}{n_{rad}} \sum_{k=1}^{n_{rad}} \int_0^r w_k(r) r dr \quad (3)$$

Here,  $w_k(r)$  is the reconstruction of the velocity profile for the path  $k$  as a function of the radius  $r$  which is integrated analytically.

### 2.3 Flow facility and test bench setup

All measurements were conducted at the heat water calibration rig at the Physikalisch-Technische Bundesanstalt in Berlin [2] at  $p = 2.5$  bar.

Using the gravimetric principle, it exhibits a measurement uncertainty of  $U = 0.04\%$  ( $k = 2$ ) for volumetric flow rates of water between 3 and 1000 m<sup>3</sup>/h and temperatures from 3 to 90 °C.

At first, the test bench was equipped with a straight DN 150 pipe ( $D_p = 158$  mm) with a length of  $50D_p$  upstream and  $10D_p$  downstream of the LFS optical access for the measurement in fully developed pipe flow.

Afterwards, an asymmetrical swirl disturbance generator was inserted into the piping at  $6D_p$  upstream of the LFS (see Figure 1).

The asymmetrical swirl disturbance generator as proposed by Tawackolian [12] features five angled blades and a disturbance plate blocking 7 % of the cross-sectional area. It was designed to emulate the flow pattern downstream of a double bend out of plane [12].

Further investigation of the resulting flow profile is described by Turiso et al. [13].

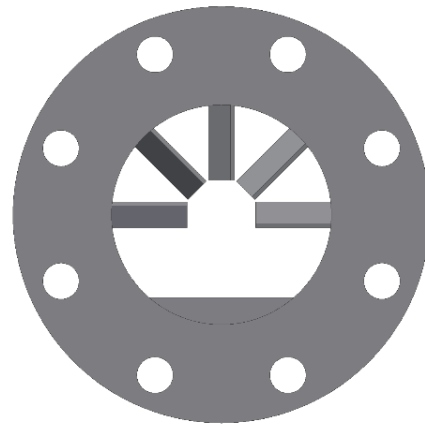


**Figure 1:** The DN 150 asymmetrical swirl disturbance generator in a DIN flange style.

For both configurations, measurements were carried out at 5 combinations of Reynolds numbers and temperatures (test cases) as shown in Table (1). For each measurement, a gravimetric flow rate measurement  $Q_{ref}$  was performed.

All Reynolds numbers are stated with respect to the DN 150 pipe upstream of the LFS as given by

$$Re = \frac{w_p D_p}{\nu} \quad (4)$$

and

$$w_p = \frac{Q_{ref}}{\frac{\pi}{4} D_p^2} \quad (5)$$

Flow rate measurements were repeated 3 times for each configuration and test case.

**Table 1:** Flow parameters of the 5 test cases.

Test case	$T$ (°C)	$Re$ ( $10^3$ )	$Q_{ref}$ (m <sup>3</sup> /h)
1	20	50	22.40
2	20	100	44.80
3	20	450	200.00
4	60	450	95.29
5	60	945	200.00

### 3. Results and discussion

In the following section, the two measurement systems are referred to as LDA1 (532 nm wavelength) and LDA2 (561 nm).

A single measurement of the volumetric flow rate took between 1.4 and 2 hours, with longer durations at low Reynolds numbers.

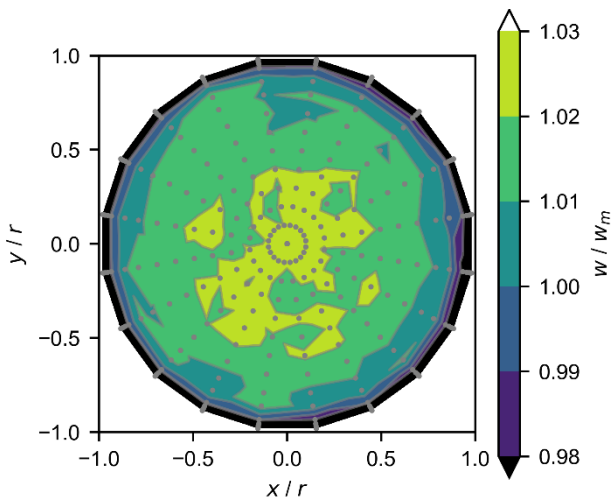


**Figure 2:** Normalized velocities of LDA2 at  $Re = 945 \cdot 10^3$  and  $60 \text{ }^\circ\text{C}$  for the undisturbed configuration.

To illustrate the flattening effect of the Venturi nozzle, Figure 2 shows the velocities measured with LDA2 under the undisturbed configuration at  $Re = 945 \cdot 10^3$  and  $60 \text{ }^\circ\text{C}$ , normalized by the mean velocity

$$w_m = \frac{Q_{LDA}}{\pi r^2} \quad (6)$$

Note that one shade of color represents velocities within a 1 % range. In the pipe center, the velocity exceeded the mean velocity by less than 3 %. Towards the pipe wall, the measured velocities stayed above  $w_m$  until around  $0.95r$ .

A fully developed turbulent flow in the same diameter and smooth walls would show a much higher center velocity of around  $1.16w_m$  and velocities lower than  $w_m$  as soon as  $0.75r$ .

As the LDA burst frequency is proportional to the velocity, the bandwidth of the raw LDA signal encountered across most of the flow field of the LFS is much narrower than in a fully developed turbulent flow. This greatly facilitates the selection of appropriate filters.

Spatial fluctuations of the velocity of less than 1 % are visible. These might be caused by imperfections that were observed on the glass pipe surface.

In Figure 3, the normalized velocity profile of LDA2 is shown for the disturbed configuration at identical flow parameters as in Figure 2.

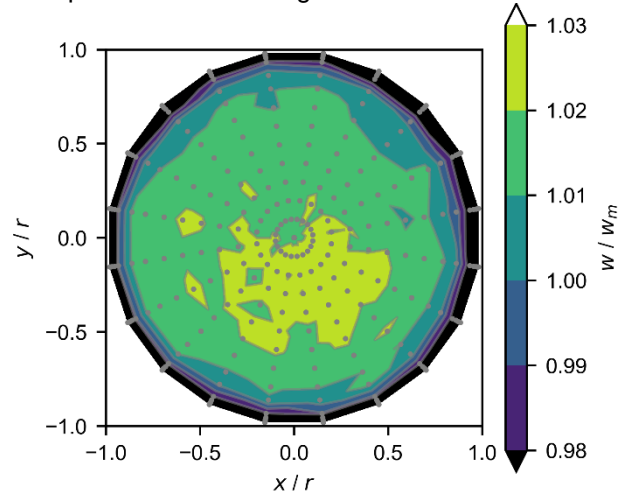


**Figure 3:** Normalized velocities of LDA2 at  $Re = 945 \cdot 10^3$  and  $60 \text{ }^\circ\text{C}$  for the disturbed configuration.

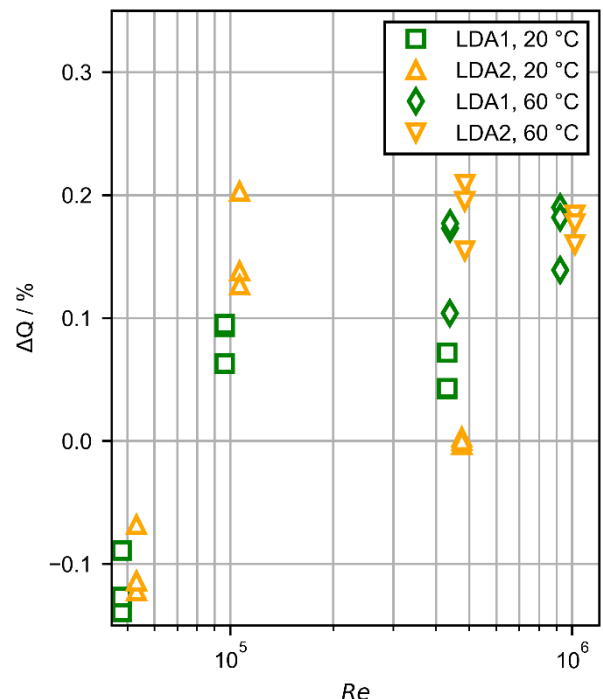


**Figure 4:** Relative deviations of the two LFS flow rates from the gravimetric reference flow rate for the undisturbed configuration.

Here, a slight shift of the location of maximal velocities towards  $-y$  can be observed. For LDA1, the shift was less pronounced. At all lower Reynolds numbers, no noticeable shift could be observed.

Figure 4 shows the deviation of the two LDA systems from the gravimetric flow rate measurement (the reference) for the undisturbed configuration and the 5 test cases in percent. The deviations were calculated as

$$\Delta Q = 100 * \frac{Q_{LDA} - Q_{ref}}{Q_{ref}} \quad (7)$$

The Reynolds numbers were slightly shifted for plotting.

For all individual measurements of the undisturbed case, the maximal deviation from the reference flow rate was 0.21 % at  $Re = 450 \cdot 10^3$  and 60 °C.

All but the measurements at the lowest Reynolds number show a positive deviation from the reference.

The mean absolute deviation between the two LDA systems was below 0.04 %, with a maximum of 0.14 % at  $Re = 100 \cdot 10^3$ .

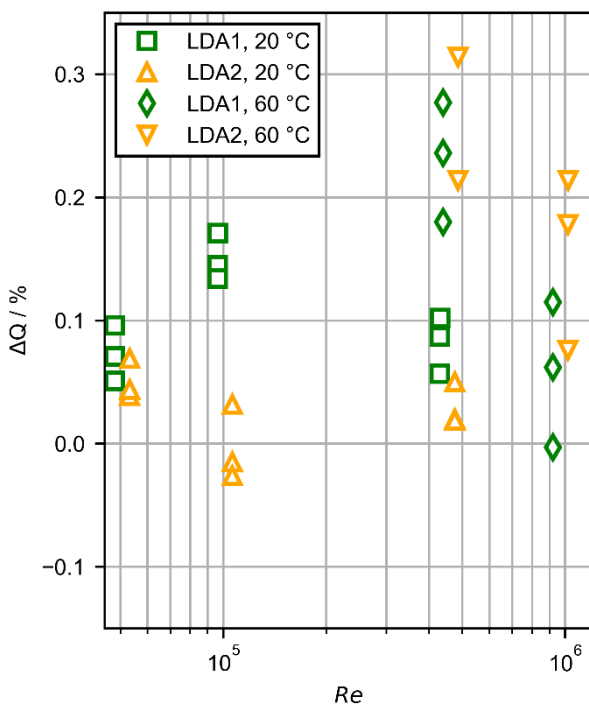


**Figure 5:** Relative deviations of the two LFS flow rates from the gravimetric reference flow rate for the disturbed configuration.

The results for the disturbed configuration are presented in Figure 5. At 20 °C, LDA1 exhibited a maximal deviation of 0.17 %, while LDA2 was better than 0.07 %.

At 60 °C however, both systems showed deviations between 0.18 % and 0.31 % for  $Re = 450 \cdot 10^3$ . At the highest Reynolds number, deviation from the reference were below 0.21 % for both systems.

For all disturbed measurements, the deviation between the two LDA systems was within 0.16 % and on average at 0.07 %. Compared to the undisturbed case, a higher variance for the test cases at 60 °C was observed.

Due to modifications to the positioning systems, the alignment procedures and for the inclusion of disturbed flow profiles, an up-to-date measurement uncertainty budget for the LFS is currently being developed.

To check for temperature and Reynolds number dependence of the LFS, further measurements across the available temperature range of the test bench must be conducted.

#### 4. Conclusion

The laser optical flow rate standard (LFS) was used to measure the volumetric flow rate of water at 20 and 60 °C and Reynolds numbers between  $50 \cdot 10^3$  and  $945 \cdot 10^3$  in a fully developed pipe flow and 6 pipe diameters behind an asymmetrical swirl disturbance generator.

Even in a heavily disturbed flow profile, both independent LDA systems exhibited low deviations from the gravimetric reference with a mean of 0.12 % and maximal deviations of 0.21 % and 0.31 %, respectively.

This is approximately one order of magnitude below the current measurement uncertainties of flow meters used in power plants, which demonstrates the potential of the LFS as a mobile, laser optical standard for the on-site calibration of industrial flow meters.

#### References

- [1] Furuichi, N., Sato, H., Terao, Y. and Takamoto, M., "A new calibration facility for water flowrate at high Reynolds number", *Flow Measurement and Instrumentation*, **20**, 38-47, 2009.
- [2] Mathies, N., "Messunsicherheit einer gravimetrischen Kalt- und Warmwasser-Normalmessanlage für große Volumenströme", Doctoral dissertation, Technische Universität Berlin, 2005.
- [3] Juling, M., "Rückgeführte Volumenstrommessung mittels ortsaufgelöster Laser-Doppler-Anemometrie", Doctoral dissertation, Technische Universität Berlin, 2016.
- [4] Mickan, B., Kramer, R., Hotze, H.J. and Dopheide, D., "Pigsar The Extended Test Facility and new German National Primary

- Standard for High-Pressure Natural Gas", in proceedings of the 5th International Symposium on Fluid Flow Measurement (ISFFM), Arlington, USA, 2002.
- [5] Müller, U., Dues, M., Utz, M., Lederer, T. and Büker, O., "Application of Laser Doppler Velocimetry for Monitoring of Measurement Uncertainty of Flow Sensors Under Installation Conditions", in proceedings of "Lasermethoden in der Strömungsmesstechnik" GALA e.V., 2007.
- [6] Steinbock, J., "Aufbau und Validierung eines laseroptischen Normal-Durchfluss-Messgeräts für die metrologische Rückführung einer Hochtemperatur-Prüfanlage", Doctoral dissertation, Technische Universität Berlin, 2017.
- [7] Juling, M., Steinbock, J., Kraume, M. and Lederer, T., "LDA volume flow rate standard for water using high spatial resolution LDA for traceable measurements in power plants", in proceedings of FLOMEKO 2016, 2016.
- [8] Steinbock, J., Weissenbrunner, A., Juling, M., Lederer and T., Thamsen, P. U., „Uncertainty evaluation for velocity–area methods”, Flow Measurement and Instrumentation, **48**, 51-56, 2016.
- [9] Heitmann, F., Juling, M., Steinbock, J. and Kraume, M., "Automated identification of the position and orientation of the LDA measuring volume with respect to flow cross section", in proceedings of "Lasermethoden in der Strömungsmesstechnik" GALA e.V., 2017.
- [10] Steinbock, J. J., Weissenbrunner, A., Juling, M. and Thamsen, P. U., "Correction for the effective measuring position of LDA in circular cross-sections", in proceedings of "Lasermethoden in der Strömungsmesstechnik" GALA e.V., 2017.
- [11] McLaughlin, D. K. and Tiederman, W. G., "Biasing correction for individual realization of laser anemometer measurements in turbulent flows", The Physics of Fluids, **16**, 2082-2088, 1973.
- [12] Tawackolian, K., „Fluiddynamische Auswirkungen auf die Messabweichung von Ultraschall-Durchflussmessgeräten“, Doctoral dissertation, Technische Universität Berlin, 2013.
- [13] Turiso, M., Straka, M., Rose, J., Bombis, C. and Hinz, D. F., "The asymmetric swirl disturbance generator: Towards a realistic and reproducible standard", Flow Measurement and Instrumentation, **60**, 144-154, 2018.

# Low-Pressure Gas Flow Standard in Russian Federation: Principles, Calibration Techniques, Intercomparisons

I.A. Isaev, V.A. Fafurin, A.V. Mingaleev, A.I. Gorchev,  
A.B. Yakovlev, O.Yu. Sladovskaya

*Federal State Unitary Enterprise «All-Russian Research Institute of Flow Metering» (VNIIR),  
St. 2<sup>nd</sup> Azinskaya, 7a, Kazan, Republic of Tatarstan, Russian Federation, 420088  
E-mail (I.A. Isaev): ilya.isaev@mail.ru*

---

## Abstract

The article deals with the basics of metrological support of low-pressure gas (air) flow measurements, describes the improved State (National) Primary Standard GET 118-2017 and methods of reproduction and transfer the gas flow rate units implemented in the Russian Federation. The improved GET 118-2017 is a complex of five test rigs that are interconnected by means of the reference sonic nozzles, which received the unit of measure on the initial test rig TR-1 of bell type. For transfer the gas flow rate units to calibratable sonic nozzles from reference sonic nozzles in GET 118-2017 a new comparing method using laminarizers (laminar flow elements) as comparators was developed and patented. The volumetric gas flow rate of the calibratable nozzle is determined by the relative change in the pressure drop on the comparator when the calibratable nozzle and two reference nozzles with nominal flow rates smaller and larger relative to the calibratable value are alternately connected after comparator. The GET 118-2017 on the scientific and technical level corresponds to the modern world achievements and is not inferior in characteristics to the best foreign analogues that is confirmed by the results of international comparisons.

---

## 1. Introduction

In 1967, work on the creation of reference facilities for the calibration of measuring instruments for measuring the volume and mass flow rate of low-pressure gas (air) was started in the Russian Federation. VNIIR developed and approved the State Primary Standard GET 62-74 of Gas Volume Rate Units in 1974 and the State Primary Standard GET 118-79 of Gas Mass Flow Rate Units in 1979.

In 2006, according to the results of the scientific and technical measures conducted by “VNIIR”, the State Primary Standard GET 118-2006 of Volume and Mass Gas Flow Rate Units was created, replacing GET 62-74 and GET 118-79. The GET 118-06 included an initial gravimetric-type reference test rig and two reference test rigs with sonic nozzles calibrated on an initial test rig with a general air flow range from  $3 \cdot 10^{-3}$  to 10000 m<sup>3</sup>/h [1]. The high level of GET 118-2006 and its compliance with the best foreign analogues were confirmed by international comparisons COOMET No.219/Sk-00 (2006-2007) and COOMET No.412/UA/07 (2010). Also, the gravimetric test rig of GET 118-06 confirmed the degree of equivalence at trilateral comparison

between NMIs of Russia, Germany and China [2], a side result of which was the confirmation of the independence of the discharge coefficient of sonic nozzles from the calibration method, since the participative reference standards had different principles of gas flow rate reproduction (gravimetric, PVTt and bell). According to the results of these intercomparisons, CMC entries VNIIR-13.01, VNIIR-13.02, VNIIR-13.03 and VNIIR-13.04 were registered in the BIPM database.

Nevertheless, the primary standard of the GET 118-2006 is already outdated by 2012 and did not meet modern requirements for accuracy, performance, reproducible flow ranges and operating pressure. Therefore, in the period from 2012 to 2017, several major steps were taken at the VNIIR to improve the Primary Standard GET-118.

## 2. Method of sonic nozzle calibration

In the Primary Standard GET 118-06 the sonic nozzles (SN) were used to transfer the gas flow rate units to working standards and measuring instruments. Sonic nozzles are distinguished by high accuracy of gas flow measurement, simplicity

of the device and reliability. With a supercritical pressure drop at the SN, the gas volume flow rate  $Q$  does not depend on the pressure in front of the nozzle, but is determined only by the geometrical parameters of the nozzle and the inlet gas temperature. Therefore SN are used as the basic elements of working standards for calibration and verification of gas flow meters, for accurate reproduction and measurement of gas volume and volume flow, as well as for testing the gas flow meters of various types. In this regard the issues of reliable calibration of the SN are extremely relevant.

The transfer of gas flow rate units to SN is usually carried out from reference standards of bell, gravimetric, piston and other types. But, as a rule, these high-precision reference standards have a high cost and relatively low productivity, that does not allow them to be used for mass calibration of measuring instruments. The use of other reference sonic nozzles (RSN) for calibration of SN at their sequential allocation using the direct comparison method is faced with a number of difficulties related to the discreteness of nozzles readings, relatively large pressure drop, the impossibility of providing identical Reynolds number, and the appearance of flow pulsations in the channel between nozzles.

Along with the direct comparison method, one of the most common methods of units transfer from reference standards to working measurement tools is comparing (or calibration using a comparator). The method consists in comparing the comparator's control parameter (related to the measured unit) on the reference sample and on the meter under test and determining from the change of this parameter the measured value on the meter under test.

In the GET 118–06 the comparing method was already used to transfer gas flow rate units from reference standard to calibratable SN. Turbine and rotary flow meters-gas meters with high-frequency output were used as comparators [3]. The volume gas flow rate  $Q$  of calibratable SN was determined in proportion to the change in the impulse frequency of the comparator output signal when the gas flows at the 1st stage successively through the comparator and the RSN with a known nominal flow rate, and at the 2nd stage through the comparator and calibratable SN. Thus, the gas flow rate indications of the comparator in the comparison procedure were not used, but only its output frequency signals were compared.

The use of the comparing method in the GET 118–06 allowed to increase productivity and, in general, to improve the characteristics of the standard.

However, significant disadvantages of this method were noted. First of all, they are connected with the difficulty of taking into account the manifest nonlinearity factor caused by friction in the rotational supports of the used comparators, as a result of which the gas flow rates of the reference and calibratable nozzles should be as close as possible (within 5%). In addition, during operation, the metrological characteristics of such comparators are deteriorated due to their wear.

In this regard, at improvement GET 118 the flow laminarizers (laminar flow elements) were used as comparators for SN calibration. Laminarizers are characterized by high sensitivity, a wide applicable flow range and the absence of moving friction joints. In such devices, there is a sharp decrease in the equivalent hydraulic diameter due to the direction of the main flow into the system of small parallel tubes or flat ducts. As a result, in a large range of operating parameters a laminar flow takes place, which, according to the Poiseuille law, is characterized by a linear dependence of the volume flow rate  $Q$  vs. the pressure drop  $\Delta p$ .

Thus, in the case of SN location directly behind the laminarizer, it is possible to establish a relationship between the  $Q$  value of the nozzle and the pressure drop  $\Delta p$  in the stabilized flow section in the comparator. It should be taken into account that in the isothermal gas flow the volume flow rate is not constant along the length of the channel due to changes in pressure, and the value  $Q$  corresponds to the gas density at average pressure  $p + \Delta p/2$  (where  $p$  is the outlet pressure from comparator, approximately equal to the pressure at the entrance to the nozzle) on the section  $L$  of the laminarizer.

Based on this, the method was developed for transfer the volume gas flow rate units from reference nozzles to calibratable ones. To improve the accuracy of SN calibration, two RSN are used - with a smaller and larger flow rate relative to the calibratable value (Figure 1), which allows to more accurately determine the character of the dependence  $\Delta p(Q)$  within the established range. The output from the comparator and the input sections of the nozzles are located in the common receiver to minimize the pressure drop between them.

For the practical implementation of the presented method in a wide range of gas flow rates, several laminarizers with flat slit channels with a height of 0.8 mm and a length of 230 mm were created.

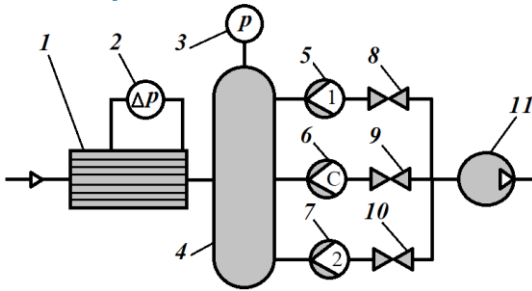


**Figure 1:** Schematic diagram of the reference installation for sonic nozzles calibrating: 1 – laminarizer (comparator); 2 – pressure differential sensor; 3 – pressure sensor; 4 – receiver; 5 – lower flow RSN; 6 – calibratable nozzle; 7 – higher flow RSN; 8, 9, 10 – gas valves; 11 – compressor.

For excluding the initial stabilization section, the first pressure tap is installed at a distance of 90 mm from the laminarizer's entrance. Comparators designed for different ranges of measured flow rates differ in width (from 20 to 120 mm) and in the number of slot channels (from 3 to 51).

SN calibration on the developed comparing method is carried out as follows. At first, the volume flow rate ( $m^3/h$ ) of the calibratable nozzle is estimated using the approximate formula  $Q_n = 0,55 \cdot d_n^2$  (where  $d_n$  is the diameter of the nozzle throat, mm). Then a comparator and two RSN with lower and higher flow rate (which differ from the value  $Q_n$  within 10%) should be selected.

Hereafter, the gas is pumped sequentially through the comparator and the calibratable nozzle, and the differential pressure  $\Delta p$  on the comparator is recorded in the first calibration stage. On the second and third stages, respectively, the pressure drops  $\Delta p_1$  and  $\Delta p_2$  are fixed at the comparator when the gas passes alternately through the first and second RSN with known nominal flow rates  $Q_1$  and  $Q_2$ , reduced to standard conditions. The volume gas flow rate of calibratable nozzle under standard conditions is determined by the formula:

$$Q = \Delta p \left[ \frac{Q_1}{\Delta p_1} + \frac{\Delta p - \Delta p_1}{\Delta p_2 - \Delta p_1} \left( \frac{Q_2}{\Delta p_2} - \frac{Q_1}{\Delta p_1} \right) \right]. \quad (1)$$

According to the results of the experiments, it was found that a simpler equation could be used instead of equation (1):

$$Q = Q_1 + (Q_2 - Q_1) \frac{\Delta p - \Delta p_1}{\Delta p_2 - \Delta p_1}. \quad (2)$$

The patent was received on the presented method and device in the form of a laminariser for SN calibration [4].

At implementing the developed method for SN calibration in the improved State Primary Standard GET 118-2017, the Yokogawa differential pressure sensors with a reduced error of  $\pm 0.04\%$  were used to measure the pressure drop at the comparator. This allows to calibrate the SN with an expanded uncertainty  $U$  (at coverage factor  $k=2$ ) not exceeding 0.1%.

### 3. The content of improved State Primary Standard GET 118-2017 of Volume and Mass Gas Flow Rate Units

To improve the GET 118 several important activities were carried out at the VNIIR.

First, as an initial test rig TR-1 for reproducing and transfer volume gas (air) flow rate units from 0.4 to 100  $m^3/h$  at atmospheric pressure the high-precision bell prover was used instead of morally and physically outdated gravimetric test rig.

Secondly, to expand the range of reproducible gas flow rate in the region of large values (up to 16000  $m^3/h$ ) at atmospheric pressure the test rig TR-2 with a SN-set was introduced into the GET 118.

Thirdly, highly-productive test rig TR-3 including a SN-set was created with reproducible gas flow rate from 1 to 64  $m^3/h$  at atmospheric pressure.

Fourthly, the test rig TR-4 with a SN-set and a reference gas meter was introduced into the GET 118 to transfer the gas flow rate units from 10 to 2300  $m^3/h$  at gage pressure up to 1 MPa.

Fifth, for reproduction gas flow rate units in ultra-low range (from  $3 \cdot 10^{-4}$  to 3  $m^3/h$ ) at atmospheric pressure a piston prover (test rig TR-5) was used.

Thus, the improved GET 118-2017 is a complex of five test rigs that are interconnected by means of the reference sonic nozzles, which received the unit of measure on the initial test rig TR-1 (Figure 2). In addition, due to the limited gas flow rate range of the TR-1, the ECS of a larger flow rate (up to 410  $m^3/h$ ) is also being calibrated at the TR-2 in several stages with an increase the flow rate using as reference standards not individual RSN, but sets of parallel-mounted reference nozzles (by the "bootstrapping" procedure). The nozzles calibrated in this way are subsequently used in the composition of both the TR-2 itself and the TR-4.

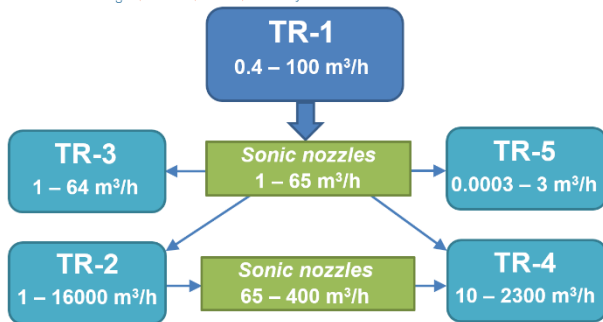


**Figure 2:** Diagram of the transfer of gas flow rate units in the GET 118-2017.

The RSN-sets are part of the test rigs TR-2, TR-3, TR-4, and also are used to calibrate the reference flow meter of test rig TR-4 and measurement cells of piston prover TR-5.

#### 4. Description of the test rigs included in the GET 118-2017

##### 4.1 Initial test rig TR-1

The initial test rig TR-1 based on a bell prover is designed to reproduce and transfer units of volume and mass flow rates, as well as to calibrate RSN and reference gas flow meters used in other test rigs of GET 118-2017 (Figure 3). It was developed and produced in collaboration with the German National Metrology Institute PTB. The created test rig is analogous to the Primary Standard of Germany [5].



**Figure 3:** Photograph of initial test rig TR-1: 1 – bell (in the highest position), 2 - oil tank, 3 - cabinet of the climate precision system, 4 - test bench, 5 - cabinet of the automated control system.

The operating principle of bell prover is based on the displacement of a certain gas volume from under the bell at its lowering into the sealing liquid.

The expanded uncertainty  $U$  of gas flow rate reproduction at the TR-1 is not more than 0.06% in the flow range from 1 to 65 m<sup>3</sup>/h and not more than 0.1% in the flow ranges from 0.4 to 1 m<sup>3</sup>/h and from 65 to 100 m<sup>3</sup>/h

To maintain the specified constant values of temperature and humidity a climate-controlled climate system based on the Clima Processor CA S01 conditioner was used.

##### 4.2 Test rig TR-2

The automated test rig TR-2 with a SN-sets includes two modules:

- module 1 designed to transfer the gas flow rate units to working standards and working measuring instruments based on positive displacement gas flowmeters in the range of volumetric flow rate from 10 to 16000 m<sup>3</sup>/h;
- module 2 designed to transfer the gas flow rate units to working standards and working measuring instruments based on sonic nozzles and positive displacement gas flowmeter in the range of volumetric flow rates from 1 to 1600 m<sup>3</sup>/h.

Gas is pumped on the suction line by means of three air blowers.

The transfer of the gas flow rate units in module 1 is carried out by comparing the mass air flow through sequentially placed calibratable gas flow meter and measuring system, which includes 45 parallelly installed RSN of various typical sizes.

The operating principle of module 2 is based on a comparison of gas flow rate through a reference nozzle (or RSN set) and a calibratable nozzle by means of the developed comparing method using laminarizers. The module contains 13 various RSN.

With the inclusion of various combinations of RSN in modules 1 and 2, the change in air flow rate is ensured. Each RSN is connected and disconnected by means of pneumatic actuated valves.

According to the research results, the test rig TR-2 ensures the reproduction of volume and mass gas flow rate units with an expanded uncertainty of no more than 0.1%.

##### 4.3 Test rig TR-3

The automated test rig TR-3 with a RSN-set is designed to transfer the volume and mass flow rate units to working standards and measuring instruments by means of direct comparison method, as well as to calibrate sonic nozzles by means of

comparing method using laminarizers. A photograph of the EU-3 reference module is shown in Figure 4.

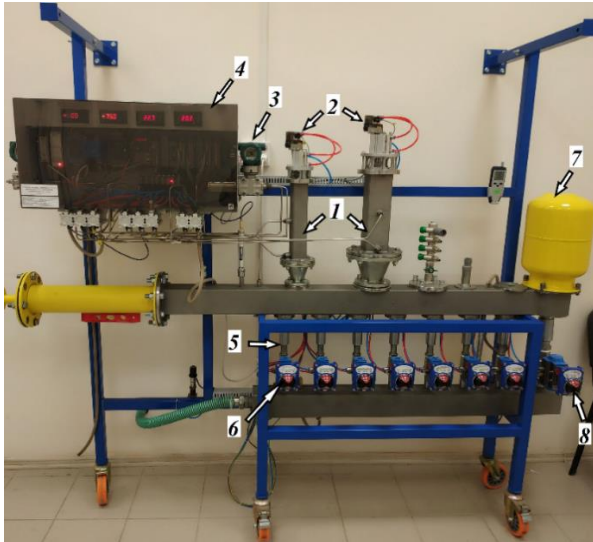


**Figure 4:** Photograph of test rig TR-3: 1 – laminarizer (comparator); 2 – inlet pneumatic valve; 3 – pressure differential sensor; 4 – control unit; 5 – set of parallel mounted RSN; 6 – pneumatic cranes of RSN; 7 – receiver with calibratable nozzle inside; 8 – pneumatic crane of calibratable nozzle.

The air flow in TR-3 is provided by gas rarefaction created by the vacuum pump in the receiver. Through various combinations of open RSN, the air flow rate is varied in the range from 1 to 64 m<sup>3</sup>/h.

The test rig TR-3 consists of an inlet and outlet manifolds, between which a receiver with a calibratable nozzle and seven reference nozzles with electric motorized ball valves are installed. Two comparators (with flow ranges of 1–10 m<sup>3</sup>/h and 8–64 m<sup>3</sup>/h, respectively) are located on the inlet manifold. Comparators are included in the operation by means of full-way electric ball valves.

According to the research results, the test rig TR-3 ensures the reproduction of volume and mass gas flow rate units with an expanded uncertainty not exceeding 0.09%.

#### 4.4 Test rig TR-4 at gage pressure up to 1.0 MPa

Reproduction of gas volume and mass flow units in TR-4 is based on a direct comparison of the air flow rate through sequentially installed meter under test and reference flow transducers (RSN-set or reference flow meter).

The flow generator is a compressor that provides a volumetric flow rate of up to 2300 m<sup>3</sup>/h (under standard conditions) and gage pressure up to 1.0

MPa. Using a system of ball valves and valves, the air flow from the compressor to the point of release into the atmosphere can be carried out either sequentially through a reference meter and meter under test or sequentially through a meter under test and RSN-set.

A rotary gas meter IRM-A-DUO with a measured flow rate of up to 400 m<sup>3</sup>/h is used as a reference flow meter (reference standard).

The RSN-set consists of inlet and outlet collectors, between which there are five various reference nozzles (with a gas flow rate from 10 to 400 m<sup>3</sup>/h), calibrated in test rigs TR-1 and TR-2.

According to the research results, the test rig TR-4 ensures the reproduction of volume and mass gas flow rate units with an expanded uncertainty not exceeding 0.11%.

#### 4.5 Test rig TR-5

The automated piston type test rig TR-5 consists of two measuring cells (Figure 5): SL-800-10 (Q=0.0003...0.03 m<sup>3</sup>/h) and SL-800-44 (Q=0.03...3 m<sup>3</sup>/h).



**Figure 5:** Photograph of test rig TR-5.

The method of reproducing the flow rate is based on the displacement of a certain volume of gas when the piston moves inside a tube during the measured time interval. The distance traveled by the piston is determined by means of photodiodes mounted on the initial and final marks. The piston is made of graphite composite having a low coefficient of friction and resistant to wear. The tube inside which the piston moves is made of borosilicate glass having a low coefficient of thermal expansion.

According to the research results, the test rig TR-5 ensures the reproduction of volume and mass gas flow rate units with an expanded uncertainty of no more than 0.1%.

## 5. Conclusion

As a result of the improvement of the GET 118, the following was achieved:

- the expanded uncertainty of reproduction of volume and mass flow rate units of gas (air) at the initial test rig in the flow range from 1 to 65 m<sup>3</sup>/h was reduced from 0.08% to 0.06%, and in general an expanded uncertainty of reproduction of volume and mass gas flow rate units in GET 118-2017 is from 0.06 to 0.11%;
- the range of reproducible gas flow rate was significantly expanded, and now it is from 0.0003 to 16000 m<sup>3</sup>/h);
- the upper value of the gage pressure of gas (air) was increased to 1 MPa in the range of gas flow rate from 10 to 2300 m<sup>3</sup>/h;
- the application of the developed comparing method using laminarizers allowed: 1) to calibrate SN with gas flow values much higher than the maximum value of the reproduction range of the initial test rig TR-1 of bell type, 2) to reduce the load and wear of the expensive initial test rig TR-1, 3) to significantly increase the productivity of calibration works.

The general metrological characteristics of State Primary Standard GET 118-2017 of Volume and Mass Gas Flow Rate Units are shown in Table 1.

**Table 1:** Metrological characteristics of GET 118-2017.

Test rig	Parameter		
	Q, m <sup>3</sup> /h	p, kPa	U, %
TR-1	1 – 65	96 – 104	0,06
	0,4 – 1		0,10
	65 – 100		0,10
TR-2	1 – 16000	96 – 104	0,10
TR-3	1 – 64	96 – 104	0,09
TR-4	10 – 2300	to 1100	0,11
TR-5	0,0003 – 3	96 – 104	0,10

In 2018, according to Euramet project No. 1396 the international comparison of the GET 118-2017 with similar national standards of Germany (PTB) and the Czech Republic (CMI) in the range from 1 to 250 m<sup>3</sup>/h was made using reference standards based on sonic nozzles [6]. Positive results were obtained: the stated metrological characteristics of the bell

prover TR-1 were confirmed over the entire flow range. Thus, the GET 118-2017 on the scientific and technical level corresponds to the modern world achievements and is not inferior in characteristics to the best foreign analogues.

Currently, GET 118-2017 participates in international comparisons of COOMET project No. 680/RU/16 in the range of gas flow rate from 20 to 6500 m<sup>3</sup>/h using reference standards based on turbine and rotary gas meters.

## References

- [1] Fishman I I, Rainchik S V, Krasavin V M, Semenova O K, “National Primary Standard of Volumetric and Mass Gas Flow GET 118-06. International Comparisons of National Standards”, *Telemechanization and Communication in Oil Industry*, **Vol. 1**, pp.17-19, 2011 (in Russian).
- [2] Li Ch, Mickan B, Isaev I, “The comparison of low pressure gas flowrate among NIM, PTB and VNIIR”, in *17th International Flow Measurement Conference, FLOMEKO 2016*, Sydney (Australia), 4 p., 2016.
- [3] Gerasimov A P, Krasavin A V, “Calibration of Critical Nozzles on Standards of the Units of the Rate of Flow of a Gas”, *Measurement Techniques*, **Vol. 56 (10)**, pp.1146-1149, 2014.
- [4] Gorchev A I, Mingaleev A V, Bykov I A, Kratirov D V, Mikheev N I, “Method for critical nozzles calibration and device for critical nozzles calibration”, Patent RU 2654934, 2018 (in Russian).
- [5] Mickan B, Kramer R, “Evaluation of two new volumetric primary standards for gas volume established by PTB”, in *7th International Symposium on Fluid Flow Measurement*, Anchorage (USA), 13 p., 2009.
- [6] Valenta T, Mickan B, “Inter-comparison in the gas flow range from 1 m<sup>3</sup>/h to 250 m<sup>3</sup>/h with sonic nozzles”, Euramet Project No. 1396, Final Report – Draft B, 32 p., 2018.

# Calculation of the flow-rate measurement uncertainty by means of Pitot tubes using the Monte Carlo Method

L. L. Martins<sup>1</sup>, A. S. Ribeiro<sup>1</sup>, J. Alves e Sousa<sup>2</sup>

<sup>1</sup>LNEC – National Laboratory for Civil Engineering, Avenida do Brasil, 101, 1700-066, Lisbon, Portugal

<sup>2</sup>IPQ – Portuguese Institute for Quality, Rua António Gião 2, 2829-513 Caparica, Portugal

E-mail (corresponding author): lfmartins@lnec.pt

---

## Abstract

This paper is dedicated to the flow-rate measurement uncertainty calculation, considering the use of Pitot tubes inside closed conduits as the applied measurement method, according to the guidelines and procedures established by the current ISO 3966 standard. The performed study aims the comparison between measurement uncertainties obtained by the conventional error approach mentioned in the method's standard and the results obtained from the application of the Monte Carlo Method (MCM). Using the same input data, a difference of 0,3% was obtained between the 95% relative expanded measurement uncertainties. The obtained probability density function of the compressibility correction factor showed a non-Gaussian asymmetric shape, however, not affecting the remaining quantities in the uncertainty propagation chain. The Pitot tube's calibration factor and the turbulence and high frequency fluctuations were identified as the main uncertainty contributions for the combined measurement uncertainties.

---

## 1. Introduction

Pitot tubes are frequently used in several scientific, technical and industrial areas, aiming the measurement of fluid flow, for example, in closed conduits. The normative framework of this measurement method is currently established in ISO 3966 [1], which addresses all the main topics related to the design and maintenance of Pitot static tubes, and describes the calculation procedures of local velocities from measured differential pressures and of the flow-rate by velocity integration.

In particular, this international standard describes a conventional approach based on the error evaluation method, in order to assess the accuracy of the volume flow-rate measurement, providing a detailed formulation of error sources related to the local velocity measurement and flow-rate calculation, being given an example of estimation of the overall uncertainty in its Annex G.

The main motivation of this study is to review and update the procedure used to evaluate the measurement accuracy in flow-rate measurements using Pitot tubes, considering the international documents published after ISO 3966:2008,

namely, the latest edition of VIM [2] and GUM Supplements [3-5], widely accepted for complex and nonlinear models such as those required to the studies in this field of knowledge.

The paper is focused on the application of the Monte Carlo Method (MCM) as the proper approach to estimate the measurement uncertainty, due to the non-linearity and complexity of the mathematical models needed to describe the measurand and procedures involved in the velocity computation, integration and corrections.

The performed numerical simulations by MCM are based on a robust pseudo-random number generator and validated computational routines are used for determining the measurement uncertainties and its computational accuracy levels, following the main guidelines of the GUM Supplement 1 [4]. As result, the estimates are obtained within related measurement uncertainties and probability distribution functions, allowing to find the main individual contributions for the output dispersion of local velocity and flow-rate. The use of the input information shown in Annex G of [1] in the simulations, will allow a robust comparison with the results obtained using the conventional error approach.

Section 2 summarizes the mathematical models applied in calculation of the local and discharge velocities and flow-rate quantities. In Section 3, the measurement uncertainty evaluation is described, namely, the probabilistic formulation of input quantities, the uncertainty propagation stages and details about the MCM numerical simulation. The obtained results are shown in Section 4, while in Section 5, conclusions are drawn about the suitability of the MCM approach for the calculation of velocity and flow-rate measurement uncertainty and giving a contribution to be considered in future revision of ISO 3966:2008 [1], namely, of its metrological contents.

## 2. Velocity and flow-rate measurements by means of Pitot tubes

### 2.1 Introduction

Pitot tubes are key elements in the measurement of flow (more extensively used gases, rather than in liquids) in closed conduits, being one of the so-called point velocity methods such as those supported by hot-wire and hot-film anemometers, vane anemometers, current meters and laser velocimetry [6]. In this method, several local velocity determinations (sub-section 2.2) are taken across a known cross-section,  $A$ , of the fluid stream, which are then spatially integrated in order to know the discharge velocity,  $U$ , (sub-section 2.3). The product of these two quantities allows the indirect measurement of the volumetric flow-rate  $q_V$ . The additional multiplication by the fluid density,  $\rho$ , allows knowing the mass flow-rate,  $q_m$ .

### 2.2 Local velocity

The application of the Bernoulli's principle to the case of a Pitot static tube, allows to express the local fluid velocity,  $v$ , at a certain point inside a closed conduit, by

$$v = \alpha \cdot \sqrt{\frac{2 \cdot \Delta p}{\rho}}, \quad (1)$$

where  $\alpha$  is the calibration factor of the Pitot tube and  $\Delta p$  is the differential pressure between the total and static pressures. The estimate of the calibration factor is equal to one for standard measurement conditions and Pitot tubes [6], and velocities above  $5 \text{ m}\cdot\text{s}^{-1}$ . Differential pressure is usually measured using a micromanometer connected to the Pitot tube. This measurement is slightly overestimated and can be corrected for head loss,  $\xi$ , due to the distance between the static (located downstream) and the total pressure tapings. Its estimate is generally negligible, being FLOMEKO 2019, Lisbon, Portugal

equal to the friction head loss in the conduit over the above mentioned distance [1].

The density of a compressible fluid is determined by

$$\rho = \frac{p \cdot M}{Z \cdot R_g \cdot T}, \quad (2)$$

where  $p$  is the local static pressure,  $R_g$ , is the molar constant of gas,  $M$  is the molar mass of the fluid,  $Z$  is the gas law deviation factor and  $T$  is the local static temperature.

In the case of compressible fluids such as air, namely for velocities above  $60 \text{ m}\cdot\text{s}^{-1}$  [6], expression (1) must include an additional compressibility correction factor,  $(1 - \varepsilon)$ , originating the following expression

$$v = \alpha \cdot (1 - \varepsilon) \cdot \sqrt{\frac{2 \cdot \Delta p}{\rho}}. \quad (3)$$

According to [1] and considering low Mach numbers, the compressibility correction factor,  $(1 - \varepsilon)$ , is almost equal to

$$(1 - \varepsilon) \approx \left[ 1 - \frac{1}{2\gamma} \cdot \frac{\Delta p}{p} + \frac{\gamma-1}{6\gamma^2} \left( \frac{\Delta p}{p} \right)^2 \right]^{\frac{1}{2}}, \quad (4)$$

where  $\gamma$  is the ratio of specific heat capacities, usually varying between 1,1 and 1,7.

### 2.3 Discharge velocity

The discharge velocity,  $U$ , is mathematically defined by the spatial integration of the fluid velocity in the conduit's circular or rectangular measuring cross-section. For this purpose, several standard methods are available [1], being briefly described in Table 1.

**Table 1: Methods for the discharge velocity determination.**

<b>Graphical integration</b>	A graphical representation of the velocity profile is performed in order to determine the area under the curve which is bounded by the measuring points closest to the conduit wall. The velocity profile in the peripheral zone is assumed to satisfy a power law and is taken into account. No specific location for the measuring points is defined.
<b>Numerical integration</b>	Similar to the previous method with the exception of the velocity profile which is defined by an algebraic curve and integration is performed analytically.
<b>Arithmetical methods</b>	The velocity distribution assumes a particular law and the discharge velocity is given by a linear combination of individual velocities measured at specific locations.

### 3. Measurement uncertainty evaluation

#### 3.1 Input probabilistic formulation and uncertainty propagation stages

In the flow-rate measurement uncertainty evaluation, four propagation stages are defined: (i) the fluid density; (ii) the local fluid velocity; (iii) the volumetric flow-rate; (iv) the mass flow-rate.

Table 2 presents the probabilistic formulation of the uncertainty components related to the input quantities, based on the standard information [1, 9] and experimental knowledge about the performed measurements.

**Table 2:** Uncertainty components related to input quantities.

Uncertainty component	Uncertainty source	PDF*	Standard uncertainty
$u(p)$	Local static pressure	Gaussian	100 Pa
$u(M)$	Molar mass of the fluid	Gaussian	$2,3 \cdot 10^{-6}$ kg·mol <sup>-1</sup>
$u(Z)$	Gas deviation factor	Uniform	0,000 5/ $\sqrt{3}$
$u(R_g)$	Molar constant of gas	Gaussian	$4,8 \cdot 10^{-6}$ J·mol <sup>-1</sup> ·K <sup>-1</sup>
$u(T)$	Local static temperature	Gaussian	0,1 K
$u(\Delta p)_{\text{inst}}$	Instrumental uncertainty	Gaussian	0,4%
$u(\Delta p)_{\text{head}}$	Correction for head loss	Gaussian	0,2%
$u(\alpha)$	Calibration factor of the Pitot tube	Gaussian	0,2%
$u(\gamma)$	Ratio of specific heat capacities	Uniform	0,3/ $\sqrt{3}$
$u(A)$	Cross-section area	Gaussian	0,2%

\*PDF – Probability Density Function.

In the case of the local velocity and volumetric flow-rate quantities, in addition to the measurement uncertainty propagated through the corresponding mathematical models, additional uncertainty components are introduced (see Table 3 for the local velocity and Table 4 for the volumetric flow-rate), based on the information shown in Annex G of [1].

**Table 3:** Additional uncertainty components related to the local velocity measurement.

Uncertainty component	Uncertainty source	PDF	Standard uncertainty
$u(v)_{\text{block}}$	Blockage effect	Gaussian	0,25%
$u(v)_{\text{high}}$	Turbulence and high frequency fluctuations	Gaussian	0,50%
$u(v)_{\text{incl}}$	Pitot tube inclination	Gaussian	0,15%
$u(v)_{\text{grad}}$	Gradient velocity	Gaussian	0,15%
$u(v)_{\text{slow}}$	Slow fluctuations	Gaussian	0,10%

**Table 4:** Additional uncertainty components related to the volumetric flow-rate measurement.

Uncertainty component	Uncertainty source	PDF	Standard uncertainty
$u(q_v)_{\text{integ}}$	Integration technique	Gaussian	0,10%
$u(q_v)_{\text{rough}}$	Roughness coefficient estimate	Gaussian	0,05%
$u(q_v)_{\text{point}}$	Insufficient number of points	Gaussian	0,10%
$u(q_v)_{\text{posit}}$	Pitot tube positioning	Gaussian	0,05%

The results shown in Section 4 are based on typical estimates values (Table 5) of the mentioned input quantities in the flow-rate measurement by means of Pitot tubes, considering air as the fluid inside the closed conduit.

**Table 5:** Estimates related to the input quantities.

$p$	105 000 Pa	$\gamma$	1,40
$M$	$28\,963,5 \cdot 10^{-6}$ kg·mol <sup>-1</sup>	$\Delta p$	10,00 Pa
$Z$	1,000 00	$\xi$	0,00 Pa
$R_g$	$8,314\,459\,8$ J·mol <sup>-1</sup> ·K <sup>-1</sup>	$\alpha$	1,000
$T$	290,0 K	$A$	0,120 0 m <sup>2</sup>

#### 3.2 Monte Carlo Method

The computational simulation algorithm was developed in Matlab<sup>®</sup>, following the guidelines of Supplement 1 of the GUM [4] to apply the MCM. In particular, the Mersenne-Twister pseudo-random number generator [10] was used in the numerical simulations of the input quantities dispersions of values.

Validated computational routines were used for the calculation of the average, mode, 95% expanded uncertainties (absolute,  $U_{95\%}$ , and relative,  $U_r 95\%$ ) and computational accuracy,  $U_c 95\%$ , values, as well as the corresponding normalized histograms of the simulated output PDF's.

The results presented in Section 4 correspond to solutions that converge for  $10^6$  trials.

## 4. Results

#### 4.1 Air density

Air density is an input quantity, not only for the local air velocity measurement, but also for the mass flow-rate. The numerical results obtained by MCM simulations are shown in Table 6, for which a Gaussian shape PDF was obtained.

**Table 6:** Air density simulation results.

Mean / kg·m <sup>-3</sup>	Mode / kg·m <sup>-3</sup>	$U_{95\%}$ / kg·m <sup>-3</sup>	$U_r 95\%$ / %	$U_c 95\%$ / kg·m <sup>-3</sup>
1,260 4	1,260 5	0,005 1	0,4	< 0,000 03

The performed sensitivity analysis revealed the main contributions for the obtained measurement uncertainty value: (i) the local static pressure (89%); (ii) the local temperature (8%); (iii) the molar constant of gas (3%); (iv) the molar mass and the gas deviation factor, with negligible contributions.

The adoption of extreme local pressure estimates of 80 000 Pa and 120 000 Pa do not produce significant changes in the obtained air density 95% expanded (absolute) measurement uncertainties, respectively,  $(0,960\ 0 \pm 0,004\ 9)\ \text{kg}\cdot\text{m}^{-3}$  and  $(1,440\ 6 \pm 0,005\ 2)\ \text{kg}\cdot\text{m}^{-3}$ . For a local temperature estimate variation, between 273 K and 373 K, the air density 95% expanded relative measurement uncertainty maintains a constant of 0,4%.

#### 4.2 Compressibility correction factor

Based on the available input data and taking into account expression (4), the MCM simulations provided the results shown in Table 7, as well as the numerical PDF shown in Figure 1.

**Table 7:** Compressibility correction factor simulation results.

Mean	Mode	$U_{95\%}$	$U_{C\ 95\%}$
0,999 982 7	0,999 985 7	$3,6\cdot 10^{-6}$	$< 7\cdot 10^{-9}$

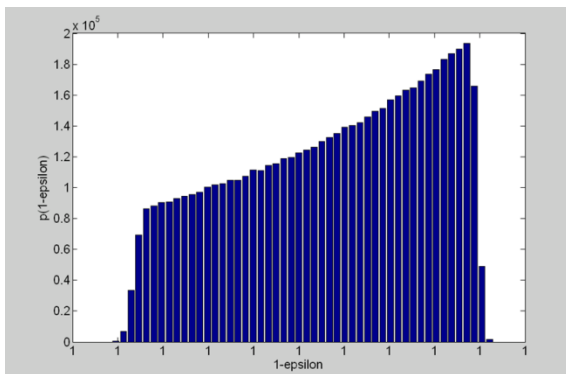


**Figure 1:** Numerical PDF of the compressibility correction factor.

The main contribution for the measurement uncertainty is related to the ratio of specific heat capacities (99,7%), which is also responsible for the obtained asymmetrical output PDF of the compressibility correction factor. This fact was confirmed by performing numerical simulations considering the specific heat capacities measurement uncertainty null, from which a Gaussian shape PDF was obtained for the compressibility correction factor. The remaining input quantities (differential and local static pressures) have reduced contributions (0,15%) for the compressibility correction factor dispersion.

#### 4.3 Local velocity

The measurement uncertainty propagation through expression (3) and the additional measurement uncertainty components shown in Table 3, allowed to obtain the local velocity results given in Table 8.

**Table 8:** Local velocity simulation results.

Mean / $\text{m}\cdot\text{s}^{-1}$	Mode / $\text{m}\cdot\text{s}^{-1}$	$U_{95\%}$ / $\text{m}\cdot\text{s}^{-1}$	$U_{F\ 95\%}$ / %	$U_{C\ 95\%}$ / $\text{m}\cdot\text{s}^{-1}$
3,983	3,978	0,069	1,7	$< 0,000\ 4$

The performed sensitivity analysis results given in Figure 2 allow to compare the weight of individual contributions to the combined measurement uncertainty.

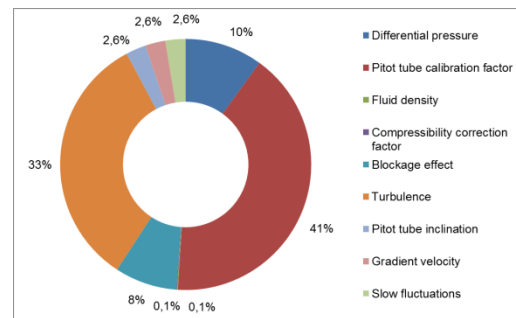


**Figure 2:** Relative weight of contributions to the local velocity combined measurement uncertainty.

Figure 2 shows two major contributions for the local velocity measurement uncertainty – the Pitot tube calibration factor (41%) and the turbulence and high frequency fluctuations uncertainty components (33%). A second group of intermediate contributions is related to the differential pressure measurement and the blockage effect uncertainty component, 10% and 8%, respectively, followed by a reduced contribution (2,6% each) concerning the Pitot tube inclination, gradient velocity, slow fluctuations uncertainty components. Both the fluid density and the compressibility correction factor have an almost null contribution (0,1% each) to the local velocity measurement uncertainty.

The numerical output PDF has a Gaussian shape, confirming the reduced influence of the compressibility correction factor (with a known asymmetric PDF – see Figure 1 – related to the specific heat capacities).

Additional simulations were performed, ranging local velocities from  $4\ \text{m}\cdot\text{s}^{-1}$  up to  $90\ \text{m}\cdot\text{s}^{-1}$ , showing a constant relative 95% expanded measurement uncertainty of 1,7%.

#### 4.4 Volumetric flow-rate

Based on the results obtained in the previous Section 4.3, concerning the local velocity measurement, and taking into account the uncertainty components mentioned in Table 4 and the measurement uncertainty assigned to the cross-section area (see Table 2), the dispersion of volumetric flow-rate was obtained by numerical simulation, being characterized by a Gaussian PDF and by the results presented in Table 9, expressed both in  $\text{m}^3 \cdot \text{s}^{-1}$  and  $\text{m}^3 \cdot \text{h}^{-1}$ .

**Table 9:** Volumetric flow-rate simulation results.

Mean / $\text{m}^3 \cdot \text{s}^{-1}$	Mode / $\text{m}^3 \cdot \text{s}^{-1}$	$U_{95\%}$ / $\text{m}^3 \cdot \text{s}^{-1}$	$U_{f, 95\%}$ /%	$U_{c, 95\%}$ / $\text{m}^3 \cdot \text{s}^{-1}$
0,478 0	0,477 9	0,008 7	1,8	< 0,000 05
Mean / $\text{m}^3 \cdot \text{h}^{-1}$	Mode / $\text{m}^3 \cdot \text{h}^{-1}$	$U_{95\%}$ / $\text{m}^3 \cdot \text{h}^{-1}$	$U_{f, 95\%}$ /%	$U_{c, 95\%}$ / $\text{m}^3 \cdot \text{h}^{-1}$
1721	1720	31	1,8	< 0,18

The major contribution for the measurement uncertainty shown in Table 9 is related to the local velocity measurement uncertainty which contributes for 91% of the obtained dispersion of values. It is followed by the cross-section area measurement (4%) and the uncertainty components of integration technique (1,5%), the Pitot tube positioning (1,5%), the number of measurement points (1,5%) and the estimation of roughness coefficient (0,5%).

The numerical simulations were extended for a volumetric flow-rate measurement interval approximately between  $0,15 \text{ m}^3 \cdot \text{s}^{-1}$  ( $544 \text{ m}^3 \cdot \text{h}^{-1}$ ) and  $1,5 \text{ m}^3 \cdot \text{s}^{-1}$  ( $5440 \text{ m}^3 \cdot \text{h}^{-1}$ ), for which a constant relative 95% relative expanded measurement uncertainty of 1,8% was obtained.

#### 4.5 Mass flow-rate

The results presented in Sections 4.1 (air density) and 4.5 (volumetric flow-rate) were used to perform the numerical simulations related to the mass flow-rate quantity. The obtained results, expressed both in  $\text{kg} \cdot \text{s}^{-1}$  and  $\text{kg} \cdot \text{h}^{-1}$ , are shown in Table 10.

**Table 10:** Mass flow-rate velocity simulation results.

Mean / $\text{kg} \cdot \text{s}^{-1}$	Mode / $\text{kg} \cdot \text{s}^{-1}$	$U_{95\%}$ / $\text{kg} \cdot \text{s}^{-1}$	$U_{f, 95\%}$ /%	$U_{c, 95\%}$ / $\text{kg} \cdot \text{s}^{-1}$
0,602	0,603	0,011	1,8	< 0,000 06
Mean / $\text{kg} \cdot \text{h}^{-1}$	Mode / $\text{kg} \cdot \text{h}^{-1}$	$U_{95\%}$ / $\text{kg} \cdot \text{h}^{-1}$	$U_{f, 95\%}$ /%	$U_{c, 95\%}$ / $\text{kg} \cdot \text{h}^{-1}$
2167	2170	40	1,8	< 0,22

The measurement uncertainty provided is given, essentially, from the dispersion of the volumetric flow-rate (99%), while the contribution of the fluid density is negligible.

Additional numerical simulations were performed, ranging mass flow-rates from  $0,2 \text{ kg} \cdot \text{s}^{-1}$  ( $720 \text{ kg} \cdot \text{h}^{-1}$ ) up to  $2,0 \text{ kg} \cdot \text{s}^{-1}$  ( $7200 \text{ kg} \cdot \text{h}^{-1}$ ), showing a constant relative 95% expanded measurement uncertainty of 1,8%.

## 5. Conclusions

The MCM allowed to evaluate the flow-rate measurement uncertainty related to the use of Pitot tubes inside closed conduits, and to consider it fit-for-purpose.

Considering the studied measurement intervals, estimates and uncertainty components and adopted assumptions, the following 95% expanded relative measurement uncertainties were obtained: (i) 1,7%, for the local velocity quantity; (ii) and 1,8%, for both the volumetric and mass flow-rates. These values are close to the ones (1,4% and 1,5%, respectively) mentioned in [1].

The reduced difference (0,3%) between the results obtained from the conventional error approach, described in [1], and the MCM approach presented in this paper, is justified by the weak non-linearity of the applied mathematical models and by the low contribution of the measurement uncertainty of quantities, such as the compressibility correction factor, which are related to non-linear models. Therefore, the conventional approach can be used as a suitable approx. solution if the noticed differences are not significant for the target measurement accuracy.

This study showed that the local velocity quantity has a significant impact in the flow-rate measurement accuracy, in particular, the measurement uncertainty of the Pitot tube calibration factor and the uncertainty component related to turbulence and high frequency fluctuations. If needed, efforts to improve the flow-rate measurement accuracy should be directed towards these two elements, noticing that the corresponding quantification presented in this study is merely illustrative [1]. In a real case scenario, the probabilistic formulation and quantification must be confirmed and updated if required.

The results achieved are considered as able to provide useful information to be taken into account in a future revision of the ISO 3966 standard Annex G, namely, as an updated example of flow-rate measurement uncertainty calculation.

## References

- [1] ISO 3966: *Measurement of fluid flow in closed conduits. Velocity area method using Pitot static tubes*, 2008.
- [2] JCGM 200: *International Vocabulary of Metrology (VIM) – Basic and general concepts and associated terms*, 2008.
- [3] JCGM 100: *Evaluation of measurement data – Guide to the expression of Uncertainty in Measurement*, 2008.
- [4] JCGM 101: *Evaluation of measurement data – Supplement 1 to the “Guide to the expression of Uncertainty in Measurement” – Propagation of distributions using a Monte Carlo method*, 2008.
- [5] JCGM 102: *Evaluation of measurement data – Supplement 2 to the “Guide to the expression of Uncertainty in Measurement” – Extension to any number of output quantities*, 2011.
- [6] Sydenham P H, *Handbook of Measurement Science. Volume 2. Practical Fundamentals* (John Wiley & Sons), 1983.
- [7] Ower E, Pankhurst R C, *The Measurement of Air Flow* (Oxford, Pergamon), 1977.
- [8] Sabersky R H, Acosta, A J, Hauptmann, E G, Gates, E M, *Fluid Flow* (New Jersey, Prentice Hall), 1999.
- [9] NIST, CODATA Internationally recommended 2018 values of the Fundamental Physical Constants,  
<https://physics.nist.gov/cuu/Constants>
- [10] Matsumoto M, Nishimura T, “Mersenne twister: a 623-dimensionally equidistributed uniform pseudo-random number generator”, *ACM Transactions on Modelling and Computer Simulation*, **8**, 3-30, 1998.

# Uncertainty evaluation of totalization of flow and volume measurements in drinking water supply networks

A. S. Ribeiro<sup>1</sup>, D. Loureiro<sup>1</sup>, M. C. Almeida<sup>1</sup>, M. G. Cox<sup>2</sup>, J. A. Sousa<sup>3</sup>, M. A. Silva<sup>1</sup>,  
L. Martins<sup>1</sup>, R. Brito<sup>1</sup>, A. C. Soares<sup>1</sup>

<sup>1</sup>LNEC – National Laboratory for Civil Engineering, Avenida do Brasil, 101, 1700-066 Lisbon, Portugal

<sup>2</sup>National Physical Laboratory, Teddington TW11 0LW, UK

<sup>3</sup>Portuguese Institute for Quality, Rua António Gião, 2, 2829-518, Caparica, Portugal

E-mail (corresponding author): [asribeiro@lnec.pt](mailto:asribeiro@lnec.pt)

---

## Abstract

Clean water and sanitation are one of the 17 sustainable development goals (SDG) of the United Nations' 2030 agenda for action, being directly related to several other objectives, namely, economic growth, sustainable cities' communities, responsible consumption and production, and climate action. Since demand for this resource is constantly growing, problems of scarcity of water and transboundary issues are becoming critical to increase water supply efficiency and to improve water management in modern society. Water providers make use of large infrastructures – water supply networks – defined as engineering systems based on hydrological and hydraulic elements able to supply water to consumers, industries, facilities, services and other users. These infrastructures rely on the quality of measurement as a condition to management, having a relevant role in the process of decision-making and to deal with the common problem of water losses. Good measurement practices and uncertainty evaluation are needed to support robust analysis in urban water supply systems. For many water utilities the evaluation of uncertainty is still considered a difficult task, often in situations of missing data for the analysis, having to deal with large amounts of raw and processed data, and requiring support to apply the provisions of the Guide to the expression of uncertainty in measurement (GUM). However, the application of the GUM to the simple mathematical models used in this context makes it possible to obtain simplified equations that can be used in specific conditions of measurement, providing support to non-expert users with more straightforward approaches. Those include measurement of constant flow, totalization of volume at a single measurement point, and sums and differences obtained by combining branches of a network.

---

## 1. Introduction

Clean water and sanitation are one of the 17 sustainable development goals (SDG) of the United Nations' 2030 agenda [1], being directly related to several other objectives, namely, economic growth, sustainable cities and communities, responsible consumption and production, and climate action. Since demand for water is continuously growing, the risk of scarcity of water together with non-sustainable water supply and transboundary issues are becoming critical, requiring the increase of water supply efficiency and the improvement of water management in our society [2].

Water utilities make use of extensive infrastructures – water supply networks – defined as engineering systems based on hydrological and hydraulic elements allowing the supply of water to

households, industries, facilities, services and other users.

Sustainable management of these infrastructures depends on the use of equipment able to measure many quantities (flow, volume, level, velocity, pressure, temperature, water quality parameters, among others). Measurements are also required to evaluate compliance with conditions established by regulations, technical specifications as well as management requirements of service and trade, becoming a relevant part of governance and of the global economy.

Management decisions are increasingly supported by information provided by measurement [3]. The lack of knowledge regarding measurement data reliability and associated uncertainty is a key issue for the management of water supply networks.

Good measurement practices and uncertainty evaluation are needed to support robust analysis in urban water supply systems, considering its complex distribution structures and the impact of hidden water losses [4-7]. Therefore, a strong motivation for this study is the assumption that the improvement of the quality of measurement will increase confidence in the results, required to support fair trade relations between service providers, clients and consumers.

The common approach in these trade relations is to measure flow or volume of water as the output quantity (e.g., measurement of flow during a time interval, knowing the cross-sectional area of a conduit, allows the volume delivered during the time interval to be calculated).

In a water network, multiple measurement locations allow network flows and water demand to be obtained and defined in a way that enables the inflow and outflow of water to be calculated and the use of this information to evaluate the net balance of the system.

The measurement process includes three stages:

1. Data acquisition of measurements with a certain frequency, generating a time series;
2. Data processing, to obtain the totalized volume for the time interval considered;
3. The combination of totalized volumes for the several locations to evaluate the net balance (sums and differences) of the system.

Frequently, the goal of the process is to have a net balance between water inflow and outflow of a system or subsystem, in some cases subsequently used in trade relations. These totalized results of flow or volume should be conveyed with their associated uncertainties (usually expressed as relative uncertainties), to promote informed decision-making as well as increasing the confidence between the involved agents.

For many water utilities, the evaluation of uncertainty is considered important but still a difficult task, requiring support to apply the provisions of the guide to the expression of uncertainty in measurement (GUM) [8]. Other situations adding complexity include missing data and dealing with large amounts of raw and processed data.

The application of the GUM to simple mathematical models used in this context enables simplified equations to be obtained that can be used in specific

conditions of measurement (e.g., measurement of constant flow, totalization of volume at a single measurement point, sums and differences obtained by combining branches of a network), allowing non-expert users to be supported by more straightforward approaches.

## 2. Measurement of total volume at a single point of a network

There are many technologies and techniques to undertake the measurement of flow and volume, supported by different physical principles (e.g., mechanical, electromechanical, electromagnetic, acoustic, mass, gravimetric) [9].

Flowmeters that are used in flow systems (liquid and gas) are intended to evaluate the rate of a fluid flow (volumetric flow rate), during a time interval (since observations are a time-dependent phenomenon). This equipment is often used because it can provide higher accuracy levels, being able to give indirectly estimates of the volume. Equipment of this kind includes electromagnetic flowmeters of the following types: vortex, swirl, ultrasonic, differential pressure, compact orifice, pitot, variable area and mass Coriolis.

Another type of equipment that can be used is based on the direct measurement of volume during a time interval, usually named as water meters based on electromechanical combinations. Such equipment usually provides less accurate measurements but is practical to use in many industrial and other infrastructures having reasonable accuracy levels for many common applications. Some examples are volume totalizers, oval gear totalizers, oscillating piston totalizers, lobed impeller gas totalizers and turbine totalizers. For such equipment, the measurement output can be interpreted as the integration of the quantity being measured over time.

The definition of volumetric flow rate,  $Q$ , is the volume of fluid that passes per unit time (sometimes referred as volume velocity using the symbol  $\dot{V}$ ) and having as SI unit  $\text{m}^3/\text{s}$ . Volumetric flow rate can be obtained using equation (1), which relates the fluid flow velocity,  $v$ , and the cross sectional vector area,  $A$ , where measurement takes place:

$$Q = v \cdot A. \quad (1)$$

Considering a closed conduit with circular geometry having an internal diameter,  $D$ , and a cross section orthogonal to the velocity vector ( $\theta = 0^\circ$ ), Equation (1) becomes

$$Q = vA \cos \theta = v \frac{\pi D^2}{4}. \quad (2)$$

Theoretically, to obtain the total volume from flow rate measurement, an integration over the time interval,  $\Delta t$ , should be made, as in (3):

$$V = \int_{\Delta t} Q dt. \quad (3)$$

At the experimental level, flow rate measurement is usually obtained at constant time intervals,  $\Delta t$ , creating a discrete set of  $n$  values in a time series. Thus, Equation (3) becomes,

$$V = \sum_{i=1}^n (Q_i \Delta t). \quad (4)$$

If a direct approach is used,  $n$  values of volume of fluid,  $V_i$ , are obtained using sampling based on a constant time interval ( $\Delta t$ ), the estimate of total volume being given by

$$V = \sum_{i=1}^n V_i. \quad (5)$$

The nature of the measuring approach is often related to the water supply process. For the purpose of this study, two types of systems were considered:

- flow with random behaviour (related to users' demands); Fig. 1 typifies the consumption of water measured during a time interval, sometimes allowing to model (predictive) the system demands; and
- constant flow (controlled by the provider or by the user), as illustrated in Fig. 2, during a time interval (e.g. filling a storage tank).

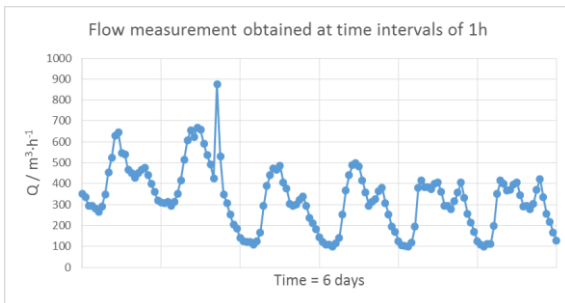


**Figure 1:** Input flow measurement experimental data obtained in a water distribution network with  $n$  users and water losses' during 6 days with time interval of sampling of 1 hour.

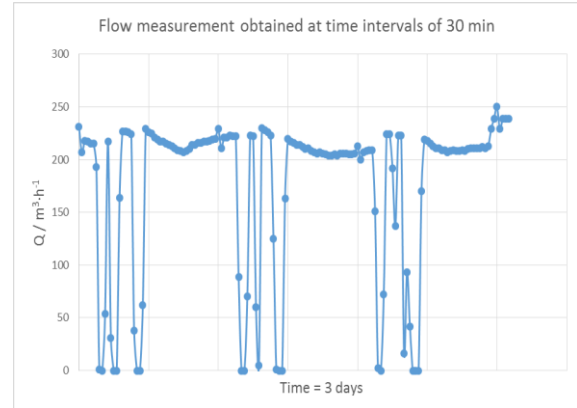


**Figure 2:** Flow measurement experimental data obtained at the entrance of a storage tank during 3 days with time interval of sampling of 30 minutes.

### 3. Total volume uncertainty at a single measurement section of a network

Equation (5) provides the functional relation used to obtain the output quantity required, the totalized volume,  $V$ , given as a sum of discrete values measured during the time of acquisition:

To obtain the standard measurement uncertainty of the totalized volume, the law of propagation of uncertainty (LPU) of the GUM [8] can be applied:

$$u^2(V) = \left(\frac{\partial V}{\partial V_1}\right)^2 \cdot u^2(V_1) + \left(\frac{\partial V}{\partial V_2}\right)^2 \cdot u^2(V_2) + \dots + \left(\frac{\partial V}{\partial V_n}\right)^2 \cdot u^2(V_n). \quad (6)$$

Considering that the partial derivatives of  $V$  with respect to the  $V_i$  are, in this case, all equal to unity, Equation (6) becomes

$$u^2(V) = u^2(V_1) + u^2(V_2) + \dots + u^2(V_n). \quad (7)$$

Flow measurement uncertainty is often known and expressed in relative form (proportional to the measured values of the quantity), being its relation with the standard uncertainty, for the case of a single measurement of volume, given by

$$w(V_i) = \frac{u(V_i)}{V_i}. \quad (8)$$

The use of Equations (7) and (8) yields an equation based on relative uncertainty contributions:

$$u^2(V) = w^2(V_1) \cdot V_1^2 + w^2(V_2) \cdot V_2^2 + \dots + w^2(V_n) \cdot V_n^2. \quad (9)$$

### 3.1 Case study of constant relative uncertainty

Measurement of flow in common cases allows to assume that the relative uncertainty is approximately constant for the measurement interval:

$$w(V_1) = w(V_2) = \dots = w(V_n) = w(V_i), \quad (10)$$

which, when applied to equation (9), gives

$$u^2(V) = w^2(V_i) \cdot [V_1^2 + V_2^2 + \dots + V_n^2]. \quad (11)$$

This expression simplifies the evaluation of the standard uncertainty of the total volume, as it requires only to know the relative standard uncertainty of the measurement of volume and the  $n$  values of this quantity. Furthermore, it facilitates the approach used to evaluate the total volume relative uncertainty, again using Equation (8):

$$w(V) = \frac{u(V)}{V}. \quad (12)$$

Consider an example with 10 measurements of volume (experimental data given in Table 1), with relative uncertainty of 2,0 %.

**Table 1:** Example of 10 measurements of volume obtained using a volumetric counter

V <sub>1</sub>	58 m <sup>3</sup>	V <sub>6</sub>	61 m <sup>3</sup>
V <sub>2</sub>	63 m <sup>3</sup>	V <sub>7</sub>	52 m <sup>3</sup>
V <sub>3</sub>	62 m <sup>3</sup>	V <sub>8</sub>	57 m <sup>3</sup>
V <sub>4</sub>	57 m <sup>3</sup>	V <sub>9</sub>	69 m <sup>3</sup>
V <sub>5</sub>	79 m <sup>3</sup>	V <sub>10</sub>	76 m <sup>3</sup>

With this information, using equations (11) and (12), the total volume standard uncertainty and relative uncertainty, respectively, would be evaluated for the total volume amount of 634 m<sup>3</sup>.

$$u(V) = \sqrt{(0,02^2) \cdot (40\ 878)} \text{ m}^3 \approx 4,0 \text{ m}^3, \quad (13)$$

$$w(V) \approx 0,64 \%. \quad (14)$$

### 3.2 Case study of constant relative uncertainty and constant flow

In some particular cases, like the filling of a storage tank, there is a constant flow during an interval of time. In this case, still considering that a constant relative uncertainty is also a condition of the system, we can assume that the relation between measurements obtained at the same interval of acquisition is

$$V_1 = V_2 = \dots = V_n = V_i. \quad (15)$$

This relation, applied to Equation (11), gives

$$u^2(V) = w^2(V_i) \cdot [n \cdot V_i^2], \quad (16)$$

from which

$$u(V) = \sqrt{n} \cdot w(V_i) \cdot V_i, \quad (17)$$

$$w(V) = \frac{\sqrt{n} \cdot w(V_i) \cdot V_i}{V}. \quad (18)$$

Equations (17) and (18) are particularly interesting to this study, because they allow the effect of the number of measurement samples ( $n$ ) in the output quantity uncertainty to be assessed, as detailed in the next section.

### 3.3 Analysis of the effect of sampling in the constant flow case study

In the design of the process applied to flow measurement, there is not a special concern with the sampling interval, since that interval is often taken according to previous practice or simply adopting the manufacturer's recommendation.

The first rationale for the definition of a sampling interval should naturally be an interval adequate to allow observations of the expected phenomenon variability. However, in special cases like that mentioned with constant flow, intuitively one could think that it had no impact in the level of accuracy of the method.

Looking to Equations (17) and (18), applicable to obtain the standard uncertainty and relative uncertainty of the total volume, respectively, it becomes clear that results depend on the number of samples,  $n$ , and on the value obtained of each observation of the volume,  $V_i$ . For a certain total volume amount fixed, when  $n$  grows, the single observation of volume decreases proportionally.

$$\hat{V}_i = \frac{V}{n}. \quad (19)$$

Using this relation in Equation (17), a simplified relation is obtained showing that the relative standard uncertainty of the total volume decreases with an increasing number of samples,  $n$ :

$$w(V) = \frac{w(V_i)}{\sqrt{n}}. \quad (20)$$

Consider a simple example, having a relative standard uncertainty of 2 %, and 10 observations each of 100 m<sup>3</sup>, or 5 observations of 200 m<sup>3</sup>, with total volume in both cases of 1 000 m<sup>3</sup>. Applying Equation (20) the results are, for the data series of 10 values,

$$w(V) = \frac{w(V_i)}{\sqrt{n}} = 0,63 \% \quad (21)$$

and, for the data series of 5 values,

$$w(V) = \frac{w(V_i)}{\sqrt{n}} = 0,89 \% \quad (22)$$

It can be concluded that sampling has a relevant role in the estimated measurement uncertainty achieved, and that it is possible to use simple and direct approaches to obtain the measurement uncertainty from the basic information provided by the acquisition data and known measurement uncertainty associated with the flowmeter.

Although it was expected that a larger number of observations would provide better knowledge about the small variations and better statistics related to the quantity measurement, the application of LPU of the GUM method also shows that the evaluation of uncertainty benefits from this practice, decreasing its value.

#### 4. Volume uncertainty related to net balance at a water supply system network

Most of water supply infrastructures are part of services provided for trade of this resource, in which it is required to make a net balance of inflow and outflow of water volume in the system and in a set period of time. The approach usually taken is based on measuring the volume at different locations and the use of sums and differences to obtain information needed in the economic process. In many cases, it also allows to identify water losses and to evaluate the efficiency of the system.

A functional relation to characterise the net balance is given by

$$V_{\text{net}} = \sum_{i=1}^n V_i - \sum_{j=1}^m \tilde{V}_j + \delta V_{\text{loss}}, \quad (23)$$

where  $V_i$  represents the  $n$  measuring locations of inflow of water into the system,  $\tilde{V}_j$  represents the  $m$  measuring locations of water outflow of water in the system, and  $\delta V_{\text{loss}}$  the water losses during the transfer process.

Applying the LPU to equation (23), noting that the partial derivatives are all equal to one, gives

$$u^2(V_{\text{net}}) = \sum_{i=1}^n u^2(V_i) + \sum_{j=1}^m u^2(\tilde{V}_j) + u^2(\delta V_{\text{loss}}). \quad (24)$$

Considering the existence of a similar uncertainty magnitude,  $u(V)$ , for the inflow and outflow measurement locations, and neglecting the contribution related to the quantity lost, a simplified equation is obtained:

$$u(V_{\text{net}}) \approx \sqrt{(n+m)} \cdot u(V), \quad (25)$$

which shows that increasing the number of locations used in the net balance will increase the measurement uncertainty of the estimated net volume.

#### 5. Conclusion

Encouraging the sustainable management of water resources is a societal imperative especially in view of the stresses over these limited resources. Adoption of the adequate strategies to increase robustness of the decision-making process supported by measurements includes the adoption of approaches to make measurements increasingly accurate and reliable, applying traceability principles, understanding the information given by uncertainty and promoting good practices.

The focus of this paper is on the evaluation and use of uncertainty for two typical processes observed in water management: measurement of water consumption and filling of storage tanks. In both cases, simple equations were obtained in order to evaluate the output measurement uncertainty associated with totalized volume, considering two stages of analysis, measuring in a single location during a time interval and making the net balance of a network system.

The second stage is particularly relevant, because it is related to a major problem that is known as "hidden losses". To perform a cause analysis able to identify the share related to measurement and with real losses, measurement uncertainty needs to be considered.

This paper also points out the relevance of an appropriate decision regarding the sampling time interval, an issue often disregarded in practice.

Finally, as expected, the number of locations used in the net balance has impact on the net measurement uncertainty, which can become relevant for large systems having multiple inflows and intermediate connections. This paper quantifies such effects.

Future work in this field includes increasing the knowledge on the impact of these conditions and effects in experimental data from different water service providers. Another topic intended to be developed is related to the influence of sampling time interval in the totalization of volume, namely, the error and uncertainty related to the assumptions of linearity usually considered.

## 6. Acknowledgements

The authors would like to acknowledge the European Metrology Programme for Innovation and Research (EMPIR) developed by EURAMET, integrated in Horizon 2020, the EU Framework Programme for Research and Innovation, for the funding of project 17NRM05 EMUE (Examples of Measurement Uncertainty Evaluation), Advancing measurement uncertainty – comprehensive examples for key international standards.

## 7. References

- [1] *Transforming our World: The 2030 Agenda for Sustainable Development. A/RES/70/1*. United Nations. Following the United Nations Sustainable Development Meeting 2015, New York, 25 – 27 Sept. 2015.
- [2] P. Reig, T. Shiao, F. Gassert, *AQUEDUCT Water Risk Framework*, World Resources Institute, Jan. 2013. Washington DC (USA).
- [3] E. Borgomeo, Climate change and water resources: risk-based approaches for decision-making, Thesis presented for the degree of Doctor of Philosophy at the University of Oxford, Christ Church College, Oxford, July 2015.
- [4] Alegre, H., Baptista, J. F., Cabrera, E., Cubillo, F., Duarte, P., Hirner, W., Parena, R. (2016) – Performance indicators for water supply services, 3rd edition, IWA Publishing, ISBN 9781780406329, London
- [5] Silva, M., Amado, C., Loureiro, D., Alegre, H. (2017). Propagation of Uncertainty in the Water Balance Calculation, Measurement, Volume 126, Pages 356-368.
- [6] Thornton, J. (2002). Water loss control manual. ISBN 0-07-137434-5, McGraw-Hill, New York.
- [7] Arregui, F., Cabrera, E., & Cobacho, R. (2006). Integrated water meter management. IWA publishing, ISBN 1843390345, London
- [8] JCGM 100:2008 (GUM 1995 with minor corrections). Evaluation of measurement data – Guide to the expression of uncertainty in measurement, Joint Committee for Guides in Metrology,
- [9] Frenzel F. *et. al.* (2011). Industrial Flow Measurements, Basics and Practice. ABB Automation Products GmbH,

# Predicting the Output Error of a Coriolis Flowmeter under Gas-Liquid Two-Phase Conditions through Analytical Modelling

J.Liu<sup>1,2</sup>, T.Wang<sup>1,2</sup>, Y.Yan<sup>1</sup>, X.Wang<sup>3</sup>

<sup>1</sup>*School of Engineering and Digital Arts, University of Kent, Canterbury, Kent CT2 7NT, U.K.*

<sup>2</sup>*KROHNE Ltd., Wellingborough NN8 6AE, U.K.*

<sup>3</sup>*School of Mathematics, Statistics and Actuarial Science, University of Kent, Canterbury, Kent CT2 7FS, U.K.*  
*E-mail (corresponding author): Y.Yan@kent.ac.uk*

---

## Abstract

Coriolis flowmeters are recognised to give excellent performance of the mass flow measurement and independent density measurement of single-phase flow. However, the large measurement error of a Coriolis flowmeter under gas-liquid two-phase flow conditions makes it unsuitable for many industrial processes where gas-liquid two-phase flow is encountered. Although analytical models have been proposed to explain the reasons behind the large output error of a Coriolis flowmeter under two-phase conditions, none of the individual theories nor their combinations can match experimental results to within 10% difference. In particular, when the gas volume fraction (GVF) exceeds 15%, the existing analytical models are not suitable. In this paper, a semi-empirical analytical model is established by combining existing analytical models with empirical terms and coefficients. The applicable range of this new analytical model is now extended to up to 40% GVF, which also better matches the experimental results. Comparisons between the modelling predictions and the experimental results for air-water two-phase flow on a two-inch Coriolis flowmeter (KROHNE OPTIMASS 6000) are made. Comparisons indicate that 2314 out of 2457 (94.2%) modelling predictions in mass flowrate fall within 10% relative error while 2403 out of 2457 (97.8%) predictions in GVF measurements fall within 5% absolute error. The outcome of this research contributes to an analytical approach to predict output error of Coriolis flowmeters under gas-liquid two-phase flow with improved accuracy and extended GVF range.

---

## 1 Introduction

Gas-liquid two-phase flow is commonly encountered in many industrial processes due to production requirement or inevitable gas entrainment from various sources. For the purposes of reducing cost, improving safety or meeting legal requirements, accurate mass metering of liquid flowrate is important but challenging to achieve under complex two-phase flow conditions.

There are many approaches to address the challenges of gas-liquid two-phase flow [1]. Phase fraction measurement techniques (e.g. electrical impedance/capacitance tomography or absorption of an electromagnetic wave such as gamma ray, X-ray microwave, infrared etc.) and phase velocity measurements (e.g. cross-correlation, Venturi) are often combined to work out the flowrate and concentration of each phase. Also, recently developed Magnetic Resonance flowmeter can achieve 3% to 5% uncertainty in volumetric measurements of liquid phase and 8% to 10% uncertainty in volumetric measurements of gas

phase [2]. However, these multi-phase flowmeter solutions could be expensive to own and maintain and not suitable for applications where single-phase can be expected for most of the time. Coriolis flowmeters as the most accurate single-phase mass flow metering devices may be an ideal candidate to address the gas-liquid flow measurement problem owing to its direct mass flow measurement and multivariable sensing nature. Recent advances in digital converters allow a Coriolis flowmeter to maintain working status and produce repeatable erroneous outputs [3], which clearly indicate additional physical interactions between the gas-liquid flow and the fluid conveying tube. Despite extensive investigations into the performance of Coriolis flowmeters under two-phase flow conditions, neither existing analytical models nor their combinations can match the experimental results [4] especially when the GVF is larger than 15%.

In this paper, we proposed a novel semi-empirical analytical model that agrees with the experimental results to within a relative error of  $\pm 10\%$  for mass flowrate and an absolute error of  $\pm 5\%$  for GVF measurements. After

investigating the behaviours of a two-inch bent-twin-tube Coriolis flowmeter under a wide range of GVF, flowrate and flow regimes [4], error terms from existing analytical models with correction factors as well as new error terms are used to predict the mass and density measurement errors of the Coriolis flowmeter.

## 2 Methodology

Firstly, the existing analytical models for decoupling and compressibility error of the Coriolis flowmeter under gas-liquid two-phase conditions are reviewed. Secondly, invalidity of the assumptions for such models under higher GVF is discussed. Thirdly, correction of existing error terms and additional error term to extend the applicability of the analytical models are described to predict the behaviours of the Coriolis flowmeter under gas-liquid two-phase flow.

### 2.1 Review of existing analytical models

There are two quantified analytical models available in the literature to describe the behaviours of the Coriolis flowmeter under gas-liquid two-phase flow, namely, decoupling error and compressibility error.

Decoupling, as a decoupling error, refers to the relative motion of gas bubbles and their surrounding liquid in the transverse direction during vibration. As it is derived in [5], the gas bubbles travel further than the surrounding liquid, resulting in a small portion of the liquid not fully coupled with the tube and therefore have less inertia sensed by the Coriolis tubes. Consequently, decoupling error leads to under-read of mass flowrate and density as shown in equations below [4]:

$$E_{d,q_m} = \frac{1-F}{1-\alpha} \alpha \quad (1)$$

$$E_{d,\rho} = -F \alpha \quad (2)$$

where E is the relative error, F is decoupling ratio between gas and liquid phases, and  $\alpha$  is cross-sectional void fraction of the pipe (in this paper we assume  $\alpha =$  GVF as the slip ratio of homogeneous gas-liquid mixture is negligible for the accuracy of the proposed analytical model). Subscription d,  $q_m$ , and  $\rho$  are decoupling error, mass flowrate, and density, respectively.

Compressibility, as its name implies, describes the deformation of the gas-liquid mixture inside the vibration tube of a Coriolis flowmeter. Although a number of formulas from different papers [6]–[9] have been used to describe the compressibility error depending on the complexity of the model, the compressibility error in its

simplest form is used in this study to the accuracy we are working at.

$$E_{C,q_m} = \frac{1}{2} \left( \frac{\omega}{c} b \right)^2 \quad (3)$$

$$E_{C,\rho} = \frac{1}{4} \left( \frac{\omega}{c} b \right)^2 \quad (4)$$

where c,  $\omega$ , and b are mixture speed of sound, tube vibration frequency and tube radius, respectively. Subscription C is compressibility error. Consequently, compressibility error leads to over-read of mass flowrate.

### 2.2 Problem in existing analytical models

Since the existing analytical models are restricted by various assumptions, they do not work at GVF larger than 15%. This GVF limit is inferred from the publications that reports the agreement between existing analytical models and experimental results up to 15% (Tables 1 and 2 from [9]). It is also confirmed from the experimental data from this work that the existing analytical model only work for GVF up to 5% (as demonstrated in Figure 1). Two main assumptions from existing analytical models are:

- No interactions among bubbles nor between bubbles and pipe wall are assumed for decoupling error model.
- The gas-liquid fluid is assumed to be a homogeneous mixture for compressibility error model.

When the number and size of bubbles increase with GVF, both assumptions are no longer valid. As a result, the decoupling ratio calculated from the analytical model will not be accurate. Similarly, when GVF increases, the gas phase will decouple from the liquid phase and therefore the mixture is no longer homogeneous. Therefore, the compressibility error from the model will not be accurate.

There are also other factors not quantified such as imbalance, asymmetry distribution of bubbles and different geometry of the fluid conveying pipe. For the most common Coriolis flowmeters which have a twin tube in structure, gas bubbles could be unevenly distributed in the tubes. Such uneven distribution results in imbalance which increase mechanical disturbances in the vibration signal. In addition, owing to the pressure drop or difference in gas distribution upstream and downstream of the same tube, mechanical disturbances can also be expected. Last but not the least, the analytical models are derived for Coriolis flowmeters with straight tubes whereas those with bent tubes are commonly used nowadays for their structural advantages (e.g. higher measurement accuracy under a wider range of temperature and more flexible resonance frequency

design). Because of all the reasons above, neither existing analytical models nor their combinations can predict the errors of Coriolis flowmeter under gas-liquid two-phase conditions to an acceptable accuracy, especially when the GVF is higher than 15%.

### 2.3 Improvements of existing analytical models

#### 2.3.1 Improvements on decoupling error prediction

According to the analytical model in [5], a decoupling ratio can be calculated based on the properties of the gas and liquid phases including densities, viscosities, bubble sizes and vibration frequency. However, this would only work when no bubble to bubble or bubble to wall interaction is assumed. When bubble to bubble or bubble to wall interaction are expected, which usually happen under higher GVF, the gas would not be able to decouple from the liquid as far as calculated. In order to account for the reduced decoupling ratio caused by the interactions, the term related to GVF is introduced to account for the bubble to bubble and bubble to wall interaction while an empirical coefficient is introduced so that the output of the model matches with experimental results. The corrected decoupling ratio  $F'$  is shown as follows:

$$F' = C_F F (1 - \alpha) \quad (5)$$

where  $C_F$  is an empirical coefficient, which has a value of 0.854, determined from the experimental results. The derivation is stated in Section 3.2.

As a result, the corrected decoupling error from Equations (1) and (2) by substituting decoupling ratio  $F'$  with  $F'$  becomes:

$$E'_{d,qm} = \frac{1-F'}{1-\alpha} \alpha \quad (6)$$

$$E'_{d,\rho} = -F' \alpha \quad (7)$$

#### 2.3.2 Adding damping term

In addition, over-reading of the Coriolis flowmeter due to compressibility or similar principle is caused by larger damping under two-phase conditions compared with single-phase flow conditions. Additionally, flowrate also affects the over-reading of the Coriolis flowmeter according to experimental results [4]. Therefore, an additional term combining damping and flowrate is added to the prediction of the output of the behaviours of the Coriolis flowmeter as shown below:

$$E_E = C_E G_D \alpha_{qm} \quad (8)$$

where  $C_E$  is an empirical constant with a value of 1.8 derived from the experimental results (Section 3.2).  $G_D$  is the normalized drive gain and  $\alpha_{qm}$  is the normalised mass flowrate of the flowmeter, respectively as shown in equations below:

$$G_D = \left( \frac{V_d}{(V_A + V_B)/2} - G_{D0} \right) \times 100\% \quad (9)$$

where  $G_{D0}$  is the drive gain of the Coriolis flowmeter measured when the fluid conveying tube is filled with water under no flow conditions.

$$\alpha_{qm} = \frac{q_m}{q_{m,n}} \times 100\% \quad (10)$$

where  $q_m$  and  $q_{m,n}$  are reference flowrates of the liquid phase and nominal flowrate of the meter under test, respectively.

#### 2.3.3 Complete Expression of the Improved Model

From the statements above, the prediction on the mass flowrate and density errors are expressed below when the properties of the liquid phase are the measurands:

$$E_{qm} = E'_{d,qm} + E_{C,qm} + E_E \quad (11)$$

$$E_\rho = E'_{d,\rho} + E_{C,\rho} \quad (12)$$

## 3 Experimental results and discussion

### 3.1 Test facility and test conditions

The experimental setup has been covered in a previously published paper [4] and therefore will not be repeated here. In summary, air-water two-phase tests were conducted on a two-inch bore rig with the Coriolis flowmeter under test (KROHNE OPTIMASS 6000 S50). The test matrix is designed in a way that the behaviours of the Coriolis flowmeter under various gas-liquid two-phase flow test conditions were recorded. The collected data is then used to derive and validate the analytical model proposed from this paper. The covered test conditions are summarised in Table 1.

Table 1: Covered test conditions

Factors	Coverage
GVF	0% to 40%
Flowrate	5000 kg/h to 35000 kg/h
Bubble size and distribution	Different length of upstream straight pipe, different gas injection points, different flow conditioners
Temperature	20 °C and 40 °C
Pressure	0.2 bar and 0.7 bar

Based on the combination of the test variation, 29 data sets with different test conditions are listed in Table 2. Three air injection points (1,2, and 4) are available either from top or bottom of the pipeline. Different flow conditioners are used, which were installed either upstream or downstream (corresponding to @4U and @4D, respectively) of the spool piece directly connected to the upstream flange of the meter under test or installed upstream (corresponding to @2U) of the spool piece directly connected to the upstream flange of the sight glass, as shown in Fig. 2 of [4]. Test temperature was controlled to be either 20 °C or 40 °C and back pressure was controlled to be either 0.2 bar or 0.7 bar.

Table 2: Test conditions

Data Sets	Injection Location	Flow conditioners	Temperature (°C)	Pressure (bar)
data01	1 bottom	Hybrid@2U	20	0.2
data02	1 bottom	Hybrid@4U	20	0.2
data03	1 top	Grid@4D	20	0.2
data04	1 top	Hybrid@2U	20	0.2
data05	1 top	Hybrid@4U	20	0.2
data06	2 bottom	Hybrid@2U	20	0.2
data07	2 bottom	Hybrid@4U	20	0.2
data08	2 top	Hybrid@2U	20	0.2
data09	2 top	Hybrid@4U	20	0.2
data10	1 top	no	20	0.2
data11	1 top	no	20	0.7
data12	1 top	no	40	0.2
data13	2 bottom	no	20	0.2
data14	2 bottom	no	20	0.7
data15	2 bottom	no	40	0.2
data16	1 bottom	no	20	0.2
data17	1 bottom	no	20	0.2
data18	2 top	no	20	0.2
data19	4 bottom	no	20	0.2
data20	1 top	no	20	0.2
data21	2 bottom	no	20	0.2
data22	1 top	no	20	0.2
data23	1 top	no	20	0.2
data24	2 bottom	no	20	0.2
data25	1 top	Swirl@2D	20	0.2
data26	2 bottom	Swirl@2D	20	0.2
data27	2 bottom	Grid@2D	20	0.2
data28	1 top	Grid@2D	20	0.2
data29	1 top	Grid@4D	20	0.2

Since there is a large number of test points in all 29 test conditions (2457 test points in total), only representative test sets are selected to demonstrate the problems in existing analytical model and to illustrate the development and validation of the analytical model. In this case, data 13 is selected as one of the datasets that best fits the analytical model while data 5 is selected as one of the few datasets that worst fits the model.

### 3.2 Comparison of experimental results with model predictions

Figure 1 shows the comparison between the experimental results and predictions using existing analytical models.

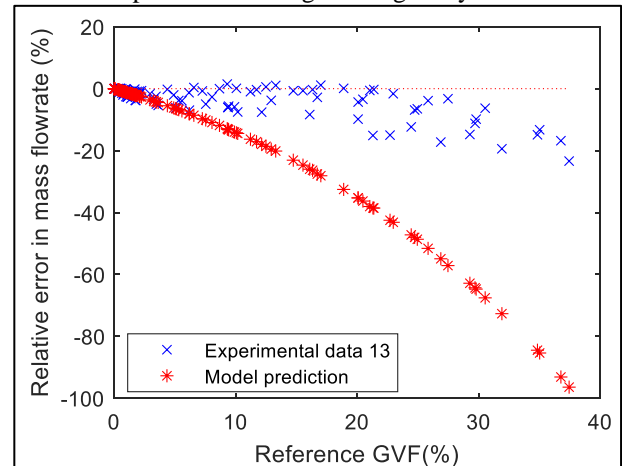
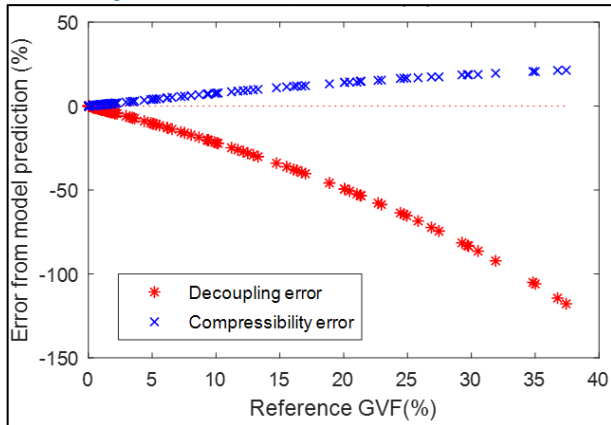


Figure 1 Comparison between model prediction and experimental results

It can be observed that the existing analytical model can predict the behaviours of the Coriolis flowmeter at very low GVF (up to 5%) and the trend is correct for the remaining GVF sections. However, the prediction error will soon become unacceptable with the increase of GVF. This error in prediction is caused by the overestimated decoupling error. For very low viscosity liquid such as water, the theoretical decoupling ratio approaches 3, which means the gas bubbles travels 3 times further than liquid in the direction of vibration. However, with the increase of GVF, bubbles start to interact with each other and the pipe wall, reducing the actual decoupling ratio. As a result, the decoupling ratio should reduce with GVF, which can be described in Equation (5). The empirical coefficient  $C_F$  is determined based on the experimental results of all 29 sets from Table 2. Output prediction using the empirical coefficient is compared with the experimental result and the coefficient that results in the lowest overall difference is found to be 0.854.

In the meantime, the scattered outputs under the same GVF is obtained when the flowrate is different. Neither existing decoupling nor compressibility model take flowrate into consideration as shown in Figure 2.



**Figure 2** Decoupling error and compressibility error terms

Since the behaviours of the Coriolis flowmeter, especially on the positive error part (as shown in Figure 1) is correlated to flowrate and damping (as shown in Figure 3) during gas-liquid two-phase flow, the error term in Equation (8) is added to the model to better predict positive error together with the compressibility error while reflect the error scatter in the experimental data. Similarly, the empirical coefficient  $C_E$  is determined through comparison with experimental results, which results in the lowest overall difference.

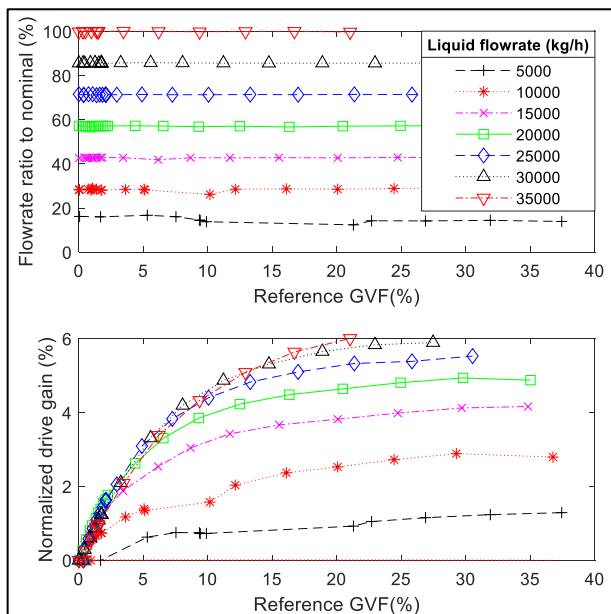


**Figure 3** Flowrate and damping plot under different flowrate

The experimental results and the prediction from the improved model are shown in Figure 4.

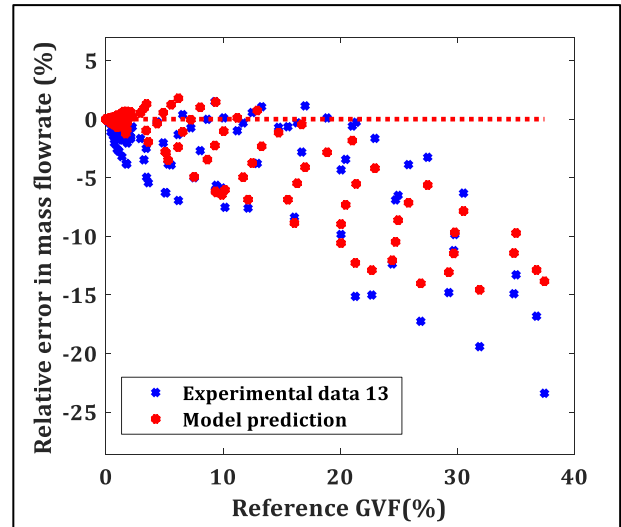


**Figure 4** Comparison between improved analytical model (data 13) and experimental results

With the empirical coefficients  $C_F$  and  $C_E$ , the experimental error can be accurately predicted. The improved physical model predicted that 2314 out of 2457 (94.2%) predictions of mass flowrate fall within 10% error while 2403 out of 2457 (97.8%) predictions of GVF measurements fall within 5% error.

Lastly, example of predictions from the improved analytical model that do not reflect experimental results is shown in Figure 5.

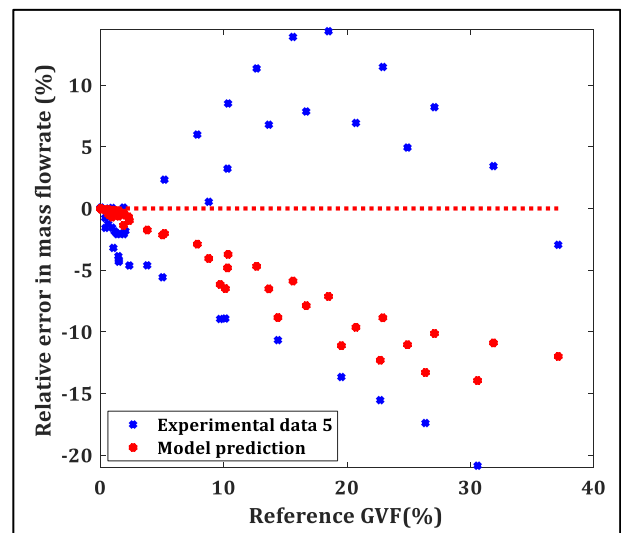


**Figure 5** Comparison between improved analytical model (data 5) and experimental results

Such poor predictions of the model occur when the flow conditioner (described in detail in [4]) is either grid mixer or hybrid mixer while installed too near (@4U and @4D) to the meter under test. In these cases, the bubbles are

assumed to be smaller since they are broken down by the flow conditioners and have no time to merge back particularly when the flowrate is high. As a result, positive error that larger than model predicted compressibility error occurred in the experiment. A solution to this problem is quite simple. Since such test conditions are deliberately created to investigate the behaviours of the Coriolis flowmeter under various test conditions, it can be simply avoided by not using flow conditioners or using sufficient straight section upstream of the Coriolis flowmeter under test. By allowing sufficient time for the gas bubble to reach equilibrium state, the improved analytical model proposed in this paper can be used to predict the output error of the Coriolis flowmeter.

#### 4 Conclusion

In this paper, an improved analytical model is presented to better predict the behaviours of the Coriolis flowmeter under air-water two-phase flow conditions. According to the comparison between the improved analytical model and experimental results, there are 2314 out of 2457 (94.2%) predictions of mass flowrate that are within 10% error while 2403 out of 2457 (97.8%) predictions of GVF measurements are within 5% error. Such performance is confirmed under a variety of test conditions and the outliers can be easily avoided by not using unusual test setups. By loosening the modelling restrictions, the applicable range of the model is also extended from maximum 15% GVF to at least 40% GVF. By utilising diagnosis signals that are already available from the Coriolis flowmeter, physical interaction inside the Coriolis flowmeter can be better described and predicted with the additional flow condition information. Furthermore, the results demonstrate the possibility of using a Coriolis flowmeter incorporating an analytical model to measure gas-liquid two-phase flow. With further GVF measurement or investigation into the correlation between GVF and mass flowrate errors, the proposed model can lead to solutions that achieve competing performance compared to the radiological measurement systems (3% to 5% uncertainty in volumetric measurements of the liquid phase in [10]) and other complex measurement systems (3% to 5% uncertainty in volumetric measurements of the liquid phase in [2]) under various test conditions. Future work will include the examination of the generalization capability of such an analytical model for Coriolis flowmeters of different size and fluids with different properties.

#### References

- [1] R. Thorn, G. A. Johansen, and B. T. Hjertaker, 'Three-phase flow measurement in the petroleum industry', *Measurement Science and Technology*, vol. 24, no. 1, p. 012003, 2013.
- [2] A. M. Bilgic, J. W. Kunze, V. Stegemann, M. Zoetewij, and J. Hogendoorn, 'Multiphase flow metering with nuclear magnetic resonance spectroscopy', in *Proceedings SENSOR 2015*, Nürnberg, Germany, 2015, pp. 292–297.
- [3] M. P. Henry *et al.*, 'A self-validating digital Coriolis mass-flow meter: an overview', *Control Engineering Practice*, vol. 8, no. 5, pp. 487–506, 2000.
- [4] J. Liu, T. Wang, Y. Yan, X. Wang, and L. Wang, 'Investigations into the behaviours of Coriolis flowmeters under air-water two-phase flow conditions on an optimized experimental platform', in *2018 IEEE International Instrumentation and Measurement Technology Conference (I2MTC)*, 2018, pp. 1551–1556.
- [5] J. A. Weinstein, D. R. Kassoy, and M. J. Bell, 'Experimental study of oscillatory motion of particles and bubbles with applications to Coriolis flow meters', *Physics of Fluids*, vol. 20, no. 10, p. 103306, 2008.
- [6] J. Hemp and J. Kutin, 'Theory of errors in Coriolis flowmeter readings due to compressibility of the fluid being metered', *Flow measurement and Instrumentation*, vol. 17, no. 6, pp. 359–369, 2006.
- [7] N. T. Basse, 'A review of the theory of Coriolis flowmeter measurement errors due to entrained particles', *Flow Measurement and Instrumentation*, vol. 37, pp. 107–118, 2014.
- [8] D. L. Gysling, 'An aeroelastic model of Coriolis mass and density meters operating on aerated mixtures', *Flow Measurement and Instrumentation*, vol. 18, no. 2, pp. 69–77, 2007.
- [9] A. Rieder, W. Drahm, and H. Zhu, 'Coriolis mass flowmeters: on measurement errors in two-phase conditions', in *Proceeding of the 13th International Flow Measurement Conference*, Peebles Hydro, Scotland, UK, 2005.
- [10] 'Roxar MPFM 2600 MVG'. [Online]. Available: <https://www.emerson.com/documents/automation/product-data-sheet-download-full-specs-roxar-en-us-170838.pdf>. [Accessed: 26-Apr-2019].

# The Discussion of Influence of the Inlet Temperature Measurement on the CFVN Calibration

Qingqiang Hou<sup>1</sup>, Meng Yang<sup>2</sup>,  
W. Han<sup>3</sup>, J. H. Niu<sup>4</sup>, K. C. Wu<sup>5</sup>

<sup>1</sup>Nanjing Branch of National Station of Petroleum & Natural Gas Flow Measurement,  
*houqingqiang@petrochina.com.cn, Nanjing, China*

<sup>2,3,4,5</sup>Nanjing Branch of National Station of Petroleum & Natural Gas Flow Measurement, Nanjing, China  
*E-mail (corresponding author): houqingqiang@petrochina.com.cn*

---

## Abstract

When the CFVN calibration is carried out, the inlet temperature measurement of the CFVN is detailed described in both “ISO 9300:2005 Measurement of gas flow by means of critical flow Venturi nozzles” and “JJG 620-2008 Critical Flow Venturi Nozzle”. But in some cases, the sensing element can not be strictly confirmed to the requirement for some reasons. To explore the influence of the inlet temperature measurement, two different kinds of installation are presented in this paper. Differences between the two installations are the diameter of the sensing element and the location of the sensing element. As the results shown, the inlet temperature measurement has non-negligible influence on the CFVN calibration. According to the comparison, to ensure the accuracy and reliability of traceability, the CFVN should be calibrated under the same installation conditions as that on site. And both the interlaboratory measurement comparison and proficiency testing of CFVN should take the installation impact as an important factor if there are some differences.

---

## 1. Introduction

The CFVN is widely used as standard of flow calibration facility for its character of good stability, with no moving part, long calibration period and so on. It is usually calibrated using the mass-time method high pressure natural gas flow primary standard facility or pVTt method facility. The installation requirements are detailed described in both ISO 9300:2005 Measurement of gas flow by means of critical flow Venturi nozzles [1] and JJG 620-2008 Critical Flow Venturi Nozzle [2]. But in some cases, the installation can not be strictly confirmed to the requirement for some reasons. To explore the influence of the inlet temperature measurement, two different kinds of installation are presented in this paper. Differences between the two installations are the diameter of the sensing element and the location of the sensing element. CFVNs at different flow rate are selected to compare the influence. And experiments are carried out using the mass-time method high pressure natural gas flow primary standard facility with natural gas as medium at different pressure.

This paper contains parts as follows: the requirements of regulations, the information of CFVN under test and the installation condition description, the results and analysis of calibration, and the conclusion.

## 2. The requirements of the regulations

According to GB/T 21188-2007/ISO 9300:2005: Measurement of gas flow by means of critical flow Venturi nozzles (ISO 9300:2005, IDT), the installation requirements of CFVN include the upstream pipeline, downstream requirements, pressure measurement, drain holes, temperature measurement, density measurement [3]. The factors of temperature measurement discussed in this paper are as follows.

### 2.1 The diameter of the sensing element

The diameter of the sensing element shall be not larger than  $0.04D$ . If the diameter of the sensing element is not less than  $0.04D$ , the sensing element shall be located at the place that the sensing element does not affect the pressure measurement.

## 2.2 The location of the sensing element

The sensing element shall not be aligned with a wall pressure tapping in the flow direction. This requirement is also proposed to make that the sensing element does not affect the pressure measurement.

## 3. The information of CFVN under test

There are two designs of standard CFVN: the toroidal-throat Venturi nozzle ( Figure 1 ) and the cylinder-throat Venturi nozzle ( Figure 2 ). [1] As the name suggests, the main difference between these two designs is that the throat of the cylinder-throat Venturi nozzle is cylinder.

CFVNs at different flow rate are selected in the experiment, and the detailed information of the CFVNs is shown in Table 1.

**Table 1:** The information of the CFVN.

CFVN No.	CFVN Type	Throat Diameter $d$ (mm)	Flow-rate ( $m^3/h$ )
A	Toroidal-throat Venturi nozzle	9.5	50
B		7.4	32
C		3.8	8

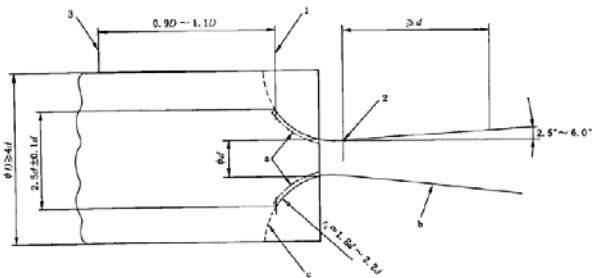


**Figure 1:** Toroidal-throat Venturi nozzle [1]

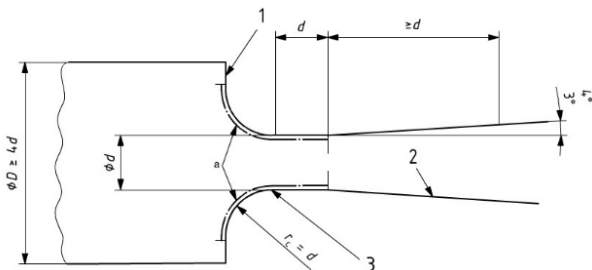


**Figure 2:** Cylindrical-throat Venturi nozzle [1]

## 4. The installation condition description

The CFVN is installed under these two conditions described in Table 2, and the sensing element location is shown in Figure 3 and Figure 4.

All the experiments are carried out using the mass-time method high pressure natural gas flow primary standard facility with natural gas as medium. The mass-time method high pressure natural gas flow primary standard facility which is used to reproduce the mass flowrate can calibrate CFVNs of natural gas at high pressure. The major components include the gyro scope, the spherical weigh tank, a pair of high speed hydraulically actuated plug valves, timer, the measuring instruments, piping components and so on. [4,5]

**Table 2:** Differences between the two installations.

Installation No.	The sensing element	
	Diameter	Location
(1)	$\leq 0.04D$	Perpendicular to the pressure measurement position
(2)	$> 0.04D$	In line with the pressure measurement position

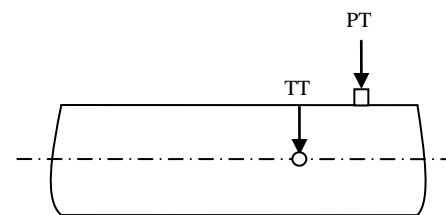


**Figure 3:** Installation No. (1).

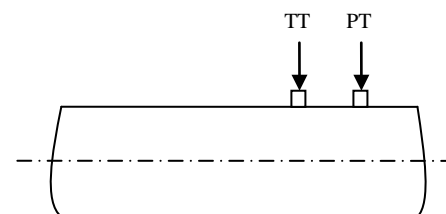


**Figure 4:** Installation No. (2).

The platinum resistance sensor of sensing element in installation No. (1) is directly installed into the pipeline, while the platinum resistance sensor of sensing element in installation No. (2) is connected to the thermowell mounted to the pipeline. So the diameter of the thermowell is more than  $0.04D$ , and the diameter of the platinum resistance sensor of sensing element in installation No. (1) is less than  $0.04D$ .

## 5. The results and analysis of calibration

The calibration results at different pressure point are compared and analysed. And the results of the CFVN calibration are shown in Table 3.

**Table 3:** The results of the CFVN calibration.

CFVN No.	Pressure (MPa)	Discharge coefficient	
		Installation No. (1)	Installation No. (2)
A	5.5	0.9945	0.9953
	5.0	0.9943	0.9953
B	5.5	0.9945	0.9952
	5.0	0.9946	0.9950
C	5.5	0.9910	0.9916
	5.0	0.9910	0.9914

As shown in Table 3, the diameter and location of the sensing element has influence on the results of CFVN calibration. Compare the discharge coefficient of each CFVN under these two conditions, the discharge coefficient of installation No. (2) is bigger than the discharge coefficient of installation No. (1).

And the deviation from the equation (10) in ISO 9300 is calculated for each installation.

$$C_d = a - bRe_{nt}^{-n} \quad (1)$$

Where,  $C_d$  stands for discharge coefficient,  $Re_{nt}$  stands for throat Reynolds number, and  $a=0.9959$ ,  $b=2.72$ ,  $n=0.5$ .

**Table 4:** The deviation from the equation (10) in ISO 9300.

CFVN No.	Pressure (MPa)	The deviation (%)	
		Installation No. (1)	Installation No. (2)
A	5.5	-0.04	0.04
	5.0	-0.06	0.04
B	5.5	-0.03	0.04
	5.0	-0.02	0.02
C	5.5	-0.34	-0.28
	5.0	-0.34	-0.30

And as shown in Table 4, the discharge coefficient of installation No.(2) is bigger than the discharge coefficient calculated from the equation (10) in ISO 9300 for CFVN No. A and B, while the discharge coefficient of installation No.(1) is smaller than the discharge coefficient calculated from the equation (10) in ISO 9300 for CFVN No. A and B. But the discharge coefficient is smaller than the discharge coefficient calculated from the equation (10) in ISO 9300 for CFVN No. C.

## 6. Conclusion

- (1) The inlet temperature measurement has non-negligible influence on the CFVN calibration.
- (2) The CFVN should be calibrated under the same installation conditions as that on site.
- (3) Both the interlaboratory measurement comparison and proficiency testing of CFVN should take the installation impact as an important factor if there are some differences.
- (4) The other two combination of diameter and location of the sensing element are not compared. More experiments should be carried out to compare the influence of the inlet temperature measurement.
- (5) Numerical simulation can be used to check the influence of sensing element in the further research.

## References

- [1] ISO 9300: *Measurement of gas flow by means of critical flow Venturi nozzles*, 2005.
- [2] JJG 620: *Critical Flow Venturi Nozzle*, 2008.
- [3] GB/T 21188-2007/ISO 9300:2005: *Measurement of gas flow by means of critical flow Venturi nozzles (ISO 9300:2005, IDT)*, 2007.
- [4] Mingchang Guo, Meng Yang, Bo Yang, Qingqiang Hou, Zhenlin Li, "The Analysis of Influence Factors and Control Measures of mass-time Method High Pressure Natural Gas Flow Primary Standard Facility", 28, 1-6, 2018.
- [5] Mingchang Guo, Bo Yang, "The Uncertainty Evaluation and Confirmation of mass-time Method High Pressure Natural Gas Flow Primary Standard Facility", 25, 57-63, 2015.

# Study on Data Collection Methods of Natural Gas Flow Verification

Chuanbo Zheng\*, Xingchuan Chen ,Yiwen Liu, Wei Han,Zhe Liu

National oil and natural gas flow metering station substation in Guangzhou, Guangzhou, China

E-mail : zhengchuanbo@petrochina.com.cn

---

## Abstract

Based on the different ways of data collection which adopted by the current domestic natural gas flow metering station, this paper first analyzes the theoretically applicability and limitations for two kinds of data collection methods: instantaneous flow and cumulative flow, and obtains the relation and distinction between these two ways. Then, the flow-meters with different diameters are actual tested in two data acquisition ways, instantaneous flow and cumulative flow, which performed by the work level standard device of substation in Guangzhou. The results show that the different methods of data collection have no evident impact on indication error but high effect on the repeatability of indication error.

---

## 1. Introduction

With the rapid development of the oil and gas industry and frequent trade in the world, China has also ushered in a period of vigorous development of this industry, a large number of natural gas pipelines have been built, and natural gas as a clean energy has been widely used in many fields. Undoubtedly, the popularization of natural gas also requires the continuous development of its metering technology. Therefore, high-pressure and large-caliber natural gas flow meters have been promoted and applied in many fields, e.g. the flow meters have been used as the settlement basis of international natural gas trade [1]. In addition, the natural gas metering is an important part of energy measurement and environmental protection, as well as an important guarantee for industrial production quality. Therefore, the accuracy of the standard device used to verify the natural gas flow meter involves the economic interests of both trading parties and is closely related to people's livelihood .

Now, for the small flow verification, multiple data collection is required to meet the requirement of repeatability due to large fluid fluctuations, which leads to low verification efficiency and fails to meet the requirements of the rapid development of domestic natural gas pipeline business for the verification of flow meters. Besides, the data collection methods of different national metrological sub-stations are different, which also need to further verify whether the collection method affects the flow meter verification result.

Therefore, this paper focuses on the influence of data collection method on the verification result of flow meters, and then explores the more effective method of data collection and processing. Finally, the accuracy and reliability of metrological verification are guaranteed while improving the verification efficiency.

## 2. Theoretical analysis

### 2.1 Instantaneous flow test

When the instantaneous flow is used for verification of the natural gas flow meter, and the sampling method is frequency collection. The instantaneous flow of the working standard flow meter ( $q$ ) and the detected flow meter ( $q_f$ ) are shown in formula (1) and (2) respectively:

$$q = \frac{f_n}{K_n} \times 3600 \quad (1)$$

$$q_f = \frac{f_f}{K_f} \times 3600 \quad (2)$$

Where  $f_f$  and  $K_f$  are the output frequency and metering coefficient of the detected flow meter, which are measured in 1/s and 1/m<sup>3</sup>, respectively;  $f_n$  and  $K_n$  are the output frequency and metering coefficient of the standard flow mete.

The standard volume flow rate ( $q_s$ ) of the detected flow meter under the operating condition is:

$$q_s = q \left( \frac{P_f}{P_n} \right) \left( \frac{T_n}{T_f} \right) \left( \frac{Z_n}{Z_f} \right) \quad (3)$$

Where  $P_f$ ,  $T_f$  and  $Z_f$  are the environment pressure, temperature and compression factor of the detected flow meter, respectively;  $P_n$ ,  $T_n$  and  $Z_n$  are the pressure, temperature and compression factor under the standard state.

The indication error ( $E_{ij}$ ) of the detected flow meter is:

$$E_{ij} = \frac{q_{ij} - (q_s)_{ij}}{(q_s)_{ij}} \times 100\% \quad (4)$$

When each flow point is repeatedly verified  $n$  times, the repeatability ( $E_r$ ) <sub>$i$</sub>  of the flow point is:

$$(E_r)_i = \left[ \frac{1}{(n-1)} \sum_{j=1}^n (E_{ij} - E_i)^2 \right]^{\frac{1}{2}} \quad (5)$$

For instance, if the system collects one frequency every 500 ms, 2t instantaneous frequency values will be acquired within a sampling period ( $t$  (s)), and the average value will be calculated to obtain the instantaneous frequency of the flow meter. The evolution of sampling frequency with collection time is shown in Figure 1.

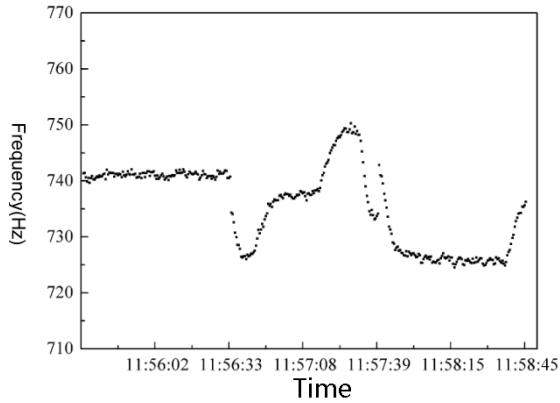


**Figure 1** Evolution of sampling frequency with collection time

## 2.2 Cumulative flow test

When using the cumulative flow to verify the natural gas flow meter, the selected sampling method is pulse acquisition. The cumulative flow of the working standard flow meter ( $Q$ ) and the detected flow meter ( $Q_f$ ) are shown in formula (5) and (6) respectively:

$$Q = \frac{N_n}{K_n} \frac{3600}{t} \quad (6)$$

$$Q_f = \frac{N_f}{K_f} \frac{3600}{t} \quad (7)$$

Where  $N_f$  and  $N_n$  are the corrected pulse counts of the detected flow meter and the standard flow meter,  $t$  is the collection time.

The standard volume flow rate ( $Q_s$ ) of the detected flow meter under the operating condition is:

$$Q_s = Q \left( \frac{P_f}{P_n} \right) \left( \frac{T_n}{T_f} \right) \left( \frac{Z_n}{Z_f} \right) \quad (8)$$

The indication error ( $E_{ij}$ ) of the detected flow meter is:

$$E_{ij} = \frac{Q_{ij} - (Q_s)_{ij}}{(Q_s)_{ij}} \times 100\% \quad (9)$$

For the cumulative flow test, the relationship between the collection time and the cumulative of pulse count is shown in Figure 2. In the whole collection process, the cumulative flow is calculated by cumulating the pulse count collected during this period.

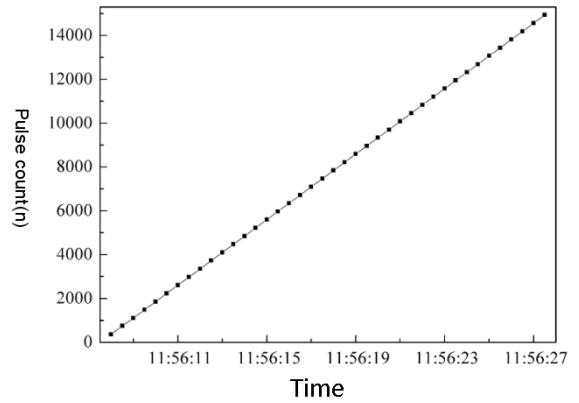


**Figure 2** Relationship between the collection time and the cumulative of pulse count

## 2.3 Comparative analysis

Due to the following relation between pulse, frequency and sampling time,

$$f = \frac{N}{t} \quad (10)$$

the instantaneous flow test and cumulative flow test have the same essence and can be derived from each other. But according to Figure 1 and 2, it can be seen that the data collected by the two methods are still different to some extent. For the cumulative flow test, its collection is the cumulative of pulse count over a period of time, which is a cumulative process and unable to collect the fluctuation of the flow state, so its anti-interference ability is poor, and it is unable to identify and eliminate abnormal data, corresponding to the lower configuration of hardware devices and low cost. On the contrary, the instantaneous flow test can obtain the fluctuation of the flow, which is convenient for timely detection and elimination of abnormal values, thus improving the effectiveness of data. However, the collection time of this method is

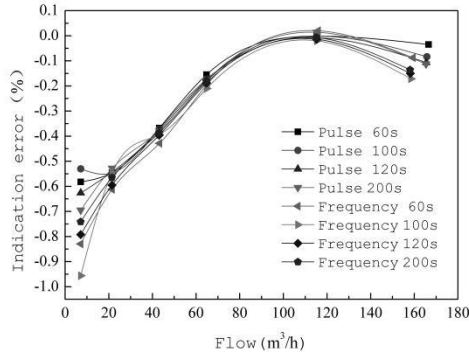
short, the requirements for hardware equipment are high, and the corresponding data processing algorithm is more complex.

### 3. Analysis of experimental results

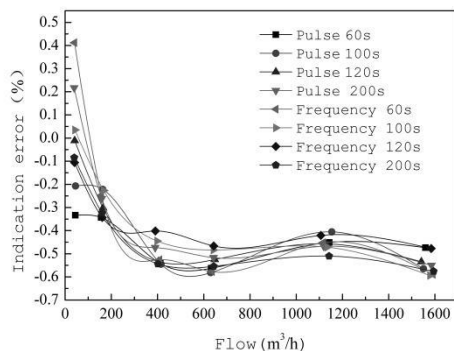
The standard turbine flow meter of National oil and natural gas flow metering station substation in Guangzhou was used to test the flow meters with different diameters by two verification methods: instantaneous flow and cumulative flow. The test flow points were  $Q_{min}$ ,  $Q_t$ ,  $0.25Q_{max}$ ,  $0.4Q_{max}$ ,  $0.7Q_{max}$  and  $Q_{max}$ , and the sampling time were 60 s, 100 s, 120 s and 200 s, respectively.

#### 3.1 Influence of collection method on verification results

In order to compare the influence of instantaneous flow collection and cumulative flow collection on verification results, the curves of operating flow and indication error under different collection methods and sampling times were compared and analyzed. The relationship between operating flow and indication error of DN80 and DN250 flow meters are shown in Figure 3 and Figure 4, respectively.



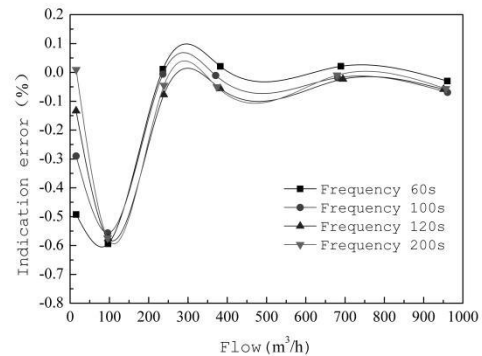
**Figure 3** Relationship between operating flow and indication error of DN80 flow meter



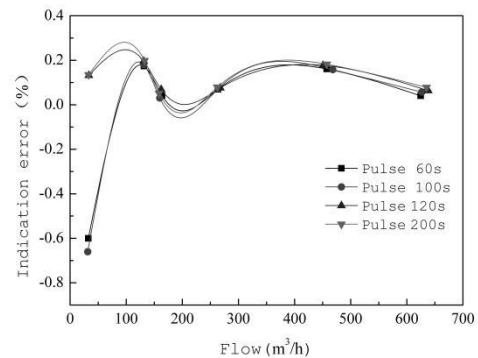
**Figure 4** Relationship between operating flow and indication error of DN250 flow meter

Based on the Figure 3 and Figure 4, under the different collection ways, the overall trend of operating flow and indication error is basically consistent, except for the small flow point. The main reason is that there are many factors affecting the indication error of the small flow point, such as the performance of the flow meter, the collection time, and the poor stability of flow. In general, it can be concluded that different collection methods have little influence on the indication error of each flow point.

#### 3.2 Influence of sampling time on verification results



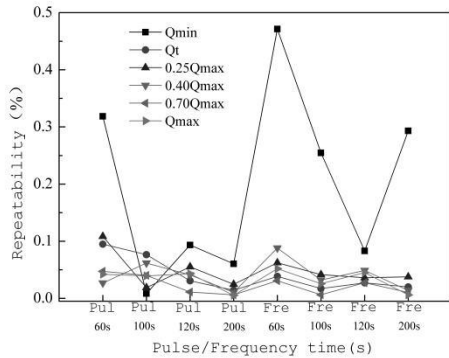
**Figure 5** Curves of the operating flow vs. indication error for the DN100 flow meter



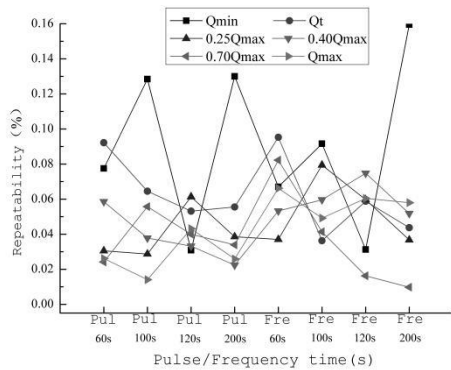
**Figure 6** Curves of the operating flow vs. indication error for the DN150 flow meter

Figure 5 and Figure 6 show the curves of the operating flow vs. indication error for the DN100 and DN150 flow meters under the same collection method and different sampling times, respectively. Under different sampling times, the difference of each flow point is mainly reflected in the small flow point, while the difference of other flow points is small. In order to display the repeatability and indication error of each flow point at different calibration stations more directly, the variation of the indication error repeatability of DN100, DN200 and DN300 flow points with pulse

or frequency are shown in Figure 7, Figure 8 and Figure 9.



**Figure 7** Indication error repeatability of each flow point for the DN100 flow meter



**Figure 8** Indication error repeatability of each flow point for the DN200 flow meter

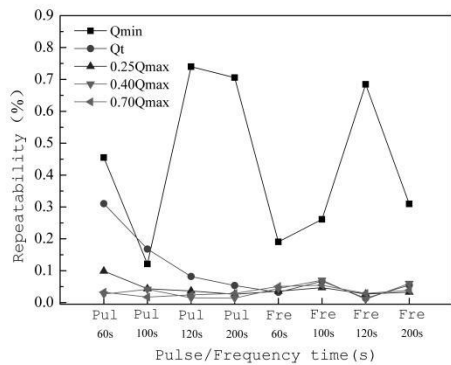


**Figure 9** Indication error repeatability of each flow point for the DN300 flow meter

As can be seen from Figure 7 to Figure 9, the sampling time has a significant influence on

repeatability, especially on small flow points. At the minimum flow point, for cumulative flow collection, the indication error repeatability is small when the sampling time is 200 s, while for instantaneous flow collection, it is 120 s. In  $Q_t$  point, the minimum indication error repeatability can be obtained at the 120 s and 200 s during the cumulative flow collection, but for the instantaneous flow collection, it can be gained is at the 100 s and 120 s. From the  $0.25Q_{max}$  to  $Q_{max}$  points, for the flow meters with small caliber calibration station, such as DN100, the sampling times corresponding to the minimum indication error repeatability are mainly at 120 s and 200 s during the cumulative flow collection, and they are at 100 s and 120 s for the instantaneous flow collection. But For the flow meters with large caliber calibration station, such as DN200 and DN300, they are mainly at 60 s and 100 s during the cumulative flow collection, and they are at 100 s and 200 s for the instantaneous flow collection.

Therefore, in order to improve the verification efficiency of the flow meter, it is necessary to select the appropriate method and sampling time according to different calibration stations.

#### 4. Conclusions

- (1) Theoretically, the instantaneous flow test and cumulative flow test have the same essence and can be derived from each other.
- (2) Experimentally, the indication error trends of the each detected flow meter verified by instantaneous flow and cumulative flow tests are basically consistent with the result of theoretical analysis.
- (3) The sampling time has a certain influence on the indication error repeatability. In order to improve the verification efficiency, it is suggested to give priority to the instantaneous flow test for the small-caliber flow meter and the cumulative flow test for the large-caliber one.

#### References

[1] Guang Zheng Jia, Jin Cai Geng, Yong Ling Fu. Development of High-Pressure Gas Test System[J].Applied Mechanics and Materials, 2013, 278-280: 873-877.

# Reproducibility of Liquid Micro-Flow Measurements

J. D. Wright and J. W. Schmidt

National Institute of Standards and Technology (NIST), 100 Bureau Drive, Gaithersburg, MD, USA 20899  
E-mail: john.wright@nist.gov

---

New applications in biology, medicine, and manufacturing require reliable measurements of liquid flows smaller than 100  $\mu\text{L}/\text{min}$ . NIST addressed this requirement by improving the reliability and ease of use of NIST's Dynamic Gravimetric Micro-Flow Standard. The meter under test is now connected to the weighing beaker by a liquid bridge that reduces variations in parasitic surface tension forces as the level of liquid in the collection beaker rises. We describe other improvements to NIST's standard (e.g. pipette positioning and evaporation reduction) and provide an uncertainty analysis for the present system. The gravimetric standard measures liquid flow between 0.1  $\mu\text{L}/\text{min}$  and 100  $\mu\text{L}/\text{min}$  with uncertainty ranging from 4.5 % to 0.04 %. Repeated calibrations of five commercially available micro-flow meters (one for nearly 2 years) show that their calibrations are reproducible within 1.5 % for many months.

## 1. Introduction

The NIST Fluid Metrology Group (FMG) builds and operates liquid flow standards that are used to calibrate flow meters and to conduct flow research. In 2014, the FMG began building a flow standard for flows of 1 mL/min and smaller [1]. The micro-flow standard uses the dynamic gravimetric flow method, *i.e.*, it periodically records the time and the mass of liquid accumulating in a beaker resting on a weigh scale (balance) and calculates the rate of change of mass with respect to time (the mass flow). This document explains the method of flow measurement in detail, gives an uncertainty analysis, and presents calibration data for five flow meters.

## 2. NIST Dynamic Gravimetric Micro-Flow Standard: Equipment and Operation

The arrangement of equipment used in NIST's Dynamic Gravimetric Micro-Flow Standard (DGMFS) is shown in Figures 1 and 2. A computer-controlled Cetoni\* Nemesys syringe pump is used as the source (or sink) of water. The system is filled with water by withdrawing the syringe while a three-way valve connects the syringe to a reservoir of pure, filtered water. Once the syringe is fully withdrawn, the three-way valve is turned so that the syringe pump pushes the water into the downstream tubing of the DGMFS, thereby pushing air out of the system. The water flows through a Systec 2.5 mL active de-bubbler. Air bubbles in the flow that reach the de-bubbler pass through a Poridex gas permeable membrane to a vacuum pump. The test section can hold several meters under test (MUTs) while recording their flow indications. Translucent plastic tubing (1.6 mm or 0.8 mm inside diameter) conducts the water between components and enables detecting air bubbles in the system. The tubing is terminated by a 0.5 mm heat-drawn glass pipette that delivers water to or from a beaker that rests on a Sartorius balance (6 g full scale, 0.1  $\mu\text{g}$ . resolution).

---

\* Certain commercial entities, equipment, or materials may be identified in this document in order to describe an experimental procedure or concept adequately. Such identification is not intended to imply recommendation or endorsement by the National Institute of Standards and Technology, nor is it intended to imply that the entities, materials, or equipment are necessarily the best available for the purpose.

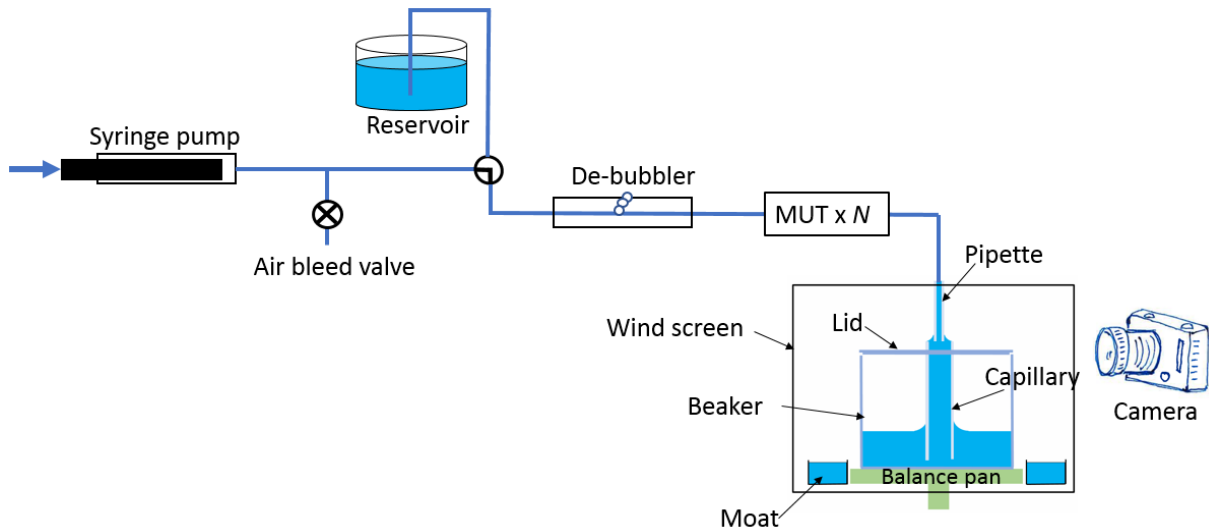


**Figure 1.** Sketch of the Dynamic Gravimetric Micro-Flow Standard (DGMFS).

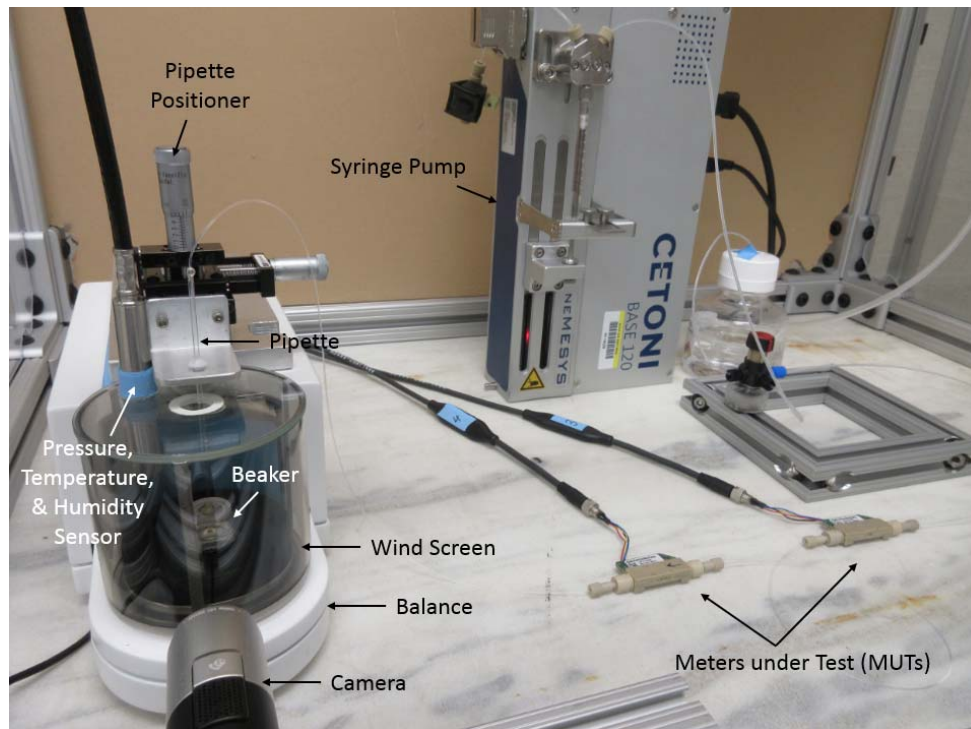


**Figure 2.** Overview of the DGMFS showing the syringe pump, connecting tubing, meters under test, and the 6 g balance.

Figures 3 and 4 show the equipment on or near the balance pan. The weighed beaker has a lid with a 1.5 mm diameter capillary passing through its center. The capillary is attached to the lid and does not reach the bottom of the beaker, so the water can flow into or out of the capillary. The beaker's lid is not air-tight;

therefore, air moves in and out of the beaker as the water level changes, but the lid does reduce evaporation of the collected water. Using a 3-axis linear stage, the pipette is positioned so that its tip is inside the capillary but it does not touch the capillary's walls. A camera provides a magnified view of the pipette / capillary interface to facilitate pipette positioning. Capillary action pulls water to the top of the capillary and once the pipette is filled and properly positioned, a liquid bridge forms between the pipette and the capillary. The water surface at the interface between the pipette and the capillary remains nearly stationary as water fills or is removed from the beaker.

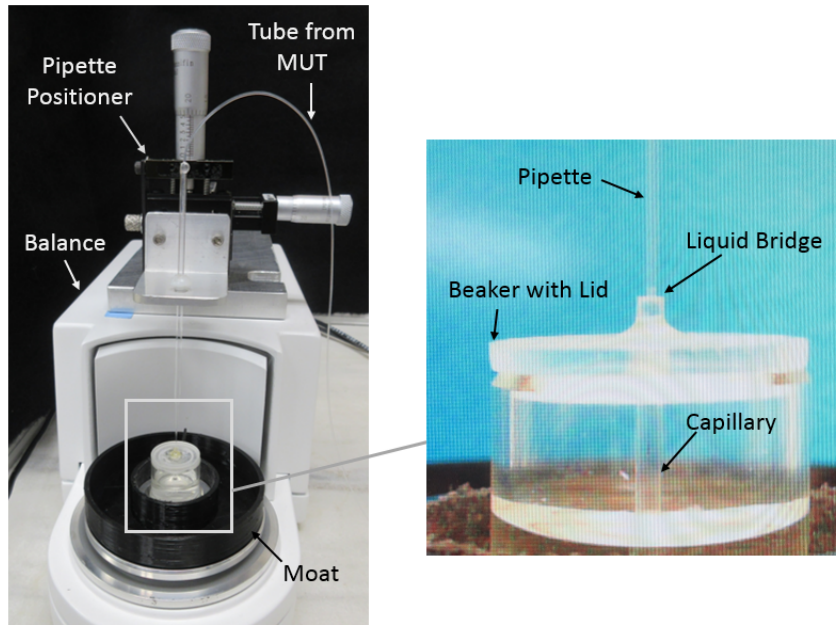


**Figure 3.** Left: Photograph of the balance (without wind screen installed), beaker, and pipette positioning system. Right: A close-up view of the beaker and the fluid coupling between the pipette and capillary.

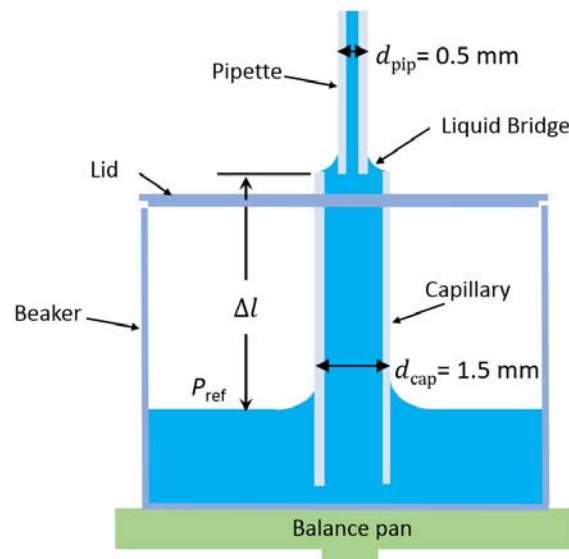
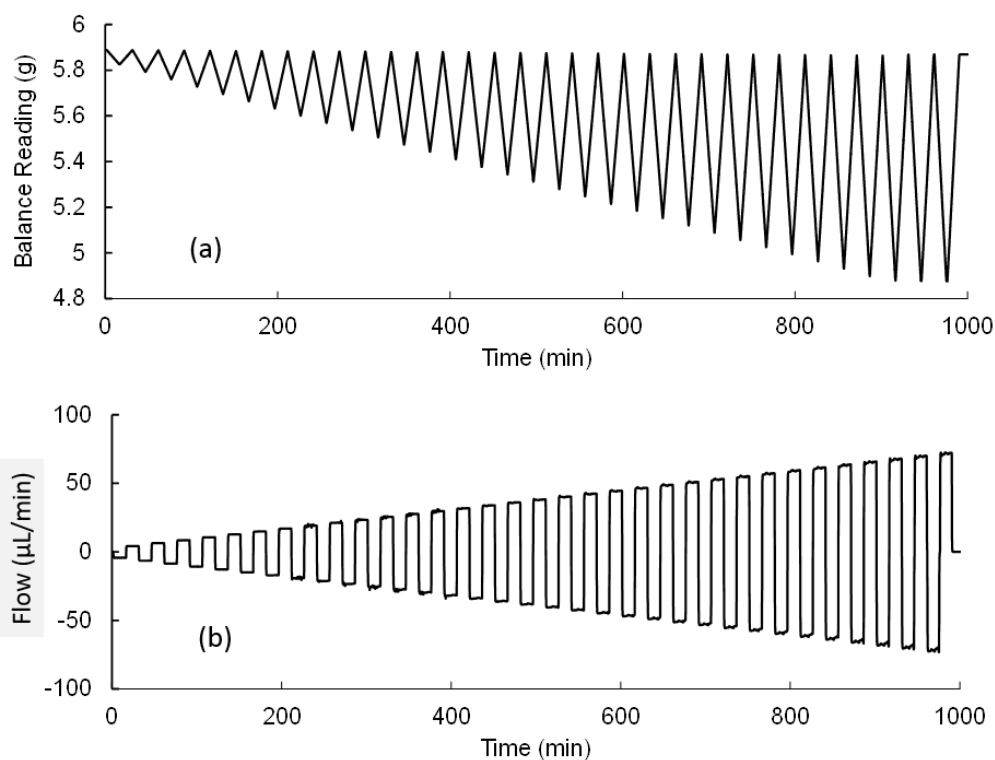


Figure 4. The beaker, capillary, and pipette used to weigh liquid in the dynamic gravimetric micro-flow standard.

The balance pan has a wind screen to block air currents that might alter the balance readings (installed in Figure 2, removed in Figure 3). A small open reservoir of water (a moat) under the wind screen (but not on the balance pan) comprises an “evaporation trap”: water vapor from it maintains approximately 90 % relative humidity under the wind screen and reduces evaporation from the liquid bridge and beaker. The pipette passes through a small hole in the wind screen. The pressure, temperature, and relative humidity of the air under the wind screen is measured in order to make buoyancy corrections for the mass of water in the beaker. The environmental conditions in the lab are stable to  $\pm 1$  °C. The DGMFS is enclosed in a plexiglass enclosure, further dampening air currents and temperature fluctuations.

A data acquisition computer and Labview program control the DGMFS, acquire mass, time, and other necessary sensor readings, and process the data to calculate flow. Flow set points are established via the syringe pump, or optionally via the elevation of a water reservoir attached to a vertical stage. The empty collection beaker weighs 4 g, so the beaker can be filled with up to 2 g of water before reaching the 6 g capacity of the balance. During normal operation, the beaker is filled with approximately 2 mL of water so that it weighs just under 6 g initially and the water supply is moved back and forth between the beaker and the syringe pump, producing negative and positive flows at the meter under test. We wait 5 minutes or more for flow stability after each set point change and then take five one-minute-long averages from the DGMFS and the MUT. Longer stabilization times and averages are used at lower flows. Upon completion of the flow set points, data are recorded at the zero flow condition (stopped syringe pump) to gravimetrically measure the evaporation from the beaker. A sample data set is shown in Figure 5.



**Figure 5.** Mass versus time (a) and flow ( $dm/dt$ ) versus time (b) for a calibration made with the DGMFS.

### 3. DGMFS Flow Equations

The DGMFS measures the mass flow through the meter under test from the time rate of change of the mass of water in the collection beaker. A force balance shows that corrections for buoyancy forces and

evaporation are necessary to obtain low uncertainty flow measurements. The forces imposed between the beaker and the balance pan are depicted in Figure 6. In Figure 6, each force has been divided by the gravitational acceleration  $g$  so that the quantities have units of mass.

- The quantity  $F_{\text{bal}}/g$  is the opposing force provided by the balance pan to the beaker and its contents divided by  $g$ . The balance software applies a correction for buoyancy using assumed values for the density of the weighed object and the surrounding air. To remove this buoyancy correction and obtain  $F_{\text{bal}}/g$ , it is necessary to multiply the balance reading by  $1 - \rho_{\text{air}^*}/\rho_{\text{std}} = 0.99985$ , where  $\rho_{\text{air}^*}$  is the density of air assumed by the balance software ( $0.0012 \text{ g/cm}^3$ ) and  $\rho_{\text{std}}$  is the assumed density for a stainless steel mass standard ( $8 \text{ g/cm}^3$ ).
- Surface tension at the liquid interface between the pipette and the capillary produces an upward force equal to the product of the circumference of the pipette  $\pi d_{\text{pip}}$ , the surface tension  $\gamma$ , and the cosine of the liquid contact angle  $\theta_{\text{liq}}$  (hereafter assumed equal to zero).
- The buoyancy forces of the water collected in the beaker and the beaker itself lead to the terms  $V_{\text{liq}} \rho_{\text{air}}$  and  $V_{\text{beaker}} \rho_{\text{air}}$  where  $V_{\text{liq}}$  and  $V_{\text{beaker}}$  are the volumes of the water and beaker respectively, and  $\rho_{\text{air}}$  is the density of the surrounding air. Note that  $\rho_{\text{air}}$  is not assumed to be a constant; it is calculated using [2] and the pressure, temperature, and relative humidity measured near the balance pan.
- The pressure at the tip of the pipette is lower than the atmospheric pressure ( $P_{\text{ref}}$ ) by the hydrostatic head of the water between the top of the capillary and the main body of water in the beaker ( $\Delta l$  in Figure 4). The beaker and its contents are partially supported by this small pressure difference ( $\rho \Delta l g \approx 150 \text{ Pa}$ ). The supporting force ( $\rho_{\text{liq}} \Delta l A_{\text{pip}}$ ) is a function of the depth of the water in the beaker.
- $m$  and  $m_{\text{beaker}}$  are the masses of the water in the beaker and of the beaker itself. Note that for the purposes of the force balance, the beaker lid and the capillary are part of the beaker.
- The term  $V_{\text{pip}} \rho_{\text{liq}}$  accounts for buoyancy forces imposed on the balance due to the tip of the pipette in the water within the capillary.

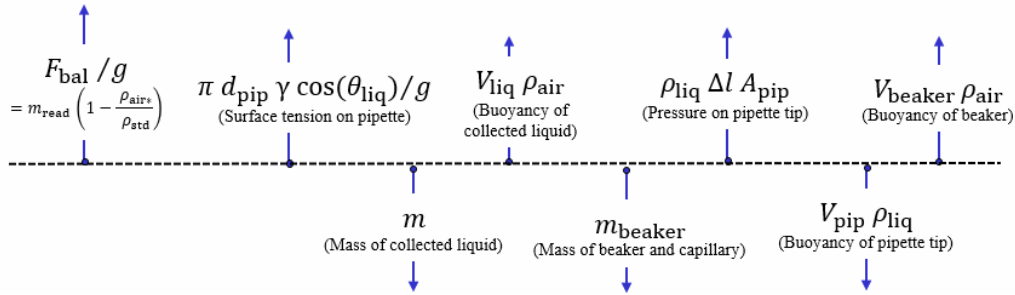


**Figure 6.** Contributions to the force balance on the beaker. The magnitudes of the vectors are not drawn to scale.

Setting the sum of the terms in Figure 6 equal to zero and solving for the mass of water in the beaker at a particular time gives:

$$m = \frac{F_{\text{bal}}}{g} + \frac{\pi d_{\text{pip}} \gamma}{g} + V_{\text{liq}} \rho_{\text{air}} + \rho_{\text{liq}} \Delta l A_{\text{pip}} + V_{\text{beaker}} \rho_{\text{air}} - m_{\text{beaker}} - V_{\text{pip}} \rho_{\text{liq}}. \quad (1)$$

Using the relationships  $F_{\text{bal}}/g = m_{\text{read}} \left(1 - \frac{\rho_{\text{air}^*}}{\rho_{\text{std}}}\right)$  and  $V_{\text{liq}} = m/\rho_{\text{liq}}$  leads to:

$$m = m_{\text{read}} \frac{\left(1 - \frac{\rho_{\text{air}^*}}{\rho_{\text{std}}}\right)}{\left(1 - \frac{\rho_{\text{air}}}{\rho_{\text{liq}}}\right)} + \rho_{\text{liq}} \Delta l A_{\text{pip}} + \frac{\pi d_{\text{pip}} \gamma}{g} + V_{\text{beaker}} \rho_{\text{air}} - m_{\text{beaker}} - V_{\text{pip}} \rho_{\text{liq}}. \quad (2)$$

The mass flow can be calculated from the difference in mass of the beaker contents divided by the time between the two mass measurements. Several of the forces represented in Equation 2 are effectively constant over time and will cancel when a mass change is calculated, i.e.,  $\pi d_{pip} \gamma / g$ ,  $V_{beaker} \rho_{air}$ ,  $m_{beaker}$ , and  $V_{pip} \rho_{liq}$ . (Note that the cancelling terms *will* be considered as sources of uncertainty.) Assuming that the density of the water and of the surrounding air remains constant, the mass change  $\Delta m$  between two mass measurements  $m_1$  and  $m_2$  is:

$$\Delta m = \Delta m_{read} \frac{\left(1 - \frac{\rho_{air*}}{\rho_{std}}\right)}{\left(1 - \frac{\rho_{air}}{\rho_{liq}}\right)} + \rho_{liq} A_{pip} (\Delta l_2 - \Delta l_1) . \quad (3)$$

The change in the level of water in the beaker can be closely approximated using the change in reading of the balance and the cross-sectional areas of the beaker and capillary:

$$\Delta l_2 - \Delta l_1 \cong - \frac{\Delta m_{read}}{\rho_{liq} (A_{beaker} - A_{cap})} \frac{\left(1 - \frac{\rho_{air*}}{\rho_{std}}\right)}{\left(1 - \frac{\rho_{air}}{\rho_{liq}}\right)} , \text{ which leads to:} \quad (4)$$

$$\Delta m \cong \Delta m_{read} \frac{\left(1 - \frac{\rho_{air*}}{\rho_{std}}\right)}{\left(1 - \frac{\rho_{air}}{\rho_{liq}}\right)} \left[ 1 - \frac{A_{pip}}{(A_{beaker} - A_{cap})} \right] . \quad (5)$$

In review, the expression  $\left(1 - \frac{\rho_{air*}}{\rho_{std}}\right)$  removes buoyancy corrections for stainless steel reference masses implemented by the balance software and the term  $\left(1 - \frac{\rho_{air}}{\rho_{liq}}\right)$  corrects for buoyancy forces on the collected water. The term in the square brackets (the pipette hydrostatic correction) accounts for hydrostatic or pressure forces on the pipette tip that change as the water level changes in the beaker.

To calculate the mass flow from two mass measurements, one could divide the change in mass by the time interval between  $m_1$  and  $m_2$ . But we can reduce the effects of random variations in the mass measurements and balance uncertainties by calculating the rate of change of mass from a larger number of mass and time values. Equation 6 gives the slope of the mass-versus-time record as determined using a first order least squares regression [3] with  $N$  pseudo-mass values  $\hat{m}$  evenly spaced in time,  $t$

$$\dot{m}_0 = \frac{d\hat{m}}{dt} \cong \frac{N \sum_{j=1}^N t_j \hat{m}_j - \sum_{j=1}^N t_j \sum_{j=1}^N \hat{m}_j}{N \sum_{j=1}^N t_j^2 - (\sum_{j=1}^N t_j)^2} . \quad (6)$$

A pseudo-mass value  $\hat{m}$  can be used to calculate the 0<sup>th</sup> order mass flow:

$$\hat{m} = m_{read} \frac{\left(1 - \frac{\rho_{air*}}{\rho_{std}}\right)}{\left(1 - \frac{\rho_{air}}{\rho_{liq}}\right)} . \quad (7)$$

The 0<sup>th</sup> order mass flow is then corrected by 1) the hydrostatic or pressure effect on the pipette tip and 2) evaporation:

$$\dot{m} = \dot{m}_0 \left[ 1 - \frac{A_{pip}}{(A_{beaker} - A_{cap})} \right] + \frac{dm_{evap}}{dt} . \quad (8)$$

The evaporation correction is based on measurements made under zero flow conditions and will be discussed in more detail later in this paper.

The volumetric flow at the meter under test (MUT) can be calculated from the mass flow and the density at the MUT via:

$$Q = \frac{\dot{m}}{\rho_{\text{liq}}} . \quad (9)$$

The density of the water depends on the temperature and the pressure of the water, so formally, the water density in the beaker and at the MUT ( $\rho_{\text{liq}}$  in equations 7 and 9 respectively) are not equal. However for the temperature uniformity and pressures in our laboratory, the water density differences are negligible compared to other uncertainty sources.

Note that Equation 1 applies to a beaker with an interface as shown in Figure 4, i. e., a system utilizing a liquid bridge so that the liquid does not rise on the externally supported pipette as the beaker fills. In an earlier version of the NIST micro-flow standard, the filling tube was directly inserted into the liquid collecting in the beaker, and an additional correction was necessary to account for increasing buoyancy forces exerted by the tube on the balance as the liquid rises around the tube [1]. A micro-flow standard that has the liquid level rising around the pipette is subject to changes in the surface tension forces imposed on the balance due to “stick-slip” behaviour of the liquid / pipette interface [1]: the liquid meniscus often varies in shape as the liquid level changes due to the pipette’s surface inhomogeneities.

#### 4. DGMFS Uncertainty Analysis

The approximately 95 % confidence level ( $k = 2$ ) uncertainty of the DGMFS for flows between 0.1  $\mu\text{L}/\text{min}$  and 100  $\mu\text{L}/\text{min}$  is plotted in Figure 7. At the largest flows, the uncertainty is dominated by the repeatability of the best MUT known to us and by the pipette hydrostatic correction. Below 1  $\mu\text{L}/\text{min}$ , uncertainty in the corrections made for evaporation and the repeatability of the best-available MUT dominate. Table 1 lists the uncertainty components, nominal values for the quantities, their uncertainty, and the contribution of each component to the total uncertainty for a 100  $\mu\text{L}/\text{min}$  flow. In the following sections, the broad uncertainty categories listed in Table 1 and their estimations are discussed.

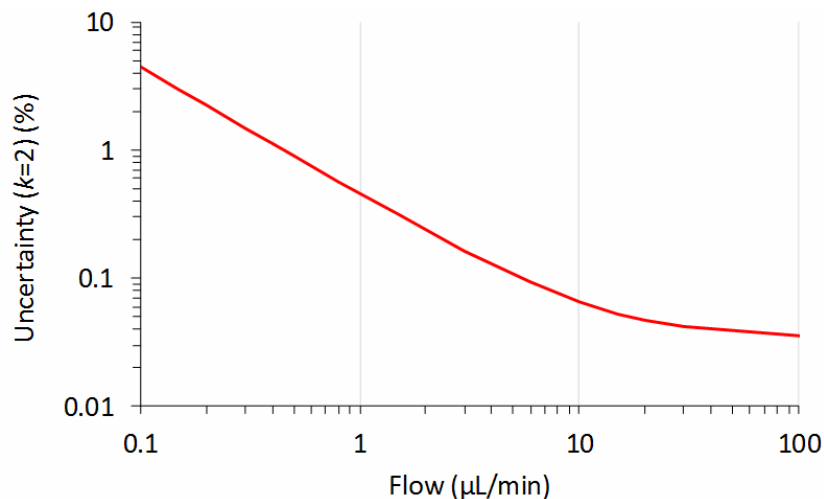


**Figure 7.** The 95 % confidence level uncertainty of the DGMFS versus flow.

**Table 1.** Uncertainty of the DGMFS for a flow of 100  $\mu\text{L}/\text{min}$ .

Uncertainty category	Value	Units	Standard unc. ( $k = 1$ )	Contrib.
			(%)	(%)
$\Delta\text{Mass}$ with buoyancy corr.	0.1	[g]	0.003	0
$\Delta\text{Time}$	1	[min]	0.002	0
Pipette hydrostatic corr.	0.999	[-]	0.008	19
Slope calculation	0	[g/min]	0	0
Evaporation	-0.01	[ $\mu\text{L}/\text{min}$ ]	0.002	1
Water density	0.998	[ $\text{g}/\text{cm}^3$ ]	0.005	0
Repeatability & flow stability	0.1	[g/min]	0.016	79
Expanded uncertainty ( $k = 2$ )	0.04	[ $\mu\text{L}/\text{min}$ ]	0.04	

Change in Mass (with Buoyancy Corrections): At low flows, the largest contributor to the mass change uncertainty is zero drift of the balance. At high flows, the largest contributor is gain (slope) errors in the balance calibration. Uncertainty due to the resolution of the balance (0.1  $\mu\text{g}$ ) is small compared to the zero drift and gain errors. Buoyancy corrections are significant (0.12 %), but their uncertainty ( $< 5$  parts in  $10^6$ ) is not significant, thanks to the low uncertainty of the sensors and equations used for air density.

Balance zero drift is indistinguishable from changes in the mass of the beaker due to water flowing into it. Zero drift data were collected by placing a reference mass on the balance pan (with the wind screen in place) and using the data acquisition system to record the balance readings. Figure 8 shows an example data set. The line shows the balance readings over a 15 hour interval and the symbols are one minute averages of the flow (or drift) calculated as done for flow calibrations. For the data in Figure 8, the largest drift value is 0.26  $\mu\text{g}/\text{min}$  and the standard deviation of the drift is 0.08  $\mu\text{g}/\text{min}$ . The maximum slopes observed in this (and other) data sets were used to quantify the standard uncertainty (68 % confidence level) due to zero drift (0.16  $\mu\text{g}/\text{min}$ ).

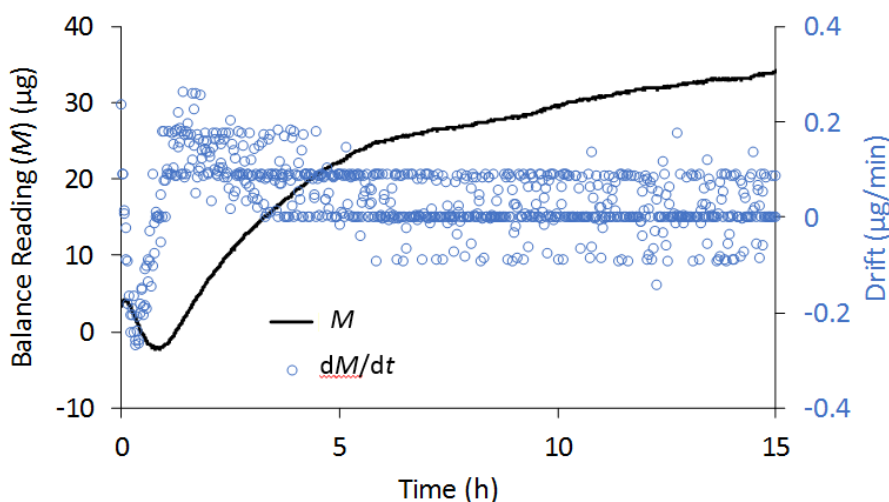


**Figure 8.** The balance reading during a 15 h interval and one minute averages of its slope (drift). This and additional, similar data sets were used to quantify the standard uncertainty of the drift in the balance calibration: 0.16  $\mu\text{g}/\text{min}$  (0.16  $\text{nL}/\text{min}$ ).

The balance is periodically calibrated using the procedure provided by the manufacturer, i.e. the zero and gain of the balance are adjusted by automatically placing an internal reference mass on or off the balance. We verified this internal calibration process by placing reference masses between zero and 6 g (in 1 g increments) on the balance and comparing the balance readings to the known reference mass values. On occasion, the reference-mass verifications were conducted 4 months after an internal calibration to reveal how well the balance holds its calibration over time. Based on the data in Figure 9, we conclude that the balance gain error and calibration stability can introduce 0.03 mg uncertainty ( $k = 1$ ) for each gram of mass change measured.

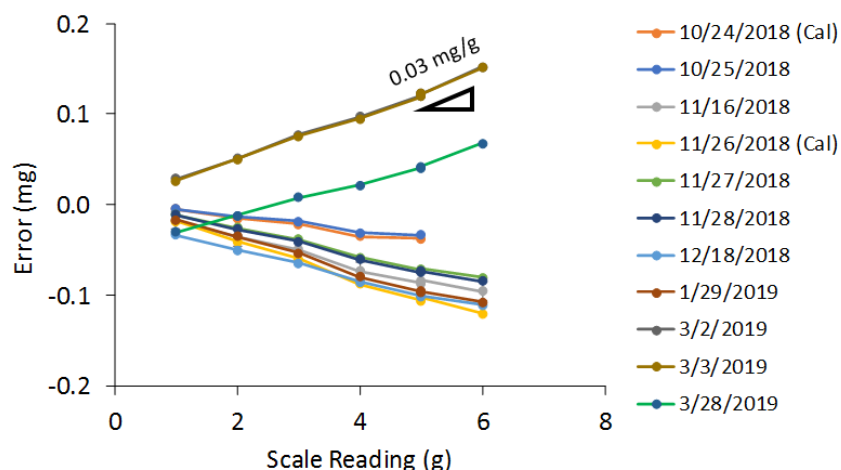


**Figure 9.** Results of balance calibrations performed using reference masses. Internal scale calibrations were performed on the dates followed by the notation (Cal) in the legend.

*Change in Time:* Mass values are acquired from the balance at 2.5 Hz. The uncertainty of the time values attributed to the mass measurements has two main sources: 1) drift in the clock of the computer that is used for data acquisition, and 2) inconsistencies in the time for communication between the balance and the computer (latency). The computer clock drift is periodically checked by disconnecting it from the computer network to prevent automatic time corrections and visually comparing the computer clock to a cell phone clock over a 72 h interval. These periodic checks show that the computer clock is correct with standard uncertainty of 20 parts in  $10^6$ .

We assessed the time uncertainties introduced by variations in the digital communications between the balance and the computer (latency) from the standard deviation of the period of the data acquisitions. The period measured via Labview timing functions (i.e. the data acquisition computer clock) is 0.39861 s and it has a standard deviation of 75  $\mu$ s. For the minimum flow data collection time (60 s), this is a standard uncertainty of 1 part in  $10^6$ . Combining clock drift and latency components gives a standard uncertainty for the time measurements of 20 parts in  $10^6$ .

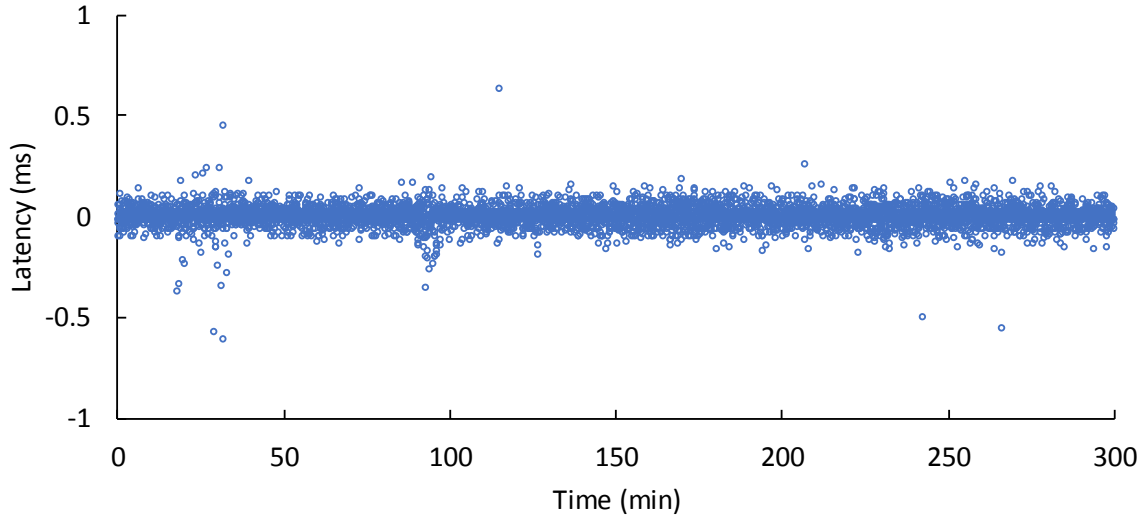


**Figure 10.** Variations in the communication time (latency) for the data acquisition computer and the balance. The standard deviation of data like these were used in the time uncertainty analysis.

*Pipette Hydrostatic Correction:* This correction accounts for the force on the balance caused by the pressure difference at the top of the capillary relative to the atmospheric pressure. The correction depends on the dimensions of the beaker, capillary, and pipette. Of these dimensions, the correction is most sensitive to uncertainty of the pipette's inside diameter, known with a standard uncertainty of 0.02 mm which leads to a standard uncertainty of 80 parts in  $10^6$  in the correction.

*Slope Calculation:* The slope of the mass-time data pairs is calculated via Equation 6 using a 20 s long moving window of data collected at 2.5 Hz. The mass flow values from the slope calculation (and the acquired output of the MUT) are averaged for a minimum of 60 s, so the effective minimum number of data points fitted is  $N = 150$ . At flows  $< 1 \mu\text{L}/\text{min}$ , the averaging time is lengthened to produce mass changes greater than 1 mg to control uncertainty due to balance resolution (0.1  $\mu\text{g}$ ). The uncertainty in the mass values (and associated corrections) is at least 2.5 times larger than the uncertainty in the time values, allowing us to apply the simplest expression for the uncertainty of the best fit slope [3]:

$$U^2(a_1) = \frac{2 \frac{\sum_{j=1}^N (m_j - a_1 t_j - a_0)^2}{N-2}}{\sum_{j=1}^N t_j^2 - \frac{(\sum_{j=1}^N t_j)^2}{N}} = \frac{4\sqrt{3} s(m)}{\sqrt{N^3 - N} \Delta t} \quad (10)$$

where  $a_0$  and  $a_1$  are the zeroeth and first-order coefficients of the fit to the mass versus time data. (Here we have used  $a_1$  instead of  $\dot{m}$  to avoid confusion: Equation 10 gives the uncertainty related to the fitting process, not the total uncertainty of the mass flow.) The quantity  $s(m)$  is the sample standard deviation of the mass fit residuals and  $\Delta t$  is the time interval between successive mass measurements. We used the sample data sets shown in Figure 11 (and others) and found that  $s(m)$  ranged from 2  $\mu\text{g}$  at the lowest flows to 12 mg at 100  $\mu\text{L}/\text{min}$ . We applied Equation 10 with these values of  $s(m)$ ,  $N = 150$ , and  $\Delta t = 0.39861$  s and found that the uncertainty introduced by the slope calculation is negligible.

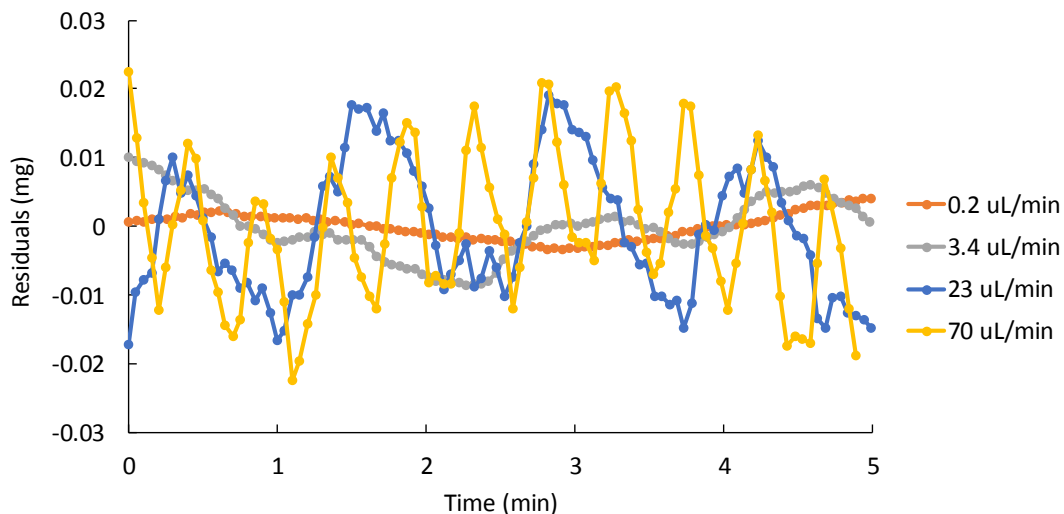


**Figure 11.** Residuals of first-order best-fits to mass measurements for flows from 0.2  $\mu\text{L}/\text{min}$  to 70  $\mu\text{L}/\text{min}$ . The periodic flow changes visible for the larger flows are probably caused by the syringe pump.

*Evaporation Correction:* Water evaporates from the liquid bridge between the pipette and the capillary and through the crevices of the beaker lid (Figures 3 and 4). The relative humidity under the balance wind screen is normally greater than 90 %. However, evaporation of the water in the beaker is significant, about  $-0.01 \mu\text{L}/\text{min}$ . After completion of all non-zero flow set points, the gravimetric standard continues to acquire data at a no-flow condition, often for many hours, to determine the evaporation correction. An example is shown in Figure 12. The standard uncertainty of the evaporation correction is  $0.002 \mu\text{L}/\text{min}$  and this is the most significant uncertainty component at flows  $< 6 \mu\text{L}/\text{min}$ .

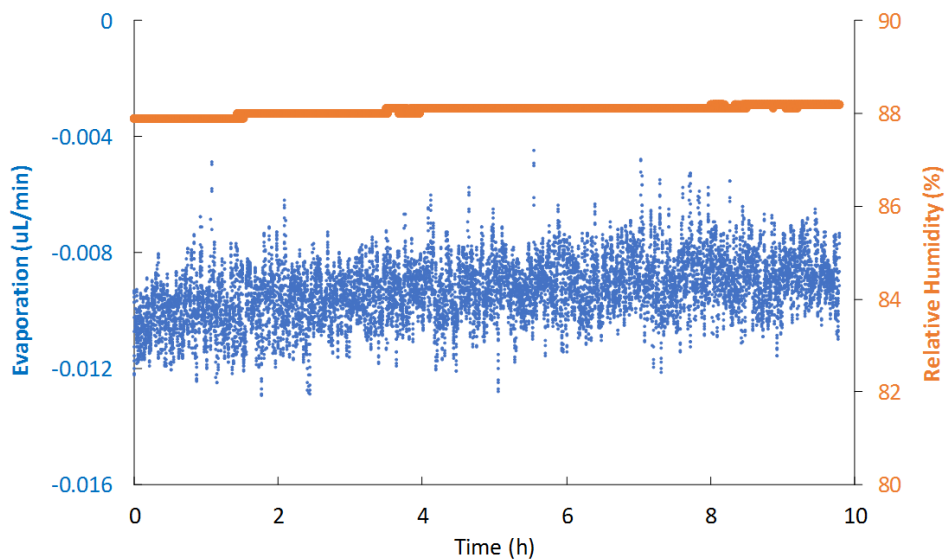


**Figure 12.** A sample of evaporation and relative humidity data collected at the end of a calibration run.

*Flow Stability and Repeatability of the Best Existing Device:* Removing air bubbles from the flow tubes is essential for good flow stability. Figure 13a shows large flow transients caused by bubbles alternately moving or sticking in the flow tubes while Figure 13b shows good flow stability when bubbles are removed. The response time of the system to step changes of the flow is markedly faster without air bubbles. Bubbles can be pushed out of the tubing by the operator using the syringe pump when the system is filled, but they

are often not easy to see. The de-bubbler is helpful too. Bubbles can be pulled into the flow tubes though loose fittings during negative flow when the pressure in the system is less than ambient pressure. Data traces like Figure 13a do not produce reliable calibration data and lead to re-testing.

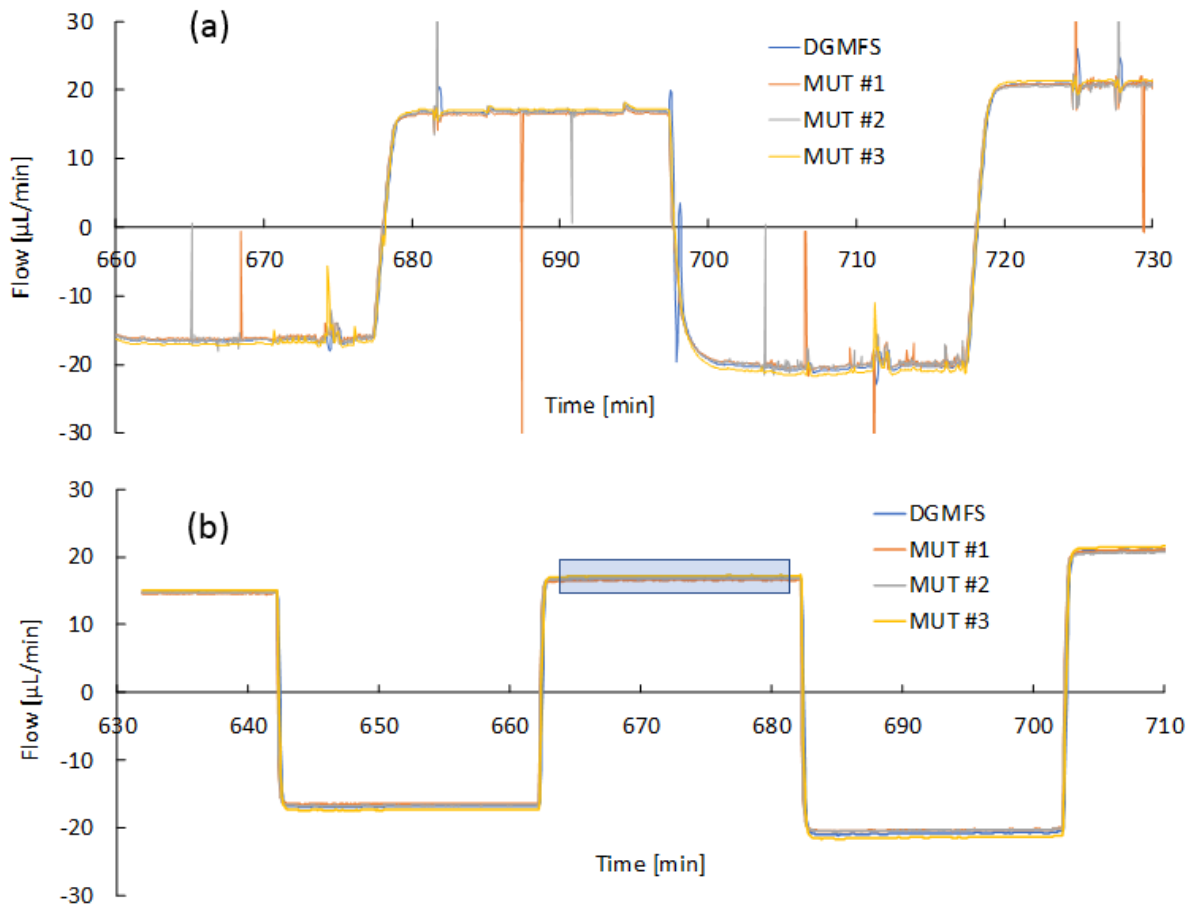


**Figure 13.** Flow records from the gravimetric standard and three MUTs (a) with air bubbles in the flow tubes and (b) without air bubbles. The data in the rectangular highlight in (b) are plotted on an expanded scale in Figure 14.

Periodic flow changes in the gravimetric standard and three meters under test are clear in Figure 14 (and Figure 11). Bissig [4] notes that, for periodic flows in micro-flow systems, time delays occur between the flows in the pump, the MUT, and the flow standard. When the flow reverses, the pressure distribution in the flexible flow tubes changes and the volumes of the tubes changes. The time required for the flow to adjust to the volume changes is not negligible. In Figure 14, the time delay between the gravimetric standard and the MUTs is approximately 9 s. Other time delays may be caused by the slope calculation using a 20 s moving window, and by the response time of the MUT. These time delays and the finite time response of the flow meters can lead to uncertainty in the flow calibration results. Most flow standards avoid these concerns by providing very steady flow conditions and by using long averages that span many periods of flow fluctuations, but that is more difficult to achieve in micro-flow systems. This subject deserves more attention, especially so that micro-flow applications that need reliable transient flow measurements are well served.

For this uncertainty analysis, we will assume that the uncertainty due to flow instability and time response is captured by the type A repeatability component. Here we use the standard deviation of the 5 repeated

flow measurements from the best existing device. When performing a customer calibration, we use the repeatability for the meter under test instead of the repeatability for the best existing device.

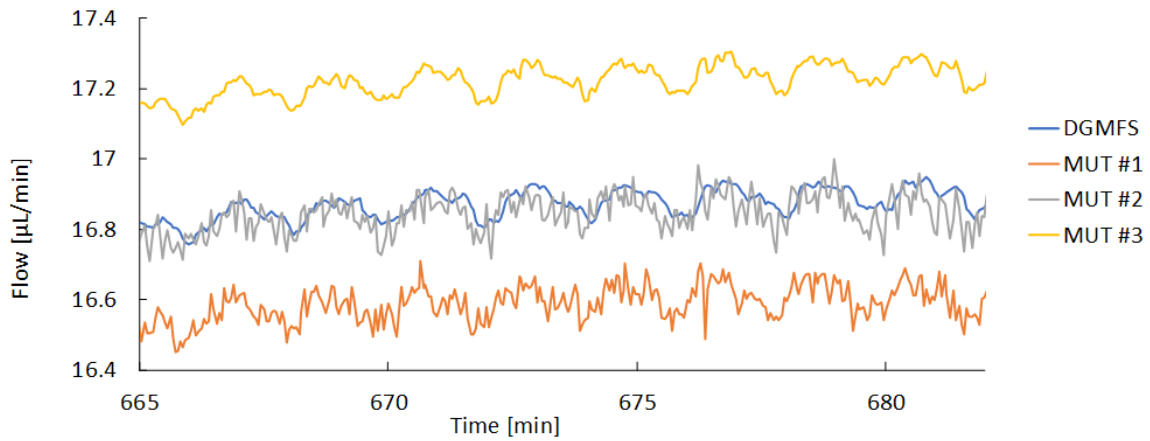


**Figure 14.** Periodic flow changes, probably caused by mechanical imperfections of the syringe pump drive screw or plunger.

## 5. Reproducibility of Micro-Flow Meters

The DGMFS was used to calibrate 5 NIST-owned, commercially-purchased flow meters multiple times. We identify these meters by the letters A, B, C, D, and E. Control charts are plotted in the following figures with the flow axis plotted on 1) a linear scale and 2) a log scale. The manufacturer's specification is shown as dashed lines.

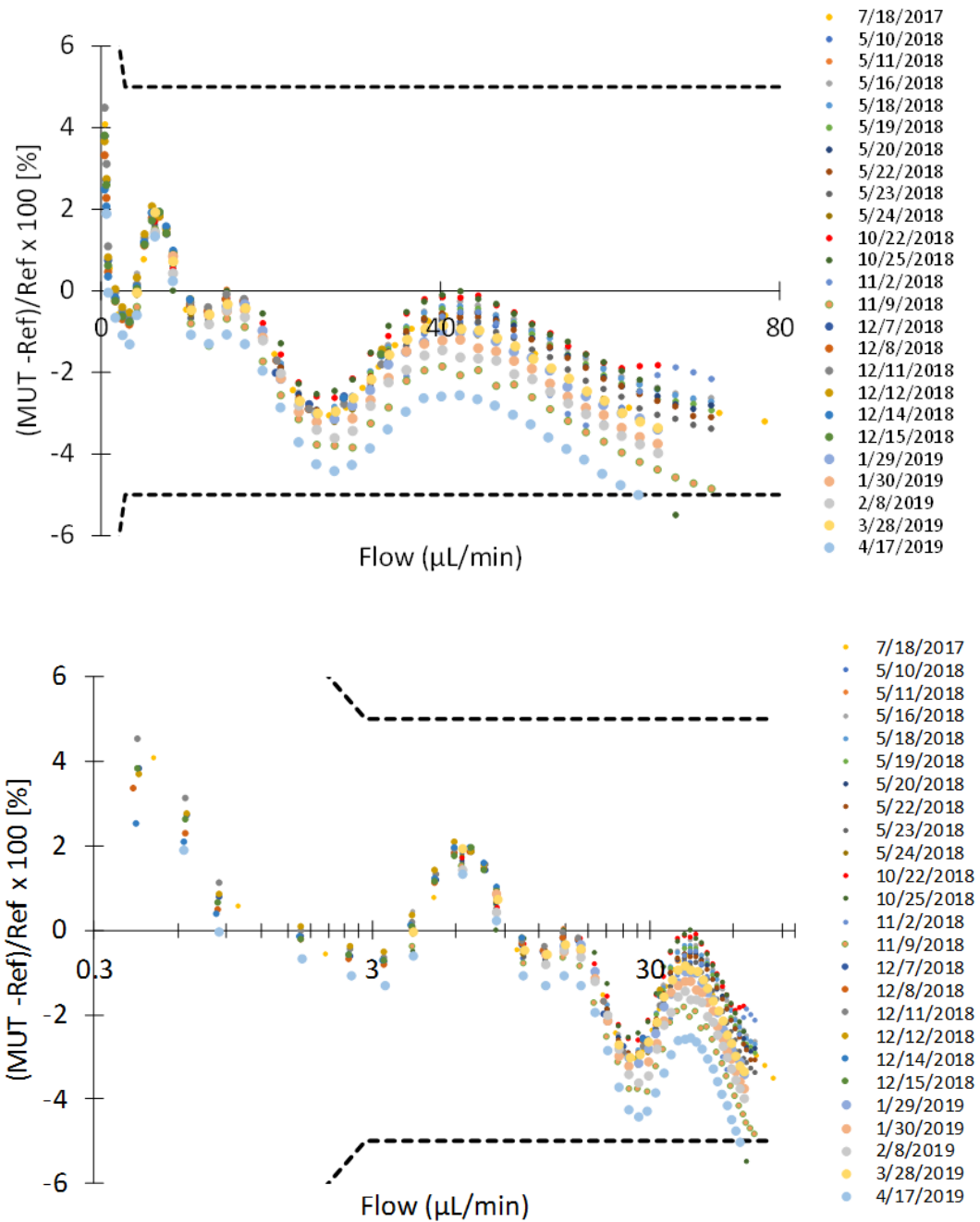


**Figure 15.** Thermal flow meter A with a 21 month long calibration history, has an error curve than could be well fit with a polynomial or a spline. The scatter of the calibration curves from 25 calibrations over 21 months has standard deviation of about 1.5 %. The calibration data shown here have a turndown ratio of 360 to 1.

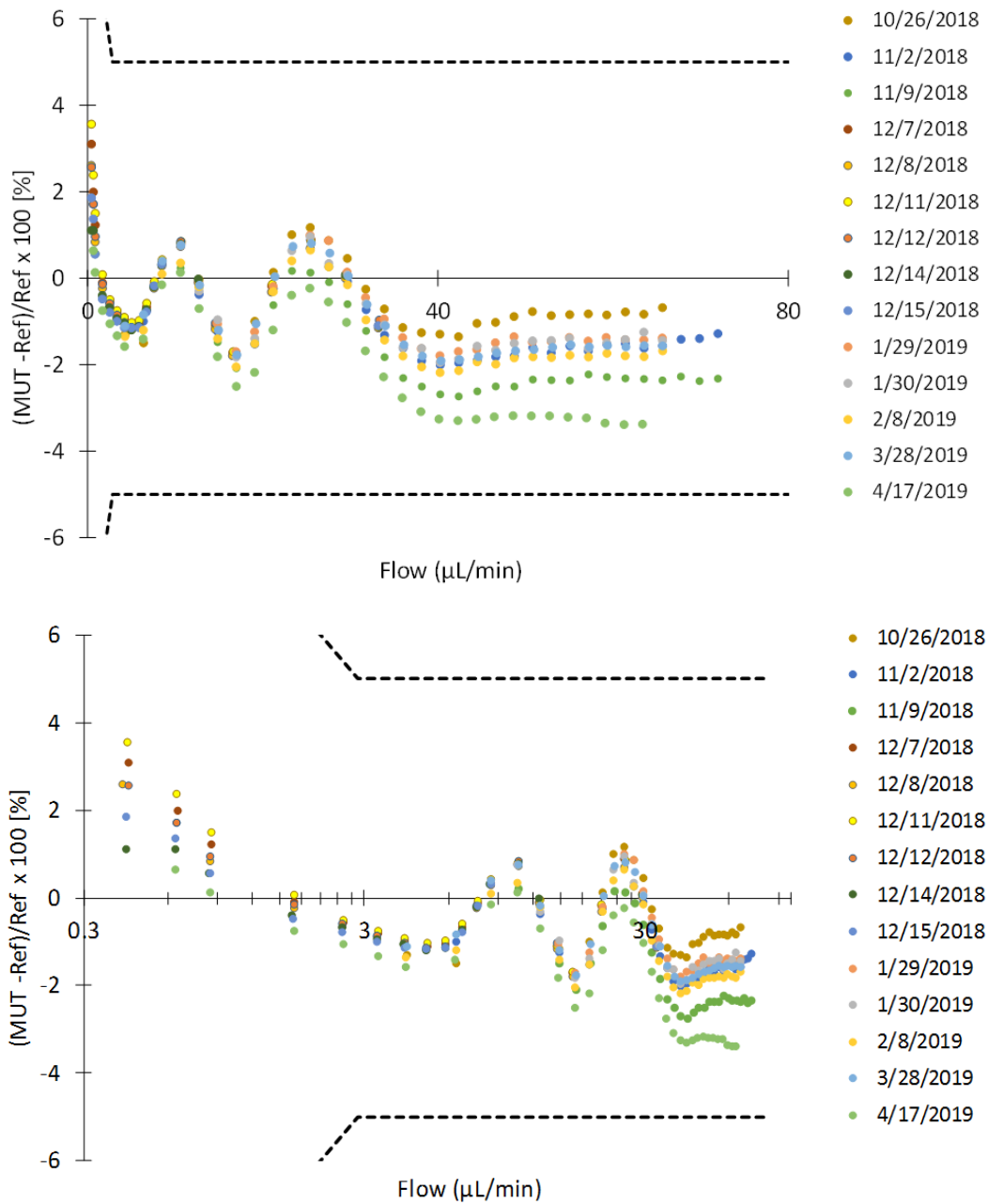


**Figure 16.** Thermal flow meter B. This meter is the same model as Meter A (Fig. 15.) The meter's 14 calibrations spanning a 6 month period show standard deviations up to 1.4 %.

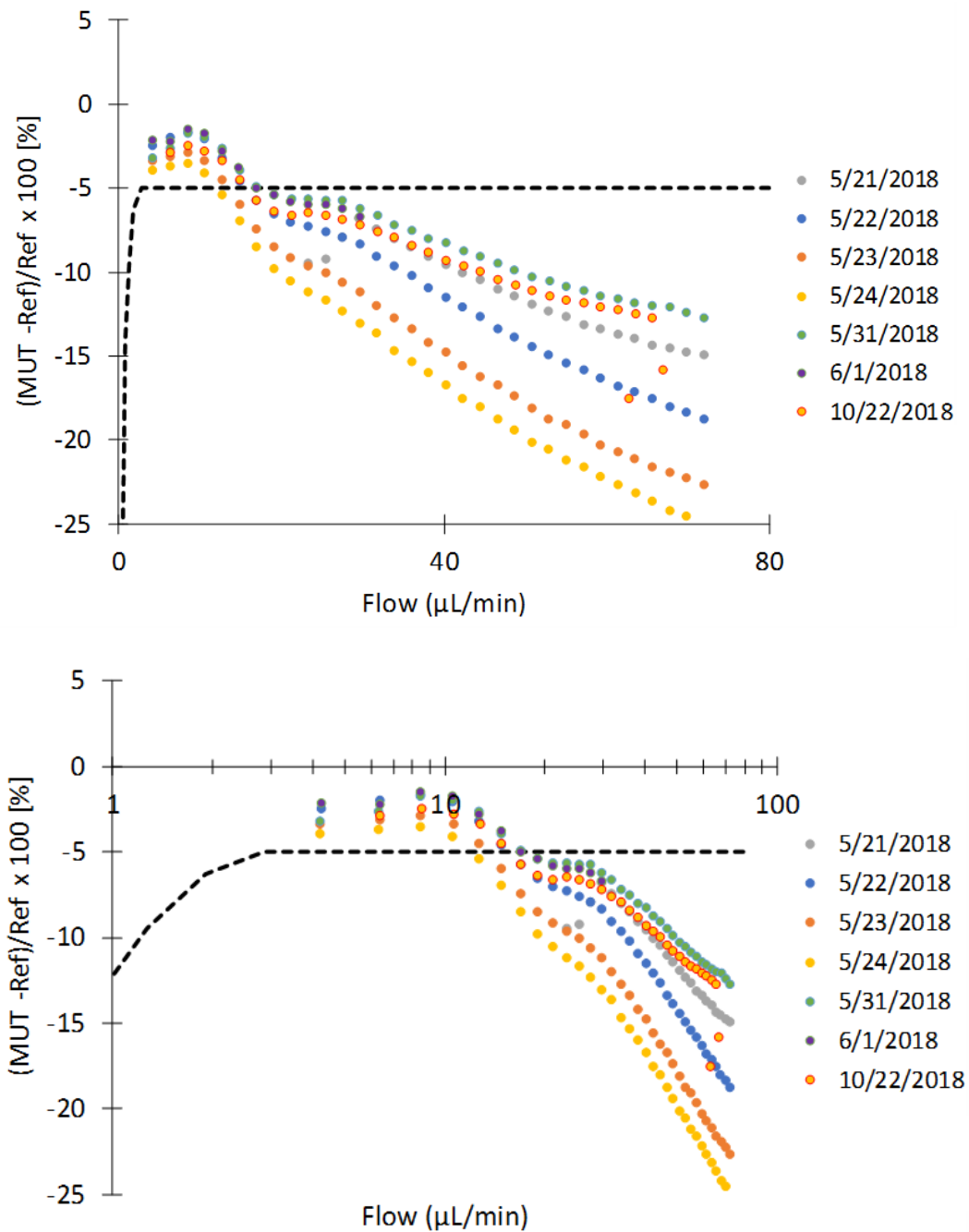


**Figure 17.** Thermal flow meter C. The calibration of this meter drifted significantly for unknown reasons. This meter was calibrated in series with other MUTs that did not show significant drift. (We always use a check meter in series with the MUT to alert us to possible problems with the DGMFS.)

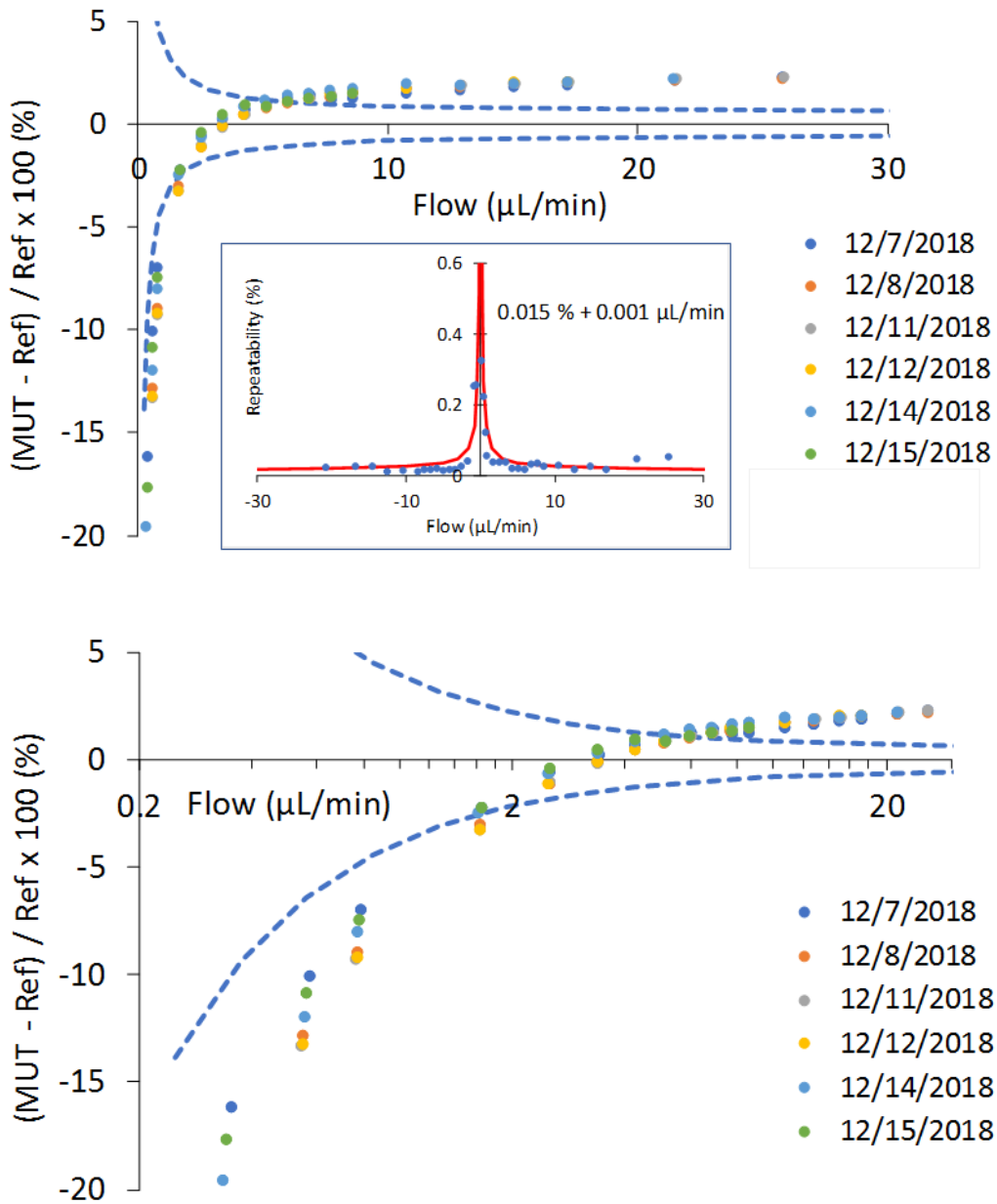


**Figure 18.** Coriolis flow meter D. These 6 calibrations over a 1-week interval have reproducibility of < 0.5 % over a 16 to 1 turndown ratio. We used meter D to quantify type A uncertainties for the DGMFS uncertainty analysis. The inset is a plot of the repeatability (standard deviation) of the 5 one minute averages for each

set point on 12/8/2018. This meter was not re-zeroed, an easy process that would improve its measurements at low flows.

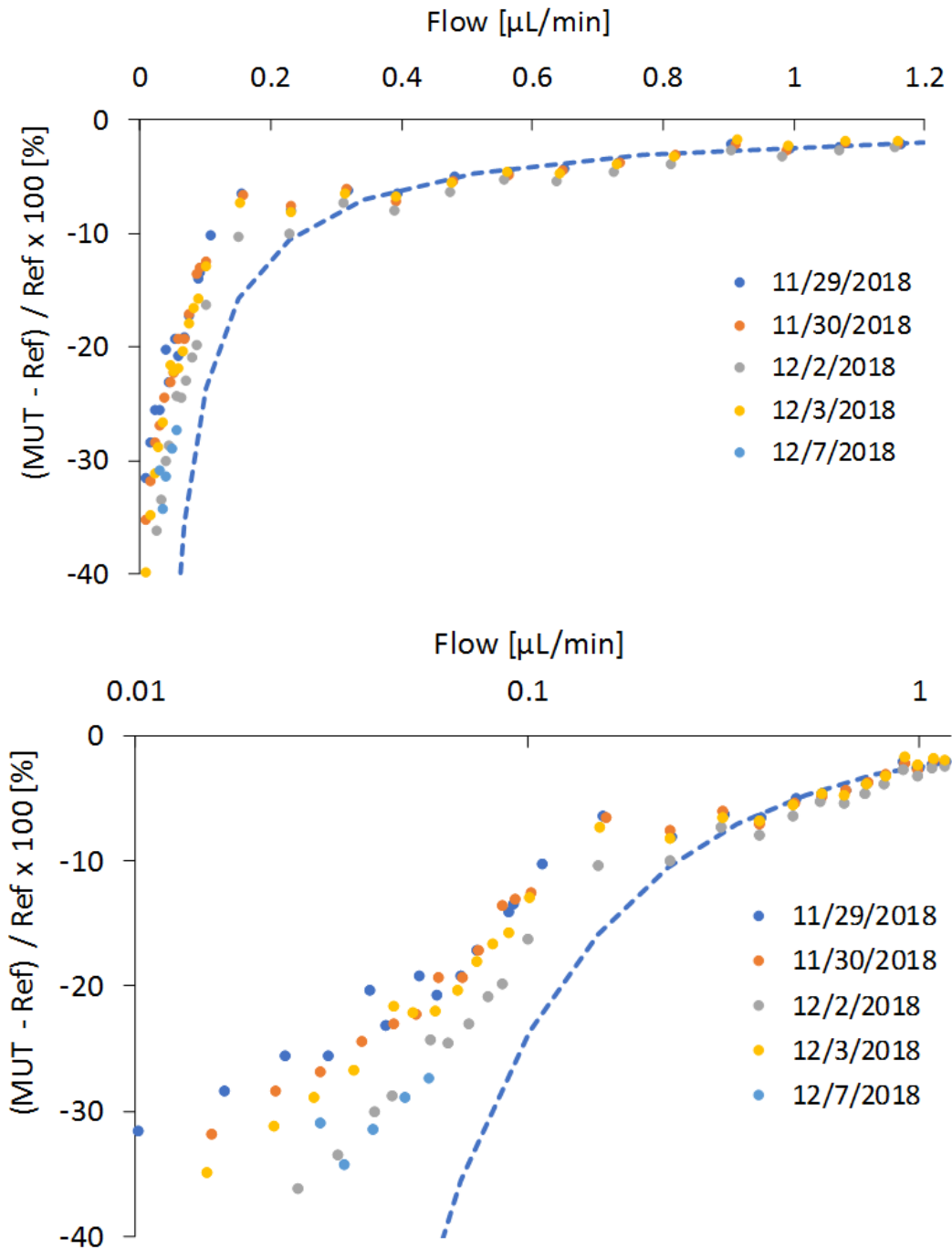


**Figure 19.** Thermal flow meter E. Meter E was not re-zeroed. If we followed this easy procedure, the results at low flows would improve.

## 6. Summary and Conclusions

Since it was first commissioned in 2015, NIST's Dynamic Gravimetric Micro-Flow Standard (DGMFS) has been improved by using a liquid bridge between the pipette and the collection beaker, and by the addition of an evaporation trap, camera, and pipette positioning equipment. The liquid bridge avoids varying surface forces on the balance due to stick / slip phenomena on a gradually immersed tube.

A detailed derivation of the equations of flow (based on a force balance) was presented. We showed experimental results quantifying the uncertainty components of mass, time, pipette hydrostatic correction, evaporation, slope calculation, and repeatability. The DGMFS measures water flow between 0.1  $\mu\text{L}/\text{min}$  and 100  $\mu\text{L}/\text{min}$  with uncertainty ranging from 4.5 % to 0.04 %. At high flows, MUT repeatability and pipette hydrostatic corrections are the largest uncertainties. At low flows, evaporation corrections and repeatability of the best existing device are the largest uncertainty components. We have used the DGMFS at flows as low as 0.01  $\mu\text{L}/\text{min}$  (Figure 19), but at that flow, the uncertainty of the standard is estimated to be 45 %, the evaporation correction is equal to the flow, and the  $k = 2$  uncertainty of the evaporation correction is 40 % of the flow. So, until we can reduce the evaporation and its uncertainty, 0.1  $\mu\text{L}/\text{min}$  is the practical lower limit of the DGMFS.

Repeated calibrations of five commercially available micro-flow meters (one for nearly 2 years) show that their calibration generally remains stable within 1.5 % for many months. The calibrations show that the flow uncertainty achieved in a user's application can be improved by applying a correction equation based on a calibration against a reference flow standard.

---

<sup>1</sup> Schmidt, J. W. and Wright, J. D., *Micro-Flow Calibration Facility at NIST*, Proceedings of the 9<sup>th</sup> International Symposium on Fluid Flow Measurement, Arlington, VA, USA, April 14 to 17, 2015.

<sup>2</sup> Jaeger, K. B. and Davis, R. S., *A Primer for Mass Metrology*, NBS Special Publication 700-1, November, 1984.

<sup>3</sup> Coleman, H. W., and Steele, W. G., *Experimentation, Validation, and Uncertainty Analysis for Engineers*, 3rd edition, A. John Wiley and Sons, 2009, Appendix E.

<sup>4</sup> Bissig, H., Tschannen, M., de Huu, M., *Traceable Response Time Characterization in Fast Changing Flow Rates*, Proceedings of the 10<sup>th</sup> International Symposium on Fluid Flow Measurement, Querétaro, Mexico, March 21 to 23, 2018.

# Automated Substitution Weighing Apparatus for Liquid Volume Measurement

J. D. Wright, S. D. Sheckels, and J. T. Boyd

*National Institute of Standards and Technology (NIST), 100 Bureau Drive, Gaithersburg, MD, USA 20899  
E-mail: john.wright@nist.gov*

---

The custody transfer of petroleum worth \$1 x 10<sup>12</sup> / year is traced to the volume delivered from provers and liquid test measures. Mistakes as small as 0.02 % in a custody meter calibration can lead to multi-million dollar corrections in bills. NIST presently uses the direct weighing method to measure the volume delivered from a test measure, by weighing (on a calibrated balance) the test measure when it is full of pure water and again after it has been drained. Recently, NIST reduced the uncertainty of its calibrations of volumes between 3.8 L and 40 L by constructing an automated substitution-weighing standard. The new standard reduces the mass measurement uncertainty by alternately placing 1) the test measure (unknown mass) and 2) approximately equal reference masses on the balance. Automated, pneumatically-driven hardware moves heavy liquid-filled volumes and reference masses on and off the weigh scale, thereby protecting the operator's safety and comfort. We describe the system's design, operation, uncertainty, and repeatability. The new standard was validated by comparison to NIST's well established direct weighing approach and by repeated calibration of a 38 L pipette during more than 2 years. The results are fully consistent with the 95 % confidence level uncertainty estimate of 0.007 % for the substitution weighing standard. Correlation between temperature and the volume of the 38 L pipette shows the need for improved environmental temperature control in the laboratory. We also describe the design of a set of four pipettes with an overflow filling system that can be used as references in an automated volume transfer standard.

---

## 1. Introduction

The NIST Fluid Metrology Group measures the volume of water delivered from test measures to provide impartial, System International traceability for petroleum custody transfer. NIST presently uses the direct weighing method for these calibrations, but has developed an automated substitution weighing standard for test measures from 3.8 L to 40 L that has uncertainty at least 6 times smaller. This paper describes the new standard and validates its performance by directly comparing it to the existing direct-weighing standard.

For the direct weighing method, a balance (weigh scale) is calibrated with reference masses and the balance is subsequently used to weigh the test measure: 1) when it is full of pure water and 2) after it is drained [1]. At NIST, a 60 kg balance is used to calibrate volumes 40 L or smaller and a 600 kg balance is used for volumes up to 380 L. Between periodic calibrations of the balance, it is evaluated with a check mass at mid-scale, and an error larger than 3 g triggers a new balance calibration. The 95 % confidence level uncertainty of the full and drained mass measurements is based on the 3 g tolerance and a rectangular probability distribution [ $u(m) = 2(3/\sqrt{3}) = 3.46$  g]. Usually, this 3.46 g uncertainty is the largest uncertainty component for test measures smaller than 40 L. The 95 % confidence level uncertainty of the delivered volume of a 3.8 L test measure is 0.32 % and for a 40 L test measure it is 0.04 %.

Single substitution weighing alternately places an unknown mass and a reference mass on a balance and uses the buoyancy-corrected reference mass and the ratio of the two balance readings to determine the unknown mass [2]. Substitution weighing is equivalent to calibrating the balance immediately before it is used to weigh the unknown mass and provides lower mass uncertainty. Our automated substitution weighing standard has uncertainty of 0.007 % or less (95 % confidence level).

We also describe a set of pipettes designed to serve as references for calibrations of test measures by volume transfer [1]. The pipettes have nominal volumes of 3.8 L, 19 L, 38 L, and 190 L. Our plan is to use the pipettes in various combinations to calibrate customer's test measures that are larger than 40 L. The pipette design is bottom-filled, has an overflow system for filling that produces a reproducible delivered volume, and is designed for automation. We present calibration results for the 38 L pipette from the substitution weighing standard that demonstrate the suitability of the design for low uncertainty volume transfer calibrations.

## 2. The Automated Substitution Weighing Standard

Figures 1 and 2 show the arrangement of equipment in the substitution weighing standard. Three aluminum plates can be placed on or off a 60 kg Mettler® balance by pneumatic actuators under the control of a data acquisition computer and a Labview program. The "bucket plate" is used to place a plastic bucket large enough to receive the delivered volume from a volume under test (VUT) on the balance. Plate #2 holds reference masses that produce approximately the same balance reading as the bucket plate when the bucket is drained. Plate #3 holds masses that produce a balance reading approximately equal to the bucket plate when the bucket is filled with water from the VUT. The pneumatic actuators (Motion Controls Inc, D12SERC SL1.5 RA1) are air driven in both directions (not spring return) and needle valves on the air inlets allow one to tune the speed that they move, thereby avoiding sudden impacts on the balance when the plate is lowered. Two wires run from a support post to the bucket plate to: 1) open or close the electrically-actuated drain valve (Plast-o-matic ¾ inch) on the collection bucket, and 2) measure the temperature of the water in the bucket. We hang the wires in a catenary shape to avoid significant changes in the forces imposed by these wires when the bucket plate is on the balance in the lowered position. Other temperature sensors measure the temperature in the volume under test. The reference masses used on Plates #2 and #3 are rectangular blocks of 316 stainless steel that were calibrated by substitution weighing and are traceable to the System International through US mass standards. A Vaisala PTU200 measures the room pressure, temperature, and relative humidity. These measurands are used to calculate the air density for buoyancy correction to mass.

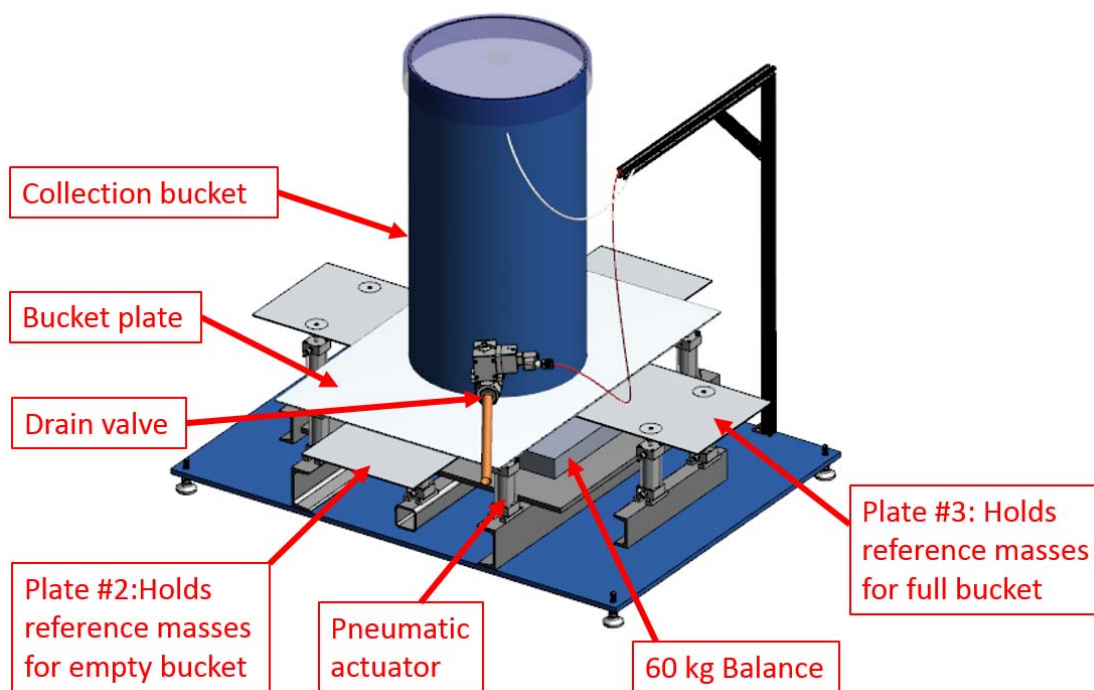


**Figure 1.** A drawing of the automated substitution weighing standard.

\* Certain commercial entities, equipment, or materials may be identified in this document in order to describe an experimental procedure or concept adequately. Such identification is not intended to imply recommendation or endorsement by the National Institute of Standards and Technology, nor is it intended to imply that the entities, materials, or equipment are necessarily the best available for the purpose.

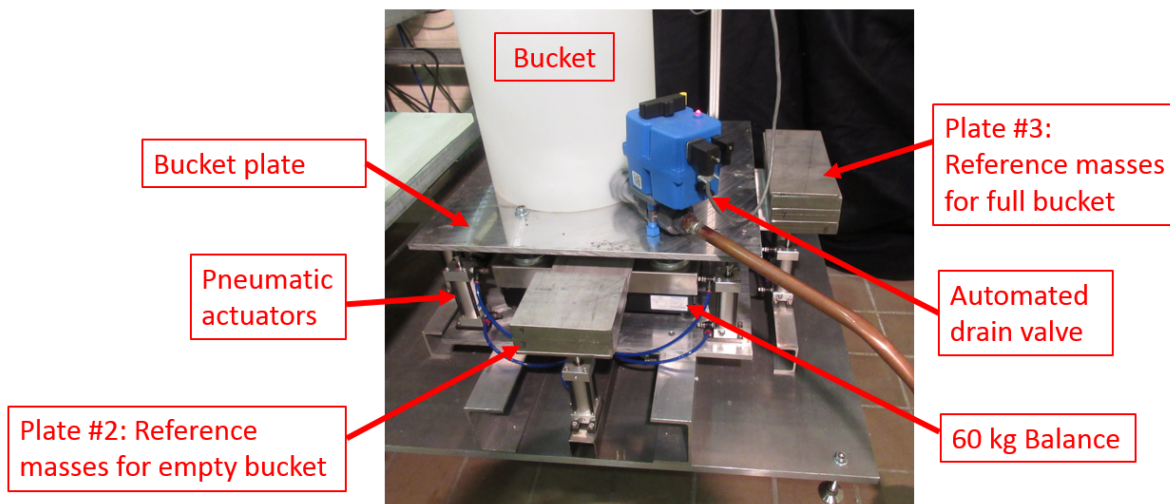


**Figure 2.** A picture of the automated substitution weighing standard.

A single volume calibration run using the substitution weighing standard has the following steps:

1. Place the VUT on a platform above the substitution weighing standard so that it can be drained by gravity into the collection bucket. Note that the VUT should be levelled, filled, and drained in the same manner as in normal use by the customer. The same drip time and if practical, the same plumbing on the drain should be used so that residual volume of liquid on the interior walls of the VUT is consistent during calibration and usage [3].
2. Check that the collection bucket is drained and the drain valve is closed. Lift all plates off the balance, wait 17 s or more for the balance reading to stabilize, re-zero the balance, and record the balance zero reading ( $R_{z1}$ ).
3. Lower the bucket plate (and the bucket) onto the balance. When stable, record the balance reading ( $R_{buc1}$ ).
4. Raise the bucket plate and when stable, record the balance zero reading ( $R_{z2}$ ).
5. Place reference masses of approximately equal weight as the bucket plate and empty bucket on Plate #2.
6. Lower Plate #2 and when stable, record the balance reading ( $R_{ref1}$ ).
7. Fill the VUT with pure water. NIST uses filtered, reverse-osmosis water so that literature correlations of water density as a function of temperature apply [4].
8. Wait for the VUT temperature sensor to reach thermal equilibrium with the water, and record the VUT water temperature. Record the volume registered by the VUT.
9. Transfer water from the VUT to the collection bucket. Take care that no water splashes out of the collection bucket during transfer from the VUT. The bucket has a lid with minimal openings to the room to reduce water loss by evaporation.
10. Raise Plate #2 and when stable, record the balance zero reading ( $R_{z3}$ ).
11. Lower the bucket plate onto the balance and when stable, record the balance reading ( $R_{buc2}$ ). Record the bucket water temperature and the environmental conditions: barometric pressure, room temperature, and relative humidity (for buoyancy corrections). Because the mass measurements are only weakly sensitive to the environmental conditions and change slowly, these values can be used for all mass buoyancy corrections for this run.
12. Raise the bucket plate and when stable, record the balance zero reading ( $R_{z4}$ ).
13. Place reference masses of approximately equal weight as the bucket plate and full bucket on Plate #3.
14. Lower Plate #3 and when stable, record the balance reading ( $R_{ref2}$ ).
15. Open the bucket valve to drain the bucket to prepare for the next run.

In a typical calibration, the appropriate steps above are repeated to produce 5 or more independent volume determinations to assess repeatability of the process.

The apparent mass of the drained bucket ( $m_{A,buc1}$ ) is calculated from the ratio of the zero-corrected readings for the bucket and reference masses multiplied by the apparent mass of the reference masses (Equation 1).

Note that the reference mass is both the stainless steel blocks and the aluminum plate supporting them, leading to:

$$m_{A,buc1} = \frac{(R_{buc1} - R_{z1})}{(R_{ref1} - R_{z2})} \left[ m_{ref,ss1} \left( 1 - \frac{\rho_{air}}{\rho_{ss}} \right) + m_{ref,Al1} \left( 1 - \frac{\rho_{air}}{\rho_{Al}} \right) \right], \quad (1)$$

where  $\rho_{air}$  is the density of the room air,  $m_{ref,ss1}$  and  $\rho_{ss}$  are the mass and density of the stainless steel reference masses, and  $m_{ref,Al1}$  and  $\rho_{Al}$  are the mass and density of the aluminum plate. Analogously, the apparent mass of the full bucket is:

$$m_{A,buc2} = \frac{(R_{buc2} - R_{z3})}{(R_{ref2} - R_{z4})} \left[ m_{ref,ss2} \left( 1 - \frac{\rho_{air}}{\rho_{ss}} \right) + m_{ref,Al2} \left( 1 - \frac{\rho_{air}}{\rho_{Al}} \right) \right]. \quad (2)$$

The density of air is calculated from the environmental pressure, temperature, and relative humidity measurements made during the calibration run. Once the apparent masses of the full and empty bucket are calculated, the volume of delivered water is calculated in the same manner as for the direct weighing method using Equations 4 and 5 in reference [1]. The 95 % confidence level uncertainty of the mass measurements for the direct weighing method is 3.46 g while the 95 % confidence level uncertainty via substitution weighing is less than 0.6 g, dominated by the uncertainty of the reference masses and balance non-linearity (10 parts in  $10^6$ ). The improvement in mass measurement reduces the expanded uncertainty ( $k = 2$ ) of the delivered volume measurement to 0.007 % or less.

We have compared volume measurements made by direct weighing and by the automated substitution weighing standard using three 20 L test measures, and the results are shown in Figure 3. Volume “A” is a slicker plate, Volume “B” is a pipette, and volume “C” is a neck scale test measure. The points in Figure 3 are based on averages of 5 or more volume measurements. The slicker plate and pipette show a six-fold improvement in uncertainty for the substitution weighing method. The neck scale test measure uncertainty is reduced by a factor of two: the poorer repeatability of the neck scale test measure relative to the slicker plate and pipette hamper uncertainty improvement somewhat. The volume measurements made by direct weighing and substitution weighing agree within 170 parts in  $10^6$ , 22 parts in  $10^6$ , and 6 parts in  $10^6$  for volumes A, B, and C respectively.

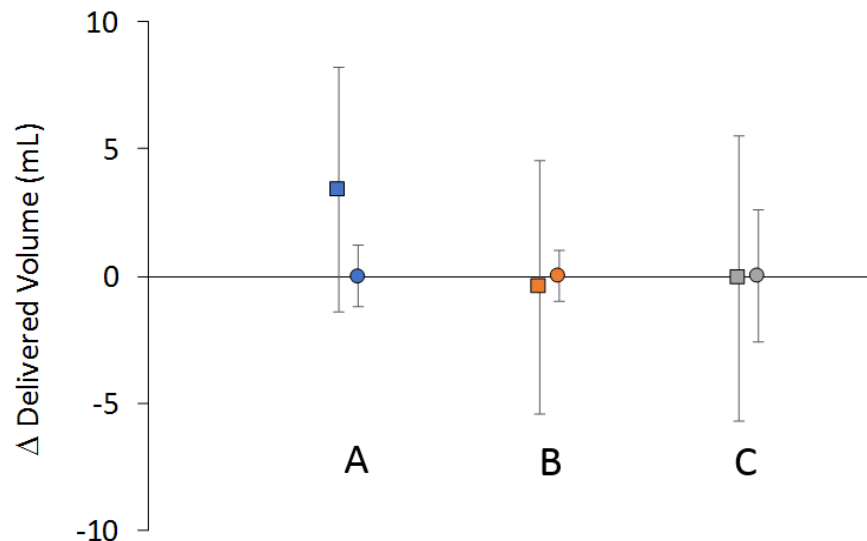


**Figure 3.** The difference in delivered volume from the direct weighing method (squares) and the automated substitution weighing standard (circles) for three 20 L test measures. Volume A is a slicker plate, volume B is a pipette, and volume C is a neck scale test measure.

### 3. Volume Transfer Pipettes

The NIST Fluid Metrology Group purchased four Seraphin Series P pipettes with nominal volumes of 3.8 L, 18.9 L, 38 L, and 189 L. With a suitable platform, we plan to calibrate these pipettes gravimetrically and then use them (in various combinations) to do volume transfer calibrations [1] of customer test measures. Figure 4(a) is a general view of the 38 L pipette where one can see the main body of the volume, the overflow system for filling, and one of the two thermowells for temperature sensors used to measure the water and pipette material

temperature. This temperature is used to calculate water density and to make thermal expansion corrections and give the VUT volume at the customer-specified reference temperature. Figure 4(b) shows the lower half of the pipette and the pneumatically actuated valves used to fill or drain the pipette via computer control. The valve is a weir-type valve made by ITT Industries that is designed to prevent any trapped air or liquid volumes in either the open or closed states. Figure 4(c) shows the overflow system that sets up a reproducible meniscus (and hence liquid volume) with the pipette. The pipette is bottom filled to reduce bubble formation. When the pipette is full, water flows out of the pipe labelled “meniscus” in Figure 4(c) and the float switch triggers the Labview program to close the fill valve. Water gravity-flows out of the overflow system through the pipe labelled “overflow” and later through a 3 mm “drain hole”. The small diameter drain hole slows the draining of the water from the overflow system and sets up a reproducible liquid level at the position labelled “meniscus”.

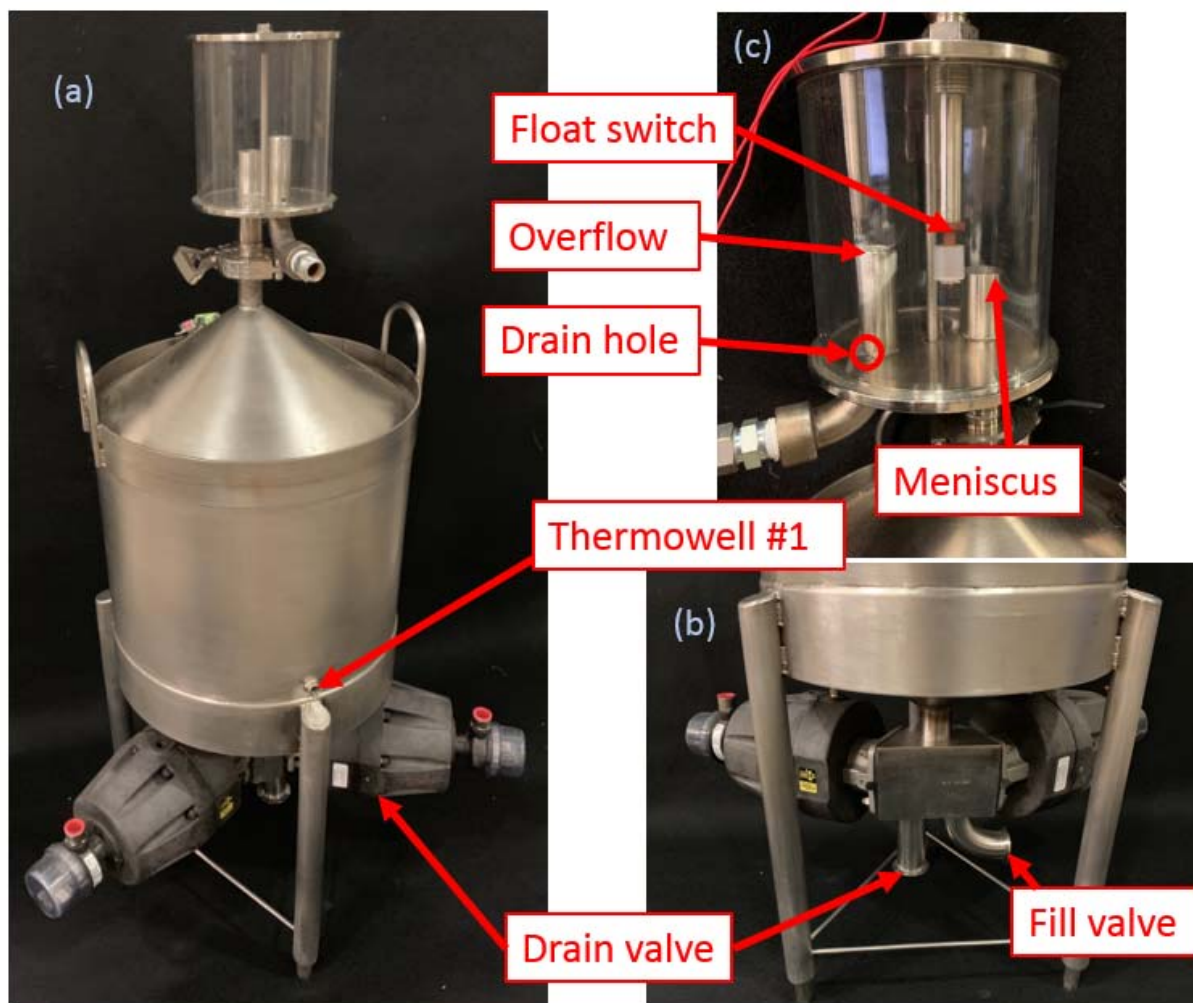


**Figure 4.** An overall view of the 38 L pipette (left), the actuated fill and drain valves (bottom right), and the overflow system (top right).

The 38 L pipette has been calibrated using the substitution weighing standard on 12 occasions spanning more than 2 years. The results are shown in Figure 5. The uncertainty bars in Figure 5 are the 95 % confidence level uncertainty of the volume calibrations (0.007 %). The standard deviation of the 5 measurements averaged to make each point in Figure 5 is 17 parts in  $10^6$  or less.

While the 12 volume values in Figure 5 agree within the uncertainty expectations, we searched the data for explanations for the 0.015 % changes over time. The room where the substitution weighing standard is presently located has poor environmental controls and the temperature in the room ranged from 17.9 °C to 26 °C depending on the season of the year. The reverse osmosis water is continuously pumped through filters and an ultraviolet light system to prevent bacterial growth in the water. The continuous pumping keeps the water about



---

<sup>2</sup> Jaeger, K. B. and Davis, R. S., *A Primer for Mass Metrology*, NBS Special Publication 700-1, November, 1984.

<sup>3</sup> Wright, J. D., Sheckels, S. D., Lachance, C., Sharifi, F., Falicki, A., and Ondoro, D., *The Effect of Liquid Kinematic Viscosity and Drain Time on the Volume Delivered from a Test Measure*, Proceedings of the 9<sup>th</sup> International Symposium on Fluid Flow Measurement, Arlington, Va, USA, April 14 to 17, 2015.

<sup>4</sup> Tanaka, M., Girard, G., Davis, R., Peuto, A., and Bignell, N., *Recommended Table for the Density of Water between 0 °C and 40°C Based on Recent Experimental Reports*, Metrologia, **38**, 2001.

# Primary Piston Prover Intercomparison Between PTB, VSL and FORCE Technology

Arnthor Gunnarsson<sup>1</sup>, Jos van der Grinten<sup>2</sup>,  
Mijndert van der Beek<sup>3</sup>, Bodo Mickan<sup>4</sup>

<sup>1</sup>FORCE Technology, Navervej 1, 6600 Vejen, Denmark

<sup>2</sup>Physikalisch-Technische Bundesanstalt, Bundesallee 100, D-38116 Braunschweig, Germany

<sup>3</sup>VSL, Thijsseweg 11, 2628 JA, Delft, The Netherlands

<sup>4</sup>Physikalisch-Technische Bundesanstalt, Bundesallee 100, D-38116 Braunschweig, Germany

E-mail (Arnthor Gunnarsson): agu@force.dk

---

## Abstract

The EuReGa members that use a Piston Prover as a primary calibration device (PTB, VSL and FORCE Technology) performed an intercomparison in 2018-2019. This paper will describe the Piston Provers used in the intercomparison after which the intercomparison results and their implication will be presented.

Degree of equivalence has been determined on multiple occasions in the past between the participants. What distinguishes this intercomparison from others is that it is performed with Piston Provers, which is the starting point in the respective participants traceability systems. This means that the CMC reported in the intercomparison is lower compared to previous intercomparisons between the participants, with reported CMC uncertainty between 0.07% and 0.086%. The traceability of the participants is independent from each other, since the results are directly traceable to the participants respective Piston Provers, the Piston Provers being primary calibration systems traceable to length.

EuReGa consists of four members with established traceability chains, LNE-LADG, PTB, FORCE Technology and VSL. LNE-LADG did not participate in the intercomparison because they use a PVTt system to establish their traceability.

The results support the CMC claims of the participants, showing that also at the starting point in the traceability, and therefore at the low end of the uncertainty spectre of the participants, there are acceptable differences between the members of EuReGa. The intercomparison report for this project has been submitted under EURAMET project no. 1301 which forms a basis for this report [1].

---

## 1. Introduction

Every three years the members of EuReGa perform a harmonization exercise for high-pressure flows of natural gas [2], [3], [4]. In the harmonization, equivalence has been demonstrated between the four EuReGa members and the differences between the laboratories are minimized through harmonizing. This project describes the results of an intercomparison using the primary standards, which are the first step in the respective participants' traceability chains. Consequently, this intercomparison has been performed at the lowest uncertainty levels achievable by the participants. Unfortunately, the French colleagues cannot participate in this intercomparison as their primary is a PVTt system. However, LNE-LADG, PTB, NIM and NIST did perform a primary intercomparison in 2015 [5]. So, using the intercomparison from 2015 and this Piston Prover intercomparison, the circle can be closed with PTB as the connecting institute in both intercomparisons.

Thus equivalence can be determined between all EuReGa members at a low uncertainty.

The meters used in this intercomparison are two of the meters used in the harmonization exercise and have been used in many intercomparisons in the past. Data from this intercomparison can be used with results from previous harmonization exercises to be analysed. Dependent on there being noticeable differences between those results, that can be used to identify where differences occur in the participants respective traceability systems.

## 2. Participants' Piston Provers

All participants in the intercomparison use a Piston Prover as a primary reference. PTB uses a 10" gas-gas Piston Prover (HPPP), it consists of a honed 250 mm diameter in which a piston can travel at a maximum speed of 3 m/s (approx. 480 m<sup>3</sup>/h) over a length of 6 m with an effective measurement length of 3 m. VSL uses a 24" gas-oil Piston Prover

(GOPP). The prover is filled with oil on one side and gas on the other side of the free moving piston. The maximum flowrate is 230 m<sup>3</sup>/h. Finally, FORCE Technology uses a 26" Twin gas-gas Piston Prover with two parallel cylinders with bidirectional pistons inside them. The actuated pistons can displace up to 400 m<sup>3</sup>/h. The characteristics of the provers can be seen in Table 1. [1]

**Table 1:** Characteristics of the participants piston provers.

Institute	VSL	PTB	FORCE
Primary device	24" Gas Oil Piston Prover (GOPP)	10" Piston Prover (HPPP)	26" Twin Piston Prover
Piston	Passive	Passive	Active
Nominal diameter	600 mm	250 mm	660 mm
Absolute operating pressure	1 – 62 bar	8-51 bar	1-66 bar
Piston stroke / effective stroke	12 m / 6.5 m	6 m / 3 m	2.8 m / 0.6-2.7 m
Flowrate range	3 – 230 m <sup>3</sup> /h	3 – 480 m <sup>3</sup> /h	2 – 400 m <sup>3</sup> /h
Maximum piston speed	0.25 m/s	3 m/s	0.17 m/s
CMC	0.070 0.086%	– 0.065 %	0.080 %

### 3. Transfer Meters and Test Protocol

Both meter packages used in this intercomparison consist of a G250 turbine meter with a fixed upstream flow conditioner, upstream spool and downstream spool with thermowell. The meter packages are designated EuReGa DN100 M1 and EuReGa DN100 M2. They are normally used in the EuReGa intercomparison every three years, the last time in 2017 and 2018 [2]. In this intercomparison, the packages were calibrated individually, not in series. The meters were calibrated at flowrates 25, 40, 65, 100, 160, 250 and 400 m<sup>3</sup>/h at absolute pressures of 8, 20 and 50 bar. At each flowrate the laboratories report the meter deviation  $e$ , which is the average of four or five successive measurements, and its expanded measurement uncertainty. PTB and FORCE cover the entire range while VSL covers the range up to 200 m<sup>3</sup>/h. In addition, VSL calibrated one meter package: EuReGa DN100 M2. [1]

In 2013, the EUREGA group published a review about the long-term performance of the transfer standards used in the harmonisation **Error! Reference source not found..** The outcome for the G250 meters was a random drift of approximately 0.1 % within 6 years or 5 applications in intercomparison rounds respectively. Assuming a pure random process (what is justified by the data base), we can

conclude an additional uncertainty contributed by the transfer meters at a level of 0.05% per intercomparison round.

### 4. Data Processing

The processing of the measurement data was done according to [6]. For each pressure and flowrate the average error of all successive measurements performed by laboratory  $i$  is  $e_{lab\ i,flow\ j}$ . The associated uncertainty  $U_{lab\ i,flow\ j}$  is calculated as the reported lab uncertainty  $U_{(lab\ i,flow\ j)}$  with the added meter stability (drift),  $U_{meter}$  uncertainty of 0.05% based on section 3.

$$U(e_{lab\ i,flow\ j}) = \sqrt{U_{(lab\ i,flow\ j)}^2 + U_{meter}^2} \quad (1)$$

For each laboratory a weighing factor  $w_{lab\ i,flow\ j}$  is calculated according to equation (2).

$$w_{lab\ i,flow\ j} = \frac{1}{U_{lab\ i,flow\ j}^2} \quad (2)$$

The sum of the weighing factor for each flowrate is

$$W_{flow\ j} = \sum_i w_{lab\ i,flow\ j} \quad (3)$$

They are used along with each laboratory's average error  $e_{lab\ i,flow\ j}$  to calculate a weighted mean error  $\bar{e}$  also called comparison reference value (CRV).

$$\bar{e}_{flow\ j} = \frac{1}{W_{flow\ j}} \sum_i w_{lab\ i,flow\ j} e_{lab\ i,flow\ j} \quad (4)$$

The uncertainty of each  $\bar{e}_{flow\ j}$  is then calculated by

$$U(\bar{e}_{flow\ j}) = \sqrt{\frac{1}{W_{flow\ j}}} \quad (5)$$

Based on each laboratory's average error  $e_{lab\ i,flow\ j}$  and the weighted mean error  $\bar{e}$ , the difference  $d_{lab\ i,flow\ j}$  is calculated for each laboratory's pressure and flow:

$$d_{lab\ i,flow\ j} = e_{lab\ i,flow\ j} - \bar{e}_{flow\ j} \quad (6)$$

Based on the values for each flow, a chi-squared test for consistency can be performed. The chi-squared test is a statistical method that in this case is performed to investigate if the observed differences correspond to what can be expected with regards to the uncertainty and it being reported with 95% confidence. This has been performed in established key comparisons in the past, see [7]. Equation (7) shows how the  $\chi_{obs}^2$  is calculated:

$$\chi_{obs,flow\ j}^2 = \sum_i \frac{d_{lab\ i,flow\ j}^2}{\left(\frac{U(e_{lab\ i,flow\ j})}{2}\right)^2} \quad (7)$$

The chi-squared consistency check fails if,  $Pr\{\chi_v^2 > \chi_{obs}^2\} < 0.05$  which corresponds to  $CHIINV(0.05; v) < \chi_{obs}^2$ . If the consistency check passes, then the CRV is accepted, but if it fails, then the laboratory with the highest value of  $\frac{d_{lab\ i,flow\ j}^2}{\left(\frac{U(e_{lab\ i,flow\ j})}{2}\right)^2}$  is excluded in the calculation of the CRV for that specific flowpoint. This means that a new calculation of the CRV is performed in that flowpoint according to equation (4), with one laboratory excluded.

For the non-excluded results, the uncertainty of the difference is obtained by

$$U(d_{lab\ i,flow\ j}) = \sqrt{U(e_{lab\ i,flow\ j})^2 - U(\bar{e}_{flow\ j})^2} \quad (8)$$

The uncertainty of a laboratory with excluded results in a flowpoint is

$$U(d_{lab\ i,flow\ j}) = \sqrt{U(e_{lab\ i,flow\ j})^2 + U(\bar{e}_{flow\ j})^2} \quad (9)$$

The only difference between equation (8) and (9) is the sign in the right-hand-side of the equation, which leads to higher uncertainties for the excluded data points. Finally, based on equations (6, 8 and 9), the degree of equivalence  $E_{N,lab\ i,flow\ j}$ , also called normalized deviation, can be determined by

$$E_{N,lab\ i,flow\ j} = \frac{|d_{lab\ i,flow\ j}|}{U(d_{lab\ i,flow\ j})} \quad (10)$$

## 5. Results

In total there were 102 points and therefore 102 differences and normalized differences ( $E_N$  values). The calibration results with Reynolds number on the x-axis are shown in figures 1 and 2. The results can be seen as points and a Reynolds fit is included with 95% uncertainty contours.

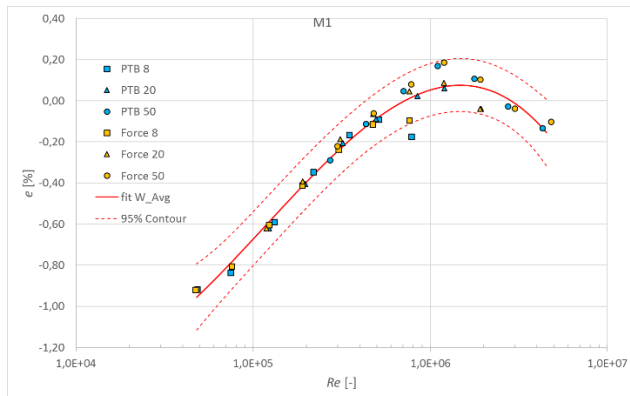


**Figure 1:** Calibration results of DN100 M1. The observed meter error  $e$  [%] is plotted versus the Reynolds number  $Re$  [-]. The

solid line is the least-squares fit and the dashed lines represent the 95% uncertainty contours.

The contour uncertainty is approximately 2.4 times higher for M1 than for M2, note that the range on the y-axis is considerably higher for M1. So, although there are more points outside of the uncertainty contours for M2, this is because the contour uncertainty is low. The uncertainty contours are an indication of how well the Reynolds fit actually represents the CRV for each flow point. Thus, M2's errors fit well to a Reynolds curve while M1 has some differences, especially in the boundary layer (high and low flowrates for each pressure) when comparing the CRV for each flow point with the Reynolds fit.

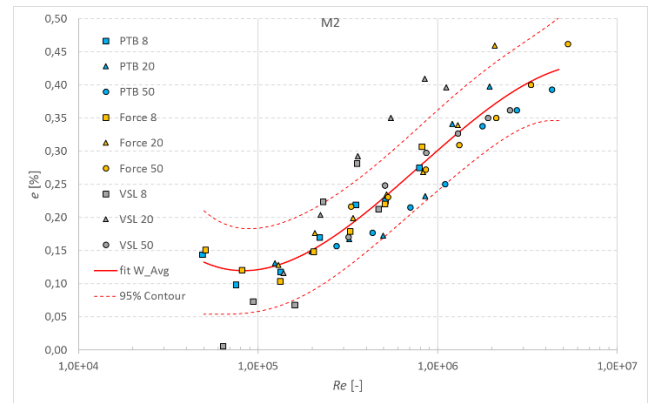


**Figure 2:** Calibration results of DN100 M2. The observed meter error  $e$  [%] is plotted versus the Reynolds number  $Re$  [-]. The solid line is the least-squares fit and the dashed lines represent the 95% uncertainty contours.

After calculating the differences, the chi-squared consistency check was performed where it was found that three points should be excluded. After excluding the three values in calculation of the CRV, the consistency check for the points was accepted. Note that the polynomials in figures 1 and 2 are based on the results after exclusion of the three points.

The differences  $d$  are shown in Figure 3 and the  $E_N$  values are shown in Figure 4. Both are plotted with Reynolds number  $Re$  on the x-axis.

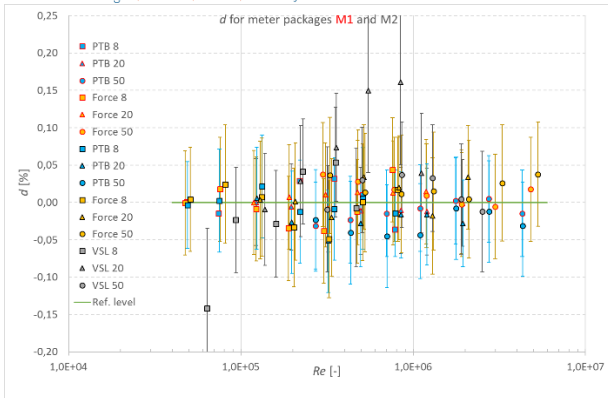


**Figure 3:** Differences  $d$  [%] with their respective expanded uncertainties shown as vertical bars versus the  $Re$  number [-].

Disregarding the three excluded points, the differences  $d$  are in the range  $-0.052\%$  to  $0.074\%$ . Additionally, PTB has an average difference  $d$  of  $-0.011\%$ , FORCE's average  $d$  is  $0.007\%$  and finally VSL has an average difference  $d$  of  $0.023\%$ . With different traceability systems, there can be systematic differences between the participants. It is evident that with these average differences that the systematic difference between the participants is low but the spread means that some of the differences are higher than what can be expected with these low reported uncertainties.

Figure 4 shows the normalized deviations ( $E_N$  values) for the intercomparison.

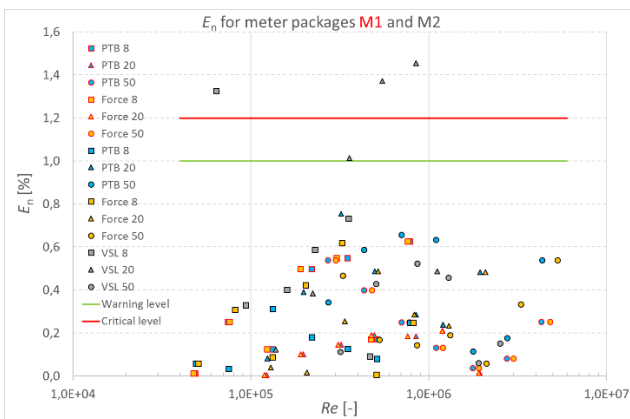


**Figure 4:**  $E_N$  values versus  $Re$  number. The green horizontal line is the warning level corresponding to  $E_N = 1$ . The horizontal red line is the critical level corresponding to  $E_N = 1.2$ .

**Table 2:** Frequency distribution of observed  $E_N$  values.

Histogram bin	Number	Percentage
$0 \leq E_N \leq 0.5$	82	80%
$0.5 < E_N \leq 1$	16	16%
$1 < E_N \leq 1.2$	1	1%
$1.2 < E_N$	3	3%

Table 2 shows the frequency distribution of the observed  $E_N$  values. The table shows that 96% of the results matches  $E_N \leq 1$ , 80% even matching  $E_N \leq 0.5$ . 3% of the  $E_N$  values lies above the critical level with the highest one being 1.45. The observed frequency distribution is consistent with the 95% confidence level of the applied statistics.

## 6. Discussion and Comparison with Historic Results

The present intercomparison demonstrates the equivalence of the primary standards. However, some test points of VSL had to be treated as outliers. Possible causes for the deviating behaviour of the calibration include:

- 1) The GOPP of VSL is designed and optimised to operate with rotary meters. Turbine meters might not be able to follow small irregularities in the applied flow rate as well as rotary meters would. This might cause over spinning of the turbine wheel.
- 2) The GOPP was operated at different temperatures than the primary standards of FORCE and PTB. A correction for the influence of the temperature on the meter dimensions and meter behaviour have been applied. These corrections could possibly be further improved.

An additional comparison between Force and VSL is currently being planned. This comparison will use rotary meters instead of turbine meters and will include an additional pressure of 61 bar.

The present intercomparison was performed with primary standards at an uncertainty level of  $0.070\% - 0.086\%$ . The observed variability of the results is consistent with the present CMCs. How much do the calibration results diverge as we go further down the traceability chains of the participants? Since the primary intercomparison can be used in conjunction with intercomparisons later in the traceability systems to measure this diversion of results, how can this be minimized? These are questions that could be of great value to investigate to better understand the respective participants traceability systems.

Since the same meter packages were also used in the 2017 EuReGa harmonization process, the results from 2017 can be compared with the results of this piston prover intercomparison. Figure 5 shows the difference between the weighted average of the meters from this Piston Prover intercomparison finalized in 2019 and the EuReGa intercomparison from 2017.

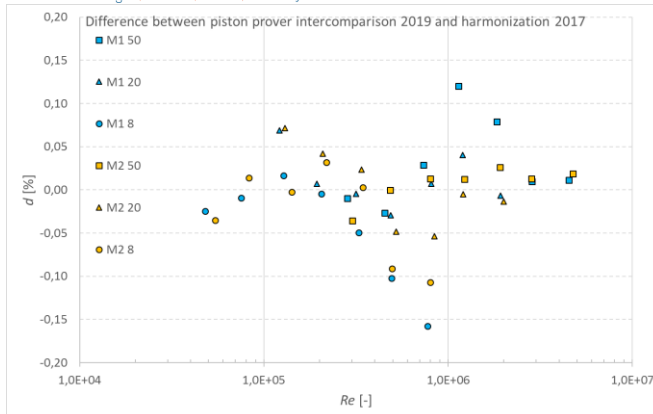


**Figure 5:** Differences between the weighted average of the Piston Prover intercomparison and the weighted average of the EuReGa intercomparison from 2017 using the same meters.

The results show that the average difference between the 2019 and 2017 comparison reference values results is -0.004%, which is small compared to the CMC values. Additionally, 50% of the absolute differences are lower than 0.024% and 95% of the absolute differences below 0.11% the maximum difference being 0.16%.

## 7. Conclusion

The results between the participants have been reported with a 95% confidence. With 96% of the  $E_N$  values lower than 1, the results are compliant. Taking into account the reasoning behind some of the high  $E_N$  values, the results support the CMC claims of the participants. Additionally, the results in this intercomparison match historic results with the same meters. This intercomparison can thus be regarded a successful demonstration of the CMC's of the participants. And as was mentioned in section 1, LNE-LADG, PTB and NIST performed a successful intercomparison in 2015 [5]. With these two intercomparison all four members of EuReGa are included and PTB is the connecting institute in both intercomparisons, This means that also at the low end of the uncertainty spectrum, there are acceptable differences between the members of EuReGa.

## Acknowledgements

The authors wish to thank their colleagues Henri Foulon, Christophe Windenberger, Abderrahim Ouerdani (LNE-LADG), Jesper Busk (FORCE), Detlef Vieth (Pigsar) and Roy van Hartingsveld (Euroloop) for their continuous support and encouragement.

## References

[1] Jos van der Grinten, Arnthor Gunnarsson, Mijndert van der Beek and Bodo Mickan, "Intercomparison of primary high pressure flow

standards", EuReGa Communiqué No 3, EURAMET F1301, 2019,

<https://tinyurl.com/y39lx5ud>.

[2] Jos van der Grinten, Henri Foulon, Arnthor Gunnarsson, Bodo Mickan (2018): Reducing measurement uncertainties of high-pressure gas flow calibrations by using reference values based on multiple independent traceability chains, *Technisches Messen*, **85**(12), pp 754-763.

<https://doi.org/10.1515/teme-2018-0019>

[3] EuReGa, "EuReGa Communiqué No. 2 (2018): Harmonized Reference Value 2018", Euramet F1301, <https://tinyurl.com/yyzhh58l>

[4] EuReGa. "Traceability chains of EuReGa Participants for high-pressure natural gas", EuReGa White Paper, Euramet F1301, 2018

<https://tinyurl.com/y98xzpad>

[5] B. Mickan, M. van der Beek, J-P. Vallet, "Review of the European Harmonised Cubic Meter 1999 – 2012", 16<sup>th</sup> International Flow Measurement Conference, FLOMEKO, Paris, 24-26 September 2013, France.

[6] Cox, M. G. [The evaluation of key comparison data](#), *Metrologia*, **39**(6), pp 589-595, 2002.

[7] Miroslava Benková et al., "[CIPM key comparison CCM.FF-K6.2011, Comparison of Primary \(National\) Standards of Low-Pressure Gas Flow](#)", *Metrologia*, **51**(1A), pp 07004-07004 doi:10.1088/0026-1394/51/1a/07004

# Reproduction of air velocity in the entrance region of the pipe

N. Pedisius<sup>1</sup>, A. Bertasiene<sup>1</sup>

<sup>1</sup>Lithuanian Energy Institute, Breslaujos str. 3, Kaunas, Lithuania  
E-mail (corresponding authors): [agne.bertasiene@lei.lt](mailto:agne.bertasiene@lei.lt)

---

## Abstract

Information about the airflow development in pipes in the entrance region is still not thoroughly investigated due to the complexity and restricted access for experiments. However, the reproduction of air velocity values, as well as calibration of the devices, is usually made in free streams from the nozzles or in the entrance region of the channels (pipes). In this study, different flow regimes have been investigated using different air velocity measurement methods for mean velocity to define. Experimental and numerical results in the entrance region of the pipe and in the test chamber of higher dimensions give a broad spectrum of information about the developing flow. Ultrasonic anemometer (UA) installed into the entrance region of the aerodynamic test facility shows reliable and highly comparable results in a wide range of velocities with another non-intrusive method – laser Doppler velocimetry (LDA). Due to the fast response, it enabled to analyse fluctuations in the flow. The mean air velocity values were determined from the single path sound propagation time in the pipe with a defined distance between the transducers placed at an angle of 45 degrees with the main axis. Local vortices identified in the flow might have influenced the low-frequency fluctuations and the scatter of measurement results. Moreover, high-frequency fluctuations found in the flow originated from the flow turbulence and the electronic or acoustic noise. The stabilisation of the entrance region and the boundary layer of the pipe influenced mean velocity value, velocity distribution and axial velocity development in different test sections of the pipe. Along with the recirculation zones in cavities of ultrasonic transducers they are the essential impact factors on velocity value defined.

---

## 1. Introduction

The airflow distribution is one of the most important characteristics used to judge the internal structure of the flow, the intensity of the mass and heat transfer processes and energy consumption. National laboratories initiate studies aimed at harmonizing the conditions and procedures for the investigation of various physical quantities, like pressure, temperature, air speed, humidity etc. measurements thus ensuring a high level of measurement accuracy with ever-increasing demands on it. Due to the lack of airflow field research, it is difficult to identify sources that influence airspeed reproduction under different conditions and provide a high level of accuracy that is important for international traceability linked to practical challenges, the transfer of accurate metrological parameters, the fulfilment of legally regulated conditions, and operational functionality. Airspeed is one of the most common measures in practice, which allows evaluating the health and safety conditions at workplaces, to ensure safe

work in the air and seaports and the functioning of lifting mechanisms, as well as measurements of emissions to the environment and wind energy [1]. However, different measuring instruments with different spatial and temporal characteristics provide different parameters and allow for different treatment of the flow. The main problem is how to determine the influence of the flow structure on the accuracy of the measurement result covering a specific and wide range of air velocities. It comes from the scientific, industrial and economic needs of the country that must meet the measurement levels achieved by National Measurement Institutes (NMI) within the European countries or even globally (USA, Japan, China etc.) as well. The EU NMIs, responsible for the international measurement interface, proper market functioning and the competitiveness of the production in a certain country, are making systematic investigations but more confined to legitimizing a particular device or studies based on measurement comparisons aiming to standardize measurements conditions and procedures of different physical

quantities. However, methodological actions to standardize the impact factors that define the structure of the flow, changes in it and the characteristics (or response) of the measuring instruments consistently are scarce. Recently some specific research activities [2-4] within the metrology platform arose on that purpose but still encounter difficulties in definition of certain and essential impact factors evoking result scattering. Nevertheless, differences in airflow reproduction conditions should be emphasized as the key factor.

In this case, the analysis and discussions remark the changes of flow structure in the entrance (developing) region of the pipe after convergent nozzles and rectangular chambers. Section 2 consists of a representation of wind tunnel specific features. Section 3 reveals the discussion concerning reproduction of air velocity value based on different measurement methods concluding into main factors emerging result scattering and flow development in the entrance region specific features. In the last section 4 the conclusions and future prospects are highlighted.

## 2. Experimental setup

Mostly used wind tunnels for airspeed measurement consist of the test section of the type like free streams, open test chambers after the closed loop and fully closed conduits with either round or rectangular shape [5-7]. All of them are restricted due to the cross-sectional area for devices under test (DUT) to place.

The aim of this investigation is to develop stable and controllable conditions reproducing low-velocity values under two different conditions. In many of analysed studies [5-8], the range of low velocities is very distinct, thus in this work, the boundaries are from 5 cm/s to 30 m/s covering the laminar, transitional and turbulent flow regimes. Experimental investigations were performed in the test facility (Figure 1, a) in the entrance region of the round channel (i.e. a pipe) with the diameter of 400 mm (D) and in the free stream from the pipe into the chamber with the length, height and width of 1000 mm (Figure 1, b). The test section as the semi-closed aerodynamic facility conditions treated due to the existing chamber. High contraction ratio of convergent nozzle (CN) (1650 / 400 mm) and the set of flow straighteners ensured low turbulence degree of about 0.5-1 % for higher than 1 m/s (later discussed more in Chapter 3). Moreover, the uniform velocity distribution in the largest part of the channel cross-section maintains the flat core along the channels' length up to the

outlet into the chamber and within it for at least 1 D.

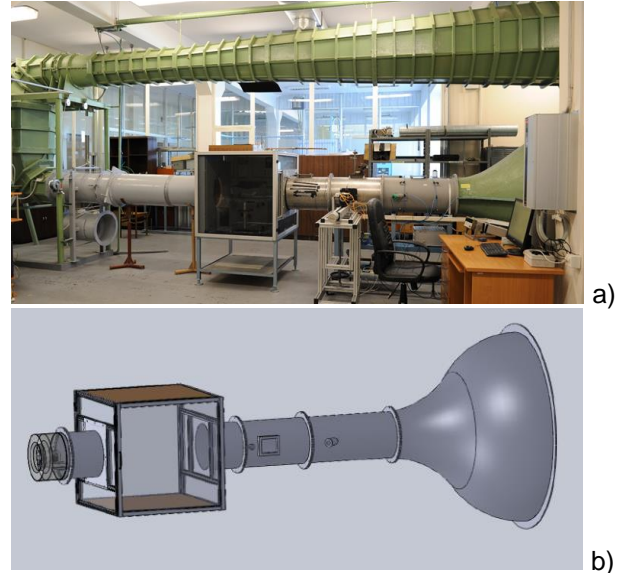


**Figure 1:** air velocity test facility general view (a) and measurement channel with CN, the straight channel and the chamber of enlarged dimensions (b)

As the main measurements are performed at the entrance region of the pipe the transversal velocity distribution is not evolved into the shape of the fully developed laminar or turbulent profile. Consequently, it is essential to have them clearly defined beforehand as the testing devices are located 1-4 D after the CN in the straight channel. The single path ultrasonic anemometer (UA) as one of the working standards is based at the distance of 1 D from the CN and the test section for laser Doppler anemometer (LDA) as the main standard is at 3 D where all DUTs are normally placed. UA anemometer gives the average velocity values as it measures velocity value at a certain angle with the axis, in this case at 45°, along some certain distance, here of 0.57 m. The transducers of UA are placed in the niches outside the pipe in order not to disturb the flow. Niches are covered with specific grids to weaken the vortices in these cavities. CN is a very accurate mean of velocity reproduction through the differential pressure measurements well related to the primary standard LDA as well as the UA. Having predefined relations of UA, CN and LDA any measurement in the test channel from the UA plane up to the chamber centre (6 D) has clear and certain evaluation with proper uncertainty level. The blockage or shielding effects with the available wake regions are also evaluated for the most common measurement devices as the hot wire anemometers of different types and the Pitot tubes of different forms with some rotating anemometers with the appropriate diameters suitable for the test section [1, 4, 9]. The

limitation concerning the dimensions of DUT in the testing plane is no more than 0.06. This is the ration of the frontal area of the DUT and the pipe taking into consideration 10 % as for open test sections.

### 3. Flow development in the entrance region. Discussion on the experimental and numerical results

The peculiarities of the entrance region, in this case, is summarized in this section and is highlighted especially for the most sensitive velocity value regions. Velocity distribution transversally and axial flow development with the turbulence degree variations are represented. Some comparison is made of experimental results with the numerical simulation based on ANSYS Fluent commercial package (CFD).

The main experimental results are from the airflow measurements in the test pipe section and the chamber using the LDA. Well-defined flow core in the pipe is evident from the velocity profiles made gradually in the straight pipe, and the chamber, for wide velocity range. As the core region of velocity distribution for higher velocities, starting from 1 m/s up to 30 m/s is not changing significantly even at different planes of the pipe (1-4 D) and in the chamber (5-7 D), basic results are depicted for lower velocities than the maximum possible value where changes and fluctuations exist.

It is clearly evident from the LDA time records, the profiles and the turbulence distributions that the test facility enables stable and repeatable air velocity values with a certain core region transversely (Figure 2) and longitudinally (Figure 3-4). Taking into consideration laminar-transitional flow regime it should be emphasized that some velocity values up to approx. 8 cm/s have not very flat profile at the centre and suffer from specific concave form, sometimes even slightly fluctuating. It is also observed in CFD results (Figure 3) though with all models in ANSYS Fluent 17.2 calculated this kind of concavity exists for higher velocities as well. Experimental results for higher than 0.1 m/s do not show it. Numerically investigated transition in pipes is represented by spatial or temporal coherent structures of vortices or travelling waves [10-12] but for experimental case transition results in contradictory states depending much on initial conditions and observation time.

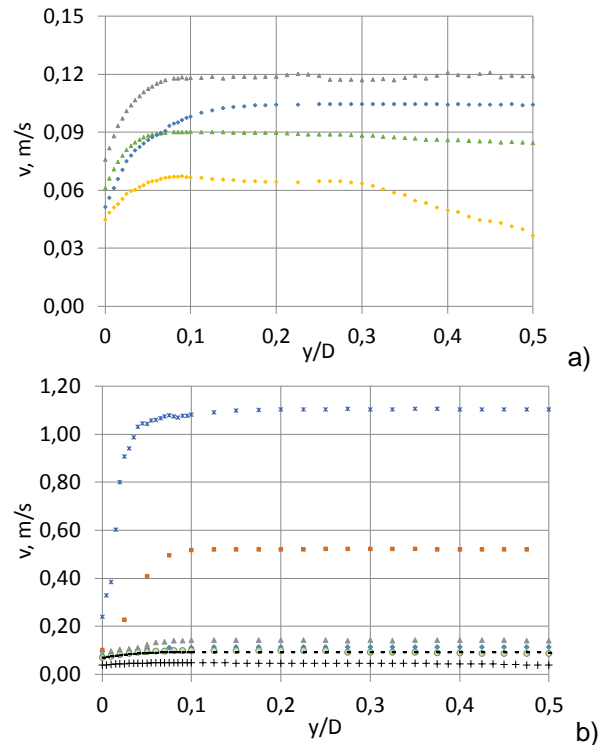


**Figure 2:** Velocity distribution across the diameter of the pipe. Different flow velocity and regimes: a) laminar-transitional flow, b) transitional to turbulent flow

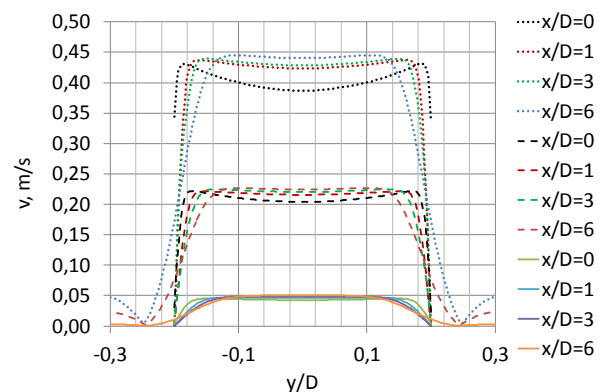


**Figure 3:** Velocity distribution across the diameter of the pipe for different flow velocity (0.45; 0.22 and 0.05 m/s) and axial distances from the inlet ( $x/D=0$ ) up to the centre of the chamber of higher dimensions ( $x/D=6$ ). The CFD results

The measured profiles in the test facility have a flat profile that covers 80-90 % of the cross section of the pipe diameter. Comparing experimental and simulation results could be stated similar distributions either in the pipe or in the test chamber (Figure 4). For testing simplicity velocity value in the test chamber is selected 10 m/s and compared with simulated value of 8.5 m/s that do not differ from each other due to the same flow regime selected and do not suffer from transition effects.

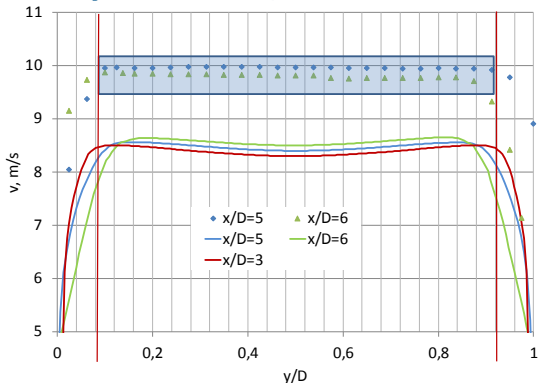


**Figure 4:** Comparison of velocity distribution calculated and measured at the outlet of the pipe ( $x/D=5$ ) and in the centre of the chamber ( $x/D=6$ ). In the CFD results  $x/D=3$  plane is the measurement plane of the LDA in the pipe

To analyse in details the changes of the flow in the chamber CFD results make it easier to reveal. A clear development of vortices in the chamber corners is noticed from Figure 5 which represents three different flow regimes. It should be noticed that in some regimes different simulation models slightly differs resulting in either still several vortices structure or one vortex in the whole chamber cavity above and under the core region covering not only one corner. As the chamber has an axial symmetry only one side of the chamber is shown in the pictures. Single elongated vortex from the almost laminar case of 0.05 m/s (a) is evolving into a several vortices in case of 0.2 m/s (b) (still transition flow regime) that develop from the right towards the left corner of the chamber near the outlet of the pipe. While transition to turbulent case with velocity value of 0.45 m/s (c) has already formed vortex covering the whole space of the side chamber niche. It is also clearly evident that flow core in the chamber is narrowing reaching the centre and more approaching the inlet to the pipe again.

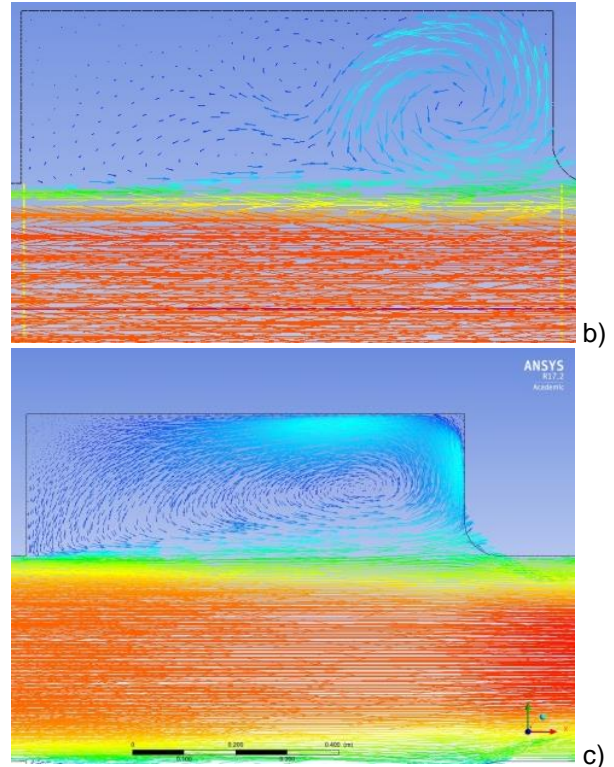
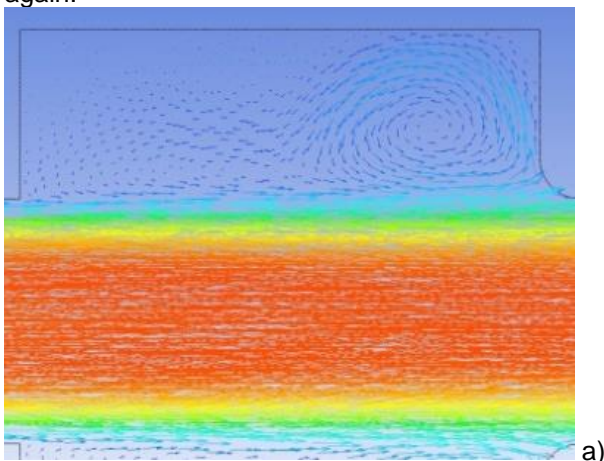


**Figure 5:** Comparison of velocity development in the chamber calculated for different flow regimes. Velocity value is in a) 0.05; b) 0.22; c) 0.45

Flow regime changes can also be noticed from the time records from LDA in Figure 6. Laminar to transition regime is accompanied with accidental disturbances. Similar results are gained using UA records. Due to its high response to fluctuation in the flow and measuring them not across the pipe but with an angle and quite a long distance low and high frequency pulsations may be raised due to some temperature effects, flow recirculation in the niches of the transducers or flow turbulence and noise in electric and acoustic fields.

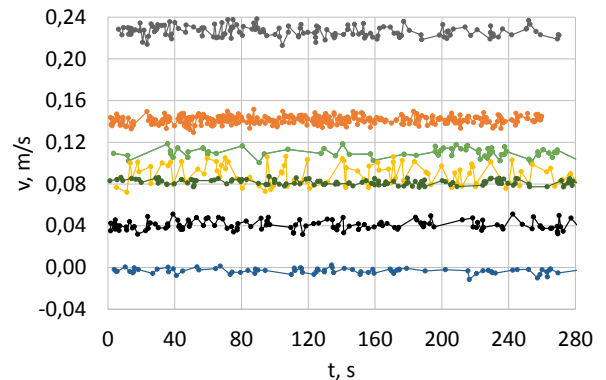


**Figure 6:** LDA time records for a series of velocities.

Wind tunnels of different types and configurations are presented with the very different degree of turbulence. Very low turbulence degree of 0.07 %

is declared in the laboratory of NIST [7]. However, starting from the velocity value of 0.2 m/s is not clear if this turbulence degree is for this velocity as it is stated that this degree is for the most air speed range that is up to 75 m/s. In this wind tunnel turbulence is higher due to some reasons and differs much on conditions and flow regimes. Figure 7 represents turbulence degree variations at different planes from the pipe to the chamber and different conditions for velocity to be achieved. It is noticed that turbulence degree is slightly increasing with the approach to the outlet of the pipe ( $x/D$  from 1 to 4.5). Moreover, with the decrease of velocity value it increases more significant starting from 0.5 m/s and extremely from 0.2 m/s. It also depends on velocity reproduction case as two different fans are used for low and higher velocities to achieve, as well as additional different grids are inserted to stabilize velocity fluctuations. Consequently, these grids increase the degree of turbulence. It is evident from the results for low velocities reproduced using different fan without any additional grid (fan 1, Figure 7). Distribution of turbulence degree across the pipe shows results relative to the velocity distribution (Figure 8). Consequently, with the decrease of velocity value approaching the wall, turbulence degree is increasing.

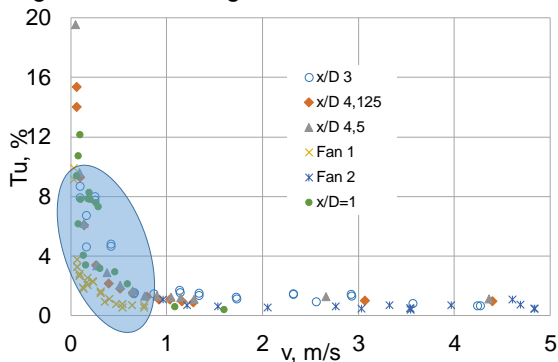


Figure 7. Turbulence degree at different planes and conditions. Fan 1 and 2 are different fans used to achieve lower and higher velocities, respectively

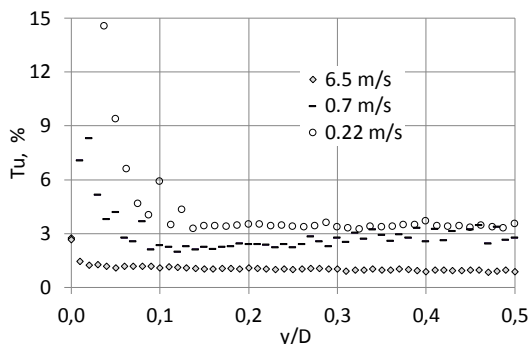
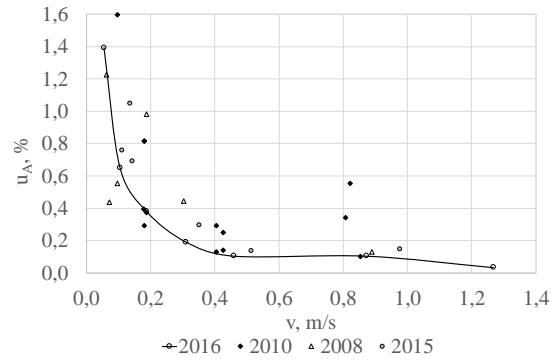
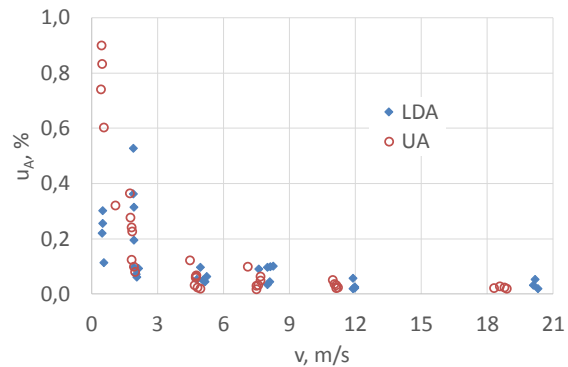


Figure 8. Distribution of turbulence degree across the pipe for different velocity values

Concluding about the flow stability and air velocity reproduction in the test facility from the results of LDA and UA repeatability is calculated and it shows the same tendency and level during the last ten years (Figure 9).



a)



b)

Figure 9. Standard type A uncertainty results: a) 2008-2016 years, LDA; b) 2018-2019 years, LDA and UA

The results of both standards (LDA and UA) show good agreement and repeatability except very low velocity range. This is a consequence of several factors such as flow regime, mean velocity definition procedure and recirculation zones. Recirculation cavities were covered with grids but they just stabilized the zones with still existing vortices as the results did not show any significant changes. It should be noted that scatter in the results is in the transition regime due to the profiles that are changing significantly in the stabilization region and especially at low velocities. Thus mean velocity value differs measured with UA and LDA as LDA measures it in the flat and already stable profile plane. Recirculation will make less impact with the velocity value increase. It was found from literature [13] that for small pipe and laminar flow the simulated results are significantly affected by these vortices in the niches.

Mean velocity value depends on the profiles as well. Moreover, it depends on the method used to calculate it. They are already discussed. And the LDA is measuring a local velocity under conditions of predefined profile. Results of mean velocity changes along the axis from the inlet into the pipe

up to the outlet into the chamber show changes up to 2-3 %. In the chamber up to its centre significant changes is not found experimentally though simulation results show a tendency of growing of velocity value.

Finally, the uncertainty of the measurements in the test facility is defined. For velocity range of 0.05 to 30 m/s it covers 8 to 0.45 % respectively. Detailed analysis is in Table 1.

**Table 1:** Example of a table.

Velocity value, m/s	Expanded Uncertainty, %	Factors for uncertainty		
		Type B, %	Repeatability	Reproducibility
0.05	8.0	0.22	3.55	1.8
0.15	4.9	0.22	2.15	1.1
0.5	2.3	0.22	1.0	0.5
1	1.9	0.22	0.83	0.42
3	1.1	0.22	0.45	0.22
5	0.8	0.22	0.3	0.16
10	0.55	0.22	0.15	0.075
30	0.45	0.22	0.04	0.02

#### 4. Conclusion

The paper reveals airflow development features in the entrance region of the pipe as the test section of the wind tunnel and in the chamber of larger dimensions.

The results of standards, Laser Doppler Anemometer and Ultrasonic anemometer show good agreement and repeatability except very low velocity range. This is a consequence of several factors such as flow regime, mean velocity definition procedure and recirculation zones.

Due to the fast response, UA enabled to analyse fluctuations in the flow. Local vortices identified in the flow might have influenced the low-frequency fluctuations and the scatter of measurement results. The high-frequency fluctuations found in the flow originated from the flow turbulence and the electronic or acoustic noise. The stabilisation of the entrance region and the boundary layer of the pipe influenced mean velocity value, velocity distribution and axial velocity development in different test sections of the pipe. Along with the recirculation zones in cavities of ultrasonic transducers they are the essential impact factors on velocity value defined.

The uncertainty of the measurements in the test facility for velocity range of 0.05 to 30 m/s covers 8 to 0.45 % respectively.

Simulation and experimental results have some differences that need to be further analysed.

For future tasks conditions of UA using simulation tools also is a key action as experimentally it is not available due to the lack of optical access.

#### References

- [1] Bertašienė A, „Investigation of air velocity value reproduction and transfer in flow regime change“, Doctoral thesis, 2011.
- [2] Pachinger D, Guideline on the Calibration of Solid Anemometers - Part 2: Thermal Anemometers. Euramet project No.1454. Coordinator BEV/E+E, Austria. 2018 till now.
- [3] Pachinger D, Development of a guide one air speed calibration solid anemometers. Euramet project No. 1312. Coordinator BEV/E+E, Austria. 2014-2018.
- [4] Sluse J, Comparison of low air speed. Euramet project No.1450. Coordinator CMI, Czech Republic.
- [5] Nader G, Dos Santos C, Jabardo Paulo J S et al, „Characterisation of low turbulence wind tunnel“, *XVIII IMEKO World Congress*, 2006.
- [6] Jian Wu, „Realisation of a primary air velocity standard using laser Doppler anemometer and precision wind tunnel“, *XIX IMEKO World Congress*, 2009.
- [7] Shinder I I, Crowley Ch J, Filla B J and Moldover M R, „Improvement to NIST’s air speed calibration service“, *Flow measurement and instrumentation*, **44**, 19-26, 2015.
- [8] Piccato A, Malvano R and Spazzini P G, “Metrological features of the rotating low speed anemometer calibration facility at INRIM”, *Metrologia*, **47**, 47-57, 2010.
- [9] Bujalski M, Gawor M and Sobczyk J, „Flow disturbance due to the presence of the vane anemometre“, *XXI Fluid mechanics Conference, Journal of physics*, **530**, 2014 (012045).
- [10] Chen J et.al. , “Numerical study of transition in a cylindrical pipe flow”, *Communication in nonlinear science and numerical simulation*, **9**, 661-668, 2004.
- [11] Willis A P et al, “Experimental and theoretical progress in pipe flow transition”, *Philosophical transactions of the royal society*, **366**, 2671-2684, 2008.
- [12] Eckhardt B et al, “Turbulence transition in pipe flow”, *Annual review of fluid mechanics*, **39**, 447-468, 2007.
- [13] Guo L et al. “The flow field analysis and flow calculation of ultrasonic flowmeter based on the fluent software”, *Hindawi. Abstracts and applied analysis*,. 2014. ID 528602.

# Non-Nulling Measurements of Flue Gas Flows in a Coal-Fired Power Plant Stack

A. N. Johnson<sup>1</sup>, I. I. Shinder<sup>1</sup>, J. B. Filla<sup>1</sup>, J. T. Boyd<sup>1</sup>, R. Bryant<sup>1</sup>, M. R. Moldover<sup>1</sup>, T. D. Martz<sup>2</sup>

<sup>1</sup>NIST 100 Bureau Drive, Gaithersburg, MD, USA

<sup>2</sup>EPRI, 3420 Hillview Ave., Palo Alto, CA 94304

(corresponding author): [Aaron.Johnson@nist.gov](mailto:Aaron.Johnson@nist.gov)

---

*Exhaust flows from coal-fired stacks are determined by measuring the flue gas velocity at prescribed points in the stack cross section. During the last 30+ years these velocity measurements have been made predominantly using S-type pitot probes. These probes are robust and inexpensive; however, S-probes measure only two components of the velocity vector and can give biased results if the stack flow has significant yaw and pitch angles. Furthermore, S-probe measurements are time intensive, requiring probe rotation (or nulling) at each traverse point to find the yaw angle. The only EPA-sanctioned alternatives to the S-probe are 5-hole probes (i.e., the prism probe and spherical probe) that also require yaw-nulling. We developed a non-nulling technique applicable to the spherical probe and two custom designed 5-hole probes that reduce testing time and may improve measurement accuracy. The non-nulling technique measures all 3 components of velocity without rotating the probe. We assessed the performance of these 5-hole probes in a coal-fired stack at the high-load (16 m/s) and the low-load (7 m/s). For the spherical probes, the non-nulling results and the nulling results were in excellent mutual agreement (< 0.1 %). For the custom probes, the non-nulling and nulling results were inconsistent: the differences were 5% at the high load and 10 % at the low load. We speculate that the nulling data for the custom probes were flawed because the non-nulling data for all the probes accurately determined the yaw and pitch angles at high and low loads. Our results demonstrate that the non-nulling technique can accurately measure flue gas flows in a coal-fired stack.*

---

## Introduction

This Introduction briefly reviews (1) the need for accurately measuring flue gas flows, (2) the current “nulling” technique for flue gas measurements and its problems, (3) the possibility of improved measurements using a non-nulling technique, and (4) the encouraging results from preliminary field tests of a non-nulling technique.

(1) The combustion gases from coal-fired power plants (CFPPs) are exhausted into large diameter (> 5 m), vertically oriented smokestacks, which emit pollutants into the atmosphere. To quantify the amount of pollutants released into the atmosphere, the total flow in these stacks must be accurately measured; however, accurate stack flow measurements are difficult. Stacks are fed by a network of elbows, reducers, fans, etc. which generate complex, difficult-to-measure flows. The flue gas itself causes additional difficulties because it can be hot (as high as 120°C),

acidic, asphyxiating, and in some cases saturated with water vapor. Nevertheless, accurate measurements of the total flue gas flow are essential to monitor emissions of greenhouse gases (GHGs) and other hazardous pollutants.

Pollutant emissions from CFPPs are quantified by continuous emission monitoring systems (CEMS) permanently installed in the stacks. The CEMS equipment measures the concentration of each regulated pollutant as well as the total flow. Federal regulations require annual calibration of the CEMS flow monitors and concentration equipment. These calibrations are performed using an EPA protocol called a relative accuracy test audit (RATA). The flow portion of the calibration is herein referred to as the flow RATA.

### (2) How Stack Flows are Currently Measured

The flow RATA maps the axial stack velocity measured along 2 orthogonal chords in the stack

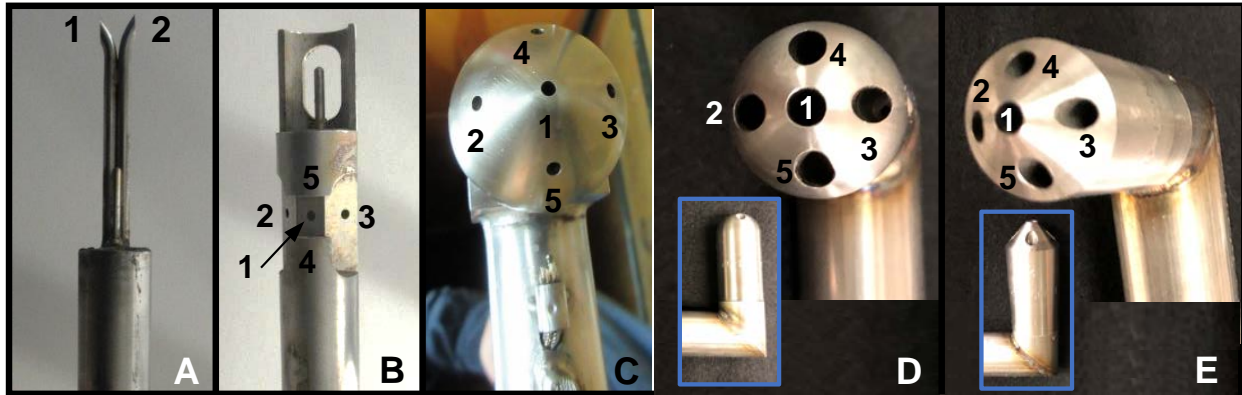


**Figure 1.** Pictures A, B, and C show the 3 EPA-sanctioned RATA probes including A) the S-probe, B) Prism probe, and C) Spherical Probe. The hemispherical and conical probes shown in D) and E), respectively are custom-made probes designed for non-nulling.

cross-section. A pitot probe is inserted into the flow through ports on the stack wall. On each chord, measurements are made at discrete points located at the centroids of equal area [1]. The discrete velocity measurements are integrated to determine the flow velocity, which in turn, is used to determine the correction factor for the CEMS flow meter.

Figures 1A, 1B, and 1C show the 3 RATA probe types sanctioned by the EPA including A) the S-probe, B) the prism probe, and C) the spherical probe. All 3 probes use the same measurement principle. The axial velocity is correlated to differential pressure measurements made across the probe's pressure ports. Both the prism and the spherical probe have 5 pressure ports and both measure the entire velocity vector including the pitch, yaw, and axial velocity components. In contrast, the S-probe measures only the yaw and axial velocities, and has been shown to give flow velocities that are biased high if significant pitch and yaw are present in the flow [2].

#### *Nulling Method*

The 3 EPA-sanctioned probes use a yaw-nulling method [3, 4, 5] to determine the angle of off-axis flow in the yaw direction, which we call the yaw-null angle ( $\beta_{null}$ ). At each point on the RATA map, the probe is *nulled* by rotating it about its axis until the vector sum of the yaw and axial

velocities align with pressure port 1. For a 3-D probe the nulling procedure can be accomplished in a single rotation. The S-probe requires 2 rotations. First the S-probe is nulled by rotating it about its axis until  $P_{12} = 0$ . A second 90° rotation orients port 1 so that it faces into the flow. Once the probe is nulled, the probe calibration parameters are used to determine the dynamic pressure ( $P_{dyn}$ ), and for 3-D probes the pitch angle ( $\alpha$ ).

#### *Errors Due to Imperfect Nulling*

If the null condition is not satisfied, significant flow measurement errors can occur. The nulling errors increase with the ratio  $\Delta P_{null}/P_{dyn}$ , where the null-differential-pressure  $\Delta P_{null} = P_{23}$  for 3-D probes and  $\Delta P_{null} = P_{12}$  for the S-probe. The errors become significant when  $\Delta P_{null}/P_{dyn}$  is not small relative to unity [6]. In most cases the nulling procedure is performed manually. A person rotates the probe while reading a differential pressure gauge to determine the exact yaw angle for which  $\Delta P_{null} = 0$ . However, transients in stack flows, noisy pressure signals, and human errors make nulling imperfect and introduce unquantified bias (e.g. high for an S-probe) into the measurement process.

When the velocity field has a significant yaw component, nulling the probe can be

time-intensive and, consequently, expensive. When mapping the flow field, several iterations are generally required to find the yaw-null angle at each traverse point. The nulling time increases in wet stacks since stack testers must frequently interrupt the measurement process to purge the probe's pressure ports of droplets or particles. Because 3-D probes have more pressure ports than S-probes, and because the diameters of these ports are smaller than the ports of S-probes, 3-D probes are more susceptible to plugging. Consequently, 3-D probes generally require more time than the S-probe to complete the flow RATA. Historically the stack flow measurement community has opted to use the more robust and economical, but less accurate, S-probe.

### (3) Non-Nulling Method

Non-nulling methods determine the axial velocity without rotating the probe at each traverse point to find  $\beta_{\text{null}}$ . Instead, the axial velocity, the pitch angle, and the yaw-null angle  $\beta_{\text{null}}$  are determined with the probe oriented at zero yaw angle (*i.e.*,  $\beta = 0^\circ$  such that port 1 on the probe is aligned with the stack axis). Compared with nulling methods, non-nulling methods reduce the time needed to perform flow RATAs. CFPPs are concerned about the duration of flow RATAs because they must maintain loads stipulated by the RATA instead of loads dictated by customer supply and demand.

The non-nulling method also has the potential to improve flow measurement accuracy compared with nulling methods. First, the S-probe measures only 2 components of the velocity vector while the non-nulling method applies to 3-D probes and thereby measures the entire velocity vector. Second, Method 2F [5], which is the EPA nulling method for 3-D probes, does not address errors resulting from imperfect nulling, as discussed above.

In this manuscript we demonstrate the feasibility of accurately determining the total flow in a CFPP stack using a non-nulling

method and commercially available flow RATA equipment. In previous work, we achieved 1 % accuracy when we performed flow RATAs in NIST's Scale-Model Smokestack Simulator (SMSS) using a spherical probe, even with highly-distorted flows [7, 8]. However, the SMSS facility uses ambient air as surrogate for flue gas and performs flow RATAs under laboratory conditions using laboratory grade instrumentation.

Using NIST's wind tunnel and NIST's smokestack simulator, we developed non-nulling algorithms for the spherical probe in Fig. 1C and for the 2 custom probes shown in Figs. 1D and 1E. At NIST, we calibrated these probes using our non-nulling method and also EPA's Method 2F, and then we used these probes to measure the flow velocity in a CFPP stack.

For assessing the accuracy and limitations of the non-nulling method, we selected a CFPP stack known to have complex flows. The selected stack's RATA measurement platform was only 3.8 stack diameters ( $D = 6.8$  m) downstream of a  $90^\circ$  elbow. Moreover, upstream of the elbow, flow from two wet scrubbers merged into a single stream. Not surprisingly, the flow at the RATA platform had significant yaw-null angles that were nearly  $-30^\circ$  at the stack wall. The flue gas was saturated with water from the wet scrubbers. The wet, particle-laden gas frequently plugged the 3-D probes; plugging increased the duration of the tests and resulted in false high (or low) axial velocity measurements both for Method 2F and the non-nulling method. We developed a statistical method based on the noisiness of the measured pressure signals to identify data affected by plugging.

The CFPP stack was equipped with an X-pattern ultrasonic flow meter system, which was used as the CEMS flow monitor. The CFPP provided us with minute by minute CEMS flow velocity data ( $V_{\text{CEMS}}$ ) for the duration of the test. On average, the stability of  $V_{\text{CEMS}}$  during the flow RATAs was better than 1.5 %. We performed a 16-point flow RATA

using both Method 2F and the non-nulling method. The flow RATAs were performed at two loads, a high load with a flue gas velocity of 16 m/s, and at a low load of 7 m/s.

**Table 1.** Normalized flow velocity ( $V_{RATA}/V_{CEMS}$ ) for Method 2F (M2F) and for the non-nulling method at zero yaw angle (NN,  $\beta = 0$ ) at a high load of 16 m/s and a low load of 7 m/s.

Probe Types	Load (Repeats)	M2F	NN ( $\beta = 0$ )	M2F/NN -1
Spherical Probes (SP)	High (4) <sup>a</sup>	0.993 (2.1 %) <sup>b</sup>	0.994 (0.4 %) <sup>b</sup>	-0.1 % <sup>c</sup>
Custom Probes (CP)	High (4)	1.053 (0.4 %)	0.990 (0.7 %)	+5.9 %
CP/SP-1	High	6.0 %	-0.4 %	
Spherical Probes (SP)	Low (6)	1.02 (1.3 %)	1.02 (1.7 %)	0 %
Custom Probes (CP)	Low (6)	1.108 (2.0 %)	0.997 (1.6 %)	+10 %
CP/SP-1	Low	8.6 %	-2.3 %	

a) Number of repeated RATA traverses for the same probe at the same flow

b) Standard deviation of normalized RATA velocity expressed as a percent

c) Percent difference computed using  $100 (M2F/NN - 1)$

(4) The CFPP test results are summarized in Table 1. The tabulated RATA velocities are normalized by the CEMS velocity ( $V_{RATA}/V_{CEMS}$ ) to help account for flow variations during and between measurements. The data in column “M2F” are the normalized flow velocities for Method 2F; the data in column “NN ( $\beta = 0$ )” are the normalized non-nulling velocities obtained with the probe at a zero yaw angle.

There are 4 primary results. First, the non-nulling method and Method 2F showed excellent agreement for the spherical probes. As indicated in the last column, the difference at high load was -0.1 % and at low load the difference was 0 %.

Second, the flow results from the non-nulling method were consistent throughout the test. The percent difference of  $V_{NN}/V_{CEMS}$  determined with

the spherical probes and the custom probes was only -0.4 % at high load and -2.3 % at low load.

Third,  $V_{NN}/V_{CEMS}$  is close to unity in all cases. This agreement between  $V_{NN}$  and  $V_{CEMS}$  is better than expected. The values of  $V_{CEMS}$  are based on an earlier S-probe RATA calibration that used the conventional nulling method. Our values of  $V_{NN}$  are based on a 16-point traverse that did not account for the lower velocities near the wall. If we had accounted the lower velocities, we would have found  $V_{NN} < V_{CEMS}$ . Note: we measured pitch angles less than 5°, so that S-probe errors related to pitch angle are negligible in this stack.

Fourth, the results of Method 2F and the non-nulling method showed poor agreement for the custom probes: the differences are 5.9 % at high load and 10 % at low load. Presently we do not understand the cause of the differences. However, we suspect these results are erroneous for the following reasons: a) the non-nulling results were consistent for all tests and agreed with the results obtained with the EPA-sanctioned spherical probe, b) in cases where RATAs based on Method 2F disagree with the S-probe nulling method, the Method 2F results are typically lower due to inherent positive biases in the S-probe [9].

### Probe Calibrations in NIST’s Wind Tunnel

We calibrated all 3 probe types in NIST’s wind tunnel using both Method 2F [5] and the non-nulling method. Calibrations were performed in the wind tunnel’s rectangular test section (1.5 m × 1.2 m) using NIST’s Laser Doppler Anemometer (LDA) working standard. The metrological traceability of the LDA working standard is documented in the following references 10, 11, and 12. We use the LDA velocity ( $U_{LDA}$ ) in conjunction with air density ( $\rho_{AIR}$ ) in the wind tunnel to determine the dynamic pressure,  $P_{dyn} = \rho_{AIR} U_{LDA}^2/2$ . The wind tunnel is equipped with an automated traversing system, which positions the pitot probes to prescribed pitch angles ( $\alpha$ ) and yaw angles ( $\beta$ ) in the test section [13, 14]. The expanded uncertainty of wind speed is less than 1 %, and the expanded uncertainties of pitch and yaw angles are 0.5°.

### Method 2F Probe Calibrations

We calibrated 4 spherical probes, 2 hemispherical probes, and 2 conical probes. All the probes were calibrated at 11 velocities ranging from 5 m/s to 30 m/s in steps of 2.5 m/s, and at 17 pitch angles ranging from  $-20^\circ$  to  $20^\circ$  in steps of  $2.5^\circ$ . Thus, for each probe we measured 187 combined velocity and pitch angle set points. We used the Curve Fit Method [6] to determine the pitch calibration factor,  $F_1$ , and the velocity calibration,  $F_2$ , at the null condition ( $P_{23} = 0$ ). The Curve Fit Method does not require rotating the probe to the exact position where  $P_{23} = 0$ ; instead the pitch pressure ratio,  $P_{45}/P_{12}$ , and the velocity pressure ratio,  $[P_{\text{dyn}}/P_{12}]^{1/2}$ , are measured over a narrow range of yaw pressures surrounding  $P_{23} = 0$ . By definition, the pitch pressure ratio and the velocity pressure ratio equal the respective calibration factors,  $F_1 = P_{45}/P_{12}$  and  $F_2 = [P_{\text{dyn}}/P_{12}]^{1/2}$  at zero yaw pressure,  $P_{23} = 0$ .

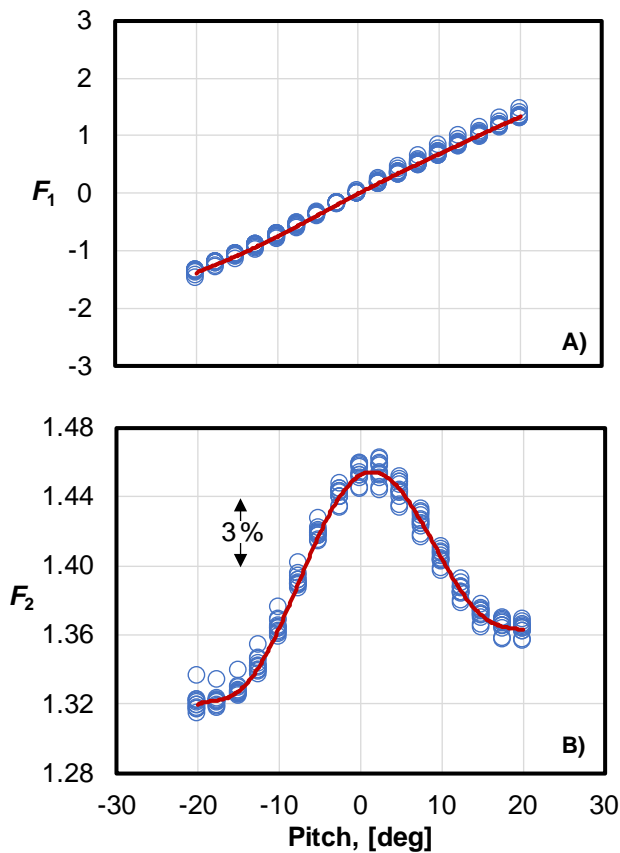


**Figure 2.** Hemispherical probe  $F_1$  and  $F_2$  calibration parameters plotted versus pitch angle. The circles (○) are data points taken at 11 different velocities and the solid line (—) is a curve fitted to the points.

The measured values of the pitch pressure ratio and the velocity pressure ratio values are fit by either a 2<sup>nd</sup> or 3<sup>rd</sup> degree polynomial function of the yaw pressure, which we evaluate at  $P_{23} = 0$  to determine the respective null parameters,  $F_1$  and  $F_2$ .

Figures 2 and 3 plot the calibration parameters  $F_1$  and  $F_2$  as functions of the pitch angle for a hemispherical probe (Fig. 1D) and a conical probe (Fig. 1E). The circles (○) are data taken at the 11 different velocities ranging from 5 m/s to 30 m/s. For both probes,  $F_1$  is nearly independent of velocity, but  $F_2$  exhibits a small, systematic velocity dependence. The solid lines (—) are curves fitted to the data. The pitch angle ( $\alpha$ ) is fitted by a 6<sup>th</sup> degree polynomial of independent variable  $F_1$ , and  $F_2$  is fit to 6<sup>th</sup> degree polynomial of  $\alpha$ .

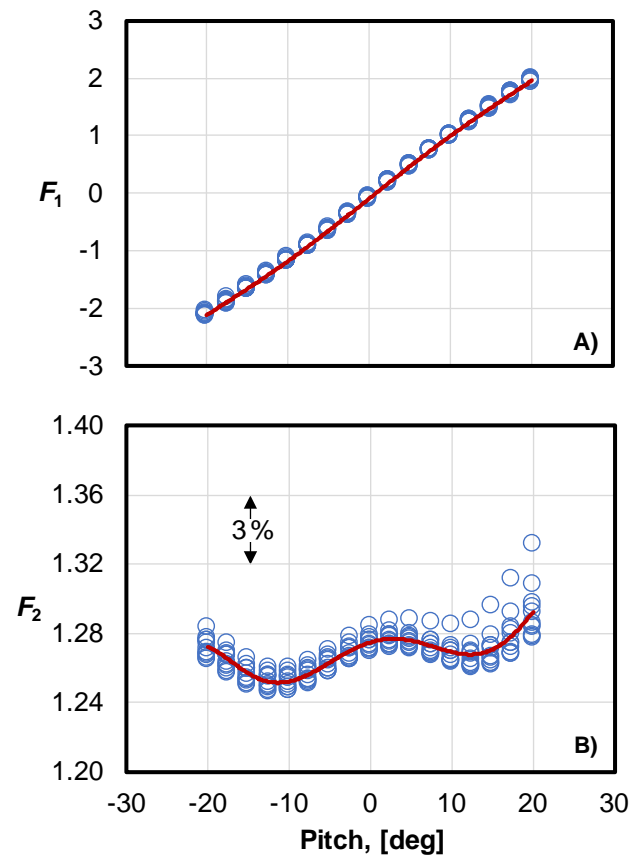


**Figure 3.** Conical probe  $F_1$  and  $F_2$  calibration parameters plotted versus pitch angle. The circles (○) are data points taken at the 11 different velocities and the solid line (—) is a curve fitted to the points.

As observed in Figs. 2B and 3B, the curve fit of  $F_2$  is essentially an average of the velocity data at each pitch angle. This approximate method of accounting for the velocity dependence is consistent with the Method 2F protocol.

For flow RATAs performed using Method 2F, we determined the axial velocity at each traverse point using the following procedure. First, we nulled the probe and measured the yaw-null angle ( $\beta_{\text{null}}$ ) with an inclinometer. Next, we determined the pitch calibration factor,  $F_1 = P_{45}/P_{12}$ , from the measured null pressures  $P_{45}$  and  $P_{12}$ . We use the 6<sup>th</sup> degree polynomial determined during calibration,  $\alpha = \alpha(F_1)$  (here expressed in generic functional form) to determine  $\alpha$ . Then, the calculated  $\alpha$  is used to determine the velocity calibration factor using the fitted curve  $F_2 = F_2(\alpha)$  developed during calibration. The differential pressure between ports 1 and 2 on the probe head along with the velocity calibration factor determine the dynamic pressure,  $P_{\text{dyn}} = F_2^2 P_{12}$ . Finally, the axial velocity at each traverse point is determined as a function of the 1) dynamic pressure, 2) yaw-null angle, and 3) pitch angle using

$$V_{\text{axial}} = \sqrt{\frac{2P_{\text{dyn}}}{\rho}} \cos(\beta_{\text{null}} - \beta_0) \cos(\alpha) \quad (1)$$

where  $\beta_0$  accounts for any yaw angle offset (or misalignment) when probes are installed into the automated traverse system used to perform the flow RATA. We followed EPA Method 4 to measure the flue gas moisture [15], and we used EPA Method 3A to determine the molar mass [16]. The flue gas density ( $\rho$ ) was determined *via* Method 2F using pressure, temperature, and molar mass measurements.

#### Non-Nulling Probe Calibrations

The non-nulling method also uses Eq. (1) to determine the axial velocity at each traverse point. The fundamental difference is that  $P_{\text{dyn}}$ ,  $\beta_{\text{null}}$ , and  $\alpha$  are determined by fitting 3000 or more data points acquired in NIST's wind tunnel. These data span velocities from 5 m/s to 30 m/s, pitch angles from -20° to 20°, and yaw angles from -42° to 42°. The fitted calibration curve is

a fifth-degree polynomial of the four independent variables:  $P_{12}$ ,  $P_{13}$ ,  $P_{14}$ , and  $P_{15}$ .

For the non-nulling method, there is no need to rotate the probe. However, since scenarios could arise where rotating the probe is beneficial (e.g., the predicted value of  $\beta_{\text{null}}$  exceeds the curve fit limits), we discuss a more general application of the non-nulling method. First the probe is rotated to a user-selected yaw angle ( $\beta$ ). Next, we simultaneously measure the four input pressures:  $P_{12}$ ,  $P_{13}$ ,  $P_{14}$ , and  $P_{15}$ , and use the non-nulling calibration curve fits to calculate  $P_{\text{dyn}}$ ,  $\beta'_{\text{null}}$ , and  $\alpha$ . Here,  $\beta'_{\text{null}}$  is the calculated yaw-null angle relative to the rotated probe position at  $\beta$ . The absolute yaw-null angle is the sum of the probe yaw angle and the yaw-null angle determined from the non-nulling algorithm,

$$\beta_{\text{null}} = \beta + \beta'_{\text{null}}. \quad (2)$$

If the probe is oriented at a zero yaw angle ( $\beta = 0^\circ$ ), then the yaw-null angle determined by the non-nulling algorithm equals the yaw angle measured from the stack axis,  $\beta'_{\text{null}} = \beta_{\text{null}}$ . Alternatively, if one rotates the probe to the yaw-null angle,  $\beta = \beta_{\text{null}}$ , then  $\beta'_{\text{null}}$  would be zero, ideally. In this case any changes in  $\beta'_{\text{null}}$  would provide an indication of how the yaw-null angle fluctuates while the probe is oriented at the yaw-angle.

#### Test Protocol for Stack Flow Measurements

We conducted 16-point flow RATAs using multiple probe types. We used a set of 4 spherical probes (see Fig. 1C), and we also used a combination of the 2 custom probes shown in Fig. 1D and 1E. We tested each probe type at 2 loads, a high load with a nominal flow velocity of 16 m/s, and a low load of 7 m/s. The test matrix shown in Table 2 lists the probes used for each test, the flow loads, and the number of repeated runs. The diagram in Fig. 4 shows the cross-sectional view of the setup. The probe installed in each port measures the axial velocity of the nearest 4 points as illustrated in the figure. A complete traverse, herein called a *run*, includes all 16 points shown in the figure. We completed 4 runs for each probe type at the high load and 6 runs for each probe type at the low load.

**Table 2.** Test matrix for 16-point flow RATAs performed in CFPP stack.

Test No.	Probe Types	Load	Repeat Runs	Port 1	Port 2	Port 3	Port 4
1	Spherical Probes	High	4	Sphere 2	Sphere 3	Sphere 5	Sphere 6
2	Custom Probes	High	4	Hemi-sphere 1	Conical 1	Hemi-sphere 1	Conical 2
3	Custom Probes	Low	6	Hemi-sphere 1	Conical 1	Hemi-sphere 1	Conical 2
4	Spherical Probes	Low	6	Sphere 2	Sphere 3	Sphere 5	Sphere 6

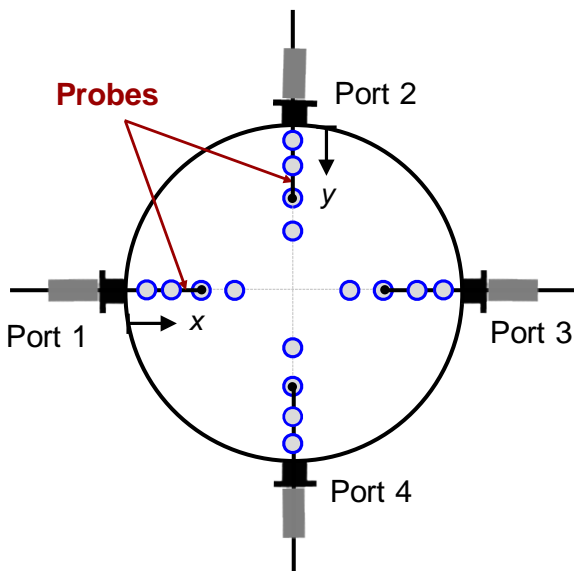


**Figure 4.** Cross-section of stack showing probes, port numbers and 16 traverse points located at centroids of equal stack area.

Our test protocol was conducted by an EPRI contractor who used commercially available RATA equipment called “Multiple Automated Probe System” (MAP)<sup>1</sup> to perform five functions: 1) move all 4 probes simultaneously to specified points; 2) periodically supply high pressure gas to purge droplets or particles plugging any of the 5 pressure ports on the probe head; 3) send a dc voltage to our data acquisition

system 5 s prior to starting a purge, 4) implement the Method 2F nulling procedure including the measurement of  $\beta_{null}$  and  $\beta_0$ ; and 5) provide time stamps at the start and stop of each non-nulling and Method 2F measurement intervals.

#### Data Acquisition System

To collect non-nulling and Method 2F data, we designed and assembled four custom data acquisition systems that were connected to a single laptop computer. Each system included inexpensive, industrial-grade differential pressure transducers, which we sampled at 10 Hz. The transducers were bidirectional with a full-scale of 1244 Pa and a time response faster than 1 kHz. We used pneumatically actuated valves to isolate the differential pressure transducers during purge events. The transducers and valves for each system were housed in a weather-proof case. Each case was placed on the floor of the RATA measurement platform just below the port where the corresponding probe was installed. Each case contained 5 pressure transducers that were connected to the 5 pressure ports on the 3-D probe using 6.35 mm inner diameter tubes approximately 13 m long. In this way, we measured the flue gas pressure (minus a near ambient reference pressure,  $P_{ref}$ , located inside the case) at all 5 pressure ports on the probe

<sup>1</sup> Certain commercial equipment, instruments, or materials are identified in this report to foster understanding. Such identification does not imply recommendation or endorsement by the National Institute of Standards and Technology, nor

does it imply that the materials or equipment identified are necessarily the best available for the purpose.

head. The required differential pressures for the non-nulling algorithm (*i.e.*,  $P_{12}$ ,  $P_{13}$ ,  $P_{14}$ ,  $P_{15}$ ) and for Method 2F (*i.e.*,  $P_{23}$ ,  $P_{12}$ ,  $P_{45}$ ) were calculated by subtracting the appropriate pressure measurements. For example, the yaw pressure was determined by subtracting the measured pressures on port 2 from port 3,  $P_{23} = (P_2 - P_{ref}) - (P_3 - P_{ref})$ .

#### Procedure for Automated Traverses

Each of the 4 tests listed in Table 2 began by starting the data acquisition unit. Pressure data were collected throughout the test except during purge events, which occurred approximately once every minute. During purge events, valves isolated the transducers from the purge pressure while simultaneously re-zeroing the transducers to the common reference pressure.

The same measurement protocol was followed at each traverse point. The MAP system simultaneously moved the 4 probes to the specified traverse point and rotated each probe to a zero yaw angle. After a 3 s stabilization period, the axial velocity ( $V_{NN@0yaw}$ ) was measured for 10 s using the non-nulling algorithm. Next, the MAP system nulled each probe and recorded its  $\beta_{null}$ . After another 3 s stabilization period we measured the axial velocity for 10 s via Method 2F ( $V_{M2F}$ ) and the non-nulling method ( $V_{NN@null}$ ). Thus, we measured 3 velocities at each traverse point: 1) non-nulling with the probe at zero yaw;  $V_{NN@0yaw}$ , 2) Method 2F at the yaw-null angle;  $V_{M2F}$ , and 3) a second non-nulling measurement coincident with  $V_{M2F}$  where the probe is oriented at the yaw-null angle;  $V_{NN@null}$ . The second non-nulling measurement provided insight regarding the steadiness of the yaw-null angle, and could be directly compared to  $V_{M2F}$  since both measurements were made simultaneously.

#### Data Processing

The 3 axial velocities (*i.e.*,  $V_{NN@0yaw}$ ,  $V_{M2F}$ , and  $V_{NN@null}$ ) measured at each traverse point are all calculated using Eq. (1). However, the

algorithms for determining  $P_{dyn}$ ,  $\beta_{null}$ , and  $\alpha$  differ for the non-nulling method and Method 2F. The calculations for both methods are outlined above in the section entitled *Probe Calibrations*. In this section, we emphasize the different approach in averaging the data in each 10 s collection interval.

Method 2F determines the average axial velocity and pitch angle from *pressure averages*. Specifically, we calculated  $P_{12,avg}$  and  $P_{45,avg}$ , which are arithmetic averages of  $P_{12}$  and  $P_{45}$  sampled at 10 Hz for 10 s.

In contrast, our implementation of the non-nulling method determines the average dynamic pressure ( $P_{dyn}$ ), yaw-null angle ( $\beta_{null}$ ), and pitch angle ( $\alpha$ ) from *time averages*. These quantities are calculated every 0.1 s when  $P_{12}$ ,  $P_{13}$ ,  $P_{14}$ , and  $P_{15}$  are updated. At the end of the 10 s collection interval, we calculate the arithmetic average of the 100 values of  $P_{dyn}$ ,  $\beta_{null}$ , and  $\alpha$ . As expected for the steady flows in NIST's wind tunnel, the values of  $P_{dyn}$ ,  $\beta_{null}$ , and  $\alpha$  computed from the pressure averages and the time averages were indistinguishable. If transients are present in the stack flow, a time average may be more accurate than a pressure average. In the CFPP stack, we compared the axial velocities  $V_{axial}$  determined from pressure averages and time averages in a few cases. For most of the comparisons, the values of  $V_{axial}$  agreed to better than 1%; in a few cases  $V_{axial}$  differed by 10% or more.

One disadvantage of time-averaging is that the noisy pressure signals occasionally yielded values of  $P_{dyn}$ ,  $\beta_{null}$ , or  $\alpha$  that exceed the limits of the non-nulling calibration curve. This problem was unexpected; we circumvented it by excluding the anomalous values from the averages. Fortunately, there were only a few cases where the calculated average did not include at least 80% of the data. In future tests we will expand the range of the non-nulling calibration curve and we will retake data points that do not include at

least 80 % (or some user-specified percentage) of data in the time averages.

Unfortunately, the data acquisition was not set up to process data during the CFPP stack measurements. Therefore, we processed the data after the field tests were completed. We used the time stamps provided by the MAP system to identify the non-nulling and Method 2F pressure data. For the low loads, approximately 20 % of the data could not be found at the indicated time stamps. At the high load less than 5 % of the data was unaccounted for.

## Results

Table 1 summarizes the average flow results. It provides solid evidence that the non-nulling method has the potential to make efficient, accurate stack flow measurements. Because we already discussed the averaged flow data, we now compare the profiles of velocity, yaw-null angle, and pitch angle determined by Method 2F to those determined by the non-nulling method. In addition, we describe how we used the noisy pressure signals to troubleshoot plugging problems.

The flow RATAs were performed along 2 orthogonal axes. We denote the axis extending from port 1 to port 3 in Fig. 4 as the “x-axis”. The y-axis extended from port 2 to port 4. Each axis included 8 traverse points. The traverse points are located at the centroids of equal area, so that flow velocity of each run is calculated by averaging the axial velocities measured at 16 traverse points [1]. The axial velocity, yaw-null angle, and pitch angle are plotted on the  $x/D$  and  $y/D$  axes, respectively, where  $D$  is the diameter of the stack.

### Axial Velocity Profiles

Figures 5A and 5B show that while the load remained constant, the flow profile had large variations (greater than 10 %) at particular locations. Figure 5 is a plot of the normalized axial velocity ( $V_{RATA}/V_{CEMS}$ ) measured using the spherical probes at high load as functions of  $x/D$  and  $y/D$ , respectively. The open circles (○) connected by dashed lines are Method 2F

data from each of the 4 runs. The spacings between the dashed lines indicate profile variations. Despite these variations, the flow velocity of each Method 2F run is stable as shown in Table 3. The standard deviation expressed as a percent was only 2.1 %.

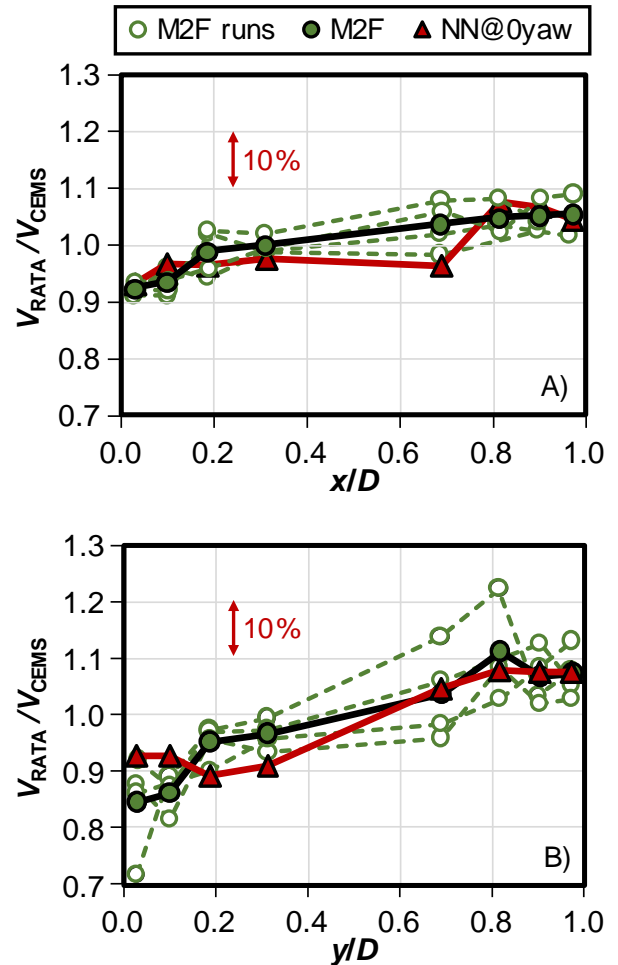


**Figure 5.** Flow RATA for spherical probes at high load: Plots of normalized axial velocity versus A)  $x/D$ , and B)  $y/D$ .

We observed similar profile variations (not plotted) in the 4 non-nulling runs even though the standard deviation of the average velocity was only 0.4 %.

The localized variations in the flow field indicated in Figs. 5A and 5B might be due to vortices. We are confident that they are not artefacts of the measurements (e.g., caused by plugging or filtering the data) because the average flow velocity for each run is stable.

The solid circles (●) and solid triangles (▲) in Fig. 5 are the averages of the Method 2F runs and the non-nulling runs, respectively. In Figs. 5A and 5B the solid lines connecting the averaged points are close to each other. This displays the good agreement of the Method 2F velocity profiles with the non-nulling velocity profiles. Table 3 shows that the difference in the averaged flow velocity is only -0.1 %. We emphasize that the normalized velocity profiles measured at both high and low loads were similar to the profiles observed in Figs. 5A and 5B.

**Table 3.** Normalized flow velocities determined by Method 2F and by the non-nulling method for the 4 repeated runs measured with spherical probe at high load (16 m/s).

Run No.	$\frac{V_{M2F}}{V_{CEMS}}$	$\frac{V_{NN@0yaw}}{V_{CEMS}}$	% Diff <sup>c</sup>
1	1.008	0.999	0.9 %
2	1.009	0.993	1.6 %
3	0.965	0.991	-2.6 %
4	0.988	0.992	-0.4 %
<b>Avg<sup>a</sup></b>	<b>0.993</b>	<b>0.994</b>	<b>-0.1 %<sup>c</sup></b>
<b>%Std Dev<sup>b</sup></b>	<b>2.1 %</b>	<b>0.4 %</b>	

- a) Avg is the average of the 4 runs  
b) %Std Dev is 100 times the standard deviation of the 4 runs dividing by the average  
c) %Diff is calculated by  $100(V_{M2F}/V_{NN@0yaw}-1)$

### Yaw Angle Profiles

Figure 6 shows the average yaw-null profiles for the spherical probe at high load. The Method 2F (●) and non-nulling (▲) yaw-null angles show the same trend and are in good agreement in Figs. 6A and 6B. Both methods show the magnitudes of yaw-null angles are largest near the wall with a value of nearly 30°. The magnitude yaw-null angle decreases monotonically as one moves away from the wall toward the center of the stack. The differences between Method 2F and the non-nulling method are smallest near the center of the stack and increase to maximum of approximately 7° near the wall in the worst case.

We found that the yaw-null profiles were nearly identical at low load. We obtained the same trends shown in Figs. 6A and 6B independent of probe type (*i.e.*, spherical or custom) and method (*i.e.*, non-nulling or Method 2F).

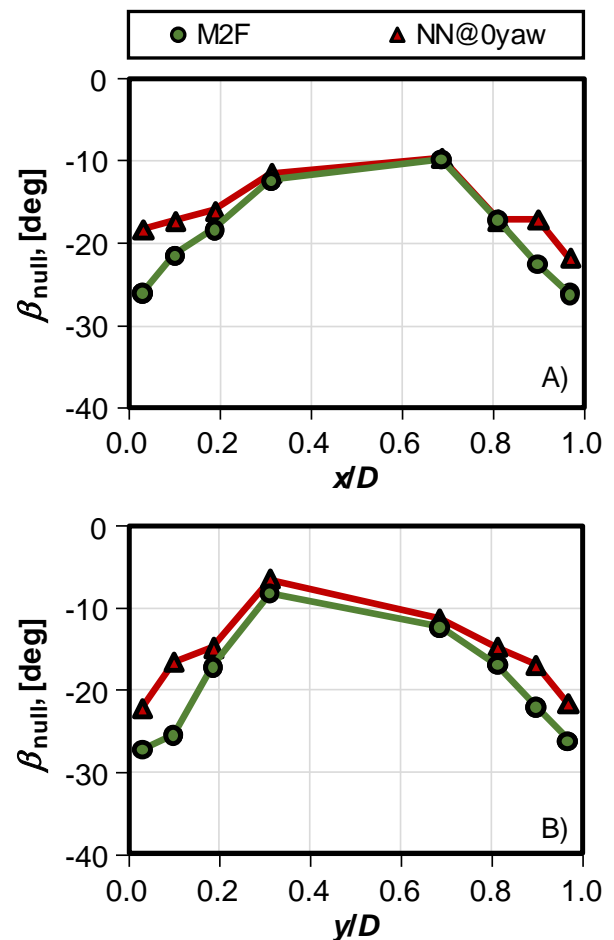


**Figure 6.** Yaw-null profiles determined using Method 2F (●) and non-nulling with  $\beta = 0^\circ$  (▲) along A) port 1 to port 3, and B) port 2 to port 4.

Figure 7 plots the yaw-null angle during a typical 10 s collection time with the probe oriented at  $\beta = \beta_{null}$ . Because the probe was nulled, the non-nulling algorithm measures  $\beta'_{null}$  defined by Eq. (2). In a steady flow with low turbulence  $\beta'_{null}$  would have a constant value close to  $0^\circ$  during the 10 s collection. In contrast, we observed (Fig. 7) the sine-like oscillations with an amplitude of nearly  $30^\circ$

and a period of approximately 4 s. Surprisingly, the integrated average of  $\beta'_{null}$  is  $-1.5^\circ$ , which is close to zero. This time-dependence of  $\beta'_{null}$  is evidence that the flow field in the CFPP stack had large transients. (Figs. 5A and 5B are additional evidence for large transients.) We note that better averages could be obtained by averaging over more cycles (*i.e.*, longer collection times) or by averaging over the 4 s period. However, since the focus of this work is to demonstrate the feasibility of the non-nulling method, we did not implement this strategy.

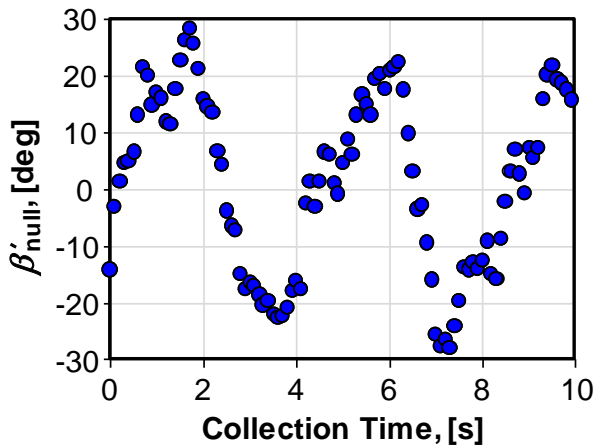


**Figure 7.** Sine-like oscillations of Yaw-null angle during 10 s Method 2F data collection. (Spherical probe is oriented at the yaw-null angle, and  $\beta'_{null}$  is determined every 0.1 s using the non-nulling algorithm.)

#### Pitch Angle Profiles

Figures 8A and 8B show profiles of the pitch angle determined by Method 2F (●) and by the non-nulling algorithm with  $\beta = 0^\circ$  (▲). These results correspond to Test #1 specified in Table 2. The pitch angles determined by Method 2F and by the non-nulling algorithm agree with each other and have similar, asymmetric dependences on  $x/D$  and  $y/D$ . We found the same characteristic profiles independent of flow load, probe type, and method. Although we hoped to perform the test in a stack with high pitch, the largest pitch angle was only about  $5^\circ$ .

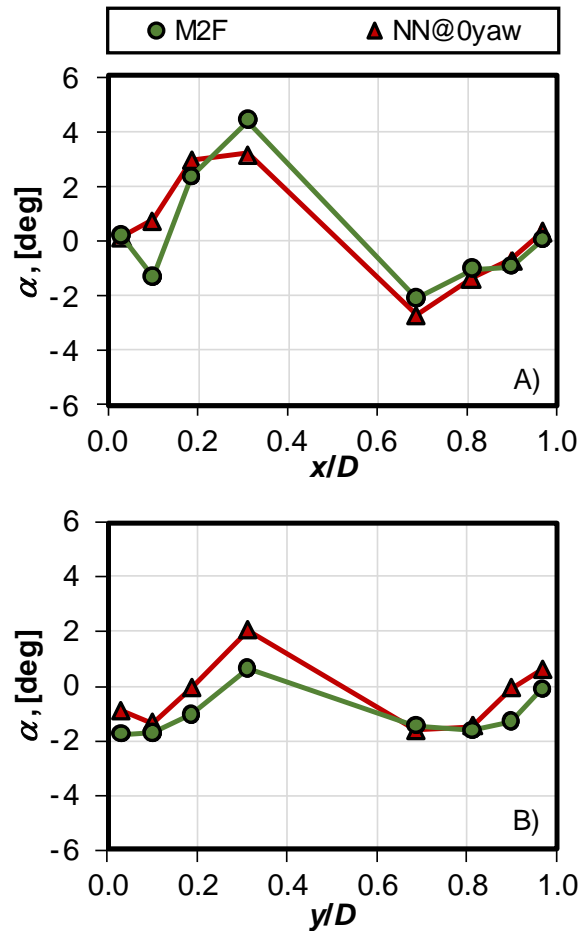


**Figure 8.** Pitch angle profile for Test #1 in Table 2 where A)  $x/D$  is the dimensionless distance from port 1 to port 3, and B)  $y/D$  is the dimensionless distance from port 2 to port 4.

#### Troubleshooting Plugging Problems

To mitigate plugging we purged the probe pressure ports every 60 s. Nevertheless, we still had problems with plugging. Plugging issues were most severe for spherical probe 2 during Test #4 in Table 2. The 4 traverse points in port 1 seemed to be the most impacted by plugging problems.

One way to detect plugging is to evaluate the consistency of repeated axial velocity measurements made at the same traverse point. If significant deviations are found at the same traverse points from run to run, then plugging could be the culprit. However, we could not be sure if deviations resulted from plugged pressure ports or from flow transients like those observed in Figs. 5A and 5B. In this

study we used a simple statistical approach to find outliers in the data caused by plugging.

The pressure signals ( $P_{n,ref}$ ;  $n = 1$  to 5) for the five pressure ports on the probe head were noisy. That is, pressures fluctuations during non-nulling and during Method 2F were usually larger than the mean of the pressure signal. We hypothesized that the noise would significantly decrease if a pressure port on the probe head was plugged. For each 10 s collection time, we computed the standard deviation of the pressure signal from each pressure port on the probe head. If the standard deviation was below the typical noise level by a statistically defined threshold, we assumed that the port was plugged.

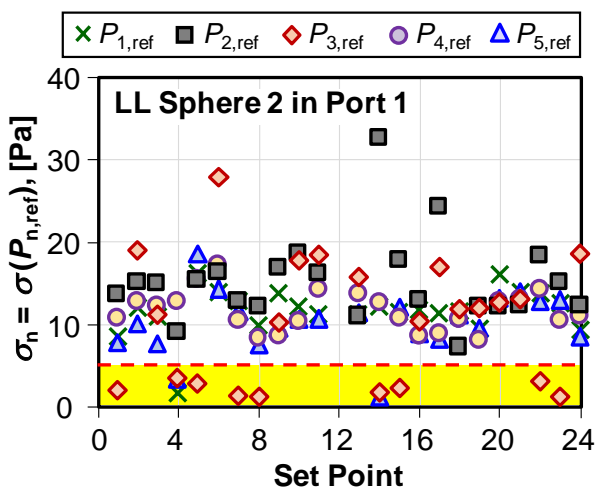


**Figure 9.** Standard deviation of pressure signals ( $\sigma_n$ ) at  $n = 1$  to 5 pressure ports on the spherical probe head. Values of  $\sigma_n$  below the dashed line (---) indicate that port  $n$  was plugged.

Figure 9 illustrates how we applied the statistical approach to detect plugged pressure ports. This example focuses on the non-nulling measurements made at low load using spherical probe 2. The 24 set points on the x-axis correspond to the 4 traverse points for port 1 multiplied by the 6 repeated runs (see Test #4, Table 2). The y-axis is the standard deviation of the pressure signals  $\sigma_n = \sigma(P_{n,ref})$  measured at the  $n = 1$  to 5

pressure ports on the probe head. We considered a pressure port plugged if the standard deviation was below the statistical limit indicated by the dashed line (---). For simplicity Fig. 9 only shows a single limit; however, in practice we used separate limits for each of the 5 pressure signals. The statistical limit for the  $n^{\text{th}}$  probe was

$$limit_n = \langle \sigma_n \rangle - k \sigma(\sigma_n) \quad (3)$$

where  $\langle \sigma_n \rangle$  is the average of the 24 values of  $\sigma_n$ ;  $\sigma(\sigma_n)$  is the standard deviation of the 24 values of  $\sigma_n$ ; and  $k$  is the coverage factor which we set equal to 1.5. (The computed normalized velocities had only a weak sensitivity to the value of  $k$ .)

Figure 10A compares two normalized velocity profiles, one affected by plugging, and the other calculated excluding the subset of data affected by plugging. The figure corresponds to traverses performed at low load using the spherical probes. The velocity ( $V_{RATA}$ ) was determined using the non-nulling algorithm with the probe oriented at zero yaw angle. Each open triangle ( $\Delta$ ) is the average of 6 repeated runs. The dashed line connecting the triangles shows the normalized axial velocity profile of the 8 traverse points between port 1 and port 3 (*i.e.*, the x-axis). The first 4 points along  $x/D$  are traversed by the spherical probe 2 installed in port 1. The statistical approach illustrated in Fig. 9 suggested that several of these points were affected by plugging. If we omit these points when calculating the average axial velocity at each traverse point, we obtain the solid triangles ( $\blacktriangle$ ). The solid line connecting the solid triangles shows the normalized velocity profile corrected to account for plugging.

If the normalized velocity profile ( $\blacktriangle$ ) in Fig. 10A is correct, we expect to find the same profile at low load independent probe type (*i.e.*, spherical or custom) and independent of the method (*i.e.*, non-nulling or Method 2F). Moreover, for these high Reynolds number flows ( $3 \times 10^6$  to  $6.5 \times 10^6$ ) we expect that the high load normalized velocity profile will have essentially the same shape as the low load. Figure 10B

shows that all normalized profiles are in good agreement with the corrected profiles. The good agreement of these profiles is 1) strong evidence that we successfully identified and removed data affected by plugging, and 2) that the non-nulling method performed well independent of probe type and flow load.

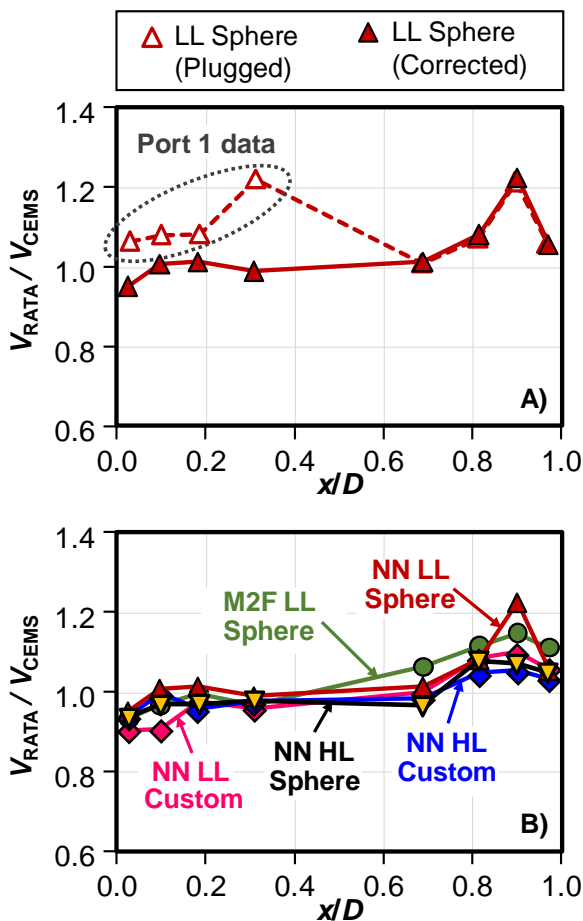


**Figure 10.** Normalized axial velocity profiles plotted against the dimensionless distance from port 1 to port 3: A)  $\triangle$  Low Load Spherical profile with plugged probe ports;  $\blacktriangle$  same profile recalculated with plugged data removed. B) Five profiles not significantly affected by plugging: 1)  $\blacklozenge$  NN LL Custom non-nulling low load, 2)  $\blacklozenge$  NN HL Custom non-nulling high; 3)  $\blacktriangledown$  NN HL Sphere non-nulling high load, 4)  $\bullet$  M2F LL Sphere, Method 2F low load 5)  $\blacktriangle$  NN LL Sphere, non-nulling, low load

### Conclusions

We demonstrated that the non-nulling method can accurately measure complex flows in CFPP stacks. We conducted 16-point flow

RATAs 3.8 stack diameters downstream of the 90° elbow at the stack inlet, and we measured yaw-null angles approaching  $-30^\circ$  near the stack wall. We found excellent agreement between the non-nulling method and Method 2F using spherical probes. The results from Table 1 show agreement of  $-0.1\%$  at a high load of 16 m/s and  $0.0\%$  at a low load of 7 m/s. We found similar levels of agreement between Method 2F and the non-nulling method when we conducted flow RATAs in NIST Scale-Model Smokestack Simulator (SMSS) [7, 8]. The non-nulling method gives the same flow results but is more time and cost efficient than Method 2F.

The SMSS facility uses air as a surrogate for flue gas and has a 1.2 m diameter test section. The facility can generate complex flows that have yaw-null angles of almost  $40^\circ$  at the wall. The excellent non-nulling flow results found in the SMSS are analogous to those found in this study of a CFPP stack. Thus, the SMSS facility is a satisfactory research facility for characterizing probes used for flow RATAs, ultrasonic CEMS, and other flow monitors for use in CFPP stacks.

We developed custom hemispherical and conical probes and compared their performance in a CFPP stack with the EPA-sanctioned spherical probe using the non-nulling method. The non-nulling flow velocities at high and low loads were consistent for all probe types. After normalizing the measured axial velocities by the CEMS velocity, we found essentially the same characteristic profiles at low and high loads across both orthogonal chords. The normalized Method 2F axial velocities also exhibited the same profiles across the chords.

The non-nulling method measured consistent pitch and yaw-null angles using all the probe types at both high and low loads. Therefore, in future flow RATA testing, a hybrid non-nulling method can be implemented. That is, if while performing a flow RATA using the non-nulling method one has reason to question the axial velocity measurement, the RATA tester can

rotate the probe to the calculated yaw-null angle and take a Method 2F measurement.

The non-nulling method requires bidirectional, fast response differential pressure transducers. We used industrial grade differential transducers for our stack measurements. We measured the pressure (minus a common reference pressure) at each of the 5 ports on the 3-D probe. Pressure measurements were sampled at 10 Hz. They revealed periodic pressure fluctuations with periods ranging between 3 s and 5 s. These transients could not be observed or adequately accounted for (e.g., averaging over the periods) using Method 2F. In contrast, the non-nulling data processing could easily be modified to perform averages over the period.

We used a commercially available automated traverse system 1) to reduce the RATA times and 2) to improve the accuracy of nulling the probes. We emphasize that the benefits of automated traverses are less important for the non-nulling method than for nulling methods because the non-nulling method does not rotate the probe rotation and eliminates errors from imperfect nulling.

Despite purging every 60 seconds, our spherical probes were plagued by plugging that was most severe at low load. We did not experience the same difficulties with the two custom probes; however, we are not sure if this is due to their designs or to good fortune. Additional field tests are needed to better understand plugging.

For accurate flow measurements, it was necessary to distinguish fluctuations of the axial velocity from plugging of one or more

pressure ports. We made this distinction by detecting the reduction in the pressure noise that occurs when a pressure port is plugged. Without plugging, the fluctuations of the pressure signals were often larger than their mean values. For each pressure signal, during each 10 s data collection period, we used the standard deviation of the pressure from its mean as a measure of its noise. In this study, we were not prepared to process the noise data in real time. After all the measurements were completed, we used a statistical criterion to discard data corrupted by plugging. In the future, we will process the noise data as they are acquired during a RATA. If the noise indicates plugging the probe can be purged and the data retaken. Thus, the noise measurements will be used as a diagnostic to guide the data acquisition and not to discard data.

In this study we performed a 3000-point calibration on each probe used for the non-nulling measurements. Such an extensive calibration is not practical for routine flow RATAs. Research efforts are underway to determine if a baseline non-nulling calibration can be applied to all probes of the same type. If so, a simple calibration will be done to correct for slight manufacturing differences.

### Acknowledgments

We thank John Wright of NIST for his continuing, enthusiastic support of this work. This research was partially funded by NIST's Greenhouse Gas and Climate Science Measurements Program. A Cooperative Research and Development Agreement (CRADA) between NIST and EPRI facilitated our access to a RATA at a CFPP.

- 
- [1] Environmental Protection Agency, **40 CFR Part 60 Application Method 1 Sample and Velocity Traverses for Stationary Sources**, Washington D.C., 1996.
- [2] Norfleet, S. K., Muzio L. J., and Martz T. D., **An Examination of Bias in Method 2 Measurements Under Controlled Non-Axial Flow Conditions**, Report by RMB

Consulting and Research, Inc., May 22, 1998.

- [3] Environmental Protection Agency, **40 CFR Part 60 Application Method 2 Velocity and S-type Pitot**, Washington D.C., 1996.
- [4] Environmental Protection Agency, **40 CFR Part 60 Application Method 2G Stack**

- Gas-Velocity/Volumetric Flow Rate-2D probe**, Washington D.C., 1996.
- [5] Environmental Protection Agency, 40 CFR Part 60 **Application Method 2F Stack Gas-Velocity/Volumetric Flow Rate-3D probe**, Washington D.C., 1996.
- [6] Shinder, I. I., Johnson, A. N., Moldover, M. R., Filla, B. J., and Khromchenko, V. B., **Characterization of Five-Hole Probes used for Flow Measurement in Stack Emission Testing**, 10th International Symposium on Fluid Flow Measurement (ISFFM), Querétaro, Mexico, MX, April 2018.
- [7] Johnson, A. N., Boyd, J. T., Harman, E., Khalil, M. Ricker, J. R., Crowley, C. J., Wright, J. D., Bryant, R. A., and Shinder, I. I., **Design and Capabilities of NIST's Scale-Model Smokestack Simulator (SMSS)**, 9th International Symposium on Fluid Flow Measurement (ISFFM), Arlington, Virginia, April 2015.
- [8] Bryant, R. A.; Johnson, A. N.; Wright, J. D.; Wong, T. M.; Whetstone, J. R.; Moldover, M. R.; Shinder, I. I.; Swiggard, S.; Gunning, C.; Elam, D.; Martz, T.; Harman, E.; Nuckols, D.; Zhang, L.; Kang, W.; and Vigil, S.; **Improving Measurement for Smokestack Emissions - Workshop Summary**, Special Publication (NIST SP) 1228, 9/21/2018.
- [9] Johnson, A. N., Shinder, I. I., Moldover, M. R., Boyd, J. T., and Filla, B. J., **Progress Towards Accurate Monitoring of Flue Gas Emissions**, 10th International Symposium on Fluid Flow Measurement (ISFFM), Querétaro, MX, March 2018.
- [10] Yeh, T. T., Hall, J. M., *Air Speed Calibration Service*, NIST Special Publication 250-79, National Institute of Standards and Technology, Gaithersburg, Maryland, 2006.
- [11] Yeh, T. T., Hall, J. M., **An Uncertainty Analysis of the NIST Airspeed Standards, ASME Paper FEDSM2007-37560**, ASME/JSME 5th Joint Fluids Engineering Conference, pp. 135-142, San Diego, California, USA, 2007.
- [12] Yeh, T. T. and Hall, J. M. **Uncertainty of NIST Airspeed Calibrations**, *Technical document of Fluid Flow Group*, NIST, Gaithersburg, Maryland, USA, 2008.
- [13] Shinder, I. I., Crowley, C. J., Filla, B. J., Moldover, M. R., **Improvements to NIST's Air Speed Calibration Service**, 16th International Flow Measurement Conference, Flomeko 2013, Paris, France September 24-26, 2013.
- [14] Shinder, I. I., Khromchenko, V. B., and Moldover, M. R., **NIST's New 3D Airspeed Calibration Rig, Addresses Turbulent Flow Measurement Challenges**, 9th International Symposium on Fluid Flow Measurement (ISFFM), Washington, DC, U. S., April 2015.
- [15] Environmental Protection Agency, **40 CFR Part 60 Application Method 4 Determination of Moisture Content in Stack Gases**, Washington D.C., 1996.
- [16] Environmental Protection Agency, **40 CFR Part 60 Application Method 3A Determination of Oxygen and Carbon Dioxide Concentrations in Emissions From Stationary Sources**, Washington D.C., 1996.

# Comparison of two different methods for calibration of Cole type Pitot tubes

I.B.S. Bispo<sup>1,2</sup>, L.C. Pacifico<sup>1</sup>, W.O. Chaves<sup>1</sup>,  
N.M. Taira<sup>1</sup>, P.J.S. Jabardo<sup>1</sup>

<sup>1</sup>Institute for Technological Research – IPT, Av. Prof. Almeida Prado, 532, São Paulo, Brazil

<sup>2</sup>e-mail (corresponding author): [ibispo@ipt.br](mailto:ibispo@ipt.br)

---

## Abstract

The Cole type Pitot tubes (Pitot-Cole tubes) are widely used by water utility companies to map fluid flow velocity profile and thus measure the flow rate in pipelines. This technique is mainly used for on-site calibration of other kind of flow meters, such as electromagnetic or ultrasonic, particularly when removing the meter from the pipeline is somehow not feasible. Therefore, when using Pitot-Cole tubes for those purposes, the determination of the calibration coefficient ( $C_d$ ) and its associated uncertainty contributes significantly to the results of such measurements.

This paper presents the description and comparison between the results of two different methodologies for calibration of Pitot-Cole tubes: in a wind-tunnel and in a towing tank. Comparisons were also performed for two configurations of the Pitot-Cole tube, with and without a central pin between the two pressure tips, in which the inclusion of this feature increases the measured differential pressure, leading to a set of more reliable measurements.

The obtained results demonstrate coherence and feasibility of the wind-tunnel calibration for normalized Reynolds numbers ( $Re/L$ ) greater than  $7 \times 10^5$ . These results also show that a more precise value can be applied along distinct velocity ranges, individually for each Pitot-Cole tube, instead of employing the usual value of  $C_d = 0.869$ , used since Cole proposed this form of Pitot tube in 1896. Another major result shows that, for lower values of  $Re/L$ , a correction of the calibration coefficient is needed, in order to reduce the uncertainty associated to the measurement. This second result is especially important since the corresponding velocities are related to lower flow rates, in which their measurements are usually followed by larger uncertainty estimates.

---

## 1. Introduction

Water distribution systems are strictly dependent on well calibrated equipment, especially when considering the measurement of its main resource: water. To correctly measure its flow through the system, flow meters must be regularly calibrated over time. One such method for calibration of flow meters is based on the so called Cole type Pitot tube (Pitot-Cole tube or also reversible pitometer, as it used to be called).

In order to guarantee the results of the aforementioned calibration method, the Pitot-Cole must also be calibrated and in doing so, the problem of the insertion of the Pitot rod into the flow arises, creating significant disturbances to the velocity profile which is being

measured. The shape of the tips and the use of a hydrodynamic profile that incurs in drag reduction, induces flow effects close to the tips that need to be mitigated by the use of a calibration coefficient, denoted here by  $C_d$ . Such coefficient can be described as a ratio of actual average velocity to the measured fluid velocity at a certain position of the Pitot-Cole tube inside the flow.

In Brazil, in the early 2000s, Pitot-Cole tubes were rarely calibrated, and until then, the  $C_d$  was usually adopted as equal to 0.869, as it was proposed long ago by Edward S. Cole [1]. However, due to numerous reasons, such as, the need of increasing reliability in measurement data, dimensioning of the catchment system and distributions to meet the continuous growth

of demand, monitoring for determination of loss rates, measurement traceability requirements for proving metrological reliability, accreditation of conformity assessment bodies and meeting normative requirements applied to laboratory quality management systems, the calibration of this type of instrument has become more relevant.

One of the methodologies for experimental determination of the  $C_d$  coefficient for this type of Pitot tube is by means of towing tank measurement, which is considered a relatively costly method (see [4]). In order to meet this demand, the Institute of Technological Research of the State of São Paulo (IPT) developed and proposed an economically more feasible methodology for calibration using the normalized Reynolds number correlation ( $Re/L$ ) so the calibration procedure could be carried out in a wind-tunnel [4].

In this work, these two different methodologies for obtaining the mentioned calibration coefficient are evaluated and have their results compared: in a wind tunnel and in a towing tank facility. Such methods are much used in this field and, therefore, are worth being evaluated. Also, two types of Pitot-Cole tubes are compared: with or without a central pin between the two reversible tips, a feature that increases the wake and provides better readings of velocities.

The attained results show reasonable agreement between the two methods for  $Re/L > 5 \times 10^5$ , a result that agrees with previous works. One interesting result is presented for values of  $Re/L < 5 \times 10^5$  and for  $Re/L > 2.5 \times 10^6$ : As Edward S. Cole proposed, the value of the calibration coefficient can be adopted as constant, although it might differ slightly for each individual instrument and also for slightly different designs, such as the introduction of the central pin.

## 2. The Cole type Pitot tube

### 2.1 Brief Historical Background

The Pitot-Cole tube, depicted schematically in Figure 1 and in detail in Figure 2, dates back to 1896, and it was proposed by Edward S. Cole [1] as a way to determine flow velocity along a large pipe by measuring the differential pressure at specific radial positions at as many diameters as one might need to measure. By employing this method, it is possible for one to establish a discrete but detailed sample of the velocity profile of the flow. It has been shown, in many other works (see [1], [2] and [3], for example) that, if conducted carefully, in a steady flow condition, even with only one mapping traverse of the velocity profile, this measurement can be used to calibrate other flow meters with reasonable accuracy.

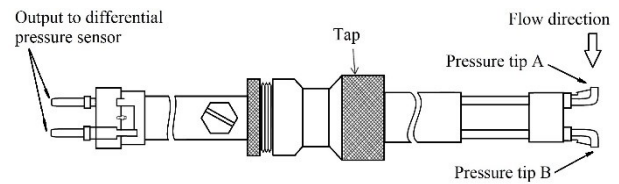


Figure 1: The Cole type Pitot tube - Schematic representation.

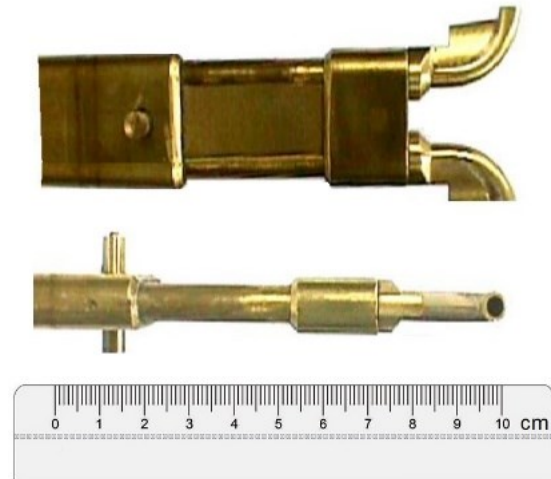


Figure 2: The Cole type Pitot tube – Detail of tips.

Albeit its age, it is a fairly conventional and robust method of calibration of flow meters, as it is suitable for on-site usage, it is easy to transport, and can be easily applied in a varied range of pipe diameters and fluid velocities, having also the advantage of low uncertainty level associated to its measurements in such harsh conditions of work. Also, it is a relatively affordable equipment, when compared to other flow meters or even with the costs required for laboratory calibration of the often large flow meters installed in water supply systems.

It sure have a few disadvantages, such as not being an automatic flow meter, which calls for the operation of a specialized technician and requires the addition of pressure transmitters connected to a computer. Another issue is that it needs to be inserted in the flow, a condition that requires a tap with a valve to be installed outside the pipe, usually close to the flow meter being calibrated.

Although this later question does not represent a major problem in terms of implementation, it leads to a more relevant matter that needs to be addressed: the inherent disturbance of the velocity profile by the insertion of the Pitot-Cole rod into the flow. As stated before, to correct the influence of the Pitot-Cole tips, a calibration coefficient,  $C_d$ , is applied to the measurements through the following relation:

$$V_0 = C_d \sqrt{\frac{2\Delta P}{\rho}} \quad (1)$$

Where  $V_0$  is the measured fluid velocity,  $\Delta P$  is the differential pressure read from the tips of the Pitot-Cole tube in each traverse position and  $\rho$  is the density of the fluid. The value of  $C_d$  is obtained in different ways depending on the calibration method and this will be detailed further ahead in this paper.

## 2.2 Effects of the Instrument Calibration

Acknowledging the issue of measurement deviation, Cole and Hubbard, respectively in [1] and [2], carried out the first experiments to estimate values of  $C_d$  in order to correct the measurements made when using the Pitot-Cole tube. The experiments were conducted at different facilities, providing a detailed study on the influence of a variety of pipe diameters and the smoothness of the velocity distribution in those conduits. At that work, it was concluded that the accuracy of the measurements was highly dependent on the calibration coefficient and that this value could be found by calibrating the Pitot-Cole tube at a location in which “the velocity distribution or disturbance is similar to that at the location in which the velocity distribution is to be determined” [1]. Tests conducted in different conditions, such as in distinct pipe diameters and in a revolving boom station, concluded that the mean value of  $C_d$  was around 0.869, but no detailed conclusions in relation to its dependency on Reynolds number was drawn.

As it is expected, the physical simulation of disturbances for large pipes in a controlled environment is costly and almost a custom implementation that makes the calibration of Pitot-Cole tubes impractical. A closer method, however, is to calibrate the Pitot-Cole tube in a towing tank, simulating the flow velocities by imposing it to the instrument along the tank. Similar to that is the usage of a circular tank, as presented in [2] and [7]. Using these methods, it is possible to obtain values of  $C_d$  for a range of flow velocities in which the water distribution systems actually operate.

As presented in [4], mainly due to the lack of availability of facilities and the costs associated with the usage of a towing tank, a new methodology was proposed at IPT – Institute for Technological Research, in Brazil, in the early 2000s. At that work, it was shown that the calibration of a Pitot-Cole tube, similarly to the calibration of a “S” type Pitot tube, could be performed in a wind tunnel and that, for  $Re/L > 5 \times 10^5$  (equivalent to 0.5 m/s in water), the obtained calibration coefficient is suitable to be used in water for on-site calibration of flow meters. This is possible due to the

Reynolds similarity relation,  $Re_{water} = Re_{air}$ , in which velocities of air from 5 m/s to 36 m/s can be mapped, respectively, to 0.3 m/s and 2.4 m/s in water. Also, for the mentioned range of  $Re/L$ , the authors concluded that the collected data showed good agreement between the calibration coefficient values obtained from the wind tunnel and from the towing tank experiments. It was noted that there are some advantages in the proposed methodology as well, such as, greater stability of readings, easily attainment of flow rate set point, assembling of the instruments for the tests, faster calibration process and no need for transducer purges.

Another important result from [4] is that the tests indicated that the periodic calibration of Pitot-Cole tubes was in great need, since it was observed that minor changes in geometry of the tips, usually occurring from the usage of the instrument, could lead to a difference of up to 5% in  $C_d$  values. Because of this result, it was recommended to identify the tip in use, since flow direction can be read from both sides of the tube, using tip A or B (see Figure 1), and their  $C_d$  values can vary significantly. The authors of [5] even conclude, from a statistical analysis of a set of individual calibrations of Pitot-Cole tubes that, the use of different sides of the same tube is equivalent to completely different tubes, since their  $C_d$  values vary greatly.

The influence of this variation is deeper evaluated in [5] through the statistical analysis of a historical database of calibration coefficients obtained from nine years of experiments at IPT. They concluded that a single mean value for  $C_d$  for all Pitot-Cole tubes can have a large impact on the uncertainty of the flow rate measurement (up to 1.5%). At that same study, it is presented a figure of  $3.5 \times 10^7$  m<sup>3</sup>/year of uncertainty in the measurement of water distributed in the metropolitan area of São Paulo, in Brazil. Also, the authors recommend the periodic calibration of each Pitot-Cole tube, despite of no significant changes on the mean value of  $C_d$  being found over that period of time.

This last reference was also influenced by the results presented in [6], in which the authors state that one of the major contributions to the overall uncertainty is given by the uncertainty of  $C_d$ . Apart from the fact that the study encompasses only the “S” type Pitot tube, it is known from the literature presented above that this is also a main issue for the Cole type Pitot tube. Another investigation carried out in that study is the influence of the Reynolds number on the calibration coefficient of that kind of Pitot tube, to which the authors concluded that this effect is negligible when compared to the total uncertainty of the flow rate measurements. In contrast, the effect of the manufacturing quality was found to be relevant, which shows that an individual calibration of Pitot tubes is always preferred, as concluded by [5].

Taking into account the conclusions and results presented by the references previously cited, this paper aims at the investigation of the influence of a specific range of Reynolds numbers on the values of  $C_d$ , employing two configurations of Pitot-Cole tubes, in two different methods of calibration. The main purpose of this study is to reduce the uncertainty on the flow rate measurements performed on-site, since the impact of this is clearly of great importance for natural resources sustainability, such as the rational use of water.

### 3. Methodology

A set of four Pitot-Cole tubes was employed in this study. Two of them, here denoted by C1 and C2, are built as the tube presented in Figure 2. The other two, P1 and P2, are built with the inclusion of a safety pin between the tips, in order to protect them when in operation, since they can easily break off when touching the pipe walls. This modified version, presented in Figure 3, is the one preferred at IPT for on-site flow meter calibration, since it is more secure to use it on the field.

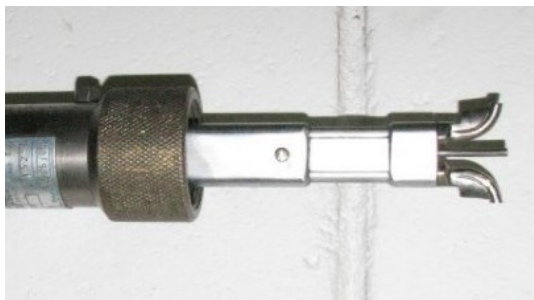


**Figure 3: Modified Cole type Pitot tube with a safety pin between tips.**

In order to compare the results, the dimensionless Reynolds number is used, divided by an unitary diameter ( $Re/L$ ). The calibration methods are described in the following subsections.

#### 3.1 Wind Tunnel Calibration

The adopted calibration procedure is the same as the one employed regularly at the IPT Fluid Flow Laboratory. An aerodynamic wind tunnel is used for the calibration of the Pitot-Cole tubes, as depicted in Figure 4. This wind tunnel was designed so that the velocity profile of the air pushed from the inside, at its test section, is uniform with low turbulence for flow velocities as high as 50 m/s.



**Figure 4: Aerodynamic wind tunnel at IPT's Fluid Flow Laboratory – On the left of the test section the standard Pitot-static tube is installed and its measurements are used as reference to obtain  $C_d$  values for the Pitot-Cole tubes being tested, which are installed on the right.**

By measuring the differential pressure using a conventional standard Pitot-static tube, the calibration coefficient of the Pitot-Cole tube,  $C_d$ , can be calculated from the following relation:

$$C_d = C_{Standard} \sqrt{\frac{\Delta P_{Standard}}{\Delta P_{Cole}}} \quad (2)$$

Where  $C_{Standard}$  is the calibration coefficient of the standard Pitot-static tube and  $\Delta P_{Cole}$  and  $\Delta P_{Standard}$  refers, respectively, to the measured differential pressure by the Pitot-Cole and the standard Pitot-static tubes.

Tests were performed for each of four Cole type Pitot tubes, for both tips of these instruments, in twenty different velocity conditions that are equivalent to  $Re/L$  values from, approximately,  $2.0 \times 10^5$  to  $2.3 \times 10^6$ . The differential pressures of both instruments were measured using inclined column manometers and no repetition was needed, since this is the standard procedure for calibration and the readings are performed only when differential pressure stability is attained.

#### 3.1 Towing Tank Calibration

This method of calibration of Pitot tubes is fairly traditional, although more expensive, since this kind of facility demands heavier maintenance and the tests are usually more time consuming. The procedure is pretty straight forward: one or a set of Pitot tubes (Cole type, "S" type, static or etc.) is attached to a carriage suspended over the tank and supported on rails on both sides. The carriage is then moved with constant speed along the tank, which is usually long, straight, relatively narrow and deep enough so that no waves are generated from reflexion on the walls and no effect of the bottom is significant. An overview of the towing tank of IPT with its carriage is presented in Figure 5. This facility is

250 m long, 5 m wide and its carriage can reach up to 3.2 m/s.



**Figure 5: Overview of Towing tank facility at IPT – The Cole type Pitot tubes can be seen on the bottom, attached to a holding structure at the lower deck of the carriage.**

An encoder system is adopted to register the revolutions per minute of one of the carriage's wheels, which are used to compute the velocity of the system. Similarly to expression (2), this velocity of the moving Pitot-Cole tubes is employed to calculate  $C_d$  values from eq. (3) below, computing the velocity directly from the differential pressures read with the Pitot-Cole tubes:

$$C_d = \frac{V_{Carriage}}{V_{Cole}} \quad (3)$$

Where  $V_{Carriage}$  is the velocity registered from the moving system and  $V_{Cole}$  is the velocity computed from the differential pressure measured by the Pitot-Cole tubes, with correction only for the calibration coefficients of the pressure transducers, which have very low individual contributions on the uncertainties of the flow rate measurements, being considered negligible for this study.

The experiment was carried out for 17 velocities, with a repetition of three runs for each. The velocity range corresponds to  $Re/L$  values from  $1.15 \times 10^5$  to  $3.4 \times 10^6$ , in order to cover and outrange the values usually employed for the wind tunnel calibration of Pitot tubes. Especial attention was given to lower and higher values in this range, since the idea is to reduce the uncertainty of flow rate measurements for more extreme values of fluid velocities, in which case the velocity profile is usually disturbed and measurements can be harder to perform with relative low uncertainties. Both sides of the four Pitot-Cole tubes were tested and had their

calibration coefficients computed for all the velocities of the test.

#### 4. Results

Assuming that each side of a single Pitot-Cole tube might correspond to a completely different instrument, as stated by the authors of [5], the sample used in this study can be regarded as two sets of four instruments each: four with a central pin and four without this feature.

The results of the measurements in the towing tank are compared to those performed using the wind tunnel and the threshold of  $Re/L = 5 \times 10^5$ , proposed in [4], is put to a test, since the sample of that study was scarce and restricted to a limited range of  $Re/L$  values for the towing tank experiments.

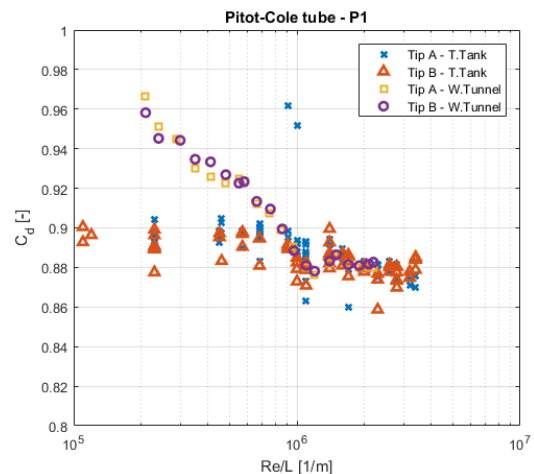


**Figure 6:  $C_d$  values for Pitot-Cole P1 (with pin).**

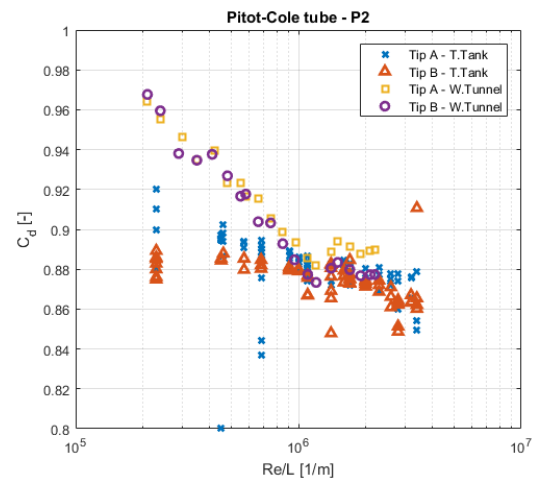


**Figure 7:  $C_d$  values for Pitot-Cole P2 (with pin).**

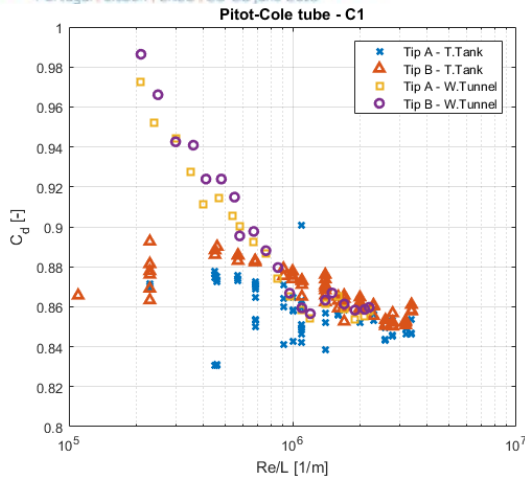


Figure 8:  $C_d$  values for Pitot-Cole C1 (without pin).

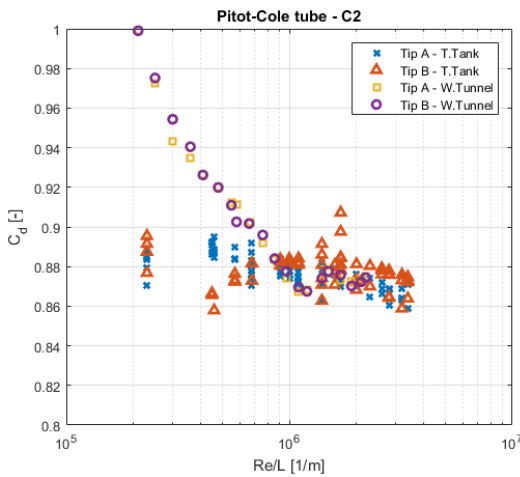


Figure 9:  $C_d$  values for Pitot-Cole C2 (without pin).

It is possible to observe from Figure 6 to Figure 9 that both methods of calibration are coherent for the expected range. Outside it, the values of  $C_d$  from the towing tank are more reliable and are in agreement with the other studies. In this figures is also shown that there is less dispersion for the data collected in the experiments with the instruments that have the central pin. As stated before, this feature increases the reliability of the readings by creating a stronger wake in the flow, and, therefore, leads to more accurate measurements.

Outliers were excluded for the analysis, so values of  $C_d$  below 0.84 and above 0.94 for the towing tank experiments are discarded for mean and standard deviation computations.

#### 4. Conclusions

Analysis of the results without differentiation of the tips (Figure 10 and Figure 11) indicate that a mean value of

$C_d$  can be used even for low and high values of  $Re/L$ , as proposed by Edward S. Cole in [1] but, nevertheless, the coefficient must be obtained for each instrument, since the standard deviation is considerably large and the uncertainties can be greatly affected, as presented in [4] and [5]. From these scatter plots it is also visible that the mean value of the calibration coefficient for the Pitot-Cole with the pin is slightly larger than the one proposed by Edward S. Cole.

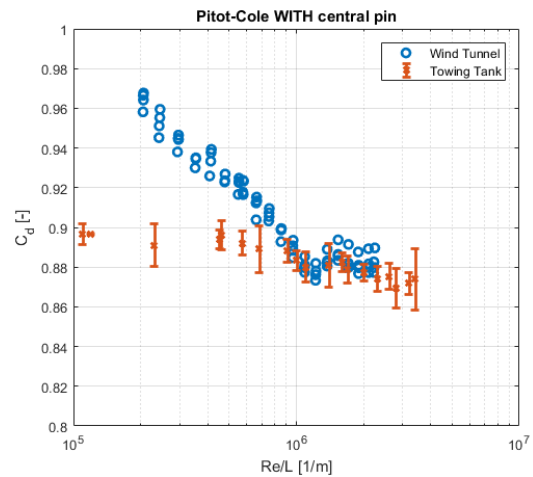


Figure 10:  $C_d$  values for both Pitot-Cole tubes with central pin - Bars indicate the standard deviation from mean values.

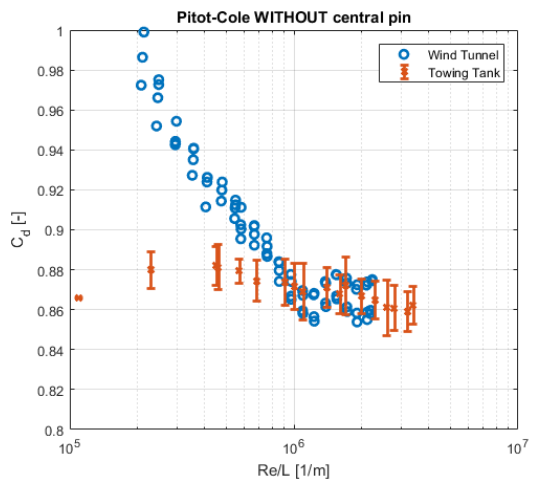


Figure 11:  $C_d$  values for both Pitot-Cole tubes without central pin - Bars indicate the standard deviation from mean values.

The attained results show good agreement with previous studies for the range  $5 \times 10^5 < Re/L < 2.5 \times 10^6$ . Also, in this range, both methods of calibration agree between them. An evaluation of the calibration coefficient for values of  $Re/L$  outside the mentioned range indicates that a constant value of  $C_d$  can be applied along the considered values of  $Re/L$ , but caution must be taken, since it is clear from the results that a value of  $C_d$  must be found for each instrument and preferably for each tip as well. From this experiments it is also identifiable that

the Pitot-Cole provided with a central pin between tips is preferable, since its calibration coefficient values are much less sparse than the results obtained from the tube without the central pin.

Overall, the results indicate that measurements for lower flow velocities can be performed with the use of a mean value of  $C_d$  obtained from the towing tank. Unfortunately, the calibration in this range cannot be performed in the wind tunnel. However, the results confirm that it is a robust method for the most common velocities measured in water distribution systems.

### Acknowledgments

The authors kindly thank the Institute for Technological Research – IPT and its support Foundation – FIPT, for the financial aid on the development of this study and on the events that follow for the disclosure of the results.

### References

- [1] Cole, E. S., & Cole, E. S.. “Pitot Tubes in Large Pipes”. *Transactions of A.S.M.E.*, 61, 465–475, 1939.
- [2] Hubbard, C. W.. “Investigation of Errors of Pitot Tubes”. *Transactions of A.S.M.E.*, 61, 477–506, 1939.
- [3] ISO 3966: *Measurement of fluid flow in closed conduits - Velocity area method using Pitot static tubes*, 2008, p. 59.
- [4] Espirito Santo, G., & Sanchez, J. G.. “Calibração De Tubos De Pitot Tipo Cole”, *20<sup>o</sup> Congresso Brasileiro de Engenharia Sanitária e Ambiental*, 2096–2105, 1999.
- [5] Buscarini, I. D. O., Barsaglini, A. C., Jabardo, P. J. S., Taira, N. M., & Nader, G.. “Impact of Pitot tube calibration on the uncertainty of water flow rate measurement”. *Journal of Physics: Conference Series*, 648, 2015.  
<https://doi.org/10.1088/1742-6596/648/1/012005>
- [6] Kang, W., Trang, N. D., Lee, S. H., Choi, H. M., Shim, J. S., Jang, H. S., & Choi, Y. M.. “Experimental and numerical investigations of the factors affecting the S-type Pitot tube coefficients”. *Flow Measurement and Instrumentation*, 44, 11–18, 2015.
- [7] Siqueira, N. A.. “Medidor de vazão de água, tipo “Pitot-Cole”, com configuração prismática hexagonal”. (São Paulo, Universidade de São Paulo), 2018.

# Experimental Study on Flow Rate Measurement Downstream of an Elbow Pipe using the Clamp-on ultrasonic Flowmeter

S. Wada<sup>1</sup>, N. Furuichi<sup>1</sup>, H. Hamada<sup>2</sup>, T. Akama<sup>2</sup>, T. Yamaguchi<sup>2</sup>, S. Suzuki<sup>2</sup>  
and S. Takatsuka<sup>2</sup>

<sup>1</sup>Advance Industrial Science and Technology, National Metrology Institute of Japan,  
Central 3, 1-1-1, Umezono, Tsukuba, Ibaraki, 305-8563, Japan

<sup>2</sup>TOKYO KEIKI INC., Tokyo, Japan

E-mail (corresponding author): wada.s@aist.go.jp

---

## Abstract

This paper presents experimental measurements using the clamp-on ultrasonic flowmeter. To obtain an uncertainty of flow rate measurement using the clamp-on ultrasonic flowmeter, experiments are carried out at the national standard calibration facility of water flow rate in Japan (the National Institute of Advanced Industrial Science and Technology, National Metrology Institute of Japan). Flow rate given by the clamp-on ultrasonic flowmeter is compared with the static gravimetric method using a tank system weighing 50 t. The uncertainty of the reference flow rate given by the 50 t weighing tank system is 0.060% ( $k = 2$ ). The transducers of clamp-on ultrasonic flowmeter are mounted downstream of an elbow pipe. The length from the elbow to the transducers is five times of the pipe diameter and ten times of the pipe diameter, respectively. The curvature radius of the elbow is equal to the pipe diameter. Flow rate measurement is based on a time of flight of pulsed ultrasound. The multi-pass mode of the clamp-on ultrasonic flowmeter is used to measure the disturbed flow condition, and the number of ultrasound pass is up to four. The pipe is made of stainless steel with the outer diameter of 216.3 mm and the thickness is 6.5mm. The flow rate condition is from 100 m<sup>3</sup>/h to 700 m<sup>3</sup>/h. The results show that the clamp-on ultrasonic flowmeter using the multi-pass mode can measure the flow rate accurately, even if the velocity profiles are disturbed by the upstream elbow pipe.

---

## 1. Introduction

It is well known that the measured flow rate given by flowmeters, such as ultrasonic, electromagnetic, and turbine flowmeters, generally depends on the velocity profile in a pipe. This dependence demonstrates that the measurement accuracy of these flowmeters is influenced by the upstream pipe configuration and flow rate conditions, even if the flowmeters are calibrated by a calibration facility. In calibration facilities, the construction of a complete equivalent pipe layout in an actual field is often difficult. In consideration of the application of these flowmeters to actual flow fields, such as industrial facilities and power plants, the issue of disturbed velocity profile influenced by the upstream pipe condition is important.

This paper presents the experimental results of flow rate measurement using the clamp-on ultrasonic flowmeter. Two upstream pipe conditions, a long straight pipe and an elbow pipe, are applied. The influence of the number of

ultrasound path on the uncertainty of flow rate measurement is evaluated.

## 2. Experimental facility and conditions

### 2.1 Experimental facility

The experiments were performed at the water flow rate calibration facility of the National Institute of Advanced Industrial Science and Technology, National Metrology Institute of Japan (AIST, NMIJ). This facility is the national standard calibration facility of water flow in Japan. The flow rate given by the clamp-on ultrasonic flowmeter was evaluated with respect to the static gravimetric method using a tank system weighing 50 t. The uncertainty of the reference flow rate given by the 50 t weighing tank system is 0.060% (the coverage factor  $k = 2$ ). For the details of the system, see reference [1].

### 2.2 Experimental conditions

Figure 1 shows the schematic of the test facility and the test section. The transducers of clamp-on

ultrasonic flowmeter are mounted downstream of a straight pipe and an elbow pipe. The length of the straight pipe is  $65D_1$ . Where,  $D_1$  is the pipe diameter of the test section. The pipe is made of stainless steel with the outer diameter of 216.3 mm and the thickness is 6.5 mm. In the case of downstream of an elbow, the length from the elbow outlet to the transducers is  $5D_1$  or  $10D_1$ . The curvature radius of the elbow is equal to the pipe diameter. The flow rate condition is from  $100 \text{ m}^3/\text{h}$  to  $700 \text{ m}^3/\text{h}$ .

Flow rate measurement is based on a time of flight of pulsed ultrasound. Figure 2 shows the layout of transducers. The multi-pass mode of the clamp-on ultrasonic flowmeter is used to measure the disturbed flow condition, and the number of ultrasound path is up to four. In four paths mode, the ultrasound paths are bisected at right angles as shown in the figure. To measure along the other circumferential path, transducers are mounted with an interval of  $30^\circ$ .

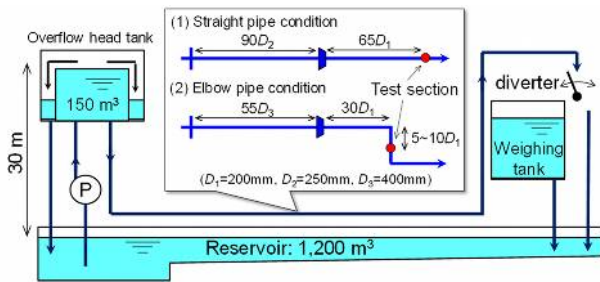


Figure 1: Experimental facility and test section.

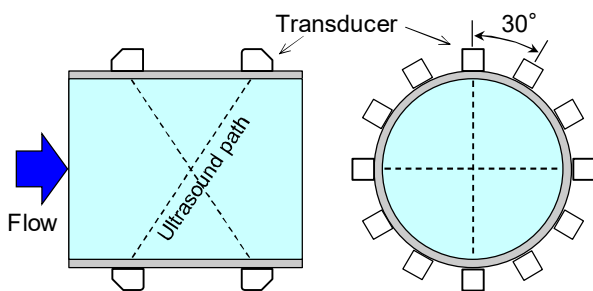


Figure 2: Setting of Transducers.

### 3. Results

Figure 3 and Figure 4 show the errors and standard deviations of flow rate measurement using the 1 path and 4 paths mode downstream of the long straight pipe. The error is obtained as following equation.

$$E = \frac{Q_u}{Q_w} - 1 \quad (1)$$

Where,  $Q_u$  and  $Q_w$  are the flow rate measured by the ultrasonic flowmeter and the weighing tank system, respectively.  $E_{arg}$  is the average value of all measured  $E$ . These results indicate clearly that 4 paths can measure the flow rate accurately compared with 1 path.

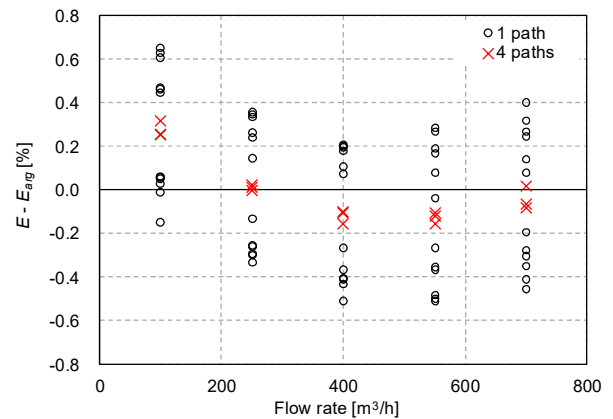


Figure 3: Errors of flow rate measurement using 1 path and 4 paths downstream of the long straight pipe.

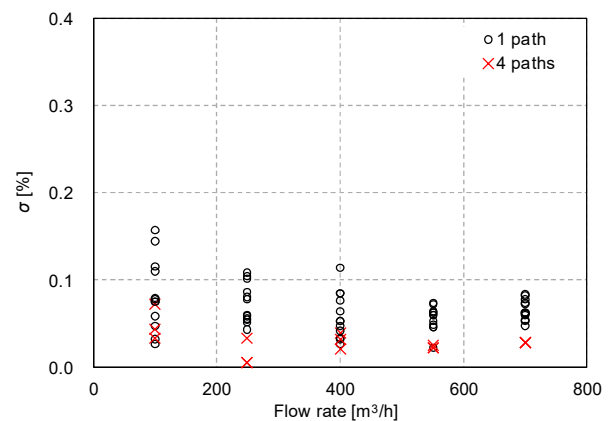
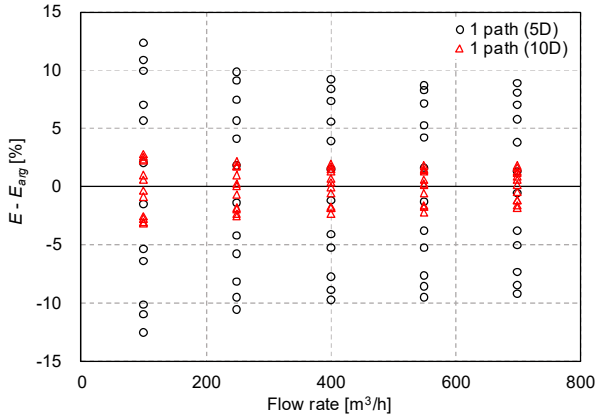


Figure 4: Standard deviations of flow rate measurement using 1 path and 4 paths downstream of the long straight pipe.

Figure 5 and Figure 6 are the errors and standard deviations of flow rate measurement using 1 path mode downstream of the elbow pipe. Both errors measured at  $5D_1$  and  $10D_1$  are plotted in these figures. These results indicate that the accuracy of flow rate measurement depends on the circumferential position of transducer because of the strongly disturbed flow by the elbow.

On the other hand, Figure 7 and Figure 8 show the results using 4 paths mode downstream of the elbow pipe. The errors and standard deviations of

flow rate measurement are almost equivalent to the errors downstream of the long straight pipe condition.



**Figure 5:** Errors of flow rate measurement using 1 path downstream of the elbow pipe.

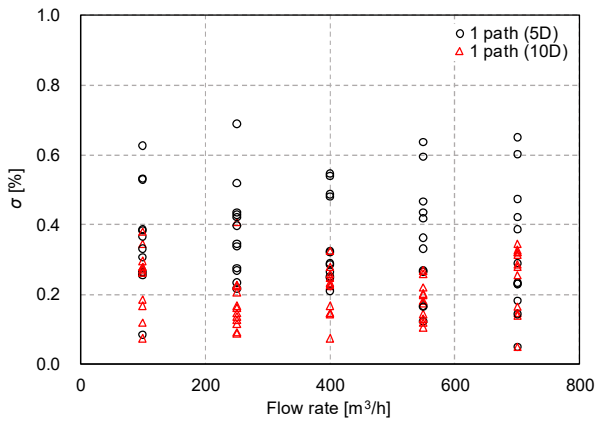


**Figure 6:** Standard deviations of flow rate measurement using 1 path downstream of the elbow pipe.

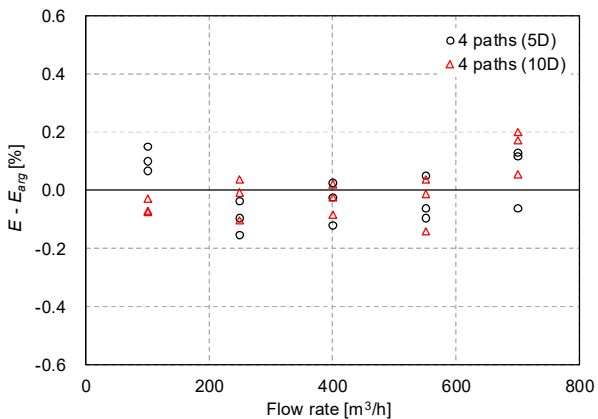


**Figure 7:** Errors of flow rate measurement using 4 paths downstream of the elbow pipe.

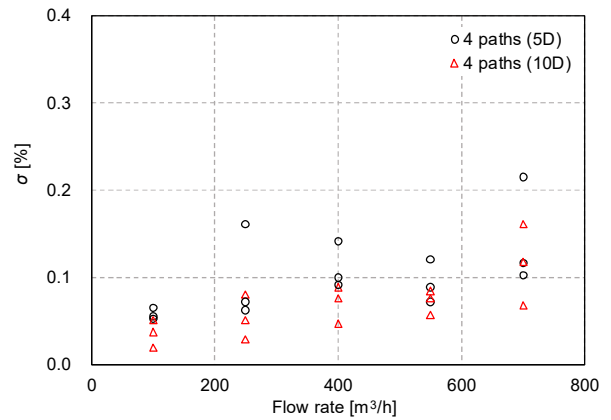


**Figure 8:** Standard deviations of flow rate measurement using 4 paths downstream of the elbow pipe.

#### 4. Conclusion

The clamp-on ultrasonic flowmeter using 4 paths can measure the flow rate accurately compared with 1 path downstream of the long straight pipe. Additionally, the errors and standard deviations measured downstream of the elbow pipe using 4 paths are equivalent to the case of the long straight pipe, even if the velocity profiles are disturbed strongly by the upstream elbow pipe.

#### References

- [1] Furuichi N, Terao Y and Takamoto M: Calibration facilities for water flowrate in NMIJ, *Proceedings of 7th International Symposium on Fluid Flow Measurement*, Anchorage, USA, August (2009), pp.12–14.

# A calibrated physical flow standard for medical perfusion imaging

G. Kok<sup>1</sup>, N. Pelevic<sup>1</sup>, A. Chiribiri<sup>2</sup>, X. Milidonis<sup>2</sup>, M. Nazir<sup>2</sup>, M. Capstick<sup>3</sup>, S. Drost<sup>4</sup>,  
C. Poelma<sup>4</sup>, T. Schaeffter<sup>5</sup>

<sup>1</sup>VSL B.V., Thijssseweg 11, 2629 JA, Delft, Netherlands

<sup>2</sup>School of Biomedical Engineering and Imaging Sciences, King's College London, London, United Kingdom,

<sup>3</sup>ZMT Zurich MedTech AG, Zurich, Switzerland,

<sup>4</sup>Laboratory for Aero- and Hydrodynamics, Technische Universiteit Delft, Delft, Netherlands,

<sup>5</sup>Physikalisch-Technische Bundesanstalt, Berlin, Germany

E-mail (corresponding author): gkok@vsl.nl

---

## Abstract

In the medical sector, various imaging methodologies or *modalities* (e.g. MRI, PET, CT) are used to assess the health of various parts of the bodies of patients. One such investigation is the blood flow or *perfusion* of the heart muscle, expressed as the (blood) flow rate normalized by the mass of the volume of interest, with unit mL/min/g. Currently there is no physical flow standard for the assessment and validation of myocardial perfusion imaging methodologies, resulting in a large proportion of medical diagnoses being inaccurate and highly dependent on the scanner type, software used and the clinical operator. In the EMPIR 15HLT05 PerfusImaging project a phantom simulating myocardial perfusion has recently been developed with which imaging modalities can be tested. In this paper the construction and validation of the phantom is described which involved several iterations with design updates, computational fluid dynamics simulations, 3D printing of the phantom, ultrasound imaging velocimetry and magnetic resonance imaging (MRI). Dynamic contrast-enhanced MRI was performed to image the passage of a tracer through the phantom and estimate perfusion. Two flow models and associated data analysis methods to relate the measurement data with the reference flow rates are presented and discussed.

---

## 1. Introduction

In the medical sector, various imaging methodologies or *modalities* (e.g. MRI, PET, CT) are used to assess the health of various parts of the bodies of patients. One such investigation is the blood flow or *perfusion* of the heart muscle, expresses as the (blood) flow rate normalized (divided) by the mass of the volume of interest, with unit mL/min/g. A decreased perfusion of the heart muscle or myocardium is an imaging biomarker for increased risk for a heart attack and can cause chest pain.

Currently there is no physical flow standard for the assessment and validation of myocardial perfusion imaging methodologies, resulting in a large proportion of medical diagnoses being inaccurate and highly dependent on the scanner type, software used and the clinical operator. In the EMPIR 15HLT05 PerfusImaging project [1] a phantom simulating myocardial perfusion has recently been developed with which imaging modalities can be

tested. The design was based on an earlier, already existing phantom made by KCL [2].

In this paper the construction and validation of the phantom is described which involved several iterations with design updates, computational fluid dynamics (CFD) simulations, 3D printing of the phantom, ultrasound imaging velocimetry (UIV) and MRI measurements involving all partners. Dynamic contrast enhanced MRI (DCE-MRI) measurements were also performed. Various flow models to interpret the data will be discussed.

## 2. Phantom design

The phantom [3] mimics the complete flow through a human heart including the four heart chambers, pulmonary volume and the blood flow through the heart muscle. The part simulating the tissue of the heart muscle or the *myocardium* is of special interest in this study. The arteries in this tissue are simulated by more than 200 parallel channels or capillaries with cross-sectional area ranging from 1

to 7 mm<sup>2</sup>. Upstream of the channels is a pre-chamber with a volume of 36 mL. This part was produced by 3D printing and is shown in Figure 1. The engineering and production of the phantom was done by the company Zurich MedTech (ZMT). In Figure 2 a schematic drawing of the phantom is shown including the location of the MRI imaging plane. The flow rates through the aorta (cardiac output) can be varied between 2 and 5 L/min and the perfusion rate through the myocardium between 1 and 5 mL/min/g, corresponding to flow rates between 85.3 and 426.5 mL/min. In this study, the flow rate through the aorta was set around 4 L/min and the full range of flow rates through the two myocardia were tested.

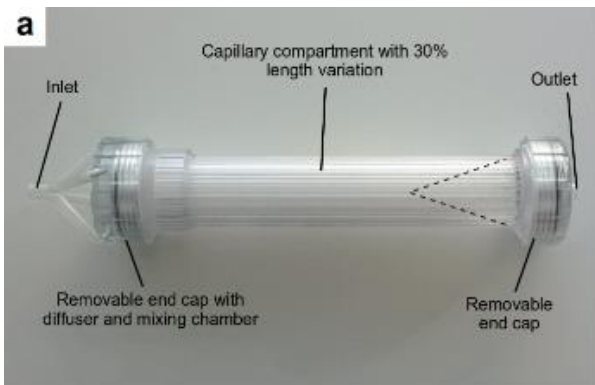


**Figure 1:** Photograph of the 3D printed myocardium indicating the main compartments.

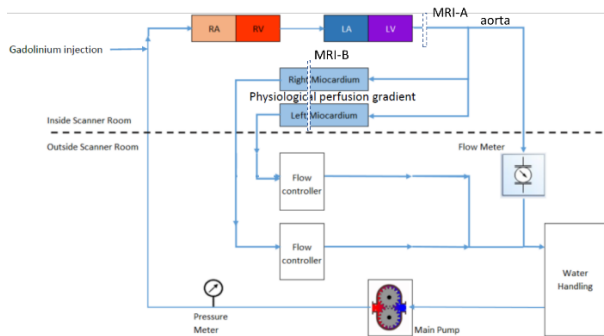


**Figure 2:** Schematic overview of the phantom. The MRI imaging locations MRI-A and MRI-B are in reality in the same plane (dashed lines). The four heart chambers are denoted by RA, RV, LA and LV (right atrium, right ventricle, left atrium, left ventricle).

### 2.1 CFD simulations

The design goal was a channel configuration with a rotationally symmetric flow profile with maximum flow velocity at the centre and linearly decreasing flow velocity to -30 % at the outer wall (for channels with identical cross sections). While Poiseuille's law for a laminar flow regime suggests a linear increase of +30 % in channel length towards the outer wall to obtain the desired linear variation in flow velocity, the OpenFOAM CFD solver was used by VSL to confirm this expectation and to ensure that the flow FLOMEKO 2019, Lisbon, Portugal

regime would be rotationally symmetric, at least in the model. The final design had four inlets from the sides to the pre-chamber in which a laminar flow element upstream of the channels was installed to remove any form of potential pressure gradient and turbulence in the cross section (the Reynolds number is below 250 in the pre-chamber). In Figure 3 two plots of the results of the CFD simulation are shown. Approximately 4 million cells were used. For the large octagonal channels the CFD results are in line with the simple analytical Poiseuille model, see Table 1. For the smaller square channels with side lengths 1.0, 1.2, 1.4 and 1.8 mm, the predicted flow rates by CFD are smaller than the analytical ones, which is probably due to the mesh size of the CFD simulation.

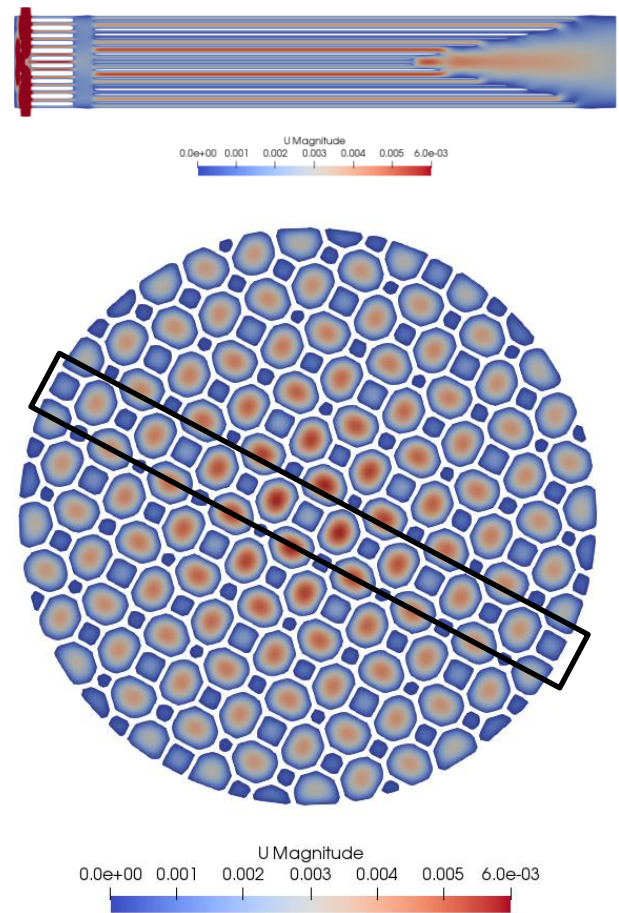


**Figure 3:** Some results of the velocity field calculated by CFD. Top: cross-cut along the main axis of the phantom. Bottom: cross cut perpendicular to the axis at the mid-myocardial level. The black box indicates the octagonal channels used in Table 1.

**Table 1:** Flow rate per channel as a fraction of the flow in the octagonal channels in the box of Figure 3 – bottom. Numbering is from top left to bottom right.

Channel nr.	1	2	3	4	5	6	7	8
Percentage	70%	78%	89%	100%	100%	89%	78%	70%

## 2.2 PIV measurements

In order to measure the actual flow rates through the channels of the phantom, measurements with ultrasound imaging velocimetry (UIV) were performed by TU Delft. The earlier version of the phantom was based on thin walled straws [2]. The current version was 3D printed and had thicker walls [3], which turned out to be problematic for the UIV measurements. Some indicative results were finally obtained suggesting linearly decreasing flow velocities with radius, but with an uncertainty higher than the target uncertainty of 10 %. In Figure 4 a schematic view of the measurement set-up and a measurement image are shown.

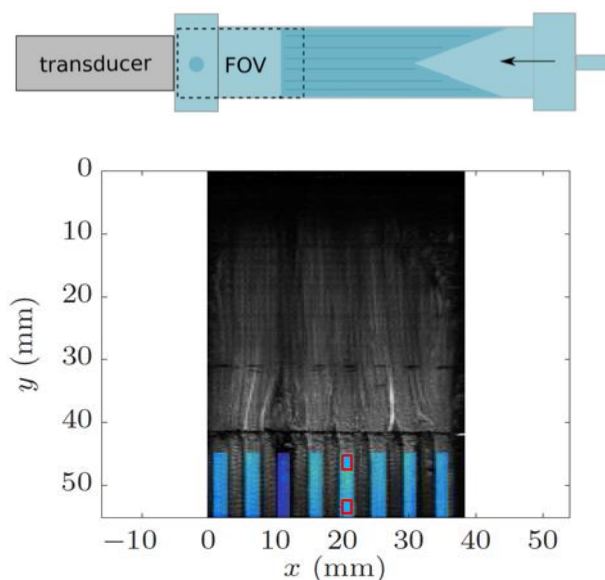


**Figure 4:** Top: Schematic drawing of the ultrasound imaging velocimetry (modified) set-up, showing the compartment in light blue and the ultrasound transducer in grey. FOV indicates field of view. Bottom: tracer visualization at the outflow. By correlating the intensity within the two red squares in the capillary in the centre, the mean flow can be determined.

## 2.3 Phase contrast MRI measurements

As alternative to the UIV measurements phase contrast (PC) MRI measurements were performed with an estimated uncertainty of 10 % for the flow velocities. Five flow rates between 85.3 and 426.5 mL/min were each measured twice, and the results were analysed in various ways by KCL and VSL. In Figure 5 one such analysis by VSL is shown. The channel geometry is slightly different than that of Figure 3, but the expected decrease in flow rate is the same. The octagonal channels on a horizontal line were identified by an algorithm, and the flow rates through channels were calculated by integrating the velocity field and expressed as a percentage relative to the flow rate in channel 5. A decrease of  $30 \pm 10$  % with respect to the maximum

flow rate is visible for all flow rates, be it not completely symmetrical between left and right side.

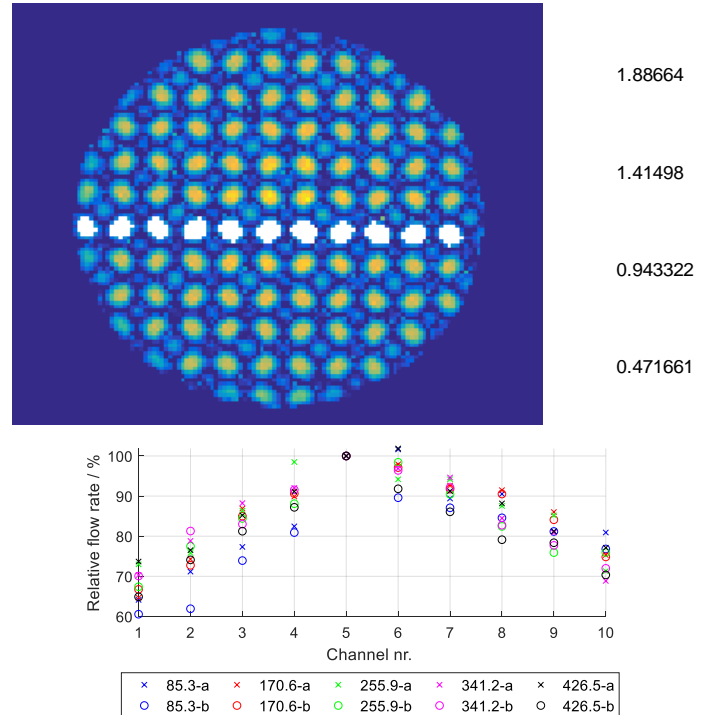


**Figure 5:** Top: PC-MRI measurement image with identified octagonal channels on a horizontal line used for integration of the measured velocity field (except for the most left one). Bottom: Relative flow rate distribution over the channels at five flow rates as measured by PC-MR, normalized to the flow rate in channel nr. 5.

## 3. DCE-MRI and flow modelling

### 3.1 Dynamic Contrast Enhanced MRI protocol

For clinical measurements of myocardial perfusion in patients a so-called Dynamic Contrast Enhanced MRI protocol is being used. A bolus of contrast agent (CA, e.g. gadolinium) is injected in the patient upstream of the heart and this is simulated by injecting such a bolus at a specific point in the phantom representing the vena cava. The CA concentration in the blood is roughly proportional to the measured MRI signal. The bolus of CA mixes with the blood (or water) and passes through the four heart chambers. Then, the MRI signal is measured as function of time in (a pipe simulating) the aorta, upstream of the myocardium. The resulting time series is called the arterial input function (AIF). In the same image, the concentration inside the myocardium is also visible. After conversion from signal intensity to CA concentration, the perfusion of the myocardium can be estimated. In patients typically three slices of the heart are being measured, though one slice at a time is used during the analysis phase. In the experimental work with the phantom one slice of the

phantom has been measured and analysed. To reduce the effect of the non-linearity of the relationship between CA concentration and MRI signal intensity a dual bolus scheme is typically used. In this scheme a first ‘pre-bolus’ diluted in saline at a ratio 1:9 is injected from which the AIF is derived and scaled by a factor 10. Subsequently, a second undiluted bolus is injected from which the myocardium signal is taken. As the CA concentration in the myocardium is much lower (and more spread out over time) than in the aorta, the MRI signal magnitudes of AIF and myocardium measurements are similar, and the effects of non-linearity and signal saturation are diminished.

In the next sections various ways of analysing the data are presented.

### 3.2 Standard theory

The standard theory and method for quantification of the perfusion assumes a system of volume  $V_{sys}$  with one inlet and one outlet, see Figure 6. The AIF is measured at the inlet by MRI-A (aorta) and is proportional to the CA concentration  $c_{in}(t)$ . The average CA concentration in  $V_{sys}$  at time  $t$  equals  $c_{sys}(t)$  and is measured by MRI-B, the measurement of the myocardium. The stationary flow rate through the system equals  $q_{in} = q_{out}$  and the quantity of interest is the perfusion  $f = q_{in}/V_{sys}$ .

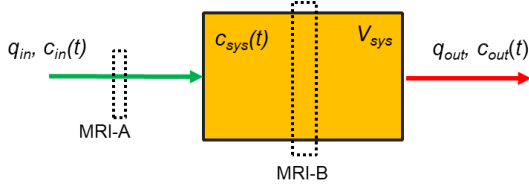


**Figure 6:** Standard system view used in perfusion quantification with DCE-MRI.

Based on a mass balance of CA in the system, the following equation can be derived

$$V_{sys}c_{sys}(t) = \int_0^t q_{in} c_{in}(s)ds - \int_0^t q_{out} c_{out}(s)ds \quad (1)$$

Assuming a linear and stationary system with impulse response function  $h(t)$ ,  $c_{in}(t) = c_{sys}(t) = 0$  for  $t < 0$  s and using  $q_{in} = q_{out}$  the outlet concentration can be written as

$$c_{out}(t) = \int_0^t c_{in}(t-s)h(s)ds = (c_{in} * h)(t) \quad (2)$$

where  $*$  denotes the convolution operation. Defining  $R_f(t) = q_{in}/V_{sys} \left(1 - \int_0^t h(s)ds\right)$  and performing some mathematical transformations one can derive that

$$c_{sys}(t) = (c_{in} * R_f)(t). \quad (3)$$

Solving convolution Equation (3) for  $R_f(t)$  the perfusion  $f$  follows from  $f = R_f(0) = \max(R_f(t))$ .

In practice a correction factor has to be applied for the accessible part of the myocardial tissue for the CA (‘volume fraction’), or the ‘non-plastic fraction’ in the case of a phantom.

Advantages of the standard approach are its relative simplicity and the fact that the volume  $V_{sys}$  doesn’t need to be known. Possible limitations are that the measured concentration by MRI-B is in practice (at least for the phantom) rather an outflow CA concentration  $c_{out}(t)$  than the system average concentration  $c_{sys}(t)$ , and interaction between different parts of the myocardium is not modelled.

### 3.3 Alternative model

An alternative model and method for calculating the perfusion is based on Figure 7, where a system with a common pre-chamber is shown and two subsequent compartments in parallel. Note that this model is not limited to three compartments, but can be generalized to an arbitrary number of compartments. For ease of presentation only three compartments are used in this paper.

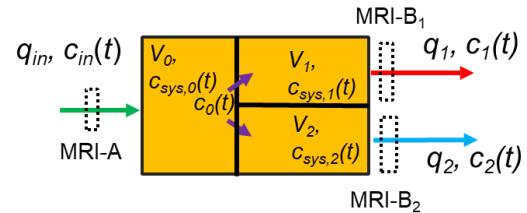


**Figure 7:** Alternative system view for perfusion quantification with DCE-MRI. The compartment volumes are denoted by  $V_i$ , compartment average concentrations as function of time are denoted by  $c_{sys,i}(t)$ , compartment outflow concentrations are denoted by  $c_i(t)$  and outflow flow rates by  $q_i$  for  $i = 0, 1, 2$ .

It is again assumed that at location MRI-A the MRI signal is proportional to the CA inlet concentration  $c_{in}(t)$ . However, at MRI-B<sub>1</sub> and MRI-B<sub>2</sub> the signal is assumed to be proportional to the respective outlet concentrations. The perfusion  $f_i$  in compartment  $i$  is defined by  $f_i = q_i/V_i$ , the impulse response function for compartment  $i$  is denoted by  $h_i(t)$  and the mean transit time  $T_i$  of a unit of CA through a compartment  $i$  is given by  $T_i = \int_0^\infty t h_i(t)dt$ . From system inlet to outlet  $i = 1$  or  $2$  the mean transit time  $T_{0i}$  is given by  $T_{0i} = T_0 + T_i$  and the impulse response function  $h_{0i}$

is given by  $h_{0i} = h_0 * h_i$ . The relationships of interest for the measured MRI signals are

$$c_i(t) = (c_{in} * h_{0i})(t), \quad i = 1, 2 \quad (4)$$

which is similar to Equation (3).

In order to be able to calculate the perfusions an additional hypothesis is needed. The assumption made is that there exists a constant tissue delay factor  $d$  for which following relation holds true for any compartment  $i$ :

$$T_i = d V_i / q_i \quad (5)$$

From Equation (5) then follows that  $f_i = d / T_i$ . Using  $q_{in} = q_1 + q_2$  all perfusions as well as flow rates can be calculated when the measurement results  $c_{in}(t)$  and  $c_i(t)$  are available.

When a dual bolus scheme is being used or when there is a significant delay before the CA arrives at the myocardium additionally an additional time offset  $\tau$  has to be used in Equation (5), leading to  $T_i = \tau + d V_i / q_i$ . Note that this is also the case for the standard method. In the assessment of the methods discarding  $\tau$  and only using the main bolus gave better results and these are shown in Table 2.

Advantages of this alternative method are that it might be more realistic and thus might yield more accurate results, as it models the measurements at MRI-B<sub>i</sub> as proportional to the compartment outflow concentration rather than the compartment's average concentration, and it models a common large blood vessel (or phantom pre-chamber) upstream of smaller myocardium blood vessels (or phantom channels) in parallel. Disadvantages are the required knowledge of the (relative) volumes of the compartments (which is possible for a phantom but very difficult for tissue of patients) and the hypothesis of constant tissue delay factor (of which the exact value is required if absolute values of perfusion are of interest). Another disadvantage is that determination of the mean transit time requires integration over the complete relevant time domain of the signals  $c_{in}(t)$  and  $c_i(t)$ , which is possible for a phantom, but problematic for patients where CA may re-enter the aorta and myocardium resulting in an undesired 'second-pass' perfusion MRI signal. Another assumption is that  $c_0(t)$  is homogeneous at the outlet plane of the initial compartment. (A similar assumption is used in the standard method.)

### 3.4 Comparison of data analysis methods

The two analysis methods described in section 3.2 and 3.3 were applied to DCE-MRI data acquired for FLOMEKO 2019, Lisbon, Portugal

the phantom described in section 2. The target quantity was the ratio  $r$  of perfusion through the outer ring to the perfusion through the inner circle, i.e.  $r = f_{out} / f_{in}$ , see also Figure 8.

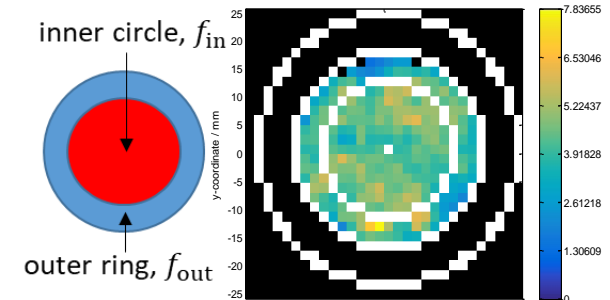


**Figure 8:** Left: Schematic partition of image in two parts of equal area. Right: Phantom with local pixel-wise perfusion values based on inverse transit times and assuming  $d = 1$ .

The two segments have equal area. The channels close to the outer boundary were taken out in this analysis, as measurement results were unreliable in this area due to partial volume effects.

The results of the calculations for both methods are shown in Table 2. In this case both methods turn out to perform equally well and are both in line with the reference value based on PC-MRI measurements (which are in-line with CFD and analytical calculations).

**Table 2:** Results of the calculations using the standard method ( $r^A$ ) and the alternative method ( $r^B$ ). The reference value based on PC-MRI measurements is  $r^A = 0.87 \pm 0.05$ .

$q_0^{ref} / (\text{mL/min})$	$r^A$	$r^B$
55	0.89	0.79
110	0.79	0.82
165	0.85	0.87
220	0.91	0.92
275	0.82	0.85

## 4. Discussion

The two analysis methods presented in this paper both rely on the validity of some additional assumptions. One of these assumptions is that the CA concentration at the inlets of all channels are equal at the same point in time and that the images are rotationally symmetric. Inspection of the raw MRI images directly shows that this is not the case, see Figure 9. Especially at the bottom the MRI signal appears to be higher.

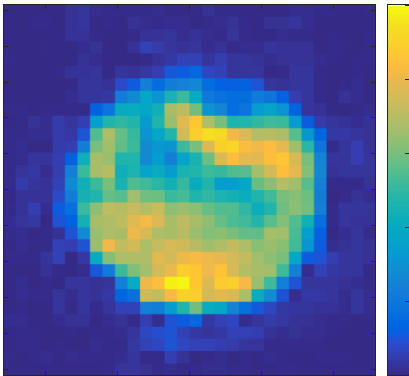


**Figure 9:** Raw MRI image of the phantom myocardium at flow rate 170 mL/min, showing imperfect rotational symmetry.

As the contrast agent has a higher density than the water some stratification seems to happen especially in the case of the lowest flow rates. Updated designs with passive mixers may improve the situation. Another practical issue that was encountered was that removing all the air bubbles from the phantom was not so straightforward.

The comparison of the performance of the methods may be obfuscated by effects such as stratification effects as discussed in the last paragraph. In the analysis algorithm various parameters need to be selected, such as an image base line value, the pixels to be included in the analysis and similarly for the selection of time points. Each of these choices has an effect on the results which in some cases is non-negligible. These issues are also encountered in medical practice and the phantom can help to assess the importance of each parameter.

The goal of the phantom is to make MRI perfusion measurements more quantitative and more comparable across different MRI manufacturers, software settings and operators when measuring real patients. Even if the alternative method would turn out to perform better in a next version of the phantom, its requirements in terms of necessary (relative) volume information and measurement time range and other assumptions may limit its applicability in a medical setting. Application to sample patient data is a necessary next step to assess the usefulness of the alternative method and this will be a next step in our research.

## 5. Conclusion

In this paper a calibrated physical flow standard for medical perfusion imaging was presented, i.e. a phantom mimicking a human heart with known flow rates through its channels which can be used to assess the performance of MRI scanners as well as of PET and CT scanners.

Reference values for the flow rates through the channels were measured with phase contrast MRI with an uncertainty of approximately 10 % and were in line with CFD and analytical calculations. PIV measurement results were only indicative due to the thickness of the 3D-printed material. Overall flow rates are being measured with flow meters.

Two models and associated analysis methods were presented that can be used to relate dynamic contrast enhanced MRI measurements with the reference flow rates. The methods performed approximately equally well for the phantom measurement data.

Current research in the project consists of measuring the phantom with different scanners, extending the phantom to a multi-compartment phantom simulating more faithfully human tissue, and applying the alternative data analysis method to real patient data in order to assess its usefulness in a medical setting.

## Acknowledgment

The authors gratefully acknowledge funding of this research by the EMPIR 15HLT05 PerfusImaging project. The EMPIR initiative is co-funded by the European Union's Horizon 2020 research and innovation programme and the EMPIR Participating States.

## References

- [1] EMPIR project 15HLT05 PerfusImaging, Metrology for multi-modality imaging of impaired tissue perfusion, <https://www.ptb.de/empir2018/perfusimaging/home/>
- [2] Chiribiri et al., "Perfusion Phantom: An Efficient and Reproducible Method to Simulate Myocardial First-Pass Perfusion Measurements With Cardiovascular Magnetic Resonance", *Magnetic Resonance in Medicine*, 2012, DOI 10.1002/mrm.24299
- [3] Milidonis et al., *Dynamic contrast-enhanced and phase contrast MRI of a novel 3D printed cardiac phantom mimicking transmural myocardial perfusion gradients*, ISMRM conference, Paris 2018.

# Results from an intercomparison between multiphase flow test facilities

G. Kok<sup>1</sup>, D. van Putten<sup>2</sup>, L. Zakharov<sup>3</sup>

<sup>1</sup>VSL, Thijssseweg 11, 2629 JA, Delft, the Netherlands

<sup>2</sup>DNV GL, Groningen, the Netherlands

<sup>3</sup>OneSubsea-Schlumberger, Bergen, Norway

E-mail (corresponding author): [gkok@vsl.nl](mailto:gkok@vsl.nl)

## Abstract

Multiphase flow meters are measurement instruments that simultaneously measure the flow rates of oil, natural gas and water flowing through a pipe line. Their traceability and the comparability of test results stemming from different multiphase test facilities is much less well established than that of single phase flow meters and single phase calibration facilities. In the (first) EMRP MultiFlowMet project an intercomparison for multiphase test facilities was organised to investigate the comparability of multiphase flow test facilities. Three facilities participated: NEL, DNV GL and OneSubsea-Schlumberger (OSS). VSL acted as independent partner auditing the uncertainty budgets, witnessing the tests and analysing the data. The outcome of this analysis was pairwise consistencies in the order of 80 %, taking into account the claimed uncertainties of the test facilities and the estimated meter reproducibility. This value was also found for the comparison with OSS, where a different inlet geometry was used. Open access to data and more extensive testing could provide means to get a better understanding of the reasons behind the inconsistency of a small part of the points.

## 1. Introduction

The traceability of single-phase flow meters is well managed by means of accredited calibration facilities performing calibrations for clients, with quality assured by means of audits on test methods and uncertainty quantification, and supplemented by the organisation of intercomparisons between the facilities. This is not the case for multiphase flow meters and multiphase test facilities.

To improve this situation an intercomparison for multiphase test facilities was organised as part of (the first) EMRP project MultiFlowMet [1]. Three facilities participated: NEL, DNV GL and OneSubsea (OSS), a Schlumberger Company. VSL acted as independent partner during the tests, arranging the tests and test protocol in close collaboration with the partners, auditing the uncertainty budgets, witnessing the tests and analysing the data.

In the next section the test protocol will be shortly presented. The paper will then focus on the analysis method and the test results. As the complete set of comparison partners could not agree on a common publication of the results, this paper is mainly based

on the project's Final Publishable JRP Report with Associated Annex [2].

## 2. Test protocol

In an earlier paper [3] at Flomeko 2016 the test protocol including flow meter package and test matrix was extensively presented. In this paper only the main points of interest will be repeated.

### 2.1 Test protocol

The test protocol defined the flow meter package (see section 2.2), the procedure of installation and configuration, and the test points (flow rates) to be used (see section 2.3). The finally performed test schedule was as indicated in Table 1 with test rounds subsequently at NEL, DNV GL, NEL and OneSubsea (owner of the meter, for practical reasons placed at the end of the schedule).

**Table 1:** Performed test schedule.

Test round	Test period
NEL Round 1	27 July 2015 – 7 August 2015
DNV GL	13 July 2016 – 19 July 2016
NEL Round 2	29 August 2016 – 12 September 2016
OneSubsea	22 November 2016 – 12 December 2016

The test protocol specified pressures and temperatures to be used in order to get flow conditions as similar as possible, see [3] for a more detailed discussion. However, due to the design of the facilities, differences remained, as illustrated by Table 2. The large range in water density at NEL is due to a different salinity in NEL Round 1 and NEL Round 2. In NEL's open loop design the nitrogen gas is vented at the separator. DNV GL tested at a higher temperature than initially specified for reasons of available testing time.

**Table 2:** Some characteristics per facility with a focus on the differences. 'Dist of mix' denotes the distance of the mixing point of the pure fluids upstream of the flow meter, '*U*' the expanded relative uncertainty, '*q*-single-phase' the single phase flow rates (oil, water, gas), and 'o&w' means 'oil & water'.

Characteristic	NEL	DNV GL	OneSubsea
Pressure at MUT / barg	2.1 to 9.5	7.3 to 8.3	15.9 to 17.1
Temperature at MUT / °C	38 to 45	19 to 21	11 to 17
Oil viscosity / cP	7.5 to 9.1	4.6 to 5.0	1.7 to 1.9
Water density / kg/m <sup>3</sup>	1015 to 1029	1029 to 1030	999 to 1000
Flow loop design	Open loop	Closed loop	Closed loop
Dist. of mix / m	11	20	3
<i>U</i> ( <i>q</i> -single-phase)	< 0.9 %	< 1.0 %	o&w: 1.5 % gas: 5 %
<i>U</i> (WLR)	< 0.23 %	< 0.17 %	< 0.6 %
<i>U</i> (GVF)	< 0.14 %	< 0.24 %	< 1.3 %

## 2.2 Flow meter package

The multiphase flow meter to be tested by each of the laboratories (MUT, Meter Under Test) was a Schlumberger PhaseTester Vx52. The meter has a pipe diameter of 4" and is based on Venturi tube with throat diameter is 52 mm. Pressure, temperature, differential pressure and gamma-ray attenuation measurements allow for determination of the oil, water and gas flow rates separately.

In order to make the flow conditions as similar as possible, it was agreed to install a 10 meter (100 D) straight inlet pipe section followed by a transparent pipe section to be used for flow regime recording by a video camera, and finally a 90° elbow connected to the inlet of the flow meter. This configuration was used at both DNV GL and NEL. At the Horsøy test facility of OneSubsea this turned out not to be possible for practical reasons and a different inlet configuration was used, which is the standard way of testing flow meters at OneSubsea. A picture of the flow meter while being tested at OneSubsea's test facility is shown in Figure 1.



**Figure 2:** Vx multiphase flow meter being tested at OneSubsea's test facility Horsøy.

## 2.3 Test matrix

It was agreed to perform both single and multiphase test points. The agreed multiphase test points ranged from liquid flow rates 9 to 90 m<sup>3</sup>/h, gas volume fractions (GVF) 25 to 96 % and water liquid ratios (WLR) 0 to 100 %. More details can be found in Table 3. Due to a limited amount of available testing time at DNV GL no tests were performed at WLR = 70 % at this facility. At both NEL and OneSubsea additional tests were carried out in order to analyse specific research questions, which are not presented in this short paper.

**Table 3:** Test matrix for multiphase points defining liquid flow rates and gas volume fractions to be tested, together with the following water cut specification: test points marked 'O' were to be carried out at water liquid ratios 0%, 25%, 45%, 70%, 90% and 100%; test points marked 'X' were to be carried out at 25%, 45%, 70% and 90% water liquid ratios.

Liquid Flow m <sup>3</sup> /h	Gas Volume Fraction / %					
	25	55	70	84	92	96
9					X	O
18				X	O	X
35		O	X	O	X	
50	O	X	O	X		
70	X	O	X			
90	O					

## 3. Analysis method

### 3.1 Validation of measurement points

The flow meter was installed and configured by an operator of OneSubsea. VSL witnessed all tests. After the data had been collected various sanity checks were performed. This included following checks: correspondence of measured time period by MUT and facility, differential pressure in throat of Venturi of MUT above 50 mbar, physical conservation laws in the reported data, correspondence of measured density with theoretical density, consistency of the noise levels

and standard deviations in the data, correspondence of actual flow rates, WLR and GVF with the nominal values prescribed by the test protocol. Points not respecting the quality criteria were removed.

Data from NEL was reprocessed by the flow meter manufacturer in order to compensate for changing fluid properties (due to the open loop design) that could have affected the flow meter performance. This resulted in only small changes.

### 3.2 Consistency assessment

An important goal of the comparisons is to assess if the claimed uncertainties by the test facilities can be validated or not. The measurand is the absolute or relative deviation  $d$  of the MUT for various multiphase quantities like water oil and gas volume flow rates, total mass flow rate, GVF (Gas Volume Fraction) and WLR (Water Liquid Ratio).

For example, let  $d$  be the relative deviation of the average MUT oil flow rate  $q_{MUT}$  with respect to the average reference oil flow rate  $q_{ref}$  provided by the test facility recorded during a test point, i.e.  $d = (q_{MUT} - q_{ref}) / q_{ref}$ . If the testing time was long enough the recorded average  $q_{MUT}$  has very small uncertainty, as the natural variability of the flow rate will be averaged out.

In the case of relative small deviations between MUT and test facility, it can be verified that  $u(d) \approx u^*(q_{ref})$ , where  $u^*(q_{ref})$  denotes the relative standard uncertainty of the reference flow rate provided by the test facility. For each facility  $k$ , and for each test point  $i$  and for each quantity of interest  $j$  a deviation  $d_{ij}^k$  with uncertainty  $u(d_{ij}^k)$  can be calculated. The results of two facilities  $A$  and  $B$  are consistent if

$$|d_{ij}^A - d_{ij}^B| \leq 2 \sqrt{u^2(d_{ij}^A) + u^2(d_{ij}^B) + 2 u^2(r_j^{MUT})} \quad (1)$$

The term  $u(r_j^{MUT})$  denotes the reproducibility uncertainty of the MUT for quantity  $j$ , which is assumed to be independent of the actual test point  $i$  (e.g. the overall reproducibility of the MUT for measured oil flow rates, as a number independent of the actual flow rate). Note that a dependence on GVF was observed (see **Fout! Verwijzingsbron niet gevonden.**4), but in the overall consistency calculations the overall value has been used. The reproducibility uncertainty accounts for the fact that the MUT itself produces slightly different measurement results, when a measurement is

repeated under the same measurement conditions. It is present at both facilities  $A$  and  $B$ , which is the reason for the factor 2 before  $u^2(r_j^{MUT})$  in equation (1).

This uncertainty contribution has been assessed by analysing the data measured at NEL in two different rounds of measurement, which were separated by approximately one year in time. The fact that the MUT may produce different results in different operating conditions (see Table 2 for the differences) is not accounted for in this consistency assessment, as it is difficult to quantify.

Thus, if results are inconsistent, either an uncertainty provided by (at least) one test facility is too low, or the flow meter has a higher reproducibility uncertainty between different facilities than the calculated value  $u(r_j^{MUT})$ .

Also note that it is impossible to thoroughly validate facility uncertainties  $u(d_{ij}^k)$  which are smaller than  $u(r_j^{MUT})$ , as in that case potential inconsistencies are obfuscated by the flow meter reproducibility. It is therefore important that the flow meter reproducibility is as low as possible, and a priori assuming a high value for  $u(r_j^{MUT})$  makes the comparison a priori of little significance. The factor 2 before the square root in equation (1) is linked to the fact that the target is 'consistency with a 95 % coverage probability (assuming a normal distribution for the uncertainties)'.

Multiphase flow patterns have a natural variability. Flow rates of oil, water and gas fluctuate over time. The reported mean values measured over a sufficient long time have been compared in this analysis. The standard deviation of the flow rates is seen as irrelevant as long as the averaging time is long enough, or, alternatively, if its effect on the uncertainty is incorporated in the uncertainty statements by the test facilities. If one would include these standard deviations in the analysis, a facility can claim any uncertainty and get consistent results as long as the natural variability in time of the multiphase flow pattern is high<sup>1</sup>.

### 1.4 Flow meter reproducibility

In this section the results for the flow meter reproducibility  $u(r_j^{MUT})$  are presented. This has been done by comparing the results of 56 multiphase test points measured at NEL in August

<sup>1</sup> This approach was followed in an alternative analysis not presented in this paper.

2015 and September 2016. The batch of single phase test points was not used in this analysis, nor some points with questionable quality (low dP values or timing error). The expanded reproducibility uncertainties  $U_{repro}$ , where  $U_{repro} = 2\sqrt{2} u(r_j^{MUT})$ , are presented in Table 4 split out to GVF range. These values are both affected both by flow meter and test facility reproducibility. The factor  $2\sqrt{2}$  has been included in order to present an expanded uncertainty (factor 2) covering the uncertainty of both measurement rounds (factor  $\sqrt{2}$ ).

**Table 4:** Results of the reproducibility analysis, split out for different GVFs. The value  $U_{repro}$  corresponds to  $2\sqrt{2} u(r_j^{MUT})$  in Equation (1).

Quantity	$U_{repro}$ (all GVFs)	$U_{repro}$ (GVF ≤ 90 %)	$U_{repro}$ (GVF = 92 %)	$U_{repro}$ (GVF = 96 %)
Total mass flow rate, $q_{m, total}$	2.2 %	2.0 %	2.3 %	3.5 %
Total volume flow rate, $q_{total}$	2.2 %	2.1 %	2.1 %	3.0 %
Gas volume flow rate, $q_{gas}$	3.2 %	3.3 %	2.1 %	2.9 %
Liquid volume flow rate, $q_{liquid}$	2.4 %	2.0 %	2.4 %	4.2 %
Water liquid ratio, WLR	1.9 %-abs	1.2 %-abs	1.6 %-abs	4.4 %-abs
Gas volume fraction, GVF	0.7 %-abs	0.8 %-abs	0.2 %-abs	0.2 %-abs
Oil volume flow rate <sup>2</sup> , $q_{oil}$	5.6 %	4.3 %	8.7 %	8.5 %
Water volume flow rate, $q_{water}$	3.4 %	3.0 %	3.0 %	5.7 %

#### 4. Pairwise comparisons

In this paper the results of NEL and DNV GL, and the results of DNV GL and OneSubsea are pairwise compared. NEL does not wish its results to be compared with OSS for reasons of the different inlet geometry used at OSS. NEL and DNV GL claim a similarly low uncertainty whereas OneSubsea claims a higher uncertainty. DNV GL and OneSubsea have tested at different operating pressure. These two facilities represent the extremes regarding the location of the mixing point of the three phase points with DNV GL having a mixing point far upstream and OneSubsea relatively close to the MUT.

##### 4.1 Measurement results

As a first step an overview of some of the main measurement results is given. Figure 3 shows the measured MUT deviations for gas volume flow rate (relative deviation in %) and Figure 4 for Water

Liquid Ratio (WLR, absolute deviation in %). The results for 100 % gas have been excluded from the plots and analysis.

Although the specifications regarding absolute accuracy of the manufacturer are strictly speaking not relevant in a comparison context, they have nevertheless been included, as it is still interesting to see how they compare with the results of the test facilities, and it can serve as a quality check of the MUT. It is seen that most points for WLR fall within specifications. For gas volume flow rate more points fall outside. For high GVF measurements at NEL this is not a complete surprise due to the low operating pressure at these points. It is not surprising that the MUT deviations as measured at OneSubsea's multiphase facility all lie within specifications, as OneSubsea is the manufacturer of the MUT. At high GVFs the various test results for the gas volume rate start to differ. This is probably due to the difference in operating pressure at the test facilities. Note that it is known that the meter uncertainty specification increases at lower pressure for high GVF.

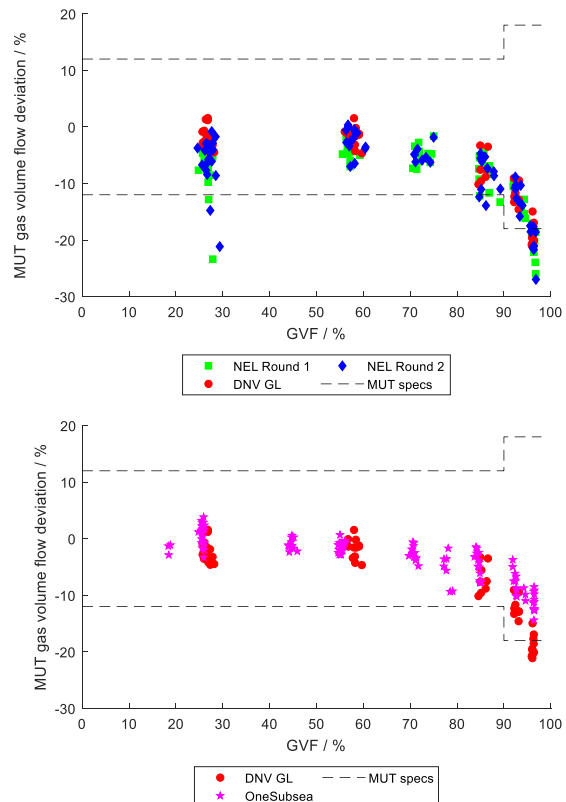


**Figure 3:** Pairwise comparison of measurement results for MUT relative gas volume flow rate deviation as function of GVF. Top: NEL and DNV GL. Bottom: DNV GL and OneSubsea.

<sup>2</sup> One value with a difference of 36 % in measured flow meter oil volume flow rate deviation between the two test rounds was removed in this calculation.

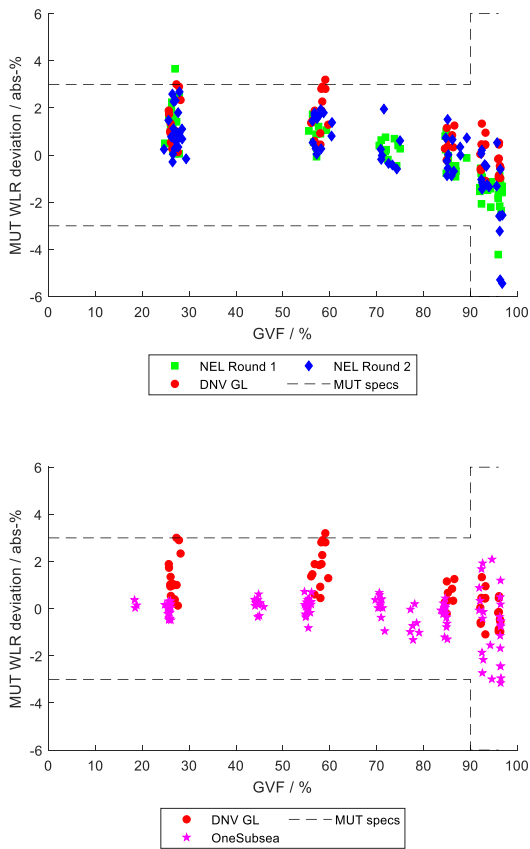


**Figure 4:** Pairwise comparison of measurement results for MUT WLR deviation as function of GVF. Top: NEL and DNV GL. Bottom: DNV GL and OneSubsea.

#### 4.2 Point-wise comparison

As a next step the test points have been compared point-wise, after checking that the actual flow rates corresponded sufficiently (and not only the nominal values). Some points were removed for this reason. It was observed that for WLR = 0 % the water volume flow rate reported by the MUT became sometimes slightly negative (down to  $-0.3 \text{ m}^3/\text{h}$ ), and for WLR = 100 % the oil flow reading became sometimes negative (down to about  $-3 \text{ m}^3/\text{h}$ ), together with an indicated WLR of almost 104 %. This deviation is possibly related to inconsistency between fluid properties as measured during the MUT setup vs. fluids properties during actual flow testing.

The results for the test points at a total liquid flow rate  $q_{\text{liquid}} = 90 \text{ m}^3/\text{h}$  and GVF = 25 % for various WLRs are shown in Figure 4 for MUT gas volume flow deviation and in Figure 5 for MUT WLR deviation. This is an interesting set of points as it contains some of the highest deviations between the facilities. The error bars indicate the expanded

uncertainty reported by the test facilities. In order to judge consistency of the results the meter reproducibility (as estimated in Table 3) has to be included as well, and equation (1) has to be applied.

For gas volume flow rate ( $U_{\text{repro}}(q_{\text{gas}}) = 3.3 \%$ ) the results of NEL and DNV GL are consistent for high WLRs, but inconsistent for low WLRs, especially for an oil-gas mixture. The results of DNV GL and OSS are consistent.

For WLR the results of NEL and DNV GL are consistent for this set of points (as  $U_{\text{repro}}(\text{WLR}) = 1.2 \%$ ), whereas this is not the case for DNV GL and OSS.

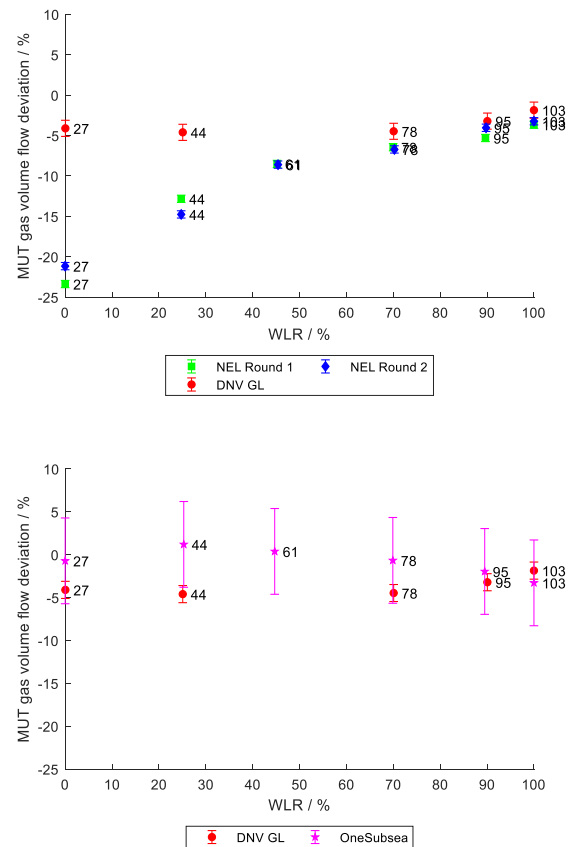


**Figure 4:** Examples of pairwise point-wise comparison of test point results for relative gas volume flow rate deviation ( $U_{\text{repro}} = 3.3 \%$ ) for GVF = 25 % and  $q_{\text{liquid}} = 90 \text{ m}^3/\text{h}$ . Error bars indicate facility uncertainties only. Top: NEL and DNV GL. Bottom: DNV GL and OneSubsea.

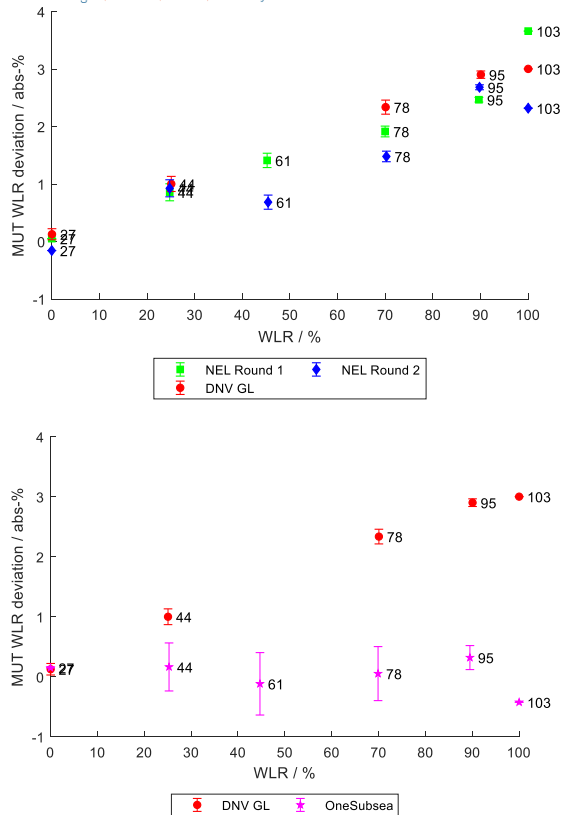


**Figure 5:** Examples of pairwise point-wise comparison of test point results for WLR deviation ( $U_{repro} = 1.2\%$ ) for GVF = 25 % and  $q_{liquid} = 90\text{ m}^3/\text{h}$ . Error bars indicate facility uncertainties only. Top: NEL and DNV GL. Bottom: DNV GL and OneSubsea.

#### 4.3 Overall numerical consistency

To summarize all results with a few numbers, the %-fraction of the cases that consistency was achieved has been calculated for different quantities, as listed in the first row of Table 5.

The large batch of single phase points has been excluded from this calculation. The row comparing NEL-R1 with NEL-R2 has a mean consistency of 95 %. This is as expected by the definition of  $U_{repro}$  and also confirms that the assumption of a normal distribution for the uncertainty is not so bad (i.e. 2 standard deviations corresponds to 95 %). The consistency between NEL and DNV GL, and between DNV GL and OSS is close to 80 %, where (at least) 95 % would be expected for complete consistency. Without more information it is unclear if the fraction of inconsistent results is mainly due to a larger reproducibility uncertainty of the flow meter installed in different facilities (see Table 3), or to one or more facilities underestimating their uncertainty of measurement (or anything else being overlooked in this analysis). Nevertheless, in view of all the differences between the facilities as listed in Table 2 and not explicitly addressed by increased

uncertainties, a consistency of 80 % is seen as a good result.

**Table 5:** Pairwise consistency of test results expressed as percentage of the number of test points. N1: NEL-Round 1, N2: NEL-Round 2, DG: DNV-GL, OS: OneSubsea. See Table 4 for the meaning of the symbols in the column headings.

Tests	$q_{m, total}$	$q_{total}$	$q_{gas}$	$q_{liquid}$	WLR	GVF	$q_{oil}$	$q_{water}$	Mean
N1 – N2	91%	95%	98%	93%	96%	96%	92%	96%	95%
N1 – DG	89%	78%	69%	87%	95%	71%	88%	90%	83%
N2 – DG	85%	75%	75%	90%	93%	79%	84%	86%	78%
DG – OS	82%	74%	78%	74%	80%	100%	58%	80%	78%

## 6. Conclusion

Pairwise comparison of test results of NEL and DNV GL, and DNV GL and OneSubsea resulted in an overall consistency of about 80 %. This is less than the desired 95 %, but still a good result in view of all the differences in e.g. fluid viscosities, operating pressures and inlet geometries, which were not explicitly incorporated in the uncertainty analysis. To get a better understanding of the results, following advices are given:

- make publicly available all measurement data of the ENG58 for further research
- organize a more extensive comparison including various types of flow meters and more partners, with open data access.

## Acknowledgment

We gratefully acknowledge funding of this research by the EMRP project ENG58 MultiFlowMet. The EMRP programme was co-funded by the European Union and the EMRP Participating States.

## References

- [1] EMRP ENG58 [MultiFlowMet](#), *Multiphase flow metrology in oil and gas production*, 2014 – 2017.
- [2] [“ENG 58 Final Publishable JRP Report and Associated Annex A”](#), Euramet, 2018.
- [3] P. Lucas, G. Kok, H. de Leeuw, T. Leonard, D. van Putten, L. Zakharov, [“Intercomparison between multiphase flow test facilities”](#), FLOMEKO 2016, Sydney, Australia.

## New EMPIR project – Metrology for Drug Delivery

E. Batista<sup>1</sup>, A. Furtado<sup>1</sup>, J. Pereira<sup>1</sup>, M. Ferreira<sup>1</sup>, H. Bissig<sup>2</sup>, E. Graham<sup>3</sup>, A. Niemann<sup>4</sup>,  
A. Timmerman<sup>5</sup>, J. Alves e Sousa<sup>1</sup>

<sup>1</sup>Instituto Português da Qualidade, I.P., Portugal

<sup>2</sup>METAS, Switzerland

<sup>3</sup>NEL, UK

<sup>4</sup>DTI, , Denmark

<sup>5</sup>UMCU, A.M.D.E.Timmerman@umcutrecht.nl, Netherlands

E-mail: ebatista@ipq.pt

---

### Abstract

This document presents the scientific and technical objectives, state of the art and expected progress beyond it, and most importantly the expected impact on metrology, science, standards, and society of the new joint research project - MeDD II, Metrology for drug delivery (follow up of project MeDD I). It was selected for funding through the EURAMET EMPIR program of the European Commission and the participating countries. The project starts in June 2019 and will last for three years. It involves 15 partners from National and Designated Metrology Institutes, companies, and academia. The main objective is to enable traceable measurements of volume, flow and pressure of existing drug delivery devices (like, infusion pumps and analysers) and inline sensors that work at flow rates lower than 100 nL/min, in order to prevent inaccurate measurement results. This project will also investigate fast changing flow rates, liquid mixing behaviour and occlusion phenomena in multi-infusion systems with the purpose of improving dosing accuracy in each infusion line.

---

### 1. Introduction

The most commonly used form of therapy in hospital environment is infusion therapy [1], which implies that drug delivery is a critical aspect in health safety. Because of the widespread application by many users in critical health situations, infusion errors are often made, with potential dramatic effects in the patients. There are various examples where adverse incidents, morbidity and even mortality, can be traced back to poor drug delivery. The authors Snijder et al [2] published a review in which medical errors associated with flow rate variability in infusion devices are described, where they emphasized the severe and lasting health damage that has occurred.

A well-defined metrological infrastructure is needed to allow infusion pump manufacturers to include robust information on the “real” dose delivered to the patient, and drug delivery devices operators to have a better metrological knowledge of these critical devices, thus preventing incorrect measurement results and significantly improving patient safety.

Metrology can bridge the knowledge gap by designing a representative multi-infusion intravenous system for

testing how different liquids mix and how this affects drugs concentrations. The increasing implementations of novel microfluidic solutions in healthcare urge the development of a metrological infrastructure for validating quality and reproducibility [3].

The new Joint Research Project - MeDD II, Metrology for drug delivery funded under the EMPIR program of the European Commission starts in June 2019, will last for three years involving 15 partners, including: 9 National and Designated Metrology Institutes (IPQ-Portugal, CETIAT - France, CMI – Chez Republic, DTI - Denmark, METAS - Switzerland, NEL – United Kingdom, NQIS - Greece, RISE – Sweden and KRIS - Korea), 4 companies (DNV GL – The Netherlands, HSG-IMIT - Germany, INESC MN - Portugal, BHT – The Netherlands) and 2 University Hospitals (THL - Germany, UMCU – The Netherlands).

This project is coordinated by IPQ, the Portuguese Institute of Quality and has the overall to improve dosing accuracy and enable traceable measurements of volume, flow and pressure of existing drug delivery devices and inline sensors operating at very low flow rates (lower than 100 nL/min). This can be achieved through the development of new calibration methods

and improved metrological infrastructures. Another goal of this project is to investigate the influence of: different flow rate regimes; physical properties of the infused fluids (e.g., viscoelasticity); and occlusion phenomena in multi-infusion systems. This knowledge will help preventing inaccurate measurement results and thus improve patient safety.

## 2. State of the art and progress beyond it

In 2004, in a metrological effort to understand and improve multi-infusion, Clark [4] defined the crucial performance aspect of an infusion system and established the importance of a patient receiving the correct dose, of the required substances, in a certain time. However, in multi-infusion, this is not an easy task. The first steps towards a better understanding of the real flow rates and of the drugs' concentration delivered to the patient were made in 2 previous projects [5, 6]. In MeDD I (Metrology for Drug Delivery I) [5] the aim was to prevent errors by upgrading calibration services and improving knowledge transfer to the end-user [5]. An infrastructure, consisting of traceable calibration services for drug delivery systems for flow rates down to 100 nL/min, was developed in five European National Metrology Institutes (NMIs) [7, 8]. Syringe pumps and peristaltic pumps with accessories were tested [9]. Additionally, the effects of variations in several physical parameters in infusion systems were incorporated in a predictive model [10].

This new project will go beyond the research conducted during the project MeDD I [5] by investigating the influence of fast changing flow rates due to a change in the pre-set flow rate. Also, a multi-infusion setup will be developed to investigate fluid flow rates and fluid compositions in the outlet of the infusion line. This setup will allow the assessment of the performance of drug delivery devices in multi-infusion systems and the determination of the concentration of each drug being administered.

## 3. Scientific Objectives

The overall goal is to enable traceable measurements of volume, flow and pressure of existing drug delivery devices and inline sensors that work at a flow rate lower than 100 nL/min. This project will also investigate different flow rate regimes, liquid mixing behaviour and occlusion phenomena in multi-infusion systems with the purpose of improving dosing accuracy in each infusion line.

The specific objectives of the project are:

1. To develop new traceable techniques for generating and measuring the response time or delay time against changes in flow rate, in the interval from 5 nL/min to 100 nL/min, using Newtonian liquids, for example, optical methods.
2. To upgrade the existing flow facilities and knowledge of the participant NMIs in order to enable traceable inline measurement of the dynamic viscosity of Newtonian liquids, as a function of the flow rate and pressure drop, with a target relative uncertainty of 2 % ( $k=2$ ).
3. To develop and validate novel calibration procedures for existing drug delivery devices traceable to a primary standard and a target relative uncertainty of 2 % for a range of 5 nL/min up to 600 mL/min. In addition, to develop a proof-of-concept of an on-chip microfluidic pump used as transfer standard in drug discovery and organ-on-a-chip applications in the flow rates from 5 nL/min to 100 nL/min.
4. To design and develop a multi infusion system containing check valves, with several options for testing the miscibility of liquids (with different viscosities and flow rates) and how this affects drugs' concentration.
5. To facilitate the take up of the technology and measurement infrastructure developed in the project by the measurement supply chain, (i.e. accredited laboratories, instrumentation manufacturers, etc.), standards developing organizations and end-users (i.e. hospitals and health centres).

## 4. Impact

### 4.1 On society and health sectors

The main goal of this project is to improve diagnostics, patient treatment and patient safety by developing new calibration methods, resulting in an adequate traceability chain for flow rate measurements performed by several drug delivery devices such as multi infusion systems, insulin pumps and pain controllers working at flow rates as low as 100 nL/min. It is known that drug errors account for a significant percentage of medical errors, with dosing errors being a significant subset of them [11-14]. Depending on the drug type, the patient characteristics and the applied therapy, dosing errors can have severe consequences, including a substantial number of fatalities.

A better understanding on how dosing errors may occur, and how to increase the accuracy of the drug delivery devices will have a noticeable impact on the health industry and significantly improve patient treatment and safety. Therefore, any attempt to prevent adverse events by improving the knowledge on actual doses can already make an enormous difference for the individual patient, especially newborn

babies, and have a significant impact on the health sector as a whole. A considerable impact on society through improved patient safety can be expected by improving the calibration and administration conditions for drug delivery devices and setups. Important examples can be found in chemotherapy, in anaesthesia, in the operating theatre and in nursery wards, especially for the neonates. The calibration methods are also important in drug injection applications in very small anatomic regions of the body, for example in the inner ear. Improving metrology for microfluidic methods in this field could help to find new horizons for the treatment of acute deafness and Meniere's disease.

Furthermore, occlusion alarms' quality can be improved, and occlusion alarm fatigue diminished by more reliable pressure measurements.

Accurate drug delivery will also have economic benefits. In modern medicine, many sophisticated pharmaceuticals are available, but only at high prices. Metrology can help prevent waste of expensive medication, by enabling the delivery of accurate dosage.

Finally, the infusion pumps analysers used by the hospitals' maintenance to calibrate the in-house used infusion devices; need to be calibrated against a reference. However, in most of the cases the traceability of the theses devices are only guarantee in hospitals with ISO 9001 certification since it is mandatory,

#### 4.2 On metrology

This project will upgrade various existing facilities for flow measurements from 5 nL/min up to 100 nL/min using different Newtonian fluids as test medium. These new facilities will be validated by means of an inter-comparison with stable transfer standards allowing the recognition of new measurement capabilities.

New calibration methods will be developed based on optical methods and this knowledge will be disseminated across the scientific community by relevant publications in scientific journals and congresses.

These new calibration methods will be beneficial for both accredited laboratories and manufacturers of drug delivery devices. These new procedures can later be updated for microfluidic devices used in health, mainly in organ-on-a-chip technology. A calibration guide for the different type of drug delivery devices will be drafted describing the calibration methods, conditions under which they are to be operated, target uncertainty and best working practices. The draft will be submitted to EURAMET and made available to end users.

#### 4.3 On standardisation

In this project, procedures and methods for the calibration of drug delivery devices already on the market are going to be developed. This information will be supplied to the relevant ISO technical committees (TC). For example, the current version of IEC 60601-2-24 used by manufacturers to develop drug delivery devices and by laboratories and maintenance departments of hospitals to verify and calibrate drug delivery devices, is roughly 20 years old and is outdated. Moreover, the given measurement methods are not suitable for very low flow rates (< 100 nL/min) relevant to implantable infusion pumps where applications are encountered. An urging need to update the measurement procedures for different types of pumps and master calibrators is widely accepted. It is envisaged that the project will impact on Section Eight of IEC 60601-2-24 (Accuracy of operating data and protection against hazardous output).

This project can also supply inputs on the Regulation (EU) 2017/745 of the European Parliament and of the Council of 5 April 2017 on medical devices that are currently lacking information regarding maximum permissible errors of several medical devices, including drug delivery devices.

### 5. Conclusion

By improving the flow rate measurements accuracy of drug delivery devices, dosing errors will be reduced, and lives will be saved. This can be achieved by wider uptake of traceable calibrations of low and ultra-low flow infusion (master) devices and by improved knowledge of calibrating drug delivery devices in clinical environments, especially in the case of multiple infusion systems. This project directly benefits the general community because it allows identifying and reducing dosing errors in drug delivery devices used for patient treatment and diagnostic.

#### Acknowledgment

The EMPIR project "MeDDII" is carried out with funding of European Union under the EMPIR. The EMPIR is jointly funded by the EMPIR participating countries within EURAMET and the European Union.

#### References

- [1] P.T. Lee, F. Thompson, H. Thimbleby, "Analysis of infusion pump error logs and their significance for health care". *Br J Nurs*. 2012 Apr 26-May 9;21(8): S12, S14, S16-20]
- [2] Roland A. Snijder\*, Maurits K. Konings, Peter Lucas, Toine C. Egberts and Annemoon D. Timmerman; Flow variability and its physical causes in infusion technology: a systematic review

- of in vitro measurement and modeling studies; *Biomed. Eng.-Biomed. Tech.* 2015; 60(4): 277–300; DOI 10.1515/bmt-2014-0148
- [3] Ronaldson-Bouchard K, Vunjak-Novakovic G. Organs-on-a-Chip: A Fast Track for Engineered Human Tissues in Drug Development. *Cell Stem Cell.* 2018 Mar 1;22(3):310-324. doi: 10.1016/j.stem.2018.02.011. Review.
- [4] C. Clark, “A study to determine the extent and impact of problems associated with poor mixing of fluids in medical infusions into the vascular system”, Project report FEOT 11a submitted to National Measurement System Directorate, 30 June 2004
- [5] Publishable JRP Summary Report for JRP HLT07 MeDD Metrology for drug delivery. [https://www.euramet.org/Media/docs/EMRP/JRP/JRP\\_Summaries\\_2011/Health\\_JRPs/HLT07\\_Publishable\\_JRP\\_Summary.pdf](https://www.euramet.org/Media/docs/EMRP/JRP/JRP_Summaries_2011/Health_JRPs/HLT07_Publishable_JRP_Summary.pdf)
- [6] Support for impact project, <https://www.drugmetrology.com/>
- [7] H. Bissig, HT. Petter, P. Lucas, E. Batista, E. Filipe, N. Almeida, L. Ribeiro, J. Gala, R. Martins, B. Savanier, F. Ogheard, AK. Niemann, J. Lötters, W. Sparreboom. “Primary standards for measuring flow rates from 100 nl/min to 1 ml/min – gravimetric principle”. *Biomed Tech (Berl)*. 2015 Aug;60(4):301-16.
- [8] P. Lucas, M. Ahrens, J. Geršl, W. Sparreboom, J. Lötters. “Primary standard for liquid flow rates between 30 and 1500 nl/min based on volume expansion”. *Biomed Tech (Berl)*. 2015 Aug;60(4):317-35
- [9] E. Batista, N. Almeida, A. Furtado, E. Filipe, L. Sousa, R. Martins, P. Lucas, HT. Petter, R. Snijder, A. Timmerman. “Assessment of drug delivery devices”. *Biomed Tech (Berl)*. 2015 Aug;60(4):347-57
- [10] MK. Konings, RA. Snijder, JH. Radermacher, AM. Timmerman. “Analytical method for calculation of deviations from intended dosages during multi-infusion”. *Biomed Eng Online.* 2017 Jan 17;16(1):18. doi: 10.1186/s12938-016-0309-4. PubMed PMID: 28095851; PubMed Central PMCID: PMC5240402
- [11] R. Kaushal, K. Shojania, D. Bates. “Effects of computerized physician order entry and clinical decision support systems on medication safety: a systematic review”. *Arch Intern Med.* 2003; 163: 1409–1416.
- [12] A. Ameer, S. Dhillon, MJ. Peters, M. Ghaleb. “Systematic literature review of hospital medication administration errors in children”. *Integr Pharm Res Pract.* 2015 Nov 5;4:153-165
- [13] M. Husch, C. Sullivan, D. Rooney, C. Barnard, M. Fotis, J. Clarke, G. Noskin. “Insights from the sharp end of intravenous medication errors: implications for infusion pump technology”. *Qual Saf Health Care.* 2005 Apr;14(2):80-6
- [14] N.C. Von Laue, D.L. Schwappach. & C.M. Koeck. (2003a) “The epidemiology of medical errors: a review of the literature”. *Wiener Klinische Wochenschrift* 115, 318–325.

# Establishment and Verification of Mercury-Sealed Piston Prover for Primary Standard

Ying-Chun Lin<sup>1</sup>, Win-Ti Lin<sup>2</sup>, Chun-Lin Chiang<sup>3</sup>,

*Flow Measurement Laboratory in Center for Measurement Standards of Industrial Technology Research Institute, No.30 Daxue Road, Hsinchu 30080, Taiwan (R.O.C)*

*<sup>1</sup>emi\_lin@itri.org.tw, <sup>2</sup>WinTiLin@itri.org.tw, <sup>3</sup>C.L.Chiang@itri.org.tw*

This paper presents the establishment and verification of a mercury-sealed piston prover, which is commonly used for low pressure gas flow calibration. The calibration gases could be dry air, nitrogen, argon, helium, oxygen and carbon dioxide. The flow capacity of the new system covers from 0.002 L/min to 40 L/min at 23 °C and 101.325 kPa, and some overlapped flows are between various columns. The relative expanded uncertainty of mass flow measurement is less than 0.08 % at 95 % confidence level.

We were also successfully altering the temperature sensor construction, temperature sensor placement, data logger system to real-time monitor the temperature difference of the entering gas. The data showed that the temperature difference between the entering gas and column could approximate in the calibration period.

The newly piston prover measurement result between different column was less than 0.01 %. A comparison between new-constructed and original CMC submitted piston prover that both are in CMS was conducted, and the *En* value was less than 0.4. The results indicate that the measurement capabilities of each column of newly piston prover were identical with expectation.

## 1. Introduction

Low pressure gas sensing components such as laminar flowmeters, rotary flowmeters, and sonic nozzles are widely used in several industries which as semiconductor, chemistry, energy, environment and safety to control, monitor gas flow and trade. Therefore, if we want to maintain the measurement accuracy and measurement traceability of the sensing components, they should be ensured by calibration. Currently, bell prover, piston prover and PVTt system are the conventional primary standard facilities of the low pressure gas flow calibration, and most laboratories are continuously to systematically improve to meet the technical development of related low pressure gas sensing components[1][2].

The original piston prover calibration system in CMS/ITRI was constructed at 1987, and each year has been done the calibration more than 100 units. Since some equipment is old and difficult to obtain, it is necessary to rebuild for the purpose of prevent the system can't provide the necessary calibration services. A renew project was created at 2017 to construct a newly system that the measurement uncertainty and cover flow rate range could meet our requirements. We were carefully considered the affect factors [3] [4] and then designed our newly piston prover calibration system. For example, how to position the thermometers that could measure a more representative temperature of

the gas inside the column during calibration [5] was described herein.

In this paper, we also describe how to evaluate the measurement uncertainty of the gas flow rate. To verify the measurement capability and performance of the newly established piston prover, an intra-comparison between original and newly piston prover was conducted. The comparison results shown that two systems are in a good agreement were also addressed in this paper. Therefore, the capability of newly piston prover calibration system was valid. Then newly piston prover calibration system could provide calibration service at flow rate from 0.002 L/min to 40 L/min at (23 ± 1) °C.

## 2. Establishment of Primary Standard

### 2.1 Piston prover design

The newly established piston prover is shown in Figure 1. It is composed of five precision-machined glass columns (inside diameter ± 0.01 mm). Each column has the independent inlet and outlet pipes, and was covered by the acrylic lid respectively to reduce the influence of temperature exchange. A standard thermometer built in each column, and it was disposed at the gas inlet and outlet junction under the column. The pressure gauge together with the standard thermometer was also same placed at the bottom of the column. We used the low

power fiber optical sensor to sensing the piston position and also it could less the heat arise.

The arrangement of five columns in different size was aligned at the central of the glass column. Then the Laser Doppler Scale (LDS) could be driven at one direction back and forth among the columns to simplify the control. Different size of columns can be selected in accordance with the flow rate for shortening the collecting time. The newly piston prover system also has auto-calibration process to use manpower sparingly.

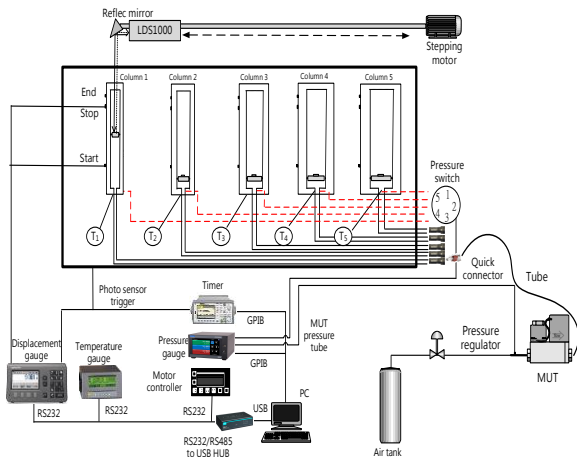


Figure 1. Diagram of newly piston prover.

## 2.2 Evaluation of uncertainty

According to the theory of the mass flow rate measurement could be obtained the equation (1). The equation (2) was shown the relative combined standard uncertainty of mass flow rate which was derived from the equation (1). The measurement uncertainty of the gas flow rate was evaluated in accordance with the recommendation by the ISO/IEC Guide 98-3: 2008 [6]. Regarding the uncertainty sources mentioned previously, the variation of temperature influences dimensional measurement, and the variations of temperature and pressure influence density. Thus, the contributions to the relative uncertainty of measured mass flow rate were evaluated from every effective factor via equations (3) to (4), which were listed below. All of the uncertainty components multiplied its sensitivity coefficients first, and then combined by the root-sum-square (RSS) and multiplied by a coverage factor to obtain the expanded uncertainty at 95 % confidence level. Subsequently, the contributions to relative uncertainty of measured mass flow rate from every effective factor were illustrated separately in follows.

$$q_{m,s} = \frac{\rho_s \times \pi \times D_s^2 \times L_s \times 60}{4t \times 10^6} + \frac{\Delta \rho_{cv} \times V_{cv} \times 60}{t} + \rho_s \times q_l \quad (1)$$

$$= f(D_s, L_s, \rho_s, t, \Delta \rho_{cv}, V_{cv}, q_l)$$

$$\frac{u_c(q_{m,s})}{q_{m,s}} = \left[ \left( \frac{2u(D_s)}{D_s} \right)^2 + \left( \frac{u(L_s)}{L_s} \right)^2 + \left( \frac{u(\rho_s)}{\rho_s} \right)^2 + \left( \frac{-u(t)}{t} \right)^2 + \left( \frac{4 \times 10^6 V_{cv} u(\Delta \rho_{cv})}{60 \pi D_s^2 L_s \rho_s} \right)^2 + \left( \frac{\Delta \rho_{cv} \times 4 \times 10^6 u(V_{cv})}{60 \pi D_s^2 L_s} \right)^2 + \left( \frac{4 \times 10^6 t u(q_l)}{60 \pi D_s^2 L_s} \right)^2 \right]^{1/2} \quad (2)$$

$$V_{cv} = \frac{\pi \times D_s^2 \times L_s}{4 \times 10^6} \quad (3)$$

$$\rho_s = \frac{P_s M}{Z(P_s, T_s) R_u T_s} \quad (4)$$

### 2.2.1. Uncertainty of column diameter

We used five ring gauges which have different diameters couple with Linear Variable Differential Transducer (LVDT) to measure the internal diameter of each column respectively. The results of average inner diameter of glass columns and uncertainty analysis were listed as the Table 1.

Table 1 Measurement data of inner diameter

Column no.	Diameter (mm)	$u_c(D_s)$ ( $\mu\text{m}$ )	$k$	$U$ ( $\mu\text{m}$ )	$\nu_i$
Column 1	16.4950	0.39	1.96	0.8	520
Column 2	27.0021	1.24	2.18	2.8	12
Column 3	44.9827	1.56	2.18	3.4	12
Column 4	79.9868	1.17	2.08	2.5	21
Column 5	160.0225	1.86	2.03	3.8	33

### 2.2.2 Relative uncertainty of the piston displacement

Laser Doppler Scale was used to measure the displacement of the piston. LDS was calibrated by Dimensional Laboratory/CMS. Uncertainty due to calibration traceability was less than 0.0001 % and can be ignored. The maximum cosine error produced by the measurement process was estimated as 0.01 mm. If we assuming the probability distributions was rectangular and then the standard uncertainty of this item was 0.006 mm, the degrees of freedom was 50.

### 2.2.3 Relative standard uncertainty of density

The density value was determined through the temperature measurement and pressure measurement, as shown in Equation (4). The relative standard uncertainty of gas density measurement could be calculated from Equation (5).

$$\left( \frac{u(\rho_s)}{\rho_s} \right) = \left\{ \left[ \frac{u(T_s)}{T_s} \right]^2 + \left[ \frac{u(P_s)}{P_s} \right]^2 + \left[ \frac{u(M)}{M} \right]^2 + \left[ \frac{u(R_u)}{R_u} \right]^2 + \left[ \frac{u(Z(P_s, T_s))}{Z(P_s, T_s)} \right]^2 \right\}^{1/2} \quad (5)$$

There were four factors in temperature measurement, (a) Calibrated uncertainty of thermometer was 0.018 °C, and the associated degrees of freedom was 60. (b) The error of calibrated thermometer was within  $\pm 0.003$  °C. If estimating with rectangular distribution, the standard

uncertainty of this term was 0.002 °C, with degrees of freedom was 50. (c) The long-term stability of temperature gauge was less than 0.01 °C. If estimated with rectangular distribution, the standard uncertainty of this term was 0.006 °C, with degrees of freedom was 50. (d) The measurement error that was caused by the non-uniform temperature distribution, around 0.10 °C and we assumed that was a rectangular distribution. Then, the uncertainty of this item was 0.058 °C, and the associated degrees of freedom was 50. Therefore, we could estimate the combined relative standard uncertainty was 0.021% at lowest operating temperature nearly 295.15 K with degrees of freedom was 62.

In pressure measurement, we estimated three factors. They were (a) Calibrated uncertainty of pressure gauge was 6 Pa, and the associated with degrees of freedom was 60. (b) Long-term stability of the pressure gauge. We using the pressure gauge drift from the manufacturer claims to evaluate. The maximum variation was estimated as 15 Pa. Then we could obtain the standard uncertainty was 8.7 Pa when we assuming that was a rectangular distribution, the degrees of freedom was 50. (c) Another uncertainty was the measurement error due to the installation position and sampling. The maximum deviation was 10 Pa between the pressure gauge sampling position and the average pressure appeared of the gas inside the column. Thus, the standard uncertainty could be calculated as 5.8 Pa, and the associated with degrees of freedom was 50. Finally, we can obtain the relative standard uncertainty at lowest operating pressure (100 kPa) was 0.012 %, degrees of freedom was 132.

Universal gas constant was a fixed number, thus the uncertainty could be ignored. The gas molecular weight was referred to as the publication of NIST [7]. The relative standard uncertainty of air was less than 0.019 %. The relative standard uncertainty of the other gases was less than 0.002 %, the associated degrees of freedom was 100. The relative standard uncertainty of gas compression was calculated by the NIST REFPROP software. Therefore, the relative standard uncertainty of gas compression can be estimated as 0.001 % and the associated degrees of freedom was 146.

Finally, the relative uncertainty due to the measurement of gas density was obtained of 0.031 % via RSS method, and the associated degrees of freedom was 200 as shown in Table 2.

**Table 2** Relative uncertainty of density

Composition of density	$u(x_i)$	$\frac{u(x_i)}{x_i}$ (%)	$c_i$	$ c_i  \frac{u(x_i)}{x_i}$ (%)	$\nu_i$
$T_s$	0.061		1/295.15	0.021	62
$P_s$	0.012		1/100	0.012	132
$M$		0.019	1	0.019	100
$R_u$		0.000	1	0.000	100
$Z_s$		0.001	1	0.001	146
$\rho_s$				<b>0.031</b>	200

### 2.2.4 Relative standard uncertainty of time

The influence factor of the time relative standard uncertainty assessment included three items. (a) Universal counter was employed as a standard timer for piston prover system. The standard uncertainty was less than 0.0001 ms according to the calibration report. Thus, the uncertainty of this item could be ignored. (b) The maximum difference between the timer and the LDS counter trigger synchronization from the experiments less than 0.001 s. If the minimum collecting time of 15 s was employed to calculate the relative standard uncertainty and assuming that was a rectangular distribution, then we could obtain the value as 0.004 % with the value of degrees of freedom was 12. (c) The resolution of timer was 0.0001 s, and it was assumed as a rectangular uncertainty distribution. Based on a minimum collecting time of 15 s, the relative standard uncertainty was 0.0004 %. The degree of freedom was 50. Then we can obtain the combine relative standard uncertainty of time measurement was 0.004 % and the degrees of freedom was 12.

### 2.2.5 Relative standard uncertainty due to gas density variation inside the control volume during the beginning and the end of collecting period

The density change of gas inside control volume during the calibration period was less than 0.00015. If estimating with rectangular distribution, the relative standard uncertainty of gas density variation was 0.009 % and the degrees of freedom was 50. The sensitivity coefficients of columns were from 0.3 to 0.7, and then the relative standard uncertainties were located at 0.0027 % to 0.0063 % as table 3.

**Table 3** Relative uncertainty of control volume during the beginning and the end of collecting period

	Column 1	Column 2	Column 3	Column 4	Column 5
$\frac{u(\Delta\rho_{CV})}{\rho_s}$	0.009 %	0.009 %	0.009 %	0.009 %	0.009 %
$\frac{4 \times 10^6 V_{CV}}{60\pi D_s^2 L_s}$	0.7	0.3	0.3	0.3	0.4
$\frac{4 \times 10^6 V_{CV} u(\Delta\rho_{CV})}{60\pi D_s^2 L_s \rho_s}$	0.0063 %	0.0027 %	0.0027 %	0.0027 %	0.0036 %
Degrees of freedom	50	50	50	50	50

### 2.2.6 Relative standard uncertainty due to volume measurement of control volume

The density change of gas inside control volume during the calibration period was less than 0.00015. The control volume was estimated by connect pipe size, thus the sensitivity coefficient could be estimated as 0.2 for all columns. Therefore, the relative standard uncertainty of control volume can be evaluated as 0.003 %, and the degrees of freedom was 12.

### 2.2.7 Relative standard uncertainty due to leakage of control surface

The leakage flow rate was assessed from the actual leakage test data. The dry air enters the column to push the piston to a position then close the inlet valve. Then, LDS continuously to monitor the variance of displacement of piston for a period, and the temperature, pressure at same time. Thus, we could use the collection values from time, temperature, pressure, and piston displacement to obtain the leakage flow. The low limit flow rate of each standard column was used as the flow rate in leakage test, the leakage flow rate of every column was shown in Table 4. Use this value to calculate the standard uncertainty of this item.

**Table 4** Uncertainty of leakage flow rate

Column no.	Flow rate (L/min)	$q_{v,l}$ (L/min)	$v_i$
Column 1	0.002	$5 \times 10^{-7}$	100
Column 2	0.025	$1 \times 10^{-6}$	100
Column 3	0.1	$2 \times 10^{-6}$	100
Column 4	0.5	$1 \times 10^{-5}$	100
Column 5	2	$5 \times 10^{-5}$	100

Table 5 and Table 6 are shown the uncertainty budgets of column 1 operated at 0.002 L/min and of column 5 operated at 40 L/min. In table 5, we could found that column 1 had  $5 \times 10^{-7}$  L/min of the actual leakage flow rate at minimum flow rate, and the relative standard uncertainty of the leakage flow rate was 0.014 %. Therefore, the relative combined standard uncertainty of

column 1 was 0.036 %. In table 6, we could found that the relative standard uncertainty of gas density was the biggest uncertainty source. The relative standard uncertainty of the leakage flow rate far less than the relative standard uncertainty of gas density. Then, we could found that the relative combined standard uncertainty of column 5 was 0.032 % is different as column 1. Also, we found that the influence of the variance of gas density in the collecting volume was different for each standard column due to the difference sensitivity coefficients.

In table 7, we shown the relative combined standard uncertainty and the flow rate ranges of each column of our newly piston prover. The capabilities of each columns were meet our requirements. The relative standard uncertainty of gas density is the biggest uncertainty source of this newly piston prover. In the relative standard uncertainty of gas density, the influence of temperature is bigger than other factors. How to reduce the temperature influence in the system is the future work.

**Table 5** Uncertainty budget of Column 1 (0.002 L/min)

Components	$\frac{u(x_i)}{x_i}$ (%)	$c_i$	$ c_i  \frac{u(x_i)}{x_i}$ (%)	$v_i$
$D_s$	0.003	2	0.006	520
$L_s$	0.002	1	0.002	58
$\rho_s$	0.031	1	0.031	200
$t$	0.000	1	0.000	12
$\Delta\rho_{CV}$	0.009	0.7	0.0063	50
$V_{CV}$	20	0.00015	0.003	12
$q_{v,l}$	0.014	1	0.014	100
$u_c(q_{m,s})/q_{m,s}$			<b>0.036</b>	329
$k$			<b>1.97</b>	
$U$			<b>0.08</b>	

**Table 6** Uncertainty budget of the Column 5 (40 L/min)

Components	$\frac{u(x_i)}{x_i}$ (%)	$c_i$	$ c_i  \frac{u(x_i)}{x_i}$ (%)	$v_i$
$D_s$	0.002	2	0.004	33
$L_s$	0.001	1	0.001	60
$\rho_s$	0.031	1	0.031	200
$t$	0.004	1	0.004	12
$\Delta\rho_{CV}$	0.009	0.4	0.0036	50
$V_{CV}$	20	0.00015	0.003	12
$q_{v,l}$	0.0001	1	0.0001	100
$u_c(q_{m,s})/q_{m,s}$			<b>0.032</b>	225
$k$			<b>1.97</b>	
$U$			<b>0.07</b>	

**Table 7** Uncertainty budget of the piston prover

Column no.	Flow rate range (L/min)	$u_c(q_{m,s})/q_{m,s}$ (%)	$k$	$U$ (%)
Column 1	(0.002 to 0.1)	0.036	1.97	0.08
Column 2	(0.01 to 0.3)	0.034	1.97	0.07
Column 3	(0.1 to 1)	0.033	1.97	0.07
Column 4	(0.5 to 5)	0.032	1.97	0.07
Column 5	(2 to 40)	0.032	1.97	0.07

Nomenclature	
$q_{m,s}$	Standard mass flow rate [g/min]
$\rho_s$	Gas density of the collecting volume [g/L]
$D_s$	Average inner diameter of the column [mm]
$L_s$	Displacement of piston [mm]
$t$	Collection time [s]
$\Delta\rho_{cv}$	Density change of gas in the control volume at the beginning and end of calibration [g/L]
$V_{cv}$	Volume in the control volume [L]
$q_{v,l}$	Leakage rate during the calibration process [L/min]
$V_c$	Collecting volume inside the column [L]
$T_s$	Absolute temperature of gas in the collecting volume [K]
$P_s$	Absolute pressure of gas in the collecting volume [kPa]
$M$	Gas molecular weight [g/mol]
$R_u$	Universal gas constant [J/mol·K]
$Z$	Gas compressibility constant [J/mol·K]
$U$	Relative expanded uncertainty
$u_c$	Relative combined standard uncertainty
$k$	Coverage factor
$u(x_i)$	Standard uncertainty
$c_i$	Sensitivity coefficient
$\nu_i$	Degrees of freedom for $u(x_i)$

### 3. Verification of the newly Piston Prover

#### 3.1 Comparison of new piston prover between different columns

A comparison between different columns was carried according to the overlap of flow rate range to confirm the performance consistency. Four Laminar flow elements have good stability that was used as the transfer standard (TS). The calibration gas was dry air. The test results were shown in Figure 2. The consistencies among different standard columns of newly piston prover were authenticated, and the maximum deviation was less than 0.01 %.

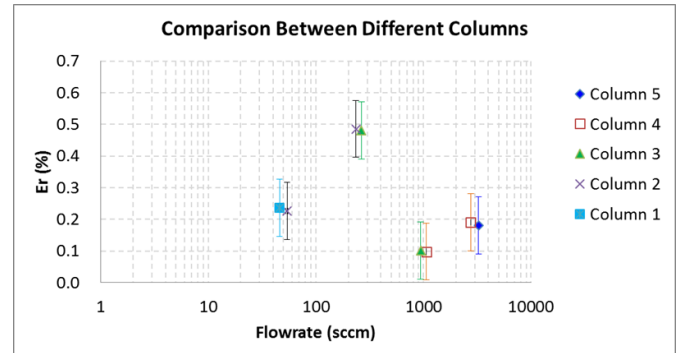


**Figure 2** Comparison between different columns

#### 3.2 Intra-comparison between original and newly established piston prover

A comparison between new-constructed and original CMC submitted piston prover was conducted to validate the capability of newly piston prover fit the bill for industry calibration needs. In table 8 were shown the results of the comparison.

The  $E_n$  value was used as the index for measuring the test capability of two systems. The calculation way of  $E_n$  value was shown in Equation (6).

$$|E_n| = \left| \frac{E_1 - E_2}{\sqrt{U_1^2 + U_2^2}} \right| \quad (6)$$

Where,  $E_1$  was the measurement result for the relative error of new piston prover.  $E_2$  was the measurement result for the relative error of original piston prover.  $U_1$  was 0.09 % of the expanded uncertainty of new Piston Prover system. Prover.  $U_2$  was 0.11 % of the expanded uncertainty of the original piston prover system. Under the same flow rate, the differences of the original system and new system were located from 0.00 % to 0.05 %. The evaluation of  $E_n$  value were equal or less than 0.4 at all tests. The verification results were identical with expectation.

**Table 8** Summary of the comparison results between different Piston Prover

Laminar flowmeter	Flow rate (sccm)	$E_1$ (%)	$E_2$ (%)	$U_1$ (%)	$U_2$ (%)	$ E_n $
m-1247	250	0.45	0.45	0.09	0.11	0
	200	0.39	0.39	0.09	0.11	0
	150	0.34	0.35	0.09	0.11	0.1
	100	0.32	0.30	0.09	0.11	0.1
	50	0.35	0.33	0.09	0.11	0.1
m-977A	1000	0.11	0.15	0.09	0.11	0.3
	750	0.09	0.12	0.09	0.11	0.2
	500	0.09	0.10	0.09	0.11	0.1
	250	0.09	0.12	0.09	0.11	0.2
m-1286	5000	0.33	0.35	0.09	0.11	0.1
	4000	0.24	0.25	0.09	0.11	0.1
	3000	0.19	0.21	0.09	0.11	0.1
	2000	0.14	0.17	0.09	0.11	0.2
	1000	0.10	0.15	0.09	0.11	0.4
m-1092	20000	0.46	0.49	0.09	0.11	0.2
	15000	0.43	0.46	0.09	0.11	0.2
	10000	0.44	0.48	0.09	0.11	0.3
	6000	0.48	0.53	0.09	0.11	0.4

Note: sccm is standard cubic centimeter per minute @0°C

#### 4. Conclusion

A newly mercury-sealed piston prover was established and verified at CMS/ITRI. The flow capacity of this new system covers from 0.002 L/min to 40 L/min at 23 °C and 101.325 kPa. The relative expanded uncertainty of mass flow measurement was less than 0.08 % at 95 % confidence level. The comparison results indicate that the measurement capabilities and system stability of each column of newly piston prover were identical with expectation.

#### 5. Acknowledgement

We acknowledge the financial support from the Bureau of Standards, Metrology and Inspection (BSMI) of the Republic of China.

#### References

- [1] Wright J D and Mattingly G E, “NIST Calibration Services for Gas Flow Meters: Piston Prover and Bell Prover Gas Flow Facilities,” (*Gaithersburg, MD: National Institute of Standards and Technology*), 1998.
- [2] C.M. Su, W.T. Lin and Masri S, “Establishment and verification of a primary low-pressure gas flow standard at NIMT MAPAN *J. Metrol. Soc. India*,” Vol. 26, pp. 173-86, 2011.
- [3] Padden H, “Uncertainty analysis of a high-speed dry piston flow prover,” *Measurement Science Conf. (Anaheim, CA)*, 2002.
- [4] Padden H, “Development of a 0.2% high-speed dry piston prover,” *Measurement Science Conf. (Anaheim, CA)*, 2003.
- [5] Kutin J, Bobovnik G and Bajsic I, “Heat exchange effects on the performance of a clearance-sealed piston prover for gas flow measurements,”
- [6] Metrologia, Vol. 52, pp. 857-863, 2015. 6. ISO/IEC Guide 98-3 : 2008, Uncertainty of measurement – Part 3 : Guide to the expression of uncertainty in measurement (GUM : 1995).
- [7] Wright J. D., Johnson A. N., and Moldover M. R. “Design and Uncertainty Analysis for a PVTt Gas Flow Standard,” *J. Res. Natl. Inst. Stand. Technol.*, 108, 21-47, 2003,

# Oil-Water Flow Measurement for Custody Transfer Applications

W. Maru<sup>1</sup>, S. Lakshmanan, N. Singh and A. Thomas

Oil & Gas Measurement (OGM) Limited  
Ely, Cambridgeshire, United Kingdom  
<sup>1</sup>Email (W. Maru): [wes.maru@oghl.co.uk](mailto:wes.maru@oghl.co.uk)

---

## Abstract

In the Oil & Gas industry, the ownership or custody transfer (CT) of crude oil is measured using Flow Metering and Sampling. Flow Metering quantifies the total amount fluid while Sampling quantifies the fluid composition – for example, the water fraction and other compounds thereby correcting the Flow Metering for its Oil-Cut. Any small inaccuracies in sampling may result in the sale or purchase of expensive water – resulting in significant financial exposure, incorrect government taxations and consequently affecting our weekly shopping too. Worse still, the absence of periodic sampling and failure to detect some undesirable compounds such as (inorganic and organic) chlorides could be catastrophic – not only economically but also politically. Therefore, the central tenet in Sampling is the creation of homogeneous mixture in the pipeline so that accurate representative samples could be extracted. However, achieving a homogeneous mixture of oil and water - two fluids that don't like to mix, is challenging. To that end, following current industry standards, OGM has developed the SmartMix<sup>®</sup> Sampling System and tested it using two flow loops of different sizes, the SMPFL and LMPFL. For prototype development at the University of Cambridge, the SMPFL together with magnetic resonance imaging (MRI) is used to characterise the mixing profile. For industrial scale testing, the LMPFL together with Multiport Profile Proving (MPP) device is used to validate the performance and integrity of the technology. The test results achieved better than 97% mixing efficiency, significantly exceeding the 90% requirement stipulated by the current industry standards.

---

## 1. Introduction

The Flow Metering and Sampling of unrefined or refined petroleum fluids are the two key components of measurement in custody transfer (CT) applications.

CT typically refers to the transaction of petroleum fluids at the point of sale where there is exchange in ownership (or custody) of the product fluid. The point of sale for these fluids could be at on-shore pipelines, off-shore floating production storage and offloading (FPSO) facilities or refinery inputs. In this paper, the petroleum fluids considered are liquids – including condensates.

In general, the CT measurements serve as the “cash register” of the Oil & Gas industry. Flow Metering is concerned in quantifying the total amount (or quantity) of liquid in transaction with uncertainties as low as  $\pm 0.15\%$  while Sampling is concerned in quantifying the composition (or

quality) of the liquid product with the objective of achieving a combined measurement uncertainty of  $\pm 0.25\%$ . For example, in an Oil-Water flow, any small inaccuracies in sampling means the sale or purchase of expensive water and may result in significant financial exposure and incorrect government taxations thereby affecting our weekly shopping too. In addition, any failure in the accurate and periodic sampling of petroleum fluids that may have inorganic chlorides (salts) could be damaging and must be detected via sampling so that it can be removed from the oil using desalting (or water washing) before entering refineries. More critically, the presence of organic chlorides, which form covalent bonding with the hydrocarbon, must be detected by sampling as its concentration ought to be maintained below 1 ppm, which otherwise may significantly damage the refinery, with serious economic and political consequences – particularly between nations that depend on transboundary energy supply.

Automatic Pipeline Sampling, invariably, undergoes through five stages as depicted by **Figure 1** and as stipulated by the major industry and international standards such as ISO 3171 [1], API 8.2 [2], IP/EI 476 [3] and ASTM D4177 [4]. In brief, the sampling stages are: a) Stream conditioning-mixing, b) iso-kinetic sample extraction, c) sample collection and handling, d) sample re-mixing for analysis and e) sample analysis and reporting. The chain of uncertainty increases with the number of stages used. But, in this paper, it is argued that a two-stage approach may be much beneficial to lower the uncertainty. In addition, although all the five stages of sampling are equally important, the first two stages – namely, the creation of homogeneous oil-water mixture through stream conditioning-mixing and the iso-kinetic extraction of representative samples in a flow or time proportional way proved to be very critical for the measurement accuracy and integrity.



**Figure 1.** The five sampling stages according to ISO 3171

It is widely understood that sampling standards such as ISO 3171 and API 8.3 require the creation of a better than 90% homogeneous mixture in the pipeline to extract representative samples. However, achieving homogeneous mixture of oil and water - two fluids that don't like to mix, particularly without creating the undesirable stable emulsion, is one of the serious challenges in CT application. Although significant effort has been made to improve the mixing efficiency of devices in sampling systems for over forty years, Sampling remains "The Elephant in the Room". In fact, the current trend in the CT community appears, may be due to the challenging nature of sampling, to look away from and focus all efforts to lower the uncertainties in Flow Metering. However, evidence suggests that as oil wells age, pipelines tend to carry crudes with larger than 5% water cuts, which is observed to affect the uncertainty of even the most modern and popular flow meters significantly [5, 6]. Moreover, iff sampling is to correct Flow Metering, the current 90% mixing efficiency or homogeneity required by the leading standards [1-4] must be significantly improved.

## 2. Flow Testing and Calibration Laboratory

OGM invested significantly and built an integrated flow testing and calibration facilities (FTCF) to conduct extensive internal and collaborative R&D projects towards our effort and vision to produce leading Products & Technologies for the CT applications that satisfy our customers' needs.

OGM's integrated FTCF is depicted by **Figure 2** and is also described elsewhere [7]. In brief, the FTCF consists of the small multiphase flow loop (SMPFL) with a 2.5" nominal pipe diameter, the large multiphase flow loop (LMPFL) with 10" nominal pipe diameter, the liquid meter calibration loop (LMCL) and the high performance computing (HPC). The LMPFL is a four times scale-up version of the SMPFL and both use de-ionised water and synthetic oil.

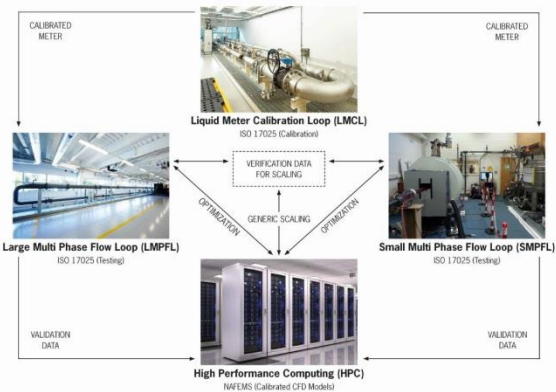


**Figure 2.** Integrated Flow Testing and Calibration Facilities.

The SMPFL has a maximum flow capacity of 18 m<sup>3</sup>/hr while the LMPFL has 148.5 m<sup>3</sup>/hr. The SMPFL has 25D straight pipe length, which is the distance between the device under test (DUT) and the water injection point. The length is 110D for LMPFL. Both the SMPFL and LMPFL are fitted with a flow through aerospace grade coalescer to separate the oil and water with better than 100 ppm separation capacity but when the water cut is not exceeding 10% (v/v). The LMCL can be used to calibrate flow meters with size ranges from 1" up to 12" and with flow range from 0.6m<sup>3</sup>/hr to 800 m<sup>3</sup>/hr. On the other hand, the HPC uses the NVIDIA K20 GPU computational hardware heterogeneously coupled with Sandy Bridge CPU cores delivering both high power efficiency and a sustained aggregate performance of 32 "Teraflops". One of the main tools that runs on the HPC is the OpenFOAM platform to develop and validate multiphase computational fluid dynamics

(MCFD) tools so that they can be used as a design guide or design tool for the development of our Products and Technologies. To this end, the key objective in the design philosophy for the FTCF is to create an ISO 17025 certified testing and calibration hub so that collaborative improvement could be to improve current CT measurement devices. In particular, the system level testing of Flow Metering and Sampling devices or skids through traceable international standards. During the commissioning of the SMPFL and LMPFL, all single phase (oil or water) flow meters are calibrated in the LMCL, whose master meters are calibrated either in an ISO 17025 certified third party laboratory or using compact provers.

Once the integrity of the measurements in the SMPFL and LMPFL are verified, the SmartMix<sup>®</sup> Sampling System tests on both loops are characterised for their performance and the data is used to validate the MCFD results.

It is now widely accepted that a validated and/or calibrated MCFD models could be used to simulate large diameter pipelines, ranging between 24" and 56", which would have been otherwise impossible to conduct physical experiments as such size flow facilities do not exist. This synergistic approach of using numerical and physical experimentation via the integrated FTCF will open up a new vista for accelerated and cost effective innovations.

## 2. The SmartMix<sup>®</sup> Sampling System

The development, validation and field installation of the SmartMix<sup>®</sup> Sampling System (here after simply called the "Sampling System"), with its LJICF Technology [8] and Advanced Control System (ACS) is described elsewhere [7, 9-11]. Therefore, the focus here is to provide only its salient features mainly focusing on the validation test results. The challenging conditions in the mixing and sampling application involve low fluid viscosity and low density while the same is true for low velocity and horizontal pipe orientations.

The Sampling System is depicted by **Figure 3**. The operating principle of the patented technology is unique at least in three ways compared to similar systems that are currently available in the market.

First, after receiving (analog or digital) signals for the flow rate and pressure inside the pipeline, the ACS actuates the variable speed drive (VSD) of the pump and the (inner, outer) automatic control valves so that the required injection flow is extracted iso-kinetically through the Scoop.

Second, at the discharge side of the pump, the flow splits in to two streams, where the Inner Stream traverses through the inner flow meter, the Sampling and Analysis Module and the inner automatic control valve before forming the Inner Jet of the Twin Nozzle<sup>™</sup>. The Outer Stream traverses through the outer flow meter and the outer automatic control valve before forming the Outer Jet of the Twin Nozzle<sup>™</sup>. The mode of interaction between the Inner and Outer Jets (as Weak-Jet and Strong-Jet) in response to the pipeline dynamic and process conditions [12-14] is one of the key basis for the technology.

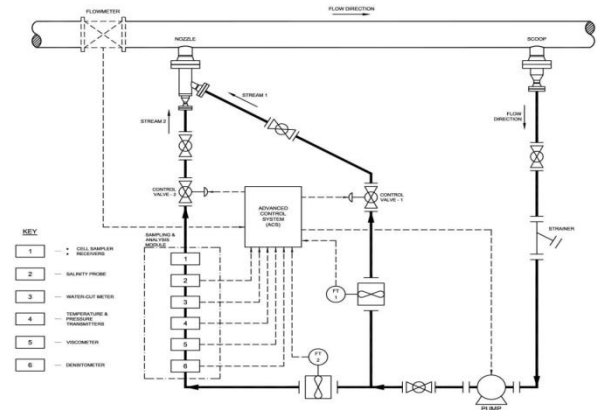


**Figure 3.** The SmartMix<sup>®</sup> Sampling System.

Third, the ACS is not only responding to the pipeline conditions, it also uses stochastic type automatic control and dynamic optimisation, where the arrays of instruments in its Sampling and Analysis Module are used to aid the control more effectively. Furthermore, the ACS also controls the (inner/outer) automatic valves so that the required flow rate and the required inner to outer stream flow ratio is ensured and achieved. These (analog, digital) readings from the water cut meter, densitometer, viscosity meter as well as pressure and temperature transmitters are the critical sensors and actuators to improve the mixing homogeneity or efficiency of the developed Sampling System.

Therefore, the operation of the Sampling System - particularly its mixing duty, is directly dependent on the real time process dynamics and fluid properties, heralding on-demand mixing that may save significant power consumption. For typical sampling systems with operational life time as long as 15-20 years, the power savings that can be gained can't be understated – both as an OpEx and in saving the environment.

## 2.1 Sampling System Proving by Water Injection

**Figure 4** depicts an industrial scale Sampling System, where proving by water injection (PWI) is used to quantify the mixing efficiency, sample extraction, sample handling, shear mixing and KF analysis, with the lowest possible chain of uncertainties.

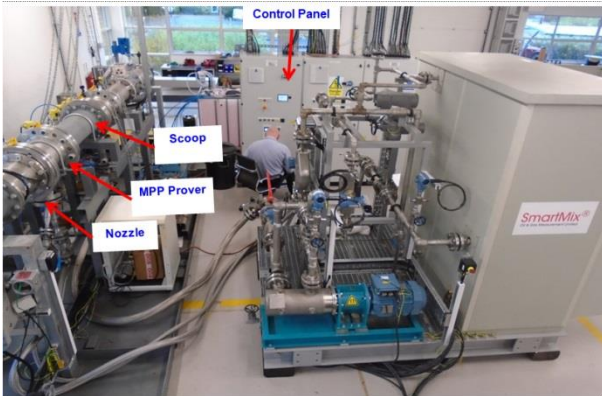


**Figure 4.** The SmartMix<sup>®</sup> Sampling System under test in OGM's Large Multi-Phase Flow Loop (LMPFL).

PWI is carried out [10,11,14] using the multiport profile proving (MPP) device which is depicted by **Figure 5**. The MPP device has six ports, where one is positioned along the pipe axis while the other four are placed symmetrically. Two of the probes are position 20 mm away from the inner wall of the pipe while the other two are positioned at half the radius ( $R/2$ ) above the pipe centre and below the pipe centre, respectively. The sixth probe is placed at the inner base of the pipe so that even the smallest water droplet could be captured. All the probes have an internal diameter of 8 mm, which is larger than the minimum 6mm diameter recommended by ISO 3171.

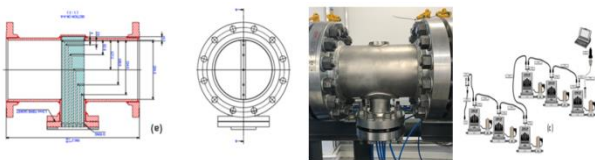


**Figure 5.** Multiport Profile Proving (MPP) device with six ports for proving by water injection (PWI).

All the six probes are each connected to six flexible tubes of equal length, which in turn are connected to six mini-Coriolis flow meters with density measurement functionality. When samples are extracted via the six probes, all the tubes open to six atmospheric receivers that are placed at a level and lower elevation. Before any PWI test, the MPP

is tested extensively and proven to achieve “true” iso-kinetic sampling with good velocity matching.

The PWI protocol follows ISO 3171 and API 8.2 and is depicted by **Figure 6**. First, for several minutes, the loop is purged using oil at its maximum flow rate. Then, a baseline water cut is introduced by selecting one of the ranges between 1% and 4%, where up on the sampling system mixing pump starts creating homogeneous mixture.

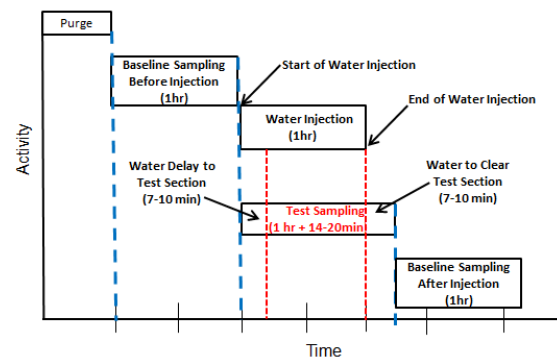


**Figure 6.** Typical Activity-Time diagram of proving by water injection (PWI) of a sampling system.

After an hour of time-proportional sampling (15 grabs/minute of 1cc each) is taken in the fast loop using the Maurer<sup>™</sup> cell sampler as shown in **Figure 6**, the ACS turns on the water pump, which allowed to raise the baseline water cut by 0.5%. However, due to the distance between the injection point and DUT (~110D), there is a delay for the water to arrive at the measuring or mixing point, which must be accounted for. Similarly, there is a delay for the water to clear when the injection is stopped. The final hour sampling is similar to the first hour sampling, which provides the steadiness of the baseline water cut. The mixing efficiency of the sampling system is evaluated according to ISO 3171 section 15.

### 3. Tests and Test Results

Two types of nozzles, SLIT Nozzle and NJ4, are considered and tested at the LMPFL. A variant of NJ4 nozzle was also tested for high water cut range between 3% and 70%, where the test was carried at an accredited flow loop in Schelkovo, which has a 6" nominal diameter.

#### 3.1 SLIT Nozzle

The test conditions are provided in **Table 1** and the PWI results are depicted by **Figure 7**. Further computational fluid dynamics (CFD) results are

depicted by **Figure 8**. The physical experiment results for the SLIT nozzle shows that the composition distribution to be homogeneous. The probe location 2 indicates the central MPP probe while positions 1 is the ratio of the probes 20 mm from the pipe wall and 3 is the ratio of those at half the radius (R/2). The result shows excellent mixing.

**Table 1:** PWI test condition for the SLIT Nozzle

	R1	R2	R3	R4	R5	R6	R7	R8	R9
U(m/s)	0.2	0.4	0.6	0.2	0.4	0.6	0.2	0.4	0.6
WC(%)	1	1	1	2	2	2	4	4	4

The results in **Figure 8a** show the initial evolution of mixing. The top and bottom contours show a slice taken parallel to the stream wise direction while the middle is a slice taken perpendicular to the stream wise direction. The pronounced vorticity provides the mixing energy dissipation rate. This is observed more clearly in **Figure 8b**, with the same slice direction as in **Figure 8a** but at a later time.

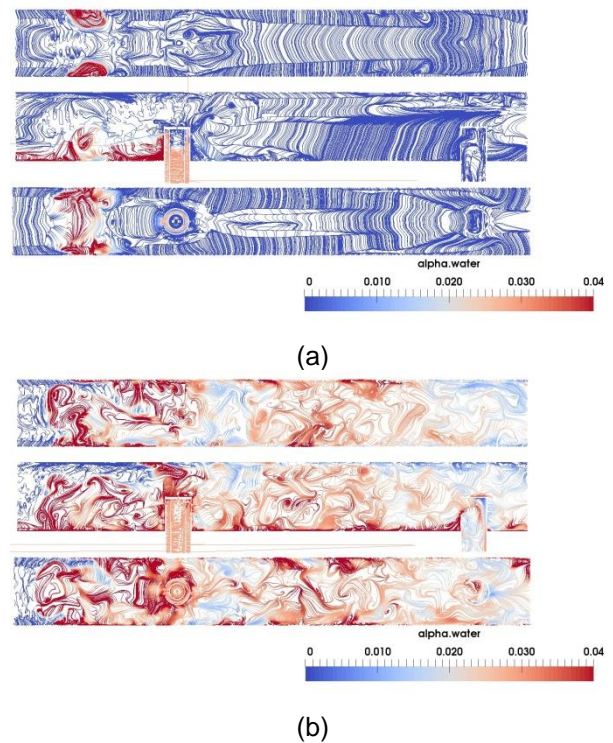


**Figure 8:** CFD simulation result of SLIT nozzle for R9 case.

**Table 2:** EPWI test condition for the SLIT Nozzle

	R2	R3	R5	R7	R8
U (m/s)	0.4	0.6	0.4	0.2	0.4
WC(%)	1.5	1.5	2.5	4.5	4

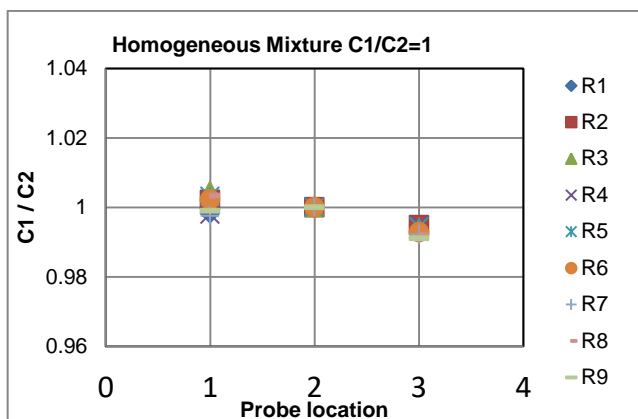


**Figure 7:** PWI results of the SLIT nozzle with probe location

Both the CFD simulation and the PWI test via the MPP device indicate very good mixing is achieved. However, the five stage sampling protocol that is in practice today appears to be a very laborious and sometimes laden with errors with increased chain of uncertainties. A direct measurement method is preferred, such as “mix and measure” [11,14].

### 3.2 NJ4 Nozzle

The test condition for the NJ4 nozzle is provided in **Table 2** and the PWI results are depicted by **Figure 9**. A CFD simulation for this case is ongoing and will be reported elsewhere. Therefore, only the physical experiment is provided, again, the result shows excellent mixing.

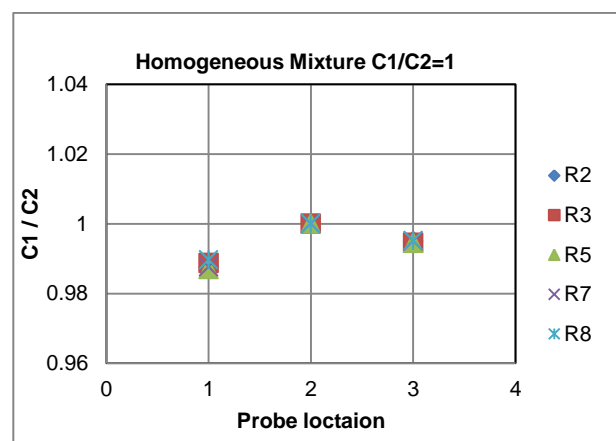


**Figure 9:** PWI results of the NJ4 nozzle with probe location

### 3.3 High Water-Cut Test at Schelkovo

The test conditions for the high water cut cases that are conducted in Schelkovo are shown in **Table 3**. The sampling results in **Figure 10** are not a proving or PWI tests as depicted by **Figure 6**.

The Schelkovo flow loop is a well instrumented facility. However, the description of the flow loop is beyond the scope of the current paper and therefore will be described elsewhere. Instead, we focus on the test condition and the result in this case. **Figure 10** shows that for the tests done, all achieved the ISO 3171 and API 8.2 mixture homogeneity requirements. The performance of the mixing device indicates that This is a remarkable

**Table 3:** PWI high water cut test condition for the NJ4 Nozzle

	R1	R2	R3	R4	R5	R6	R7	R8	R9	R10	R11	R12
U(m/s)	0.45	0.65	0.85	0.45	0.65	0.85	0.45	0.65	0.85	0.45	0.65	0.85
WC(%)	3	3	3	20	20	20	45	45	45	70	70	70

The well instrumented Schelkovo facility allowed to

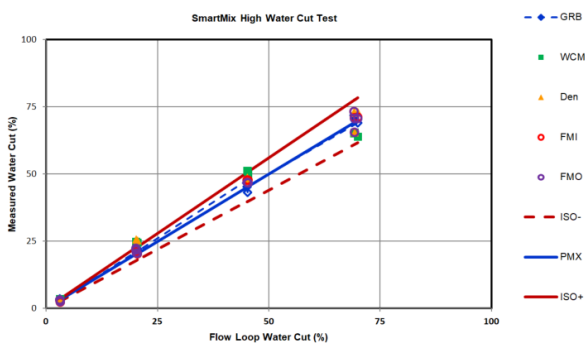


**Figure 10:** High water cut test at the Schelkovo facility

The high water cut test was a significant success as our initial product proving tests were limited to only 6% water cut. This demonstrates the versatility of the technology. The laboratory analysis (for the oil-water sample) proved repeatable and it is also proved that the Sampling System’s compliance and its high performance in mixing. For the entire test data presented, the mean absolute error is  $\pm 0.14\%$  with a standard deviation of  $\pm 0.117\%$ .

## 7. Conclusion

The Sampling system developed was tested with two nozzle families. The performance of both the SLIT and NJ4 Nozzles were excellent, providing higher than 97% mixing efficiency, compared to the 90% mixing efficiency stipulated by international standards. The challenging Schelkovo test with high water cut doesn’t appear to affect the performance of the Sampling System, showing its versatility.

## References

- [1] ISO 3171, *Petroleum liquids - Automatic pipeline sampling*, 2004.
- [2] API MPMS Chapter 8.2 *Standard Practice for Automatic Sampling of Petroleum and Petroleum Products*, Fourth Edition, 2016.
- [3] IP 476: *Petroleum liquids - Automatic pipeline sampling*, 2002
- [4] ASTM D4177–95, *Standard Practice for Automatic Sampling of Petroleum and Petroleum Products*, 1998.
- [5] Brown, G., Cousins, T., and Almeida, M. “Oil/Water Tests on a 4-Path Ultrasonic Meter at Low Flow Velocities”, 24th International North Sea Flow Measurement Workshop 24–25 October 2006
- [6] Cousin, T., Steven, R., and Kegel, T. “Coriolis Meter Testing Under Variable Water Cut, Oil Water Conditions”, 24th International North Sea Flow Measurement Workshop 24–25 October 2006
- [7] Lakshmanan, S., Maru, W., Holland, D., Thomas, T. and Sederman, A. J., “Quantifying Mixing Efficiency in automatic pipeline sampling”, North Sea Flow Measurement Conference, Norway, 2017.
- [8] Mahesh, K., The Interaction of Jets with Crossflow, *Annual Review of Fluid Mechanics Vol. 45:379-407*, 2013.
- [9] Lakshmanan, S., Maru, W., Holland, D. J., Mantle, M, D., and Sederman, A. J., Measurement of a multiphase flow process using magnetic resonance imaging, *J. Flow Measurement and Instrumentation*, **53:161-171**, 2016.
- [10] Lakshmanan, S., Maru, W., Holland, D.J., and Sederman A., “Multiphase flow quantification using Computational Fluid Dynamics and Magnetic Resonance Imaging”, *North sea Flow measurement Conference, Norway, 2015*
- [11] Maru, W. Holland, D. Lakshmanan, S , Thomas, A and Sederman, A. J. “Multiphase Flow and Mixing Quantification using Computational Fluid Dynamics and Magnetic Resonance Imaging”, *Special Issue in Recent Global Developments in the Measurement of Oil and Gas Flows (2019) to appear*
- [12] Aftosmis, M.J., and Rogers, E.R., Effects of Jet-Interaction on Pitch Control of a Launch Abort Vehicle, *46th AIAA Aerospace Sciences Meeting and Exhibit, 7-10 Jan 2008*
- [13] Yimer, I., Becker, H.A., Grandmaison, E.W., The strong-jet/weak-jet problem: New experiments and CFD, *Combustion and Flame* **124(3):481-502**, 2001.
- [14] Lakshmana, S., Maru, W., Takotue, A., “SmartMix<sup>®</sup> Sampling System: How to make more money from your pipeline”, *NEL Oil & Gas Focus Group Meeting, 1 May 2019*.

# Problems to note when using the nozzle to nozzle test method

Shinichi Nakao <sup>1)</sup>, Hiroshi Asano <sup>2)</sup> and Takeshi Yakuwa <sup>2)</sup>

<sup>1</sup> Flow Col<sup>®</sup>, flowcol@flowcol.com, Yokohama, Japan

<sup>2</sup> HIRAI Co., Ltd., Tokyo, Japan

## Abstract

The strange behaviors of the discharge coefficient of the critical nozzle were found when gradually changing the back pressure ratio ( $P_d/P_u$ ) from the almost zero to the critical back pressure ratio in the nozzle to nozzle test method. When the test gas is Helium, the change amount of the discharge coefficients at these strange behaviors is quite large and seems significantly to influence to flow measurements. The causes of the strange behaviors are different in the ranges of  $P_d/P_u < 0.1$  and of  $P_d/P_u > 0.1$ , and in either case are considered to be due to the measurement principle of the nozzle to nozzle test method that the mass flow rate through the system is constant. Under the condition that the mass flow rate is constant, the discharge coefficient of the critical nozzle on the downstream side in the nozzle to nozzle test method must definitely change in inverse proportion to its upstream pressure change. The flow models are suggested to explain the reason why the upstream pressure changes when changing the back pressure ratio. The more important point of the present results is that the equivalence of the discharge coefficient determined by the general calibration methods and by the nozzle to nozzle test method may be not always hold.

## 1. Introduction

A nozzle to nozzle test method is commonly used to evaluate the characteristics of critical nozzles, for example, to decide the discharge coefficient or to examine a critical back pressure ratio. In this test method, a back pressure ratio of a critical nozzle under test is constant during measurements. On the other hand, when a critical nozzle is calibrated by a PVTt method or a gravimetric method, a pressure in a constant volume tank or in a collecting tank increases continuously during calibration. Therefore, its back pressure ratio is not constant on the determination of discharge coefficient. So far, there has been no doubt about the equivalence of the discharge coefficients determined by these calibration methods at least. However, the recent experimental results have raised some doubt about their equivalence. One of them is a premature unchoking<sup>[1][2]</sup>. When a critical nozzle is calibrated by a PVTt method or a gravimetric method, whether a premature unchoking occurs cannot know in advance so that the discharge coefficient obtained is possible to include significant error. On the other hand, the nozzle to nozzle test method can decide a discharge coefficient by avoiding the range of the back pressure ratio where the premature unchoking occurs. From that respect, the nozzle to nozzle test method can be said to be a reliable and useful method. This paper describes about the strange behaviors of the discharge coefficient found in the nozzle to nozzle test method. The present results raise another and more serious problems for the

equivalence of discharge coefficient determined by these calibration methods.

## 2. Experimental apparatus and dimensions of critical nozzles

The nozzle to nozzle test method used in the present experiments is shown in Fig.1. The standard critical nozzles are calibrated by the gravimetric system of HIRAI Co., Ltd., which is the accreditation laboratory and has the gravimetric system similar to NMIJ. The standard critical nozzle and the critical nozzle under test are connected in series and the discharge coefficient of the latter critical nozzle is calculated from Eq.(1). When the diameters of both critical nozzles and the upstream condition of the standard critical nozzle are given, the upstream pressure of the critical nozzle under test is uniquely decided from Eq.(1).

$$C_d = C_{dS} \times \left(\frac{d_S}{d}\right)^2 \times \left(\frac{P_S}{P_u}\right) \times \sqrt{\frac{T_u}{T_S}} \quad (1)$$

Here,  $C_d$ : a discharge coefficient,  $d$ : a throat diameter,  $P$  and  $T$ : an upstream pressure and a upstream temperature of critical nozzles. Subscript "s" and "u" mean the standard critical nozzle and the critical nozzle under test, respectively. Both critical nozzles used here are the troidal throat Venturi nozzle and made of Nickel, which are manufactured by Toray Precision Co., Ltd. The throat diameters of the standard critical nozzle and the critical nozzle under test are 0.248 mm and 0.424 mm, respectively. Their inlet curvature is about  $2d$ , their diffuser length is about  $3d$  and their diffuse half angle

is about 3 degrees. The expanded relative uncertainty of  $C_{ds}$  is 0.13% for Nitrogen and 0.24% for Helium.

The pressure sensors to measure  $P_s$  and  $P_u$  are YOKOGAWA 2653-S7, which are calibrated by the piston gauge of HIRAI from 50 kPa to 700 kPa and their standard uncertainties are 10 Pa. The four wire Pt resistance thermometer to measure  $T_s$  and  $T_u$  are also calibrated at HIRAI and their standard uncertainties are 0.1 deg.C. The automatic pressure controller developed by HIRAI can control the setting pressure with  $\pm 10$  Pa  $\sim \pm 30$  Pa, depending on a setting pressure and a flow rate.

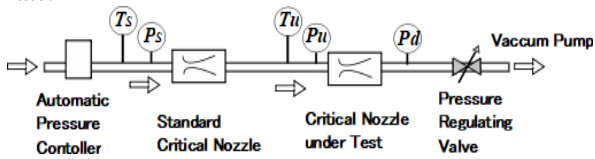


Figure 1 Experimental apparatus of the nozzle to nozzle test method

### 3. Experimental results

Figures 2 show the behaviors of the discharge coefficient of the critical nozzle under test when changing a back pressure ratio.  $C_{d0}$  of the symbol of the vertical axis is the discharge coefficient at  $P_d/P_u=0.1$ . Figure 2(a) is the results of Helium and Fig.2(b) is that of Nitrogen. The theoretical Reynolds numbers  $R_{eth}$  is adjusted as close as possible in comparing both experimental results, though it is difficult to adjust  $R_{eth}$  in these gases. The theoretical Reynolds number is defined as follows;

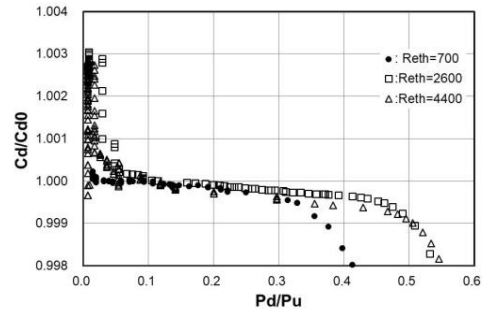
$$R_{eth} = \frac{Q_{mth}d}{A\mu}$$

Here,  $Q_{mth}$ : a theoretical mass flow rate given in Eq.(3),  $A = d^2\pi/4$ ,  $\mu$ : a viscosity of gas.

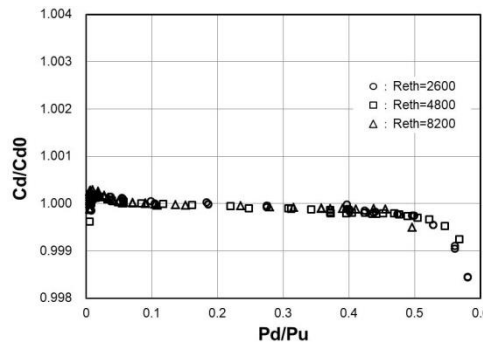
One of the strange behaviors found in these figures is the peaks of discharge coefficient in the range of  $P_d/P_u < 0.1$ . The maximum peak value in Helium is quite large and reaches to about 0.3% larger than the value of  $P_d/P_u=0.1$ . On the other hand, the maximum value in Nitrogen is only 1.0004 times the value of  $P_d/P_u=0.1$  at maximum. Another is the behaviors of the discharge coefficient in  $P_d/P_u > 0.1$  found in Helium. The discharge coefficients gradually decrease toward the critical back pressure ratio, at which the discharge coefficient decreases quickly. It should be noticed that the decrease of the discharge coefficients even in Nitrogen is slightly but definitely recognized. In this paper, the flow models are suggested to explain the reasons why these strange behaviors of the discharge coefficient occur.<sup>[3]</sup>

#### 3.1 Behaviors of the discharge coefficient in $P_d/P_u < 0.1$

Figures 3 show how the discharge coefficient changes with time. The numerals in Figs.3 are the values of  $P_d/P_u$ , which is kept constant in the range of the horizontal arrow, and the vertical arrows indicate the

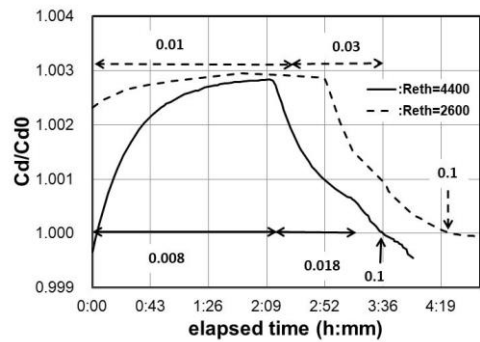


(a) Helium

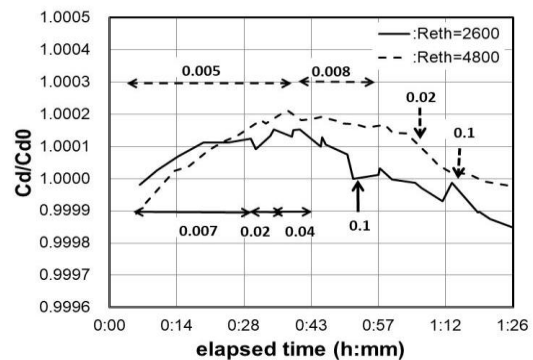


(b) Nitrogen

Figure 2 Behaviors of the discharge coefficient against the back pressure ratio



(a) Helium



(b) Nitrogen

Figure 3 Variation of the discharge coefficient with time

position of the value of  $Pd/Pu$ .

Next, let's look at the results of Helium at  $Re_{th}=4400$  in Fig.3(a) in details. When  $Pd/Pu=0.008$ , the discharge coefficient increase gradually to the maximum value over about two hours. When the back pressure ratio changes from 0.008 to 0.018, the discharge coefficient begins to decrease toward  $Pd/Pu = 0.1$ . The situation is similar in the case of  $Re_{th} = 2600$ . In Nitrogen of Fig.3(b), the changes of the discharge coefficient are much gentle compared with that in Helium. In both  $Re_{th}=2600$  and  $Re_{th}=4800$ , the discharge coefficients increase gradually and reach to their maximum value after about 40 minutes, and then the discharge coefficients begin to decrease gradually.

Figures 4 (a) and (b) show how the pressure changes with time in Helium at  $Re_{th}=4400$  and in Nitrogen at  $Re_{th}=4800$ , respectively.  $P_s$  is the upstream pressure of the standard critical nozzle and  $P_u$  is the upstream pressure of the critical nozzle under test. The change of  $P_s$  is about 0.05% in Helium and 0.02% in Nitrogen so that  $P_s$  in both gases is considered to be constant during measurements.  $P_u$  in Helium changes largely and its change amount reaches to 0.3 %. On the other hand, the change of  $P_u$  in Nitrogen is only 0.04% and is about the same as that of  $P_s$ , but the aspect of the change of  $P_u$  is similar to that of Helium, that is, increases after decreasing. It is understood from Fig.3 and Fig.4 that the change of the discharge coefficient of the critical nozzle under test and that of its upstream pressure are linked each other.

The behaviors of the discharge coefficient found in Figs.3 might be considered to be able to explain as the thermal non-equilibrium of a nozzle body and a flow field. However, the discharge coefficients of Figs.3 increase and then decrease taking long time as the back pressure ratio changes and does not seem to approach to a certain steady state in the range of  $Pd/Pu < 0.1$ . Furthermore, the pressure changes shown in Figs.4 would not be explained by the thermal non-equilibrium.

Therefore, another idea is proposed to explain the reason that the discharge coefficient changes.

Equation (2) is the definition of  $C_d$ .

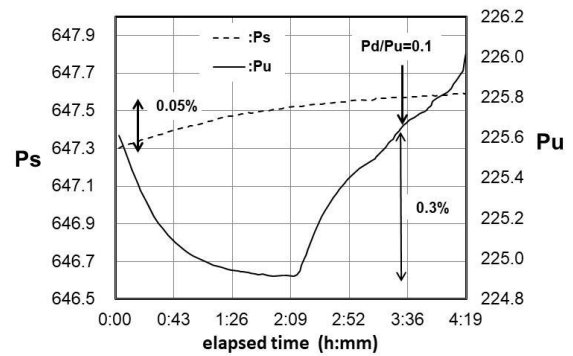
$$C_d = \frac{Q_m}{Q_{mth}} \quad (2)$$

$Q_{mth}$  in Eq.(2) is a theoretical mass flow rate and given as follows;

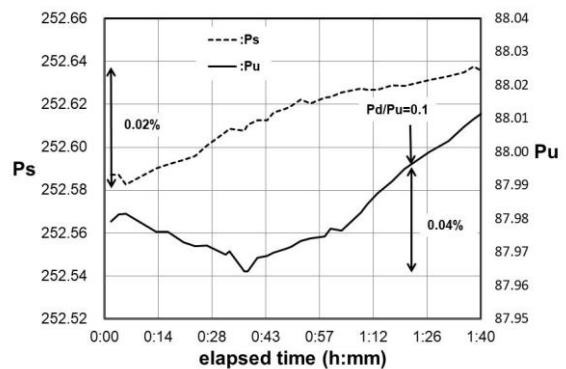
$$Q_{mth} = P_u A^* C^* \sqrt{\frac{Ng}{RT_u Z_u}} \quad (3)$$

Here,  $Q_m$  : a mass flow rate,  $A^*$ : a cross sectional area of throat,  $C^*$ : a critical flow function,  $Ng$ : a molecular weight of gas,  $R$ : an universal gas constant,  $P_u$ ,  $T_u$ : a pressure and a temperature upstream of critical nozzle and  $Z_u$ : a compressible factor at upstream condition.

The change of  $C_d$  can simply be explained as the change of the effective sonic plain area, which is caused by the change of the boundary layer thickness at the throat. That is, when the boundary layer becomes



(a) Helium :  $Re_{th} = 4400$



(b) Nitrogen :  $Re_{th} = 4800$

Figure 4 Variation of the upstream pressure in  $Pd/Pu < 0.1$

thinner, the effective sonic plain area increases. At this time, if the upstream condition is maintained, more mass flow flows and  $C_d$  increases. If the boundary layer becomes thicker, the opposite occurs.

However, in the nozzle to nozzle test method, the mass flow rate through the system is equal to that obtained from the standard critical nozzle and is constant as long as the upstream condition of the standard critical nozzle does not change. If the mass flow rate through the critical nozzle is constant, when the boundary layer becomes thinner and the effective sonic plain area increases,  $P_u$  must decrease to keep a mass flow rate constant and resultantly  $C_d$  must increase. The problem is why the boundary layer becomes thinner and why  $P_u$  decreases taking a long time.

The flow field at the nozzle exit is simply considered to consist of a core flow having almost constant Mach number and a boundary layer having subsonic velocity. When a back pressure ratio is less than  $Pd/Pu=0.1$ , a flow field outside a nozzle exit is in state of an under expanded jet and a strong expansion wave generates from the edge of nozzle exit. At this time, a flow along a boundary layer, which develops over the diffuser wall including the throat area, is strongly accelerated so that the boundary layer on the nozzle wall becomes thinner and resultantly the effective sonic plain area becomes larger. Therefore, as mentioned above, when the effective sonic plain becomes larger, the upstream

pressure decreases and resultantly the discharge coefficient increases under the condition that the mass flow rate is constant like in a nozzle to nozzle test method. It might take a long time to reach the stable upstream pressure condition because the flow field changes slowly by the pressure wave traveling from the downstream through the thin boundary layer.

When a flow field at a critical nozzle exit is an under expanded jet, a core flow in a diffuser is an isentropic flow from a throat to a nozzle exit so that the Mach number, the pressure and the cross sectional area of the diffuser have a following relations;

$$\left(\frac{A}{A^*}\right)^2 = \frac{1}{M^2} \left[ \frac{2}{\gamma+1} \left( 1 + \frac{\gamma-1}{2} M^2 \right) \right]^{(\gamma+1)/(\gamma-1)} \quad (4)$$

$$\frac{P_0}{P_e} = \left( 1 + \frac{\gamma-1}{2} M^2 \right)^{\frac{\gamma}{\gamma-1}} \quad (5)$$

Here,  $A$  and  $M$  : a cross sectional area of diffuser section at any place and the Mach number at that place, respectively,  $A_e$  : a cross sectional area of a nozzle exit,  $P_0$  : a stagnation pressure,  $P_e$  : a nozzle exit pressure,  $\gamma$  : a specific heat ratio.

As  $(A_e/A^*)$  of the critical nozzle under test used here is 1.72,  $M_e$  and  $P_e/P_0$  are 2 and 0.12 in Nitrogen, and 2.2 and 0.09 in Helium from Eq.(4) and Eq.(5). The back pressure ratio at the nozzle exit,  $P_e/P_0$ , is almost coincident to the back pressure ratio that the strange behaviors of the discharge coefficient found in Figs.3 disappear. This simple calculation results might support qualitatively the explanation that the behaviors of the discharge coefficient in the region of  $P_d/P_u < 0.1$  is caused by the strong expansion fan generated at the nozzle exit. The differences of the behaviors of the discharge coefficient between Nitrogen and Helium would come from the difference of the characteristics of the boundary layer due to thermal properties of these gases. However, it is difficult quantitatively to confirm this explanation by experiments.

The influence of this undesirable behavior of the discharge coefficient found in  $P_d/P_u < 0.1$  would be able to avoid by using a critical nozzle under the condition of  $P_d/P_u > 0.1$ . However, this problem is not so simple. When a critical nozzle is calibrated by a PVTt method or a gravimetric method, a test gas flows into a constant volume tank or a measuring tank from an almost zero back pressure ratio to a near critical back pressure ratio so that the discharge coefficient of the critical nozzle obtained should be noticed to be the value at an average value of back pressure ratios. The change of discharge coefficient found in  $P_d/P_u < 0.1$  in Nitrogen is at most 0.03% so that its change may be negligible within measurement uncertainty. However, in the cases that a test gas is Helium or the high precision measurement is required in Nitrogen, this change of the discharge coefficient in  $P_d/P_u < 0.1$  would be unable to neglect and the discharge coefficient obtained might be suspicious.

### 3.2 Behaviors of discharge coefficient in $P_d/P_u > 0.1$

Figures 5 are the enlarged view of the part of  $P_d/P_u > 0.1$  in Figs.2. The discharge coefficients in both gases decrease gradually toward the critical back pressure ratio that the discharge coefficient decreases quickly, its value depending on the theoretical Reynolds number. In the measurement in the range of  $P_d/P_u > 0.1$ , the back pressure ratio is kept for about 10 minutes, during which the discharge coefficient does not change at all. The change amount of the discharge coefficient between  $P_d/P_u = 0.1$  and  $P_d/P_u = 0.5$  is only 0.01% ~ 0.02% in Nitrogen, but is 0.05% ~ 0.08% in Helium. This change amount in Helium would be unable to be overlooked for flow measurement.

Figures 6 show the variations with time of the upstream pressures and the upstream temperatures of the standard critical nozzle and the critical nozzle under test in Nitrogen at  $Re_{th}=4800$ . The change amounts of  $P_s$  and  $P_u$  are about 15 Pa.  $T_u$  and  $T_s$  are stable within 0.1 deg.C. These are the conditions of pressure and temperature normally expected in the nozzle to nozzle test method. Figures 7 show the variations with time of  $P_s$ ,  $P_u$ ,  $T_s$  and  $T_u$  in Helium at  $Re_{th}=4400$ .  $P_s$  is quite stable and its change amount is only about 5 Pa between  $P_d/P_u=0.1$  and  $P_d/P_u=0.5$ , but  $P_u$  increases about 5 kPa in the same range.  $T_s$  is stable within 0.03 deg.C, and the change of  $T_u$  is about 0.1 deg.C.

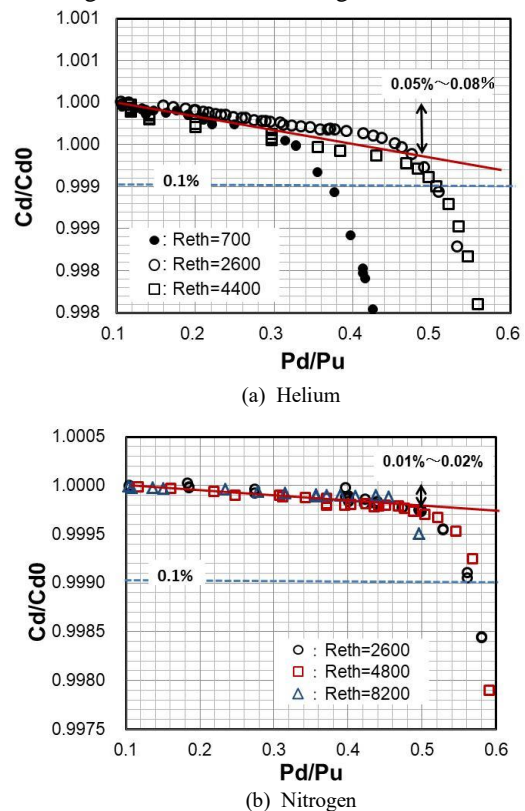
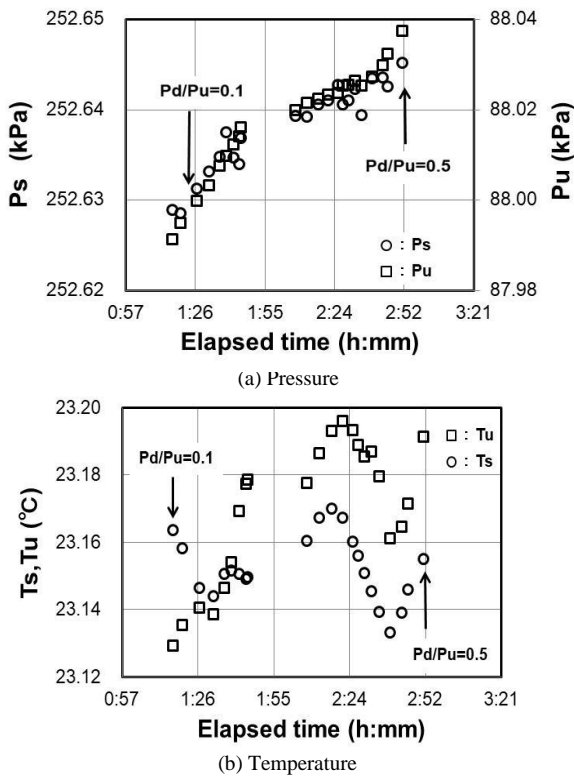
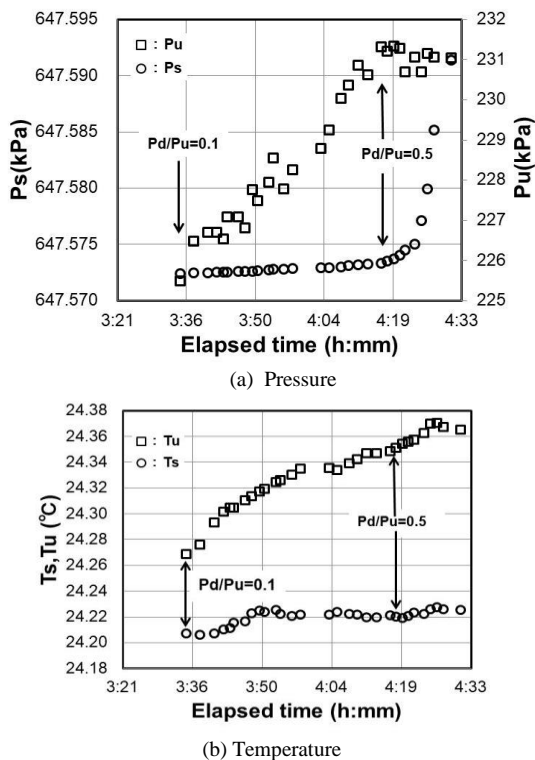


Figure 5 Enlarged view of the discharge coefficient in  $P_d/P_u > 0.1$



**Figure 6** Variations of the pressure and the temperature with time  
Nitrogen:  $Pd/Pu > 0.1$ ,  $R_{eth} = 4800$



**Figure 7** Variations of the pressure and the temperature with time  
Helium:  $Pd/Pu > 0.1$ ,  $R_{eth} = 4400$

As the temperature change is similar to that in Nitrogen, the large change of the discharge coefficient in Helium is considered to be caused by the upstream pressure change. Therefore, it is necessary to explain the reason why  $Pu$  increases largely as shown in Fig.7 (a).

The choked flow is defined as an upstream side and a downstream side of a critical nozzle are completely separated by a sonic plain and a flow field of an upstream side is not affected by that of a downstream side. However, actually, the pressure wave travels through the boundary layer from the downstream side of a critical nozzle to its upstream side or vice versa. Therefore, the upstream pressure changes definitely when a flow field changes by a change of a back pressure ratio, even if there is a difference in degree, depending on a kind of gases or on the theoretical Reynolds number. Normally, an upstream pressure change of a critical nozzle appears as a change of a mass flow rate. However, as discussed in 3.1, in the nozzle to nozzle test method that the mass flow rate is constant, the upstream pressure change results in the change of the discharge coefficient. The behaviors of the discharge coefficient shown in Figs.5 would be explained as follows; when the back pressure ratio changes, since the thickness of the boundary layer at the throat changes, the upstream pressure changes to the value of the new state of the flow field. And the discharge coefficient changes according to the pressure change. This change of the discharge coefficient caused by the pressure change is usually small and can be negligible like the case of Nitrogen, but the change of the upstream pressure in Helium of Fig.5 (a) is larger than expected and resultantly the discharge coefficient will show a significant change.

There is not any definite evidence quantitatively to explain the differences of the change amount of the discharge coefficient found in Helium and in Nitrogen, besides the differences of the characteristics of the boundary layer due to thermal properties of gases. Unfortunately, there have been few researches investigating the characteristics of the boundary layer for gases other than Air.

#### 4. Conclusion

The strange behaviors of the discharge coefficient reported here are considered to be due to the measurement principle of the nozzle to nozzle test method, in which the critical nozzle under test is evaluated under the condition that the mass flow rate is constant. Therefore, even the slight change of the upstream pressure must come out as the change of the discharge coefficient. On the other hand, in the PVTt method or in the gravimetric method, when the upstream pressure changes, since the mass flow rate changes simply in proportion to the upstream pressure, the discharge coefficient does not necessarily need to

change. This is an important and essential difference between the general calibration methods and the nozzle to nozzle test method.

The strange behaviors of the discharge coefficient might appear only under the limited measurement conditions, for example, a gas such as Helium or Hydrogen, and at low or moderate theoretical Reynolds number, etc. Also, the flow models suggested to explain these behaviors might be not correct because there are not any clear experimental evidences to support the flow models. Although, the important thing of the present results is to raise doubts about the equivalence of the discharge coefficient determined by the general calibration method like a PVTt method and that determined by the nozzle to nozzle test method. The nozzle to nozzle test method is not only easy to use, but also is definitely a reliable test method that can investigate the characteristics of critical nozzle. On the other hand, the results obtained by this test method must be examined carefully because the discharge coefficient obtained might be not coincident to that determined by other calibration method depending on calibration conditions.

#### **Afterword**

In this paper, the interesting experimental results about the discharge coefficient of the critical nozzle were shown and also the flow models to explain these phenomena were suggested. However, we could not show any clear evidence or any physical explanation to support the suggested flow models. In that sense, this paper is considered to be incomplete as an academic paper. Furthermore, the unfortunate thing is difficult for us to confirm these phenomena experimentally. We expect that CFD may give some correct explanation about these phenomena.

#### **References**

- [1] C.L.Britton & R.W.Caron : “ Unchoking pressure ratio for critical flow Venturis”, FEDSM97-3004, 1997.
- [2] E.von Lavante, A Zachcial, D.Zeitz, B.Nath, & H.Dietrich : “ Effects of various geometric parameters on Flow behavior in sonic nozzles”, FLOMEKO'00, 2000.
- [3] S.Nakao : “Critical Flow Venturi Nozzles: theory and problems”, (in Japanese), The Nikkan Kogyo Simbun, 2017.

# Measurement of water volume fraction in oil-water upward flow by using microwave cylindrical resonant cavity

Chao Yuan<sup>1,2</sup>, Georgios Dimitrakis<sup>2</sup>, Buddhika Hewakandamby<sup>3</sup>

<sup>1</sup>Imperial College London, *c.yuan@imperial.ac.uk*, London, United Kingdom

<sup>2,3</sup>University of Nottingham, Nottingham, United Kingdom

E-mail (corresponding author): *c.yuan@imperial.ac.uk*

---

## Abstract

A microwave resonant cavity was used for the determination of water volume fraction in oil-water upward flow, the frequency shift and changes in the quality factor of the cavity resonator were the vital parameters. During the experiments, the flow rates of silicon oil were 75, 100 and 125 L/min and the water volume fraction ranged from 0 to 20.1%. The relative error between the predicted and measured water volume fraction of oil-water upward flow ranged from -3.9% to 4.32% and -2.58% to 4.44% for the TM<sub>010</sub> and TM<sub>110</sub> modes.

---

## 1. Introduction

It is a requirement in the oil and gas industry to minimize the water content in crude oil as it is associated with corrosion issues in downstream processing units as well as costs of transportation. It in fact is a part of the quality defining parameter of the crude. For this reason, a reasonably accurate measurement of water in crude oil is required. In addition, monitoring water cut at various points during the processing facility may optimize the separation efficiency in oil production operations [1]. Crude oil usually contains oil, gas and water components, and it is difficult to timely and accurately measure the fraction of each component in flow.

Microwaves are electromagnetic waves having a wavelength in the approximate range from 1mm to 1 m and occupy the region between infrared and radio frequency wavelengths [2]. Microwave sensors are used for a wide range of applications (1) measurement of distance, (2) movement, shape, and (3) particle size, but the largest group of applications are related to measurement of material properties [3]. The major advantage offered by microwave sensors is the capability to characterise materials non-destructively, in a contactless manner, without posing any health hazard to the personnel.

Microwave measurement techniques are low power applications of microwave energy. The complex effective permittivity of crude oil, which is closely related to the water volume fraction, can be measured using microwave techniques and relies in the great difference of dielectric properties between water and oil.

Therefore, the effect that water volume fraction has on the microwave characteristics of crude oil can be established through complex permittivity measurements [4]. Yang [5] described an oscillator load-pull to accurately determine the water-cut of an oil-water emulsion and discussed the necessary microwave oscillator source and control electronics. Avila [6] determined water fraction measurement by the frequency shift of the first resonant peak in a non-intrusive way based on a radio frequency resonant cavity sensor. Oon [7] utilised the resonant frequencies that occurred in a cylindrical cavity and monitored the changes in the permittivity of the measured phases to differentiate between the volume fractions of air, water and oil. Ashton [8] developed a prototype non-intrusive microwave multiphase flow meter for measurement of oil, water and gas flow rates on production pipelines. Hogan [9] developed a real-time, non-intrusive multiphase dielectric meter capable of measuring the dielectric properties of different mixtures of oil, gas and water in full well stream flow. Wylie [4] developed an electromagnetic cavity resonator-based sensor, which was non-intrusive and transmitted low power (10 mW) radio frequencies in the range of 100-350 MHz, to detect the pipeline contents using resonant peaks captured instantaneously. Although these studies, including static and dynamic experiments, have proved that water-cut measurements using microwave techniques are possible, they have not provided any quantitative correlation that could be actually used for the water-cut determination of upward oil-water flow. The present study focused on the upward oil-water flow and a cylindrical resonant cavity operating at frequencies between 100 MHz and 2 GHz

was proposed to measure the water volume fraction in upward oil-water flow and helped derive a semi-empirical correlation that could be utilised in the fast and accurate determination of water-cut in oil water mixtures.

## 2. Laboratory Setup

### 2.1 Resonant cavity and vector network analyzer

During a microwave resonance there is a balance between the energy stored and the energy dissipated in the resonator. Microwave resonators are used in a variety of applications, including filters, oscillators, frequency meters and tuned amplifiers [10]. The microwave resonator, which is used in the present study, is a common type of cylindrical cavity resonator. Various resonant modes like TM (transverse magnetic) and TE (transverse electronic) modes can exist simultaneously in the cavity resonator and each one with its own resonant frequency. The electromagnetic field pattern that correspond to each one of these resonant frequencies is termed mode:

$$\text{TE mode: } f_{mnl} = \frac{1}{2\pi\sqrt{\mu\epsilon}} \sqrt{\left(\frac{p'_{nm}}{a}\right)^2 + \left(\frac{l\pi}{d}\right)^2} \quad (1)$$

$$\text{TM mode: } f_{mnl} = \frac{1}{2\pi\sqrt{\mu\epsilon}} \sqrt{\left(\frac{p_{nm}}{a}\right)^2 + \left(\frac{l\pi}{d}\right)^2} \quad (2)$$

Where  $l$ ,  $m$  and  $n$  are the number of variations in the standing wave pattern in the cavity directions,  $\mu$  and  $\epsilon$  are the permeability and permittivity of the material,  $a$  and  $d$  is the internal radius and height of cylindrical resonant cavity,  $p_{nm}$  is the  $m^{\text{th}}$  root of the Bessel function of  $n^{\text{th}}$  order,  $p'_{nm}$  is the  $m^{\text{th}}$  root of the derivative of Bessel function of  $n^{\text{th}}$  order.

The modes used in the present study are the  $\text{TM}_{010}$  and  $\text{TM}_{110}$  mode and the resonant frequencies of the unloaded  $\text{TM}_{010}$  and  $\text{TM}_{110}$  mode were 937MHz and 1.49 GHz respectively and correspond to the cavity dimensions.

In order to observe the relationship between insert loss and frequency, the scattering  $S_{21}$  parameters, which is the ratio of output and input power, were collected with the use of a Vector Network Analysers (VNA).  $S$  parameters are related to the reflected power and transmitted power in a microwave network as a function of frequency. The “Network” could be a coaxial cable, passive antenna, active amplifier, microwave filter, etc. The  $S$  parameters have magnitude and phase. Typically, magnitude is measured in dB and phase is measured in degrees.

The system was arranged by connecting network analyser and resonant cavity with two cables (Figure 1).



**Figure 1:** Measurement system

Figure 2 shows the resonant cavity, which is made of copper and has non-intrusive antennas. The energy of microwave was set to 20 dBm by the use of network analyser, the IF Bandwidth and averaging factor were adjusted to 100Hz and 4.



**Figure 2:** Resonant cavity

### 2.2 Liquid-liquid flow facility

Experiments were carried out on the liquid-liquid flow facility at the laboratory of the Faculty of Engineering in the University of Nottingham. Figure 3 displays the schematic diagram of this facility. It mainly consists of liquid supply systems, flowmeters, regulating valves, test sections and a separator. Silicon oil and water were supplied separately from two storage tanks, and the flow rates are then measured using electromagnetic flow meters immediately before the mixing unit. After the mixer where a fine dispersion is obtained, the oil-water mixture flows through a 2.8 m long vertical test section and a 4.5m long horizontal test section, and the inner diameter of these two test sections are 34 mm and 63 mm respectively. Resonant cavity with Plexiglas tube is placed at 1050 mm downstream of the bottom bend of the U-type tube (refer to Figure 3). A sampling valve is fitted at the lower end of the U section. Oil flow rates reported here were 75, 100 and 125 L/min, while varying the water fractions from 0% to 20.1% for each oil flow rate. After the test sections, oil-water mixture finally flowed into the separator and returned to the storage tanks for recycling use.

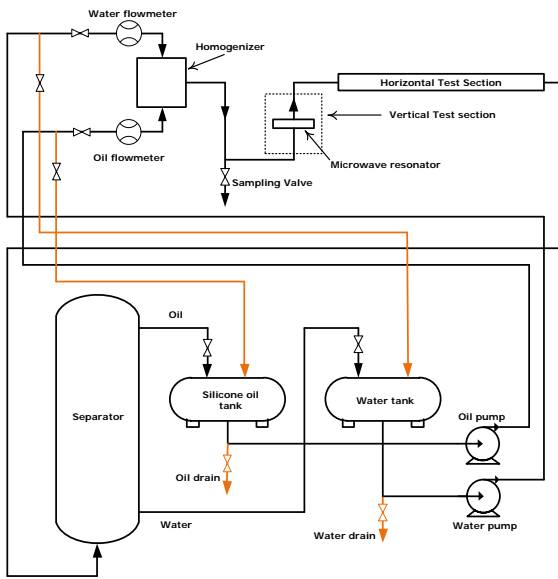
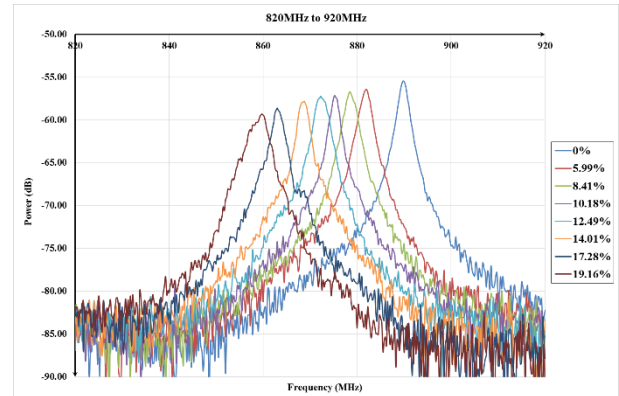


**Figure 3:** Schematic diagram of the liquid-liquid facility

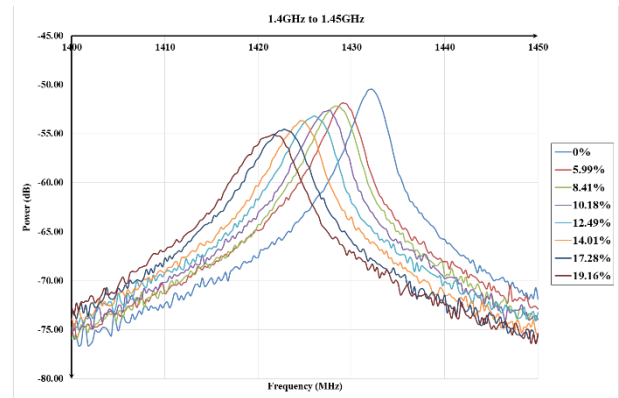
### 3. Results and discussion

In the experiments, flow rates of silicon oil and water were set at first, and then frequency and power of the peaks were collected three times after the oil and liquid flow rates stabilised. In order to acquire the actual water volume fraction of the flow in the pipe, taking a liquid sample was a necessary process when the collection of frequency and power was finished. After getting the sample, waiting for 30 minutes for the separation. And then the oil was on the top and the water was at the bottom, then majority of oil was poured into a beaker and the remaining oil-water mixture was poured into a measuring cylinder. Finally measuring the density of oil and weighing the beaker and cylinder, the volume of water and water-cut could be calculated.

Figure 4 display the resonant peaks of the cavity resonator for oil flow velocity which was 125L/min and the others flow rates showed the similar trend. According to the figures, as the increased of the water fraction, resonant frequencies continuous shift from approximately 890 MHz to 860 MHz and 1.433 GHz to 1.422 GHz. In addition, the amplitude of the resonant peaks also decreases by about 5dB with the increase of the water fraction. It means that the variation of water fraction in oil-water fraction could be described by the frequency shift and the amplitude decrease.



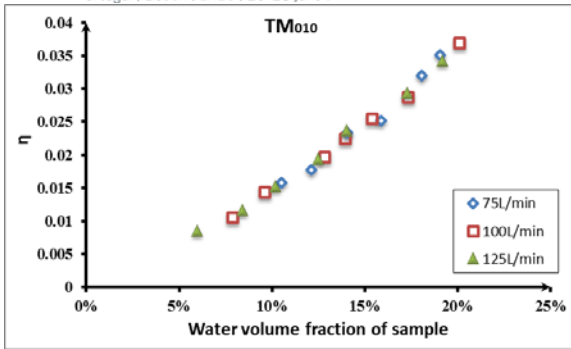
(a)  $TM_{010}$  mode,  $u_{oil}=125L/min$



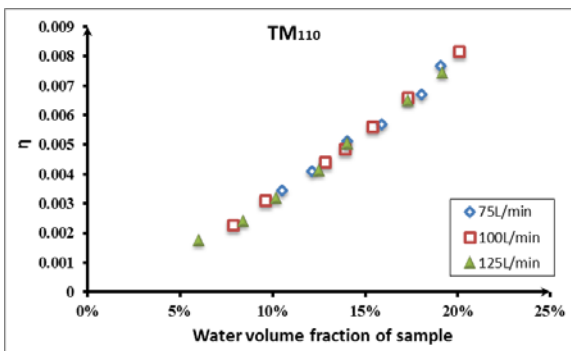
(b)  $TM_{110}$  mode,  $u_{oil}=125L/min$

**Figure 4.** Resonant peaks of the cavity resonator

In order to describe the frequency shift due to the different water-cut,  $(f-f_0)/f_0$ , termed as  $\eta$ , was introduced here to give the approximate fractional change in resonant frequency, where  $f$  and  $f_0$  were the resonant frequency of loaded and unloaded cavity respectively.  $\eta$  also was an important parameter in the simple perturbation theory of the resonant cavity to measure water cut due to the relationship between the resonant frequency and the dielectric property of the fluids. Although the system used in this study was not strictly complying with the simple perturbation theory criteria, any changes in the complex permittivity can be traced via the changes in frequency shift according to Figure 4. Figure 5 (a) and (b) show the  $\eta$  versus water volume fraction of the liquid sample and the deviations of each points. All the data points in these two figures were the average values of the three times measurement and the biggest standard deviation of each  $\eta$  was 0.0011.



(a) TM<sub>010</sub> mode



(b) TM<sub>110</sub> mode

Figure 5. Relationship between  $\eta$  and water volume fraction

Data points were overlapping in Figure 5, which indicates that although the oil and water flow rates were different, the performance of resonant cavity only depended on the water fraction of the mixture based on the former analysis. Therefore, water volume fraction,  $\theta$ , could be calculated by using resonant frequencies of different peaks and two equations (Eq. (3) and (4)) were established based on half numbers of the data points which were selected random.

$$TM_{010} : \theta = -65.805\eta^2 + 7.8178\eta - 0.002 \quad (3)$$

$$TM_{110} : \theta = -1127.6\eta^2 + 32.702\eta + 0.008 \quad (4)$$

The performance of the above equations with the other data points were displayed in Figure 6. Results showed that the relative deviations between the predicted and actual water-cut ranged from -3.9% to 4.32% and -2.58% to 4.44% for TM<sub>010</sub> and TM<sub>110</sub> mode respectively, which indicated that the resonant cavity could be applied in the prediction of oil-water upward two phase flow and the accuracy was acceptable.

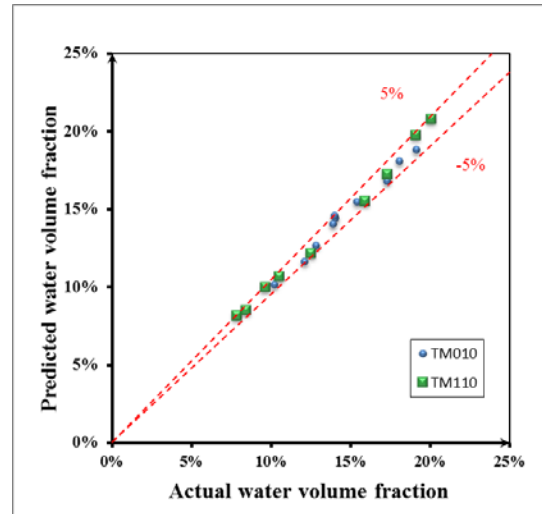


Figure 6. Performance of equation (3) and (4) in the measurement of water volume fraction

Due to the difference in the velocities of oil and water, slip may exist in the oil-water upward flow and water volume fraction measured using the microwave resonance cavity would be different from the values computed using the inlet flow rates or even from the sampling. In order to check whether the slip had affected the volume fraction measurement, water-cut from sampling and reference meters were compared as shown in Figure 7. From Figure 7 we can observe that the water-cut determined via sampling was very similar to the one determined by the reference meters which indicated that for the conditions of the experiments in the present case, there was almost no slip in the upward oil-water flow.

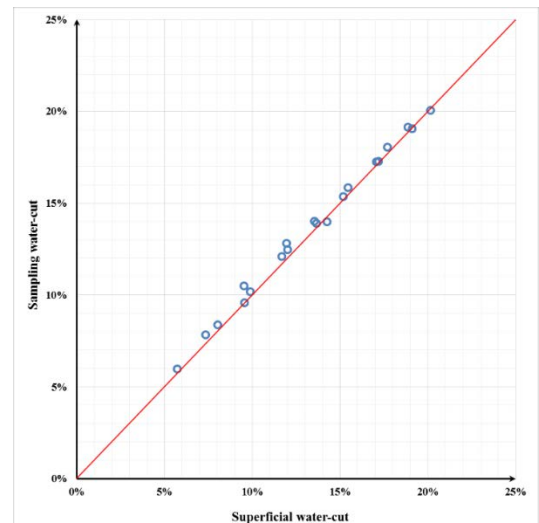


Figure 7. Sampling and superficial water cut

#### 4. Conclusion

Water volume fraction of oil-water mixture was measured by using a cylindrical resonant cavity. The results showed that the resonant frequency was sensitive

to the variation of water cut with very good repeatability. The experiments of the oil-water flow indicated that the measurement of water content in the continuous flow it was feasible and robust and was not affected by the changing flow rates. Two semi-empirical equations were established for water-cut determination corresponding to the change of two resonant modes in the resonator. The relative error between the measured and the predicted water volume fraction in oil ranged from -3.9% to 4.32% and -2.58% to 4.44% for TM<sub>010</sub> and TM<sub>110</sub> mode respectively.

### Acknowledgments

This work was financially supported by the International Postdoctoral Exchange Fellowship Program of China (No. 20160049).

### References

- [1] Mohamed, A.-M.O., M. El Gamal, and A.Y. Zekri, *Effect of salinity and temperature on water cut determination in oil reservoirs*. Journal of Petroleum Science and Engineering, 2003. **40**(3-4): p. 177-188.
- [2] Berube, M., *The American Heritage Dictionary: Second College Edition*. 1985: Houghton Mifflin.
- [3] Nyfors, E., *Industrial microwave sensors—A review*. Subsurface Sensing Technologies and Applications, 2000. **1**(1): p. 23-43.
- [4] Wylie, S.R., A. Shaw, and A.I. Al-Shamma'a, *RF sensor for multiphase flow measurement through an oil pipeline*. Measurement Science and Technology, 2006. **17**(8): p. 2141-2149.
- [5] Yang, Y., B. Scott, and B. Cregger. *The design, development, and field testing of a water-cut meter based on a microwave technique*. in *SPE Annual Technical Conference and Exhibition*. 1990. Society of Petroleum Engineers.
- [6] Ávila, H.E., D.J. Pagano, and F. Rangel de Sousa, *Water fraction measurement using a RF resonant cavity sensor*. Instrumentation viewpoint, 2013(14): p. 12-12.
- [7] Oon, C.S., et al., *Experimental study on a feasibility of using electromagnetic wave cylindrical cavity sensor to monitor the percentage of water fraction in a two phase system*. Sensors and Actuators A: Physical, 2016. **245**: p. 140-149.
- [8] Ashton, S., et al. *Development and trial of microwave techniques for measurement of multiphase flow of oil, water and gas*. in *SPE Asia Pacific Oil and Gas Conference*. 1994. Society of Petroleum Engineers.
- [9] Hogan, B., A. Al-Shamma a, and J. Lucas. *Real-time multiphase metering using non-intrusive microwave sensor*. in *BHR GROUP CONFERENCE SERIES PUBLICATION*. 2000. Bury St. Edmunds; Professional Engineering Publishing; 1998.
- [10] Pozar, D.M., *Microwave engineering*. 2009: John Wiley & Sons.

# Fuel dispensers in Slovenia - Between compliance and fairness

G. Vindišar<sup>1</sup>, D. Škrbič<sup>1</sup>, B. Simšič<sup>2</sup>

<sup>1</sup>Metrology Institute of the Republic of Slovenia, Grudnovo nabrežje 17, 1000 Ljubljana, Slovenia

<sup>2</sup>Metrology Institute of the Republic of Slovenia, Tkalska ulica 15, 3000 Celje, Slovenia

E-mail: gasper.vindisar@gov.si

## Abstract

High level of public and legal interest concerning fuel dispensers' measurements accuracy is always present. Surveillance of dispensers prior to 2013 reported undesired high error values. To limit possibilities of systematic favoring of single parties Slovenian national regulative was adapted. In year 2013 value of maximum permissible error at periodic verifications for higher flow rates of fuel dispensers was reduced.

After one verification period passed Surveillance service of Metrology Institute of the Republic of Slovenia (MIRS) performed a surveillance of fuel dispensers seeking feedback information on implementation of modified requirements.

On over 150 petrol stations over 300 nozzles serving four different fuel types were controlled at two different fuel flow rates. More than 600 evaluated control results showed among others, that the average measured error at maximum flow rate  $Q_{max}$  amounted up to + 0,23 %, depending of the fuel type. Almost all measured errors were in line with the metrological requirements, 76 % of which however appeared to be in favor of the petrol station owner. Average deliveries at  $Q_{max}$  were less favorable to an end customer than deliveries at  $Q_{min}$ .

After another verification period surveillance was performed again. Average measured errors showed further reduction. Measurements also improved their symmetry.

Compliance of measuring instruments is not hindered by adapted regulative, while level of measurement fairness is apparently elevated.

## 1. Introduction

Public and legal interest concerning fuel dispensers and their reliable measurements is always strong. Customer complaints and media responses considering doubtful fuel quantity measurements on petrol stations arise occasionally.

The Metrology Institute of the Republic of Slovenia (MIRS) is a body that performs multiple roles: it acts as a legislative advisory, verification office and well as the market surveillance authority. Fuel dispensers are not verified by MIRS itself but by three external enterprises. They are all accredited control bodies and are both authorized and surveilled by MIRS.

Thence the possibility and obligation to survey and react to the market, protect customers and enforce metrological legislative requirements.

As a legislative advisory office, in 2013 MIRS adopted national regulative [1] allowing diminished maximum permissible errors (MPE) for fuel dispensers (Table 1). The idea was to take advantage of technical capabilities of state of the art measuring instruments and limit both excess errors as well as the extent of a potential systematic favoring of a single party.

**Table 1:** Maximum permissible errors for fuel dispensers prior and after adoption of national regulation in year 2013

	Periodic verification		In-service control	
	< 2013	> 2013	< 2013	> 2013
$Q_{min}$	0,5 %	0,5 %	1,0 %	0,5 %
$Q_{max}$	0,5 %	0,3 %	1,0 %	0,5 %

Diesel road fuel demand in EU-28 members is still on the rise and is amounted to 265,3 Mt in 2017 [2]. Shifting measuring results for only 0,1 % i.e. only one fifth of MPE, would therefore represent a significant impact.

To evaluate implementation of adopted regulative after time span of one verification period MIRS surveillance authority performed targeted surveillance on more than 150 petrol stations across Slovenia.

After another verification period passed surveillance was repeated and the impact of the adapted national regulative was validated.

## 2. Test method

Surveillances were performed by trained MIRS officers following standard surveillance procedure derived from the accredited verification method.

### 2.1 Standards

According to the fuel flow rate  $Q$  of a single control appropriate standard volumes were used. Either 10 l, 50 l or 200 l standards (Figure 1) were used. Standards are regularly calibrated with a reference temperature of 15 °C.



Figure 1: Used measurement standards (10 l and 50 l)

### 2.2 Temperature impact

Albeit annual mean air temperatures in Slovenia (Figure 2) are in general below reference temperature of 15 °C and one party may potentially be favored it is not required in Slovenia for fuel dispensers to deliver fuel quantities compensated to a reference temperature.

Test measurements are instant and no correction of a measured error due to a difference of a fuel temperature in a fuel dispenser and in a standard is done. Same goes for a correction of an error due to a temperature difference between standard reference temperature and fuel temperature.

Both corrections are transposed into measurement uncertainty. Together with other uncertainty FLOMEKO 2019, Lisbon, Portugal

contributions the expanded uncertainty of a measurement with a coverage factor  $k = 2$  is estimated to not exceed  $U = 0,1 \%$ .

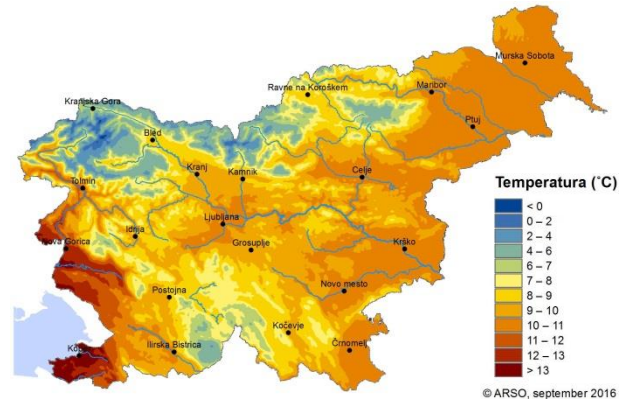


Figure 2: Annual mean air temperature in years 1981-2010 in Slovenia [3]

Measurement error is therefore calculated by Equation (1):

$$Err = \frac{V_d - V_s}{V_s} \times 100 [\%] \quad (1)$$

$V_d$  [l] ... Volume measured by fuel dispenser  
 $V_s$  [l] ... Volume measured by volume standard

## 3. First round of surveillance (2016)

Surveillance of fuel dispensers prior to 2013 detected certain measured errors to be up to 0,7 % or even 0,8 % in favor to fuel distributor. Although measured errors were in general in line with valid MPE (Table 1), MIRS believed customers could be protected even more.

An adapted national regulative with reduced MPE came into force in 2013 and systematic surveillance was done in 2016, i.e. after one verification period time passed. 325 fuel dispenser nozzles located on over 150 fuel stations across Slovenia were surveilled. Fuel dispensers were of eight different producers and delivered four different fuel types. Population of dispensers delivering Diesel and Gasoline 95 was big enough to allow discussion. Due to too small statistical relevance results gained on dispensers delivering Gasoline 100 and Heating Oil are not presented.

### 3.1 Results of 1<sup>st</sup> round of surveillance (2016)

Figure 3 presents measured errors of all, i.e. 105, tested fuel dispensers delivering Diesel fuel. Axis X presents consecutive count of a tested nozzle as

rearranged for a presentation and axis Y measured errors.

Graph lines present errors measured while testing dispensers at minimum and maximum flow rate:  $Err(Q_{min})$  – red colored and  $Err(Q_{max})$  – green colored, bold line. Calculated average measured errors  $Avg Err(Q_{min})$  and  $Avg Err(Q_{max})$  are presented by two dashed lines of corresponding colors and line styles. MPE values for in-service control are noted by full black straight lines.

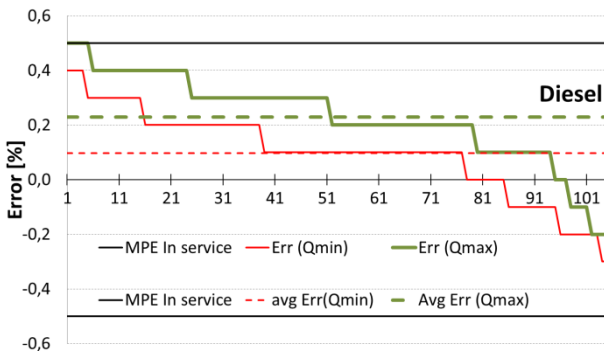


Figure 3: Errors of diesel fuel dispensers,  $n = 105$  (2016)

All measured errors complied with MPE requirements for in-service control. Average calculated errors for Diesel nozzles are  $+0,10\%$  for measurements, proceeded at  $Q_{min}$  and  $+0,23\%$  for measurements, done at  $Q_{max}$ .

Values of calculated average errors belonging to nozzles delivering both considered types of fuel and for both fuel flow rates are given in Table 2.

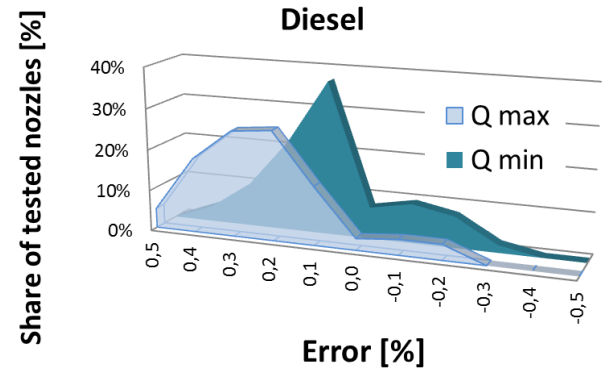
Table 2: Average measured errors of 1<sup>st</sup> surveillance round (2016)

Fuel	No. of tests	Avg Err ( $Q_{min}$ )	Avg Err ( $Q_{max}$ )
Diesel	105	$+0,10\%$	$+0,23\%$
95	103	$+0,10\%$	$+0,15\%$

If average errors measured at  $Q_{min}$  are in a range of expanded measurement uncertainty, average errors measured at  $Q_{max}$ , at which flow rate most of deliveries are done, reach up to half the value of MPE for in-service control. All average errors, however, are compliant. Single measurements exceeding relevant MPE are very rare and sporadic.

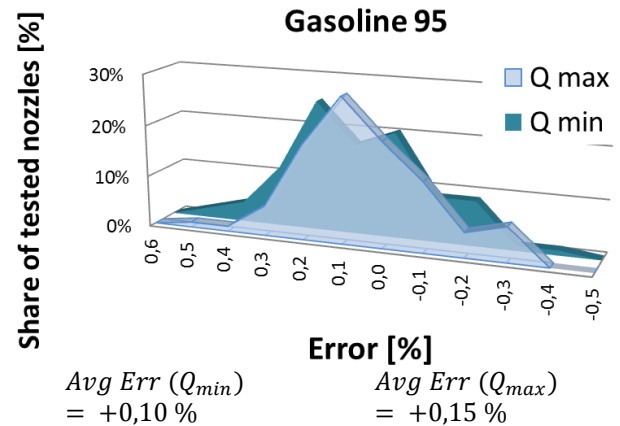
More descriptive perspective on gained results is achieved by presenting a density distribution of share of tested nozzles with a certain value of measured error. Distributions are presented separately for two test fuel rates  $Q_{min}$  and  $Q_{max}$  and for both fuel types (Figure 4 and Figure 5). On

figures also values of relevant average measured errors are stated.



$$Avg Err(Q_{min}) = +0,10\% \quad Avg Err(Q_{max}) = +0,23\%$$

Figure 4: Share of tested nozzles with a certain error for both flow rates – Diesel (2016)



$$Avg Err(Q_{min}) = +0,10\% \quad Avg Err(Q_{max}) = +0,15\%$$

Figure 5: Share of tested nozzles with a certain error for both flow rates – Gasoline 95 (2016)

A fact that all density distributions of shares of tested nozzles with a certain error values are highly or yet barely moderately skewed (Table 3) and besides that have a same sign, deserved further attention.

Table 3: Skewness coefficient of 1<sup>st</sup> surveillance round

Fuel	skewness coeff. $Q_{min}$	skewness coeff. $Q_{max}$
Diesel	0,905	1,796
95	1,014	0,840

#### 4. Second round of surveillance (2019)

After another verification period passed, effect of adapted MPE value was validated in 2018 and 2019. Only Diesel and Gasoline 95 delivering nozzles were surveilled. Sample size was approximately three quarters of the 1<sup>st</sup> round sample size.

Density distributions of the share of tested Diesel and Gasoline 95 nozzles with a certain value of measured error are for both flow rates presented on Figure 6 and Figure 7. Values of relevant average measured errors are also stated.

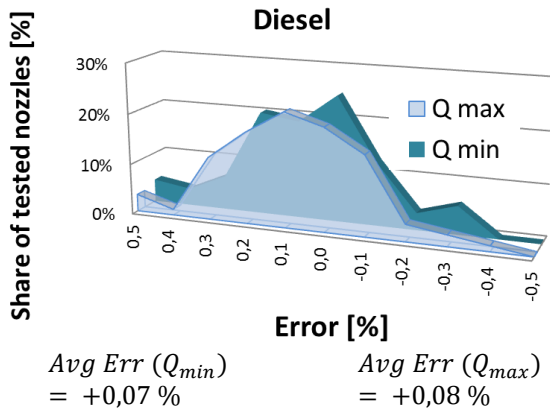


**Figure 6:** Share of tested nozzles with a certain error for both flow rates – Diesel (2019)

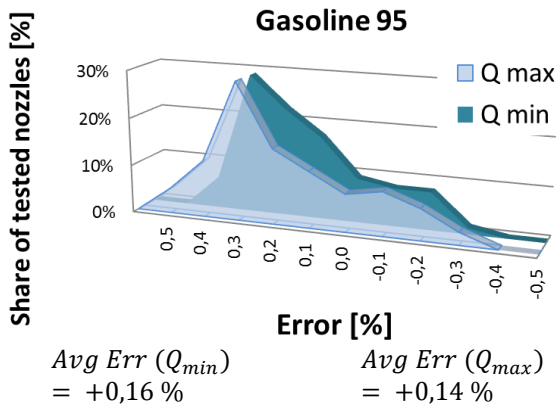


**Figure 7:** Share of tested nozzles with a certain error for both flow rates – Gasoline 95 (2019)

Meanwhile implementation of new measures continued to be supported by intense promotion and continuous trainings of verification bodies and instrument owners.

#### 4.1 Comparison of results of 1<sup>st</sup> and 2<sup>nd</sup> round of surveillance

The compared average measured errors values at  $Q_{max}$  of the 2<sup>nd</sup> surveillance round were except in one case lower as the average measured errors of the 1<sup>st</sup> surveillance round (Table 4).

The skewness coefficient values show that the 2<sup>nd</sup> surveillance round density distributions of shares of tested nozzles with a certain error values are significantly less skewed in case of Diesel (Table

5). In case of Gasoline 95 nozzles skewness factors are enlarged. However, the absolute values of reduction of skewness factors at Diesel nozzles are approximately four times bigger than the absolute values of enlargements at Gasoline 95 nozzles.

**Table 4:** Compared average measured errors of 1<sup>st</sup> and 2<sup>nd</sup> surveillance round

Fuel	No. of tests	Surveillance round	Avg Err ( $Q_{min}$ )	Avg Err ( $Q_{max}$ )
Diesel	105	1 <sup>st</sup>	+ 0,10 %	+ 0,23 %
	89	2 <sup>nd</sup>	+ 0,07 %	+ 0,08 %
95	103	1 <sup>st</sup>	+ 0,10 %	+ 0,15 %
	76	2 <sup>nd</sup>	+ 0,16 %	+ 0,14 %

**Table 5:** Compared skewness coefficient of 1<sup>st</sup> and 2<sup>nd</sup> surveillance round

Fuel	Surveillance round	skewness ( $Q_{min}$ )	skewness ( $Q_{max}$ )
Diesel	1 <sup>st</sup>	1,796	0,905
	2 <sup>nd</sup>	0,794	0,434
95	1 <sup>st</sup>	0,840	1,014
	2 <sup>nd</sup>	1,000	1,368

Effectiveness of the adapted regulative in terms of improved trust and expectations of final customers was confirmed by in generally lowered average measured errors. Improved or at least maintained skewness classes of density distributions of measured errors offered further support to such findings.

To achieve these results, set goals were strictly followed and verification procedures performed with enhanced attention. Fuel dispensers' technical capability proved that enforcement of strictly set metrology rules is feasible.

## 5. Compiled results compared

Compiling all measured results gained on fuel dispensers for both considered fuel types with the only criteria of fuel flow rate ( $Q_{min}$  or  $Q_{max}$ ) contributed to enlarged sample size and enhanced reliability of result comparison. 208 measurement results of the 1<sup>st</sup> round were compared to 165 results of the 2<sup>nd</sup> round of surveillance.

Calculated average measured errors of all results for a single flow rate in a single surveillance round along with skewness coefficients of corresponding density distributions are presented in Table 6.

**Table 6:** Compared average errors and skewness coefficients of compiled results for both surveillance rounds (1<sup>st</sup> and 2<sup>nd</sup>)

	Average error [%]		Skewness coefficient	
	2016	2019	2016	2019
$Q_{max}$	0,19	0,11	0,938	0,338
$Q_{min}$	0,10	0,11	1,000	0,093

Density distributions of share of tested nozzles with a certain value of measured error are presented separately for two test fuel rates  $Q_{min}$  and  $Q_{max}$  and for both surveillance rounds on Figure 8 and Figure 9. Values of relevant average measured errors are also stated.

Values confirm visual observations of Figure 8 and Figure 9. Average measured error is significantly diminished for in praxis mostly operated flow rate  $Q_{max}$ . Besides that, values of average errors for both flow rates are already in a vicinity of expanded measurement uncertainty value of used method.

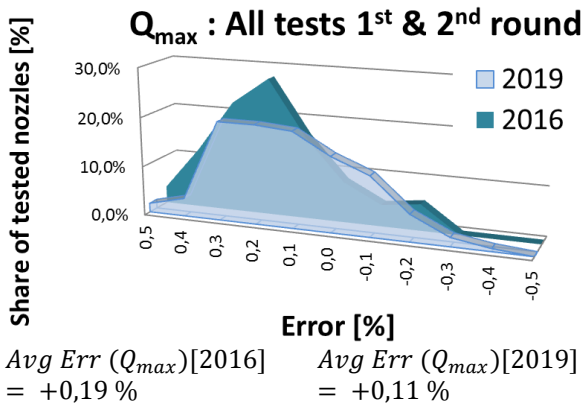


**Figure 8:** Share of tested nozzles with a certain error ( $Q_{max}$ ) - summary of results of both fuels and both surveillance rounds

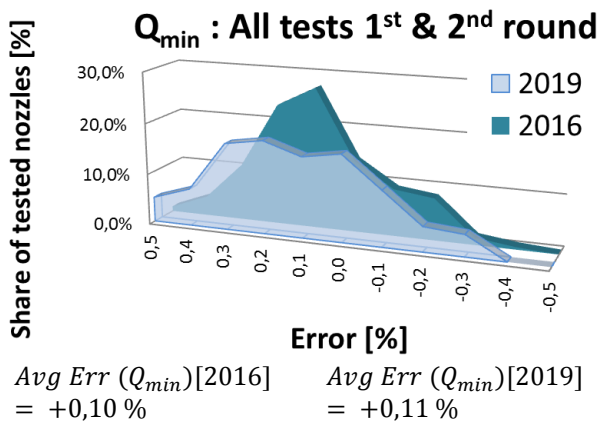


**Figure 9:** Share of tested nozzles with a certain error ( $Q_{min}$ ) - summary of results of both fuels and both surveillance rounds

Different skewness coefficient values reflect well improved symmetry of measured results.

Both findings confirm eligibility of metrology rules modification. Owners of fuel dispensers are capable of ensuring compliance of their measuring

instruments and customers can expect results with decreased deviations.

## 6. Conclusion

In 2013 reduced values of MPE for fuel dispensers in use and in service were introduced in Slovenia's national regulative. Change pursued the idea of MID annex VII Art. 2.8 [4] trying to prevent favoring any party and systematic exploitation of allowed MPE. MIRS believed state of the art measuring instruments are capable of fulfilling such requirements.

Thorough and successful implementation of new MPE values was supported by intense promotion, continuous trainings and regular surveillance.

A resume of over 1000 measurement results accomplished in two consecutive rounds of surveillance of fuel dispensers reports significantly lower average measured errors and enhanced symmetry of results. High levels of technical capability of measuring instruments were confirmed. Along with competent skills of verification officers the fulfilment of stricter metrology requirements was enabled. Expectation of a significant step towards enhanced equity of measurements bringing a satisfaction to all parties was therefore justified.

To confirm present results, MIRS will continue with the surveillance of fuel dispensers increasing their population number. Surveillance results can be enriched by added criteria like a micro location of a fuel dispenser on a petrol station, year of production of a fuel dispenser, type and producer of measuring instrument, temperature conditions, etc.

Current observations are satisfactory and encouraging enough to aim for maintaining stable values of average measured errors. Even further shifts of those values as well as enhanced symmetry of measured results may be anticipated.

Compliance of measuring results shall therefore be guaranteed while their fairness improved.

## References

- [1] Pravilnik o merilnih instrumentih (Uradni list RS, št. 19/16, 22.3.2013) [*Rules on measuring instruments, No 19/16, Official Journal of the Republic of Slovenia, 22.3.2013*]



18<sup>th</sup> International Flow Measurement Conference

Portugal | Lisbon | LNEC | 26-28 June 2019

- [2] European petroleum refineries association AISBL, Statistical report 2018, <https://www.fuelseurope.eu/wp-content/uploads/FuelsEurope-Statistical-Report-2018.pdf>
- [3] ARSO, [http://meteo.arso.gov.si/uploads/probase/www/climate/image/sl/by\\_variable/temperature/annual-mean-air-temperature\\_81-10.png](http://meteo.arso.gov.si/uploads/probase/www/climate/image/sl/by_variable/temperature/annual-mean-air-temperature_81-10.png)
- [4] DIRECTIVE 2014/32/EU OF THE EUROPEAN PARLIAMENT AND OF THE COUNCIL of 26 February 2014 on the harmonisation of the laws of the Member States relating to the making available on the market of measuring instruments (recast); Official Journal of the European Union 29.3.2014

# Effects of step in CFVN on Premature Unchoking Phenomena

N. Takegawa, M. Ishibashi and T. Morioka

National Metrology Institute of Japan, 305-8563, 1-1-1, Umezono, Tsukuba, Ibaraki, Japan  
E-mail: takegawa-naoki@aist.go.jp

## Abstract

CFVNs (Critical Flow Venturi Nozzles) are widely used as transfer standards and can realize the accurate measurement of the flow rate. However, previous research has reported that the pressure recovery effect of the diffuser decreases significantly in some CFVNs, and it has been called PUP (Premature Unchoking Phenomenon). In this study, we conducted experiments and investigated the CBPR (Critical Back Pressure Ratio) of the CFVNs. Additionally, in order to solve the PUP, we focused on the step in the diffuser and verified the its effect. As a result, although a backward facing step (causing increase of diameter) at the throat is effective for improving the CBPR at the Reynolds number of about 44000, it does not provide the improvement when the Reynolds number decreases to 11000. A forward facing step (causing decrease of diameter) in the diffuser delivers the desired pressure recovery even in the low Reynolds number of about 5000, and the CBPR can be improved. Therefore, the forward facing step in the diffuser is suggested to be a new countermeasure against the PUP in the low Reynolds number.

## 1. Introduction

Gas flow measurement is one of the most important industrial measurements, and CFVNs (Critical Flow Venturi Nozzles) are widely used as transfer standards. When the back pressure ratio (downstream pressure / upstream pressure) is lower than CBPR (Critical Back Pressure Ratio), flow velocity at the throat reaches the speed of sound, and the flow condition becomes stable. Therefore, the CFVNs can realize the accurate measurement of the flow rate. However, in the CFVNs, there is an essential problem where low back pressure ratio is required to produce choked flow. Assuming ideal gas and isentropic flow, the CBPR of the CFVNs without diffuser is about 0.528. In the subsonic flow after the transition occurred from the supersonic flow, the flow velocity decreases with the expansion of the flow path. Therefore, the diffuser plays a role as a pressure recovery system, and the its presence enable the CFVNs to choke at high back pressure ratio. However, previous research has reported that the pressure recovery effect of the diffuser decreases significantly in some CFVNs, and it is called Unchoking Phenomenon, the PUP (Premature Unchoking Phenomenon) or DPI (Diffuser Performance Inversion) [1] [2] [3] [4] [5]. In this study, we use the term “PUP”. The discharge coefficient usually shows a constant value up to a certain back pressure ratio and then decreases. When the PUP occurs, a decrease and a recover of the discharge coefficient are observed in a certain pressure ratio range (**Figure 1**). Many studies

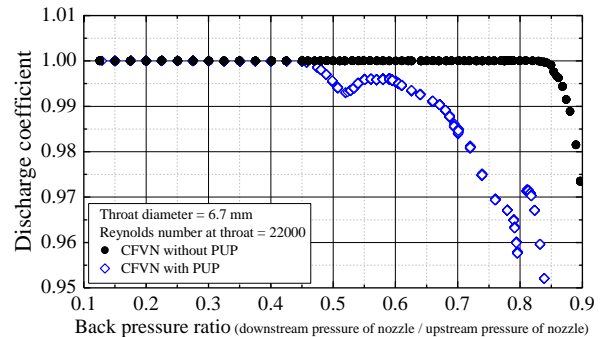


**Figure 1:** An example of PUP.

have been conducted on the relationship between the diffuser shape (length and angle) and the PUP. Cater et al. [5] [6] conducted experiments to verify the CBPR of the various CFVNs, and stated that a diffuser which was 10 times or more longer than the throat diameter was effective to suppress the PUP ( $R_e > 14000$ ). Park et al. [7] concluded from the experimental results that the effect of the diffuser angle on the CBPR was small when it was in the range of  $2^\circ$  to  $6^\circ$ . Conversely, Asano et al. [8] claimed that the diffuser angle was optimal at around  $3.5^\circ$ , and their conclusions are conflicting. This may be attributed to different Reynolds numbers in the experiment. ISO 9300 [9] provides the relationship between the ratio of the diffuser exit area  $A_{ex}$  to the throat area  $A_{th}$  and the CBPR, assuming isentropic flow. However, the

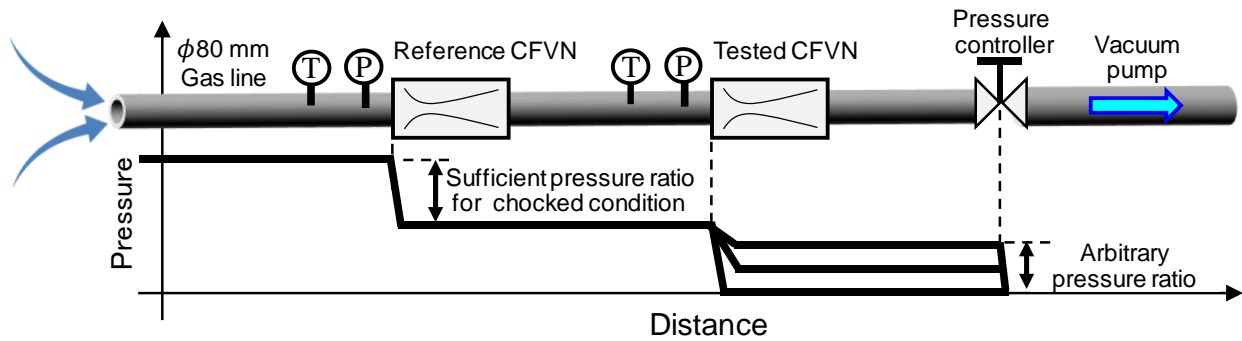


Figure 2: Schematic diagram of experiment.

relationship is applicable to Reynolds numbers greater than  $2.0 \times 10^5$ , and under low Reynolds number conditions, it is recommended in ISO 9300 [9] that the users maintain back pressure ratio of 0.25 or less. As seen in these studies, the PUP is a complex phenomenon, and the CBPR is different depending on Reynolds number and diffuser shape (length, angle, diffuser exit area). Especially in the low Reynolds number region, the discharge coefficient is strongly influenced by the PUP, and rational criteria for the CFVNs have not been established.

Since it is extremely difficult to uniquely determine the effective diffuser length and angle to suppress the PUP, a different approach in which a step is provided immediately after the throat has been proposed. von Lavante et al. [10] [11] indicated from experiments and numerical analyses that pressure fluctuation due to the oscillating shock in the diffuser led to unchoked condition, and by providing a backward facing step (causing increase of diameter) immediately after the throat, time variation of mass flow was suppressed. Cater et al. [6] verified the CBPR of the CFVNs with throat diameter  $d$  of 1.6 mm and diffuser length of  $5.3d$ , and indicated that the CBPR was greatly increased by the backward facing step after the throat when Reynolds number was about  $2.0 \times 10^5$ . Therefore, although providing a step in the diffuser seems to be effective to suppress the PUP, the detailed verification of the Step Location and step size has not been conducted. In this study, we investigate the effect of the Step Location and step height on the CBPR. Especially, we report in detail the experimental results of a forward facing step (causing decrease of diameter) in the diffuser that is effective against the PUP.

## 2. Experimental setup

Figure 2 and Figure 3 shows a schematic diagram of the experiment and measurement locations of the temperature and pressure respectively. On the upstream side of the test line, a reference CFVN whose discharge coefficient is known, and on the downstream side, a

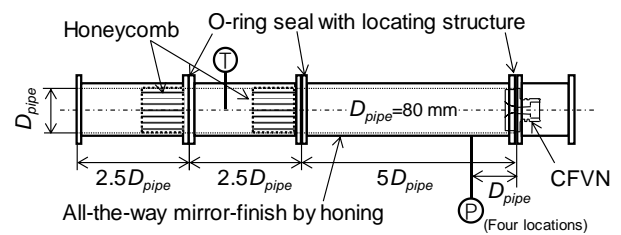


Figure 3: Measurement locations of temperature and pressure

tested CFVN are installed in series. Since the mass flow rate is constant in the test line, when the flow is steady, Equation (1) is derived as follows.

$$C_{d\_REF} Q_{theo\_REF} = C_{d\_DUT} Q_{theo\_DUT} \quad (1)$$

where  $C_d$  is the discharge coefficient and  $Q_{theo}$  is the theoretical mass flow rate. The theoretical mass flow rate was derived by the same method as Ishibashi [12]. Additionally, the subscripts REF and DUT represent the values of the reference CFVN and tested CFVN respectively. During the experiment, a flow is generated in the test line by vacuum pumps, and  $C_{d\_DUT}$  is calculated from Equation (1). The discharge coefficient shows a constant value if it is less than the CBPR. The back pressure ratio of the tested CFVN is changed by the pressure controller, and the back pressure ratio where the discharge coefficient decreases by 0.2% is defined as the CBPR.

In this study, as the CFVNs for the countermeasure against the PUP, a step is provided immediately at the throat, at the end of the toroid and in the diffuser, and their locations are called Step Location A, Step Location B and Step Location C (Figure 4). The CFVNs with steps are not a one piece, and the diffusers are attached to each CFVN. Table 1 shows the experimental cases. Large and small backward facing steps are provided at Step Location A (at the throat) for Case 3 to 6 and Step Location B (at the end of toroid) for Case 7 to 10. For Case 15 and 16, a forward facing step is provided at Step Location C (in the diffuser).

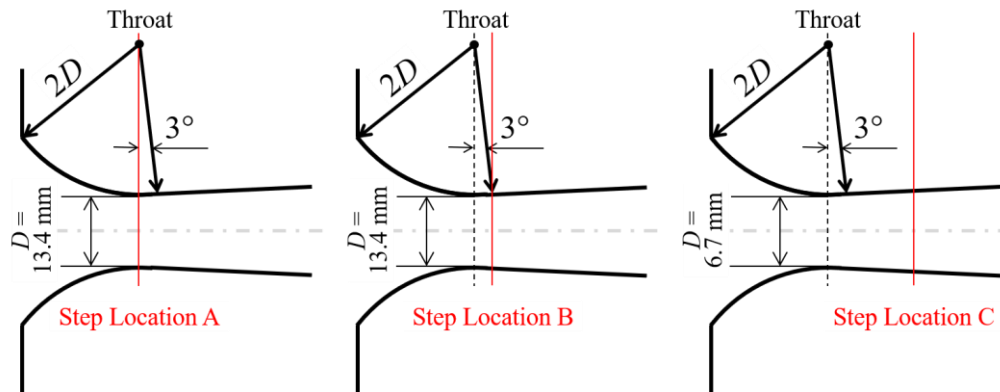


**Figure 4:** Outline of step location (Step Location A: at the throat, Step Location B: at the end of toroid and Step Location C: in the diffuser).

**Table 1:** Experimental Case.

Case	Throat Diameter $d$	Reynolds Number at throat $Re$	Diffuser Angle $\theta$	Ratio of Diffuser Length to Throat Diameter $L/d$	Ratio of Diffuser Exit Area to Throat Area $A_e/A_{th}$	Step Location	Diameter change ratio before and after step $(d_{as}/d_{bs}-1.0)*100$
1	13.4 mm	44000	3.0	2.3	1.6	Step Location A (Step at the throat)	1.1
2		11000					
3		44000					
4		11000					
5		44000					
6		11000		2.4		Step Location B (Step at end of toroid)	0.6
7		44000					
8		11000					
9		44000					
10		11000					
11	6.7 mm	22000	3.0	2.4	1.6	Step Location C (Step in diffuser)	-8.5
12		5500					
13		22000		8.7			
14		5500					
15		22000		10.5			
16		5500					

### 3. Experimental results and discussion

#### 3.1 Step at the throat and at the end of toroid (Step Location A and Step Location B)

**Figure 5** shows the relationship between the back pressure ratio and the discharge coefficient for Case 1 to Case 10. Two types of large and small backward facing step (causing increase of diameter) are provided at Step Location A for Case 3 to 6 and Step Location B for Case 7 to 10. Additionally, in **Figure 5 (a)** (Case 1, 3, 5, 7 and 9), the Reynolds number at the throat is about 44000, and in **Figure 5 (b)** (Case 2, 4, 6, 8 and 10), it is about 11000.

In **Figure 5 (a)**, where the Reynolds number at the throat is about 44000, the CBPR of the CFVNs with steps (Case FLOMEKO 2019, Lisbon, Portugal

3, 5, 7 and 9) is higher than that without a step (Case 1). This tendency is the same as previous studies [6] [13], and Wright et al. [13] discussed the improvement of the CBPR by the step at the throat from the following perspectives. A step 1) reduces the boundary layer thickness, 2) trips boundary layer from laminar to turbulent and 3) anchors a Prandtl-Meyer expansion fan and forces normal shocks further downstream, away from the throat. Comparing the CFVNs with a step, for Case 3 and 7 (small step height), the discharge coefficient decreases and recovers about 0.3% to 0.4% when the back pressure ratio is in the range of 0.6 to 0.65. Conversely, for Case 5 and 9 (large step height) the discharge coefficient is constant until the back pressure ratio reaches 0.75. Therefore, when the Reynolds number

of is about 44000, step height is an important parameter for the CBPR. There is no significant difference in the CBPR depending on the step position (at the throat or at the end of the toroid).

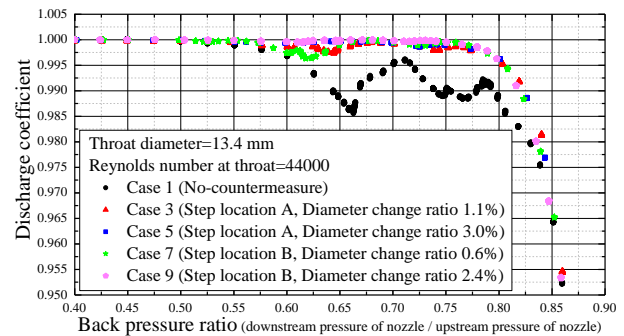
In **Figure 5 (b)**, where the Reynolds number at the throat is about 11000, the CBPR of the CFVNs with steps (Case 4, 6, 8 and 10) is equal to or less than that without a step (Case 2). This means that Although the steps at the throat or at the end of the toroid is effective for improving the CBPR at the Reynolds number of about 44000, it does not provide the improvement when the Reynolds number decreases to 11000. The behavior of the discharge coefficient to the back pressure ratio is similar in Case 4 and Case 6 (also, Case 8 and Case 10). In other words, when the Reynolds number is about 11000, the CBPR varies depending on the step position. This is different from the experimental results when the Reynolds number is about 44000. From the above results, the effect of the step at the throat or the step at the end of the toroid is largely dependent on the Reynolds number, and it is extremely important to verify whether the countermeasures are effective even in the low Reynolds numbers.

### 3.2 Step in the diffuser (Step Location C)

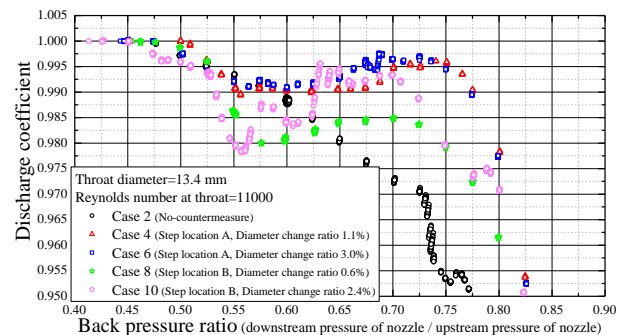
#### 3.2.1 CBPR of a CFVN with the step in the diffuser

**Figure 6** shows the relationship between the back pressure ratio and the discharge coefficient for Case 11 to Case 16. For Case 15 and 16, a forward facing step (causing decrease of diameter) is provided at Step Location C. When Reynolds number at the throat is about 22000, the CBPR for Case 11, Case 13 and Case 15 are about 0.48, 0.83, and 0.85, respectively. In Case 11 where the diffuser length is short, the CBPR is lower than in Case 13 and Case 15, and the short diffuser is not effective on pressure recovery. There is no significant difference in the behavior of the discharge coefficient to the back pressure ratio between Case 13 and Case 15.

When Reynolds number at the throat is about 5500, the CBPR for Case 12, Case 14 and Case 16 are about 0.60, 0.46, and 0.75, respectively. In Case 14, the CBPR is lower than in Case 12, and strong influence of the PUP can be seen. Cater et al. [5] [6] stated that at Reynolds numbers of 14,000 or more, the CFVNs with the long diffuser longer was effective for the PUP. Although this tendency is also confirmed in this experiment (Case 13), the effect of the long diffuser is small at low Reynolds numbers (Case 14). As described above, the PUP due to the interaction of shocks in the diffuser with the boundary layer is a very complicated phenomenon, and it is extremely difficult to derive a general rule from the experimental results. In Case 16, the CBPR is significantly increased compared to Case 14 having approximately the same diffuser length. From these results, it is clarified that a forward facing step in the



(a) Case 1, Case 3, Case 5, Case 7 and Case 9.



(b) Case 2, Case 4, Case 6, Case 8 and Case 10.

**Figure 5:** Relationship between back pressure ratio and discharge coefficient for Case 1~Case 10.

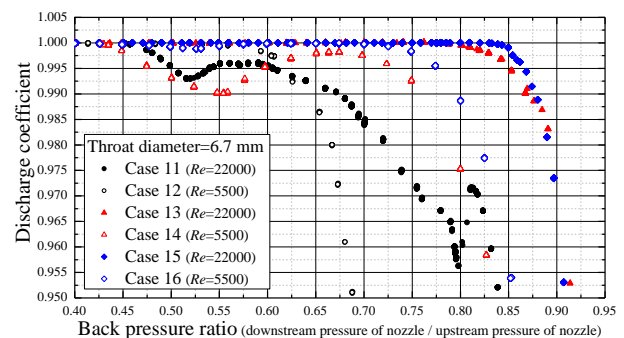


**Figure 6:** Relationship between back pressure ratio and discharge coefficient for Case 11~Case 16.

diffuser delivers the desired pressure recovery even in the low Reynolds number of about 5000, and the CBPR can be improved. The above-mentioned methods of “using the long diffuser” and “providing a step at the throat or at the end of toroid” have small effects in the low Reynolds numbers. Therefore, the forward facing step in the diffuser is suggested to be a new countermeasure for the PUP in the low Reynolds number, and it is very useful finding in establishing rational and practical design guidelines for the CFVNs.

### 3.2.2 Pressure recovery effect and pressure distribution in the diffuser

Assuming isentropic flow, the relationship between the cross sectional area of the diffuser  $A$  and the pressure  $P$  is expressed by **Equation (2)**.

$$\frac{A}{A_{th}} = \frac{\sqrt{\frac{\gamma-1}{2\left\{\left(\frac{P_0}{P}\right)^{1-\frac{1}{\gamma}}-1\right\}}}}{\left\{\frac{2\left(\frac{P_0}{P}\right)^{1-\frac{1}{\gamma}}}{\gamma+1}\right\}^{\frac{\gamma+1}{2(\gamma-1)}}} \quad (2)$$

where  $P_0$  is the stagnation pressure and  $\gamma$  is specific heat ratio. The degree of pressure recovery is determined by the diffuser exit area from **Equation (2)**. Even in ISO 9300 [5], based on isentropic flow, the CBPR is estimated from the relationship between the ratio of the diffuser exit area of  $A_{ex}$  to the throat area  $A_{th}$ . However, the flow after the throat is supersonic, and a phenomenon with an increase in entropy due to shocks occurs in the diffuser.

Additionally, the shocks in the diffuser are also one of the causes of flow separation, and, therefore, the actual diffuser does not provide the expected pressure recovery. In order to estimate the CBPR, it is necessary to consider not only the diffuser shape but also the shocks in diffuser. The pressure ratio before and after the normal shock is expressed as follows from Rankine-Hugoniot equation. Using **Equation (3)** and the relationship between the cross-sectional area  $A$  and the Mach number  $M$  shown in **Equation (4)**, it is possible to calculate the downstream pressure of the normal shock generated at any position in the diffuser. **Figure 7** shows the relationship between the cross-sectional area  $A$  and the pressure  $P$  (**Equation (2)**) and the downstream pressure after the normal shock.

$$\frac{P_{as}}{P_0} = \frac{2\gamma M^2 - \gamma + 1}{\gamma + 1} \left(1 + \frac{\gamma - 1}{2} M^2\right)^{\frac{\gamma}{\gamma - 1}} \quad (3)$$

$$\frac{A}{A_{th}} = \frac{1}{M} \left\{ \frac{(\gamma - 1)M^2 + 2}{\gamma + 1} \right\}^{\frac{\gamma + 1}{2(\gamma - 1)}} \quad (4)$$

where  $P_{as}$  is the downstream pressure of the shock. It is confirmed from **Figure 7** that the downstream pressure of the shock does not coincide with the pressure assuming transonic and isentropic flows. Assuming that, the pressure is recovered isentropically at the downstream of the normal shock, by determining the throat area, the diffuser exit area and the downstream pressure of CFVNs, it is possible to theoretically calculate the shock location and the amount of pressure recovery. **Figure 8** shows a value by subtracting the pressure in the supersonic flow from the downstream pressure after the normal shock. The value is derived assuming the diffuser angle of  $3^\circ$ , and the horizontal axis is the ratio of the throat diameter to the distance from the throat. From **Figure 8**, the amount of pressure recovery is different depending on the shock location. The amount

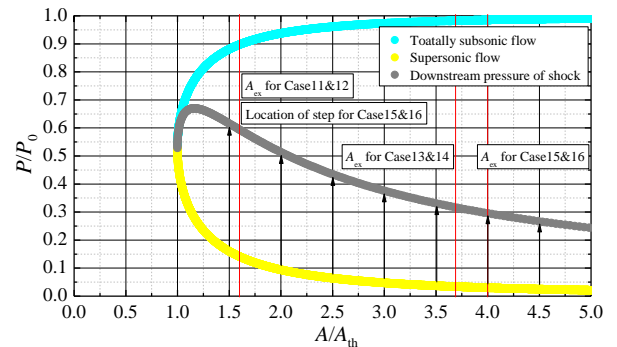


**Figure 7:** Relationship between cross-sectional area of diffuser and pressure.

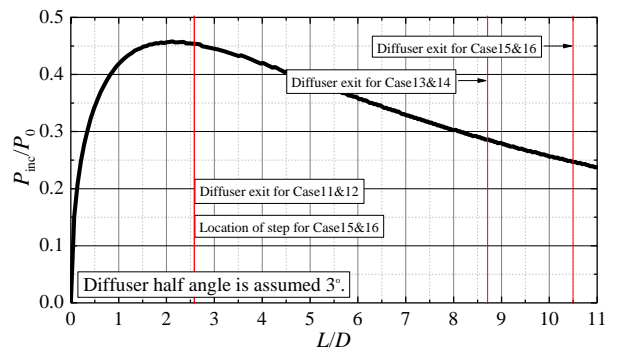


**Figure 8:** Relationship between shock location and amount of pressure recovery.

of pressure recovery becomes the maximum value of  $P_{inc}/P_0 = 0.46$  when the normal shock occurs at  $L/d = 2.1$ . From the viewpoint of the pressure recovery, it is desirable that the amount obtained by the diffuser is large. However, the strong adverse pressure gradient due to the normal shock as shown in **Figure 8** causes flow separation. Since the forward facing step in the diffuser blocks the flow, an pressure increase is expected in vicinity of the step. This means that the forward facing step in the diffuser gives the same recompression as the normal shock with a different mechanism. From the reasons, we infer that the recompression, that is, the pressure gradient around the forward facing step is weaker than the that around the normal shock, and the CBPR increases by the suppressing flow separation.

## 4. Summary

In this study, we conducted experiments to investigate the CBPR (critical back pressure ratio) of CFVNs. In order to improve the CBPR, we focused on the step in the diffuser and verified the its effect. As a result, the following conclusions were obtained.

- The step at the throat and the step at the end of toroid are effective for improving the CBPR at the Reynolds number of about 44000. Conversely, they

do not provide the improvement when the Reynolds number decreases to 11000.

- Since the effect of the step height on the CBPR depends on the Reynolds number, it is difficult to conclude the optimal step height (diameter change ratio before and after step). Therefore, it is extremely important to verify whether the countermeasures are effective even in the low Reynolds numbers.
- A forward facing step (causing decrease of diameter) in the diffuser delivers the desired pressure recovery even in the low Reynolds number. Although the CBPR is 0.46 without the forward facing step, it resulted the CBPR of 0.75 at the Reynolds number of 5000. Therefore, the forward facing step in the diffuser is suggested to be a new countermeasure against the PUP in the low Reynolds number.

#### References

- [1] C. Britton and R. Caron “Unchoking pressure ratio for critical flow venturis” *ASME Fluids Engineering Division Summer Meeting*, 3004, 1997.
- [2] S. Nakao Shinichi and M. Takamoto “Choking phenomena of sonic nozzles at low Reynolds numbers” *Flow measurement and Instrumentation*, 11(4), 285-291, 2000.
- [3] R. Caron, C. Britton and T. Kegel “Investigation into the premature unchoking phenomena of critical flow venturis” *ASME Fluids Engineering Division Summer Meeting*, 11108, 2000.
- [4] R. Caron, C. Britton and T. Kegel “The ongoing investigation into the premature unchoking phenomena of critical flow venturis” *ASME Fluids Engineering Division Summer Meeting*, 18034, 2001.
- [5] M. Carter, B. Sims, C. Britton and R. Mckee “Choking pressure ratio guidelines for small critical flow venturis and the effects of diffuser geometry” *Proceedings of 16th Conference on FLOMEKO*, 2013.
- [6] M. Carter, B. Sims and R. Mckee “Choking pressure ratio guidelines for small critical flow venturis and the effects of diffuser geometry” *Proceedings of 9th Conference on ISFFM*, 2015.
- [7] K. Park, Y. Choi, H. Choi, T. Cha. And B. Yoon “The Evaluation of Critical Pressure Ratio of Sonic Nozzles at Low Reynolds Numbers” *Flow Measurement and Instrumentation*, 12(1), 37–41, 2001.
- [8] H. Asano, S. Nakao and T. Yakuwa “Optimum shape of critical nozzles on low Reynolds number” *Transactions of the Japan Society of Mechanical Engineers Series B*, 77, 1550-1556, 2015.
- [9] International Organization for Standardization “Measurement of Gas Flow by Means of Critical Flow Venturi Nozzles” 2005.
- [10] E. Von Lavante, A. Zachcial, B. Nath and H. Dietrich “Numerical and experimental investigation of unsteady effects in critical venturi nozzles” *Flow measurement and instrumentation*, 11(4), 257-264, 2000.
- [11] E. Von Lavante, A. Zachcial, D. Zeits, B. Nath and H. Dietrich “Effects of Various Geometric Parameters on Flow” *Proceedings of 10th Conference on FLOMEKO*, 2000.
- [12] M. Ishibashi “Discharge coefficient equation for critical-flow toroidal-throat venturi nozzles covering the boundary-layer transition regime” *Flow Measurement and Instrumentation*, 44, 107–121, 2015.
- [13] J. Wright, K. Gillis, A. Johnson and I. Shinder “Back pressure ratio and the transonic resonance mechanism of low unchoking in critical flow venturis” *Proceedings of 17th Conference on FLOMEKO*, 2016.

# Application and Uncertainty Analysis of a New Balance used in Natural Gas Primary Standard up to 60bar

Jia Ren<sup>1,2</sup>, Jiqin Duan<sup>1,2</sup>, Yang Dong<sup>3</sup>

<sup>1,2</sup>Chengdu Verification Branch for Oil & Gas Large Flow rate Measurement station,  
Huayang Town 610213, Chengdu, China

<sup>2</sup>Key Lab for Natural Gas Quality Control and Energy Measurement of PetroChina, Chengdu, China

<sup>3</sup>Shenyang Chuangyuan Measurement Instrument Ltd., Shenyang, China

E-mail : renjia@petrochina.com.cn

## Abstract

A new 3-ton electromagnetic balance system was designed and built up for a high level mass-time primary standard of natural gas up to 60bar in CVB. The system is composed of a 3-ton electromagnetic balance, two tanks with thermal isolation, two platforms, two roller guide rails and two big weights which are used for special test. To achieve a lower uncertainty and the security application in natural gas measurement, several special methods were used in the system. Firstly, the tanks and platforms can be moved together steadily on the roller guide rail to be connected with pipeline system or to be weighted by the balance which also reduces the pipeline length between tanks and pipeline system. Secondly, the substitute weighing method is used for high accurate weighting. Finally, the whole system is located in a thermal isolated room with temperature and humidity controlling. Technical details, performance tests, uncertainty analysis and the future improvement ideas of the balance system are presented in the paper. The uncertainty analysis shows that the mass measurement uncertainty of gas can achieve less than 1.0g and the relative standard uncertainty of natural gas mass measurement can achieve less than 0.02%.

## 1.Introduction

Large tonnage balances are used as the mechanics instruments with high accuracy for weights traceability, mass measurement of gas or liquid as well as torque or tension pressure measurement. Gyroscopes and electromagnetic balances are the most common devices used for mass measurement in mass-time gas facility in the world. Relatively electromagnetic balances are more accurate than gyroscope, so they are popularly used in mass-time natural gas primary facility(see figure 1) over low to medium pressure.

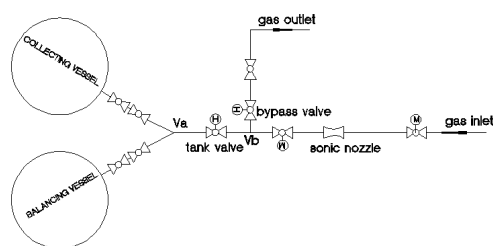


Figure 1: Sketch of the mass-time primary test rig

In 1996, CVB set up a 3-ton balance weighting system and updated the electronic controlling system to improve measurement accuracy in 2003<sup>[1]</sup>. This system was used for mass measurement in a natural gas primary standard facility which was operated under 4bar to 38bar with the maximum flow rate of 2.63kg/s. And the calibration uncertainty of sonic nozzles was 0.22% ( $k=2$ ). The weighting range of this balance was from 10kg to 110kg, the electromagnetic weighting range was from 0g-500g, the sensitive quantity was 1g, the actual scale interval was 0.1g and the repeatability of weighting is about 2g. The structure of this balance was unequal-armed which was efficient to reduce the balance weights on another side. However there were three main disadvantages in this weighting system. Firstly, it was possible that uneven change of the arms occurred because of this special structure. So the measurement accuracy would be affected. Secondly, direct weighting method was used which meant the reference weights were on the opposite side to the gas collecting vessel. Then the measurement accuracy would decline because

of the difference of arm length between two sides caused by the change of temperature and humidity. Thirdly, there were risks of beam shifting which would cause the position change of the coil and magnetic steel even scratching. The reason was that the position of the beaming system was achieved by the groove cutter bearings which were not capable for horizontal position. Then the accuracy of weighting system was declined.

To improve the measurement performance and capability, CVB started to set up a new mass and time primary standard facility for (4-60) bar natural gas with maximum mass flow rate of 5.4kg/s in 2014. So a new 3-ton balance weighting was designed for this standard (see figure 2). The new electromagnetic balance is completely equal-armed. The weighting range is from 4kg to 132.1kg, the electromagnetic weighting range was from 0g-300g, the sensitive quantity was 1g, the actual scale interval was 0.1g and the repeatability of weighting is about 0.5g. Based on this new weighting system, mass measurement uncertainty of the balance achieves less than 1g and the calibration uncertainty of sonic nozzles also improves a lot.



**Figure 2:** Picture of the weighting system

The structure, operation principle, technical details and uncertainty evaluation have been presented in this paper.

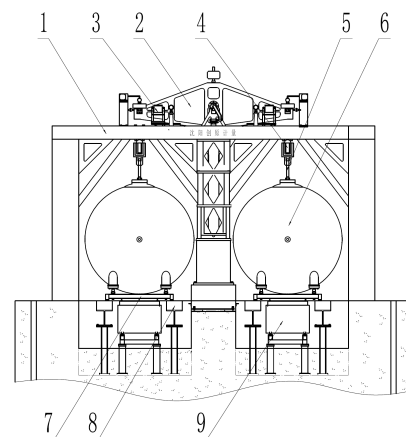
## 2. Structure and the principle

### 2.1 The structure of the new weighting system

For high pressure natural gas mass measurement, the thick-walled collecting vessels with massive weight up to several tons must be used. So the practical gas mass measurement of the balance is relatively limited. This

means a big challenge to achieve high accuracy and lower uncertainty for the heavy-loaded balance which used in natural gas mass measurement.

The new electromagnetic balance is based on the theory of lever equilibrium and electromagnetic force equilibrium (see figure 3). On this way, the mass of the thick-walled collecting vessel can be balanced by the beam system which can bear heavy loads and balance the main weights as well as the imbalance value can be measured accurately by electromagnetic force system.



1-supporting system 2-beam system 3-measuring system  
4-automatic weighting system 5-hanging system 6-weighting tank  
7-movable platform 8-roller rail 9-precision positioning platform

**Figure 3:** diagram of the weighting system

The beam system is equal-armed (see figure 4) and is made of high speed tool steel. The high and low temperature aging and natural aging are applied to eliminate the inner stress and the supporting points of the beam system are quenched to ensure a good toughness as well as high hardness. So the supporting points can be very sharp lines.

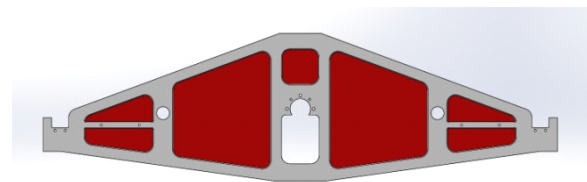


**Figure 4:** Picture of the beam

By optimizing the structure, the deformation of the beam system under heavy loads can be minimized. In addition, the left and right part of the beam would keep in equal when the environmental temperature and humidity change because of the totally symmetrical structure which could avoid the inaccuracy measurement caused by uneven change of two sides.

As shown in figure 5, two equal vessels are located in each side of the balance. One is for gas collection and another is for balance weight. The difference of air buoyancy of two vessels, which cause by the change of environmental temperature and humidity, can be minimized to achieve high accurate mass measurement.

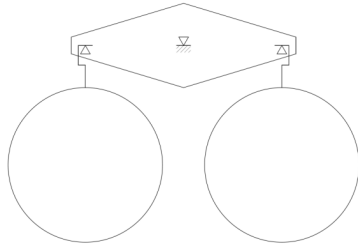


**Figure 4:** Diagram of beam and vessels

## 2.2 The weighting method

According to the state of the art in mass measurement, substitution weighing method is the most accurate one for mass measurement of high pressure natural gas which can minimize the effect of arm difference.<sup>[2]</sup>

Natural gas is a kind of inflammable and explosive greenhouse gas which can't be vented directly to atmosphere, so the weighting method is as following.

Firstly, load all reference weights on two sides of balance while the natural gas has been vented properly. Turn on the balance and get  $I_0$  as the initial measurement result without gas filing. Secondly, fill the collecting vessel with expectant quantity of natural gas and unload the relevant reference weights as  $m_{weights}$  on the same side. Turn on the balance and get  $I_p$  as the final measurement result. Finally, the mass of natural gas  $m_{gas}$  in the vessel can be calculated by equation 1.

$$m_{gas} = m_{weights} - (I_0 - I_p) \quad (1)$$

Figure 6 shows the pneumatic system which loads or unloads reference weights automatically. The system is explosion-proof which achieves the accurate loading of unloading of different weights from 100g to 132.1kg.



**Figure 6:** Picture of automatic loading and unloading system

## 2.3 The moving and positioning of collecting vessel

In general, the installing and uninstalling point between collecting vessel and test pipeline is located outside of the weighting room to avoid the change of environmental temperature and air turbulence in the room. So collecting vessel is movable to minimize the "line-pack" volume between the collecting vessel and under test meter.

Swing of the collecting vessel causes adverse effect for weighting. It would lead to unstable reading and inaccurate measurement because of centrifugal force which causes force difference on each side of supporting point of bearing. So it is critical to minimize the swing while the collecting vessel is hanging on the beam system of balance after gas filling. There are several accurate locating devices to achieve this.

Firstly, there are mechanical positioning between the collecting vessel and the movable platform which loads the vessel and moves together on the roller rail system stably and quickly. Secondly, there are electrical positioning between the movable platform, the roller rail system and the docking system which can guide the vessel to connect with the test pipeline automatically. Thirdly, there is a precision positioning platform combined with the roller guide and located under the balance (see figure 6). When the vessel and movable platform moves underneath the balance where the precision positioning platform also locates, the precision positioning platform raises up the vessel and movable platform together referring to the left part of figure 2, and makes the vessel match with the hanging system properly and stably. Then the precision positioning platform goes down with the movable platform. Then the vessel can be weighted by the balance separately.

Additionally, the docking system is specially designed to be adjusted on 6 different directions (see figure 7) to adapt the deviation caused by installation stress etc. Then the collecting vessel can connect to test pipeline properly for long term.

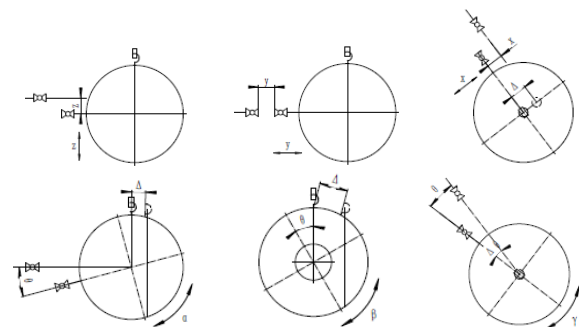


**Figure 7:** Diagram of 6 directions adjusting

## 2.4 The controlling and security system

The weighting system is operated automatically by PLC (see figure 8). So staffs can operate the whole system on the touch panel including moving, docking, hanging and weighting of the vessel before gas filling and after gas filling in the controlling room as well as data acquisition and processing which minimize the manual operation uncertainty.

**Figure 8:** Diagram of weighting controlling principle

The sensors in the security unit are independent from the measurement system. When the mechanical actuators or driving system go wrong and the vessel or platform is not in the correct position, the security system would send alarm signals to PLC and PLC would stop the whole system and remind operators check the specific part of the system.

## 2.5 Temperature and humidity controlling system

It very important to achieve stable temperature and humidity, turbulence free around the balance to minimize the effect of air buoyancy. For the new weighting system, thermal isolation walls, explosion-proof air-conditioning and micro-hole plates are applied to ensure the temperature stability and turbulence free. The test data shows the fluctuation of temperature is less than 0.5°C over two weighting runs.

# 3. Uncertainty evaluation

Uncertainty of gas mass measurement can be written as following equation [3] according to Equation (1).

$$u(m_{gas}) = u^2(m_{weights}) + u^2(I_0) + u^2(I_p) \quad (2)$$

Because  $I_0$  and  $I_p$  is balancing reading before and after gas filling respectively, both of them are related to the

performance of the balance. So  $u(I_0)$  and  $u(I_p)$  are positively strong correlation uncertainty. Then equation (2) can be rewritten as following.

$$u^2(m_{gas}) = 2 \times u^2(m_{balance}) + u^2(F_{buoyancy}) \quad (3)$$

$$u_r(m_{gas}) = \frac{u(m_{gas})}{m_{gas}} \quad (4)$$

Where  $u(m_{balance})$  is the standard uncertainty of mass measurement of balance before gas filling and  $u(F_{buoyancy})$  is the standard uncertainty of air buoyancy effect after gas filling.

The mass measurement range of the balance is from 4kg to 132.1kg. So the uncertainty evaluation of 4kg could be representative for mass measurement uncertainty of the balance system.

### 3.1 $u(m_{balance})$

According to the principle of the balance system,  $u(m_{balance})$  is composed of the uncertainty of reference weights  $u(m_{weights})$  which are class F<sub>1</sub>, measurement repeatability  $u(E_r)$ , resolution of the balance  $u(I)$  and electromagnetic force measurement  $u(EM)$  while all the sensitivity coefficient is 1. So  $u(m_{balance})$  can be calculated according to equation (5).

$$u(m_{balance}) = \sqrt{u(m_{weights}) + u(E_r) + u(I) + u(EM)} \quad (5)$$

#### (1) $u(m_{weights})$

The reference weights for gas measurement are F<sub>1</sub> class weights. Two 2kg reference weights are used for gas weighing, so  $u(m_{weights})$  can be calculated as following [4].

$$u(m_{weights}) = |MPE| / 3 = 30mg \times \sqrt{2} / 3 = 0.006g$$

#### (2) $u(E_r)$

From the test data, the maximum repeatability of the balance is 0.5g. Gas weighing would repeat three times, so  $u(E_r) = 0.5g / \sqrt{3} = 0.288g$ .

#### (3) $u(I)$

The actual scale interval is 0.1g, so  $u(I) = 0.1g / 2 / \sqrt{3} = 0.029g$ .

#### (4) $u(EM)$

The maximum unbalancing reading of electromagnetic force is 100g which traces to another group of F<sub>1</sub> reference weights. So  $u(EM) = 1.6mg / 3 = 0.0005g$ .

### 3.2 $u(F_{buoyancy})$

Of course it is necessary to consider the uncertainty component of air buoyancy effect after gas filling which

would raise the temperature of the gas inside the collecting vessel and lead to change of buoyancy of the collecting vessel and mass measurement. It is a tough job to evaluate this uncertainty accurately because there is no mathematical model to calculate the temperature effect of the collecting while gas filling because the thick wall of 24mm. So it is more practical to get  $u(F_{buoyancy})$  from the test data which means calculate it according to the measurement results for several times.

### 3.3 calculation of $u(m_{gas})$ and $u_r(m_{gas})$

The calculated result of  $u(m_{gas})$  and  $u_r(m_{gas})$  are shown in table 1 referring to equation (2).

Table 1 gas mass measurement uncertainty results of the new balance

name	quantities	Sensitive coefficient	Standard uncertainty component
$u(m_{weights})$	0.06g	1	0.06g
$u(E_r)$	0.288g	1	0.288g
$u(I)$	0.029g	1	0.029g
$u(EM)$	0.005g	1	0.005g
$u(F_{buoyancy})$	0.2g	1	0.2g
$u(m_{gas})$	0.591g		
$u_r(m_{gas})$	0.018%		

## 4. conclusions

The performance of the new weighting system has achieved a high level because of the application of proper structure, substitution weighting method, precision positioning system etc. The mass measurement of natural gas is no more than 0.6g and the relative uncertainty is less than 0.02%. According to uncertainty evaluation, repeatability of balance and air buoyancy effect after gas filling are the main uncertainty components for mass measurement of natural gas after gas filling. So it is efficient to minimize temperature change around the collecting vessel over gas filling procedure. CVB is doing some further research on it.

## References

- [1] Duan Jiqin, Liu Chunyan, et al, "Research of Improving Accuracy of the 3-ton Electric Balance for Gas Flow Measurement", FLOMEKO 2004, Guilin, China.
- [2] Zhang Zeguang, Li Xinwu, "Uncertainty Evaluation of Mass Substitution Weighing Method", Metrology & Measurement Technology, 2004, 24(04): 23-25, 47.

[3] ISO/IEC Guide 98-3:2008, "the Guide to the Expression of Uncertainty in Measurement".

[4] OIML R111:2004, "weights of classes E<sub>1</sub>, E<sub>2</sub>, F<sub>1</sub>, F<sub>2</sub>, M<sub>1</sub>, M<sub>1-2</sub>, ...".

## Flow4Link - The flow in the hand

**D.V. Silva<sup>1</sup>, M. J. Sampaio<sup>2</sup>, C. Milagres<sup>3</sup>, V. Alves<sup>4</sup>, F. Ferreira<sup>5</sup>**

<sup>1</sup>*Duarte Veloso Silva, duarte.silva@adp.pt, Águas do Norte, Barcelos, Portugal*

<sup>2</sup>*Maurício Sampaio, m.sampaio@adp.pt, Águas do Norte, Vila Real, Portugal*

<sup>3</sup>*Carlos Milagres, carlos.milagres@adp.pt, Águas do Norte, Barcelos, Portugal*

<sup>4</sup>*Vítor Ferreira Alves, v.ferreiraalves@adp.pt, Águas do Norte, Vila Real, Portugal*

<sup>5</sup>*Flora Ferreira, fjf@estg.ipp.pt, ESTG – Instituto Politécnico do Porto, Felgueiras, Portugal*

---

### Abstract

Due to greater awareness of the rationalization of water resources, Águas do Norte SA has a need to implement new methodologies to control water losses in order to improve the efficiency of their systems.

The Instrumentation&Automation team has developed some procedures, whose objective is to characterize the performance of the various flow meters, trying to reduce one of the components that define the apparent losses in water balance: measurement errors.

The present study has as scope the development of a work tool able to anticipate problems of measurement and equipment operation, in a park of flowmeters that totals about 950 flowmeters, some with about 20 years old and in different installation conditions than the initials. Safeguarding a minimum measurement chain uncertainties, several methods for information acquisition and identification of the flowmeters operating point and associated error were tested. For the calculation of the water balance, the improvement in the flow measurement will allow to quantify and possibly reduce a part of the apparent losses related to the measurement, which can be done in several ways: by replacing flowmeters with other more appropriate ones (reduction of diameter or measurement technology) or the change in operating way of some infrastructures.

The conclusions reached, highlighting the initial stage of the project, suggest that a part of the existing flow meters operate in operating ranges that are not the most adequate, taking into account the metrological characteristics of the meters, causing reading errors that contribute to the increase of apparent losses.

---

### 1. Introduction

Founded in 1999, the International Water Association (IWA) aims to monitor the phases of the urban water cycle, serving as a link between the various public and private entities operating in the water sector. Several scientific articles and "best practices" orientations for sustainable water management are published by International Water Association (IWA). In 2003, launched the publication of a series of articles on the results of experiments and guidelines aimed at combating the problem of water losses and, above all, reducing future water demand [1].

In 2018, in Águas do Norte SA, the losses reached an aggregate volume of 2,700,000 cubic meters of unbilled water, corresponding to 3.67% of the water value entered into the system.

To achieve these values, Águas do Norte SA has implemented several practices in the field, namely:

- Effective strategies to control and reduce water losses;
- Promotion of improvement of the quality of the cadastre;
- Definition of performance indicators of the supply systems;
- Replacement of sections of pipes with an abnormal history of breaks.

### 2. Definition and Quantification of Water Losses

The IWA, faced with the need to assess the volume of water losses and its components and thus allow an international comparison between the performance of different management entities, has developed a tool that has become the basis of all the analysis that is carried out around this theme - the water balance.

Added to the water balance concept is a set of definitions of the components related to water consumption and losses in the supply systems, which are articulated and outlined in Table 1.

**Table 1: IWA Water Balance Table**

System Input Volume	Authorized Consumption	Billed Authorized Consumption	Billed Metered Consumption	Revenue Water
			Billed Unmetered Consumption	
	Unbilled Authorized Consumption	Unbilled Metered Consumption	Non- Revenue Water	
		Unbilled Unmetered Consumption		
	Water Losses	Apparent Losses		Unauthorized Consumption
		Real Losses		Metering inaccuracies and Data Handling Errors
Leakage on Transmission and/or Distribution Mains				
Leakage and Overflows at Utility's Storage Tanks				
	Leakage on Service Connections up to Point of Customer Metering			

The meaning of each component of the water balance is as follows:

- System input volume - annual volume of water entering the supply system;
- Authorized consumption - annual volume of water measured or not measured but actually consumed by customers, by the supplier or by those who are implicitly or explicitly authorized to consume.
- Water losses - the difference between the volume of water introduced into the system and the authorized consumption, representing the total of actual and apparent losses;
- Unbilled water - is the difference between the volume of water introduced into the system and the authorized consumption that is actually billed.
- Apparent losses - corresponds to illicit consumption, theft or measurement failure.
- Real losses - annual volume that is lost through all types of leaks, ruptures, and extravasation of pipes, reservoirs and branches, up to the point of measurement of the customer.

The work reported here will focus on the component of "Metering inaccuracies and Data Handling Errors" in the water balance, with the attempt to define the error of measurement of a flow meter and, after this, obtaining the expanded error of a FLOMEKO 2019, Lisbon, Portugal

subsystem of water supply and, subsequently, the value of apparent losses.

### 3. Scope and phases of project implementation

Formed in 2017, the Instrumentation & Automation team has been working on the methodologies for the development of a tool, called "Flow4Link", which will allow the operation and maintenance technicians to obtain data on the efficiency of a subsystem of water supply in real time. However, the other aspect of the project is also the creation of functionalities that allow the online and predictive monitoring of the state of the measuring equipment of Águas do Norte SA.

Aims of the Flow4Link project:

- Collection of billing equipment;
- Obtaining the operating point of the flow meter;
- Calculation of global measurement error of a water supply subsystem;
- Instantaneous water balance;
- Operational management, configuration and remote diagnosis of instrumentation equipment;
- Proactive management of flowmeter problems;
- Reduction of costs in the travel of technical staff (municipal counts combined) and maintenance technicians.

To achieve these goals, there were defined the following phases for its implementation:

1. Installation of communications interface between flowmeters and Control Center;
2. Development of functionalities intended for telemetry and water balance, setting the current operating point and estimated error of each flow meter and calculation of the overall error per subsystem;
3. Development of functionalities intended for predictive maintenance and remote diagnostics of a flowmeter;
4. Link to the manufacturer's cloud for equipment park management, spares and documentation.

### 4. Implementation of the method of data communication

In order to obtain data from the meters, a register of the Águas do Norte SA flowmeter park was carried out. Some 950 flowmeters were identified and the ages can reach 20 years of operation.

Analyzing the characteristics of the various existing protocols and the limitations that each had, it was understood that the most comprehensive protocols available in most flowmeters regardless of age would be three:

- HART- Highway Addressable Remote Transducer;
- Profibus DP;
- Modbus RTU;

The more comprehensive and lower cost option fell on the HART protocol, as it would be the most functional and more information to obtain from the flow meter. In addition, it is the universal and widely expanded protocol able to reconcile communication between new and old flowmeters (Figure 1).

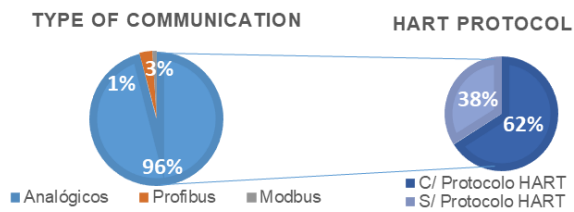


Figure 1: Communications protocols available in Águas do Norte flowmeters

Once the protocol to be used has been defined, several tests were carried out with flowmeters from different manufacturers for a common platform for the management of instrumentation equipment, using communication equipment between flowmeters and the Control Center, according to the Figure 2.

After this first phase, the exact digital data taken from the flowmeter will allow for greater accuracy in the information since this method does not add uncertainty or external disturbances in the transmission/measurement chain.

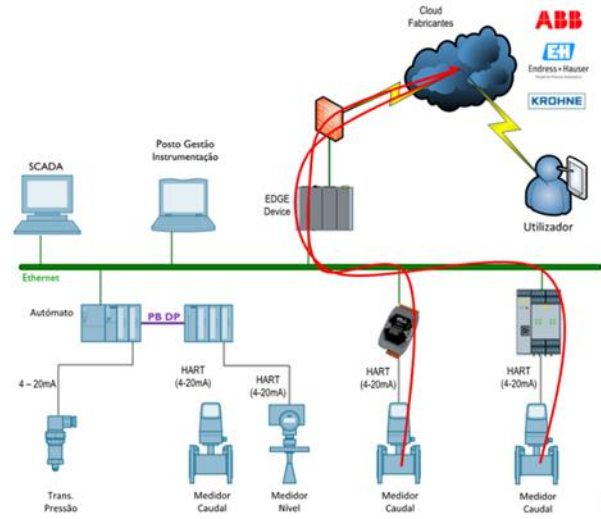


Figure 2: Diagram of data connection between flow and platform meters

To illustrate the advantage of data transmission in digital form, the example of Figure 3 illustrates a meter which is counting water volume and transmitting the information in two ways: electrical to the PLC and by digital communication.

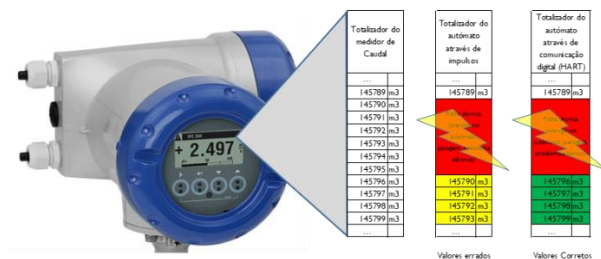


Figure 3: Example of data failure due to power failure

In a hypothetical power failure or failure of some electrical component, in the impulse data transmission chain, there was a failure of counting values in the supervision systems (SCADA). In turn, using a digital communication protocol, the count values will be the same as on the meter display.

This functionality will immediately allow some improvements in the efficiency of operations:

- Decreased travel of technicians to gauge monthly readings;
- Distance billing of a "click";
- Increased customer confidence.

## 5. Development of functionalities intended for telemetry and water balance

Establishing the communication of telemetry data between flowmeters and supervisory software, the

development of equipment productivity and analysis tools began.

### 5.1 Definition of the current operating point and estimated error of each flow meter

Considering as an example a flowmeter from a reservoir, instantaneous flow, and volume data were obtained over a period of 30 days, with minute-to-minute sampling, which resulted in about 43 000 flow measurements for the year in question. With this data, the statistical indicators presented in Table 2 were worked out.

**Table 2: Statistical indicators of flow measurements (about 43000)**

	<b>Cavado.RME_FT001</b>
Minimum flow (m3/h)	0,034
Mean flow (m3/h)	3,352
Maximum flow (m3/h)	28,306
Num. samples	42938
Calculation. Classes	16
Standard deviation (SD)	2,243
Increment	1,767
Mean + 2xSD	7,837
Corrected Average -2xSD	0,034
Mean - 2xDP	-1,134
Mode	0,955
Median	2,879

About the meter concerned, the calibration tests at the manufacturer indicated the deviations presented in Table 3 at the two reference flow points. Although not considered in the statistical treatment.

**Table 3: Deviation values on the calibration test**

Flow (m <sup>3</sup> /h)	Deviation
20,952	-0,09%
4,623	0,14%

Figure 4 shows the histogram of the sampling distribution of flow measurements. Around 80.61% of flow measurements are between 0 and 5 m3/h.

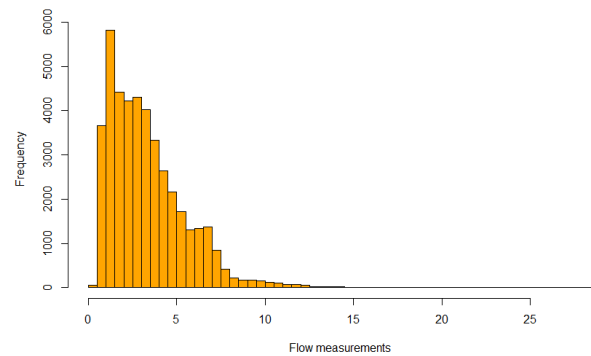


**Figure 4: Histogram of flow measurements**

Considering 20 000 random samples of size 50, by the central limit theorem, we can infer that 95% of sample means will lie within 2.735 m3/h to 3.967 m3/h and that the flow measurement means value converges to 3.352. The histogram of sample means is shown in Figure 5.

$$\mu = 3,352 \text{ m}^3/\text{h} \pm 0,615$$

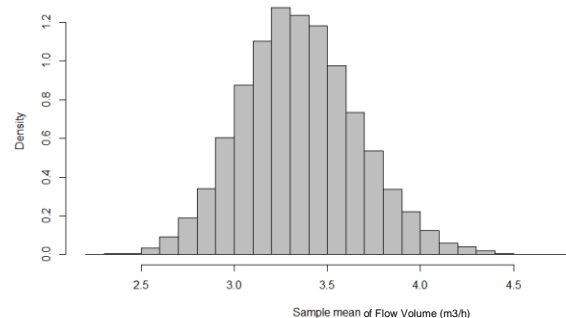


**Figure 5: Histogram of sample means from 20 000 random samples of size 50**

Taking into account the flow values for a given pipe diameter, it is possible to extract the flow velocity:

$$Q = 3600\pi \cdot v \left(\frac{d}{2}\right)^2$$

Where Q: flow (m<sup>3</sup> / h)  
v: flow velocity (m / s)  
d: pipe diameter (mm)

In the practical case, corresponding to a flowmeter of diameter 90mm, used for billing, the values of minimum, average and maximum velocity of the flows observed are shown in Table 4.

**Table 4: Calculated flow speed**

**Flowmeter Nominal Diameter = 90mm**

Minimum Flow Speed (m/s)	0,002
Average Flow Speed (m/s)	0,146
Maximum Flow Speed (m/s)	0,342

For the calculation of the estimated maximum error, for the manufacturer's reference conditions, it is given by the following equation:

$$Er (\%) = \frac{1}{v * 1000} \times 100 + T_{Er}$$

Where Er: Maximum error (%),  
V: flow velocity in (m / s)  
Ter: Transmitter error (%)

One of the components of the error that is fixed is the transmitter, which many manufacturers commercialize with different precision, but in this example was considered of 0.2% taking into account the existing measurement.

In graphical terms, the error equation translates into the curve represented in Figure 6.

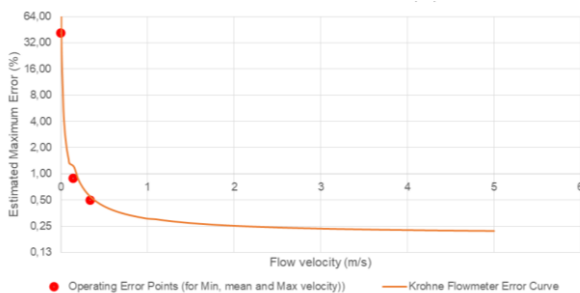


Figure 6: Operating Error Points for the Min, Mean and Max flow velocity

The maximum errors estimated for the above-mentioned flow values are presented in Table 5.

Table 5: Estimated errors for different flow speed

Flowmeter Nominal Diameter = 90mm	
Estimated Maximum Error (%)	±40,862
Estimated Average Error (%)	±0,883
Minimum Estimated Error (%)	±0,492

To calculate the expected maximum error of the flowmeter of this example, a resolution increase of the flow classes was made and the application of a weighted average. In this scenario, the result is:

Estimated maximum operating error (%)	±1,404
---------------------------------------	--------

It is important to state that although the error equations were defined for the manufacturer's reference conditions, other installation criteria were verified, such as upstream and downstream diameters, water conductivity, etc, to ensure minimum interference.

### 5.2 Measures to be implemented in cases of errors above 1%

With the goal of 1% tolerance error in the equipment, some of the measures to be implemented can be:

- Resizing the meter;
- Changing the mode of operation of infrastructure.

For the first case, considering that it is a billing meter, replacing and resizing the new equipment would improve accuracy. For example, for a diameter of 50mm, the estimated error values are given in Table 6.

Table 6: Estimated error for new flowmeter

Flowmeter Nominal Diameter = 50mm	
Estimated Maximum Error (%)	±20,772
Estimated Average Error (%)	±0,411
Minimum Estimated Error (%)	±0,290

In this case, the result for the example in question is about 50% below the previous value:

Estimated maximum operating error (%)	±0,571
---------------------------------------	--------

### 5.3 Calculation of the apparent losses of each subsystem

The second component to be developed in this project is the calculation of the global error resulting from the conjugation of several flow meters, in series or in parallel.

Normally, in the calculation of the water balance, in certain water subsystems, it happens that the sum of the partial volumes of the billing flowmeters does not coincide with the system input values, subtracting the actual losses.

After an analysis of a calibration data set of several flow gauges of the same diameter, it is possible to verify that, for smaller flow velocities, the reading

deviation tends to be positive and greater than in higher velocities, whose error tends to be lower and negative. An example is shown in Figure 7.

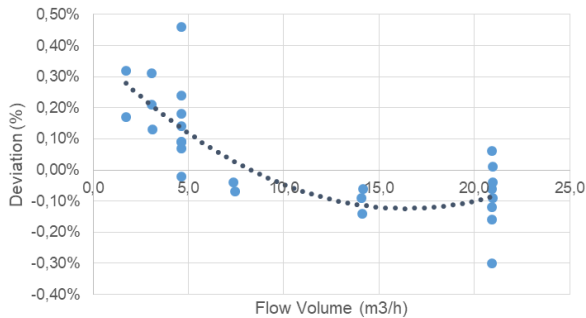


Figure 7: Deviation measurements for flowmeters with DN = 50mm

In this sense, due to the work developed, we can minimize the errors of the meter in lower flow operating regimes, avoiding the exposure to readings with greater measurement error. Considering the S. Jorge subsystem, which has a very extensive pipeline, it has a set of meters (Figure 8).

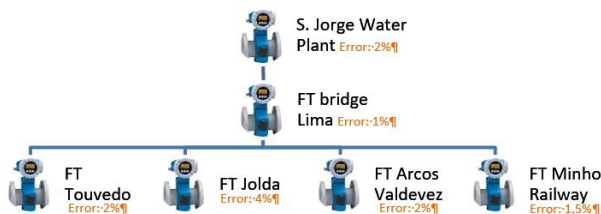


Figure 8: Illustration of a part of the flow measurement of the pipeline of the subsystem of S. Jorge - Minho

The work will go through the individual analysis of the behavior of each flowmeter, so as to ensure that all have an estimated error value less than or equal to 1%.

### 7. Development of functionalities intended for predictive maintenance and remote diagnostics of a flowmeter

Through the HART communication, it is possible to diagnose the state of the equipment and the reading of the variables of the same.

Up to now, functions have been developed to interconnect the PLC with the flowmeters so that the SCADA systems have the same field values and information on the state of the equipment.

In most meters it is possible to remove about 10 measurement variables using open software, like Pactware in Figure 9:

FLOMEKO 2019, Lisbon, Portugal

- Flow Speed
- Volume Flow
- Conductivity
- Coil Temperature
- Counter 1
- Counter 2
- Counter 3
- Counter 4
- Diagnosis Value

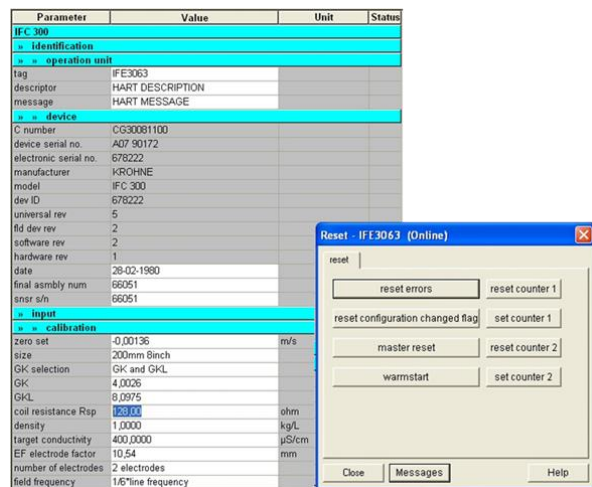


Figure 9: Example of meter configuration performed through HART protocol (Pactware)

### 7. Conclusion

The initial phase of the project has demonstrated practical and valuable results in obtaining data through digital communication, resulting in a very reliable level of data and the reduction of some of the tasks of field teams (e.g. monthly readings). Flowmeter status diagnostics, although using third-party tools, allow us to obtain important information that anticipates some actions on the ground, but to obtain them, manual verification routines are necessary.

The development of the functionalities related to the determination of the operating point of a flow meter allowed to identify some cases of meters that do not operate in the best operating zone and to estimate the average operating error, which in some specific situations results in an abnormal reading error for certain flow ranges. However, the statistical methods that support this component need to be further checked to see which are the most appropriate. Finally, the calculation of the global error of a water supply system has been more complex with the combination of the various uncertainties, lacking other tests to get a mathematical model.

## References

- [1] Farley, Malcolm, and Stuart Trow. *Losses in water distribution networks*. IWA publishing, 2003.
- [2] Pedrosa, António Carvalho; Gama, Sílvia Marques, *Introdução computacional à probabilidade e estatística* (Porto, Porto Editora), 2004.
- [3] Henriques, José Duarte; Palma, João Carlos Pires; Ribeiro, Álvaro Silva; *Medição de caudal em sistemas de abastecimento de água e de saneamento de águas residuais urbanas* (Lisboa, Instituto Regulador de Águas e resíduos / Laboratório Nacional de Engenharia Civil), 2007
- [4] Sardinha, José; Serranito, Francisco; Donnelly, Andrew; Marmelo, Vera; Saraiva, Dias, Pedro; Guimarães, Nuno Ricardo; Morais, Daniel; Rocha, Vitor; *Active Water Loss Control* (Lisboa, EPAL Technical Editions), 2007.

# A New Gravimetric Primary Standard for Natural Gas Flow Measurement at KOGAS

Young-Cheol Ha<sup>1</sup>, Myoung-Seok Kwak<sup>1</sup>, Woong Kang<sup>2</sup>

<sup>1</sup> Korea Gas Corporation (KOGAS), 950 Incheonsinhangdeora-ro, Incheon 21993, South Korea

<sup>2</sup> Korea Research Institute of Standards and Science (KRISS), Daejeon 34113, South Korea

E-mail (corresponding author): [fractals@kogas.or.kr](mailto:fractals@kogas.or.kr)

## Abstract

A new static gravimetric primary standard facility, which was constructed at the Incheon LNG terminal of Korea Gas Corporation (KOGAS) in 2017, is currently operated at pressures up to 5 MPa. Its main tasks include calibrating the secondary flow standard of the KOGAS high-pressure calibration facility (closed-loop type) and establishing the national primary standard for high-pressure natural gas flow measurement. To these aims, 1) the systematic error, which occurred due to an overlap diverter and has not yet been identified, was experimentally estimated for this facility, and 2) an inter-laboratory comparison between KOGAS and Korea Research Institute of Standard and Science (KRISS) was performed using five critical flow Venturi nozzles in 2018. Consequently, the systematic error was estimated to be about 0.06 %, and the degree of equivalence between KOGAS and KRISS was evaluated to be within  $\pm 0.23$ . The paper describes the standard facility and the comparison results.

## 1. Introduction

A new static gravimetric primary standard facility, which was constructed at the Incheon LNG terminal of Korea Gas Corporation (KOGAS) in 2017, is currently operated at pressures up to 5 MPa.

The standard facility is intended to establish the national primary standard for high-pressure (HP) natural gas (NG) flow measurement. One of its main tasks is to calibrate the secondary flow standard (i.e., the critical flow Venturi nozzles (CFVNs)) of the KOGAS HP calibration facility (closed-loop type) [1] and to prove its own accuracy. To achieve this aim, 1) the effects of an overlap diverter, especially for the systematic error, were estimated for this facility, and 2) an inter-laboratory comparison between KOGAS and Korea Research Institute of Standard and Science (KRISS) was performed using five CFVNs in 2018. The comparison was carried out at NG pressures of 1 MPa and 3 MPa (which are among the three calibration pressures of KOGAS's CFVNs), but not at 5 MPa. This is because the maximum pressure of the KRISS primary air-flow standard is 4 MPa, which is only 3 MPa in terms of NG Reynolds number under choked flow conditions. However, as the calibration method and procedure for CFVNs at 1 MPa and 3 MPa are identical to those at 5 MPa, the comparison results at both pressures can cover the measurement results at 5 MPa.

This paper describes the standard facility and the comparison results.

## 2. Description of the standard facility

### 2.1 Design and operation

Figure 1 shows a schematic of KOGAS's static gravimetric flow standard facility and Table 1 provides its specifications. The standard facility consists of a flow supply system, pressure control valves, and a standard system that includes various pressure and temperature sensors, a gas chromatograph, a molar mass meter, a flow diverter (pinion-rack type) with overlapping valves, a collection tank, and a weigh scale.

For generating and stabilizing gas flow from 10 m<sup>3</sup>/h to 170 m<sup>3</sup>/h at pressures up to 5 MPa, the flow supply system has three



HP storage tanks with a total volume of 140 m<sup>3</sup>, two low-pressure (LP) storage tanks with a total volume of 58 m<sup>3</sup>, a set of three pressure control valves that are arranged in parallel, and one measuring section with nominal diameter of DN 100 mm. For the diameter ( $D$ ) of the measuring section, the upstream straight pipe length of the CFVN is more than 30  $D$ . The 10  $D$

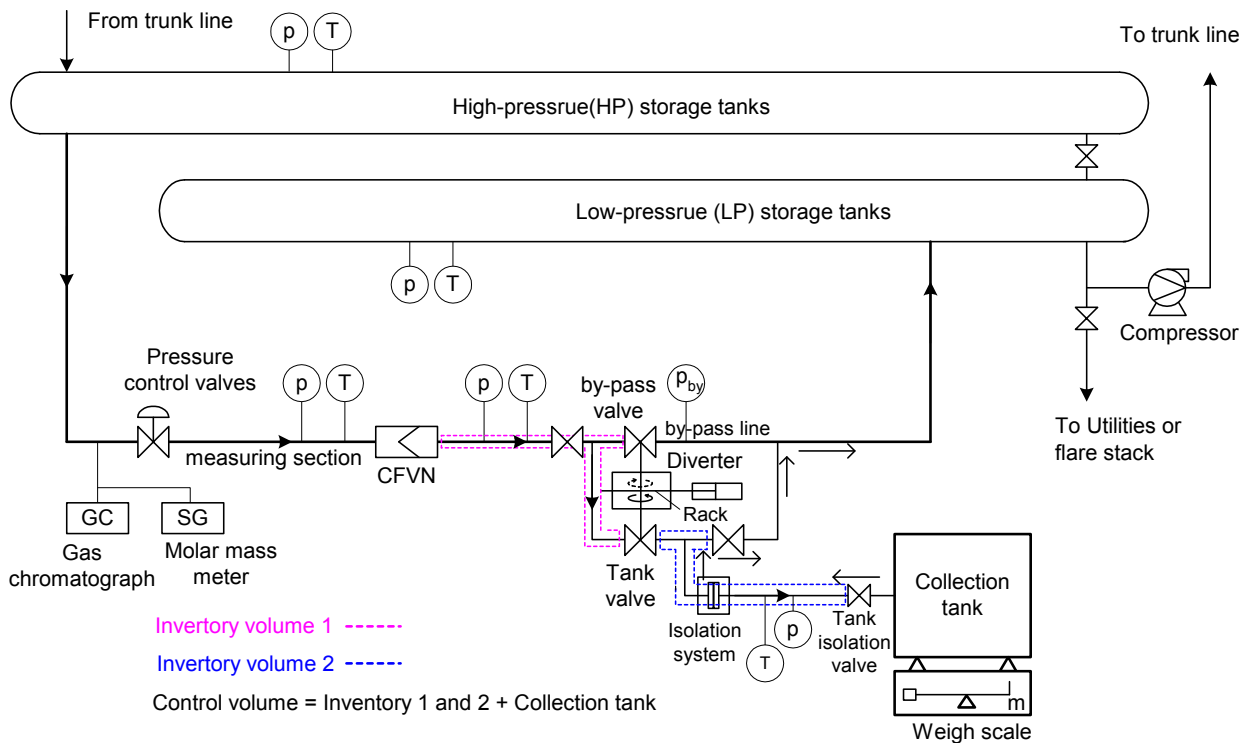


Figure 1: Schematic of the standard facility.

upstream pipe of the CFVN is made of stainless steel, while the inner surface, pressure wall taps and temperature sensor holes were carefully machined according to ISO 9300 [2]. The pressure in the measuring section is adjustable from 0.5 MPa to 5 MPa using the pressure control valves, and the pressure stability is maintained relatively well during a collection time due to the large volume of the HP storage tanks.

The process of making the gravimetric flow measurement entails the following steps:

- 1) Evacuate the gas in the collection tank down to atmospheric pressure.
- 2) Wait for pressure and temperature conditions in the collection tank to stabilize, and then measure the initial mass of gas in the collection tank.

- 3) Connect the collection tank to the piping using the isolation system (see Figure 1).
- 4) Establish a stable flow through the CFVN with flow going through the bypass valve.
- 5) Start the initial diversion for the flow into the collection tank and start the registration of the outputs (i.e., pressure, temperature, gas composition, and molar mass of gas) of the CFVN. At the same time, measure the pressures and temperatures in inventory volume 1 and 2. A collection start time is obtained at an accurately predetermined trigger point (see subsection 2.3) in the diverter-rack travel path because the diverter valves (i.e., bypass and tank valves, see Figure 1) is operated with valve overlap (hereafter ‘overlap diverter’), i.e., one valve begins to open before the other is fully closed.
- 6) Wait for the tank fill to a prescribed upper pressure,

Table 1: Specification of the standard facility.

Figures	Provisions	Parameters
Operation mode	Blow down, fluid flow via HP and LP storage tanks	Three HP storage tanks of a total volume of 140 m <sup>3</sup> ; two LP storage tanks of a total volume of 58 m <sup>3</sup>
Calibration method	Static gravimetric method, i.e. time-mass method	100 kg weigh scale with resolution 2 g; 3.09 m <sup>3</sup> collection tank; counterbalancing the tare weight of the collection tank; flow diverter with its valves overlapping
Medium	Natural gas (regasified LNG)	Concentration of inert gas less than 1 mol %
Flow ranges		10 m <sup>3</sup> /h to 170 m <sup>3</sup> /h
Pressure	0.5 MPa to 5 MPa	At maximum flow
Gas properties	Gas chromatograph, molar mass meter	GERG-2008 equation of state [3-4]
Uncertainty ( $k = 2$ )	0.12 %	Flow ranges from 10 m <sup>3</sup> /h to 170 m <sup>3</sup> /h

and then switch back the diverter and measure the temperatures in inventory volume 1 and 2. Stop the registration of the outputs of the CFVN. Shortly after the tank valve is fully closed, measure the pressure in inventory volume 2; because the tank isolation valve is open at this time, the pressure in inventory 2 is equal to the pressure in the collection tank. The stop time is obtained as described above.

- 7) Close the tank isolation valve and vent the gas from inventory volume 2. Thereafter, isolate the collection tank from the piping using the isolation system. Wait for the scale indication to stabilize, and then measure the final mass of gas in the tank.

## 2.2 Model of measurement

With an overlap flow diverter (see subsection 2.1: step 5), non-negligible lost mass and/or extra mass can occur during the diversions if the diverter operating time is not very short. In the initial diversion in which the bypass line pressure under a high flow rate is higher than the initial collection-tank pressure (atmospheric for this standard system), then when both diverter valves are partially opened, extra flow can enter the control volume from the bypass valve (see Figure 1). In the final diversion in which the final tank pressure is usually much higher than that of the bypass line, extra flow can escape from the control volume. Hence, a mathematical model of the mass flow using this standard system with an overlap diverter can be

proposed as Equation (1). All terms in the first line of Equation (1) represent the general formula for the time-averaged mass flow calculation. The two terms in the second line of Equation (1) arise from the overlap of the diverter valves during the diversions. The first term represents extra inflow occurring during the initial diversion, and the second term, of which the final tank pressure ( $p_{tk,2}$ ) is expressed in the form of the CFVN flow ( $q_{m,cfvn}$ ) multiplied by the collection time ( $t$ ), represents extra outflow occurring during the final diversion. Here, it can be seen that the second term has three distinctive characteristics from the form of its formula: first, the term is almost independent of the collection time and the flow rate through a CFVN; second, the fraction of the term in Equation (1) is almost constant if the final tank pressure-ratio ( $p_{by,2}/p_{tk,2}$ ) is small enough (for instance, not more than 0.3); third, for the previous two reasons, the term does not vanish through the process of determining the optimal trigger point of a diverter. Therefore, the term becomes a nearly constant normalized bias (systematic error) of this standard system.

In order to evaluate the effects from the overlap diverter somewhat quantitatively, especially for the amount of the extra outflow (i.e., bias), a test was performed. In this test, a CFVN (40 m<sup>3</sup>/h) of 7.724 mm in throat diameter was used, and the collection time was fixed at 180 s. The error of the discharge coefficient (marked by

$$\overline{q_{m,cfvn}} = \frac{1}{t} [m + V_{inv 1}(\rho_{inv 2,2} - \rho_{inv 1,1}) + V_{inv 2}(\rho_{inv 2,2} - \rho_{inv 2,1})] + C_{buoy} + \frac{1}{t} C_s p_{by,1} \sqrt{1 - \left(\frac{p_{tk,1}}{p_{by,1}}\right)^2} \Delta t_{div,1} - \frac{1}{t} C_e C q_{m,cfvn} \cdot (t + t_{atm}) \sqrt{1 - \left(\frac{p_{by,2}}{C q_{m,cfvn} \cdot (t + t_{atm})}\right)^2} \Delta t_{div,2} \quad (1)$$

$\overline{q_{m,cfvn}}$	Time-averaged mass flow through a critical flow Venturi nozzle during a collection time
$q_{m,cfvn}$	Instant mass flow through a critical flow Venturi nozzle, $q_{m,cfvn} \cong \overline{q_{m,cfvn}}$
$t$	Collection time
$m$	Mass of gas collected in the collection tank during a collection time
$V_{inv 1}$	Inventory volume 1 (see Figure 1)
$V_{inv 2}$	Inventory volume 2 (see Figure 1)
$\rho_{inv 1}$	Gas density of inventory volume 1
$\rho_{inv 2}$	Gas density of inventory volume 2
$C_{buoy}$	Buoyancy correction
$C$	Pressure coefficient
$C_s, C_e$	Flow coefficients
$p_{by}$	Gas pressure of bypass line
$p_{tk}$	Gas pressure of collection tank, the initial pressure is atmospheric
$t_{atm}$	Time required to raise the pressure of collection tank from vacuum to atmospheric pressure with a flow rate, $q_{m,cfvn}$ ; for this standard, initial pressure of collection tank is atmospheric
$\Delta t_{div}$	Diverter operation time

### Subscripts

1, 2 Numbers 1 and 2 after a comma refer to initial and final values, respectively

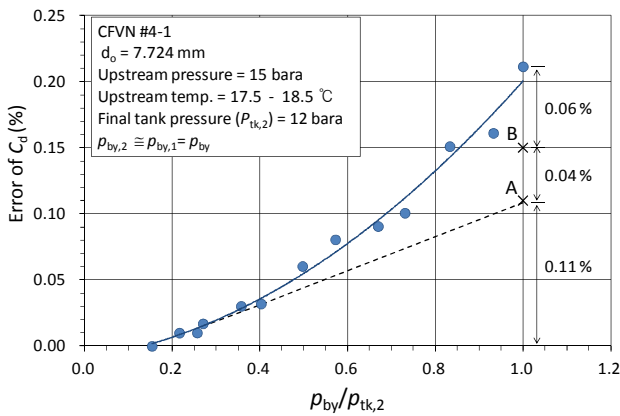


**Figure 2: Effects of the overlap diverter.**

$C_d$  hereafter) for the CFVN was measured by increasing the bypass line pressure (or the LP storage tank pressure) from 0.18 MPa up to the final tank pressure under the initial and final tank pressures fixed at atmospheric pressure and 1.2 MPa, respectively. The final pressures in inventory volume 1 and 2, as in a regular calibration process, took the final tank pressure, which yields the effect of reducing the gas mass escaping from the control volume during the final diversion.

Figure 2 shows the test results, which indicates that, due to the overlap diverter, the error quadratically increases with the increase in pressure ratio ( $p_{by}/p_{tk,2}$ ). However, because the error is a result of a combination of influence quantities (i.e., during the diversions, the extra CVFN-flow captured in the control volume, the extra inflow, and the extra outflow), it is necessary to separate the error in terms of each of the influence quantities. To achieve this goal, a best fitting curve of the error data is first obtained. Then, when the tangent line is drawn at the pressure ratio of 0.25, around which the error contributions of the extra outflow and the captured CFVN-flow are almost the same as those at the reference pressure ratio of 0.15, the error contribution of the extra inflow, 0.11 %, at the pressure ratio of 1.0 is obtained (marked A in Figure 2); the extra inflow term in Equation (1) is almost linear at the pressure ratio above 0.25. Considering that the error contribution of the extra captured-CFVN flow at the pressure ratio of 1.0 is about 0.04 % [5] (marked B in Figure 2), the error contribution of the extra outflow becomes about 0.06 %. Therefore, unlike in this test, in a regular calibration where the final tank pressure-ratio ( $p_{by,2}/p_{tk,2}$ ) is less than 0.3, it can be seen that the error contribution of the extra outflow is almost constant at 0.06 % regardless of the CFVN flow and the collection time. From the view point of the piping structure, it is plausible that the error contributions of the extra inflow and outflow are almost the same under the pressure ratio of 1.0. However, because the final pressures in inventory volume 1 and 2 take the final tank pressure, the error contribution of the

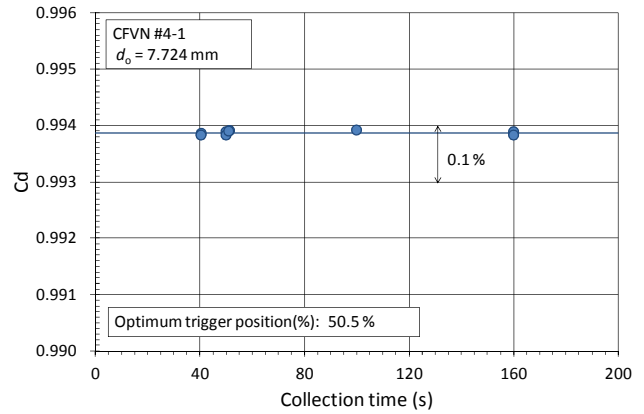


**Figure 3:  $C_d$  values at an optimal trigger point.**

extra outflow becomes less than that of the extra inflow, as explained above. Here, one thing to keep in mind is that if the  $C_d$  is measured from at the pressure ratio of 0.084, meaning that  $p_{by}$  is atmospheric, then the error contribution of the extra inflow will be greater than 0.11 %.

### 2.3 Determination of optimal trigger point and uncertainty

The motion of the diverter (pinion-rack type) is detected with an optical sensor that generates start and stop trigger signals for timer. Because the diverter operation time of this standard system is considerably long (~90 ms), the optical sensor position (hereafter, the 'trigger point') must be accurately determined in order to minimize the timing error of the diverter. For this determination, a reference CFVN (40 m<sup>3</sup>/h) of 7.724 mm in throat diameter is used and the test is carried out at 5 MPa, with the bypass line pressure (or the LP tank pressure) fixed at 0.25 MPa. An optimal trigger point, at which the  $C_d$  has one value regardless of the collection time, is found using the trial and error method, and the

**Table 2: Uncertainty contribution.**

Uncertainty category	Uncertainty ( $k=1$ )	
	Root-sum-squared term	Add term
Weigh scale readout	0.010 %	
Weigh scale calibration	0.008 %	
Timing of diverter - optimal trigger point - overlap diverter	0.007 %	0.015 %
Stability of optical sensor of timer system (background noise effect)	0.014 %	
Gas pressure	0.021 %	
Gas temperature	0.018 %	
Total effects from gas composition	0.013 %	
Critical flow function	0.024 %	
Mass of inventory	0.005 %	
Repeatability	0.010 %	
Gas leakage	0.010 %	
Combined standard uncertainty	0.061 %	
Extended uncertainty ( $k=2$ )	0.12 %	

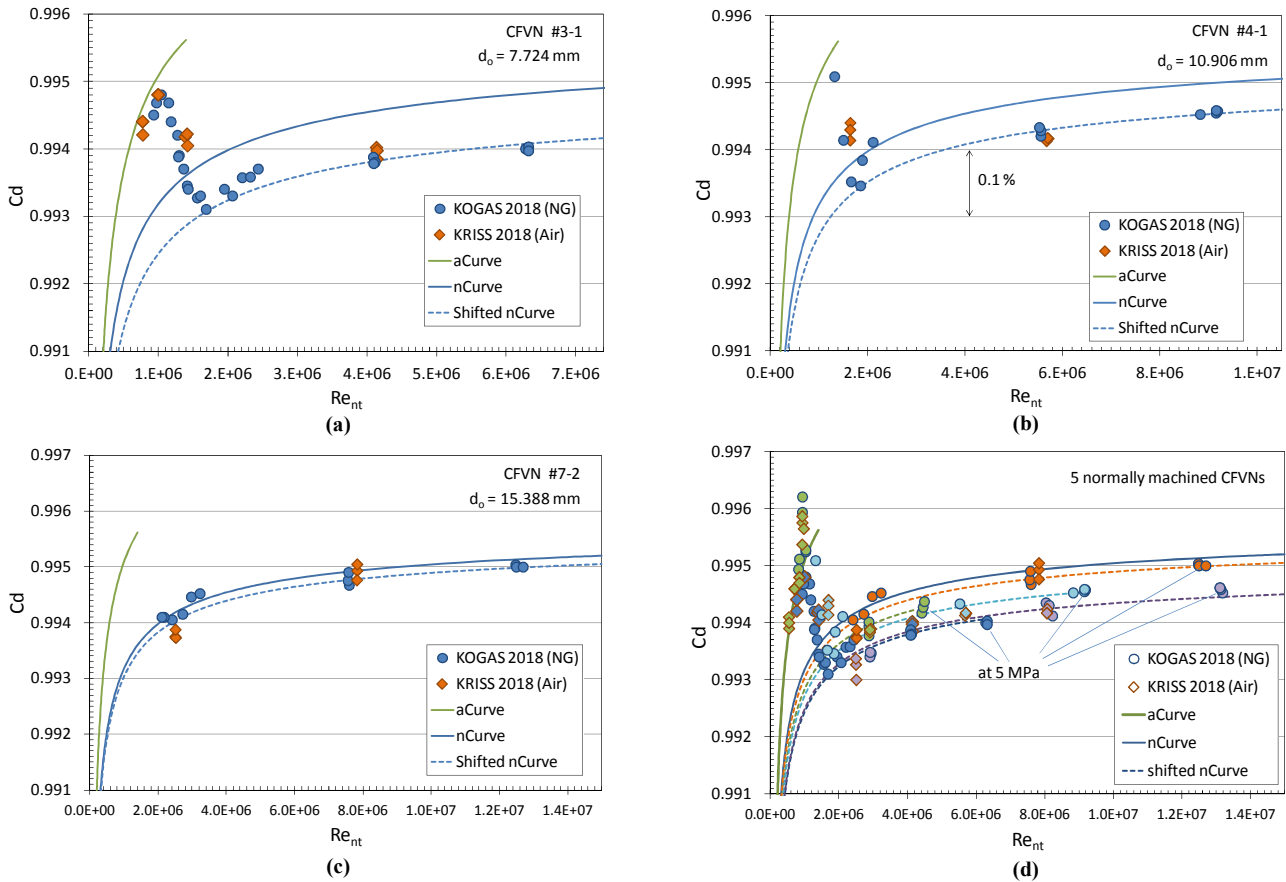


**Figure 4: Inter-laboratory comparison results.**

result is given in Figure 3. The result shows that  $C_d$  values are constant down to 40 s, which is the minimum collection time of the standard system. This implies three things: first, the extra inflow term—that is, the first term in the second line of Equation (1)—is vanished in the process of determining the optimal trigger point; second, the error due to the extra outflow (a bias of this standard system) is not detected in the process; third, for the previous two reasons, a standard system with an overlap diverter also has a converted  $C_d$  value in the process.

When the trigger point is determined to have a constant  $C_d$  value of down to 40 s, the uncertainty contribution of the diverter timing is about 0.014 % ( $k=2$ ). The error of extra outflow, which is a kind of diverter timing error [6], was corrected to only 0.03 %, but the remaining error of 0.03 % was left without correction. This is because, when the flow through a CFVN is much larger than 40 m<sup>3</sup>/h (i.e., the flow used to optimize the trigger point), some error appears due to the extra inflow, and the remaining error serves to offset this error. However, to avoid underestimating the uncertainty of this standard system, the remaining error of 0.03 % was taken as an uncertainty that adds to the combined standard

uncertainty. The uncertainty of this standard system is summarized in Table 2.

### 3. The inter-laboratory comparison result

In 2018, an inter-laboratory comparison between KOGAS and KRISS was carried out using five toroidal-throat CFVNs. The goal of the comparison was to prove the equivalence of the primary flow standards of KOGAS and KRISS using pressurized air (KRISS) and NG (KOGAS) at pressures of 0.9 MPa ( $\approx 1$  MPa) and 3 MPa. The maximum pressure of the KOGAS primary NG-flow standard is 5 MPa, but the upper pressure was limited to 3 MPa because the maximum pressure of the KRISS primary air-flow standard is 4 MPa (which is 3 MPa in terms of NG Reynolds number under choked flow conditions). The number of measurements for each CFVN was limited to three for each pressure, except for the boundary layer transition region (i.e., the flow-transition region in CFVN throat from the laminar to turbulent boundary layer [7]). The reason for this was that, at that time, all CFVNs used as the secondary standard of the KOGAS HP calibration facility had to be calibrated at a pressure of 5 MPa, so it was necessary to minimize the period required for the comparison.

The evaluation of the data utilized the discharge coefficient  $C_d$  of the CFVNs as a function of the Reynolds number and the results are summarized in Figure 4, along with the  $C_d$  values of KOGAS, which were measured at a pressure of 5 MPa. The results show that the  $C_d$  values of KOGAS are 0.04 % to 0.05 % smaller than those of KRISS in the boundary transition region, and 0.02 % to 0.04 % larger in the non-transition region when the measurement point is at an NG pressure of near 1 MPa. When the measurement point is at an NG pressure of 3 MPa, the deviations of the  $C_d$  values between KOGAS and KRISS are within 0.03 % for all five CFVNs. At an NG pressure of 5 MPa, in which there are no  $C_d$  values of KRISS, it can be seen that the  $C_d$  values of KOGAS for each CFVN are located very close to a shifted nCurve (where ‘nCurve’ denotes ISO’s  $C_d$  curve for the normally machined CFVN [2]), passing through the center of the KOGAS  $C_d$ s at 3 MPa of the CFVN. Since the CMCs ( $k=2$ ) of KOGAS and KRISS are 0.12 % ( $U_{CM,C,KOGAS}$ ) and 0.18 % ( $U_{CM,C,KRES}$ ), respectively, the degrees of equivalence ( $E_N$ ) between KOGAS and KRISS at pressures of 1 MPa and 3 MPa using Equation (2) are within  $\pm 0.23$  and  $\pm 0.14$ , respectively.

$$E_{N,KOGAS,KRES} = \frac{C_{d,KOGAS} - C_{d,KRES}}{\sqrt{U_{CM,C,KOGAS}^2 + U_{CM,C,KRES}^2}} \quad (2)$$

#### 4. Conclusion

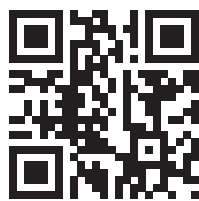
To prove the accuracy of the new static gravimetric primary standard facility at KOGAS, the systematic error, which occurred due to an overlap diverter and has not yet been identified, was estimated for this facility, and an inter-laboratory comparison between KOGAS and KRISS was performed using five CFVNs in 2018. The systematic error due to the overlap diverter of this standard system was estimated to be about 0.06 %. The degrees of equivalence between KOGAS and KRISS at pressures of 1 MPa and 3 MPa were evaluated to be within  $\pm 0.23$  and  $\pm 0.14$ , respectively, which indicates that the measurement deviations between the two laboratories are very small. Although a comparison at a pressure of 5 MPa was not possible, the comparison results at pressures of 1 MPa and 3 MPa can cover the measurement results at 5 MPa because the calibration method and procedure for CFVNs at both pressures are identical to those at 5 MPa.

This primary standard facility is now used to calibrate the secondary standard of the KOGAS HP calibration facility and is expected to become the national standard in the near future for the HP gas flow that KRISS can not cover.

#### References

- [1] Ha, Y. C., Park, K. A., “Design of a large-capacity flow calibration/test facility for natural gas flow-meter,” *Proceedings of the 16<sup>th</sup> Int. Flow Measurement Conference FLOMEKO 2013*, Paris, 2013.
- [2] ISO 9300: *Measurement of gas flow by means of critical flow Venturi nozzles*, 2005.
- [3] Kunz, O., Klimeck, R., Wagner, W., Jaeschke, M., *The GERG-2004: Wide-Range Equation of State for Natural Gases and Other Mixtures*, GERG Technical Monograph 15, GERG, 2007.
- [4] ISO 20765-2: *Natural Gas — Calculation of thermodynamic properties — Part 2: Single-phase properties (Gas, liquid and dense fluid) for extended ranges of application*, 2015.
- [5] Ha, Y. C. et al., *A study on the construction and operation of the KOGAS flow calibration /test facility for natural gas flow-meter*, Project No. RD 2012-0070, Korea Gas Corporation, Korea, 2018.
- [6] Cordova, L., Lederer, T., “A practical method to assess the performance of gravimetric flow test rigs by using the timing error,” *Flow Measurement and Instrumentation*, **44**, pp. 61-70, 2015.
- [7] Ishibashi, M., “Discharge coefficient equation for critical-flow toroidal-throat Venturi nozzles covering the boundary-layer transition regime,” *Flow Measurement and Instrumentation*, **44**, pp. 107-121, 2015.





<http://flomeko2019.inec.pt/>